

Framatome ANP, Inc.

BAW-10164NP-06

BAW-10164NP
Topical Report
Revision 6
January 2006

- RELAP5/MOD2-B&W -

An Advanced Computer Program for
Light Water Reactor LOCA and Non-LOCA
Transient Analysis

Framatome ANP Inc.
P. O. Box 10935
Lynchburg, Virginia 24506

This page is intentionally left blank.

Framatome ANP Inc.
Lynchburg, Virginia

Topical Report BAW-10164NP
Revision 6
January 2006

RELAP5/MOD2-B&W

An Advanced Computer Program for
Light Water Reactor LOCA and Non-LOCA
Transient Analysis

Key Words: RELAP5/MOD2, LOCA, Transient, Water Reactors

Abstract

This document describes the physical solution technique used by the RELAP5/MOD2-B&W computer code. RELAP5/MOD2-B&W is a Framatome ANP Incorporated (previously known as and referred to in the text as Framatome Technologies, Inc, B&W, or B&W Nuclear Technologies) adaption of the Idaho National Engineering Laboratory RELAP5/MOD2. The code developed for best estimate transient simulation of pressurized water reactors has been modified to include models required for licensing analysis of zircaloy or zirconium-based alloy fuel assemblies. Modeling capabilities are simulation of large and small break loss-of-coolant accidents, as well as operational transients such as anticipated transient without SCRAM, loss-of-offsite power, loss of feedwater, and loss of flow. The solution technique contains two energy equations, a two-step numerics option, a gap conductance model, constitutive models, and component and control system models. Control system and secondary system components have been added to permit modeling of plant controls, turbines, condensers, and secondary feedwater conditioning systems. Some discussion of the numerical techniques is presented. Benchmark comparison of code predictions to integral system test results are presented in an appendix.

This page is intentionally left blank.

ACKNOWLEDGMENT

RELAP5/MOD2-B&W is a modified version of the RELAP5/MOD2 advanced system code developed by the Idaho National Engineering Laboratory. A majority of the RELAP5/MOD2-B&W coding and the descriptive text of this document originates from the INEL personnel connected with the RELAP5 project and acknowledgment is given to their efforts.

B&W Nuclear Technologies (BWNT) also acknowledges the contribution of Nuclear Fuel Industries of Japan for the programming and documentation of the B&W modifications developed under a joint program.

The primary contributors at BWNT to this effort are: J. R. Biller, B. M. Dunn, J. A. Klingenfus, M. E. Mays, C. K. Nithianandan, K. C. Shieh, C. A. Schamp, N. H. Shah, W. T. Sneed, C. R. Williamson, and G. J. Wissinger. Their efforts are acknowledged in creating the modifications necessary to produce RELAP5/MOD2-B&W.

This page is intentionally left blank.

Topical Revision Record

Documentation <u>Revision</u>	<u>Description</u>	Program <u>Change?</u>	Program <u>Version</u>
0	Original issue	_____	8.0
1	Typographical corrections Replace CSO correlation with Condie-Bengston IV	yes	10.0
2	SBLOCA modifications Miscellaneous corrections	yes	18.0
3	EM Pin Enhancements Filtered Flows for Hot Channel Heat Transfer Rupture Area Enhancement for Surface Heat Transfer OTSG Improvements and Benchmarks using the Becker CHF, Slug Drag, and Chen Void Ramp	yes	19.0
4	Zirconium-based alloy pin model changes Option for multiple pin channels in a single core fluid channel Void-dependent core cross flow option Zirconium-based alloy rupture temperature	yes	24.0

Topical Revision Record (cont'd)

Document Revision	Description	Program Change	Program Version
5	Added capability of combined RELAP5/BEACH to simulate entire LBLOCA transient, Added distributed rupture model (Not approved.)	yes	25.0
6	Add BHTP EM CHF Option, User-Input BHTP EM CHF Option, and User-Input BWU EM CHF Option Typographical corrections (Change pages from Rev. 5 are not included in Rev. 6)	yes	26.0

TABLE OF CONTENTS

	Page
1. INTRODUCTION	1-1
2. METHOD OF SOLUTION	2.1-1
2.1. Hydrodynamics	2.1-1
2.1.1. Field Equations	2.1-3
2.1.2. State Relationships	2.1-28
2.1.3. Constitutive Models	2.1-41
2.1.4. Special Process Models	2.1-88
2.1.5. Special Component Models	2.1-134
2.2. Heat Structure Models	2.2-1
2.2.1. Heat Conduction Model	2.2-1
2.2.2. Heat Structure Convective Boundary Conditions and Heat Transfer Models.	2.2-17
2.3. Reactor Core	2.3-1
2.3.1. Reactor Kinetics	2.3-1
2.3.2. Core Heat Structure Model	2.3-25
2.3.3. Core Heat Transfer Models	2.3-58.11
2.4. Initial Conditions, Boundary Conditions, and Steady-State Calculations	2.4-1
2.4.1. Initial Conditions	2.4-2
2.4.2. Steady-State Initialization	2.4-3
2.4.3. Boundary Conditions	2.4-21
2.5. Control System	2.5-1
2.5.1. Control Variable Components	2.5-1
2.5.2. Trip System	2.5-13
3. PROGRAMMING METHODS	3.1-1
3.1. Top Level Organization	3.1-1
3.2. Transient and Steady-State Overview	3.2-1
3.3. Solution Accuracy	3.3-1
3.3.1. Time Step Control	3.3-1
3.3.2. Mass/Energy Mitigation	3.3-3
3.3.3. Velocity Flip-Flop	3.3-4

TABLE OF CONTENTS (Cont'd)

	Page
4. REFERENCES	4-1
5. LICENSING DOCUMENTS	5-1
5.1 Responses to Revision 1 Questions: Round 1	5-3
5.2 Responses to Revision 1 Questions: Round 2	5-101
5.3 Revision 1 Safety Evaluation Report (SER)	5-191
5.4 Responses to Revision 2 Questions	5-254
5.5 Responses to Revision 3 Questions	5-268
5.6 Supplemental Information to Revisions 2 and 3	5-300
5.7 Revisions 2 and 3 SER	5-325
5.8 Responses to Revision 4 Questions.	5-403
5.9 Revision 4 SER	5-533
5.10 Pages replaced from Revision 3	5-543
5.11 SER Directed Changes and Typographical Corrections.	5-570

This page is intentionally left blank.

TABLE OF CONTENTS (cont'd)

Appendices

A.	RELAP5/MOD2 Models Not Employed in Evaluations	A-1
B.	List of Symbols	B-1
C.	EM Critical Flow Tables	C-1
D.	Thermodynamic Properties	D-1
E.	RELAP5/MOD2 Internally Stored Material Default Properties	E-1
F.	Heat Transfer Regimes and Correlations Identification	F-1
G.	Benchmarks	G-1
	G.1. LBLOCA Benchmark of Semiscale MOD1 Experiment S-04-6	G-2
	G.2. SBLOCA Benchmark of LOFT Experiment L3-5	G-32
	G.3. Conclusion - Large and Small LOCA Benchmark	G-48
H.	Wilson Drag Model Benchmarks	H-1
I.	BWUMV Critical Heat Flux Correlation	I-1
J.	SBLOCA EM Benchmark	J-1
K.	19-Tube OTSG Benchmarks	K-1
L.	MIST Benchmark	L-1

LIST OF TABLES

Table	Page
2.1.3-1. RELAP5/MOD2 Interfacial Mass Transfer in Bulk Fluid	2.1-76
2.1.4-1. Critical Flow Logic	2.1-111
2.1.5-1. Semiscale Dimensionless Head Ratio Difference Data	2.1-149
2.1.5-2. Head Multiplier and Void Fraction Data	2.1-150
2.3.2-1. Constants Used in Gas Thermal Conductivity Correlation	2.3-31
2.3.2-2. Radial Thermal Strain of Zircaloy for 1073 K < T < 1273 K	2.3-37
2.3.2-3. NUREG-0630 Slow-Ramp Correlations for Burst Strain and Flow Blockage	2.3-42
2.3.2-4. NUREG-0630 Fast-Ramp Correlations for Burst Strain and Flow Blockage	2.3-43
2.3.3-1. English-SI Conversion Factors	2.3-78
C.1. Moody Critical Flow Table	C-3
C.2. Henry Model Critical Flow Tables	C-6
C.3. Homogeneous Equilibrium Model Critical Flow Tables	C-8
C.4. Murdock-Bauman Critical Flow Table for Superheated Vapor	C-13
G.1-1. Sequence of Events During Test S-04-6	G-13
G.1-2. Conditions at Blowdown Initiation	G-13
G.2-1. Initial Conditions for LOFT L3-5	G-39
G.2-2. Sequence of Events for LOFT L3-5	G-40
H.1. FOAM2 Comparison Benchmark Cases	H-5
H.2. ORNL Thermohydraulics Test Facility (THTF) Benchmark Cases	H-6
I.1. Geometry of Westinghouse Bundles 121, 160, and 164	I-9

LIST OF TABLES (Cont'd)

Table	Page
I.2. Local Condition Analysis: Subchannel Parameters	I-10
I.3. Calculated Local Condition Values	I-11
J.1. Major Design Parameters of LSTF and PWR	J-14
J.2. Initial Test Conditions	J-15
J.3. Sequence of Events	J-16
K.1. Model 19-Tube OTSG Conditions for Steady-State Boiling Length Tests	K-8
K.2. Comparison of Predicted and Measured Boiling Lengths for a 19-Tube Model OTSG	K-8
K.3. Initial Conditions for 19-Tube Model OTSG LOFW Test	K-9
L.1. Comparison of MIST Initial Conditions to RELAP5/MOD2-B&W Values	L-13
L.2. Sequence of Events	L-13

LIST OF FIGURES

Figure	Page
2.1.1-1. Relation of Central Angle θ to Void Fraction α_g	2.1-22
2.1.1-2. Difference Equation Nodalization Schematic	2.1-24
2.1.3-1. Sketch of Vertical Flow Regime Map	2.1-42
2.1.3-2. Vertical Flow Regime Map Including the Vertically Stratified Regime	2.1-43
2.1.3-3. Slug-Flow Pattern	2.1-51
2.1.3-3.1 Typical RELAP5 Void Profile: Smoothed and Unsmoothed Curves	2.1-52.4
2.1.3-4. Comparison of Friction Factors for the Colebrook and Improved RELAP5 Friction Factor Models	2.1-73

LIST OF FIGURES (Cont'd)

Figure	Page
2.1.3-5. Two Vertical Vapor/Liquid Volumes	2.1-87
2.1.4-1. Equilibrium Speed of Sound as a Function of Void Fraction and Virtual Mass Coefficient . . .	2.1-95
2.1.4-2. Coefficient of Relative Mach Number for Thermal Equilibrium Flow as a Function of Void Fraction and Virtual Mass Coefficient . . .	2.1-96
2.1.4-3. Subcooled Choking Process	2.1-98
2.1.4-4. Orifice at Abrupt Area Change	2.1-114
2.1.4-5. Schematic Flow of Two-Phase Mixture at Abrupt Area Change	2.1-117
2.1.4-6. Simplified Tee Crossflow	2.1-124
2.1.4-7. Modeling of Crossflows or Leak	2.1-125
2.1.4-8. Leak Flow Modeling	2.1-127
2.1.4-9. One-dimensional Branch	2.1-130
2.1.4-10. Gravity Effects on a Tee	2.1-132
2.1.4-11. Volumes and Junction Configurations Available for CCFL Model	2.1-133.1
2.1.5-1. Typical Separator Volume and Junctions	2.1-135
2.1.5-2. Vapor Outflow Void Donoring	2.1-136
2.1.5-3. Liquid Fallback Void Donoring	2.1-136
2.1.5-4. Typical Pump Characteristic Four- Quadrant Curves	2.1-141
2.1.5-5. Typical Pump Homologous Head Curves	2.1-142
2.1.5-6. Typical Pump Homologous Torque Curves	2.1-143
2.1.5-7. Single-Phase Homologous Head Curves for 1-1/2 Loop MOD1 Semiscale Pumps	2.1-145
2.1.5-8. Fully Degraded Two-Phase Homologous Head Curves for 1-1/2 Loop MOD1 Semiscale Pumps . . .	2.1-146
2.1.5-9. Torque Versus Speed, Type 93A Pump Motor	2.1-152

LIST OF FIGURES (Cont'd)

Figure	Page
2.1.5-10. Schematic of a Typical Relief Valve in the Closed Position	2.1-162
2.1.5-11. Schematic of a Typical Relief Valve in the Partially Open Position	2.1-163
2.1.5-12. Schematic of a Typical Relief Valve in the Fully Open Position	2.1-163
2.1.5-13. Typical Accumulator	2.1-170
2.2.1-1. Mesh Point Layout	2.2-3
2.2.1-2. Typical Mesh Points	2.2-4
2.2.1-3. Boundary Mesh Points	2.2-5
2.2.2-1. Logic Chart for System Wall Heat Transfer Regime Selection	2.2-34
2.3.2-1. Gap Conductance Options	2.3-27.1
2.3.2-2. Fuel Pin Representation	2.3-34
2.3.2-3. Fuel Pin Swell and Rupture Logic and Calculation Diagram	2.3-48
2.3.3-1. Core Model Heat Transfer Selection Logic	
a) Main Driver for EM Heat Transfer	2.3-62
b) Driver Routine for Pre-CHF and CHF Correlations	2.3-63
c) Driver Routine for CHF Correlations	2.3-64
d) Driver Routine for Post-CHF Correlations	2.3-65
3.1-1. RELAP5 Top Level Structure	3.1-1
3.2-1. Transient (Steady-State) Structure	3.2-1
G.1-1. Semiscale MOD1 Test Facility - Cold Leg Break Configuration	G-14
G.1-2. Semiscale MOD1 Rod Locations for Test S-04-6	G-15

LIST OF FIGURES (Cont'd)

Figure	Page
G.1-3. Semiscale MOD1 Test S-04-6; Pressure Near the Vessel Side Break	G-16
G.1-4. Semiscale MOD1 Test S-04-6; Pressure Near the Pump Side Break	G-16
G.1-5. Semiscale MOD1 Test S-04-6; Pressure Near the Intact Loop Pump Exit	G-17
G.1-6. Semiscale MOD1 Test S-04-6; Pressure in the Broken Loop Near the Pump Simulator Inlet . . .	G-17
G.1-7. Semiscale MOD1 Test S-04-6; Pressure in the Lower Plenum	G-18
G.1-8. Semiscale MOD1 Test S-04-6; Pressure in the Upper Plenum	G-18
G.1-9. Semiscale MOD1 Test S-04-6; Pressure Near the Top of the Pressurizer	G-19
G.1-10. Semiscale MOD1 Test S-04-6; Pressure in the Intact Loop Accumulator	G-19
G.1-11. Semiscale MOD1 Test S-04-6; Pressure in the Broken Loop Accumulator	G-20
G.1-12. Semiscale MOD1 Test S-04-6; Mass Flow Rate Near the Vessel Side Break	G-20
G.1-13. Semiscale MOD1 Test S-04-6; Mass Flow Rate Near Pump Side Break (Before ECC Injection Point)	G-21
G.1-14. Semiscale MOD1 Test S-04-6; Mass Flow Rate in the Intact Loop Hot Leg	G-21
G.1-15. Semiscale MOD1 Test S-04-6; Mass Flow Rate Near the Pump Simulator Inlet	G-22
G.1-16. Semiscale MOD1 Test S-04-6; Mass Flow Rate in Intact Loop Cold Leg (Before Accumulator Injection Point)	G-22

LIST OF FIGURES (Cont'd)

Figure	Page
G.1-17. Semiscale MOD1 Test S-04-6; Downcomer Inlet Flow Rate from the Intact Loop	G-23
G.1-18. Semiscale MOD1 Test S-04-6; Mass Flow Rate at the Core Inlet	G-23
G.1-19. Semiscale MOD1 Test S-04-6; Mass Flow Rate from the Intact Loop Accumulator	G-24
G.1-20. Semiscale MOD1 Test S-04-6; Mass Flow Rate from the Broken Loop Accumulator	G-24
G.1-21. Semiscale MOD1 Test S-04-6; Density Near the Vessel Side Break	G-25
G.1-22. Semiscale MOD1 Test S-04-6; Density Near the Pump Side Break (Before the ECC Injection Location)	G-25
G.1-23. Semiscale MOD1 Test S-04-6; Density Near the Core Inlet	G-26
G.1-24. Semiscale MOD1 Test S-04-6; Fluid Temperature Near the Vessel Side Break	G-26
G.1-25. Semiscale MOD1 Test S-04-6; Fluid Temperature Near Pump Side Break (Before ECC Injection Location)	G-27
G.1-26. Semiscale MOD1 Test S-04-6; Fluid Temperature in the Intact Loop Hot Leg	G-27
G.1-27. Semiscale MOD1 Test S-04-6; Fluid Temperature in Intact Loop Cold Leg (Near ECC Injection Point)	G-28
G.1-28. Semiscale MOD1 Test S-04-6; Fluid Temperature Near the Core Inlet	G-28
G.1-29. Semiscale MOD1 Test S-04-6; Fluid Temperature in Upper Plenum	G-29
G.1-30. Semiscale MOD1 Test S-04-6; Average Power Rod Cladding Temperature at Peak Power Location . .	G-29

LIST OF FIGURES (Cont'd)

Figure		Page
G.1-31.	Semiscale MOD1 Test S-04-6; High Power Rod Cladding Temperature Near Peak Power Location	G-30
G.1-32.	RELAP5 Node and Junction Diagram	G-31
G.2-1.	LOFT System Configuration	G-41
G.2-2.	RELAP5 LOFT Nodalization for Test L-3-5	G-42
G.2-3.	RELAP5 Nodalization for LOFT Test L-3-5 Benchmark Analysis	G-43
G.2-4.	LOFT Test L-3-5; Core Pressure	G-44
G.2-5.	LOFT Test L-3-5; Steam Generator Pressure	G-44
G.2-6.	LOFT Test L-3-5; Pressurizer Water Level	G-45
G.2-7.	LOFT Test L-3-5; Pump Velocity	G-45
G.2-8.	LOFT Test L-3-5; Hot Leg Mass Flow Rate	G-46
G.2-9.	LOFT Test L-3-5; HPIS Mass Flow Rate	G-46
G.2-10.	LOFT Test L-3-5; Leak Node Pressure	G-47
G.2-11.	LOFT Test L-3-5; Steam Generator Pressure	G-47
H.1.	RELAP5 Model of Hypothetical Reactor Core	H-7
H.2.	Comparison of RELAP5 and FOAM2 Predictions: 5% Decay Power, 100 Psia	H-8
H.3.	Comparison of RELAP5 and FOAM2 Predictions: 5% Decay Power, 200 Psia	H-8
H.4.	Comparison of RELAP5 and FOAM2 Predictions: 5% Decay Power, 400 Psia	H-9
H.5.	Comparison of RELAP5 and FOAM2 Predictions: 5% Decay Power, 600 Psia	H-9
H.6.	Comparison of RELAP5 and FOAM2 Predictions: 5% Decay Power, 800 Psia	H-10

LIST OF FIGURES (Cont'd)

Figure		Page
H.7.	Comparison of RELAP5 and FOAM2 Predictions: 5% Decay Power, 1200 Psia	H-10
H.8.	Comparison of RELAP5 and FOAM2 Predictions: 2.5% Decay Power, 100 Psia	H-11
H.9.	Comparison of RELAP5 and FOAM2 Predictions: 2.5% Decay Power, 400 Psia	H-11
H.10.	Comparison of RELAP5 and FOAM2 Predictions: 2.5% Decay Power, 800 Psia	H-12
H.11.	Comparison of RELAP5 and FOAM2 Predictions: 2.5% Decay Power, 1200 Psia	H-12
H.12.	Comparison of RELAP5 and FOAM2 Predictions: 1.5% Decay Power, 1200 Psia	H-13
H.13.	Comparison of RELAP5 and FOAM2 Predictions: 1.5% Decay Power, 1600 Psia	H-13
H.14.	THTF in Small Break Test Configuration	H-14
H.15.	RELAP Model of ORNL Thermal-Hydraulic Test Facility (THTF)	H-15
H.16.	Comparison Between RELAP5 Prediction and ORNL Test Data: Experiment 3.09.10i, 0.68 Kw/ft, 650 Psia	H-16
H.17.	Comparison Between RELAP5 Prediction and ORNL Test Data: Experiment 3.09.10j, 0.33 Kw/ft, 610 Psia	H-16
H.18.	Comparison Between RELAP5 Prediction and ORNL Test Data: Experiment 3.09.10k, 0.10 Kw/ft, 580 Psia	H-17
H.19.	Comparison Between RELAP5 Prediction and ORNL Test Data: Experiment 3.09.10l, 0.66 Kw/ft, 1090 Psia	H-17
H.20.	Comparison Between RELAP5 Prediction and ORNL Test Data: Experiment 3.09.10m, 0.31 Kw/ft, 1010 Psia	H-18

LIST OF FIGURES (Cont'd)

Figure	Page
H.21. Comparison Between RELAP5 Prediction and ORNL Test Data: Experiment 3.09.10n, 0.14 Kw/ft, 1030 Psia	H-18
H.22. Comparison Between RELAP5 Prediction and ORNL Test Data: Experiment 3.09.10aa, 0.39 Kw/ft, 590 Psia	H-19
H.23. Comparison Between RELAP5 Prediction and ORNL Test Data: Experiment 3.09.10bb, 0.20 Kw/ft, 560 Psia	H-19
H.24. Comparison Between RELAP5 Prediction and ORNL Test Data: Experiment 3.09.10cc, 0.10 Kw/ft, 520 Psia	H-20
H.25. Comparison Between RELAP5 Prediction and ORNL Test Data: Experiment 3.09.10dd, 0.39 Kw/ft, 1170 Psia	H-20
H.26. Comparison Between RELAP5 Prediction and ORNL Test Data: Experiment 3.09.10ee, 0.19 Kw/ft, 1120 Psia	H-21
H.27. Comparison Between RELAP5 Prediction and ORNL Test Data: Experiment 3.09.10ff, 0.08 Kw/ft, 1090 Psia	H-21
H.28. Comparison Between RELAP5 Prediction and ORNL Test Data: Experiment 3.09.10i, 0.68 Kw/ft, 650 Psia	H-22
H.29. Comparison Between RELAP5 Prediction and ORNL Test Data: Experiment 3.09.10j, 0.33 Kw/ft, 610 Psia	H-22
H.30. Comparison Between RELAP5 Prediction and ORNL Test Data: Experiment 3.09.10k, 0.10 Kw/ft, 580 Psia	H-23
H.31. Comparison Between RELAP5 Prediction and ORNL Test Data: Experiment 3.09.10l, 0.66 Kw/ft, 1090 Psia	H-23

LIST OF FIGURES (Cont'd)

Figure		Page
H.32.	Comparison Between RELAP5 Prediction and ORNL Test Data: Experiment 3.09.10m, 0.31 Kw/ft, 1010 Psia	H-24
H.33.	Comparison Between RELAP5 Prediction and ORNL Test Data: Experiment 3.09.10n, 0.14 Kw/ft, 1030 Psia	H-24
I.1.	Subchannel Model for Westinghouse Test 121 . . .	I-13
I.2.	Subchannel Model for Westinghouse Tests 160 and 164	I-13
I.3.	Frequency Distribution of Mixing Vane CHF Data	I-14
I.4.	Measured-to-Predicted Ratios of BWUMV Data: Quality	I-14
I.5.	Measured-to-Predicted Ratios of BWUMV Data: Pressure	I-15
I.6.	Measured-to-Predicted Ratios of BWUMV Data: Mass Flux	I-15
J.1.	ROSA Large Scale Test Facility Configuration	J-17
J.2.	ROSA Noding Diagram Pressure Vessel	J-18
J.3.	ROSA Noding Diagram for Primary Loops	J-19
J.4.	ROSA SBLOCA EM Noding Diagram for Pressure Vessel	J-20
J.5.	ROSA SBLOCA EM Noding Diagram for Primary Loops	J-21
J.6.	Leak Flow Rate	J-22
J.7.	Primary System Pressure	J-22
J.8.	Core Differential Pressure	J-23
J.9.	Intact Loop Pump Suction Seal Downflow Differential Pressure	J-23

LIST OF FIGURES (Cont'd)

Figure		Page
J.10.	Broken Loop Pump Suction Seal Downflow Differential Pressure	J-24
J.11.	Leak Flow Rate	J-24
J.12.	Primary System Pressure	J-25
J.13.	Pressurizer Level	J-25
J.14.	Intact Loop Steam Generator Pressure	J-26
J.15.	Broken Loop Steam Generator Pressure	J-26
J.16.	Intact Loop Pump Suction Seal Downflow Differential Pressure	J-27
J.17.	Intact Loop Pump Suction Seal Upflow Differential Pressure	J-27
J.18.	Broken Loop Pump Suction Seal Downflow Differential Pressure	J-28
J.19.	Broken Loop Pump Suction Seal Upflow Differential Pressure	J-28
J.20.	Core Differential Pressure	J-29
J.21.	Downcomer Differential Pressure	J-29
J.22.	Intact Loop Steam Generator Inlet Plenum Differential Pressure	J-30
J.23.	Broken Loop Steam Generator Inlet Plenum Differential Pressure	J-30
J.24.	Inlet Loop Steam Generator Tube Upflow Differential Pressure	J-31
J.25.	Broken Loop Steam Generator Tube Upflow Differential Pressure	J-31
J.26.	Upper Plenum Differential Pressure	J-32
J.27.	Inlet Loop Steam Generator Tube Downflow Differential Pressure	J-32

LIST OF FIGURES (Cont'd)

Figure		Page
J.28.	Broken Loop Steam Generator Tube Downflow Differential Pressure	J-33
J.29.	Intact Loop Accumulator Flow Rate	J-33
J.30.	Broken Loop Accumulator Flow Rate	J-34
J.31.	Hot Rod Surface Temperature - Elevation 0.05 Meters	J-34
J.32.	Hot Rod Surface Temperature - Elevation 1.018 Meters	J-35
J.33.	Hot Rod Surface Temperature - Elevation 1.83 Meters	J-35
J.34.	Hot Rod Surface Temperature - Elevation 2.236 Meters	J-36
J.35.	Hot Rod Surface Temperature - Elevation 3.048 Meters	J-36
J.36.	Hot Rod Surface Temperature - Elevation 3.61 Meters	J-37
J.37.	Dimensionless Liquid Velocity at Steam Generator Tube Inlet	J-37
J.38.	Dimensionless Vapor Velocity at Steam Generator Tube Inlet	J-38
J.39.	Wallis Constant at Steam Generator Tube Inlet	J-38
J.40.	Dimensionless Liquid Velocity at Steam Generator Plenum Inlet	J-39
J.41.	Dimensionless Vapor Velocity at Steam Generator Plenum Inlet	J-39
J.42.	Wallis Constant at Steam Generator Plenum Inlet	J-40

LIST OF FIGURES (Cont'd)

Figure		Page
K-1.	Schematic Diagram of the Nuclear Steam Generator Test Facility	K-10
K-2.	19-Tube Once-Through Steam Generator and Downcomer	K-11
K-3.	RELAP5/MOD2-B&W Model of 19-Tube OTSG	K-12
K-4.	Comparison of Measured and Predicted Boiling Lengths in a Model 19-Tube OTSG	K-13
K-5.	Comparison of Measured and Predicted Initial Primary System Fluid Temperatures for 19-Tube OTSG LOFW Test	K-13
K-6.	Comparison of Measured and Predicted Initial Secondary System Fluid Temperatures for 19-Tube OTSG LOFW Test	K-14
K-7.	Comparison of Measured and Predicted Steam Flow During 19-Tube OTSG LOFW Test	K-14
K-8.	Comparison of Measured and Predicted Primary Outlet Temperatures During 19-Tube OTSG LOFW Test	K-15
L-1.	MIST Facility	L-14
L-2.	RELAP5/MOD2-B&W Model of The MIST Facility	L-15
L-3.	Comparison of Predicted and Observed Primary System Pressures for MIST Test 320201	L-16
L-4.	Comparison of Predicted and Observed Secondary System Pressures for MIST Test 320201	L-16
L-5.	Comparison of Predicted and Observed Reactor Vessel Liquid Levels for MIST Test 320201	L-17
L-6.	Comparison of Predicted and Observed SG Secondary Liquid Levels for MIST Test 320201	L-17

This page is intentionally left blank.

1. INTRODUCTION

RELAP5/MOD2 is an advanced system analysis computer code designed to analyze a variety of thermal-hydraulic transients in light water reactor systems. It is the latest of the RELAP series of codes, developed by the Idaho National Engineering Laboratory (INEL) under the NRC Advanced Code Program. RELAP5/MOD2 is advanced over its predecessors by its six-equation, full nonequilibrium two-fluid model for the vapor-liquid flow field and partially implicit numerical integration scheme for more rapid execution. As a system code, it provides simulation capabilities for the reactor primary coolant system, secondary system, feedwater trains, control systems, and core neutronics. Special component models include pumps, valves, heat structures, electric heaters, turbines, separators, and accumulators. Code applications include the full range of safety evaluation transients, loss-of-coolant accidents (LOCAs), and operating events.

RELAP5/MOD2 has been adopted and modified by B&W for licensing and best estimate analyses of PWR transients in both the LOCA and non-LOCA categories. RELAP5/MOD2-B&W retains virtually all of the features of the original RELAP5/MOD2. Certain modifications have been made either to add to the predictive capabilities of the constitutive models or to improve code execution. More significant, however, are the B&W additions to RELAP5/MOD2 of models and features to meet the 10CFR50 Appendix K requirements for ECCS evaluation models. The Appendix K modifications are concentrated in the following areas: (1) critical flow and break discharge, (2) fuel pin heat transfer correlations and switching, and (3) fuel clad swelling and rupture for both zircaloy and zirconium-based alloy cladding types.

This report describes the physical models, formulation, and structure of the B&W version of RELAP5/MOD2 as it will be applied to ECCS and system safety analyses. It has been prepared as a stand-alone document; therefore substantial portions of the text that describe the formulation and numerics have been taken directly from original public domain reports, particularly NUREG/CR-4312¹. Chapter 2 presents the method of solution in a series of subsections, beginning with the basic hydrodynamic solution including the field equations, state equations, and constitutive models in section 2.1. Certain special process models, which require some modification of the basic hydrodynamic approach, and component models are also described. The general solution for heat structures is discussed in section 2.2. Because of the importance of the reactor core and the thermal and hydraulic interaction between the core region and the rest of the system, a separate section is dedicated to core modeling. Contained in section 2.3 are the reactor kinetics solution, the core heat structure model, and the modeling for fuel rod rupture and its consequences. Auxiliary equipment and other boundary conditions are discussed in section 2.4 and reactor control and trip function techniques in section 2.5. Chapter 3 provides an overview of the code structure, numerical solution technique, method and order of advancement, and initialization. Time step limitation and error control are presented in section 3.3.

The INEL versions of RELAP5/MOD2 contain certain solution techniques, correlations, and physical models that have not been selected for use by B&W. These options have been left intact in the coding of the B&W version, but descriptions have not been included in the main body of this report. Appendix A contains a list of those options that remain in the RELAP5/MOD2 programming but are not used by B&W and not submitted for review. A brief description of each along with a reference to an appropriate full discussion is provided in the appendix. Appendix B defines the nomenclature used throughout this report. Appendix G documents

the benchmark calculations performed by BWNT to support the application of RELAP5/MOD2 to safety and ECCS evaluations. Appendix H provides comparisons between Wilson drag benchmarks and the NRC-approved core water level swell code, FOAM2, and between Wilson and ORNL Thermal-Hydraulic Test Facility (THTF) small break LOCA test data. Appendix I provides the derivation of the BWUMV critical heat flux (CHF) correlation. Appendix J presents the small break LOCA evaluation model benchmark. Appendix K presents the once-through steam generator (OTSG) steady-state and loss-of-feedwater with feedwater reactivation benchmarks to validate the OTSG model improvements. Appendix L contains Multi-Loop Integral System Test (MIST) facility benchmarks to demonstrate the integral system performance of RELAP5/MOD2-B&W and further validate the OTSG and drag model improvements.

This page is intentionally left blank.

2. METHOD OF SOLUTION

The general formulation and structure of RELAP5/MOD2 allow the user to define a nodal finite difference model for system transient predictions. Coupling of the major system models (hydrodynamics, heat structures, reactor core, and control system) provides the capability to simulate a range of transients from LBLOCA to operational upsets. In RELAP5/MOD2, the transients are calculated by advancing the one-dimensional differential equations representing a two-fluid, nonhomogeneous, nonequilibrium, two-phase system. Six flow field equations are coupled with the state- and flow regime-dependent constitutive relations in a partially-implicit numerical solution. The control system, heat structures, and reactor core models employ explicitly formulated terms that interface with the solution techniques. Also, special models are included for some system components such as pumps, separators, valves, and accumulators. A description of the formulation and solution method is contained in this section of the report.

2.1. Hydrodynamics

The RELAP5/MOD2-B&W hydrodynamic model is a one-dimensional, transient, two-fluid model for flow of a two-phase steam-water mixture that can contain a noncondensable component in the steam phase and/or a nonvolatile component in the liquid phase. The hydrodynamic model contains several options for invoking simpler hydrodynamic models. These include homogeneous flow, thermal equilibrium, and frictionless flow models, which can be used independently or in combination.

The two-fluid equations of motion that are used as the basis for the RELAP5/MOD2-B&W hydrodynamic model are formulated in terms of area and time average parameters of the flow. Phenomena that depend upon transverse gradients such as friction and heat transfer are formulated in terms of the bulk potentials using empirical transfer coefficient formulations. The system model is solved numerically using a semi-implicit finite difference technique. The user can select an option for solving the system model using a nearly-implicit finite difference technique, which allows violation of the material Courant limit. This option is suitable for steady state calculations and for slowly-varying, quasi-steady transient calculations.

The basic two-fluid differential equations possess complex characteristic roots that give the system a partially elliptic character and thus constitute an ill-posed initial boundary value problem. In RELAP5 the numerical problem is rendered well posed by the introduction of artificial viscosity terms in the difference equation formulation that damp the high frequency spatial components of the solution.

The semi-implicit numerical solution scheme uses a direct sparse matrix solution technique for time step advancement. It is an efficient scheme and results in an overall grind time on the CDC Cyber-176 of approximately 0.0015 seconds. The method has a material Courant time step stability limit. However, this limit is implemented in such a way that single node Courant violations are permitted without adverse stability effects. Thus, single small nodes embedded in a series of larger nodes will not adversely affect the time step and computing cost. The nearly-implicit numerical solution scheme also uses a direct sparse matrix solution technique for time step advancement. This scheme has a grind time that is 25 to 60 percent greater than the semi-implicit scheme but allows violation of the material Courant limit for all nodes.

2.1.1. Field Equations

RELAP5/MOD2-B&W has six dependent variables (seven if a noncondensable component is present), P (pressure), U_g and U_f (gas and fluid internal energies), α_g (void fraction), v_g and v_f (phasic velocities), and X_n (noncondensable mass fraction). The noncondensable quality is defined as the ratio of the noncondensable gas mass to the total gaseous phase mass (i.e., $X_n = M_n / (M_n + M_g)$, where M_n = mass of noncondensable in the gaseous phase and M_g = mass of steam in the gaseous phase). The eight secondary dependent variables used in the equations are phasic densities (ρ_g, ρ_f), vapor generation rate per unit volume (Γ_g), phasic interphase heat transfer rates per unit volume (Q_{ig}, Q_{if}), phasic temperatures (T_g, T_f), and saturation temperature (T^s).

In the following sections, the basic two-fluid differential equations that form the basis for the hydrodynamic model are presented. The discussion is followed by the development of a convenient form of the differential equations used as the basis for the numerical solution scheme. The modifications necessary to model horizontal stratified flow are also discussed. Subsequently, the semi-implicit scheme difference equations, the volume-averaged velocity formulations, and the time advancement scheme are discussed. Finally, the nearly-implicit scheme difference equations are presented.

2.1.1.1. Basic Differential Equations

The differential form of the one-dimensional transient field equations is first presented for a one-component system. The modifications necessary to consider noncondensibles as a component of the gaseous phase and boron as a nonvolatile solute component of the liquid phase are discussed separately.

Vapor/Liquid System

The basic field equations for the two-fluid nonequilibrium model consist of two phasic continuity equations, two phasic momentum equations, and two phasic energy equations. The equations are recorded in differential streamtube form with time and one space dimension as independent variables and in terms of time and volume-average dependent variables.^a The development of such equations for the two-phase process has been recorded in several references^{11,12} and is not repeated here. The equations are cast in the basic form with discussion of those terms that may differ from other developments. Manipulations required to obtain the form of the equations from which the numerical scheme was developed are described in section 2.1.1.2.

The phasic continuity equations are

$$\frac{\partial}{\partial t} (\alpha_g \rho_g) + \frac{1}{A} \frac{\partial}{\partial x} (\alpha_g \rho_g v_g A) = \Gamma_g \quad 2.1.1-1$$

and

$$\frac{\partial}{\partial t} (\alpha_f \rho_f) + \frac{1}{A} \frac{\partial}{\partial x} (\alpha_f \rho_f v_f A) = -\Gamma_g \quad 2.1.1-2$$

Generally, the flow does not include mass sources or sinks and overall continuity consideration yields the requirement that the liquid generation term be the negative of the vapor generation; that is,

$$\Gamma_f = -\Gamma_g \quad 2.1.1-3$$

^aIn all the field equations shown herein, the correlation coefficients are assumed unity so the average of a product of variables is equal to the product of the averaged variables.

The interfacial mass transfer model assumes that total mass transfer consists of mass transfer in the bulk fluid (Γ_{ig}) and mass transfer at the wall (Γ_w); that is,

$$\Gamma_g = \Gamma_{ig} + \Gamma_w \quad 2.1.1-4$$

The phasic conservation of momentum equations are used, and recorded here, in the so-called nonconservative form. For the vapor phase it is

$$\begin{aligned} \alpha_g \rho_g A \frac{\partial v_g}{\partial t} + \frac{1}{2} \alpha_g \rho_g A \frac{\partial v_g^2}{\partial x} = & - \alpha_g A \frac{\partial P}{\partial x} + \alpha_g \rho_g B_x A \\ & - (\alpha_g \rho_g A) F_{WG}(v_g) + \Gamma_g A (v_{gI} - v_g) - (\alpha_g \rho_g A) F_{IG}(v_g - v_f) \\ & - C \alpha_g \alpha_f \rho A \frac{\partial (v_g - v_f)}{\partial t} \end{aligned} \quad 2.1.1-5$$

and for the liquid phase it is,

$$\begin{aligned} \alpha_f \rho_f A \frac{\partial v_f}{\partial t} + \frac{1}{2} \alpha_f \rho_f A \frac{\partial v_f^2}{\partial x} = & - \alpha_f A \frac{\partial P}{\partial x} + \alpha_f \rho_f B_x A \\ & - (\alpha_f \rho_f A) F_{WF}(v_f) - \Gamma_g A (v_{fI} - v_f) - (\alpha_f \rho_f A) F_{IF}(v_f - v_g) \\ & - C \alpha_f \alpha_g \rho A \frac{\partial (v_f - v_g)}{\partial t} \end{aligned} \quad 2.1.1-6$$

The force terms on the right sides of Equations 2.1.1-5 and 2.1.1-6 are, respectively: the pressure gradient, the body force, wall friction, momenta due to interphase mass transfer, interphase frictional drag, and force due to virtual mass. The terms FWG and FWF are part of the wall frictional drag, which is linear in velocity and are products of the friction coefficient, the frictional reference area per unit volume, and the magnitude of the fluid bulk velocity. The interfacial velocity in the

interphase momentum transfer term is the unit momentum with which phase appearance or disappearance occurs. The coefficients FIG and FIF are parts of the interphase frictional drag, which is linear in relative velocity, and are products of the interphase friction coefficients, the frictional reference area per unit volume, and the magnitude of interphase relative velocity.

The coefficient of virtual mass is the same as that used by Anderson¹³ in the RISQUE code, where the value for C depends on the flow regime. A value of $C > 1/2$ has been shown to be appropriate for bubbly or dispersed flows,^{14,15} while $C = 0$ may be appropriate for a separated or stratified flow.

The virtual mass term in Equations 2.1.1-5 and 2.1.1-6 is a simplification of the objective formulation^{16,17} used in RELAP5/MOD1. In particular, the spatial derivative portion of the term is deleted. The reason for this change is that inaccuracies in approximating spatial derivatives for the relatively coarse nodalizations used in system representations can lead to nonphysical characteristics in the numerical solution. The primary effect of the virtual mass terms is on the mixture sound speed, thus, the simplified form is adequate since critical flows are calculated in RELAP5 using an integral model¹⁸ in which the sound speed is based on an objective formulation for the added mass terms.

Conservation of interphase momentum requires that the force terms associated with interphase mass and momentum exchange sum to zero, and is shown as

$$\begin{aligned} \Gamma_g v_{gI} - (\alpha_g \rho_g) FIG(v_g - v_f) - C\alpha_g \alpha_f \rho [\partial(v_f - v_g)/\partial t] \\ + \Gamma_f v_{fI} - (\alpha_f \rho_f) FIF(v_f - v_g) - C\alpha_f \alpha_g \rho [\partial(v_f - v_g)/\partial t] = 0. \end{aligned}$$

2.1.1-7

This particular form for interphase momentum balance results from consideration of the momentum equations in conservative form. The force terms associated with virtual mass acceleration in Equation 2.1.1-7 sum to zero identically as a result of the particular form chosen. In addition, it is usually assumed (although not required by any basic conservation principle) that the interphase momentum transfer due to friction and due to mass transfer independently sum to zero, that is,

$$v_{gI} = v_{fI} = v_I \quad 2.1.1-8$$

and

$$\alpha_g \rho_g F_{IG} = \alpha_f \rho_f F_{IF} = \alpha_g \alpha_f \rho_g \rho_f F_{I}. \quad 2.1.1-9$$

These conditions are sufficient to ensure that Equation 2.1.1-7 is satisfied.

The phasic energy equations are

$$\begin{aligned} \frac{\partial}{\partial t} (\alpha_g \rho_g U_g) + \frac{1}{A} \frac{\partial}{\partial x} (\alpha_g \rho_g U_g v_g A) = -P \frac{\partial \alpha_g}{\partial t} - \frac{P}{A} \frac{\partial}{\partial x} (\alpha_g v_g A) \\ + Q_{wg} + Q_{ig} + \Gamma_{ig} h_g^* + \Gamma_w h_g^s + \text{DISS}_g \end{aligned} \quad 2.1.1-10$$

and

$$\begin{aligned} \frac{\partial}{\partial t} (\alpha_f \rho_f U_f) + \frac{1}{A} \frac{\partial}{\partial x} (\alpha_f \rho_f U_f v_f A) = -P \frac{\partial \alpha_f}{\partial t} - \frac{P}{A} \frac{\partial}{\partial x} (\alpha_f v_f A) \\ + Q_{wf} + Q_{if} - \Gamma_{ig} h_f^* - \Gamma_w h_f^s + \text{DISS}_f. \end{aligned} \quad 2.1.1-11$$

In the phasic energy equations, Q_{wg} and Q_{wf} are the phasic wall heat transfer rates per unit volume. These phasic wall heat transfer rates satisfy the equation

$$Q = Q_{wg} + Q_{wf}, \quad 2.1.1-12$$

where Q is the total wall heat transfer rate to the fluid per unit volume.

The phasic enthalpies (h_g^* , h_f^*) associated with interphase mass transfer in Equations 2.1.1-10 and 2.1.1-11 are defined in such a way that the interface energy jump conditions at the liquid vapor are satisfied. In particular, the h_g^* and vapor interface h_f^s are chosen to be h_g and h_f , respectively for the case of vaporization and h_g and h_f^s , respectively for the case of condensation. The logic for this choice will be further explained in the development of the mass transfer model.

The phasic energy dissipation terms, $DISS_g$ and $DISS_f$, are the sums of wall friction and pump effects. The wall friction dissipations are defined as

$$DISS_g = \alpha_g \rho_g FWF v_g^2 \quad 2.1.1-13$$

and

$$DISS_f = \alpha_f \rho_f FWF v_f^2 \quad 2.1.1-14$$

The phasic energy dissipation terms satisfy the relation

$$\text{DISS} = \text{DISS}_g + \text{DISS}_f, \quad 2.1.1-15$$

where DISS is the energy dissipation. When a pump component is present the associated energy dissipation is also included in the dissipation terms (see section 2.1.5.2).

The vapor generation (or condensation) consists of two parts, that which results from bulk energy exchange (Γ_{ig}) and that due to wall heat transfer effects (Γ_w). Each of the vapor generation (or condensation) processes involves interface heat transfer effects. The interface heat transfer terms appearing in Equations 2.1.1-10 and 2.1.1-11 include heat transfer from the bulk states to the interface due to both interface energy exchange and wall heat transfer effects. The vapor generation (or condensation) rates are established from energy balance considerations at the interface.

The summation of Equations 2.1.1-10 and 2.1.1-11 produces the mixture energy equation, from which it is required that the interface transfer terms vanish, that is,

$$Q_{ig} + Q_{if} + \Gamma_{ig}(h_g^* - h_f^*) + \Gamma_w(h_g^s - h_f^s) = 0 \quad 2.1.1-16$$

The interphase heat transfer terms consist of two parts, that is,

$$Q_{ig} = H_{ig}(T^s - T_g) + Q_{ig}^w \quad 2.1.1-17$$

and

$$Q_{if} = H_{if}(T^s - T_f) + Q_{if}^w \quad 2.1.1-18$$

H_{ig} and H_{if} are the interphase heat transfer coefficients per unit volume and Q_{ig}^W and Q_{if}^W are the wall heat transfer terms. The first term on the right side of Equations 2.1.1-17 and 2.1.1-18 is the thermal energy exchange between the fluid bulk states and the fluid interface, while the second term is that due to wall heat transfer effects and will be defined in terms of the wall vapor generation (or condensation) process.

Although it is not a fundamental requirement, it is assumed that Equation 2.1.1-16 will be satisfied by requiring that the wall heat transfer terms and the bulk exchange terms each sum to zero independently. Thus,

$$H_{ig}(T^S - T_g) + H_{if}(T^S - T_f) + \Gamma_{ig}(h_g^* - h_f^*) = 0 \quad 2.1.1-19$$

and

$$Q_{ig}^W + Q_{if}^W + \Gamma_w(h_g^S - h_f^S) = 0 \quad 2.1.1-20$$

In addition, it is assumed that $Q_{ig}^W = 0$ for boiling processes where $\Gamma_w > 0$. Equation 2.1.1-20 can then be solved for the wall vaporization rate to give

$$\Gamma_w = \frac{-Q_{if}^W}{h_g^S - h_f^S}, \quad \Gamma_w > 0 \quad 2.1.1-21$$

Similarly, it is assumed that $Q_{if}^W = 0$ for condensation processes in which $r_w < 0$. Equation 2.1.1-20 can then be solved for the wall condensation rate to give

$$r_w = \frac{-Q_{ig}^W}{h_g^s - h_f^s}, \quad r_w < 0 \quad . \quad 2.1.1-22$$

The interphase energy transfer terms Q_{ig} and Q_{if} can thus be expressed in a general way as

$$Q_{ig} = H_{ig}(T^s - T_g) - \left(\frac{1-\epsilon}{2}\right) r_w(h_g^s - h_f^s) \quad 2.1.1-23$$

and

$$Q_{if} = H_{if}(T^s - T_f) - \left(\frac{1+\epsilon}{2}\right) r_w(h_g^s - h_f^s), \quad 2.1.1-24$$

where $\epsilon = 1$ for $r_w > 0$ and $\epsilon = -1$ for $r_w < 0$. Finally, Equation 2.1.1-16 can be used to define the interphase vaporization (or condensation) rate

$$r_{ig} = - \frac{Q_{ig} + Q_{if}}{h_g^* - h_f^*} - r_w \frac{(h_g^s - h_f^s)}{h_g^* - h_f^*}, \quad 2.1.1-25$$

which, upon substitution of Equations 2.1.1-23 and 2.1.1-24, becomes

$$r_{ig} = - \frac{H_{ig}(T^s - T_g) + H_{if}(T^s - T_f)}{h_g^* - h_f^*} \quad . \quad 2.1.1-26$$

The phase change process that occurs at the interface is envisioned as a process in which bulk fluid is heated or cooled to the saturation temperature and phase change occurs at the saturation state. The interphase energy exchange process from each phase must be such that at least the sensible energy change to reach the saturation state occurs. Otherwise, it can be shown that the phase change process implies energy transfer from a lower temperature to a higher temperature. Such conditions can be avoided by the proper choice of the variables h_g^* and h_f^* . In particular, it can be shown that they should be

$$h_g^* = \frac{1}{2}[(h_g^s + h_g) + \eta(h_g^s - h_g)] \quad 2.1.1-27$$

and

$$h_f^* = \frac{1}{2}[(h_f^s + h_f) - \eta(h_f^s - h_f)] , \quad 2.1.1-28$$

where

$$\eta = \begin{cases} 1 & \text{for } \Gamma_{ig} \geq 0 \\ -1 & \text{for } \Gamma_{ig} < 0 \end{cases} \quad 2.1.1-29$$

$$2.1.1-30$$

Substituting Equation 2.1.1-26 into Equation 2.1.1-4 gives the final expression for the total interphase mass transfer as

$$\Gamma_g = - \frac{H_{ig}(T^s - T_g) + H_{if}(T^s - T_f)}{h_g^* - h_f^*} + \Gamma_w. \quad 2.1.1-31$$

Noncondensibles in the Gas Phase

The basic, two-phase, single-component model just discussed can be extended to include a noncondensable component in the gas phase. The noncondensable component is assumed to be in mechanical and thermal equilibrium with the vapor phase, so that

$$v_n = v_g \quad 2.1.1-32$$

and

$$T_n = T_g, \quad 2.1.1-33$$

where the subscript, n , is used to designate the noncondensable component.

The general approach for inclusion of the noncondensable component consists of assuming that all properties of the gas phase (subscript g) are mixture properties of the steam/noncondensable mixture. The quality, X , is likewise defined as the mass fraction of the entire gas phase. Thus, the two basic continuity equations (Equations 2.1.1-1 and 2.1.1-2) are unchanged. However, it is necessary to add an additional mass conservation equation for the noncondensable component

$$\frac{\partial}{\partial t}(\alpha_g \rho_g X_n) + \frac{1}{A} \frac{\partial}{\partial x}(\alpha_g \rho_g X_n v_g A) = 0, \quad 2.1.1-34$$

where X_n is the mass fraction of the noncondensable component based on the gaseous phase mass.

The remaining field equations for energy and phasic momentum are unchanged, but the vapor field properties are now evaluated for the steam/noncondensable mixture. The modifications appropriate to the state relationships are described in section 2.1.2.

Boron Concentration in the Liquid Field

An Eulerian boron tracking model is used in RELAP5 which simulates the transport of a dissolved component in the liquid phase. The solution is assumed to be sufficiently dilute that the following assumptions are valid:

1. Liquid properties are not altered by the presence of the solute.
2. Solute is transported only in the liquid phase and at the velocity of the liquid phase.
3. Energy transported by the solute is negligible.
4. Inertia of the solute is negligible.
5. Solute is transported at the velocity of the vapor phase if no liquid is present.

Under these assumptions, only an additional field equation for the conservation of the solute is required. In differential form, the added equation is

$$\frac{\partial \rho_B}{\partial t} + \frac{1}{A} \frac{\partial (C_B \alpha_f \rho_f v_f A)}{\partial x} = 0, \quad 2.1.1-35$$

where the concentration parameter, C_B , is defined as

$$C_B = \frac{\rho_B}{\rho(1 - X)} \quad 2.1.1-36$$

C_B is the concentration of dissolved solid in mass units per mass unit of liquid phase.

2.1.1.2. Numerically Convenient Set of Differential Equations

A more convenient set of differential equations upon which to base the numerical scheme is obtained from the basic density and energy differential equations by expanding the time derivative in each equation using the product rule. When the product rule is used to evaluate the time derivative, we will refer to this form as the expanded form.

A sum density equation is obtained by expanding the time derivative in the phasic density equations, Equations 2.1.1-1 and 2.1.1-2, adding these two new equations, and using the relation

$$\frac{\partial \alpha_f}{\partial t} = - \frac{\partial \alpha_g}{\partial t} \quad 2.1.1-37$$

This gives

$$\alpha_g \frac{\partial \rho_g}{\partial t} + \alpha_f \frac{\partial \rho_f}{\partial t} + (\rho_g - \rho_f) \frac{\partial \alpha_g}{\partial t} + \frac{1}{A} \frac{\partial}{\partial x} (\alpha_g \rho_g v_g A + \alpha_f \rho_f v_f A) = 0 \quad 2.1.1-38$$

A difference density equation is obtained by expanding the time derivative in the phasic density equations, Equations 2.1.1-1 and 2.1.1-2, subtracting these two new equations, again using the relation

$$\frac{\partial \alpha_f}{\partial t} = - \frac{\partial \alpha_g}{\partial t} \quad 2.1.1-39$$

and substituting Equation 2.1.1-31 for Γ_g . This gives

$$\begin{aligned} & \alpha_g \frac{\partial \rho_g}{\partial t} - \alpha_f \frac{\partial \rho_f}{\partial t} + (\rho_g + \rho_f) \frac{\partial \alpha_g}{\partial t} + \frac{1}{A} \frac{\partial}{\partial x} (\alpha_g \rho_g v_g A - \alpha_f \rho_f v_f A) \\ & = - \frac{2[H_{i,g}(T^S - T_g) + H_{i,f}(T^S - T_f)]}{h_g^* - h_f^*} + 2\Gamma_w \end{aligned} \quad 2.1.1-40$$

The time derivative of the noncondensable density equation, Equation 2.1.1-34, is expanded to give

$$\rho_g X_n \frac{\partial \alpha_g}{\partial t} + \alpha_g X_n \frac{\partial \rho_g}{\partial t} + \alpha_g \rho_g \frac{\partial X_n}{\partial t} + \frac{1}{A} \frac{\partial}{\partial x} (\alpha_g \rho_g X_n v_g A) = 0 \quad 2.1.1-41$$

The momentum equations are also rearranged into a sum and difference form. The sum momentum equation is obtained by direct summation of Equations 2.1.1-5 and 2.1.1-6 with the interface conditions (Equations 2.1.1-7, 2.1.1-8, and 2.1.1-9) substituted where appropriate and the cross-sectional area canceled throughout. The resulting sum equation is

$$\begin{aligned} & \alpha_g \rho_g \frac{\partial v_g}{\partial t} + \alpha_f \rho_f \frac{\partial v_f}{\partial t} + \frac{1}{2} \alpha_g \rho_g + \frac{\partial v_g^2}{\partial x} + \frac{1}{2} \alpha_f \rho_f \frac{\partial v_f^2}{\partial x} \\ & = - \frac{\partial P}{\partial x} + \rho B_x - \alpha_g \rho_g v_g^{FWG} - \alpha_f \rho_f v_f^{FWF} - \Gamma_g (v_g - v_f) \end{aligned} \quad 2.1.1-42$$

The difference of the phasic momentum equations is obtained by first dividing the vapor and liquid phasic momentum equations by $\alpha_g \rho_g$ and $\alpha_f \rho_f$, respectively, and subsequently subtracting. Here

again, the interface conditions are used and the common area is divided out. The resulting equation is

$$\begin{aligned} \frac{\partial v_g}{\partial t} - \frac{\partial v_f}{\partial t} + \frac{1}{2} \frac{\partial v_g^2}{\partial x} - \frac{1}{2} \frac{\partial v_f^2}{\partial x} = - \left(\frac{1}{\rho_g} - \frac{1}{\rho_f} \right) \frac{\partial P}{\partial x} \\ - v_g^{FWG} + v_f^{FWF} + \Gamma_g [\rho v_I - (\alpha_f \rho_f v_g + \alpha_g \rho_g v_f)] / \\ (\alpha_g \rho_g \alpha_f \rho_f) - \rho FI (v_g - v_f) - C [\rho^2 / (\rho_g \rho_f)] \\ \cdot \frac{\partial (v_g - v_f)}{\partial t} , \end{aligned} \quad 2.1.1-43$$

where the interfacial velocity, v_I , is defined as

$$v_I = \lambda v_g + (1 - \lambda) v_f . \quad 2.1.1-44$$

This definition for v_I has the property that if $\lambda = 1/2$, the interphase momentum transfer process associated with mass transfer is reversible. This value leads to either an entropy sink or source, depending on the sign of Γ_g . However if λ is chosen to be 0 for positive values of Γ_g and +1 for negative values of Γ_g (that is, a donor formulation), the mass exchange process is always dissipative. The latter model for v_I is the most realistic for the momentum exchange process and is used for the numerical scheme development.

To develop an expanded form of the vapor energy Equation 2.1.1-10 the time derivative of the vapor energy equation, Equation 2.1.1-10, is expanded, the Q_{ig} Equation 2.1.1-23 and the Γ_{ig} Equation 2.1.1-26 are substituted, and the H_{ig} , H_{if} , $\delta \alpha_g / \delta t$,

and convective terms are collected. This gives the desired form for the vapor energy equation

$$\begin{aligned}
 & (\rho_g U_g + P) \frac{\partial \alpha_g}{\partial t} + \alpha_g U_g \frac{\partial \rho_g}{\partial t} + \alpha_g \rho_g \frac{\partial U_g}{\partial t} + \frac{1}{A} \left[\frac{\partial}{\partial x} (\alpha_g \rho_g U_g v_g A) \right. \\
 & \left. + P \frac{\partial}{\partial x} (\alpha_g v_g A) \right] = - \left[\frac{h_f^*}{h_g^* - h_f^*} \right] H_{ig} (T^S - T_g) \\
 & - \left[\frac{h_g^*}{h_g^* - h_f^*} \right] H_{if} (T^S - T_f) + \left[\left(\frac{1+\epsilon}{2} \right) h_g^S \right. \\
 & \left. + \left(\frac{1-\epsilon}{2} \right) h_f^S \right] \Gamma_w + Q_{wg} + DISS_g .
 \end{aligned} \tag{2.1.1-45}$$

To develop an expanded form of the liquid energy Equation 2.1.1-11 the time derivative is expanded, the Q_{if} Equation 2.1.1-24 and the Γ_{ig} Equation 2.1.1-26 are substituted, and

$$\frac{\partial \alpha_f}{\partial t} = - \frac{\partial \alpha_g}{\partial t} \tag{2.1.1-46}$$

is used, then the H_{ig} , H_{if} , $\delta \alpha_g / \delta t$, and convective terms are collected. This gives the desired form for the liquid energy equation

$$\begin{aligned}
 & - (\rho_f U_f + P) \frac{\partial \alpha_g}{\partial t} + \alpha_f U_f \frac{\partial \rho_f}{\partial t} + \alpha_f \rho_f \frac{\partial U_f}{\partial t} \\
 & + \frac{1}{A} \left[\frac{\partial}{\partial x} (\alpha_f \rho_f U_f v_f A) + P \frac{\partial}{\partial x} (\alpha_f v_f A) \right] \\
 & = \left[\frac{h_f^*}{h_g^* - h_f^*} \right] H_{ig} (T^S - T_g) + \left[\frac{h_g^*}{h_g^* - h_f^*} \right] H_{if} (T^S - T_f) \\
 & - \left[\left(\frac{1+\epsilon}{2} \right) h_g^S + \left(\frac{1-\epsilon}{2} \right) h_f^S \right] \Gamma_w + Q_{wf} + DISS_f .
 \end{aligned} \tag{2.1.1-47}$$

The basic density and energy differential equations are used in nonexpanded form in the back substitution part of the numerical scheme. When the product rule is not used to evaluate the time derivative, we will refer to this form as the nonexpanded form.

The vapor, liquid, and noncondensable density equations, Equations 2.1.1-1, 2.1.1-2, and 2.1.1-34, are in nonexpanded form. The Γ_g , from Equation 2.1.1-31, is not substituted into the vapor and liquid density equations (the reason is apparent in the Time Step Solution Scheme, see section 3.1.1.6 of NUREG/CR-4312¹). The vapor energy equation, Equation 2.1.1-10, is altered by substituting Equation 2.1.1-23 for Q_{ig} , substituting Equation 2.1.1-26 for Γ_{ig} and collecting the H_{ig} , H_{if} , and convective terms. This gives

$$\begin{aligned} & \frac{\partial}{\partial t}(\alpha_g \rho_g U_g) + \frac{1}{A} \left[\frac{\partial}{\partial x}(\alpha_g \rho_g U_g v_g A) + P \frac{\partial}{\partial x}(\alpha_g v_g A) \right] \\ & = -P \frac{\partial \alpha_g}{\partial t} - \left[\frac{h_f^*}{h_g^* - h_f^*} \right] H_{ig} (T^S - T_g) - \left[\frac{h_g^*}{h_g^* - h_f^*} \right] H_{if} (T^S - T_f) \\ & + \left[\left(\frac{1+\epsilon}{2} \right) h_g^S + \left(\frac{1-\epsilon}{2} \right) h_f^S \right] \Gamma_w + Q_{wg} + DISS_g . \end{aligned} \quad 2.1.1-48$$

The liquid energy equation, Equation 2.1.1-11, is also altered by substituting Equation 2.1.1-24 for Q_{if} , substituting Equation 2.1.1-26 for Γ_{ig} , using

$$\frac{\partial \alpha_f}{\partial t} = - \frac{\partial \alpha_g}{\partial t} , \quad 2.1.1-49$$

and collecting the H_{ig} , H_{if} , and convective terms. This gives

$$\begin{aligned} & \frac{\partial}{\partial t}(\alpha_f \rho_f U_f) + \frac{1}{A} \left[\frac{\partial}{\partial x}(\alpha_f \rho_f U_f v_f A) + P \frac{\partial}{\partial x}(\alpha_f v_f A) \right] \\ & = P \frac{\partial \alpha_g}{\partial t} + \left[\frac{h_f^*}{h_g^* - h_f^*} \right] H_{ig}(T^S - T_g) + \left[\frac{h_g^*}{h_g^* - h_f^*} \right] H_{if}(T^S - T_f) \\ & - \left[\left(\frac{1+\epsilon}{2} \right) h_g^S + \left(\frac{1-\epsilon}{2} \right) h_f^S \right] \Gamma_w + Q_{wf} + DISS_f . \end{aligned} \quad 2.1.1-50$$

2.1.1.3. Horizontal Stratified Flow

Flow at low velocity in a horizontal passage can be stratified as a result of buoyancy forces caused by density differences between vapor and liquid. When the flow is stratified, the area average pressures are affected by nonuniform transverse distribution of the phases. Appropriate modifications to the basic field equations when stratified flow exists are obtained by considering separate area average pressures for the vapor and liquid phases, and the interfacial pressure between them. Using this model, the pressure gradient force terms of Equations 2.1.1-5 and 2.1.1-6 become

$$- \alpha_g A \left(\frac{\partial P}{\partial x} \right) \rightarrow - \alpha_g A \left(\frac{\partial P_g}{\partial x} \right) + (P_I - P_g) A \left(\frac{\partial \alpha_g}{\partial x} \right) \quad 2.1.1-51$$

and

$$- \alpha_f A \left(\frac{\partial P}{\partial x} \right) \rightarrow - \alpha_f A \left(\frac{\partial P_f}{\partial x} \right) + (P_I - P_f) A \left(\frac{\partial \alpha_f}{\partial x} \right) . \quad 2.1.1-52$$

The area average pressure for the entire cross section of the flow is expressed in terms of the phasic area average pressures by

$$P = \alpha_g P_g + \alpha_f P_f \quad . \quad 2.1.1-53$$

With these definitions, the sum of the phasic momentum equations, written in terms of the cross section average pressure (Equation 2.1.1-42) remains unchanged. However, the difference of the phasic momentum equations (Equation 2.1.1-43), contains on the right side the following additional terms

$$[\rho / (\alpha_g \alpha_f \rho_g \rho_f)] [-\alpha_f \partial (\alpha_g P_g) / \partial x + \alpha_g \partial (\alpha_f P_f) / \partial x + P_I (\partial \alpha_g / \partial x)] \quad . \quad 2.1.1-54$$

The interface and phasic cross-sectional average pressures, P_I , P_g , and P_f , can be found by means of the assumption of a transverse hydrostatic pressure in a round pipe. For a pipe having diameter D , pressures P_I , P_g , and P_f are given by

$$P_g = P_I - \rho_g B_y D [\sin^3 \theta / (3\pi \alpha_g) - \cos \theta / 2] \quad 2.1.1-55$$

and

$$P_f = P_I + \rho_f B_y D [\sin^3 \theta / (3\pi \alpha_f) + \cos \theta / 2] \quad . \quad 2.1.1-56$$

The angle, θ , is defined by the void fraction as illustrated in Figure 2.1.1-1. The algebraic relationship between α_g and θ is

$$\alpha_g \pi = (\theta - \sin \theta \cos \theta) \quad . \quad 2.1.1-57$$

The additional term in the momentum difference equation (Equation 2.1.1-54) can be simplified using Equations 2.1.1-55, 2.1.1-56, and 2.1.1-57 to obtain

$$- [\rho / (\rho_g \rho_f)] (\rho_f - \rho_g) \pi D B_y / (4 \sin \theta) (\partial \alpha_g / \partial x) \quad 2.1.1-58$$

where θ is related to the void fraction using Equation 2.1.1-57.

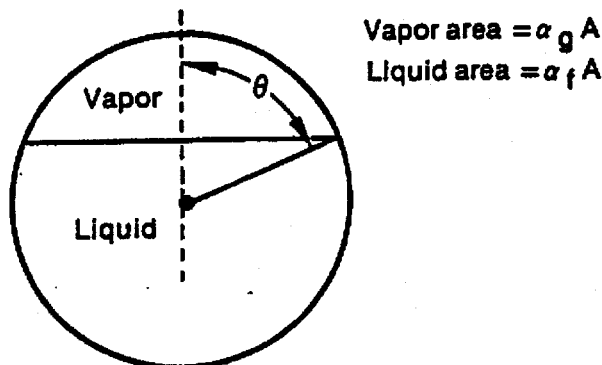


Figure 2.1.1-1. Relation of Central Angle θ to Void Fraction α_g .

The additional force term that arises for a stratified flow geometry in horizontal pipes is added to the basic equation when the flow is established to be stratified from flow regime considerations.

2.1.1.4. Semi-Implicit Scheme Difference Equations

The semi-implicit numerical solution scheme is based on replacing the system of differential equations with a system of finite-difference equations partially implicit in time. The terms evaluated implicitly are identified as the scheme is developed. In all cases, the implicit terms are formulated to be

linear in the dependent variables at new time. This results in a linear time-advancement matrix that is solved by direct inversion using a sparse matrix routine.¹⁹ An additional feature of the scheme is that implicitness is selected such that the field equations can be reduced to a single difference equation per fluid control volume or mesh cell, which is in terms of the hydrodynamic pressure. Thus, only an $N \times N$ system of the difference equations must be solved simultaneously at each time step (N is the total number of control volumes used to simulate the fluid system).

A well-posed numerical problem is obtained by several means. These include the selective implicit evaluation of spatial gradient terms at the new time, donor formulations for the mass and energy flux terms, and use of a donor-like formulation for the momentum flux terms. The term, donor-like, is used because the momentum flux formulation consists of a centered formulation for the spatial velocity gradient plus a numerical viscosity term similar to the form obtained when the momentum flux terms are donored with the conservative form of the momentum equations.

The difference equations are based on the concept of a control volume (or mesh cell) in which mass and energy are conserved by equating accumulation to rate of influx through the cell boundaries. This model results in defining mass and energy volume average properties and requiring knowledge of velocities at the volume boundaries. The velocities at boundaries are most conveniently defined through use of momentum control volumes (cells) centered on the mass and energy cell boundaries. This approach results in a numerical scheme having a staggered spatial mesh. The scalar properties (pressure, energies, and void fraction) of the flow are defined at cell centers, and vector quantities (velocities) are defined on the cell boundaries. The resulting one-dimensional spatial noding is illustrated in Figure

2.1.1-2. The term, cell, means an increment in the spatial variable, x , corresponding to the mass and energy control volume. The difference equations for each cell are obtained by integrating the mass and energy equations (Equations 2.1.1-38, 2.1.1-40, 2.1.1-41, 2.1.1-45, and 2.1.1-47) with respect to the spatial variable, x , from the junction at x_j to x_{j+1} . The momentum equations (Equations 2.1.1-42 and 2.1.1-43) are integrated with respect to the spatial variable from cell center to adjoining cell center (x_K to x_L , Figure 2.1.1-2). The equations are listed for the case of a pipe with no branching.

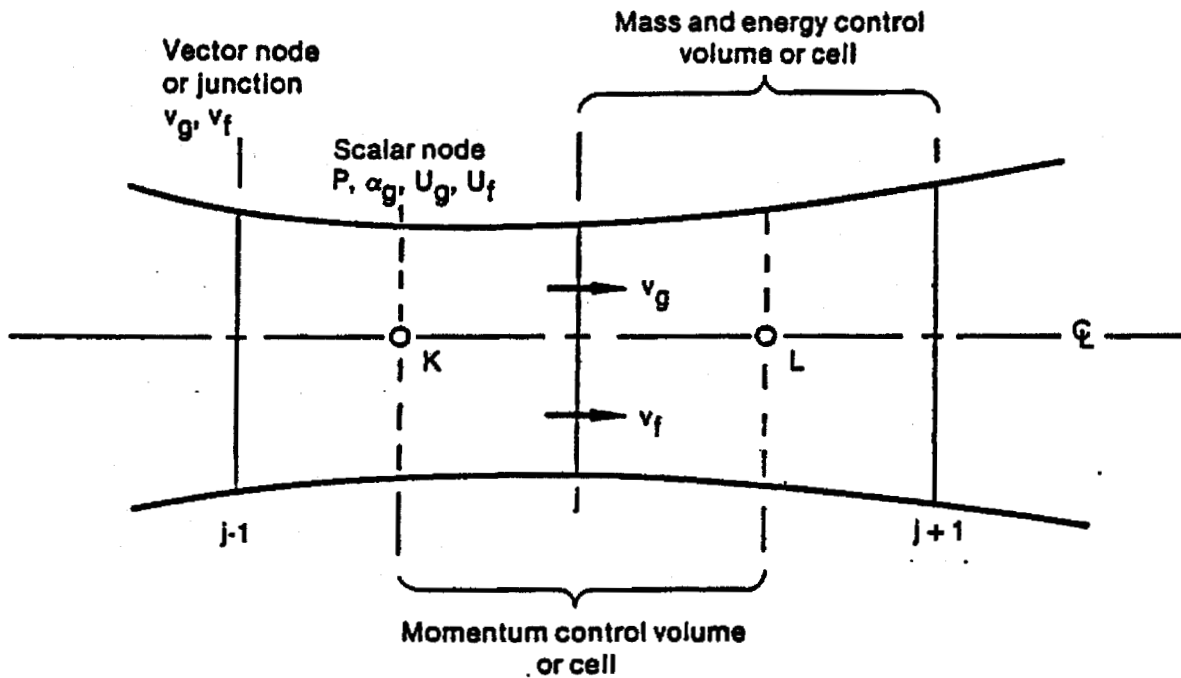


Figure 2.1.1-2. Difference Equation Nodalization Schematic.

When the mass and energy equations (Equations 2.1.1-38, 2.1.1-40, 2.1.1-41, 2.1.1-45, and 2.1.1-47) are integrated with respect to the spatial variable from junction j to $j+1$, differential equations in terms of cell-average properties and cell boundary fluxes are obtained. The development and form of

these finite-difference equations is described in detail in NUREG/CR-4312¹, section 3.1.1.4. The advancement techniques are also given in NUREG/CR-4312, section 3.1.1.6.

2.1.1.5. Volume-Average Velocities

Volume-average velocities are required for the momentum flux calculation, evaluation of the frictional forces and the Courant time step limit. In a simple constant area passage, the arithmetic-average between the inlet and outlet is a satisfactory approximation. However, at branch volumes with multiple inlets and/or outlets, or for volumes with abrupt area change, use of the arithmetic average results in nonphysical behavior.

The RELAP5 volume-average velocity formulas have the form

$$\begin{aligned}
 (v_f)_L^n &= \frac{\left[\sum_j (\alpha_f \rho_f v_f)_j^n A_j \cdot \sum_j A_j \right] \text{ inlets}}{\left[\sum_j (\alpha_f \rho_f)_j^n A_j \cdot A_L \right] \text{ inlets and outlets}} \\
 &+ \frac{\left[\sum_j (\alpha_f \rho_f v_f)_j^n A_j \cdot \sum_j A_j \right] \text{ outlets}}{\left[\sum_j (\alpha_f \rho_f)_j^n A_j \cdot A_L \right] \text{ inlets and outlets}}
 \end{aligned}
 \tag{2.1.1-59}$$

and

$$\begin{aligned}
 (v_g)_L^n &= \frac{\left[\sum_j (\alpha_g \rho_g v_g)_j^n A_j \cdot \sum_j A_j \right] \text{ inlets}}{\left[\sum_j (\alpha_g \rho_g)_j^n A_j \cdot A_L \right] \text{ inlets and outlets}} \\
 &+ \frac{\left[\sum_j (\alpha_g \rho_g v_g)_j^n A_j \cdot \sum_j A_j \right] \text{ outlets}}{\left[\sum_j (\alpha_g \rho_g)_j^n A_j \cdot A_L \right] \text{ inlets and outlets}}
 \end{aligned}
 \tag{2.1.1-60}$$

2.1.1.6. Nearly-Implicit Scheme Difference Equations and Time Advancement

For problems where the flow is expected to change very slowly with time, it is possible to obtain adequate information from an approximate solution based on very large time steps. This would be advantageous if a reliable and efficient means could be found for solving difference equations treating all terms--phase exchanges, pressure propagation, and convection--by implicit differences. Unfortunately, the state-of-the-art is less satisfactory here than in the case of semi-implicit (convection-explicit) schemes. A fully-implicit scheme for the six equation model of a 100 cell problem would require the solution of 600 coupled algebraic equations. If these equations were linearized for a straight pipe, inversion of a block tri-diagonal 600 x 600 matrix with 6 x 6 blocks would be required. This would yield a matrix of bandwidth 23 containing 13,800 nonzero elements, resulting in an extremely costly time advancement scheme.

To reduce the number of calculations required for solving fully implicit difference schemes, fractional step (sometimes called multiple step) methods have been tried. The equations can be split into fractional steps based upon physical phenomena. This is the basic idea in the nearly-implicit scheme. Fractional step methods for two-phase flow problems have been developed in References 24 and 25. These earlier efforts have been used to guide the development of the nearly-implicit scheme. The fractional step method described here differs significantly from prior efforts in the reduced number of steps used to evaluate the momentum equations.

The nearly-implicit scheme consists of a first step that solves all seven conservation equations treating all interphase exchange processes, the pressure propagation process, and the momentum convection process implicitly. These finite difference equations

are exactly the expanded ones solved in the semi-implicit scheme with one major change. The convective terms in the momentum equations are evaluated implicitly (in a linearized form) instead of in an explicit donored fashion as is done in the semi-implicit scheme. Development of this technique is given in NUREG-4312, Reference 1, section 3.1.1.7.

2.1.2. State Relationships

The six equation model with an additional equation for the noncondensable gas component has five independent state variables. The independent variables are chosen to be P , α_g , U_g , U_f , and X_n . All the remaining thermodynamic variables (temperatures, densities, partial pressures, qualities, etc.) are expressed as functions of these five independent properties. In addition to these properties several state derivatives are needed because of the linearization used in the numerical scheme. This section contains three parts. The first discusses the state property derivatives needed in the numerical scheme. The second section develops the appropriate derivative formulas for the single component case and the third section does the same for the two-phase, two-component case.

The values of thermodynamic state variables are stored in tabular form within a controlled environmental library which is attached by the code. The environmental library was received from EG&G with the base RELAP5 code version.

2.1.2.1. State Equations

To expand the time derivatives of the phasic densities in terms of these dependent variables using two-term Taylor series expansions, the following derivatives of the phasic densities are needed:

$$\left(\frac{\partial \rho_g}{\partial P}\right)_{U_g, X_n}, \quad \left(\frac{\partial \rho_g}{\partial U_g}\right)_{P, X_n}, \quad \left(\frac{\partial \rho_g}{\partial X_n}\right)_{P, U_g}, \quad \left(\frac{\partial \rho_f}{\partial P}\right)_{U_f}, \quad \text{and} \quad \left(\frac{\partial \rho_f}{\partial U_f}\right)_P.$$

The interphase mass and heat transfer requires an implicit (linearized) evaluation of the interphase temperature potentials

$T_f - T_I$ and $T_g - T_I$. T_I is the temperature that exists at the phase interface. For a single component mixture,

$$T_I = T^S(P) , \quad 2.1.2-1$$

where the superscript s denotes a saturation value. In the presence of a noncondensable mixed with the steam,

$$T_I = T^S(P_s) , \quad 2.1.2-2$$

where P_s is the partial pressure of the steam in the gaseous phase. The gaseous phase properties for a two-component mixture can be described with three independent properties. In particular, the steam partial pressure, P_s , can be expressed as

$$P_s = P_s(P, X_n, U_g) . \quad 2.1.2-3$$

Substituting Equation 2.1.2-3 into Equation 2.1.2-2 gives the interface temperature, T_I , as the desired function of P , X_n , and U_g .^a The implicit evaluation of the temperature potential in the numerical scheme requires the following derivatives of the phasic and interface temperatures, such as

$$\left(\frac{\partial T_g}{\partial P} \right)_{U_g, X_n} , \quad \left(\frac{\partial T_g}{\partial U_g} \right)_{P, X_n} , \quad \left(\frac{\partial T_g}{\partial X_n} \right)_{P, U_g} ,$$

$$\left(\frac{\partial T_f}{\partial P} \right)_{U_f} , \quad \left(\frac{\partial T_f}{\partial U_f} \right)_P , \quad \left(\frac{\partial T^S}{\partial P} \right)_{U_g, X_n} , \quad \left(\frac{\partial T^S}{\partial U_g} \right)_{P, X_n} , \text{ and } \left(\frac{\partial T^S}{\partial X_n} \right)_{P, U_g} .$$

^a ρ_g and T_g could have initially been written with P_s , X_n , U_f as the independent arguments. Equation 2.1.2-3 would then be used to write ρ_g and T_g with P , X_n , and U_g as the independent variables.

For a single component mixture the X_n derivatives are zero and

$$\left(\frac{\partial T^S}{\partial U_g} \right)_P = 0 ; \quad 2.1.2-4$$

since T^S is only a function of P for this case.

In addition to these derivatives, the basic phasic properties as functions of P , α_g , U_g , U_f , and X_n are needed along with the homogeneous equilibrium sound speed for the critical flow model.

The basic properties are obtained from steam tables that tabulate for each phase the phasic properties and three phasic derivatives: the isobaric thermal expansion coefficient (β), the isothermal compressibility (κ), and the specific heat at constant pressure (C_p).

2.1.2.2. Single Component Two-Phase Mixture

For the purposes of this discussion, a single component two-phase mixture will be referred to as Case 1. Case 1 is straight forward. Liquid properties are obtained from the steam tables given P and U_f . All the desired density and temperature derivatives can then be obtained from κ_f , β_f , and C_{pf} . The desired derivatives are given as

$$\left(\frac{\partial \rho_f}{\partial U_f} \right)_P = - \left(\frac{V_f \beta_f}{C_{pf} - V_f \beta_f P} \right) / V_f^2 , \quad 2.1.2-5$$

$$\left(\frac{\partial T_f}{\partial U_f} \right)_P = \frac{1}{C_{pf} - V_f \beta_f P} , \quad 2.1.2-6$$

$$\left(\frac{\partial \rho_f}{\partial P}\right)_{U_f} = \left[\frac{C_{pf} V_f \kappa_f - T_f (V_f \beta_f)^2}{C_{pf} - V_f \beta_f P} \right] / V_f^2, \text{ and} \quad 2.1.2-7$$

$$\left(\frac{\partial T_f}{\partial P}\right)_{U_f} = - \left[\frac{P V_f \kappa_f - T V_f \beta_f}{C_{pf} - V_f \beta_f P} \right]. \quad 2.1.2-8$$

Parallel formulas hold for the vapor phase with P and U_g as the independent variables.

The only nonstandard feature involved in the evaluation of the formulas in Equation 2.1.2-8 is the calculation of V , T , κ , β , and C_p if the steam is subcooled or the liquid is superheated, that is, metastable states. The extrapolation used for these cases is a constant pressure extrapolation from the saturation state for the temperature and specific volume. Using the first two terms of a Taylor series gives

$$T = T(P) + \frac{1}{C_p(P) - P V(P) \beta(P)} [U - U(P)] \quad 2.1.2-9$$

and

$$V = V(P) + V(P) \beta(P) [T - T(P)] \quad 2.1.2-10$$

In Equations 2.1.2-9 and 2.1.2-10 the argument P indicates a saturation value.

To obtain the β , κ , and C_p corresponding to the extrapolated V and T , the extrapolation formulas are differentiated. Taking the appropriate derivatives of Equations 2.1.2-9 and 2.1.2-10 gives

$$C_p(P, T) \triangleq \left(\frac{\partial h}{\partial T}\right)_P = \left(\frac{\partial U}{\partial T}\right)_P + P \left(\frac{\partial V}{\partial T}\right)_P = C_p(P), \quad 2.1.2-11$$

$$\beta(P, T) \triangleq \frac{1}{V} \left(\frac{\partial V}{\partial T}\right)_P = \frac{V(P) \beta(P)}{V(P, T)}, \text{ and} \quad 2.1.2-12$$

$$\kappa(P, T) \triangleq - \frac{1}{V} \left(\frac{\partial V}{\partial P} \right)_T = \{V(P) + [T - T(P)]V(P)\beta(P)\} \frac{\kappa(P)}{V(P, T)} \\ - [T - T(P)] V(P) \left[\frac{d\beta(P)}{dP} + \beta^2(P) \frac{dT}{dP}(P) \right] / V(P, T).$$

2.1.2-13

Equation 2.1.2-11 shows that a consistently extrapolated C_p is just the saturation value $C_p(P)$. Equation 2.1.2-12 gives the extrapolated β as a function of the saturation properties and the extrapolated V . Equation 2.1.2-13 gives the consistently extrapolated κ as a function of the extrapolated and saturation properties. The extrapolated κ in Equation 2.1.2-13 involves a change of saturation properties along the saturation line. In particular, $\frac{d\beta}{dP}(P)$ involves a second derivative of specific volume. Since no second-order derivatives are available from the steam property tables, this term was approximated for the vapor phase by assuming the fluid behaves as an ideal gas. With this assumption the appropriate formula for the vapor phase κ is

$$\kappa_g(P, T) = \{V_g(P) + [T_g - T(P)] V_g(P)\beta_g(P)\} \kappa_g(P) / V_g(P, T).$$

2.1.2-14

For the liquid phase extrapolation (superheated liquid) only the specific volume correction factor in Equation 2.1.2-13 was retained, that is,

$$\kappa_f(P, T) = \frac{V_f(P)\kappa_f(P)}{V_f(P, T)}.$$

2.1.2-15

The homogeneous equilibrium sound speed is calculated from standard formulas using the saturation κ 's, β 's, and C_p 's. The sound speed formula

$$a^2 = v^2 \left(\frac{dp^s}{dT} \right)^2 \left\{ x \left[\frac{C_{pg}}{T_g} + v_g \frac{dp^s}{dT} \left(\kappa_g \frac{dp^s}{dT} - 2\beta_g \right) \right] + (1-x) \left[\frac{C_{pf}}{T_f} + v_f \frac{dp^s}{dT} \left(\kappa_f \frac{dp^s}{dT} - 2\beta_f \right) \right] \right\} \quad 2.1.2-16$$

is used, where from the Clapeyron equation

$$\frac{dp^s}{dT} = \frac{h_g^s - h_f^s}{T^s (v_g^s - v_f^s)} \quad , \quad 2.1.2-17$$

and X is the steam quality based on the mixture mass.

2.1.2.3. Two Component, Two-Phase Mixture

This case is referred to as Case 2. The liquid phasic properties and derivatives are calculated in exactly the same manner as described in Case 1 (see section 2.1.2.2), assuming the noncondensable component is present only in the gaseous phase.

The properties for the gaseous phase are calculated assuming a Gibbs-Dalton mixture of steam and an ideal noncondensable gas. A Gibbs-Dalton mixture is based upon the following assumptions:

$$1. \quad P = P_n + P_s \quad , \quad 2.1.2-18$$

$$2. \quad U_g = X_n U_n + (1 - X_n) U_s \quad , \quad \text{and} \quad 2.1.2-19$$

$$3. \quad X_n V_n = (1 - X_n) V_s = V_g, \quad 2.1.2-20$$

where P_s and P_n are the partial pressures of the steam and noncondensable components, respectively. The internal energies U_s , U_n , and the specific volumes V_s , V_n are evaluated at the gas temperature and the respective partial pressures. The vapor properties are obtained from the steam tables and the noncondensable state equations are^a

$$P_n V_n = R_n T_g \quad \text{and} \quad 2.1.2-21$$

$$U_n = \begin{cases} C_o T_g + U_o & T_g < T_o \\ C_o T_g + \frac{1}{2} D_o (T_g - T_o)^2 + U_o & T_g \geq T_o \end{cases} \quad 2.1.2-22$$

Given P , U_g , and X_n , Equations 2.1.2-18 through 2.1.2-20 are solved implicitly to find the state of the gaseous phase. If Equation 2.1.2-18 is used to eliminate P_n and Equation 2.1.2-21 is used for V_n , Equations 2.1.2-19 and 2.1.2-20 can be written as

$$(1 - X_n) U_s + X_n U_n \left[T_g(U_s, P_s) \right] - U_g = 0 \quad 2.1.2-23$$

and

$$(1 - X_n) \left[\frac{V_s(U_s, P_s) P_s}{T_g(U_s, P_s)} \right] (P - P_s) - X_n R_n P_s = 0. \quad 2.1.2-24$$

Given P , U_g , and X_n , Equations 2.1.2-23 and 2.1.2-24 implicitly determine U_s and P_s . (Equation 2.1.2-20 was divided by the temperature and multiplied by the partial pressures to obtain Equation 2.1.2-24.)

^aThe code input permits selection of any one of six noncondensable gases. The constants used to represent air are in SI units: $T_o = 250.0$ K, $C_o = 715.0$ J/(kg/K), $U_o = 158990.52$ J/kg, $D_o = 0.10329$ J/(kg K²), and $R_n = 287.066$ N m/(kg K).

To obtain the derivatives needed in the numerical scheme, the derivatives of U_s and P_s are taken with respect to P , U_g , and X_n . These derivatives can be obtained from Equations 2.1.2-23 and 2.1.2-24 by the use of the chain rule and implicit differentiation. For example, taking the derivative of Equations 2.1.2-23 and 2.1.2-24 with respect to P [recall that $P_s = P_s(P, U_g, X_n)$ and $U_s = U_s(P, U_g, X_n)$] yields

$$\begin{bmatrix} X_n \left(\frac{dU_n}{dT_g} \right) \left(\frac{\partial T_g}{\partial P_s} \right) & 1 - X_n + X_n \left(\frac{\delta U_n}{dT_g} \right) \left(\frac{\partial T_g}{\partial U_s} \right) \\ -X_n R_n - (1 - X_n) R_s & 0 + \text{TERM2} \\ + R_s + \text{TERM1} & \end{bmatrix} \times \begin{bmatrix} \left(\frac{\partial P_s}{\partial P} \right)_{U_g, X_n} \\ \left(\frac{\partial U_s}{\partial P} \right)_{U_g, X_n} \end{bmatrix} = \begin{bmatrix} 0 \\ (1 - X_n) R_s \end{bmatrix} \tag{2.1.2-25}$$

as a linear system of two equations determining

$$\left(\frac{\partial P_s}{\partial P} \right)_{U_g, X_n} \quad \text{and} \quad \left(\frac{\partial U_s}{\partial P} \right)_{U_g, X_n}$$

In Equation 2.1.2-25

$$R_s = \frac{P_s V_s}{T_g} \tag{2.1.2-26}$$

is the equivalent gas constant for the steam vapor,

$$\text{TERM1} = (1 - X_n) P_n R_s \left[\frac{1}{P_s} + \frac{1}{V_s} \left(\frac{\partial V_s}{\partial P_s} \right)_{U_s} - \frac{1}{T_g} \left(\frac{\partial T_g}{\partial P_s} \right)_{U_s} \right] \tag{2.1.2-27}$$

and

$$\text{TERM2} = (1 - X_n) P_n R_s \left[\frac{1}{V_s} \left(\frac{\partial V_s}{\partial U_s} \right)_{P_s} - \frac{1}{T_g} \left(\frac{\partial T_g}{\partial U_s} \right)_{P_s} \right]. \quad 2.1.2-28$$

The TERM factors have been singled out as they are treated in a special manner in the numerical scheme. To obtain the derivatives P_s and U_s with respect to U_g and X_n the above development is repeated, taking derivatives of Equations 2.1.2-23 and 2.1.2-24 with respect to U_g and X_n . In each case, linear equations parallel to those in Equation 2.1.2-25 are obtained. In fact, the left side matrix is exactly the same, only the right side vector changes.

Having obtained all the derivatives of P_s and U_s , it is relatively easy to obtain the derivatives needed for the gaseous phase. From the chain rule,

$$\left(\frac{\partial T_g}{\partial P} \right)_{U_g, X_n} = \left(\frac{\partial T_g}{\partial P_s} \right)_{U_s} \left(\frac{\partial P_s}{\partial P} \right)_{U_g, X_n} + \left(\frac{\partial T_g}{\partial U_s} \right)_{P_s} \left(\frac{\partial U_s}{\partial P} \right)_{U_g, X_n}, \quad 2.1.2-29$$

$$\left(\frac{\partial T_g}{\partial U_g} \right)_{P, X_n} = \left(\frac{\partial T_g}{\partial P_s} \right)_{U_s} \left(\frac{\partial P_s}{\partial U_g} \right)_{P_g, X_n} + \left(\frac{\partial T_g}{\partial U_s} \right)_{P_s} \left(\frac{\partial U_s}{\partial U_g} \right)_{P, X_n}, \quad \text{and} \quad 2.1.2-30$$

$$\left(\frac{\partial T_g}{\partial X_n} \right)_{P, U_g} = \left(\frac{\partial T_g}{\partial P_s} \right)_{U_s} \left(\frac{\partial P_s}{\partial X_n} \right)_{P, U_g} + \left(\frac{\partial T_g}{\partial U_s} \right)_{P_s} \left(\frac{\partial U_s}{\partial X_n} \right)_{P, U_g}, \quad 2.1.2-31$$

where

$$\left(\frac{\partial T_g}{\partial P_s}\right)_{U_s} \quad \text{and} \quad \left(\frac{\partial T_g}{\partial U_s}\right)_{P_s}$$

are the standard phasic derivatives for the vapor phase. Equations 2.1.2-29 through 2.1.2-31 give all the desired gaseous temperature derivatives. The interface temperature derivatives are obtained from the Clapeyron equation and the known P_s derivatives, that is,

$$\left(\frac{\partial T_i}{\partial P}\right)_{U_g, X_n} = \frac{dT_i}{dP_s} \left(\frac{\partial P_s}{\partial P}\right)_{U_s, X_n}, \quad 2.1.2-32$$

$$\left(\frac{\partial T_i}{\partial U_g}\right)_{P, X_n} = \frac{dT_i}{dP_s} \left(\frac{\partial P_s}{\partial U_g}\right)_{P, X_n}, \quad \text{and} \quad 2.1.2-33$$

$$\left(\frac{\partial T_i}{\partial X_n}\right)_{P, U_g} = \frac{dT_i}{dP_s} \left(\frac{\partial P_s}{\partial X_n}\right)_{P, U_g}, \quad 2.1.2-34$$

where dT_i/dP_s is given by the reciprocal of Equation 2.1.2-17.

The density derivatives can be obtained from $V_g = X_n V_n$ or $V_g = (1 - X_n)V_s$ as these two formulas for the gaseous specific volume are equivalent (see Equation 2.1.2-20). A symmetric formula can be obtained by eliminating X_n from the above two formulas giving

$$v_g = \frac{v_s v_n}{v_s + v_n}. \quad 2.1.2-35$$

Using Equation 2.1.2-35 the ρ_g derivatives with respect to P are obtained

$$\left(\frac{\partial \rho_g}{\partial P}\right)_{U_g, X_n} = -\frac{1}{V_n^2} \left(\frac{\partial V_n}{\partial P}\right)_{U_g, X_n} - \frac{1}{V_s^2} \left(\frac{\partial V_s}{\partial P}\right)_{U_g, X_n} \quad 2.1.2-36$$

Parallel formulas are obtained when U_g or X_n is the independent variable. The partial derivatives on the right side of Equation 2.1.2-36 are obtained from formulas exactly parallel to those in Equations 2.1.2-29 through 2.1.2-31 with T_g replaced by V_s or V_n . When taking the derivatives of V_n ,

$$V_n = \frac{R T_g(P_s, V_s)}{P - P_s} \quad 2.1.2-37$$

Hence, an additional term appears in Equation 2.1.2-29 due to the direct dependence of V_n on P.

The homogeneous equilibrium sound speed for a noncondensable-steam-water mixture is derived in Reference 113.

The sound speed formula in Reference 113 is

$$\begin{aligned} a^2 = & V^2 (P'_s)^2 / \left\{ \left[-\hat{X}_n V_n P'_s \beta_n - \hat{X}_f V_f P'_s (\beta_f - P'_s \kappa_f) \right] \right. \\ & + \left\{ \hat{X}_s P'_s \left[\frac{C_{ps}}{T_s} + P'_s V_s (-2\beta_s + \kappa_s P'_s) \right] + \hat{X}_n P'_s \left[\frac{C_{pn}}{T_s} + P'_s V_n \beta_n \right] \right. \\ & \left. \left. + \hat{X}_f P'_s \left[\frac{C_{pf}}{T_s} - P'_s V_s \beta_s \right] \right\} \left(\frac{\partial T}{\partial P} \right)_{S, X_n} \right\} \quad 2.1.2-38 \end{aligned}$$

where

$$p'_s = \frac{dp^s}{dT} = \frac{h_s^s - h_f^s}{T^s (v_s^s - v_f^s)} \quad 2.1.2-39$$

and

$$\left(\frac{\partial T}{\partial P}\right)_{s, X_n} = \left\{ 1 + \left[\hat{X}_n v_n \beta_n + X_f v_f \beta_f \right] / \left[\hat{X}_s \kappa_n (s_s - s_f) \right] \right\} /$$

$$\left\{ p'_s + \left[\frac{\kappa_s}{\kappa_n} \right] \left\{ p'_s + \left[\frac{\beta_n - \beta_s}{\kappa_s} \right] + \left[\left(\hat{X}_n v_n \beta_n - \hat{X}_s v_s \beta_s \right) p'_s + \left(\hat{X}_n c_{pn} + \hat{X}_s c_{ps} + \hat{X}_f c_{pf} \right) / T^s \right] / \left[\hat{X}_s \kappa_s (s_s - s_f) \right] \right\} \right\} .$$

2.1.2-40

In the above formulas \hat{X}_s , \hat{X}_n , and \hat{X}_f are mass qualities based on the total mixture mass.

Evaluation of the sound speed formulas at the saturated equilibrium state requires a second iteration. To avoid this extra iteration the sound speed formulas were evaluated using the nonequilibrium state properties.

The liquid properties and derivatives are obtained as above for Case 1. To obtain the gaseous properties, Equations 2.1.2-23 and 2.1.2-24 must be solved iteratively. A standard Newton iteration in two variables is used. The iteration variables are P_s and U_s . The steam table Subroutine STH2X6 is called once during each iteration to obtain all the needed steam vapor properties and Equations 2.1.2-21 and 2.1.2-22 are used to obtain the air properties. To save calculation time only an approximate

Jacobian is used inside the iteration loop. From Equation 2.1.2-24, it is clear that if the steam behaves as an ideal gas, that is, $R_g = (V_g P_g / T_g)$ is constant, then Equation 2.1.2-24 is a simple linear equation determining P_g directly in terms of P and X_n . It simplifies the iteration to neglect the derivatives of R_g in the Jacobian, making it equal the left side matrix in Equation 2.1.2-25, with TERM1 and TERM2 terms absent. This iteration has been tested with P_g ranging from 2000 Pa to P and has always converged. The iteration is terminated when $|\Delta P_g|/P$ and $|\Delta V_g|/V_g$ are both < 0.0005 . Hand calculations have been performed to compare both the properties and derivatives with the code calculations. In all cases the scheme converged in 4 iterations or less.

Once the iteration has converged the gaseous properties are determined from the formulas in this section. In the evaluations of all these derivatives the full matrix in Equation 2.1.2-25 is used including TERM1 and TERM2.

2.1.3. Constitutive Models

The constitutive relations include models for defining flow regimes and flow regime related models for interphase drag, wall friction, heat transfer, interphase heat and mass transfer, horizontal and vertical stratification, and water packing mitigation.

2.1.3.1. Flow Regime Maps

In RELAP5 the constitutive relations include flow regime effects for which simplified mapping techniques have been developed to control the use of constitutive relation correlations. Three flow regime maps are utilized. They are vertical and horizontal maps for flow in pipes, and a high mixing map for flow in pumps. The flow regime maps are based on the work of Taitel and Dukler^{27,28} and Ishii.²⁹⁻³¹

Taitel and Dukler have simplified flow regime classification and developed semi-empirical relations to describe flow regime transitions. However, some of their transition criteria are complex and further simplification has been carried out in order to apply these criteria efficiently in RELAP5. In addition, post-CHF regimes as suggested by Ishii²⁹ are included.

Vertical Flow Regime Map

The vertical flow regime map is modeled as seven regimes, three of which are for pre-CHF heat transfer, three of which are for post-CHF heat transfer, and one of which is for vertical stratification. For pre-CHF heat transfer, the regimes modeled are the bubbly, slug, and annular mist regimes. Formulations for these three regimes were utilized by Vince and Lahey³² to analyze their data. For post-CHF heat transfer, the bubbly, slug, and annular mist regimes are transformed to the inverted annular,

inverted slug, and mist regimes, respectively, as suggested by Ishii.²⁹ Unheated components are also modeled utilizing the pre-CHF map. A schematic representing the pre- and post-CHF regimes of the vertical flow regime map is shown in Figure 2.1.3-1. The vertically stratified regime may exist at low flow conditions and a schematic showing its relationship in the vertical flow regime map is given in Figure 2.1.3-2. The criteria for defining the boundaries for transition from one regime to another are given by the following correlations.

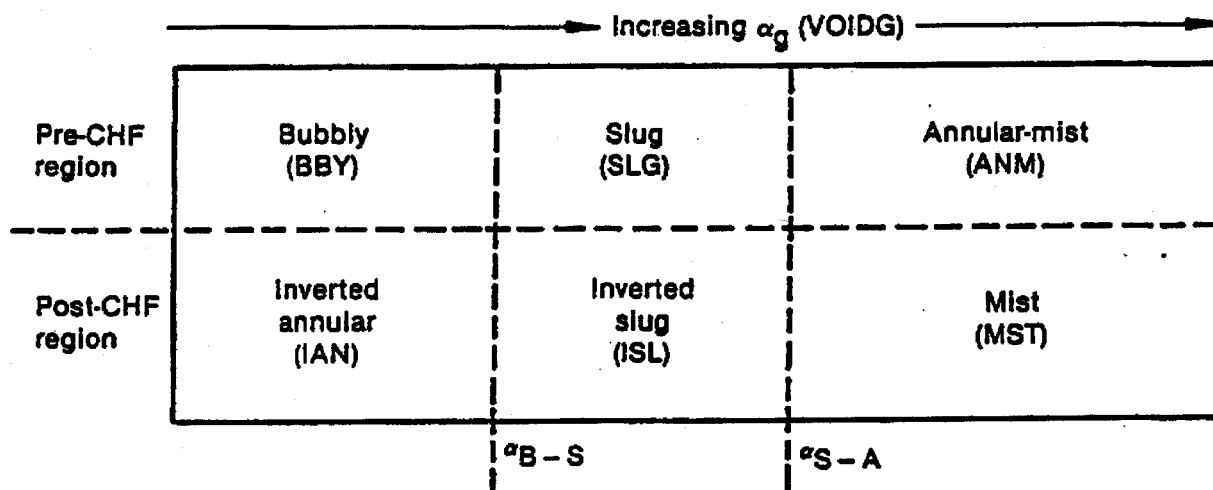


Figure 2.1.3-1. Sketch of Vertical Flow Regime Map.

For the bubbly to slug transition, Taitel and Dukler^{27,28} suggested that bubbly flow may not exist in tubes of small diameter where the rise velocity of small bubbles exceeds that of Taylor bubbles. The small bubble rise velocity is given by the correlation²⁸

$$v_{sb} = 1.53 \left[\frac{g(\rho_f - \rho_g)\sigma}{\rho_f^2} \right]^{1/4} \quad 2.1.3-1$$

and the Taylor bubble rise velocity is given by the correlation¹¹

$$v_{Tb} = 0.35 \left[\frac{gD(\rho_f - \rho_g)}{\rho_f} \right]^{1/2} \quad 2.1.3-2$$

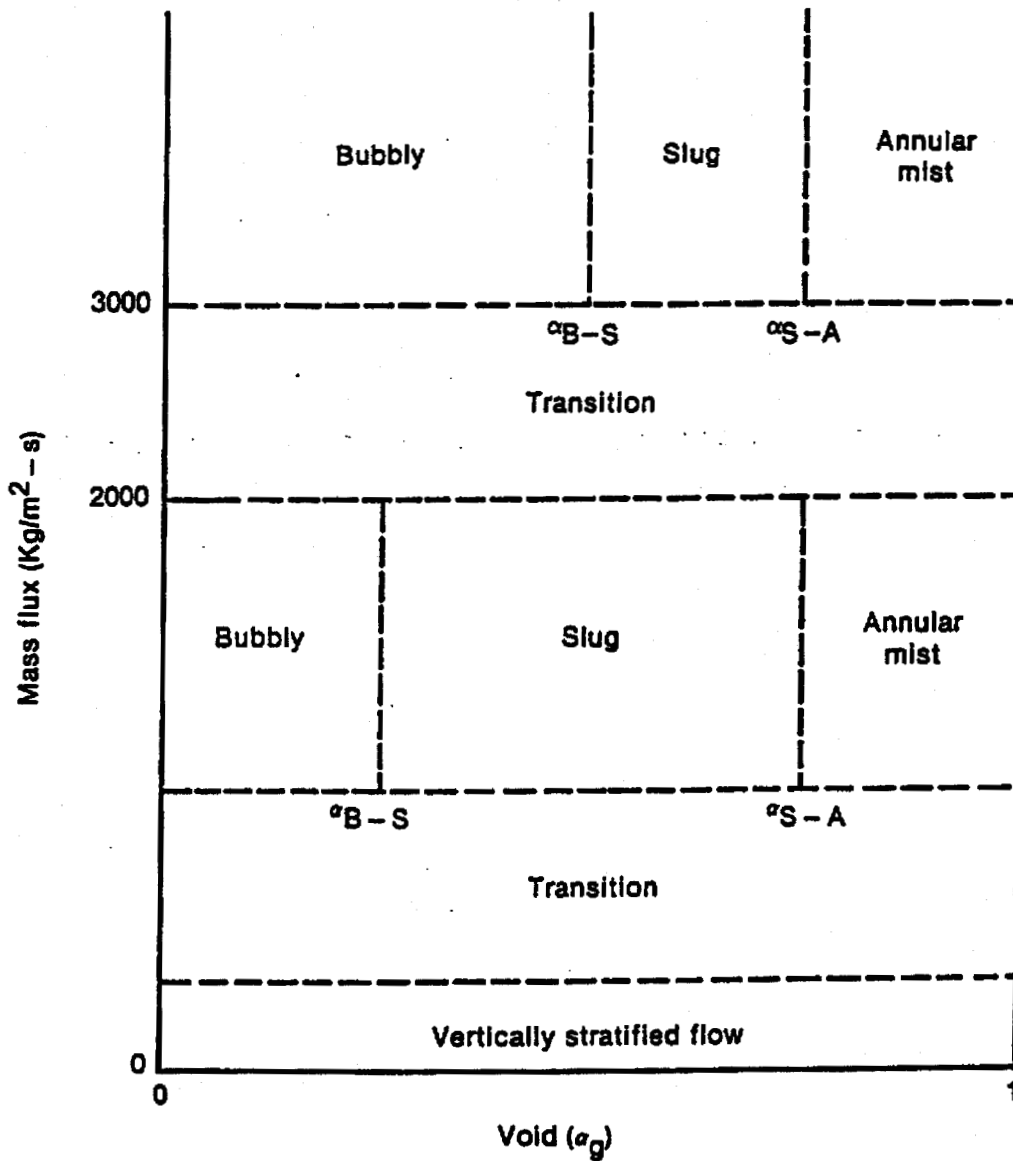


Figure 2.1.3-2. Vertical Flow Regime Map Including the Vertically Stratified Regime.

(Note: in Reference 28, $\rho_f - \rho_g$ is approximated as ρ_f , see also References 30 and 33). Accordingly, the limiting tube diameter allowing the presence of bubbly flow is

$$D^* \geq 19 , \quad 2.1.3-3$$

where D^* is the dimensionless tube diameter,

$$D^* = D[g(\rho_f - \rho_g)/\sigma]^{1/2} . \quad 2.1.3-4$$

Equation 2.1.3-2 is the dimensionless ratio of tube diameter to film thickness times the Deryagin number, where the Deryagin number is the ratio of film thickness to capillary length. Also, in the limit, as the fluid properties approach the thermodynamic critical pressure, $D^* = D$.

For tubes with diameters satisfying the condition of Equation 2.1.3-3 the bubble-slug transition occurs at a void fraction $\alpha_g = 0.25$ for low mass fluxes of $G \leq 2000 \text{ kg/m}^2\text{s}$. By combining this void criterion with Equation 2.1.3-3 the bubble-slug transition criterion can be defined such that

$$\alpha_L = 0.25 \text{ MIN } [1.0, (D^*/19)^8] . \quad 2.1.3-5$$

Hence, if the local void fraction, α_g^V , exceeds the criterion of Equation 2.1.3-5 then bubbly flow cannot exist since the rise velocity of small bubbles exceeds that of Taylor bubbles. The exponential power of 8 is used to provide a smooth variation of α_L as D^* decreases.

At high mass fluxes of $G \geq 3000 \text{ kg/m}^2\text{s}$, bubbly flow with finely-dispersed bubbles can exist up to a void fraction, α_g , of 0.5. Then, if the criterion is linearly interpolated between the upper

and lower void limits, the bubbly-slug transition criterion can be written as

$$\alpha_{B-S} = \alpha_L \quad 2.1.3-6$$

for mass fluxes of $G \leq 2000 \text{ kg/m}^2\text{s}$,

$$\alpha_{B-S} = \alpha_L + 0.001 (G - 2000) (0.5 - \alpha_L) \quad 2.1.3-7$$

for mass fluxes of $2000 < G < 3000 \text{ kg/m}^2\text{s}$, and

$$\alpha_{B-S} = 0.5 \quad 2.1.3-8$$

for mass fluxes of $G \geq 3000 \text{ kg/m}^2\text{s}$. The flow regime can therefore be in the bubbly regime if $\alpha_g < \alpha_{B-S}$ and in the slug regime if $\alpha_g \geq \alpha_{B-S}$.

The bubble-slug transition defined by Equations 2.1.3-6 to 2.1.3-8 is similar to that given by Taitel and Dukler,²⁸ except that the void fraction relation is converted into a form based on liquid and vapor superficial velocities and finely dispersed bubbles are also distinguished from ordinary bubbles.

For the slug to annular flow transition, Taitel and Dukler²⁸ developed a criterion based on the critical vapor velocity required to suspend a liquid droplet. The critical velocity, u_c , is written as

$$u_c = 3.1[\sigma g(\rho_f - \rho_g)]^{1/4} / \rho_g^{1/2} = (\alpha_g v_g)_c \quad 2.1.3-9$$

The value 3.1 for the numerical coefficient is somewhat larger than the value of 1.4 reported by Wallis³⁴ but is a better fit to the data reported by Vince and Lahey.³² In comparing RELAP5 code results to data, however, the coefficient value of 1.4 gives better results. The void fraction must also be greater than 0.75

in order to get good comparisons between code results and data. Hence, solving Equation 2.1.3-9 for void fraction and imposing a lower void limit of 0.75 yields the slug to annular transition criterion for which

$$\alpha_{S-A} = \text{MAX} \left[0.75, 1.4 [\sigma g (\rho_f - \rho_g)]^{1/4} / (v_g \rho_g^{1/2}) \right], \quad 2.1.3-10$$

where the flow regime is said to be in the slug regime if

$\alpha_g \leq \alpha_{S-A}$ and in the annular-mist regime if $\alpha_g > \alpha_{S-A}$.

For post-CHF heat transfer the same formulations are used to define the inverted flow regime transition criteria in that Equations 2.1.3-6 through 2.1.3-8 also define the inverted slug regime transition and Equation 2.1.3-10 defines the inverted slug to mist regime transition.

At low mass fluxes the possibility exists for vertically stratified conditions. In RELAP5 vertical flow in a volume cell is considered to be stratified if the difference in void fraction of the volumes above and below is greater than 0.5 and if the magnitude of the volume average mixture mass flux is less than the Taylor bubble rise velocity mass flux. The Taylor bubble criterion is based on the Taylor bubble velocity given by Equation 2.1.3-2 such that

$$|G| < \rho v_{Tb} \quad , \quad 2.1.3-11$$

where v_{Tb} is the Taylor bubble velocity and

$$|G| = |\alpha_g \rho_g v_g + \alpha_f \rho_f v_f| \quad . \quad 2.1.3-12$$

Hence, if Equation 2.1.3-11 is true, then transition to vertical stratification exists and if Equation 2.1.3-11 is false, then transition to vertical stratification does not exist.

Horizontal Flow Regime Map

The horizontal flow regime map is similar to the vertical flow regime map except that the post-CHF regimes are not included and a horizontal stratification regime is modeled that replaces the vertical stratification regime. The horizontal flow regime map therefore consists of horizontally stratified, bubbly, slug and annular mist regimes. The criteria for the bubbly to slug and the slug to annular mist regimes are also similar to those for the vertical map except that the bubbly to slug transition criterion is a constant

$$\alpha_{B-S} = \alpha_L = 0.25. \quad 2.1.3-13$$

The slug to annular mist transition criterion is also a constant

$$\alpha_{S-A} = 0.8. \quad 2.1.3-14$$

The criterion defining the horizontally stratified regime is one developed by Taitel and Dukler.²⁷

According to Taitel and Dukler, the flow field is horizontally stratified if the vapor velocity satisfies the condition that

$$v_g < v_{gL} \quad 2.1.3-15$$

where

$$v_{gL} = \frac{1}{2} \left[\frac{(\rho_f - \rho_g) g a A}{\rho_g D \sin \theta} \right]^{1/2} (1 - \cos \theta) \quad 2.1.3-16$$

The angle θ is related to the liquid level, ll , and the void fraction, α_g , by the relationships

$$ll = D (1 + \cos\theta)/2 \quad 2.1.3-17$$

and

$$\alpha_g \pi = \theta - \sin\theta \cos\theta \quad 2.1.3-18$$

If the horizontal stratification condition of Equation 2.1.3-15 is met, then the flow field undergoes a transition to horizontally stratified. If the condition of Equation 2.1.3-15 is not met, then the flow field undergoes a transition to the bubbly, slug, or annular mist flow regime.

High Mixing Flow Regime Map

The high mixing flow regime map is based on vapor void fraction, α_g , and consists of a bubbly regime for $\alpha_g \leq 0.5$, a mist regime for $\alpha_g \geq 0.95$, and a transition regime for $0.5 < \alpha_g < 0.95$. The transition regime is modeled as a mixture of bubbles dispersed in liquid and droplets dispersed in vapor.

2.1.3.2. Interphase Drag

The interphase drag force per unit volume expressed in terms of relative phasic velocity is

$$F_{I_{gf}} = - f_{gf} |v_g - v_f| (v_g - v_f) \quad 2.1.3-19$$

with

$$f_{gf} = \rho_c S_F a_{gf} C_D / 8 \quad 2.1.3-20$$

where

- ρ_c = density of the continuous phase,
- C_D = drag coefficient,
- a_{gf} = interfacial area per unit volume, and
- S_F = shape factor.

The shape factor³⁰, S_F , is assumed to be unity (1.0). The evaluation of a_{gf} and C_D for different flow regimes is covered in the following discussion.

Dispersed Flow

The bubbly and mist flow regimes are both considered as dispersed flow. According to Wallis³⁴ and Shapiro,³⁵ the dispersed bubbles or droplets can be assumed to be spherical particles with a size distribution of the Nukiyama-Tanasawa form. The Nukiyama-Tanasawa distribution function in nondimensional form is

$$p^* = 4d^{*2} e^{-2d^*} \quad , \quad 2.1.3-21$$

where $d^* = d/d'$; d' is the most probable particle diameter, and p^* is the probability of particles with a nondimensional diameter of d^* . With this distribution, it can be shown that the average particle diameter $d_0 = 1.5 d'$, and the surface area per unit volume is

$$a_{gf} = \frac{6\bar{a}}{d'} \int \frac{d^{*2} p^* dd^*}{d^{*3} p^* dd^*} = \frac{2.4\bar{a}}{d'} \quad , \quad 2.1.3-22$$

where $\bar{\alpha} = \alpha_g$ for bubbles and $\bar{\alpha} = \alpha_f$ for droplets. In terms of the average diameter, d_o , the interfacial area per unit volume, a_{gf} , is

$$a_{gf} = 3.6\bar{\alpha}/d_o \quad . \quad 2.1.3-23$$

The average diameter d_o is obtained by assuming that $d_o = 1/2 d_{max}$. The maximum diameter, d_{max} , is related to the critical Weber number, We , by

$$We = d_{max} \rho_c (v_g - v_f)^2 / \sigma \quad . \quad 2.1.3-24$$

The values for We are presently taken as $We = 10$ for bubbles and $We = 3.0$ for droplets.

The drag coefficient is given by Ishii and Chawla³⁰ for the viscous regime as

$$C_D = 24(1 + 0.1 Re_p^{0.75}) / Re_p \quad , \quad 2.1.3-25$$

where the particle Reynolds number Re_p is defined as

$$Re_p = |v_g - v_f| d_o \rho_c / \mu_m \quad . \quad 2.1.3-26$$

The mixture viscosity, μ_m , is $\mu_m = \mu_f / \alpha_f$ for bubbles and $\mu_m = \mu_g / (\alpha_g)^{2.5}$ for droplets.

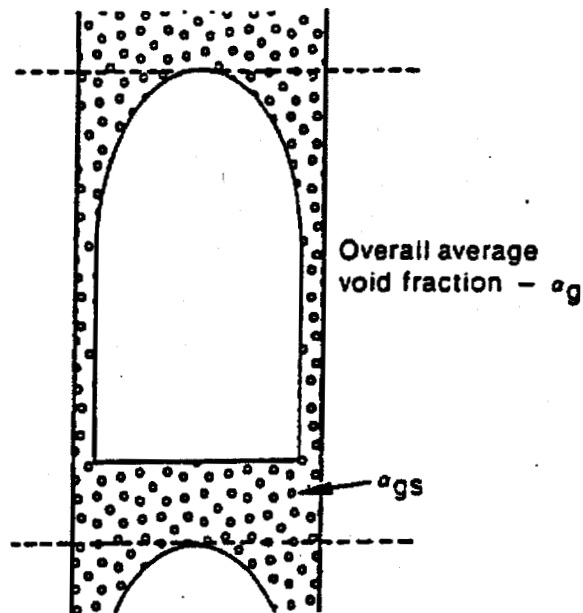


Figure 2.1.3-3. Slug Flow Pattern

Slug Flow

Slug flow is modeled as a series of Taylor bubbles separated by liquid slugs containing small bubbles. A sketch of a slug flow pattern is shown in Figure 2.1.3-3. The Taylor bubble has a diameter nearly equal to the pipe diameter and a length varying from one to one hundred pipe diameters.

The total drag in slug flow is partitioned into small bubble and Taylor bubble drag components:

$$f_{gf} = (f_{gf})_{sb} + (f_{gf})_T \quad 2.1.3-26.1$$

The interphasic friction term for small bubbles, $(f_{gf})_{sb}$, is of the form given in Equation 2.1.3-20 and is determined with the a_{gf} and C_D derived for dispersed flow (Equations 2.1.3-23 and 2.1.3-25).

The void fraction of a single Taylor bubble, α_b , in the total mixture is

$$\alpha_b = (\alpha_g - \alpha_{gs}) / (1 - \alpha_{gs}) \quad . \quad 2.1.3-27$$

where α_{gs} is the average void fraction in the liquid film and slug region.

To provide a smooth transition into and out of slug flow, α_{gs} , in Equation 2.1.3-27, is considered as a free parameter varying from the void fraction (α_{B-S}) at the bubbly to slug flow regime transition to nearly zero at the slug to annular mist flow regime transition. The variation is represented by the exponential expression

$$\alpha_{gs} = \alpha_{B-S} \exp[-10(\alpha_g - \alpha_{B-S}) / (\alpha_{S-A} - \alpha_{B-S})] \quad . \quad 2.1.3-28$$

Three options are available for computing the Taylor bubble interphase drag in slug flow: the base INEL drag, the Wilson drag, and the B&W modified slug-drag model. The Wilson drag is based on the Wilson bubble rise velocity in a vertical pipe.¹³⁵

The BWNT modified slug-drag model uses coefficients that are a function of pressure and void fraction to adjust the INEL drag model. The default is the INEL model.

INEL Drag Model

By approximating the ratio of the Taylor bubble diameter to the tube diameter and the diameter-to-length ratio of a Taylor bubble, Ishii and Mishima³¹ obtained the surface-to-volume ratio of a Taylor bubble as $4.5/D$. In the INEL drag model, this is used to obtain the interfacial area per unit volume, a_{gf} , for slug flow:

$$a_{gf} = (4.5 C_t/D) \alpha_b + (3.6 \alpha_{gs}/d_o)(1 - \alpha_b) \quad , \quad 2.1.3-29$$

in which the first term pertains to Taylor bubbles and the second term to small bubbles. C_t is a roughness parameter that is introduced to account for irregularities in the surface of large Taylor bubbles. At the present time, C_t is assumed to be unity (1.0).

The INEL model drag coefficient for Taylor bubbles is given by Ishii and Chawla³⁰ as

$$(C_D)_T = 9.8 (1 - \alpha_b)^3 \quad , \quad 2.1.3-30$$

where α_b is given by combining Equations 2.1.3-27 and 2.1.3-28.

The Wilson Drag Model

The Wilson drag model was first derived for reflood applications using BEACH¹³⁶ and is now applied to non-reflood conditions in RELAP5/MOD2-B&W.

b,c,d,e

b,c,d,e

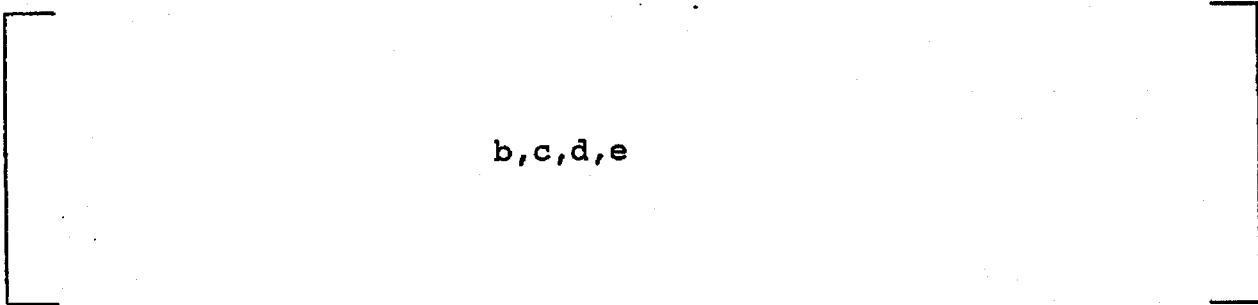
The estimate of the phasic slip, Δv , is obtained from a modified set of the Wilson¹³⁵ bubble rise model:

b,c,d,e

The coefficients a_j and b_j for $j = 1$ and 2 are from the original correlation. The third set ($j = 3$), however, was added to obtain a better match to the original data at high α_g^* (greater than about 6.526). As implemented in RELAP5/MOD2-B&W, the bubble velocity is multiplied by a user-defined multiplier, C_{WB} :

$$v_{bub} = C_{WB} \Delta v.$$

2.1.3-30.6



where C_{WSL} is a user-defined multiplier for slug flow conditions which, at the present time, is set equal to one.

In RELAP5, an interphase drag for each volume is calculated and then the drag for the junctions between connecting volumes are determined. RELAP5 uses several techniques to smooth the void behavior across the junction. One of these smoothing techniques is used when the difference between the void fractions of adjoining volumes is greater than 0.001. For some situations (for example, in RSG PWR small break LOCA, during the hot leg draining period and during the period preceding core uncover), it is expected that discontinuous void behavior will occur at the core-upper plenum boundary. The unmodified junction drag logic calculates void behavior reasonably well. However, because RELAP5 smooths the void behavior across the junction when the difference between connecting nodes is greater than 0.001, a flat

void profile is calculated for some cases as illustrated in Figure 2.1.3-3.1. Therefore, as an option to the Wilson drag model, the void difference threshold for curve smoothing is increased to 0.5.

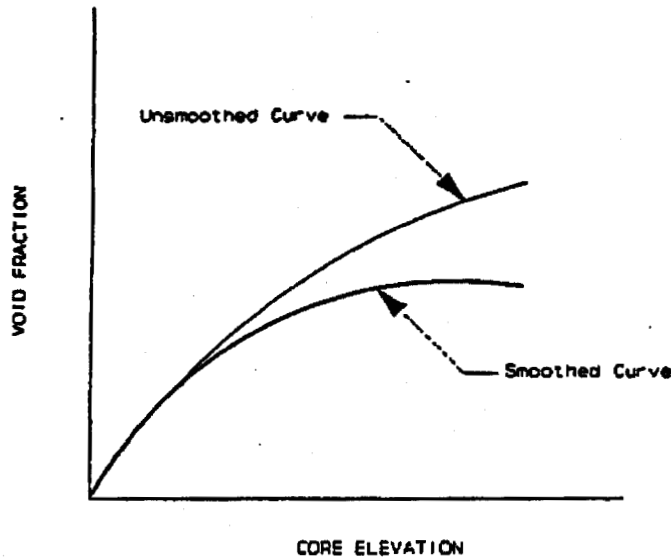


Figure 2.1.3-3.1. Typical RELAP5 Void Profile: Smoothed and Unsmoothed Curves.

BWNT has added an option to adjust the slug interphase drag for non-reflood applications via coefficients added to Equation 2.1.3-26.1. The adjustments, based on numerous benchmarks, are functions of pressure and void fraction as shown in the following equations.

$$f_{gf} = M_{st} [(f_{gf})_{sb} + M_s (f_{gf})_T] \quad , \quad 2.1.3-30.7.1$$

where

$$\left[\quad \quad \quad b, c, d, e \quad \quad \quad \right]$$

b,c,d,e

The values given in parentheses are the default coefficients. These are selected by the user through input of a control volume flag which refers back to a tabular default table number containing the five coefficients that are listed. A different set of coefficients may be specified by the user on input. Use of the default drag adjustments are appropriate for two-phase applications in heated tube bundles and small diameter pipes during non-reflood calculations.

Annular Mist Flow

Annular mist flow is characterized by a liquid film along the wall and a vapor core containing entrained liquid droplets. The INEL drag is the sum of the annular vapor and liquid droplet drag components

$$f_{gf} = (f_{gf})_{ann} + (f_{gf})_{drp} \quad 2.1.3-30.8$$

Let α_{ff} be the average liquid volume fraction of the liquid film along the wall. Then, from simple geometric considerations, the interfacial area per unit volume can be shown to be

$$\alpha_{gf} = (4C_{an}/D)(1 - \alpha_{ff})^{1/2} + (3.6\alpha_{fd}/d_o)(1 - \alpha_{ff}), \quad 2.1.3-31$$

where C_{an} is a roughness parameter introduced to account for waves in the liquid wall film and α_{fd} is the average liquid volume fraction in the vapor core, for which

$$\alpha_{fd} = (\alpha_f - \alpha_{ff}) / (1 - \alpha_{ff}) \quad . \quad 2.1.3-32$$

A simple relation based on the flow regime transition criterion and liquid Reynolds number is used to correlate the average liquid film volume fraction. For vertical flow regimes, the entrainment relation is

$$\alpha_{ff} = \alpha_f C_f \exp \left\{ -7.5 \cdot 10^{-5} (\alpha_g v_g / u_c)^6 \right\}, \quad 2.1.3-33$$

where u_c is the entrainment critical velocity given by Equation 2.1.3-9 with the coefficient 3.1 replaced by 1.4. For horizontal flow regimes, the entrainment relation is

$$\alpha_{ff} = \alpha_f C_f \exp \left\{ -4.0 \cdot 10^{-5} (v_g / v_{gl})^6 \right\}, \quad 2.1.3-34$$

where v_{gl} is the horizontal stratification critical velocity given by Equation 2.1.3-16. The term C_f is expressed as

$$C_f = 10^{-4} \rho_f \alpha_f v_f D / \mu_f \quad .$$

The interfacial friction factor, f_1 , for the liquid film takes the place of C_D in Equation 2.1.3-20, and is described by a correlation obtained by Bharathan et al.³⁶ for which

$$f_1 = 4 (0.005 + A(\delta^*)^B) , \quad 2.1.3-35$$

where

$$\log_{10} A = -0.56 + 9.07/D^* , \quad 2.1.3-36$$

$$B = 1.63 + 4.74/D^* , \text{ and} \quad 2.1.3-37$$

$$\delta^* = \delta \left\{ \frac{(\rho_f - \rho_g) g}{\sigma} \right\}^{1/2} . \quad 2.1.3-38$$

The term δ^* is the liquid wall film Deryagin number for which δ is the film thickness, and D^* is the dimensionless diameter given by Equation 2.1.3-5.

BWNT has added an option to include a multiplicative coefficient on the overall drag computed for control volumes in an annular mist flow regime. This coefficient is available for non-reflood applications. The default coefficient, xms , is 1.0; however, it may be changed on input specified by the user. The coefficient is applied as follows

$$f_{gf} = xms [(f_{gf})_{ann} + (f_{gf})_{drp}] \quad 2.1.3-38.1$$

Vertical Stratified Flow

For vertically stratified flow the previously discussed interphase drag relationships are applied except that a low interphase drag coefficient of $0.1 \text{ N-s}^2/\text{m}^5$ is imposed for the junction above the vertically stratified volume.

Horizontal Stratified Flow

By simple geometric consideration, one can show that the interfacial area per unit volume is

$$a_{gf} = 4C_{st} \sin \theta (\pi D) , \quad 2.1.3-39$$

where C_{st} is a roughness parameter introduced to account for surface waves and is set to 1 at the present time.

The interface Reynolds number is defined with the vapor properties and regarding liquid as the continuous phase for which

$$Re_i = D_i \rho_g | v_g - v_f | \mu_g , \quad 2.1.3-40$$

where the equivalent wetted diameter, D_i , for the interface is

$$D_i = \alpha \pi D / (\theta + \sin \theta) . \quad 2.1.3-41$$

The interfacial friction factor, f_i , replaces C_D in Equation 2.1.3-20 and is obtained by assuming typical friction factor relationships for which

$$f_i = 64/Re_i \quad 2.1.3-42$$

for laminar flow, where $Re_i \leq 1187$,

$$f_i = 0.3164/Re_i^{0.25} \quad 2.1.3-43$$

for turbulent flow, where $Re_i \geq 4000$, and

$$f_i = 0.0539 \quad 2.1.3-44$$

for the laminar to turbulent transition where $1187 < Re_i < 4000$.

Inverted Flow Regimes

The interphase drag relationships for post-CHF inverted flow regimes are treated in a similar fashion to the corresponding pre-CHF flow regimes except that the roles of vapor and liquid are interchanged.

2.1.3.3. Wall Friction

In RELAP5, the wall friction force terms include only wall shear effects. Losses due to abrupt area change are calculated using mechanistic form loss models. Other losses due to elbows or complicated flow passage geometry are modeled using energy loss coefficients that must be input by the user.

In the development of the RELAP5/MOD2 wall friction model, emphasis was placed on obtaining reasonable values for wall friction in all flow regimes. The flow regime models are discussed in section 2.1.3.1.

The wall friction model is based on a two-phase multiplier approach in which the two-phase multiplier is calculated from the Heat Transfer and Fluid Flow Service (HTFS) modified Baroczy correlation.³⁷ The individual phasic wall friction components are calculated by apportioning the two-phase friction between the

phases using a technique derived from the Lockhart-Martinelli³⁸ model. The model is based on the assumption that the frictional pressure drop may be calculated using a quasi-steady form of the momentum equation.

The Two-Phase Friction Multiplier Approach

The overall friction pressure drop can be expressed in terms of the liquid-alone wall friction pressure drop

$$\left(\frac{\partial P}{\partial x}\right)_{2\phi} = \phi_f^2 \left(\frac{\partial P}{\partial x}\right)_f \quad 2.1.3-45$$

or the vapor-alone wall friction pressure drop

$$\left(\frac{\partial P}{\partial x}\right)_{2\phi} = \phi_g^2 \left(\frac{\partial P}{\partial x}\right)_g \quad 2.1.3-46$$

where ϕ_f and ϕ_g are the liquid-alone and vapor-alone two-phase friction multipliers, respectively. The phasic wall friction pressure gradients are expressed as

$$\left(\frac{\partial P}{\partial x}\right)_f = \frac{\lambda'_f M_f^2}{2D\rho_f A^2} \quad 2.1.3-47$$

for the liquid-alone, and

$$\left(\frac{\partial P}{\partial x}\right)_g = \frac{\lambda'_g M_g^2}{2D\rho_g A^2} \quad 2.1.3-48$$

for the vapor-alone, where the prime indicates the liquid and vapor-alone friction factors, respectively, calculated at the respective Reynolds numbers

$$Re'_f = \frac{\alpha_f \rho_f |v_f| D}{\mu_f} \quad 2.1.3-49$$

and

$$Re'_g = \frac{\alpha_g \rho_g |v_g| D}{\mu_g} \quad 2.1.3-50$$

The liquid and vapor mass flow rates, respectively, are defined as

$$M_f = \alpha_f \rho_f v_f A \quad 2.1.3-51$$

and

$$M_g = \alpha_g \rho_g v_g A \quad 2.1.3-52$$

Throughout the current literature the overall two-phase friction pressure gradient is calculated using two-phase friction multiplier correlations. However, regardless of the correlation used, the multipliers may be interrelated using Equations 2.1.3-45 through 2.1.3-48 and the Lockhart-Martinelli³⁸ ratio defined as

$$x^2 = \frac{\left(\frac{dP}{dx}\right)_f}{\left(\frac{dP}{dx}\right)_g} = \frac{\phi_g^2}{\phi_f^2} \quad 2.1.3-53$$

In RELAP5 these equations are used to apportion the overall wall friction into liquid and vapor wall friction coefficients.

Flow Regime Effects

Two-phase friction can be modeled in terms of two-phase friction multipliers and known friction factors using the method developed by Lockhart-Martinelli.³⁹ Chisholm³⁸ also developed a theoretical basis for the Lockhart-Martinelli model that provides a rationale for relating the equations to empirical results.

From the theoretical basis developed by Chisholm, irrespective of flow regime, the quasi-steady phasic momentum equations can be expressed in scalar form as

$$\alpha_f A \left(\frac{\partial P}{\partial x} \right)_{2\phi} - \tau_f P_f - S_{FI} = 0 \quad 2.1.3-54$$

for the liquid, and

$$\alpha_g A \left(\frac{\partial P}{\partial x} \right)_{2\phi} - \tau_g P_g - S_{FI} = 0 \quad 2.1.3-55$$

for the vapor, where τ_f and τ_g are the liquid and vapor wall shear stresses, respectively, p_f and p_g are the liquid and vapor wetted wall perimeter, respectively, and S_{FI} is a stress gradient due to interphase friction. These equations can be expressed in terms of Darcy friction factors and simplified so that

$$\left(\frac{dP}{dx} \right)_{2\phi} \left[1 + S_R \frac{\alpha_g}{\alpha_f} \right] = \frac{\lambda_f' \rho_f v_f^2}{2D} \left(\frac{\alpha_{fw}}{\alpha_f} \right) \quad 2.1.3-56$$

for the liquid, and

$$\left(\frac{dP}{dx}\right)_{2\phi} (1 + S_R) = \frac{\lambda_g \rho_g v_g^2}{2D} \left(\frac{\alpha_{gw}}{\alpha_g}\right) \quad 2.1.3-57$$

for the vapor, where the interphase friction term, S_R , is defined as

$$S_R = \frac{S_{FI}}{\alpha_g A \left(\frac{\partial P}{\partial x}\right)_{2\phi}} \quad 2.1.3-58$$

The terms α_{fw} and α_{gw} are the liquid and vapor volume fractions, respectively, at the wall, and α_f and α_g are the overall liquid and vapor volume fractions, respectively. Taking the ratio of Equation 2.1.3-56 to 2.1.3-57 gives

$$z^2 = \frac{\lambda_f \rho_f v_f^2 \left(\frac{\alpha_{fw}}{\alpha_f}\right)}{\lambda_g \rho_g v_g^2 \left(\frac{\alpha_{gw}}{\alpha_g}\right)} = \frac{1 + S_R \frac{\alpha_g}{\alpha_f}}{(1 - S_R)} \quad 2.1.3-59$$

Consider the pure liquid case where $\alpha_g = 0$ and $\alpha_{fw} = \alpha_f$ and for which Equation 2.1.3-56 reduces to

$$\left(\frac{\partial P}{\partial x}\right)_{2\phi} = \left(\frac{\partial P}{\partial x}\right)_f = \frac{\lambda_f \rho_f v_f^2}{2D} \quad 2.1.3-60$$

For this case, the friction factor, λ_f , can be precisely calculated based on a Reynolds number expressed in terms of D .

Similarly, for the two-phase case, liquid and vapor friction factors can be calculated based on Reynolds number of

$$R_f = \frac{\rho_f \left(\frac{\alpha_f}{\alpha_{fw}} \right) D |v_f|}{\mu_f} \quad \text{and} \quad 2.1.3-61$$

$$R_g = \frac{\rho_g \left(\frac{\alpha_g}{\alpha_{gw}} \right) D |v_g|}{\mu_g} \quad 2.1.3-62$$

for the liquid and vapor, respectively. These terms have the property that, as one phase or the other disappears, the friction factors calculated reduce to their single-phase formulations.

Equations 2.1.3-56 and 2.1.3-57 can be rewritten as

$$\left(\frac{dp}{dx} \right)_{2\phi} \left[\frac{z^2}{\alpha_g + \alpha_f z^2} \right] = \frac{\lambda_f \rho_f v_f^2}{2D} \left(\frac{\alpha_{fw}}{\alpha_f} \right) \quad 2.1.3-63$$

and

$$\left(\frac{dp}{dx} \right)_{2\phi} \left[\frac{1}{\alpha_g + \alpha_f z^2} \right] = \frac{\lambda_g \rho_g v_g^2}{2D} \left(\frac{\alpha_{gw}}{\alpha_g} \right) \quad 2.1.3-64$$

for the liquid and vapor, respectively. However, these equations are now flow regime dependent since knowledge of the wetted wall and overall void fractions is required in order to calculate the friction factors. The term z^2 can also be considered as a correlating factor relating the overall two-phase friction pressure gradient to the known phasic friction factors.

The quasi-steady phasic momentum equations similar to Equations 2.1.3-63 and 2.1.3-64 can also be written in terms of the RELAP5 friction coefficient, where

$$\alpha_f \left(\frac{dP}{dx} \right)_{2\phi} \left[\frac{Z^2}{\alpha_g + \alpha_f Z^2} \right] = FWF(\alpha_f \rho_f v_f) \quad 2.1.3-65$$

for the liquid, and

$$\alpha_g \left(\frac{dP}{dx} \right)_{2\phi} \left[\frac{1}{\alpha_g + \alpha_f Z^2} \right] = FWG(\alpha_g \rho_g v_g) \quad 2.1.3-66$$

for the vapor. Taking the sum of these two equations gives the overall quasi-steady two-phase pressure gradient as

$$\left(\frac{dP}{dx} \right)_{2\phi} = FWF(\alpha_f \rho_f v_f) + FWG(\alpha_g \rho_g v_g) \quad 2.1.3-67$$

It should be noted that the calculation of the phasic friction factors using the Reynolds numbers given by Equation 2.1.3-61 and the assumption that two-phase flows behave similarly to single-phase flows in the laminar, transition, and turbulent regimes provides the rationale relating Equations 2.1.3-63 and 2.1.3-64 to empirical data. It is this same rationale that allows expressing the correlating term, Z^2 , in terms of friction factors that are independent of interphase friction as given by Equation 2.1.3-59. It is this equation that forms the basis for apportioning the overall two-phase wall friction between the phases.

Apportioning Wall Friction

Overall two-phase wall friction can be apportioned into phasic components by combining Equations 2.1.3-65 and 2.1.3-66 with

Equations 2.1.3-45 through 2.1.3-48 and 2.1.3-59, 2.1.3-62, and 2.1.3-64 which results in

$$\phi_f^2 \frac{\lambda'_{f\rho_f} (\alpha_f v_f)^2}{2D} \frac{\alpha_{fw} \lambda_{f\rho_f} v_f^2}{\alpha_{gw} \lambda_{g\rho_g} v_g^2 + \alpha_{fw} \lambda_{f\rho_f} v_f^2} = FWF(\alpha_{f\rho_f} v_f) \quad 2.1.3-68$$

for the liquid, and

$$\phi_g^2 \frac{\lambda'_{g\rho_g} (\alpha_g v_g)^2}{2D} \frac{\alpha_{gw} \lambda_{g\rho_g} v_g^2}{\alpha_{gw} \lambda_{g\rho_g} v_g^2 + \alpha_{fw} \lambda_{f\rho_f} v_f^2} = FWG(\alpha_{g\rho_g} v_g) \quad 2.1.3-69$$

for the vapor, where the two-phase multiplier terms are calculated using a two-phase friction multiplier correlation. Flow regime effects are also included in the relationships between wetted wall and overall void fractions and their effect in calculating the friction factor terms.

The H.T.F.S. Two-Phase Friction Multiplier Correlation

In RELAP5 only the H.T.F.S. correlation³⁷ is used to calculate two-phase friction multipliers. This correlation was chosen because it is correlated to empirical data over very broad ranges of phasic volume fractions, phasic flowrates and flow regimes. The correlation has also been shown to give good agreement with empirical data.

The H.T.F.S. correlation for two-phase friction multiplier³⁷ is expressed as

$$\phi_f^2 = 1 + \frac{C}{x} + \frac{1}{x^2} \quad 2.1.3-70$$

for the liquid-alone multiplier, or

$$\phi_g^2 = x^2 + Cx + 1 \quad 2.1.3-71$$

for the vapor-alone multiplier, where C is the correlation term and x is the Lockhart-Martinelli ratio given by Equation 2.1.3-53. The correlation term is expressed in terms of scalar mass flux, G, and the Baroczy dimensionless property index, Λ , such that

$$2 \leq C = -2 + f_1(G) T_1, \quad 2.1.3-72$$

where

$$f_1(G) = 28 - 0.3 G^{0.5}, \quad 2.1.3-73$$

$$T_1 = \exp - \left[\frac{(\log_{10} \Lambda + 2.5)^2}{2.4 - G(10^{-4})} \right], \quad 2.1.3-74$$

$$\Lambda = \frac{\rho_g}{\rho_f} \left[\frac{\mu_f}{\mu_g} \right]^{0.2}, \text{ and} \quad 2.1.3-75$$

$$G = \alpha_f \rho_f v_f + \alpha_g \rho_g v_g \quad 2.1.3-76$$

The terms ρ , μ , α and v denote the density, viscosity, volume fraction and velocity, respectively.

If the H.T.F.S. correlation is combined with the wall friction formulations by combining Equations 2.1.3-45 through 2.1.3-48, 2.1.3-51 through 2.1.3-53, 2.1.3-70, and 2.1.3-71, then

$$\begin{aligned} \left(\frac{dP}{dx}\right)_{2\phi} &= \phi_f^2 \left(\frac{dP}{dx}\right)_f = \phi_g^2 \left(\frac{dP}{dx}\right)_g \\ &= \frac{1}{2D} \left\{ \lambda_f' \rho_f (\alpha_f v_f)^2 + c \left[\lambda_f' \rho_f (\alpha_f v_f)^2 \lambda_g' \rho_g (\alpha_g v_g)^2 \right]^{0.5} \right. \\ &\quad \left. + \lambda_g' \rho_g (\alpha_g v_g)^2 \right\}. \end{aligned} \quad 2.1.3-77$$

This equation can then be combined with Equation 2.1.3-68 and 2.1.3-69 and simplified such that

$$\begin{aligned} FWF(\alpha_f \rho_f) &= \alpha_{fw} \frac{\rho_f \lambda_f |v_f|}{2D} \left\{ \lambda_f' \rho_f (\alpha_f v_f)^2 \right. \\ &\quad \left. + c \left[\lambda_f' \rho_f (\alpha_f v_f)^2 \lambda_g' \rho_g (\alpha_g v_g)^2 \right]^{0.5} \right. \\ &\quad \left. + \lambda_g' \rho_g (\alpha_g v_g)^2 \right\} / \left[\alpha_{gw} \lambda_g \rho_g v_g^2 + \alpha_{fw} \lambda_f \rho_f v_f^2 \right] \end{aligned} \quad 2.1.3-78$$

for the liquid, and

$$\begin{aligned} FWG(\alpha_g \rho_g) &= \alpha_{gw} \frac{\rho_g \lambda_g |v_g|}{2D} \left\{ \lambda_f' \rho_f (\alpha_f v_f)^2 \right. \\ &\quad \left. + c \left[\lambda_f' \rho_f (\alpha_f v_f)^2 \lambda_g' \rho_g (\alpha_g v_g)^2 \right] \right. \\ &\quad \left. + \lambda_g' \rho_g (\alpha_g v_g)^2 \right\} / \left[\alpha_{gw} \lambda_g \rho_g v_g^2 + \alpha_{fw} \lambda_f \rho_f v_f^2 \right] \end{aligned} \quad 2.1.3-79$$

for the vapor.

In RELAP5 the friction factor and velocity terms are calculated in such a manner that as the velocity terms disappear the equations give the correct limits. For example, the friction factor terms are evaluated such that

$$\lim_{\left| \left[\frac{\alpha_f}{\alpha_{fw}} \right] v_f \right| \rightarrow 0} \left[\lambda_f \left| \left[\frac{\alpha_f}{\alpha_{fw}} \right] v_f \right| \right] = \frac{64\mu_f}{D\rho_f} = \lim_{|\alpha_f v_f| \rightarrow 0} (\lambda'_f |\alpha_f v_f|),$$

$$\lim_{\left| \left[\frac{\alpha_g}{\alpha_{gw}} \right] v_g \right| \rightarrow 0} \left[\lambda_g \left| \left[\frac{\alpha_g}{\alpha_{gw}} \right] v_g \right| \right] = \frac{64\mu_g}{D\rho_g} = \lim_{|\alpha_g v_g| \rightarrow 0} (\lambda'_g |\alpha_g v_g|),$$

2.1.3-80

and the velocity terms are evaluated such that

$$\lim_{|v_f| \rightarrow 0} |v_f| = \epsilon = \lim_{|v_g| \rightarrow 0} |v_g| .$$

2.1.3-81

Hence, for stagnant flow or single-phase conditions, a positive and finite friction coefficient is always calculated. Thus, the numerical possibility of an infinite or negative friction coefficient is eliminated.

In Equations 2.1.3-78 and 2.1.3-79, flow regime effects are included in the terms (α_{fw}/α_f) and (α_{gw}/α_g) for the liquid and vapor, respectively. These terms are such that

$$\alpha_{fw} = 1 - \alpha_{gw} \quad 2.1.3-82$$

and

$$\alpha_f = 1 - \alpha_g . \quad 2.1.3-83$$

Equations 2.1.3-80 and 2.1.3-83 are restricted such that as overall phasic volume fraction disappears its corresponding wall film volume fraction disappears so that

$$\lim_{\alpha_f \rightarrow 0} \left(\frac{\alpha_{fw}}{\alpha_f} \right) = 1 \quad \text{and} \quad \lim_{\alpha_f \rightarrow 0} \left(\frac{\alpha_{gw}}{\alpha_g} \right) = 1, \quad 2.1.3-84$$

and similarly,

$$\lim_{\alpha_g \rightarrow 0} \left(\frac{\alpha_{gw}}{\alpha_g} \right) = 1 \quad \text{and} \quad \lim_{\alpha_g \rightarrow 0} \left(\frac{\alpha_{fw}}{\alpha_f} \right) = 1. \quad 2.1.3-85$$

Flow Regime Factors for Phasic Wall Friction

Phasic wall friction is expressed in terms of wall shear stress, which in turn requires knowledge of the surface area wetted by each phase. From the flow regime model discussed in section 2.1.3.1, expressions for the wall film phasic volume fractions can be derived. Using these expressions, the phasic wall friction factors that appear in Equations 2.1.3-56 and 2.1.3-57 may then be completed.

In the flow regime map, seven flow regimes are modeled, which are: for pre-CHF heat transfer, the bubbly, slug, and annular mist; for post-CHF heat transfer, the inverted-annular, inverted-slug and mist; and for stratified flow, the vertically and horizontally stratified. For the transition regime between pre- and post-CHF heat transfer, an interpolation scheme is also implemented in the code.

To implement flow regime effects in the two-phase wall friction model, first consider the wall liquid and vapor volume fractions.

These terms are

$$\frac{p_f}{p} = \alpha_{fw} \quad , \quad 2.1.3-86$$

which represents the liquid volume fraction in the wall film, and

$$\frac{p_g}{p} = \alpha_{gw} \quad , \quad 2.1.3-87$$

which represents the vapor volume fraction in the wall film where the terms p_f , p_g , and p are the perimeters wetted by the liquid, vapor, and mixture, respectively. Then, from the flow regime model these are formulated for all of the flow regimes as follows:

For the bubbly regime

$$\alpha_{fw} = \alpha_f \text{ and } \alpha_{gw} = \alpha_g \quad , \quad 2.1.3-88$$

where α_f , α_g are the overall liquid and vapor volume fraction, respectively.

For the slug regime

$$\alpha_{fw} = 1 - \alpha_{gs} \text{ and } \alpha_{gw} = \alpha_{gs} \quad , \quad 2.1.3-89$$

where α_{gs} is given by Equation 2.1.3-29.

For the annular-mist regime

$$\alpha_{fw} = (\alpha_{ff})^{\frac{1}{4}} \text{ and } \alpha_{gw} = 1 - (\alpha_{ff})^{\frac{1}{4}} \quad , \quad 2.1.3-90$$

where α_{ff} is given by Equation 2.1.3-34.

For the inverted-annular regime

$$\alpha_{gw} = (\alpha_{gg})^{\frac{1}{4}} \quad \text{and} \quad \alpha_{fw} = 1 - (\alpha_{gg})^{\frac{1}{4}} , \quad 2.1.3-91$$

where α_{gg} is the inverted form of Equation 2.1.3-34.

For the inverted-slug regime

$$\alpha_{fw} = \alpha_{fs} \quad \text{and} \quad \alpha_{gw} = 1 - \alpha_{fs} , \quad 2.1.3-92$$

where α_{fs} is the inverted form of Equation 2.1.3-29.

For the mist regime

$$\alpha_{fw} = \alpha_f \quad \text{and} \quad \alpha_{gw} = \alpha_g , \quad 2.1.3-93$$

which is similar to the bubbly regime.

For the vertically stratified regime

$$\alpha_{fw} = \alpha_f \quad \text{and} \quad \alpha_{gw} = \alpha_g . \quad 2.1.3-94$$

For the horizontally stratified regime

$$\alpha_{fw} = 1 - \frac{\theta}{\pi} \quad \text{and} \quad \alpha_{gw} = \frac{\theta}{\pi} , \quad 2.1.3-95$$

where θ results from the solution of Equations 2.1.3-17 and 2.1.3-18.

The Friction Factor Model

In RELAP5, the friction factor is computed using a high speed calculational scheme representing an engineering approximation to the Colebrook correlation.³⁹

The friction factor model is simply an interpolation scheme linking the laminar, laminar-turbulent transition, and turbulent-full turbulent transition regimes. The laminar friction factor is calculated as

$$\lambda_L = \frac{64}{R} \quad 0 \leq R \leq 2000, \quad 2.1.3-96$$

where R is the Reynolds number. The laminar-turbulent friction factor is interpolated as

$$\lambda_{L,T} = 5.285[1.189 - (4000/R)^{0.25}](\lambda_{t,4000} - \lambda_{L,2000}) + \lambda_{L,2000} \quad 2000 < R < 4000, \quad 2.1.3-97$$

where $\lambda_{L,2000}$ is the laminar factor at a Reynolds number of 2000 and where $\lambda_{t,4000}$ is the turbulent friction factor at a Reynolds number of 4000. The interpolation factor is defined such that

$$0 \leq 5.285 \left[1.189 - \left(\frac{4000}{R} \right)^{0.25} \right] \leq 1.0 \quad 2.1.3-98$$

The turbulent-full turbulent friction factor is interpolated as

$$\lambda_{t,tt} = \frac{\left[1 - \left(\frac{4000}{R} \right)^{0.25} \right]}{\left[1 - \left(\frac{4000}{R_c} \right)^{0.25} \right]} (\lambda_{tt} - \lambda_{t,4000}) + \lambda_{t,4000} \quad 4000 \leq R \leq R_c, \quad 2.1.3-99$$

where the interpolation factor is defined such that

$$0 \leq \frac{\left[1 - \left(\frac{4000}{R}\right)^{0.25}\right]}{\left[1 - \left(\frac{4000}{R_c}\right)^{0.25}\right]} \leq 1 \quad 2.1.3-100$$

and R_c is the critical Reynolds number at which the Colebrook equation gives a constant friction factor of

$$\lambda_{tt} = [1.74 - 2\text{Log}_{10}(2\epsilon/D)]^{-2}, \quad 2.1.3-101$$

and where ϵ is the surface roughness.

The critical Reynolds number is given as

$$R_c = \frac{378.3}{\frac{2\epsilon}{D} \lambda_{tt}^{0.5}}, \quad 2.1.3-102$$

where $2\epsilon/D \geq 10^{-9}$.

If precise values for $\lambda_{t,4000}$ are used, Equations 2.1.3-96 and 2.1.3-97 are identical to the formulations used in the Colebrook friction factor model for the laminar and transition regimes. Equation 2.1.3-101 is also identical to the solution of the Colebrook model for Reynolds numbers greater than the critical Reynolds number. Therefore, the interpolation scheme in the friction factor model lies in the formulation of Equation 2.1.3-99, which is linear in $(1/R)^{0.25}$. The maximum deviation between the friction factor calculated using Equation 2.1.3-99 and that calculated using the Colebrook correlation is within the third significant figure for a moderate ϵ/D of 0.0003, and as ϵ/D increases the deviation decreases until at an ϵ/D such that $R_c <$

4000 the value given by Equation 2.1.3-99 is precisely that of Equation 2.1.3-101. In any case, the results calculated using Equation 2.1.3-99 are negligibly different from those calculated by the Colebrook equation. This accuracy is achieved using a good estimate for $\lambda_{t,4000}$ given by

$$\lambda_{t,4000} = \lambda_0 + K(\lambda_{tt} - \lambda_1) , \quad 2.1.3-103$$

where λ_0 is a constant evaluated from the Blasius smooth pipe formula at a Reynolds number of 4000, such that

$$\lambda_0 = 0.0398. \quad 2.1.3-104$$

The coefficients have been evaluated as

$$K = 0.558 \quad \text{and} \quad \lambda_1 = 0.0158 \quad 2.1.3-105$$

by the method of least squares.

In calculational schemes, it is desirable to evaluate the friction factor in terms of $\lambda|\psi v|$ so that the limiting terms will be correctly calculated as defined by Equations 2.1.3-80. For this case, the Reynolds number must be defined as

$$R = \frac{\rho D}{\mu} |\psi v| \quad 2.1.3-106$$

and Equation 2.1.3-97 can be rewritten as

$$\lambda|\psi v| = \lambda_L^* + L[5.285(1.189 - R^*)]\{L[(1 - R^*)/(1 - R_C^*)]\} \cdot$$

$$(\lambda_{tt} - \lambda_{t,4000})|\psi v| + \lambda_{t,4000}|\psi v| - \lambda_L^* , \quad 2.1.3-107$$

where $L(y)$ denotes a general limit function such that

$$0 \leq L(y) \leq 1 \quad , \quad 2.1.3-108$$

$$R^* = (4000/R)^{.25} \quad \text{and} \quad R_C^* = (4000/R_C)^{.25} \quad , \quad \text{and} \quad 2.1.3-109$$

$$R \geq 2000 \quad \text{and} \quad R_C \geq 4000 \quad , \quad 2.1.3-110$$

and where the laminar term is

$$\lambda_L^* = \frac{64\mu}{\rho D} \quad . \quad 2.1.3-111$$

The accuracy of the improved friction factor model can be observed in Figure 2.1.3-4, which is a plot of results calculated by Equation 2.1.3-107 compared to similar results calculated by the Colebrook equation. Four curves are plotted for each model representing roughness to diameter ratios of $2\epsilon/D = 0.0, 0.0006, 0.02, \text{ and } 0.1$, respectively. Equation 2.1.3-107 results are plotted and labeled as INTERP in the plot legend. Colebrook equation results are plotted and labeled as COLBRK in the plot legend. The axes of the plot are scaled logarithmically.

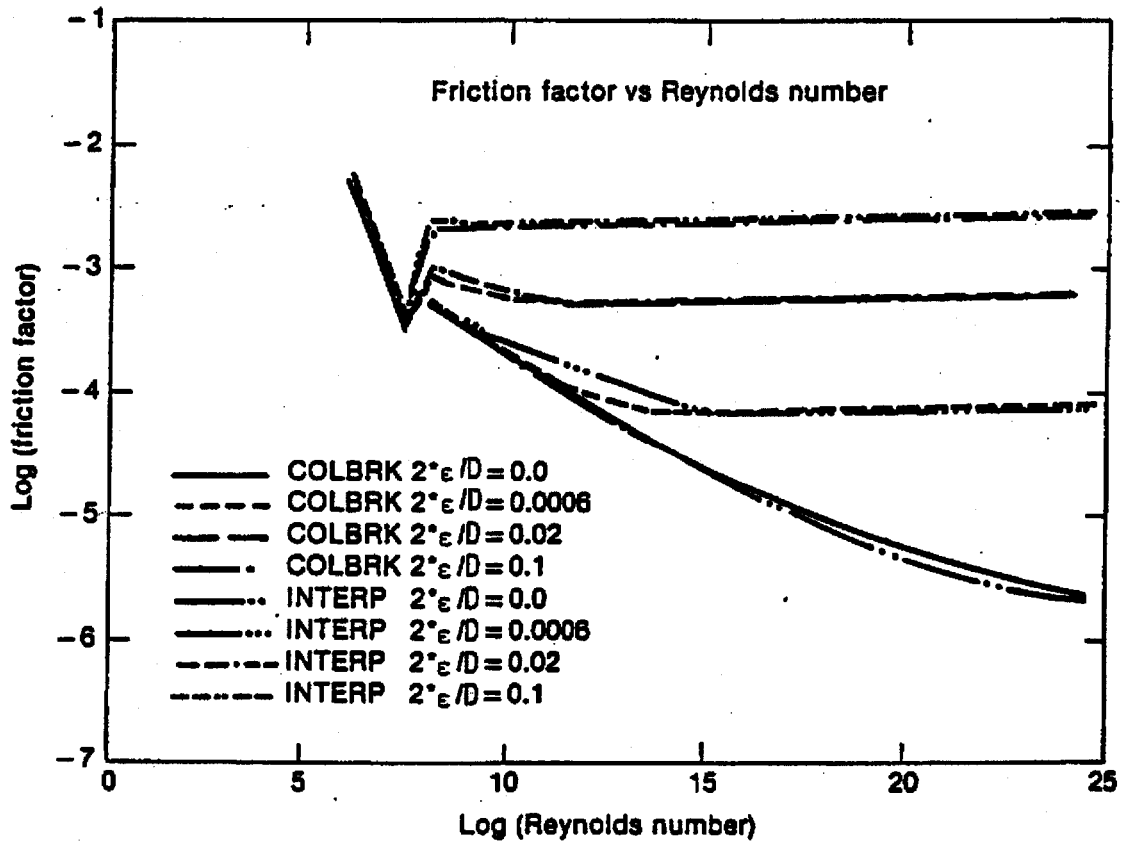


Figure 2.1.3-4. Comparison of Friction Factor for the Colebrook and the Improved RELAP5 Friction Factor Models.

2.1.3.4. Interphase Heat and Mass Transfer

The interface mass transfer is modeled according to the thermodynamic process, interphase heat transfer regime, and flow regime. After the thermodynamic process is decided, the flow regime map discussed in section 2.1.3.1 is used to determine the phasic interfacial area and to select the interphase heat transfer correlation.

The mass transfer model is formulated so that the net interfacial mass transfer rate is composed of two components which are the mass transfer rate at the wall and the mass transfer rate in the bulk fluid, which is expressed as

$$\Gamma_g = \Gamma_w + \Gamma_{ig} \quad . \quad 2.1.3-112$$

For system components in which wall heat transfer is modeled, mass transfer at the wall is calculated according to the wall heat transfer model and mass transfer to the bulk fluid is calculated according to the interphase heat transfer regime and flow regime. For system components in which wall heat transfer is not modeled, mass transfer at the wall is ignored and mass transfer in the bulk fluid is modeled according to the interphase heat transfer regime and flow regime.

For components modeling wall heat transfer processes, the interfacial mass transfer at the wall is calculated from the total wall-to-liquid heat transfer minus the wall-to-liquid convective heat transfer. For these processes, the heat transfer model developed by Chen, as discussed in section 2.2.2.1, is used to model the total wall to liquid heat transfer. The Chen model assumes that the total wall-to-liquid heat transfer is composed of boiling and convective heat transfer and that the interfacial mass transfer at the wall is mainly due to boiling heat transfer. Consequently, the contribution due to convective heat transfer must be subtracted from the total wall to liquid heat transfer in

order to calculate the interfacial mass transfer at the wall. Correlations used to calculate interfacial mass transfer at the wall for different heat transfer regimes are discussed in section 2.2.2.

For components not modeling wall heat transfer and for the general bulk mass transfer processes, the interfacial mass transfer in the bulk fluid is modeled according to the flow regime. In the bubbly flow regime, for the liquid side, interfacial mass transfer is the larger of either the model for bubble growth developed by Plesset and Zwick⁴⁷ or the model for convective heat transfer for a spherical bubble,⁴⁸ and for the vapor side, an interphase heat transfer coefficient is assumed that is high enough to drive the vapor temperature toward saturation. Analogously, in the annular mist regime, for the vapor side, a convective heat transfer model for a spherical droplet is used for the interphase heat transfer coefficient, and for the liquid side, an interphase heat transfer coefficient is assumed that is high enough to drive the liquid temperature toward saturation. Correlations used to calculate interfacial mass transfer in the bulk fluid are summarized in Table 2.1.3-1.

For condensation processes, the interfacial mass transfer in the bulk fluid, for the liquid side, is calculated by the Unal bubble collapse model⁴⁹ in the bubbly flow regime and by the Theofanous interfacial condensation model⁵¹ in the annular mist flow regime and for the vapor side, a large interphase heat transfer coefficient is assumed in order to drive the vapor temperature toward saturation.

Table 2.1.3-1. RELAP/MOD2 Interfacial Mass Transfer in Bulk Fluid.

Depressurization Process ($T_f > T_{sat}$)

1. Bubbly Flow Regimes:

$$Q_{if} = H_{if} (T_s - T_f) ,$$

where

$$H_{if} = \text{MAX} \left[\begin{array}{l} \frac{12}{\pi d_b^2} \Delta T_{sat} \frac{\rho_f (C_p) k_f}{\rho_g h_{fg}} \quad (\text{Plesset-Zwick})^{47} \quad (\text{w/m}^3\text{-K}) \\ \frac{6\alpha_g K_f}{d_b^2} (2 + 0.74 \text{Re}_b^{0.5} \text{Pr}_f^{0.333}) \quad (\text{Force convection for single bubble}),^{42} \end{array} \right.$$

$$\text{Re}_b = \frac{\rho_f d_b |v_g - v_f|}{\mu_f} \quad (\text{Bubble Reynolds number}),$$

d_b = bubble diameter (m),

$$Q_{ig} = H_{ig} (T_s - T_g), \text{ and}$$

where

$$H_{ig} = \frac{6\alpha_g}{d_b^2} k_g \text{Nu}_{ib} \quad \text{and}$$

$$\text{Nu}_{ib} = 10^4 .$$

2. Annular-Mist Regime:

$$Q_{if} = H_{if} (T_s - T_f),$$

Table 2.1.3-1. (Continued)

where

$$H_{if} = \frac{6(1-\alpha_g)}{d_b^2} k_f Nu_{id}$$

$$Nu_{id} = 10^5, \text{ and}$$

$$Q_{ig} = H_{ig} (T_s - T_g),$$

where

$$H_{ig} = \frac{6(1-\alpha_g)}{d_d^2} \cdot k_g (2. + 0.74 Re_d^{0.5} Pr_g^{0.33})$$

$$+ 0.0023 (Re)_g^{0.8} \cdot k_g \cdot \frac{(\alpha_g)^{0.5}}{D_e^2},$$

$$Re_d = \frac{\rho_g d_d |v_g - v_f|}{\mu_g} \text{ (Droplet Reynolds number), and}$$

$$d_d = \text{drop diameter (m).}$$

Heat Transfer Process ($T_f \leq T_{sat}$)

1. Bubbly Flow Regime:

$$Q_{if} = H_{if} (T_s - T_f),$$

Table 2.1.3-1. (Continued)

where

$$H_{if} = \frac{3\phi C h_{fg} \alpha_g}{\frac{1}{\rho_g} - \frac{1}{\rho_f}} \quad (\text{Unal's correlation}),^{49} \quad \text{and}$$

where

$$\phi = \begin{cases} 1 & v_f \leq 0.61 \text{ (m/s)} \\ [1.639 v_f]^{0.47} & v_f > 0.61 \text{ (m/s)} \end{cases}$$

$$C = \begin{cases} 61 - 6.489 \cdot 10^{-5} (P - 1.7 \cdot 10^5) & P \leq 10^6 \text{ (Pa)} \\ 2.3 \cdot 10^9 / P^{1.418} & P > 10^6 \text{ (Pa)} \end{cases}$$

P = pressure (Pa), and

$$Q_{ig} = H_{ig} (T_s - T_g),$$

where

$$H_{ig} = \frac{6\alpha_g}{d_b^2} k_g \text{Nu}_{ib} \quad \text{and}$$

$$\text{Nu}_{ib} = 10^4.$$

Table 2.1.3-1. (Continued)

2. Annular-Mist Flow Regime:

Similar to the depressurization process.

Condensation Process

1. Bubbly Flow Regime:

Similar to the heat transfer process.

2. Annular-Mist Flow Regime:

$$Q_{if} = H_{if} (T_s - T_f),$$

where

$$H_{if} = 6 \left[2. + \frac{8. (T_s - T_f)}{T_m - T_f} \right] k_f (1 - \alpha_g) / d_d^2 \\ + 10^{-3} \cdot \rho_f \cdot v_f \cdot C_{pf} \cdot A_{film},$$

A_{film} = area of film per unit volume, and

$$T_m = \frac{T_s - T_f}{1 + C_{pg}(T_g - T_s)/h_{fg}}$$

The first term on the right side uses the condensation of a single droplet in superheated steam model developed by Brown.⁵⁰

Table 2.1.3-1. (Continued)

The second term on the right side uses the film condensation model developed by Theofanous.⁵¹

$$Q_{ig} = H_{ig} (T_s - T_f) ,$$

where

$$H_{ig} = \frac{6 \cdot (1-\alpha)}{d_d^2} k_g \cdot Nu_{id} \text{ and}$$

$$Nu_{id} = 10^5 .$$

2.1.3.5. Horizontal Stratification Entrainment Model

Under stratified conditions in horizontal components, the void fraction of flow through a junction may be different from the upstream volume void fraction. Consequently, the regular donoring scheme for junction void fraction is no longer appropriate because vapor may be pulled through the junction and liquid may also be entrained and pulled through the junction. The correlations describing the onset of vapor pull through and liquid entrainment for various geometrical conditions were summarized by Zuber.⁷³

The incipient liquid entrainment is determined by the criterion that

$$v_g \geq v_{ge} \quad , \quad 2.1.3-113$$

where v_{ge} is given by the expressions

$$v_{ge} = 5.7 \left[\frac{D-ll}{d} \right]^{3/2} \left[\frac{B_y (\rho_f - \rho_g) (D-ll)}{\rho_g} \right]^{1/2} \quad 2.1.3-114$$

for an upwardly oriented junction⁷³, and

$$v_{ge} = 3.25 \left[\frac{D/2-ll}{d} \right]^2 \left[\frac{B_y (\rho_f - \rho_g) (D/2-ll)}{\rho_g} \right]^{1/2} \quad 2.1.3-115$$

for a centrally oriented junction,^{74,75} where d is the junction diameter and ll is the liquid level.

The condition for the onset of vapor pull-through is determined by the criterion

$$v_f > v_{fp} \quad , \quad 2.1.3-116$$

where

$$v_{fp} = 3.25 \left(\frac{ll - D_c/2}{d} \right)^{5/2} \left[\frac{B_y (\rho_f - \rho_g) d}{\rho_f} \right]^{1/2}, \quad 2.1.3-117$$

and where

$$c = \begin{cases} 1 & \text{for a centrally located or side junction} \\ 0 & \text{for downward oriented junction.}^{76,77} \end{cases}$$

Equations 2.1.3-113 through 2.1.3-117 together with the horizontal stratification criterion (Equation 2.1.3-15) from section 2.1.3.1, form the basis for calculating the junction void fraction under stratification conditions.

For liquid entrainment, the junction liquid fraction, $\alpha_{f,j}$, is related to the donor volume liquid fraction, $\alpha_{f,K}$, by the expression

$$\alpha_{f,j} = \alpha_{f,K} \left[1 - \exp(-C_1 v_g/v_{ge} - 10v_g^2/v_{gL}^2) \right], \quad 2.1.3-118$$

where v_{gL} is from Equation 2.1.3-16. For vapor pull-through, the junction void fraction, $\alpha_{g,j}$, is given by the expression

$$\alpha_{g,j} = \alpha_{g,K} \left[1 - \exp(-C_2 v_f/v_{fp} - 10v_g^2/v_{gL}^2) \right]. \quad 2.1.3-119$$

The constants C_1 and C_2 for Equations 2.1.3-118 and 2.1.3-119 are obtained by comparisons of code calculations with experimental data.⁷⁸⁻⁸⁰

2.1.3.6. Vertical Stratification Model

The vertical stratification model has been installed so that the nonequilibrium modeling capability can include repressurization transients in which subcooled liquid and superheated vapor may coexist in the pressurizer and/or other locations in the primary coolant system. A version⁸⁸ of this model has been modified, and this modified version is described in this section.

For this model, a vertically stratified flow regime is included in the vertical flow regime map as shown in Figure 2.1.3-2. A vertical volume is detected as being vertically stratified when the difference between the void fraction in the volume above and that in the volume below is greater than 0.50.

The criterion is based on the Taylor bubble velocity in Reference 28. The factor F is calculated first.

$$F = \left[\frac{v_g}{0.35 [gD(\rho_f - \rho_g)/\rho_f]^{1/2}} \right]^3 \quad 2.1.3-120$$

If $F \leq 1$, then the vertical stratification model is not used and the normal vertical flow regime map is used. If $F > 1$, then a linear interpolation is used between the normal flow regime values for the interphase mass transfer, wall heat transfer, and the interphase drag coefficients.

For a vertically stratified volume, the interphase mass transfer, wall heat transfer, and interphase drag coefficients are modified. The interphase mass transfer is given in terms of the interphase heat transfer. The interphase heat transfer rate per unit volume (neglecting contribution from the wall) is given as

$$Q_{if} = h_{if} \frac{A_c}{V} (T^s - T_f) \quad 2.1.3-121$$

and

$$Q_{ig} = h_{ig} \frac{A_c}{V} (T^S - T_g), \quad 2.1.3-122$$

where h_{if} and h_{ig} are the liquid side and vapor side interface heat transfer coefficients, A_c is the cross-sectional flow area (equal to the interfacial area when stratified), and V is the volume. A value of $10 \text{ w/m}^2\text{-K}$ is used for both h_{if} and h_{ig} in the vertical stratification model. The wall heat transfer coefficients h_{wf} and h_{wg} are partitioned with respect to their corresponding vapor and liquid fractions (α_f and α_g) when vertical stratification occurs. For the junction above the vertically stratified volume, an interphase drag coefficient of $10^{-1} \text{ N-s}^2/\text{m}^5$ is used.

There is no specific edit information output for a vertically stratified volume.

2.1.3.7. Water Packing Mitigation Scheme

Large pressure spikes that cannot be explained by known physical phenomena are at times encountered when Eulerian type codes are used to analyze integral systems tests or reactor accidents. These spikes usually do not affect overall transient behavior, but in some cases may affect important localized behavior (e.g. delivery of coolant to the reactor core). A water packing scheme has been installed to mitigate these spikes.

The water packing scheme closely follows the method used in the TRAC code.^{89,90} It involves a detection scheme to determine when a pressure change occurs in a volume containing mostly liquid. It then imposes changes to the momentum equations, followed by a recalculation of the pressure solution using the sparse matrix solver.

The detection logic used in the water packing scheme evolved from experience gained in running a vertical fill problem.⁹¹ The scheme requires a pressure increase of 0.23% or more, a void fraction (α_g) less than or equal to 0.12, the liquid temperature (T_f) to be less than the saturation temperature (T^S), the volume to be flagged as vertically stratified, and the volume above to be highly voided. Thus a legitimate water hammer would not be detected in the water packing scheme.

The next part of the scheme involves altering the momentum equations so that only small pressure changes will occur in the volume that fills with water. The scheme involves modifying the coefficient that multiplies the pressure change in the filling volume. The modification multiplies this coefficient by 10^6 . This is discussed in more detail in the next paragraph. Since the pressure solution is rejected when water packing occurs, the pressure calculation is repeated using the sparse matrix solver.

The finite difference form of the phasic momentum equations used can be written

$$v_{f,j}^{n+1} = v_{f,j}^{n,exp} - (VFDP)_j^n \left[(P_L^{n+1} - P_L^n) - (P_K^{n+1} - P_K^n) \right] \quad 2.1.3-123$$

and

$$v_{g,j}^{n+1} = v_{g,j}^{n,exp} - (VGDP)_j^n \left[(P_L^{n+1} - P_L^n) - (P_K^{n+1} - P_K^n) \right] \quad 2.1.3-124$$

where $v_{f,j}^{n,exp}$ and $v_{g,j}^{n,exp}$ contain all the old time terms and $(VFDP)_j^n$ and $(VGDP)_j^n$ contain all the terms that multiply the pressure change. Consider the filling example in Figure 2.1.3-5 where volume K is full of liquid and volume L is full of steam. The change to the momentum equations is to multiply the $(P_K^{n+1} - P_K^n)$ terms by 10^6 , which forces P_K^{n+1} to be approximately the

same as P_K^n . Thus, the water filled K volume will not show a pressure spike. The momentum equations then have the form

$$v_{f,j}^{n+1} = v_{f,j}^{n,exp} - (VFDP)_j^n (P_L^{n+1} - P_L^n) + (VFDP)_j^n (10^6) (P_K^{n+1} - P_K^n)$$

2.1.3-125

and

$$v_{g,j}^{n+1} = v_{g,j}^{n,exp} - (VGDP)_j^n (P_L^{n+1} - P_L^n) + (VGDP)_j^n (10^6) (P_K^{n+1} - P_K^n).$$

2.1.3-126

In addition to the modification of the momentum equation, the interphase drag is reduced to $10^{-1} (N - s^2)/m^5$ for junction j.

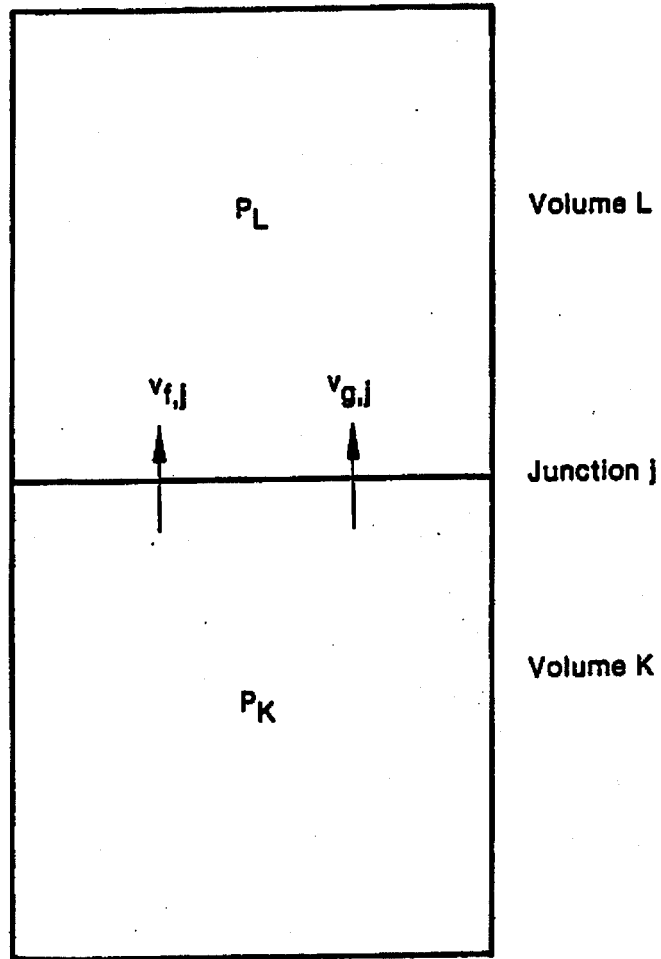


Figure 2.1.3-5. Two Vertical Vapor/Liquid Volumes.

2.1.4. Special Process Models

Certain models in RELAP5/MOD2 have been developed to simulate special processes. These models, described in the following subsections, include: choked flow, abrupt area change, crossflow junction, and branch models.

2.1.4.1. Choked Flow Models

Two mutually exclusive models are available for calculating choked flow in RELAP5/MOD2. The first option uses the original built-in Ransom-Trapp method. The second option uses a table interpolation with any of the four following critical mass flux tables: Extended Henry-Fauske, Moody, HEM, or Murdock-Bauman.

Ransom-Trapp Choked Model

A choked flow model developed by Ransom and Trapp^{62,18} is included in RELAP5 primarily for calculation of the mass discharge from the system at a pipe break or a nozzle. Generally, the flow at the break or nozzle is choked until the system pressure nears the containment pressure. The choked flow model is used to predict if the flow is choked at the break or nozzle and, if it is, to establish the discharge boundary condition. In addition, the choked flow model can be used to predict existence of and calculate choked flow at internal points in the system.

Choking is defined as the condition wherein the mass flow rate becomes independent of the downstream conditions (that point at which further reduction in the downstream pressure does not change the mass flow rate). The fundamental reason that choking occurs is that acoustic signals can no longer propagate upstream. This occurs when the fluid velocity equals or exceeds the propagation velocity. The choked flow model is based on a definition that is established by a characteristic analysis using time-dependent differential equations.

Consider a system of n first-order quasi-linear, partial differential equations of the form

$$A(U) (\partial U / \partial t) + B(U) (\partial U / \partial x) + C(U) = 0 \quad . \quad 2.1.4-1$$

The characteristic directions (or characterization velocities) of the system are defined^{63,64} as the roots, $\lambda_i (i \leq n)$, of the characteristic polynomial

$$(A\lambda - B) = 0 \quad . \quad 2.1.4-2$$

The real part of any root, λ_i , give the velocity of signal propagation along the corresponding characteristic path in the space/time plane. An imaginary part of any complex root, λ_i , gives the rate of growth or decay of the signal propagating along the respective path. For a hyperbolic system in which all the roots of Equation 2.1.4-2 are real and nonzero, the number of boundary conditions required at any boundary point equals the number of characteristic lines entering the solution region as time increases. If we consider the system (Equation 2.1.4-1) for a particular region $0 \leq x \leq L$, and examine the boundary conditions at $x = L$, as long as any λ_i is less than zero, we must supply some boundary information to obtain the solution. If λ_i is greater than or equal to zero, no boundary conditions are needed at $x = L$, and the interior solution is unaffected by conditions beyond this boundary.

A choked condition exists when no information can propagate into the solution region from the exterior. Such a condition exists at the boundary point, $x = L$, when

$$\lambda_j \geq 0 \text{ for all } j \leq n \quad . \quad 2.1.4-3$$

These are the mathematical conditions satisfied by the equations of motion for a flowing fluid when reduction in downstream

pressure ceases to result in increased flow rate. It is well-known⁶⁵ that the choked condition for single-phase flow occurs when the fluid velocity just equals the local sound speed. For this case, one of the λ_j 's is just equal to zero. For the two-phase case, it is possible for all λ_j 's to be greater than zero under special conditions which can exist during discharge of a subcooled liquid.

During the course of the RELAP5 development, extensive investigation was carried out to determine two-phase choked flow criterion under two assumed conditions:^a (a) thermal equilibrium between phases, and (b) adiabatic phases without phase change (frozen).⁶⁶ The frozen assumption was in poor agreement with data, compared to the thermal equilibrium assumption. Therefore, the thermal equilibrium assumption with slip is used as the basis for the RELAP5 choked flow criterion. In the following paragraphs, theoretical aspects of choked flow are discussed.

Ransom-Trapp Model Choking Criterion for Nonhomogeneous, Equilibrium Two-Phase Flow

The two-fluid model for the conditions of thermal equilibrium (equilibrium interphase mass transfer) is described by the overall mass continuity equation, two phasic momentum equations, and the mixture entropy equation. This system of equations is

$$\partial(\alpha_g \rho_g + \alpha_f \rho_f) / \partial t + \partial(\alpha_g \rho_g v_g + \alpha_f \rho_f v_f) / \partial x = 0, \quad 2.1.4-4$$

$$\begin{aligned} \alpha_g \rho_g [\partial v_g / \partial t + v_g (\partial v_g / \partial x)] + \alpha_g (\partial P / \partial x) \\ + C \alpha_g \alpha_f \rho (\partial v_g / \partial t - \partial v_f / \partial t) = 0, \quad 2.1.4-5 \end{aligned}$$

^aThe hydrodynamic model is not based on either of these assumptions; however, the purpose of this analysis is simply to establish a criterion for choked flow and thus, there is no conflict with the basic hydrodynamic model.

$$\alpha_f \rho_f [\partial v_f / \partial t + v_f (\partial v_f / \partial x)] + \alpha_f (\partial P / \partial x) + C \alpha_f \alpha_g \rho (\partial v_f / \partial t - \partial v_g / \partial t) = 0, \quad 2.1.4-6$$

and

$$\partial (\alpha_g \rho_g S_g + \alpha_f \rho_f S_f) / \partial t + \partial (\alpha_g \rho_g S_g v_g + \alpha_f \rho_f S_f v_f) / \partial x = 0. \quad 2.1.4-7$$

The momentum equations include the interphase force terms due to relative acceleration.¹⁶ These force terms have a significant effect on wave propagation velocity and consequently on the choked flow velocity. The particular form chosen is frame invariant and symmetrical, and the coefficient of virtual mass, $C \alpha_g \alpha_f \rho$, is chosen to ensure a smooth transition between pure vapor and pure liquid. For a dispersed flow, the constant, C , has a theoretical value of 0.5, whereas for a separated flow, the value may approach zero. The energy equation is written in terms of mixture entropy, which is constant for adiabatic flow (the energy dissipation associated with interphase mass transfer and relative phase acceleration is neglected).

The nondifferential source terms, $C(U)$, in Equation 2.1.4-1 do not enter into the characteristic analysis or affect the propagation velocities. For this reason, the source terms associated with wall friction, interphase drag, and heat transfer are omitted for brevity in Equations 2.1.4-4 through 2.1.4-7.

In the thermal equilibrium case, ρ_g , ρ_f , S_g , and S_f are known functions of the pressure only (the vapor and liquid values along the saturation curve). The derivatives of these variables are designated by an asterisk as follows

$$\rho_f^* = d\rho_f^S / dP \text{ and } \rho_g^* = d\rho_g^S / dP, \quad 2.1.4-8$$

and

$$s_f^* = ds_f^s/dP \text{ and } s_g^* = ds_g^s/dP \quad . \quad 2.1.4-9$$

The system of governing equations (Equations 2.1.4-4 through 2.1.4-7) can be written in terms of the four dependent variables, α_g , P , v_g , and v_f , by application of the chain rule and the property derivatives (Equations 2.1.4-8 and 2.1.4-9). Thus, the system of equations can be written in the form of Equation 2.1.4-1 where the A and B are fourth-order square coefficient matrices.

The characteristic polynomial that results is fourth-order in λ and factorization can only be carried out approximately to obtain the roots for λ , and establish the choking criterion. The first two roots are

$$\lambda_{1,2} = \frac{\left[\begin{aligned} & \left\{ \alpha_{fg} \rho_g + \rho C/2 \pm \left[(\rho C/2)^2 - \alpha_g \alpha_{fg} \rho_g \rho_f \right]^{1/2} \right\} v_g \\ & + \left\{ \alpha_{gf} \rho_f + \rho C/2 + \left[(\rho C/2)^2 - \alpha_g \alpha_{fg} \rho_g \rho_f \right]^{1/2} \right\} v_f \end{aligned} \right]}{(\alpha_{fg} \rho_g + \rho C/2) + (\alpha_{gf} \rho_f + \rho C/2)} \quad .$$

2.1.4-10

These two roots are obtained by neglecting the fourth-order factors relative to the second-order factors in $(\lambda - v_g)$ and $(\lambda - v_f)$. There are no first- or third-order factors. Inspection of Equation 2.1.4-10 shows that $\lambda_{1,2}$ have values between v_g and v_f ; thus, the fourth-order factors $(\lambda - v_g)$ and $(\lambda - v_f)$ are small (i.e., neglecting these terms is justified). The values for $\lambda_{1,2}$ may be real or complex depending on the sign of the quantity $[(\rho C/2)^2 - \alpha_g \alpha_{fg} \rho_g \rho_f]$.

The remaining two roots are obtained by dividing out the quadratic factor containing $\lambda_{1,2}$, neglecting the remainder, and subsequent factorization of the remaining quadratic terms. [This procedure can be shown to be analogous to neglecting the second- and higher-order terms in the relative velocity, $(v_g - v_f)$.] The remaining roots are

$$\lambda_{3,4} = v + D(v_g - v_f) \pm a, \quad 2.1.4-11$$

where

$$v = (\alpha_g \rho_g v_g + \alpha_f \rho_f v_f) / \rho, \quad 2.1.4-12$$

$$a = a_{\text{He}} \left\{ [C_p^2 + \rho(\alpha_g \rho_f + \alpha_f \rho_g)] / (C_p^2 + \rho_g \rho_f) \right\}^{1/2}, \quad 2.1.4-13$$

and

$$D = 0.5 \left[\frac{(\alpha_g \rho_f - \alpha_f \rho_g)}{(\rho C + \alpha_f \rho_g + \alpha_g \rho_f)} + \frac{\rho_g \rho_f (\alpha_f \rho_f - \alpha_g \rho_g)}{\rho (\rho_g \rho_f + C_p^2)} \right. \\ \left. - a_{\text{He}}^2 \frac{\rho [\alpha_g \rho_g^2 S_g^* + \alpha_f \rho_f^2 S_f^*]}{\rho_g \rho_f (S_g - S_f)} \right]. \quad 2.1.4-14$$

The quantity, a_{He} , is the homogeneous equilibrium speed of sound. The roots, $\lambda_{3,4}$, have only real values.

The general nature and significance of these roots is revealed by applying the characteristic considerations. The speed of propagation of small disturbances is related to the values of the characteristic roots. In general, the velocity of propagation corresponds to the real part of a root and the growth or attenuation is associated with the complex part of the root.

Choking will occur when the signal, which propagates with the largest velocity relative to the fluid, is just stationary, that is,

$$\lambda^R = 0 \text{ for } j \leq 4 \quad 2.1.4-15$$

and

$$\lambda^R \geq 0 \text{ for all } i \neq j \quad 2.1.4-16$$

The existence of complex roots for $\lambda_{1,2}$ makes the initial boundary value problem ill-posed. This problem has been discussed by many investigators^{13,20} and the addition of any small, second-order viscous effects renders the problem well-posed.^{13,21} The whole phenomenon of systems with mixed orders of derivatives and a first-order system with the addition of a small, second-order term, has been discussed and analyzed by Whitham.⁶⁴ He has shown that the second-order viscous terms give infinite characteristic velocities. However, very little information is propagated along these characteristic lines and the bulk of the information is propagated along characteristic lines defined by the first-order system. We conclude that the ill-posed nature of Equations 2.1.4-4 through 2.1.4-7 can be removed by the addition of small, second-order viscous terms that have little effect upon the propagation of information. Therefore, the choking criterion for the two-phase flow system analyzed here is established from Equation 2.1.4-15.

The explicit character of the choking criterion for the two-phase flow model defined by Equations 2.1.4-4 through 2.1.4-7 is examined. Since the two roots, $\lambda_{1,2}$, are between the phase velocities, v_f and v_g , the choking criterion is established from the roots, $\lambda_{3,4}$, and Equation 2.1.4-15. The choking criterion is

$$v + D(v_g - v_f) = \pm a. \quad 2.1.4-17$$

The choking criterion can be rewritten in terms of the mass mean and relative Mach numbers

$$M_v = v/a \text{ and } M_r = (v_g - v_f)/a \quad 2.1.4-18$$

as

$$M_v + DM_r = 1. \quad 2.1.4-19$$

This relation is similar to the choking criterion for single-phase flow where only the mass average Mach number appears and choking corresponds to a Mach number of unity.

The choking criterion (Equation 2.1.4-19) is a function of the two parameters, D and a . In Figure 2.1.4-1, a is plotted as a function of the void fraction, α_g , for a typical steam/water system at 7.5 MPa with C equal to zero (the stratified equilibrium sound speed), C equal to 0.5 (the typical value for a dispersed flow model), and in the limiting case when C become infinite (homogeneous equilibrium sound speed). From Figure 2.1.4-1 it is evident that the virtual mass coefficient has a

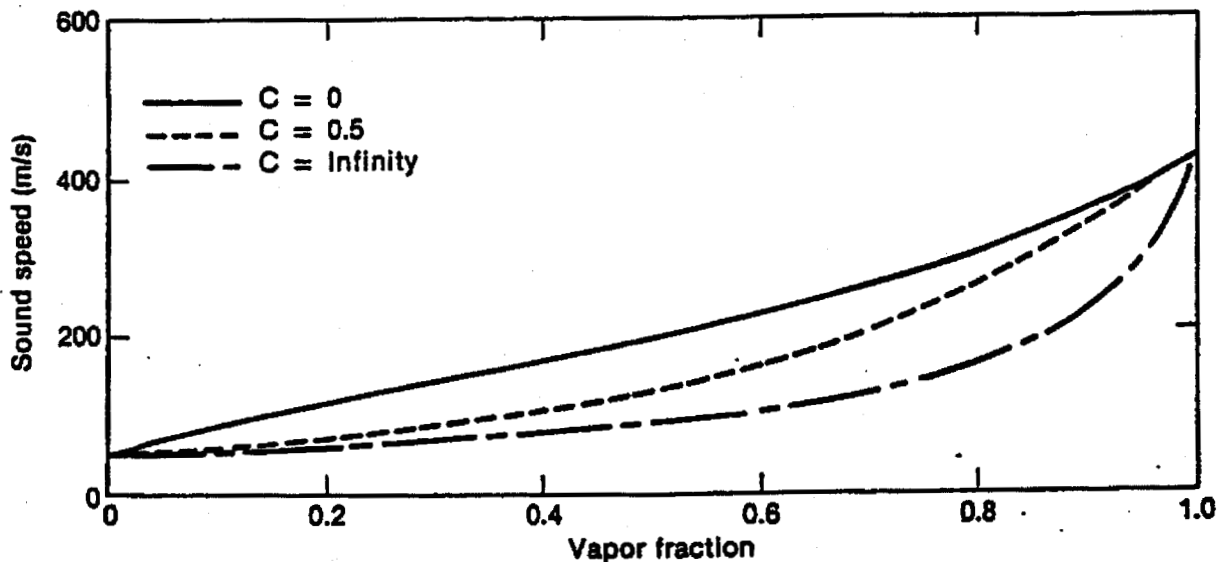


Figure 2.1.4-1. Equilibrium Speed of Sound as a Function of Void Fraction and Virtual Mass Coefficient.

significant effect upon the choked two-phase flow dynamics.¹⁴

To establish the actual choked flow rate for two-phase flow with slip, the relative velocity term in Equation 2.1.4-19 must also be considered. The relative Mach number coefficient, D , is shown in Figure 2.1.4-2 for values of C equal to 0, 0.5, and ∞ . It is evident from these results that the choked flow velocity can differ appreciably from the mass mean velocity when slip occurs. It is significant that the variation of the choked flow criterion from the homogeneous result is entirely due to velocity nonequilibrium, since these results have been obtained under the assumption of thermal equilibrium. The particular values of

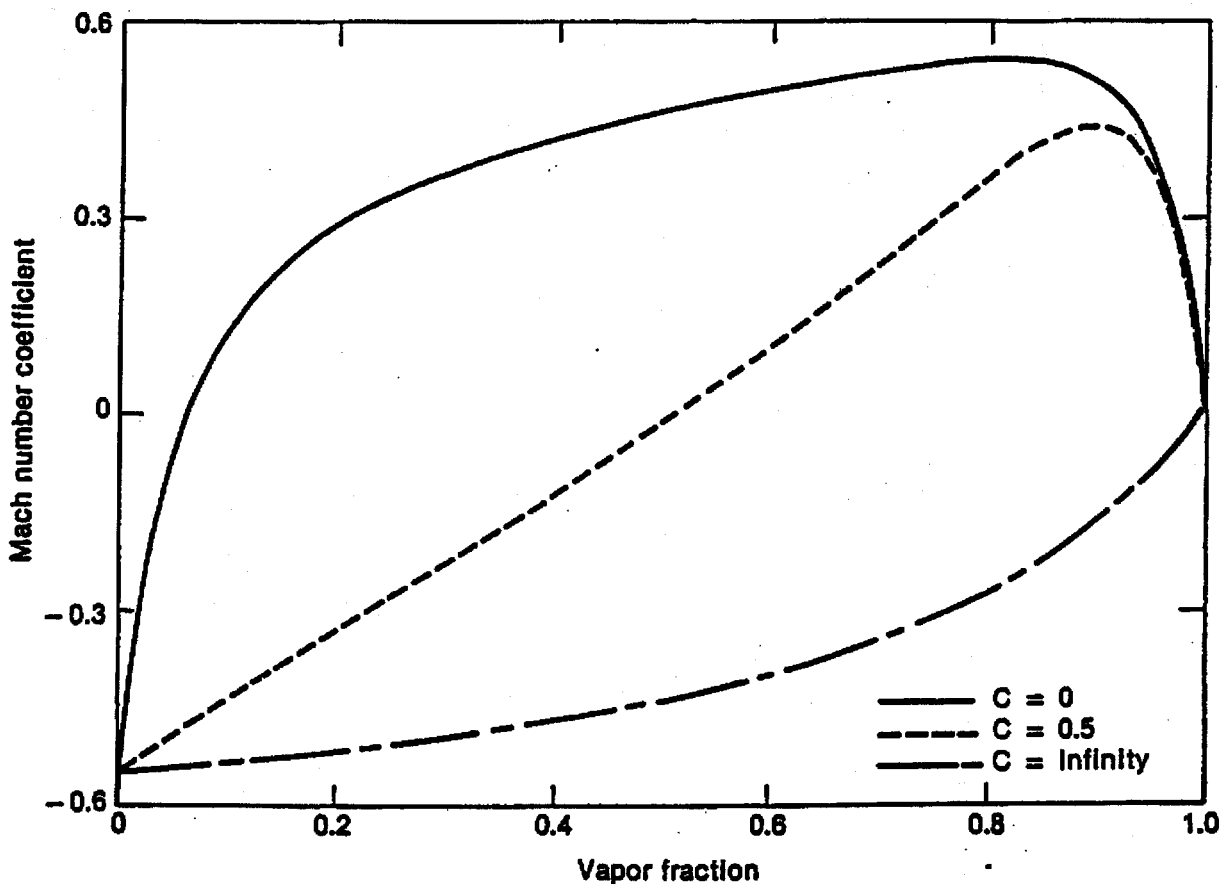


Figure 2.1.4-2. Coefficient of Relative Mach Number for Thermal Equilibrium Flow as a Function of Void Fraction and Virtual Mass Coefficient.

these parameters used in the model are discussed later in this section.

Ransom-Trapp Subcooled Choking Criterion

The previous analysis assumes two-phase conditions exist throughout the break flow process. However, initially and in the early phase of blowdown, the flow approaching the break or break nozzle will be subcooled liquid. Under most conditions of interest in LWR systems, the fluid undergoes a phase change at the break. The transition from single- to two-phase flow is accompanied by a discontinuous change in the fluid bulk modulus. This is especially true for the liquid-to-liquid/vapor transition. For example, at 600 KPa, the ratio of the single- to two-phase sound speed at the liquid boundary is 339.4. Thus, considerable care must be exercised when analyzing a flow having transitions to or from a pure phase (a discontinuity is also present at the vapor boundary, but the ratio is only 1.069).

To understand the physical process that occurs for subcooled upstream conditions, consider the flow through a converging/diverging nozzle connected to an upstream plenum with subcooled water at a high pressure. For a downstream pressure only slightly lower than the upstream pressure, subcooled liquid flow will exist throughout the nozzle. Under these conditions the flow can be analyzed using Bernoulli's equation, which predicts a minimum pressure, P_t , at the throat.^a As the downstream pressure is lowered further, a point is reached where the throat pressure equals the local saturation pressure, P_{sat} . If the downstream pressure is lowered further, vaporization will take place at the throat.^b When this happens, the fluid sound

^aFor all practical cases of choking, the subcooled water can be considered incompressible with infinite sound speed.

^bAn idealized one-dimensional homogeneous equilibrium model is assumed in the example.

speed lowers drastically, but continuity considerations dictate that the velocity, v_t , of the two-phase mixture (at the point of minuscule void fraction) just equals the velocity of the subcooled water slightly upstream of the throat. When this occurs, v_t in the subcooled region is less than the water sound speed, but in the two-phase region, v_t can be greater than the two-phase sound speed. Hence, the subcooled water has a Mach number (M) less than one, whereas the two-phase mixture at the throat has a Mach number greater than one. Under these conditions (Mach numbers greater than one in the two-phase region), downstream pressure effects are not propagated upstream and the flow is choked. In particular, the supersonic two-phase fluid at the throat must increase in velocity and the pressure drop as it expands in the diverging section^a (transition back to

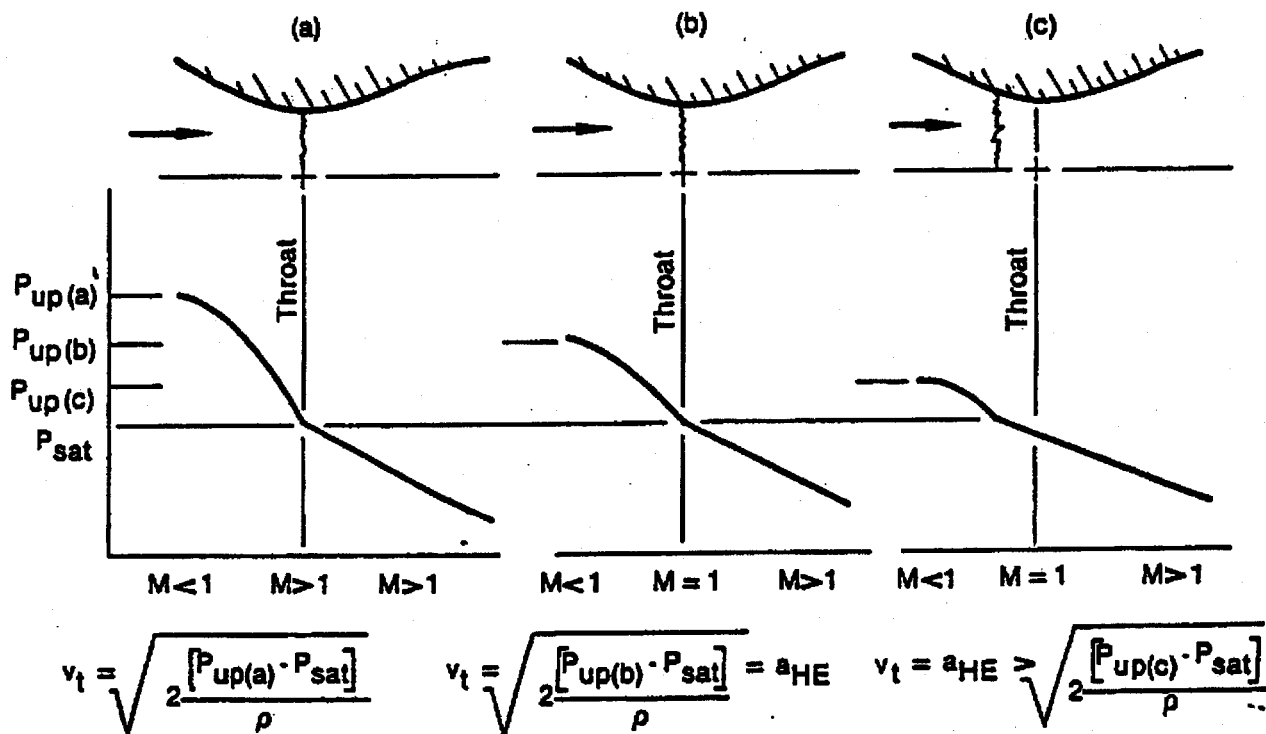


Figure 2.1.4-3. Subcooled Choking Process.

^aIn a supersonic flow, a diverging nozzle implies an increase in velocity.

subsonic flow can occur in the nozzle as a result of a shock wave). The choked condition is shown in Figure 2.1.4-3(a).

Contrary to the usual single-phase choked flow in a converging/diverging nozzle, there is no point in the flow field where $M = 1$. This is because in the homogeneous equilibrium model the fluid undergoes a discontinuous change in sound speed from single-phase subcooled conditions to two-phase conditions, although the fluid properties are continuous through the transition point.

When this condition prevails, the flow rate can be established from application of Bernoulli's equation ($1/2 \rho v_t^2 = P_{up} - P_{sat}$). For a further decrease in the downstream pressure, no further increase in upstream fluid velocity will occur as long as the upstream conditions are maintained constant.

Now consider the process where a subcooled choked flow, as described above, initially exists (with a very low downstream pressure) and the upstream pressure is lowered. As the upstream pressure decreases, the pressure at the throat will remain at P_{sat} and Bernoulli's equation will give a smaller subcooled water velocity (v_t) at the throat. As P_{up} is lowered further, a point is reached where $v_t = a_{HE}$ and $M = 1$ on the two-phase side of the throat (the Mach number in the subcooled portion upstream of the throat is much less than one). This situation is shown schematically in Figure 2.1.4-3(b).

As the upstream pressure is lowered further, the point where the pressure reaches P_{sat} must move upstream of the throat [see Figure 2.1.4-3(c)]. The subcooled water velocity at the P_{sat} location is smaller than the two-phase sound speed and the flow is subsonic. In the two-phase region between the point at which P_{sat} is reached and the throat, the Mach number is less than 1, but increases to $M = 1$ at the throat, that is, the two-phase

sonic velocity is reached at the throat (as in the case of choked flow having a continuous variation of sound speed with pressure). As P_{up} is lowered still further, the P_{sat} point moves upstream until the flow becomes completely two-phase.

The homogeneous assumption applied in the above subcooled choking description is very close to the real situation when vapor is first formed. However, nonequilibrium can result in a superheated liquid state at a throat pressure, P_t , much lower than the saturation pressure, P_{sat} . The onset of vaporization occurs at P_t instead of P_{sat} .

The pressure undershoot, $P_{sat} - P_t$, can be described by the Alamgir-Lienhard-Jones correlation⁶⁷⁻⁶⁹

$$P_{sat} - P_t = \text{MAX} (\Delta P, 0) , \quad 2.1.4-20$$

with

$$\Delta P = 0.258 \sigma^{3/2} T^{13.76} \left[1 + 13.25 \sum'^{0.8} \right]^{1/2} / \left[(k_B T_c)^{1/2} (1 - v_f v_g) \right] - 0.07^2 (A_t/A) \left[\rho v_c^2 / 2 \right] . \quad 2.1.4-21$$

The first term in ΔP represents the static depressurization effect and is derived by Alamgir and Lienhard⁶⁸ based on classical nucleation theory. For steady flow in a nozzle, the depressurization rate, Σ' , can be shown to be

$$\Sigma' = \left[\rho v_c^3 / A_t \right] (dA/dx)_t . \quad 2.1.4-22$$

Note that in Equation 2.1.4-21 Σ' is in units of Matm/s, but in Equation 2.1.4-22, Σ' is in units of Pa/s. Here, $(dA/dx)_t$ is the variation of area with respect to axial length and is to be

evaluated at the throat. The second term in ΔP (Equation 2.1.4-21) represents the turbulence effect and is developed by Jones.⁶⁹

The choking velocity, based upon the process shown in Figure 2.1.4-3(a), can be calculated by applying Bernoulli's equation

$$v_c = \left[v_{up}^2 + 2 (P_{up} - P_t) / \rho \right]^{1/2}, \quad 2.1.4-23$$

where P_t is to be computed from Equation 2.1.4-20.

For the process shown in Figures 2.1.4-3(b) and (c)

$$v_c = a_{HE}, \quad 2.1.4-24$$

and the two-phase choking criterion applies.

To determine which of the above situations exists, both v_c 's are calculated and the larger is used as the choking velocity to be imposed at the throat. This velocity is imposed numerically at the throat in exactly the same manner as the choking criterion used for the two-phase condition described previously.

The subcooled choking model is very similar to models proposed by Burnell⁷⁰ and Moody;⁷¹ however, the criterion for transition from subcooled choking to two-phase choking is now better understood and is in agreement with the physics of two-phase flow. The model here is also in agreement with cavitating venturi experience (experimentally confirmed behavior).

Ransom-Trapp Horizontal Stratified Choked Flow

Under stratified conditions, the void fraction of the flow out of a small break may be quite different from the upstream void

fraction. The usual definition of the outlet void fraction as a donored void fraction is no longer applicable. A simple approach based on the height of the liquid level and a criterion for the stability of small disturbances is used to determine the junction void fraction for stratified break flow.

By balancing the upward pressure force due to the Bernoulli effect and the downward gravitational force acting on a small surface perturbation, Taitel and Dukler²⁷ developed the following criterion for transition from the stratified horizontal flow regime in a round pipe

$$v_g > \left[\frac{(\rho_f - \rho_g) B_v A_g}{\rho_g dA_f/dH_f} \right]^{1/2} \left(1 - \frac{H_f}{D} \right) . \quad 2.1.4-25$$

In Equation 2.1.4-25, A_g and A_f are the flow areas of vapor and liquid, respectively. The right side of Equation 2.1.4-25 is the limiting vapor velocity designated by v_{gL} . The following geometrical relationships define H_g and H_f .

$$H_g = D (1 - \cos\theta)/2 \quad 2.1.4-26$$

and

$$H_f = D (1 + \cos\theta)/2 , \quad 2.1.4-27$$

where θ is the central angle formed by a vertical cord and a radius to the liquid vapor interface. It can be shown that dA_f/dH_f equals $D \sin \theta$ and hence v_{gL} becomes

$$v_{gL} = 1/2 \left[\frac{(\rho_f - \rho_g) B_v \alpha A}{\rho_g D \sin\theta} \right]^{1/2} (1 - \cos\theta) . \quad 2.1.4-28$$

Let D_t be the diameter of the break area. When the liquid level is above the break [i.e., $H_f > (D + D_t)/2$], the outlet void fraction, $\alpha_{g,j}$, which accounts for the pull-through of vapor, is defined as

$$\alpha_{g,j} = \alpha_{g,K} (v_g/v_{gL})^{1/2}, \quad 2.1.4-29$$

where $\alpha_{g,K}$ and v_g are the void fraction and vapor velocity upstream of the outlet. If the liquid level falls below the break [i.e., $H_f < (D - D_t)/2$], liquid entrainment is modeled by defining the outlet liquid fraction, $\alpha_{f,j}$, as

$$\alpha_{f,j} = \alpha_{f,K} (v_g/v_{gL})^{1/2}, \quad 2.1.4-30$$

where $\alpha_{f,K}$ is the liquid volume fraction upstream of the outlet. The equality, $\alpha_{g,j} + \alpha_{f,j} = 1$, is used to obtain $\alpha_{g,j}$ ($\alpha_{f,j}$), if $\alpha_{f,j}$ ($\alpha_{g,j}$) is known. When the liquid level lies within the outlet area [i.e., $(D + D_t)/2 > H_f > (D - D_t)/2$], the void fraction is obtained by interpolation of the two void fractions computed at the boundaries.

Implementation of the Ransom-Trapp Choked Flow Model

Ideally, the two-phase choking criterion (Equation 2.1.4-17) can be used as a boundary condition for obtaining flow solutions. However, the applicability of Equation 2.1.4-17 has not been fully explored. Instead, an approximate criterion

$$(\alpha_g \rho_f v_g + \alpha_f \rho_g v_f) / (\alpha_g \rho_f + \alpha_f \rho_g) = \pm a_{HE} \quad 2.1.4-31$$

has been applied extensively and has produced good code/data comparisons. Equation 2.1.4-31 can be derived from Equation 2.1.4-17 by neglecting the third term in D and setting $C = 0$ (stratified) on the right side of Equation 2.1.4-17 and $C = \infty$

(homogeneous) on the left side. Because of extensive experience with this approximate model, Equation 2.1.4-31 is currently used in RELAP5/MOD2 choked flow calculations.

At each time step and at each flow junction where two-phase cocurrent flow exists, the choking criterion (Equation 2.1.4-31) is checked using explicitly calculated values. When choking occurs, Equation 2.1.4-31 is solved semi-implicitly with the upstream vapor and liquid momentum equations for v_g , v_f , and P_t , throat pressure, at the point of flow choking (upstream is with reference to v_g and v_f). As P_t is not needed in system calculations, we can eliminate $\partial P/\partial x$ from the vapor and liquid momentum equations to obtain

$$\begin{aligned} & \rho_g \left[\partial v_g / \partial t + 1/2 \partial v_g^2 / \partial x \right] - \rho_f \left[\partial v_f / \partial t + 1/2 \partial v_f^2 / \partial x \right] \\ & = \rho_g - \rho_f B_x + \Gamma_g (v_I - \alpha_f v_g - \alpha_g v_f) / \alpha_f \alpha_g \\ & - \rho_g v_g^{FWG} + \rho_f v_f^{FWF} - \rho_f \rho_g (v_g - v_f) FI \\ & - C \rho \partial (v_g - v_f) / \partial t \end{aligned} \quad 2.1.4-32$$

The finite difference form of this equation is obtained by integrating with respect to the spatial variable from the upstream volume center to the junction. In this finite-difference equation, all junction velocities are evaluated implicitly; a_{HE}^{n+1} is approximated by

$$a_{HE}^{n+1} = a_{HE}^n + (\partial a_{HE} / \partial P) (P^{n+1} - P^n), \quad 2.1.4-33$$

where P is the upstream volume pressure. The finite-difference equations corresponding to Equations 2.1.4-31 and 2.1.4-32 can be solved for v_g^{n+1} and v_f^{n+1} in terms of P^{n+1} and old time values.

In the case of subcooled choking, the choking criterion (Equation 2.1.4-31) and the velocity equation (Equation 2.1.4-32) reduce to

$$v_f = v_g = \pm v_c . \quad 2.1.4-34$$

Here, v_c is determined according to the procedures described previously. The frictional pressure losses and gravity head, which do not appear in the ideal Equation 2.1.4-23 are properly taken into account in the actual calculation.

In general, there is a large drop in critical velocity when the fluid changes from a subcooled state to a two-phase state. This sudden change often leads to unrealistic velocity oscillations and causes the time step size to be reduced considerably. To provide a smooth transition from subcooled to two-phase, a transition region is defined as in the low void region. Within the transition region, an underrelaxation scheme,

$$v_g^{n+1} = v_g^n + 0.1 \left(v_g^{n+1} - v_g^n \right)$$

and

2.1.4-35

$$v_f^{n+1} = v_f^n + 0.1 \left(v_f^{n+1} - v_f^n \right)$$

is implemented. Experience with this scheme indicates that it works satisfactorily.

Tabular Choked Flow Models

The extended Henry-Fauske¹¹³, Moody¹¹⁴, HEM and Murdock-Bauman¹¹⁵ critical flow models are new options added for evaluation model calculations. Each of these models, extracted from the RELAP46D code, consist of tabular critical mass fluxes as functions of upstream volume stagnation pressure and enthalpy. These tables are listed in Appendix C.

$$G_c = f(P_0, h_0) ,$$

2.1.4-36

where

G_c = critical mass flux (lbm/ft²-s),

P_0 = upstream volume stagnation pressure (psia), and

h_0 = upstream volume stagnation enthalpy (Btu/lbm).

The user has the option to select static volume pressure and enthalpy or stagnation properties for the interpolation within these supplied models. The calculated critical mass flux will be compared with the mass flux calculated by the RELAP5 momentum equations at each time step. If the former is smaller than the latter, choking is assumed to occur and phasic velocities will be calculated based on the critical mass flux.

Since the RELAP5 code derives the total junction mass fluxes only in terms of the junction phasic velocities, the total mass flux from the tables must be translated into equivalent liquid and vapor velocities. The energy flux calculations must be separated similarly.

$$G_c = \alpha_g \rho_g V_g + \alpha_f \rho_f V_f$$

2.1.4-37

and

$$G_{ch} = \alpha_g \rho_g V_{gh} + \alpha_f \rho_f V_{fh} ,$$

2.1.4-38

where

α = volume fraction,

ρ = density (lbm/ft³),

V = velocity (ft/s),

h = static upstream enthalpy (Btu/lbm),

and the subscripts denote

g = vapor phase and

f = liquid phase.

The phasic velocities are defined by the slip between the liquid and steam during two-phase conditions where the slip ratio, s , is defined as

$$s = V_g / V_f. \quad 2.1.4-39$$

There are several slip models available in the code. These models include homogeneous (no slip), constant slip, Moody's slip, RELAP5 momentum equation slip, and upstream volume equilibrium quality slip. They are described as follows:

1. Homogeneous

$$V_f = V_g. \quad 2.1.4-40$$

2. Constant slip ratio

s = user input constant .

3. Moody's slip ratio

$$s = (v_g / v_f)^{1/3}, \quad 2.1.4-41..$$

where

v_g = saturated steam specific volume and

v_f = saturated liquid specific volume.

4. RELAP5 momentum equation slip ratio

$$s = V_g / V_f , \quad 2.1.4-42$$

where the phasic velocities are calculated by the momentum equation.

5. Equilibrium quality slip ratio

$$s = \begin{cases} X_e \rho_f \alpha_f / [(1 - X_e) \rho_g \alpha_g] & X_e \leq 0.5 \\ (1 - X_e) \rho_g \alpha_g / [X_e \rho_f \alpha_f] & X_e > 0.5 . \end{cases} \quad 2.1.4-43$$

Each slip model has the option to smooth the slip ratio and specify a minimum and maximum value. The smoothing is provided in the form

$$s^{n+1} = 0.1 s^{n+1} + 0.9 s^n . \quad 2.1.4-44$$

The slip ratio calculated by one of the above models will be used to determine the phasic velocity.

$$V_f = G_c / (\alpha_g \rho_g s + \alpha_f \rho_f) \quad 2.1.4-45$$

and

$$V_g = s V_f . \quad 2.1.4-46$$

Note that all these slip models may not be consistent with the tabular critical flow model formulations.

Some of the added critical flow models may have limitations imposed over which fluid conditions they can be applied. Table 2.1.4-1 shows the conditions over which the individual models may be applied. A discontinuity arises at the saturation boundaries

because two separate models without consistent end points meet. To prevent unreasonable time step size reductions and to provide a smooth transition from the subcooled region to the two-phase region, where the critical mass flux decreases significantly, the following smoothing options are available. Based on either a quality or void fraction criteria the smoothing

$$v^{n+1} = v^n + 0.1 (v^{n+1} - v^n) \quad 2.1.4-47$$

is applied if

$$0.0 < |(h_0 - h_{f0}) / h_{fg}| < e \quad \text{for quality, or}$$

$$\alpha_{g1} \leq \alpha_g \leq \alpha_{gu} \quad \text{for void fraction,}$$

where

- h_{fg} = latent heat of vaporization at P_0 ,
- $n+1, n$ = time step,
- e = transition criteria (based on user input),
- α_{g1} = lower void fraction transition limit (input), and
- α_{gu} = upper void fraction transition limit (input).

Equation 2.1.4-47 is the same technique used in the original RELAP5 choked flow model.

The stagnation properties are the theoretical basis of the critical flow models described above. The stagnation pressure and enthalpy are calculated from the static upstream volume pressure and enthalpy assuming isentropic flow. The stagnation enthalpy is calculated from the kinetic energy relationship using a calculated fluid velocity.

$$h_0 = h_1 + v^2/2c, \quad 2.1.4-48$$

where

h_1 = upstream volume static enthalpy (Btu/lbm) and
 C = conversion factor from (ft-lbm) to (Btu):

Applying the basic energy equation in differential form,

$$Tds = dh - vdp, \quad 2.1.4-49$$

and assuming an isentropic process ($ds = 0$),

$$dp = dh / v. \quad 2.1.4-50$$

Integrating Equation 2.1.4-50 over the change in enthalpy from static to stagnation limit gives

$$P_0 = P_1 + \int_{h_1}^{h_0} dh/v, \quad 2.1.4-51$$

where

P_1 = upstream volume static pressure (psia) and
 v = specific volume (ft³/lbm).

Equation 2.4.1-51 is evaluated between the limits (h_1, P_1) and (h_0, P_0) by a fourth-order Runge-Kutta technique. The specific volume is obtained from the steam tables.

In order to minimize computational time, the stagnation property will not be calculated if the upstream volume phase is not liquid and at the same time the Mach number of the average volume flow is less than 0.3. Also if

$$(h_0 - h_1) / h_1 \leq \text{THDTH}, \quad 2.1.4-52$$

where

THDTH = user input criteria (defaulted to 0.001)

stagnation properties are not calculated.

Table 2.1.4-1. Critical Flow Logic.

		TWO PHASE MODEL	JCHOKE FLAGS			
			0	1	3	4
SUBCOOLED MODEL			ORIGINAL RANSOM TRAPP	EXTENDED HENRY-FAUSKE	MOODY	HOMOGENEOUS EQUILIBRIUM
			I C H O K E F L A G	0	ORIGINAL RANSOM TRAPP	
1	EXTENDED HENRY-FAUSKE			X		
3	MOODY	X		X	X	X
4	HOMOGENEOUS EQUILIBRIUM			X		

NOTES

X DENOTES IMPROPER MODEL COMBINATIONS

MURDOCK-BAUMAN IS CHOSEN BY SETTING JCHOKE TO -3 OR -4

THE |JCHOKE| THEN IS USED TO SELECT THE TWO PHASE MODE

2.1.4.2. Abrupt Area Change

The general reactor system contains piping networks with many sudden area changes and orifices. To apply the RELAP5 hydrodynamic model to such systems, analytical models for these components have been developed.⁸¹ The basic hydrodynamic model is formulated for slowly varying (continuous) flow area variations; therefore, special models are not required for this case.

The abrupt area change model discussed here and developed in detail in Reference 81, is based on the Bourda-Carnot⁸² formulation for a sudden enlargement and standard pipe flow relations, including the vena-contracta effect for a sudden contraction or an orifice or both. Quasi-steady continuity and momentum balances are employed at points of abrupt area change. The numerical implementation of these balances is such that hydrodynamic losses are independent of upstream and downstream nodalization. In effect, the quasi-steady balances are employed as jump conditions that couple fluid components having abrupt changes in cross-sectional area. This coupling process is achieved without change to the basic linear semi-implicit numerical time-advancement scheme.

Abrupt Area Change Modeling Assumptions

The basic assumption used for the transient calculation of two-phase flow in flow passages with points of abrupt area change is that the transient flow process can be approximated as a quasi-steady flow process that is instantaneously satisfied by the upstream and downstream conditions (i.e., transient inertia, mass, and energy storage are neglected at abrupt area changes). However, the upstream and downstream flows are treated as fully transient flows.

There are several bases for the above assumption. A primary consideration is that available loss correlations are based on data taken during steady flow processes; however, transient investigations⁸³ have verified the adequacy of the quasi-steady assumption. The volume of fluid and associated mass, energy, and inertia at points of abrupt area change is generally small compared with the volume of upstream and downstream fluid components. The transient mass, energy, and inertia effects are approximated by lumping them into upstream and downstream flow volumes. Finally, the quasi-steady approach is consistent with modeling of other important phenomena in transient codes (i.e., heat transfer, pumps, and valves).

Review of Single-Phase Abrupt Area Change Models

The modeling techniques used for dynamic pressure losses associated with abrupt area change in a single-phase flow are reviewed briefly before discussing the extension of these methods to two-phase flows. In a steady incompressible flow, losses at an area change are modeled by the inclusion of an appropriate dynamic head loss term, h_L , in the one-dimensional modified Bernoulli equation

$$(v^2/2 + P/\rho)_1 = (v^2/2 + P/\rho)_2 + h_L . \quad 2.1.4-53$$

The particular form of the dynamic head loss is obtained by employing the Bourda-Carnot⁸² assumption for calculating losses associated with the expansion part of the flow process. Losses associated with the contracting part of the flow process are small relative to the expansion losses, and are neglected.

The most general case of an abrupt area change is a contraction with an orifice at the point of contraction. Such a configuration is shown in Figure 2.1.4-4. Three area ratios are used throughout this development. The first is the contraction

area ratio at the vena-contracta relative to the minimum physical area, $\epsilon_c = A_c/A_T$. The second is the ratio of the minimum physical area to the upstream flow area, $\epsilon_T = A_T/A_1$. The third is the ratio of the downstream to upstream area, $\epsilon = A_2/A_1$.

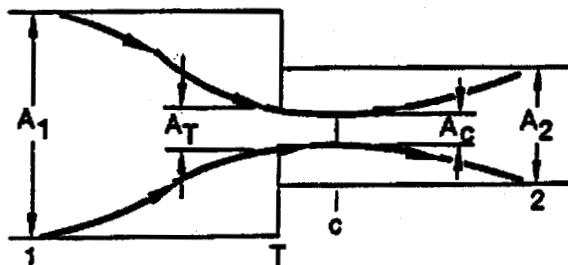


Figure 2.1.4-4. Orifice at Abrupt Area Change.

The loss associated with the contracting fluid stream from Station 1 to c (the point of vena-contracta) is neglected [measurements indicate that the contracting flow experiences a loss no larger than $\Delta P_f = 0.05 (1/2 \rho v_c^2)$ where v_c is the velocity at the vena-contracta] whereas the dynamic pressure loss associated with the expansion from the vena-contracta to the downstream section is given by

$$\Delta P_f = 1/2 \rho (1 - A_c/A_2)^2 v_c^2 \quad 2.1.4-54$$

The contraction ratio, $\epsilon_c = A_c/A_T$, is an empirical function of $\epsilon_T = A_T/A_1$. Using the continuity equation, $v_c = \frac{A_T v_T}{A_c} = v_T / \epsilon_c$, and $v_T = \frac{A_2 v_2}{A_T} = \frac{\epsilon}{\epsilon_T} v_2$, Equation 2.1.4-54 can be written as

$$\Delta P_f = 1/2 \rho \left(1 - \frac{\epsilon}{\epsilon_c \epsilon_T} \right)^2 v_2^2 \quad . \quad 2.1.4-55$$

Equation 2.1.4-55 is applicable to all the cases of interest. For a pure expansion, $\epsilon_T = 1$, $\epsilon_c = 1$, and $\epsilon > 1$; for a contraction, $\epsilon_T = \epsilon < 1$ and $\epsilon_c < 1$. Each of these is a special case of Equation 2.1.4-55. The two-phase dynamic pressure loss model is based on an adaptation of the general single-phase head loss given by this equation.

Two-Phase Abrupt Area Change Model

The two-phase flow through an abrupt area change is modeled in a manner very similar to that for single-phase flow by defining phasic flow areas. The two phases are coupled through the interphase drag, a common pressure gradient, and the requirement that the phases coexist in the flow passage.

The one-dimensional phasic stream-tube momentum equations are given in section 2.1.1.1. The flow at points of abrupt area change is assumed to be quasi-steady and incompressible. In addition, the terms in the momentum equations due to body force, wall friction, and mass transfer are assumed to be small in the region affected by the area change. The interphase drag terms are retained since the gradient in relative velocity can be large at points of abrupt area changes.

Equations 2.1.1-5 and 2.1.1-6 can be integrated approximately for a steady incompressible, smoothly varying flow to obtain modified Bernoulli-type equations.

$$\begin{aligned} \left[\frac{1}{2} \rho_f v_f^2 + P \right]_1 &= \left[\frac{1}{2} \rho_f v_f^2 + P \right]_2 + \left[\frac{FI'}{\alpha_f} \right]_1 (v_{f1} - v_{g1}) L_1 \\ &+ \left[\frac{FI'}{\alpha_f} \right]_2 (v_{f2} - v_{g2}) L_2 \end{aligned} \quad 2.1.4-56$$

and

$$\begin{aligned} \left[\frac{1}{2} \rho_g v_g^2 + P \right]_1 &= \left[\frac{1}{2} \rho_g v_g^2 + P \right]_2 + \left[\frac{FI'}{\alpha_f} \right]_1 (v_{g1} - v_{f1}) L_1 \\ &+ \left[\frac{FI'}{\alpha_f} \right]_2 (v_{g2} - v_{f2}) L_2, \end{aligned} \quad 2.1.4-57$$

where $FI' = \alpha_f \alpha_g \rho_f \rho_g FI$. The interphase drag is divided into two parts associated with the upstream and downstream parts of the flow affected by the area change.

General Model

Consider the application of Equations 2.1.4-56 and 2.1.4-57 to the flow of a two-phase fluid through a passage having a generalized abrupt area change (the flow passage shown in Figure 2.1.4-5).^a Here, the area A_T is the throat or minimum area associated with an orifice located at the point of the abrupt area change. Since each phase is governed by a modified Bernoulli-type equation, it is reasonable to assume that losses associated with changes in the phasic flow area can be modeled by separate dynamic pressure loss terms for both the liquid and gas phases. Hence, we assume that the liquid sustains a loss as if it alone (except for the interphase drag) were experiencing an area change from $\alpha_{f1} A_1$ to $\alpha_{fT} A_T$ to $\alpha_{f2} A_2$, and the gas phase

^aIn Figure 2.1.4-5, the flow is shown as a separated flow for clarity. The models developed are equally applicable to separated and dispersed flow regimes.

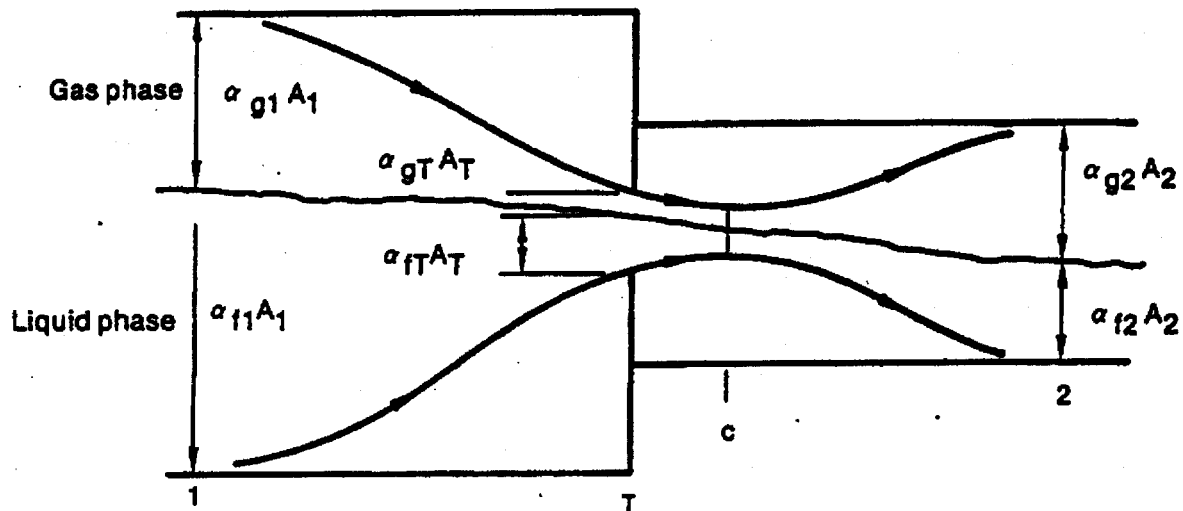


Figure 2.1.4-5. Schematic Flow of Two-Phase Mixture at Abrupt Area Change.

experiences a loss as if it alone were flowing through an area change from $\alpha_{g1} A_1$ to $\alpha_{gT} A_T$ to $\alpha_{g2} A_2$. The area changes for each phase are the phasic area changes (see Figure 2.1.4-5). When the losses for these respective area changes (based on the Bourda-Carnot model and given by Equation 2.1.4-55) are added to Equations 2.1.4-56 and 2.1.4-57, the following phasic momentum equations are obtained

$$\left[\frac{1}{2} \rho_f v_f^2 + P \right]_1 = \left[\frac{1}{2} \rho_f v_f^2 + P \right]_2 + \frac{1}{2} \rho_f \left[1 - \frac{\alpha_{f2} \epsilon}{\alpha_{fT} \epsilon_{fc} \epsilon_T} \right]^2 \cdot (v_{f2})^2 + \left[\frac{F I'}{\alpha_f} \right]_2 (v_{f1} - v_{g1}) L_1 + \left[\frac{F I'}{\alpha_f} \right]_2 (v_{f2} - v_{g2}) L_2$$

2.1.4-58

and

$$\left[\frac{1}{2} \rho_g v_g^2 + P \right]_1 = \left[\frac{1}{2} \rho_g v_g^2 + P \right]_2 + \frac{1}{2} \rho_g \left[1 - \frac{\alpha_{f2} \epsilon'}{\alpha_{gT} \epsilon_{gc} \epsilon_T} \right]^2 \cdot (v_{g2})^2 + \left[\frac{FI'}{\alpha_g} \right]_2 (v_{g1} - v_{f1}) L_1 + \left[\frac{FI'}{\alpha_g} \right]_2 (v_{g2} - v_{f2}) L_2.$$

2.1.4-59

These phasic momentum equations are used across an abrupt area change. In Equations 2.1.4-58 and 2.1.4-59, ϵ_{fc} and ϵ_{gc} are the same tabular function of area ratio as in the single-phase case except that the area ratios used are the phasic area ratios

$$\epsilon_{fT} = (\alpha_{fT}/\alpha_{f1}) \epsilon_T \quad 2.1.4-60$$

and

$$\epsilon_{gT} = (\alpha_{gT}/\alpha_{g1}) \epsilon_T \quad 2.1.4-61$$

respectively. The area ratios, $\epsilon = A_2/A_1$ and $\epsilon_T = A_T/A_1$, are the same as for single-phase flow.

The interphase drag effects in Equations 2.1.4-58 and 2.1.4-59 are important. These terms govern the amount of slip induced by an abrupt area change, and if they are omitted, the model will always predict a slip at the area change appropriate to a completely separated flow situation and give erroneous results for a dispersed flow.

Model Application

A few remarks concerning the way Equations 2.1.4-58 and 2.1.4-59 are applied to expansions and contractions, both with and without an orifice, are necessary. In a single-phase steady flow situation, given the upstream conditions, v_1 and P_1 , using the

continuity equation ($v_1 A_1 = v_2 A_2$) and Equation 2.1.4-53 one can solve for v_2 and P_2 . Equations 2.1.4-58 and 2.1.4-59 along with the two phasic continuity equations can be used in a similar manner except now the downstream void fraction is an additional unknown which must be determined.

Expansion

For the purpose of explanation, consider the case of an expansion ($\alpha_{fT} = \alpha_{f1}$, $\epsilon > 0$, $\epsilon_T = 1$, $\epsilon_{fc} = \epsilon_{gc} = 1$, $FI'_1 = 0$, $L_1 = 0$) for which Equations 2.1.4-58 and 2.1.4-59 reduce to

$$\begin{aligned} \left[\frac{1}{2} \rho_f v_f^2 + P \right]_1 &= \left[\frac{1}{2} \rho_f v_f^2 + P \right]_2 + \frac{1}{2} \rho_f \left[1 - \frac{\alpha_{f2} \epsilon}{\alpha_{f1}} \right]^2 (v_{f2})^2 \\ &+ \left[\frac{FI'}{\alpha_f} \right]_2 (v_{f2} - v_{g2}) L_2 \end{aligned} \quad 2.1.4-62$$

and

$$\begin{aligned} \left[\frac{1}{2} \rho_g v_g^2 + P \right]_1 &= \left[\frac{1}{2} \rho_g v_g^2 + P \right]_2 + \frac{1}{2} \rho_g \left[1 - \frac{\alpha_{g2} \epsilon}{\alpha_{g1}} \right]^2 (v_{g2})^2 \\ &+ \left[\frac{FI'}{\alpha_g} \right]_2 (v_{g2} - v_{f2}) L_2 \end{aligned} \quad 2.1.4-63$$

These two equations with the incompressible continuity equations

$$\alpha_{f1} v_{f1} A_1 = \alpha_{f2} v_{f2} A_2 \quad 2.1.4-64$$

and

$$\alpha_{g1} v_{g1} A_1 = \alpha_{g2} v_{g2} A_2 \quad 2.1.4-65$$

are a system of four equations having four unknowns, α_{f2} ($\alpha_{g2} = 1 - \alpha_{f2}$), v_{f2} , v_{g2} , and P_2 , in terms of the upstream conditions, α_{f1} ($\alpha_{g1} = 1 - \alpha_{f1}$), v_{f1} , v_{g1} , and P_1 . (The

interphase drag, FI' , is a known function of the flow properties.) It is important to note that the downstream value of the liquid fraction (α_{f2}) is an additional unknown compared with the single-phase case and is determined (with the downstream velocities and pressure) by simultaneous solution of Equations 2.1.4-62 through 2.1.4-65 without additional assumptions. It is reassuring that by taking a proper linear combination of Equations 2.1.4-58 and 2.1.4-59 the usual overall momentum balance obtained using the Bourda-Carnot⁸² assumption can be obtained.⁸⁴⁻⁸⁵

If, as in the cited literature,⁸⁴⁻⁸⁷ only the overall momentum balance is used at an expansion, there will be an insufficient number of equations to determine all the downstream flow parameters, α_{f2} , v_{f2} , v_{g2} , and P_2 . The indeterminacy has been overcome in cited works by means of several different assumptions concerning the downstream void fraction.^a In the model developed here (Equations 2.1.4-62 and 2.1.4-63), division of the overall loss into liquid and gas parts, respectively, results in sufficient conditions to determine all downstream flow variables including α_{f2} . In addition, the present model includes force terms due to interphase drag in Equations 2.1.4-62 and 2.1.4-63, which are necessary to predict the proper amount of slip and void redistribution that occur at points of area change.

Contraction

Consider the application of Equations 2.1.4-61 and 2.1.4-62 to a contraction. To determine both the downstream conditions and throat conditions from the upstream values of α_{f1} (α_{g1}), v_{f1} , v_{g1} , and P_1 , an additional consideration needs to be made. To obtain

^aJ. G. Collier⁸⁴ mentions three different assumptions that have been used: (i) $\alpha_{f2} = \alpha_{f1}$, (ii) α_{f2} is given by a homogeneous model, and (iii) α_{f2} is given by the Hughmark void fraction correlation.

the throat values, apply the momentum equations valid for the contracting section of flow (here, the L_1 portion of the interphase force is associated with the contraction), that is,

$$\left[\frac{1}{2} \rho_f v_f^2 + P \right]_1 = \left[\frac{1}{2} \rho_f v_f^2 + P \right]_T + \left[\frac{FI'}{\alpha_f} \right]_1 (v_{f1} - v_{g1}) L_1, \quad 2.1.4-66$$

$$\left[\frac{1}{2} \rho_g v_g^2 + P \right]_1 = \left[\frac{1}{2} \rho_g v_g^2 + P \right]_T + \left[\frac{FI'}{\alpha_g} \right]_1 (v_{g1} - v_{f1}) L_1, \quad 2.1.4-67$$

$$\alpha_{f1} v_{f1} A_1 = \alpha_{fT} v_{fT} A_T, \quad 2.1.4-68$$

and

$$\alpha_{g1} v_{g1} A_1 = \alpha_{gT} v_{gT} A_T. \quad 2.1.4-69$$

These four equations are solved simultaneously for the values of α_{fT} (α_{gT}), v_{fT} , v_{gT} , and P_T at the throat section (the minimum physical area). No additional or special assumptions are made concerning the throat conditions since they follow as a direct consequence of the unique head loss models for each phase. After the throat values have been obtained, the conditions at the point of vena-contracta are established assuming the void fraction is the same as that at the throat. Thus, ϵ_{fc} and ϵ_{gc} are established using the tabular function in Appendix A of Reference 81 and the throat area ratios, ϵ_{fT} and ϵ_{gT} , defined by Equations 2.1.4-60 and 2.1.4-61. To determine the downstream values, Equations 2.1.4-58 and 2.1.4-59 can be applied directly from stations 1 to 2 with the throat values known or the expansion loss equations can be used from the throat section to station 2. Both approaches produce identical downstream solutions. As in the case of an expansion, because the proper upstream and

downstream interphase drag is included, this modeling approach establishes the phase slip and resulting void redistribution. An orifice at an abrupt area change is treated exactly as the contraction explained above (i.e., with two separate calculations to establish first the throat and then the downstream flow variables).

Countercurrent Flow

The preceding development implicitly assumed a cocurrent flow. For countercurrent flow, Equations 2.1.4-58 and 2.1.4-59 are applied exactly as in cocurrent flow except that the upstream sections for the respective phases are located on different sides of the abrupt area change. The difference appears in how the throat and downstream voids are determined. To determine the throat properties, equations similar to Equations 2.1.4-66 through 2.1.4-67 are used with the upstream values appropriate for each phase. These four equations are then solved for $\alpha_{FT}(\alpha_{GT})$, v_{FT} , v_{GT} , and P_T . To determine the downstream values for each phase, only the head loss terms are needed for the downstream voids (the downstream v_f , v_g , and P do not appear). For countercurrent flow, these voids are set such that the downstream void of each phase plus the upstream void of the opposite phase adds to one (both phases together must fill the flow channel). With the throat and downstream voids now known, Equations 2.1.4-58 and 2.1.4-59 can be used directly to determine the total loss for each phase at the abrupt area change.

2.1.4.3. Crossflow Junction

The RELAP5 numerical scheme is generally formulated using one-dimensional elements. However, there are several applications where an approximate treatment of crossflow provides an improved physical simulation. Three different applications for a crossflow formulation are described in the following paragraphs.

The first application concerns a small crossflow between two essentially axial flow streams. This situation is typical of regions such as a reactor core or a steam generator because the component geometry provides a large resistance to crossflow and a small resistance to axial flow. Hence, simplified crossflow momentum equations can be used to couple a hot flow channel to a bulk flow channel.

The second application of a crossflow junction is to provide a tee model. In this case, the momentum flux in the side branch is assumed to be perpendicular to the main stream and thus the main stream momentum flux does not contribute to the crossflow momentum formulation.

The third application is modeling of leak flow paths. In this case, the flow is small and governed primarily by pressure differential, gravity, and flow resistance. Thus, the momentum flux terms can be neglected.

The vapor momentum finite difference equation used in the basic numerical scheme is

$$\begin{aligned} & \left(\alpha_g \rho_g \right)_j^n \left(v_g^{n+1} - v_g^n \right)_j \Delta x_j^n + \frac{1}{2} \left(\alpha_g \rho_g \right)_j^n \left[\left(v_g^2 \right)_L^n - \left(v_g^2 \right)_K^n \right] \Delta t + \text{VISCOUS} \\ & \qquad \qquad \qquad \text{TERMS} \\ & = - \alpha_{g,j}^n \left(P_L^{n+1} - P_K^{n+1} \right) \Delta t \\ & - \left(\alpha_g \rho_g \right)_j^n \left[\left(\text{FWG}_K^n + \text{FWG}_L^n \right) \Delta x_j + \text{HLOSSG}_j^n \right] v_{g,j}^{n+1} \Delta t \\ & - \left(\alpha_g \rho_g \right)_j^n \text{FIG}_j^n \left(v_{g,j}^{n+1} - v_{f,j}^{n+1} \right) \Delta x_j \Delta t + \left(\alpha_g \rho_g \right)_j^n B_x \Delta x_j \Delta t \\ & + \text{ADDED MASS} + \text{MASS TRANSFER MOMENTUM} \\ & + \text{HORIZONTAL STRATIFIED PRESSURE GRADIENT EFFECT,} \end{aligned}$$

2.1.4-70

where

$$\Delta x_j = \frac{1}{2}(\Delta x_K + \Delta x_L) \quad . \quad 2.1.4-71$$

A parallel equation holds for the liquid phase. It should be noted that the momentum Equation 2.1.4-70 is in reality the sum of half the K cell momentum plus half the L cell momentum. This is the reason for Equation 2.1.4-71.

There are two areas in which the crossflow modeling affects the numerical scheme. One concerns the approximations made in the junction momentum equations; the other concerns the volume average velocities in a volume.

If the junction is to model crossflow perpendicular to the main or axial-flow direction then the volume average velocity in the K and L cells, which represent the axial flow velocity, should not include crossflow junction velocity components. For the simple leak flow situation shown in Figure 2.1.4-6, this requires that

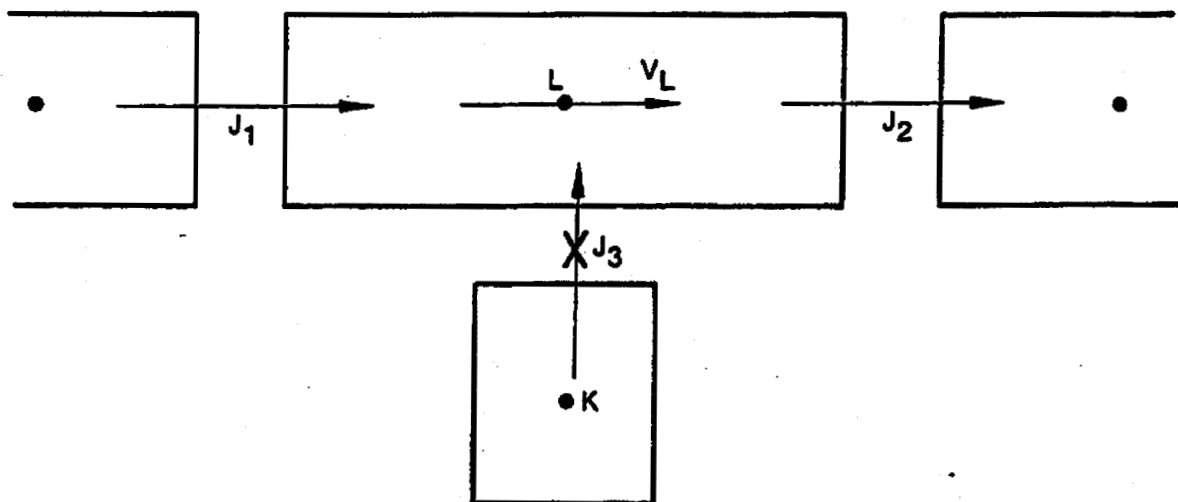


Figure 2.1.4-6. Simplified Tee Crossflow.

$v_{J,3}$ not be included in the volume average (axial) velocity calculation for cell L.

The second area of numerical modification relates to the reduced form of the momentum equations to be used at a crossflow junction. In crossflow junctions, the cross product momentum flux terms are neglected, that is, there is no x-direction transport of momentum due to the y velocity.

For the case of a small crossflow junction between two axial-flow streams (J_2 in Figure 2.1.4-7) all the geometric input (AVOL, DX, DZ) for both of the volumes relates to the axial flow direction as does the wall drag and code calculated form losses. Since the crossflow has a different flow geometry and resistance (for example, crossflow resistance in a rod bundle) the friction and form losses must be user input and must be appropriate for the crossflow direction geometry. For crossflow junctions the user input form losses should include all crossflow resistance (form losses and wall drag). The normal terms representing wall drag and abrupt area change losses are not included in the formulation of the momentum equation at a crossflow junction as these refer to the axial properties of the K and L volumes.

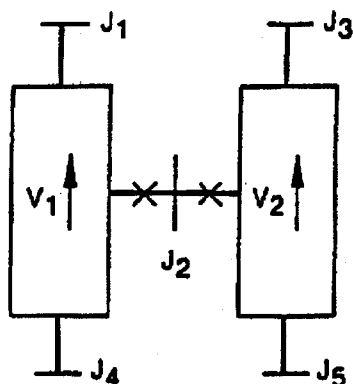


Figure 2.1.4-7. Modeling of Crossflows or Leak.

Since the connecting K and L volumes are assumed to be predominately axial-flow volumes, the crossflow junction momentum flux (related to the axial volume velocity in K and L) is neglected along with the associated numerical viscous term. In addition, the horizontal stratified pressure gradient is neglected.

All lengths and elevation changes in the one-dimensional representation are based upon the axial geometry of the K and L volumes and the crossflow junction is assumed to be perpendicular to the axial direction and of zero elevation change, thus, no gravity force term is included.

The resulting vapor momentum finite difference equation for a crossflow junction is

$$\begin{aligned} & \left(\alpha_g \rho_g \right)_j^n \left(v_{g,j}^{n+1} - v_{g,j}^n \right) \Delta x_j = - \alpha_{g,j}^n (P_L - P_K)^{n+1} \Delta t \\ & - \left(\alpha_g \rho_g \right)_j^n H_{LOSSG_j}^n v_{g,j}^{n+1} \Delta t \\ & - \left(\alpha_g \rho_g \right)_j^n F_{IG_j}^n \left(v_{g,j}^{n+1} - v_{f,j}^{n+1} \right) \Delta x_j \Delta t \end{aligned}$$

+ ADDED MASS + MASS TRANSFER MOMENTUM.

2.1.4-72

A similar equation can be written for the liquid phase. In Equation 2.1.4-72, $H_{LOSSG_j}^n$ contains only the user-input crossflow resistance. The Δx_j term that is used to estimate the inertial length associated with crossflow is defined using the diameters of volumes K and L,

$$\Delta x_j = \frac{1}{2} [D(K) + D(L)] .$$

2.1.4-73

A special void-dependent form loss option of the full crossflow model has been added for certain multi-core channel applications. This option allows the user to alter the input constant form loss coefficient based on the void fraction in the upstream volume. The specific applications are possibly multi-channel core analyses such as SBLOCA scenarios with significant core uncovering or future multi-channel BEACH reflooding calculations. This model allows the regions of the core covered by a two-phase mixture or pool to have a resistance that is different from that in the uncovered or steam region. The crossflow resistance changes can alter the volume-average axial velocities that are used to determine the core surface heat transfer. Any cross flow is excluded from the volume average velocity used for heat transfer.

The model uses the input form loss coefficients whenever the upstream steam void fraction is less than a user-supplied minimum void fraction value given as $\alpha_{\min-Kcross}$. The model allows user input of a forward, $M_{K-forward}$, and reverse, $M_{K-reverse}$, crossflow resistance multiplier when the upstream steam void fraction is greater than the maximum user-input void fraction, $\alpha_{\max-Kcross}$. Linear interpolation is used to determine the multiplicative factor when the void fraction is between minimum and maximum input void fractions as indicated in the following equations. For the forward flow direction (from Volume K to Volume L),

If	$\alpha_g(K) < \alpha_{\min-Kcross}$	$K_{jun} = K_{jun \text{ forward}}$
If	$\alpha_{\max-Kcross} \leq \alpha_g(K)$	$K_{jun} = K_{jun \text{ forward}} * M_{K-forward}$
If	$\alpha_{\min-Kcross} \leq \alpha_g(K) < \alpha_{\max-Kcross}$	$K_{jun} = K_{jun \text{ forward}} * M_{Kf \text{ interp}}$

2.1.4-73.1

where

$$M_{Kf \text{ interp}} = 1 - (1 - M_{K\text{-forward}}) * [\alpha_{\text{min-Kcross}} - \alpha_g(K)] / (\alpha_{\text{min-Kcross}} - \alpha_{\text{max-Kcross}})$$

and $K_{\text{jun forward}}$ is the user-supplied forward loss coefficient specified in this junction input.

The equation for the reverse flow direction (from Volume L to Volume K) is similar.

IF	$\alpha_g(L) < \alpha_{\text{min-Kcross}}$	$K_{\text{jun}} = K_{\text{jun reverse}}$
IF	$\alpha_{\text{max-Kcross}} \leq \alpha_g(L)$	$K_{\text{jun}} = K_{\text{jun reverse}} * M_{K\text{-reverse}}$
IF	$\alpha_{\text{min-Kcross}} \leq \alpha_g(L) < \alpha_{\text{max-Kcross}}$	$K_{\text{jun}} = K_{\text{jun reverse}} * M_{Kf \text{ interp}}$

2.1.4-73.2

where

$$M_{Kr \text{ interp}} = 1 - (1 - M_{K\text{-reverse}}) * [\alpha_{\text{min-Kcross}} - \alpha_g(L)] / (\alpha_{\text{min-Kcross}} - \alpha_{\text{max-Kcross}})$$

and $K_{\text{jun reverse}}$ is the user-supplied reverse loss coefficient specified in this junction input.

The code performs several input checks to ensure that the user input will not cause code failures. These checks include tests to see if the input form loss multipliers are greater than zero. The minimum void fraction must be greater than zero and less than the maximum void fraction input. The maximum void fraction must be less than or equal to one.

The crossflow option can be used with the crossflow junction perpendicular to the axial flow in Volume L (or K) but parallel

to the axial flow in volume K (or L) (see Figure 2.1.4-6). Here, the situation regarding the half cell momentum contribution associated with volume K is the same as for a normal junction. Hence, this crossflow junction has all the terms in Equation 2.1.4-70 except that; (a) wall friction, momentum flux, and gravity only include the K cell contribution, (b) the $HLOSSG_j^n$ term is only the user input loss, and (c) the Δx cell in the inertial term and interphase drag includes the normal K cell contribution and a term of the form in Equation 2.1.4-73 for the L cell. This type of crossflow modeling can be used for a 90 degree tee simulation.

For leak flows and minor flow paths the modeling approach shown in Figure 2.1.4-8 is recommended. Here, J_3 is the normal flow path, whereas junction J_1 , volume M, and junction J_2 represent the leak flow path. Junctions J_1 and J_2 should be modeled as tee junctions described above. The only reason for using volume M is

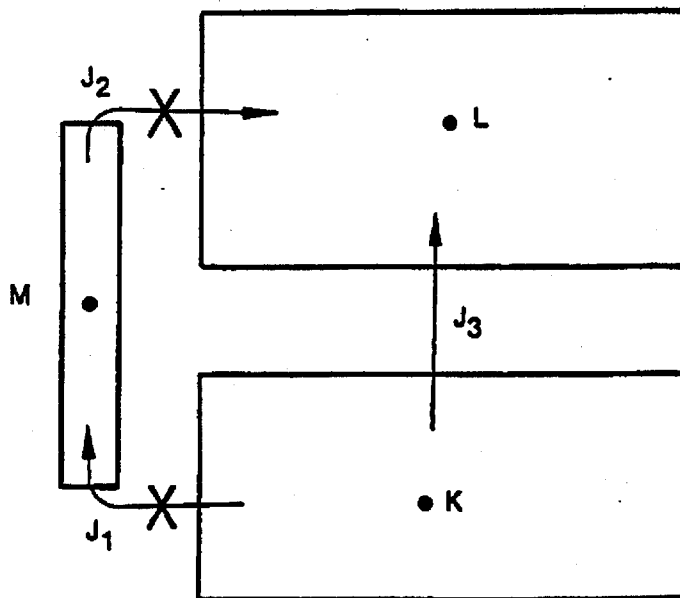


Figure 2.1.4-8. Leak Flow Modeling.

to obtain a correct representation of the gravity head from K to L. If a crossflow junction were modeled directly between volumes K and L then there would be no gravity head in the leak flow junction equation. Leak paths may also be modeled using a crossflow junction that is perpendicular to both the K and L volumes when the leak flow is between volumes having the same volume center elevation.

2.1.4.4. Branch

The branch component is a model designed for convenient interconnection of hydrodynamic components. The identical result can be obtained by using a single volume component and several single junction components. Thus the branch is a separate component only in the input processing scheme.

In RELAP5/MOD2 the crossflow junction has been added in which the junction velocities are assumed to be normal to the one-dimensional flow path of the hydrodynamic volume. Thus, the branch component can include multiple connections at the inlet, outlet, or in the crossflow direction.

Specialized modeling considerations are applied to any volume having multiple junctions connected at either volume end (the ends of a hydrodynamic volume are the inlet and outlet as defined in section 2.1.1.1).

These special calculations include both the method for calculating the volume average velocities and the method for partitioning the volume cross-sectional area between the multiple inlet or multiple outlet junctions. The partitioned volume areas are used both in the abrupt area change model to calculate kinetic loss factors and in the momentum equations to simulate the stream-tube area.

In applications, the multiple junction and crossflow models are used in three distinct ways to model branching flows. These are the one-dimensional branching, a tee branch, and a crossflow branch. Combination of the three basic branches may also occur. Each of the three basic models will be discussed in turn.

One-Dimensional Branching

This basic branch model is consistent with the one-dimensional approximation for a piping network and assumes that multidimensional effects at branches are small compared to system interaction effects. In the case of branched flows that occur in headers or plena, the model gives an accurate physical description of the flow division or merging process and the one-dimensional branch model is intended primarily for use in modeling such branched flows. Examples of such situations in LWR systems are flow division at the core inlet if parallel flow paths through the core are modeled, steam generator inlet and outlet plena when several parallel tube groups are modeled (for the effect of tube height and length), or at a wye connection.

The one-dimensional branch is illustrated in Figure 2.1.4-9 for a volume having two inlet junctions and one outlet junction. The junctions J_1 and J_2 are the inlet junctions and junction J_3 is the outlet junction. The multiple flows are assumed to merge in such a way that they come to the common velocity equal to the inlet volume average velocity for volume V_3 . The volume cross-sectional area is then divided in proportion to the volume flow of the respective inlet junctions. This method of apportioning volume cross-sectional area satisfies continuity but does not conserve momentum, particularly for high velocity differences between the merging streams (for flow splitting, however, the method does preserve momentum). For this reason the special jet mixer component was developed for merging flows having high relative velocities such as in a jet pump. The jet-mixer can be used for one-dimensional mixing, but is limited to two inlet

streams and a single outlet stream (see Appendix A for a reference to the jet-mixer model). The volume partitioned areas are calculated as follows

$$(A_K)_j = \frac{[|\alpha_f)_j^n (v_f)_j^n| + |\alpha_g)_j^n (v_g)_j^n|] A_j A_k}{\sum_{i=J_1}^{J_N} [|\alpha_f)_i^n (v_f)_i^n| + |\alpha_g)_i^n (v_g)_i^n|] A_i} \quad 2.1.4-74$$

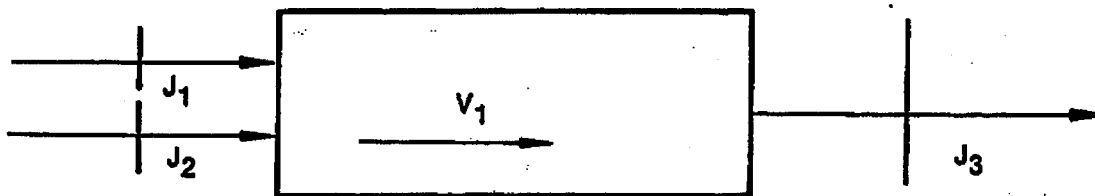


Figure 2.1.4-9. One-Dimensional Branch.

The apportioned volume areas for each junction are used with the abrupt area change model, section 2.1.4.2, to calculate energy loss coefficients for the liquid and vapor streams at each junction.

Ninety-Degree Tee Model

The crossflow junction (see section 2.1.4.3) is used to form a 90-degree tee as shown in Figure 2.1.4-6. In this particular application the side connection to the tee is modeled using a junction in which only one-half of the junction momentum equation has the crossflow form (the half of the junction J_3 associated with volume V_L is a crossflow junction and is designated by an X, see Figure 2.1.4-6).

No special component is provided to accomplish the input associated with a model such as illustrated in Figure 2.1.4-6. The volume V_L may be specified as a branch with the associated junctions or as a single volume with single junctions used to specify the connecting junctions. In either case, junctions J_1 and J_2 should be specified as smooth unless actual abrupt changes in area occur at either junction. The junction J_3 should be specified as smooth with a user input form loss factor to account for the turning and entrance losses. In addition, junction J_3 must be specified so that the half of the junction associated with volume V_L is modeled as a crossflow junction and the half associated with volume V_K is a normal junction. These options are specified through input of junction control flags.

It is also possible to model a 90-degree tee with the RELAP5/MOD2 code, however, unphysical numerical results may be obtained. Thus, the 90-degree tee model described previously is recommended and is a closer approximation to the actual fluid momentum interaction which occurs at a tee.

Gravity Effects at a Tee

In some branching situations where the through flow is small or where the flow is constrained by the geometry, body force effects may be significant. Examples that occur in PWR systems are the cold leg connections to the inlet annulus and downcomer, and the hot leg connection to the upper plenum and core. This type of branched flow is modeled as shown in Figure 2.1.4-10. Here the vertical direction is modeled as the through-flow direction (indicated by the volume orientation arrows). The cold or hot leg connections are modeled by crossflow junctions. The through flow direction of volume V_3 is chosen to correspond to the major flow path. In the case of a PWR inlet annulus through-flow in the horizontal direction is inhibited by the annular structure and in the case of the upper plenum to core connection the area for flow in the vertical direction is large compared to the flow

area in the horizontal direction. Some judgment is required to select the orientation. However, the crossflow branch connection will permit through-flow in the horizontal direction but with some accompanying pressure rise and drop associated with the fact that the momentum flux terms are neglected in the crossflow part of the junction.

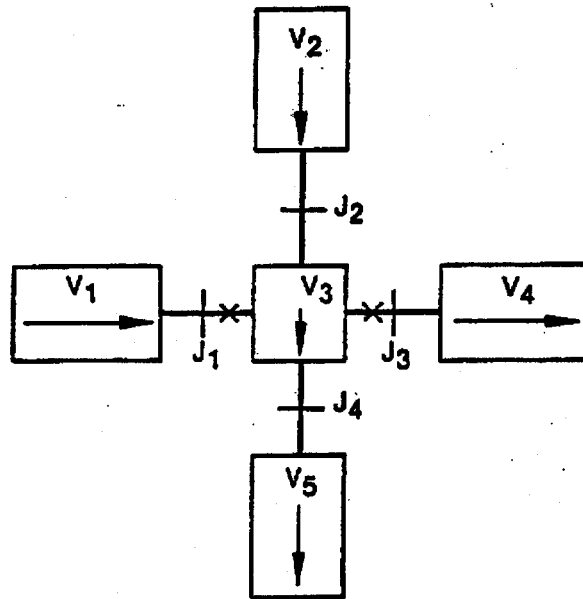


Figure 2.1.4-10. Gravity Effects on a Tee.

The model illustrated in Figure 2.1.4-10 has the additional advantage that the effect of vertical void gradients in the flow out of the horizontal connections may be more sharply defined as a result of the central volume, V_3 , which has a vertical height equal to the diameter of branch volumes V_1 and V_4 .

No special component model is provided for modeling the vertical tee and either a branch or a single volume may be used for volume V_3 . The branch component is more convenient since all junctions connecting to volume V_3 can be specified with the branch component.

Crossflow Branch

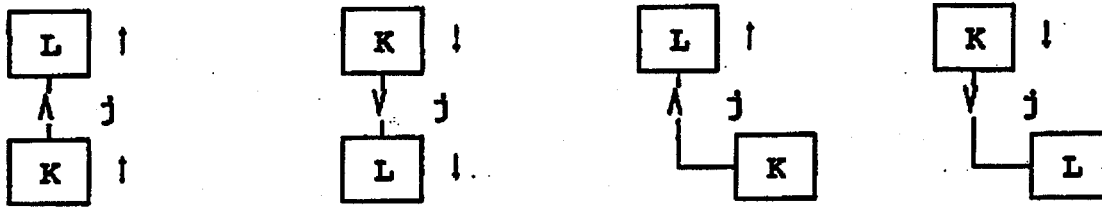
A fourth type of branch flow path can be created by the use of a crossflow junction to couple two volumes. This type of branch is used to model crossflow between columns having centers at the same vertical elevation. The crossflow junction is assumed to have no elevation change; thus, one limitation of this type of branch is that the volume centers that are coupled must be at the same elevation. If volumes of differing elevation are coupled, an input processing error will occur in the loop elevation checking routines. The application of the crossflow junction for crossflow or leak path modeling is illustrated in Figure 2.1.4-7. The length scale associated with the crossflow junction is one half the diameter of the L volume. This length is only used for modeling the fluid inertia terms in the momentum equation and is always assumed to lie in a horizontal plane.

The pure crossflow branch is most easily modeled using a single junction component for the crossflow junction. However, either volume, V_1 or V_2 in Figure 2.1.4-7, can be modeled using the branch component and specifying the coupling junctions with that component.

2.1.4.5. Countercurrent Flow Limit (CCFL) Model

During the reflux condensation period of a small break LOCA transient in a PWR with U-tube steam generator, countercurrent flow limitation (CCFL) often will occur at the hot leg bend and at the U-tube inlet. The Wallis CCFL correlation³⁴ is added to calculate the steam and liquid flow rates for certain RELAP5 junctions. The applicability of the CCFL model is limited to the volume and junction configurations shown in Figure 2.1.4-11, in which K and L are RELAP5 volumes, the junction j is from the exit of volume K to the inlet of volume L, and ΔZ is the elevation change of each volume.

This page is intentionally left blank.



- a) $\Delta Z(K) > 0$ & $\Delta Z(L) > 0$ b) $\Delta Z(K) < 0$ & $\Delta Z(L) < 0$ c) $\Delta Z(K) = 0$ & $\Delta Z(L) > 0$ d) $\Delta Z(K) < 0$ & $\Delta Z(L) = 0$

Figure 2.1.4-11. Volumes and Junction Configurations Available for CCFL Model.

The general form of the Wallis CCFL correlation³⁴ is:

$$\left(j_g^* \right)^{1/2} + m \left(j_f^* \right)^{1/2} = c, \quad 2.1.4-75$$

where m is the negative slope and c is the y-intercept, respectively, of a plot of j_g^* versus j_f^* . The dimensionless gas flux, j_g^* , and the liquid flux, j_f^* , are defined by

$$j_g^* = j_g \left[\frac{\rho_g}{g D_j (\rho_f - \rho_g)} \right]^{1/2} \quad 2.1.4-76$$

and

$$j_f^* = j_f \left[\frac{\rho_f}{g D_j (\rho_f - \rho_g)} \right]^{1/2}, \quad 2.1.4-77$$

respectively, where j_g is the gas superficial velocity, j_f is the liquid superficial velocity, and D_j is the junction hydraulic diameter.

With regard to the solution method, if the CCFL model is requested by the user, the coding checks if countercurrent flow exists and if the liquid downflow exceeds the limit imposed by equation 2.1.4-75. If this is true, the sum momentum equation and the flooding limit equation is applied as has been done in RELAP5/MOD3.¹⁴⁴ The code's difference equation is replaced with the flooding limit equation during the semi-implicit intermediate velocity calculation (Subroutine VEXPLT). The difference equation contains the interphase friction, whereas the sum equation does not. This method is advantageous in that the phasic velocities still must satisfy the the sum equation which contains gravity and pressure terms. The numerical form of Equation 2.1.4-75 needed by the code is obtained by letting $c_g = j_g^*/v_g$ and $c_f = j_f^*/v_f$, solving for $m j_f^{1/2}$, and squaring the equation. This results in

$$m^2 c_{f,j}^n v_{f,j}^{n+1} = c^2 - 2c (c_{g,j}^n)^{1/2} (v_{g,j}^{n+1})^{1/2} + c_{g,j}^n v_{g,j}^{n+1} \quad 2.1.4-78$$

Linearization of $(v_{g,j}^{n+1})^{1/2}$ gives

$$(v_{g,j}^{n+1})^{1/2} = (v_{g,j}^n)^{1/2} + \frac{1}{2} (v_{g,j}^n)^{-1/2} (v_{g,j}^{n+1} - v_{g,j}^n) \quad 2.1.4-79$$

and substitution into equation 2.1.4-75 produces

$$\begin{aligned} m^2 c_{f,j}^n v_{f,j}^{n+1} + [c (c_{g,j}^n)^{1/2} (v_{g,j}^n)^{-1/2} - c_{g,j}^n] v_{g,j}^{n+1} \\ = c^2 - c (c_{g,j}^n)^{1/2} (v_{g,j}^n)^{1/2} \end{aligned} \quad 2.1.4-80$$

The above method can be used when both the RELAP5 momentum equations and the CCFL correlation predict countercurrent flow. In situations where RELAP5 predicts countercurrent flow and the

CCFL correlation predicts current flow based on the RELAP5 calculated velocities, a different approach is used. The present RELAP5/MOD2 model does not address this situation. When this situation arises an iterative approach between the RELAP5 momentum solution and the CCFL correlation prediction is used until both solutions predict consistent flow behavior. During the iteration, the junction interphase drag of k-th iteration, f_{gf}^k , is multiplied by

$$C_{ccfl} = |v_{g,j}^k + v_{f,j}^k| / [(v_{g,j}^k)^2 + (v_{f,j}^k)^2]^{1/2}, \quad 2.1.4-81$$

such that

$$f_{gf}^{k+1} = C_{ccfl}^k f_{gf}^k . \quad 2.1.4-82$$

This page intentionally left blank.

2.1.5. Special Component Models

RELAP5 consists of a variety of generic models which are used to build system models. The general philosophy has been to avoid system component models such as pressurizer, steam generator, core, etc. However, certain subsystem components are unavoidable due to unique processes or performance. RELAP5 contains models for subsystem components such as a separator, pump, valve, and accumulator. A summary of each of these models is included here.

2.1.5.1. Separator

The RELAP5 separator model is a nonmechanistic or black box model consisting of a special volume with junction flows as pictured in Figure 2.1.5-1. A steam-water inflowing mixture is separated by defining the quality of the outflow streams using empirical functions. No attempt is made to model the actual separation process from first principles.

The separator vapor outlet performance is defined by means of a special function for the vapor void fraction at J_1 . The donored junction vapor void fraction used to flux mass through the steam outlet is related to the vapor void fraction in the separator volume using the curve in Figure 2.1.5-2. For separator volume void fractions above the value of VOVER (an input parameter) a perfect separation is assumed and pure vapor is fluxed out junction J_1 . For separator volume void fractions less than VOVER a two-phase mixture is fluxed out. The VOVER parameter governs the vapor void fraction of the outflow. If VOVER is small the vapor outflow corresponds to an ideal separator. If VOVER equals 1.0 the vapor outlet junction behaves as a normal junction and the vapor outlet junction void fraction is equal to the separator volume average void fraction.

This page is intentionally left blank.

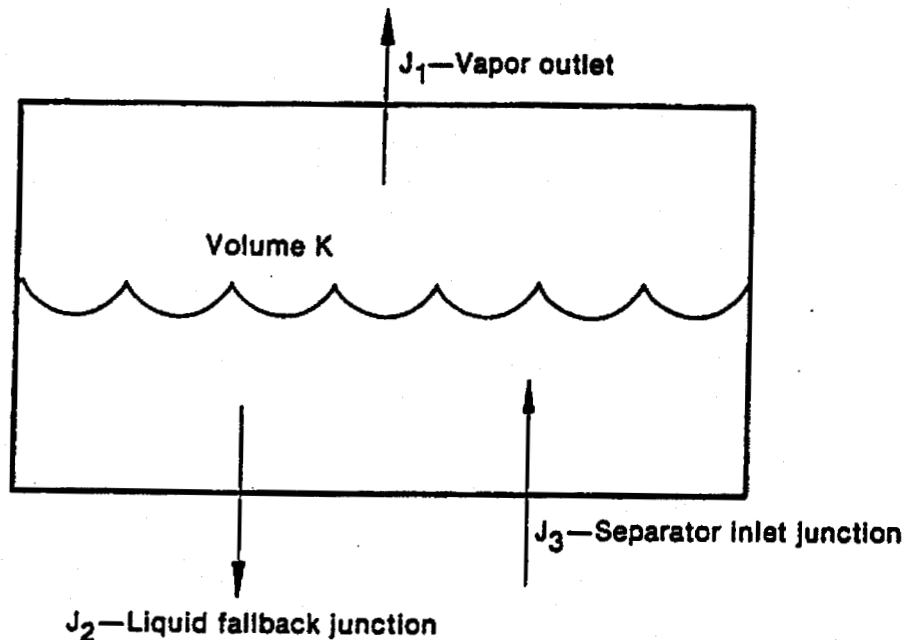


Figure 2.1.5-1. Typical Separator Volume and Junctions.

The flow of the separator liquid drain junction is modeled in a manner similar to the steam outlet except pure liquid outflow is assumed when the volume void fraction is less than the value of $VUNDER$, see Figure 2.1.5-3. Normal donor fluxes are used for the separator inlet junction. Although the void fractions used to flux mass and energy from the separator volumes are modified, the normal junction momentum equations are used to calculate the flow velocities.

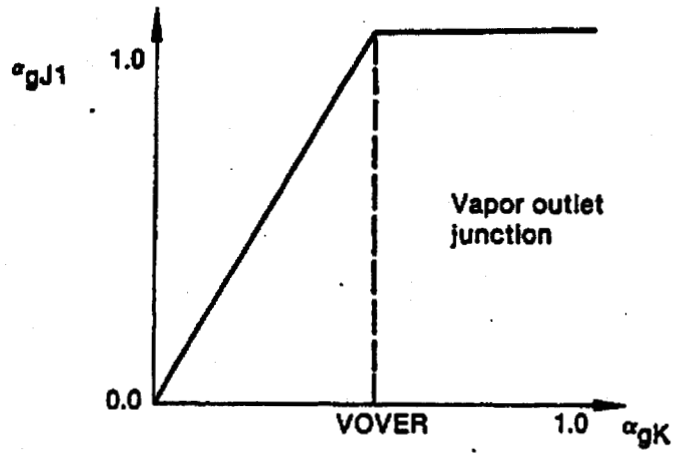


Figure 2.1.5-2. Vapor Outflow Void Donoring.

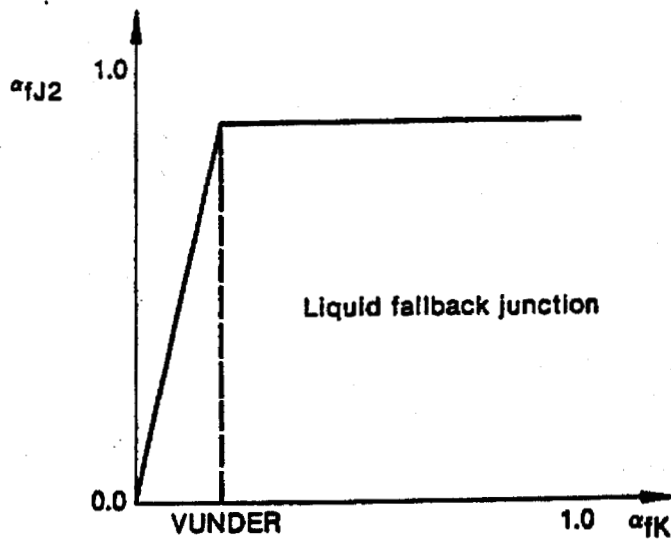


Figure 2.1.5-3. Liquid Fallback Void Donoring.

2.1.5.2. Pump Model

The pump is a volume oriented component and the head developed by the pump is apportioned equally between the suction and discharge junctions that connect the pump volume to the system. The pump model is interfaced with the two fluid hydrodynamic model by assuming the head developed by the pump is similar to a body force. Thus, the head term appears in the mixture momentum equation, but like the gravity body force, it does not appear in the momentum difference equation used in RELAP5. The term that is added to the mixture momentum equation is

$$\frac{1}{2}\rho gH ,$$

2.1.5-1

where H is the total head rise of the pump (m), ρ is the fluid density (kg/m^3), and g is the acceleration due to gravity (m/s^2). The factor 1/2 is needed because the term is applied at both the suction and discharge junctions.

In the semi-implicit numerical scheme, the pump is coupled explicitly so the numerical equivalent of Equation 2.1.5-1 is

$$\frac{1}{2}\rho^n g H^n \Delta t ,$$

2.1.5-2

where the n designates the previous time level and Δt is the time integration interval. This term is added to the right side of the mixture momentum equation.

In the nearly-implicit numerical scheme, the pump is coupled implicitly by way of its dependence on the volumetric flow rate (Q). It is assumed that the head depends on the volumetric flow rate, and a first order Taylor series expansion is used

$$H^{n+1} = H^n + \left(\frac{dH}{dQ} \right)^n (Q^{n+1} - Q^n) \quad . \quad 2.1.5-3$$

Thus, the numerical equivalent of Equation 2.1.5-1 in the nearly-implicit scheme is

$$\frac{1}{2} \rho_g^n g H^n \Delta t + \frac{1}{2} \rho_g^n g \left(\frac{dH}{dQ} \right)^n (Q^{n+1} - Q^n) \Delta t \quad . \quad 2.1.5-4$$

This term is added to the right side of the mixture momentum equation, which uses the linear implicit convection term from NUREG-4312¹ sections 3.1.1.4 and 3.1.1.7.

The pump dissipation is calculated for the pump volume as

$$r\omega - \frac{gH}{\rho} (\alpha_f \rho_f v_f + \alpha_g \rho_g v_g) A \quad , \quad 2.1.5-5$$

where r is the pump torque and ω is the pump speed.

This term is evaluated explicitly in both the semi-implicit and nearly-implicit schemes, and it is partitioned between the liquid and vapor thermal energy equations in such a way that the rise in temperature due to dissipation is equal in each phase (the details of the dissipation mechanism in a two-phase system are unknown so the assumption is made that the mechanism acts in such a way that thermal equilibrium between the phases is maintained without phase change). Thus, the terms that are added to the right sides of the liquid and vapor thermal energy equations, are

$$\frac{\left[r\omega^n - \frac{gH^n}{\rho^n} \left(\alpha_f^n \rho_f^n \bar{v}_f^n + \alpha_g^n \rho_g^n \bar{v}_g^n \right) A \right] \Delta t \left[\alpha_f^n \rho_f^n C_{pf}^n \right]}{\left[\alpha_f^n \rho_f^n C_{pf}^n + \alpha_g^n \rho_g^n C_{pg}^n \right]} \quad 2.1.5-6$$

and

$$\frac{\left[r_{\omega}^n - \frac{gH^n}{\rho^n} \left(\alpha_f^n \rho_f^n \bar{v}_f^n + \alpha_g^n \rho_g^n \bar{v}_g^n \right) A \right] \Delta t \left(\alpha_g^n \rho_g^n C_{pg}^n \right)}{\left(\alpha_f^n \rho_f^n C_{pf}^n + \alpha_g^n \rho_g^n C_{pg}^n \right)} \quad 2.1.5-7$$

respectively.

The pump head, H , and torque, τ , are defined by means of an empirical homologous pump performance model and the pump speed, ω , is defined by a pump drive model. The derivative of the pump head with respect to the volumetric flow rate, dH/dQ , is obtained from the empirical homologous pump performance model using the assumption that the pump speed is constant.

Centrifugal Pump Performance Model

The basic pump performance data must be generated experimentally. Analytical programs have been developed that are reasonably successful in predicting near design pump performance for single-phase fluids. For off design operation or for operation with a two-phase fluid, the problems of analytical pump performance prediction are nearly insurmountable. The basic parameters that characterize the pump performance are the rotational speed, ω or N , the volumetric through flow, Q , the head rise, H , and the shaft torque, τ . The relationship between these four parameters can be uniquely displayed by a four-quadrant representation of such data. A typical four quadrant curve is shown in Figure 2.1.5-4. Both positive and negative values for each of the four parameters are represented. The disadvantages in using such a data map for numerical purposes are the need for two-dimensional interpolation, the large number of points needed to define the entire range, and the fact that the map is infinite in extent. These objections can be largely

overcome by use of a homologous transformation based on the centrifugal pump similarity relationships. Such a transformation collapses the four quadrant data onto a single bounded dimensionless curve having eight basic octants. Typical homologous curves for the head and torque are illustrated in Figures 2.1.5-5 and 2.1.5-6 respectively where ω_r , Q_R , H_R , and τ_R are the rated values for the pump speed, volumetric flow rate, head, and torque, respectively. The homologous transformation is not unique and not all points of Figure 2.1.5-4 lie on the curves of Figures 2.1.5-5 and 2.1.5-6. However, the data are closely grouped and the single curve is a good approximation for the global pump performance.

The pump model allows the user the option of accounting for cavitation or two-phase degradation effects on pump performance. The user must supply a separate set of homologous, two-phase curves for head and torque that are in the form of difference curves. Difference curves are used because analysis of available two-phase pump data indicated that when the fluid being pumped had a void fraction between 0.2 and 0.9, little head was developed by the pump being tested. Outside this range of void fraction, the pump developed head varied from zero to undegraded single-phase performance. To consider the degraded performance, a set of dimensionless homologous curves was fit to the head data. Thus the fully-degraded two-phase head was expressed as a function of the standard pump model arguments.

To consider the ranges of void fraction where the pump was able to develop head (0 to 0.2 and 0.9 to 1.0), a multiplier as a function of void fraction was used. The multiplier varied from 0 to about 1.0 as the void fraction varied from 0 to 0.2, and the multiplier varied from about 1.0 to 0 as the void fraction varied from 0.9 to 1.0.

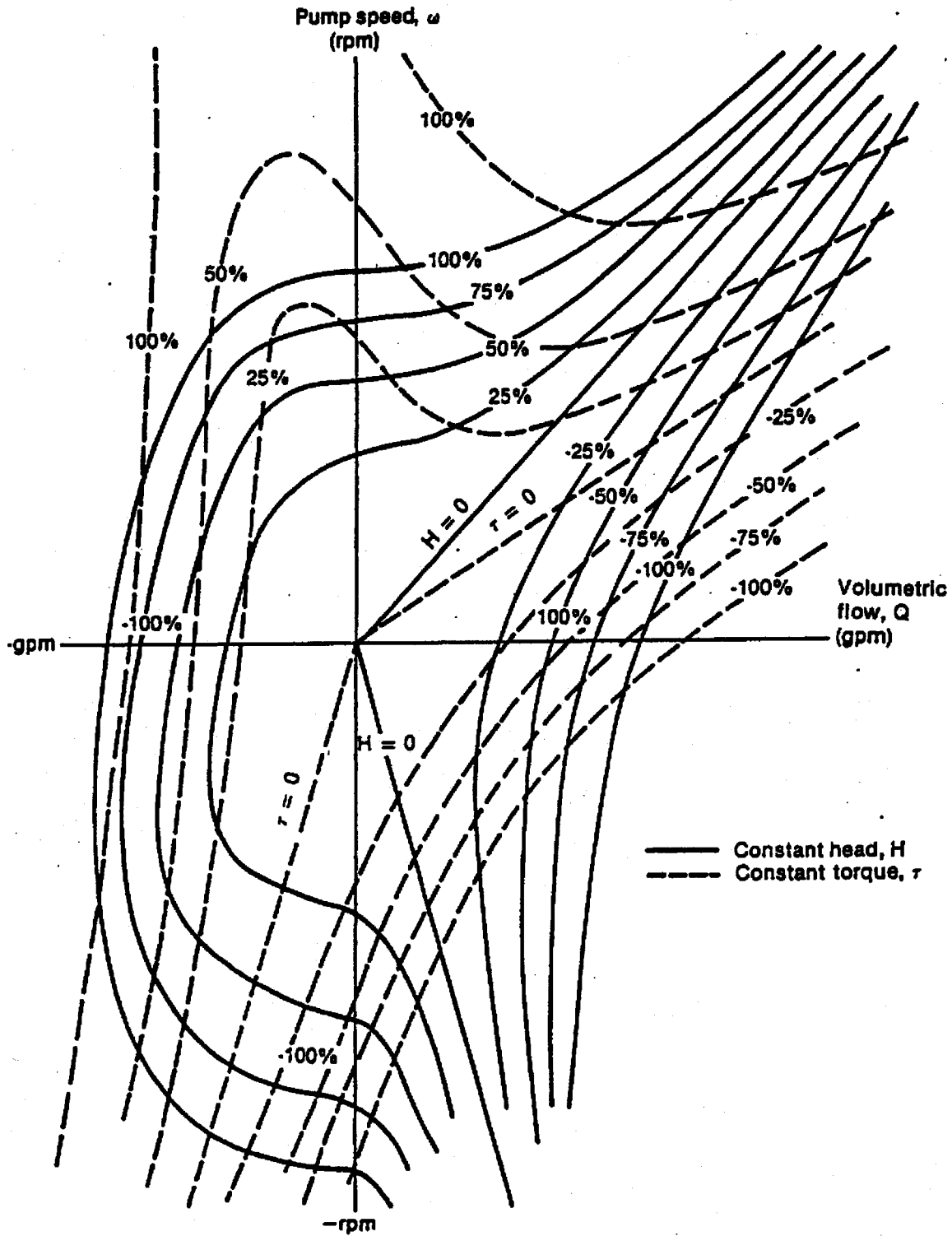


Figure 2.1.5-4. Typical Pump Characteristic Four-Quadrant Curves.

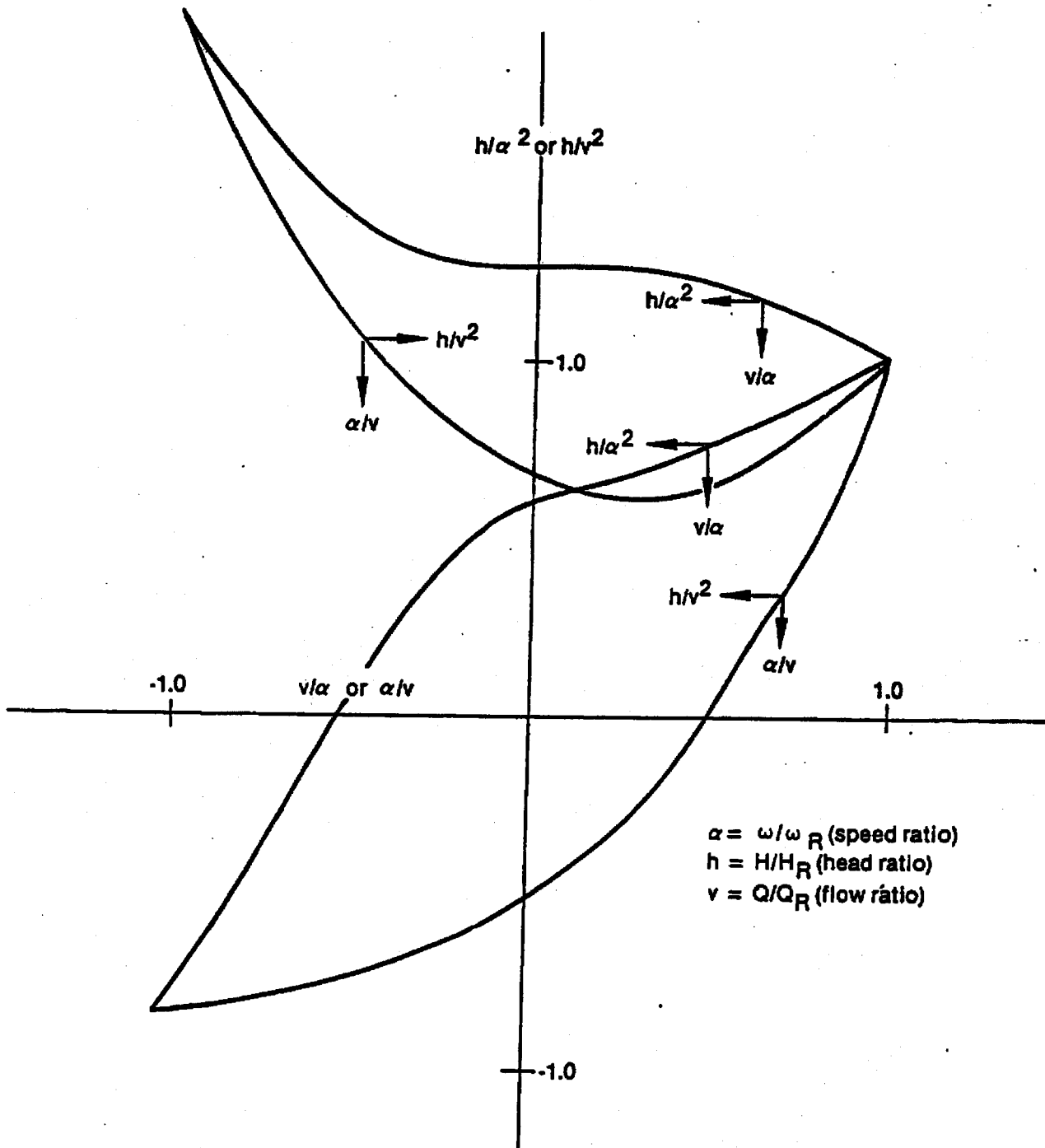


Figure 2.1.5-5. Typical Pump Homologous Head Curves.

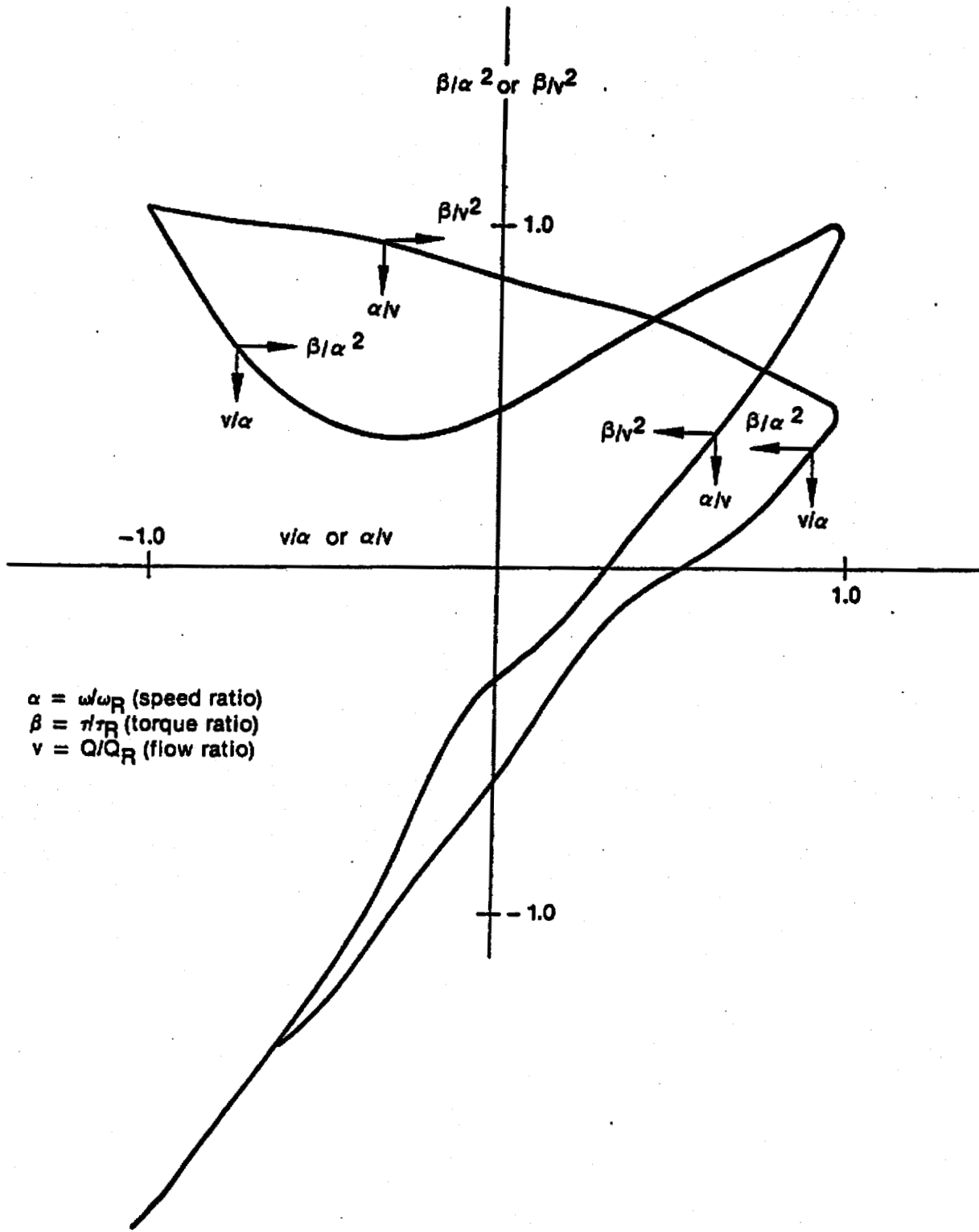


Figure 2.1.5-6. Typical Pump Homologous Torque Curves.

Available pump data from the 1-1/2 Loop Model Semiscale and Westinghouse Canada Limited (WCL) experiments were used in developing the two-phase pump data. Assumptions inherent in the pump model for two-phase flow include:

1. The head multiplier, $M_H(\alpha_g)$, determined empirically for the normal operating region of the pump, is also valid as an interpolating factor in all other operating regions.
2. The relationship of the two-phase to the single-phase behavior of the Semiscale pump is applicable to large reactor pumps. This assumes that the pump model of two-phase flow is independent of pump specific speed.

The single-phase pump head (dimensionless) curve for the Semiscale pump is shown in Figure 2.1.5-7 and the fully degraded two-phase pump head curves are shown in Figure 2.1.5-8. These represent complete pump characteristics (except for the reverse pump fully degraded region) for the Semiscale pump operating under two-phase conditions with the average of the void fractions of the pump inlet and outlet mixtures between 0.2 and 0.9. The lines drawn through the data were determined by least square polynomial fits to the data using known constraints.

A comparison of the two-phase data in Figure 2.1.5-8 with the single-phase data in Figure 2.1.5-7 shows that the two-phase dimensionless head ratio (h/v^2 or h/α^2) is significantly less than the single-phase dimensionless head ratio for the normal pump operation region (HAN and HVN). For negative ratios of v/α , such as those that occur in the HAD region, the pump flow becomes negative. When the pump flow is negative, the two-phase dimensionless head ratio is greater than the single-phase dimensionless head ratio. Two-phase flow friction losses are

Normal pump	$(+Q, +\alpha)$	}	HAN
			HVN
Energy dissipation	$(-Q, +\alpha)$	}	HAD
			HVD
Normal turbine	$(-Q, -\alpha)$	}	HAT
			HVT
Reverse pump	$(+Q, -\alpha)$	}	HAR
			HVR

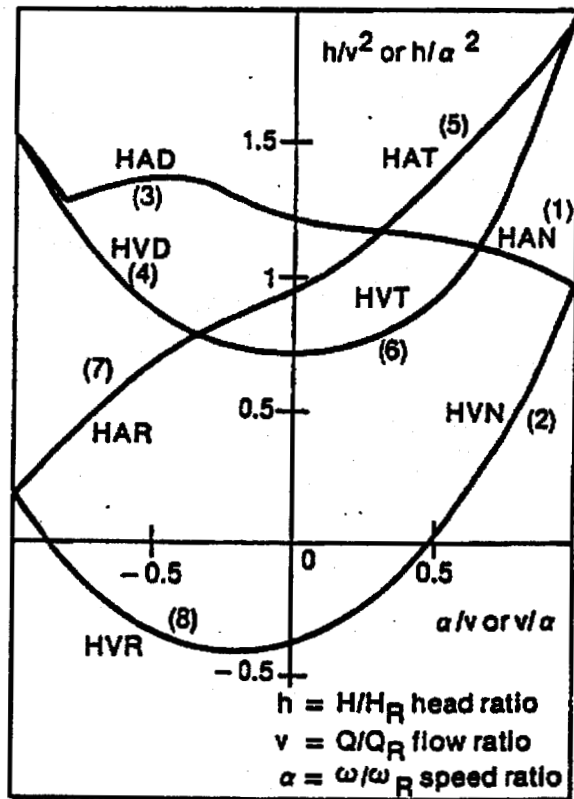


Figure 2.1.5-7. Single-Phase Homologous Head Curves for 1-1/2 Loop MOD1 Semiscale Pumps.

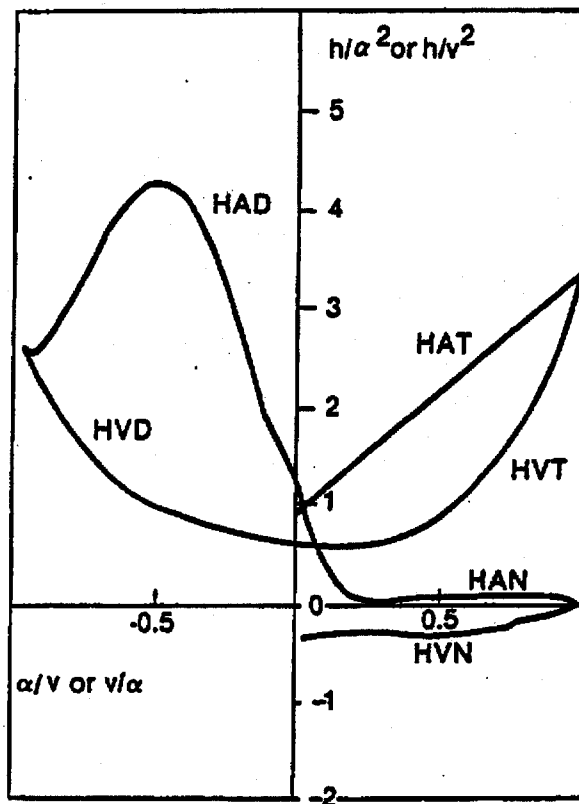


Figure 2.1.5-8. Fully Degraded Two-Phase Homologous Head Curves for 1-1/2 Loop MOD1 Semiscale Pumps.

generally greater than single-phase losses, and friction is controlling in this energy dissipation region (HAD). The other regions of two-phase dimensionless head ratio data show similar deviations from single-phase data.

Table 2.1.5-1 shows the difference between the single- and two-phase dimensionless head ratio data as a function of v/α and α/v for the various pumping regions shown in Figures 2.1.5-7 and 2.1.5-8. The differences shown in Table 2.1.5-1 are for the eight curve types used for determining pump head.

The head multiplier, $M_H(\alpha_g)$, and void fraction data shown in Table 2.1.5-2 were obtained in the following manner. The Semiscale and WCL pump data⁹² were converted to dimensionless head ratios of h/α^2 or h/v^2 . Values of the dimensionless head ratios were obtained for pump speeds and volumetric flow rates within 50% of the rated speed and flow rate for the pumps. The difference between the single- and two-phase dimensionless ratios was developed as a function of the average void fractions for the pump inlet and outlet mixtures. The difference between the single- and two-phase dimensionless ratios was then normalized to a value between 0 and 1.0. The normalized result was tabulated as a function of the void fraction.

If the two-phase option is selected, the pump head and torque are calculated from

$$H = H_{1\phi} - M_H(\alpha_g) (H_{1\phi} - H_{2\phi}) \quad 2.1.5-8$$

and

$$\tau = \tau_{1\phi} - M_r(\alpha_g) (\tau_{1\phi} - \tau_{\phi}) \quad 2.1.5-9$$

where

1ϕ = single-phase value,

2ϕ = two-phase, fully degraded value, $0.2 < \alpha_g < 0.9$,

M = multiplier on difference curve, and

α_g = average volume void fraction.

Centrifugal Pump Drive Model

The pump torque is used to calculate the pump speed after the pump has been shut off by the input trip signal. The speed is calculated by the deceleration equation

$$I \frac{d\omega}{dt} = r \quad . \quad 2.1.5-10$$

The solution of this equation is

$$\omega_{t+\Delta t} = \omega_t + \frac{r\Delta t}{I} \quad , \quad 2.1.5-11$$

where

r = net torque,

I = moment of inertia,

t = time,

Δt = time step, and

ω = angular velocity.

The rate of energy addition to the pump system is given by ωr and has been used in Equation 2.1.5-5 to calculate the pump dissipation.

Table 2.1.5-1. Semiscale Dimensionless Head Ratio Difference (single-phase minus two-phase) Data.

$$x = \frac{v}{\alpha} \quad \text{or} \quad \frac{\alpha}{v}$$

$$y = \frac{h}{\alpha^2} \Big|_{1\phi} - \frac{h}{\alpha^2} \Big|_{2\phi} \quad \text{or} \quad \frac{h}{v^2} \Big|_{1\phi} - \frac{h}{v^2} \Big|_{2\phi}$$

Curve Type	x	y	Curve Type	x	y
1 (HAN)	0.00	0.00	4 (HVD)	-1.00	-1.16
	0.10	0.83		-0.90	-0.78
	0.20	1.09		-0.80	-0.50
	0.50	1.02		-0.70	-0.31
	0.70	1.01		-0.60	-0.17
	0.90	0.94		-0.50	-0.08
	1.00	1.00		-0.35	0.00
2 (HVN)	0.00	0.00	-0.20	0.05	
	0.10	-0.04	-0.10	0.08	
	0.20	0.00	0.00	0.11	
	0.30	0.10	5 (HAT)	0.00	0.00
	0.40	0.21		0.20	-0.34
	0.80	0.67		0.40	-0.65
	0.90	0.80		0.60	-0.95
1.00	1.00	0.80	-1.19		
3 (HAD)	-1.00	<u>-1.16</u>	1.00	-1.47	
	-0.90	-1.24	6 (HVT)	0.00	0.11
	-0.80	-1.77		0.10	0.13
	-0.70	-2.36		0.25	0.15
	-0.60	-2.79		0.40	0.13
	-0.50	-2.91		0.50	0.07
	-0.40	-2.67		0.60	-0.04
	-0.25	-1.69		0.70	-0.23
	-0.10	-0.50		0.80	-0.51
	0.00	0.00		0.90	-0.91
				1.00	-1.47
		7 (HAR)		-1.00	0.00
			0.00	0.00	
		8 (HVR)	-1.00	0.00	
			0.00	0.00	

Table 2.1.5-2. Head Multiplier and Void Fraction Data.

α_g	$M_H(\alpha_g)$
0.00	0.00
0.10	0.00
0.15	0.05
0.24	0.80
0.30	0.96
0.40	0.98
0.60	0.97
0.80	0.90
0.90	0.80
0.96	0.50
1.00	0.00

The total pump torque is calculated by considering the hydraulic torque from the homologous curves and the pump frictional torque. The net torque with the drive motor shut off is

$$\tau = \tau_{hy} + \tau_{fr}$$

2.1.5-12

where

τ_{hy} = hydraulic torque and

τ_{fr} = frictional torque.

Pump frictional torque ($\tau_{fr} = TF$) is modeled as a cubic function of the pump rotational velocity. The FORTRAN notation for the cubic function is

$$S = \frac{V}{VR}$$

2.1.5-13

$$SA = |S| , \text{ and} \quad 2.1.5-14$$

$$TF = -SIGN(TFO + TF1 \cdot SA + TF2 \cdot SA^2 + TF3 \cdot SA^3, S) , \quad 2.1.5-15$$

where V is pump rotational velocity, VR is rated pump rotational velocity, TFO, TF1, TF2, and TF3 are input data, and SIGN is a function whose result is the magnitude of the first argument with the sign of the second argument. An option is available to specify whether reverse rotation of the pump is allowed.

The electric drive motor will affect the speed behavior of the pump while the motor remains connected to its power source. The net torque with the drive motor on is incorporated into the pump model by adding the value of motor torque, r_m , to the torque summation

$$r = r_{hy} + r_{fr} - r_m , \quad 2.1.5-16$$

where the sign of the motor torque is the same as that of the hydraulic and frictional torque for steady operating conditions, that is, zero net torque.

Induction motors are used to drive primary coolant pumps. At constant voltage, the motor torque is an explicit function of speed. This torque/speed relationship is normally available from the motor manufacturer.

Motor torque is supplied to the pump model as a tabular function of torque versus speed as given by the manufacturer's data. A typical torque/speed curve for an induction motor is shown in Figure 2.1.5-9.

The capability to simulate a locked rotor condition of the pump is included in RELAP5. This option provides for simulation of the pump rotor lockup as a function of input elapsed time,

maximum forward speed, or maximum reverse speed. At the time the rotor locks (and at all times thereafter), the pump speed is set equal to zero.

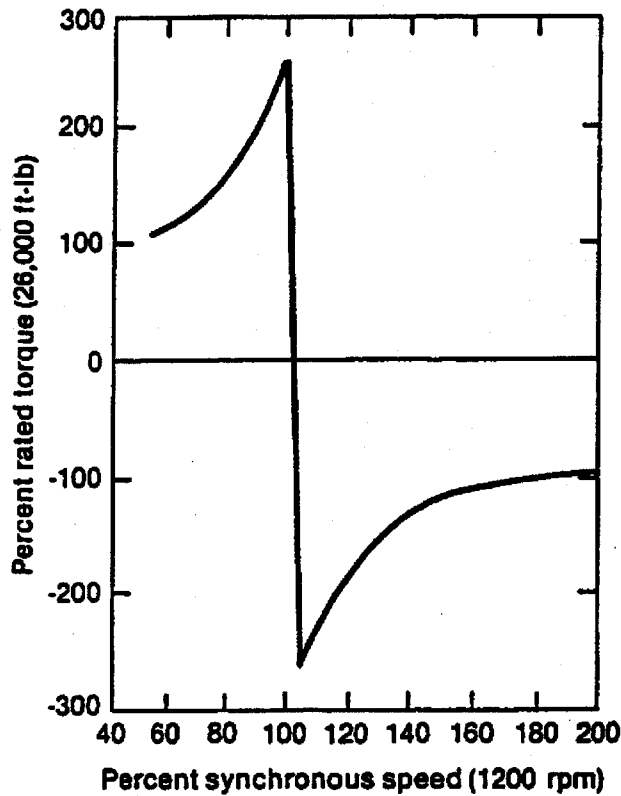


Figure 2.1.5-9. Torque Versus Speed, Type 93A Pump Motor (Rated Voltage).

2.1.5.3. Valves

Valves are quasi-steady models that are used either to specify an option in a system model or to simulate control mechanisms in a hydrodynamic system. The RELAP5 valve models can be classified into two categories: (a) valves that open or close instantly, and (b) valves that open or close gradually. Either type can be operated by control systems or by flow dynamics.

Valves in the first category are trip valves and check valves. The model for these valves does not include valve inertia or momentum effects. If the valve is used as a junction with an abrupt area change, then the abrupt area change model is used to calculate kinetic loss factors when the valve is open.

Valves in the second category are the inertial swing check valve, the motor valve, the servo valve, and the relief valve. The inertial valve and relief valve behavior is modeled using Newton's second law of motion. The abrupt area change model controls losses through the valve as the cross-sectional flow area varies with valve assembly movement. The motor and servo valve use differential equations to control valve movement. These two valves include the options to use the abrupt area change model to calculate losses across the valve or to use flow coefficients (C_v) input by the user. The C_v 's are converted to energy loss coefficients within the numerical scheme.

Valves are modeled in RELAP5 as junction components. The types of valves are defined as follows.

Trip Valve

The operation of a trip valve is solely dependent on the trip selected. With an appropriate trip, an abrupt full opening or full closing of the valve will occur. A latch option is also included for latching the valve in the open or closed position.

Check Valve

The operation of a check valve can be specified to open or close by static differential pressure, to open by static differential pressure and close by flow reversal, or to open by static differential pressure and close by dynamic differential pressure.

All of the check valves will be opened or closed based on static differential pressure across the junction according to

$$\left[P_K + \Delta P_{Kg} \right] - \left[P_L + \Delta P_{Lg} \right] - PCV > 0, \text{ valve opens, 2.1.5-17}$$

where

P_K, P_L = junction from and to volume thermodynamic pressures,

$\Delta P_{Kg}, \Delta P_{Lg}$ = static pressure head due to gravity, and

PCV = back pressure required to close the valve (user input).

For a static pressure controlled check valve the valve will open if Equation 2.1.5-17 becomes positive and will close if Equation 2.1.5-17 becomes negative. If Equation 2.1.5-17 is zero, the valve will remain as previously defined.

For a flow controlled check valve, the valve will open if Equation 2.1.5-17 is positive and will close only if a flow reversal occurs such that

$$GC < 0 ,$$

where GC is the dynamic pressure given as

$$GC = \frac{1}{2}(|\bar{\rho}\bar{v}| \bar{v})_j = \frac{1}{2}|\alpha_f \rho_f v_f + \alpha_g \rho_g v_g|_j (\alpha_f v_f + \alpha_g v_g)_j \quad 2.1.5-18$$

For a dynamic pressure controlled check valve, the valve opens if Equation 2.1.5-17 is greater than zero. Once the valve is open, the forces due to pressure differential and momentum hold the valve open until

$$\left(P_K - \Delta P_{K_g} \right) - \left(P_L + \Delta P_{L_g} \right) + GC - PCV \begin{cases} < 0, \text{ valve closes} \\ = 0, \text{ remains as} \\ & \text{previously} \\ & \text{defined.} \end{cases} \quad 2.1.5-19$$

The terms α_f and α_g are the junction liquid and vapor volume fractions, respectively, ρ_f and ρ_g are the junction liquid and vapor densities, respectively, and v_f and v_g are the junction liquid and vapor velocities, respectively.

All check valves may be initialized as either open or closed. Leakage is also allowed if the valve is closed and the abrupt area change model is used to calculate the valve form losses.

Inertial Valve

This valve models the motion of the valve flapper assembly in an inertial type check valve. The abrupt area change model is used to calculate kinetic form losses assuming that the area between the flapper and the valve seat behaves as an orifice whose area changes in time as a function of the inertial valve geometry.

The motion of the flapper about the shaft axis is given by Newton's second law (angular version) as

$$\tau = I \alpha ,$$

2.1.5-20

where the external torques acting on the valve disk are given by

$$\tau = -W L \sin(\theta + \phi) - A_D L(\Delta P + P_{BP} + G_{head}) , \quad 2.1.5-21$$

where ΔP is the pressure drop across the valve, and α is the angular acceleration. Substituting Equation 2.1.5-20 into Equation 2.1.5-21 gives

$$I\alpha = -WL \sin\theta - \pi R^2 L(\Delta P + P_{BP} + G_{head}) , \quad 2.1.5-22$$

where ϕ has been dropped by assuming the valve is a horizontal pipe. Equation 2.1.5-22 is then written in finite-difference form as

$$\alpha^n = \frac{1}{I} - WL \sin\theta^n - \pi R^2 L(\Delta P^n + P_{BP} + G_{head}) , \quad 2.1.5-23$$

where the superscript, n , indicates the time level, $t + n \Delta t$. Integrating Equation 2.1.5-23 with respect to time yields the angular velocity

$$\omega^{n+1} = \omega^n + \alpha^n \Delta t . \quad 2.1.5-24$$

Similarly integrating Equation 2.1.5-24 gives the angular position

$$\theta^{n+1} = \theta^n + \omega^{n+1} \Delta t . \quad 2.1.5-25$$

The throat flow area for the valve is set by the following function^{94,95}.

$$A_{throat} = \begin{cases} 2\pi R^2 \tan(\theta^{n+1}) & \theta \leq 26.565 \\ \pi R^2 & \theta > 26.565 . \end{cases} \quad 2.1.5-26$$

Several options are allowed with the use of this valve such as specifying minimum and maximum flapper angular positions when the valve is closed, specifying latch or no latch options, and specifying leakage.

Motor Valve

This valve model has the capability of controlling the junction flow area between two control volumes as a function of time. The operation of the valve is controlled by two trips: one for opening the valve, and a second for closing the valve. A constant rate parameter controls the speed at which valve area changes. The motor valve area variation can also be specified using a general table. When the general table is specified, the constant rate parameter controls the valve stem position and the general table relates the stem position to the valve flow area. Conversely, when the general table is not specified, the constant rate parameter controls the rate of change in valve area.

The abrupt area change model is used to calculate kinetic form losses with respect to the valve area. However, if the normalized valve flow area has a value less than 1.0E-10, the valve is assumed to be closed.

A second option allowed for the motor valve is the specification of valve flow coefficients, C_v . These coefficients may be specified using a general table of C_v versus normalized stem position and the smooth junction option must be specified. The conversion of C_v to an energy loss coefficient, K , is done in the numerical scheme using the formula

$$K = 2 \frac{A_{\text{valve}}^2}{C_v^2 \rho_0}$$

2.1.5-27

where

ρ_0 = density of water at 288.71 K (60.0 F).

Provisions also exist for applying multipliers to both stem position and C_v .

Servo Valve

The servo valve operation is similar to that for the motor valve. However, the valve area or stem position is controlled by a control variable rather than by a specified rate parameter. The servo valve also has the same options as the motor valve.

Relief Valve

For thermal-hydraulic analysis of overpressure transients it is necessary to simulate the effects of relief valves. In particular, it is desirable to model the valve dynamic behavior, including simulation of valve flutter and hysteresis effects.

To assist in understanding the relief valve model three schematics of a typical relief valve are shown in Figures 2.1.5-10, 2.1.5-11, and 2.1.5-12. The three schematics represent the valve in the closed (Figure 2.1.5-10), partially open (Figure 2.1.5-11), and fully open (Figure 2.1.5-12) modes, respectively. In the schematics, the seven main components of a relief valve are shown, which are: the valve housing, inlet, outlet, piston rod assembly, spring, bellows, and valve adjusting ring assembly. The numerical model of the valve simply approximates the fluid forces acting on the valve piston and the valve reaction to these forces. The model of the fluid forces is based on a quasi-steady-state form of the impulse momentum principle and the valve reaction force is based on Newton's Second Law of motion.

A qualitative understanding of the operation of the relief valve can be gained by referring again to Figures 2.1.5-10, 2.1.5-11, and 2.1.5-12. If the valve inlet pressure is low the valve is closed, as shown in Figure 2.1.5-10. As the inlet pressure increases the valve piston will remain closed until the force of the upstream pressure on the valve exceeds the setpoint forces. The setpoint forces are the combined forces of the piston and rod assembly weight, the valve spring, the atmospheric pressure inside the bellows and the downstream back pressure around the outside of the bellows. Once the setpoint forces are exceeded the valve piston will begin to lift. Upon opening, the upstream fluid will begin to expand through the opening into the valve ring region. This initial expansion occurs through the angle α_0 and the flow changes direction through an average angle θ_0 as shown in Figure 2.1.5-10. As the flow accelerates, the momentum effects of the expansion and change in flow direction exert a thrust on the valve piston causing the valve to open further. As the valve partially opens the angle of expansion decreases to α_1 and the change in flow direction increases to θ_1 as shown in Figure 2.1.5-11. This effect in turn further increases the thrust on the valve piston causing it to fully open as shown in Figure 2.1.5-12. As these processes occur the valve reaction forces and fluid momentum forces vary in such a manner that the valve will not close until the upstream pressure decreases significantly below the valve setpoint pressure. In this respect a hysteresis effect is observed that is characteristic of relief valves.

The relief valve model consists of a set of equations designed to approximate the behavior described above. In implementing the model, the dynamic behavior of the fluid is calculated at each time step by the RELAP5/MOD2-B&W hydrodynamic solution scheme. The resultant phasic velocities and thermodynamic properties are then utilized to solve a quasi-steady equation approximating the fluid forces on the valve piston. The valve dynamic reaction

forces are then calculated and the new time valve piston speed and position are estimated.

The relief valve model is formulated by applying D'Alembert's principle in which the forces acting on the face of the valve piston are balanced, for which the valve reaction forces can be written as

$$(\text{Reaction Forces}) = F_R = m_v a_{v,x} + B (v_{v,x} - v_{\text{housing}}) + K_s x ,$$

2.1.5-28

where

m_v = mass of the valve mechanism that is in motion
(i.e., the valve piston and rod assembly combined with the spring and bellows),

$a_{v,x}$ = valve assembly acceleration in the x-direction,

B = damping coefficient,

$v_{v,x}$ = velocity of the valve mechanism in the x-direction,

$v_{\text{housing}} = 0$ = velocity of the valve housing,

K_s = spring constant, and

x = piston position (i.e., x-coordinate).

The positive x-direction is assumed to be in the direction of fluid flow at the valve inlet. The fluid forces can be formulated by summing the forces acting over the surfaces of the fluid flow channel such that

$$(\text{Fluid Forces}) = F_F = (P_i A_D) x$$

$$- (P_a A_{Ba}) x - (P_o A_{Bo}) - (P_e A_e) x - F_R ,$$

2.1.5-29

where

F_R = reaction forces,

P_i = valve inlet pressure,

A_D = valve piston face area exposed to the inlet flow stream,

P_a = atmospheric pressure inside the bellows,

A_{Ba} = valve piston area inside the bellows,

P_o = valve back pressure outside the bellows,

A_{Bo} = valve piston area outside the bellows,

A_e = valve ring exit area, and

P_e = valve ring exit pressure.

The subscript x denotes that the force component is in the x-direction. Since the fluid is flowing through a channel that both expands and changes direction, the fluid undergoes a change in momentum expressed by the impulse momentum principle as

$$F_F = \Delta(mv) = \dot{m}_F (v_{e,x} - v_{i,x}) , \quad 2.1.5-30$$

where

\dot{m}_F = mass flow rate of the fluid through the valve,

$v_{e,x}$ = fluid velocity exiting through the rings, and

$v_{i,x}$ = fluid velocity entering the valve inlet.

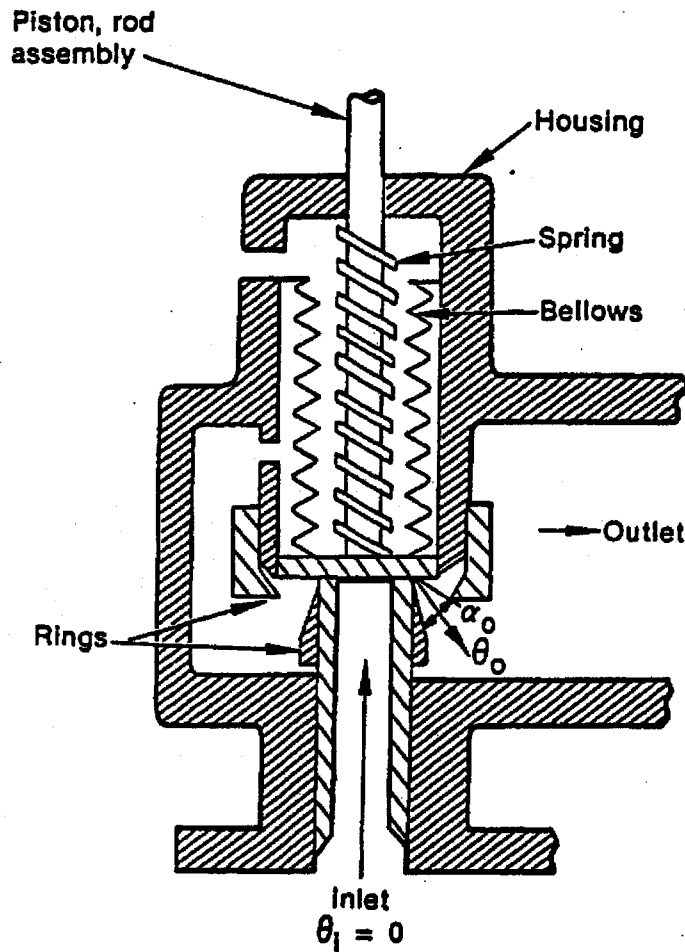
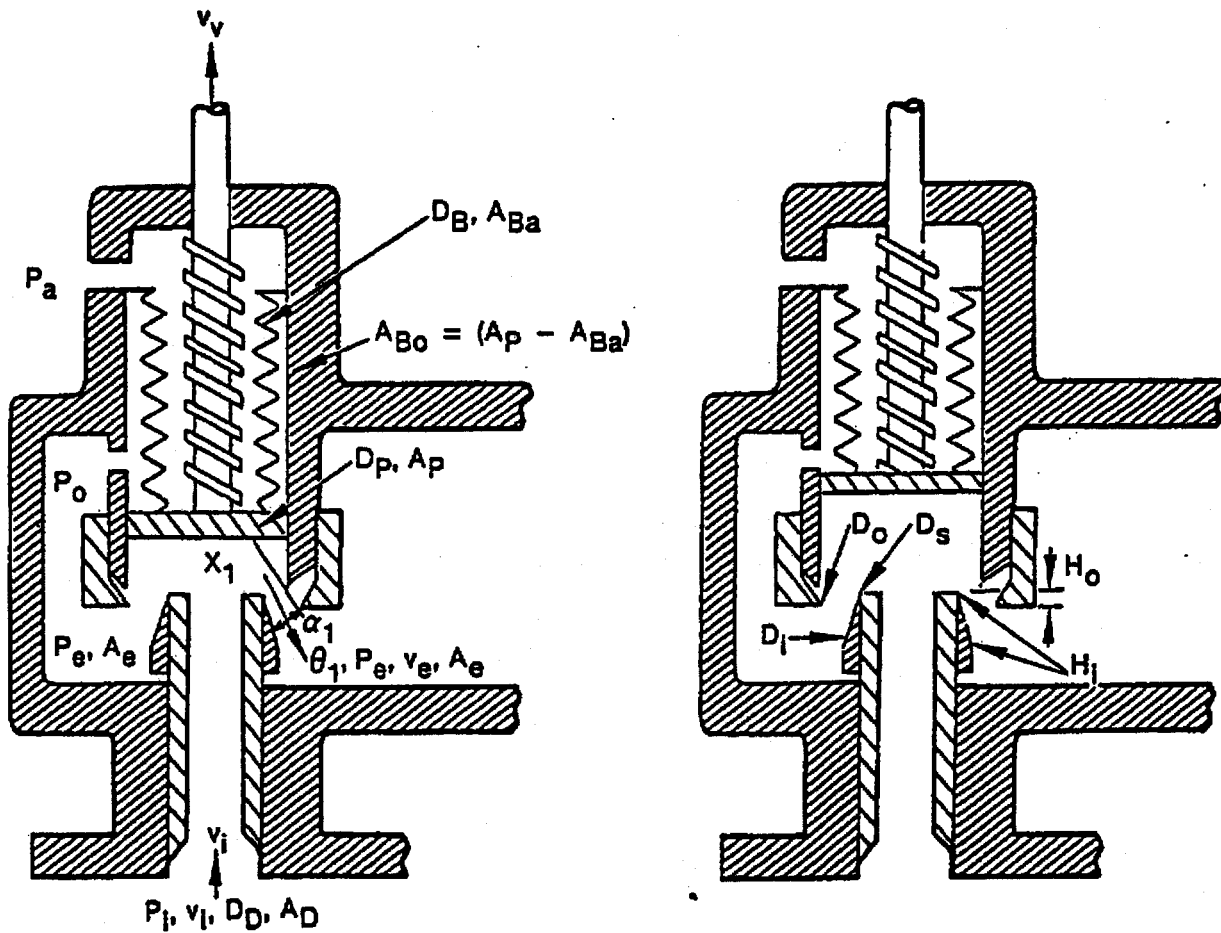


Figure 2.1.5-10. Schematic of a Typical Relief Valve in the Closed Position.



Figures 2.1.5-11. and 2.1.5-12. Schematic of a Typical Relief Valve in the Partially and Fully Open Positions, respectively.

Hence balancing the forces by combining Equations 2.1.5-28, 2.1.5-29 and 2.1.5-30 gives

$$m_v a_{v,x} + Bv_{v,x} + K_s x = -(P_a A_{Ba}) - (P_o A_{Bo}) - (P_e A_e) \cos \theta - \dot{m}_F (v_e \cos \theta - v_i) + P_i A_D \quad 2.1.5-31$$

The valve acceleration can be expressed in terms of the valve velocity as

$$a_{v,x} = \frac{dv_{v,x}}{dt} + g, \quad 2.1.5-32$$

where g is the acceleration of gravity.

Combining Equations 2.1.5-31 and 2.1.5-32, treating the velocity damping term and spring force position terms implicitly and integrating over the time step gives

$$m_v (v_{v,x}^{n+1} - v_{v,x}^n) + Bv_{v,x}^{n+1} dt + K_s x^{n+1} dt + m_v g dt = [(P_i^n A_D) - (P_a A_{Ba}) - (P_o^n A_{Bo}) - (P_e^n A_e) \cos \theta_e^n - \dot{m}_F^n (v_e \cos \theta_e^n - v_i)] dt, \quad 2.1.5-33$$

where the superscripts n and $n+1$ represent the old and new time terms, respectively.

The position term, x^{n+1} , can be written in terms of the valve velocity by considering that

$$v_{v,x} = \frac{dx}{dt} \quad 2.1.5-34$$

If Equation 2.1.5-34 is integrated over the time step then

$$x^{n+1} = x^n + v_{v,x}^{n+1} dt \quad . \quad 2.1.5-35$$

If the valve setpoint pressure is equated to $K_s x_0$ then combining Equations 2.1.5-33 and 2.1.5-35 and both adding and subtracting the term $K_s x_0$ gives the numerical form of the relief valve model, for which

$$\begin{aligned} m_v (v_{v,x}^{n+1} - v_{v,x}^n) + [(B + K_s dt) v_{v,x}^{n+1} + K_s (x^n - x_0) + m_v g] dt \\ = K_s x_0 dt + [(P_i^n A_D) - (P_a A_{Ba}) - (P_o^n A_{Bo}) - (P_e^n A_e) \cos \theta_e^n \\ - \dot{m}_F^n (v_e^n \cos \theta_e^n - v_i^n)] dt \quad . \quad 2.1.5-36 \end{aligned}$$

The size of the gravity term, g , is dependent on the valve orientation. For example, if the valve is oriented upward (i.e., $+x$ is upward) then the gravity term is expressed as $g = -|g|$.

In the numerical scheme, Equation 2.1.5-36 is solved for the new time valve piston velocity, v_v^{n+1} , in terms of the current time terms with superscript, n . The terms required to model the valve geometry and the valve damping, spring, and back pressure forces are input by the user.

The characteristic relief valve hysteresis effects are inherent in the formulation of Equation 2.1.5-36. For example, if the valve is closed then all velocity terms are zero and $x = x_0$. Therefore, acceleration of the valve piston in the positive x direction cannot occur until the upstream force $P_i A_D$ exceeds the spring set point and valve weight. Once the valve opens and the fluid accelerates, the forces due to the change in fluid momentum aid in holding the valve open. Therefore, the valve cannot close until the combined fluid pressure and momentum terms decrease

below the set point forces. Hence, the desired hysteresis is incorporated in the model.

2.1.5.4. Accumulator Model

An accumulator model is included in RELAP5/MOD2-B&W that features mechanistic relationships for the hydrodynamics, heat transfer from the tank wall and water surface, condensation in the vapor dome, and vaporization from the water surface to the vapor dome.

Hydrodynamic Model

An accumulator is modeled in RELAP5 as a lumped-parameter component. This modeling was chosen for two reasons; the spatial gradients in the accumulator tank are expected to be small, and special treatment of the equation of state can be utilized.

The accumulator model and associated notations are shown in Figure 2.1.5-13. The basic model assumptions are:

1. Heat transfer from the accumulator walls and heat and mass transfer from the liquid are modeled using natural convection correlations assuming similarity between heat and mass transfer from the liquid surface.
2. The gas in the gas dome is modeled as a closed expanding system composed of an ideal gas with constant specific heat. The steam in the dome exists at a very low partial pressure and hence its effect on the nitrogen state is neglected. However, energy transport to the gas dome as a result of vaporization/condensation is included.
3. Because of the high heat capacity and large mass of water below the interface, the water is modeled as an isothermal system.

4. The model for liquid flow includes inertia, wall friction, form loss and gravity effects.

Using these assumptions, the basic equations governing the thermal-hydraulics of the tank and discharge line for conservation of mass (nitrogen) can be written as

$$M_n = \text{constant} = \rho_n V_n \quad 2.1.5-37$$

where

M_n and ρ_n = gas mass and density, respectively, and
 V_n = gas dome volume

for conservation of energy.

Nitrogen

$$M_n \frac{\partial u_n}{\partial t} = - P_D \frac{\partial V_v}{\partial t} + \dot{Q}_D \quad 2.1.5-38$$

where

u_n = nitrogen internal energy
 P_D = vapor dome pressure, and
 \dot{Q}_D = heat transfer rate to the gas dome.

Wall

$$M_{\text{wall}} C_{v\text{wall}} \frac{\partial T_{\text{wall}}}{\partial t} = -\dot{Q}_{\text{wall}} \quad 2.1.5-39$$

where

M_{wall} = metal mass in the tank wall,

$C_{V \text{ wall}}$ = metal specific heat,

T_{wall} = mean metal temperature, and

Q_{wall} = heat transfer rate to the wall.

For momentum^a

$$\rho A \left(L \frac{\partial v}{\partial t} + \frac{1}{2} v^2 \right) + Fv = - A \frac{\partial P}{\partial x} + \Delta P_z, \quad 2.1.5-40$$

where

A = flow channel cross-sectional area,

v = velocity,

F = frictional loss coefficient, and

ΔP_z = elevation pressure differential.

For the gas state relationships

$$P_D V_v = M_n R_n T_D \quad 2.1.5-41$$

and

$$U_n = M_n C_{V_n} T_D \quad 2.1.5-42$$

^aEquation 2.1.5-40 is the combined tank and discharge line momentum equations. The wall drag coefficient, F , is given as $1/2 p_{wf} L_L/D A_{LV}$, where D = surge line diameter.

Using Equations 2.1.5-41 and 2.1.5-42, the nitrogen energy equation (Equation 2.1.5-40), can be rewritten as

$$M_n C_{v_n} \frac{dT_D}{dt} = - P_D v A_L + \dot{Q}_D \quad . \quad 2.1.5-43$$

Differentiating Equation 2.1.5-41, eliminating the constant term $M_n R_n$ and substituting the result into Equation 2.1.5-43 yields

$$P_D \left(1 + \frac{R_n}{C_{v_n}} \right) \frac{dv_v}{dt} + v_v \frac{dP_D}{dt} = \frac{R_n}{C_{v_n}} \dot{Q}_D \quad . \quad 2.1.5-44$$

Equations 2.1.5-40, 2.1.5-43, and 2.1.5-44 comprise the system of three differential equations used in the accumulator hydrodynamic model. They are used to numerically advance T_D , v_v , and P_D in time.

Heat Transfer to the Gas Dome

In the accumulator, energy transport by heat transfer is modeled to the gas dome using a typical convective transport equation of the form

$$Q_i = h_i A_i (T_i - T_d) \quad , \quad 2.1.5-45$$

where

subscript i = thermal transport interface,

h_i = convective transport coefficient,

A_i = interface surface area, and

$T_i - T_d$ = interface to gas dome temperature difference.

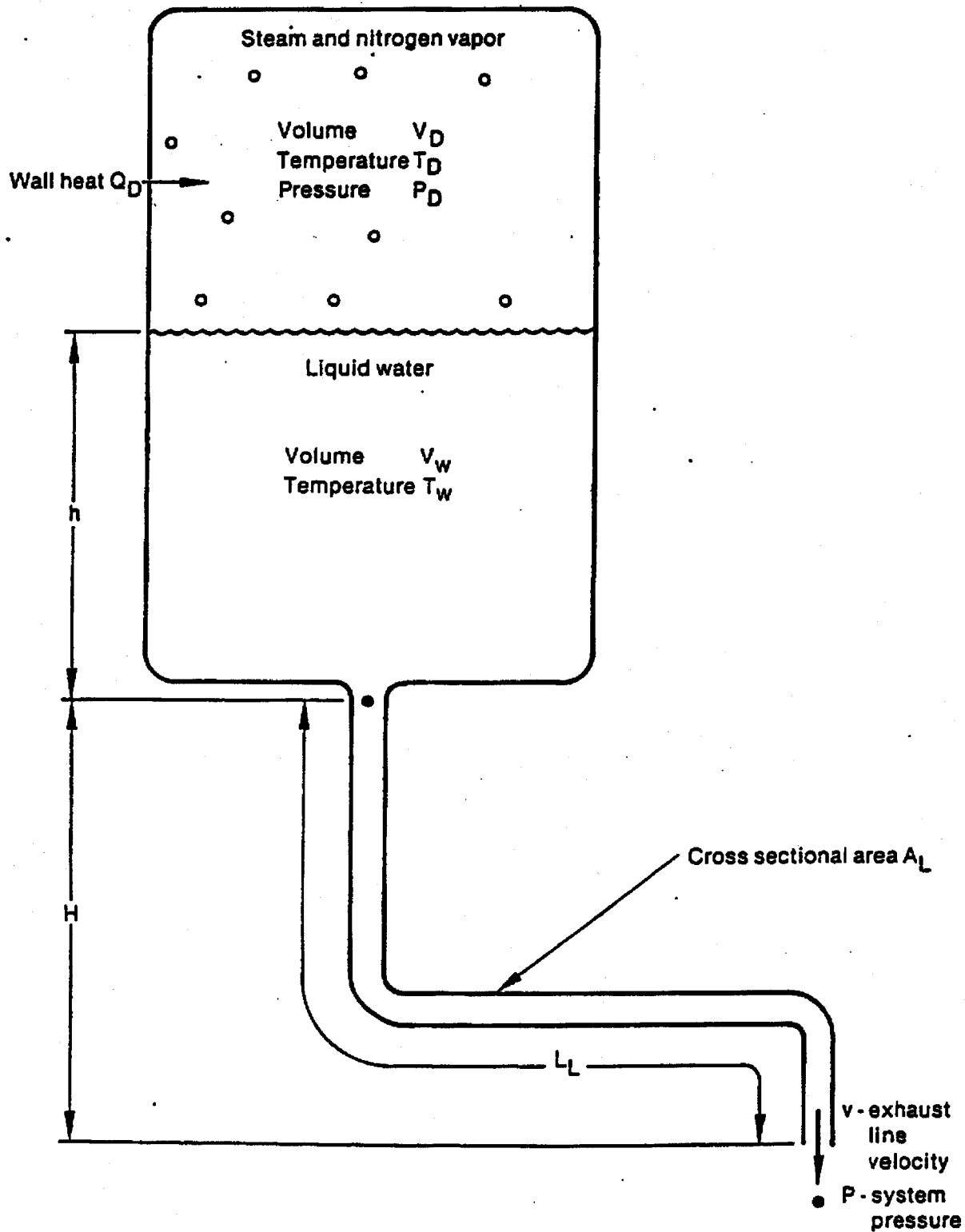


Figure 2.1.5-13. Typical Accumulator.

It should be noted that heat and mass transfer in the accumulator surge line are neglected.

Two turbulent natural convection heat transfer models are used and combined by superposition. First, heat transfer with the cylindrical walls of the tank is considered using a turbulent natural convection correlation⁹⁶ for heat transfer within a vertical cylinder with closed ends for which

$$h_1 = 0.1 \frac{k_d}{\frac{1}{2} D_{TK}} (Gr Pr)^{\frac{1}{3}} \frac{L}{\delta} \quad 2.1.5-46$$

and

$$A_1 = \pi D_{TK} L, \quad 2.1.5-47$$

where

h_1 = gas dome to cylinder heat transfer coefficient,

L = gas dome cylinder length,

δ = gas dome characteristic diameter,

k_d = gas thermal conductivity,

$1/2 D_{TK}$ = integration interval normal to the surface of the cylinder,

Gr = gas dome Grashof number, and

Pr = gas dome Prandtl number.

Second, heat transfer with the disk shaped ends of the cylinder is considered, where the top disk is the metal top of the tank and the bottom disk is the liquid-gas interface. For this model a turbulent natural convection correlation⁵⁶ is used for heat

transfer between two horizontal disks separated vertically where, for each disk,

$$h_2 = 0.15 \frac{k_d}{L} (Gr Pr)^{\frac{1}{3}} \frac{L}{\delta} \quad 2.1.5-48$$

and

$$A_2 = \frac{\pi D_{TK}^2}{4} \quad 2.1.5-49$$

In the correlations given by Equations 2.1.5-46 and 2.1.5-49 the product of the Grashof and Prandtl numbers represents the convective thermal circulation in the gas dome, where the Grashof number represents the circulation and the Prandtl number represents the thermal diffusion. Only the Grashof number is a function of the gas dome dimensions and temperature difference for which

$$Gr = \frac{g \beta_d |T_i - T_d| \delta^3}{\nu_i^2}, \quad 2.1.5-50$$

where

g = acceleration due to gravity,

β_d = gas isobaric coefficient of thermal expansion,

$T_i - T_d$ = magnitude of the interface, gas dome temperature difference,

ν_i = gas kinematic viscosity, and

δ = characteristic overall diameter of the gas dome.

If the Prandtl number is written in terms of the gas dome thermal diffusivity then

$$Pr = \frac{\mu_d}{\rho_d \alpha_d}, \quad 2.1.5-51$$

where

ρ_d = gas density and
 α_d = thermal diffusivity.

The characteristic diameter is defined in terms of the typical volume to surface area ratio as

$$\delta = \frac{4 V_d}{A_i}, \quad 2.1.5-52$$

where

A_i = combined gas dome cylinder, disk top, and bottom surface areas.

Mass Transfer to the Gas Dome

When the accumulator is in its stagnant initial condition the gas dome and liquid are in thermal equilibrium and the gas dome is at essentially 100% humidity. However, as the accumulator blows down, the gas dome expands and cools while the liquid remains essentially isothermal. As a result there is simultaneous vaporization at the liquid-gas interface and condensation in the gas dome.

At the liquid-gas interface as vaporization occurs the vapor diffuses across the temperature gradient into the gas dome. Assuming that the process can be approximated by a quasi-steady

formulation, then for diffusion in a stagnant gas the mass transfer for the process can be written as

$$\dot{M}_{\text{vap}} = - \zeta A_i \frac{dC}{dx}, \quad 2.1.5-53$$

where

\dot{M}_{vap} = rate of vapor diffusion,

ζ = diffusion coefficient,

A_i = surface area of the liquid-gas interface, and

$\frac{dC}{dx}$ = vapor concentration gradient.

The concentration can be expressed in terms of partial pressure such that

$$C = \frac{P_v}{P_d} \rho_g, \quad 2.1.5-54$$

where

C = vapor concentration,

P_v = local vapor partial pressure, and

ρ_g = vapor density (saturated vapor at P_v).

Hence at the dome pressure, the concentration gradient can be written as

$$\frac{dC}{dx} = \frac{1}{P_d} \frac{dP_v \rho_g}{dx}. \quad 2.1.5-55$$

Combining Equations 2.1.5-53 and 2.1.5-55 and integrating gives

$$\dot{M}_{\text{vap}} L_d = - \frac{\zeta A_d}{P_d} \left[\bar{P}_v \int_{x=0}^{x=L_d} d\rho_g + \bar{\rho} \int_{x=0}^{x=L_d} dP_v \right], \quad 2.1.5-56$$

where the integration is performed by parts.

Both of the differential terms $d\rho_g$ and dP_v can be written in terms of temperature differentials if 100% relative humidity is assumed, so that

$$P_v = P^S(T_g),$$

where

$$P^S(T_g) = \text{saturation pressure at the temperature } T_g.$$

Hence the density differential can be expanded as

$$d\rho_g = \left[\left(\frac{\partial \rho_g}{\partial P_g} \right)_T \frac{dP_g}{dT} + \left(\frac{\partial \rho_g}{\partial T} \right)_{P_g} \right] \Delta T, \quad 2.1.5-57$$

where

$$\left(\frac{\partial \rho_g}{\partial P_g} \right)_T = \kappa_g \rho_g \quad \text{and} \quad 2.1.5-58$$

$$\left(\frac{\partial \rho_g}{\partial T} \right)_{P_g} = - \beta_g \rho_g. \quad 2.1.5-59$$

Combining Equations 2.1.5-57, 2.1.5-58, and 2.1.5-59, and substituting Clapeyron's equation for the dP_g/dT term gives

$$d\rho_g = \bar{\rho}_g \left[\kappa_g \left(\frac{h_{fg}}{T_g v_{fg}} \right) - \beta_g \right] dT, \quad 2.1.5-60$$

where Clapeyron's equation is

$$dP^s = \left(\frac{h_{fg}}{T_g v_{fg}} \right) dT, \quad 2.1.5-61$$

and where the term $(h_{fg}/T_g v_{fg})$ is treated as a constant. Combining Equations 2.1.5-56, 2.1.5-60, and 2.1.5-61 the diffusion equation can be rewritten as

$$\dot{M}_{\text{vap}} = \frac{c}{L_d} \frac{A_i}{P_d} \left\{ \bar{P}_g \bar{\rho}_g \left[\kappa_g \left(\frac{h_{fg}}{T_g v_{fg}} \right) - \beta_g \right] + \bar{\rho}_g \left(\frac{h_{fg}}{T_g v_{fg}} \right) \right\} (T_f - T_w). \quad 2.1.5-62$$

The dome average terms are evaluated at the dome average temperature, $T_g = T_d$, and T_w is the tank top wall temperature.

Equation 2.1.5-62 can be made analogous to a convective equation by expressing the mass transfer coefficient as

$$h_{2s} = \frac{c}{L_d}, \quad 2.1.5-63$$

where

h_{2s} = mass transfer coefficient in a stagnant gas.

Then, by applying Reynold's analogy a turbulent natural convection mass transfer coefficient can be derived in terms of the heat transfer coefficient, h_2 , from Equation 2.1.5-48 such that

$$h_{2s} = h_2 \left(\frac{r}{k_d}\right) \left(\frac{\alpha_d}{r}\right)^{1/3} \quad 2.1.5-64$$

Equation 2.1.5-64 can then be substituted in place of (r/L) in Equation 2.1.5-63 such that

$$\begin{aligned} \dot{M}_{\text{vap}} = h_2 \left(\frac{r}{k_d}\right) \left(\frac{\alpha_d}{r}\right)^{1/3} \left(\frac{A_i}{P_d}\right) \left\{ \bar{p}_g \bar{\rho}_g \left[k_g \left(\frac{h_{fg}}{T_d v_{fg}}\right) - \beta_g \right] \right. \\ \left. + \bar{\rho}_g \left(\frac{h_{fg}}{T_g v_{fg}}\right) \right\} (T_f - T_w) , \quad 2.1.5-65 \end{aligned}$$

which gives the rate at which water vapor is transported into the accumulator gas dome by turbulent diffusion.

Since the energy transported to the gas dome by the vaporization process must come from the liquid and since the energy per unit mass required for vaporization is h_{fg} , then the rate of energy transport to the gas dome by vaporization is

$$\dot{Q}_{\text{vap}} = \Gamma_{\text{vap}} (h_{fg})_{T_f} = \dot{M}_{\text{vap}} (h_g)_{T_f} , \quad 2.1.5-66$$

where Γ_{vap} is the rate of vaporization at the liquid gas interface.

In the gas dome, as the accumulator blows down, the gas cools and condensation by turbulent diffusion occurs. The rate of condensation may be approximated by assuming that the gas dome

remains at 100% humidity and considering simple humidity relationships. The humidity ratio can be written as

$$w = \frac{M_g}{M_n} = \frac{N_g P_g}{N_n P_D} \quad , \quad 2.1.5-67$$

where

M_g, M_n = vapor, gas masses, respectively,

N_g, N_n = vapor, gas molecular weights, respectively, and

P_g = vapor partial pressure.

Taking the derivative of Equation 2.1.5-67 gives

$$\frac{dM_g}{dt} = \frac{1}{P_D} \left[M_n \frac{N_g}{N_n} \frac{dP_g}{dt} - M_g \frac{dP_D}{dt} \right] \quad . \quad 2.1.5-68$$

From Gibb's equation, the relationship between the vapor and liquid condensate in the dome is

$$v_{g_{P_g, T_D}} \frac{dP_g}{dT_D} - s_{g_{P_g, T_D}} = v_{f_{P_D, T_D}} \frac{dP_D}{dT_D} - s_{f_{P_D, T_D}} \quad . \quad 2.1.5-69$$

Substituting the relationship

$$\frac{dP}{dt} = \frac{dP}{dT} \frac{dT}{dt} \quad 2.1.5-70$$

into Equation 2.1.5-69 and rearranging gives

$$\frac{dP_g}{dt} = \frac{v_{f_{P_D, T_D}}}{v_{g_{P_g, T_D}}} \frac{dP_D}{dt} - \frac{(h_{g_{P_g, T_D}} - h_{f_{P_D, T_D}})}{T_D v_{g_{P_g, T_D}}} \frac{dT_D}{dt} \quad . \quad 2.1.5-71$$

Combining Equations 2.1.5-68 and 2.1.5-71 with Equations 2.1.5-43 and 2.1.5-44 gives

$$\frac{dM_g}{dt} = \frac{1}{P_D} \left(M_a \frac{N_g}{N_a} - M_g \right) \frac{V_{f_{P_D, T_D}}}{V_{g_{P_g, T_D}}} \frac{1}{V_v} \left[\dot{Q}_D \frac{R_H}{C_v} - P_D \left(1 + \frac{R_H}{C_v} \right) A_1 V \right]$$

$$+ \frac{1}{P_D} \frac{N_g}{N_a} \left[\frac{h_{g_{P_g, T_D}} - h_{f_{P_D, T_D}}}{T_D V_{g_{P_g, T_D}}} \right] \frac{1}{C_v} (\dot{Q}_D - P_D A_1 V) \quad 2.1.5-72$$

and the rate of condensate formation is given as

$$\dot{M}_C = - \frac{dM_g}{dt} + \dot{M}_{vap} \quad 2.1.5-73$$

The energy transported by the condensate to the interface can be expressed as

$$\dot{Q}_{m_C} = \dot{m}_C h_{f_{T_D}} \quad 2.1.5-74$$

Also, since the condensation is taking place in the gas dome, the energy given up by the condensation process is given up to the gas dome at the rate expressed as

$$\dot{Q}_{M_C} = \dot{M}_C h_{fg_{T_D}} \quad 2.1.5-75$$

Finally, since it is assumed that the condensate is transported to the interface at the condensation rate

$$\dot{m}_C = \dot{M}_C \quad 2.1.5-76$$

and the net energy given up to the gas dome by the condensation process can be expressed as

$$\dot{Q}_C = \dot{Q}_{\dot{M}_C} - \dot{Q}_{\dot{m}_C} = \dot{m}_C (h_{fg_{T_D}} - h_{f_{T_D}}) \quad . \quad 2.1.5-77$$

Energy Transported to the Gas Dome by Combined Heat and Mass Transfer

The total energy transported to the gas dome can be rewritten by combining Equations 2.1.5-45, 2.1.5-46, 2.1.5-48, 2.1.5-66, and 2.1.5-77 and summing to give

$$\begin{aligned} \dot{Q}_D = & (h_1 A_1 + h_2 A_2) (T_w - T_d) + h_2 A_2 (T_f - T_d) + \dot{M}_{vap} h_{g_{T_f}} \\ & + \dot{m}_C \left(h_{fg_{T_d}} - h_{f_{T_d}} \right) \quad . \quad 2.1.5-78 \end{aligned}$$

Numerical Implementation

The numerical scheme used for the accumulator model includes special features for coupling the solution scheme to the main code in such a way that it is time step independent. This scheme, as in RELAP5, is semi-implicit and special considerations are employed to preserve the nitrogen energy and mass.

The numerical scheme uses finite difference techniques to solve the differential equations. The momentum equation is formulated

by integrating Equation 2.1.5-40 over space and writing the time variation in difference form as

$$\begin{aligned} & \left[\rho_f \left(L_{f_L} + L_{f_{TK}} \right) \left(\frac{A_L}{A_{TK}} \right) + F_f \Delta t + \rho_g \left(L_{g_L} + L_{g_{TK}} \right) \left(\frac{A_L}{A_{TK}} \right) + F_g \Delta t \right] v_{f_L}^{n+1} \\ & = - \left(P^{n+1} - P_D^{n+1} \right) \Delta t + \Delta P_z \Delta t + \left[\rho_f \left(L_{f_L} + L_{f_{TK}} \right) \left(\frac{A_L}{A_{TK}} \right) \right. \\ & \quad \left. + \rho_g \left(L_{g_L} + L_{g_{TK}} \right) \left(\frac{A_L}{A_{TK}} \right) \right] v_{f_L}^n - \text{CONVF} - \text{CONVG} , \quad 2.1.5-79 \end{aligned}$$

where

P^{n+1} = pressure downstream from the accumulator junction.

The inertia term is represented by

$$\rho_f \left(L_{f_L} + L_{f_{TK}} \right) \left(\frac{A_L}{A_{TK}} \right) + \rho_g \left(L_{g_L} + L_{g_{TK}} \right) \left(\frac{A_L}{A_{TK}} \right) , \quad 2.1.5-80$$

where L_{f_L} , $L_{f_{TK}}$, L_{g_L} , and $L_{g_{TK}}$ are the lengths of the liquid and gas in the surge line and tank, respectively. These terms are computed at each time step and hence vary explicitly with time having the effect that as the accumulator blows down the inertia term changes from a liquid dominant to a vapor dominant term. The liquid and gas friction terms, respectively, are formulated as

$$F_f = \frac{\rho_f}{2} \left(\lambda \frac{L_{f_L}}{D_L} + K_L \frac{L_{f_L}}{L_L} \right) v_{f_L}^n \quad 2.1.5-81$$

for the liquid, and

$$F_g = \frac{\rho_g}{2} \left(\lambda \frac{L_{g_L}}{D_L} + K_L \frac{L_{g_L}}{L_L} \right) v_{g_L}^n \quad 2.1.5-82$$

for the vapor. Friction is neglected in the tank and the line friction factor is assumed to be the constant turbulent-turbulent Darcy friction factor given as

$$\lambda = \left[1.74 - 2 \log \frac{2\epsilon}{D_L} \right]^{-2} \quad 2.1.5-83$$

The loss factor term, K_L , is assumed to be distributed over the surge line length, L_L . The term D_L is the surge line hydraulic diameter and ϵ is the surge line wall roughness. The elevation head term, ΔP_z , is formulated as

$$\Delta P_z = - \frac{g \Delta z_{TK} \left(\rho_f L_{f_{TK}} + \frac{1}{2} \rho_g L_{g_{TK}} \right)}{L_{TK}} - \frac{g \Delta z_L \left(\rho_f L_{f_L} + \rho_g L_{g_L} \right)}{L_L} \quad 2.1.5-84$$

where Δz_{TK} and Δz_L are the tank and surge line elevation changes, respectively, and g is the gravitational acceleration. The liquid and vapor momentum flux terms, $CONVF$ and $CONVG$, respectively are formulated as

$$CONVF = \frac{1}{2} \rho_f \left[1 - \left(\frac{A_L}{A_{TK}} \right)^2 \right] \Delta t v_{f_L}^n \left(2v_{f_L}^{n+1} - v_{f_L}^n \right) \quad 2.1.5-85$$

if there is liquid in the tank,

$$CONVF = 0.0 \quad 2.1.5-86$$

when there is no liquid in the tank,

$$\text{CONVG} = \frac{1}{2} \rho_g \left[\left(\frac{A_L}{A_{TK}} \right)^2 - \frac{1}{4} \left(\frac{A_L}{A_{TK}} \right)^2 \right] \Delta t v_{g_L}^n \left(2 v_{g_L}^{n+1} - v_{g_L}^n \right) \quad 2.1.5-87$$

if there is vapor in the surge line, and

$$\text{CONVG} = 0.0 \quad 2.1.5-88$$

where there is no vapor in the surge line. By formulation in this manner the momentum equation is solved over the pressure gradient from the centroid of the gas dome to the accumulator junction. However, the momentum of the fluid downstream from the accumulator junction is not included. Also since fluxing of the gas through the junction is not allowed, we have

$$v_{g_L}^{n, n+1} = v_{f_L}^{n, n+1} \quad 2.1.5-89$$

until the accumulator empties of liquid. The effect of this formulation is that as the accumulator blowsdown the liquid-gas interface moves out of the accumulator tank and surge line. Thus, the centroid of the gas dome moves towards the centroid of the combined tank and surge line.

The pressure solution is obtained by combining Equations 2.1.5-38 and 2.1.5-42 and multiplying by R_n/C_{v_n} , which results in

$$M_n R_n \frac{dT}{dt} = - \frac{R_n P_D}{C_{v_n}} \frac{dv_v}{dt} + \frac{R_n}{C_{v_n}} \dot{Q}_D, \quad 2.1.5-90$$

where Q_D is given by Equation 2.1.5-78. Equations 2.1.5-41 and 2.1.5-90 are then combined resulting in

$$P_D \left(1 + \frac{R_n}{C_{v_n}} \right) \frac{dv_v}{dt} + v_v \frac{dP_D}{dt} = \frac{R_n}{C_{v_n}} \dot{Q}_D . \quad 2.1.5-91$$

Since the liquid is incompressible

$$\frac{dv_v}{dt} = - \frac{dv_f}{dt} = A_L v_{f_L} \quad 2.1.5-92$$

and substitution in Equation 2.1.5-91 and expanding in nonconservative finite difference form gives

$$P_D^n \left(1 + \frac{R_n}{C_{v_n}} \right) A_L \Delta t v_{f_L}^{n+1} + v_v^n (P_D^{n+1} - P_D^n) = \frac{R_n}{C_{v_n}} \dot{Q}_D^n \Delta t . \quad 2.1.5-93$$

The energy equation may then be solved directly for the new time gas temperature by combining Equations 2.1.5-41, 2.1.5-44, 2.1.5-91, and integrating, which gives

$$T_D^{n+1} = T_D^n e^{\left[\frac{R_n}{C_{v_n}} \ln \left[\frac{v_v^n}{v_v^{n+1}} \right] + \Delta t \frac{\dot{Q}_D^n}{P_D^n v_v^n} \right]} . \quad 2.1.5-94$$

2.2. Heat Structure Models

Heat structures provided in RELAP5/MOD2-B&W permit calculation of the heat transferred across solid boundaries of hydrodynamic volumes. Modeling capabilities of heat structures include fuel pins or plates with nuclear or electrical heating, heat transfer across steam generator tubes, and heat transfer from pipe or vessel walls. The general conduction solution for the structures, heat transfer coupling, and source and boundary condition treatment are discussed in this section. The special treatment of the reactor core including kinetics, decay heat, gap conductance, clad rupture, metal water reaction and the core heat transfer correlations are contained in section 2.3.

2.2.1. Heat Conduction Model

Heat structures are assumed to be represented by one-dimensional heat conduction in rectangular, cylindrical, or spherical geometry. Surface multipliers are used to convert the unit surface of the one-dimensional calculation to the actual surface of the heat structure. Temperature-dependent thermal conductivities and volumetric heat capacities are provided in tabular or functional form either from built-in or user-supplied data.

Finite differences are used to advance the heat conduction solutions. Each mesh interval may contain a different mesh spacing, a different material, or both. The spatial dependence of the internal heat source may vary over each mesh interval. The time-dependence of the heat source can be obtained from reactor kinetics, one of several tables of power versus time, or a control system variable. Symmetry or insulated conditions and tables of surface temperature versus time, heat transfer rate versus time, heat transfer coefficient versus time, or surface temperature are allowed for boundary conditions. For heat structure surfaces connected to hydrodynamic volumes, a heat

transfer package containing correlations for convective, nucleate boiling, transition boiling, and film heat transfer from the wall to water and reverse transfer from water to wall is provided.

The following describes the numerical techniques for heat conduction. The integral form of the heat conduction equation is

$$\iiint_V \rho(T, \bar{x}) \frac{\partial T}{\partial t}(\bar{x}, t) dV = \iint_S -k(T, \bar{x}) \nabla T(\bar{x}, t) \cdot d\bar{s} + \iiint_V S(\bar{x}, t) dV, \quad 2.2.1-1$$

where k is the thermal conductivity, s is the surface, S is the internal heat source, t is time, T is temperature, V is volume, x represents the space coordinates, and ρ is the volumetric heat capacity. The boundary condition applied to the exterior surface has the form

$$A(T)T(t) + B(T) \frac{\partial T(t)}{\partial \bar{n}} = D(T) \quad . \quad 2.2.1-2$$

The \bar{n} denotes the unit normal vector away from the boundary surface. The desired boundary condition is that the heat transferred out of the surface equals a heat transfer coefficient, h , times the difference between the surface temperature, T_w , and the sink temperature, T_s .

$$-k \frac{\partial T}{\partial \bar{n}} = h(T_w - T_s) \quad . \quad 2.2.1-3$$

The correspondence between the above expression and Equation 2.2.1-2 yields

$$A = h, \quad B = k \quad \text{and} \quad D = h T_s \quad . \quad 2.2.1-4$$

In one dimensional problems, boundary conditions are applied on the left and right surfaces. In steady state problems, a valid physical problem requires that A be nonzero on at least one of the two boundary surfaces. If a transient or steady state problem has cylindrical or spherical geometry and a zero radius for the left surface (i.e., a solid cylinder or sphere), the left boundary condition is normally the symmetry condition,

$\frac{\partial T}{\partial n} = 0$. Under these conditions, if B is nonzero, the numerical technique forces the symmetry boundary condition, even if it is not specified.

2.2.1.1. Mesh Point and Thermal Property Layout

Figure 2.2.1-1 illustrates the placement of mesh points at temperatures to be calculated. The mesh point spacing for a rectangular problem is taken in the positive x-direction. For cylindrical and spherical problems, the mesh point spacing is in the positive radial direction. Mesh points are placed on the external boundaries of the problem, at the interfaces between different materials, and at desired intervals between the interfaces, boundaries, or both.

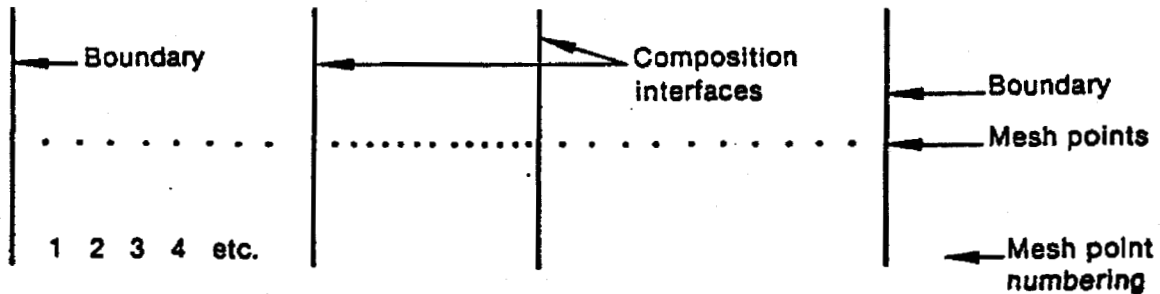


Figure 2.2.1-1. Mesh Point Layout.

Figure 2.2.1-2 represents three typical mesh points. The subscripts are space indexes indicating the mesh point number, and l and r (if present) designate quantities to the left and right, respectively, of the mesh point. The δ 's indicate mesh point spacings that are not necessarily equal. Between mesh points, the thermal properties, k and ρ and the source term, S , are assumed spatially constant, but k_{lm} is not necessarily equal to k_{rm} and similarly for ρ and S .

To obtain the spatial-difference approximation for the m^{th} interior mesh point, Equation 2.2.1-1 is applied to the volume and surfaces indicated by the dashed line shown in Figure 2.2.1-2. For the spatial-difference approximation at the boundaries, Equations 2.2.1-1 and 2.2.1-2 are used to define the gradient along the exterior surfaces and applied to the volumes and surfaces indicated by the dashed lines shown in Figure 2.2.1-3. If the coefficient of the gradient in the boundary equation is zero, the surface temperature is given directly from Equation

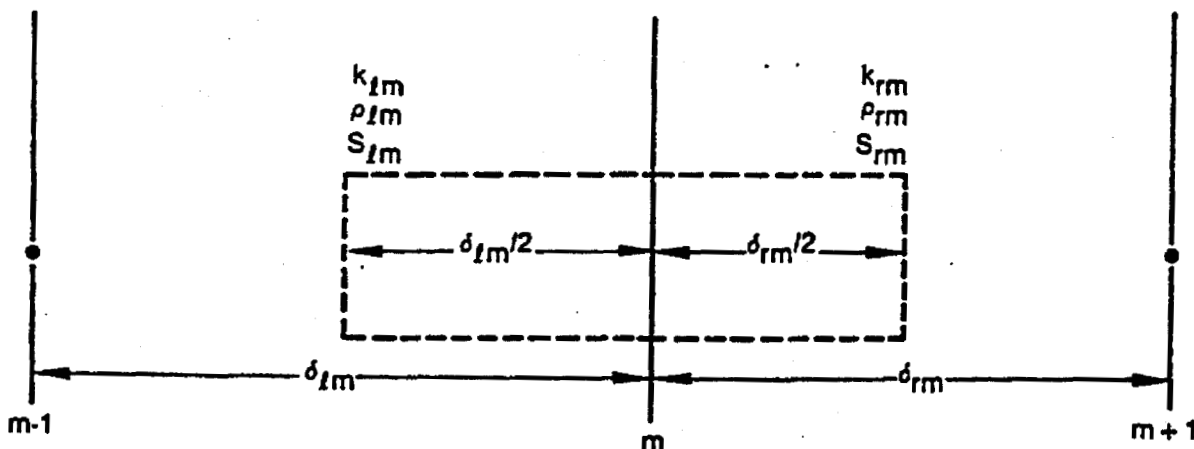


Figure 2.2.1-2. Typical Mesh Points.

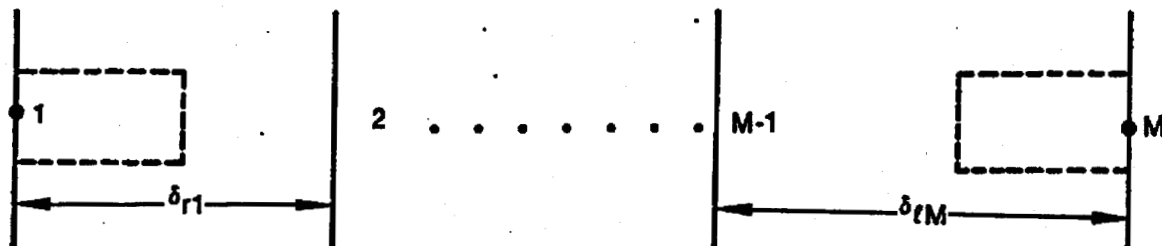


Figure 2.2.1-3. Boundary Mesh Points.

2.2.1-2. Since the code is one-dimensional, the dimensions of the volume for other than the x or r coordinate are set to one. For rectangular geometry, the volume is a rectangular solid. For cylindrical geometry, the volume is a cylindrical annulus, and for spherical geometry, the volume is a spherical shell.

The spatial finite-difference approximations use exact expressions for the space and volume factors and simple differences for the gradient terms.

To condense the expressions defining the numerical approximations and to avoid writing expressions unique to each geometry, the following quantities are defined.

For rectangular geometry

$$\delta_{lm}^s = \frac{1}{\delta_{lm}} \quad \text{and} \quad \delta_{rm}^s = \frac{1}{\delta_{rm}}, \quad 2.2.1-5$$

$$\delta_{lm}^v = \frac{\delta_{lm}}{2} \quad \text{and} \quad \delta_{rm}^v = \frac{\delta_{rm}}{2}, \quad 2.2.1-6$$

and

$$\delta_m^b = 1. \quad 2.2.1-7$$

For cylindrical geometry

$$\delta_{lm}^v = 2\pi \frac{\delta_{lm}}{2} \left[x_m - \frac{\delta_{lm}}{4} \right] \quad \text{and} \quad \delta_{rm}^v = 2\pi \frac{\delta_{rm}}{2} \left[x_m + \frac{\delta_{rm}}{4} \right], \quad 2.2.1-8$$

$$\delta_{lm}^s = \frac{2\pi}{\delta_{lm}} \left[x_m - \frac{\delta_{lm}}{2} \right] \quad \text{and} \quad \delta_{rm}^s = \frac{2\pi}{\delta_{rm}} \left[x_m + \frac{\delta_{rm}}{2} \right], \quad 2.2.1-9$$

and

$$\delta_m^b = 2\pi x_m. \quad 2.2.1-10$$

For spherical geometry

$$\delta_{lm}^v = \frac{4\pi}{3} \left[x_m^3 - \left(x_m - \frac{\delta_{lm}}{2} \right)^3 \right], \quad 2.2.1-11$$

$$\delta_{rm}^v = \frac{4\pi}{3} \left[\left(x_m + \frac{\delta_{rm}}{4} \right)^3 - x_m^3 \right],$$

$$\delta_{lm}^s = \frac{4\pi}{\delta_{lm}} \left(x_m - \frac{\delta_{lm}}{2} \right)^2 \quad \text{and} \quad \delta_{rm}^s = \frac{4\pi}{\delta_{rm}} \left(x_m + \frac{\delta_{rm}}{2} \right)^2, \quad 2.2.1-12$$

and

$$\delta_m^b = 4\pi x_m^2. \quad 2.2.1-13$$

For all geometries

$$G_m = \rho_{lm} \delta_{lm}^v + \rho_{rm} \delta_{rm}^v. \quad 2.2.1-14$$

The superscripts, v and s, refer to volume and surface-gradient weights. The δ_m^b is a surface weight used at exterior boundaries and in heat transfer rate equations.

2.2.1.2. Difference Approximation at Internal Mesh Points

Using a forward difference for the time derivative, the first term of Equation 2.2.1-1 for the volume of Figure 2.2.1-2 is approximated by

$$\iiint_V \rho(T, \bar{x}) \frac{\partial T}{\partial t}(\bar{x}, t) dV = \left(T_m^{n+1} - T_m^n \right) \frac{G_m}{\Delta t}. \quad 2.2.1-15$$

The superscript n refers to time; thus, T_m^n indicates the temperature at mesh point m at time t^n , and T_m^{n+1} indicates the temperature at mesh point m at time $t^{n+1} = t^n + \Delta t$. The second term of Equation 2.2.1-1 for the surfaces of Figure 2.2.1-2 is approximately by

$$\iint_S k(T, \bar{x}) \nabla T(\bar{x}, t) \cdot d\bar{s} = (T_{m-1} - T_m) k_{lm} \delta_{lm}^s + (T_{m+1} - T_m) k_{rm} \delta_{rm}^s. \quad 2.2.1-16$$

Note that the above expression includes the standard interface conditions of continuity of temperature and heat flow. The surface integral of Equation 2.2.1-1 is usually evaluated by

integrating only along the exterior surfaces of the volume indicated by the dashed line in Figure 2.2.1-2. If, however, the volume is divided into two sub-volumes by the interface line and the surface integrals of these sub-volumes are added, the surface integrals along the common interface cancel because of the continuity of heat flow. The continuity of temperature is implied by use of a single-valued temperature at the interface.

A contact-resistance interface condition cannot be specified directly since the temperature, instead of being continuous at the interface, is given by $q = h_c \Delta T$, where q is the heat transfer rate across the interface, h_c is the contact conductivity, and ΔT is the temperature change across the interface. This condition can be specified by defining a small mesh interval with thermal properties of $k = h_c$ and $\rho = 0$. The size of the mesh interval, δ , is arbitrary except in cylindrical or spherical geometry, where the surface and volume weights are dependent on the radius. This mesh interval is usually chosen very small with respect to the dimensions of the problem.

The space and time-dependence of the source term in Equation 2.2.1-1 are assumed to be separable functions, that is,

$$S(x,t) = P_f P(t) Q(x) , \quad 2.2.1-17$$

where P_f is the factor that relates the reactor power (or power from a table) to the heat generation rate for a particular heat structure, $P(t)$ is the time varying function and may be reactor power, power from a table, or a control variable, and $Q(x)$ is the space-dependent function. The value of $Q(x)$ is assumed constant over a mesh interval, but each interval can have a different

value. The third term of Equation 2.2.1-1 is then approximated as

$$\iiint_V s(\bar{x}, t) dV = \left[Q_{lm} \delta_{lm}^V + Q_{rm} \delta_{rm}^V \right] P_f P(t) . \quad 2.2.1-18$$

Gathering the approximations of terms in Equation 2.2.1-1, the basic difference equation for the m^{th} mesh point is

$$\begin{aligned} \frac{(T_m^{n+1} - T_m^n) G_m}{\Delta t} &= -(T_m - T_{m-1}) k_{lm} \delta_{lm}^S + (T_{m+1} - T_m) k_{rm} \delta_{rm}^S \\ &+ \left[Q_{lm} \delta_{lm}^V + Q_{rm} \delta_{rm}^V \right] P_f P(t) . \end{aligned} \quad 2.2.1-19$$

Using the symbol ζ_m to represent the right side, Equation 2.2.1-19 can be written as

$$\frac{(T_m^{n+1} - T_m^n) G_m}{\Delta t} = \zeta_m . \quad 2.2.1-20$$

Thus far, the time superscripts for G_m and ζ_m have been omitted and the procedure for approximating the temperature-dependence of the thermal properties has not been mentioned. The procedures for temperature-dependent thermal properties are discussed later. However, superscripts for thermal properties are written here even though their significance is not explained until later. For steady state, the difference approximation becomes

$$\zeta_m = 0 , \quad 2.2.1-21$$

and no time superscripts are needed. For the time-dependent case, an equation of the type

$$\frac{(T_m^{n+1} - T_m^n) G_m}{\Delta t} = w \zeta_m^{n+1} + (1 - w) \zeta_m^n \quad 2.2.1-22$$

is an explicit formula if w is zero, and is an implicit formula when w is nonzero. RELAP5 uses the implicit formulation with $w = 1/2$.

Writing Equation 2.2.1-22, in full, the difference approximation for the m^{th} interior mesh point for transient and steady state cases is

$$a_m^n T_{m-1}^{n+1} + b_m^n T_m^{n+1} + c_m^n T_{m+1}^{n+1} = d_m, \quad 2.2.1-23$$

where

$$a_m^n = - \frac{k_{lm}^n \delta_{lm}^s \Delta t}{\sigma + 1}, \quad 2.2.1-24$$

$$b_m^n = \sigma G_m^n - a_m^n - c_m^n, \quad 2.2.1-25$$

$$c_m^n = - \frac{k_{rm}^n \delta_{rm}^s \Delta t}{\sigma + 1}, \quad 2.2.1-26$$

$$d_m = -\sigma a_m^n T_{m-1}^n + \sigma (G_m^n + a_m^n + c_m^n) T_m^n - \sigma c_m^n T_{m+1}^n + \Delta t P_f \left(\frac{P^{n+1} + \sigma P^n}{\sigma + 1} \right) \left(Q_{lm} \delta_{lm}^v + Q_{rm} \delta_{rm}^v \right), \quad 2.2.1-27$$

and σ is 1 for transient cases and 0 for steady state cases.

2.2.1.3. Difference Approximation at Boundaries

To obtain the difference approximations for the mesh points at the boundaries, Equation 2.2.1-1 is applied to the volumes of Figure 2.2.2-3 with Equation 2.2.1-2 used to define the gradient at the surface. The second term of Equation 2.2.1-1 at $x = x_1$ is approximated by

$$\iint_S k(T, \bar{x}) \nabla T(\bar{x}, t) \cdot d\bar{s} = -\frac{k_{r1}}{B_1} (A_1 T_1 - D_1) \delta_1^b + k_{r1} (T_2 - T_1) \delta_{r1}^s. \quad 2.2.1-28$$

The complete basic expression for the left boundary mesh point becomes

$$\frac{(T_1^{n+1} - T_1^n)}{\Delta t} \rho_{r1} \delta_{r1}^v = -\frac{k_{r1}}{B_1} (A_1 T_1 - D_1) \delta_1^b + k_{r1} (T_2 - T_1) \delta_{r1}^s + Q_{r1} \delta_{r1}^v P_f^P(t). \quad 2.2.1-29$$

If B in the boundary condition equation is zero, the above equation is not used since the boundary condition determines the temperature. Also in that case, a division by zero would be indicated if Equation 2.2.1-29 were used. Approximations for the boundary at $x = x_m$ are derived in a similar fashion. These equations for the boundary mesh points are converted to the implicit formulas in the same manner as for the interior mesh points, except that the surface temperature appearing in the boundary condition is evaluated completely at the $n+1$ time level. Thus, for the left boundary

$$b_1^{n,n+1} T_1^{n+1} + c_1^{n,n+1} T_2^{n+1} = d_1, \quad 2.2.1-30$$

$$b_1^n = \sigma \rho_{r1}^n \delta_{r1}^v + \frac{k_{r1}^n A_{r1}^n \delta_{r1}^b \Delta t}{B_1^n} - c_1^n, \quad 2.2.1-31$$

$$c_1^n = - \frac{k_{r1}^n \delta_{r1}^s \Delta t}{\sigma + 1}, \text{ and} \quad 2.2.1-32$$

$$d_1 = - \sigma c_1^n T_2^n + \sigma \left(\rho_{r1}^n \delta_{r1}^v + c_1^n \right) T_1^n + \frac{k_{r1}^n \delta_{r1}^b D_1^n \Delta t}{B_1^n} + P_f \frac{(\sigma P^n + P^{n+1}) Q_{r1} \delta_{r1}^v \Delta t}{\sigma + 1}. \quad 2.2.1-33$$

In the coding, a variable, HTBCCO, is defined as $C_1^n = A_1^n T_1^n - D_1^n$. Substituting this relation into Equation 2.2.1-33 gives

$$d_1 = - \sigma c_1^n T_2^n + \left[\sigma \rho_{r1}^n \delta_{r1}^v + \sigma c_1^n + \frac{k_{r1}^n \delta_{r1}^b A_1^n \Delta t}{B_1^n} \right] T_1^n - \frac{k_{r1}^n \delta_{r1}^b C_1^n \Delta t}{B_1^n} + \frac{P_f (\sigma P^n + P^{n+1}) Q_{r1} \delta_{r1}^v \Delta t}{\sigma + 1}. \quad 2.2.1-34$$

For the right boundary

$$a_{M^{TM-1}}^{n,n+1} + b_{M^{TM}}^{n,n+1} = d_M, \quad 2.2.1-35$$

$$a_M^n = \frac{-k_{\ell M}^n \delta_{\ell M}^s \Delta t}{\sigma + 1}, \quad 2.2.1-36$$

$$b_M^n = \sigma \rho_{\ell M}^n \delta_{\ell M}^v + \frac{k_{\ell M}^n A_{\ell M}^n \delta_{\ell M}^b \Delta t}{B_M^n} - a_M^n, \text{ and} \quad 2.2.1-37$$

$$d_M = -\sigma a_{M-1}^{nT} + \sigma \left[\rho_{LM}^n \delta_{LM}^v + a_M^n \right] T_M^n + \frac{k_{LM}^n \delta_{LM}^b D_M^n \Delta t}{B_M^n} \tag{2.2.1-38}$$

$$+ P_f \frac{(\sigma P^n + P^{n+1}) Q_{LM} \delta_{LM}^v \Delta t}{\sigma + 1}$$

In the coding, a variable, HTBCCN, is defined as $C_M^n = A_M^n T_M^n - D_M^n$. Substituting this relation into Equation 2.2.1-38 gives

$$d_M = -\sigma a_{M-1}^{nT} + \left[\sigma \rho_{LM}^n \delta_{LM}^v + a_M^n + \frac{k_{LM}^n \delta_{LM}^b A_M^n \Delta t}{B_M^n} \right] T_M^n \tag{2.2.1-39}$$

$$- \frac{k_{LM}^n \delta_{LM}^b D_M^n \Delta t}{B_M^n} + \frac{P_f (\sigma P^n + P^{n+1}) Q_{LM} \delta_{LM}^v \Delta t}{\sigma + 1}$$

2.2.1.4. Solution of Simultaneous Equations

The difference approximations for the mesh points (Equations 2.2.1-27, 2.2.1-38, and 2.2.1-39) lead to a tri-diagonal set of M equations. The coefficient matrix is symmetric unless the boundary condition specifies the surface temperature. In that case, the elements, c_1 and a_M , are 0, and destroy the symmetry. The solution to the above equations is obtained by:

1. Form $E_1 = \frac{c_1}{b_1}$ and $F_1 = \frac{d_1}{b_1}$. 2.2.1-40

2. Form $E_j = \frac{c_j}{b_j - a_j E_{j-1}}$ and $F_j = \frac{d_j - a_j F_{j-1}}{b_j - a_j E_{j-1}}$

for $j = 2, 3, \dots, M-1$. 2.2.1-41

$$3. \text{ Form } T_M^{n+1} = \frac{d_M - a_M F_{M-1}}{b_M - a_M E_{M-1}} \quad 2.2.1-42$$

$$4. \text{ Form } T_j^{n+1} = -E_j T_{j+1}^{n+1} + F_j$$

for $j = M-1, M-2, \dots, 3, 2, 1.$ 2.2.1-43

These procedures can be derived by applying the rules for Gaussian elimination. This method of solution introduces little roundoff error if the off-diagonal elements are negative and the diagonal is greater than the sum of the magnitudes of the off-diagonal elements. From the form of the difference equations, these conditions are satisfied for any values of the mesh point spacing, time step, and thermal properties.

2.2.1.5. Thermal Properties, Boundary Condition Parameters, and Iteration Procedures

The thermal conductivity, k , and the volumetric heat capacity, ρ , are considered functions of temperature and space. These thermal properties are obtained for each interval by using the average of the mesh point temperatures bounding the interval

$$k_{lm} = k \left(\frac{T_{r,m-1} + T_{l,m}}{2} \right) = k_{r,m-1} \quad 2.2.1-44$$

and

$$k_{rm} = k \left(\frac{T_{r,m} + T_{l,m+1}}{2} \right) = k_{l,m+1} \quad 2.2.1-45$$

The quantity, ρ , is treated in the same manner. The boundary condition parameters, A , B , and D , are considered functions of temperature and time. In steady state problems, no superscripts would be required for the thermal parameters, k , ρ , A , B , and D . Accordingly in Equations 2.2.1-23, 2.2.1-30, and 2.2.1-35, those

quantities written with superscript n are ignored since they are multiplied by $\sigma = 0$, and only quantities with superscript $n + 1$ are used. If these quantities are not temperature-dependent, the solution of Equations 2.2.1-23, 2.2.1-30, and 2.2.1-35 will immediately give steady state temperatures. When these parameters are temperature-dependent, iterations are used to resolve the difficulty of obtaining thermal parameters as a function of temperature when the temperatures are unknown.

In transient problems, the thermal properties, k , ρ , A , B , and D , with superscript n are evaluated as a function of the temperatures, T^n , at the beginning of a time step. Since these are either initial temperatures or results of the last time-advancement, the corresponding thermal parameters can be determined. Those thermal parameters with superscript $n + 1$ are evaluated as a function of the temperatures, T^{n+1} , at the end of the time step. Since these temperatures are not available, the initial estimate of the thermal parameters is obtained using $k^{n+1} = k^n$ and similarly for ρ , A , B , and D . The superscript $n + 1/2$ indicates an average of the quantities with superscript n and $n + 1$, or

$$\rho^{n+1/2} = \frac{\rho^{n+1} + \rho^n}{2} \quad 2.2.1-46$$

If thermal parameters and boundary conditions are constant, or do not vary greatly during a time step, the temperatures obtained from the solution of Equations 2.2.1-27, 2.2.1-30, and 2.2.1-31 with $k^{n+1} = k^n$, etc., are satisfactory. This is presently assumed in RELAP5.

2.2.1.6. Difference Approximation for Boundary Conditions

The development of the difference equations uses a general form for the boundary conditions, but RELAP5 uses only the following conditions.

$$-k \frac{\partial T}{\partial x} = 0 , \quad 2.2.1-47$$

$$-k \frac{\partial T}{\partial x} = q_T(t) , \quad 2.2.1-48$$

$$-k \frac{\partial T}{\partial x} = h(T - T_B) , \text{ or} \quad 2.2.1-49$$

$$T = T_T(t) , \quad 2.2.1-50$$

where q_T and T_T are tabular functions of time. For the convective boundary condition Equation 2.2.1-49, the heat transfer coefficient, h , can either be input or calculated initially by the code. For the first three conditions, the heat transfer rate is given directly by the boundary conditions once the surface temperature has been calculated. For the temperature boundary condition, the heat transfer rate is obtained from the difference equation. The general expression, shown here, for the right boundary is

$$q_M^{n+1} \delta_M^b = \frac{k_{LM}^n}{\sigma + 1} \left[T_{M-1}^{n+1} - T_M^{n+1} \right] \delta_{LM}^s + \frac{\sigma k_{LM}^n}{\sigma + 1} \left[T_{M-1}^n - T_M^n \right] \delta_{LM}^s$$

$$+ P_f \frac{(\sigma P^n + P^{n+1})}{\sigma + 1} Q_{LM} \delta_{LM}^v - \frac{\sigma \rho_{LM}^n}{\Delta t} \left[T_M^{n+1} - T_M^n \right] \delta_{LM}^v$$

2.2.1-51

2.2.2. Heat Structure Convective Boundary Conditions and Heat Transfer Models

When the internal convective boundary condition is specified, the wall to fluid volumetric heat transfer, Q_{wf} and Q_{wg} , and the mass transfer rate due to wall heat transfer, Γ_w , are calculated as described in this section. A boiling curve is used to govern the selection of heat transfer correlations. The following two options are available to calculate the wall heat transfer:

Option 1: System Heat Transfer

Option 2: Core Heat Transfer

Although both can be applied throughout the simulation, Option 1 is intended primarily for use outside the core, that is, the steam generator or component or piping walls. Option 2 is intended for the fuel rod heat transfer and has specific logic based on Appendix K. Only Option 1 will be described in this section of the report. Option 2, core heat transfer, is presented in the section on the reactor core, section 2.3.3.

In Option 1, the system heat transfer model, the heat transfer regimes modeled are classified as pre-CHF, CHF, and post-CHF regimes. Condensation heat transfer and the heat transfer to air-water mixtures are also modeled. Figure 2.2.2-1 gives a chart of the logic scheme for selecting the heat transfer models. Q_{wf} , Q_{wg} , the total heat flux, q , and the total heat transfer coefficient, h are calculated as follows

$$Q_{wf} = q_{wf} A_w / V, \quad 2.2.2-1$$

$$Q_{wg} = q_{wg} A_w / V, \quad 2.2.2-2$$

$$q = q_{wf} + q_{wg}, \quad 2.2.2-3$$

and

$$h = h_{wf} + h_{wg} , \quad 2.2.2-4$$

where q_{wf} and q_{wg} are the effective wall to liquid and vapor heat flux, respectively, based on the total heat slab area, A_w . The calculation of q_{wf} , q_{wg} , and Γ_w for each heat transfer regime are summarized below.

2.2.2.1. Pre-CHF Heat Transfer Correlations

The pre-CHF regime consists of models for single-phase liquid convection, subcooled nucleate boiling, and saturated nucleate boiling. In this regime, the model assumes that the wall is totally wetted by liquid. Therefore, the heat transfer from the wall to the vapor, Q_{wg} , is equal to zero.

Single-Phase Liquid Convection

In single-phase liquid convection, the heat transfer coefficient is the maximum of the Dittus-Boelter or Rohsenow-Choi correlations under forced convection conditions or the maximum of the Dittus-Boelter⁴⁰, Rohsenow-Choi, or the natural convection correlation for natural convection conditions.

$$h = h_{wf} = \text{MAX} (C1_{DB} h_{DB}, C1_{RC} h_{RC}, C1_{NCi} h_{NC}). \quad 2.2.2-5$$

The Dittus-Boelter correlation is

$$h_{DB} = 0.023 \frac{k_f}{D_e} Pr_f^{0.4} Re_f^{0.8} , \quad 2.2.2-6$$

and Rohsenow-Choi is given by

$$h_{RC} = 4.36 \frac{k_f}{D_e} \quad 2.2.2-7$$

The natural convection correlation,

$$h_{NC} = a \frac{k_f}{D_e} (Gr \cdot Pr)^b \quad 2.2.2-8$$

is dependent on the flow regime as follows.

Laminar flow, ($Gr \leq 10^9$)

$$a = 0.59$$

$$b = 0.25$$

$$Cl_{NCi} = Cl_{NCl}$$

Transition flow, ($10^9 < Gr \leq 10^{13}$)

$$a = 0.021$$

$$b = 0.4$$

$$Cl_{NCi} = Cl_{NCtrn}$$

Turbulent flow, ($Gr > 10^{13}$)

$$a = 0.1$$

$$b = 0.3333$$

$$Cl_{NCi} = Cl_{NCtur} \quad 2.2.2-9$$

q_{wg} and Γ_w are zero throughout this heat transfer regime and q_{wf} is given by

$$q_{wf} = h(T_w - T_f) \quad 2.2.2-10$$

Subcooled and Saturated Nucleate Boiling

The subcooled and saturated nucleate boiling heat transfer coefficients are calculated using the modified Chen⁴⁴ and the Chen⁴¹ correlation, respectively. Because of the nonequilibrium nature of RELAP5, the subcooled-to-saturated nucleate boiling boundary cannot be defined precisely. In addition, the vapor generation in the subcooled boiling regime has to be included. Hence, the Chen correlation is modified as follows.

The heat transfer coefficient in nucleate boiling is given by the sum of the two effects: microscopic (boiling) and macroscopic (convection)

$$h = h_{mic}^* + h_{mac}^* \quad 2.2.2-11$$

In RELAP5, it is assumed that the wall-to-fluid heat transfer is by convection only, until the subcooled vapor generation criteria is satisfied. This is achieved by using a subcooled vapor generation factor, f_{subvap} , as follows

$$h_{mic}^* = C1_{mic} h_{mic} f_{subvap} \quad 2.2.2-12$$

where h_{mic} is the Chen microscopic heat transfer coefficient

$$h_{mic} = 0.00122 \left\{ \frac{k_f^{0.79} C_{pf}^{0.45} \rho_f^{0.49}}{\sigma^{0.5} \mu_f^{0.29} h_{fg}^{0.24} \rho_g^{0.24}} \right\} \Delta T_{sat}^{0.24} \Delta P^{0.75} \text{ S.} \quad 2.2.2-13$$

The subcooled vapor generation factor, f_{subvap} , a measure of the first appearance of bubbles on the heat slab surface, is calculated based on the onset of nucleate boiling criteria given by Bergels and Rohsenow⁵² and the net vapor generation criteria

given by Saha and Zuber.¹²¹ The calculation of f_{subvap} is discussed later in this section.

The convection part, h_{mac}^* , is taken as the maximum of the Rohsenow-Choi correlation and Chen's macroscopic heat transfer coefficient, h_{mac} . Thus,

$$h_{\text{mac}}^* = \text{MAX}(C1_{\text{mac}} h_{\text{mac}}, C1_{\text{RC}} 4.36 k_f/D_e) \quad 2.2.2-14$$

and

$$h_{\text{mac}} = 0.023 (k_f/D_e) (\text{Pr}_f)^{0.4} [G(1-X) D_e/\mu_f]^{0.8} F. \quad 2.2.2-15$$

The modified Chen correlation is obtained by setting $F = 1$ in the Chen correlation. Because of the nonequilibrium nature of RELAP5, F is calculated as follows.

$$F = 1.0,$$

if the liquid flow is negative ($\alpha_f \rho_f v_f \leq 0.0$) or liquid subcooling is greater than or equal to 5K or the Martinelli parameter

$$X_{\text{tt}}^{-1} = \left[\frac{\alpha_g \rho_g v_g}{\alpha_f \rho_f v_f} \right]^{0.9} \left[\frac{\rho_f}{\rho_g} \right]^{0.5} \left[\frac{\mu_g}{\mu_f} \right]^{0.1} < 0.1. \quad 2.2.2-16$$

Otherwise

$$F = F' - 0.2(F' - 1) \text{MAX}(0.0, T_{\text{sat}} - T_f), \quad 2.2.2-17$$

where F' is a fit to Chen's F-factor

$$F' = 2.35(X_{tt}^{-1} + 0.213)^{0.736} \quad 2.2.2-18$$

The suppression factor, S , is calculated based on the void fraction as

$$S = W_{\alpha} \begin{cases} 1 & \alpha_g \leq 0.3 \\ 1 - 2(1 - S') (\alpha_g - 0.3) & 0.3 < \alpha_g < 0.8 \\ S' & \alpha_g \geq 0.8 \end{cases} \quad 2.2.2-19$$

The W_{α} multiplicative factor is a weighting factor that was added to force the S factor, and consequently h_{mic} , to zero as the steam void fraction approaches unity. The factor is defined as follows

$$W_{\alpha} = \begin{cases} 1.0 & \alpha_g \leq \alpha_{gr} \\ (1 - \alpha_g)/(1 - \alpha_{gr}) & \alpha_{gr} < \alpha_g \end{cases} \quad 2.2.2-19.1$$

α_{gr} is a user specified void fraction at which to begin the S ramp. Its value must be less than 0.991 to activate the ramp. The default value of this parameter is 1.0 (i.e. the ramp is not used). For once-through steam generator applications, a value less than 0.991 is needed to preclude observed sharp increases in S that results in disproportionally high overall heat transfer as the void fraction approaches unity.

S' is a fit to Chen's suppression factor given by the following expression

$$S' = \begin{cases} [1 + 0.12(\text{Re}_{\text{TP}})^{1.14}]^{-1} & \text{Re}_{\text{TP}} < 32.5 \\ [1 + 0.42(\text{Re}_{\text{TP}})^{0.78}]^{-1} & 32.5 \leq \text{Re}_{\text{TP}} < 70.0 \\ 0.0797 & \text{Re}_{\text{TP}} \geq 70 \end{cases} \quad 2.2.2-20$$

where

$$\text{Re}_{\text{TP}} = 10^{-4} \left(\frac{\alpha_f \rho_f v_f D_e}{\mu_f} \right) F^{1.25} ,$$

$$\Delta T_{\text{sat}} = T_w - T_{\text{sat}} , \text{ and} \quad 2.2.2-21$$

ΔP = difference in vapor pressure corresponding to ΔT_{sat} .

The subcooled vapor generation factor, f_{subvap} , is calculated as follows. The onset of boiling occurs when $T_w \geq T_{w\text{ONB}}$, where $T_{w\text{ONB}}$ is the wall temperature at the onset of nucleate boiling. However, the net vapor generation will not occur until the liquid subcooling, ΔTh_{sub} , is less than the subcooling for net vapor generation, ΔTh_{NVG} . RELAP5 uses both criteria and allows vapor generation when either of the two conditions are satisfied. The onset of nucleate boiling is calculated using the Bergels and Rohsenow correlation and ΔT_{NVG} is calculated using the Saha-Zuber correlation. f_{subvap} is calculated based on these two conditions.

The Bergels and Rohsenow⁵² correlation is

$$\Delta T_{w\text{ONB}} = 0.5556 [556.7 q p^{-1.156}] [0.35355 p^{0.0234}] ,$$

2.2.2-22

where

$$\Delta T_{w_{ONB}} = T_{w_{ONB}} - T_{sat}$$

The bubble formation on the wall occurs when $T_w = T_{w_{ONB}}$. In order to make it continuous, no vapor formation occurs when $T_w \leq T_{w_{ONB}} - 2$ and increases linearly based on $T_w - T_{w_{ONB}}$, such that when $T_w = T_{w_{ONB}}$, all the q_{vap} is allowed to form vapors. This is achieved by defining a function,

$$f_{ONB} = \frac{1}{2} \text{MAX} [-2, \text{MIN} (\Delta T_s - \Delta T_{w_{ONB}}, 0.0)] + 1. \quad 2.2.2-23$$

The Saha Zuber¹²¹ correlation for ΔT_{NVG} is

$$\Delta T_{NVG} = \begin{cases} 0.002198 q D / k_f & P_e \leq 70,000 \\ 153.85 q / (G C_{pf}) & P_e > 70,000 \end{cases}, \quad 2.2.2-24$$

where

$$P_e = \text{Peclet number, } G D C_{pf} / k.$$

In order to make the net vapor generation continuous, vapor generation is allowed to begin at $T_f = (T_{f_{NVG}} - 2.0)$ and increase linearly, based on $T_f - T_{f_{NVG}}$, such that all q_{vap} is allowed to form vapor at $T_f = T_{f_{NVG}}$. This is achieved by defining a function

$$f_{NVG} = \frac{1}{2} \text{MAX} [-2, \text{MIN} (\Delta T_{NVG} - (T_{sat} - T_f), 0.0)] + 1. \quad 2.2.2-25$$

RELAP5/MOD2 allows the vapor to form when either f_{NVG} or f_{ONB} becomes greater than zero, and thus,

$$f_{subvap} = \text{MAX} (f_{ONB}, f_{NVG}) \quad 2.2.2-26$$

In subcooled and saturated nucleate boiling, h_{wg} and q_{wg} are zero. Then

$$h_{wf} = h,$$

$$q = h_{mic}^* \Delta T_{sat} + h_{mac}^* (T_w - T_f), \quad 2.2.2-27$$

and

$$\Gamma_w = q_{vap} A_w / \left[v h_{fg} \left\{ 1 + \frac{(\rho C_p)_f \cdot \text{MAX}(0.0, T_{sat} - T_f)}{\rho_g h_{fg}} \right\}^2 \right], \quad 2.2.2-28$$

where q_{vap} is the portion of q_{wf} available for vapor generation. It is calculated by

$$q_{vap} = (q_{wf} - q_{conv}), \quad 2.2.2-29$$

where

$$q_{conv} = h_{mac}^* (T_w - T_f) \psi, \text{ and} \quad 2.2.2-30$$

$$\psi = \begin{cases} 1 & T_f > T_w \\ 0.5 \text{ MIN}[2.0, \text{MAX}(0.0, T_{sat} - T_f)] & \text{otherwise.} \end{cases}$$

2.2.2.2. Critical Heat Flux (CHF) Correlations

Two options are available for best-estimate computation of the critical heat flux, q_{crit} . An option is provided to use the Biasi and modified Zuber correlations or the Becker¹⁴⁹ rod bundle correlation. Analyses have shown that the previous best-estimate default CHF correlation in RELAP5/MOD2, Biasi-Zuber, inadequately predicts once-through steam generator (OTSG) CHF at lower power levels. Consequently, Biasi-Zuber causes poor prediction of shell-side heat transfer regimes and dryout behavior at power levels less than 80 percent. The Becker CHF correlation provides a substantially improved prediction of dryout location and dryout quality and overall better response of OTSG steady-state and transient phenomena. Therefore, the Becker correlation is added to RELAP5 and is recommended for OTSG secondary shell-side heat structures. The Becker CHF correlation is limited by pressure and is only used up to 90 bar, which is more than ample for any OTSG transient. A linear interpolation scheme activates at 80 bar to 90 bar and interpolates between the two CHF correlations to ensure a smooth and continuous transition from Becker to Biasi-Zuber at 90 bar. The Biasi-Zuber correlation is considered to be applicable for all other geometries, without any restriction of input conditions. The Becker correlation is restricted by pressure and can only be used up to 90 bar. For pressures above 90 bar, the Biasi-Zuber correlation will be used with either option.

Biasi-Zuber

This correlation is primarily flow dependent, that is, when the mass flux, G , is greater than or equal to $300 \text{ Kg/m}^2\text{-s}$, q_{crit} is calculated as the maximum of the Biasi correlation for the low quality region

$$q_{crit} = C1_{BA} \frac{1.883 \cdot 10^7}{(100D_e)^n (0.1G)^{1/6}} \left[\frac{f(P)}{(0.1G)^{1/6}} - X_e \right], \quad 2.2.2-31$$

and for the high quality region

$$q_{\text{crit}} = C1_{\text{BB}} \frac{3.78 \cdot 10^7 h(P)}{(100D_e)^n (0.1G)^{0.6}} [1 - x_e], \quad 2.2.2-32$$

where

$$n = \begin{cases} 0.4 & D_e \geq 0.01 \text{ m} \\ 0.6 & D_e < 0.01 \text{ m}, \end{cases}$$

$$f(P) = 0.7249 + 0.099 P' \exp(-0.032P'),$$

$$h(P) = -1.159 + 0.149 P' \exp(-0.019P') \\ + 8.99P' / [10 + P'^2], \quad \text{and}$$

$$P' = \text{MAX}(10^{-5} P, 2.7) \text{ bar.}$$

When G is between 200 and 300 $\text{Kg/m}^2\text{-s}$, q_{crit} is calculated using the Biasi correlation for the high quality region. When G is between 100 and 200 $\text{Kg/m}^2\text{-s}$, q_{crit} is calculated using a linear interpolation, with respect to G , between the maximum value of the two Biasi correlations (using $G = 200 \text{ Kg/m}^2\text{-s}$) and the modified Zuber correlation, that is,

$$q_{\text{crit}} = C1_{\text{ZB}} 0.131 h_{\text{fg}} \rho_g^{0.5} [\sigma g (\rho_f - \rho_g)]^{0.25} \left[\frac{\rho_f \cdot}{\rho_f + \rho_g} \right]^{0.5} \\ \cdot (1.0 - \alpha_g) \quad 2.2.2-35$$

When $G < 100 \text{ Kg/m}^2\text{-s}$, q_{crit} is given by the modified Zuber correlation.

Becker

The Becker correlation is separated into two major components based upon equilibrium quality. For each quality regime, each component is further subdivided based upon pressure. For the Becker correlation, the mass flux, G , is limited to a minimum value of $30.0 \text{ Kg/m}^2\text{-sec}$ by $G = \text{Max}(30.0, G)$.

For the low quality region, where the equilibrium quality is between 0.0 and 0.25, q_{crit} is computed by

$$q_{\text{crit}} = \frac{10^8}{G^{0.5}} \left[\left(\frac{x_e}{a_0} + a_1 \right)^{-1} \right] \quad 2.2.2-35.1$$

where,

$$a_0 = f_2(P_{\text{bar}}) / h_{\text{fg}}^* \quad 2.2.2-35.2$$

$$a_1 = f_1(P_{\text{bar}}) / f_2(P_{\text{bar}}) \quad 2.2.2-35.3$$

$$P_{\text{bar}} = \text{MAX}(10^{-5} P, 2.7) = \text{Pressure, (bar)}$$

$$h_{\text{fg}}^* = \text{enthalpy of vaporization, (KJ/Kg)}$$

and where,

$$f_1(P_{\text{bar}}) = 27.8763 \cdot P_{\text{bar}} \quad 2.2.2-35.4$$

$$f_2(P_{\text{bar}}) = 73.5845 \cdot P_{\text{bar}} \quad 2.2.2-35.5$$

for low pressures between 2.70 and 20 bar. For higher pressures within the range of 20 to 90 bar, the f -parameter is computed by

$$f_1(P_1) = 182.79 - P_1 \left\{ 114.99 - P_1 \left[2766.6 + P_1 (14457 + P_1 [40523 + P_1 (48283 + P_1 19608)]) \right] \right\} \quad 2.2.2-35.6$$

$$f_2(P_1) = 432.07 - P_1 \left\{ 244.75 - P_1 \left[5751.7 + P_1 (21745 + P_1 [64025 + P_1 (83304 + P_1 35767)]) \right] \right\}$$

2.2.2-35.7

and where,

$$P_1 = (P_{\text{bar}} - 100.5) / 100.0 .$$

For the high quality region, where X_e is greater than 0.25, several logarithmic equations are used to calculate the critical heat flux, q_{crit} . The equations are transcendental, requiring an iterative solution method. The logarithmic nature of the equations, however, is an asset and allows the solution method to be simple and quick, usually converging within three to four iterations. The high quality q_{crit} is given by:

$$q_{\text{crit}} = \frac{10^3 b h_{fg}^*}{G^{1/2} (B0) (v_g - v_f)} ,$$

2.2.2-35.8

where

$$B0 = (B1 + B2 + B3) / B4$$

2.2.2-35.9

$$B1 = -\ln (1.0 - X_e)$$

2.2.2-35.10

$$B2 = \ln \left(\text{Max} [1.0E-5, \left[0.98 - \left[\frac{E v B0^{1/2}}{X_e^{1/4} (B0 + 1.0)} \right] \right] \right)$$

2.2.2-35.11

$$B3 = -\ln \left(\text{Max} [1.0E-5, \left[1.0 - \left[\frac{E (X_e + v) B0^{1/2}}{(1 - X_e) X_e^{1/4} (B0 + 1.0)} \right] \right] \right)$$

2.2.2-35.12

$$B_4 = \ln \left(\frac{X_e + v}{v} \right) \quad 2.2.2-35.13$$

with

$$v = v_f / (v_g - v_f) .$$

The coefficients E and b are functions of pressure:

$$E (P_1) = 0.25354 + P_1 \{ 0.9575 + P_1 [0.7287 - P_1 (0.56389)] \} . \quad 2.2.2-35.14$$

For very low pressures, between 2.7 and 5.0 bar,

$$b (P_1) = 65.841 + P_1 [143.336 + P_1 (79.213)] . \quad 2.2.2-35.15$$

For intermediate pressures, between 5.0 and 20.0 bar,

$$b (P_1) = 7.3694 + P_1 [17.536 + P_1 (11.60)] . \quad 2.2.2-35.16$$

For high pressures, between 20.0 and 90.0 bar,

$$b (P_1) = 0.23884 - P_1 \{ 0.15999 - P_1 [0.14662 - P_1 (0.59071)] \} . \quad 2.2.2-35.17$$

2.2.2.3. Post-CHF Correlation

The post-CHF heat transfer regime includes the transition boiling, film boiling, and single-phase vapor heat transfer. The heat transfer in each of the regimes is described below.

Transition Boiling

In the transition boiling, the heat transfer is calculated based on the approach given by Chen.⁴³ In this regime, it is assumed that a portion of the heat slab surface given by the Chen factor, F_L (modified to make its value equal 1 at $T_w = T_{wCHF}$), is wetted by the liquid. The wall-to-liquid heat transfer is calculated as follows

$$q_{wf} = q_{crit} \cdot F_L \quad 2.2.2-36$$

and

$$h_{wf} = q_{wf} / \Delta T_{sat} \quad 2.2.2-37$$

The modified Chen's liquid contact area weighting fraction, F_L , is calculated by

$$F_L = e^{-\lambda \Delta T^*}, \quad 2.2.2-38$$

where

$$\Delta T^* = 1.34164 \text{ MIN}(|T_w - T_{wCHF}|, \sqrt{\Delta T_{sat}}),$$

$$\lambda = \text{MAX}(\lambda_1, \lambda_2),$$

$$\lambda_1 = C_1 - 7.373381 \cdot 10^{-3} C_2 G,$$

$$\lambda_2 = 7.373381 \cdot 10^{-3} C_3 G,$$

$$C_2 = 0.05 / [1 - \alpha_g^{*40}] + 0.075 \alpha_g^*,$$

$$C_1 = 2.4 C_2,$$

$$\alpha_g^* = \text{MIN}(\alpha_g, 0.999), \text{ and}$$

$$C_3 = 0.2 C_2.$$

The vapor heat transfer is calculated as

$$h_{wg} = h_{vc}(1 - F_L) \quad 2.2.2-39$$

and

$$q_{wg} = h_{wg}(T_w - T_g). \quad 2.2.2-40$$

The vapor heat transfer coefficient, h_{vc} , is calculated using the Dittus-Boelter (Equation 2.2.2-6) Rohsenow-Choi (Equation 2.2.2-7) and natural convection (Equation 2.2.2-8) correlations, based on vapor properties as follows

$$h_{vc} = \text{MAX}[\alpha_g \cdot \text{MAX}(C1_{DBV} h_{DB}, C1_{RCV} h_{RC}), C1_{NCi} h_{NC}]. \quad 2.2.2-41$$

The constants $a = 0.23$, $b = 1/3$, and $C1_{NCi} = C1_{NCV}$ are used in the natural convection correlation (Equation 2.2.2-8).

The vapor generation rate, Γ_w , is calculated using the following equation

$$\Gamma_w = q_{wf} A_w / [V(h_{fg} + 0.5 C_{p_g} \text{MAX}(0.0, T_g - T_{sat}))] \quad 2.2.2-42$$

Film Boiling

In the film boiling regime, the vapor void fraction, α_g , is used to partition the wall-to-fluid energy between the liquid and the vapor phases. In addition, wall-to-droplet radiation is added to

the liquid heat transfer. The total wall-to-liquid heat transfer is calculated as follows

$$q_{wf} = h_{wf} \Delta T_{sat} ,$$

where

$$h_{wf} = (1 - \alpha_g) h_{fB} + C1_{RD} q_{wd,rad}/\Delta T_{sat} . \quad 2.2.2-43$$

The film heat transfer coefficient, h_{fB} , is calculated using the modified Bromley correlation

$$h_{fB} = C1_{BR} 0.620 \left[\frac{k_g^3 \rho_g (\rho_f - \rho_g) h'_{fg} g}{\lambda_c \mu_g \Delta T_{sat}} \right]^{0.25} , \quad 2.2.2-44$$

where

$$h'_{fg} = h_{fg} + 0.5 C_p g \Delta T_{sat} , \text{ and}$$

$$\lambda_c = 2\pi \left[\frac{\sigma}{g(\rho_f - \rho_g)} \right]^{0.5} .$$

The wall-to-liquid droplet radiation $q_{wd,rad}$ is calculated using a model developed by Sun⁶⁰ (the wall-to-vapor and vapor-to-liquid radiation terms of the Sun correlation are neglected).

$$q_{wd,rad} = F_{wf} \sigma_{SB} (T_w^4 - T_{sat}^4) , \quad 2.2.2-45$$

where

$$\sigma_{SB} = \text{Stephen-Boltzman constant } (5.67 \cdot 10^{-8} \text{ w/m}^2\text{-k}^4),$$

$$F_{wf} = 1/[R_2(1 + R_3/R_1 + R_3/R_2)],$$

$$R_1 = (1 - \epsilon_g) / [\epsilon_g(1 - \epsilon_g \epsilon_f)],$$

$$R_2 = (1 - \epsilon_f) / [\epsilon_f(1 - \epsilon_g \epsilon_f)], \text{ and}$$

$$R_3 = 1 / (1 - \epsilon_g \epsilon_f) + (1 - \epsilon_w) / \epsilon_w,$$

for which the emissivities are given as

$$\epsilon_g = 0.02,$$

$$\epsilon_f = \text{MIN}[1 - \exp(-a_f L_m), 0.75], \text{ and}$$

$$\epsilon_w = 0.9,$$

where L_m is a mean length and a_f is the liquid absorption coefficient, respectively. The mean length L_m is roughly equal to $0.9 D_{hy}$, where D_{hy} is the hydraulic diameter of the fluid channel. The absorption coefficient, a_f , for droplets is given by

$$a_f = 1.11 \alpha_f / d_d.$$

The droplet diameter, d_d , is calculated based on a critical droplet Weber number

$$We = d_d \rho_g (v_g - v_f)^2 / \sigma = 7.5, \quad 2.2.2-46$$

and limited to

$$d_d \leq \alpha_f^{0.5} D_{hy}.$$

The wall-to-vapor heat transfer, q_{wg} , is calculated using Equation 2.2.2-40, and h_{wg} is equal to h_{vc} (Equation 2.2.2-41). The vapor generation rate, Γ_w , is given by Equation 2.2.2-36.

Single-Phase Vapor Heat Transfer

The heat transfer coefficient in this regime is calculated using the Dittus-Boelter (Equation 2.2.2-6) Rohsenow-Choi (Equation 2.2.2-7) and natural convection (Equation 2.2.2-8) correlations, based on the vapor properties as given below.

$$h = \text{MAX}(C1_{DBV} h_{DB}, C1_{RCV} h_{RC}, C1_{NCi} h_{NC}) . \quad 2.2.2-47$$

The constants $a = 0.23$, $b = 1/3$, and $C1_{NCi} = C1_{NCV}$ are used in Equation 2.2.2-8.

For single-phase vapor, h_{wf} , q_{wf} , and Γ_w are zero, and

$$h_{wg} = h \quad 2.2.2-48$$

and

$$q_{wg} = h(T_w - T_g) . \quad 2.2.2-49$$

2.2.2.4. Condensation Heat Transfer

When two-phase or single-phase vapor passes over a heat structure whose surface temperature is below the saturation temperature of the mixture or vapor, heat transfer occurs from the fluid to the structure by a condensation process. The condensation heat transfer coefficient⁴⁴ is calculated as the maximum of the Nusselt laminar film correlation and the Carpenter and Colburn turbulent film correlation.

$$h_{con} = \text{MAX}(h_{nlf}, h_{cctf}) . \quad 2.2.2-50$$

The Nusselt laminar film correlation⁴⁴ used in RELAP5/MOD2-B&W depends on the orientation of the condensing surface. For a condensation on a horizontal surface, laminar film condensation in a horizontal tube with stratified flow is assumed and a modified form of the Nusselt equation is used:

$$h_{nlf} = 0.296 \left[\frac{\rho_f (\rho_f - \rho_g) g h_{fg} k_f^3}{D_e \mu_f (T_{sat} - T_w)} \right]^{0.25} \quad 2.2.2-51$$

For a vertical surface, the Nusselt laminar film condensation correlation is used

$$h_{nlf} = 0.943 \left[\frac{\rho_f (\rho_f - \rho_g) g \sin \theta h_{fg} k_f^3}{\mu_f L_v (T_{sat} - T_w)} \right]^{0.25} \quad , \quad 2.2.2-51.1$$

where

θ = angle of inclination to the horizontal

and

L_v = volume length.

When the average liquid velocity is less than or equal to 0.001 m/s, only laminar film condensation is used.

The Carpenter and Colburn turbulent film correlation is

$$h_{cctf} = 0.065 \frac{\rho_f^{0.5}}{\mu_f} (\text{Pr})_f^{0.5} r_i^{0.5} k_f \quad , \quad 2.2.2-52$$

with

$$r_i = \frac{0.0792}{(\text{Re})_g^{0.25}} \left[\frac{\rho_g v_g^2}{2} \right] \quad . \quad 2.2.2-53$$

The heat transfer coefficient from the gas is determined by proportioning the pure condensation coefficient with the gas void fraction

$$h_{wg} = \alpha_g h_{con} \cdot \text{MIN}(1.0, 10\alpha_g) , \quad 2.2.2-54$$

and the heat flux is determined in the usual way

$$q_{wg} = h_{wg} \Delta T_{sat} . \quad 2.2.2-55$$

Heat transfer to or from the liquid is also likely under these conditions. This process is modeled similar to heat transfer to subcooled liquid, section 2.2.2.1, using the maximum of the Dittus-Boelter or the Rohsenow-Choi correlations proportioned to the liquid void fraction

$$h_{wf} = \alpha_f \text{MAX}(h_{DB}, h_{RC}) . \quad 2.2.2-56$$

Both correlations are evaluated at the liquid conditions. The heat flux is again straightforward

$$q_{wf} = h_{wf} (T_w - T_f) . \quad 2.2.2-57$$

The volumetric vapor condensation rate, Γ_w , is given by

$$\Gamma_w = q_{wg} A_w / \{V[h_{fg} + 0.375 C_{pg} \text{MAX}(0.0, T_g - T_{sat})]\} . \quad 2.2.2-58$$

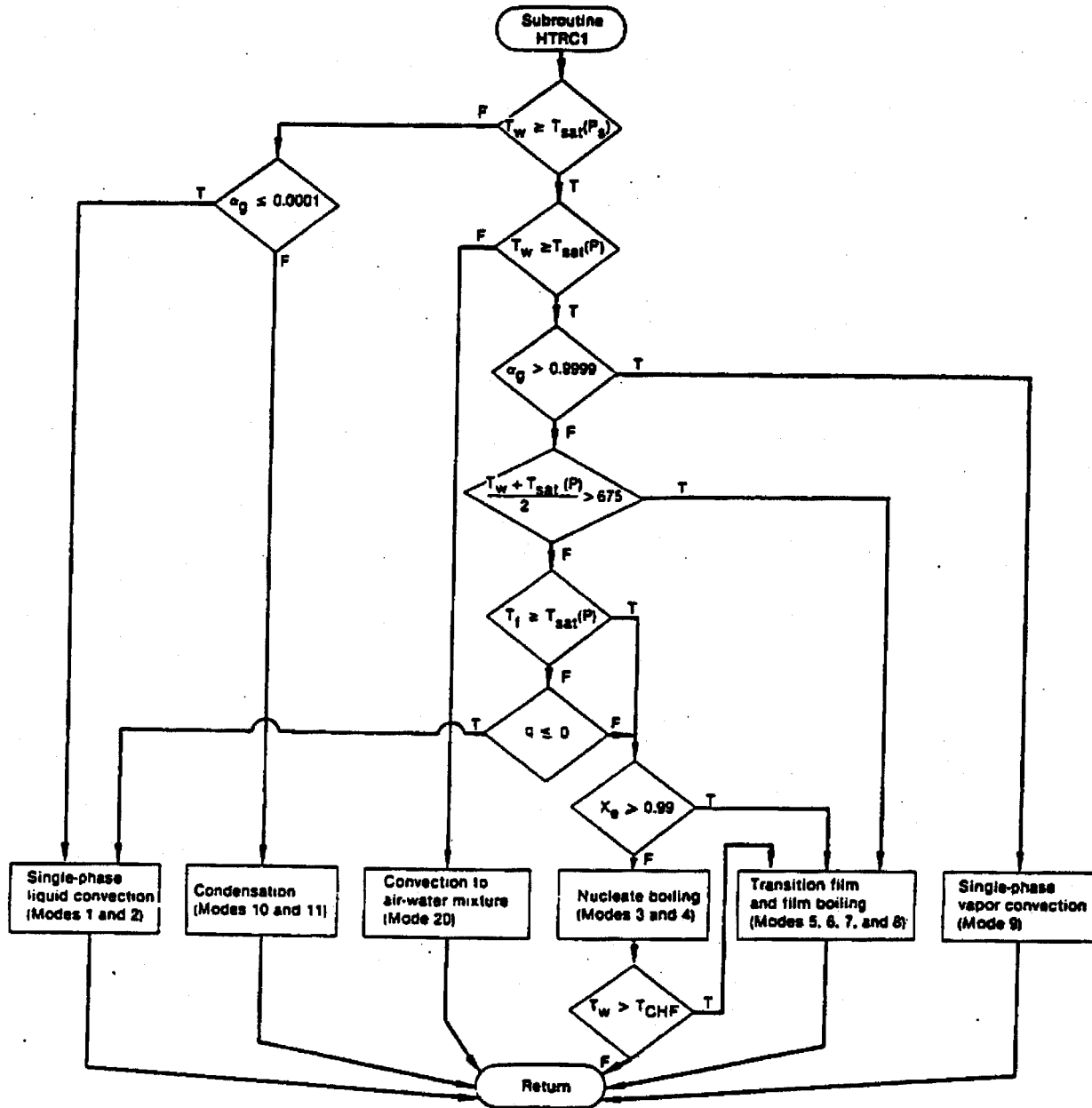


Figure 2.2.2-1. Logic Chart for System Wall Heat Transfer Regime Selection.

2.2.2.5. Auxiliary Feedwater Model

An auxiliary feedwater (AFW) model developed by B&W is incorporated in RELAP5/MOD2 to calculate the B&W once-through steam generator (OTSG) heat transfer correctly during auxiliary feedwater AFW injection from high elevation locations. The model consists of two parts:

1. A heat transfer surface area change model to calculate the number of tubes wetted by auxiliary feedwater at a given location.
2. Heat and mass transfer models to calculate energy transfer from the tube walls to the falling liquid film and to the steam.

The surface area change model and the heat transfer models are taken directly from REDBL5 code manual. In the RELAP5/MOD2 formulation the total energy transfer from the tubes to the fluid is partitioned between the phases. A mass transfer model is added to calculate the mass transfer between the phases.

In most B&W plants the subcooled auxiliary feedwater is injected near the top of the steam generator. As the water cascades down through the broached tube support plates, the number of tubes wetted by the falling film increases. This is modeled using a heat transfer area change model, and the falling film heat and mass transfer correlations described in this section. The AFW model selection logic is also described in this section.

Heat Transfer Area Change Model

At the point of injection of AFW, the fraction of the tubes wetted is a function of the injection rate. The total fraction of the tubes wetted by AFW at the injection location is given by

$$\frac{N_o}{N_t} = C_1 \frac{W_{AFW}}{\rho_l} , \quad 2.2.2-59$$

where

- N_o = number of tubes wetted at the injection location,
- N_t = total number of tubes in a steam generator (input),
- W_{AFW} = AFW flow rate into a steam generator (kg/s),
- ρ_l = density of AFW (kg/m³), and
- C_1 = user input constant (default = 0.5278).

As the liquid drains downward it spreads out, thereby increasing the fraction of tubes wetted. The number of tubes wetted by AFW at a distance Z from the injection location is given by

$$\frac{N(Z)}{N_o} = \text{MIN}[1.0 + C_2 Z, C_3] , \quad 2.2.2-60$$

where C_2 and C_3 are user input constants. (The default values are $C_2 = 1.788$ and $C_3 = 10.0$.)

Combining Equations 2.2.2-59 and 2.2.2-60

$$\frac{N(Z)}{N_t} = C_1 \frac{W_{AFW}}{\rho_l} \cdot \text{MIN}[1.0 + C_2 Z, C_3] . \quad 2.2.2-61$$

Multiple radial channels may be used to model the wetted and dry tube bundles. If the steam generator is modeled using multiple radial regions, the maximum number of tubes wetted by AFW will be equal to the number of tubes (N_{AFW}) in the radial region which is connected to AFW source. Thus,

$$\frac{N(Z)}{N_t} \leq \frac{N_{AFW}}{N_t} \quad (N_{AFW} = N_t \text{ for one radial region model}). \quad 2.2.2-62$$

The tube heat structure heat transfer areas connected to the secondary control volume are partitioned by

$$A_{wet} = \frac{N(Z)}{N_{AFW}} \cdot A_{slab} \quad 2.2.2-63$$

and

$$A_{dry} = A_{slab} - A_{wet} \quad 2.2.2-64$$

where A_{slab} is the total right side heat structure surface area. It should be noted that $N(Z)/N_{AFW}$ is limited between zero and one to prevent unrealistic calculations.

Heat and Mass Transfer Calculations

The wetted and dry heat transfer coefficients of the individual tube bundle regions will be associated with the wetted and dry areas determined in Equations 2.2.2-63 and 2.2.2-64. The wall to steam heat transfer to the dry area is determined by the Dittus-Boelter forced convection correlation with the steam properties.

$$h_g = h_{DB} = 0.023 \frac{k_g}{D_e} Pr_g^{0.4} Re_g^{0.8} \quad 2.2.2-65$$

The liquid heat transfer coefficient for the wetted region is determined by a combination of models. It is assumed that the AFW falls down the outside of the tubes as a thin film which spreads according to the wetted heat transfer area correlations. The heat transfer coefficient is based on the liquid conditions. If the liquid is subcooled, ($T_l \leq T_{sat} - 4K$), then the wall to subcooled liquid film heat transfer is defined by the Drew falling film correlation.

$$h_l = h_{Drew} = C_{Drew} \left[\frac{k_l^3 \rho_l^2 g}{(\mu_l)^2} \right]^{1/3} \left(Pr \cdot Re \right)^{1/3}, \quad (w/m^2), \quad 2.2.2-66$$

where

C_{Drew} = Drew correlation constant (input), default = 0.01,

Pr = Prandtl number $(\mu C_p/k)_l$,

Re = Reynolds number $(4 \Gamma/\mu_l)$,

Γ = flow/wetted perimeter $(W_{AUX}/N(Z)\pi D_o)$,

k_l = thermal conductivity (w/m-K),

ρ_l = density of the liquid film (kg/m^3) ,

g = gravitational constant (m/s^2) ,

$N(Z)$ = number of wetted tubes given by Equations 2.2.2-61 or 2.2.2-62,

D_o = outside tube diameter (m),

W_{AUX} = average AFW flow rate in a control volume (kg/s),
and

μ_l = liquid viscosity (kg/m-s).

If the liquid is saturated ($T_l \geq T_{sat}$), then the liquid heat transfer coefficient is defined by the Chen nucleate boiling correlation (see section 2.2.2.1).

$$h_l = h_{Chen} = h_{mic} + h_{mac} . \quad 2.2.2-67$$

If the liquid temperature is $(T_{sat} - 4) < T_l < T_{sat}$, then an interpolation between the two correlations is used.

$$h_l = h_{Chen} - \left[\left(h_{Chen} - h_{Drew} \right) \left(\frac{T_{sat} - T_l}{4.0} \right) \right] . \quad 2.2.2-68$$

The mass transfer, Γ_w , is determined separately depending on the liquid condition.

For $T_l \leq (T_{sat} - 4.0)$,

$$\Gamma_{wg} = \Gamma_{wf} = 0.0 . \quad 2.2.2-69$$

For $T_l \geq T_{sat}$,

$$\Gamma_{wf} = \Gamma_{wChen} = \frac{\left[q_{Chen} - h_{mac} \left(|T_{sat} - T_l| \right) \right] A_{wet}}{V h_{fg} \left[1.0 + C_p \left(|T_{sat} - T_l| \right) \rho_l \left(\rho_g h_{fg} \right) \right]^2} \quad 2.2.2-70$$

and

$$\Gamma_{wg} = 0.0 , \quad 2.2.2-71$$

where

$$q_{Chen} = h_{mac} (T_w - T_l) + h_{mic} (T_w - T_{sat}) . \quad 2.2.2-72$$

For $(T_{\text{sat}} - 4.0) < T_l < T_{\text{sat}}$,

$$\Gamma_{\text{wf}} = \Gamma_{\text{wChen}} - [(\Gamma_{\text{wChen}} - 0.0)(T_{\text{sat}} - T_l)/4.0] \quad 2.2.2-73$$

and

$$\Gamma_{\text{wg}} = 0.0 \quad 2.2.2-74$$

In the cases where $(T_{\text{sat}} - 4.0) > T_l$, there is an additional limit applied to Γ_{wf} . If Γ_{wf} calculated by Equations 2.2.2-70 or 2.2.2-72 exceeds 80% of the liquid available for boiling within a control volume, then the wetted area is reduced accordingly to give a value which can only equal 80%. This limit avoids the possibility of introducing an artificial mass error by vaporizing more liquid than is available.

Average Heat Flux and Heat Transfer Coefficients

The average values of heat flux and heat transfer coefficients are calculated as follows

$$h_{\text{fff}} = h_l A_{\text{wet}}/A_{\text{slab}} \quad 2.2.2-75$$

$$h_{\text{ffg}} = h_g (1 - A_{\text{wet}}/A_{\text{slab}}) \quad 2.2.2-76 \quad | \quad s$$

$$h_{\text{ff}} = h_{\text{fff}} + h_{\text{ffg}} \quad 2.2.2-77$$

$$q_{\text{fff}} = h_{\text{fff}}(T_w - T_l) \quad 2.2.2-78$$

$$q_{\text{ffg}} = h_{\text{ffg}}(T_w - T_g) \quad \text{and} \quad 2.2.2-79$$

$$q_{\text{ff}} = q_{\text{fff}} + q_{\text{ffg}} \quad 2.2.2-80$$

AFW Model Selection Logic

The falling film heat transfer is calculated only when the liquid velocity in the user-specified junction representing the AFW inlet is greater than or equal to 0.0, that is, the AFW is on. When the AFW is on the falling film and/or the regular RELAP5 heat transfer logic is selected based on the following conditions:

1. It is assumed that the falling film heat transfer correlation is applicable only above the slug flow regime. Hence, RELAP5 heat transfer logic is used in all the secondary nodes associated with AFW below a secondary control volume where $\alpha_g \geq 0.65$.
2. It is assumed that the falling film heat transfer correlation is applicable only when the volume average liquid flow is downwards. Hence, the default RELAP5 heat transfer logic requires the volume average liquid velocity to be greater than or equal to -0.001 m/s. A user over-ride option does exist to remove this criteria. Use of the default criteria can result in a significant heat transfer change if the volume average liquid velocity fluctuates due to a valve opening, STGR, pool heat transfer coupling, etc.
3. Use falling heat transfer logic in all the secondary control volumes above a lowermost volume where $\alpha_g \geq 0.85$, provided that the void fraction α_g in a given volume is less than or equal to 0.9999. In this region of the steam generator model, even if the void fraction is below 0.85 due to artificial liquid holdup, falling film heat transfer logic is used (MODE = 13). In this case, set

$$h_f = h_{fff} ,$$

2.2.2-81

$$h_g = h_{ffg} , \quad 2.2.2-82$$

$$h_f = h_g + h , \quad 2.2.2-83$$

$$q_f = q_{fff} , \quad 2.2.2-84$$

$$q_g = q_{ffg} , \text{ and} \quad 2.2.2-85$$

$$q_f = q_g + q . \quad 2.2.2-86$$

4. In the volumes between the lowermost control volume where $\alpha_g \geq 0.65$ and the lowermost volume where $\alpha_g \geq 0.85$, the heat transfer is calculated by linear interpolation (MODE = 14).

$$h_f = [(0.85 - \alpha_g) h_{fR} + (\alpha_g - 0.65) h_{fff}]/0.2 , \quad 2.2.2-87$$

$$h_g = [(0.85 - \alpha_g) h_{gR} + (\alpha_g - 0.65) h_{ffg}]/0.2 , \quad 2.2.2-88$$

$$h_f = h_g + h , \quad 2.2.2-89$$

$$q_f = h_f(T_w - T_l) , \text{ and} \quad 2.2.2-90$$

$$q_g = h_g(T_w - T_g) , \quad 2.2.2-91$$

where h_{fR} and h_{gR} are liquid and vapor heat transfer coefficients, respectively, calculated by the normal RELAP5 heat transfer logic.

5. When the equilibrium quality is greater than or equal to 1, it is assumed that AFW has not reached to that control volume. This might be due to evaporation or artificial holdup of the falling liquid in the region above the node.

2.3. Reactor Core

Simulation of the reactor core requires several special models not used in the rest of the reactor coolant system. The core thermo- and hydrodynamics are identical to any other region of the simulation excepting that the possibility of fuel cladding rupture during a LOCA may require the addition of resistance to some of the flow junctions. The heat structure modeling is similar to the rest of the simulation excepting the heat source, a nuclear reaction, the fuel-to-clad gap model, the potential of zirconium oxidation, and the use of a different heat transfer package. These features are described in the following sections. The section on the fuel pin model describes both the thermal behavior modeling and the hydraulic effects of the occurrence of rupture.

2.3.1. Reactor Kinetics

The reactor kinetics capability can be used to compute the power behavior in a nuclear reactor. The power is computed using the space-independent or point kinetics approximation that assumes that power can be separated into space and time functions. This approximation is adequate for cases in which the space distribution remains nearly constant.

The reactor kinetics model of RELAP5/MOD2 computes both the immediate fission power and the power from decay or fission fragments. The immediate power is that released at the time of fission and includes power from fission fragment kinetic energy and neutron moderation. Decay power is generated as the fission products undergo radioactive decay. The user can select the decay power model based on either an ANS Standard¹⁰² proposed in 1973 or on the 1979 ANS Standard for Decay Heat Power in Light Water Reactors.¹⁰³

2.3.1.1. Reactor Kinetics Equations

The point kinetics equations are

$$\frac{d\phi(t)}{dt} = \frac{[\rho(t) - \beta]}{\Lambda} \phi(t) + \sum_{i=1}^N \lambda_i C_i(t) + S, \quad 2.3.1-1$$

$$\frac{dC_i(t)}{dt} = \frac{\beta f_i}{\Lambda} \phi(t) - \lambda_i C_i(t) \quad i = 1, 2, \dots, N, \quad 2.3.1-2$$

$$\psi(t) = \Sigma_f \phi(t), \quad 2.3.1-3$$

and

$$P_f(t) = Q_f \psi(t), \quad 2.3.1-4$$

where

t = time,

ϕ = neutron flux,

C_i = number of delayed neutron precursors of group i ,

β = effective delayed neutron fraction,

Λ = prompt neutron generation time,

ρ = reactivity (only the time dependence has been indicated; however, the reactivity is dependent on other variables),

f_i = fraction of delayed neutrons of group i ,

λ_i = decay constant of group i ,

S = source,

ψ = fission rate in #/s,

Σ_f = fission cross section,

P_f = immediate fission power in MeV/s, and

Q_f = immediate fission energy per fission in MeV.

2.3.1.2. Fission Fragment Decay Model .

The 1979 standard expresses the power $P_\alpha(t)$ in MeV/s as a function of time t resulting from one fission of isotope α at $t = 0$ as

$$P_\alpha(t) = \sum_{j=1}^{N_\alpha} a_{\alpha j} \exp(-\lambda_{\alpha j} t) . \quad 2.3.1-5$$

Data are presented for three isotopes, U^{235} , U^{238} , and Pu^{239} . The parameters a and λ were obtained by fitting to fission decay power data. The fitting for each isotope used 23 groups ($N_\alpha = 23$). The above expression is an impulse response to one fission and can be extended to an arbitrary fission rate $\psi_\alpha(t)$ through the convolution integral

$$P_\alpha(t) = \sum_{j=1}^{N_\alpha} a_{\alpha j} \exp(-\lambda_{\alpha j} t) \psi_\alpha(t) , \quad 2.3.1-6$$

where the convolution operation is defined by

$$A(t)B(t) = \int_0^t A(t - \tau) B(\tau) d\tau = \int_0^t A(\tau) B(t - \tau) d\tau . \quad 2.3.1-7$$

Since numerical evaluation of convolution integrals is cumbersome, a set of differential equations equivalent to the convolution integral is derived.

Assume that the power from each group is from radioactive decay of a fission fragment i . Then

$$P_{\alpha j}(t) = \lambda_{\alpha j} \gamma_{\alpha j} = a_{\alpha j} \exp(-\lambda_{\alpha j} t) . \quad 2.3.1-8$$

For simplification in the following derivation, the α and j subscripts are dropped and the following expressions represent an equation for one group for one isotope. From Equation 2.3.1-8 we have

$$\gamma(t) = \frac{a}{\lambda} \exp(-\lambda t) . \quad 2.3.1-9$$

Laplace transforming Equation 2.3.1-8 gives

$$\gamma(s) = \frac{a}{\lambda(s + \lambda)} . \quad 2.3.1-10$$

Rearranging gives

$$s\gamma(s) = \frac{a}{\lambda} - \lambda\gamma(s) . \quad 2.3.1-11$$

Transforming to real time yields

$$\frac{d\gamma(t)}{dt} = \frac{a}{\lambda} \delta(0) - \lambda\gamma(t) , \quad 2.3.1-12$$

where $\delta(0)$ is the impulse function. Applying a time dependent fission rate $\psi(t)$ in place of the single fission (impulse response), Equations 2.3.1-11 and 2.3.1-12 become

$$s\gamma(s) = \frac{a}{\lambda} \psi(s) - \lambda\gamma(s) \quad 2.3.1-13$$

and

$$\frac{d\gamma(t)}{dt} = \frac{\beta}{\lambda} \psi(t) - \lambda \gamma(t) . \quad 2.3.1-14$$

The solution of Equations 2.3.1-13 or 2.3.1-14 (remembering that $P = \lambda\gamma$) for an impulse yields Equation 2.3.1-5 and a similar expression in the standard. Solution of Equations 2.3.1-13 or 2.3.1-14 for an arbitrary fission source yields Equation 2.3.1-7. When specifying

$$\psi(t) = 1 \text{ for } 0 \leq t \leq T \text{ and } \psi(t) = 0 \text{ for } t > T . \quad 2.3.1-15$$

Equations 2.3.1-13 and 2.3.1-14 yield another solution given in the standard (note that the standard defines t as starting at 0 after fissioning for T seconds).

A physical model can be attached to the terms in Equation 2.3.1-14. The first term on the right represents production of the isotope during fission; the last term is the loss of the isotope due to decay. A more mechanistic model would provide for production of one isotope due to the decay of another (see actinide model).

As shown above, the 1979 ANS standard for decay power can be implemented by advancing the differential equations, which become

$$\frac{d\gamma_{\alpha j}(t)}{dt} = \frac{F_{\gamma} a_{\alpha j}}{\lambda_{\alpha j}} F_{\alpha} \psi(t) - \lambda_{\alpha j} \gamma_{\alpha j}(t)$$

$$j = 1, 2, \dots, N_{\alpha}$$

$$\alpha = 1, 2, 3 \quad 2.3.1-16$$

and

$$P_{\gamma}(t) = \sum_{\alpha=1}^3 \sum_{j=1}^{N_{\alpha}} \lambda_{\alpha j} \gamma_{\alpha j}(t) , \quad 2.3.1-17$$

where ψ is the fission rate from all isotopes, F_{α} is the fraction of fissions from isotope α , and P_{γ} is the decay power. Summation of F_{α} over α is 1.0. The value F_{γ} is an input factor to allow easy specification of a conservative calculation. It is usually 1.0 for best estimate calculations and 1.2 was recommended for a conservative calculation with the 1973 data. The 1979 data should allow consistent use of 1.0 for F_{γ} .

The 1973 proposed standard as implemented in RELAP5/MOD1 used one isotope and prescribed data for 11 groups. The 1979 standard lists data for three isotopes, U^{235} , U^{238} , and Pu^{239} , and uses 23 groups for each isotope. A user option also allows only the 1979 standard data for U^{235} to be used. The data for both standards are built into the code as default data, but the user may enter different data.

2.3.1.3. Actinide Decay Model

In RELAP5/MOD1, the actinide model was simply the optional selection of another isotope and would be identical to using two isotopes. The MOD1 actinide default data used two groups. The RELAP5/MOD2 model uses

$$\frac{d\gamma_u(t)}{dt} = F_u \psi(t) - \lambda_u \gamma_u(t) , \quad 2.3.1-18$$

$$\frac{d\gamma_N(t)}{dt} = \lambda_u \gamma_u(t) - \lambda_N \gamma_N(t) , \quad 2.3.1-19$$

and

$$P_{\alpha} = \eta_d \lambda_u \gamma_u + \eta_N \lambda_N \gamma_N . \quad 2.3.1-20$$

The quantity F_u is user input and is the number of atoms of U^{239} produced by neutron capture in U^{238} per fission from all isotopes. A conservative factor if desired should be factored into F_u . The λ and η values can be user input or default values equal to those stated in the standard can be used.

The first equation describes the rate of change of atoms of U^{239} . The first term on the right represents the production of U^{239} ; the last term is the loss of U^{239} due to beta decay. The second equation describes the rate of change of N_p^{239} . The production of N_p from the beta decay of U^{239} and Pu^{239} is formed from the decay of N_p^{239} . Solution of the actinide equations, Equations 2.3.1-18 and 2.3.1-19, for the fission source given in Equation 2.3.1-15 yields the result quoted in the 1979 standard.

2.3.1.4. Transformation of Equations for Solution

The differential equations to be advanced in time are Equations 2.3.1-1, 2.3.1-2, 2.3.1-16, 2.3.1-18, and 2.3.1-19. (The equations are ordered in storage as listed for programming convenience and to enhance vectorization.) Multiplying by Σ_f and X , the conversion from MeV/s to watts, as needed, the equations become

$$\frac{d}{dt}[X \psi(t)] = \frac{[\rho(t) - \beta] X \psi(t)}{\Lambda} + \sum_{i=1}^N \lambda_i X \Sigma_f C_i(t) , \quad 2.3.1-21$$

$$\frac{d}{dt} [X \Sigma_f C_i(t)] = \frac{\beta f_i X \psi(t)}{\Lambda} - \lambda_i X \Sigma_f C_i(t)$$

$$i = 1, 2, \dots, N,$$

2.3.1-22

$$\frac{d}{dt} [X \gamma_{\alpha j}(t)] = \frac{F_{\gamma} a_{\alpha j} F_{\alpha} X}{\lambda_{\alpha j}} \psi(t) - \lambda_{\alpha j} X \gamma_{\alpha j}(t)$$

$$j = 1, 2, \dots, N_{\alpha}$$

$$\alpha = 1, 2, 3, \quad 2.3.1-23$$

$$\frac{d}{dt} [X \gamma_u(t)] = F_u X \psi(t) - \lambda_u X \gamma_u(t),$$

and

$$\frac{d}{dt} [X \gamma_N(t)] = \lambda_u X \gamma_u(t) - \lambda_N X \gamma_N(t). \quad 2.3.1-24$$

The total power P_T is the sum of immediate fission power, fission product decay, and actinide decay, and now in units of watts is

$$P_T(t) = Q_F X \psi(t) + \sum_{a=1}^3 \sum_{j=1}^{N_a} \lambda_{aj} X \gamma_{aj}(t) + \eta_u g_u X g_u(t)$$

$$+ \eta_N \gamma_N X \lambda_N(t). \quad 2.3.1-25$$

For solution convenience, the following substitutions are made

$$\rho(t) = \beta r(t), \quad 2.3.1-26$$

$$X \psi(t) = \psi'(t), \quad 2.3.1-27$$

$$X \frac{\Delta S}{\beta} = S', \quad 2.3.1-28$$

$$X \Sigma_f C_i(t) = \frac{\beta f_i W_i(t)}{\Lambda \lambda_i}, \quad 2.3.1-29$$

$$X \gamma_{\alpha j}(t) = \frac{F_{\gamma} a_{\alpha j} F_{\alpha}}{\lambda_{\alpha j}^2} Z_{\alpha j}(t), \quad 2.3.1-30$$

$$X \gamma_u(t) = \frac{F_u}{\lambda_u} Z_u(t), \quad 2.3.1-31$$

and

$$X q_N(t) = Z_N(t). \quad 2.3.1-32$$

The equations to be advanced are now

$$\frac{d\psi'}{dt}(t) = \frac{\beta}{\Lambda} [r(t) - 1] \psi'(t) + \sum_{i=1}^N f_i W_i(t) + S', \quad 2.3.1-33$$

$$\frac{d}{dt} W_i(t) = \lambda_i \psi'(t) - \lambda_i W_i(t) \quad i = 1, 2, \dots, N, \quad 2.3.1-34$$

$$\frac{d}{dt} Z_u(t) = \lambda_u \psi'(t) - \lambda_u Z_u(t), \quad 2.3.1-35$$

$$\frac{d}{dt} Z_N(t) = F_u Z_u(t) - \lambda_N Z_N(t), \quad 2.3.1-36$$

and

$$P_T(t) = Q_f \psi'(t) + \sum_{a=1}^3 \sum_{j=1}^{N_a} \frac{F_{\gamma a} \lambda_{aj} F_a Z_{aj}(t)}{q_{aj}} + F_u \eta_u Z_u(t) + \eta_N \lambda_N Z_N(t) . \quad 2.3.1-37$$

These equations are advanced using the modified Runge-Kutta method¹⁰⁵ described in section 2.3.1.7.

2.3.1.5. Initialization

Two initialization options are provided. In both options, the fission rate and delayed neutrons are in steady state or equilibrium conditions, that is, their time derivatives are zero. With $r(0)$ as an input quantity

$$W_i(0) = \psi(0) \quad i = 1, 2, \dots, N \quad 2.3.1-38$$

and

$$S' = -r(0) \psi(0) . \quad 2.3.1-39$$

The first option assumes that the fission product decay and actinides are also in equilibrium. This is equivalent to assuming that the reactor has been operating at a constant total power for an infinite period of time. The initial conditions are

$$Z_{aj}(0) = \psi(0) \quad j = 1, 2, 3, \dots, N_a \\ a = 1, 2, 3 , \quad 2.3.1-40$$

$$Z_u(0) = \psi(0) , \quad 2.3.1-41$$

$$Z_N(o) = \frac{F_u}{q_u} \psi(o) , \quad 2.3.1-42$$

$$P_T(o) = Q \psi(o) , \quad 2.3.1-43$$

and

$$Q = Q_f + \sum_{\alpha=1}^3 \sum_{j=1}^{N_{\alpha}} \frac{F_{\alpha} a_{\alpha j} F_{\alpha}}{\lambda_{\alpha j}} + F_u \eta_u + F_u \eta_N . \quad 2.3.1-44$$

The quantity Q , which is the total energy in MeV generated per fission, is either an input value or can be defaulted to 200 MeV. The quantity Q_f is defined from Equation 2.3.1-44 and the user input or defaulted data even if the second initialization option is used. The total power is an input quantity, and the source ψ is computed from Equation 2.3.1-43.

The second option uses a power history to determine the initial values of the fission product and actinide quantities. The power history consists of one or more periods of constant total power. For each period, the input consists of the total power, the time duration at that power, and in the case of three isotopes, the fraction of power from each isotope. The fission product and actinide differential equations, Equations 2.3.1-34, 2.3.1-35, and 2.3.1-36 are advanced in time starting with initial values of zero. The fission rate ψ is defined from Equation 2.3.1-37. The fission rate is reset to zero whenever a negative value is computed. This would occur whenever the user entered total power is less than the current fission product and actinide decay power. Thus for shutdown periods, the user may conveniently enter zero total power even though significant decay power remains. The fission product and actinide values at the end of the power history become the initial values for the transient.

The initial fission rate is computed from Equation 2.3.1-37 using the total reactor power at the start of the transient (which may be different from the last power history value). If this fission rate is negative or zero, it is reset such that the immediate fission power is 10^{-12} times the decay power.

The differential equations for the power history calculation are advanced using the same numerical technique as for the transient advancement except for a simplified time step control. Time step control consists of starting the advancement of each history period with a time step of 1 second. The time step is doubled after each advancement. When the next advancement would exceed the time duration, the last advancement is with the remaining time. This scheme was selected since with each different power value, the solution moves toward a new equilibrium condition asymptotically and the most rapid change is at the beginning of a power change.

2.3.1.6. Reactivity Feedback

One of two models can be selected for reactivity feedback. The separable model is defined by

$$r(t) = r_0 - r_B + \sum_i^{n_s} r_{si}(t) + \sum_i^{n_c} v_{ci} + \sum_i^{n_p} [w_{\rho i} R_{\rho} \rho_I(t) + \alpha_{wi} T_{wi}(t)] \\ + \sum_i^{n_F} [w_{Fi} R_F T_{Fi}(t) + \alpha_{Fi} T_{Fi}(t)] . \quad 2.3.1-45$$

The quantity, r_0 , is an input quantity and represents the reactivity corresponding to the assumed steady state reactor power at time equal zero. The quantity, r_B , is calculated during input processing such that $r(0) = r_0$.

The quantities, r_{si} , are obtained from input tables defining n_s reactivity curves as a function of time. The quantities, V_{ci} , are N_c control variables that can be user defined as reactivity contributions. R_p is a table defining reactivity as a function of the current density of water, $\rho_i(t)$, in the hydrodynamic volume i ; $W_{p,i}$ is the density weighting factor for volume i ; T_{wi} is the equilibrium temperature of volume i ; α_{wi} is the temperature coefficient (not including density changes) for volume i ; and n_p is the number of hydrodynamic volumes in the reactor core. The value R_f is a table defining reactivity as a function of the average fuel temperature T_{fi} in a heat structure; W_{fi} and α_{fi} are the fuel temperature weighting factor and the fuel temperature coefficient, respectively; and n_f is the number of heat structures in the reactor core.

This model assumes nonlinear feedback effects from moderator density and fuel temperature changes and linear feedback from moderator temperature changes. The name, separable, is attached to this model since each effect is assumed to be independent of the other effects. Boron feedback is not provided, but a user defined boron feedback can be implemented with the control system.

The separable model can be used if boron changes are quite small and the reactor is near critical about only one state point.

A postulated BWR ATWS accident is an example where the reactor could be nearly critical for two different state points. One point is at normal power operating conditions: high moderator and fuel temperatures, highly voided, and no boron. During accident recovery, the reactor might approach a critical condition with relatively cold moderator and fuel temperatures, with no voids, but with some boron concentration. The reactivity could be nearly critical for both states, but the contribution from the different feedback effects is vastly different. The

assumptions of no interactions among the different feedback mechanisms, especially boron, cannot be justified. The tabular model defines reactivity as

$$r(t) = r_o + r_B + \sum_i^{N_S} r_{Si} + \sum_i^{n_C} v_{Ci} + R[\bar{\rho}(t), \bar{T}_W(t), \bar{T}_F(t), \bar{B}(t)] ,$$

2.3.1-46

$$\bar{\rho}(t) = \sum_i^{n_P} W_{\rho i} \rho_i(t) ,$$

2.3.1-47

$$\bar{T}_W(t) = \sum_i^{n_P} W_{\rho i} T_{Wi}(t) ,$$

2.3.1-48

$$\bar{B}(t) = \sum_i^{n_P} W_{\rho i} B_i(t) ,$$

2.3.1-49

and

$$\bar{T}_F(t) = \sum_i^{n_F} W_{Fi} T_{Fi}(t) ,$$

2.3.1-50

where B is boron density. The average quantities are obtained with the use of one weighting factor for each hydrodynamic volume and each heat structure contributing to reactivity feedback. The reactivity function R is defined by a table input by the user. In the Table 4 option, the table is four-dimensional; the Table 3

option assumes no boron dependence and the table is then three-dimensional.

The tabular model overcomes the objections of the separable model since all feedback mechanisms can be nonlinear and interactions among the mechanisms are included. The penalty for the expanded modeling capability greatly increases the input data requirements.

The reactivity function R is evaluated by a direct extension of the one-dimensional table lookup and linear interpolation scheme to multiple dimensions. One-dimensional table lookup and interpolation of the function $V = F(W)$ uses an ordered set of N_w independent variable values W_i with the corresponding values of the dependent variable V_i to determine the value of V corresponding to a search argument W . The independent variable is searched such that W_i and W_{i+1} bracket W ; an equation for a straight line is fitted to the points W_i, V_i , and W_{i+1}, V_{i+1} ; and the straight line equation is evaluated for the given W .

Using subscripts 0 and 1 for bracketing independent values and corresponding dependent values, and defining $w = (W - W_0)/(W_1 - W_0)$ so that w varies from 0 through 1 as W varies from W_0 through W_1 , the interpolation equations are

$$a_0 = V_0 \quad \text{and} \quad a_1 = V_1 - V_0 \quad . \quad 2.3.1-51$$

For two-dimensional interpolation of $V = F(W, X)$, two sets of independent variables are used: N_w values of W_i , and N_x values of X_j . A total of $N_w N_x$ dependent values of V_{ij} are entered, one for each combination of variables from the two sets of independent variables. Graphically, the two sets of independent variables form a rectangular grid when the W_i and X_j variables are plotted on horizontal and vertical coordinates, respectively. The dependent variables are entered corresponding to the

intersections of the mesh lines. The search for bracketing values in each independent set locates a mesh rectangle and the dependent values at the four corners are used to form an interpolation equation which is the product of two straight line functions, one for each independent variable. Using 0 and 1 subscripts for the bracketing values

$$v = \sum_{i=0}^1 \sum_{j=0}^1 a_{ij} w^i x^j , \quad 2.3.1-52$$

$$x = \frac{x - x_0}{x_1 - x_0} ,$$

$$a_{00} = v_{00}, \quad a_{01} = v_{01} - v_{00}, \quad a_{10} = v_{10} - v_{00} ,$$

and

$$a_{11} = v_{11} - v_{01} - v_{10} + v_{00} .$$

This process is simply extended to three- and four-dimensions. Three sets of independent variables define a three-dimensional rectangular grid and eight dependent quantities corresponding to the corners of a rectangular solid are used to define the interpolation equation which is the product of three straight line functions. In four-dimensions, four sets of independent variables are defined and 16 dependent values are used to define the interpolation equations, which is the product of four straight line functions.

For three-dimensional interpolation

$$V = F(W, X, Y) , \quad 2.3.1-53$$

$$y = \frac{Y - Y_0}{Y_1 - Y_0} ,$$

and

$$v = \sum_{i=0}^1 \sum_{j=0}^1 \sum_{k=0}^1 a_{ijk} w^i x^j y^k . \quad 2.3.1-54$$

For four-dimensional interpolation

$$v = F(W, X, Y, Z) , \quad 2.3.1-55$$

$$z = \frac{Z - Z_0}{Z_1 - Z_0} , \quad 2.3.1-56$$

and

$$v = \sum_{i=0}^1 \sum_{j=0}^1 \sum_{k=0}^1 \sum_{l=0}^1 a_{ijkl} w^i x^j y^k z^l . \quad 2.3.1-57$$

The interpolating equations define a continuous function, that is, there is no discontinuity in the dependent quantity as any one or combination of dependent variables pass to the next bracketing pair of values.

Using N_w , N_x , N_y , and N_z as the number of values in the four sets of independent variables, the number of data points for a three-dimensional table is $N_w N_x N_y$ and is $N_w N_x N_y N_z$ for a four-dimensional table. Using only four values for each independent variable, a four-dimensional table requires 256 data points.

2.3.1.7. Reactor Kinetics Numerical Procedures

The reactor kinetics equations are advanced in time using the modified Runge-Kutta Method of Cohen.¹⁰⁴ A first-order differential equation is written as

$$\dot{n}(t) = \alpha n(t) + R(n,t) , \quad 2.3.1-58$$

where α is constant over the time step, and $R(n,t)$ contains the remaining terms of the differential equation, including the nonconstant portion of any coefficient of $n(t)$. If the coefficient of $n(t)$ is $\beta(n,t)$, α would be $\beta[n(0),0]$, and $R(n,t)$ would contain a term of the form, $\beta[n(t),t] - \alpha n(t)$. Multiplying Equation 2.3.1-58 by an integrating factor and integrating gives

$$n(t) = n(0) e^{\alpha t} + \int_0^t e^{\alpha(t-\lambda)} R(n,\lambda) d\lambda . \quad 2.3.1-59$$

Since

$$n(0) e^{\alpha t} = n(0) + \int_0^t \alpha n(0) e^{\alpha(t-\lambda)} d\lambda , \quad 2.3.1-60$$

then

$$n(t) = n(0) + \int_0^t [\alpha n(0) + R(n,\lambda)] e^{\alpha(t-\lambda)} d\lambda . \quad 2.3.1-61$$

Letting $\lambda = ut$, then $d\lambda = tdu$, and

$$n(t) = n(0) + t \int_0^1 [\alpha n(0) + R(n,u)] e^{\alpha t(1-u)} du . \quad 2.3.1-62$$

The numerical technique for advancing the solution over the time step consists of making approximations to the behavior of $R(n,u)$ over the time step. For convenience in the following expressions, the following function is defined

$$C_m(x) = \int_0^1 u^{m-1} e^{x(1-u)} du . \quad 2.3.1-63$$

Stage 1:

Assume $R(n,\lambda) = R[n(0),0] = R_0$ and write $n(0)$ as n_0 ; then compute $n\left(\frac{h}{2}\right)$.

$$n_1 = n\left(\frac{h}{2}\right) = n_0 + \frac{h}{2} \left[\alpha n_0 + R_0 \right] C_1 \left[\alpha \frac{h}{2} \right] . \quad 2.3.1-64$$

Stage 2:

Assume a straight-line variation of $R(n,\lambda)$ between R_0 and $R_1 = R\left(n_1, \frac{h}{2}\right)$ and compute $n\left(\frac{h}{2}\right)$.

$$R(n,\lambda) = R_0 + \frac{2(R_1 - R_0)\lambda}{h} , \quad 2.3.1-65$$

$$R(n,\lambda) = R_0 + (R_1 - R_0) u \quad \left(\text{using } \lambda = u \frac{h}{2}\right) , \quad 2.3.1-66$$

and

$$n_2 = n\left(\frac{h}{2}\right) = n_1 + \frac{h}{2} (R_1 - R_0) C_2 \left[\alpha \frac{h}{2} \right] . \quad 2.3.1-67$$

Stage 3:

Assume a straight-line variation of $R(n, \lambda)$ between R_0 and $R_2 = R\left(n_2, \frac{h}{2}\right)$ and compute $n(h)$.

$$R(n, \lambda) = R_0 + \frac{2(R_2 - R_0)g}{h}, \quad 2.3.1-68$$

$$R(n, u) = R_0 + 2(R_2 - R_0) \quad (\text{using } g = uh), \quad 2.3.1-69$$

and

$$n_3 = n(h) = n_2 + h(\alpha n_0 + R_0) C_1(\alpha h) + 2h(R_2 - R_0) C_2(\alpha h). \quad 2.3.1-70$$

Stage 4:

Assume a quadratic through the points $R_0, R_2,$ and $R_3 = R(n_3, h)$ and compute $n(h)$.

$$R(n, u) = (2R_0 + 4R_2 + 2R_3)^2 u + (-3R_0 + 4R_2 - R_3) u + R_0 \quad 2.3.1-71$$

and

$$n_4 = n(h) = n_3 + h(R_4 - R_3) [2C_3(\alpha h) - C_2(\alpha h)]. \quad 2.3.1-72$$

Stage 5:

Assume a quadratic through the points $R_0, R_2,$ and $R_4 = R(n_4, h)$ and compute $n(h)$.

$$n_5 = n(h) = n_4 + h(R_4 - R_3) [2C_3(\alpha h) - C_2(\alpha h)]. \quad 2.3.1-73$$

Third-, fourth-, and fifth-order approximations are obtained by terminating the process at the end of the third, fourth, and fifth stages, respectively. RELAP5 uses only the fifth-order approximation.

By direct integration, the function, $C_1(x)$, is given by

$$C_1(x) = \frac{e^x - 1}{x} . \quad 2.3.1-74$$

Using integration by parts, a recursion relation for $C_m(x)$ is

$$C_{m+1}(x) = \frac{mC_m(x) - 1}{x} . \quad 2.3.1-75$$

During machine calculations of the $C_m(x)$ functions for $X \leq 1$, excessive loss of significance occurs. For this range, $C_3(x)$ is computed from its MacClaurin series expansion

$$C_3(x) = 2 \left[\frac{1}{3!} + \frac{x}{4!} + \frac{x^2}{5!} + \frac{x^3}{6!} + \frac{x^4}{7!} + \frac{x^5}{8!} + \frac{x^6}{9!} + \frac{x^7}{10!} \right] . \quad 2.3.1-76$$

C_2 and C_1 are evaluated by solving Equation 2.3.1-75 for $C_m(x)$.

During the advancement in time of the solution, the time increment is automatically increased or decreased to maintain a specified degree of accuracy. After the calculations for a reactor kinetics time-advancement, an empirical formula is used to estimate the error. If the error is excessive, the time increment is halved, and the advancement calculation is redone. If the error is sufficiently small, the time interval is doubled for the next time step. If the estimated error is between limits, the same interval is used for the next time-advancement.

These procedures for time step control, taken from the AIREK¹⁰⁵ code, are as follows

$$\omega_1 = \frac{\dot{\phi}(0)}{\phi(0)}$$

and

$$\omega_3 = \frac{\dot{\phi}(h)}{\phi(h)} .$$

2.3.1-77

$\bar{\omega}$ is defined by $\phi(h) = \phi(0)e^{-\bar{\omega}h}$.

$$Q = \frac{h_2 C(\alpha h)}{1 + C_1(\alpha h)} \left[\omega_1 - 2\bar{\omega} + \omega_3 \right] .$$

2.3.1-78

The α in Equation 2.3.1-78 is that of the neutron flux equation, Equation 2.3.1-23. The quantity, δ , is defined as the maximum (taken over all differential equations) of the quantity

$$\frac{n_1 - n_0}{n_1} .$$

The Q_L and Q_H appearing below are 0.0001 and 0.001, respectively.

1. If $\delta < 2^{-15}$ and $Q \geq Q_L$, the program continues with the same time step.
2. If $\delta < 2^{-15}$ and $Q < Q_L$, the program doubles the time step for the next advancement.
3. If $\delta \geq 2^{-15}$ and
 - a. $Q < Q_L$, the time step is doubled for the next advancement.

- b. $Q \leq Q_H$, the same time step is used for the next advancement.
 - c. $Q > Q_H$, the time advancement is recalculated with half the time step.
4. The time advancement is also recomputed with the time step halved if
- a. αh (of any equation) > 88.0 .
 - b. Negative or zero power is computed.

If the coefficient of the neutron flux in Equation 2.3.1-23 is negative, a subtraction is involved in determination of the derivative and a loss of significant figures can occur. If this coefficient is negative, a check is made of the number of bits lost in the subtraction. If more than nine bits are lost, the value of neutron flux computed by the current stage of the advancement procedure is discarded; instead, neutron flux is determined from the expression obtained by setting the neutron flux derivative to zero

$$D(t) = \frac{- \sum_{i=1}^I f_i W_i(t) - \frac{SA}{b}}{r(t) - 1} \quad 2.3.1-79$$

The transfer of information between the reactor kinetics calculation and the other RELAP5 calculations is explicit. Hydrodynamic and heat conduction/transfer calculations precede reactor kinetics, and the control system calculation follows reactor kinetics. The reactor power used in hydrodynamics and heat conduction is the value at the beginning of the time step. The reactivity used as an end-of-time step value in the kinetics

advancement uses end-of-time step values from hydrodynamics and heat conduction and beginning-of-time step values from the control system.

The reactor kinetics equations are advanced at the same time step rate as the hydrodynamics and reactivity is assumed to vary linearly between time step values. The maximum time step for the reactor kinetics advancement is the hydrodynamic time step. That time step is reduced if necessary as described above.

2.3.2. Core Heat Structure Model

The ordinary RELAP5 heat structures are general in nature and can be used for modeling core fuel pins; however, licensing calculations require special treatment of the fuel pin heat transfer. To accommodate these requirements, two additional models, commonly referred to as the EM (Evaluation Model) pin and core surface heat transfer models, were added to the code. The EM pin model calculates dynamic fuel-clad gap conductance, fuel rod swell and rupture using either NUREG-0630¹¹⁷ or user input options (for modeling M5 cladding or other zirconium-based alloy cladding material types), and cladding metal-water reaction. The core fuel pin surface heat transfer is calculated with a flow regime-dependent set of correlations that include restrictions on which correlations can be selected per NRC licensing requirements. These new models are independent and mutually exclusive of the original system heat transfer model (described in section 2.2.2) and the existing simple gap conductance model¹¹⁸ (referenced in Appendix A). The new models are explicitly coupled to the solution scheme through the modification of the gap conductance term, addition of fluid hydraulic resistance upon rupture, deposition of metal-water reaction energy in the clad, and determination of fuel pin surface heat transfer. The new EM pin model calculations are described in this section, while the EM heat transfer description is contained in section 2.3.3.

The EM pin model consists of three basic parts:

1. Dynamic fuel-clad gap conductance,
2. Fuel rod swell and rupture using NUREG-0630 or user specified swell and rupture options, and
3. Clad metal-water reaction,

which couple explicitly to the heat structure solution scheme or add fluid hydraulic resistance upon rupture. The model may be executed either in a steady-state initialization or transient mode determined by user input.

The pin calculations are performed on single fuel rod which represent the average behavior of a large number of rods. Each rod (also termed channel) can be broken into up to ninety heat structures, each having an associated pin segment. The gap conductance, deformation mode, and metal-water reaction are determined for each individual segment based on the channel specific pin pressure.

The changes to the EM pin model included in Version 21 and later code versions are:

1. User options to model zircaloy and/or M5 cladding (or other zirconium-based alloy material types) in the same problem,
2. User options to specify the pin channel as a primary or supplemental channel for additive form loss and BEACH droplet breakup calculations upon pin rupture, and
3. Integration of the NRC SER limitation (BEACH code-BAW-10166, Rev. 2 dated 8/13/90) for use of a maximum flow blockage of 60 percent in the ruptured cladding droplet breakup calculations.

The option to allow zirconium-based alloy cladding types requires user input to identify which pin channels are zircaloy and which are not. The zirconium-based alloy cladding also requires additional user input to specify the material properties necessary to calculate the transient cladding swell and rupture behavior.

The supplemental pin capability was added to improve the calculational methods that require modeling of multiple EM pin channels within a single hydrodynamic fluid channel (i.e., an assembly or a group of assemblies) for LOCA applications. The relationship between the supplemental pin and the remainder of the pins in a common fluid channel is one in which the supplemental pin swell and rupture will not define the rupture flow blockage for the entire channel. Rather it will define a local effect that should not be used in determination of the channel droplet breakup parameters and the additive form loss due to rupture. These parameters should be controlled by the larger group of pins (i.e. primary channel) and not the smaller grouping (i.e. supplemental channel). The supplemental rod modeling is particularly useful for gadolinia or lead test pin (M5) analyses. It may also be used in future EM revisions for hot pin applications, in which the hot pin has a higher radial peak or a different initial fuel temperature.

2.3.2.1. Transient Dynamic Fuel-Clad Gap Conductance

The RELAP5 heat structure conduction scheme uses cold, unstressed geometrical dimensions for its solution technique. The dynamic gap conductance, h_{gap} , is calculated from hot stressed conditions from which an effective gap thermal conductivity, \bar{k}_{gap} , based on cold gap size, $r_{\text{g cold}}$, is determined for each pin segment.

$$\bar{k}_{\text{gap}} = h_{\text{gap}} \cdot r_{\text{g cold}}$$

2.3.2-1

The gap conductance is determined by calculating the gap gas conductivity, temperature jump gap distance, radiation component, and dynamic fuel-clad gap from the deformation models. An

This page is intentionally left blank.

additive fuel-clad contact conductance term has also been included as an option to simulate the closed gap contribution for high fuel rod burn-up applications. Two options are provided to calculate the conductance. The first option assumes that the fuel pellet is concentric within the clad, while the second option assumes the fuel pellet is non-concentric within the clad as illustrated in Figure 2.3.2-1.

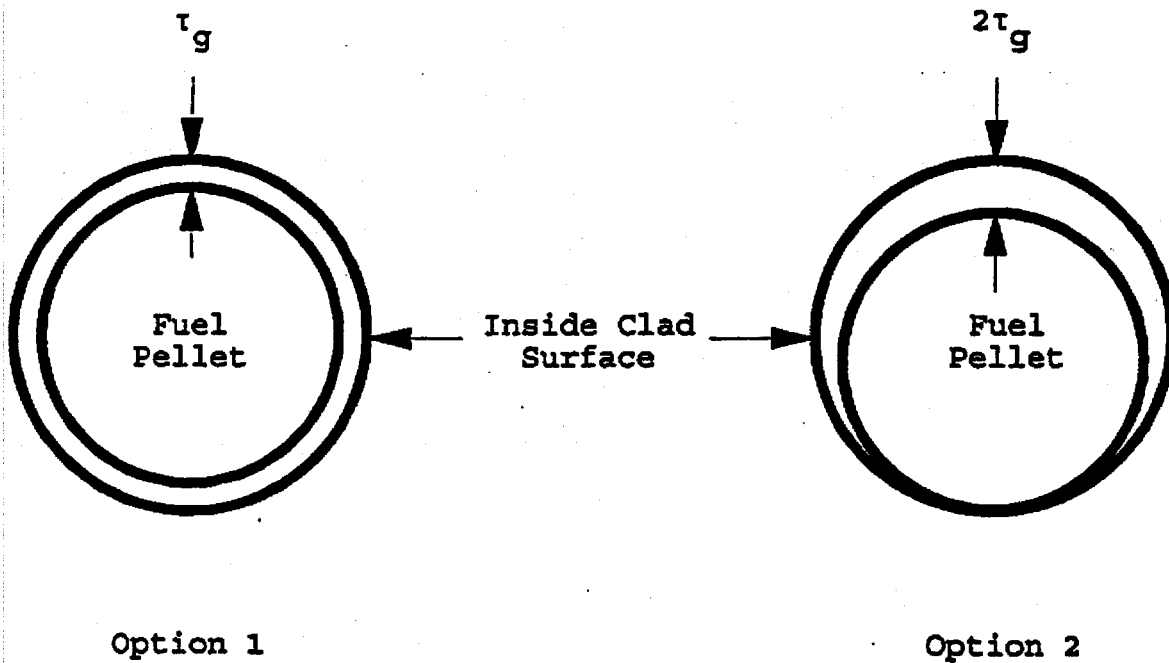


Figure 2.3.2-1. Gap Conductance Options.

Eight half-symmetrical azimuthal sections are used for determining the overall conductance for the second option without calculating an azimuthal temperature gradient. The total gap conductance is determined by

$$h_{\text{gap}} = M_g h_{\text{gap gas}} + h_{\text{rad}} + h_{\text{fcc}} \quad 2.3.2-2$$

with

h_{gap} = conductance through gap gas ($\text{w/m}^2\text{-K}$),

M_g = user input multiplier used to acquire correct initial temperature within fuel,

$h_{\text{gap gas}}$ = gap gas conductance contribution ($\text{w/m}^2\text{-K}$),

h_{rad} = conductance due to radiation contribution from fuel to clad ($\text{w/m}^2\text{-K}$), and

h_{fcc} = gap contact conductance contribution due to fuel-cladding mechanical interaction ($\text{w/m}^2\text{-K}$).

The radiation gap conductance contribution is calculated by

$$h_{\text{rad}} = \frac{\sigma}{\frac{1}{e_f} + \frac{r_f}{r_{ic}} \left(\frac{1}{e_c} - 1 \right)} \left[\frac{T_{fs}^4 - T_{ics}^4}{T_{fs} - T_{ics}} \right]$$

$$= \frac{\sigma (T_{fs}^2 + T_{ics}^2) (T_{fs} + T_{ics})}{\frac{1}{e_f} + \frac{r_f}{r_{ic}} \left(\frac{1}{e_c} - 1 \right)},$$

2.3.2-2.1

where

σ = Stefan-Boltzmann constant,

= 5.6697×10^{-8} (w/m²-K⁴),

e_f = emissivity of fuel surface,

e_c = emissivity of clad-inside surface,

T_{fs} = fuel outside surface temperature (K), and

T_{ics} = clad-inside surface temperature (K).

This page is intentionally left blank.

The optional fuel-cladding contact conductance, h_{fcc} , contribution is calculated by¹⁵⁰

$$h_{fcc} = 0.1565 (k_h/R_{eff}) \cdot M_{2h} \cdot (P_{fcc}/H_m)^{0.5} \cdot \max (1 , [P_{fcc}/(6.89 \times 10^6)]^{0.5}) , \quad 2.3.2-2.2$$

where

k_h = harmonic mean conductivity, (w/m-K),

R_{eff} = effective surface roughness, (m),

M_{2h} = ratio of RHR fuel surface roughness to wavelength
(RHR is defined as Relative-Height-Rating),

P_{fcc} = interface contact pressure, (Pa), and

H_m = Meyer hardness for the cladding, (Pa).

The harmonic mean conductivity is defined as

$$k_h = \frac{2 k_f k_c}{(k_f + k_c)} , \quad 2.3.2-2.3$$

where k_f is the fuel surface thermal conductivity, (w/m-K), evaluated at the average temperature of the outer two fuel mesh points. k_c is the cladding conductivity, (w/m-K), evaluated at the average temperature of the inner two cladding mesh points.

The effective surface roughness is given by

$$R_{eff} = \left[R_F^2 + R_C^2 \right]^{0.5} . \quad 2.3.2-2.4$$

The fuel surface roughness to wavelength ratio^{150,147} is given by

$$M_{2h} = 29.28 \cdot R_F^{0.528} \quad 2.3.2-2.5$$

The Meyer hardness for the cladding is defined as a function of the inside cladding surface temperature, T_{ics} , as

$$H_m = \text{Max} (\exp [C_1 T_{ics}^3 + C_2 T_{ics}^2 + C_3 T_{ics} + C_4], 10^5) \quad 2.3.2-2.6$$

The constants C_1 , C_2 , C_3 , and C_4 are user input or defaults¹¹⁹ to

$$C_1 = -2.5621 \times 10^{-8} \quad , \quad (K^{-3}),$$

$$C_2 = 4.3502 \times 10^{-5} \quad , \quad (K^{-2}),$$

$$C_3 = -2.6394 \times 10^{-2} \quad , \quad (K^{-1}), \text{ and}$$

$$C_4 = 26.034 \quad , \quad (\text{dimensionless}).$$

The contact pressure between the fuel and cladding is¹⁵¹

$$P_{fcc} = \frac{[u_{fcc} \cdot E_c] / r_{ic}}{\left[\frac{r_{oc}^2 + r_{ic}^2}{r_{oc}^2 - r_{ic}^2} \right] + \nu_c + \frac{E_c (1 - \nu_f)}{E_f}} \quad , \quad 2.3.2-2.7$$

where

u_{fcc} = cladding radial displacement due to contact (from Equation 2.3.2-41.9 through 2.3.2-41.12), (m),

E_c = Young's modulus for the cladding (see Equation 2.3.2-29), (Pa),

r_{ic} = hot, stressed inside cladding radius (m),

r_{oc} = hot, stressed outside cladding radius (m),

ν_c = Poisson's ratio for the cladding (dimensionless input),
(default value is 0.3),

ν_f = Poisson's ratio for the fuel (dimensionless input),
(default value is 0.314), and

E_f = Young's modulus for the fuel given either by the
code for UO_2 fuel (Pa) as,

$$= \begin{cases} 1.8863 \times 10^{11} - 9.0627 \times 10^7 T_f ; & T_f \leq 2000 \text{ K} \\ 7.0 \times 10^8 & ; T_f > 2000 \text{ K} \end{cases} \quad 2.3.2-2.8$$

or by a user specified cubic equation

$$= C_1 T_f^3 + C_2 T_f^2 + C_3 T_f + C_4 \quad 2.3.2-2.9$$

The gap gas conductance is calculated by

$$h_{\text{gap gas}} = \frac{M_g K_{\text{gas}}}{N} \sum_{n=1}^N \frac{1}{[r_n + 3.6(R_f + R_c) + (g_1 + g_2)]} \quad 2.3.2-3$$

where

n = number of the azimuthal segment,

N = user controlled total number of azimuthal segments;

$$= \begin{cases} 1, & \text{for option 1 or concentric fuel pellets,} \\ 8, & \text{for option 2 or non-concentric fuel pellets,} \end{cases}$$

K_{gas} = thermal conductivity of gap gases (w/m-K),

r_n = width of fuel-clad gap at the midpoint of the n-th azimuthal segment (m),

R_F = user input surface roughness of the fuel (m),

R_C = user input surface roughness of the clad (m),

$g_1 + g_2$ = temperature jump distance terms for fuel and cladding (m), with

$$r_n = \left[\frac{2n-1}{N} \right] r_g, \quad 2.3.2-4$$

where

r_g = hot fuel-clad gap size (m)

$$= r_{ic} - r_f,$$

r_{ic} = hot, stressed inside clad radius (m), and

r_f = hot fuel outside radius (m).

The temperature jump distance terms account for the temperature discontinuity caused by incomplete thermal accommodation of gas

molecules to surface temperatures. The terms also account for the inability of gas molecules leaving the fuel and cladding surfaces to completely exchange their energy with neighboring gas molecules, which produces a nonlinear temperature gradient near the fuel and cladding surfaces. The terms are calculated by the equation

$$g_1 + g_2 = 0.024688 K_g T_g^{1/2} / P_g \sum_i f_i a_i M_i^{-1/2}, \quad 2.3.2-5$$

where

$$T_g = \text{temperature of gas in fuel-cladding gap (K),} \\ = (T_{ics} + T_{fs})/2,$$

$$P_g = \text{channel gas pressure (Pa),}$$

$$f_i = \text{mole fractions of } i\text{-th component of gas,}$$

$$a_i = \text{accommodation coefficient of the } i\text{-th component of gas, and}$$

$$M_i = \text{molecular weight of } i\text{-th component of gas.}$$

The accommodation coefficients for helium and xenon are obtained by using curve fits to the data.¹⁰⁰

$$a_{He} = 0.425 - 2.3 \cdot 10^{-4} T_g \quad (\text{Helium}) \quad 2.3.2-6$$

and

$$a_{Xe} = 0.749 - 2.5 \cdot 10^{-4} T_g \quad (\text{Xenon}) \quad 2.3.2-7$$

If T_g is greater than 1000 K, T_g is set to 1000K. The accommodation coefficients for other gases are determined by interpolation.

$$a_j = a_{He} + \frac{(M_j - M_{He})}{(M_{Xe} - M_{He})} (a_{Xe} - a_{He}) . \quad 2.3.2-8$$

The volumetric heat capacity and thermal conductivity of the fuel rod materials, except the thermal conductivity of the gap gas, must be supplied by the user. For the computation of gas thermal conductivity, the user is required to provide the gas composition in terms of mole fractions of seven common gases included in the model.

The conductivity as a function of temperature for a pure noble or diatomic gas is calculated using the following correlation

$$K_{gas} = AT_g^B . \quad 2.3.2-9$$

The constants A and B for seven common gases are given in Table 2.3.2-1. The thermal conductivity of a gas mixture is calculated from the expression

$$K_{gas} = \sum_{i=1}^{N_g} \left\{ \frac{(k_i X_i)}{\left(X_i + \sum_{\substack{j=1 \\ j \neq i}}^{N_g} \phi_{ij} X_j \right)} \right\} , \quad 2.3.2-10$$

where

$$\phi_{ij} = \left[1 + (K_i/K_j)^{1/2} (M_i/M_j)^{1/4} \right]^2 \left[8 \left(1 + M_i/M_j \right) \right]^{-1/2} , \quad 2.3.2-11$$

and

N_g = number of components in the mixture,

M_i = molecular weight of component i ,

X_i = mole fraction of component i , and

K_i = thermal conductivity of component i (w/mK).

Table 2.3.2-1. Constants Used in Gas Thermal Conductivity Correlation.

Gas	Constant	
	A	B
He	$2.639 \cdot 10^{-3}$	0.7085
Ar	$2.986 \cdot 10^{-4}$	0.7224
Kr	$8.247 \cdot 10^{-5}$	0.8363
Xe	$4.351 \cdot 10^{-5}$	0.8616
H ₂	$1.097 \cdot 10^{-3}$	0.8785
N ₂	$5.314 \cdot 10^{-4}$	0.6898
O ₂	$1.853 \cdot 10^{-4}$	0.8729

Fuel Rod Swell and Rupture

The hot fuel-clad gap distance used to compute the total gap conductance for each pin segment is defined as before.

$$r_g = r_{ic} - r_f \quad 2.3.2-12$$

The thermally expanded fuel outside radius, r_f , is determined from

$$r_f = r_{f \text{ cold}} + u_{TF} + u_{FC} \quad 2.3.2-13$$

where

$r_{f\text{cold}}$ = cold unstressed fuel outside radius (m),

u_{TF} = radial displacement due to fuel thermal expansion (m), and

u_{FC} = fuel radius over-specification factor determined during pin transient initiation (m).

The thermal expansion of the fuel is determined by summing the diametrical expansion of each fuel mesh interval input on the general heat structure card series.

$$u_{TF} = \sum_{n=1}^{N_f} (r_{n+1} - r_n) \epsilon_{TF}, \quad 2.3.2-14$$

where

N_f = total number of fuel mesh intervals,

r_n = heat structure radius at the inside of mesh interval n (m),

ϵ_{TF} = radial strain function defining the fuel thermal expansion as a function of fuel temperature,

$$\epsilon_{TF} = C_1 T_f + C_2 + C_3 [\exp(C_4/T_f)], \quad 2.3.2-15$$

with

$$T_f = (T_{f_n} + T_{f_{n+1}}) / 2, \quad 2.3.2-16$$

= average mesh interval temperature, (K), and constants C_1 , C_2 , C_3 , and C_4 are user input or defaulted to (from MATPRO 11 Rev. 2¹¹⁹),

$$\begin{aligned}
 C_1 &= 1.0 \cdot 10^{-5} \text{ (K}^{-1}\text{)}, \\
 C_2 &= -3.0 \cdot 10^{-3}, \\
 C_3 &= 4.0 \cdot 10^{-2}, \text{ and} \\
 C_4 &= -5.0 \cdot 10^3 \text{ (K)}.
 \end{aligned}$$

The fuel is defined by the first material type specified in the heat structure input, with the next material type being the gap and the third the clad as shown in Figure 2.3.2-2. Any deviation from the geometry will result in an error or misinterpretation of the information by the pin model. The gap can only be one mesh interval wide, while fuel or clad must be greater than or equal to one mesh interval. Currently no provisions are made for annular fuel pellets.

The calculation of the inside clad radius is not as straightforward as the fuel outside radius. Seven different calculational modes are required to cover the possible clad conditions. They are defined as:

1. Elastic and thermal expansion within an unruptured channel,
2. Elastic and thermal expansion within 166.7K (300°F) of the clad rupture temperature within an unruptured channel,
3. Plastic deformation within an unruptured channel,
4. Elastic thermal expansion within a ruptured channel,
5. Plastic deformation in a ruptured channel,
6. Ruptured segment, and
7. Fuel-cladding mechanical iteration (closed gap).

Each mode is related to the NUREG-0630 calculated rupture temperature for zircaloy cladding by the equation:

$$T_{\text{rupt}} = 4233 - \frac{20.4\sigma_h}{1 + H} - \frac{(8.51 \cdot 10^6) \sigma_h}{100(1 + H) + 2790\sigma_h}, \quad 2.3.2-17$$

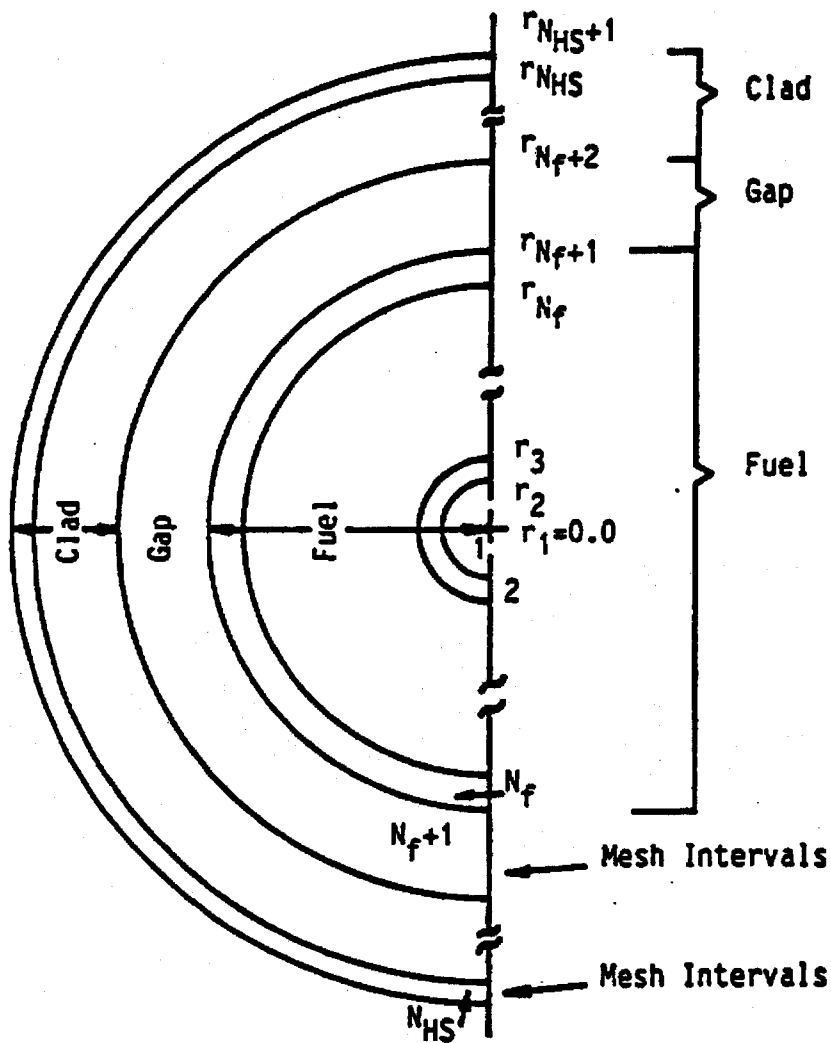


Figure 2.3.2-2. Fuel Pin Representation.

where

T_{rupt} = cladding rupture temperature (K),

σ_h = clad hoop stress (kpsi), and

H = dimensionless clad heating ramp rate, $0 \leq H \leq 1$.

The rupture temperature for other zirconium-based alloys is calculated by the following equation:

$$T_{rupt} = a_1 - \frac{a_2(\sigma_h - a_7)}{a_4 + H} - \frac{a_3(\sigma_h - a_7)}{a_5(a_4 + H) + a_6(\sigma_h - a_7)} \quad 2.3.2-17a$$

where a_1 through a_7 are user-specified input constants. The clad hoop stress for any pin segment in either equation is given by

$$\sigma_h = C_p (P_g r_{ic_{cold}} - P_f r_{oc_{cold}}) / (r_{oc_{cold}} - r_{ic_{cold}}), \quad 2.3.2-18$$

with

$r_{ic_{cold}}$ = cold unstressed inside clad radius (m),

$r_{oc_{cold}}$ = cold unstressed outside clad radius (m),

P_g = internal fuel rod pin pressure for that channel (Pa), and

P_f = external fluid pressure of the right-hand side heat structure associated volume (Pa).

$$C_p = 1 / 6.894757 \times 10^6$$

The heating rate can be either a user input constant or one of three additional transient-dependent algorithms discussed in detail later in this section.

At the beginning of each new time step following a successful RELAP5 time step advancement, the hoop stress and normalized heating ramp rate are computed for each pin segment. The clad average temperature is also known at this time. If the clad

average temperature is greater than the rupture temperature, then rupture occurs. Should the segment still be elastic and the rupture minus the clad temperature is less than 166.7K (300 F), then the segment stays elastic. Between these two temperatures the clad can be either elastic or plastic depending upon this temperature difference and the burst strain as described in the following paragraphs for ruptured or unruptured channels.

Mode 1: Unruptured Elastic and Thermal Deformation

Within an unruptured channel, the clad is considered purely elastic if it has never gone plastic, ruptured, or the temperature difference between rupture and clad average temperatures is less than 166.7 K (300 F). The inside clad radius for this pure elastic mode is determined by

$$r_{ic} = r_{ic_{cold}} + u_{TC} + u_{CC} + u_e, \quad 2.3.2-19$$

where

u_{TC} = clad radial displacement due to thermal expansion (m),

u_{CC} = clad radius over-specification factor (m),
determined during pin transient initiation, and

u_e = clad radial displacement due to elastic deformation (m).

The clad thermal expansion is determined similarly to that for the fuel.

$$u_{TC} = (r_{N_{HS}+1} + r_{N_f+2}) \epsilon_{TC} / 2, \quad 2.3.2-20$$

with

N_{HS} = total number of mesh intervals in the heat structure,

r_n = heat structure radius at the inside of mesh interval n or outside of n-1 (m), and

ϵ_{TC} = radial strain function defining clad thermal expansion as a function of clad average temperature.

The radial strain function is defined by either a user input table as a function of cladding temperature for zirconium-based material types other than zircaloy or a built in code correlation set for zircaloy cladding¹¹⁹ consisting of

$$\epsilon_{TC} = -2.0731 \cdot 10^{-3} + 6.721 \cdot 10^{-6} T_C \quad 2.3.2-22$$

for $T_C \leq 1073.15$ K (α phase), and

$$\epsilon_{TC} = -9.4495 \cdot 10^{-3} + 9.7 \cdot 10^{-6} T_C \quad 2.3.2-23$$

for $T_C \geq 1273.15$ K (β phase), where T_C is the average cladding temperature (K). In the α phase to β phase transition zone, 1073.15 K $< T_C < 1273.15$ K, a table lookup is used. Some selected values are listed in Table 2.3.2-2.

Table 2.3.2-2. Thermal Strain of Zircaloy for 1073.15 K $< T < 1273.15$ K.

<u>T(K)</u>	<u>Radial Strain</u> ϵ_{TC}	<u>Axial Strain</u> ϵ_{ATC}
1073.15	$5.14 \cdot 10^{-3}$	$3.53 \cdot 10^{-3}$
1093.15	$5.25 \cdot 10^{-3}$	$3.50 \cdot 10^{-3}$
1103.15	$5.28 \cdot 10^{-3}$	$3.46 \cdot 10^{-3}$
1123.15	$5.24 \cdot 10^{-3}$	$3.33 \cdot 10^{-3}$
1143.15	$5.15 \cdot 10^{-3}$	$3.07 \cdot 10^{-3}$
1183.15	$4.45 \cdot 10^{-3}$	$1.50 \cdot 10^{-3}$
1223.15	$2.97 \cdot 10^{-3}$	$1.10 \cdot 10^{-3}$
1273.15	$2.90 \cdot 10^{-3}$	$1.40 \cdot 10^{-3}$

The average clad temperature is calculated via a volume weighted average.

$$T_C = \sum_{n=N_f+2}^{N_{HS}} \frac{(r_{n+1}^2 - r_n^2)}{(r_{N_{HS}+1}^2 - r_{N_f+2}^2)} \left[\frac{(T_{n+1} + T_n)}{2} \right]. \quad 2.3.2-24$$

The maximum clad average temperature is calculated for each EM pin channel and written at each major edit and at the end of each case. The segment number and time of the peak cladding temperature is also specified. The fuel volume weighted average temperature, \bar{T}_f , is calculated similarly to the cladding.

$$\bar{T}_f = \sum_{n=1}^{N_f} \frac{(r_{n+1}^2 - r_n^2)}{(r_{N_f+1}^2 - r_1^2)} \left[\frac{(T_{n+1} + T_n)}{2} \right]. \quad 2.3.2-25$$

The elastic deformation, u_e , is calculated by

$$u_e = \left[\frac{r_{N_{HS}+1} + r_{N_f+2}}{2} \right] \left[\frac{\sigma_h - \nu \sigma_z}{E} \right], \quad 2.3.2-26$$

where

E = Young's modulus for clad (Pa),

σ_h = segment clad hoop stress (Pa),

σ_z = channel clad axial stress (Pa), and

ν = Poisson's ratio for clad (dimensionless).

The channel axial stress is the same for all segments in the channel and is determined by

$$\sigma_z = \frac{P_g r_{ic\ cold}^2 - P_f r_{oc\ cold}^2}{r_{oc\ cold}^2 - r_{ic\ cold}^2}. \quad 2.3.2-27$$

Young's modulus is given either by the code for zircaloy cladding as

$$E = \begin{cases} 1.088 \cdot 10^{11} - 5.475 \cdot 10^7 T_C; & \text{for } 1090K \geq T_C \\ 1.017 \cdot 10^{11} - 4.827 \cdot 10^7 T_C; & \text{for } 1240K \geq T_C > 1090K \\ 9.21 \cdot 10^{10} - 4.05 \cdot 10^7 T_C; & \text{for } 2027K \geq T_C > 1240K \\ 1.0 \cdot 10^{10} & ; \text{ for } T_C > 2027K, \end{cases}$$

2.3.2-28

or by a user-specified cubic equation that can be used for zirconium-based alloy cladding

$$E = C_1 T_C^3 + C_2 T_C^2 + C_3 T_C + C_4 \quad 2.3.2-29$$

Poisson's ratio is a constant which is defined as 0.30 for zircaloy by the code, however, the user can over-ride this value for zirconium-based alloy cladding types.

The normalized heating ramp rate for the elastic mode is determined by one of two methods. The code calculates an instantaneous heating rate for one method, while the other method sets the rate to a normalized user-input value between 0 and 1. The calculated heating rate is normalized via a constant value, H_{Rnorm} , of 28 K/s for zircaloy cladding or a user input for other zirconium-based alloy cladding materials.

$$H = \left\{ \frac{dT_C}{dt} \right\} / H_{Rnorm}$$

$$= \left\{ \frac{T_C^n - T_C^{n-1}}{t^n - t^{n-1}} \right\} / H_{Rnorm} \quad 2.3.2-30$$

The normalized heating rate is always limited to values between 0 and 1 or $(0 \text{ K/s} / H_{Rnorm}) \leq H \leq (28 \text{ K/s} / H_{Rnorm} = 1)$ for zircaloy cladding and between $(H_{slow \text{ input}} / H_{Rnorm}) \leq H \leq (H_{fast \text{ input}} / H_{Rnorm})$ for

other zirconium-based alloy cladding types. This limit is applied to H prior to using it in any subsequent checking or calculations. The superscripts reflect the current time, n, and old time, n-1, values. The zirconium-based alloy slow or fast ramp rate divided by the normalized rate is still limited between 0 and 1, but they do not have to be equal to 0 or 1. Values greater than 0 or less than 1 activate the slow or fast ramp curves at different normalized heating rates.

Mode 2: Unruptured Elastic and Thermal Deformation Within 166.7K
(300 F) of the Rupture Temperature

When the clad average temperature is within 166.7K (300 F) of the rupture temperature, the elastic inside clad radius is calculated as shown in Mode 1. This radius is compared against the plastic inside clad radius calculated in Mode 3. If the elastic radius is greater than the plastic radius, then Mode 2 is retained and the inside clad radius is set to the elastic radius. If not, the clad becomes plastic (Mode 3) and the plastic clad calculations are used. An informative message is printed when a segment first becomes plastic. No return to elastic Modes (1 or 2) is permitted once the clad becomes plastic.

$$r_{ic} = \text{MAX}(r_{ic_{\text{elastic}}}, r_{ic_{\text{plastic}}}) \quad 2.3.2-31$$

If $r_{ic_{\text{elastic}}} \geq r_{ic_{\text{plastic}}}$, Mode = 2 .

If $r_{ic_{\text{elastic}}} < r_{ic_{\text{plastic}}}$, Mode = 3 .

Mode 3: Unruptured Plastic Deformation

The unruptured plastic deformation is determined by the plastic strain, e_p .

$$r_{ic} = r_{ic_{\text{cold}}} (1 + e_p), \quad 2.3.2-32$$

with

$$e_p = e_{cps} \exp[-0.02754(T_{rupt} - T_c)], \quad 2.3.2-33$$

where e_{cps} is $0.2 * e_b$ (e_b is the burst strain) based on NUREG-0630 for maximum cladding plastic strain and on user input tables for zirconium-based alloy cladding. The plastic strain or burst strain is determined by a double interpolation, relative to H and T_{rupt} in the user input or default NUREG-0630 burst strain Tables 2.3.2-3 and 2.3.2-4. The plastic strain behaves as a ratchet. Once a given plastic strain is reached, no decrease in its value is allowed. In other words, for plastic mode calculations

$$r_{ic} = \text{MAX}(r_{ic}^n, r_{ic}^{n-1}), \quad 2.3.2-34$$

where the superscripts refer to the current and old time values.

If the plastic mode is selected, the normalized heating ramp rate is calculated from any of three user options: user input constant, average ramp rate, or plastic weighted ramp rate. The normalized average ramp rate is calculated from

$$H = \left\{ \frac{T_c^n - T_c^p}{t^n - t^p} \right\} / H_{Rnorm}, \quad 2.3.2-35$$

where

t = time (s),

n = superscript defining the current time, and

p = superscript defining the time in which the clad first went plastic.

The normalized plastic weighted ramp is calculated by

$$H = \left[\frac{\int_{t^p}^{t^n} W(T) \left\{ \frac{dT_c}{dt} \right\} dt}{\int_{t^p}^{t^n} W(T) dt} \right] / H_{Rnorm} \quad 2.3.2-36$$

Table 2.3.2-3. NUREG-0630 Slow-Ramp Correlations for Burst Strain and Flow Blockage.

<u>Rupture temperature, C</u>	<u>≤10 C/S burst strain, %</u>	<u>≤10 C/S flow blockage, %</u>
600	10	6.5
625	11	7.0
650	13	8.4
675	20	13.8
700	45	33.5
725	67	52.5
750	82	65.8
775	89	71.0
800	90	71.5
825	89	71.0
850	82	65.8
875	67	52.5
900	48	35.7
925	28	20.0
950	25	18.0
975	28	20.0
1000	33	24.1
1025	35	25.7
1050	33	24.1
1075	25	18.0
1100	14	9.2
1125	11	7.0
1150	10	6.5
1175	10	6.5
1200	10	6.5

Table 2.3.2-4. NUREG-0630 Fast-Ramp Correlations for Burst Strain and Flow Blockage.

<u>Rupture temperature, C</u>	<u>≥25 C/S burst strain, %</u>	<u>≥25 C/S flow blockage, %</u>
600	10	6.5
625	10	6.5
650	12	7.5
675	15	10.0
700	20	13.8
725	28	20.0
750	38	27.5
775	48	35.7
800	57	43.3
825	60	46.0
850	60	46.0
875	57	43.3
900	45	33.5
925	28	20.0
950	25	18.0
975	28	20.0
1000	35	25.7
1025	48	35.7
1050	77	61.6
1075	80	64.5
1100	77	61.6
1125	39	28.5
1150	26	18.3
1175	26	18.3
1200	36	26.2

with

$$W(T) = \exp[-0.02754(T_{rupt} - T_c)]. \quad 2.3.2-37$$

All three options have H limited to between 0 and 1.

Mode 4: Elastic Thermal Expansion in Ruptured Channel

When a segment within the channel ruptures, the remaining segments in that channel are effected. Following rupture all external mechanical forces are removed from the clad. For any elastic segments (Mode 1 or 2) the clad can shrink back to a thermally expanded state marked by Mode 4. The inside clad radius is calculated by

$$r_{ic} = r_{ic_{cold}} + U_{TC} + U_{CC} \quad 2.3.2-38$$

for segments in this mode.

Mode 5: Plastic Deformation in a Ruptured Channel

Any segment which was plastic in a channel when another segment ruptured has its mode redefined from 3 to 5. The clad inside radius remains frozen from that time forth. The gap size can change, however, due to thermal expansion or contraction of the fuel pellet.

Mode 6: Ruptured Segment

A segment ruptures when the clad temperature exceeds the calculated rupture temperature. An edit is provided at the time of rupture for clearly identifying the rupture segment and time. Mode 6 is associated with a ruptured segment.

Upon rupture various calculations and changes occur. All other segments in that channel have redefined modes. The clad rupture radius is calculated by one of two methods (fine or coarse mesh

nodding options) chosen by the user. The fine mesh nodding option computes the inside radius as

$$r_{ic} = r_{ic_{cold}} (1 + \epsilon_B) . \quad 2.3.2-39$$

With this option, the gap conductance is calculated as though there is steam in the gap. The steam thermal conductivity is evaluated at the gap temperature and used with the hot gap size to compute the conductance. This option also calculates inside metal-water reaction for the ruptured segment.

The coarse mesh nodding option computes the inside clad radius as

$$r_{ic} = r_{ic_{cold}} (1 + \epsilon_{cps}) . \quad 2.3.2-40$$

This option uses the regular gap gas conductance and does not consider inside metal-water reaction. It is intended for use nominally when the expected rupture length is small when compared to the total segment length. The microscopic effects at the rupture site considered with the fine mesh option are expected to be negligible when compared to the longer segment behavior. With the coarse mesh option, the overall behavior will be more closely controlled by the entire segment rather than just the rupture site conditions.

Within the ruptured channel various calculations are modified at the time of rupture. Each segment within that channel undergoes a mode change. The pin pressure becomes that of the hydrodynamic volume associated with the ruptured segment. An additive form loss coefficient is calculated at rupture based on the clad flow blockage by a simple expression for an abrupt contraction-expansion.

$$K_{\text{add}} = \frac{0.5(1 - \beta^2) + (1 - \beta^2)^2}{(\beta^2)^2},$$

2.3.2-41

where

$$\begin{aligned} \beta^2 &= \text{fraction of the channel flow area } \underline{\text{unblocked}}, \\ &= (1.0 - A_{\text{blocked}}/A_{\text{channel}}). \end{aligned}$$

| t

The flow blockage is obtained via a double table interpolation relative to the normalized heating ramp rate and rupture temperature similarly to the clad burst strain. The table is either user supplied or default NUREG-0630 values listed in Tables 2.3.2-3 and 2.3.2-4. The additive value of the loss coefficient is edited at the time of rupture. The flow blockage loss coefficient is added automatically to the problem for a primary pin channel unless the user overrides via a new optional input. If added, the form loss is applied to the forward flow direction for the inlet (bottom) junction and the reverse flow direction for the exit (top) junction attached to the volume in which the clad ruptured. The user option to exclude this form loss addition from the junctions has been included for supplemental pin channels or for certain non-licensing sensitivity studies with multiple cross-connected channels.

Another option has been added to the EM Pin model to help minimize user burden when running EM reflooding heat transfer analyses with BEACH (BAW-10166 Section 2.1.3.8.4). This user-controlled option automatically includes code-calculated pin rupture, droplet break-up (up to 60 percent blockage) for primary pin channels and convective enhancement adjustments for primary or supplemental pin channels. The input grid parameters are modified with the ruptured values and will be retained for use in the reflooding heat transfer calculations. This model is optional and requires input to activate the calculations. If no input is specified the default is that no rupture enhancements will be calculated and no droplet

breakup calculations will be performed for any supplemental pin channels.

When this option is activated, Equations 2.3.2-41.1 through 2.3.2-41.4 will be calculated following cladding rupture for primary pin channels, only. The first calculation performed determines the midpoint elevation of ruptured segment, referenced from the bottom of the pin channel (which coincides with the bottom of the heat structure geometry or reflood stack). This midpoint elevation, Z_{grid} , is the location where the new "grid" is inserted. This elevation is used to determine the droplet break-up effects for the ruptured segment.

$$Z_{grid} = 0.5 \cdot \Delta Z_{rupt\ seg} + \sum_{j=1}^{rupt\ seg-1} \Delta Z_{seg_j}, \quad 2.3.2-41.1$$

where

ΔZ_{seg} = elevation change of pin segment.

The second set of calculations is to calculate rupture droplet breakup efficiency. These calculations are identical to those described in Sections 2.1.3.7. and 2.1.3.8. of Reference 123. The rupture atomization factor, η_{etamax} , is calculated as

$$\eta_{etamax} = \frac{1}{[1 + \{(n^{1/3} - 1) \cdot \min(0.60, e_{fb})\}]}, \quad 2.3.2-41.2$$

where

n = number of equal size droplets resulting from the split-up of the larger droplets,

e_{fb} = flow blockage fraction (limited to a maximum of 0.60).

The increase in the droplet surface area from that used for interface heat transfer is defined in Equation 2.1.3-105¹²³ as

$$\Delta a_{gf} = C_{\max DB} \theta a_{gf}$$

The proportionality constant, $C_{\max DB}$, is determined from the constant, C_1 , the rupture flow blockage fraction (limited to a maximum of 0.60), and the length of the ruptured segment.

$$C_{\max DB} = \frac{C_1 \cdot \min(0.6, e_{fb})}{\Delta Z_{\text{rupt seg}}} \quad 2.3.2-41.3$$

The velocity of the fluid at the ruptured location increases because of the flow area reduction. The physical area in the code calculations is not modified, but a velocity multiplier, used for determining the droplet Weber number, is calculated from

$$\text{VELMULT} = \frac{1}{1 - \min(0.6, e_{fb})} \quad 2.3.2-41.4$$

The cladding rupture results in an increase in the pin outside heat transfer surface area. The increase in area is not directly included in the conduction solution in the code calculations. It is accounted for by using the rupture convective enhancement factor and applying it to the grid wall heat transfer enhancement factor, $F_{gg'}$ for primary or supplemental channels. The rupture enhancement, M_{RAR} , is an multiplicative contribution determined by

M_{RAR} = Rupture Area Ratio

$$= \frac{2\pi r_{\text{rupt oc}} L}{2\pi r_{\text{oc cold}} L} = \frac{r_{\text{rupt oc}}}{r_{\text{oc cold}}} \quad 2.3.2-41.5$$

where

$r_{rupt_{oc}}$ = outside clad radius of the ruptured node given by

$$= r_{ic} + \left[r_{oc_{cold}} - r_{ic_{cold}} \right] \left[r_{ic_{cold}} / r_{ic} \right] \quad 2.3.2-41.6$$

The total wall heat transfer convective factor then becomes

$$F_{gq_{tot}} = F_{gq_{grid}} \cdot M_{RAR} \quad 2.3.2-41.7$$

These droplet break-up and convective enhancement terms are optionally calculated and edited at rupture by the EM pin model.

This page intentionally blank.

They are stored for use when the reflooding heat transfer option (BEACH) is activated.

Mode 7: Fuel Cladding Mechanical Interaction (Closed Gap Conductance)

The inside cladding radius obtained from any of the previous six modes is checked for further displacement due to fuel cladding mechanical interaction if the closed gap option is active. If the fuel radius plus the residual gap adjustment term is greater than the cladding radius without the mechanical interaction, then the cladding radius is adjusted for the overlap assuming the fuel is an incompressible rigid body. That is, if

$$r_f + u_{cg} > r_{ic}^* , \quad 2.3.2-41.8$$

then this is a mechanically deformed, closed gap condition with

$$u_{fcc} = r_f + u_{cg} - r_{ic}^* \quad \text{and} \quad 2.3.2-41.9$$

$$r_{ic} = r_f + u_{cg} \quad 2.3.2-41.10$$

$$= r_{ic}^* + u_{fcc} . \quad 2.3.2-41.11$$

Otherwise, the gap is open and

$$u_{fcc} = 0.0 \quad \text{and} \quad 2.3.2-41.12$$

$$r_{ic} = r_{ic}^* , \quad 2.3.2-41.13$$

where

$$r_{ic} = \text{hot stressed inside clad radius (m)},$$

r_{ic}^* = inside cladding radius, r_{ic} , without gap contact determined by calculational modes 1 through 6 (m),

r_f = thermally expanded fuel outside radius (m),

u_{cg} = residual gap size during contact, determined during pin transient initiation (m), and

u_{fcc} = clad radius displacement due to contact (m).

The closed gap option, if selected, is turned off once reflood (BEACH) is initiated.

All Calculational Modes

Once the inside clad radius is calculated, the clad thickness, r_c , can be determined by the thin shell approximation

$$r_c = \frac{r_{ic\text{cold}}}{r_{ic}} r_{c\text{cold}} = \frac{r_{ic\text{cold}}}{r_{ic}} \left[r_{oc\text{cold}} - r_{ic\text{cold}} \right]$$

2.3.2-42

regardless of the deformation mode. This value is used to compute the hot stressed clad outside radius, r_{oc} .

$$r_{oc} = r_{ic} + r_c$$

2.3.2-43

The logic block diagram and calculational order for the fuel rod swell and rupture is shown in Figure 2.3.2-3. The selection logic and calculational details were included in this section.

2.3.2.2. Transient Internal Pin Pressure Calculations

The channel internal pin pressure is determined by the perfect gas relationship

$$P_g = \frac{n_g \bar{R} T_g}{V_g}, \quad 2.3.2-44$$

where the relationship is broken into parts by pin segments or end plena components.

$$P_g = P_{g_i} = n_{g_i} \frac{\bar{R} T_{g_i}}{V_{g_i}}, \quad 2.3.2-45$$

with

- P_g = internal pin gas pressure (Pa),
- n_g = number of moles of gas (Kg mole),
- T_g = gas temperature (K),
- V_g = gas volume (m^3),
- R = universal gas constant (J/Kg mole K), and
- i = pin segment or plenum designation.

The number of pin segments may include all segments or exclude a top and/or bottom unheated segment as specified by the user. The option to exclude these unheated segments was added to allow modeling of the upper and lower end fittings.

The total gas moles, n_{g_T} , inside the clad pressure boundary is

$$n_{g_T} = \sum_i n_{g_i}, \quad 2.3.2-46$$



Figure 2.3.2-3. Fuel Pin Swell and Rupture
Logic and Calculation Diagram.

which is assumed constant during the transient until rupture occurs. Therefore,

$$n_{gT} = \sum_i \frac{P_{g_i} V_{g_i}}{\bar{R} T_{g_i}} = \frac{P_g}{\bar{R}} \sum_i \frac{V_{g_i}}{T_{g_i}} \quad 2.3-2-47$$

Since the number of moles is constant

$$\frac{N_{gT}^*}{N_{gT}^o} = 1 = \frac{P_g^* \sum_i \frac{V_{g_i}^*}{T_{g_i}^*}}{P_g^o \sum_i \frac{V_{g_i}^o}{T_{g_i}^o}} \quad 2.3.2-48$$

reduces to

$$P_g^* = P_g^o \frac{\sum_i \frac{V_{g_i}^o}{T_{g_i}^o}}{\sum_i \frac{V_{g_i}^*}{T_{g_i}^*}} \quad 2.3.2-49$$

where the superscript * denotes the transient and ^o denotes final steady-state values.

The summation can be broken up further by

$$P_g^* = P_g^o \frac{\left[\frac{V_{P_u}}{T_{P_u}} + \sum_{j=bot}^{top} \frac{V_{g_j}}{T_{g_j}} + \frac{V_{P_\ell}}{T_{P_\ell}} \right]^o}{\left[\frac{V_{P_u}}{T_{P_u}} + \sum_{j=bot}^{top} \frac{V_{g_j}}{T_{g_j}} + \frac{V_{P_\ell}}{T_{P_\ell}} \right]^*} \quad 2.3.2-50$$

where

V_{P_u} = dynamic gas volume in upper pin plenum (m^3),

T_{P_u} = upper pin plenum temperature (K),

= T_{ic} of the top pin segment,

V_{P_l} = constant gas volume in lower pin plenum (m^3),

T_{P_l} = lower pin plenum temperature (K),

= T_{ic} of the bottom pin segment,

V_{g_j} = hot dynamic gap volume for segment j (m^3),

$$= \pi L (r_{ic}^2 - r_f^2), \quad 2.3.2-51$$

T_{g_j} = gap average temperature for segment j (K),

bot = $\begin{cases} 1; & \text{without unheated bottom segment,} \\ 2; & \text{with bottom unheated segment, and} \end{cases}$

top = $\begin{cases} \text{Top seg;} & \text{without unheated top segment,} \\ (\text{Top seg} - 1); & \text{with top unheated segment.} \end{cases}$

The dynamic gas volume in the upper pin plenum is calculated by

$$V_{P_u} = V_{P_u}^O + \Delta V_{P_u}, \quad 2.3.2-51.1$$

if an axial expansion option is selected by the user. Otherwise, the code defaults to

$$V_{P_u} = V_{P_u}^O, \quad 2.3.2-51.2$$

where

$V_{P_u}^O$ = initial hot gas volume in upper pin plenum (m^3),
(user input),

$$\begin{aligned} \Delta V_{P_u} &= \text{change in gas volume in upper pin plenum } (m^3), \\ &= \pi r_{ic_u}^2 \Delta L_p, \quad 2.3.2-51.3 \end{aligned}$$

r_{ic_u} = inside clad radius of the top pin segment (m), and

ΔL_p = change in gas plenum length (m).

The change in gas plenum length is calculated from the net change in the fuel and clad stack lengths due to axial thermal expansions as follows. Let

$$\begin{aligned} \Delta L_{cf} &= \text{change in gas plenum length from cold condition (m),} \\ &= \Delta L_c - \Delta L_f, \end{aligned} \quad 2.3.2-51.4$$

where

ΔL_c = total axial thermal expansion of clad from cold condition (m),

$$\begin{aligned} &\# \text{ seg} \\ &= \sum_{j=1} (L_j \epsilon_{ATC_j}), \text{ and} \end{aligned} \quad 2.3.2-51.5$$

ΔL_f = total axial thermal expansion of fuel from cold condition (m),

$$\begin{aligned} &\# \text{ seg} \\ &= \sum_{j=1} (L_j \epsilon_{ATF_j}). \end{aligned} \quad 2.3.2-51.6$$

Then

$$\begin{aligned} \Delta L_p &= \text{change in gas plenum length from hot initial} \\ &\quad \text{condition (m),} \\ &= \Delta L_{cf} - \Delta L_{cf}^0, \end{aligned} \quad 2.3.2-51.7$$

where

ΔL_{cf}^0 = initial over-specification in gas plenum length (m), determined during pin transient initiation,

L_j = axial length of the jth segment (m),

ϵ_{ATF} = fuel strain function of Equation 2.3.2-15, evaluated at fuel volume weighted average temperature \bar{T}_f of Equation 2.3.2-25, (dimensionless), and

ϵ_{ATC} = axial strain function defining clad axial thermal expansion as a function of clad volume average temperature, (dimensionless),

The axial strain for the cladding is defined by either a user-input table versus cladding temperature for zirconium-based alloy cladding (Note: This table replaces the cubic fit from Rev. 3 Eqn 2.3.2-51.8.) or a built in code correlation set for zircaloy cladding¹¹⁹

$$\begin{aligned}\epsilon_{ATC} &= -2.506 \times 10^{-5} + (T_C - 273.15) 4.441 \times 10^{-6} \\ &= -1.2381 \times 10^{-3} + 4.441 \times 10^{-6} T_C\end{aligned}\quad 2.3.2-51.9$$

for $T_C \leq 1073.15$ K (α phase), or

$$\begin{aligned}\epsilon_{ATC} &= -8.3 \times 10^{-3} + (T_C - 273.15) 9.7 \times 10^{-6} \\ &= -1.0950 \times 10^{-2} + 9.7 \times 10^{-6} T_C\end{aligned}\quad 2.3.2-51.10$$

for $T_C \geq 1273.15$ K (β phase), where T_C is the volume average cladding temperature (K) of Equation 2.3.2-24. In the α phase to β phase transition zone, 1073.15 K $< T_C < 1273.15$ K, a table lookup is used. Some selected values are listed in Table 2.3.2-2.

2.3.2.3. Steady-State and Initialization Calculations for the EM Pin Gap Conductance Model

The pin model gap conductance calculations are divided into two separate periods, steady-state and transient. The transient calculations were discussed in the preceding subsection with some references to the initialization values set up at the end of the pin steady-state calculations. These values are related to over-specification of the initial boundary values and conditions obtained from a steady-state fuel code. The set-up and details of these initialization calculations are contained in the following paragraphs.

The steady-state pin calculations are performed when any one of the following conditions apply:

1. RELAP5 is being executed in its steady-state mode.
2. RELAP5 is being executed in its transient mode and the pin model transient initiation trip was input and has always been false.
3. RELAP5 is being executed in its transient mode without a pin model trip prior to the second time step after the transient calculations begin.

During the steady-state pin calculations, the gap conductance is computed as described earlier in the transient dynamic gap section; however, the user supplied steady-state hot stressed outside fuel and inside clad radii as well as the initial pin pressure remain at the input values. The gap conductance is calculated across the constant gap thickness as a combination of gap gas, fuel-cladding mechanical contact, and radiation conductances by

$$h_{\text{gap}} = M_g h_{\text{gap, gas}} + h_{\text{rad}} + h_{\text{fcc}}$$

2.3.2-52

The multiplier, M_g , is provided to allow user adjustment of the initial stored fuel energy for each individual pin segment determined by the steady-state fuel code. The multiplier is intended as a compensation for neglected terms or differences between RELAP5 and the steady-state fuel code. Its value may be user input or calculated by the code during initialization via an iteration to match a user supplied volume average fuel temperature. The input or calculated value remains constant throughout the initialization and transient calculations. The method for determining the gap multiplier is based on a gap multiplier input for each pin segment. Input of a positive value sets the gap multiplier to the input value. Input of a negative value equal to the fuel volume average temperature selects the iterative code calculation for the gap multiplier. The iteration uses the input mesh point temperature distribution and a multiplier of one to calculate the gap conductance. That value is used to advance the conduction solution one iteration. The calculated fuel volume average temperature (Equation 2.3.2-25) is subtracted from the absolute value of the input value.

$$\Delta \bar{T}_f = (|\bar{T}_{f, \text{input}}| - \bar{T}_f) . \quad 2.3.2-52.1$$

The gap temperature differential at the end of the iteration is calculated from the fuel outside surface to the cladding inside surface.

$$\Delta T_{\text{gap}} = (T_{fs} - T_{ics}) . \quad 2.3.2-52.2$$

Using the assumption that both the slope of the fuel mesh point temperatures and the overall gap conductance will not change significantly, the last gap multiplier (1.0 for the first iteration) can be adjusted via a ratio to give a new multiplier,

$$M_g^{\eta+1} = \frac{\Delta T_{\text{gap}}}{(\Delta T_{\text{gap}} + \Delta \bar{T}_f)} M_g^{\eta} \quad 2.3.2-52.3$$

After calculation of the new gap multiplier, another conduction solution iteration step is taken. The fuel volume average temperature differential is recalculated via Equation 2.3.2-52.1. If the absolute value is greater than 2 K, then another iteration step is taken after recalculating a new multiplier via Equations 2.3.2-52.2 and 2.3.2-52.3. If the absolute value is less than 2 K, then the iteration has converged and the last multiplier calculated is edited and used during the steady-state and transient EM pin calculations. Up to twenty-one iterations are allowed. If convergence is not obtained in twenty-one iterations, then the code will stop at the end of the initialization process and appropriate failure messages will be edited. Failure of the iteration to converge is generally related to poor estimates given for the initial mesh point temperature distribution. An improved estimate will normally allow the iteration to converge properly. If convergence is still a problem, user specification of the multiplier is also available.

At the completion of the EM pin steady-state calculations (i.e., after EM pin steady-state trip becomes true or during the first time step if there is no trip) several calculations are required to initiate the pin transient calculations. The user-supplied cold unstressed pin geometry input via the heat structure cards is elastically expanded using the final code calculated temperature and mechanical stresses.

$$r_{f_o} = r_{f_{cold}} + u_{TF} \quad 2.3.2-53$$

and

$$r_{ic_o} = r_{ic_{cold}} + u_{TC} + u_e + u_{fcc} \quad 2.3.2-54$$

with

r_{f_o} = thermally expanded outside fuel radius (m),

r_{ic_o} = thermally and mechanically expanded inside clad radius (m),

u_e = elastic deformation due to mechanical stresses (m),
and

u_{fcc} = elastic deformation from gap mechanical contact (m).
This term is calculated from the user supplied input contact pressure and cladding radii during the initialization.

$$u_{fcc} = \frac{P_{fcc} \cdot r_{ic}}{E_c} \left\{ \left[\frac{r_{oc}^2 + r_{ic}^2}{r_{oc}^2 - r_{ic}^2} \right] + \nu_c + \frac{E_c}{E_f} (1 - \nu_f) \right\} \quad 2.3.2-54.1$$

The calculated radii are compared against the input values by

$$u_{FC} = r_{f_{input}} - r_{f_o} \quad 2.3.2-55$$

$$u_{CC} = r_{ic_{input}} - r_{ic_o} \quad 2.3.2-56$$

and

$$u_{cg} = \begin{cases} 0.0 & \text{for } P_{fcc_{input}} = 0.0 \\ r_{ic_{input}} - r_{f_{input}} & \text{for } P_{fcc_{input}} > 0.0 \end{cases} \quad 2.3.2-56.1$$

where

u_{FC} = difference in the outside fuel final steady-state calculated and input radius termed fuel radius over-specification factor (m),

u_{CC} = difference in the inside cladding final steady-state calculated and input radius termed clad radius over-specification factor, and

u_{cg} = final steady-state residual gap during mechanical contact.

These three terms compensate for differences between the steady-state fuel code and RELAP5 for effects such as cladding creepdown, fission gas induced fuel swelling, or gap contact. They are retained at these initial values and used as described in the transient calculations.

Terms for the transient pin pressure advancement are also calculated at the end of the pin steady-state calculations. The steady-state terms

$$n_T \bar{R} = p_g^o \left[\frac{v_{g_{up}}}{T_{g_{up}}} + \sum_{j=bot}^{top} \frac{v_{g_j}}{T_{g_j}} + \frac{v_{g_\ell}}{T_{g_\ell}} \right]^o \quad 2.3.2-57$$

and

$$\Delta L_{cf}^o = (\Delta L_c - \Delta L_f)^o \quad 2.3.2-57.1$$

are computed for each channel within the pin model and used during transient pin pressure calculations.

2.3.2.4. Metal-Water Reaction Model

When zircaloy cladding is raised to an elevated temperature in a steam atmosphere, an exothermic reaction will occur. The steam reacts with the zircaloy cladding causing oxidation of the cladding and liberation of hydrogen gas based on the following chemical reaction equation



Baker and Just¹²⁰ derived a parabolic relationship to describe the rate of metal reacted

$$W^2 = K_{MN} t \exp [-\Delta E / (R T)] , \quad 2.3.2-57.3$$

where

W = weight of metal reacted per unit area (g/cm^2),

K_{MN} = rate constant $\left[\frac{\text{g}^2}{\text{cm}^4 \text{s}} \right]$,

t = time (seconds),

ΔE = activation energy $\left[\frac{\text{cal}}{\text{gmole}} \right]$,

R = gas constant = 1.987 $\left[\frac{\text{cal}}{\text{gmole K}} \right]$, and

T = cladding surface temperature (K).

The method of solution for determining the energy addition from the Zr - H₂O reaction or metal-water reaction (MWR) has two options available within the code. The original or default method uses an explicit formulation to calculate the velocity of

the oxide boundary. The second, user-selected option uses an implicit method for determining the thickness of the oxide layer. Both solutions are acceptable for licensing applications since they are based on the parabolic rate relationship derived by Baker and Just¹²⁰ as required for 10 CFR 50 Appendix K applications.

For applications that use relatively coarse time step sizes, it has been noted that under certain conditions the explicit method can produce a large spike in the MWR energy generation rate calculated just after cladding rupture. The thin inside oxide thickness calculated over large time steps can lead to excessive MWR energy on the first few time steps after rupture, especially if little cladding surface heat transfer is predicted. If the inside cladding temperature is near 1800 °F or above, the energy addition can quickly lead to an increase in cladding temperature, that further enhances the MWR energy addition rate. These conditions may be encountered following cladding ruptures during SBLOCA events that uncover the core for extended time periods. They may also occur during the later portions of the adiabatic heatup phase of an LBLOCA. The implicit formulation calculates a smoother, but still conservatively high, energy addition rate and correspondingly more realistic cladding temperature response than that from the original implementation of the explicit model during this period. The energy additions from the two formulations will approach each other after a short time interval.

The details of the two implementations will be discussed in this section. The explicit model formulation is the default model that will be used if not specifically requested by the user for any application. The specified method will be used for both inside and outside MWR calculations to determine the MWR energy addition, hydrogen gas liberations, and oxide growth rates.

Explicit Metal-Water Reaction Option

The explicit implementation of the cladding outside metal-water reaction rate in cylindrical coordinates is determined by the parabolic rate relationship derived by Baker and Just for describing the clad metal-oxide interface velocity dr_{ox}/dt .

$$\left. \frac{dr_{ox}}{dt} \right|_{out} = - \frac{K_{MN}}{(2 \cdot 10^4) \rho_c^2 r_{ox}^{\eta-1} \left|_{out} \ln \left[\frac{r_{oc}}{r_{ox}^{\eta-1} \left|_{out} \right.} \right]} \exp \left[- \frac{AE}{R T_{oc}} \right],$$

2.3.2-58

where

T_{oc} = clad outside surface temperature (K),

ρ_c = cladding density $\left(\frac{g}{cm^3} \right)$,

$r_{ox}^{\eta-1} \left|_{out}$ = old outside oxide radius (m), and

r_{oc} = outside clad radius (m).

The reaction calculation begins after the clad surface temperature exceeds the specified initiation temperature and assumes the process to be isothermal with an unlimited steam supply. The initiation temperature is not a true threshold for the reaction to begin; however, it should correspond to a temperature below which the reaction has a negligible effect on the oxide thickness or energy generation rate during the transient. The rate equation can be simplified by considering the actual clad dimensions. The entire clad thickness is small with respect to the actual cladding outside radius. The $r_{oc}/r_{ox}^{\eta-1}$ term therefore will be close to but greater than one, and may be approximated by

$$\ln \left(\frac{r_{oc}}{r_{ox}^{\eta-1}} \right) = \frac{r_{oc}}{r_{ox}^{\eta-1}} - 1 \quad 2.3.2-59$$

Simplifying, given that, $r_{ox}^{\eta-1} = r_{oc}^{\eta} - r_{ox}^{\eta-1}$, one gets

$$\left. \frac{dr_{ox}}{dt} \right|_{out} = - \frac{K_{MN}}{(2 \cdot 10^4) \rho_c^2 \left(r_{ox}^{\eta-1} \right|_{out})} \exp \left[- \frac{\Delta E}{RT_{oc}} \right] \quad 2.3.2-60$$

If the clad is oxidized up to its limited maximum of 17% of the total clad thickness, the error due to the approximation for a typical PWR fuel pin is only one to two percent.

The explicit implementation of the inside metal water reaction is calculated for the ruptured segments only when the fine nodding option is selected. The equations solved are nearly identical to the outside calculations; however, the geometry terms are described with inside radii.

Given that

$$r_{ox}^{\eta-1} \Big|_{in} = r_{ox}^{\eta-1} \Big|_{in} - r_{ic}^{\eta} \quad 2.3.2-60.1$$

$$\left. \frac{dr_{ox}}{dt} \right|_{in} = \frac{K_{MN}}{(2 \cdot 10^4) \rho_c^2 \left(r_{ox}^{\eta-1} \Big|_{in} \right)} \exp \left[- \frac{\Delta E}{RT_{ic}} \right] \quad 2.3.2-61.2$$

Implicit Metal-Water Reaction Option

The implicit formulation of the Baker-Just equation implemented into RELAP5/MOD2 takes its formulation from the NRC-approved, FRAP-T6-B&W¹⁴⁸ computer code (BAW-10165). The outside oxide thickness finite difference form is given by:

$$\left[\tau_{\text{ox}}^{\eta} \Big|_{\text{out}} \right]^2 = \left[\tau_{\text{ox}}^{\eta-1} \Big|_{\text{out}} \right]^2 + \left[\frac{K_{\text{MN}} \Delta t}{10^4 \cdot \rho_c^2} \right] \exp \left[\frac{-\Delta E}{R T_{\text{oc}}} \right]$$

2.3.2-62.3

and the rate of oxide thickness change is then calculated by

$$\frac{d(\tau_{\text{ox}}^{\eta})}{dt} \Big|_{\text{out}} = \frac{\tau_{\text{ox}}^{\eta} - \tau_{\text{ox}}^{\eta-1}}{\Delta t} \Big|_{\text{out}} = - \frac{dr_{\text{ox}}}{dt} \Big|_{\text{out}} .$$

2.3.2-62.4

The inside oxide thickness finite difference form is given by:

$$\left[\tau_{\text{ox}}^{\eta} \Big|_{\text{in}} \right]^2 = \left[\tau_{\text{ox}}^{\eta-1} \Big|_{\text{in}} \right]^2 + \left[\frac{K_{\text{MN}} \Delta t}{10^4 \cdot \rho_c^2} \right] \exp \left[\frac{-\Delta E}{R T_{\text{ic}}} \right]$$

2.3.2-62.5

and the rate of oxide thickness change is then calculated by

$$\frac{d(\tau_{\text{ox}}^{\eta})}{dt} \Big|_{\text{in}} = \frac{\tau_{\text{ox}}^{\eta} - \tau_{\text{ox}}^{\eta-1}}{\Delta t} \Big|_{\text{in}} = \frac{dr_{\text{ox}}}{dt} \Big|_{\text{in}} .$$

2.3.2-62.6

Metal-Water Energy Addition and Hydrogen Evolution

Once the oxide interface velocity (or oxide thickness change) is calculated with either method, the metal-water heat generation rate can be computed. First, the old oxide interface radius, $r_{\text{ox}}^{\eta-1} \Big|_{\text{out}}$, is calculated.

$$r_{\text{ox}}^{\eta-1} \Big|_{\text{out}} = r_{\text{oc}}^{\eta} - r_{\text{ox}}^{\eta-1} \Big|_{\text{out}} .$$

2.3.2-61

Then the energy generation rate is computed.

$$\dot{Q}_{MW} \Big|_{out} = 4184 \left[\frac{dr_{ox}}{dt} \Big|_{out} \right] (A_{SHT}) \left[\frac{r_{ox}^{\eta-1} \Big|_{out}}{r_{oc\ cold}} \right] \frac{\rho_c \Delta H}{Z_c}, \quad 2.3.2-62$$

where

\dot{Q}_{MW} = energy generation rate (w),

A_{SHT} = outside heat structure surface area for heat transfer (m²),

ΔH = heat of reaction $\left(\frac{Kcal}{gmole} \right)$,

Z_c = atomic weight of clad (g/gmole), and

4184 = conversion factor (w-s/kcal).

The molar rate of hydrogen gas production, $\left[\frac{dN_{H_2}}{dt} \Big|_{out} \right]$ and/or steam consumption, $\left[\frac{dN_{H_2O}}{dt} \Big|_{out} \right]$, can be determined from the chemical reaction equation (Equation 2.3.2-57.2). The molar production rate is

$$\begin{aligned} \frac{dN_{H_2}}{dt} \Big|_{out} &= \frac{dN_{H_2O}}{dt} \Big|_{out} = \left[\frac{dr_{ox}}{dt} \Big|_{out} \right] \left[\frac{\rho_c N_{H_2} A_{SHT} \left[\frac{r_{ox}^{\eta-1} \Big|_{out}}{r_{oc\ cold}} \right]}{N_c Z_c} \right] \\ &= \left[\frac{g\ moles\ H_2}{s} \right] \text{ or } \left[\frac{g\ moles\ H_2O}{s} \right]. \quad 2.3.2-63 \end{aligned}$$

The hydrogen gas mass production rate is

$$\frac{dM_{H_2}}{dt} \Big|_{out} = \frac{dN_{H_2}}{dt} \Big|_{out} Z_{H_2} = 0.002 \frac{dN_{H_2}}{dt} \Big|_{out} \left[\frac{Kg}{s} \right], \quad 2.3.2-64$$

and the corresponding water mass reacted is

$$\left. \frac{dM_{H_2O}}{dt} \right|_{out} = \left(\frac{N_{H_2O}}{N_{H_2}} \right) \left. \frac{dN_{H_2}}{dt} \right|_{out} z_{H_2O} = 0.018 \left. \frac{dN_{H_2O}}{dt} \right|_{out} \left(\frac{Kg}{s} \right)$$

2.3.2-65

for zircaloy cladding.

For an isothermal process, the steam required for reaction must be brought up to the surface temperature with the following energy

$$\dot{Q}_{steam} = \left. \frac{dM_{H_2O}}{dt} \right|_{out} C_p (T_{oc} - T_{steam}) ,$$

2.3.2-66

with

C_p = specific heat capacity (J/Kg - K) evaluated at $\bar{T} = (T_{oc} + T_{steam})/2$,

T_{oc} = associated heat structure outside surface temperature (K),

T_{steam} = associated right hand side volume steam temperature (K),

\dot{Q}_{steam} = energy needed to bring the steam to reaction temperature (w), and

$$\dot{Q}_{steam} = \text{MIN} (\dot{Q}_{steam}, \dot{Q}_{MW}|_{out}) .$$

The energy added into the clad is

$$\dot{Q}_{clad} = \dot{Q}_{MW}|_{out} , (w) .$$

2.3.2-67

(Note: Equations 2.3.2-68 and 2.3.2-69 from revisions 2 and before have been deleted.)

The inside metal water reaction is calculated for the ruptured segments only when the fine nodding option is selected. The equations solved are nearly identical to the outside calculations, however, the geometry terms are described with inside radii.

Given

$$r_{ox}^{\eta-1} \Big|_{in} = r_{ox}^{\eta-1} \Big|_{in} - r_{ic}^{\eta} \quad , \quad 2.3.2-70$$

the inside MWR energy addition can be calculated. The inside energy addition can be computed based on either the entire heat structure or on a ratio of a three inch segment to the total length of the heat structure segment. The user has the option to override the default option of the entire heat structure area with the ratio option. The area for inside metal-water energy addition is defined as either

1. Entire heat structure surface area (default option)

$$A_{SHT} = A_{\text{outside heat structure}} \quad \text{or}$$

2. A three inch ratio to the length of the heat structure pin segment

$$A_{SHT} = \left(\frac{0.0762}{\Delta Z_{\text{seg}}} \right) A_{\text{outside heat structure}}$$

where

0.0762 = a converted three inch length (m), and

ΔZ_{seg} = heat structure channel length if input
or the control volume elevation change
if no input was supplied (m).

This surface area is used for the associated hydrogen production rate calculations as well.

$$\dot{Q}_{MW}|_{in} = 4184 \left(\frac{dr_{ox}}{dt} \Big|_{in} \right) (A_{SHT}) \left(\frac{r_{ox}^{\eta-1} |_{in}}{r_{oc} |_{cold}} \right) \left(\frac{\rho_c \Delta H}{z_c} \right), (w).$$

2.3.2-71

The molar production or consumption rates are

$$\frac{dN_{H_2}}{dt} \Big|_{in} = \frac{dN_{H_2O}}{dt} \Big|_{in} = \frac{dr_{ox}}{dt} \Big|_{in} \left[\frac{\rho_c N_{H_2}}{N_c z_c} \frac{A_{SHT} r_{ox}^{\eta-1} |_{in}}{r_{oc} |_{cold}} \right],$$

2.3.2-72

$$\frac{dM_{H_2}}{dt} \Big|_{in} = 0.002 \frac{dN_{H_2}}{dt}, \left(\frac{Kg}{s} \right),$$

2.3.2-73

and

$$\frac{dM_{H_2O}}{dt} \Big|_{in} = 0.018 \frac{dN_{H_2O}}{dt}, \left(\frac{Kg}{s} \right).$$

2.3.2-74

The inside metal-water reaction should occur with steam that is hotter than the clad inside surface temperature. Therefore, all the reaction energy should be deposited in the clad.

The last step in the metal-water calculations is advancement of the energies, radii, and production masses. The total energy added to the clad for a time step of Δt is

$$\dot{Q}_{MW} = \left[\dot{Q}_{MW}|_{out} + \dot{Q}_{MW}|_{in} - \dot{Q}_{steam} \right] \Delta t, (w). \quad 2.3.2-75$$

The oxide thicknesses are also updated

$$r_{ox}^{\eta}|_{out} = r_{ox}^{\eta-1}|_{out} + \left(\frac{dr_{ox}}{dt} \Big|_{out} \right) \Delta t \quad 2.3.2-76$$

and

$$r_{ox}^{\eta}|_{in} = r_{ox}^{\eta-1}|_{in} + \left(\frac{dr_{ox}}{dt} \Big|_{in} \right) \Delta t. \quad 2.3.2-77$$

The hydrogen mass evolved is summed.

$$M_{H_2}^{\eta} = M_{H_2}^{\eta-1} + \left[\frac{dM_{H_2}}{dt} \Big|_{in} + \frac{dM_{H_2}}{dt} \Big|_{out} \right] \Delta t, (kg H_2). \quad 2.3.2-78$$

The metal-water oxide layer thicknesses are adjusted during certain periods in the pin swell and rupture calculations. Since the metal-water reaction rate is inversely proportional to the oxide thickness, it is nonconservative to neglect thinning due to clad swelling. The swelling is insignificant while the clad is elastic; however, during plastic deformation and at rupture the thinning may be significant. Therefore, during plastic calculations (Mode 3) or at rupture (Mode 6), the oxide thicknesses are adjusted by

$$r_{ox}|_{out} = r_{ox}|_{out} \frac{r_{ic}^{\eta-1}}{r_{ic}^{\eta}} \quad 2.3.2-79$$

and

$$r_{ox}|_{in} = r_{ox}|_{in} \frac{r_{ic}^{\eta-1}}{r_{ic}^{\eta}}$$

2.3.2-80

where η and $\eta-1$ are the current and last time step values, respectively. Recall that the inside clad radius cannot shrink during these identified periods; therefore, the ratio $(r_{ic}^{\eta-1}/r_{ic}^{\eta})$ will always be less than or equal to one.

2.3.2.5. EM Pin Model Additional Edit Variables

Several new parameters have been added to the EM pin model edit to aid the user in confirming that all Appendix K requirements have been met. These parameters include the channel peak cladding temperature (PCT), T_C , time of PCT, and the maximum metal-water oxidation fraction. The pin segment within each channel in which the PCT and maximum oxidation are found are also specified in the output.

The volumetric fraction of the cladding that is oxidized is computed for each pin segment or heat structure by

$$\text{Frac}_{ox}|_{seg} = \frac{r_{oc}^2 - (r_{oc} - r_{ox}|_{out})^2 + (r_{ic} + r_{ox}|_{in})^2 - r_{ic}^2}{r_{oc}^2 - r_{ic}^2}$$

2.3.2-81

The channel average oxidation fraction is computed for the heated segments by

$$\text{Frac}_{ox}|_{chan} = \frac{\sum_{j=bot}^{top} \Delta Z_{seg} \text{Frac}_{ox}|_{seg}}{\sum_{j=bot}^{top} \Delta Z_{seg}}$$

where

top = the index of the uppermost heated segment, and
 bot = the index of the lowermost heated segment.

The channel oxidation fraction was added to provide a quick evaluation of the whole-core metal-water hydrogen generation. This is not a whole-core value, however.

2.3.3. Core Heat Transfer Models

The system heat transfer regime classifications are used in the core heat transfer model except that the pre-CHF regime includes condensation heat transfer. As indicated in section 2.2.2 (Heat Transfer Model, Heat Sources and Boundary Conditions), the core heat transfer option can be used throughout the simulation but has been developed specifically for application within the core region. The following sections present first the heat transfer switching logic and then the heat transfer and CHF correlations used in the core model.

A filtered flow option has been included specifically for use with the core heat transfer package. This option was added to address the Appendix K requirement to eliminate any calculated rapid flow oscillations of a periods less than 0.1 seconds during the LBLOCA blowdown phase. The general non-homogeneous, non-equilibrium code formulation dictates that the flow should be tracked in two separate phasic components. Therefore, the individual phasic mass fluxes, G_g and G_f , will be filtered separately. They will be filtered by passing the instantaneous flux value through the equation for a low pass filter.

$$\frac{dZ}{dt} = -P (Z - G) ,$$

where

Z = filtered mass flux,
 P = filter break frequency, and
 G = instantaneous mass flux, G_g or G_f

with

$$G_g = \rho_g \alpha_g v_g$$

and

$$G_f = \rho_f \alpha_f v_f$$

The filter break frequency is set to remove perturbations in the mass fluxes of periods less than 0.1 seconds. The break frequency is user specified, through the value of an individual control variable. The user also designates core heat structure geometries in which the flow filtering is applied. Each phase is filtered independently at time step, η , and summed to give a total. These three filtered mass fluxes are used in the core heat transfer and CHF calculations when this option is selected.

$$Z_g^\eta = (Z_g^{\eta-1} + \Delta t \cdot P \cdot G_g) / (1 + \Delta t \cdot P)$$

$$Z_f^\eta = (Z_f^{\eta-1} + \Delta t \cdot P \cdot G_f) / (1 + \Delta t \cdot P)$$

$$Z_{Tot} = Z_g + Z_f$$

The individual filtered mass fluxes were added as a parameter which may be plotted or used in control system applications.

2.3.3.1. Core Heat Transfer Selection Logic

This section presents the SBLOCA and LBLOCA logic to select the heat transfer regimes and correlations applied under the core

heat transfer option. The switching logic for LBLOCA is responsive to two main goals: (1) once departure from nucleate boiling (DNB) has occurred, it does not allow the use of nucleate boiling or other pre-CHF heat transfer correlations for the rest of the simulation, and (2) after DNB, it locks into film boiling or convection to steam once the wall superheat (ΔT_{sat}) is greater than or equal to 166.667K (300 F). Liquid convection (single-phase) or condensation (two-phase) is allowed when T_w is less than T_{sat} even though the DNB or film boiling lock-in has occurred.

The no return to nucleate boiling and the lock into film boiling restrictions of Appendix K are not applicable to SBLOCA. Therefore, an SBLOCA option was added to the LBLOCA logic by removing these restrictions. All other LBLOCA logic and correlations are equally applicable for SBLOCA.

The core heat transfer switching logic is diagrammed in Figure 2.3.3-1. The pre-CHF correlations are used if anyone of the following conditions are satisfied:

1. The surface temperature of a heat slab, T_w , is less than the saturation temperature, T_{sat} , based on the total pressure, P .
2. The total pressure, P , is greater than or equal to the critical pressure, P_{crit} (3208.2 psia).
3. $T_w \geq T_{sat}$, $P < P_{crit}$, and the critical heat flux has not been exceeded at this time or before.

A result of the third criteria is that in the unlikely event that the wall experiences dryout without passing through CHF, there is

no prohibition against a return to pre-CHF heat transfer correlations.

The post-CHF correlations are used when $T_w \geq T_{sat}$, $P < P_{crit}$, and the critical heat flux has been exceeded at the present time or before.

Once CHF has been exceeded, a lock-in to film boiling occurs if the wall superheat ($T_w - T_{sat}$) equals or exceeds 300 F. A film boiling heat transfer coefficient is also used if a transition boiling value is calculated such that its value exceeds a pre-CHF value.^a

Pre-CHF Heat Transfer Correlation Selection

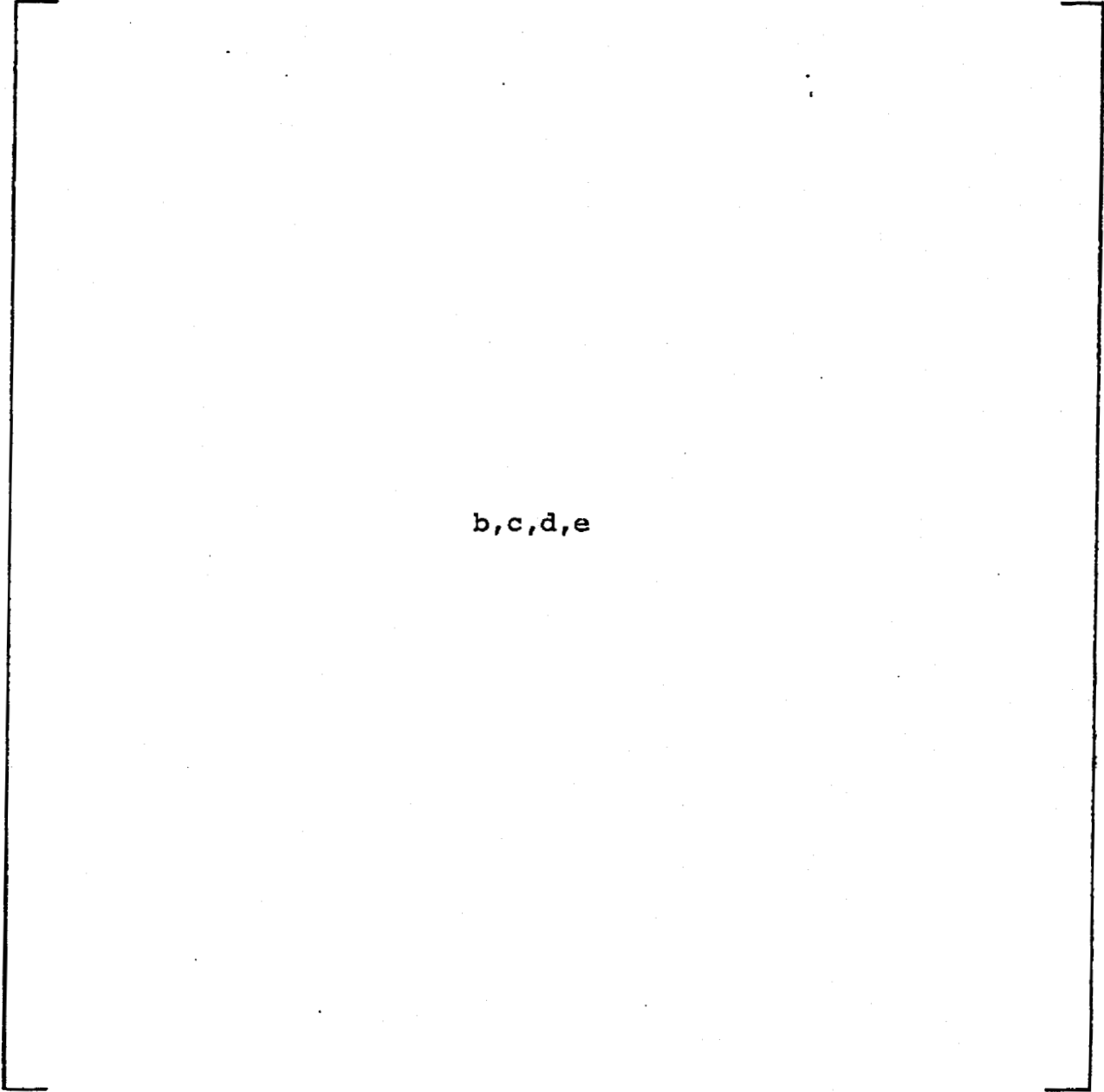
When the wall temperature is less than the fluid saturation temperature, the heat transfer is calculated using the maximum of the Rohsenow-Choi or the Dittus-Boelter correlations.

$$h = \text{MAX}(h_{RC}, h_{DB}) \quad T_w < T_{sat} \quad 2.3.3-1$$

Under these conditions, the fluid would normally be subcooled single-phase water. There is no prohibition, and the same correlations apply, to heat transfer from steam or a two-phase mixture to the heat slab.

^a A permanent lock-in to film boiling option may be specified by user input. If this option is chosen and film boiling is ever predicted, then a return to transition boiling is prohibited.

This page intentionally left blank.



b,c,d,e

Figure 2.3.3-1. Core Model Heat Transfer Selection Logic.
a) Main Drive Routine for EM Heat Transfer.

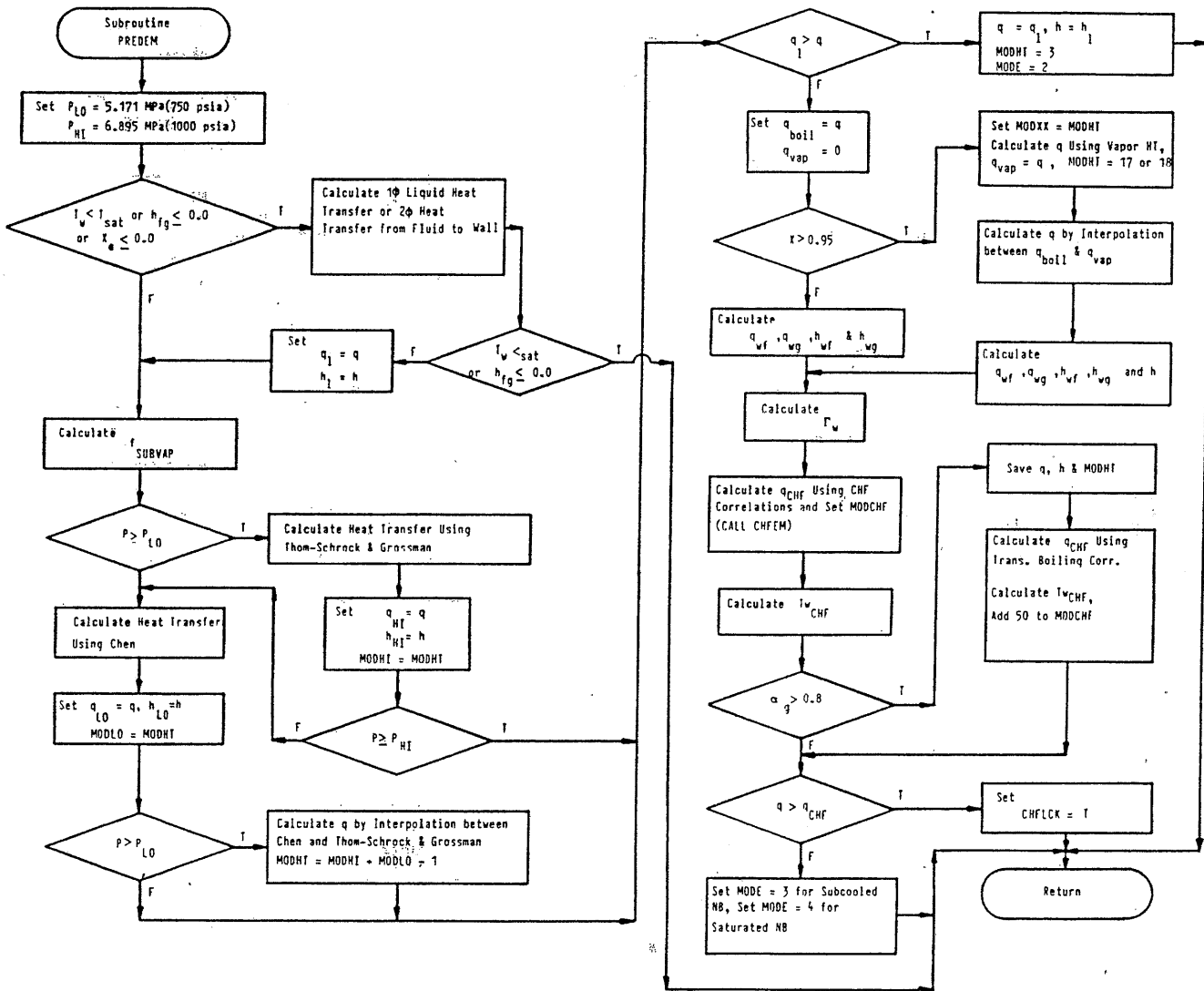


Figure 2.3.3-1. Core Model Heat Transfer Selection Logic.
b) Driver Routine for Pre-CHF and CHF Correlations.

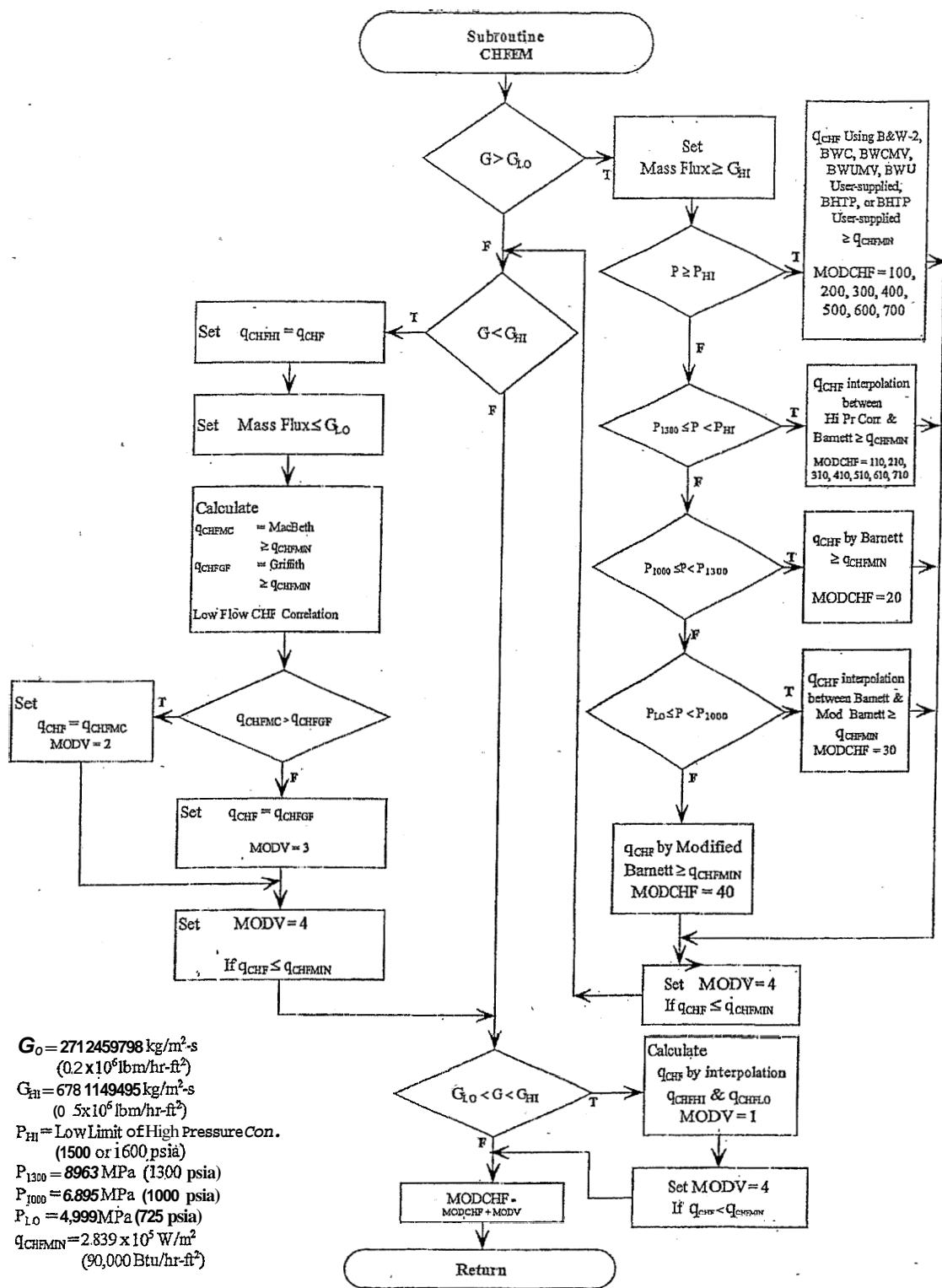


Figure 2.3.3-1. Core Model Heat Transfer Selection Logic.
c) Driver Routine for CHF Correlations.

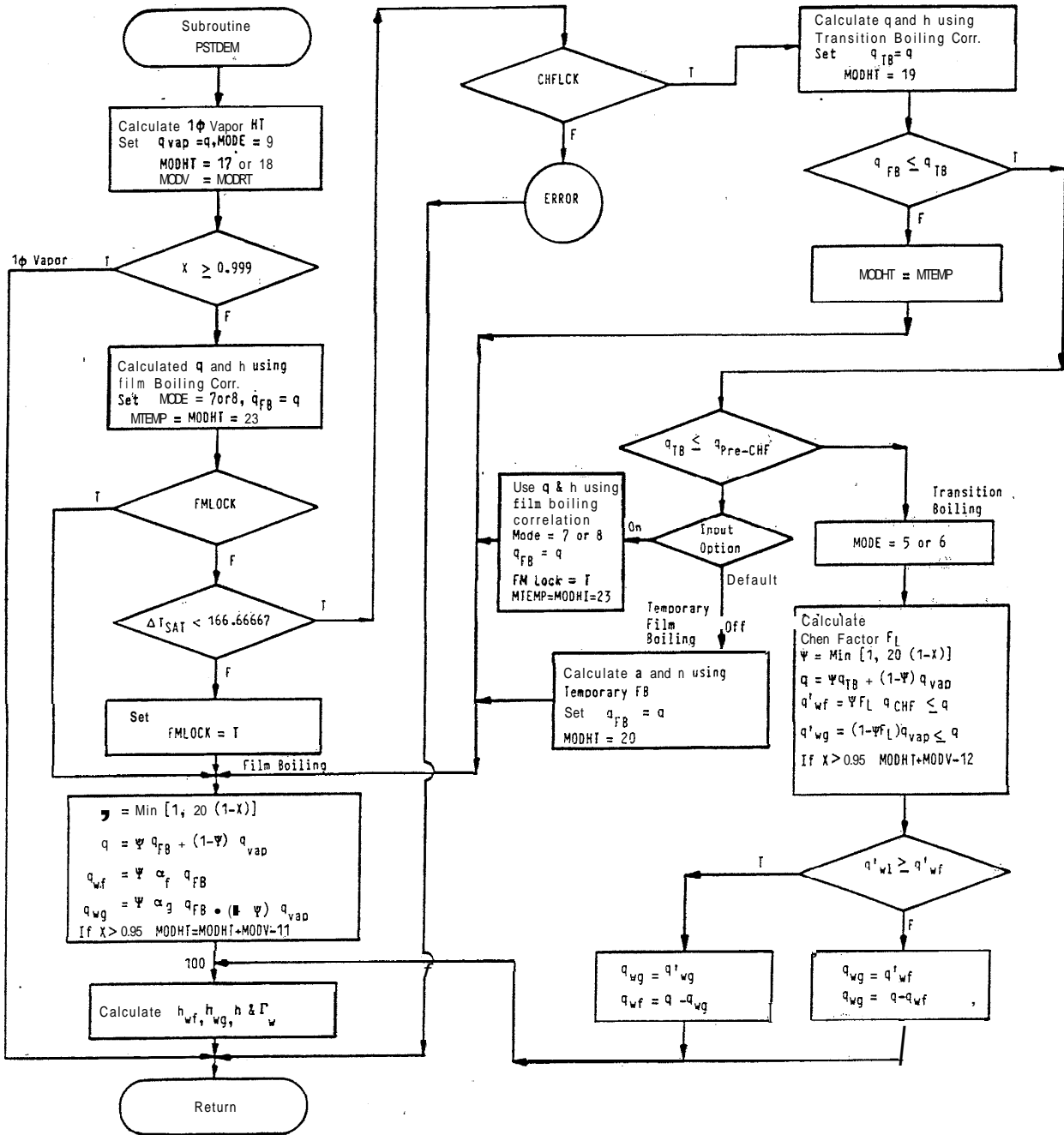


Figure 2.3.3-1. Core Model Heat Transfer Selection Logic. d) Driver Routine for Post-CHF correlations.

When the wall temperature is equal to or greater than the fluid saturation temperature and the equilibrium quality is less than or equal to zero, the maximum of the single-phase liquid and the nucleate boiling heat transfer correlations is used. However, when the quality is greater than zero, only the nucleate boiling correlation is used.

$$h = \begin{cases} \text{MAX}(h_{DB}, h_{RC}, h_{NB}) & T_w \geq T_{sat} \text{ and } X_e \leq 0.0 \\ h_{NB} & T_w \geq T_{sat} \text{ and } X_e > 0 \end{cases} \quad 2.3.3-2$$

A combination of the Chen, Thom, and Schrock-Grossman correlations are used for the nucleate boiling and the forced convection vaporization regimes. Switching between the correlations is dependent on pressure and void fraction and in accordance with the ranges of the correlations. Linear interpolation between the ranges of application of the correlation is employed to eliminate discontinuities in the value of heat transfer. Specifically,

$$h_{NB} = \begin{cases} h_{Chen} & \text{if } P \leq P_{750}, \\ h_{Thom} & \text{if } P \geq P_{1000} \text{ and } \alpha_g \leq 0.8, \\ h_{SG} & \text{if } P \geq P_{1000} \text{ and } \alpha_g \geq 0.9, \\ \text{Linear on } \alpha_g & \text{if } P \geq P_{1000} \\ (h_{Thom}, h_{SG}) & \text{and } 0.8 < \alpha_g < 0.9, \\ \text{Linear on } P & \text{if } P_{750} < P < P_{1000}, \\ (h_{Chen}, h_{Thom} - h_{SG}(\alpha_g)) & \end{cases} \quad 2.3.3-3$$

where

$$P_{750} = 5.171 \cdot 10^6 \text{ Pa (750 psia), and}$$

$$P_{1000} = 6.895 \cdot 10^6 \text{ Pa (1000 psia) .}$$

For very high quality, $X \geq 0.95$, the total heat flux is calculated by a linear interpolation on quality between the nucleate boiling value and the value for single-phase vapor heat transfer.

CHF Correlation Selection

The appropriate CHF correlation can be dependent on the fuel design being evaluated. RELAP5/MOD2-B&W allows seven options in the core heat transfer logic for high flow-high pressure CHF in order to accommodate this design dependence. For lower pressure and lower flow conditions, a single set of correlations, dependent on flow and pressure, have been selected. The high flow regime is defined as the mass flux, G , greater than or equal to G_{HI} (500,000 lbm/hr-ft²). In this area, the user may specify the high pressure CHF correlation, CHF_{HP} , as:

- | | |
|-----------------------------------|---|
| 1. B&W-2 applied at | $P \geq P_{HI} = P_{1500}, G \geq G_{HI},$ |
| 2. BWC applied at | $P \geq P_{HI} = P_{1600}, G \geq G_{HI},$ |
| 3. BWCMV applied at | $P \geq P_{HI} = P_{1500}, G \geq G_{HI},$ |
| 4. BWUMV applied at | $P \geq P_{HI} = P_{1500}, G \geq G_{HI},$ |
| 5. BWU User-Specified applied at | $P \geq P_{HI} = P_{1500}, G \geq G_{HI},$ |
| 6. BHTP applied at | $P \geq P_{HI} = P_{1600}, G \geq G_{HI}, \text{ or}$ |
| 7. BHTP User-Specified applied at | $P \geq P_{HI} = P_{1600}, G \geq G_{HI},$ |

where

$$P_{1500} = 10.342 \cdot 10^6 \text{ Pa (1500 psia),}$$

$$P_{1600} = 11.032 \cdot 10^6 \text{ Pa (1600 psia), and}$$

$$G_{HI} = \text{default of } 678.115 \text{ kg/m}^2\text{-sec (500,000 lbm/hr-ft}^2\text{),}$$

or user-input value for BHTP and BHTP user-specified.

Under each selection the value of the pressure above which the correlation will be applied, P_{HI} , is specified. Lower pressures for the high flow regime are covered by a combination of the Barnett and modified Barnett correlations and interpolation.

$$\text{CHF} = \begin{cases} \text{Linear on pressure} \\ \text{\{CHF}_{HP}, \text{Barnett}\}} & P_{1300} \leq P < P_{HI}, \\ \\ \text{Barnett} & P_{1000} \leq P < P_{1300}, \\ \\ \text{Linear on pressure} \\ \text{\{Barnett, Modified Barnett}\}} & P_{725} \leq P < P_{1000} \text{ psia}, \\ \\ \text{Modified Barnett} & P < P_{725} \end{cases}$$

2.3.3-5

where

$$\begin{aligned}
 P_{1300} &= 8.963 \cdot 10^6 \text{ Pa (1300 psia), and} \\
 P_{725} &= 4.999 \cdot 10^6 \text{ Pa (725 psia).}
 \end{aligned}$$

For the low flow regime, $G < G_{LO}$, the CHF value is the maximum of the low flow MacBeth correlation or the Griffith correlation for all pressures.

$$\text{CHF} = \text{MAX} \{ \text{MacBeth}, \text{Griffith} \}, \quad 2.3.3-6$$

where

$$G_{LO} = 271.246 \text{ kg/m}^2\text{-sec (200,000 lbm/hr-ft}^2\text{), or user-input value.}$$

In the middle flow regime, $G_{LO} \leq G < G_{HI}$, the CHF value is determined by the linear interpolation on mass flux between the high flow CHF at its low flow limit and the low flow CHF at its high flow limit.

In all regimes, two additional constraints are applied:

1. An absolute lower limit of CHF is set at $2.839 \cdot 10^5 \text{ w/m}^2$ (90,000 Btu/hr-ft²).

2. For vapor fractions greater than 0.8, ($\alpha_g > 0.8$), the value of CHF is taken as the value of the heat flux calculated using the transition boiling heat transfer correlation.

Post-CHF Heat Transfer Correlation Selection

Three post-CHF heat transfer regimes: transition boiling, film boiling, and single-phase vapor are considered. For wall temperatures before the film boiling lock-in ($\Delta T_{\text{sat}} < 300 \text{ F}$), the heat flux is taken as the maximum of the transition or film boiling correlations. An exception to this occurs if transition is selected and the heat flux value would be larger than that calculated using the pre-CHF heat flux correlation at the current surface temperature and fluid conditions. For such a case, the film boiling heat flux (identified as temporary film boiling) is used. This exception is needed to prevent post-CHF heat transfer values higher than or equal to pre-CHF nucleate boiling heat transfer.

$$q = \text{MAX}(q_{\text{TB}}, q_{\text{FB}}) \quad \Delta T_{\text{sat}} < 166.667 \text{ K (300 F)},$$

unless

$$q_{\text{TB}} \geq q_{\text{pre-CHF}}, \quad 2.3.3-7$$

then

$$q = q_{\text{FB}}.$$

Once the wall temperature is 166.667 K (300 F) greater than or equal to the fluid saturation temperature, the heat transfer is locked into film boiling or single-phase vapor. Film boiling is used up to a quality of 0.95, and single-phase forced convection is applied above 0.999 with a linear interpolation between 0.95 and 0.999.

$$q = \begin{cases} q_{FB} \text{ or } q_{TB} & X < 0.95, \\ \text{Linear on } X \text{ } ((q_{FB} \text{ or } q_{TB}), q_{SPV}) & 0.95 \leq X < 0.999, \\ q_{SPVC} & 0.999 \leq X. \end{cases}$$

2.3.3-8

A permanent film boiling lock-in option is also available through user control which will only allow film boiling or single-phase vapor heat transfer once film boiling is calculated. This option may prevent oscillations caused by film boiling to transition boiling switching prior to reaching the permanent film boiling lock-in temperature criteria.

2.3.3.2. Pre-CHF Heat Transfer Correlations (Core Model)

As in the system heat transfer model, the core heat transfer regimes included are classified as pre-CHF and post-CHF regimes. Condensation heat transfer is also included. Figure 2.3.3-1 gives a chart of the logic scheme for selecting the heat transfer models. The volumetric heat transfer rates for each phase are calculated as

$$Q_{wf} = q_{wf} A_w/V \quad 2.3.3-9$$

and

$$Q_{wg} = q_{wg} A_w/V. \quad 2.3.3-10$$

The total heat flux from the heat structure is

$$q = q_{wf} + q_{wg}, \quad 2.3.3-11$$

and the corresponding heat transfer coefficient is

$$h = h_{wf} + h_{wg}, \quad 2.3.3-12$$

where q_{wf} and q_{wg} are the effective wall-to-liquid and vapor heat flux, respectively, based on the total heat slab area, A_w . The pre-CHF heat transfer regime consists of convection to subcooled or a two-phase fluid and nucleate boiling.

Convection

For convection from the wall to the fluid, the maximum of Rohsenow-Choi⁵⁹ or the Dittus-Boelter⁴⁰ correlation is used. |

$$h = \text{MAX}(Cl_{DB} h_{DB}, Cl_{RC} h_{RC}) . \quad 2.3.3-13$$

The Dittus-Boelter correlation is

$$h_{DB} = 0.023 \frac{k_f}{D_e} (Pr_f)^{0.4} (Re_f)^{0.8} , \quad 2.3.3-14$$

and Rohsenow-Choi is given by

$$h_{RC} = 4 \frac{k_f}{D_e} . \quad 2.3.3-15$$

Cl_{DB} and Cl_{RC} are user input constants (default = 1). Q_{wg} and Γ_w are zero throughout this heat transfer regime and q_{wf} is given by $q_{wf} = h(T_w - T_f)$.

Condensation

Since condensation is not expected to occur on the fuel rod surface during LOCA, a simple heat transfer model is added. The vapor and liquid heat transfer coefficients, h'_g and h'_f , are calculated using Equation 2.3.3-13 and using the total mass flux, G , and the appropriate (liquid or vapor) fluid properties. The heat transfer is partitioned based on the void fraction as follows

$$h_{wf} = \alpha_f h'_f$$

and

$$h_{wg} = \alpha_g h'_g .$$

The condensation parameters, q_{wf} , q_{wg} , and Γ_w , are calculated as given below

$$q_{wf} = h_{wf} (T_w - T_f) ,$$

$$q_{wg} = h_{wg} (T_w - T_g) ,$$

and

$$\Gamma_w = q_{wg} A_w / (V h_{fg}) .$$

Nucleate Boiling

For nucleate boiling, the heat transfer logic, section 2.3.3.1, makes use of the Chen, Thom, and the Schrock-Grossman correlations.

Chen and Modified Chen

The implementation of the Chen⁴¹ and modified Chen⁴⁴ correlations, is slightly altered by the core model switching logic. It is the same as the system heat transfer model, section 2.2.2.1, except for the use of the subcooled vapor generation factor, f_{subvap} . Again, because of the nonequilibrium nature of RELAP5, the subcooled-to-saturated nucleate boiling boundary cannot be defined precisely. In addition, the vapor generation in the subcooled boiling regime has to be included. Hence, the Chen correlation is modified as follows.

The heat transfer coefficient in nucleate boiling is given by the sum of the two effects: microscopic (boiling) and macroscopic (convection)

$$h_{Chen} = C1_{mic} h_{mic}^* + C1_{mac} h_{mac}^* \quad 2.3.3-16$$

and

$$q = C1_{mic} h_{mic}^* \Delta T_{sat} + C1_{mic} h_{mac}^* (T_w - T_f) ,$$

where

$C1_{mic}$ and $C1_{mac}$ are user input constants (default = 1).

In the system model, the Chen microscopic component is altered by the subcooled vapor generation factor, f_{subvap} , to give the contribution above.

$$h_{mic}^* = h_{mic} f_{subvap} . \quad 2.3.3-17$$

In the core model, the modification takes place in the development of the vapor generation rate, Γ_w , and no direct alteration of h_{mic} is made. Thus,

$$h_{mic}^* = h_{mic} , \quad 2.3.3-18$$

where h_{mic} is Chen's microscopic heat transfer coefficient,

$$h_{mic} = 0.00122 \frac{k_f^{0.79} C_{pf}^{0.45} \rho_f^{0.49}}{\sigma^{0.5} \mu_f^{0.29} h_{fg}^{0.24} \rho_g^{0.24}} \Delta T_{sat}^{0.24} \Delta P^{0.75} S .$$

2.3.3-19

The subcooled vapor generation factor, which is a measure of the first appearance of bubbles in the channel, is calculated based on the onset of nucleate boiling criteria given by Bergels and Rohsenow⁵² and the net vapor generation criteria given by Saha and Zuber.¹³⁰ The calculation of f_{subvap} is discussed in section 2.2.2.1.

The convection part, h_{mac}^* , is taken as the maximum of the Rohsenow-Choi correlation and the Chen macroscopic heat transfer coefficient, h_{mac} . Thus,

$$h_{\text{mac}}^* = \text{MAX}(h_{\text{mac}}, 4k_f/D_e), \quad 2.3.3-20$$

where

$$h_{\text{mac}} = 0.023 (k_f/D_e) (\text{Pr}_f)^{0.4} \left[|\alpha_f \rho_f v_f| D_e / \mu_f \right]^{0.8} F. \quad 2.3.3-21$$

The modified Chen correlation is obtained by setting $F = 1$ in the Chen correlation. Because of the nonequilibrium nature of RELAP5, F is calculated as follows.

$$F = 1.0 ,$$

if the liquid flow is zero or liquid subcooling is greater than or equal to 5K. Otherwise,

$$F = F' - 0.2(F' - 1) \text{MAX}(0, T_{\text{sat}} - T_f), \quad 2.3.3-22$$

where F' is equal to 1.0 if the inverse of the Martinelli parameter

$$x_{\text{tt}}^{-1} = \left[\frac{|\alpha_g \rho_g v_g|}{|\alpha_f \rho_f v_f|} \right]^{0.9} \left(\frac{\rho_f}{\rho_g} \right)^{0.5} \left(\frac{\mu_g}{\mu_f} \right)^{0.1} \leq 0.1 . \quad 2.3.3-23$$

Otherwise, F' is a fit to the Chen F-factor

$$F' = 2.35(X_{tt}^{-1} + 0.213)^{0.736}$$

The suppression factor, S , is calculated based on the void fraction as

$$S = \begin{cases} 1 & \alpha_g \leq 0.3 \\ 1 - 2(1 - S') (\alpha_g - 0.3) & 0.3 < \alpha_g < 0.8 \\ S' & \alpha_g \geq 0.8, \end{cases} \quad 2.3.3-24$$

where S' is a fit to the Chen suppression factor given by the following expression.

$$S' = \begin{cases} [1 + 0.12(Re_{TP})^{1.14}]^{-1} & Re_{TP} < 32.5 \\ [1 + 0.42(Re_{TP})^{0.78}]^{-1} & 32.5 \leq Re_{TP} < 70.0 \\ 0.0797 & Re_{TP} \geq 70, \end{cases} \quad 2.3.3-25$$

where

$$Re_{TP} = 10^{-4} \left[\frac{\alpha_f \rho_f v_f D_e}{\mu_f} \right] F^{1.25}, \quad 2.3.3-26$$

$$\Delta T_{sat} = T_w - T_{sat}, \text{ and} \quad 2.3.3-27$$

ΔP is the difference in vapor pressure corresponding to ΔT_{sat} .

Thom

The Thom nucleate boiling correlation is given by

$$q = C_{1T} \cdot C_{1EF} \left[\frac{\Delta T_{sat} \exp(P/(1260 C_{1P}))}{0.04} \right]^2 \quad 2.3.3-28$$

and

$$h_{Thom} = q/\Delta T_{sat} , \quad 2.3.3-29$$

where

C_{1T} is a user input constant (default = 1) and the conversion factors C_{1EF} and C_{1P} are given in Table 2.3.3-1.

Schrock and Grossman

The Schrock and Grossman¹³¹ correlation is

$$h_{SG} = 2.5 C_{1SG}^{0.023} \frac{k_f}{D_e} (Pr_f)^{0.4} \left[\frac{\alpha_f \rho_f v_f D_e}{\mu_f} \right]^{0.8} \left[\frac{1}{X_{tt}} \right]^{0.75} \quad 2.3.3-30$$

and

$$q = h_{SG} \Delta T_{sat} , \quad 2.3.3-31$$

where the inverse of the Martinelli parameter, X_{tt}^{-1} , is given by Equation 2.3.3-22 and C_{1SG} is a user input constant (default = 1).

Heat Flux Calculation

When $X \leq 0.95$ and q_{wg} and h_{wg} are zero

$$q_{wf} = q, \quad 2.3.3-32$$

and

$$h_{wf} = h. \quad 2.3.3-33$$

When $X > 0.95$, it is assumed that the liquid heat flux, q_{wf} , decreases linearly based on X from the value calculated by the nucleate boiling correlation to zero at $X = 1$. Similarly, the vapor heat flux, q_{wg} , increases linearly from zero at $X = 0.95$ to the value calculated using the single-phase vapor heat transfer correlations described in section 2.3.3.4 at $X = 1$. Thus,

$$q = q_{wf} + q_{wg} \quad 2.3.3-34$$

and

$$h = h_{wf} + h_{wg}, \quad 2.3.3-35$$

where

$$q_{wf} = q_{NB} \cdot f,$$

$$q_{wg} = q_v(1 - f),$$

$$h_{wf} = q_{wf}/\Delta T_{sat},$$

$$h_{wg} = q_{wg}/(T_w - T_g),$$

$$f = 20(1 - X),$$

q_{NB} = heat flux, q , calculated using nucleate boiling correlations, and

q_v = total heat flux calculated using the vapor heat transfer correlation described in section 2.3.3-4 (Equation 2.3.3-64).

Table 2.2.3-1. English - SI Conversion Factors

	<u>Parameter</u>
$C1_{IN} = 0.0254 \text{ m/in}$	length
$C1_L = 0.3048 \text{ m/ft}$	length
$C1_M = 0.45359237 \text{ kg/lbm}$	mass
$C1_P = 6894.757293 \text{ Pa/psia}$	pressure
$C1_E = 1055.05585 \text{ J/Btu}$	energy
$C1_{SE} = 2326.0 \text{ (J/kg)/(Btu/lbm)}$	specific energy
$C1_{EF} = 3.154590745 \text{ (w/m}^2\text{)/(Btu/hr-ft}^2\text{)}$	heat flux
$C1_{MF} = 1.356229899 \cdot 10^{-3} \text{ (kg/m}^2\text{-s)/(lbm/hr-ft}^2\text{)}$	mass flux

In order to make the transition from single-phase liquid heat transfer to nucleate boiling continuous, the heat flux in the subcooled boiling regime, where $T_w > T_{sat}$ and $X_e \leq 0.0$, is taken as the maximum of the values calculated using single-phase liquid and nucleate boiling correlations. That is,

$$q = \text{MAX}(q_{liq}, q_{NB}) , \quad 2.3.3-36$$

where

q_{liq} = single-phase liquid heat flux calculated using the convection correlations given in section 2.2.2.1 and

q_{NB} = heat flux, calculated using nucleate boiling correlations.

When $q = q_{liq}$, all the additional heat transfer parameters are calculated using the equations for convection given in section 2.2.2.1. When $q = q_{NB}$, the additional parameters are calculated using the equations for nucleate boiling.

Calculation of Γ_w

In nucleate boiling, Γ_w is calculated using Equation 2.2.2-28. The q_{vap} in this equation is slightly different than that used in system heat transfer. This is because the subcooled vapor generation function, f_{subvap} , calculated in section 2.2.2.1, is used differently here than that used in the system model. In the system model, the microscopic heat transfer portion (h_{mic}) of the Chen correlation remained zero when $f_{subvap} \leq 0.0$ (when T_w or T_f does not satisfy the vapor generation criteria). In the core model, the macroscopic portion of the heat is added to liquid until $f_{subvap} > 0.0$.

In the core model, q_{vap} is calculated as follows

$$q_{vap} = (q_{wf} - q_{conv}) f_{subvap} \quad 2.3.3-37$$

where

$$q_{conv} = h_{conv}(T_w - T_f) \Psi,$$

with

$$\Psi = \begin{cases} 1.0 & T_f > T_w \\ 1/2 \text{ MIN } [2.0, \text{MAX}(0.0, T_{sat} - T_f)] & T_f \leq T_w \end{cases}$$

Ψ is a linear interpolation function to make $q_{conv} = 0$ at

$$T_f = T_{sat},$$

$$h_{conv} = \text{MAX}(C1_{DB} h_{DB}, C1_{RC} 4 k_f / D_e).$$

The Reynolds number, Re_f , in h_{DB} is calculated using

$$Re_f = |\alpha_f \rho_f v_f| D_e / \mu_f \quad 2.3.3-38$$

2.3.3.3. Critical Heat Flux Correlations

The CHF correlations used in the core heat transfer model are B&W-2, BWC, BWCMV, BWUMV, BWU User-Specified, BHTP, BHTP User-Specified, Barnett, modified Barnett for high flow, and MacBeth and Griffith low flow. The first seven were developed by B&W specifically for B&W fuel and serve as the high flow-high pressure correlations depending on the fuel type. The later four are public domain and serve in the low flow regime for low pressures. The switching logic is described in section 2.3.3.1.

B&W-2

The B&W-2¹⁰⁶ correlation was developed by B&W in the early 1970's for application to B&W's 15 by 15 fuel assembly design. It is given by

$$q_{crit} = C1_{BW2} C1_{EF} \left[\frac{1.15509 - 0.40703 (D_e/C1_{IN})}{12.710(3.0545(G \cdot 10^{-6}/C1_{MF})^A)} \right] \\ \cdot \left[0.3702 \cdot 10^8 (0.59137(G \cdot 10^{-6}/C1_{MF})^B) \right. \\ \left. - 0.15208 X_{eth} (h_{fg}/C1_{SE})(G/C1_{MF}) \right] , \quad 2.3.3-39$$

where

$C1_{BW2}$ = user input constant (default = 1),

$$A = 0.71186 + (0.20729 \cdot 10^{-3}) [(P/C1_p) - 2000.0] ,$$

$$B = 0.8304 + (0.68479 \cdot 10^{-3}) [(P/C1_p) - 2000.0] ,$$

$$X_{eth} = \begin{cases} X_e & \text{if } h \geq h_{f,sat} \text{ or } X_a > 0.0 \\ (h - h_{f,sat}) / (h_{g,sat} - h_{f,sat}) \leq 1 & \text{otherwise,} \end{cases}$$

$$h = XU_g + (1 - X) U_f + P/\rho , \text{ and}$$

$h_{f,sat}$ and $h_{g,sat}$ are liquid and vapor saturation enthalpies.

The conversion factors $C1_{EF}$, $C1_{IN}$, $C1_{MF}$, $C1_p$ and $C1_{SE}$ are given in Table 2.3.3-1.

BWC¹⁰⁷

The BWC correlation was developed by B&W in the late 1970's for application to the B&W 17 by 17 fuel assembly and zirconium grid

15 by 15 assembly. The correlation is held proprietary by B&W and given by

$$q_{crit} = C1_{BWC} C1_{EF} A_5 \frac{(A_3 + A_4 (P/C1_P - 2000)) \left[\frac{A_1 G/C1_{MF}}{(A_6 + A_7 (P/C1_P - 2000))} - A_8 X_{eth} \left(\frac{h_{fg}/C1_{SE}}{G/C1_{MF}} \right) \right] \left[G/C1_{MF} \right]}{[A_2 G/C1_{MF}]}$$

2.3.3-40

where

$C1_{BWC}$ = user input constant (default = 1),

$$A_1 = 0.309191 \cdot 10^{-6},$$

$$A_2 = 0.388223 \cdot 10^{-5},$$

$$A_3 = 0.964882,$$

$$A_4 = 0.301423 \cdot 10^{-3},$$

$$A_5 = 0.554836 \cdot 10^7,$$

$$A_6 = 0.727729,$$

$$A_7 = 0.189646 \cdot 10^{-4}, \text{ and}$$

$$A_8 = 0.175233 \cdot 10^{-8}.$$

BWCMV¹⁰⁸

The BWCMV correlation was developed in the mid 1980's for application to the 17 by 17 fuel assembly with mixing vane, MV, grids. The correlation is held proprietary by B&W and given by

$$q_{crit} = C1_{BWV} C1_{EF}^{FLS} A_5 \frac{(A_3 + A_4 (P/C1_P - 2000)) \left[\frac{A_1 G/C1_{MF}}{(A_6 + A_7 (P/C1_P - 2000))} - A_8 X_{eth} \left(\frac{h_{fg}/C1_{SE}}{G/G1_{MF}} \right) \right] \left[G/G1_{MF} \right]}{[A_2 G/C1_{MF}]}$$

2.3.3-41

where

- $C1_{BWV}$ = user input constant (default = 1),
 $FLS = C_1 + C_2L + C_3S + C_4LS + C_5L^2 + C_6S^2$ (input)
 dimensionless,
 L = heated (active) length of the core (inches),
 S = spacer grid spacing (inches),

b, c, d, e

BWUMV

The BWUMV correlation was developed from the same database as BWCVM¹³⁹, but with additional data in the mid-range flow regime. It is applicable to 17 x 17 fuel assemblies with mixing vanes for wide pressure, mass flux, and quality ranges. Derivation of the BWUMV correlation is given in Appendix I of this report. The correlation, as implemented in RELAP5/MOD2-B&W, is given by:

$$q_{crit} = C1_{BWU} C1_{EF} FLS (a_0 + a_1x_1 + a_2x_2 + a_3x_3 + a_4x_1^2 + a_5x_2^2 + a_6x_3|x_3| + a_7x_1x_2 + a_8x_1x_3 + a_9x_2x_3 + a_{10}x_1^3 + a_{11}x_2^3 + a_{12}x_3^3 + a_{13}x_1x_2x_3), \quad 2.3.3-41.1$$

where

- $C1_{BWU}$ = user input constant (default = 1) and
 FLS = the spacer grid spacing factor used in BWCVM.

BWUMV is dependent on the variables:

This page is intentionally left blank.

$$\begin{aligned}x_1 &= \exp [P / (1000 \cdot C1_p)], \\x_2 &= G / (10^6 * C1_{MF}), \text{ and} \\x_3 &= X_{eth}\end{aligned}$$

where P is the system pressure in Pa, G is mass flux in kg/m²-s, X_{eth} is the quality at CHF, and C1_p and C1_{MF} are the English-to-metric conversion factors for pressure and mass flux, respectively.

The empirical coefficients are:



BWU User-Specified CHF Model

There are several general CHF correlations using the form of the BWU correlation for high pressure, high flow CHF applications of different fuel designs. The code has been modified to allow user input of the new CHF coefficients with the generalized BWU CHF correlation form given by:

$$\begin{aligned}q_{crit} &= C1_{BWUUS} C1_{EF} FLS (a_0 + a_1 x_1 + a_2 x_2 + a_3 x_3 + a_4 x_1^2 + \\& a_5 x_2^2 + a_6 x_3 |x_3| + a_7 x_1 x_2 + a_8 x_1 x_3 + a_9 x_2 x_3 + a_{10} x_1^3 + \\& a_{11} x_2^3 + a_{12} x_3^3 + a_{13} x_1 x_2 x_3), \quad 2.3.3-41.2\end{aligned}$$

where

Cl_{BWUUS} = user input constant (default = 1) and
 FLS = the spacer grid spacing factor given for BWCMV.

The BWU user-supplied CHF model is dependent on the variables:

$$x_1 = \exp [P / (a_{14} * Cl_p)],$$

$$x_2 = G / (10^6 * Cl_{MF}) , \text{ and}$$

$$x_3 = X_{eth}$$

where P is the system pressure in Pa, G is mass flux in kg/m^2-s , X_{eth} is the quality at CHF, and Cl_p and Cl_{MF} are the English-to-metric conversion factors for pressure and mass flux, respectively.

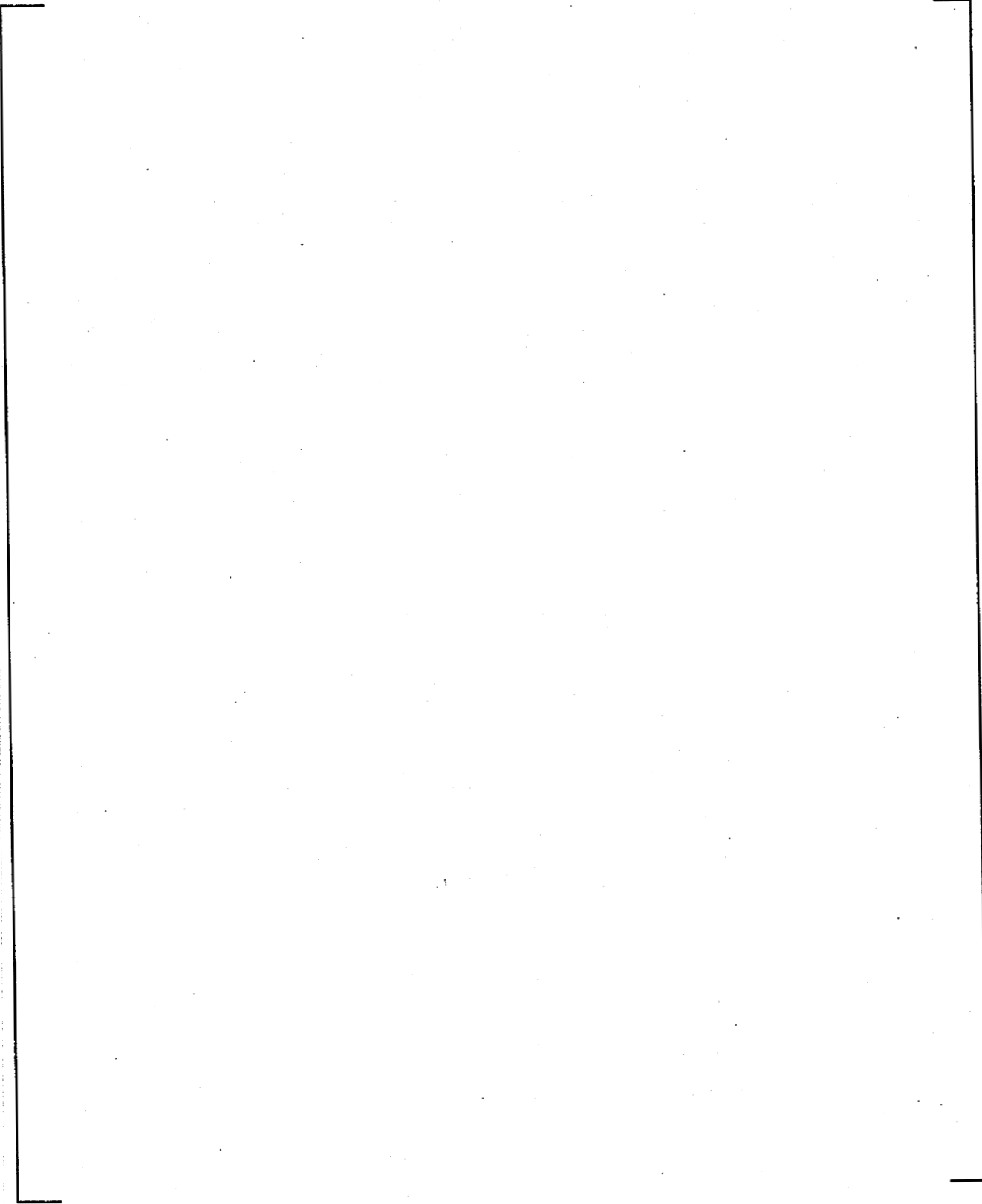
The incorporation of the general form of the BWU CHF correlation into the code with empirical coefficients, a_0 through a_{14} , allows options for user input of a new BWU CHF correlation that may be developed from CHF performance testing of new or modified fuel designs. Therefore, the new correlation could be implemented without a future coding change if the form of the correlation is unchanged.

BHTP

The general form of the approved HTP CHF correlation¹⁶⁵ is as follows:

	2.3.3-41.3
	2.3.3-41.4

where q_{base}'' has been converted from its correlated units of MBtu/(ht-ft²) into the SI units, W/m² via the 10⁶ and Cl_{EF} terms.



The implementation in RELAP5/MOD2 sets the F_{ax} parameter to 1.0 for LBLOCA applications that could have flow direction changes during the blowdown phase. (This is a similar approach that was previously adopted for the Tong non-uniform flux distribution factor in the BWUMV correlation in Appendix I of BAW-10164.) An axial power shape-dependent value for the F_{ax} factor is applied in the determination of CHF for the SBLOCA analyses, which do not predict an initial core flow direction change.

The BHTP CHF correlation is the same form as the HTP CHF correlation described above however, the coefficients used in the equations to calculate the A, B, and HTERM parameters have been optimized for use in the NRC-approved thermal-hydraulics LYNXT code (Reference 164) and these have been incorporated into RELAP5/MOD2. The following table contains the BHTP CHF correlation coefficients defined in Reference 164 as follows:

--	--

The ranges of applicability for the coolant conditions that have been approved by the NRC for the BHTP CHF correlation (Reference 164) used in DNB analyses and the values applied to the RELAP5/MOD2 applications as coded are given in the following table. Another table provides the ranges for the fuel design parameters.

	<u>Acceptable Range</u>	<u>Code Range</u>
Coolant conditions		
Pressure, psia	1385-2425	> 1600*
Local mass flux, Mlbm/(hr-ft ²)	0.492-3.549	> 0.5**
Inlet enthalpy, Btu/lbm	383.9-644.3	Not limited
Local quality	< 0.512	Not limited

* The HTP correlation is used exclusively down to 1600 psia and based on linear interpolation with the Barnett CHF correlation down to 1300 psia.

** The HTP correlation is used exclusively down to 0.5 Mlbm/hr/ft² and based on linear interpolation with the low flow CHF correlations down to 0.2 Mlbm/hr/ft².

Test Section Geometry

Fuel rod diameter, in	0.360-0.440
Fuel rod pitch, in	0.496-0.580
Axial spacer span, in	10.5-26.2
Hydraulic diameter, in	0.4571-0.5334
Heated length, ft	9.8-14.0

The EM core heat transfer package used for LOCA analyses includes a variety of generic CHF correlations that are used for lower pressures and flow conditions. Linear interpolation regions are used to provide smooth transitions from the high-pressure high-flow CHF correlations to the other generic correlations. Generally the high-pressure high-flow CHF correlation is used exclusively within its approved range of applicability with extrapolation to pressures and flows outside the range for the linear interpolations.

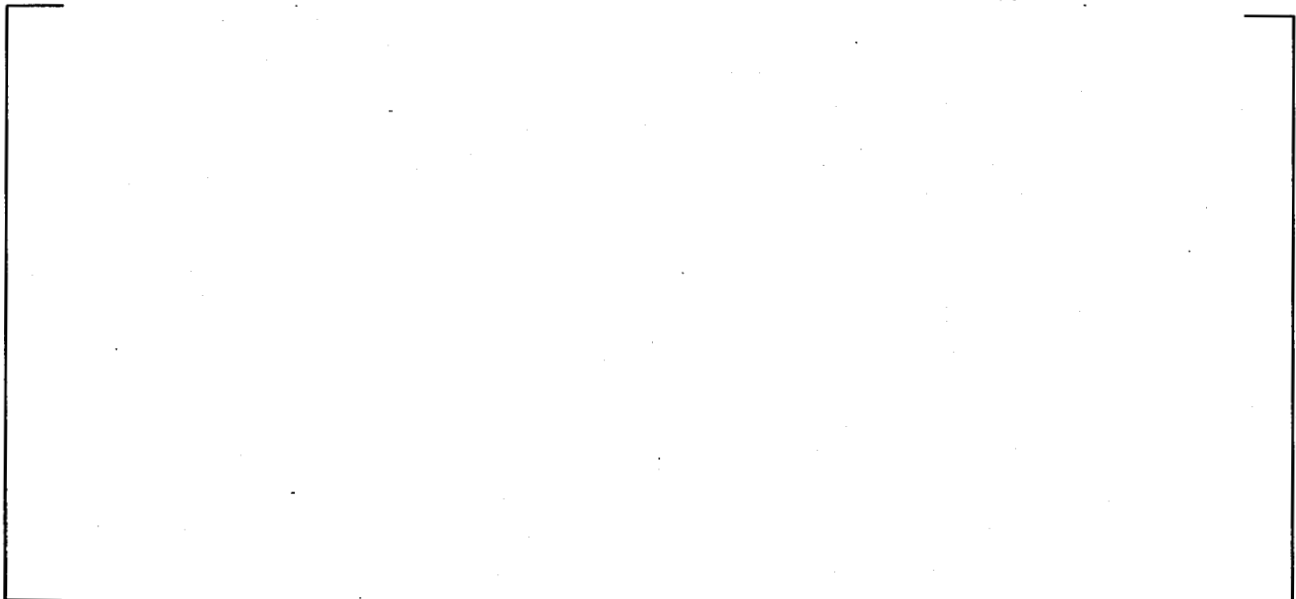
In order to retain flexibility in the ranges used for the BHTP CHF correlation, an option was added to allow the user to change the minimum pressure and mass flux range via input when the BHTP correlation is used. A code input option allows the user to change the default high pressure CHF transition (P_{HI} of 1600 psia) and high mass flux transition ranges (G_{HI} of 0.5 Mlbm/hr-ft²), respectively, on the BHTP correlation options.

BHTP User-Supplied CHF Model

An option has been added to RELAP5 to allow for the user to select the general form of the HTP CHF correlation



and specify inputs for the coefficients defining the A, B, and HTERM parameters given in the previous section and repeated here for clarity.



In order to retain flexibility in the ranges used for the user-supplied BHTP CHF correlation, an option was added to allow the user to change the minimum pressure and mass flux range via input when the BHTP correlation is used. A code input option allows the user to change the default high pressure CHF transition (P_{HI} of 1600 psia) and high mass flux transition ranges (G_{HI} of 0.5 Mlbm/hr-ft²), respectively, on the BHTP correlation options.

High to Low Flow CHF Transition

Figure 2.3.3-1 highlights the methods used for calculating CHF over the entire pressure and flow range. When the mass flux is above G_{HI} the high flow correlations are used and when it is less than G_{LO} the low flow correlations are applied. The high-to-low flow interpolation is performed when the mass flux is between G_{HI} and G_{LO} . G_{HI} is defaulted to 0.5 Mlbm/hr-ft² (678.115 kg/m²-s) as listed in Figure 2.3.3-1 and also discussed in the text in Section 2.3.3.1. (Note that G_{HI} can be changed by user input for the BHTP and user-supplied BHTP CHF options if necessary.) This option was added along with the BHTP and user-supplied forms of the BHTP CHF

correlations to allow a change in the default value of 0.2 Mlbm/hr-ft² (271.25 kg/m²-s) for G_{LO} if needed. This option was also added to facilitate mass flux transition changes if needed without requiring a future code modification. It is noted that any application that applied a change in the default value of G_{LO} (or G_{HT} for the BHTP options) would require additional justification to support its use.

Barnett¹⁰⁹

The Barnett correlation is widely accepted and applied within the industry for high flow medium pressure CHF. The correlation is given by

$$q_{crit} = 10^6 C_{1BR} C_{1EF} \frac{A+B(h_f - h_{in})/C_{1SE}}{C+L/C_{1in}}, \quad 2.3.3-42$$

where

C_{1BR} = user input constant (default = 1),

This page is intentionally left blank.

$$A = 67.45 (D_{he}/Cl_{IN})^{0.68} (G \cdot 10^{-6}/Cl_{MF})^{0.192} \\ \cdot \{1.0 - 0.744 \exp[-6.512(D_{hy}/Cl_{IN}) (G \cdot 10^{-6}/Cl_{MF})]\},$$

$$B = 0.2587 (D_{he}/Cl_{IN})^{1.261} (G \cdot 10^{-6}/Cl_{MF})^{0.817},$$

$$C = 185.0 (D_{hy}/Cl_{IN})^{1.415} (G \cdot 10^{-6}/Cl_{MF})^{0.212},$$

L = segment length (input) (m),

D_{he} = heated equivalent diameter (input) (m),

D_{hy} = $[D_r(D_r + D_{he})]^{1/2} - D_r$ (m), and

D_r = rod diameter calculated using the heat slab input (m).

Modified Barnett¹¹⁰

As with the Barnett correlation, the modified Barnett has been widely accepted and is applied in the high flow, low pressure regime. The correlation is given by

$$q_{crit} = 10^6 Cl_{MBR} Cl_{EF} \frac{A + B(h_f - h_{in})/Cl_{SE}}{C + L/Cl_{IN}}, \quad 2.3.3-43$$

where

Cl_{MBR} = user input constant (default = 1),

$$A = 73.71 \left[\frac{D_{he}}{Cl_{IN}} \right]^{0.0523} (G \cdot 10^{-6}/Cl_{MF})^{0.663} \left[\frac{888.6}{h_{fg}/Cl_{SE}} \right]$$

$$\cdot [1 - 0.315 \exp\{-11.34(D_{hy}/Cl_{IN}) (G \cdot 10^{-6}/Cl_{MF})\}],$$

This page is intentionally left blank.

$$B = 0.104 \left[\frac{D_{he}}{Cl_{in}} \right]^{1.445} (G \cdot 10^{-6} / Cl_{MF})^{0.691} ,$$

$$C = 45.55 \left[\frac{D_{hy}}{Cl_{in}} \right]^{0.0817} (G \cdot 10^{-6} / Cl_{MF})^{0.587} ,$$

and the other variables are the same as in Barnett.

Macbeth Correlation¹¹¹

The MacBeth low-flow correlation is applied in combination with the Griffith correlation over the entire pressure range. The correlation is given by

$$q_{crit} = Cl_{MAC} \left[\frac{10^6}{158} Cl_{EF} \right] (h_{fg} / Cl_{SE}) (G \cdot 10^{-6} / Cl_{MF})^{0.51} \cdot (D_e / Cl_{IN})^{-0.1} (1 - X_{eth}) , \quad 2.3.3-44$$

where

Cl_{MAC} = user input constant (default = 1).

Griffith¹¹²

The Griffith correlation applied in converse with MacBeth low flow is given by -

$$q_{crit} = Cl_{GRF} \left(\frac{\pi}{30} \right) \cos[\pi(49 \alpha_g + 1)/100] h_{fg} \cdot \left[\frac{\rho_f \rho_g}{\rho_f + \rho_g} \right]^{0.5} [\sigma(\rho_f - \rho_g)]^{0.25} , \quad 2.3.3-45$$

where

$C1_{GRF}$ = user input constant (default = 1).

2.3.3.4. Post-CHF Heat Transfer Correlations

As in the system model, the post-CHF heat transfer regimes in the core model include the transition, film boiling, and single-phase steam heat transfer.

Transition Boiling

The total heat flux from wall-to-fluid is calculated using the McDonough, Milich, and King correlation.¹³²

$$q = q_{TR} = C1_{TR} [q_{crit} - C1_{TR1} C (T_w - T_{wCHF})] , \quad 2.3.3-46$$

where

$C1_{TR}$ and $C1_{TR1}$ = user input constants (default = 1), and

q_{crit} = critical heat flux calculated using the correlations given in section 2.3.3.3.

The slope of the heat flux C is calculated by the linear interpolation between the values given below

<u>Pressure, MPa (psia)</u>	<u>C, w/m²-k (Btu/hr-ft²-F)</u>
13.7895149 (2000)	5560.155464 (979.2)
8.273708752 (1200)	6704.893353 (1180.8)
5.515805834 (800)	8524.208928 (1501.2)

The wall temperature corresponding to q_{crit} , T_{wCHF} , is calculated using the Thom correlation given by Equation 2.3.3-28, by setting $q = q_{crit}$.

When the quality $X > 0.95$, the heat flux is calculated by linear interpolation, based on quality, between q_{TR} and the value calculated using the single-phase vapor correlation given later in this section.

$$q = \psi q_{TB} + (1 - \psi) q_v, \quad 2.3.3-47$$

where

$$\psi = \begin{cases} 1 & X \leq 0.95 \\ 20(1 - X) & X > 0.95 \end{cases},$$

and

q_v = single-phase vapor heat flux (q of Equation 2.3.3-64).

The partitioning of the energy between the phases, q_{wf} and q_{wg} , is done slightly differently than that in the system model transition boiling. This is because in the core model the total heat flux has to satisfy the value calculated using Equations 2.3.3-46 or 2.2.2-47. q_{wf} and q_{wg} are calculated as follows.

$$q'_{wf} = \psi \cdot F_L \cdot q_{crit} \leq q \quad 2.3.3-48$$

and

$$q'_{wg} = (1 - \psi F_L) q_v \leq q, \quad 2.3.3-49$$

where

F_L = the Chen factor given by Equation 2.2.2-38.

If $q'_{wf} \geq q'_{wg}$,

$$q_{wg} = (q - q'_{wg})$$

and

$$q_{wg} = q'_{wg}$$

If $q'_{wf} < q'_{wg}$,

$$q_{wg} = q'_{wg}$$

and

$$q_{wg} = q - q'_{wf}$$

The other heat transfer parameters are calculated as follows.

$$h_{wf} = q_{wf}/\Delta T_{sat}, \quad 2.3.3-50$$

$$h_{wg} = q_{wg}/(T_w - T_g), \quad 2.3.3-51$$

$$h = h_{wf} + h_{wg}, \quad 2.3.3-52$$

and

r_w is calculated using Equation 2.2.2-42.

Film Boiling

The total wall-to-fluid heat flux in the film boiling heat transfer regime is calculated using either the CSO correlation¹²⁵⁻¹²⁹ or the Condie-Bengston IV¹³⁴ correlation. The choice of correlations is determined by the user through the use of the heat transfer multipliers.

$$q = q_{FB} = h(T_w - T_v). \quad 2.3.3-53$$

This heat flux is calculated based on the cold heat transfer surface area. This area is used in all heat structures with only one exception. A user option has been added to allow adjustment of the surface heat transfer coefficient following clad rupture. When this option has been requested, the heat flux in a ruptured segment single heat structure is multiplied by the ratio of the ruptured-to-cold outside cladding radius to approximate the enhanced pin surface area. The heat flux for any of the core heat transfer film boiling correlations under these conditions is computed by

$$q = q_{FB} = \left[\frac{r_{oc_rupt}}{r_{oc_cold}} \right] h(T_w - T_v). \quad 2.3.3-53.1$$

CSO Correlation

The vapor temperature, T_v , calculation is determined by a user input option. It is the RELAP5 volume steam temperature, T_g , or it is obtained by solving the following two equations simultaneously for a given system pressure, P , and wall temperature, T_w .

$$X_{ac}/X_e = h_{fg}/(h_v - h_{f,sat}) \quad 2.3.3-54$$

and

$$X_{ac}/X_e = 1 - B(P) (T_v - T_{sat}) / (T_w - T_v) , \quad 2.3.3-55$$

where

$$B(P) = 0.26 / [1.15 - (P/P_c)^{0.65}] , \text{ and}$$

P_c = critical pressure, 22.12 MPa (3208.2 psia).

The solution of Equations 2.3.3-54 and 2.3.3-55 also gives the actual quality X_{ac} . From physical considerations, the following limits apply

$$T_{sat} \leq T_v \leq [T_w + B(P) T_{sat}] / [1 + B(P)] , \quad 2.3.3-56$$

$$0.0 \leq X_{ac}/X_e \leq 1 , \text{ and} \quad 2.3.3-57$$

$$0 \leq X_{ac} \leq 1. \quad 2.3.3-58$$

The total heat transfer coefficient, h , is calculated by

$$h = \text{MAX} [Cl_{FLM} h_{vc} (1 + F_s) , Cl_{RC} 4 k_g / D_e] , \quad 2.3.3-59$$

where

Cl_{FLM} = user input constant (default = 1).

The Chen CSO heat transfer coefficient, h_{vc} , is given by

$$h_{vc} = f/2 G X_{ac} Cp_{vf} (Pr)_{vf}^{-2/3} , \quad 2.3.3-60$$

where

$$f = 0.037 \text{ Re}^{-0.17}$$

Subscript v_f refers to properties evaluated at $(T_w + T_v)/2$.

$$\text{Re}_e = D_e \rho_v \langle j \rangle / \mu_v$$

and

$$\langle j \rangle = G [X_{ac} / \rho_v + (1 - X_{ac}) / \rho_f] \quad 2.3.3-61$$

F_s is the heat transfer enhancement factor to account for the effect of the entrained liquid droplets, and it is calculated using the following equation

$$F_s = 250 (P/P_c)^{0.69} [(1 - X_{ac}) / X_{ac}]^{0.49} (\text{Re}_v)^{-0.55} \quad 2.3.3-62$$

where

$$\text{Re}_v = G X_{ac} D_e / \mu_v$$

When X_e is less than or equal to zero, T_v is set equal to T_{sat} and h_{vc} is set equal to zero.

When the quality $X > 0.95$, the heat flux is calculated as

$$q = \psi q_{FB} + (1 - \psi) q_v \quad 2.3.3-63$$

where

$$\psi = \begin{cases} 1 & X \leq 0.95 \\ 20(1 - X) & X > 0.95 \end{cases}$$

and

q_v = single-phase vapor heat flux given by Equation 2.3.3-64.

The partitioning of the energy between the phases is done as described below.

$$q_{wf} = \psi \alpha_f q_{FB},$$

$$q_{wg} = \psi \alpha_g q_{FB} + (1 - \psi) q_v,$$

$$h_{wf} = q_{wf} / \Delta T_{sat},$$

$$h_{wg} = q_{wg} / (T_w - T_g),$$

and

Γ_w is calculated using Equation 2.2.2-42.

Condie-Bengston IV Correlation¹³⁴

The vapor temperature, T_v , is the saturation temperature, T_{sat} . The heat transfer coefficient, h , is calculated by:

$$h = a \frac{K_g^{0.4593} Pr^{2.2598} Re_g^{[0.6249 + 0.2043 \ln(x + 1)]}}{D_e^{0.8095} (x + 1)^{2.0514}},$$

where

$$a = 0.05345; \left[\frac{W}{m \cdot K} \right]^{0.5407} \left[\frac{1}{m} \right]^{0.1905}$$

K_g = thermal conductivity at T_{sat} ,

Pr = Prandtl number evaluated at T_{wall} ,

Re_g = Reynold's number = $G_{tot} D_e / \mu_g$,

x = equilibrium quality,

D_e = hydraulic diameter.

The total heat transfer coefficient, h , is calculated by

$$h = \text{MAX} [Cl_{FLM} h_{CB}, Cl_{RC} 4K_g/D_e] ,$$

where

Cl_{FLM} = user input constant (default = 1).

The partitioning of the energy between the phases is done as described in the previous section on the CSO correlation.

Single-Phase Vapor Heat Transfer

In single-phase vapor convection h_{wf} , q_{wf} , and Γ_w are zero,

$$q = q_{wg} = q_{conv} + q_{rad} \quad 2.3.3-64$$

This heat flux is calculated based on the cold heat transfer surface area. This area is used in all heat structures with only one exception. A user option has been added to allow adjustment of the surface heat coefficient following clad rupture. When this option has been requested, the heat flux in a ruptured segment heat structure is multiplied by the ratio of the ruptured-to-cold outside cladding radius to approximate the enhanced pin surface area. The heat flux for the steam heat transfer under these conditions is computed by

$$q = \left[\frac{r_{oc_rupt}}{r_{oc_cold}} \right] q_{wg} \quad 2.3.3-64.1$$

The heat transfer coefficient is computed from q as

$$h = h_{wg} = q / (T_w - T_g) \quad 2.3.3-65$$

The convection heat flux, q_{conv} , is calculated as the maximum of the McEligot and Rohsenow-Choi correlations.

$$q_{conv} = \text{MAX}[Cl_{MC} h_{MC}, Cl_{RC} 4.0 k_g/D_e](T_w - T_g) \quad 2.3.3-66$$

where

$$h_{MC} = 0.021 k_g/D_e (Re_g)^{0.8} (Pr_g)^{0.4} (T_g/T_w)^{0.5} \quad 2.3.3-67$$

(McEligot correlation),

and

Cl_{MC} and Cl_{RC} are user input constants (default = 1).

The radiation heat flux, q_{rad} , is calculated using the correlation by Sun⁶⁰ provided T_w is greater than 650 K and T_w is greater than T_g .

$$q_{rad} = F_{wg} \sigma_{SB} (T_w^4 - T_g^4) \quad 2.3.3-68$$

where

σ_{SB} = Stefan-Boltzman constant ($5.67 \cdot 10^{-8} \text{ w/m}^2\text{K}^4$), and

$$F_{wg} = \frac{1}{[(1 - \epsilon_w)/\epsilon_w + 1/\epsilon_g]}$$

The emissivity of water vapor, ϵ_g , is given by

$$\epsilon_g = 1 - \exp(-a_g L_m),$$

where

L_m is the mean beam length, $0.85 D_e$. The absorption coefficient, a_g , for vapor⁶¹ is given by

$$a_g = 1.813244 \cdot 10^{-4} P \left[\frac{555.56}{T_g} \right]^2 \left\{ 1 - 0.05357 \left[\frac{555.56}{T_g} \right]^2 \right\} .$$

2.3.3-69

For the wall emissivity, ϵ_w , the user has the following options.

$$\epsilon_w = \text{user input (default = 0.67)}, \quad 2.3.3-70$$

or if the core heat transfer model is coupled with the core pin model, ϵ_w can be calculated using the MATPRO-Version 10 correlation¹³³ as given below.

If $T_w \leq 1500 \text{ K}$,

$$\epsilon_w = \begin{cases} 0.325 + 0.1246 \cdot 10^6 \delta & \delta \geq 3.88 \cdot 10^{-6} \text{ m} \quad 2.3.3-71 \\ 0.808642 - 50 \delta & \delta < 3.88 \cdot 10^{-6} \text{ m}, \quad 2.3.3-72 \end{cases}$$

where

δ is the oxide thickness.

If $T_w > 1500$ K

$$\epsilon_w = \text{MAX}\{0.325, \epsilon_w^i \exp[(1500 - T_w)/300]\}, \quad 2.3.3-73$$

where ϵ_w^i is the wall emissivity calculated using the Equation 2.3.3-71 or Equation 2.3.3-72.

2.4. Initial Conditions, Boundary Conditions, and Steady-State Calculations

All transient analysis problems require initial conditions from which to begin the transient simulation. Usually the initial conditions will correspond to a steady-state with the transient initiated from a change at some boundary condition. In general, the initial conditions required are a determinate set of the dependent variables of the problem. The hydrodynamic model requires four thermodynamic state variables at each hydrodynamic volume and the two velocities at each junction. Heat structures require the initial temperature at each node, control systems require the initial value of all control variables, and the kinetics calculations require the initial power and reactivity. All of these parameters are established through the code input and initialization process for a new problem. For a restarted problem, the values are established from the previous calculation. For restart with renodalization or some problem changes, the initialization will result from a combination of the two processes.

Typically, detailed problems require a period of code execution with constant boundary conditions in order to acquire consistent steady-state values of the hydrodynamic variables. The code may be executed in either the normal transient mode or a special steady-state mode determined by user control. The transient mode requires the user to determine if steady-state exists, while the code evaluates the convergence with the steady-state option. A discussion of the special steady-state calculation treatment is included in this section.

Boundary conditions may be required for hydrodynamic models, heat structures, or control components if there are parameters governed by conditions outside of the problem boundaries. These could be mass and energy in flows or an externally specified control parameter. A description of the generalized boundary conditions is included in this section.

2.4.1. Initial Conditions

All variables of the problem which are established by integration require initial values in order to begin a calculation or simulation. Problem variables which are related through quasi-steady relationships to the integration variables do not require initial conditions since they can be established from the initial values required in integration variables. An example is the pump head which is related to the pump flow and speed, both of which are obtained by integration and thus require initial conditions.

Input initial values are required in order to begin a new problem whether a steady-state or transient run is selected. These initial values are supplied by the user through card input for each component (heat structure is an exception and can be initialized by input or by a steady-state initialization using the heat structure boundary conditions at time zero).

The hydrodynamic volume components have seven options for specifying the volume initial conditions. Four options are provided for pure steam/water systems. The remaining three options allow noncondensibles. Boron concentration can be specified with all seven options. Regardless of what option is used, the initialization computes initial values for all primary and secondary dependent variables. The primary variables are the pressure, void fractions, the two phase energies, the noncondensable quality, and the boron concentration. Secondary variables are quality, density, temperature, etc.

Heat structure initial temperatures must be input. Depending upon the initialization option selected these temperatures are either used as initial temperatures or as an initial guess for an iterative solution to the steady-state temperature profile. The iteration solution option will attempt to satisfy the boundary conditions and heat sources/sinks that have been specified through input.

Initial conditions must be specified for each control component which is used, even if the option to compute the initial condition is selected. Theoretically only the integral functions should require initial conditions; however, a sequential single pass solution scheme is used for control components and unless the control variables are input in an order so that no control variables appear as arguments until after they are defined will the input initial condition not be needed for non-integral functions. The specified initial value for a control variable defined by integration is always needed.

The reactor kinetics model requires specification of an initial power and reactivity, and previous power history data may be entered.

2.4.2. Steady-State Initialization

RELAPS/MOD2 contains an option for steady-state calculations. This option uses the transient hydrodynamic, kinetics, and controls algorithms and a modified thermal transient algorithm to converge to a steady-state. The differences between the steady-state and transient options are that a lowered thermal inertia is used to accelerate the response of the thermal transient and a testing scheme is used to check if a steady-state has been achieved. When steady-state is achieved, the run is terminated, thus, saving computer time. The results of the steady-state calculation are saved so that a restart can be made in the transient mode. In this case, all initial conditions for the transient are supplied from the steady-state calculation. It is possible to restart in either the transient or steady-state mode from either a steady-state or transient prior run. The following subsections describe the fundamental concepts of steady-state during transient calculations.

2.4.2.1. Fundamental Concepts for Detecting Hydrodynamic Steady-State During Transient Calculations

The fundamental concept of steady-state is that the state of a system being modeled does not change with respect to time. In the hydrodynamic solution scheme three terms can be monitored whose variation in time include the variation of all of the other terms. These three terms are the thermodynamic density, internal energy, and pressure. Furthermore, these three terms can be combined into a single term, enthalpy. Hence, monitoring the time variation of enthalpy is equivalent to monitoring the time variation of all of the other variables in the solution scheme. For each volume cell in the system model the enthalpy can be written as

$$V_i \rho_i^n h_i^n = V_i \left[\rho_i^n U_i^n + P_i^n \right] , \quad 2.4-1$$

where subscript i denotes the i^{th} volume element, superscript n denotes the solution time, t^n , h_i is the volume element enthalpy in units of energy per unit mass, V_i is the element volume that is constant, and ρ_i , U_i , and P_i are the thermodynamic density, internal energy and pressure, respectively, of the substance within the volume. Since volume is constant, Equation 2.4-1 can be simplified as

$$\rho_i^n h_i^n = \rho_i^n U_i^n + P_i^n . \quad 2.4-2$$

The rate of variation with respect to time can be expressed numerically as

$$\left(\frac{d\rho h}{dt} \right)_i^n = \frac{\left[\rho_i^{n+1} U_i^{n+1} + P_i^{n+1} \right] - \left[\rho_i^n U_i^n + P_i^n \right]}{\Delta t^n} , \quad 2.4-3$$

where superscripts n and $n+1$ denote the old and new time values, respectively. Absolute hydrodynamic steady-state occurs when

Equation 2.4-3 is zero for each of the volume elements in the modeled system.

In order to simplify the task of detecting steady-state a system mean enthalpy can be expressed as

$$\bar{\rho h}^n = \frac{\sum_{i=1}^{NVOLS} v_i (\rho_i^n U_i^n + P_i^n)}{\sum_{i=1}^{NVOLS} v_i} \quad 2.4-4$$

A system mean rate of change can also be formulated as

$$\frac{d\bar{\rho h}}{dt}^n = \frac{1}{\Delta t_n} \frac{\sum_{i=1}^{NVOLS} \left[v_i (\rho_i^{n+1} U_i^{n+1} + P_i^{n+1}) - (\rho_i^n U_i^n + P_i^n) \right]}{\sum_{i=1}^{NVOLS} v_i} \quad 2.4-5$$

However, since the rate of change in any volume element can be positive or negative these terms would tend to cancel. Hence, a better formulation for the mean rate of change is as a mean square summation that can be written as

$$\frac{d\bar{\rho h}}{dt}^2 = \frac{1}{\Delta t_n^2} \frac{\sum_{i=1}^{NVOLS} v_i^2 \left[(\rho_i^{n+1} U_i^{n+1} + P_i^{n+1}) - (\rho_i^n U_i^n + P_i^n) \right]^2}{\sum_{i=1}^{NVOLS} v_i^2} \quad 2.4-6$$

During the course of the problem solution, Equation 2.4-6 can be used to monitor the system approach to steady-state because, as each volume element approaches steady-state, its rate of change

goes to zero and drops out of the summation. The detection of absolute steady-state is therefore relatively simple, since the calculations need only be monitored until Equation 2.4-6 becomes zero. However, another property of Equation 2.4-6 is that it will fluctuate wildly, varying between small and large magnitudes. These fluctuations decrease in magnitude as the calculations proceed toward steady-state. Hence, Equation 2.4-6 is not a well behaved function and it is therefore difficult to monitor its behavior. However, a well behaved function can be curve fitted to the results of this equation over reasonable time intervals. An exponential function is of this type and if

$$\overline{\left(\frac{d\phi h}{dt}\right)^2}^n = y = e^{[\alpha + \beta t^n + \gamma t^{n^2} + \phi t^{n^3}]}$$

$$t_0 \leq t^n \leq t, \quad 2.4-7$$

the coefficients α , β , γ , and ϕ may be computed by the method of least squares over any reasonable time interval greater than four time steps. Equation 2.4-7 has the property that it can increase to large values at small values of time and then decrease to small values as time increases and the system approaches steady state. Equation 2.4-7 represents the time smoothed root mean square (RMS) rate of change in system enthalpy.

Because the user must provide boundary conditions, controls, or trips to guide the transient solution to steady-state, it may not be possible to achieve an absolute steady-state. For example, a steam generator water level control may be modeled so that the water level oscillates between high and low setpoints. In addition, since numerical schemes are inexact, it may only be possible to calculate absolute steady-state within a small limit of precision. For this kind of fluctuating average steady-state, the RMS $(d\phi h/dt)$ will approach a constant positive non-zero value. As a result, an additional method must be used to detect an average steady state over limited time intervals.

If the system $\overline{\rho h}^n$ is varying with time over the interval

$$t_1 \leq t^n \leq t_2 , \quad 2.4-8$$

its variation can be expressed approximately in the form of a straight line such that

$$H^n = b + at^n \approx \overline{\rho h}^n . \quad 2.4-9$$

If the system is approaching an absolute steady state, then the line rate of change will be zero and Equation 2.4-9 will give the system time average ρh such that

$$\overline{\rho h}^{t_1 t_2} = b \quad t_1 \leq t^n \leq t_2 , \quad 2.4-10$$

where the superscript t_1 — t_2 denotes a time average over the interval $t_1 \leq t^n \leq t_2$.

The second testing method consists of monitoring the system ρh^n at the completion of each successful time step and at reasonable time intervals solving for the straight line coefficients a and b using the method of least squares.

In performing the method of least squares, the mean system enthalpy is computed at the successful completion of each time step in the interval

$$t_1 \leq t^n \leq t_2 ,$$

and an equation expressing the sum of the squares of the differences between ρh^n and Equation 2.4-9 can be written as

$$\xi_{\rho h}^2 \left|_{t_1}^{t_2} = \sum_{n=n1}^{n2} \left(\overline{\rho h}^n - b - at^n \right)^2 . \quad 2.4-11$$

The coefficients a and b can then be calculated by the method of least squares.

A measure of the RMS fluctuation of ρh^n with respect to the line of Equation 2.4-9 can also be computed using the mean square form of Equation 2.4-11 where

$$\frac{t_1}{\xi_{\rho h}^2} \frac{t_2}{t_1} = \left[\frac{1}{(n2 - n1)} \xi_{\rho h}^2 \left|_{t_1}^{t_2} \right]^{1/2} . \quad 2.4-12$$

The RMS fluctuation then represents a measure of the typical difference between the mean system enthalpy and the line of Equation 2.4-9. However, the coefficients a and b cannot be calculated with any better precision than the overall precision of the solution scheme for the entire system.

2.4.2.2. Calculational Precision and the Steady-State Convergence Criteria

In the RELAP5/MOD2 solution scheme, after the successful completion of calculations over a time step, three fundamental variables are computed for each volume element in the system modeled. These variables are:

1. $\rho_{m_i}^{n+1}$, the thermodynamic density of the volume substance, where subscript m denotes the solution by conservation of mass.

2. U_i^{n+1} , the thermodynamic internal energy of the volume substance resulting from conservation of energy.
3. P_i^{n+1} , the thermodynamic pressure of the volume substance resulting from the combined solution conserving momentum, mass and energy.

The superscript $n+1$ denotes the new time solution at time $t^{n+1} = t^n + \Delta t^n$. Only three of these variables are required to define the thermodynamic state of the volume substance.

In RELAP5/MOD2, the thermodynamic pressure, phasic internal energies, and vapor volume fraction are used to compute the state utilizing a set of properties tables. In the resulting calculations, a thermodynamic density ρ^{n+1} is calculated corresponding to the solution results. If the pressure and overall internal energy are preserved then the precision of the calculations can be defined as

$$\epsilon_{\rho,i}^{n+1} = \rho_i^{n+1} - \rho_{m,i}^{n+1} \quad 2.4-13$$

for each volume element in the system. If the calculations were exact then Equation 2.4-13 would be zero. However the properties tables are limited in precision to a tolerance of ± 1 in the fifth significant figure and in statistical terminology the mean expected precision would be approximately ± 5 in the sixth significant figure. If the mean expected precision is considered to be a standard precision, an approximate expression can be written in terms of the property table density

$$\epsilon_{\text{std},\rho,i}^{n+1} = \pm (5 \cdot 10^{-6}) \rho_i^{n+1} \quad 2.4-14$$

which is approximately ± 5 in the density sixth significant figure and which represents the best expected precision for the calculational scheme.

In the steady-state testing scheme, the precision of the volume enthalpy can be written as

$$\epsilon_{\rho h, i}^{n+1} = \rho_i^{n+1} U_i^{n+1} + P_i^{n+1} - \rho_{m_i}^{n+1} U_i^{n+1} + P_i^{n+1} \quad 2.4-15$$

or

$$\epsilon_{\rho h, i}^{n+1} = \left(\rho_i^{n+1} - \rho_{m_i}^{n+1} \right) U_i^{n+1} \quad 2.4-16$$

Similarly, the precision of the rate of change in volume enthalpy can be written as

$$\begin{aligned} \epsilon_{\left(\frac{d\rho h}{dt}\right), i}^{n+1} = \frac{1}{\Delta t^n} \left\{ \left[\left(\rho_i^{n+1} U_i^{n+1} + P_i^{n+1} \right) - \left(\rho_i^n U_i^n + P_i^n \right) \right] \right. \\ \left. - \left[\left(\rho_{m_i}^{n+1} U_i^{n+1} + P_i^{n+1} \right) - \left(\rho_{m_i}^n U_i^n + P_i^n \right) \right] \right\} \quad 2.4-17 \end{aligned}$$

which simplifies to

$$\epsilon_{\left(\frac{d\rho h}{dt}\right), i}^{n+1} = \frac{1}{\Delta t^n} \epsilon_{\rho h, i}^{n+1} \quad 2.4-18$$

For the entire system at the current time step, a statistical precision can be defined, where

$$\epsilon_{\rho h}^{n+1} = \left[\frac{\sum_{i=1}^{NVOLS} v_i^2 \left[\left(\rho_i^{n+1} - \rho_{m_i}^{n+1} \right) U_i^{n+1} \right]^2}{\sum_{i=1}^{NVOLS} v_i^2} \right]^{1/2} \quad 2.4-19$$

for the system mean enthalpy, and where

$$\epsilon \left(\frac{d\rho h}{dt} \right)^{n+1} = \left[\frac{1}{(\Delta t^n)^2} \overline{\epsilon_{\rho h}^2}^{n+1} \right]^{1/2} \quad 2.4-20$$

for the system rate of change in enthalpy.

Simple mean differences for the entire system can also be written as

$$\overline{\delta}_{\rho h}^{n+1} = \frac{\sum_{i=1}^{NVOLS} v_i \left(\rho_i^{n+1} - \rho_{m_i}^{n+1} \right) U_i^{n+1}}{\sum_{i=1}^{NVOLS} v_i} \quad 2.4-21$$

for the system mean enthalpy, and as

$$\overline{\delta} \left(\frac{d\rho h}{dt} \right)^{n+1} = \frac{1}{\Delta t^n} \overline{\delta}_{\rho h}^{n+1} \quad 2.4-22$$

for the system rate of change in enthalpy.

The relationship between the mean difference and precision terms defines the uncertainty characteristics of the overall solution scheme. From Equations 2.4-19 through 2.4-22, it is obvious that

$$-\epsilon_n \leq \delta_n \leq \epsilon_n , \quad 2.4-23$$

where subscript n denotes the particular term, ρh or $d(\rho h/dt)$, being considered. In particular, if ϵ_n is small it can be concluded that calculations are made with a high degree of precision throughout the entire system modeled. If the mean difference term is such that

$$\delta_n \approx 0 , \quad 2.4-24$$

then the overall system solution is said to be unbiased. This means that the overall system mass, energy, and momentum are precisely conserved. However, if

$$\delta_n = \epsilon_n , \quad 2.4-25$$

then the overall system solution is said to be biased. This means that if Equation 2.4-23 is true and

$$\delta_n < 0 , \quad 2.4-26$$

then the overall system solution behaves as if it were losing mass, energy, or momentum. If

$$\delta_n > 0 , \quad 2.4-27$$

then the system solution behaves as if it were gaining mass, energy, or momentum. In RELAP5 the size of the calculational time steps are controlled to maintain a high degree of precision which in turn limits the system bias. However, the

characteristics just described can have an effect in determining time average steady-state.

Since the time average straight line test defined by Equation 2.4-9 is conducted over a time interval, time average precision and mean difference terms must be calculated over the same time interval using the relationships

$$t_1 \frac{t_2}{\epsilon_{\rho h}^2} = \frac{\sum_{n=n1}^{n2} \Delta t^n (\epsilon_{\rho h}^n)^2}{\sum_{n=n1}^{n2} \Delta t^n}, \quad 2.4-28$$

$$t_1 \frac{t_2}{\epsilon_{\frac{d\rho h}{dt}}^2} = \frac{\sum_{n=n1}^{n2} \Delta t^n \left(\epsilon_{\frac{d\rho h}{dt}}^n \right)^2}{\sum_{n=n1}^{n2} \Delta t^n}, \quad 2.4-29$$

$$t_1 \frac{t_2}{\delta_{\rho h}} = \frac{\sum_{n=n1}^{n2} \Delta t^n \delta_{\rho h}^n}{\sum_{n=n1}^{n2} \Delta t^n}, \quad 2.4-30$$

and

$$t_1 \frac{t_2}{\delta_{\left(\frac{d\rho h}{dt}\right)}} = \frac{\sum_{n=n1}^{n2} \Delta t^n \delta_{\left(\frac{d\rho h}{dt}\right)}^n}{\sum_{n=n1}^{n2} \Delta t^n}, \quad 2.4-31$$

where superscript t_1 — t_2 denotes a time average over the time interval and the summation terms n_1 and n_2 denote the number of time steps taken over the interval from t_1 to t_2 , respectively.

Equations 2.4-28 through 2.4-31 represent the precision of the actual calculations relative to the thermodynamic state algorithm. These equations have the characteristic that if the system approaches absolute steady-state both Equations 2.4-28 and 2.4-29 will become very small. Since the properties tables are limited in precision, it is useless in a practical sense to continue calculations if absolute steady-state is achieved with a precision better than that for the properties tables. This criteria can be defined by considering equations similar to Equations 2.4-28 and 2.4-29 but written in terms of the properties tables standard precision. These equations can be derived by simply substituting Equation 2.4-14 for the density difference term in the equations leading to Equations 2.4-28 and 2.4-29.

The steady-state convergence criteria can then be defined by combining the calculational and standard precisions such that

$$\epsilon_{c, \rho h}^{t_1-t_2} = \left\{ \frac{1}{2} \left[\left(\epsilon_{std, \rho h}^{t_1-t_2} \right)^2 + \left(\epsilon_{\rho h}^{t_1-t_2} \right)^2 \right] \right\}^{1/2} \quad 2.4-32$$

for the system mean enthalpy, and

$$\epsilon_{c, \left(\frac{d\phi h}{dt} \right)}^{t_1-t_2} = \left\{ \frac{1}{2} \left[\left(\epsilon_{std, \left(\frac{d\phi h}{dt} \right)}^{t_1-t_2} \right)^2 + \left(\epsilon_{\left(\frac{d\phi h}{dt} \right)}^{t_1-t_2} \right)^2 \right] \right\}^{1/2} \quad 2.4-33$$

for the system rate of change in enthalpy.

These equations represent the steady-state convergence criteria and it can be said that within the limits of calculational and properties precision, time average steady-state is achieved when the mean rate of change in system enthalpy is within the limits of

$$t_1 \frac{t_2}{\epsilon_{c, d\phi h}} \leq a \leq + t_1 \frac{t_2}{\epsilon_{c, d\phi h}} \quad , \quad 2.4-34$$

where a is the mean rate of change in system enthalpy given by Equation 2.4-9. If Equation 2.4-34 is true and if Equation 2.4-7 is such that

$$y \leq t_1 \frac{t_2}{\epsilon_{c, d\phi h}} \quad , \quad 2.4-35$$

then absolute steady-state is achieved. If Equation 2.4-34 is true and

$$y > t_1 \frac{t_2}{\epsilon_{c, d\phi h}} \quad , \quad 2.4-36$$

then the system is fluctuating and time average steady-state is achieved.

2.4.2.3. Steady-State Testing Scheme, Time Interval Control and Output

In the steady-state testing scheme, the concepts discussed for detecting steady-state are used and calculations are performed over time intervals composed of a number of time steps. Because the nature of each problem is different a systematic method of varying the test time intervals is performed.

These tests are performed in two parts. First the system model overall state and rate of change in state are monitored by evaluating Equations 2.4-1 through 2.4-6 and including these results in the least square terms for Equation 2.4-7. At time intervals computed internally, Equation 2.4-7 is evaluated and the current system rate of change is determined. If the rate of change in state is increasing, then a divergent condition is indicated. If the rate of change in state is decreasing or zero, then a convergent condition is indicated. Second, if a convergent condition is indicated, then calculations are performed to determine the system average state and average rate of change in state over the internally computed time intervals. These time averages are formed by obtaining successive overlapping least square solutions for Equation 2.4-8. These successive time average values are compared and the achievement or nonachievement of a time average steady-state is determined. In performing these tests the calculational precision is accounted for by using Equations 2.4-13 through 2.4-36.

In the steady-state scheme, each time a solution for Equation 2.4-7 is obtained, the overall state and steady-state convergence test results are printed. This printout is composed of current time results and time smoothed results integrated over the test time interval. The current time results are (a) the state and rates of change in state resulting from Equations 2.4-4, 2.4-5, and 2.4-6, (b) the current time uncertainties resulting from Equations 2.4-19 through 2.4-22, and (c) the current time mean and root mean square (RMS) mass errors. The time smoothed results that are printed are the current time evaluation of Equation 2.4-7 and the resultant coefficients of Equation 2.4-7 determined by the least squares solution over the time interval from t_1 to the current time TIMEHY. The time, t_1 , corresponds to the time at the successful completion of calculations for the

first time step after problem initiation. For example, if the problem is a NEW problem then t_1 , corresponds to

$$t_1 = 0 + \Delta t_1 , \quad 2.4-37$$

where Δt_1 is the first successful time step. If the problem is a RESTART problem, then t_1 corresponds to

$$t_1 = TREST + \Delta t , \quad 2.4-38$$

where TREST is the time of restart and Δt is the first successful time step after restart. If the results of the overall state tests indicate a convergent condition, then time average tests are initiated.

The time average tests consist of approximating the overall state with a set of three straight lines where each test line is fitted to the calculational results over successive test intervals. The time rates of change of these test lines are then monitored to determine time average steady-state. In the testing scheme, when the time average tests are initiated, calculations continue until the successive test time interval is exceeded. At this time the first test line, Line A, is defined and its results are printed. Calculations then continue until the next successive test time interval is exceeded. At this time, the second test line, Line B, is defined for the second test interval and the third test line, Line C, is defined for the combined first and second test intervals. The results for the three test lines are then printed and tests are performed to determine the achievement of time average steady-state. If steady-state has not been achieved, then test Line A is reset to Line B and the process is repeated until steady-state is achieved.

In the printed edit for time average steady-state tests the results for each of the three test lines are printed. The test line results are obtained by curve fitting Equation 2.4-7 over

each of the line test intervals. The results printed are the endpoints of Equation 2.4-9 evaluated at the test interval start and end times and the time rate of change of Equation 2.4-7. Also printed are the time average uncertainties from Equations 2.4-28 through 2.4-31, the RMS fluctuation of system mean ρh about the line from Equation 2.4-12, and the mass error integrated over the line test interval.

In performing both the overall and the time average sets of tests, calculations proceed through a logic scheme to perform tests that monitor the solution scheme's approach to steady-state. After completing the logic scheme calculations, the steady-state conclusions and next course of action are printed. This printout is composed of statements of the mode of convergence and the state of the system in alphanumeric terms. These statements are defined as the calculations proceed through the logic scheme. To prevent excessive printout during the overall state convergence tests, the first test for overall convergence is not performed until the completion of ten successful time steps. At this time a current test time interval is initialized as $\Delta t_c = \text{TIMEHY} - t_1$. If this test indicates a divergent condition, then the test time interval is increased and the test procedure is repeated. To increase the test time interval, three tests are performed. First, the current test time interval is halved and the time t_2 is estimated as

$$t_2 = \text{TIMEHY} + \frac{1}{2} \Delta t_c . \quad 2.4-39$$

Then Equation 2.4-7 is evaluated as $y(t_2)$. If $y(t_2)$ is greater than the current value of y , then the time t_2 is reset to

$$t_2 = \text{TIMEHY} + \Delta t_c , \quad 2.4-40$$

and Equation 2.4-7 is reevaluated, which results in resetting $y(t_2)$. If $y(t_2)$ is again greater than y , then the time t_2 is again reset to

$$t_2 = \text{TIMEHY} + 2\Delta t_c . \quad 2.4-41$$

In any case, the test time interval is expanded by either maintaining, halving, or doubling the current test time interval based on a projected estimate of the current time smoothed convergence function. This test procedure is then successively repeated until a convergent condition is calculated.

To provide efficiency for the time average testing scheme, upon the first occurrence of an overall state convergent condition the time average testing scheme is activated and the test time interval is redefined by estimating the time interval over which a 10% change in state will occur. This time interval is approximately

$$\Delta t_c \approx 0.1(\overline{\rho h^n})/y . \quad 2.4-42$$

However, to prevent excessively small or large intervals, the time interval is limited such that

$$10 dt \leq \Delta t_c \leq 100 dt , \quad 2.4-43$$

where dt is the current calculational time step. The calculations for the time average scheme then proceed with each successive test time interval specified 10% larger than the time interval just completed. As the calculations progress and approach steady-state, the line segments approach a constant value within the steady-state convergence criteria. When this condition is met, the test time interval is doubled. If this condition is recursively maintained for two more successive test intervals then a final steady-state has been achieved and the

calculations are terminated. If the line segment tests indicate that the solution is diverging from steady-state the results of the time average tests are discarded. When the conditions of Equation 2.4-7 again become true, the time average tests are reinitiated and the procedure is continued until steady-state is achieved.

2.4.2.4. Heat Structure Heat Conductance Scheme for Steady-State

In both the steady-state and transient solution schemes the same transient heat transfer algorithm is utilized. However, in the steady-state scheme the heat structure heat capacity data input by the user are ignored. Instead, this term is evaluated as an artificially small number such that

$$\frac{\rho C_p (\Delta x)^2}{k \Delta t_{ht}} \geq 2 ,$$

2.4-44

where ρC_p is the heat capacity term, Δx is the heat structure mesh interval, k is the heat structure thermal conductivity and Δt_{ht} is the heat transfer scheme calculational time step. Equation 2.4-44 corresponds to the explicit stability criteria for a transient numerical heat conduction scheme.

In a transient solution scheme, the heat capacity term is treated analogously to a thermal inertia and its magnitude determines the characteristic response time of the conduction solution. For example, ρC_p is typically quite large and on the order of 10^5 or larger. Hence, a large value of ρC_p results in a characteristic response time much greater than the hydrodynamic response time. Indeed, hydrodynamic steady-state can be approximately achieved in reasonably short calculational times before large heat structures have even begun to respond.

2.4.3. Boundary Conditions

Boundary conditions are required in most transient calculations. In reality, boundary conditions take the form of the containment atmosphere, operator actions, or mass and energy sources which are not explicitly modeled as part of the system. Such boundary conditions are simulated by means of a time dependent volume, a time dependent junction, a specified heat flux on a heat structure surface, an energy source, or a specified variation of parameters in control components to simulate an operator action. The time variation of the boundary conditions are specified by input tables or can be varied dynamically by use of trips and control variables which effect step changes based on time or any other dependent variable of the simulation. A few of the possible boundary conditions and suggested ways of modeling them will be described.

2.4.3.1. Mass Sources or Sinks

Hydrodynamic mass sources or sinks are simulated by the use of a time dependent volume with a time dependent junction. The thermodynamic state of the fluid is specified as a function of time by input or by a control variable. The time dependent junction flows or velocities are also specified. This approach can be used to model either an inflow or an outflow.

Typical pressurized water reactor applications require simulation of high pressure injection, low pressure injection, main feedwater, and auxiliary feedwater. These inflow conditions are specified for these sources with time dependent junctions which use the flow rate contained within a control variable. Other control variables, trips, functions, or general tables may be used in defining the value of the control variable used for flow control.

2.4.3.2. Pressure Boundary

A pressure boundary condition is modeled using a time dependent volume in which the pressure and thermodynamic state variables are specified as a function of time through input by tables or by a control variable. The time dependent volume is connected to the system through a normal junction, thus, inflow or outflow will result depending upon the pressure difference. For inflow conditions, time dependent volume conditions represent the state of fluid which enters the system. Only the static energy of an incoming flow is fixed by a time dependent volume. The total energy will depend upon the inflow velocity and increases with increasing velocity due to kinetic energy.

The additional boundary conditions represented by a time dependent volume concern the viscous damping terms inherent in the momentum formulation. For this purpose the derivative of velocity across the time dependent volume is zero and the length and volume are assumed to be zero (regardless of the required input). The fact that the energy of inflow increases with velocity can lead to a nonphysical result since the stagnation pressure also increases and for a fixed system pressure an unmitigated increase in inflow velocity can result. This effect can be avoided by making the cross sectional area of the time dependent volume large compared to the junction so that the volume velocity of the time dependent volume is small and thus, the total energy of the inflow is constant. When a large area ratio exists between the time dependent volume and the junction connecting it to the system, a reservoir or plenum is simulated. As a general rule, all pressure boundary conditions having either inflow or outflow should be modeled as plenums for stability and realism. In particular, when an outflow is choked the critical flow models more closely approximate the conditions at large expansions (i.e., little or no diffusion occurs). Thus, this assumption is consistent with the choked flow models and is recommended.

2.5. Control System

The control system provides the capability to evaluate simultaneous algebraic and ordinary differential equations. The capability is primarily intended to simulate control systems typically used in hydrodynamic systems but it can also model other phenomena described by algebraic and ordinary differential equations. Another use is to define auxiliary output quantities such as differential pressures so they can be printed in major and minor edits and be plotted.

The control system consists of both control variables and trip functions. Each component is defined by a specific function of time-advanced quantities. The time advanced quantities include: hydrodynamic volumes, junctions, pumps, valves, heat structures, reactor kinetics, trip quantities, and the control variables themselves (including the control variable being defined). This permits a multitude of control components to be developed that perform basic operations, including such things as valve position control, safety system initiation and control, and boundary system flow or pressure control.

2.5.1. Control Variable Components

Nearly every standard engineering function is available in the RELAP5 control variables. The control variables provide arithmetic, integral, differential, proportional-integral, lag, lead-lag, and shaft operation components for user defined calculations. The individual operations are described in detail in the following sections.

In the following equations that define the control components and associated numerical techniques, Y_i is the control variable defined by the i^{th} control component; A_j , R , and S are real constants input by the user; I is an integer constant input by the user; V_j is a quantity advanced in time by RELAP5 and can

include Y_i ; t is time; and s is the Laplace transform variable. Superscripts involving the index n denote time levels. The name in parentheses to the right of the definition is used in input data to specify the component.

2.5.1.1. Arithmetic Control Components

Constant

$$Y_i = S \quad (\text{CONSTANT}) \quad . \quad 2.5.1-1$$

Addition-Subtraction

$$Y_i = S(A_0 + A_1 V_1 + A_2 V_2 + \dots) \quad (\text{SUM}) \quad . \quad 2.5.1-2$$

Multiplication

$$Y_i = S V_1 V_2 \dots \quad (\text{MULT}) \quad . \quad 2.5.1-3$$

Division

$$Y_i = \frac{S}{V_1} \text{ or } Y_i = \frac{S V_2}{V_1} \quad (\text{DIV}) \quad . \quad 2.5.1-4$$

Exponentiation

$$Y_i = S V_1^I \quad (\text{POWERI}) \quad , \quad 2.5.1-5$$

$$Y_i = S V_1^R \quad (\text{POWERR}) \quad , \quad 2.5.1-6$$

and

$$Y_i = S V_1^{V_2} \quad (\text{POWERX}) \quad 2.5.1-7$$

Table Lookup Function

$$Y_i = S F(V_1) \quad (\text{FUNCTION}) \quad 2.5.1-8$$

where F is a function defined by table lookup and interpolation.

Standard Functions

$$Y_i = SF(V_1, V_2, V_3, \dots) \quad (\text{STDFNCTN}) \quad 2.5.1-9$$

where F can be $|V_1|$, $\exp(V_1)$, $\ln(V_1)$, $\sin(V_1)$, $\cos(V_1)$, $\tan(V_1)$, $\tan^{-1}(V_1)$, V_1 , $(V_1)^{1/2}$, $\text{MAX}(V_1, V_2, V_3, \dots)$, and $\text{MIN}(V_1, V_2, V_3, \dots)$. Only MAX and MIN may have multiple arguments.

Delay

$$Y_i = S V_1(t - t_d) \quad (\text{DELAY}) \quad 2.5.1-10$$

where t_d is the delay time. A user input, h, determines the length of the table used to store past values of V_1 . The maximum number of time-function pairs is $h+2$. The delay table time increment is t_d/h . The delayed function is obtained by linear interpolation using the stored past history. As time is advanced, new time values are added to the table. Once the table fills, new values replace values that are older than the delay time.

Unit Trip

$$Y_i = SU (\pm t_r) \quad (\text{TRIPUNIT}) \quad . \quad 2.5.1-11$$

Trip Delay

$$Y_i = ST_r(t_r) \quad (\text{TRIPDLAY}) \quad . \quad 2.5.1-12$$

In the above two trip related components, t_r is a trip number and a negative indicates that the complement of the trip is to be used. U is 0.0 or 1.0 depending on trip t_r (or its complement if t_r is negative) being false or true, and T_r is -1.0 if the trip is false and the time the trip was last set true if the trip is true.

No numerical approximations are involved in evaluating the algebraic components. Evaluation is by simply performing the indicated operations. In the sequence of operations that perform a time advancement of the trip, heat conduction, hydrodynamic, reactor kinetic, and control systems of RELAP5, the control system is processed last. Thus, the end of time step (n+1) values for trip variables t_r and all V_i variables except control variables Y_i are available. The control components are evaluated in component number order. As the first control variable Y_i is being evaluated, only old time values are available for all control component variables. Once Y_i is evaluated, the new time value is available for the remaining control variable evaluations of Y_i . In general, while Y_i is being evaluated, new time values are available for Y_k , $k < i$, and only old time values are available for Y_k , $k \geq i$.

In the example,

$$Y_{10}^{n+1} = A_0 + A_1 T^{n+1} + A_2 P^{n+1} + A_3 Y_8^{n+1} + A_4 Y_{10}^n + A_5 Y_{15}^n, \quad 2.5.1-13$$

T and P, which represent a temperature and pressure from the heat structure or hydrodynamic systems, are new time values. The value Y_8 is also a new time value because it was advanced before control component 10, and Y_{10} and Y_{15} are old time values.

Initialization of the algebraic control components is very similar to a time advancement. At the start of control component initialization, all other time advanced quantities have been initialized. Control component input includes an initial value and a flag that indicates if initialization is to be performed. The initialization proceeds in the order of component numbers. The initial value entered becomes the initial value if no initialization is specified. If initialization is specified, it is simply the specified computation using the available data. If component i references Y_k , $k < i$, the initialized value of Y_k is used; if $k \geq i$, the entered initial value is used.

2.5.1.2. Integration Control Component

The integration component evaluates

$$Y_i = S \int_{t_1}^t V dt_1 \quad (\text{INTEGRAL}), \quad 2.5.1-14$$

where t_1 is the time the component is added to the system, and the initial value at t_1 is the input item regardless of the initialization flag.

The integral is advanced by the trapezoidal approximation

$$y_1^{n+1} = y_1^n + s[v_1^n + v_1^{n+1}] \frac{\Delta t}{2} . \quad 2.5.1-15$$

Both new time (n+1) and old time (n) values are available for V_1 except when it is a control variable Y_k , $k \geq i$. For the case when $V_1 = Y_k$, $k \geq i$, the v^n and v^{n+1} are instead v^{n-1} and v^n .

$$y_1^{n+1} = y_1^n + s[v_1^{n-1} + v_1^n] \frac{\Delta t}{2} . \quad 2.5.1-16$$

Use of the integral component when old time values will be used should be avoided. Consider the example

$$a = P_1 - P_2 - BV - kd, \quad 2.5.1-17$$

$$v = \int a dt, \quad 2.5.1-18$$

and

$$d = \int v dt. \quad 2.5.1-19$$

This acceleration-velocity-distance system cannot be advanced without use of old values. As a general rule, it is considered better to use the old value in the algebraic expression and not in the integral expressions.

Thus, using $Y_1 = a$, $Y_2 = V$, and $Y_3 = d$;

$$Y_1 = P_1 - P_2 - BY_2 - kY_3, \quad 2.5.1-20$$

$$Y_2 = \text{INTEGRAL } (Y_1), \quad 2.5.1-21$$

and

$$Y_3 = \text{INTEGRAL}(Y_2).$$

2.5.1-22

2.5.1.3. Differentiation Control Components

Two components provide for differentiation

$$Y_i = \frac{dV_1}{dt}$$

One component evaluates the derivative by the inverse of the integration technique

$$Y_i = \frac{2S}{\Delta t} (V_1^{n+1} - V_1^n) - Y_i^n \quad (\text{DIFFERNI}) \quad 2.5.1-23$$

This component is not recommended since it can be unstable, requires an accurate initial value, and does not recover from a bad initial value. The recommended derivative component, uses a simple difference expression

$$Y_i = S \frac{(V_1^{n+1} - V_1^n)}{\Delta t} \quad (\text{DIFFERNI}) \quad 2.5.1-24$$

Differentiation is a noisy process and should be avoided. Differentiation of control system variables can almost always be avoided. Filtering the result of differentiation of other variables should be considered. Similar to the case of the integral component, old time values are used when advancement of Y_1 involves $V_1 = Y_k, k \geq i$.

2.5.1.4. Proportional-Integral Component

This component evaluates

$$Y_1 = S \left[A_1 V_1 + A_2 \int_{t_1}^t V_1 dt \right] \quad (\text{PROP-INT}) \quad 2.5.1-25$$

or in Laplace transform notation

$$Y_1(s) = S \left[A_1 + \frac{A_2}{s} \right] V_1(s). \quad 2.5.1-26$$

This component is advanced in time by

$$I^{n+1} = I^n + \left(V_1^n + V_1^{n+1} \right) \frac{\Delta t}{2} \quad 2.5.1-27$$

and

$$Y_i^{n+1} = S \left(A_1 V_1^{n+1} + A_2 I^{n+1} \right) \quad 2.5.1-28$$

The comments in the previous section concerning integration with $V_1 = Y_k$ hold for this component.

If the initialization flag is off, Y^* is the entered initial value and

$$I^* = \frac{1}{A_2} \left(\frac{Y_i^*}{S} - A_1 V_1^* \right) \quad 2.5.1-29$$

If the initialization flag is on

$$I^* = 0 \quad 2.5.1-30$$

and

$$Y_i = SA_1 V_1 \quad . \quad 2.5.1-31$$

2.5.1.5. Lag Control Component

The lag component is defined in Laplace transform notation as

$$Y_i(s) = S \left[\frac{1}{1 + A_1 s} \right] V_1(s) \quad (\text{LAG}) \quad . \quad 2.5.1-32$$

Through algebraic rearrangement

$$Y_i(s) + A_1 s Y_i(s) = S V_1(s) \quad , \quad 2.5.1-33$$

$$\frac{Y_i(s)}{s} + A_1 Y_i(s) = \frac{S V_1(s)}{s} \quad , \quad 2.5.1-34$$

or

$$Y_i(s) = \frac{S V_1(s) - Y_i(s)}{A_1 s} \quad . \quad 2.5.1-35$$

Transforming to the time domain gives

$$Y_i = \int_0^t [S V_1 - Y_i] dt \quad . \quad 2.5.1-36$$

The above expression is advanced numerically by

$$Y_i^{n+1} = Y_i^n + \left[S(V_1^n + V_1^{n+1}) - Y_i^n - Y_i^{n+1} \right] \frac{\Delta t}{2A_1} \quad 2.5.1-37$$

or

$$y_i^{n+1} = \frac{y_i^n \left[1 - \frac{\Delta t}{2A_1} \right] + s \left[v_1^n + v_1^{n+1} \right] \frac{\Delta t}{2A_1}}{1 + \frac{\Delta t}{2A_1}} \quad 2.5.1-38$$

If the initialization flag is set,

$$y_i^* = s v_1^* \quad 2.5.1-39$$

2.5.1.6. Lead-Lag Control Component

The lead-lag component is defined in Laplace transform notation as

$$Y_i(s) = s \left[\frac{1 + A_1 s}{1 + A_2 s} \right] V_1(s) \quad (\text{LEAD-LAG}) \quad 2.5.1-40$$

Rearranging algebraically, this yields

$$Y_i(s) + A_2 s Y_i(s) = s V_1(s) + A_1 s s V_1(s) \quad 2.5.1-41$$

or

$$Y_i(s) = \frac{A_1 s V_1(s)}{A_2} + \frac{s V_1(s) - Y_i(s)}{A_2 s} \quad 2.5.1-42$$

Transforming to the time domain gives

$$y_i = \frac{A_1 s V_1}{A_2} + \int_0^t \left[\frac{s V_1 - y_i}{A_2} \right] dt \quad 2.5.1-43$$

Note that the differentiation implied by the $sv_1(s)$ term has been avoided.

The above expression is advanced numerically by

$$y_i^{n+1} = \frac{A_1}{A_2} s v_1^{n+1} + I^n + \left[s \left[v_1^n + v_1^{n+1} \right] - y_i^n - y_i^{n+1} \right] \frac{\Delta t}{2A_2} \quad 2.5.1-44$$

or

$$y_i^{n+1} = \frac{\frac{A_1}{A_2} s v_1^{n+1} + I^n + \left[s \left[v_1^n + v_1^{n+1} \right] - y_i^n \right] \frac{\Delta t}{2A_2}}{1 + \frac{\Delta t}{2A_2}} \quad 2.5.1-45$$

and finally

$$I^{n+1} = I^n + \left[s \left[v_1^n + v_1^{n+1} \right] - y_i^n - y_i^{n+1} \right] \frac{\Delta t}{2A_2}. \quad 2.5.1-46$$

If no initialization is specified, $I^* = 0$ and Y_i is the entered initial value. If initialization is specified, then

$$y_i^* = sv_1^* \text{ and } I^* = \left[1 - \frac{A_1}{A_2} \right] sv_1^*. \quad 2.5.1-47$$

For both lag and lead-lag components, if $v_1 = Y_k$: $k = i$ is an error; when $k < i$, old and new values are used as indicated; if $k > i$, v_1^n and v_1^{n+1} are really y_k^{n-1} and y_k^n .

2.5.1.7. Shaft Component

The shaft component is a specialized control component that advances the rotational velocity

$$\sum_i I_i \frac{d\omega}{dt} = \sum_i r_i - \sum_i f_i \omega + r_c \quad (\text{SHAFT}) , \quad 2.5.1-48$$

where I is the moment of inertia, r_i is the torque from component i , f_i is friction, and r_c is an optional torque from a control component. The summations are over the pump, generator, motor, or turbine components that might be connected to the shaft and the shaft itself. The shaft and each associated component contains its own model, data, and storage for inertia, friction, and torque, and has storage for its rotational velocity. Each associated component also has a disconnect trip number. If zero (no trip) the component is always connected to the shaft. If a trip is specified, the component is connected when false and disconnected when true. Any disconnected component is advanced separately and thus can have a different rotational velocity than the shaft. All connected components have the same rotational velocity.

The shaft equation is advanced explicitly by

$$\sum_i I_i \frac{(\omega^{n+1} - \omega^n)}{\Delta t} = \sum_i r_i^n - \sum_i f_i^n \omega^n + r_c. \quad 2.5.1-49$$

Inertias, torques, and friction are evaluated using old time information. The torque from the control system, r_c , would be in terms of new time values for quantities other than control variables and would use new or old time values for control variables depending on their component numbers relative to the shaft component number. Except when a generator component is involved, the shaft component calculations consist of solving

Equation 2.5.1-49 for ω_{n+1} separately for each component disconnected from the shaft (if any) and for the shaft and the connected components as one system. For separated components, the new rotational velocity is stored with the component data and the summations are only over terms within the component. For the shaft and the connected components, the summations are over the shaft and the connected components, and the new rotational velocity is stored as the shaft's and each connected component's rotational velocity. A tripped generator, attached or connected, is treated as described above. An untripped generator rotates at the input synchronous speed, and if connected to the shaft, the shaft and all connected components are forced to the synchronous speed.

2.5.2. Trip System

The trip system consists of the evaluation of logical statements. Each trip statement is a simple logical statement which has a true or false result and an associated variable, TIMEOF. The TIMEOF variable is -1.0 whenever the trip is false and contains the time the trip was last set true whenever the trip is true. This variable allows for time delays and unit step functions based on events during the transient.

Within the structure of RELAP5, the trip system is considered to be only the evaluation of the logical statements. The decision of what action is needed, based on trip status resides within other models. For example, valve models are provided that open or close the valve based on trip values; pump models test trip status to determine whether a pump electrical breaker has tripped.

Two types of trip statements are provided, variable and logical trips. Since logical trips involve variable trips and other logical trips, complex logical expressions can be constructed from simple logical statements. Both types of trips can be

latched or unlatched. A latched trip, once set true, is no longer tested and remains true for the remainder of the problem or until reset at a restart. An unlatched trip is evaluated every time step.

2.5.2.1. Variable Trips

A variable trip evaluates the statement

$$T_{ri} = V_1 \text{ OP } (V_2 + C) \quad . \quad 2.5.2-1$$

The value T_{ri} is the i^{th} trip variable that may be true or false. Values V_1 and V_2 are quantities from the heat structures, hydrodynamics, reactor kinetics, control systems, or may be a TIMEOF quantity. C is a constant; OP is one of the arithmetic relational operations; EQ is equal; NE is not equal; GT is greater than; GE is greater than or equal; LT is less than; and LE is less than or equal.

Trips are evaluated at the beginning of the overall RELAP5 time advancement and are evaluated in numerical order. Except for TIMEOF variables, all other V quantities have beginning of time step values and the results of the trip evaluation are independent of the evaluation order. But when a variable trip statement references TIMEOF (T_{rk}), the new value of TIMEOF is used if $k < i$.

2.5.2.2. Logical Trips

A logical trip evaluates

$$T_{ri} = \pm T_{rj} \text{ OP } \pm T_{rp} \quad . \quad 2.5.2-2$$

The values T_{rj} and T_{rp} are variable or logical trips and the minus sign if present denotes the complement of the trip value.

The value OP is one of the logical operations, AND, OR (inclusive or), or XOR (exclusive or).

Logical trips are evaluated following the evaluation of variable trips and are evaluated in numerical order. When T_{rj} (or T_{rp}) is a variable trip, new trip values are used; when T_{rj} is a logical trip used in logical trip expression i , new values are used when $j < i$, and old values are used when $j \geq i$.

This page is intentionally left blank.

3. PROGRAMMING METHODS

The RELAP5 code architecture is the result of experience with the development of large thermal-hydraulic computer codes at INEL. Convenience, allowance for future modifications, and computer efficiency were primary considerations in designing RELAP5. This section presents the basic organization of the code, a brief discussion of the numerical approach, the order of processing of the solution, and a discussion of the treatment of approximations and accumulated mass and energy decrements.

3.1. Top Level Organization

RELAP5 is coded in a modular fashion using top down structuring. The various models and procedures are isolated in separate subroutines. The top level structure is shown in Figure 3.1-1 and consists of input, steady-state, transient, plotting, and stripping blocks.

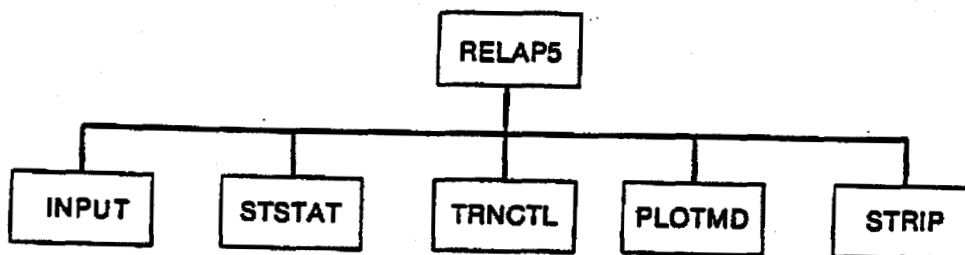


Figure 3.1-1. RELAP5 Top Level Structure.

The input block processes input, checks input data, and prepares required data blocks for all program options.

The steady-state block determines the steady state conditions if a properly posed steady-state problem is presented. The steady-state is obtained by running an accelerated transient until the time derivatives approach zero. Thus, the steady-state block is very similar to the transient block but contains convergence testing algorithms to determine satisfactory steady-state, divergence from steady-state, or cyclic operation. With this technique, approach to steady-state from an initial condition would be identical to a plant transient from the initial condition. Pressures, densities, and flow distributions would adjust quickly, but thermal effects would occur more slowly. To reduce the transient time required to reach steady-state, the steady-state option artificially accelerates heat conduction by reducing the heat capacity of the conductors.

The transient block advances the transient solution. Further discussion of this and the equivalent portions of the steady-state block is given in section 3.2.

The plotting block produces time history plots of simulation results generated from the steady-state or transient blocks. This block can also produce plots from data saved on a restart-plot file from an earlier simulation.

The strip block extracts simulation data from a plot-restart file for convenient passing of RELAP5 simulation results to other computer programs.

3.2. Transient and Steady-State Overview

Figure 3.2-1 shows the second-level structures for the transient and steady-state blocks or subroutines. Since these blocks are nearly identical, the transient blocks are discussed with equivalent steady-state block names shown in parentheses.

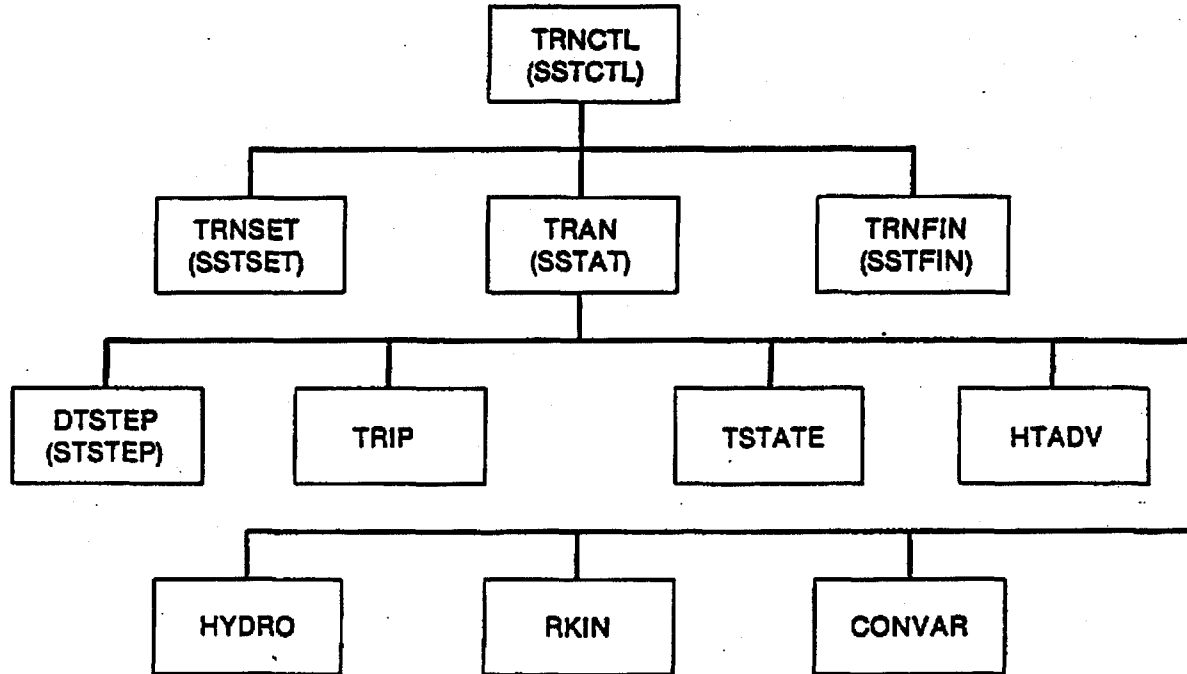


Figure 3.2-1. Transient (Steady-State) Structure.

The Subroutine TRNCTL (SSTCTL) consists only of the logic to call the next lower level routines. Subroutine TRNSET (SSTSET) brings dynamic blocks required for transient execution from disk into SCM or LCM, performs final cross-linking of information between data blocks, sets up arrays to control the sparse matrix solution, establishes scratch work space, and returns unneeded SCM and LCM memory. Subroutine TRAN (SSTAT) controls the transient advancement of the solution. Nearly all the execution time is spent in this block and this block is the most demanding of memory. Nearly all the dynamic data blocks must be in SCM and LCM, and the memory required for instruction storage is high

since coding to advance all models resides in this block. The TRAN block is a single segment. Further segmentation results in a significant execution time penalty because the processing time to complete one advancement is of the same order of magnitude as required to load one segment from disk. In order to avoid the excessive delay in waiting for disk transfers of segments, a segment when first loaded is copied to LCM. Subsequent references to the segment use the fast LCM-SCM transfer. The Subroutine TRNFIN (SSTFIN) releases space for the dynamic data blocks that are no longer needed and prints the transient timing summary.

Figure 3.2-1 also shows the structure of the TRAN (SSTAT) block. DTSTEP (STSTEP) determines the time step size and whether transient advancement should be terminated. TSTATE applies hydrodynamic boundary conditions by computing thermodynamic conditions for time dependent volumes and velocities for time dependent junctions. The remaining blocks perform or control the calculations for major models within RELAP5: trip logic (TRIP), heat structure advancement (HTADV), hydrodynamic advancement (HYDRO), reactor kinetics advancement (RKIN), and control system advancement (CONVAR). The blocks are executed in the order shown in the figure from left to right, top to bottom. Although implicit techniques are used within some of the blocks (HTADV and HYDRO), data exchange between blocks is explicit, and the order of block execution dictates the time levels of feedback data between models. Thus, HTADV advances heat conduction/convection solutions using only old time reactor kinetics power and old time hydrodynamic conditions. HYDRO, since it follows HTADV, can use both new and old time heat transfer rates to compute heat transferred into a hydrodynamic volume.

3.3. Solution Accuracy

The semi-implicit and nearly-implicit solution methods are mass and energy conservative. The mass from the state relationship is compared to the mass from the continuity equation, and the difference is a measure of the truncation error inherent in the numerical solution. This is the main method used to control the time step and thus control the truncation error even though mass and energy are preserved in the solution scheme.

3.3.1. Time Step Control

A variety of checks on solution acceptability are used to control the time step. These include material Courant limit checks, mass error checks, material properties out of defined ranges, water property errors, excessive extrapolation of state properties in the meta-stable regimes, and a change in heat slab temperature of more than 50 K.

The material Courant limit check is made before a hydrodynamic advancement takes place and, thus, it may reduce the time step, but it does not cause a time step to be repeated. All of the other checks may cause all or part of the time advancement to be repeated at a smaller time step. The material Courant limit is evaluated for each hydrodynamic volume using the volume mass average velocity, that is,

$$(\Delta t_c)_i = [\Delta x \text{MAX}(\alpha_f^n, \alpha_g^n) / \text{MAX}(|\alpha_f^n v_f^n|, |\alpha_g^n v_g^n|)]_i \quad 3.3.1-1$$

$$i = 1, 2, \dots, N.$$

The N volumes are sequentially divided into five subsets, that is, (1, 6, 11, ...) volumes belong to the first subset, (2, 7,

12, ...) volumes belong to the second subset, etc. The five Courant limits for the five subsets are rearranged in ascending order, that is,

$$\Delta t_C^1 \leq \Delta t_C^2 \leq \Delta t_C^3 \leq \Delta t_C^4 \leq \Delta t_C^5 . \quad 3.3.1-2$$

Obviously, Δt_C^1 is the Courant limit for the entire system. This is the number printed at each major edit under "CRNT. DT = ". For the semi-implicit scheme, Δt_C^2 is used for limiting time step size. Thus, partial violation of the material Courant limit is allowed for this scheme. There is no user input option to select the degree of partial Courant limit violation. For the nearly-implicit scheme, five times Δt_C^2 is used for limiting the time step size for the transient mode and 10 times Δt_C^2 is used for limiting the time step size for the steady-state mode.

The mass error check is made after the time step solution is nearly complete and, thus, if excessive mass error is detected then the time step is repeated at a reduced interval. Two types of mass error measures are computed. The first one is designed to check the validity of density linearization and is defined as

$$\epsilon_m = \text{MAX} (|\rho_{mi} - \rho_{si}|/\rho_{fi}, i = 1, 2, \dots, N) , \quad 3.3.1-3$$

where ρ_{mi} is the total density obtained from the mass continuity equation, ρ_{si} is the total density computed from the state relationship, and ρ_{fi} is the liquid density computed from the state relationship. The second one is a measure of overall system mass error and is given by

$$\epsilon_{\text{rms}} = 2 \frac{\sum_{i=1}^N [V_i(\rho_{si} - \rho_{mi})]^2}{\sum_{i=1}^N (V_i \rho_{si})^2} . \quad 3.3.1-4$$

If either ϵ_m or ϵ_{rms} is greater than $2 \cdot 10^{-3}$, the time step is rejected and repeated with one half of the time step size. Otherwise, the time step is accepted and the next time step size is doubled if both ϵ_m and ϵ_{rms} are less than $2 \cdot 10^{-4}$.

At any point in the solution flow if a material property is found to lie outside the defined range then the time step is halved and repeated. This process will proceed until the user specified minimum time step is reached. If the minimum time step is reached without obtaining a valid solution, then the code calculation is terminated and the last time step is repeated with a diagnostic dump printed. A program stop is encountered after completion of this step. This same procedure is applied for all property or extrapolation failures.

3.3.2. Mass/Energy Mitigation

The semi-implicit numerical scheme described in sections 2.1.1.4 and 2.1.1.6 has two calculations of the new time variables α_g , U_g , U_f , and X_n . These variables are first calculated in connection with a linearization of all the product terms involved in the time derivatives and are referred to as tentative new time variables. They are denoted by a tilde in sections 2.1.1.4 and 2.1.1.6. This first calculation uses a numerically conservative form for all flux calculations of mass and energy but because the products in the time derivatives are linearized the quantities $\alpha_g \rho_g$, $\alpha_f \rho_f$, $\alpha_g \rho_g U_g$, $\alpha_f \rho_f U_f$, and $\alpha_g \rho_g X_n$ are not numerically conserved. These tentative new time values are only used to evaluate the interphase heat and mass transfer terms to be used in the second evaluation of the basic equations. In this second evaluation of the basic equations the products appearing in the time derivatives are not linearized. This second step also uses the numerically conservative form for the flux terms. Hence, the final end of time step values have been calculated using an accurate numerically conservative form of differencing.

The truncation errors in the linearization procedure may produce errors in the solution of pressure, phasic energies and void fraction. Since the state is computed from these basic variables, the resultant density may have some error. This error is used in the time step control presented in section 3.3.1. Furthermore, the convective terms in the field equations are computed with donored properties determined by the directions of phasic velocities. There are chances that the final velocities may differ in directions from the explicit velocities used to define the donored properties. This may result in mass/energy errors due to incorrect properties used in the numerical scheme. The scheme used to handle this situation will be presented next.

3.3.3. Velocity Flip-Flop

The term velocity flip-flop refers to the situation in which the final velocities and the explicit velocities differ in sign. In the RELAP5 numerical scheme the pressures and final velocities are calculated using the donor properties based on the explicit velocities. The velocity flip-flop implies that inconsistent donor properties were used for the pressure computation and the final mass/energy computation. This may result in bad velocity and energy solutions and large mass errors.

Let $\bar{\alpha}_{fj}$, $\bar{\rho}_{fj}$, \bar{u}_{fj} , $\bar{\alpha}_{gj}$, $\bar{\rho}_{gj}$, and \bar{u}_{gj} be the junction liquid fraction, liquid density, liquid energy, void fraction, vapor density, and vapor energy respectively, based on the explicit velocities and $\tilde{\alpha}_{fj}$, $\tilde{\rho}_{fj}$, \tilde{u}_{fj} , $\tilde{\alpha}_{gj}$, $\tilde{\rho}_{gj}$, and \tilde{u}_{gj} be the same variables based on the final velocities. A velocity flip-flop has occurred when one of the junctions in a system satisfies the following condition

$$|\bar{\alpha}_{fj} \bar{\rho}_{fj} \bar{u}_{fj} + \bar{\alpha}_{gj} \bar{\rho}_{gj} \bar{u}_{gj} - \tilde{\alpha}_{fj} \tilde{\rho}_{fj} \tilde{u}_{fj} - \tilde{\alpha}_{gj} \tilde{\rho}_{gj} \tilde{u}_{gj}| > 0.20 (\bar{\alpha}_{fj} \bar{\rho}_{fj} \bar{u}_{fj} + \bar{\alpha}_{gj} \bar{\rho}_{gj} \bar{u}_{gj}). \quad 3.3.3-1$$

Under such circumstances, the pressures and final velocities are recalculated using the donor properties of the previously calculated final velocities. The solution is then accepted if no velocity flip-flop exists between the previous final velocities and new final velocities. Otherwise, the time-step size is reduced.

This page is intentionally left blank.

4. REFERENCES

1. V. H. Ransom et al., RELAP5/MOD2 Code Manual, Volumes 1 and 2, NUREG/CR-4312, EGG-2396, August 1985.
2. K. G. Condie, et al., Four Inch Equivalent Break Loss-of-Coolant Experiment Post-Test Analysis of LOFT Experiment L3-1, L3-5, and L3-6, EG&G-LOFT-5480, October 1981.
3. D. L. Reeder, LOFT System and Test Description, NUREG/CR-0247, TREE-1208, July 1978.
4. L.T.L. Dao and J. M. Carpenter, Experimental Data Report for LOFT Nuclear Small Break Experiment L3-5/L3-5A; NUREG/CR-1695, EG&G-2060, November 1980.
5. H. S. Crapo, et al., Experiment Data Report for Semiscale MOD-1 Test S-04-5 and S-04-6 (Baseline ECC Tests), TREE-NUREG-1045, January 1977.
6. L. J. Ball et al., Semiscale Program Description, TREE-NUREG-1210, May 1978.
7. M. S. Sahota, Comparisons of RELAP4/MOD6 With Semiscale Blowdown Data, CVAP-TR-78-023, July 1978.
8. V. H. Ransom, et al., RELAP5/MOD0 Code Description Volume 2 - RELAP5 Code Development Update and Sample Problems, CDAP-TR-057 (Volume 2), July 1978.
9. Deleted.
10. Deleted.
11. M. Ishii, Thermo-Fluid Dynamic Theory of Two-Phase Flow, Direction des Etudes et Recherches of Electricite de France, 1975.
12. F. H. Harlow and A. A. Amsden, "Flow of Interpreting Material Phase," Journal of Computational Physics, 18, pp. 440-464, 1975.

13. P. S. Anderson, P. Astrup, L. Eget, and O. Rathman, "Numerical Experience with the Two-Fluid Model RISQUE," ANS Water Reactor Safety Meeting, July 31-August 4, 1977.
14. N. Zuber, "On the Dispersed Two-Phase Flow in the Laminar Flow Regime," American Institute of Chemical Engineers, 19, pp. 897-917, 1964.
15. L. Van Wijngaarden, "Hydrodynamic Interaction between Gas and Bubbles in Liquid," Journal of Fluid Mechanics, 77, 1, pp. 27-44, 1976.
16. R. T. Lahey, Jr., "RPI Two-Phase Flow Modeling Program," Fifth Water Reactor Safety Research Information Meeting, Washington, D.C., November 7-11, 1977.
17. D. A. Drew, L. Y. Cheng, and R. T. Lahey, Jr., "The Analysis of Virtual Mass Effects in Two-Phase Flow," International Journal of Multiphase Flow, 5, pp 233-242, 1979.
18. J. A. Trapp and V. H. Ransom, "A Choked-Flow Calculation Criterion for Nonhomogeneous, Nonequilibrium Two-Phase Flows," International Journal of Multiphase Flow, 8, 6, pp. 669-681, 1982.
19. A. R. Curtis and J. K. Reid, FORTTRAN Subroutines for the Solution of Sparse Sets of Linear Equations, AERE-R6844, Atomic Energy Research Establishment, 1971.
20. D. Gidaspow (Chairman), "Modeling of Two-Phase Flow," Proceedings of Round Table Discussion RT-1-2 at the Fifth International Heat Transfer Conference, Tokyo, Japan, September 3-7, 1974, also in ASME Journal of Heat Transfer, 3, 1974.
21. J. D. Ramshaw and J. A. Trapp, "Characteristics, Stability, and Short-Wavelength Phenomena in Two-Phase Flow Equation Systems," Nuclear Science and Engineering, 66, pp. 93-102, 1978.
22. Deleted.

23. Deleted.
24. H. B. Stewart, "Fractional Step Methods for Thermodynamic Calculations," Journal of Computational Physics, 40, pp. 77-90, 1981.
25. J. H. Mahaffy, "A Stability-Enhancing Two-Step Method for Fluid Flow Calculations," Journal of Computational Physics, 46, pp. 329-341, 1982.
26. Deleted.
27. Y. Taitel and A. E. Dukler, "A Model of Predicting Flow Regime Transitions in Horizontal and Near Horizontal Gas-Liquid Flow," AIChE Journal, Vol. 22, pp. 47-55, 1976.
28. Y. Taitel, D. Bornea, and A. E. Dukler, "Modeling Flow Pattern Transitions for Steady Upward Gas-Liquid Flow in Vertical Tubes," AIChE Journal, Vol. 26, pp. 345-354, 1980.
29. M. Ishii and G. De Jarlais, "Inverted Annular Flow Modeling," presented at EG&G, July 27, 1982.
30. M. Ishii and T. C. Chawla, Local Drag Laws in Dispersed Two-Phase Flow, NUREG/CR-1230, ANL-79-105, 1979.
31. M. Ishii and K. Mishima, Study of Two-Fluid Model and Interfacial Area, NUREG/CR-1873, ANL-80-111, 1980.
32. M. A. Vince and R. T. Lahey, Jr., "On the Development of An Objective Flow Regime Indicator," International Journal of Multiphase Flow, 8, pp. 93-124, 1982.
33. D. T. Dumitrescu, "Stomung an einer Luftblase in senkrechten Rohr," Z. Angew Math. Mech. 23, 139, 1943.
34. G. B. Wallis, One-Dimensional Two-Phase Flow, McGraw-Hill Book Company, New York, 1969.
35. A. H. Shapiro and A. J. Erickson, Transactions of ASME, 79, p. 775, 1957.

36. D. Bharathan, H. T. Richter, and G. B. Wallis, Air-Water Counter-Current Annular Flow in Vertical Tubes, EPRI, NP-786, 1978.
37. K. T. Chaxton, J. G. Collier, and A. J. War, H.T.F.S. Correlation for Two-Phase Pressure Drop and Void Fraction in Tubes, AERE-R7162, 1972.
38. D. Chisholm, "A Theoretical Basis for the Lockhart-Martinelli Correlation for Two-Phase Flow," J. Heat-Mass Transfer, Vol. 10, pp. 1767-1778, Pergamon Press Ltd., 1967; Great Britain.
39. R. W. Lockhart and R. C. Martinelli, "Proposed Correlation of Data for Isothermal Two-Phase, Two-Component Flow in Pipes," Chemical Engineering Progress, 45, 1, pp. 39-48, 1949.
40. F. W. Dittus and L. M. K. Boelter, "Heat Transfer in Automobile Radiators of the Tubular Type," Publications in Engineering, University of California, Berkeley, 2, pp. 443-461, 1930.
41. J. C. Chen, "A Correlation for Boiling Heat Transfer to Saturated Fluids in Convective Flow," Process Design Development, 5, pp. 322-327, 1966.
42. L. S. Tong, and J. D. Young, "A Phenomenological Transition and Film Boiling Correlation," Proceedings of the 5th International Heat Transfer Conference, Vol. IV, B 3.9, Tokyo, 1974.
43. J. C. Chen et al., A Phenomenological Correlation for Post-CHF Heat Transfer, TS-774, Dept. of M. E., Lehigh University, April 1977.
44. J. G. Collier, Convection Boiling and Condensation, London: McGraw-Hill Book Company, Inc., 1972.
45. Deleted.
46. Deleted.

47. M. S. Plesset and S. A. Zwick, "Growth of Vapor Bubbles in Superheated Liquids," Journal of Applied Physics, 25, 4, 493-500, 1954.
48. F. Kreith, Principles of Heat Transfer, New York: Intext Press, Inc., 1973.
49. H. C. Unal, "Maximum Bubble Diameter, Maximum Bubble-Growth Time and Bubble-Growth Rate During the Subcooled Nucleate Flow Boiling of Water Up to $17. \text{MN/m}^2$," International Journal of Heat Mass Transfer, 19, pp. 643-649, 1976.
50. G. Brown, "Heat Transmission by Condensation of Steam on a Spray of Water Drops," Institute of Mechanical Engineers, pp. 49-52, 1951.
51. T. G. Theofanous, "Modeling of Basic Condensation Processes," The Water Reactor Safety Research Workshop on Condensation, Silver Springs, MD, May 24-25, 1979.
52. A. E. Bergles and W. M. Rohsenow, "The Determination of Forced-Convection Surface-Boiling Heat Transfer," Journal of Heat Transfer, Transactions of ASME, 86, p. 365, 1964.
53. Deleted.
54. T. A. Bjornard and P. Griffith, "PWR Blowdown Heat Transfer," Thermal and Hydraulic Aspects of Nuclear Reactor Safety, ASME, New York, Vol. 1, 17, 1977.
55. Deleted.
56. S. Wang, Y. K. Kao, and J. Weisman "Studies of Transition Boiling Heat Transfer with Saturated Water at 1-4 Bar," Nuclear Engineering Design, 70, p. 223, 1982.
57. Deleted.
58. Deleted.
59. J. M. Delhaye, M. Giot and M. L. Reithmuller, Thermohydraulics of Two-Phase Systems for Industrial Design and Nuclear Engineering, pp. 261-262, 1981.

60. K. H. Sun, J. M. Gonzalez, and C. L. Tien, "Calculations of Combined Radiation and Convection Heat Transfer in Rod Bundles under Emergency Cooling Conditions," Journal of Heat Transfer, Transactions of ASME, 98, p. 414, 1976.
61. W. L. Kirchner, Reflood Heat Transfer in Light Water Reactors, NUREG-0106, August 1976.
62. V. H. Ransom and J. A. Trapp, "The RELAP5 Choked Flow Model and Application to a Large Scale flow Test," Proceedings of the ANS/ASME/NRC International Topical Meeting on Nuclear Reactor Thermal-Hydraulics, Saratoga Springs, New York, October 5-8, 1980.
63. P. R. Garabedian, Partial Differential Equations, New York: John Wiley and Sons, 1964.
64. G. B. Whitham, Linear and Nonlinear Waves, New York: John Wiley and Sons, 1974.
65. A. H. Shapiro, The Dynamics and Thermodynamics of Compressible Fluid Flow. II, New York: Ronald, 1954.
66. V. H. Ransom and J. A. Trapp, RELAP5 Progress Summary Analytical Choking Criterion for Two-Phase Flow, CDAP-TR-013, EG&G Idaho, Inc., 1978.
67. N. Abuaf, O. C. Jones, Jr., and B. J. C. Wu, Critical Flashing Flow in Nozzles with Subcooled Inlet Conditions, BNL Informal Report, BNL-NUREG-27512, 1980.
68. M. D. Alamgir and J. H. Lienhard, "Correlation of Pressure Undershoot During Hot Water Depressurization," ASME Journal of Heat Transfer, 103, pp. 52-73, 1981.
69. O. C. Jones, Jr., "Flashing Inception in Flowing Liquids," ASME Journal of Heat Transfer, 102, pp. 439-444, 1980.
70. J. W. Burnell, "Flow of Boiling Water through Nozzles, Orifices, and Pipes," Engineering, pp. 572-576, 1947.

71. F. J. Moody, "Maximum Flow Rate of a Single Component, Two-Phase Mixture," Transactions of the American Society of Mechanical Engineers, February 1965, pp. 136-143.
72. W. M. Bryce, Improvements to the RELAP5/MOD1/014 LOCA Code: The RELAP5/MOD1/WIN001 Code, AEEW-R-1649, pp. 64-65, May 1983.
73. N. Zuber, Problems in Modeling of Small Break LOCA, NUREG-0724, October 1980.
74. H. Rouse, "Seven Exploratory Studies in Hydraulics," Proceedings of ASCE, Vol. 82, 1956.
75. A. Craya, "Theoretical Research on the Flow of Non-Homogeneous Fluids," La Houille Blanche, pp. 44-45, January-February 1949.
76. P. Gariel, "Experimental Research on the Flow of Non-Homogeneous Fluids," La Houille Blanche, pp. 56-64, January-February 1949.
77. B. Lubin and M. Hurwitz "Vapor Pull-Through at A Tank Drain--With and Without Dielectrophoretic Baffling," Proc. Conf. Long Term Cryo-Propellant Storage in Space, NASA Marshall Space Center, Huntsville, Alabama, p. 173, October 1966.
78. J. C. Lin, G. E. Gruen, and W. J. Quapp, "Critical Flow in Small Nozzles for Saturated and Subcooled Water at High Pressures," ASME Winter Annual Meeting, Chicago, Illinois, November 1980.
79. C. J. Crowley and P. H. Rothe, "Flow Visualization and Break Mass Flow Measurements in Small Break Separate Effects Experiments," ANS Specialists Meeting on Small Break Loss-of-Coolant Accident Analyses in LWRs, Monterey, California, August 1981.

80. J. Reiman and M. Khan, "Flow Through a Small Break at the Bottom of a Large Pipe With Stratified Flow," The Second International Topical Meeting on Nuclear Reactor Thermal-Hydraulics, Santa Barbara, California, January 1983.
81. J. A. Trapp and V. H. Ransom, RELAP5 Hydrodynamic Model Progress Summary--Abrupt Area Changes and Parallel Branching, PG-R-77-92, EG&G Idaho, Inc., November 1977.
82. J. K. Vennard, Elementary Fluid Mechanics, 4th Edition, New York: John Wiley and Sons, 1965.
83. J. Weisman, T. Ake, and R. Knott, "Two-Phase Pressure Drop Across Abrupt Area Changes in Oscillatory Flow," Nuclear Science and Engineering, 61, pp. 297-309, 1976.
84. J. G. Collier, "Advanced Study Institute on Two-Phase Flows and Heat Transfer," ASI Proceedings, Istanbul-Turkey, August 1976.
85. M. M. El-Wakil, Nuclear Heat Transport, Scranton: International Textbook Company, 1971.
86. B. Harshc, A. Hussain, and J. Weisman, Two-Phase Pressure Drop Across Restrictions and Other Abrupt Area Changes, NUREG-0062, University of Cincinnati, April 1976.
87. P. A. Lottes, "Expansion Losses in Two-Phase Flows," Nuclear Science and Energy, 9, pp. 26-31, 1961.
88. J. C. Lin, R. A. Riemke, V. H. Ransom, and G. W. Johnsen, "RELAP5/MOD2 Pressurizer Modeling," ASME Winter Annual Meeting, New Orleans, Louisiana, December 1984.
89. D. R. Liles et al., TRAC-PF1/MOD1: An Advanced Best-Estimate Computer Program for Pressurized Water Reactor Thermal-Hydraulic Analyses, Los Alamos National Laboratory, DRAFT, December 1983.

90. J. H. Mahaffy and D. R. Liles, "Numerically Induced Pressure Excursions in Two-Phase-Flow Calculations," 2nd International Topical Meeting on Nuclear Reactor Thermal Hydraulics, Santa Barbara, California, January 11-14, 1983.
91. V. H. Ransom et al., RELAP5/MOD0 Code Description, Volume 2, Code Development Update and Sample Problems, CDAP-TR-057, May 1979.
92. EG&G Idaho, Inc., RELAP4/MOD6: A Computer Program for Transient Thermal-Hydraulic Analysis of Nuclear Reactors and Related Systems, Users Manual, CDAP-TR-003, EG&G Idaho, Inc., May 1978.
93. Deleted.
94. R. A. Berry, An Analysis Tool for Predicting Transient Hydrodynamics in Nuclear Piping Systems Containing Swing Check Valves, RE-A-78-261, Rev. 2, EG&G Idaho, Inc., 1978.
95. R. S. Samra, "Impact Energy Calculations for a Steam Check Valve Following a Postulated Pipe Rupture," ASME Winter Annual Meeting, December 1978, 76-WA/FE-8.
96. J. P. Holman, Heat Transfer, 4th Edition, New York: McGraw-Hill Book Company, Inc., pp. 244-245, 280, 1976.
97. Deleted.
98. Deleted.
99. Deleted.
100. A. Ullman, R. Acharya and D. R. Olander, "Thermal Accommodation Coefficients of Inert Gases on Stainless Steel and UO_2 ," Journal of Nuclear Materials 51, pp. 277-279, 1974.
101. Deleted.
102. "American Nuclear Society Proposed Standard ANS 5.1, Decay Energy Release Rates Following Shutdown of Uranium-Fueled Thermal Reactors," October 1971, revised October 1973.

103. "American National Standard for Decay Heat Power in Light Water Reactors," ANSI/ANS-5.1, 1979.
104. E. R. Cohen, "Some Topics in Reactor Kinetics," A/CONF. 15, p. 629, 1958.
105. A. Schwartz, Generalized Reactor Kinetics Code AIREK II, NAA-SR-Memo-4980, 1960.
106. Correlation of Critical Heat Flux in a Bundle Cooled by Pressurized Water, BAW-10000, March 1970.
107. R. H. Wilson, D. A. Farnsworth, and R. H. Stoudt, BWC Correlation of Critical Heat Flux, BAW-10143P-A, Babcock & Wilcox, April 1985.
108. D. A. Farnsworth and G. A. Meyer, BWCMV Correlation of Critical Heat Flux in Mixing Vane Grid Fuel Assemblies, BAW-10159P, Babcock & Wilcox, May 1986.
109. P. G. Barnett, A Correlation of Burnout Data for Uniformly Heated Annuli and its Use for Predicting Burnout in Uniformly Heated Rod Bundles, AEEW-R463, September 1966.
110. E. D. Hughes, A Correlation of Rod Bundle Critical Heat Flux for Water in the Pressure Range 150 to 725 psia, IN-1412, Idaho Nuclear, July 1970.
111. R. V. Macbeth, Burn-out Analysis Part 4: Application of a Local Conditions Hypothesis to World Data for Uniformly Heated Round Tubes and Rectangular Channels, AEEW-R267, August 1963.
112. C. T. Avedisian, Critical Heat Flux in Countercurrent Flow, M. S. Thesis, Mass. Inst. Technology, 1974.
113. R. E. Henry and H. K. Fauske, "The Two-Phase Critical Flow of One-Component Mixtures in Nozzles, Orifices, and Short Tubes," ASME Journal of Heat Transfer, 93, Series C, No. 2, 179, May 1971.

114. F. J. Moody, "Maximum Flow Rate of a Single-Component, Two-Phase Mixture," ASME Paper 64-HT-35, 1964.
115. J. W. Murdock and J. M. Bauman, "The Critical Flow Function for Superheated Steam," Journal of Basic Engineering, Transactions of ASME, September 1964.
116. Deleted.
117. D. A. Powers and R. O. Meyers, Cladding Swelling and Rupture Models for LOCA Analysis, NUREG-0630, April 1980.
118. L. J. Siefken, "Calculation of Transient Gap Conductance in TRAC and RELAP5," private communication.
119. D. L. Hagrman, G. A. Reymann, and R. E. Mason, MATPRO-Version 11 (Revision 2), NUREG/CR-4079, TREE-1280, Rev. 2, August 1981.
120. L. Baker, Jr. and L. C. Just, Studies of Metal-Water Reactions at High Temperatures, III - Experimental and Theoretical Studies of Zirconium-Water Reaction, ANL-6548, Argonne, May 1962.
121. P. Saha and N. Zuber, "Point of Net Vapor Generation and Vapor Void Fraction in Subcooled Boiling," Proc. Fifth Int. Heat Transfer Conf., Vol. IV, 1974.
122. Deleted.
123. BAW-10166P, BEACH - A Computer Code for Reflood Heat Transfer During LOCA.
124. Deleted.
125. J. C. Chen, R. K. Sundaram, and F. T. Ozkaynak, A Phenomenological Correlation for Post-CHF Heat Transfer, NUREG-0237, June 1977.
126. S. W. Webb and J. C. Chen, Assessment of Post-Critical Heat Flux Models with Lehigh Nonequilibrium Data, NUREG/CR-4353, April 1986.

127. S. W. Webb and J. C. Chen, "Inferring Nonequilibrium Vapor Conditions in Convective Film Boiling," Thermal-Hydraulics of Nuclear Reactors, Volume 1, The Second International Topical Meeting on Nuclear Reactor Thermal-Hydraulics, Santa Barbara, California, January 11-14, 1983, pp. 326-334.
128. S. W. Webb and J. C. Chen, A Two-Region Vapor Generation Rate Model for Convective Film Boiling, NUREG/CP-0060, The First International Workshop on Fundamental Aspects of Post-Dryout Heat Transfer, Salt Lake City, Utah, April 2-4, 1984, pp. 485-508.
129. J. C. Chen, R. Sundaram, and K. L. Chen, Analysis of Babcock & Wilcox Data on Film Boiling Heat Transfer, Report TS-811, Lehigh University, March 1, 1981.
130. P. Saha and N. Zuber, "Point of Net Vapor Generation and Vapor Void Fraction in Subcooled Boiling," Proc. Fifth Int. Heat Transfer Conf., Vol. IV, 1974.
131. V. H. Schrock and L. M. Grossman, Forced Convection Boiling Studies, Final Report on Forced Convection Vaporization Project, TID-14632, 1959.
132. J. B. McDonough, W. Milich, and E. C. King, Partial Film Boiling with Water at 2000 psia in a Round Tube, MSA Research Corporation, Technical Report 62, 1958.
133. G. A. Reymann, et al., MATPRO-Version 10: A Handbook of Materials Properties for Use in the Analysis of Light Water Reactor Fuel Rod Behavior, TREE-NUREG-1180, February 1978.
134. K. G. Condie, S. J. Bengston, and S. L. Richlin, "Post-CHF Heat Transfer Data Analysis, Comparison and Correlation," EG&G unpublished report.

135. J. F. Wilson, R. J. Grenda, and J. F. Patterson, "The Velocity of Rising Steam in a Bubbling Two-Phase Mixture," Transactions of the American Nuclear Society, Vol. 5, 1962, pp. 151-152.
136. "BEACH -- Best Estimate Analysis Core Heat Transfer," BAW-10166P-A, September 1989.
137. Akimoto, H., T. Iwamura, A. Ohnuki, Y. Abe, and Y. Marao, "Status of J-TRAC Code Development," NUREG/CP-0082, Vol. 5, pp. 381-394, (Proceedings of USNRC's Fourteenth WRSM, October 27-31, 1986).
138. Rousseau, J.C. and G. Houdayer, Advanced Safety Code CATHERE, Summary of Verification Studies on 'Separate Effects' Experiments.
139. Farnsworth, D.A. and Meyer, G.A., "BWCMV Correlation of Critical Heat Flux in Mixing Vane Grid Fuel Assemblies," BAW-10159P-A, Babcock and Wilcox, July 1990.
140. "FOAM2 Computer Program to Calculate Swell Level and Mass Flow Rate During Small-Break LOCA", BAW-10155A, October 1990.
141. Anklam, T.M., R.J. Miller, and M.D. White, "Experimental Investigations of Uncovered-Bundle Heat Transfer and Two-Phase Mixture Level Swell Under High-Pressure Low Heat Flux Conditions", NUREG/CR-2456, 1982.
142. "ROSA-4 Large Scale Test Facility (LSTF) System Description," JAERI-M-84-237, Japan Atomic Energy Research Institute, January 1985.
143. "ROSA-4 LSTF 5% Cold Leg Break LOCA Experiment Run SB-CL-18 Data Report," JAERI-M-89-027, Japan Atomic Energy Research Institute, March 1989.
144. Riemke, R.A., "Report on CCFL and Interphase Drag Models for RELAP5/MOD3", EGG-TFM-8012, INEL, February 1988.

145. "Natural Circulation Cooling In U. S. Pressurized Water Reactors," NUREG/CR-5769, January 1992.
146. "Reactor Safety Issues Resolved By The 2D/3D Program (Draft)," MPR Associates, Inc., November 1991.
147. D. D. Lanning and C. R. Hann, "Review of Methods Applicable to the Calculation of Gap Conductance in Zircaloy-Clad UO₂ Fuel Rods," BNWL-1894, UC-768, April 1975.
148. FRAP-T6-B&W - A Computer Code for the Transient Analysis of Light Water Reactor Fuel Rods, BAW-10165P, October 1988.
149. Sardh, Lars, and K. M. Becker, "Assessments of CHF Correlations Based on Full-Scale Rod Bundle Experiments," Stockholm Royal Institute of Technology, February 1986.
150. "TACO3 - Fuel Pin Thermal Analysis Computer Code," BAW-10162P-A, October 1989.
151. M. P. Bohn, et al., The Licensing Audit Calculation (LACE) Models in the FRAP-T4 Code - Description and Developmental Assessment, EGG-CDAP-5144, April 1980.
152. E. W. Dotson, "19-Tube OTSG Integral Economizer Tests -- Second Series," LR:69:6323-01:1, August 4, 1969.
153. H. R. Carter and D. D. Schleppi, "Nuclear Once-Through Steam Generator (OTSG and IEOTSG) Loss of Feedwater Flow (LOFW) Test," ARC-4707, April 1980.
154. J. A. Klingenfus and M. V. Parece, "RELAP5/MOD2 MIST Analysis Comparisons," Multiloop Integral System Test (MIST): Final Report, Vol. 10, NUREG/CR-5395, December 1989.
155. J. A. Klingenfus and G. E. Anderson, "RELAP5/MOD2 Post-Test Benchmark of Test No. 320201 - 50 CM² Pump Discharge Break," BAW-2002, 77-1168638-00, April 1987.

156. C. A. Schamp and J. A. Klingenfus, "RELAP5/MOD2 MIST Post-Test Benchmark of MIST TEST 3601AA - ATOG With Pumps Available," BAW-2033, 77-1171774-00, December 1988.
157. M. K. Smith and M. V. Parece, "RELAP5/MOD2 MIST Post-Test Benchmark of Test No. 320604 - 10 CM² Pump Discharge Break," BAW-2029, 77-1171643-00, December 1988.
158. M. B. McGuirk and M. V. Parece, "RELAP5/MOD2 MIST Post-Test Benchmark of Test No. 350101 - 10 CM² Primary System Break With High Point Vents," BAW-2032, 77-1168638-00, December 1988.
159. J. C. Seals and P. W. Ploch, "RELAP5/MOD2 MIST Post-Test Benchmark of Test No. 3404AA - Double-Ended Rupture of 10 Steam Generator Tubes," BAW-2031, 77-1171708-00, February 1989.
160. M. K. Smith and M. V. Parece, "RELAP5/MOD2 MIST Post-Test Benchmark of Test No. 3105AA - 10 CM² Pump Discharge Break," BAW-2030, 77-1171703-00, December 1988.
161. N. H. Shah, et al., "FOAM2 - Computer Program to Calculate Core Swell Level and Mass Flow Rate During Small-Break LOCA," BAW-10155, October 1987.
162. Babcock & Wilcox, "Multi-Loop Integral System Test (MIST) Facility Specification," 31-RDD:84:4091-01-01:01.
163. J. A. Klingenfus and J. C. Seals, "RELAP5/MOD2 MIST Post-Test Model Description," BAW-1997, 77-1168359-00, March 1987.
164. D. Farnsworth and K.R. Greene, "BHTP DNB Correlation Applied with LYNXT," BAW-10241(P)(A), Revision 1, July 2005.
165. F.T. Adams, "HTP: Departure From Nucleate Boiling Correlation for High Thermal Performance Fuel," EMF-92-153(P)(A), Revision 1, January 2005.

This page is intentionally left blank.

5.0 LICENSING DOCUMENTS

This section contains documents generated as a result of U.S. Nuclear Regulatory Commission (NRC) review of previous versions of this topical report. Sections 5.1 and 5.2 contain responses to rounds one and two questions, respectively, for revision 1 of this report. These documents were previously issued in the approved proprietary and non-proprietary versions as appendices H and I. Section 5.3 contains the Safety Evaluation Report (SER) issued for revision 1.

Section 5.4 and 5.5 contain responses to NRC questions on revisions 2 and 3, respectively, of this report. Section 5.6 contain supplemental information to revisions 2 and 3. Section 5.7 contains the SER issued for revisions 2 and 3. Section 5.8 contains responses to NRC questions on revision 4. Section 5.9 contains the SER issued for revision 4. Finally, Section 5.10 contains the pages removed or replaced from revision 3 to create revision 4 and Section 5.11 contains pages that were replaced due to SER direction and typographical errors.

This page intentionally left blank.

Rev. 2

8/92

5.1 Responses to Round 1 Request for Additional Information

This section contains round one questions transmitted to B&W by M.W. Hodges of the NRC in his letter of March 31, 1988, and responses transmitted by B&W to the NRC in letters dated August 15, 1988, November 23, 1988, and December 23, 1988.

1. Question: The RELAP5/MOD2 - B&W code manual (BAW-10164P) was reviewed and compared to the RELAP5/MOD2 code manual (NUREG/CR-4312, EGG-2396). Some discrepancies between the two manuals were noted in the equations shown below. Clarify why the equations are different and verify that the equations in the RELAP5/MOD2 - B&W manual reflect the actual coding in the program.
 - a. Eq. 2.2.1-27 in RELAP5/MOD2 B&W versus Eq. 528 in RELAP5/MOD2.
 - b. Eq. 2.2.1-33 in RELAP5/MOD2 B&W versus Eq. 534 in RELAP5/MOD2.
 - c. Eq. 2.2.1-34 in RELAP5/MOD2 B&W versus Eq. 535 in RELAP5/MOD2.
 - d. Eq. 2.2.1-37 in RELAP5/MOD2 B&W versus Eq. 538 in RELAP5/MOD2.
 - e. Eq. 2.2.2-13 in RELAP5/MOD2 B&W versus h_{mic} on pg. 107 in RELAP5/MOD2.
 - f. Eq. 2.2.2-38 in RELAP5/MOD2 B&W versus A_{wf} on pg. 111 in RELAP5/MOD2.
 - g. Eq. 2.2.2-58 in RELAP5/MOD2 B&W versus the condensation model given on pg. 116 in RELAP5/MOD2.
 - h. Eq. 2.3.2-2 in RELAP5/MOD2 B&W versus Eq. 575 in RELAP5/MOD2.
 - i. Eq. 2.3.2-3 in RELAP5/MOD2 B&W versus Eq. 576 in RELAP5/MOD2.

- j. Eq. 2.3.2-5 in RELAP5/MOD2 B&W versus Eq. 577 in RELAP5/MOD2.
- k. Eq. 2.3.2-10 in RELAP5/MOD2 B&W versus Eq. 592 in RELAP5/MOD2.
- l. Eq. 2.3.2-11 in RELAP5/MOD2 B&W versus Eq. 593 in RELAP5/MOD2.
- m. Eq. 2.1.3-24 in RELAP5/MOD2 B&W versus Eq. 181 in RELAP5/MOD2.
- n. Eq. 2.1.3-53 in RELAP5/MOD2 B&W versus Eq. 210 in RELAP5/MOD2.
- o. Eq. 2.1.3-97 in RELAP5/MOD2 B&W versus Eq. 253 in RELAP5/MOD2.
- p. Eq. 2.1.3-102 in RELAP5/MOD2 B&W versus Eq. 258 in RELAP5/MOD2.
- q. Eq. 2.3.1-8 in RELAP5/MOD2 B&W versus Eq. 659 in RELAP5/MOD2.

Response: The following text responds by parts:

- a. The term d_m in the difference approximation for the m^{th} interior mesh point for the one dimensional heat conduction solution in BAW-10164P is defined correctly by Equation 2.2.1-27. The RELAP5/MOD2 coding (subroutine HT1TDP) agrees with Equation 2.2.1-27. Equation 528 of NUREG/CR-4312 and EGG-2396 contains two typographical errors.

In Equation 2.2.1-24 of BAW-10164 and Equation 525 of NUREG/CR-4312 and EGG-2396 K_{1m}^n should be k_{1m}^n .

In Equation 2.2.1-26 of BAW-10164 and Equation 527 of NUREG/CR-4312 and EGG-2396 K_{rm}^n should be k_{rm}^n .

There should be a minus "-" sign on the right hand side of Equation 2.2.1-32 of BAW-10164 and Equation 533 of NUREG/CR-4312 and EGG-2396.

Changes to BAW-10164 will be prepared and released in the first revision to the document.

- b. The term d_1 in the left boundary condition for the conduction solution (Equation 2.2.1-30) in BAW-10164 is defined correctly by Equation 2.2.1-33. The RELAP5/MOD2 coding (subroutine HT1TDP) agrees with Equation 2.2.1-33. Equation 534 of NUREG/CR-4312 and EGG-2396 contains two typographical errors.
- c. There are several typographical errors in both Equation 535 of NUREG/CR-4312 and EGG-2396 and Equation 2.2.1-34 of BAW-10164. Equation 2.2.1-34 should read as follows:

$\sigma c_1^n T_2^n$ should be $-\sigma c_1^n T_2^n$,

$-\frac{k_{r1} \delta_1^b c_1 \Delta t}{B_1^n}$ should be $-\frac{k_{r1} \delta_1^b C_1^n \Delta t}{B_1^n}$, and

$Q_{r1} \delta_{r1}$ in the last term should be $Q_{r1} \delta_{r1}^v$.

The equation is coded correctly in RELAP5/MOD2.

Changes to BAW-10164 will be prepared and released in the first revision to the document.

- d. Equation 2.2.1-37 of BAW-10164 is correct and the coding of RELAP5/MOD2 agrees with the equation. There are two typographical errors in NUREG/CR-4312 and EGG-2396 Equation 538.

In the first line of text after Equation 2.2.1-38

$$C_M^n = A_M^n T_M^n - D_M^n \text{ should be replaced by } C_M^n = A_M^n T_M^n - D_M^n$$

A similar typographical error exists on page 245 of NUREG/CR-4312 and EGG-2396.

- e. Equation 2.2.2-13 of BAW-10164 is incorrect. It should read:

$$h_{mic} = 0.00122 \left[\frac{K_f^{0.79} C_{pf}^{0.45} P_f^{0.49}}{\sigma^{0.5} \mu_f^{0.29} h_{fg}^{0.24} \rho_g^{0.24}} \right] \Delta T_{sat}^{0.24} \Delta P^{0.75} S$$

The Equation on page 107 of NUREG/CR-4312 and EGG-2396 is correct. The coding of RELAP5/MOD2 is correct and agrees with the above equation.

Changes to BAW-10164 will be prepared and released in the first revision to the document.

- f. The F_L factor given by Equation 2.2.2-38 of BAW-10164 is the fraction of wall surface area wetted and equivalent to A_{wf}/A_w on page 111 of the RELAP5/MOD2 manual. Equation 2.2.2-38 is correct whereas the form of the correlation on page 111 of NUREG/CR-4312 and EGG-2396 is incorrect. The coding for RELAP5/MOD2 agrees with the equation in BAW-10164. Note should be taken of the difference in units for these correlations

in the two reports. SI units are used for Equation 2.2.2-38 in BAW-10164 while British units are used on page 111 of NUREG/CR-4312 and EGG-2396.

- g. The volumetric vapor generation rate, Γ_w , for condensation is given correctly by Equation 2.2.2-58 of BAW-10164. The coding for RELAP5/MOD2 agrees with this equation. The equation on page 116 of NUREG/CR-4312 and EGG-2396 misrepresents Γ_w for condensation.
- h. The core heat transfer models, Section 2.3.2 and 2.3.3 of BAW-10164, are essentially new models which were added to RELAP5/MOD2-B&W to enhance the reactor core simulation. The original RELAP5/MOD2 heat transfer model has been maintained in RELAP5/MOD2-B&W and is referred to as the System Heat Transfer Model. The System Heat Transfer Model is applied to the reactor coolant system exterior to the reactor core and to the secondary side. While maintaining the basic heat structure form of RELAP5/MOD2, the Core Heat Transfer Model contains new heat transfer coefficients, a pin model with a different gap conductance approach, a pin rupture model, and a metal-water reaction model. There is unlikely to be good correspondence between BAW-10164 and NUREG/CR-4312 and EGG-2396 within the features of the core heat transfer and fuel pin packages.

Equation 2.3.2-2 is part of the new fuel pin model for the core. It is printed correctly and the coding in RELAP5/MOD2-B&W agrees with the equation.

Note: The formulation of Equation 2.3.2-2 is identical to the formulation used in FRAP-T6-B&W, BAW-10165, Equations 2.1.3-1 and 2.1.3-2.

- i. Equation 2.3.2-3 is incorrect. It should be:

$$r_n = \left(\frac{2n-1}{N} \right) r_g .$$

There is no intended correspondence to Equation 576 of NUREG/CR-4312 and EGG-2396. Equation 2.3.2-3 is a simplified form of the FRAP-T6-B&W, BAW-10165, formulation of Equation 2.1.3-3 with r'_g always taken as the average hot fuel to cladding gap width.

Changes to BAW-10164 will be prepared and released in the first revision to the document.

- j. Equation 2.3.2-5 is stated correctly for the new core heat transfer and fuel pin models. Equation 577 of NUREG/CR-4312 and EGG-2396 is incorrect.
- k. Equation 2.3.2-10 of BAW-10164 contains a typographical error. It should read:

$$K_{\text{gas}} = \frac{\sum_{i=1}^{N_g} K_i X_i}{\left(X_i + \sum_{j=1}^{N_g} \phi_{ij} X_j \right)} ,$$

The coding of RELAP5/MOD2 is correct and agrees with the above equation.

Changes to BAW-10164 will be prepared and released in the first revision to the document.

- l. Equation 2.3.2-11 of BAW-10164 and Equation 593 of NUREG/CR-4312 and EGG-2396 are equivalent but in different forms.
- m. Equation 2.1.3-24 in BAW-10164 correctly defines the critical Weber Number. The coding of RELAP5/MOD2 corresponds to Equation 2.1.3-24. Equation 181 of

NUREG/CR-4312 and EGG-2396 contains a typographical error.

- n. Equation 2.1.3-53 correctly defines the relationship between the Lockhart - Martinelli parameter "x" and the ratio of the phasic pressure drops. There is a typographical error in equation 210 of NUREG/CR-4312 and EGG-2396.

Equation 2.1.3-53 enters into the coding through Equation 2.1.3-77 whose exponents are specified by the definition of the "x" term. Equations 2.1.3-53 and 2.1.3-77 are consistent as given in BAW-10164 and the coding of RELAP5/MOD2 is properly represented by Equation 2.1.3-77.

Equation 2.1.3-71 contains a typographical error. The second term of the quadratic C_x should be $C x$.

Changes to BAW-10164 will be prepared and released in the first revision to the document.

- o. The definition of the friction factor, $\lambda_{L,T}$, for the transition regime between laminar and turbulent flow is calculated correctly by Equation 2.1.3-97 in BAW-10164. Equation 253 of NUREG/CR-4312 and EGG-2396 contains typographical errors.

Equation 2.1.3-97 enters into the coding as part of the derivation for Equation 2.1.3-107 which corresponds to RELAP5/MOD2 as programed. Equation 2.1.3-107 can not be derived from Equation 253 of NUREG/CR-4312 and EGG-2396.

Equations 2.1.3-98 of BAW-10164 and Equation 254 of NUREG/CR-4312 and EGG-2396 are both incorrect and should read as follows:

$$0 \leq 5.285 \left[1.189 - \left(\frac{4000}{R} \right)^{0.25} \right] \leq 1.0$$

The coding of RELAP5/MOD2 is correct and agrees with the above equation.

$L(2-R^*)$ in Equation 2.1.3-107 of BAW-10164 and in Equation 263 of NUREG/CR-4312 and EGG-2396 should be replaced by $L [5.285 (1.189 - R^*)]$.

The coding of RELAP5/MOD2 is correct and agrees with the above.

Changes to BAW-10164 will be prepared and released in the first revision to the document.

p. The critical Reynold's number is properly given by Equation 2.1.3-102 BAW-10164 and the coding of RELAP5/MOD2 corresponds to Equation 2.1.3-102. Equation 258 of NUREG/CR-4312 and EGG-2396 contains typographical errors.

q. Equation 2.3.1-8 of BAW-10164 contains a typographical error. It should read:

$$P_{aj}(t) = \lambda_{aj} \tau_{aj} = a_{aj} \exp(-\lambda_{aj}t).$$

The coding of RELAP5/MOD2 is correct and agrees with the above equation.

Changes to BAW-10164 will be prepared and released in the first revision to the document.

2. Question: Verify the correctness or typographic error for each of the following items.

- a. Verify that Eq. 2.2.2-25 is shown correctly. Define ΔT_{NVG} . Also, should T_f be T_w ?
- b. Are R_2 and R_3 defined correctly on pg. 2.2-30?
- c. Page 2.2-30 refers to Eq. 2.2.2-34/35. Should this page actually refer to Eq. 2.2.2-40/41.
- d. On page 2.1-46 reference is made to Eq. 2.1.3-1. Should reference be to Eq. 2.1.3-2?

Response: The following text responds by parts:

- a. Equation 2.2.2-25 and the use of T_f are correct in BAW-10164. The term ΔT_{NVG} is defined as:

$$\Delta T_{\text{NVG}} = T_{\text{sat}} - T_{\text{fNVG}}$$

where

T_{fNVG} = the liquid temperature above which net vapor generation can occur.

This modeling agrees with RELAP5/MOD2 coding.

- b. Equation 2.2.2-45 and its subcomponents, namely R_1 , R_2 , and R_3 , are correct in BAW-10164. Typographical errors exist in NUREG/CR-4312 and EGG-2396 on pages 126 and 127 for these terms. Reference can be made to K. H. Sun, J. M. Gonzales, and C. L. Tien, "Calculation of Combined Radiation and Convection Heat Transfer in Rod Bundles under Emergency Cooling Conditions," Journal of Heat Transfer, Transactions of ASME, 98, 1976 page 414.

- c. The references in the last paragraph on page 2.2-30 to Equations 2.2.2-34 and 2.2.2-35 are in error; reference should be made to Equations 2.2.2-40 and 2.2.2-41 respectively.

Changes to BAW-10164 will be prepared and released in the first revision to the document.

- d. The reference in the middle paragraph on page 2.1-46 to Equation 2.1.3-1 is not correct; reference should be made to Equation 2.1.3-2.

Changes to BAW-10164 will be prepared and released in the first revision to the document.

3. Question: Eq. 2.2.2-51 is a Nusselt condensation correlation. Describe where and how this correlation is used in the code.

Response: In the RELAP5/MOD2 and RELAP5/MOD2-B&W computer codes, a form of the Nusselt laminar film condensation correlation is used that differs from the form given by Equation 2.2.2-51 of BAW-10164 (and also on page 114 of NUREG/CR-4312). The correlation as used in these codes depends on the orientation of the condensing surface as described below.

- a. Horizontal Surface (inclination angle of the volume to the horizontal is zero)

For condensation on a horizontal surface, laminar film condensation in a horizontal tube with stratified flow is assumed, and a modified form of the Nusselt equation (page 341 of Reference 44 in BAW-10164), given by

$$h_{nlf} = 0.296 \left[\frac{\rho_f (\rho_f - \rho_g) g h_{fg} k_f^3}{D_e \mu_f (T_{sat} - T_w)} \right]^{0.25}$$

is used.

- b. Vertical Surface

For condensation on a vertical surface, the Nusselt laminar film condensation correlation (Reference 44 in BAW-10164), given by

$$h_{nlf} = 0.943 \left[\frac{\rho_f (\rho_f - \rho_g) g \sin \theta h_{fg} k_f^3}{\mu_f L_v (T_{sat} - T_w)} \right]^{0.25}$$

where

θ = angle of inclination to the horizontal

and

L_v = volume length,

is used.

When the volume average liquid velocity is less than or equal to 0.001 m/s, only laminar film condensation is used. These changes will be incorporated into the next revision to BAW-10164.

4. Question: Clarify why Eq. 2.2.2-54 is multiplied by the $\min(1.0, 10 \cdot \text{VOIDG})$.

Response: Equation 2.2.2-54 would be more clearly written as,

$$h_{wg} = h_{con} \cdot (\alpha_g \text{ MIN}(1.0, 10 \alpha_g)).$$

The weighting of h_{con} by void fraction is to restrict the surface area available for condensation. At high void fraction straight α_g weighting is adequate; however, at very low void fraction α_g weighting may under predict the rate of condensation. The term $\text{MIN}(1.0, 10 \alpha_g)$ is applied to adjust the weighting at low void fractions.

This weighting of h_{con} exists in the RELAP5/MOD2 coding.

5. Question: Clarify why the coefficient in the Rohsenow-Choi correlation is 4.36 in the system model (Eq. 2.2.2-7) but 4.0 in the core model (Eq. 2.3.3-15).

Response: The coefficient in the Rohsenow-Choi correlation, as originally given (W. M. Rohsenow and H. Y. Choi; Heat, Mass, and Momentum Transfer; Prentice-Hall, Inc.; 1961; page 166), depends on the wall conditions:

<u>Wall Condition</u>	<u>Coefficient</u>
Uniform T_w	3.66
Uniform heat flux	4.36

Y. Y. Hsu recommends a value of 4.0 for this coefficient for blowdown heat transfer. This is a compromise between the laminar forced convection condition of uniform heat flux and the uniform temperature condition. Refer to Thermohydraulics of Two-Phase Systems for Industrial Design and Nuclear Engineering; Edited by J. M. Delhaye, M. Giot, and M. L. Reithmuller, Hemisphere Publishing Corporation, 1981, pages 261 and 262. B&W feels that the compromise coefficient is more appropriate for the conditions in the core than the uniform heat flux value.

On page 2.3-71 of BAW-10164 an incorrect reference was given for the Rohsenow-Choi correlation. The correct reference is given above.

Changes to BAW-10164 will be prepared and released in the first revision to the document.

6. Question: All of the heat transfer coefficients are coded with a user input multiplier. Clarify whether a multiplier other than 1.0 will ever be used in a licensing calculation, and provide justifications or bases for those multipliers with values other than 1.0.

Response: The incorporation of multipliers on the heat transfer was to provide some degree of user flexibility for general code use and to allow for sensitivity studies which may form part of a plant licensing basis. The multipliers to be used in evaluations are documented in the applicable evaluation model report (BAW-10168 for applications to Westinghouse designed NSSS).

Note: As of 7/8/88 it is B&W's intention to use a multiplier of 1.0 on all RELAP5/MOD2-B&W heat transfer coefficients for application on Westinghouse designed NSSS with the exception of certain sensitivity studies.

7. Question: Eq. 2.3.3-59 sets the film boiling heat transfer coefficient to the maximum of the CSO film boiling correlation and the Rohsenow-Choi correlation. Clarify the applicability of the Rohsenow-Choi correlation to film boiling heat transfer and why the film boiling heat transfer coefficient is calculated in this manner.

Response: The lower bound of single phase wall to vapor convective heat transfer is given by the Rohsenow-Choi correlation (Equation 2.3.3-66 of BAW-10164). The lower bound for flow film boiling is convective heat transfer to vapor. Therefore it is reasonable to use the lower bound convective heat transfer correlation as the lower bound for the flow film boiling regime. The CSO correlation is, in fact, the product of a convective to vapor heat transfer term (Equation 2.3.3-60 of BAW-10164) and liquid content based enhancement term, $(1 + F_g)$.

Recent modifications to RELAP5/MOD2-B&W, FRAP-T6-B&W, and the B&W Evaluation Model for Westinghouse-designed NSSS's have replaced the CSO flow film boiling correlation with the Condie-Bengston IV correlation (K. G. Condie, S. J. Bengston and S. L. Richlin; Post-CHF Heat Transfer Data Analysis, Comparison and Correlation; EG&G unpublished report). The same reasoning applies to the lower bound of the flow film boiling heat transfer regime and the use of Rohsenow-Choi is maintained.

A telephone conversation has been conducted with the NRC informing them of the change. A letter formally advising of this modification to the RELAP5/MOD2-B&W and FRAP-T6-B&W is being prepared for submittal in the near future.

Appropriate changes to BAW-10164, RELAP5/MOD2-B&W, and BAW-10165, FRAP-T6-B&W, will be prepared and released in the first revision to those documents. The B&W evaluation model report for Westinghouse-designed NSSS, BAW-10168, as submitted on July 25, 1988, uses and properly reflects the use of the Condie-Bengston correlation.

8. Question: Provide an assessment of the CSO film boiling heat transfer correlation and the McEligot single-phase steam correlation to verify the correlations' accuracy for calculating film boiling and single-phase steam heat transfer.

Response: In the RELAP5/MOD2-B&W EM heat transfer package, the film boiling heat transfer coefficient is calculated using either the CSO or the Condie-Bengston IV correlation. For EM applications, B&W will use the Condie-Bengston IV correlation to calculate film boiling heat transfer. Therefore, an assessment of the Condie-Bengston correlation instead of the CSO correlation will be made in response to this question. The applicability of Condie-Bengston IV and McEligot correlations for LBLOCA applications is demonstrated by the simulation of the Semiscale MOD1 test S-04-6, which is discussed in detail as a response to question 12. Additional assessments of these correlations are discussed below.

Assessment of the Condie-Bengston IV Correlation

Yoder^{8.1} evaluated the Condie-Bengston IV correlation using the available rod bundle film boiling data base. Figure 4.3 of Reference 8.1 shows the comparison between the correlation predicted heat flux and the film boiling data. From this figure, the correlation can be characterized as producing reasonable to conservative predictions. Yoder, in fact, concluded that "the Condie-Bengston IV correlation does a reasonable job in predicting film boiling heat fluxes." Therefore, B&W concludes that the Condie-Bengston IV correlation is appropriate for the prediction of film boiling heat transfer in the B&W RSG LOCA Evaluation Model.

McEligot Single-Phase Steam Correlation

The McEligot convective steam cooling correlation has been used in other approved computer code for EM applications. It is also the approved correlation used by the Japanese Nuclear Safety Commission to calculate convective heat transfer to steam in their evaluation model. Experimental studies of convective steam cooling heat transfer in single tubes and rod bundles support the use of the McEligot correlation to calculate convective heat transfer to steam.

Larsen and Lord^{8.4} studied convection and radiation heat transfer to superheated steam in heated tubes. Their results (Figure 12 in Reference 8.4) show that the correlation properly predicts convective heat transfer to steam for bulk Reynolds numbers, Re_b , (calculated based on the bulk steam temperature) above 5000, but overpredicts the heat transfer for Reynolds numbers below 5000. However, in rod bundles, such as in a nuclear core, the convective heat transfer at low Re_b would be higher than in a single tube due to the mixed convection in rod bundles.

Wong and Hochreiter^{8.5} studied low Reynolds number forced convection steam cooling using the 161-rod FLECHT-SEASET bundle. The inlet Reynolds number was varied from 2500 to 17,000. Their results show that the Dittus-Boelter correlation underpredicts the heat transfer over this range of Reynolds numbers and that the degree of underprediction increases with decreasing Reynolds number. For a given set of conditions, the Dittus-Boelter correlation predicts larger heat transfer coefficients than does the McEligot correlation. Therefore, from the Wong and Hochreiter study it can be concluded that the McEligot correlation will in general underpredict the heat transfer for Reynolds numbers below 17,000.

Yoder^{8.1} also evaluated the rod bundle steam cooling data base. The results (Figure 4.9 of Reference 8.1) show that the Dittus-Boelter correlation is appropriate for use in calculating convective heat transfer to steam for Re_b less than 20,000. This is consistent with the study by Wong and Hochreiter. Thus, from Yoder's work, it can also be concluded that the McEligot correlation is valid for use at low Reynolds numbers. Sozer, Anklam and Dodds also reached this same conclusion.

Recently, Kumamaru, et al^{8.7} evaluated various convective steam cooling correlations using the uncovered bundle heat transfer test data under high pressure boil-off conditions in the Two-Phase Flow Test Facility (TPTF). These tests covered a pressure range from 3 to 12 MPa and vapor Reynolds numbers from 10,000 to 62,000. The results of the evaluation (Figure 13 in Reference 8.7) showed that the McEligot correlation reasonably predicts convective heat transfer to steam.

From the evaluation of the available literature on convective heat transfer to steam, it is concluded that the McEligot correlation is reasonable and appropriate for use in calculating convective heat transfer to steam in both the transition (low Reynolds number) and the turbulent (high Reynolds number) flow regimes.

References

- 8.1 G. L. Yoder, Rod Bundle Film Boiling and Steam Cooling Data Base and Correlation Evaluation, NUREG/CR-4394, ORNL-TM-9628, August 1986.
- 8.2 F. M. Bordelon, et al, LOCTA-IV Program: Loss of Coolant Transient Analysis, WCAP-8305, June 1974.
- 8.3 Guideline for the Evaluation of ECCS of Light Water Reactor, Nuclear Safety Commission of Japan, July 20, 1981.
- 8.4 P. S. Larsen and H. A. Lord, Convective and Radiative Heat Transfer to Superheated Steam in Uniformly and Non-Uniformly Heated Tubes, ORA Project 08742, Dept. of Mech. Eng., University of Michigan, February 1969.
- 8.5 S. Wong and L. E. Hochreiter, "Low Reynolds Number Forced Convective Steam Cooling Heat Transfer in Rod Bundles," Paper presented at ASME Winter Annual Meeting, November 16-21, 1980, Chicago, Illinois.
- 8.6 A. Sozer, T. M. Anklam and H. L. Dodds, "Convection-Radiation Heat Transfer to Steam in Rod Bundle Geometry," Nuc. Technology 67, pp. 452-462, December 1984.
- 8.7 H. Kumamaru, et al, "Investigation of Uncovered Bundle Heat Transfer Under High Pressure Boil-Off Conditions," Nuc. Eng. and Design, 96, pp. 81-94, 1986.

9. Question: The Schrock and Grossman correlation is applied at pressures greater than 1000 psia. However, based on the information in the THETA1-B code manual, the data base for the correlation only goes to 505 psia. Clarify the accuracy and applicability of this correlation for pressures greater than 1000 psia.

Response: The data base for the Schrock and Grossman correlation is limited to below 505 psia. However, the correlation has been used in NRC-approved codes for licensing applications and in audit calculation codes (for example WREM, FRAPT-6, and TOODEE2). Extension of the correlation for use at high pressures is supported by its sound theoretical development which accounts for pressure effects.

The heat-momentum analogy is used in the development of the Schrock and Grossman correlation. Analogies between heat, mass and momentum transfer have been successfully used by the thermal hydraulic research community to transfer information between these parameters. Schrock and Grossman assumed that the ratio between the two-phase and the single-phase liquid heat transfer coefficients, h_{TP}/h_l , was a function of the Lockhart-Martinelli parameter, X_{tt} , given by Equation 2.3.3-23 in the RELAP5/MOD2-B&W topical report (BAW-10164).

$$h_{TP} / h_l = f(X_{tt}) ,$$

where the single-phase liquid heat transfer coefficient is given by the Dittus-Boelter correlation. It should also be noted that the Lockhart-Martinelli parameter is the square-

root of the ratio between the single-phase liquid pressure drop and the single-phase vapor pressure drop (Equation 2.1.3-53 in BAW-10164). The two-phase pressure drop is calculated using the assumption that the pressure ratio between the two-phase and the single-phase is a function of X_{tt} . This approach has been successfully applied in calculating two-phase pressure drops over the range from atmospheric pressure to the critical pressure. Based on this result, it is concluded that the Schrock and Grossman correlation is applicable at pressures above 1000 psia.

10. Question: Provide an assessment of the fuel behavior models (gap conductance, clad deformation, and metal-water reaction) added to RELAP5/MOD2-B&W.

Response: The fuel behavior models incorporated into RELAP5/MOD2-B&W by B&W were obtained from current technology computer codes, such as FRAPT-6, RELAP5/MOD2 and MATPRO-Version 11, and implemented according to the requirements of 10CFR50.46 Appendix K. An assessment of each of these models is presented below.

Gap Conductance

The RELAP5/MOD2-B&W gap conductance model was developed based on the models in FRAPT-6 and RELAP5/MOD2. Recently, EG&G^{10.2} evaluated the RELAP5/MOD2 dynamic gap conductance model using the Power Burst Facility (PBF) test LOC-11C. Figure 9-10, in Reference 10.2, shows the variation of fuel centerline temperature with local fuel rod power; the calculated results using FRAPT-6 are also shown. From the results shown in this figure, it can be concluded that the gap conductance models in both RELAP5/MOD2 and FRAPT-6 realistically predict fuel temperatures. The FRAPT-6 code has been widely used in calculating cladding and fuel thermal and mechanical responses during transients. In addition, RELAP5/MOD2-B&W gap conductance at steady-state is adjusted, using the gap multiplier M_g (discussed below), to match the NRC-approved fuel pin code results. Based on this assessment, it can be concluded that RELAP5/MOD2-B&W would calculate realistic fuel rod temperatures. The sources of each of the terms in the gap conductance model are given below.

The correlation for the gap conductance in RELAP5/MOD2-B&W (Equation 2.3.2-2 in BAW-10164) is the same as that used in FRAP-T6-B&W (BAW-10165 Equation 2.1.3-2). It is to be noted

that the constant 3.6 in Equation 2.3.2-2 is the same as that used in FRAP-T6 code, even though the FRAP-T6 manual (NUREG/CR-2148, Equation 2) states 3.2.

The correlation for the temperature jump distance term, $(g_1 + g_2)$, in RELAP5/MOD2-B&W (Equation 2.3.2-5 in BAW-10164) is the same as that in FRAPT-6 (Equation 4 in NUREG/CR-2148). RELAP5/MOD2-B&W uses a value of 0.74 for the constant term in the equation for the accommodation coefficient of Xenon, while FRAPT-6 uses a value of 0.749, which is consistent with the value reported by Lanning and Hann.^{10.1} It is concluded that the value used in RELAP5/MOD2-B&W should be updated to 0.749. This was accomplished in Revision 2 to BAW-10164. The gap radiation heat transfer in RELAP5/MOD2-B&W (Equation 2.3.2-4 in BAW-10164) is calculated in the same way as in FRAPT-6 (Equation 7 in NUREG/CR-2148).

RELAP5/MOD2-B&W (Equations 2.3.2-10 and 2.3.2-11 in BAW-10164) and FRAPT-6 (based on the coding) use the same correlation to calculate the thermal conductivity of the gas mixture, K_{gas} . The individual gas thermal conductivities, k_i , in RELAP5/MOD2-B&W are calculated using the correlations given in MATPRO Version 11 (Revision 2). These same correlations are also used in RELAP5/MOD2.

The gap width at the mid-point of the n -th azimuthal segment, r_n , is calculated using a simplified form of the equation given in FRAPT-6. This would have a minimal impact on the results because of the use of the gap multiplier, M_g , as explained below.

During the steady-state initialization of RELAP5/MOD2-B&W, h_{gap} is adjusted using the multiplier, M_g , such that the gap stored energy calculated by RELAP5/MOD2-B&W is greater

than or equal to the value calculated using the NRC-approved fuel pin code, TACO2 (or TACO3 upon NRC approval). The multiplier calculated during steady-state remains constant throughout the transient. A similar method has been used by B&W in the NRC-approved topical report BAW-10104-A.

The transient internal pin pressure, P_g , is calculated using the methodology in the NRC-approved CRAFT2 computer code (BAW-10092-A).

Fuel Rod Swelling, Clad Deformation, and Rupture

The hot fuel-cladding gap distance, r_g , is calculated using Equation 2.3.2-12 in BAW-10164. The fuel thermal expansion, u_{TF} (Equation 2.3.2-14 in BAW-10164), is calculated in the same manner as in RELAP5/MOD2 (NUREG/CR-4312, Equation 583). The fuel radial thermal strain function, ϵ_{TF} (Equation 2.3.2-15 in BAW-10164), the cladding strain function, ϵ_{TC} (Equation 2.3.2-21 in BAW-10164), and Young's modulus of elasticity, E (Equation 2.3.2-28 in BAW-10164), are calculated using the correlations given in MATPRO Version 11 (Revision 2). RELAP5/MOD2 also uses these same correlations in calculating the fuel-cladding gap.

The cladding thermal expansion, u_{TC} (Equation 2.3.2-20 in BAW-10164), required updating in RELAP5/MOD2-B&W. u_{TC} should be calculated based on the cladding thickness rather than the cladding radius as was done in RELAP5/MOD2 (NUREG/CR-4312, Equation 585). This update has been recorded in Revision 2 of BAW-10164.

The steady-state fuel and cladding radii calculated by RELAP5/MOD2-B&W and the corresponding values calculated using the NRC-approved fuel pin code (TACO2 at present or TACO3 after its approval) are made equal by using the over-specification factors, u_{FC} (Equation 2.3.2-13 in BAW-10164)

and u_{cc} (Equation 2.3.2-19 in BAW-10164). The values of u_{fc} and u_{cc} remain constant during the transient. In RELAP5/MOD2, similar adjustment parameters can be input to the code. In CRAFT2 and THETA1-B, the cold unstressed dimensions are calculated from the hot stressed dimension code inputs (as determined by the steady-state fuel pin code). These values are used as the basis for calculating the fuel and cladding geometry changes during a transient. Thus, using adjustments in thermal-hydraulic codes to match calculated fuel and cladding radii with values calculated from a steady-state fuel pin computer program is a standard procedure.

The clad swelling and rupture models used in RELAP5/MOD2-B&W are from NUREG-0630. The NUREG-0630 models were developed as licensing standards for LOCA analysis using the data base generated from an extensive research program sponsored by the NRC. During plastic deformation, the normalized ramp rate, H , is calculated using a plastic weighted time average equation (Equation 2.3.2-36 in BAW-10164). Its basis is an NRC letter from G. N. Lauben to L. E. Phillips^{10.3} regarding TOODEE2 models for swelling and rupture. It is concluded that RELAP5/MOD2-B&W properly calculates clad swelling and rupture as per NRC requirements.

Metal Water Reaction

The metal-water reaction rate in RELAP5/MOD2-B&W is calculated using the parametric relationship derived by Baker and Just (Reference 120 in BAW-10164) as required by Appendix K.

10.1 D. D. Lanning and C. R. Hann, Review of Methods Applicable to the Calculation of Gap Conductance in Zircaloy-Clad UO₂ Fuel Rods, BNWL-1894.

10.2 R. A. Dimenna, et al, RELAP5/MOD2 Models and Correlations, NUREG/CR-5194, August 1988.

10.3 Letter from Richard P. Denise (Acting Assistant Director for Reactor Safety, Division of Systems Safety), NRC to J. H. Taylor, B&W, January 31, 1980 (Transmitting letter from G. N. Lauben, NRC to L. E. Phillips, NRC, Subject: TOODEE2 Models for Swelling and Rupture, January 15, 1980).

11. Question: Does the fine node option discussed on page 2.3-57 of the RELAP5/MOD2-B&W manual allow for the metal-water reaction to occur no less than 1.5 inches axially from the ruptured point as required by Appendix K?

Response: The fine node option described on page 2.3-57 of BAW-10164 has no restriction on the node size. However, in a system code like RELAP5/MOD2-B&W, it is unlikely to use a node size smaller than 3 inches due to execution time. Furthermore, fuel rod thermal behavior is calculated using FRAP-T6-B&W (BAW-10165), not RELAP5/MOD2-B&W. As such, compliance with Appendix K restrictions on the amount of local and whole core metal-water reaction is demonstrated via FRAP-T6-B&W calculations. Hence, RELAP5/MOD2-B&W metal-water calculations are not significant to the overall result. Core node size used in the RELAP5/MOD2-B&W (and FRAP-T6-B&W) LOCA EM is defined in BAW-10168.

12. Question: In the large break loss-of-coolant (LBLOCA) assessment using data from Semiscale MOD-1 Test S-04-6, the depressurization calculated with the RELAP5/MOD2, cycle 36.04 code was faster than in the experiment (Figures G.1-3 to G.1-9).

- a. Clarify why the faster depressurization was calculated even though the break flow in this calculation compared reasonably well to the data.
- b. Clarify why the densities upstream of the vessel side break calculated in the two RELAP5/MOD2 calculations were lower than the measured data (Figure G.1-21).
- c. Clarify why the mass flow in the intact loop hot leg was underpredicted for the first 10s in both calculations (Figure G.1-14).
- d. In Figures G.1-30 and G.1-31, the RELAP5/MOD2-B&W evaluation model (EM) calculation showed slightly better cooling than the RELAP5/MOD2, cycle 36.04 calculation in the period after approximately 12 or 13 s. Clarify what caused this difference between the two calculations.

Response:

The Semiscale MOD1 test S-04-6 was reanalyzed using RELAP5/MOD2-B&W due to the following changes in the B&W evaluation model (BAW-10168):

1. The CSO film boiling correlation was replaced by the Condie-Bengston IV correlation.

2. The B&W-2 CHF correlation was replaced by the BWCMV correlation for the high flow, high pressure flow condition.
3. Moody slip was assumed at the break junction.
4. The ECCS bypass flow modeling was updated (see Section 4.3.4.2 of the LOCA EM topical report, BAW-10168 Volume I).

The test data and BE prediction reported in Section G.1 of BAW-10168 Volume I still remain valid and are reproduced herein for completeness of the comparison with the new EM benchmark. The responses to questions 12 and 13 are incorporated into the following discussion.

Test S-04-6 was one of the 200 percent offset shear double-ended cold leg break tests conducted in the Semiscale MOD1 test facility. RELAP5/MOD2-B&W was used to predict the test, first using the INEL Cycle 36.04 options (base case) and second using the B&W installed evaluation model (EM) options. Both cases predicted higher break mass flow rates than shown by the data, and, as a result, the predicted depressurization rates were higher than the data. The predicted cladding temperature at the peak power location of the high powered rod using the EM option was higher than the Cycle 36.04 prediction. Both cases predicted higher cladding temperatures than the measured data. From this study, it is concluded that the EM option would properly predict the system behavior during the blowdown phase of a PWR large break loss of coolant accident (LBLOCA).

Description of Experiment

An isometric view of the Semiscale MOD1 test facility used for the cold leg break tests is shown in Figure 12.1. It is a small scale model of a typical four-loop recirculating steam generator PWR. It consists of the following major PWR components: a pressure vessel with the core simulator, lower and upper plenums, and downcomer; an intact loop with a steam generator, a pump and a pressurizer; a broken loop with a simulated steam generator and a simulated pump; emergency coolant systems (ECC) in both loops that include an accumulator, and high and low pressure injection pumps; and a pressure suppression system with a suppression tank. The configuration of the electrically-heated 40-rod bundle, shown in Figure 12.2, is typical of a 15 by 15 fuel assembly (0.422 inch rod outside diameter and 0.563 inch pitch) except that the heated length of the test rods is 5.5 feet compared with 12 feet for commercial rods. The bundle has an inlet peaked axial power profile (peak at 26 inches from the bottom of the heated section). Three of the four center rods have a peak power density of 12 kw/ft and the fourth rod is unpowered. Of the remaining 36 rods, 33 rods have a peak power density of 11.46 kw/ft and three rods are unpowered.

The transient was initiated after the system reached steady-state by breaking two rupture assemblies that allowed the flow of the primary fluid into the suppression tank through two blowdown nozzles, each having a break area of 0.00262 ft². The suppression system was maintained at a constant pressure of 34.8 psia. At blowdown initiation, the power to the primary coolant pump was reduced and the pump was allowed to coast down to a speed of 1500 rpm, which was then maintained for the duration of the test. During the

transient, the power to the core was automatically controlled to simulate the thermal response of nuclear rods. The measurements made during the transient included pressure, flow, density, and fluid temperatures at different locations in the primary and secondary systems, and surface temperatures at different elevations of the selected heated rods. The sequence of events relative to the transient initiation is given in Table 12.1.

RELAP5 Input Model

The nodalization of the RELAP5 input model for the Semiscale MOD1 test facility is shown in Figure 12.3. The nodalization of the primary system is very similar to the RELAP4 model given in Reference 12.3. The geometry and other needed input information for the primary system was obtained from this RELAP4 model.^{12.3} The geometry and other input information for the secondary side of the steam generator were obtained from the RELAP5/MOD0 input model given in Reference 12.4. The input information obtained from the RELAP4 and the RELAP5/MOD0 input models were verified using the geometry values given in Reference 12.2.

The RELAP5 base input model consisted of 89 volumes, 98 junctions, and 50 heat structures. Some of the important features of the model are given below.

1. The core was modeled with two channels to account for the radially peaked power profile. The fluid volumes associated with the three high powered rods were modeled as a hot channel. The remaining core fluid volumes were modeled as an average channel. Each channel was axially divided into six volumes in order to make the model consistent with the EM plant model.

The axial division coincided with selected axial steps in the power shape curve. Crossflow junctions were used to connect the hot and average channel volumes.

2. The active heater rods in each channel were modeled using ten heat slabs, that is, one heat slab per power step.
3. The pressurizer was modeled using an eight-equal-volume pipe component.
4. The accumulator was modeled using the accumulator component.
5. The high and low pressure pumps were simulated using time-dependent volumes and junctions.
6. The suppression system was modeled as a time-dependent volume.
7. Break nozzles were modeled as trip valves.
8. The homologous curves for the intact loop pump were obtained from the RELAP4 input model.^{12.3} The measured pump speed versus time data were input to simulate the pump coastdown during the transient.
9. The measured power versus time data were input to simulate the electrical power supplied to the heater rods during the transient.
10. The moisture separator on the secondary side of the steam generator was simulated using the separator component.

11. Nonequilibrium and nonhomogeneous options were selected for each volume and junction.
12. The break junctions and the pressurizer surge line junction were treated as choked flow junctions using a discharge coefficient of one.

EM Input Options

The following modifications to the base model were made to select the EM options. These options are the same as those used in the EM plant model reported in BAW-10168 Volume I.

1. The equilibrium option was selected for the core inlet, outlet, and core volumes.
2. The homogeneous option was selected for the core inlet, outlet, and the normal (vertical) core junctions.
3. The EM heat transfer option with the B&W high pressure CHF correlation with mixing vanes (BWCMV) was selected for all the core heat slabs. The post-CHF lock-in option, that would force temporary film boiling if CHF is exceeded and conditions would permit a return to nucleate boiling, was used.
4. The 90/10 weighting factor was used in the underrelaxation of the interphase heat transfer.
5. Break junctions used the EM choked flow correlations, Extended Henry-Fauske in the subcooled regime, Moody for the saturated fluid, and Murdock-Bauman for superheated steam, with static properties. A discharge coefficient of one was used for subcooled flow and 0.6

for saturated and superheated flow conditions. These coefficients were chosen to reasonably approximate the leak flow boundary conditions from the test.

6. The break junctions in the base model were selected as EM choked flow junctions. An additional junction and a time- dependent volume were added at each break plane. These junctions were used to switch the flow from choked flow to a flow calculated by the RELAP5 momentum equations when the system pressure was close to the suppression tank pressure and choked flow was no longer appropriate. The non-choking option was selected for these junctions. When the velocity calculated using the orifice equation is less than the choked junction velocity, the choked junction is closed and the second junction is opened, and will remain open during the remainder of the transient.
7. EM ECC bypass flow modeling was used.
8. The EM heat transfer package, including the Condie-Bengston IV film boiling correlation, was used.

Transient Simulation

The base case and the EM case were run with constant boundary conditions to obtain steady-state test conditions. The steam generator secondary side pressure was adjusted to obtain the desired primary system conditions. The measured and the predicted steady-state conditions are given in Table 12.2. Trips were used to initiate the sequence of events, given in Table 12.1, during the transient.

Results and Discussion

The measured and predicted pressure variations near the vessel side break are shown in Figure 12.4. Both Cycle 36.04 and the EM predicted lower pressures than the data during the entire transient. The EM calculated a relatively faster depressurization rate than Cycle 36.04 after about 10 seconds from the transient initiation. As a result, the pressure near the break location reached the suppression tank pressure at about 21.1 seconds in the EM case, and at 25.7 seconds in the base case as compared to 37 seconds in the test.

The pressure response near the pump side break is shown in Figure 12.5. The predicted pressure response near this break location, using the EM option, was similar to the prediction near the vessel side break. Between 1.0 and 8.0 seconds, the base case predicted a higher pressure than the data. The difference between the measured and the input values of the HPI flow rates near this break location is the cause of this difference. The break plane pressure reached the suppression tank pressure at 19.3 seconds in the EM test case, and 25.6 seconds in the base case as compared to 27.0 seconds in the test.

The pressure responses at other locations in the primary system are shown in Figures 12.6 through 12.10. From these figures it can be concluded that the pressure response in the primary system is similar to the pressure response near the vessel side break shown in Figure 12.4. The Cycle 36.04 pressure response near the broken loop simulated pump suction side, as shown in Figure 12.7, supports the conclusion made from Figure 12.5 that the HPI flow rate difference is the cause for the prediction of higher pressure than the data in the 1.0 to 8.0 second time period.

The pressure responses in the intact and the broken loop accumulators, shown in Figures 12.11 and 12.12 respectively, are consistent with the primary system pressure response. The sudden drop in measured pressure in the broken loop accumulator at about 2.5 seconds was caused by the opening of a valve in the surge line before the onset of injection.^{12.3} In the present model, the initial pressure in this accumulator was set to 520 psia as was done in the RELAP4 model given in Reference 12.3.

The differential pressure across the pressurizer, which reflects the pressurizer liquid level, is shown in Figure 12.13. Both the EM and Cycle 36.04 predicted a faster decrease in liquid level than the data. Again this is consistent with the system pressure response.

The mass flow rates at different locations in the primary system are shown in Figures 12.14 through 12.20. In the test, the mass flow rate was estimated from the measured density and the volume flow rate. The mass flow rates given in the data report^{12.1} were digitized to generate the comparison plots. During the digitalization the oscillations in the original data plots were smoothed out. The vessel side break flow rate for the EM option, shown in Figure 12.14, includes the break junction flow rate and the ECC liquid bypassed.

Figure 12.14 shows that, near the vessel side break, both Cycle 36.04 and the EM predicted higher flow rates than the data during the early part of the transient. Cycle 36.04 correctly predicted the transition from single-phase to two-phase conditions which occurred at about 2.8 seconds, while the EM predicted an earlier transition than the data. The prediction also showed oscillatory flow behavior between two

and four seconds from the initiation of the transient. These oscillations are caused by the critical flow transition switching logic from Extended Henry-Fauske to Moody and the non-equilibrium nature of the flow near the break location at this time. In the EM model, the transition from the Extended Henry-Fauske to Moody occurs when the upstream node equilibrium enthalpy is close to the saturation enthalpy. Until this condition is reached only liquid is allowed to flow through the break. Since the non-equilibrium option is selected, vapor can exist in this volume, even though the equilibrium enthalpy is lower than the saturation enthalpy. As a result, the void fraction increases until the condition to switch to Moody is reached. As the choked flow correlation is switched to Moody, the break node void fraction decreases due to the high slip between the phases as calculated by the Moody slip correlation. This reduction in void fraction causes the equilibrium enthalpy to decrease below saturation which in turn causes a switch in the critical flow correlation. The switching between the two choked flow correlations continues until the liquid reaches saturation. When the system pressure was close to the suppression tank pressure, large spikes were observed in the data as well as in the prediction. These spikes were caused by the movement of liquid slugs from the accumulator injection location to the break.

The system depressurization rate depends on the mass and energy crossing the boundaries of the system. In the EM case, the use of the Moody discharge correlation causes the system to lose more energy than mass. This is due to the high slip ratio between the phases at the break location as compared to the RELAP5 Cycle 36.04 choked flow model. Thus, a lower C_D value needs to be used with the Moody correlation to approximate the depressurization rate predicted by Cycle 36.04.

The upper plenum to hot leg flow rates were biased more towards the broken loop than the intact loop for about ten seconds as shown in Figures 12.16 and 12.17. The large flow reversal in the broken loop hot leg, observed in the test at about one second after transient initiation, was not predicted by the code. This flow bias is due to the relative differences between the depressurization rates of the two hot legs.

The data as well as the prediction show that the core inlet flow remains negative during the entire blowdown period as shown in Figure 12.20. For the first second after the initiation of the transient, both cases predicted higher values than the measured negative flow rate. From 7 to 12 seconds, the EM predicted less of a negative flow rate than the data and the Cycle 36.04 prediction.

The flow rates from the intact and the broken loop accumulators are shown in Figures 12.21 and 12.22, respectively. The starting points for the accumulator injection as well as the flow rates are consistent with the pressure response near the injection location. The spike in the broken loop accumulator flow data was caused by the opening of a valve^{12.3} and therefore the actual flow did not start until about 3 seconds after transient initiation. The oscillations in the Cycle 36.04 prediction of this accumulator flow were due to the time steps taken by the code. The time steps were larger than those allowed by the Courant limit. Similar oscillations were observed in an EM case when the code used the same time step as in the Cycle 36.04 case. The EM case discussed here was run using time steps which were smaller than that allowed by the Courant limit and it calculated a smooth flow rate as shown in Figure 12.22.

The density variations near the vessel side and the pump side breaks and near the core inlet are shown in Figures 12.23, 12.24, and 12.25, respectively. The spikes in the data as well as in the predictions, during the later part of the transient, were caused by movement of liquid slugs from the ECC injection location to the break. Near the vessel side break the EM calculated density decreased rapidly at about 1.5 seconds after transient initiation. From 1.5 seconds to 5 seconds, oscillation were observed in this density calculation which coincided with the break flow oscillations shown in Figure 12.14. The early decrease in density and its oscillatory behavior are attributable to the switching in the choked flow models as described earlier. After about 5 seconds, the EM calculated density agreed reasonably well with the data until the end of blowdown. Cycle 36.04 underpredicted the density from about 3 to 11 seconds into the transient even though the code predicted the break flow reasonably well (Figure 12.14). Relatively lower slip between the phases, calculated by the Cycle 36.04 choked flow model, caused more than the required amount of liquid to be discharged from the break volume; thus, resulting in a lower volume average density prediction.

Near the pump side break, both the EM and Cycle 36.04 overpredicted the density from 1.5 to 6.0 seconds and underpredicted it during the remainder of the transient which is consistent with the pressure prediction shown in Figure 12.5. Both Cycle 36.04 and the EM overpredicted the density near the core inlet as shown in Figure 12.25. A lower core heat transfer prediction, which is discussed later in this Section, is the major cause of the high density fluid near the core inlet.

Fluid temperature variations at different locations in the primary system are shown in Figures 12.26 through 12.31. The calculated liquid and vapor temperatures are shown in these figures. The figures show that, once the system fluid condition has switched from a subcooled liquid to a two-phase mixture, the liquid and vapor temperatures generally remain near saturation during the major portion of the blowdown period. During the accumulator injection period, the data as well as the prediction show subcooled liquid and saturated steam at the injection location (Figure 12.29). As the liquid slugs move toward the break, the fluid conditions along the path change from a saturation condition to saturated steam and subcooled liquid (Figures 12.27 and 12.28). The effect of lower core heat transfer during the later part of the transient can be observed in the fluid conditions near the core inlet (Figure 12.30) and exit (Figure 12.31).

The cladding temperature variations at the peak power location in the average and the high powered rods are shown in Figures 12.32 and 12.33, respectively. From an examination of the data given in Reference 12.1, it was observed that the cladding temperatures of the rods near the vessel wall were much higher than those of other rods (data D8-27 in Figure 12.32). The unpowered rods in the bundle could reduce the temperatures of the nearby heated rods. However, test S-04-5, which is the counterpart of test S-04-6 (with all rods powered) showed a similar trend in its results. For most of the inner rods, both tests gave about the same temperatures at the peak power locations. Therefore, only the cladding temperatures for the inner rods should be used for comparing the data with predictions.

The predicted cladding surface temperatures are shown in Figures 12.32 and 12.33. In the test, the thermocouples

were located in the creases of the inner sheath. In the model, the cladding was modeled using two radial nodes. Therefore, the inner node temperature would and should be closer to the data. However, in RELAP5 only surface temperatures are stored in the plot file. At steady-state, the calculated temperature of the inner node, in both cases, was found to be close to the data. During the transient, the difference between the surface temperature and the inner node temperature was about 10 F. Hence, the surface temperature is sufficient for comparison purposes.

The EM CHF correlations were found to be conservative in predicting DNB. Cycle 36.04 predicted DNB early by about 1 second for the average powered rods and correctly predicted DNB for the high powered rods. The EM predicted DNB within 0.5 seconds for the average powered rods and within 0.1 seconds for the high powered rods after the initiation of the transient. The DNB in the test occurred at about 3 seconds after the initiation of the transient.

Cycle 36.04 and the EM both predicted higher cladding temperatures than the data during the entire transient period with the EM being even higher than Cycle 36.04. The EM calculated cooling of the high and average powered rods, after reaching the peak cladding temperatures, agreed well with the cooling rate for rod D8-27. Both the test and the EM prediction show a slow cooling of the core after 10 seconds from the initiation of the transient while Cycle 36.04 shows a slow heatup during the same period. From Figure 12.20, it can be concluded that the magnitude of the core flow during this period is slightly higher in the test than it is in either predictions. In the test, this higher core flow promotes added core cooling. In the EM calculation, even though the core flow is lower, the very high cladding temperatures before 10 seconds causes a slow

cooling of the core during the later part of the transient. In the Cycle 30.04 calculation, the lower core flow calculation in the later part of the blowdown and the approximately correct cladding temperature prediction at 10 seconds cause the cladding temperature to increase slowly during the later part of the transient.

Summary and Conclusion

Semiscale MOD1 large break LOCA test S-04-6 was simulated using RELAP5/MOD2-B&W with one case using the Cycle 36.04 options and the other using the B&W EM options. The EM options selected in this study are the same as those selected for actual plant modeling (BAW-10168). As expected, both cases predicted higher break flow rates, faster system depressurization rates, and higher cladding temperatures than the data; the EM generally predicted higher values for these parameters than Cycle 36.04.

The consistency between the transient behavior predicted by the RELAP5/MOD2-B&W evaluation model version and the test data, given allowances for the effects of the EM discharge and core heat transfer models, supports application of B&W's EM version for conservative calculations of blowdown during large LOCA transients. When applied according to Appendix K requirements, using a spectrum of effective break area-discharge coefficient combinations, RELAP5/MOD2-B&W should prove effective in defining limiting end-of-blowdown conditions.

- 12.1 H. S. Crapo, et al, Experiment Data Report for Semiscale MOD-1 Test S-04-5 and S-04-6 (Baseline ECC Tests), TREE-NUREG-1045, January 1977.
- 12.2 L. J. Ball et al, Semiscale Program Description, TREE-NUREG-1210, May 1978.
- 12.3 M. S. Sahota, Comparisons of RELAP4/MOD2 With Semiscale Blowdown Data, CVAP-TR-78-023, July 1978.
- 12.4 V. H. Ransom, et al, RELAP5/MOD0 Code Description Volume 2 - RELAP5 Code Development Update and Sample Problems, CDAP-TR-057 (Volume 2), July 1978.

Table 12.1. Sequence of Events During Test S-04-6 .

<u>Event</u>	<u>Time (sec)</u>
Blowdown Initiated	0.0
ECC Accumulators Initiated	0.0
HPI Pumps Started	0.0
Steam Generator Feedwater and Discharge Valves Closed	1.0
LPI Started	30.0

Table 12.2. Conditions at Blowdown Initiation .

<u>Parameter</u>	<u>Data</u>	<u>Cycle 36.04</u>	<u>EM</u>
Core Power, kW	1.44	1.44	1.44
Cold Leg Fluid Temperature, F	543.0	543.5	543.0
Hot Leg Fluid Temperature, F	610.0	610.3	609.5
Pressurizer Pressure, psia	2252.0	2253.3	2252.6
Pump Speed, RPM	2400.0	2400.0	2400.0
ICL Flow Rate, lbm/s	15.5	15.4	15.4
Steam Generator Pressure, psia	850.0	809.5	803.5
Pressure Suppression Tank Pressure, psia	34.8	34.8	34.8

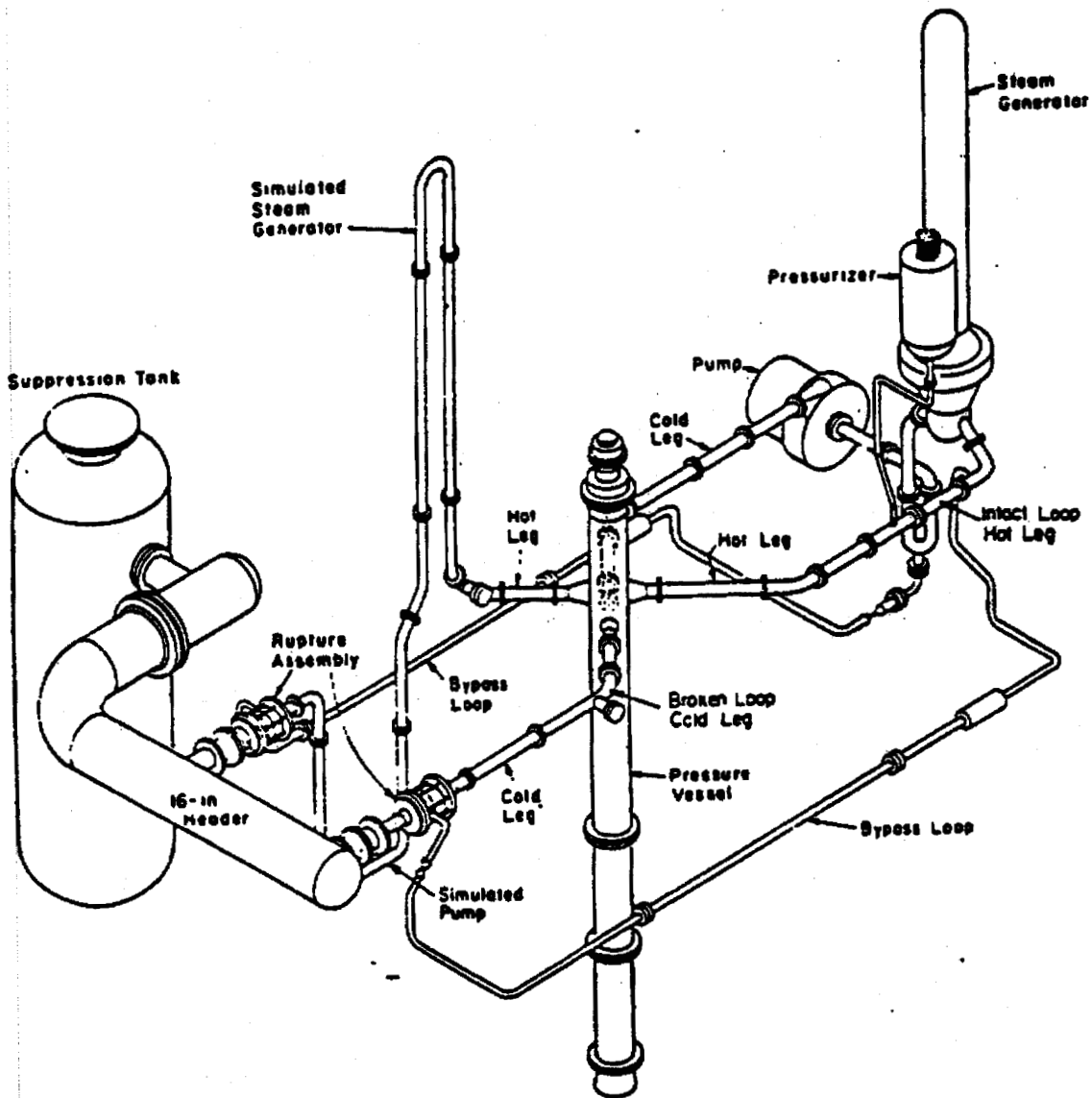


Figure 12.1. Semiscale MOD1 Test Facility - Cold Leg Break Configuration.

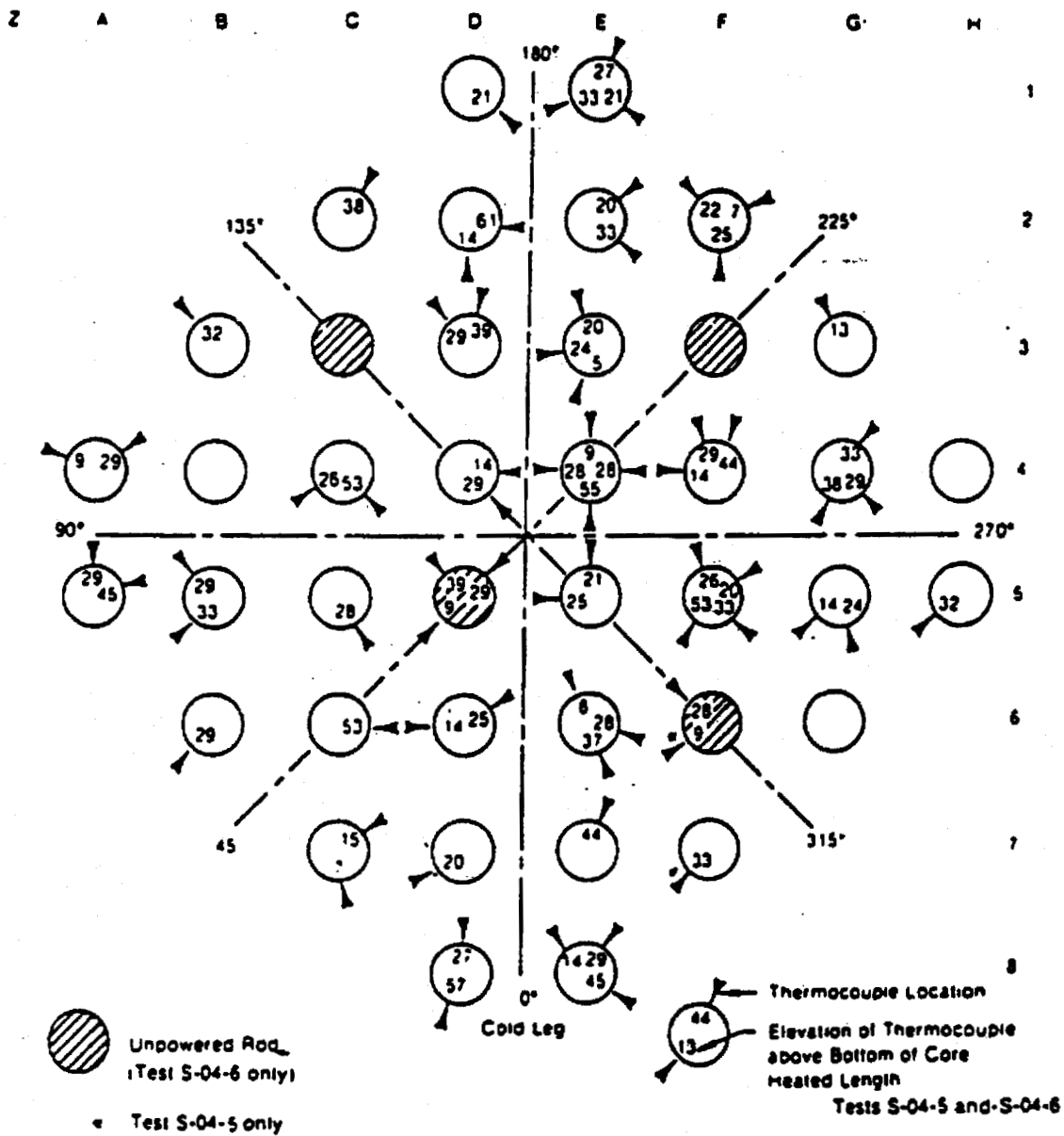


Figure 12.2. Semiscale MOD1 Rod Locations for Test S-04-6.

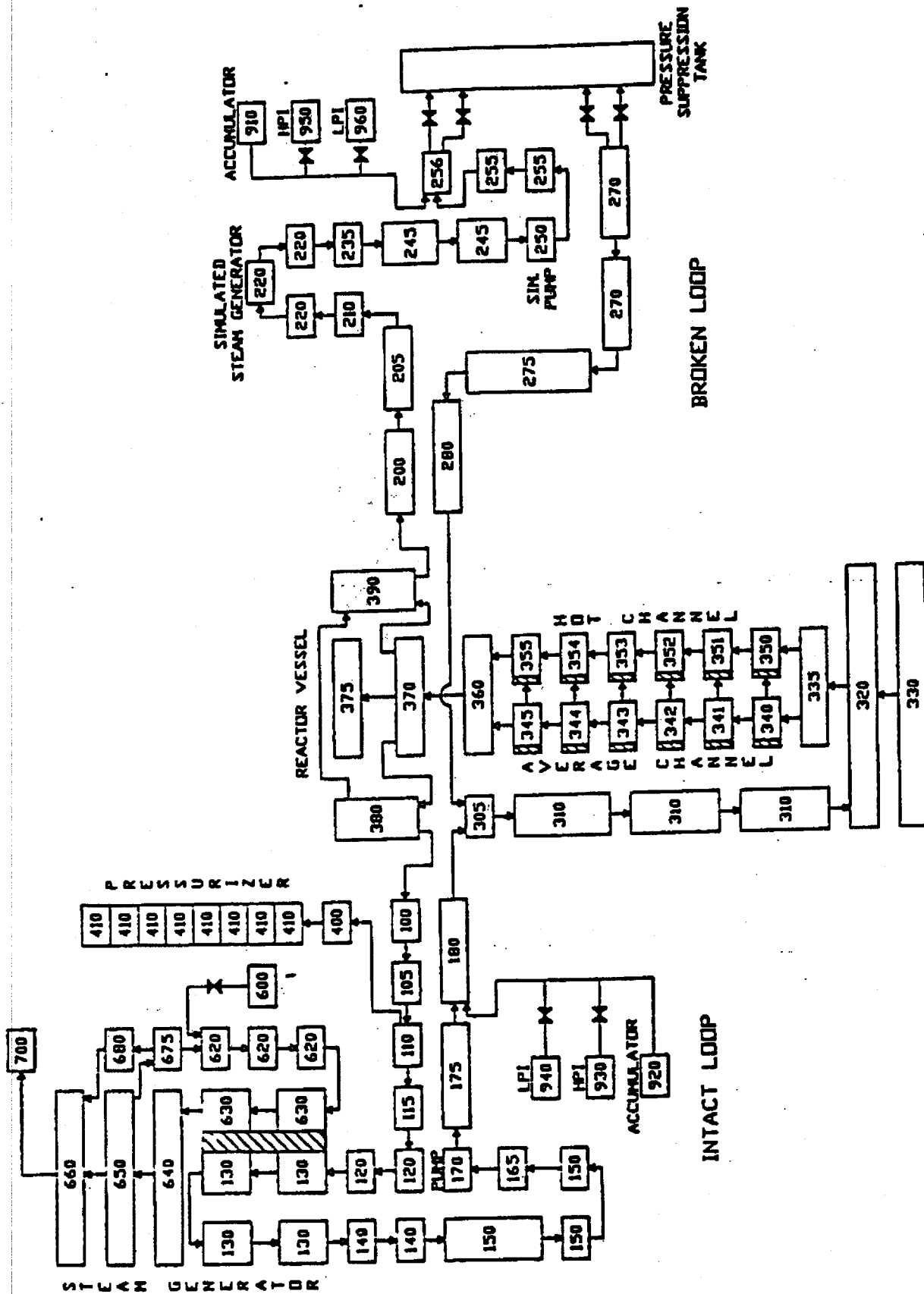


Figure 12.3. RELAP5 Node and Junction Diagram.

FIGURE 12.4. SEMSCALE MOD1 TEST S-04-6; PRESSURE NEAR THE VESSEL SIDE BREAK.

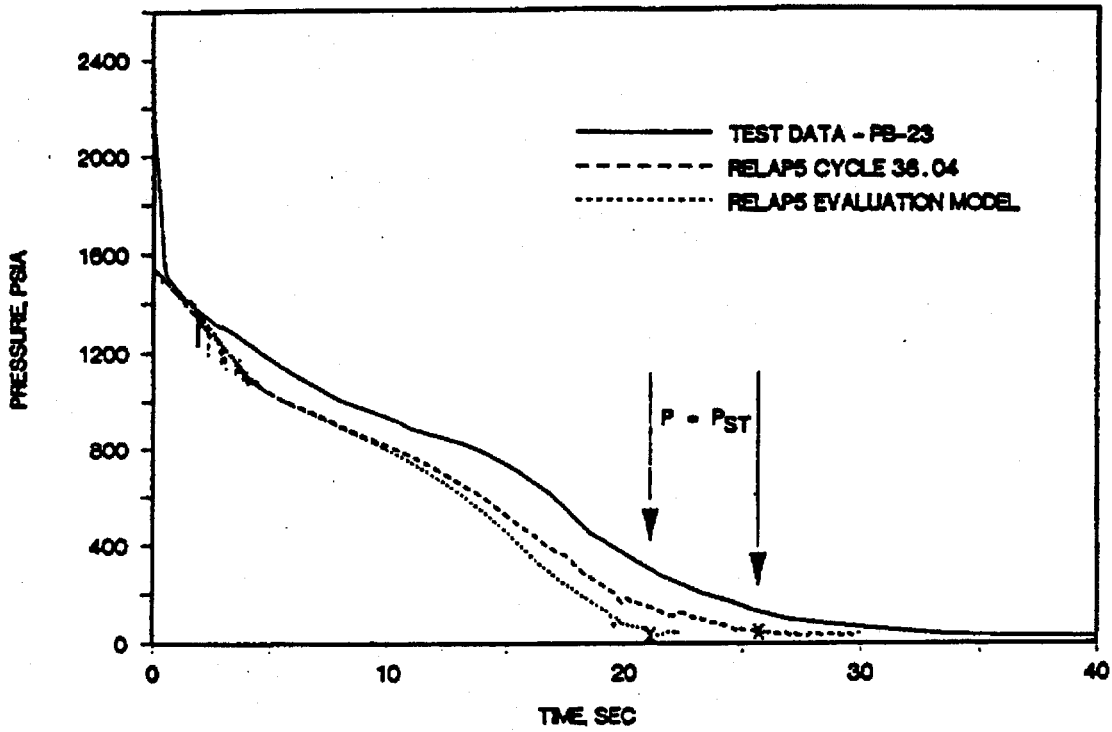


FIGURE 12.5. SEMSCALE MOD1 TEST S-04-6; PRESSURE NEAR THE PUMP SIDE BREAK.

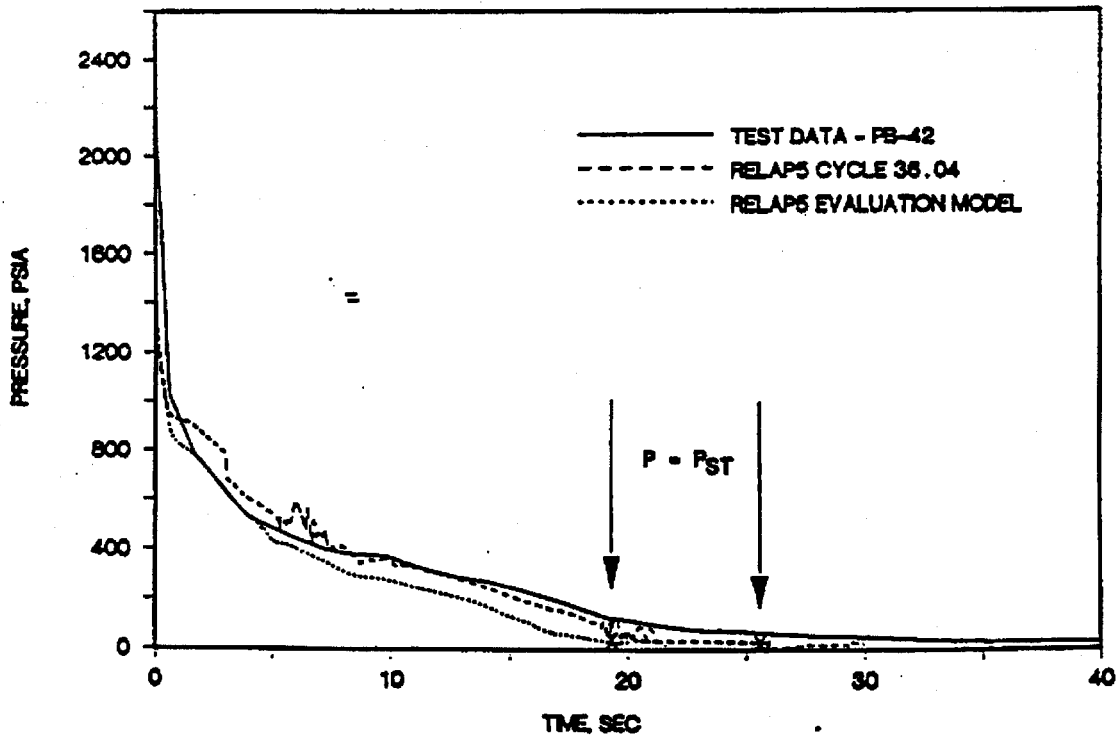


FIGURE 12.6. SEMISCALE MOD1 TEST S-04-6; PRESSURE NEAR THE INTACT LOOP PUMP EXIT.

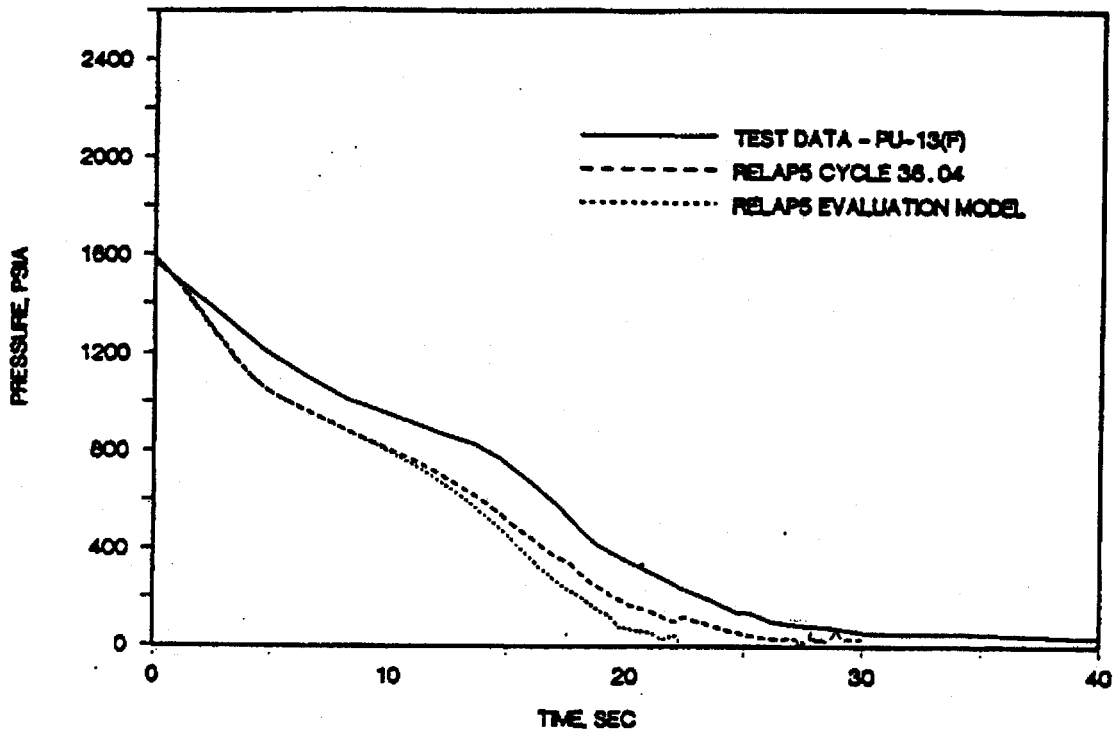


FIGURE 12.7. SEMISCALE MOD1 TEST S-04-6; PRESSURE IN THE BROKEN LOOP NEAR THE PUMP SIMULATOR INLET.

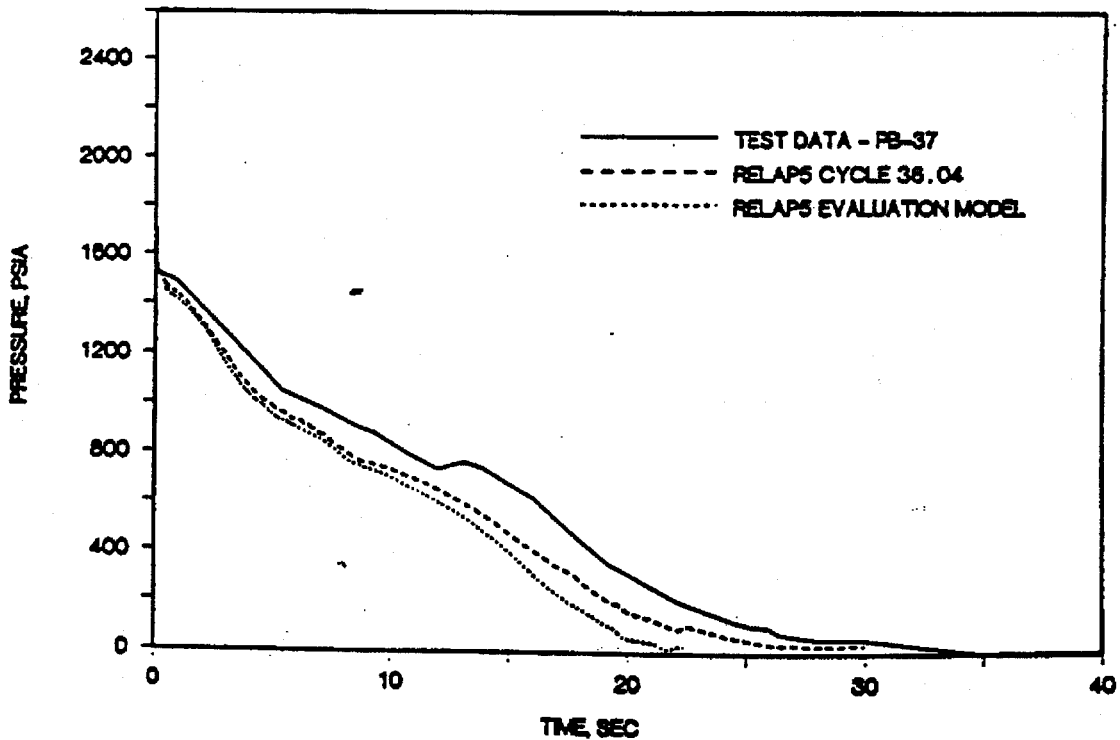


FIGURE 12.8. SEMISCALE MOD1 TEST S-04-6; PRESSURE IN THE LOWER PLENUM.

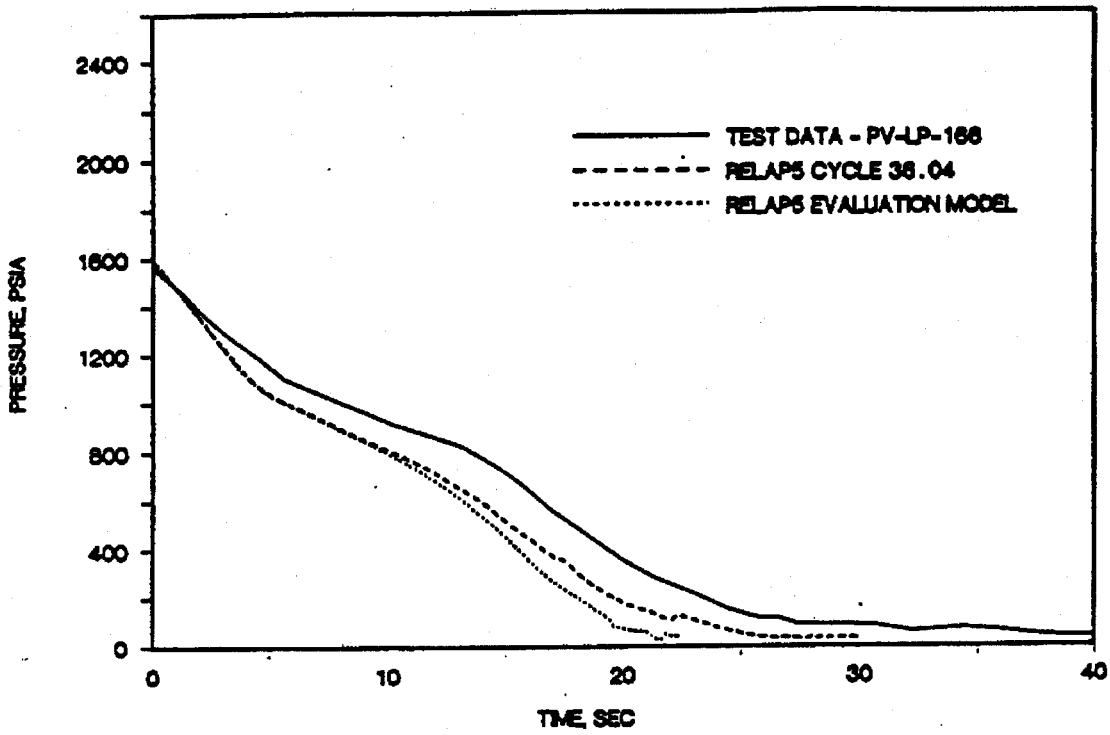


FIGURE 12.9. SEMISCALE MOD1 TEST S-04-6; PRESSURE IN THE UPPER PLENUM.

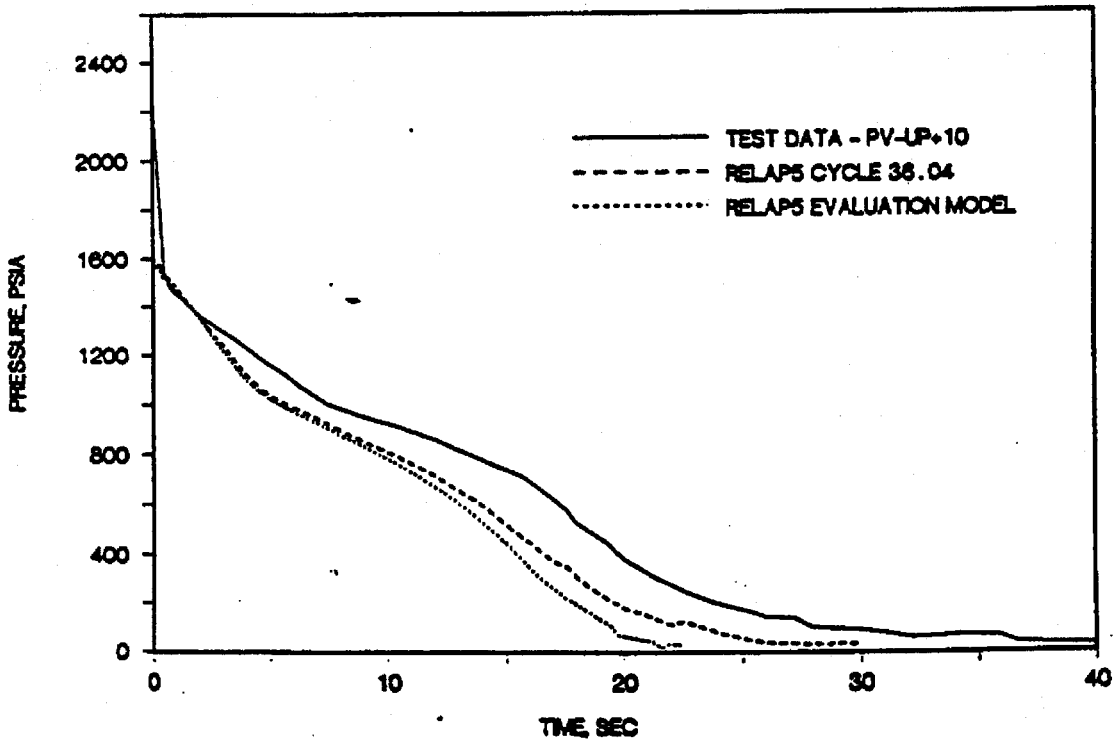


FIGURE 12. 10. SEMISCALE MOD1 TEST S-04-6; PRESSURE NEAR THE TOP OF THE PRESSURIZER.

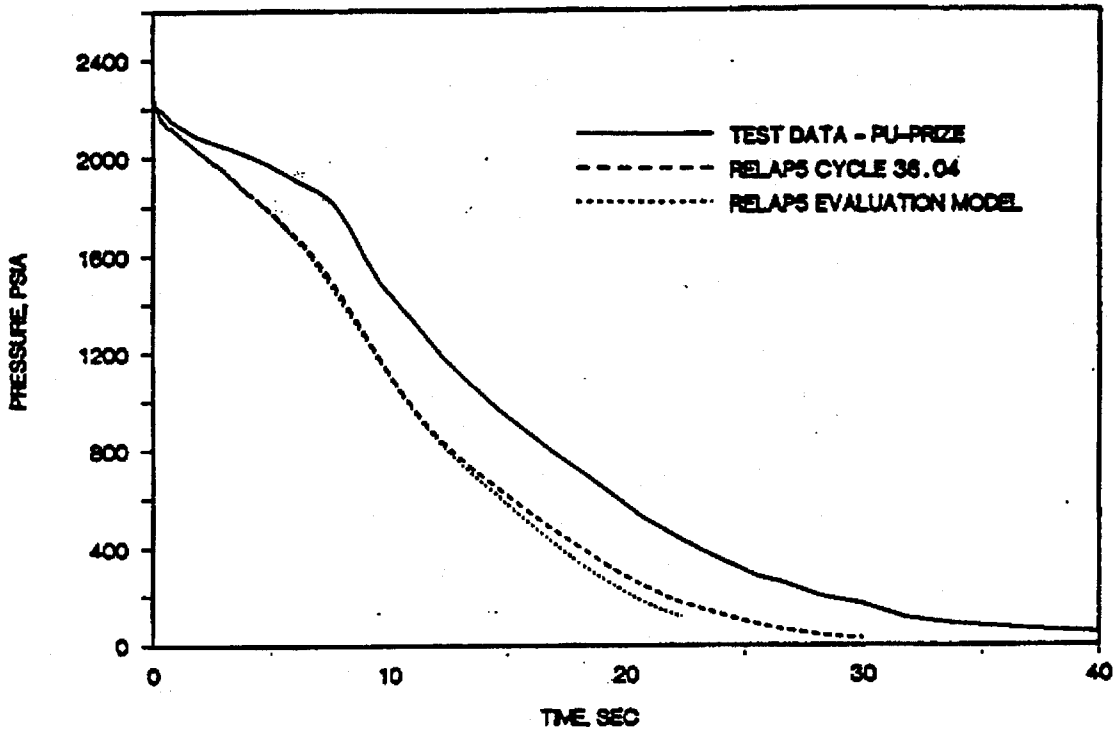


FIGURE 12. 11. SEMISCALE MOD1 TEST S-04-6; PRESSURE IN THE INTACT LOOP ACCUMULATOR.

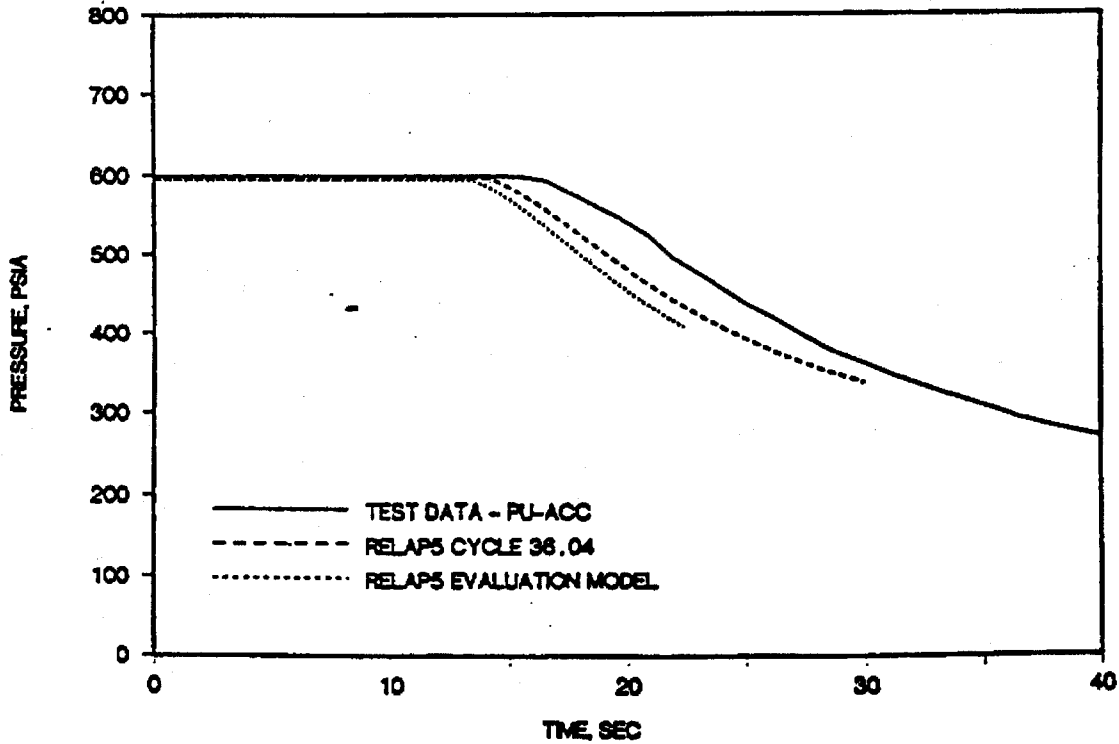


FIGURE 12. 12. SEMISCALE MOD1 TEST S-04-6; PRESSURE IN THE BROKEN LOOP ACCUMULATOR.

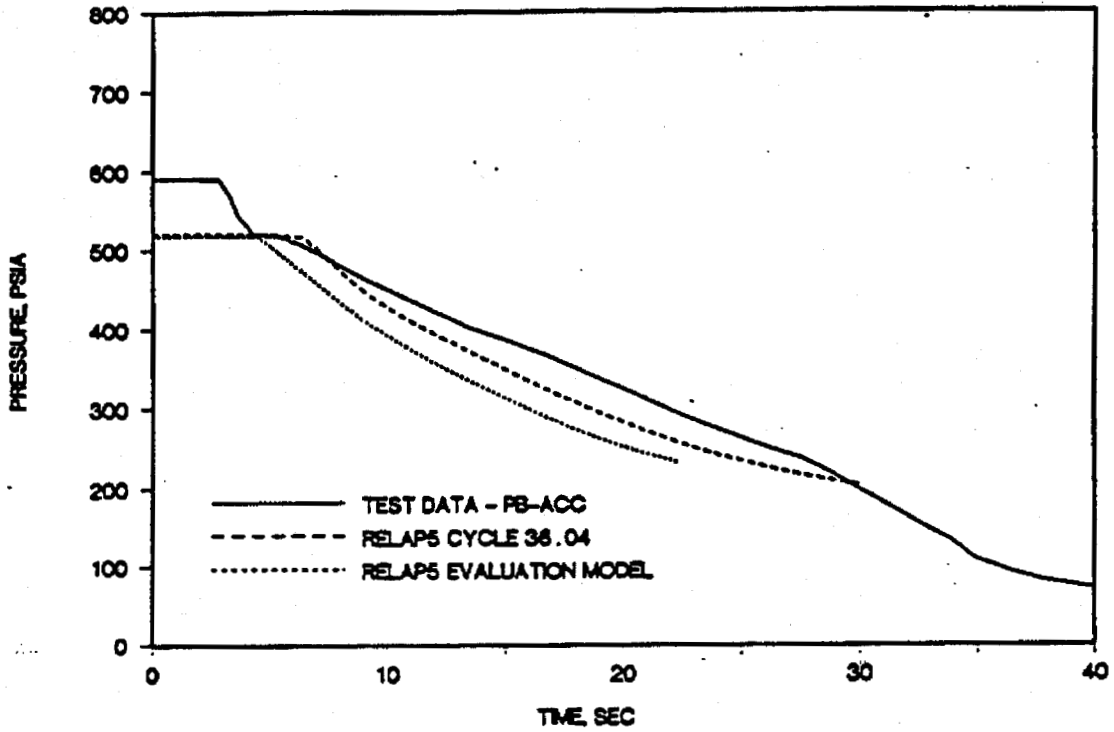


FIGURE 12. 13. SEMISCALE MOD1 TEST S-04-6; DIFFERENTIAL PRESSURE IN THE PRESSURIZER.

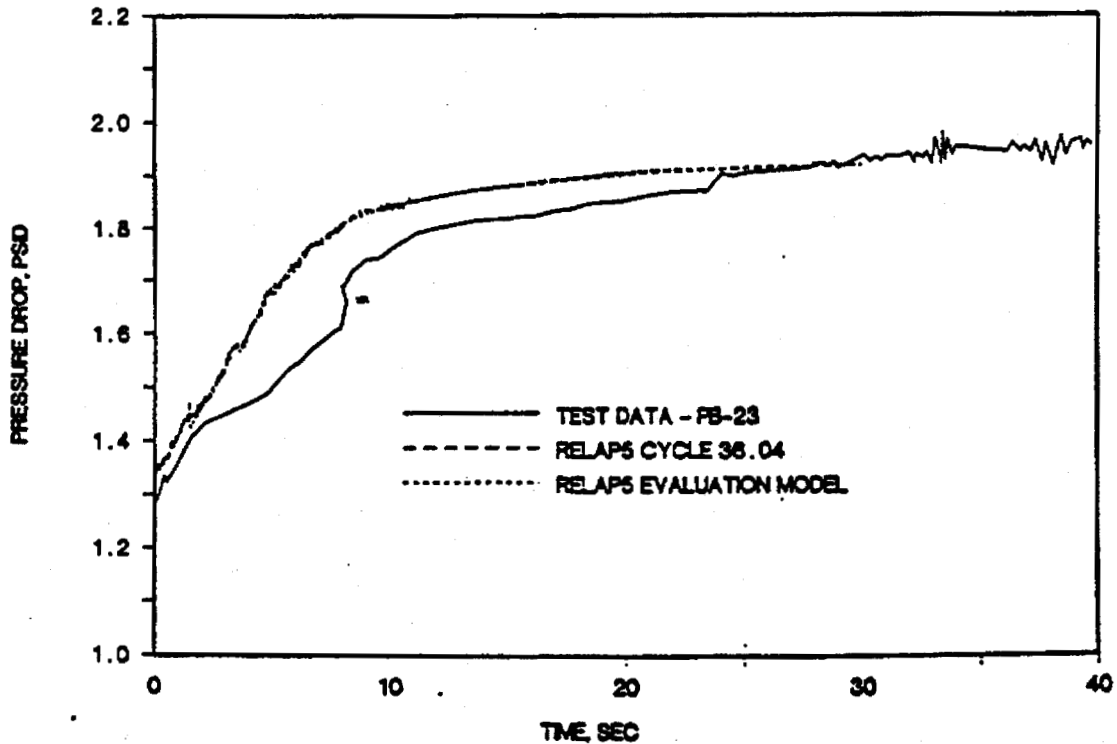


FIGURE 12. 14. SEMISCALE MOD1 TEST S-04-6; MASS FLOW RATE NEAR THE VESSEL SIDE BREAK.

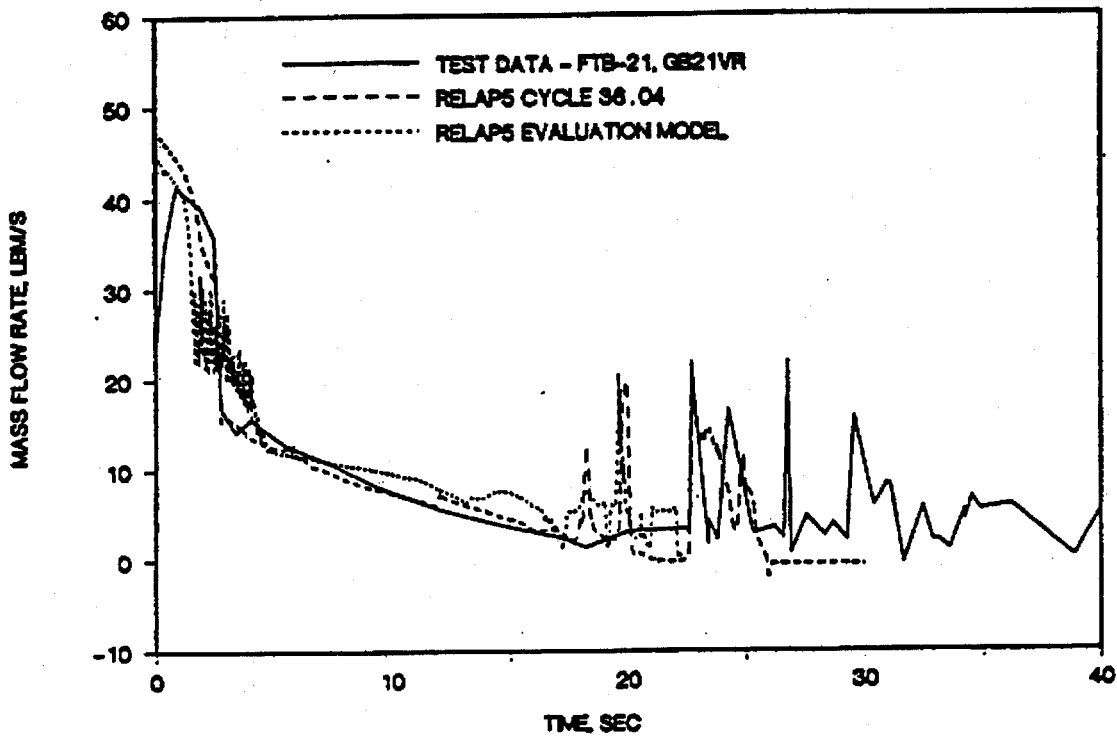


FIGURE 12. 15. SEMISCALE MOD1 TEST S-04-6; MASS FLOW RATE NEAR PUMP SIDE BREAK (BEFORE ECC INJECTION POINT).

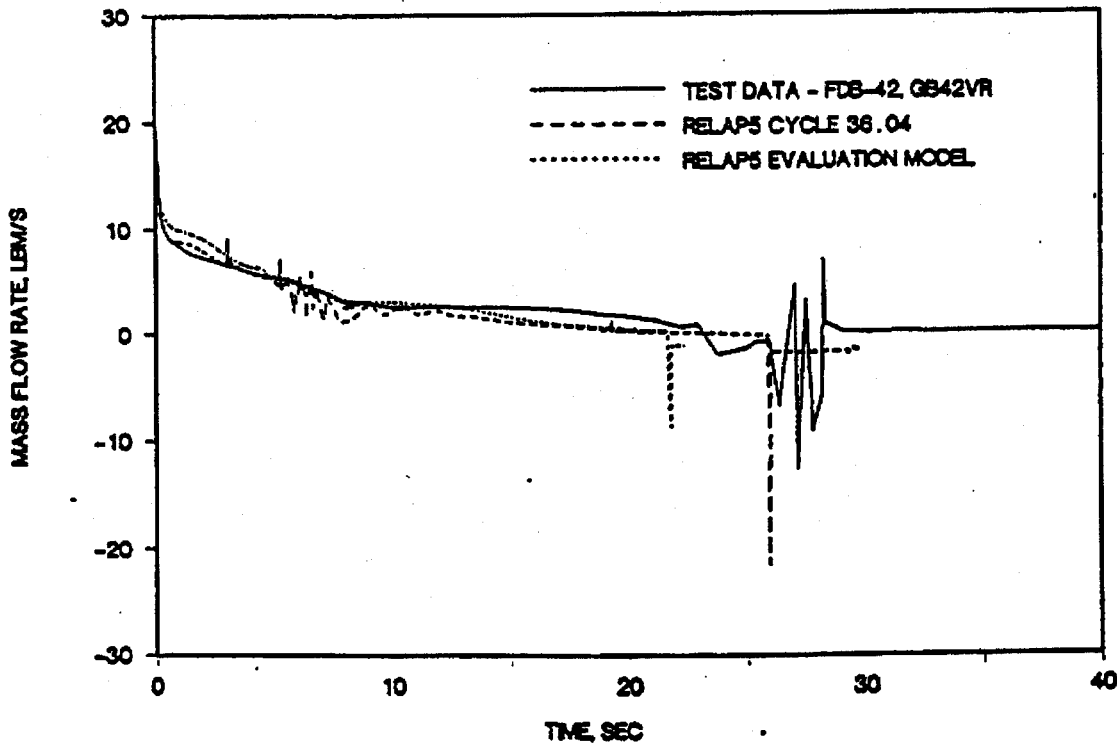


FIGURE 12. 16. SEMISCALE MOD1 TEST S-04-6; MASS FLOW RATE IN THE INTACT LOOP HOT LEG.

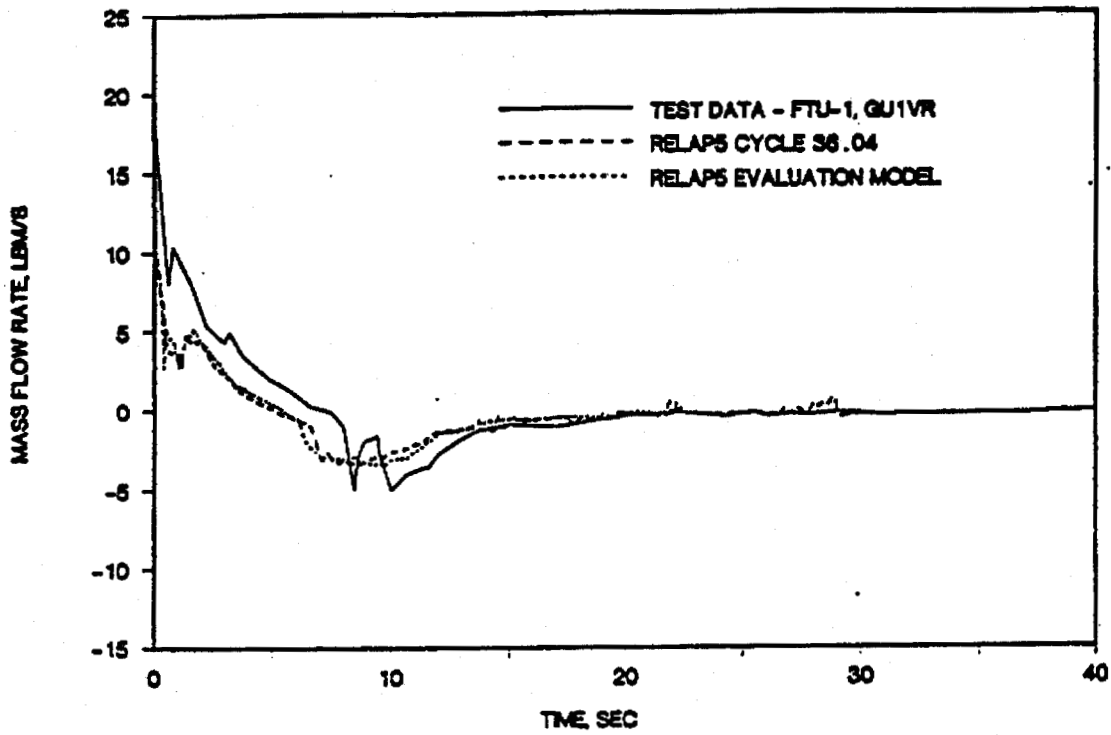


FIGURE 12. 17. SEMISCALE MOD1 TEST S-04-6; MASS FLOW RATE NEAR THE PUMP SIMULATOR INLET.

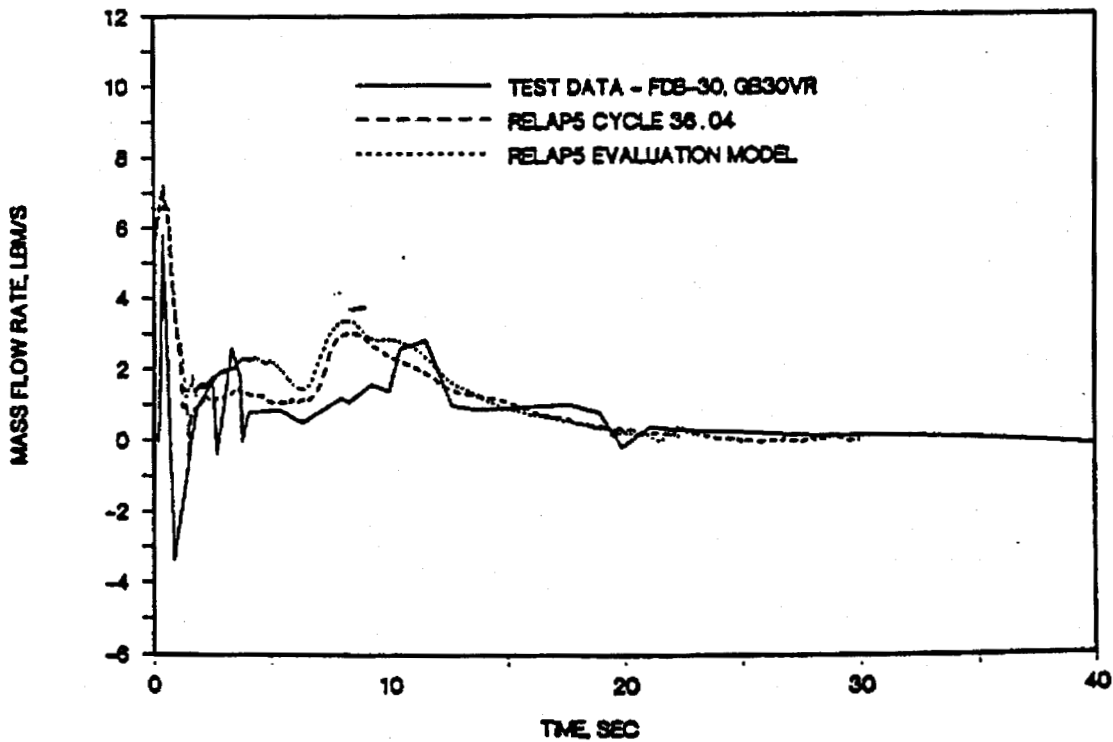


FIGURE 12. 18. SEMISCALE MOD1 TEST S-04-6; MASS FLOW RATE IN INTACT LOOP COLD LEG (BEFORE ACCUMULATOR INJECTION POINT).

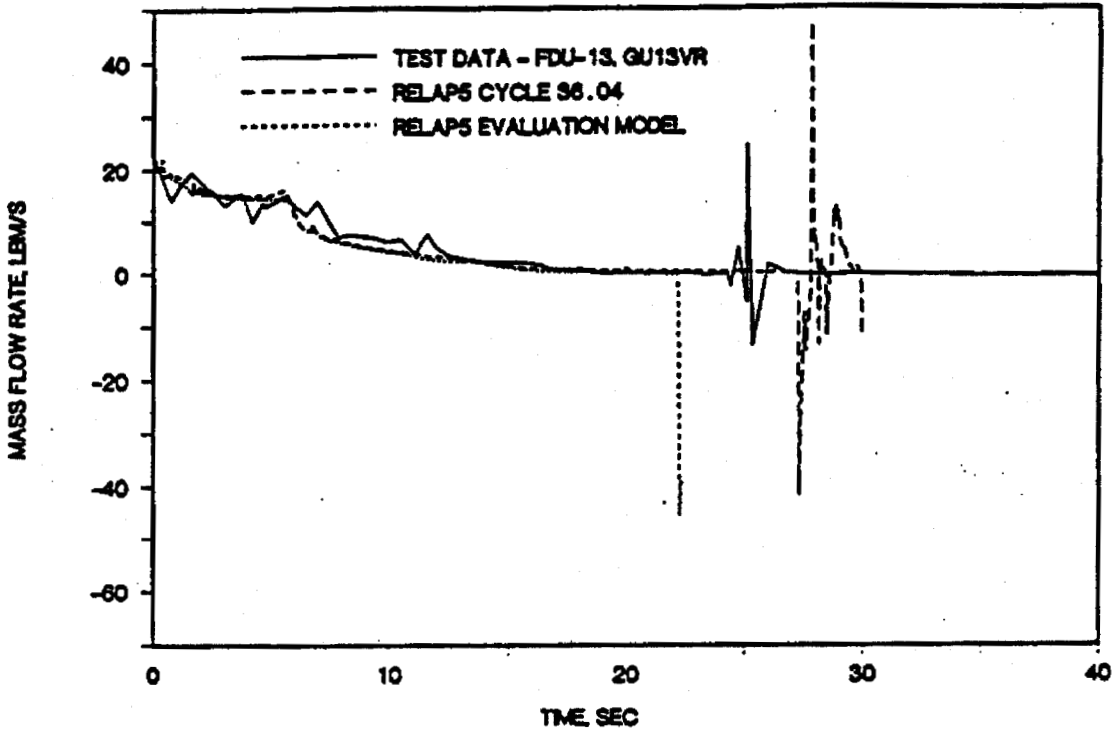


FIGURE 12. 19. SEMISCALE MOD1 TEST S-04-6; DOWNCOMER INLET FLOW RATE FROM THE INTACT LOOP.

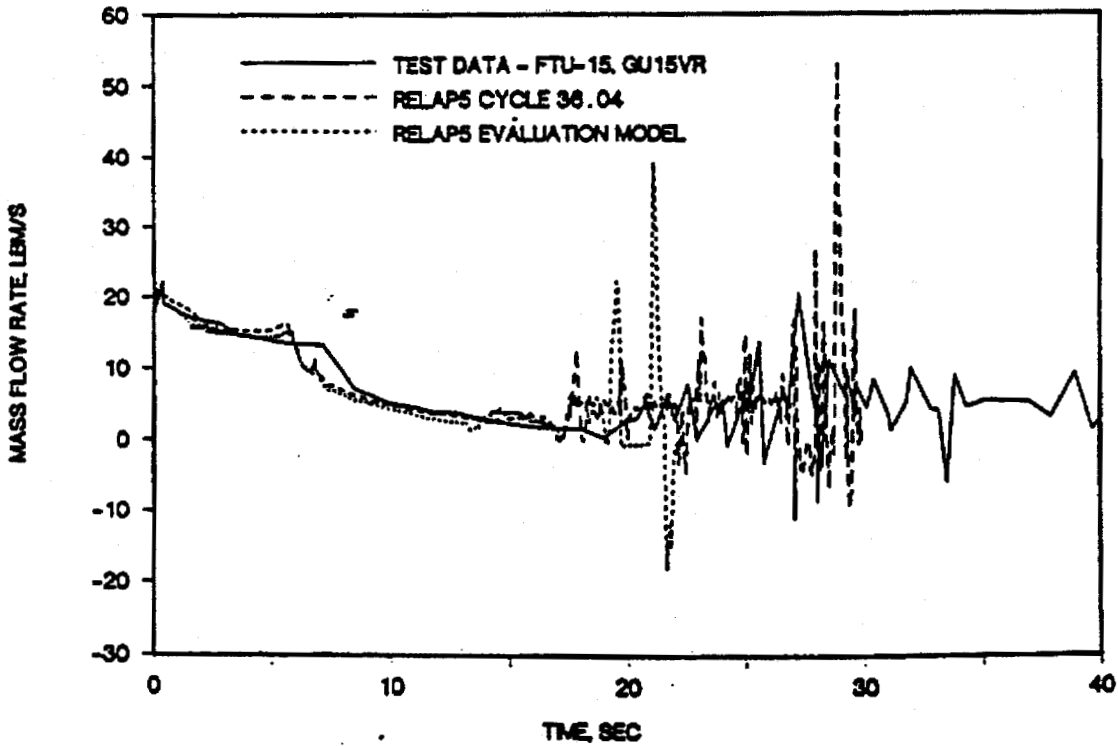


FIGURE 12.20. SEMISCALE MOD1 TEST S-04-6; MASS FLOW RATE AT THE CORE INLET.

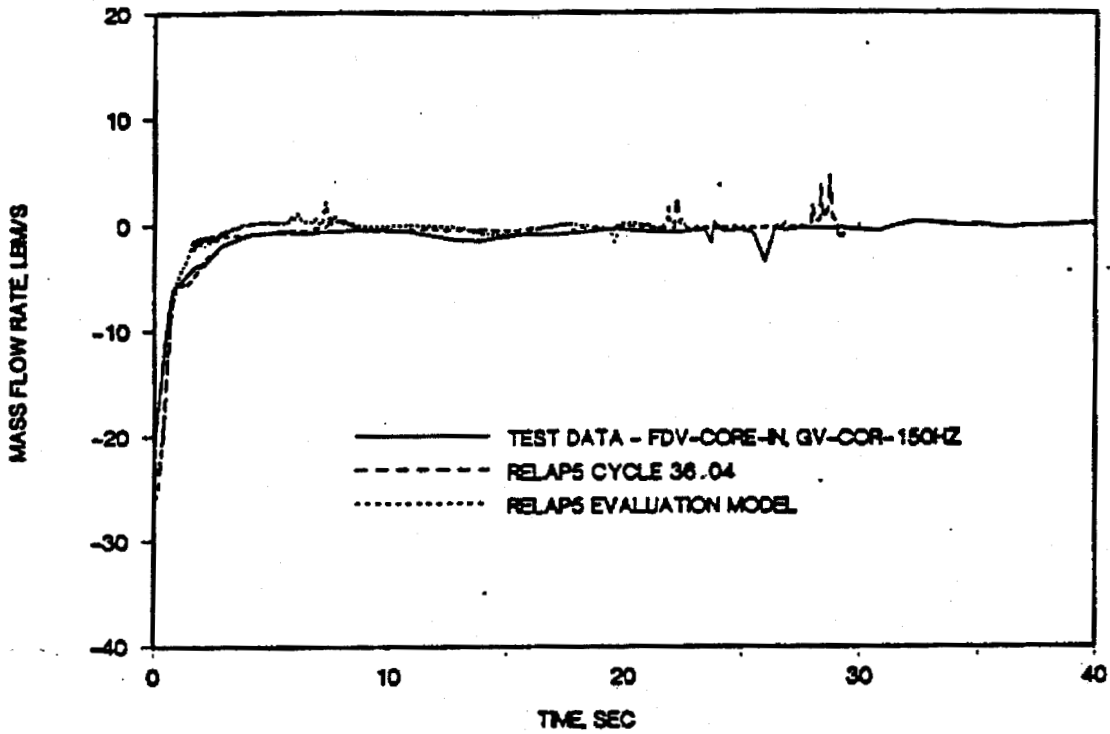


FIGURE 12.21. SEMISCALE MOD1 TEST S-04-6; MASS FLOW RATE FROM THE INTACT LOOP ACCUMULATOR.

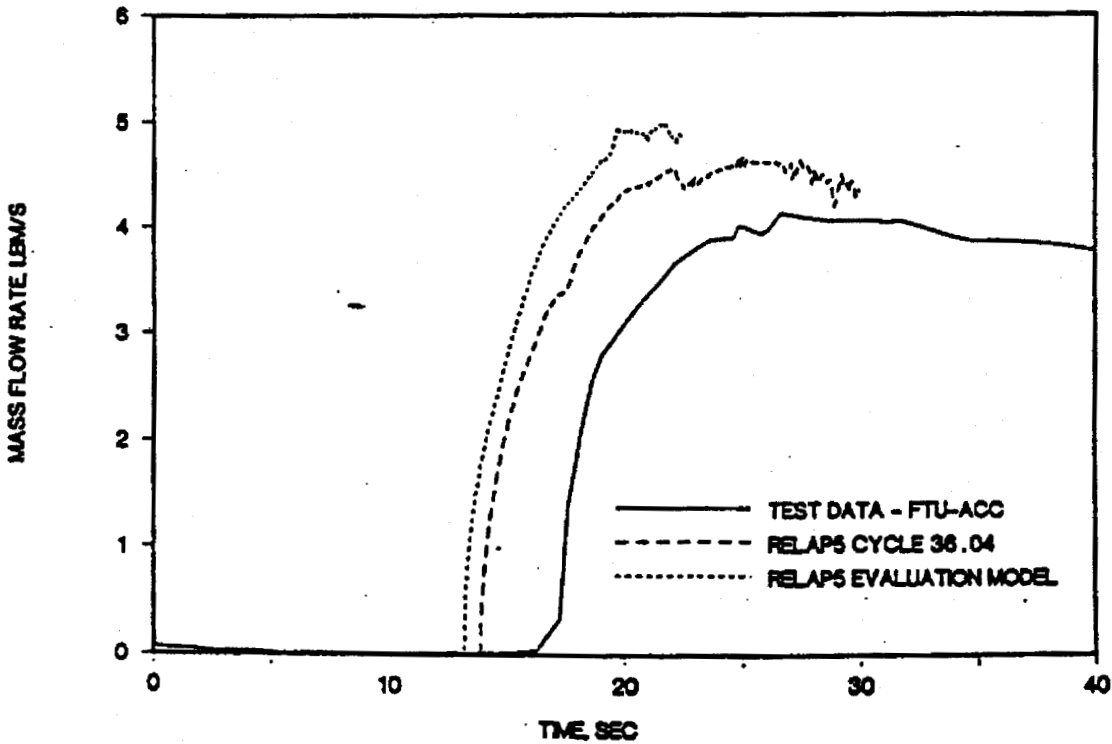


FIGURE 12.22. SEMISCALE MOD1 TEST S-04-6: MASS FLOW RATE FROM THE BROKEN LOOP ACCUMULATOR.

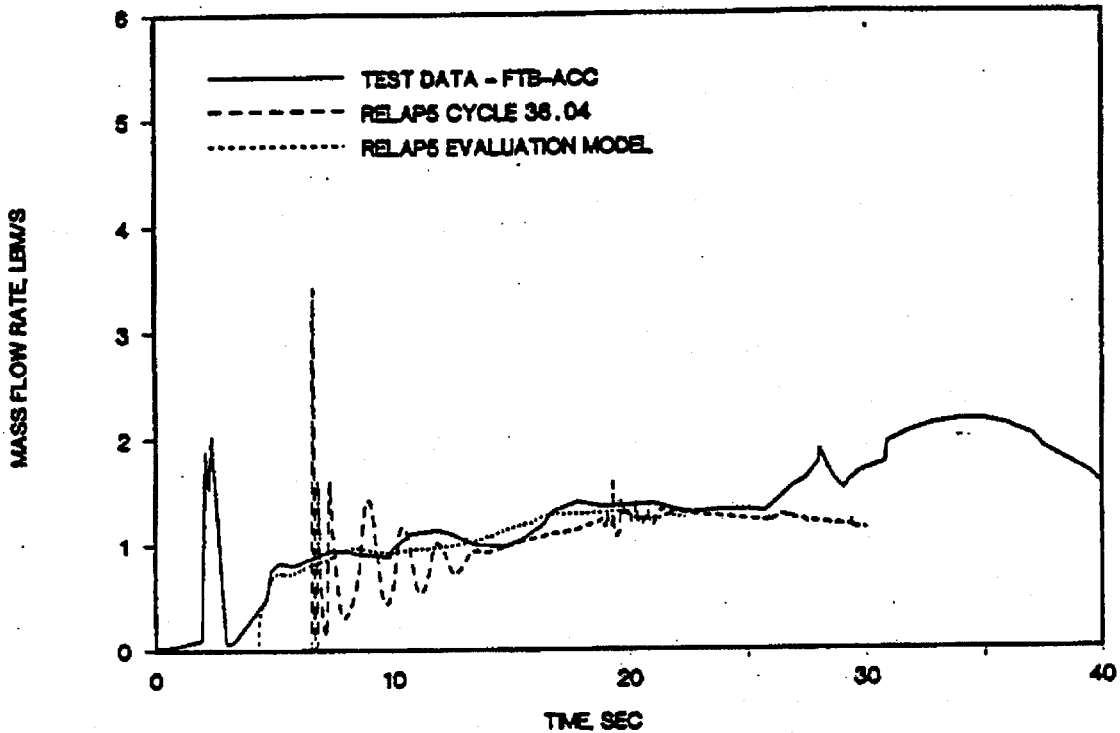


FIGURE 12.23. SEMISCALE MOD1 TEST S-04-6: DENSITY NEAR THE VESSEL SIDE BREAK.

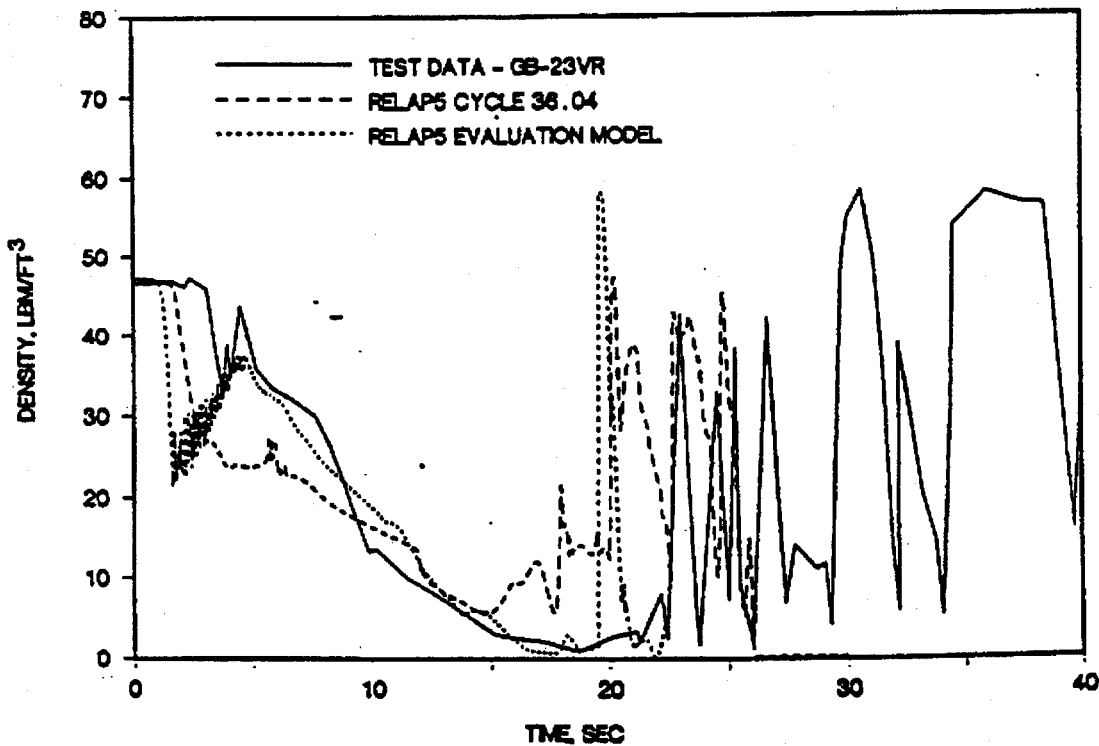


FIGURE 12.24. SEMISCALE MOD1 TEST S-04-6; DENSITY NEAR THE PUMP SIDE BREAK (BEFORE THE ECC INJECTION LOCATION).

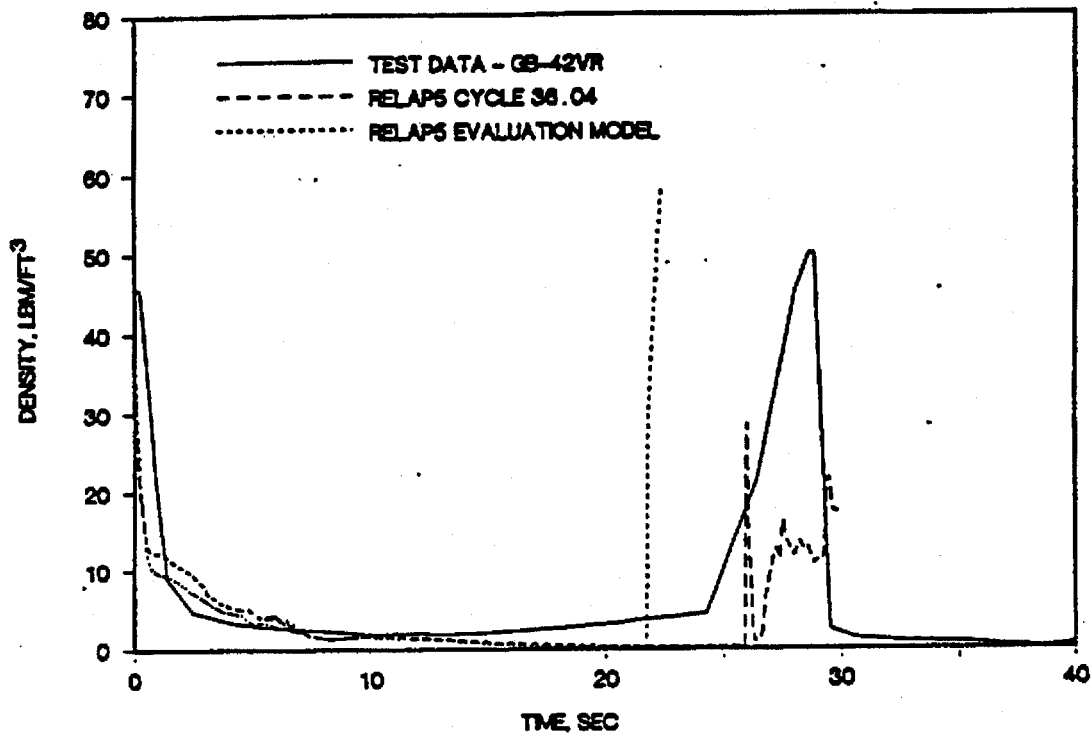


FIGURE 12.25. SEMISCALE MOD1 TEST S-04-6; DENSITY NEAR THE CORE INLET.

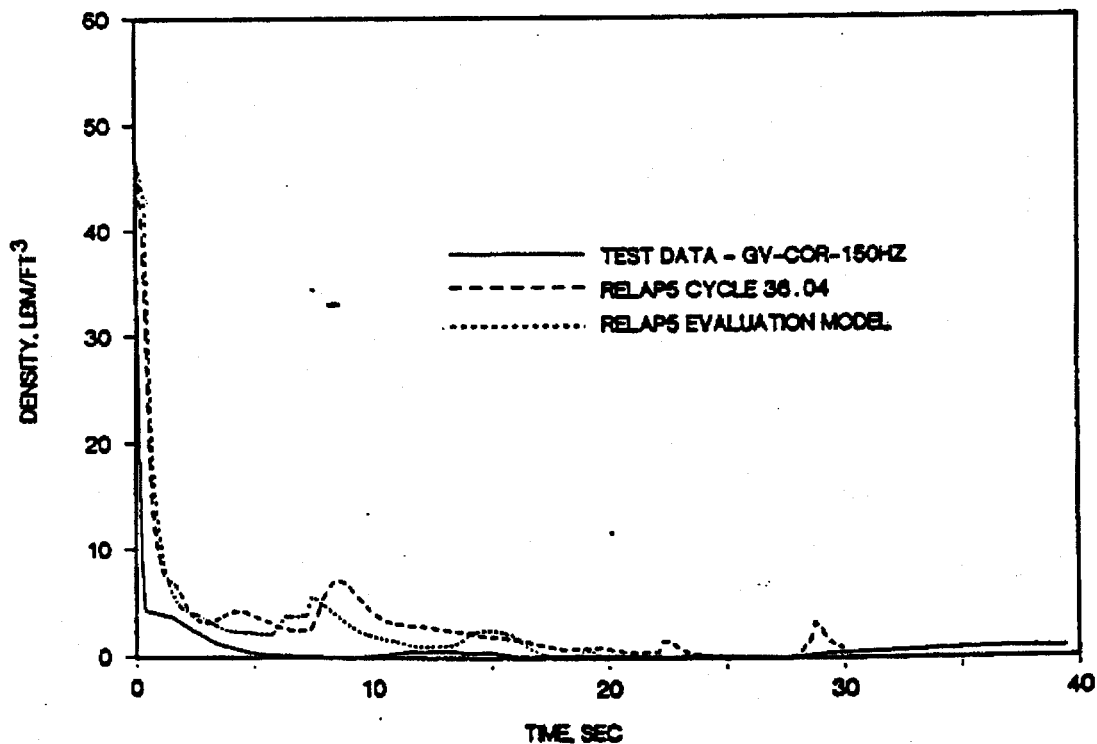


FIGURE 12.26. SEMISCALE MOD1 TEST S-04-6; FLUID TEMPERATURE NEAR THE VESSEL SIDE BREAK.

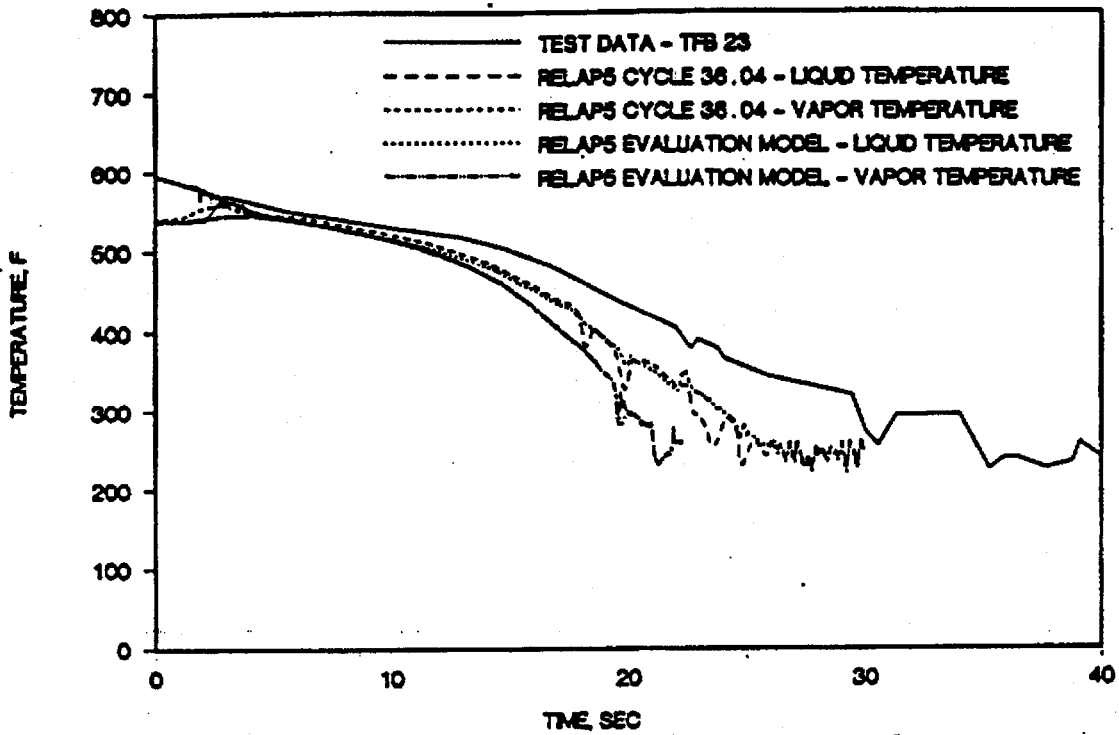


FIGURE 12.27. SEMISCALE MOD1 TEST S-04-6; FLUID TEMPERATURE NEAR PUMP SIDE BREAK (BEFORE ECC INJECTION LOCATION).

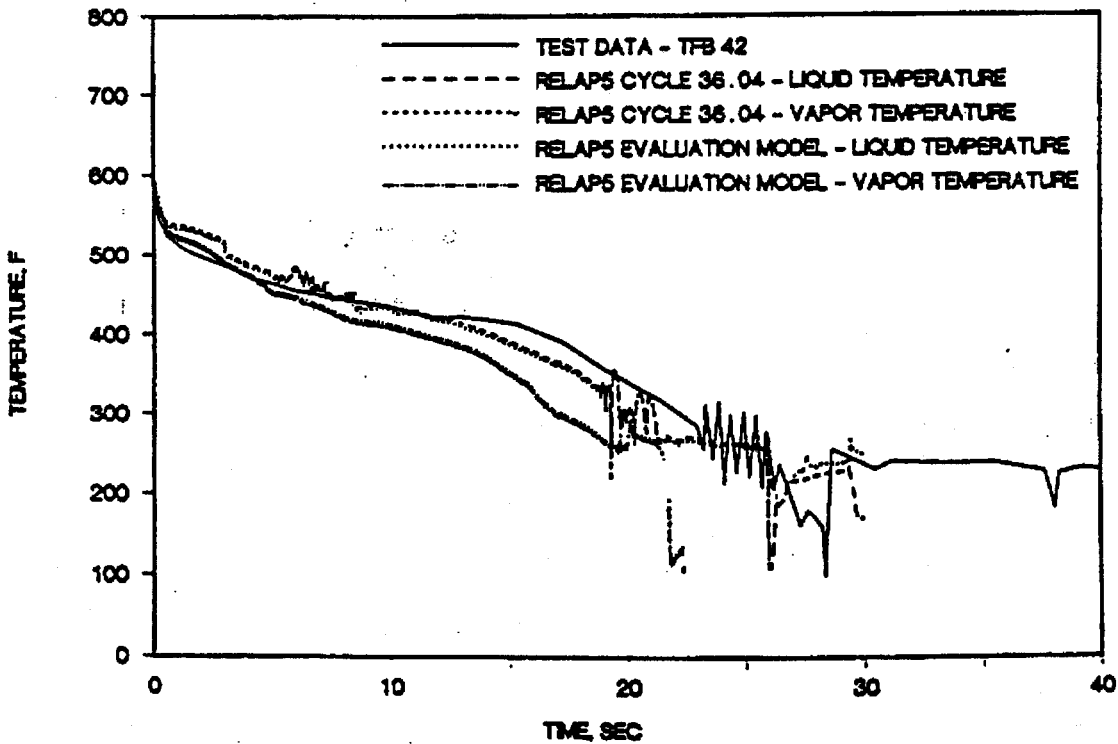


FIGURE 12.28. SEMISCALE MOD1 TEST S-04-6; FLUID TEMPERATURE IN THE INTACT LOOP HOT LEG.

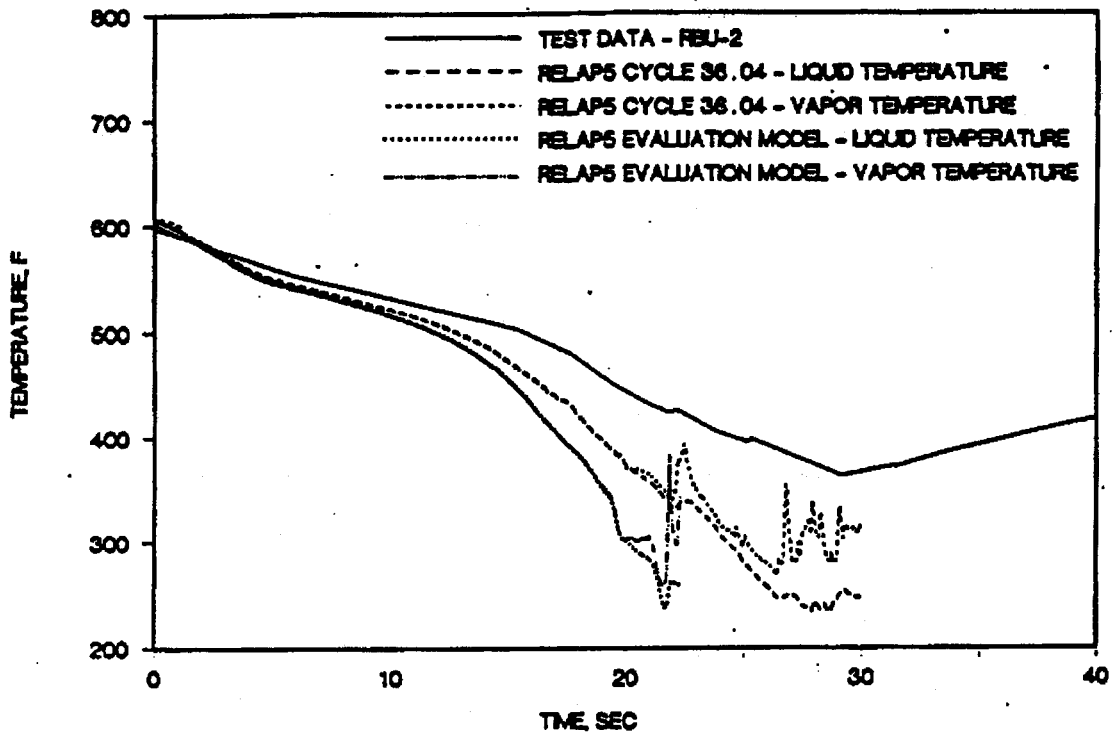


FIGURE 12.29. SEMISCALE MOD1 TEST S-04-6; FLUID TEMPERATURE IN INTACT LOOP COLD LEG (NEAR ECC INJECTION POINT).

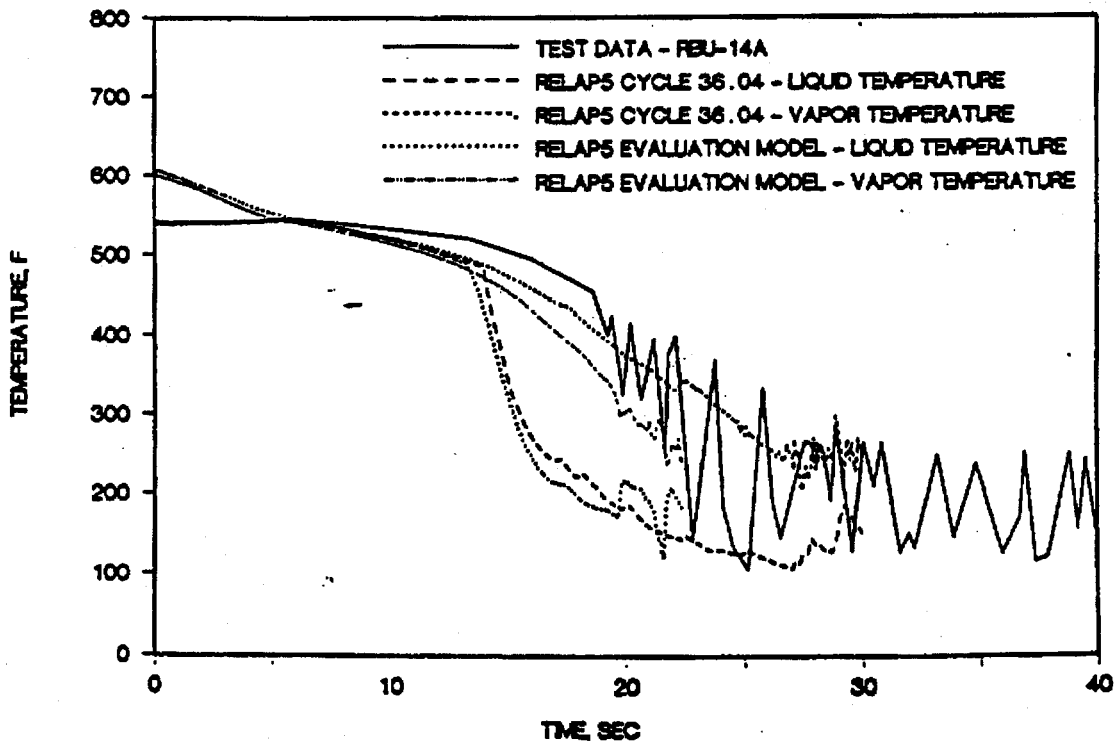


FIGURE 12.30. SEMISCALE MOD1 TEST S-04-6; FLUID TEMPERATURE NEAR THE CORE INLET.

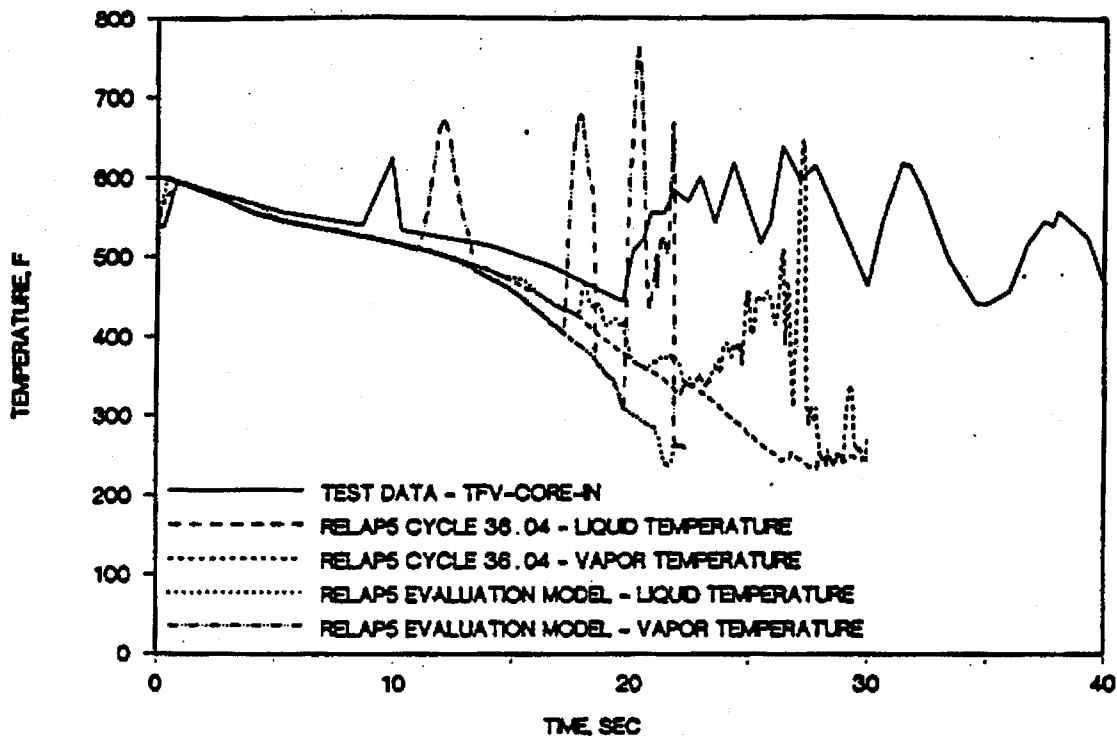


FIGURE 12.31. SEMISCALE MOD1 TEST S-04-6; FLUID TEMPERATURE IN UPPER PLENUM.

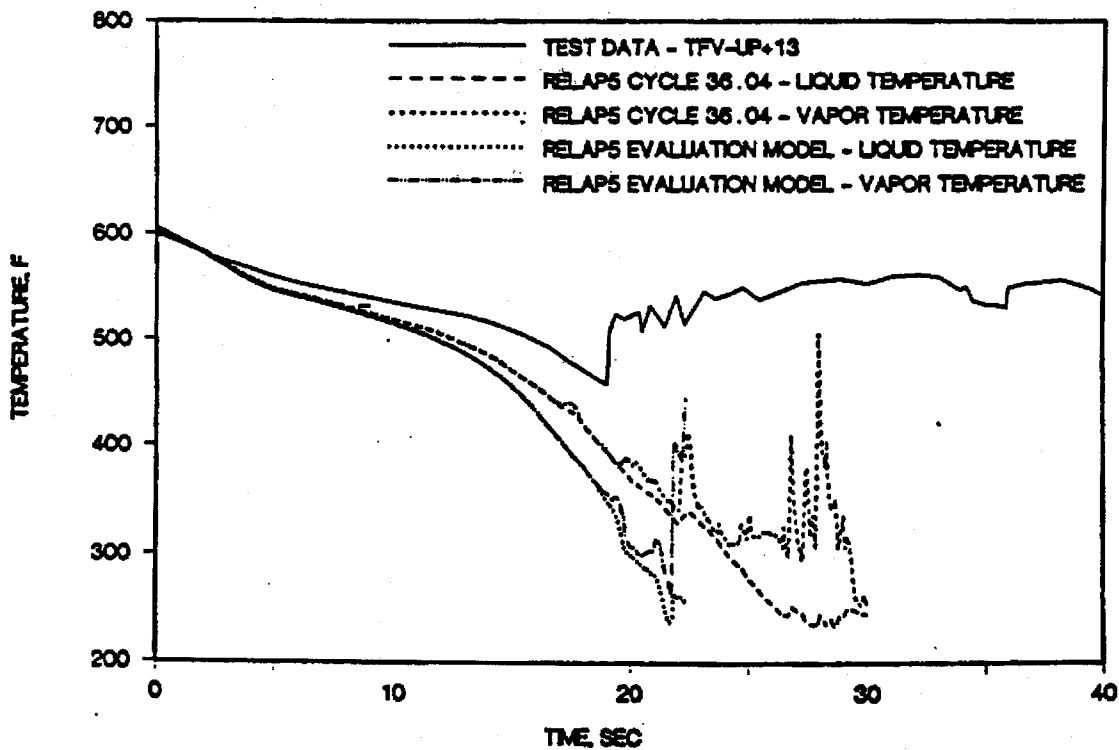


FIGURE 12.32. SEMISCALE MOD1 TEST S-04-6; AVERAGE POWER ROD CLADDING TEMPERATURE AT PEAK POWER LOCATION.

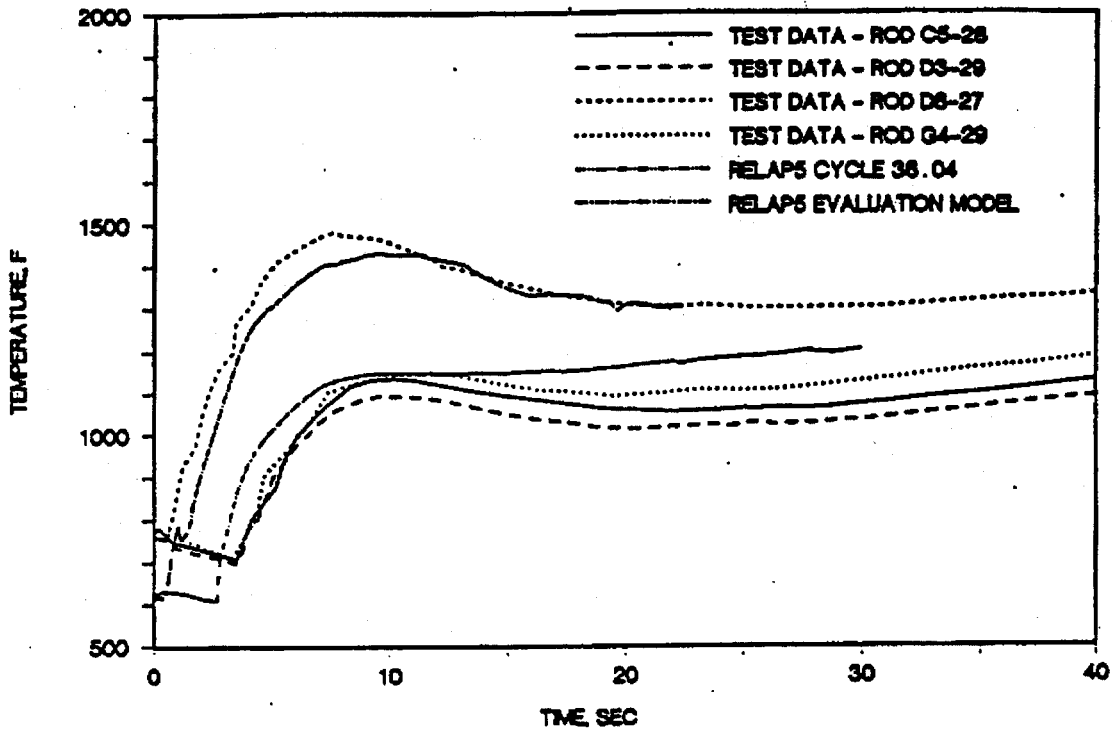
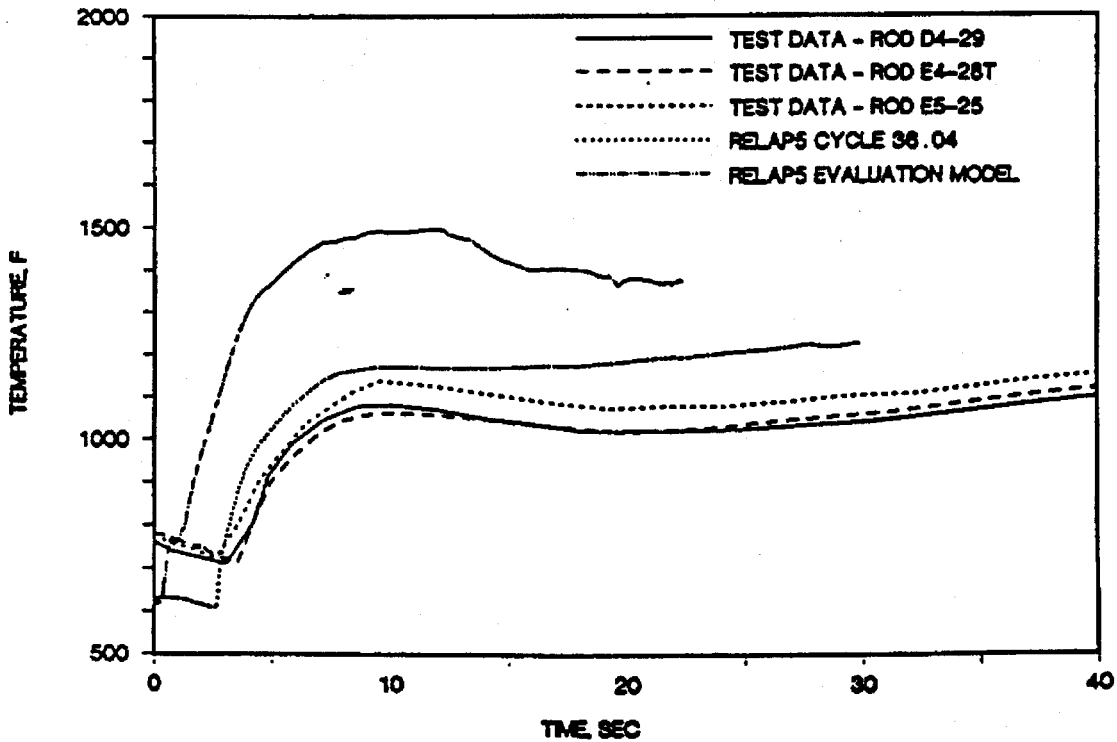


FIGURE 12.33. SEMISCALE MOD1 TEST S-04-6; HIGH POWER ROD CLADDING TEMPERATURE NEAR PEAK POWER LOCATION.



13. Question: The S-04-6 results presented by B&W did not compare the calculated and measured pressurizer level response. Provide this comparison to verify the code and system models B&W intends to use in plant calculations adequately calculate this phenomenon.

Response: See the response to question 12:

14. Question: In small break LOCAs (SBLOCAs), accurately calculating the mass distribution in the primary system is important to predicting the overall system response. The code/data comparisons provided by B&W for the LOFT L3-5 assessment calculation did not include any comparisons that would indicate how well RELAP5/MOD2-B&W calculated the mass distribution.
- a. Provide plots comparing calculated and measured densities around the primary system to verify the mass distribution was accurately calculated by the code.
 - b. Compare the calculated and measured times of loop seal clearing and provide a comparison of the calculated and measured primary system mass inventories.
 - c. Provide a comparison of the calculated and measured break flows for LOFT L3-5.
 - d. Clarify why the pump coasted down more rapidly in the calculation for LOFT3-5 than in the experiment (Figure G.2-7).

Response:

As indicated in Section G.2 of BAW-10164, RELAP5/MOD2-B&W predicted the overall system response, including primary and secondary system pressure, pump coastdown, natural circulation and long-term cooling, reasonably well. Despite the underprediction of the BE discharge model, which in large measure reflects the need to use a discharge coefficient greater than one, such uncertainties are generally accounted for in EM applications through a spectrum study. This is equivalent to varying the discharge coefficient in search of the bounding or most severe (highest peak clad temperature) SBLOCA.

a&b. The calculated and measured values for the intact loop hot leg density, cold leg density, loop seal and primary system mass inventory are presented in Figures 14.1, 14.2, 14.3, and 14.4, respectively. The loop seal plot (Figure 14.3) indicates that the loop seal blow-out phenomenon was not observed because core bypass and reflood assisted bypass were utilized in the test. The discrepancy in the loop seal height is due to a difference between the ΔP tap location and the level calculation by RELAP5 control variable that consists of the vertical section of the pump suction piping including the pump volume. Although the upper elevation of the ΔP tap was not available, the main point of this plot is to demonstrate that both the prediction and the test data showed that the loop seal was not cleared due to a core bypass designed to prevent core uncover. Test measurements during the pump coastdown (0 - 30s in Figure 14.3) do not accurately reflect the actual loop seal liquid level. The calculated hot and cold leg densities and mass inventory are consistently higher than the test data as a result of an underprediction of the BE discharge model.

c. The calculated and measured leak flowrates are presented in Figure 14.5. In general, the RELAP5 BE discharge model underpredicts the discharge flowrate. This is reflected in the primary system pressure shown in Figure G.2-10 (BAW-10164) and the mass inventory plot in Figure 14.4.

d. The pump coastdown is affected by the leak flowrate, which is substantially higher than the measured data during the coastdown period as shown in Figure 14.5. As a result, the reverse flow fluid torque exerted upon the pump reduces its speed more rapidly. This phenomenon is also observed in the benchmark calculation with RELAP4/MOD6. The RELAP4 model was obtained from EGG-LOFT-5089, Best Estimate Prediction for LOFT Nuclear Experiment L3-2, which has the same homologous pump data.

FIGURE 14.1. LOFT TEST L-3-5; HOT LEG DENSITY.

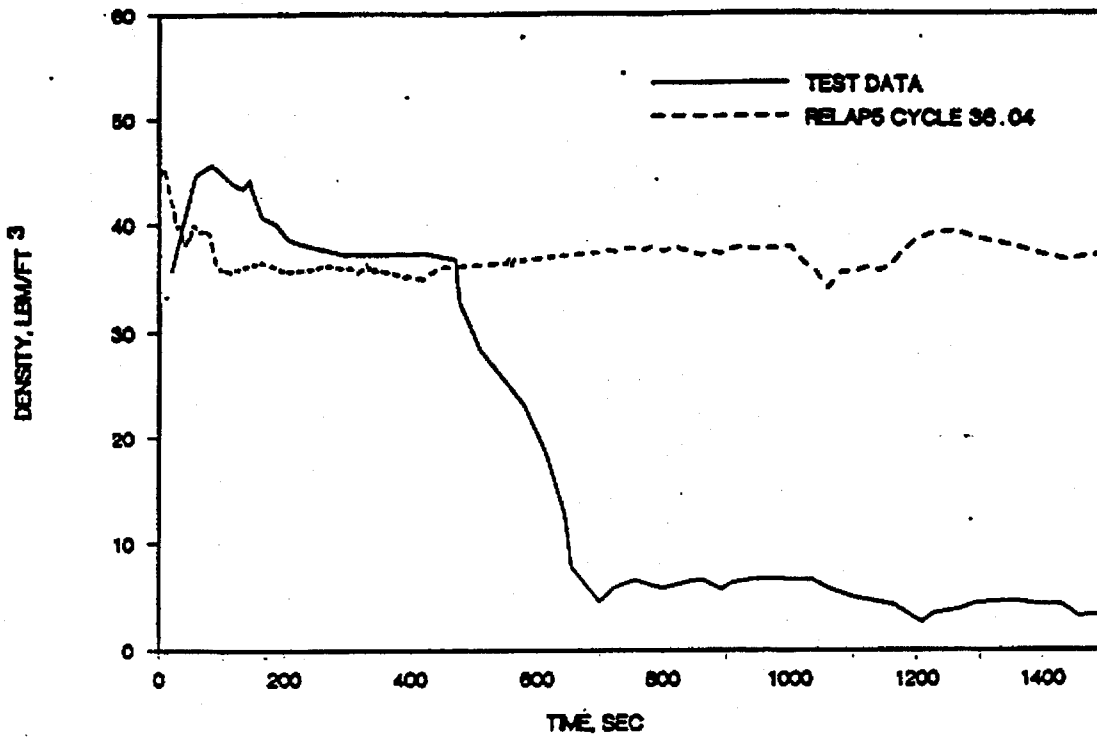


FIGURE 14.2. LOFT TEST L-3-5; COLD LEG DENSITY (PUMP DISCHARGE).

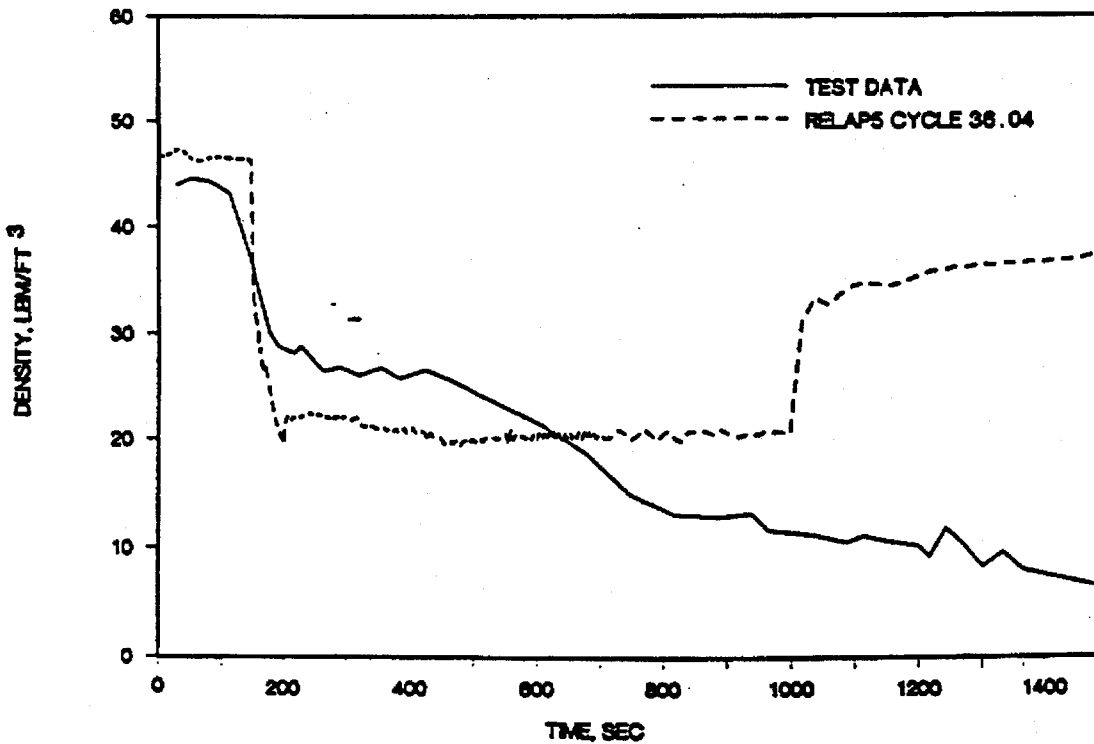


FIGURE 14.3. LOFT TEST L-3-5; LOOP SEAL HEIGHT (PUMP SUCTION PIPE).

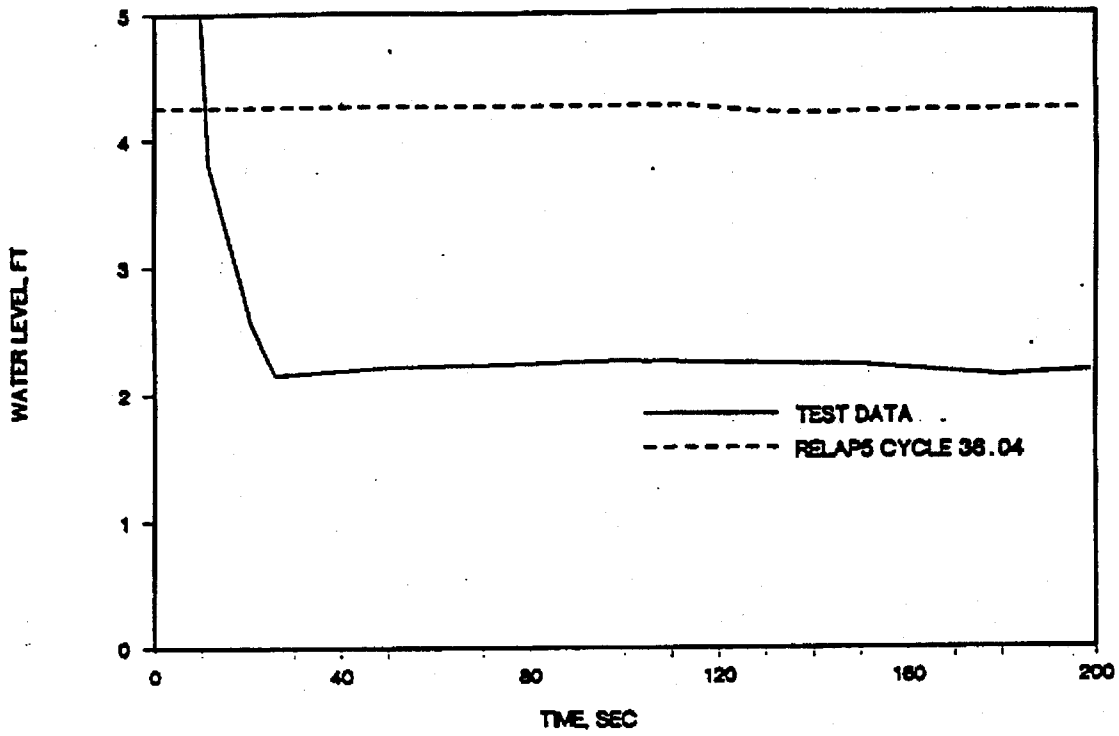


FIGURE 14.4. LOFT TEST L-3-5; NORMALIZED RCS INVENTORY.

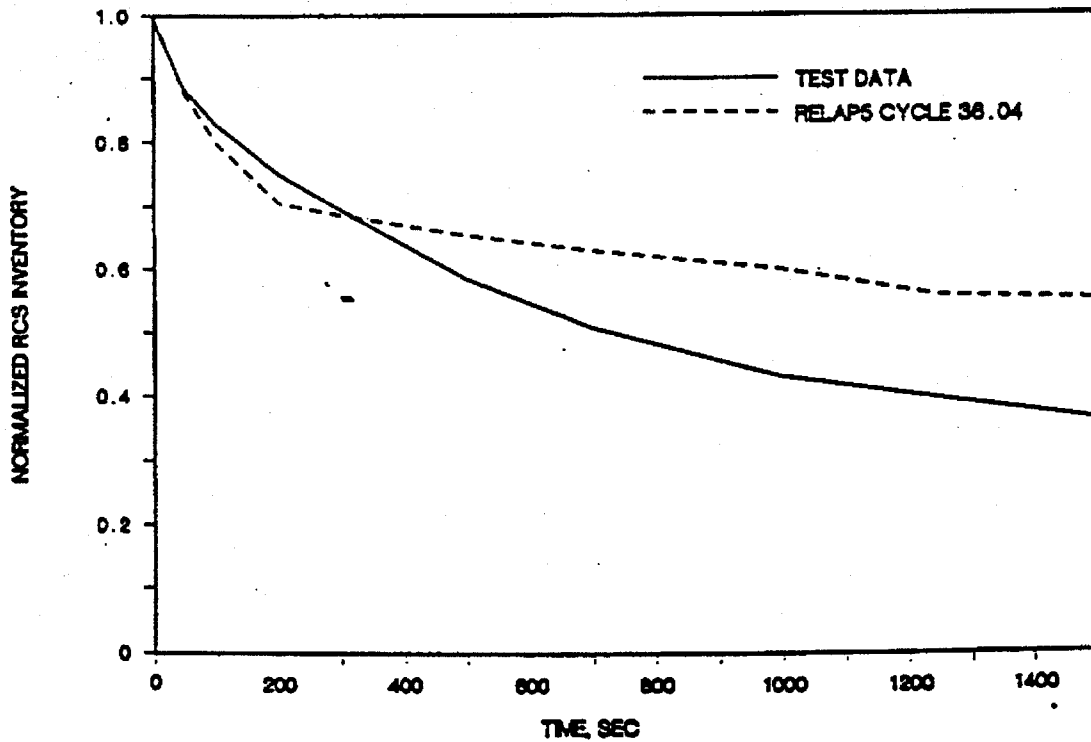
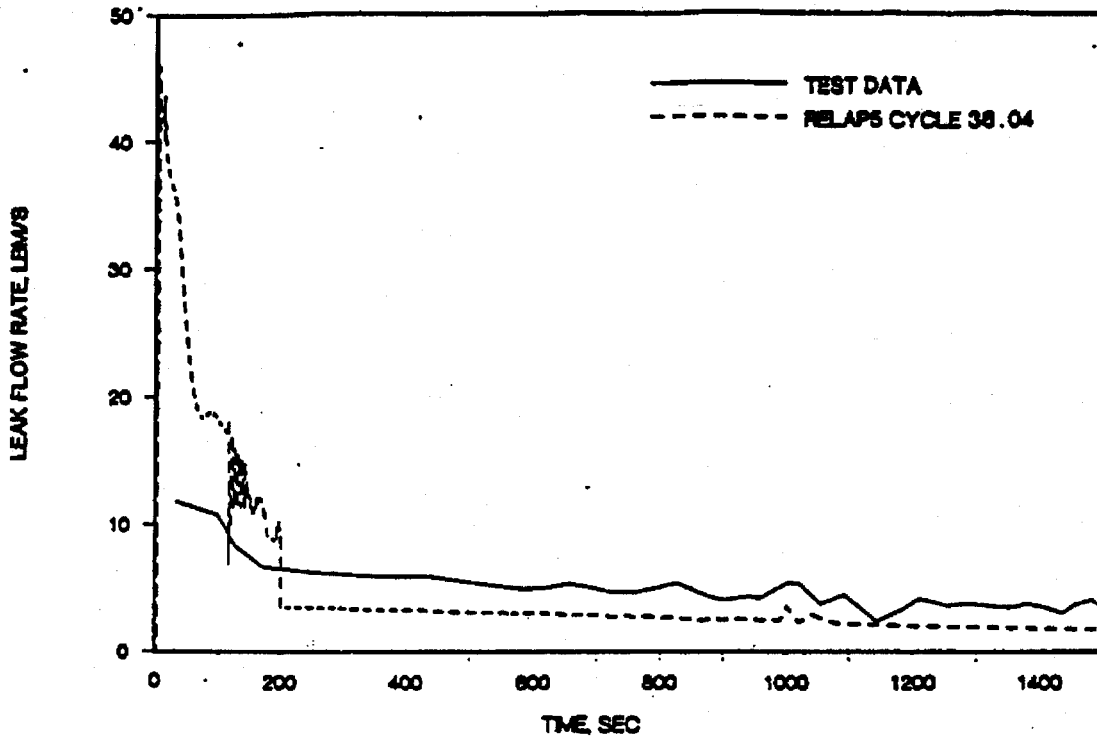


FIGURE 14.5. LOFT TEST L-3-5; LEAK FLOWRATE.



15. Question: In the B&W SBLOCA methodology, RELAP5/MOD2-B&W is used to calculate the system response including partial or total core uncover. Because LOFT L3-5 did not include core uncover, the code's ability to calculate the core inventory during core uncover in a SBLOCA was not demonstrated. To demonstrate this capability of RELAP5/MOD2-B&W, provide the result of SBLOCA assessment calculation involving core uncover.

Response: To verify RELAP5/MOD2-B&W capability to calculate core uncover/recovery and loop seal clearing, a benchmark analysis was performed on Semiscale Test S-LH-1. The results of the benchmark are presented in the response to question 17.

16. Question: NUREG-0737, Item II.K3.30, required that codes to be used to perform SBLOCA licensing calculations be verified with respect to their ability to calculate phenomena associated with noncondensibles in the primary system; the single-phase, two-phase, and reflux modes of natural circulation; and condensation heat transfer. The information provided thus far by B&W has not addressed these items. In addition, integral assessment against data for LOFT Test L3-1 and Semiscale Test S-07-10 was requested in NUREG-0737, Item II.K.3.30. The staff agrees that assessment of RELAP5/MOD2-B&W against these specific tests is not required because the SBLOCA data base is considerably larger than when NUREG-0737 was written. However, the tests used to assess the code should cover the range of phenomena typical of small break LOCAs (natural circulation, core uncover/recovery, loop seal clearing phenomena, pumps on/off, etc.). Provide the assessment calculations needed to verify that RELAP5/MOD2-B&W is capable for accurately calculating all the phenomena expected to occur in SBLOCAs.

Response: The primary system response to SBLOCA is mainly controlled by break size and decay heat removal via the steam generator. The MIST and OTIS benchmark results provided in Chapter 10 of the MIST final report and the RELAP5/MOD2 benchmark of the OTIS Feed and Bleed Test, respectively demonstrate that RELAP5 is capable of properly predicting SBLOCA phenomena. The benchmarks show that the primary system pressure response and primary system mass inventory were well predicted. Further discussion of SBLOCA phenomena, such as liquid entrainment, core uncover/recovery, loop seal clearing, and pump trip and coastdown, is presented in the response to question 17. The reflux and natural circulation modes of core cooling, and the effect of noncondensable gas on condensation heat transfer are addressed herein.

Noncondensable Gas

A mechanistic model to calculate surface condensation in the presence of noncondensable gas was developed, based on the stagnant film model of Colburn and Hogen, and was incorporated in RELAP5/MOD2-B&W. This model was benchmarked against single tube separate effects tests performed at the B&W Alliance Research Center and at MIT. The results of the benchmark calculation are published in the "Proceedings of the Eighth International Heat Transfer Conference," San Francisco, 1986, pages 1627-1634. The results show that the prediction of RELAP5 is in good agreement with the test data.

Reflux and Natural Circulation

The results of the Westinghouse small break spectrum analysis presented in WCAP-10081A show that the most limiting case is generally predicted for break areas equivalent to between 2 and 6 inches in diameter. The break sizes in this range do not depend heavily on the steam generator to remove decay heat because the primary system pressure rapidly falls below the secondary side pressure. On the other hand, the natural circulation and reflux modes of core cooling become important for smaller breaks (less than 2 inches in diameter - 0.5% break) because the primary system pressure remains above the secondary side pressure for an extended period of time. Thus, for licensing applications, to determine the most limiting break in the SBLOCA category, the ability of RELAP5 to accurately calculate steam generator heat removal will not significantly impact overall results. Furthermore, RELAP5/MOD1 benchmark results of the Semiscale MOD-2A natural circulation tests shown in EGG-SEMI-6315 and NUREG/CR-3690 have demonstrated that the code can qualitatively predict all modes of natural circulation including reflux cooling. The hydrodynamic model improvements made to RELAP5/MOD2 further enhance its accuracy in predicting natural circulation phenomena.

Additional benchmarks on natural circulation and reflux cooling using RELAP5/MOD2 (Cycle 36) were performed separately by S. Guntay of Switzerland, and by K. H. Ardron and P. C. Hall of the United Kingdom. The results of the post-test calculations of OECD-LOFT Experiment LP-SB-03 (0.4% cold leg break) demonstrate that RELAP5/MOD2 generally performed well, predicting all the key events in the correct sequence and with reasonable accuracy in timing. Except for the leak discharge and core heat transfer models, B&W's SBLOCA EM utilizes the BE options in RELAP5/MOD2 for hydrodynamic models, nonhomogeneous frictional flow and nonequilibrium models that were used in the above mentioned analyses. Thus, the B&W version of RELAP5/MOD2-B&W will perform as well as RELAP5/MOD2 Cycle 36.

17. Question: The experience with advanced thermal-hydraulic computer programs has shown an important sensitivity to modeling of the steam generators when analyzing SBLOCAs. Specifically, the modeling of liquid entrainment, condensation, and hydraulic resistance (i.e., flow regime maps) could significantly depress the mixture level in the core. This phenomenon was observed in Semiscale Test S-UT-8 and later studied in Semiscale Tests S-LH-1 and S-LH-2. Recognizing Semiscale's atypicality, the staff nevertheless believes this phenomenon to be real and, therefore, possible in a full scale reactor. It is for this reason that we request validation of your computer program to predict this phenomenon, should it occur in a full scale reactor. Validation with Semiscale Tests S-LH-1 and S-LH-2 or demonstrating that the phenomenon observed in the Semiscale experiments is calculated to occur in a plant calculation would be acceptable. Use of other integral experiments for validation requires that these experiments simulate the hydraulic behavior observed in the Semiscale tests.

Response: In response to the above request, RELAP5/MOD2-B&W was benchmarked against Semiscale test S-LH-1. S-LH-1 is a 5% break at the pump discharge pipe with a 0.9% core bypass flow from the downcomer to the upper head. The simulation of S-LH-1, using RELAP5/MOD2-B&W, demonstrates the capability of the code to predict SBLOCA phenomena, such as core uncover/recovery, natural circulation including reflux boiling, loop seal clearing, and ECCS performance. The results of the Westinghouse break spectrum analysis in WCAP-10081A show that the peak clad temperature (PCT) is generally predicted for break sizes greater than two inches in diameter (0.5% cross-sectional area of the cold leg pipe). For breaks above this size, the primary system depressurizes rapidly and falls below the secondary side pressure. Thus, decay heat removal via the steam generator is provided only briefly during the early phase of such transients, and the steam generators do not play a significant role in mitigating these accidents. For smaller breaks, that depend mainly on the steam generator for core cooling, numerous benchmarks of Semiscale test series S-NC, that demonstrate the adequacy of RELAP5/MOD2 to predict long-term core cooling by reflux boiling and natural circulation, have been performed.^{17-1,17-2} S-LH-1 addresses important SBLOCA phenomena, such as loop seal clearing and core uncover/recovery, that are observed in larger break size SBLOCAs.

Test Facility

The S-LH-1 test was conducted using the Semiscale MOD-2C facility shown in Figure 17-1. It consisted of a pressure vessel with simulated reactor internals and an external downcomer. The intact loop simulated three unaffected loops of a typical Westinghouse 4-loop PWR, while the broken loop simulated an affected loop in which the break is assumed to

occur. The intact loop steam generator contained six inverted U-tubes, and the broken loop steam generator contained two inverted U-tubes. The reactor core simulator was a 5 x 5 bundle with electrically heated rods (23 rods were powered during the test). The upper head region contained a simulated control rod guide tube and two simulated support columns. The bypass line that extended from the external downcomer to the upperhead was used to simulate the core bypass flow. A pressurizer was connected by a surgeline to the intact loop hot leg. Both loops had primary coolant circulation pumps. Emergency core coolant from an accumulator and pumped injection system (LPI and HPI) were routed to the loop cold legs. An open loop secondary coolant system was used to control the secondary side pressure with feedwater and steam control valves.

Model Description

The Semiscale MOD-2C RELAP5 model was originally developed by EG&G for the post-test analysis of experiments S-LH-1 and S-LH-2 (NUREG/CR-4438). The nodalization diagram is shown in Figure 17-2. The model consists of 181 hydrodynamic volumes, 172 junctions, and 256 heat structures. All volume and junction parameters are calculated with nonequilibrium and nonhomogeneous models. Steam generator secondaries, ECC injection, system environmental heat losses, and both vessel and piping external heaters are modelled in detail. The core axial power profile is modelled with twelve stacked heat structures over six two-foot long axial fluid volumes. The upper head region is nodalized to allow for junctions to be connected at the elevations of the top of the control rod guide tube, core bypass line and support columns, and at the elevation of the holes in the guide tube below the upper core support plate.

Several changes were made to the original EG&G model to properly account for and distribute unrecoverable losses due to pipe bends, orifices at the pump discharge pipes, area changes at the steam generator inlet and outlet plenums, and flowmeters in the hot and cold leg pipes. A steady-state calculation was made with these changes to obtain the initial conditions presented in Table 17-1. The calculated initial conditions compared well with the test conditions except for the secondary side masses and pressures. These were adjusted to achieve the desired primary cold leg temperatures. The calculated pump speeds are slightly higher than the test measurements (8% and 3% for the intact and broken loops, respectively) as a result of higher pump discharge orifice resistances calculated by RELAP5.

Prior to transient analysis, additional changes, that do not affect the steady-state initial conditions, were made to incorporate B&W's SBLOCA EM options into the model; they are: the core surface heat transfer model, the leak discharge model (BAW-10164P), and thermal equilibrium in the core region. A leak discharge coefficient of one was applied to both the subcooled and saturated choke flow models. The external heaters were modelled mechanistically in RELAP5, and the measured power to the heaters as a function of time was input as a boundary condition. The core decay power and pump coastdown speeds as a function of time were also input to the model. There was limited secondary side steam valve model information available from this experiment. Since the secondary system responses have an impact on the natural circulation and reflux boiling phases of the transient, the secondary side pressure responses from the experiment were used as boundary conditions in the calculation (see Table 17-2).

Results of Analysis

The sequence of major events is presented in Table 17-2. The transient was initiated at zero seconds by opening the leak, and thereby causing a flow of subcooled primary fluid out the break, resulting in a rapid system depressurization. Figure 17-3 shows good agreement in the leak flowrate between the RELAP5 calculation and the experimental data. The primary system pressure response is controlled by the leak flow, and Figure 17-4 shows that the calculated pressure is in good agreement with the experimental pressure up to 200 seconds. The calculated time to reach the safety injection system (SIS) setpoint of 1827.5 psia (pressurizer) is approximately 3 seconds later than the experiment, primarily due to a slower draining in the pressurizer. This is believed to be caused by a higher overall intact loop resistance observed in the initialization analysis. The calculated steady-state pump speed in the intact loop is approximately 8% higher than that of the experiment.

The draining of the steam generator tubes occurred after the pump speed coasted down to zero at 100 seconds. At this point, the primary system entered a reflux condensation cooling mode. Figures 17-5 through 17-8 show U-tube liquid levels in both the intact and broken loops. It should be noted that the measured liquid levels using differential pressure cells can lead to considerable error during the pump coastdown period (0 - 100 sec).¹⁷⁻³ Both the prediction and the experimental data show that the upflow side of the U-tube consistently drained later than the downflow side due to de-entrainment and reflux condensation on the tube surface. Following draining of the steam generator U-tubes, a liquid seal was formed in the pump suction of both loops. The seals caused a blockage of steam flow to the break. As a result, the primary system entered

a period of manometric level depression in both the downflow side of the pump suction seals and in the core liquid level. To clear the pump suction loop seals, the liquid head imbalance between the downcomer and the core must accrue to the total of the loop seal level plus the liquid holdup, due to reflux condensation, in the upflow side of the U-tubes. As shown in Figures 17-5 and 17-7, the liquid level in the upflow side of the steam generator U-tubes is a significant contributor to the total ΔP , that opposes loop seal clearing. The loop seals cleared at 175 seconds and 214 seconds for the intact loop and the broken loop, respectively.

Figures 17-9 through 17-12 show the liquid level in the pump suction pipes. The intact loop seal cleared first, followed by the broken loop, because the primary-to-secondary heat transfer was terminated earlier in the intact loop than in the broken loop. Clearing of the loop seals produces a continuous path to the break for steam generated in the core. The steam conditions at the leak result in lower leak mass flows, but higher volumetric flows. As a result, the primary system began a rapid depressurization.

Following loop seal clearing, the RELAP5 depressurization rate was faster than was observed in the experiment, in spite of good agreement in discharge mass flowrate between the calculation and the experiment. The energy discharge rate and heat-loss to the ambient surroundings of the test, were not available to confirm the reasonable hypothesis that steam venting is the primary cause of the larger depressurization rate in the RELAP5 prediction.

One of the important parameters used as an indicator for SBLOCA mitigation is core collapsed liquid level. This is shown in Figure 17-13. As a result of correctly predicting

primary system mass inventory and reflux heat transfer, the agreement in the first core level depression between the calculation and the experiment is excellent. After clearing the loop seals, core decay heat continues to boil-off fluid in the core region and, since the HPIS flow alone is not sufficient to makeup for fluid lost out the break, the core liquid level continues to decrease until accumulator actuation is achieved.

Accumulator injection occurred much earlier in the calculation than in the experiment due to the faster depressurization rate. However, the shortened core boil-off period was compensated for by increased flashing. Thus, the second core level depression was calculated to be nearly the same as the measurement except for its timing. The experiment shows that a more significant and uniform core heat-up occurred during the second core level depression. The ability of RELAP5 to correctly predict the two distinct core liquid level depressions demonstrates that the code can accurately calculate important thermal-hydraulic system parameters, that are used to determine the most limiting SBLOCA. Figure 17-14 shows the normalized primary system mass inventory. It confirms the adequacy of the EM discharge model. The mass inventory increased following accumulator injection. The HPIS injection flow rates for both the intact and broken loops are presented in Figure 17-15 and 17-16, respectively. The calculated flow rates are higher than those of the experiment due to the faster depressurization rate predicted by RELAP5.

Conclusions

In conclusion, the benchmark results show that the calculated overall system responses are in a good agreement with the experimental data. RELAP5/MOD2-B&W calculated the

major events of the transient, namely two-phase natural circulation, reflux and liquid holdup, pump suction loop seal clearing, core liquid level depression, ECCS injection and core recovery, in the proper sequence. The benchmark demonstrates that RELAP5/MOD2-B&W can adequately predict the system thermal-hydraulic responses during a SBLOCA.

References

- 17-1. K. P. Ardron and P. C. Hall, "UK Experience with RELAP5/MOD2," Central Electricity Generating Board, Generation Development and Construction Division, Barnwood, Gloucester, UK (Private Communication).
- 17-2. P. Ting, R. Hanson, and R. Jenks, International Code Assessment and Applications Program, NUREG-1270, Vol. 1, March 1987.
- 17-3. G. G. Loomis and J. E. Streit, Results of Semiscale MOD-2C Small-Break (5%) Loss-of-Coolant Accident Experiments S-LH-1 and S-LH-2, NUREG/CR-4438, November 1985.

Table 17-1. Comparison of Calculated and Measured Initial Conditions for Semiscale Test S-LH-1.

<u>Parameter</u>	<u>RELAP5</u>	<u>Measured</u>
Pressurizer Pressure, psia	2243.7	2243.8
Core Power, Kw	2014.75	2014.75
Pressurizer Liquid Level, inches	155.5	155.6
Cold Leg Fluid Temperature, F		
Intact Loop	552.1	552.2
Broken Loop	555.6	556.7
Primary System Flowrate, lbm/s		
Intact Loop	15.7	15.6
Broken Loop	5.2	5.2
Core Bypass Flow (% of total core flow)	0.9	1.0
SG Secondary Pressure, psia		
Intact Loop	829.6	859.7
Broken Loop	881.8	857.2
Core ΔT , F	67.8	67.4
SG Secondary Side Mass, lbm		
Intact Loop	421.0	374.8
Broken Loop	94.8	78.0

Table 17-2. Comparison of Calculated and Measured Sequence of Events for Semiscale Test S-LH-1.

Time, seconds

<u>Event</u>	<u>Measured</u>	<u>RELAP5</u>
Break Opened	0.5	0.0
Pressurizer at 1827.5 psia (SIS)	14.67	17.65
Reactor Scram	19.57	22.60
Pump Coastdown Initiated		
Intact Loop	21.35	24.35
Broken Loop	20.76	23.75
Feedwater Off		
Intact Loop	19.67	22.70
Broken Loop	19.00	22.00
MSIV Closure		
Intact Loop	22.0	25.00
Broken Loop	22.0	25.00
HPIS Initiated		
Intact Loop	41.60	44.60
Broken Loop	40.98	44.60
Pressurizer Emptied	33.90	44.00
Intact Loop Seal Cleared	171.4	175.0
Broken Loop Seal Cleared	262.3	214.0

Table 17-2. Comparison of Calculated and Measured Sequence of Events for Semiscale Test S-LH-1 (continued).

<u>Event</u>	<u>Time, seconds</u>	
	<u>Measured</u>	<u>RELAP5</u>
Accumulator Injection		
Intact Loop	503.8	324.0
Broken Loop	501.4	324.0

SG Secondary Side Pressure Used in the RELAP5 Prediction

<u>Time, seconds</u>	<u>Pressure, PSIA</u>	
	<u>Intact Loop</u>	<u>Broken Loop</u>
0	860	858
20	860	888
40	1016	1021
60	1000	1010
100	995	995
200	989	974
300	958	926
1000	863	700

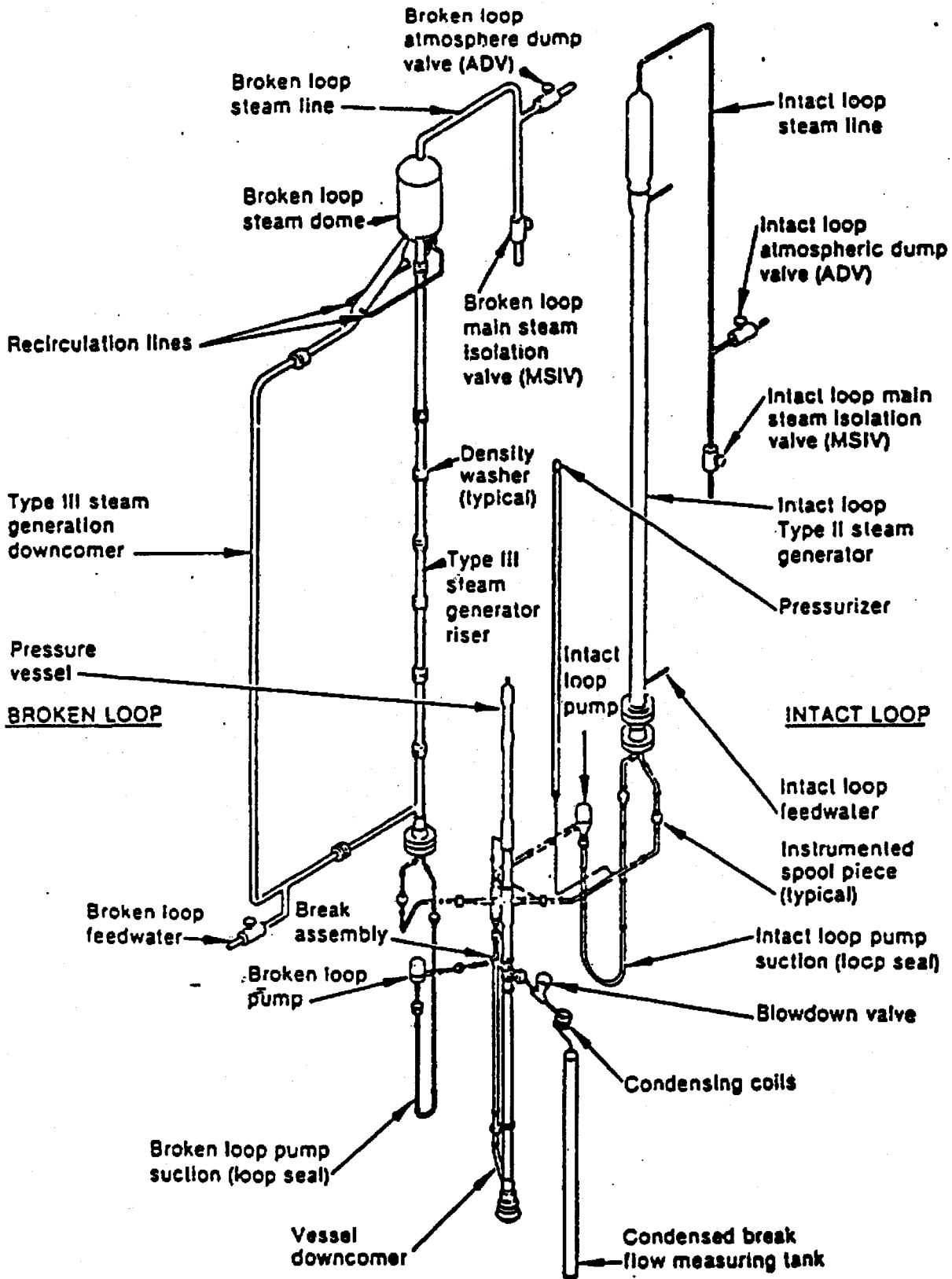


Figure 17-1. Semiscale MOD-2C System Configuration.

FIGURE 17-3. SEMISCALE TEST S-LH-1; LEAK FLOW RATE.

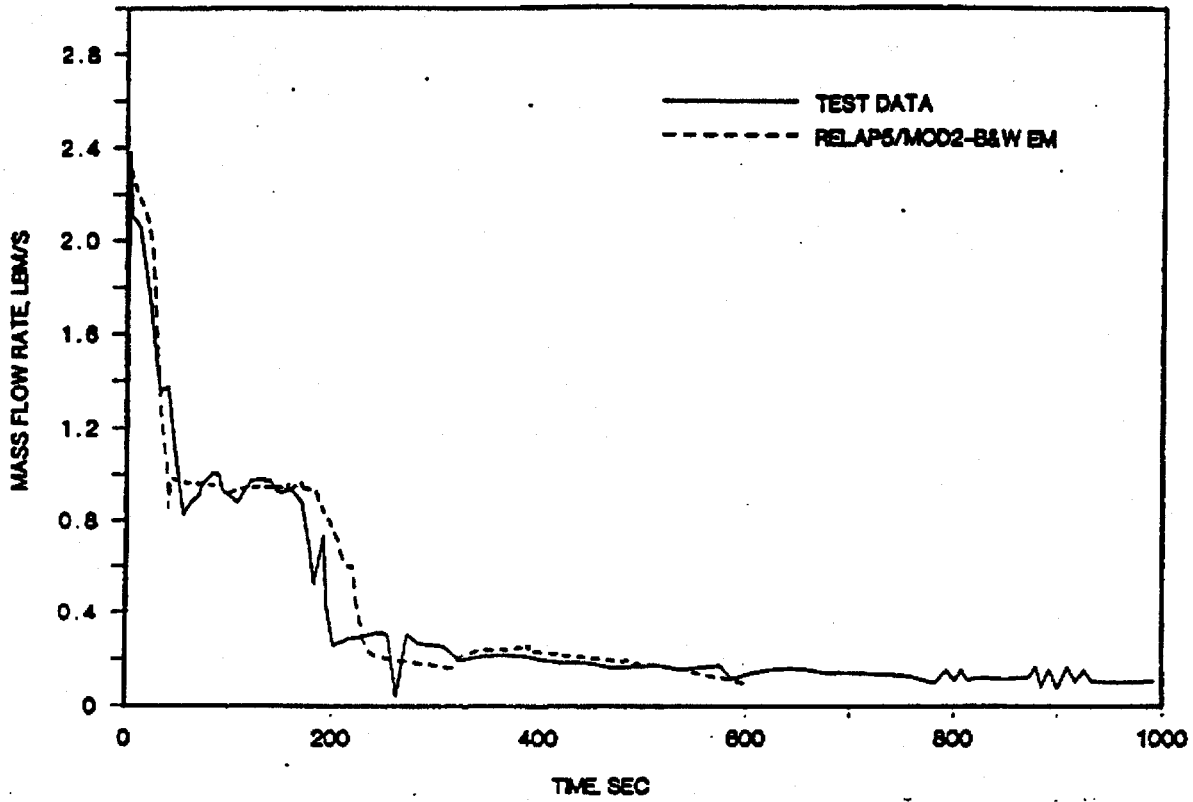


FIGURE 17-4. SEMISCALE TEST S-LH-1; PRIMARY SYSTEM PRESSURE.

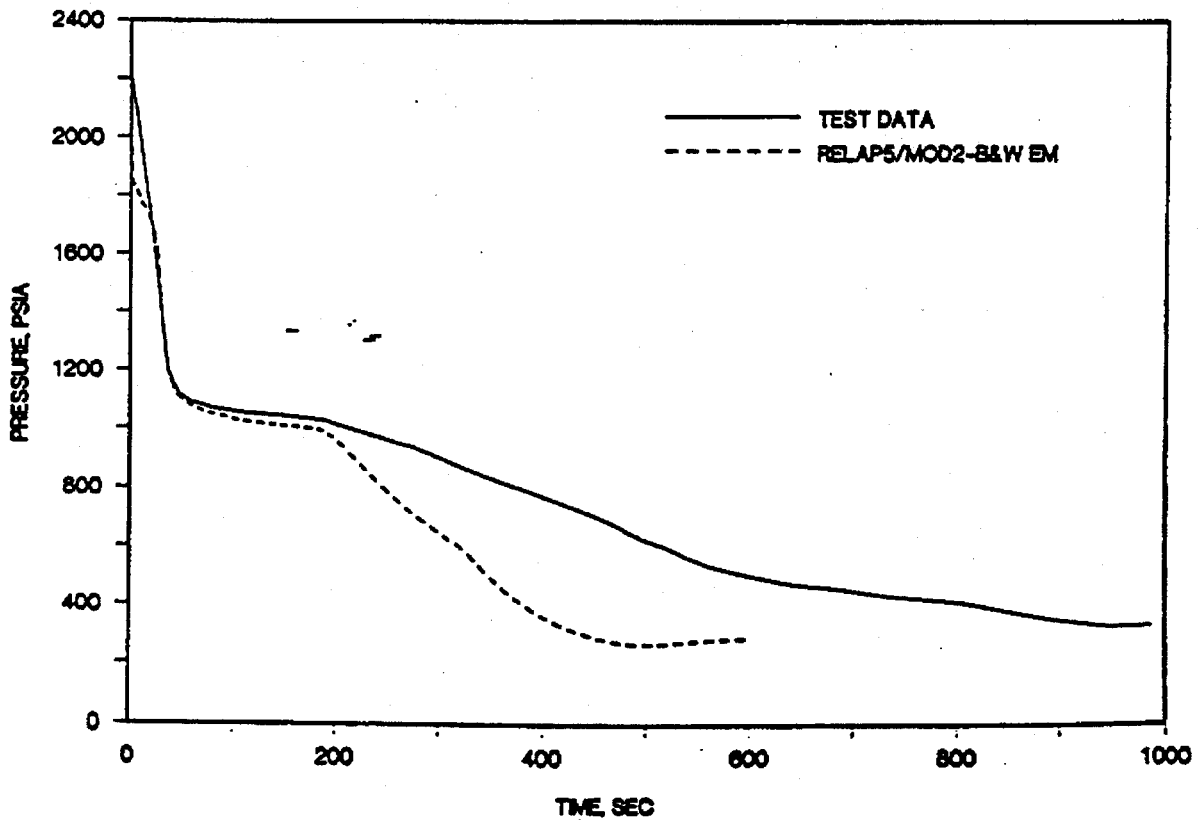


FIGURE 17-5. SEMISCALE TEST S-LH-1; INTACT LOOP STEAM GENERATOR
TUBE LEVEL - UP SIDE.

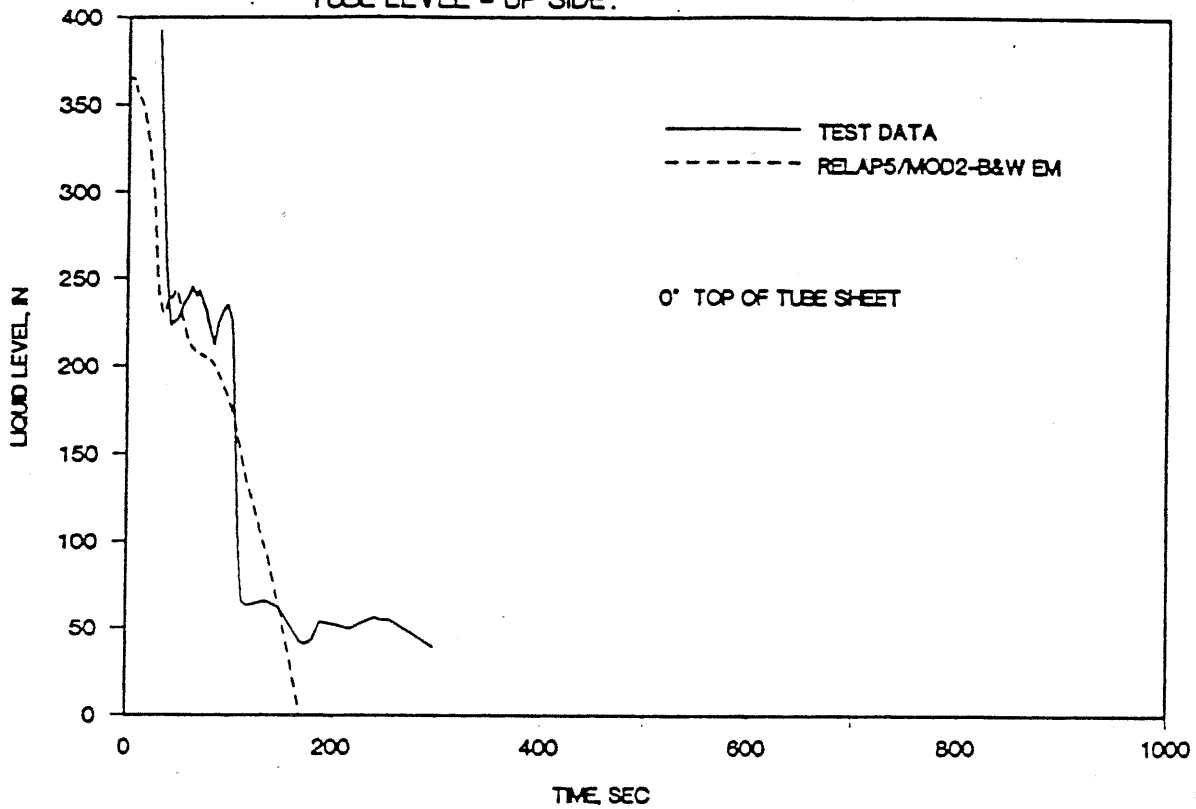


FIGURE 17-6. SEMISCALE TEST S-LH-1; INTACT LOOP STEAM GENERATOR
TUBE LEVEL - DOWN SIDE.

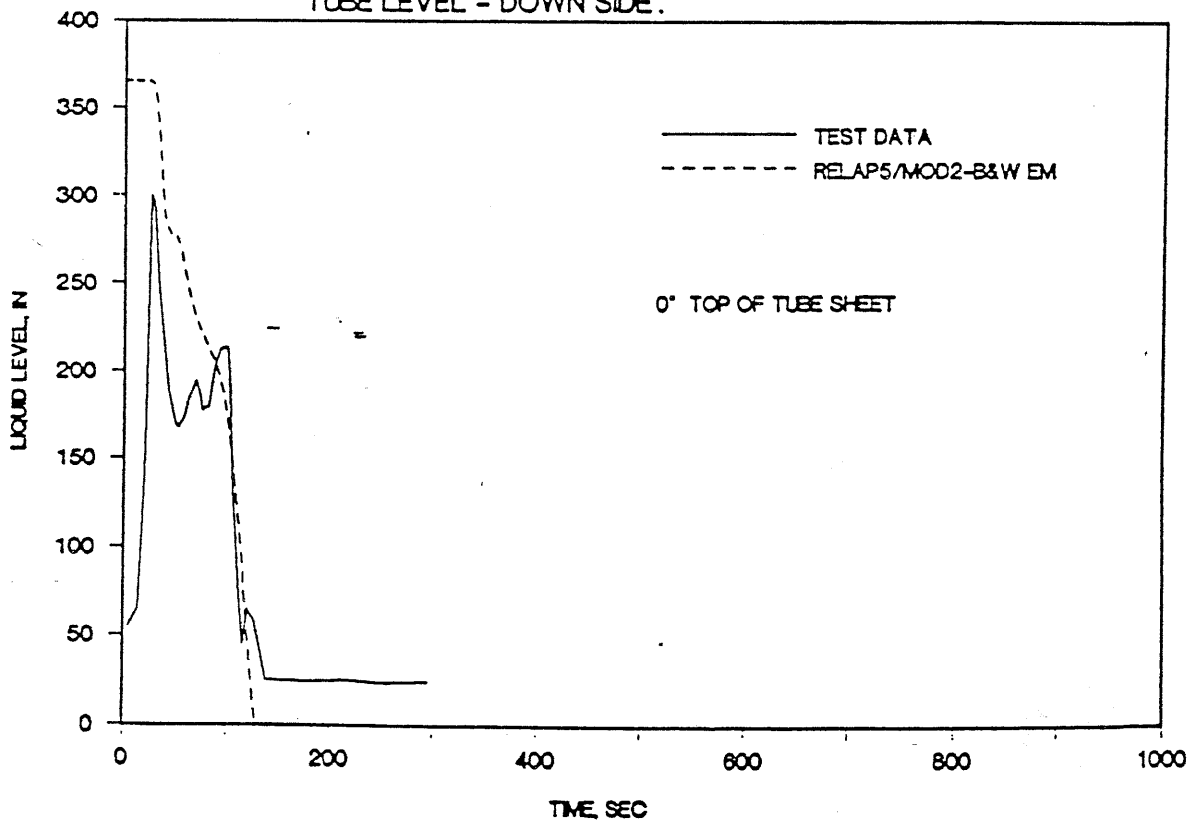


FIGURE 17-7. SEMISCALE TEST S-LH-1; BROKEN LOOP STEAM GENERATOR
TUBE LEVEL - UP SIDE.

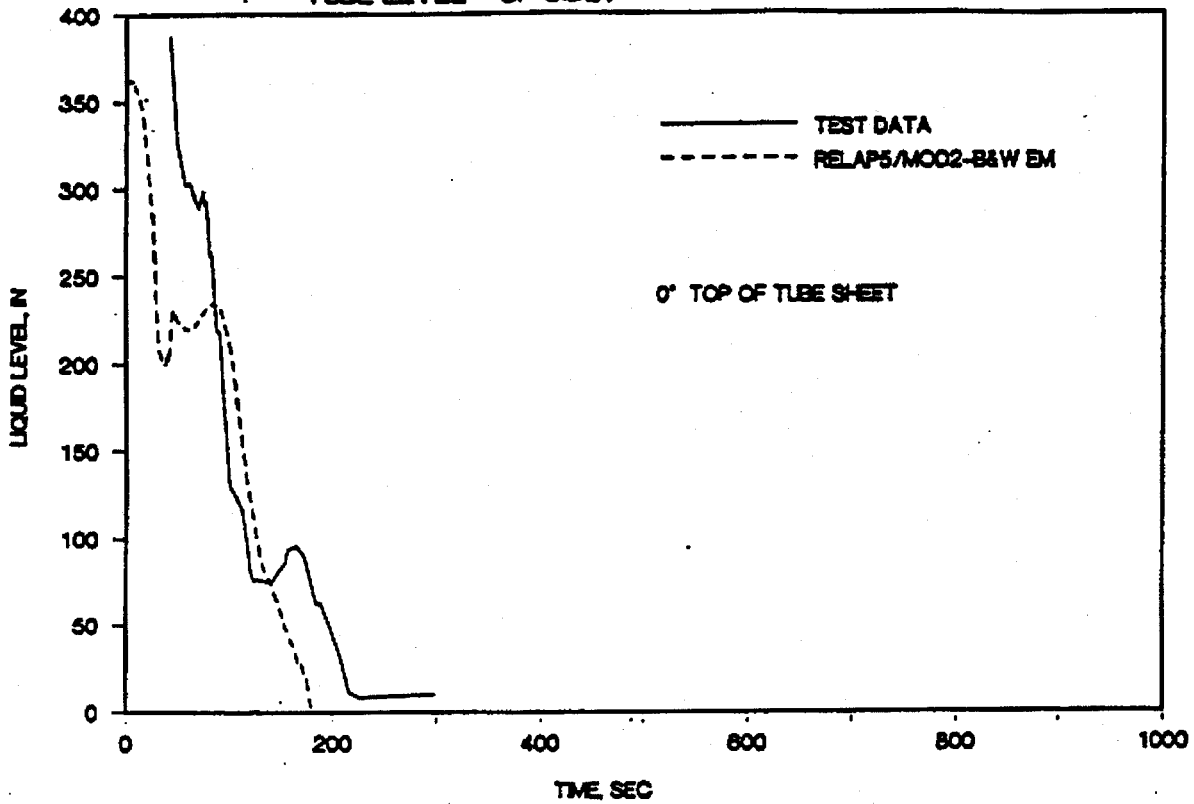


FIGURE 17-8. SEMISCALE TEST S-LH-1; BROKEN LOOP STEAM GENERATOR
TUBE LEVEL - DOWN SIDE.

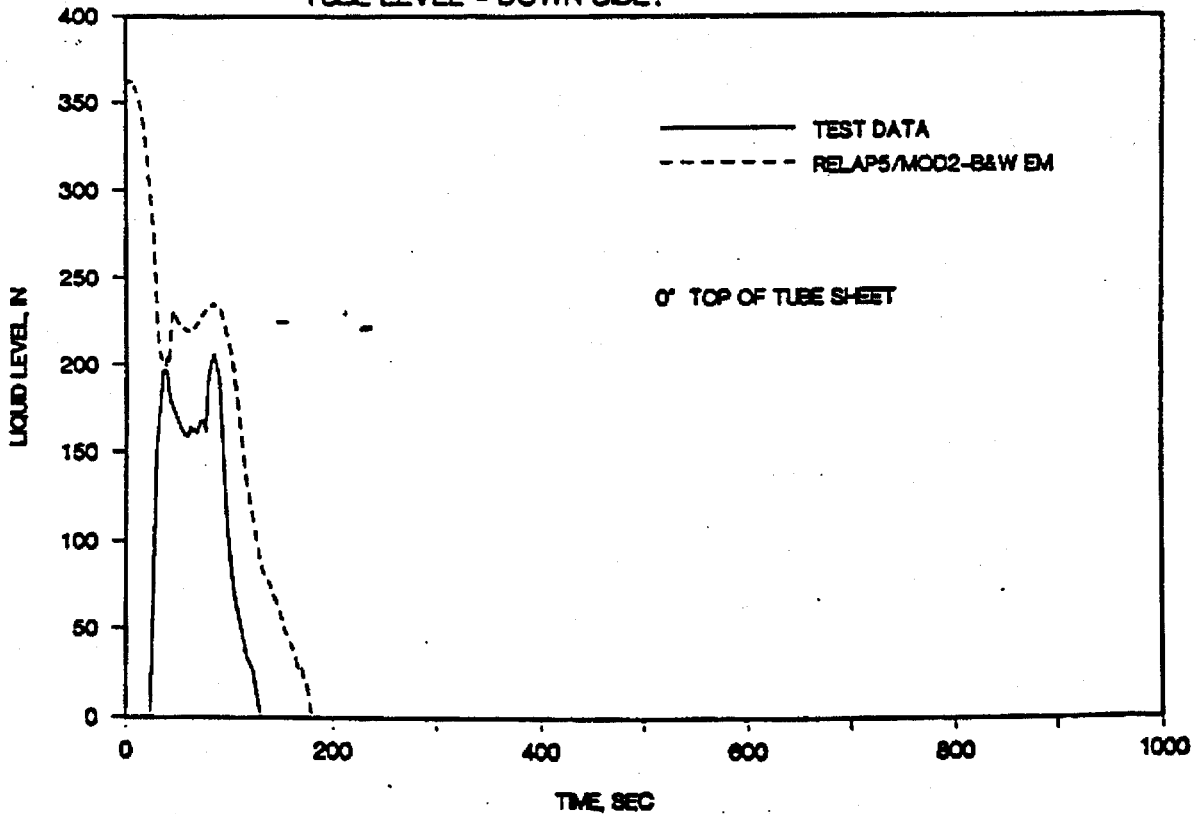


FIGURE 17-9. SEMISCALE TEST S-LH-1; INTACT LOOP PUMP SUCTION LEVEL - DOWN SIDE.

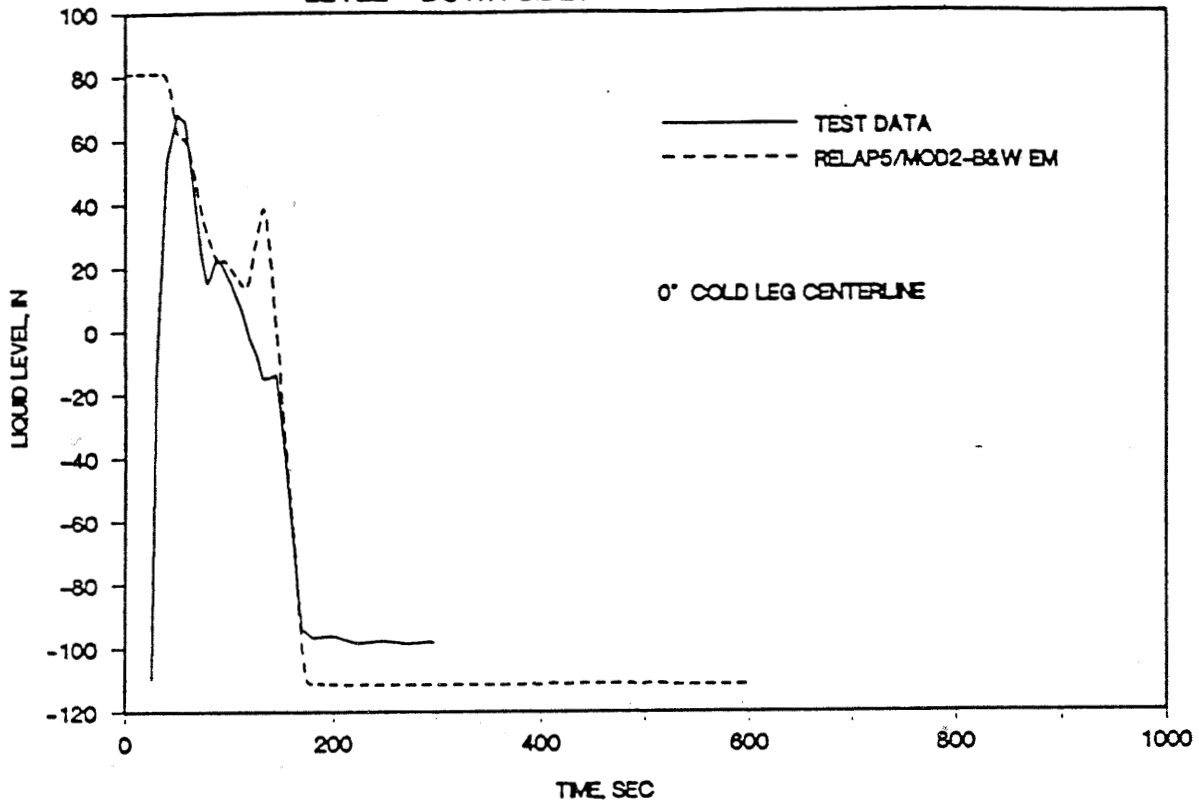


FIGURE 17-10. SEMISCALE TEST S-LH-1; INTACT LOOP PUMP SUCTION LEVEL - UP SIDE.

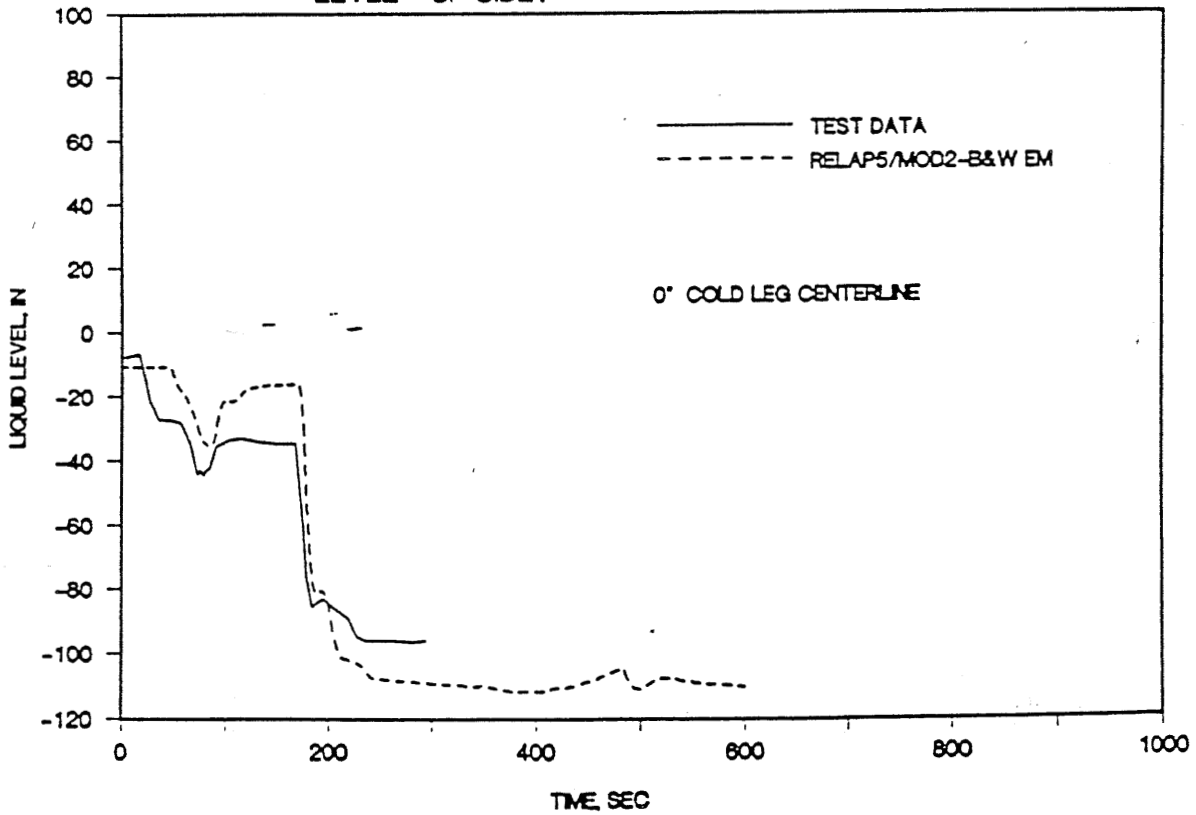


FIGURE 17-11. SEMISCALE TEST S-LH-1; BROKEN LOOP PUMP SUCTION LEVEL - DOWN SIDE.

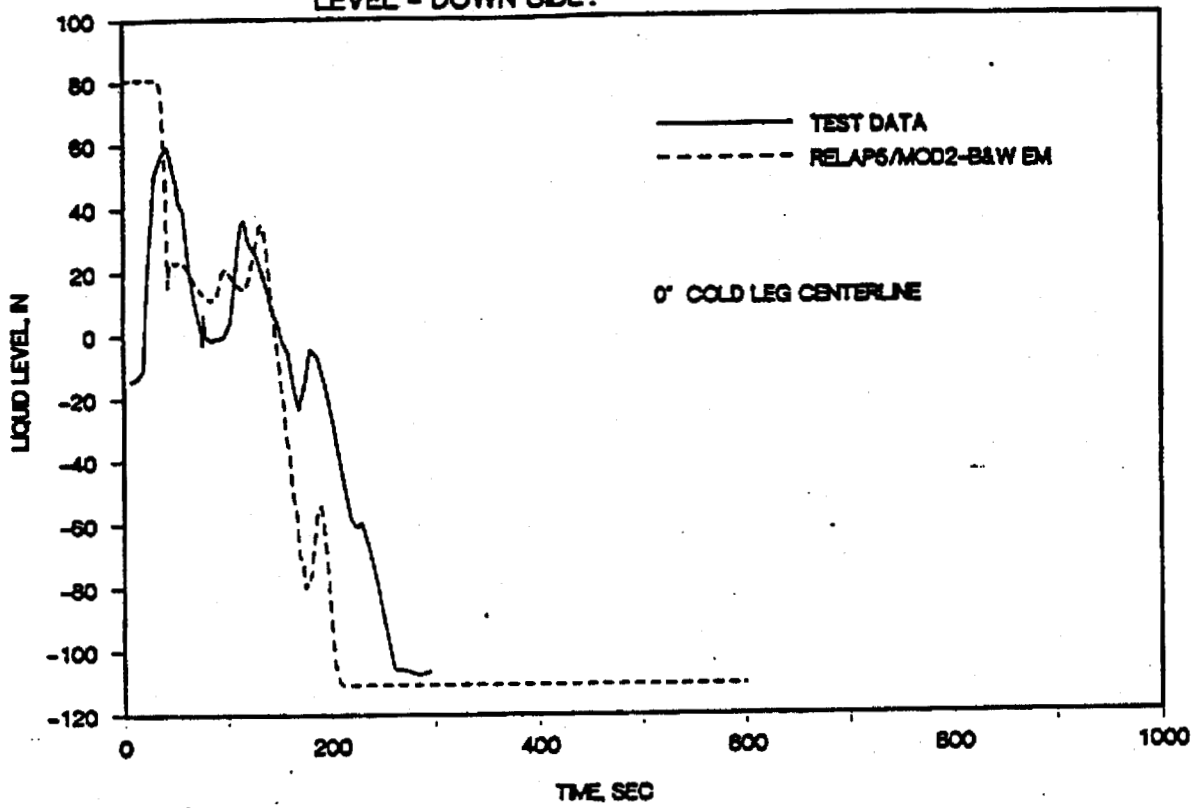


FIGURE 17-12. SEMISCALE TEST S-LH-1; BROKEN LOOP PUMP SUCTION LEVEL - UP SIDE.

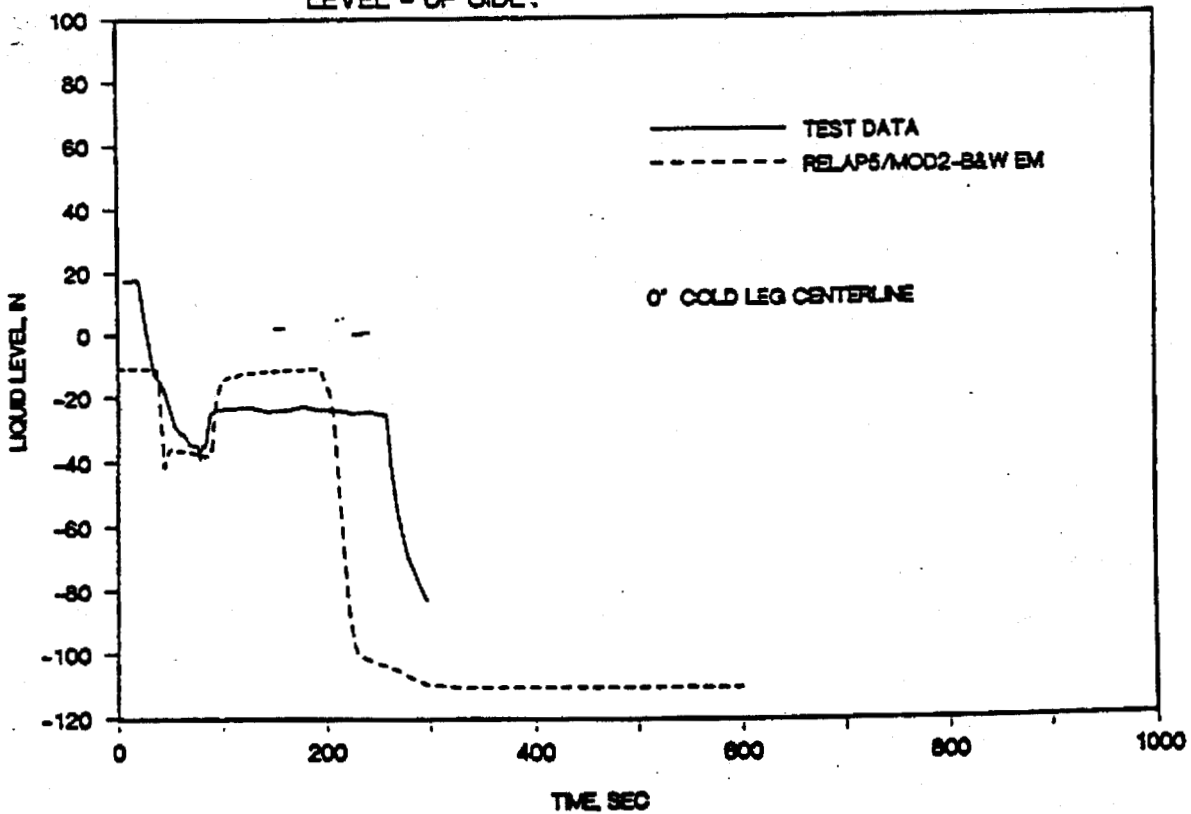


FIGURE 17-13. SEMISCALE TEST S-LH-1; VESSEL LIQUID LEVEL.

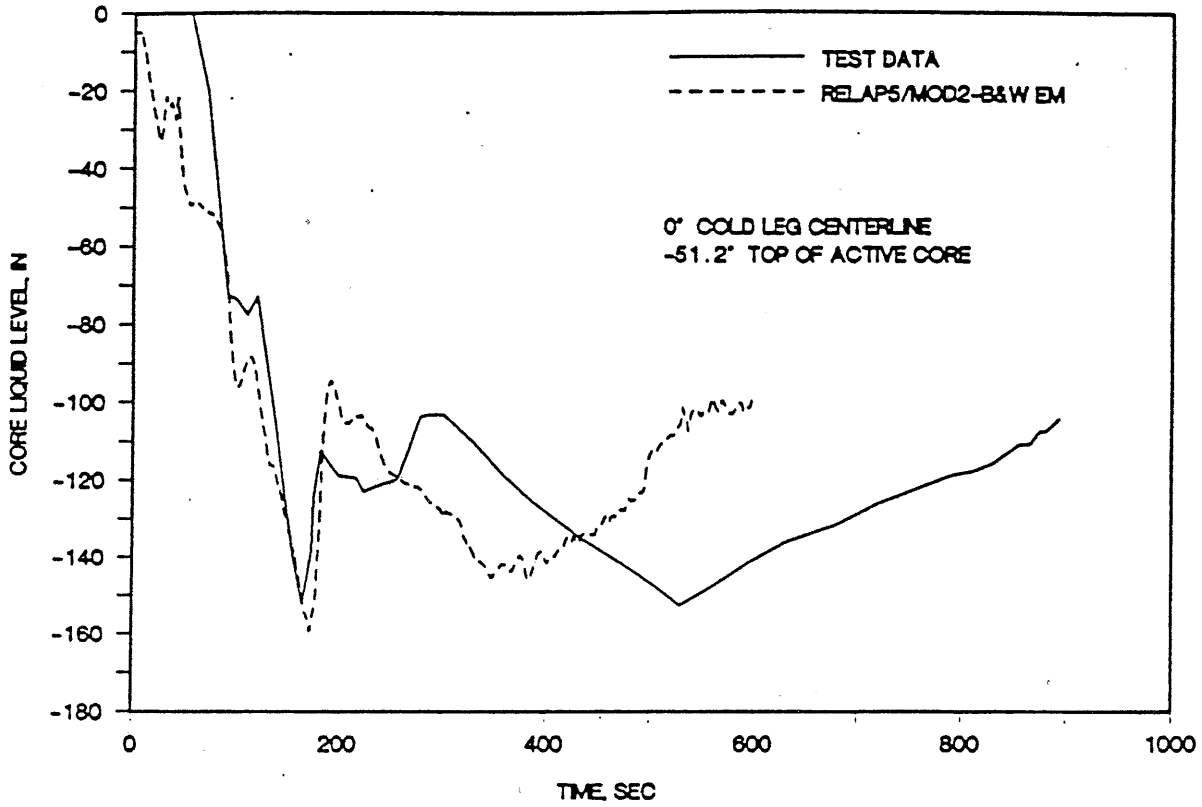


FIGURE 17-14. SEMISCALE TEST S-LH-1; PRIMARY SYSTEM NORMALIZED MASS.

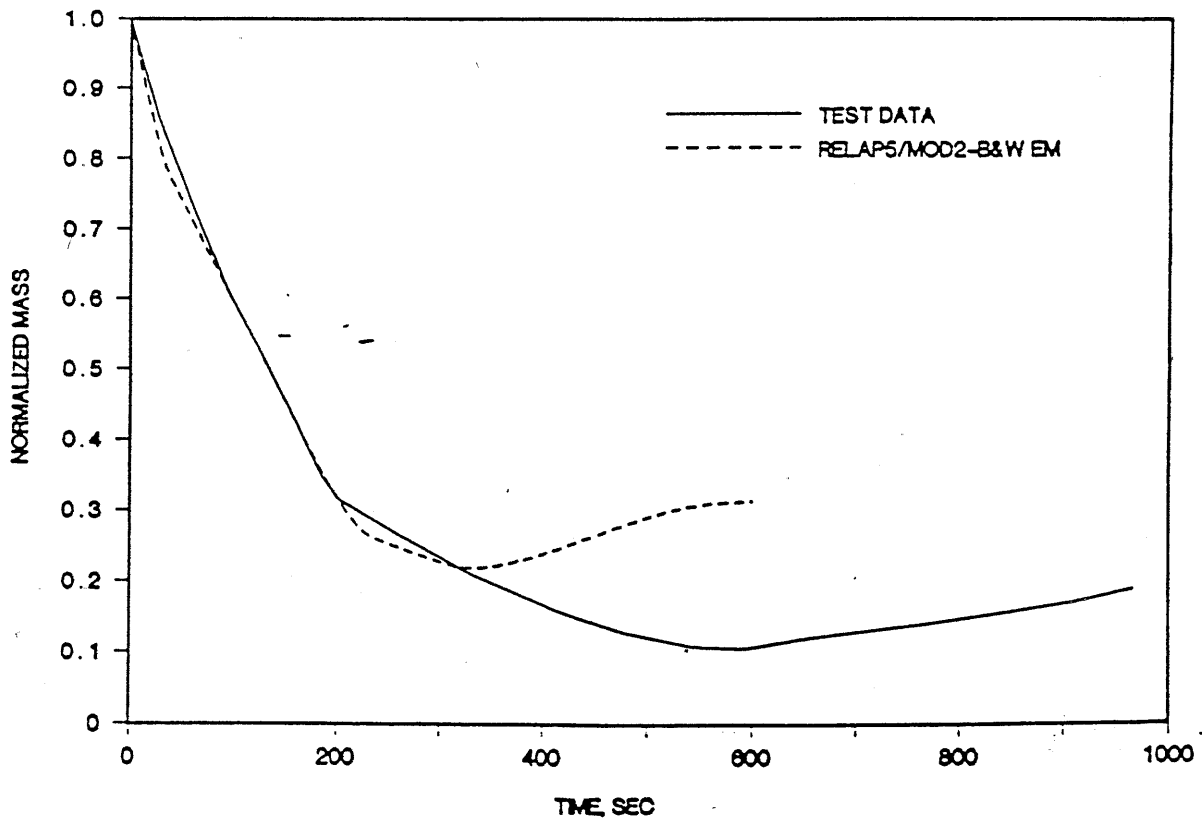


FIGURE 17-15. SEMISCALE TEST S-LH-1; INTACT LOOP ECC FLOW RATE.

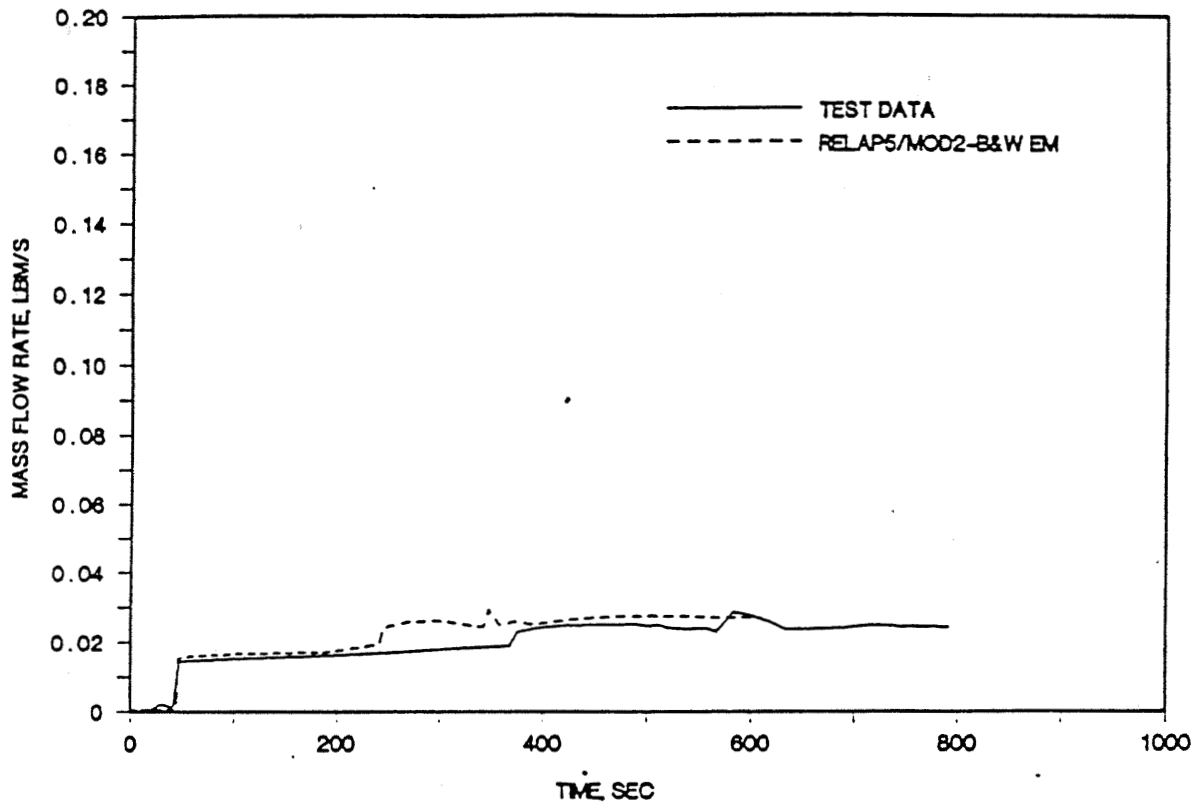
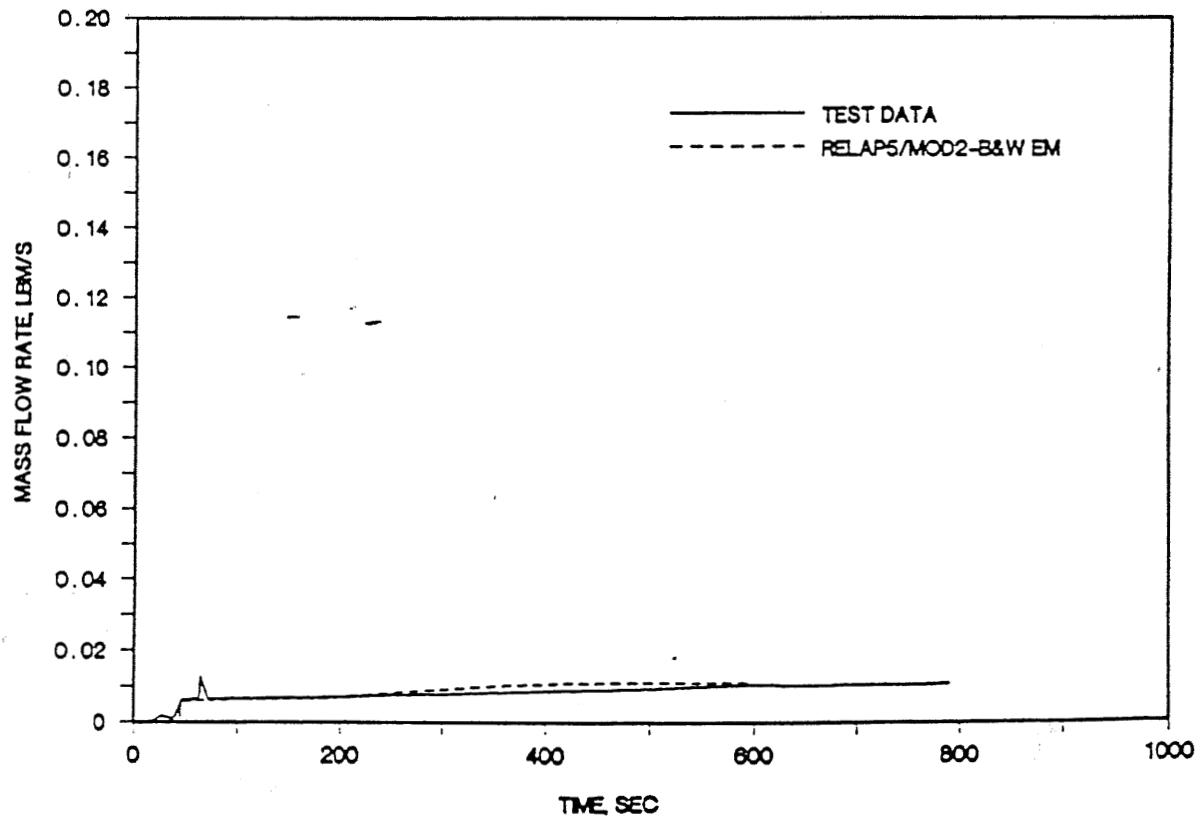


FIGURE 17-16. SEMISCALE TEST S-LH-1; BROKEN LOOP ECC FLOW RATE.



18. Question: In BAW-10168P, B&W Loss-of-Coolant Accident Evaluation Model for Recirculating Steam Generator Plants, B&W stated that the SBLOCA methodology would be applied to breaks up to approximately 1 ft². The one SBLOCA assessment provided for review by B&W was LOFT Test L3-5. The break in LOFT Test L3-5 was equivalent to a break size of approximately 0.1 ft² in a PWR. Because of the factor of ten difference between the break size analyzed and the largest break size to be analyzed, provide a RELAP5/MOD2-B&W assessment calculation where the break size analyzed is approximately 1 ft².

Response: For small breaks, the reactor vessel does not empty, and the LBLOCA phenomena such as ECC bypass, reactor refill (adiabatic heatup period), and reflooding do not occur. Based on experience, B&W selected the 1.0 ft² break as a transition point in switching EM methodology. This is consistent with the criterion employed by Westinghouse. Furthermore, over a sustained period of time, Westinghouse has shown that this break size is not the limiting case in either the large or small break LOCA category. As such, B&W believes it is not necessary to perform a demonstration analysis of a 1 ft² SBLOCA case.

5.2 Responses to Round 2 Request for Additional Information

This section contains round two questions transmitted to B&W by M.W. Hodges of the NRC in his letter of March 23, 1989 and responses transmitted to the NRC in letters from J. H. Taylor of B&W dated May 11, 1989 and July 20, 1989.

1. Question: The following questions are related to the response to Question 10 in the discussion of the sources of the fuel behavior models added to RELAP5/MOD2-B&W.

- a. The response provided the sources of the gap conductance, clad deformation and metal-water reaction models, but did not provide calculations to verify proper implementation of the models in the code. Provide the results of calculations that demonstrate these models are properly implemented.

Response: Demonstration of proper implementation of computer models is available in the code predictions and benchmarks that have been supplied within the evaluation model topical reports and in the code certification documentation maintained at B&W. The topical studies provide overall validation of the code and any changes made to it including model interactions. These are already available for review in the topicals. The code certification process provides detailed validation of model implementation on a model by model basis. All models that B&W incorporates into its computer codes are implemented in accordance with B&W procedures for computer code development and certification. The B&W procedure for certification requires that a change be: 1) described in a change specification document. 2) be verified by independent calculations of the coded results (usually manual calculations performed on a time step per time step basis). 3) have the verification calculations independently reviewed and approved for accuracy, comprehensiveness, and conclusions. 4) have all steps

documented in files stored permanently at B&W. The process and the files are subject to audit by the B&W quality assurance organization and NRC audit teams. Because of the detail involved in the files, it is not considered practical to publish the results; however, the files are readily available and open for audit at the B&W offices at any time. B&W believes that the procedure and filing of detailed results is sufficient to assure that the code models, as described in the topical reports, are properly implemented.

The following is additional information regarding the implementation of the Baker-Just correlation in RELAP5/MOD2-B&W.

Equation 2.3.2-58 in RELAP5/MOD2-B&W is derived based on the Equations 10, B5a and B5b in Reference 120 of BAW-10164. To obtain Equation 2.3.2-58, the plane geometry assumption in Equation 10 is replaced by the cylindrical geometry assumption using Equations B5a and B5b. Equation 2.3.2-58 is reduced to the equation for a plane geometry as given by the Equation 2.2.2-60 which is essentially the same as the Equation 10 in the Reference 120. Equation 10 is also the starting point for the metal water reaction Equation 2.2.2-1 in FRAP-T6-B&W.

The method used in RELAP5/MOD2-B&W to solve the differential equation (Equation 10) is slightly different from the one used in FRAP-T6-B&W. In RELAP5/MOD2-B&W it is assumed that

$$-dx/dt = \psi(t) / (x_0 - x)_{old} ,$$

where $\psi(t)$ represents the remaining terms in Equation 10.

On the other hand, FRAPT6-B&W assumes that

$$dx^2/dt = \psi(t).$$

It is to be noted that the method used in RELAP5/MOD2-B&W is consistent with that used in CRAFT2 and the method used in FRAPT6-B&W is consistent with that used in THETA1B.

- b. On comparison of the equations in RELAP5/MOD2-B&W to the source codes, a possible units problem was noted in Section 2.3. On page 2.3-35, the cladding hoop stress is defined in units of kpsi. However, the units for Eqn. 2.3.2-18 would give the hoop stress in units of Pa. Clarify this discrepancy.

Response: As stated in the question, there is an inconsistency in the unit for the hoop stress σ_h in Equations 2.3.2-17 and 2.3.2-18. The inconsistency is in the topical report not in the code. In the code, the hoop stress calculated using Equation 2.3.2-18 is divided by 6.894757×10^6 (to convert Pa to kpsi) before it is used in Equation 2.3.2-17. In order to make the unit for σ_h consistent in these two equations, Equation 2.3.2-18 should be written as

$$\sigma_h = C_p (P_g r_{icold} - P_f r_{ocold}) / (r_{ocold} - r_{icold})$$

where

$$C_p = 1/6.894757 \times 10^6,$$

and the other variables are defined in the topical report.

This modification to Equation 2.3.2-18 will be made in the next revision to the topical report.

2. Question: The following questions are regarding the new assessment calculation for Semiscale Mod-1 Test S-04-6 provided in response to Question 12.

- a. The EM and BE calculations over-predicted the system depressurization rate and the peak cladding temperature. Clarify if the PCT would still be over predicted if the calculated pressures matched the measured pressure.

Response: From Figures 12.32 and 12.33 in Round-1 question 12, it can be seen that the main reason for the EM calculation of higher cladding temperature is the prediction of the early CHF. In the EM calculation the CHF occurred within 0.2 seconds whereas in the test CHF occurred at about 3 seconds after the initiation of the transient. From Figures 12.8 and 12.9 it can be seen that during the first 3 seconds of the transient the code predicted the core pressure response reasonably well. Therefore the over-prediction of the cladding temperature in the EM calculation will not change even if the calculated pressure matched the data during the later part of the transient.

In an attempt to match the calculated pressure response with the data, the EM case was rerun using $CD = 0.4$ during the two phase and steam blowdown period. It is to be noted that $CD = 0.6$ was used in the EM calculations given in the response to question 12. From Figure 2.1 it can be seen that the code calculated pressure response agreed reasonably well with the data. The calculated cladding temperature is lower than the $CD = 0.6$ case during the later part of the transient, as shown in Figure 2.2. However, it is still much higher than the data. All other parameters, except the

density near the core inlet, Figure 2.3, showed similar behavior as in the $CD = 0.6$ case. From about 7.5 seconds to 14 seconds the $CD = 0.4$ case calculated density was higher than the data. During this period the intact loop cold leg (ICL) flow rate was higher than the broken loop cold leg (BCL) flow rate. The excess flow from the ICL flowed down to lower plenum through the downcomer. As a result of the flow reversal in the downcomer, high density fluid from the lower plenum entered the core inlet volume (volume 335). It is to be noted that the code calculated density is a volume average density in the lower plenum (volume 235 in Figure 12.3) where as the measurement is at a local point.

From this study it can be concluded that the EM would calculate higher cladding temperatures than the data even if the correct depressurization rate is calculated. A similar trend is expected in the BE calculation even though the difference between the calculated and the measured cladding temperature would be much smaller.

- b. The response noted the EM and BE RELAP5/MOD2-B&W calculations predicted a faster decrease in the pressurizer liquid level (Figure 12.13) than the data and stated this was consistent with the system pressure response. The response, however, does not explain why the level decreases were different. Clarify why the calculated and measured levels were different.

Response: The faster decrease in the calculated pressurizer level shown in Figure 12.13 was primarily caused by the pump side break flow rate shown in Figure 12.15. From Figure 12.15 and 12.17 it can be seen that

during the early part of the transient the flow in the broken loop hot leg is higher than the data. As a result, the intact loop hot leg flow rate is lower than the data as shown in Figure 12.16. From Figure 12.19 it can be seen that the intact loop cold leg flow rate is in reasonable agreement with the data. This flow is mainly controlled by the pump. The lower intact loop hot leg flow rate caused the pump to pull additional flow from the pressurizer.

- c. The response stated the calculated upper plenum to hot leg flows (Figures 12.16 and 12.17) were biased towards the broken loop over the intact loop due to relative differences in the depressurization rates between the two hot legs. B&W also noted that a flow reversal in the broken loop hot leg at 1 s observed in the test was not calculated in either analysis. Clarify the reasons for the differences between the measured data and the calculated results.

Response: The difference between the calculated flow rates and data in the intact and the broken loop hot legs is mainly due to the over-prediction of the pump side break flow as discussed with the response to question 2b.

- d. The oscillations in the calculated EM break flow after 2 s (Figure 12.14) were attributed to the critical flow switching logic between the Extended Henry-Fauske and Moody models. Was the same switching logic used in the original Test S-04-6 calculation? If so, why were the oscillation only seen in the new S-04-6 calculation? Also Section 4.3.4.1 of BAW-10168P discussed an EM method of smoothing the transition from the Extended Henry-Fauske model to the Moody model using a linear

weighting technique over the very low quality range. Clarify if this technique was used and, if so, clarify why it was not effective in providing a smooth transition between the critical flow models.

Response: The main cause for the oscillations in the EM calculated vessel flow rate, shown in Figure 12.14, from 2 to 4 seconds after the initiation of the transient was due to the use of $CD = 1.0$ for subcooled and $CD = 0.6$ for the saturated and two phase break flow conditions. Even though the extended Henry-Fauske and the Moody correlation flow rates are made continuous at the transition boundary, the use of a smaller CD value for the Moody calculated flow rate causes the flow discontinuity at the transition point. The discontinuity in the CD along with the criteria used to switch between the two correlations, as explained in question 12, caused the flow to oscillate for about 2 seconds. After about 4 seconds the flow remained two-phase and the calculated flow rate was smooth.

In the EM applications the same CD value is used with the extended Henry-Fauske and the Moody break flow correlations. Therefore, these flow oscillations will not be present in the EM calculations.

It is to be noted that the method used to smooth the flow rate at the transition point is different from that given in Section 4.3.4.1 of the EM topical report BAW-10168. Instead of linear weighting, an under relaxation of velocity as described by the equation 2.1.4-47 of RELAP5/MOD2-B&W topical report BAW 10164 is

used. This is further discussed in response to question 12 of the first set of questions on the EM topical report BAW-10168.

- e. An early decrease and subsequent oscillations in the density near the vessel side break in the EM calculation from 1.5 to 5 s were attributed to the switching in the choked flow model (See Figure 12.23). During the oscillatory period from 1.5 to 5 s, the EM calculated density showed an increasing trend that contributed to the good agreement between the EM calculation and the test data after 5 s. Was this increasing trend also caused by the switching in the choked flow model? If so, was the good agreement after 5 s fortuitous because the switching in the choked flow model is an unphysical condition? If not, clarify why the density increased in the EM calculation. Because the early density decrease was also calculated in the old EM analysis (and the BE calculation), clarify further how the early decrease was caused by the switching logic.

Response: The causes for the vessel side break flow oscillations during the 1.5 to 3.5 seconds transient period (Figure 12.14) are the discontinuities in the break flow at the subcooled to saturated transition boundary as discussed with the response to question 2d. As a result of these discontinuities, the density near the vessel side break shows similar oscillations during this period (Figure 12.23). Once the break flow condition stabilizes and becomes completely two phase (after about 5 seconds) the break flow and the density near the break show smooth behavior. The good agreement between the density calculation and the data after 5 seconds is not fortuitous, but caused by

accurate code predictions after the calculated flow regime passes the transition zone and becomes two phase. This result shows that for the test S-04-6 two different CD values have to be used with the EM break flow model, in order to calculate the correct system behavior. The flow behavior in the transition zone could be made smoother if the CD in the transition zone is made continuous. It is to be noted that the two CD values in this test simulation are used to match the break flow boundary condition with the data. In the EM applications, the same CD value is used during subcooled, two phase and single phase vapor flow conditions. Therefore, the discontinuities in the break flow and the density near the break will not exist in the EM calculations.

- f. Better cooling of the cladding after 12 s in the EM calculation as compared to the BE calculation was related to differences in core flow and the higher cladding temperatures in the EM calculation. Provide additional information on calculated heat transfer coefficients, heat fluxes, etc., to support the discussion in the response.

Response: In the EM calculation of Semiscale test S-04-6, the better cooling of the cladding after 12 seconds (Figures 12.32 and 12.33 of Round-1 question 12 related to RELAP5/MOD2-B&W topical report 10164) as compared to the Cycle 36.04 calculation was related to differences in core flow and higher cladding temperatures in the EM calculations.

From Figures 12.32 and 12.33 it can be observed that the EM calculated cladding temperatures are higher than the Cycle 36.04 calculation. Figure 2.4 shows the

calculated core flow rates near the peak power location in the hot channel. It can be seen that after about 12 seconds the EM flow rate is generally larger than that of Cycle 36.04. As a result, the EM calculated a higher heat transfer coefficient than the Cycle 36.04 prediction as shown in Figure 2.5. The higher wall temperature and higher heat transfer coefficient prediction in the EM calculation results in a higher heat flux prediction than Cycle 36.04 as shown in Figure 2.6. The prediction of higher heat flux after 12 seconds in the EM calculation caused better cooling of the cladding as shown in Figures 12.32 and 12.33.

FIGURE 2.1. SEMISCALE MOD1 TEST S-04-6; PRESSURE IN THE LOWER PLENUM.

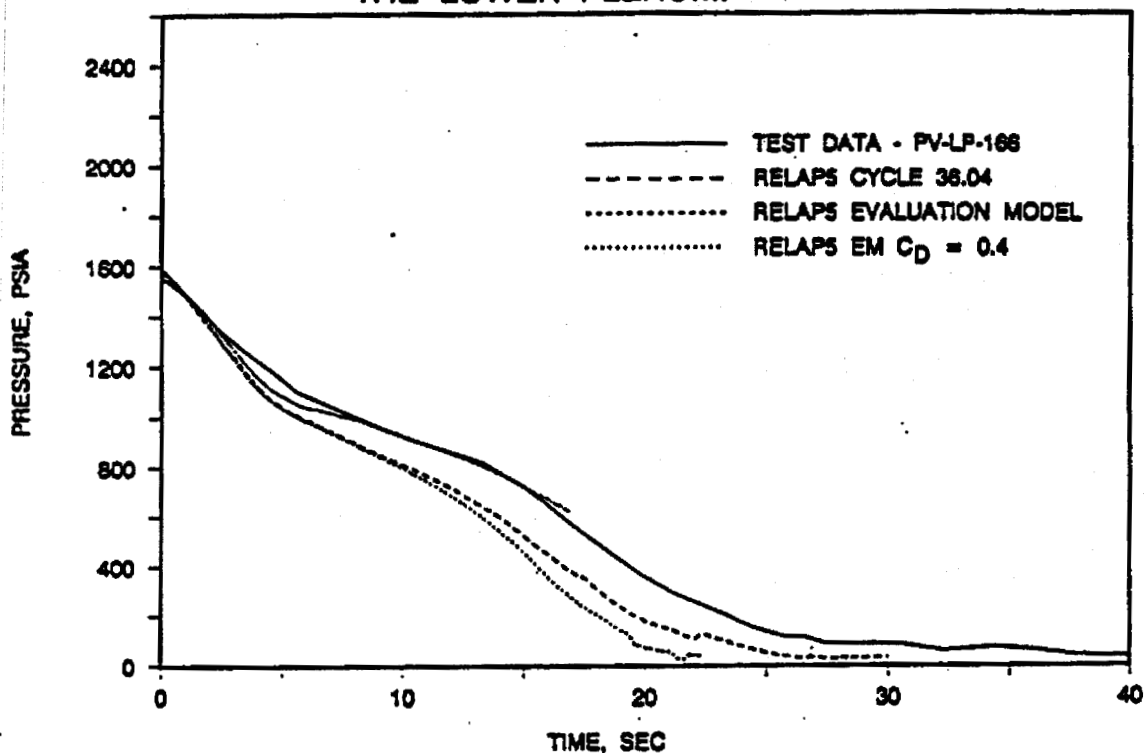


FIGURE 2.2. SEMISCALE MOD1 TEST S-04-6; HIGH POWER ROD CLAD TEMPERATURE NEAR THE PEAK POWER LOCATION.

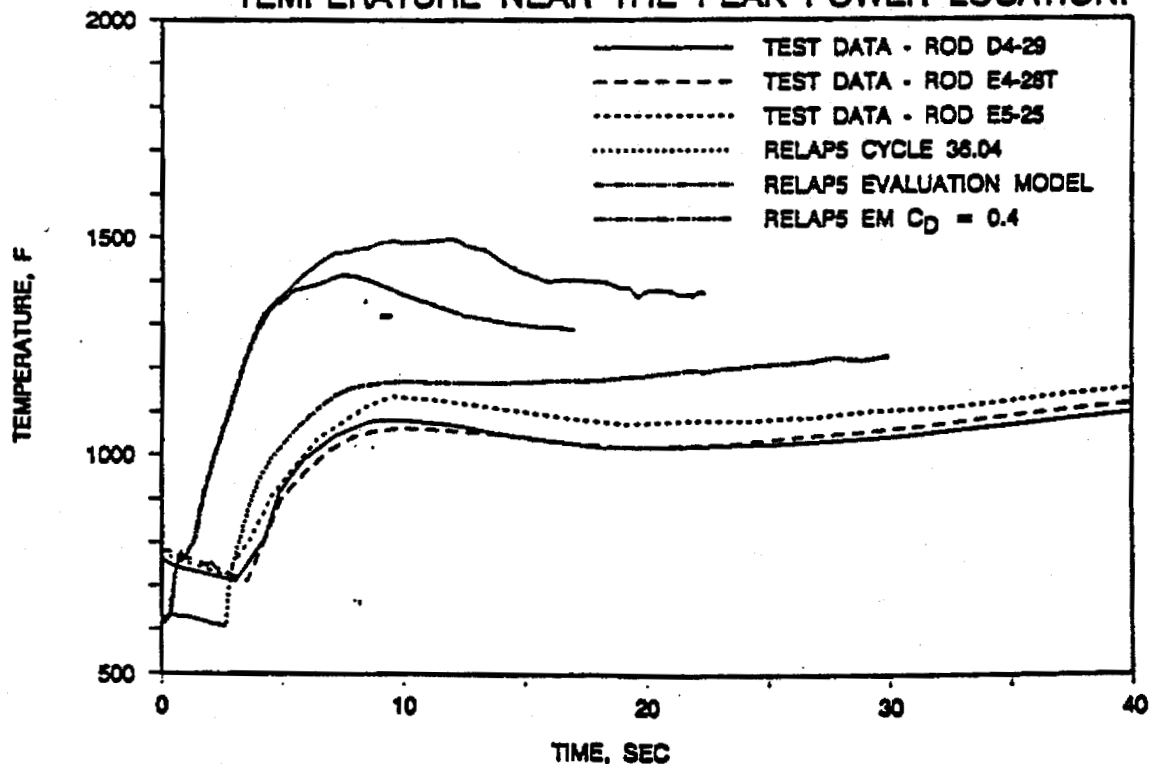


FIGURE 2.3. SEMISCALE MOD1 TEST S-04-6; DENSITY NEAR THE CORE INLET.

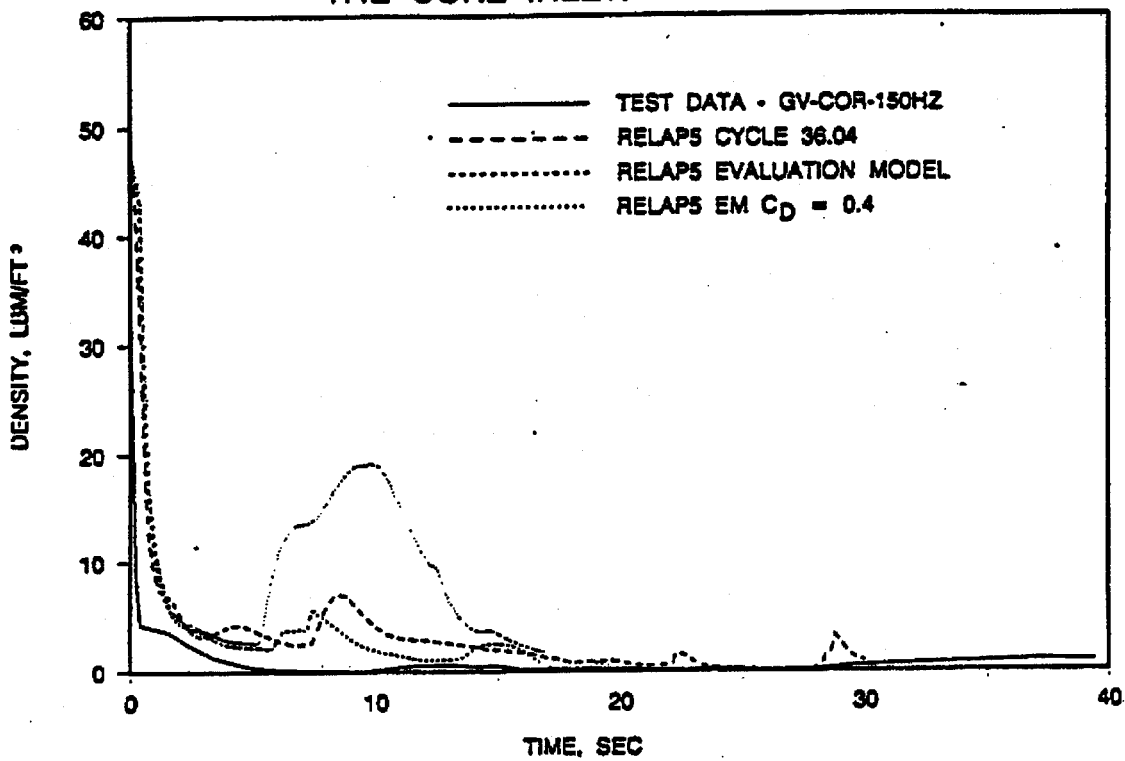


FIGURE 2.4. SEMISCALE MOD1 TEST S-04-6; MASS FLOW RATE IN THE HOT CHANNEL AT THE HIGH POWER LOCATION.

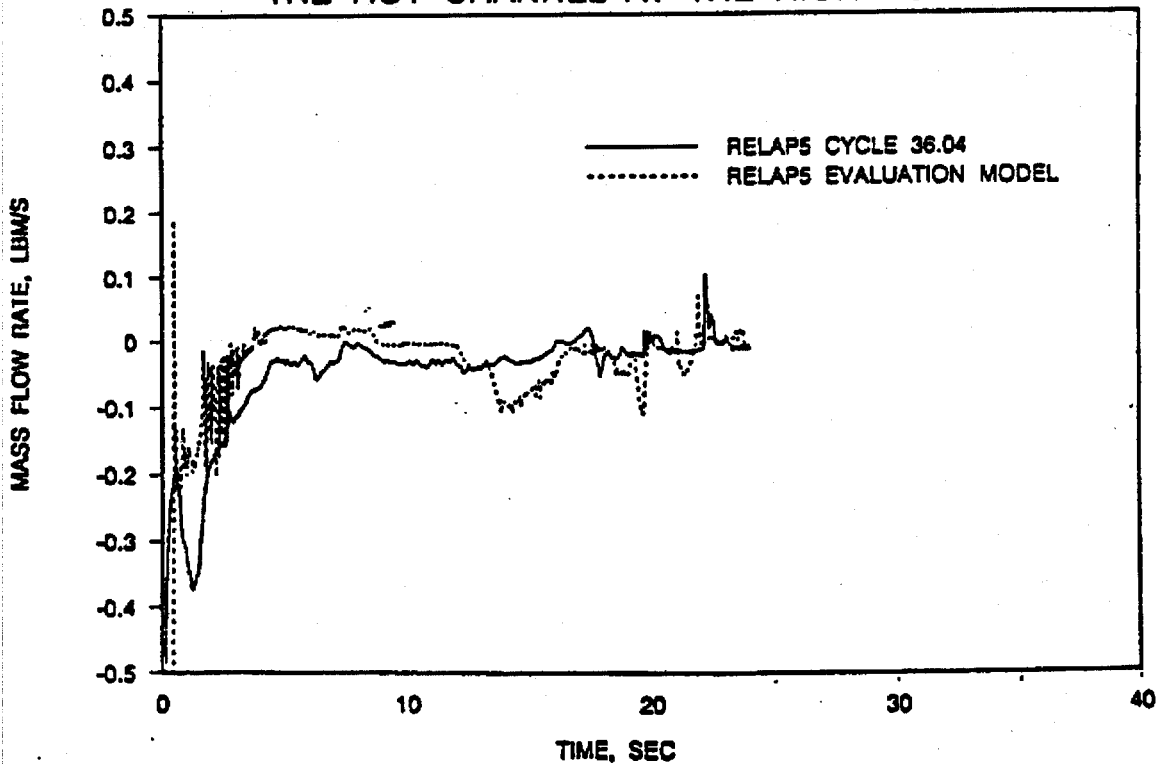


FIGURE 2.5. SEMISCALE MOD1 TEST S-04-6; HEAT TRANSFER COEFFICIENT IN THE HOT CHANNEL AT THE HIGH POWER LOCATION.

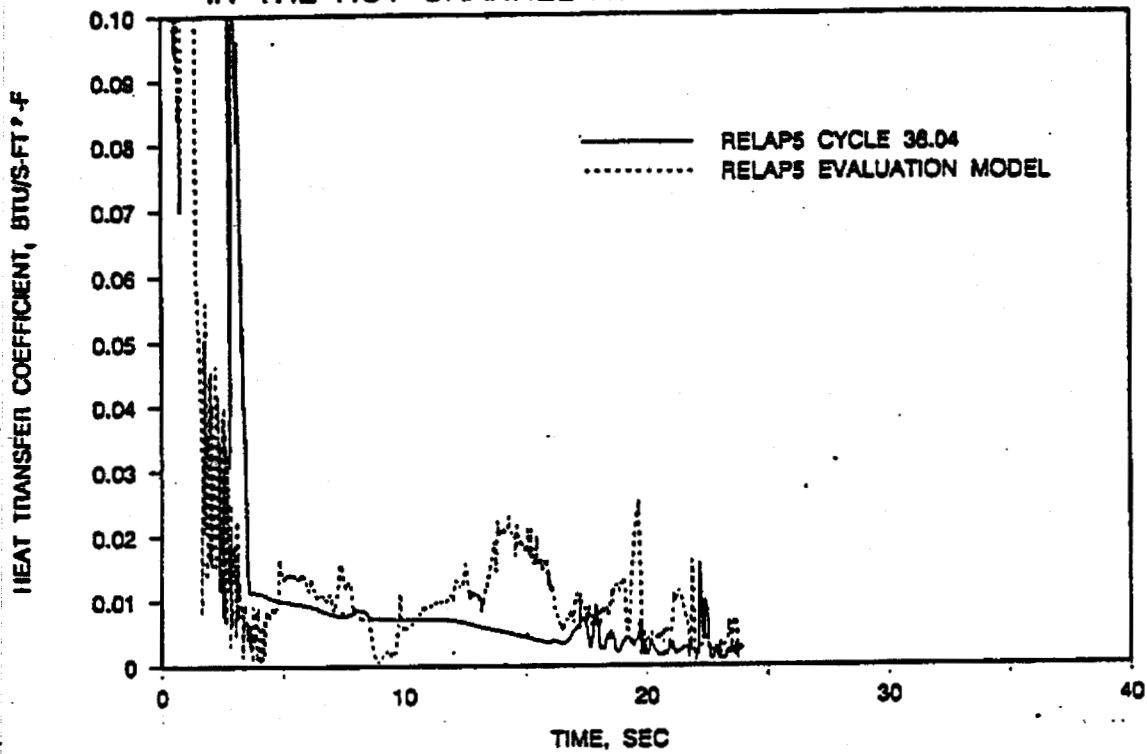
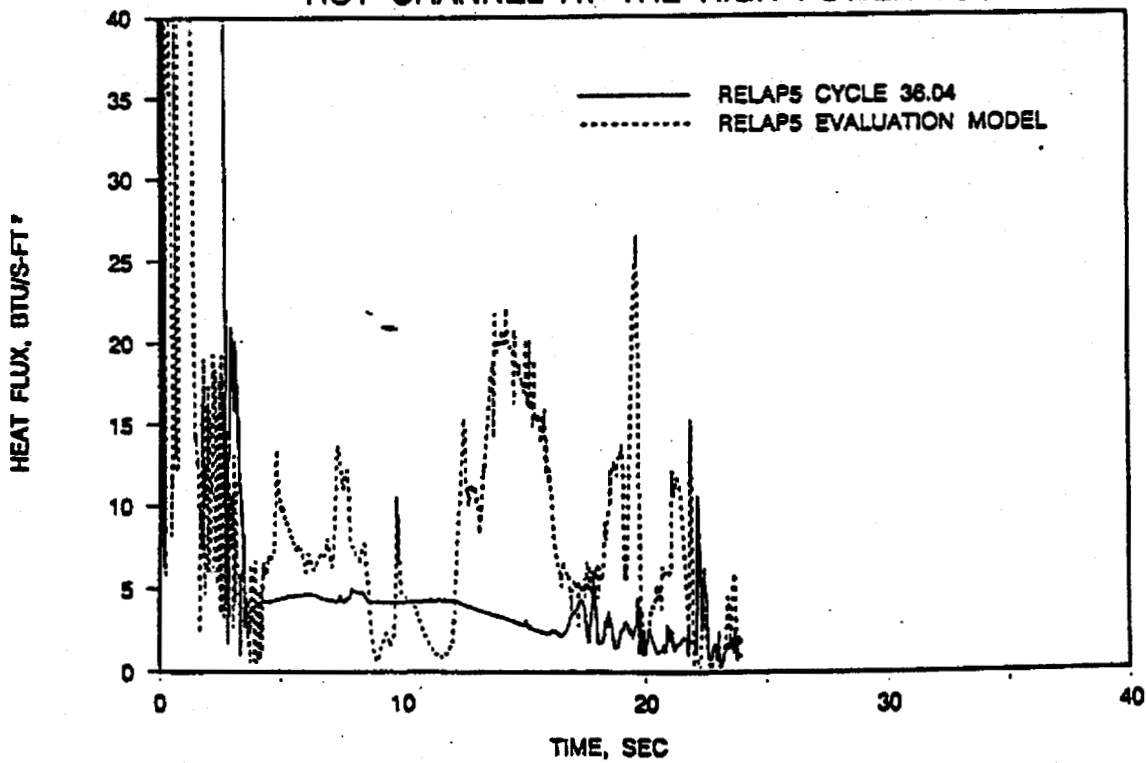


FIGURE 2.6. SEMISCALE MOD1 TEST S-04-6; HEAT FLUX IN THE HOT CHANNEL AT THE HIGH POWER LOCATION.



3. The following questions are related to the information provided in the response to Question 14 on LOFT L3-5 benchmark calculation.

- a. For several of the parameters presented, the differences between the calculated and measured results were related to the underprediction of the break flow in the RELAP5/MOD2-B&W calculation (see Figure 14.5). Clarify why the break flow was under-predicted.

Response: The purpose of the LOFT L-3-5 benchmark analysis presented in Appendix G Section 2 of BAW 10164P is to demonstrate that the B&W version of RELAP5/MOD2-36.04 can adequately predict the small break phenomena observed in the L-3-5 experiment. Although this version is not used for the licensing application, it is important to establish a baseline for the development of the SBLOCA EM. As discussed in Appendix G Section 2, the Ransom-Trapp discharge model in RELAP5/MOD2-36.04 under-predicted the two-phase discharge flow rate. As a result, the calculated primary system inventory is higher than the experiment, and the primary system depressurization is slower for the RELAP5 calculation than for the experiment.

B&W has reanalyzed the L-3-5 experiment with the EM discharge models using discharge coefficients of 1.0 and 0.6 respectively for subcooled and saturated blowdown. In addition, the core bypass resistance from the inlet annulus to the upper plenum region is reduced to achieve approximately 6.1% bypass flow (estimated bypass flow rate is 6.6% per EGG-LOFT5480). The original analysis has approximately 4.4% bypass flow. The results of this reanalysis form the basis for the response to this question.

The blowdown was initiated 4.8 seconds after the reactor scram as shown in Table 3.1. The RC pump trip, main feedwater isolation, and auxiliary feedwater initiation are identical to the original analysis presented in Table G.2-2. A comparison of the timing of events during the early phase of the blowdown between the two cases shows good agreement. This confirms the consistent subcooled leak flow calculations between the B&W EM and Ranson-Trapp discharge models. As the primary system enters the saturated discharge phase, the discharge rate between the two models vary substantially. The EM discharge model calculates a higher leak flow rate than the measurements as shown in Figure 3-1. The effects of a higher leak flow rate are reflected in the primary system depressurization rate and normalized mass inventory presented in Figures 3-2 and 3-3 respectively. Although the experimental data for the leak flow during the early phase of the blowdown are not available, Figure 3-3 seems to indicate that the calculated subcooled leak flow is higher than the test data.

A comparison of the calculated hot leg and cold leg densities with those of the experiment shows that RELAP5 can correctly calculate the primary system mass distribution. Water in the hot leg drained at approximately 600 seconds as shown in Figure 3-4. As a result of the higher leak flow calculated by the EM discharge model, water in the cold leg pipe drained earlier than the experiment as shown in Figure 3-5. This causes a sudden reduction in the leak flow rate at 670 seconds as the fluid density changes drastically following the draining.

The secondary side pressure exceeds the primary side pressure at 707 seconds, approximately 43 seconds earlier than the experiment due to the higher depressurization rate calculated by the EM discharge model. This leads to a loss of natural circulation and is conservative for the SBLOCA analysis.

The results of the analysis demonstrate that RELAP5-MOD2-B&W can adequately predict the important phenomena observed in the L-3-5 experiment such as pressurizer draining, pump coastdown, natural circulation, ECC injection, loss of natural circulation, hot let draining, and long-term cooling. Furthermore, the comparison plots confirm that B&W's SBLOCA evaluation model is conservative in predicting the overall system thermal hydraulic responses to a small break LOCA.

- b. The response also stated that the pump in the RELAP5/MOD2-B&W calculation had a faster coastdown than the pump in the test because of greater reverse flow fluid torque acting on the pump in the calculation during the coastdown period, and that the faster reverse flow torque was due to the larger break flow calculated. The connection between the reverse flow fluid torque acting on the pump and the break flow rate is not clear. Clarify how the break flow affected the pump performance. Also, in Figure 14.5, the measured break flow during the pump coastdown period (approximately the first 30 s) is not shown. How was the conclusion reached that the calculated break flow was larger than the measured break flow during this period?

Response: The response to question 14-3 with regard to the pump coastdown was inaccurate. The break flow has only a slight effect on the RC pump coast down. The difference in pump coast down appears to be due to the pump descriptive data used in the analysis. The initial several seconds of coast down are governed by the moment of inertia and the frictional torques of the pump and motor. Fluid interactions with the pump during small breaks do not contribute significantly. In order to predict the coast down observed in the test, the reported moment of inertia must be increased by a factor of 4 to 5 or the frictional torques reduced by the same factor. A comparison of the moment of inertia reported for the LOFT facility to a typical RC pump value shows that the moment of inertia of the LOFT pump is 0.0001 that of a full sized pump. This small a value is surprising in light of the scaling of the LOFT facility. At present B&W can only speculate along the line described to explain the pump behavior in the L-3-5 test prediction.

As discussed in the response to part a of this question, the lack of experimental data in the first 30 seconds of the transient and the uncertainty associated with the measurements available, make it difficult to confirm that the calculated leak flow is higher than the experiment. However, the comparison of the primary systems mass inventory logically leads to that conclusion.

Table 3.1. Sequence of Events for LOFT L-3-5 with EM Discharge Models

Events	Time (sec)	
	Experiment	RELAP5/MOD2 with EM Discharges
Reactor scrammed	0.0	0.0
LOCA Initiated	4.8	4.8
RC Pump Tripped	5.6	5.6
HPIS Initiated	8.8	9.3
Pressurizer Emptied	27.0	39.0
RC Pump Coastdown	35.0	20.0
SG Auxiliary Feedwater Initiated	67.8	67.8
Secondary side Pressure Exceeded		
Primary Side	749.8	706.6
SG Auxiliary Feedwater Terminated	1804.8	----
Leak Isolation	2313.9	----

FIGURE 3-1. LOFT TEST L-3-5, LEAK FLOW RATE.

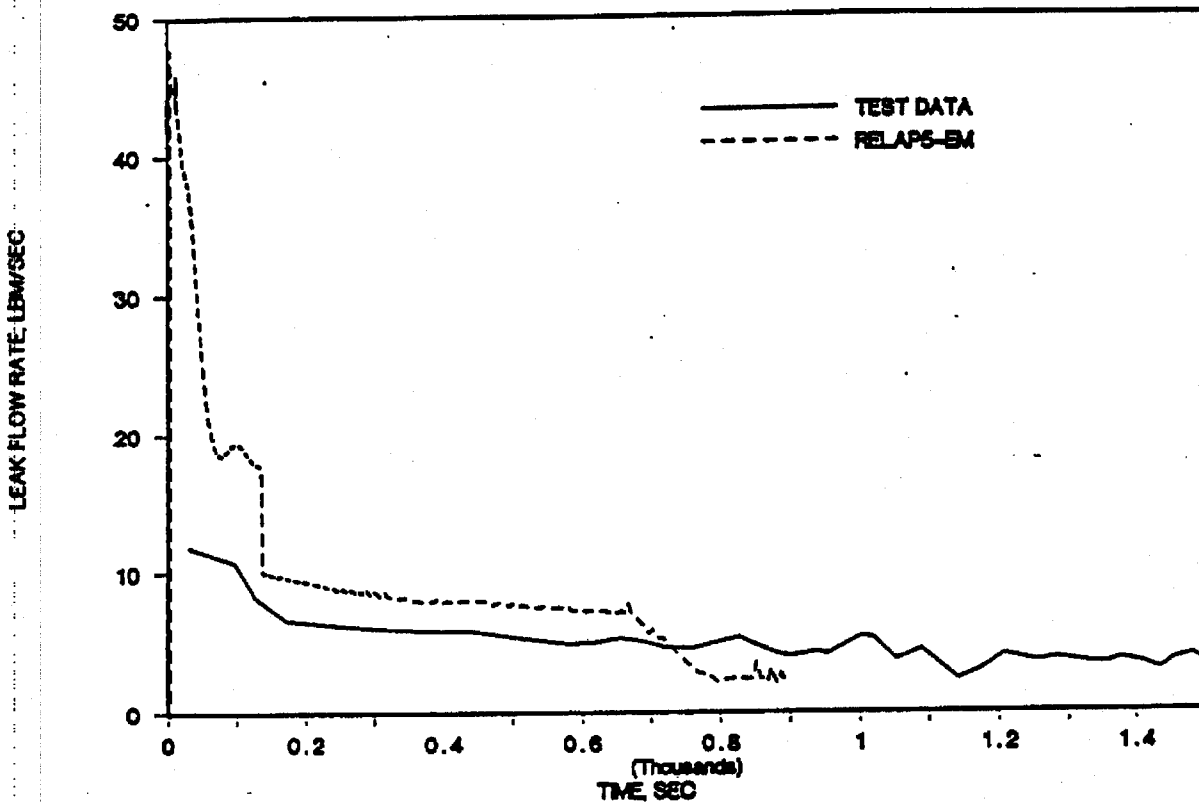


FIGURE 3-2. LOFT TEST L-3-5, LEAK NODE PRESSURE.

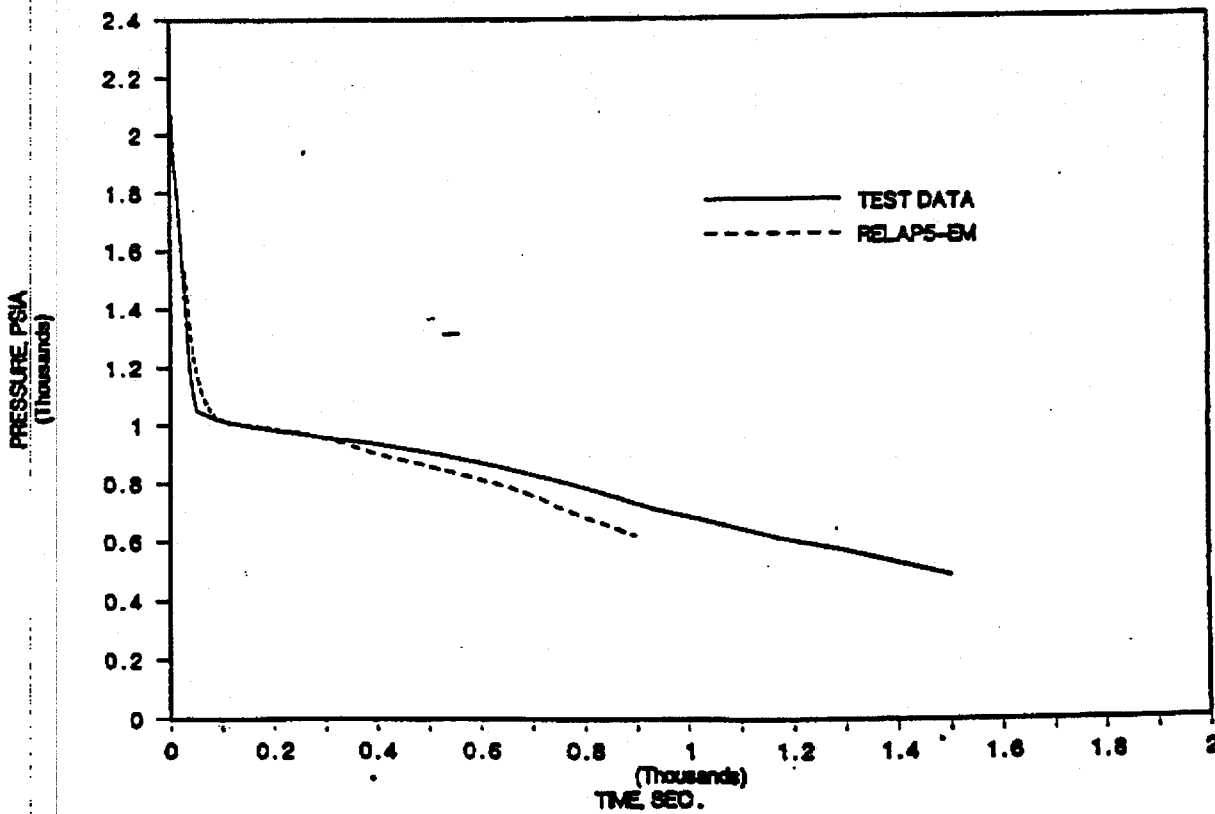


FIGURE 3-3. LOFT L-3-5, NORMALIZED RCS INVENTORY.

NORMALIZED RCS INVENTORY

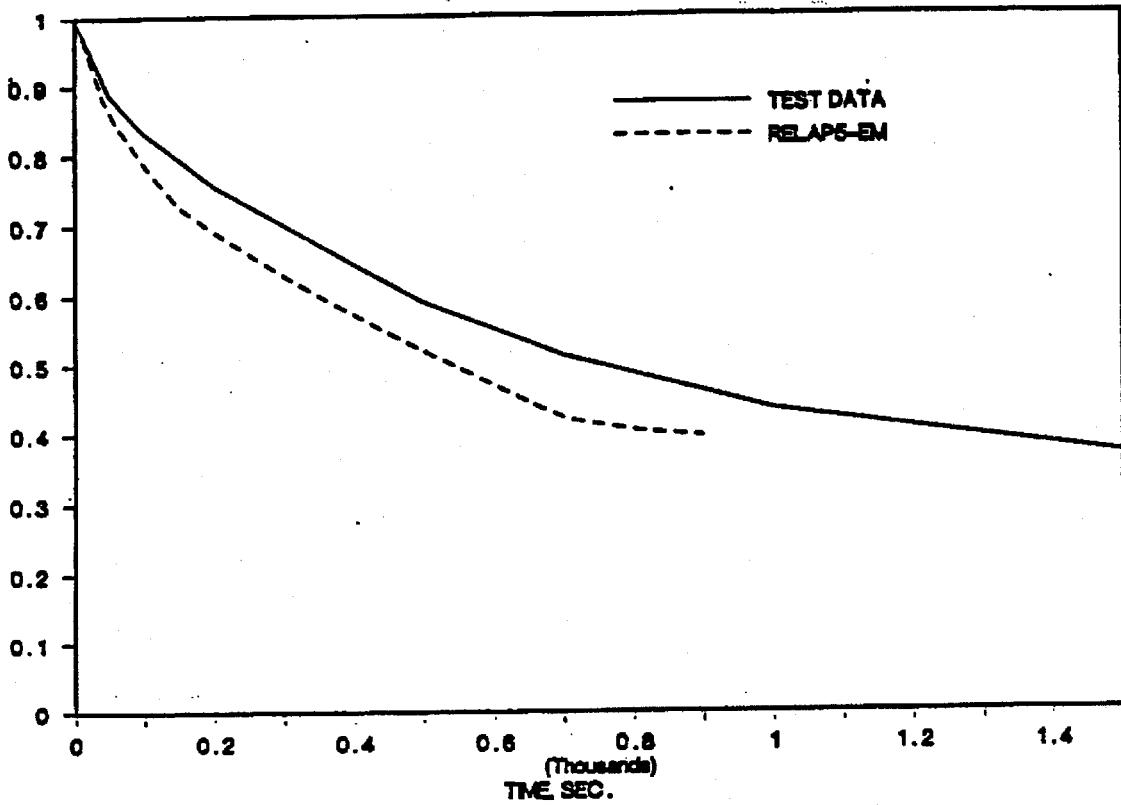


FIGURE 3-4. LOFT TEST L-3-5, HOT LEG DENSITY.

DENSITY, LB/FT³

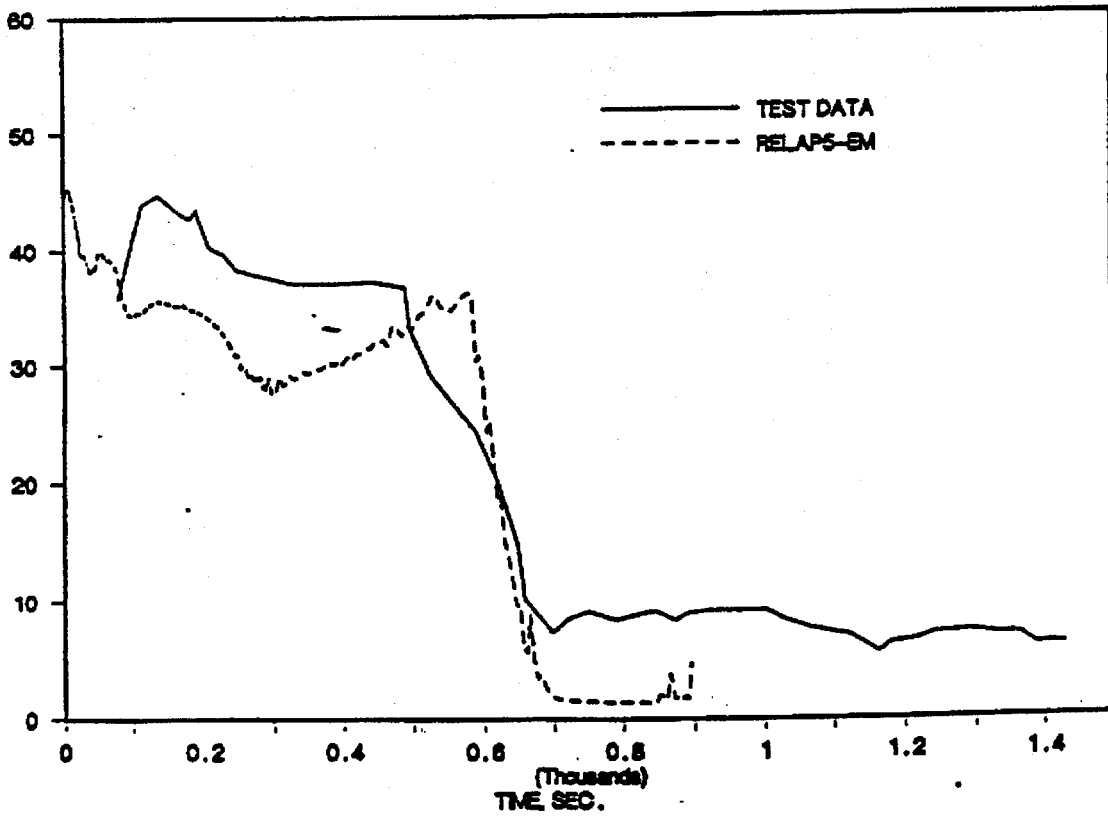
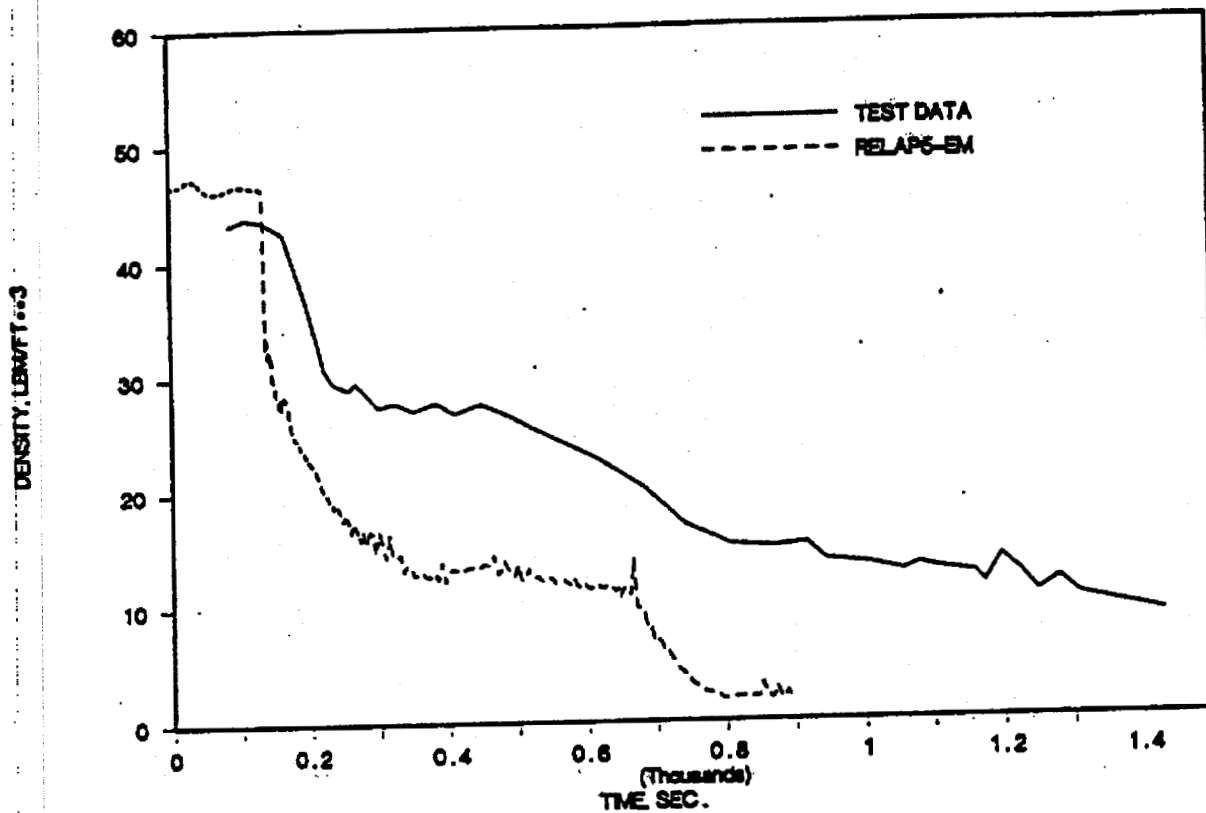


FIGURE 3-5. LOFT TEST L-3-5. COLD LEG DENSITY(PUMP DISCHARGE).



4. The following questions are related to the response to Question 16 regarding how RELAP5/MOD2-B&W meets the requirements of NUREG-0737, Item II.K.3.30.

- a. The response stated that the RELAP5/MOD2 calculations of OTIS and MIST tests demonstrated the code was capable of properly predicting SBLOCA phenomena, and that the results showed the primary system pressure and mass inventory were well predicted. However, no comparisons were provided. Also, the OTIS and MIST tests were performed with the once through steam generator geometry of B&W plants whereas the RELAP5/MOD2-B&W is intended for use for plants with recirculating steam generators. Provide additional benchmark results for facilities with a RSG design to demonstrate the LOCA evaluation model and RELAP5/MOD2-B&W'S ability to calculate small break phenomena with RSG plants.

Response: A SBLOCA transient is characterized by a relatively slow depressurization of the RCS. It begins with subcooled blowdown to saturation pressure followed by saturated depressurization for an extended period of time. Following the RC pump trip, the primary system undergoes a transition from forced flow to natural circulation, and distinct liquid levels are developed in the reactor vessel and in portions of the primary loops. Manometric balances are developed in the primary system while the core decay heat is removed via the break, natural circulation, and reflux boiling. As the core liquid level continues to decrease, the hydrostatic balance causes clearing of the pump suction loop seals. The primary system liquid inventory

continues to decrease until the ECCS overcomes the leak flow. The phenomena involved are generally common to both RSG and OTSG plant designs (excepting reflux boiling) and demonstration of code capabilities can be extended from one design to the other. The ability of RELAP5/MOD2-B&W to correctly predict these key phenomena and associated parameters is demonstrated by the results of benchmark analyses on three different facilities MIST (OTSG) test 320503, Semi-scale (RSG) S-LH-1 and LOFT (RSG) L-3-5.

Although the MIST facility represents a scaled B&W NSSS, and the performance of the OTSGs and its impact on natural circulation are not directly applicable to the RSG plant, the primary system inventory and depressurization rate are primarily controlled by the break size. The predictions of the primary system inventory and mass distribution within the primary system for the MIST test are applicable to any plant configuration. The benchmark of MIST test 320503 and the other benchmarks contained in reference 4.1 demonstrate RELAP5/MOD2s ability in fluid tracking, phase distribution, and heat removal through the natural circulation period and into the steam water separated boiling pot period.

The issue of the effects of the steam generator performance on natural circulation and reflux boiling is addressed by the benchmark of Semiscale test S-LH-1. As discussed in the response to question 17 of the round one questions on RELAP5/MOD2-B&W and question 5 of this question set, the results demonstrate the code's ability to correctly predict the SBLOCA

transient. In addition, fluid velocities in the uphill side of the steam generators are provided, in response to question 5, to demonstrate that the code calculates natural circulation and reflux boiling during the period when the steam generators are effective. Figures 10-1 and 10-2 (round one questions on RELAP5/MOD2-B&W) show liquid and vapor velocities in the uphill side of the steam generator tubes. The negative liquid velocity (fall back) indicates the reflux mode cooling. No experimental data are available for comparison.

- b. In discussing RELAP5/MOD2-B&W's ability to calculate the effects of non-condensable gases on the system response, the addition of a model to calculate surface condensation in the presence of a non-condensable was discussed. Benchmarking of this model against separate effects tests was also discussed by referencing a paper presented at the Eighth International Heat Transfer Conference in 1986 without providing the results. Provide appropriate results from this paper. Also, provide results which verify the code's ability to calculate the effects of non-condensibles on the overall system responses, including system pressure, heat transfer, natural circulation, and non-condensable transport, etc.

Response: The reference paper presented at the Eighth International Heat Transfer Conference is attached. The benchmark results of the separate effects tests demonstrate that RELAP5/MOD2-B&W is capable of handling the effect of noncondensable gas on surface

condensation. However, the volume of noncondensable gas that can be trapped in the primary system during small break LOCA (SBLOCA) is too small to impact steam generator performance in the liquid natural circulation, two-phase natural circulation, or reflux boiling modes. Thus, the effects of noncondensable gas are not directly considered in the analysis. The remainder of this response deals comprehensively with the impact of noncondensibles on the results of SBLOCAs in five subsections: (1) the general effects of noncondensable gas on SBLOCA, (2) potential sources of gas, (3) effects on steam generator performance, (4) gas effects on larger SBLOCAs, and (5) conclusions.

Generalized Effects of Noncondensable Gas on SBLOCA

For the purpose of discussing the impact of noncondensable gas, SBLOCAs can be considered in two groups: (1) those that require the steam generator to remove energy for a substantial period of time and (2) those that do not. After reactor trip, pump coast down, and removal of the initial core stored energy, an SBLOCA depressurizes (or not) in accordance with a balance between the energy source of the core and the energy sinks of the break and the steam generators. If break flow is insufficient to cause a decrease in the system average specific energy then the system will depressurize to the just above the secondary pressure, and the energy removal necessary to keep the system from repressurizing will be accomplished by the steam generators. If break flow is sufficient to cause a decrease in system average specific energy then the

system will depressurize until the break flow and the core decay heat are in balance. This balance point may vary with time, as different energy and fluid sources (the ECCS) and sinks (generally break quality) develop, but will generally act with the decay heat to produce a gradual system depressurization as decay heat is reduced. Similarly, the first group of SBLOCAs will become independent of the steam generators as the decay heat drops.

If sufficient noncondensable gas is present to interfere with the performance of the steam generators, the first group of small breaks either will not depressurize or will repressurize depending on the timing of the appearance of the gas. LOCAs of this class may depend strongly upon the ECCS injection capability for successful termination, such that, if the resultant pressure increase significantly decreases the injection capability of the ECCS, more severe core uncover may be experienced. As will be shown below, however, the amount of gas releasable to the RCS is so small for these accidents that it does not substantially interfere with the performance of the steam generators.

The effect of noncondensibles on the second class of SBLOCAs is a result and consequence of the design of the ECCS. As the break size increases, depressurization becomes more rapid and the pressure at which the leak and decay heat balance becomes lower. At some break size, the balance point will coincide with the initiation of flow from the low pressure (RHR)

injection system. If it is also true that the flow from the RHR system is required to assure core decay heat removal, it might be possible for the nitrogen cover gas from the accumulators to pressurize the system such that the flow from the low pressure system would be momentarily cutoff. As will be shown later, although it is possible that nitrogen is injected for these types of SBLOCA, the injection is insufficient to raise the RCS pressure up to the RHR system shutoff pressure or the gas enters at such a late time that the high pressure system can supply all of the required ECCS.

Sources of Noncondensable Gas

The sources of noncondensable gas that can affect steam generator performance during SBLOCA are the dissolved gas in the reactor coolant system (including the pressurizer liquid region, the charging system, and the refueling water storage tank); the gas in the steam space of the pressurizer; the gas generated by radiolytic decomposition of the coolant; the gas in the gap and plenum volumes of the fuel; and possibly gas resulting from cladding metal-water reaction. These can become free gas within the reactor coolant system (RCS) by boiling or flashing of liquid, by alteration of the solubility of the gas in water, or by direct generation. All three processes occur, to some extent, in LOCAs, resulting in a time varying concentration of free gas within the RCS. Accordingly, most arguments that the gas is inconsequential are based on the maximum releasable amounts of gas as opposed to the

actual amount of gas expected. For typical small breaks this amounts to an overprediction of the gas volume by more than 500 percent.

Accounting for all sources of gas, except hydrogen from metal-water reaction, the total volume of gas available for release within the RCS of a 4-loop Westinghouse designed plant, including one hour of radiolytic decomposition, is about 117 cubic feet at the secondary control pressure of 1150 psia and 562 F. This amounts to 29 cubic feet per steam generator or about 5.7 percent of the tube volume (assuming 10% tube plugging). If the potential for metal-water reaction is included up to the limit allowed by 10CFR50.46 (1% of the core oxidizes), the total available gas would be about 231 cubic feet at 1150 psia and 561 F. This gives 58 cubic feet per generator or about 11 percent of the tube volume (again considering 10% tube plugging). Realistically, SBLOCAs are resolved in about half an hour or less with peak cladding temperatures below 1500 F. Under these conditions, only about 10% of the water storage tank is injected into the RCS, there is essentially no metal-water reaction, and only one half of the RCS is flashed or boiled. Thus the amount of released gas is only 36 cubic feet for the system or 9 cubic feet per generator, about 1.8% of the generator tube space. Notwithstanding this, the remainder of this answer considers the maximum releasable amounts of gas.

Effect of Noncondensibles on SBLOCAs Which Require Steam Generator Heat Removal

In sufficient quantity, noncondensable gas can impede the ability of the steam generator to transfer energy. For those SBLOCAs that rely on the steam generators to remove part or most of the decay heat, an alteration of steam generator performance might seriously change the course and consequences of the accident. The steam generators remove energy by liquid natural circulation, two-phase natural circulation, or reflux boiling. Typically, an SBLOCA will proceed through all three of these phases. The reflux mode is the most significant because it is during this mode that the core has a possibility of experiencing a cladding temperature excursion. During the other two modes, the core is covered with water or a two-phase mixture. The potential impact of noncondensable gas on each of these modes of cooling is discussed below.

Liquid natural circulation is characterized by the transfer of energy from the core to the steam generator by water in its liquid state. The process may occur with steam in the system but the steam must be trapped in regions away from the circulation path since the water in the circulation path is by definition subcooled (if saturated water is present then the plant is in two-phase natural circulation). Heat exchange within the steam generators is by a convection process and will not be interfered with by the presence of noncondensable gas. The only way that such gas could interfere would be to block the circulation flow. The

total amount of noncondensable gas releasable, for a plant in this mode, is 29 cubic feet at the steam generator control pressure. If released, this gas would exist as small bubbles suspended within the RSC coolant and would be circulated around the coolant loop with the coolant. Separation may occur in regions of low velocity such as the steam generator plenums, the RC pump casings, the upper downcomer, or the reactor vessel upper head. Collection in any of these regions will not interfere with circulation because if collection threatens to interfere, the gas would be swept back into the circulating system to collect elsewhere.

A worst case assumption is that the gas all collects in the steam generator tube region. The maximum amount of the tube bundle length that could be occupied by the gas is less than three feet. Under this hypothesis, the gas would be pushed to the downside of the tubes and cause a 12 percent (51 feet is the length of the average steam generator tube) reduction in the cold side driving head for circulation. This, in turn, would slow the flow quickly causing an increase in heating of the coolant in the core, compensating for the loss of cold side head. The end result would be a slightly slower circulation rate operating at a slightly wider temperature differential, but transferring the same amount of energy. The effect would be barely noticeable.

As, or if, the primary coolant system continues to loose inventory, the capability to keep the hot leg

temperature below saturation and still transfer the required heat will be lost. The core will start to generate steam that will flow to the steam generators and be condensed. The return coolant from the steam generator will remain subcooled and the process continue much like liquid natural circulation. This is the beginning of the two-phase natural circulation period. Noncondensibles, if present, will continue to flow throughout the system as in liquid natural circulation. Again, a worst case assumption could be made that the noncondensibles accumulate in the middle of the steam generator tubes. The existence of the plug of noncondensibles in the middle of the generator would be compensated for in the same way as occurs in liquid natural circulation. The circulation rate would slow slightly and the hot leg would develop a higher void fraction.

As two-phase circulation proceeds, the fluid loss is such that the downside of the steam generator tubes can no longer support a column of saturated water and steam to the height of the center of the tubes. At this time the plant makes a gradual transition into the reflux mode. The upper or highest of the steam generator tubes will make the transition first and the generator will perform in a mixed mode for a period of time. The noncondensable impact is also mixed. For those steam generator tubes in two-phase circulation the impact is as described above, very little. For those tubes in the reflux mode, the impact is a reduction in the tube surface area available for condensation. The noncondensibles collect in the steam generator tubes on

the tube down side and act to reduce the heat transfer. As with the other modes, and as detailed below, the volume of the noncondensibles available is so small that little impact is possible.

Full refluxing in the presence of noncondensable gas has been studied experimentally. Single tube tests^{1,2} and tests performed in the Semiscale Mod 2A facility^{1,3} show that the addition of noncondensable gas to an RSG results in the division of the tube length into two zones. The upstream, active zone, experiences nearly no effect from the injection of noncondensibles, while the downstream passive zone experiences nearly total heat transfer blockage. The steam generators act as if their heat transfer areas have been reduced in proportion to the gas concentration. According to tests in the Semiscale facility^{1,3}, gas volumes up to about 5 percent of the tube volume have no detrimental impact on steam generator performance. Gas volumes above 5 percent require gradually increasing thermal potentials to maintain full heat transfer rates.

For SBLOCAs that do not involve cladding temperature excursions above 1500 F, an assumption that there is no significant core wide metal-water reaction is reasonable, and the maximum gas volume available for release is limited to 5.7 percent of the steam generator tubes. As this is essentially the upper limit for no effect demonstrated by Semiscale, there will be no detrimental effect on steam generator performance. Should the LOCA involve higher cladding temperatures, the inclusion of a 1 percent oxidation of

the core zirconium would produce a maximum gas concentration of 11 percent of the steam generator tube volume. For this concentration the Semiscale tests show a 50 psia increase in system pressure to be required to compensate for the lowered steam generator heat transfer area. Such an increase, above the steam generator control pressure of 1150 psia, would not substantially reduce the injection capabilities for the centrifugal charging and safety injection systems. Therefore, for those SBLOCAs that rely on the steam generators for partial energy removal and pressure control, the evaluation need not directly consider the consequences of noncondensable gas in the RCS.

Effect of Noncondensibles on SBLOCAs Which Do Not Require Steam Generator Heat Removal

As discussed previously, the larger SBLOCAs will depressurize rapidly to pressures at which an equilibrium exists between the core decay heat and the break flow. During the depressurization, such gas as is present will expand, but, since the steam generators are now a heat source rather than a heat sink, the effect on steam generator performance is beneficial. A possible adverse effect of noncondensable gas occurs for SBLOCAs that reach approximate equilibrium at pressures just below the RHR injection system dead head pressure. If mitigation of these events requires RHR flow, and if the plant accumulators were to expel nitrogen at the critical time, the gas might repressurize the system above the dead head pressure and stop RHR injection. The system would shortly bleed

down and reestablish RHR injection, but, if timing were crucial, the momentary lack of RHR injection could increase the severity of the event.

The effect of accumulator discharge of nitrogen has been studied for large break LOCA in the Semiscale facility^{4,4}. Depending on the amount and rate of gas discharge into the RCS, the system responded with an abrupt pressure increase followed in a few seconds by a pressure decay to a stabilized value that was 20 to 30 psi above the pre-discharge pressure. The pressure increase continued far past the end of gas injection, indicating an interference with steam condensation. By the end of the reported data, the pressure seems to be falling gradually back to the pre-injection pressure. Aside from the pressure impact, the effect of the injection of gas was to push water from the downcomer into the core and momentarily increase the flooding rate. This, in turn, slightly reduced the cladding temperatures.

These experimental results are directly applicable only for large breaks. For SBLOCA, the slower system depressurization will alter the impact of nitrogen injection. System pressure will not be increased; rather the rate of depressurization will be slowed. The interference with steam condensation will not be as noticeable as in the Semiscale tests because condensation is not a strong effect in an SBLOCA at the time of nitrogen discharge. These trends are observable in the Semiscale results in Figure 31 of reference 4.4. Here the initial pressure spike is

reduced as the rate of nitrogen injection is slowed. For the slowest injection rate there is no pressure surge but only a gradual pressure increase. SBLOCA injection rates will be considerably below the slowest of rates used in the Semiscale tests.

To address the potential for an adverse impact on SBLOCA because of accumulator gas injection, the break spectrum is divided into three more parts: (1) those breaks that will depressurize to inject nitrogen but will do so only after other ECCS systems (the two high pressure systems) can assure adequate core cooling without the RHR system, (2) those events that depressurize sooner than that but which do not fall to pressures well below the shutoff head of the RHR system, and (3) those events that depressurize to pressures well below the shutoff head of the RHR injection system. The demarkation of each category will be developed and finally the characteristics of the nitrogen effects identified to show that no adverse consequences occur.

For RCS pressures around 200 psia, both the centrifugal charging system (CC) and the safety injection system (SI) have reached a runout condition with a total injection flow of about 100 lbm/s. Such an injection flow is capable of removing all core decay heat for a 3500 Mwt plant at and after 300 seconds. Also, an expansion of the nitrogen in the accumulators at constant temperature shows that the accumulator gas will not expand beyond the tank at pressures above 200 psia. Therefore, any event that takes longer than 300

seconds to depressurize to 200 psia or lower does not require the RHR injection system to mitigate the accident and there are no adverse effects of nitrogen injection.

From the Semiscale results, the maximum impact on system pressure was about 30 psia. An examination of the system designs to be covered by this evaluation model shows that the lowest RHR injection system shutoff head is about 165 psia. As RHR injection builds fairly quickly with decreasing primary pressure, any accident that can be assured to hold pressure below 150 psia will receive abundant ECCS flow. Therefore, any accident that would depressurize to 120 psia (maximum impact is 30 psia) without nitrogen effects will not be adversely affected should gas injection occur.

The breaks between these two categories, those that depressurize to less than 200 psia prior to 300 seconds but stabilize at pressures greater than 120 psia, range from approximately 0.3 to 0.5 square feet in area. The break area is not actually significant but is useful as a tag for a normalized leak flow rate. An examination of the rate of system depressurization and the rate of accumulator depressurization for these accidents shows that accumulator injection takes place in two phases. The initial phase is predominately adiabatic and controlled by the initial energy of the pressurizing gas. This phase is responsible for the rapid injection of coolant and is active for 10 to 20 seconds longer than the system depressurization. The second phase is

controlled by the heating of the gas within the tank by natural convection with the walls of the tank. This phase causes a very slow expansion of gas and/or water into the RCS.

An examination of a break that depressurizes to a stable pressure of 140 psia shows that the adiabatic expansion of the nitrogen does not cause gas expansion beyond the volume of the tank and that, with gas heating, the gas does not expand into the RCS until about 340 seconds. At this time the expansion of the gas into the RCS, allowing for heating to RCS temperatures, is about 2 cubic feet per second with excess leak flow (potential for steam leak flow above that required to relieve core decay heat) at 80 cubic feet per second.

For events that depressurize to 130 psia, the adiabatic expansion phase is essentially over at the same time that gas expansion into the RCS is predicted. Comparing the gas expansion rate for this event to the excess volumetric leak flow at 150 psia shows that the cumulative gas added to the RCS by 300 seconds could have been vented within 15 seconds if system pressure were to increase to 150 psia.

For an event that depressurizes to 120 psia, the adiabatic expansion is still effective as gas is being expanded into the RCS. A comparison of the nitrogen injection rate, with the gas heated to the RCS temperature after injection, to the excess volumetric leak flow at 150 psia shows that there is 30% more

excess volumetric leak flow than is required to vent the accumulator gas being discharged. The rate of discharge continues to drop with time.

Taken together, these studies show that, for events that do not depressurize below 140 psia, accumulator gas discharge will not occur while the RHR injection system is required for core cooling, and that, for those events that do depressurize to below 140 psia, the effect of nitrogen injection would be to slow the depressurization of the system rather than cause a repressurization. This demonstrates that there are no adverse effects of nitrogen injection from the accumulators for SBLOCAs. To the contrary there are most likely beneficial effects. Semiscale observed that some water was pushed out of the downcomer and into the core. To a small degree that might occur during an SBLOCA. A larger benefit could accrue if the gas were flushed into the steam generators where it might interfere with the reverse heat transfer taking place.

Conclusions

An examination of the consequences of noncondensable gas on the results of SBLOCAs has shown that for smaller breaks which require the steam generators for energy removal, the amount of gas available for release to the RCS is small, the gas expected to be released is less than 20% of that releasable, and that the impact of a postulated nonmechanistic release of all available gas into the RCS is negligible. For larger breaks, it

has been demonstrated that a potential adverse impact of nitrogen injection from the accumulators, as the accumulator water is depleted, does not occur and that there may in fact be a benefit from such an injection. Therefore, it is reasonable to neglect the effects of noncondensable gas within the small break LOCA evaluation model.

- c. In discussing RELAP5/MOD2-B&W's ability to calculate natural circulation, two calculations of LOFT-OECD Test LP-SB-03 (by S. Guntay and P Hall, respectively) were referenced as demonstrating RELAP5/MOD2's ability to calculate natural circulation. You concluded that RELAP5/MOD2-B&W should perform as well as RELAP5/MOD2 because of the similarities between the two codes. However, no results were provided in the response to support this assertion. References to support the assertion that the code adequately calculates natural circulation were provided in response to Question 17. Because of the similarity of the references, it was concluded the reference for the work by Guntay was to a summary in an International Code Assessment Program report that did not discuss natural circulation. Also, the work by Ardron and Hass was shown as a private communication. This material does not acceptably demonstrate the code's ability to calculate natural circulation. Provide results of RELAP5/MOD2-B&W assessment calculations of a RSG geometry that verify the code's ability to calculate all three modes of natural circulation: single-phase, two-phase, and reflux.

Response: The calculation of natural circulation in a PWR is mainly dependent on the temperature difference between primary and secondary sides and the hydrodynamic models that affect flow regime and heat transfer. It is independent of steam generator design. For single-phase natural circulation, the benchmark results of MIST test 340213 are acceptable to demonstrate that RELAP5/MOD2-B&W is capable of calculating single-phase natural circulation when a positive temperature difference exists between the primary and secondary sides.

B&W's benchmark of the LOFT Experiment L-3-5 also demonstrates the ability of the code to calculate natural circulation. The code predicted single-phase natural circulation for the requisite period of time as shown in Figure G.2-8 of BAW-10164P and Figure 14.1. in the response to round one Question 14 on the RELAP5/MOD2-B&W topical report (BAW-10164P).

To demonstrate the code's ability to predict two-phase natural circulation and reflux cooling in the predicted and test benchmark of the S-LH-1 experiment, a comparison of flows, through the hot legs or steam generator tubes, was considered. However, test flow and density data are not readily usable to make a meaningful comparison. Therefore, a qualitative assessment is provided below.

The two-phase circulation and reflux mode cooling is believed to start after pump coastdown to zero speed, at about 90 seconds (Figure 24 in NUREG/CR-4438), and

continues to approximately 250 seconds until the primary system pressure falls below the secondary side pressure. During this period, two-phase circulation and reflux cooling co-exist with two-phase natural circulation predominanting in the earlier period when the core, liquid level remains near the top of the core as shown in Figure 31 of NUREG/CR-4438, and with the reflux cooling mode dominant in the later period when the core is substantially uncovered. The primary system pressure and steam generator tube levels shown in Figures 5-4 through 5-8 (of Question 5 of this set of questions) indicate that the required conditions for two-phase circulation and reflux cooling exist during this period for both the test and prediction. An examination of the calculated steam generator tube phasic velocities in Figure 5-21 confirms that the RELAPS/MOD2-B&W code predicted two-phase circulation and reflux cooling.

To confirm that these modes of steam generator cooling existed in the experiment, the data from NUREG/CR-4438 (results of Semiscale MOD-2C Small break Loss-of-Coolant Accident Experiments S-LH-1 and S-LH-2) are used. The hot leg volumetric flow rates and densities shown in Figures 26 and 25, respectively, indicate that there is a two-phase natural circulation period to at least 140 seconds (end of data). The collapsed liquid level in the intact loop steam generator downflow leg, shown in Figure 23, actually increases at approximately 120 seconds. This is caused by two-phase mixture entering from the uphill side of the steam generator tubes, and further supports the existence of two-phase

natural circulation in the test.

The characteristic signature of reflux cooling is to have a voided hot leg pipe and uphill side of the steam generator tubes in addition to a positive primary to secondary differential temperature. This is the case for both the intact and broken loops. An increase in hot leg volumetric flow (Figure 26) occurs at 105 seconds as steam travels to the intact loop tubes to replace fluid that is draining out. This is a good example of counter-current two-phase flow.

Additional evidence of reflux cooling can be seen in Figure 23 in NUREG/CR-4438. The collapsed liquid levels in the uphill sides of the steam generator tubes remain stable after 120 seconds while the downhill sides of the tubes continue to drain. This indicates a continuous supply of condensate to the uphill sides as a result of reflux cooling. Although no distinct period of transition from two-phase circulation to reflux cooling can be determined, the data indicate that, following the pump coastdown, steam generator cooling begins with predominantly two-phase natural circulation and changes to predominantly reflux of cooling at approximately 120 seconds as the primary system inventory continues to decrease.

Based on the above discussion, it is concluded that the RELAP5 code can adequately predict two-phase natural circulation and reflux cooling. In addition, good agreement in the leak flow rate (Figure 5-3) and the primary system pressure response (Figure 5-4) between

the test and the calculation confirms that the quantitative performance of the code with respect to energy removal via two-phase natural circulation and reflux cooling is excellent.

In conclusion, the range of test comparisons provided is diverse to the extent that all phenomena involved in the prediction of single-phase and two-phase natural circulation, and reflux cooling in an RSG plant have been demonstrated. Therefore, B&W does not believe it is necessary to provide additional benchmarks.

- d. The response did not discuss how the requirements of NUREG-0737, Item II.K.3.30, were met with respect to condensation/vaporization heat transfer in RELAP5/MOD2-B&W. Clarify how these processes are modeled in the code and how well the models represent the condensation/vaporization processes important to accurately calculating the system response to a small break LOCA. At a minimum, how well the models represent the condensation of steam in the steam generator U-tubes, condensation due to the mixing of cold ECC water with steam in the primary system, and the vaporization of the core fluid and calculation of vapor superheat should be discussed.

Response: An assessment of the RELAP5/MOD2-B&W condensation-vaporization models is given below. From this assessment it is concluded that the RELAP5/MOD2-B&W condensation-vaporization models reasonably meet the NUREG-0737 requirements.

The RELAP5/MOD2 heat transfer package is used to calculate surface condensation in steam generator tubes. Nithianandan et al.^{4,5} have evaluated these models using the B&W single tube test and MIT pressurizer test and found them to be satisfactory.

The vaporization of core fluid and the vapor superheat prediction depend on the surface heat transfer as well as the interphase heat transfer. All interphase heat transfer models in RELAP5/MOD2-B&W are the same as in RELAP5/MOD2. Dimenna et al.^{4,6} at EG&G have made a detailed assessment of the interphase heat transfer models. They concluded that the models are reasonable approximations of the current understanding of the interphase heat transfer technology.

In the EM heat transfer package, the wall heat transfer during the subcooled and saturated nucleate boiling regimes is calculated using the Thom, Chen, and Schrock and Grossman correlations. These correlations have been widely used in the nuclear industry and are accepted by the heat transfer community. In the saturated nucleate boiling regime both vapor and liquid are near saturation condition and all the surface heat transfer is used to generate saturated steam. The voiding during the subcooled boiling heat transfer depends on the interphase heat transfer. Nithianandan et al.^{4,7} has assessed the subcooled vapor generation models in RELAP5/MOD2 using two of Christensen's subcooled boiling tests and concluded that these models are satisfactory.

The wall heat transfer in the film boiling regime is calculated using the Condie-Bengston IV correlation. The McEligot correlation along with wall to vapor

radiation are used to calculate the single-phase vapor heat transfer. In the response to Question 8 (round one on RELAP5/MOD2-B&W), the Condie-Bengston IV and McEligot correlations were assessed and concluded to be acceptable. The wall to vapor radiation is calculated using the Sun et al. correlation which is widely used in the industry.

The prediction of vapor superheat during film boiling depends on the interphase heat transfer. Lin et al.^{4,8} assessed the RELAP5/MOD2 heat and mass transfer models using Chen's single tube tests conducted using the Lehigh test facility. The code was found to over-predict the vapor temperature for the high quality test and under-predict it for the low quality test. It is to be noted that it is difficult to measure the correct vapor temperature during two-phase flow conditions.

Even if RELAP5/MOD2-B&W does not calculate the vapor superheat correctly, it will have very little impact on the prediction of the peak cladding temperature. In the B&W SBLOCA methodology only the core collapsed liquid level is used from RELAP5/MOD2-B&W. The FOAM2 computer code uses this collapsed liquid level to calculate the mixture level and the steaming rate which are used in FRAP-T6-B&W. In FRAP-T6-B&W single-phase heat transfer is assumed above the mixture level irrespective of the vapor generation below the mixture level. This method conservatively eliminates pool entrainment of liquid. Therefore, the peak cladding temperature calculated by FRAP-T6-B&W will be conservative. In response to question 5 of this set, the methodology has been verified by simulating the Semiscale SBLOCA test S-LH-1 cladding heatup.

The condensation of steam in the cold legs by subcooled ECC water depends on the interphase heat transfer model. As mentioned earlier, from a detailed assessment of the interphase heat transfer models, Dimenna et al.^{4,5}, concluded that the models are reasonable. Development assessment at EG&G^{6,7}, using Bankoff's stratified flow condensation test and Aoki's steam water mixing tests provide indications of the applicability of these models.

Additional information regarding the acceptability of the interphase condensation models can be obtained from the B&W simulation of Semiscale LBLOCA test S-04-6, Semiscale SBLOCA test S-LH-1 and the LOFT SBLOCA test L-3-5. The S-04-6 results are given in response to question 12 (round one questions on RELAP5/MOD2-B&W). From the fluid temperature prediction near the injection location, shown in Figure 12.29, it can be concluded that the code calculated fluid temperature agrees reasonably well with the test data during the accumulator injection period. The mass flow rates near the injection location, shown in Figures 12.18 and 12.19, and the system pressure response, shown in Figures 12.4 through 12.19, do not show non-physical behavior during the accumulator injection period. Similar observations can be made from the pressure and temperature calculations near the injection location for tests S-LH-1 and L-3-5, Figures 4.1 through 4.4.

From this assessment of the RELAP5/MOD2-B&W condensation-vaporization models, it is concluded that these models reasonably meet the NUREG/0737 requirements.

References

- 4.1 J. A. Klingenfus, Mist Final Report Chapter 10: RELAP5/MOD2 Mist Analysis Comparisons, NRC-04-83-168, RP 2399-1, Preliminary copy NRC publication pending, February 1988.
- 4.2 D. Hein, R. Rippel, & P. Weiss, "The Distribution of Gas in a U-Tube Heat Exchanger and its Influence on the Condensation Process," International Heat Transfer Conference, Munich Germany, September 1982.
- 4.3 G. G. Loomis, Summary of the Semiscale Program (1965-1986), NUREG/CR-4945, EGG-2509, Idaho National Engineering Laboratory, July 1987, pages 197 - 199.
- 4.4 J. M. Cozzuol, Thermal-Hydraulic Analysis of Semiscale Mod-1 Integral Blowdown-Reflood Tests (Baseline ECC Series), TREE-NUREG-1077, Idaho National Engineering Laboratory, March 1977, pages 37 - 50.
- 4.5 Nithianandan, Morgan, Shah, & Miller, "RELAP5/MOD2 Models for Surface Condensation in the Presence of Non-condensable Gases," pp 1627-1633, Proceedings of the 8th Int. Heat Transfer Conference held in 1986 at San Francisco, USA, Published by Hemisphere Publishing Corporation.
- 4.6 R. A. Dimenna, et al., RELAP5/MOD2 Models and Correlations, NUREG/CR-5194, August 1988.

- 4.7 Nithianandan, Shah, Schomaker, & Turk, "RELAP5/MOD2 Assessment at Babcock & Wilcox," NUREG/CP-0072 Volume 5, pp 271-295, February 1986.
- 4.8 J. C. Lin, et al., "RELAP5/MOD2 Post-CHF Heat And Mass Transfer Models," Paper presented at the Int. Workshop on Fundamental Aspect of Post Dryout Heat Transfer, Salt Lake City, Utah, April 1-4, 1984.
- 4.9 V. H. Ransom, et al., RELAP5/MOD2 Code Manual Volume 3: Developmental Assessment Problems, EGG-SAAM-6377, April 1984.

FIGURE 4.1. S-LH-1 BROKEN LOOP ECC INJECTION
NODE PRESSURE.

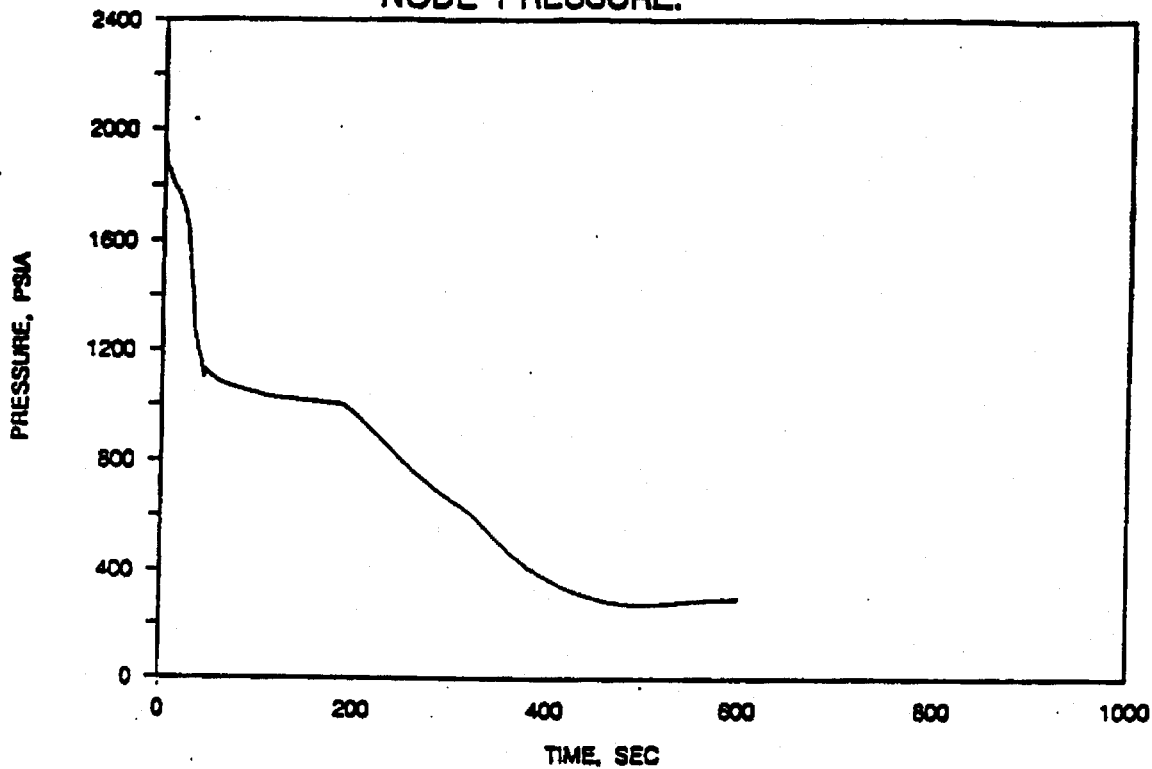


FIGURE 4.2. S-LH-1 BROKEN LOOP ECC INJECTION
NODE TEMPERATURE.

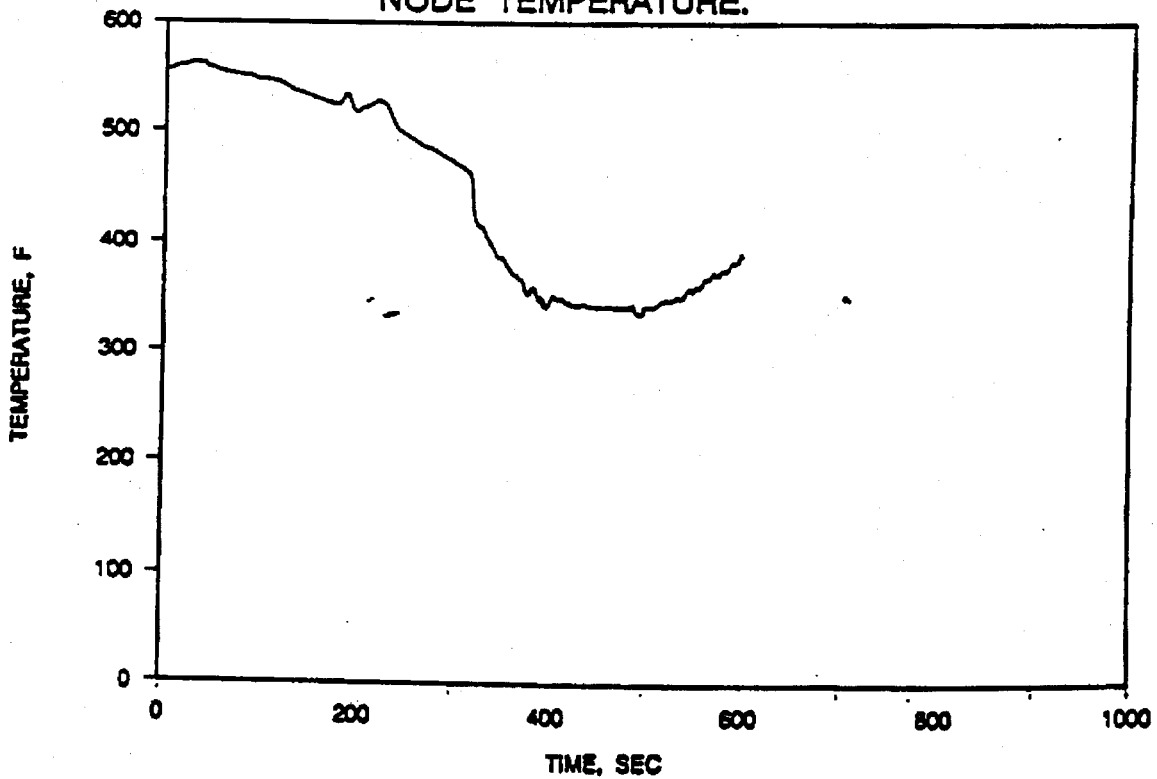


FIGURE 4.3. L-3-5 DOWNCOMER ECC INJECTION
NODE PRESSURE.

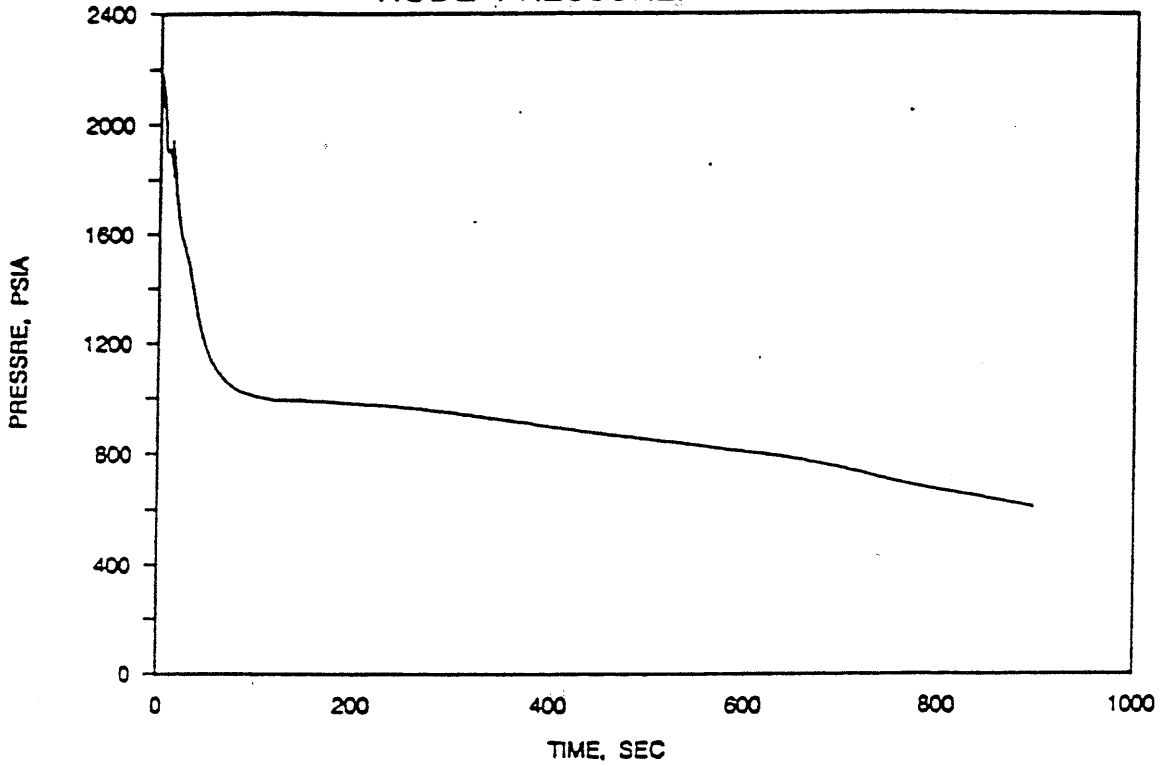
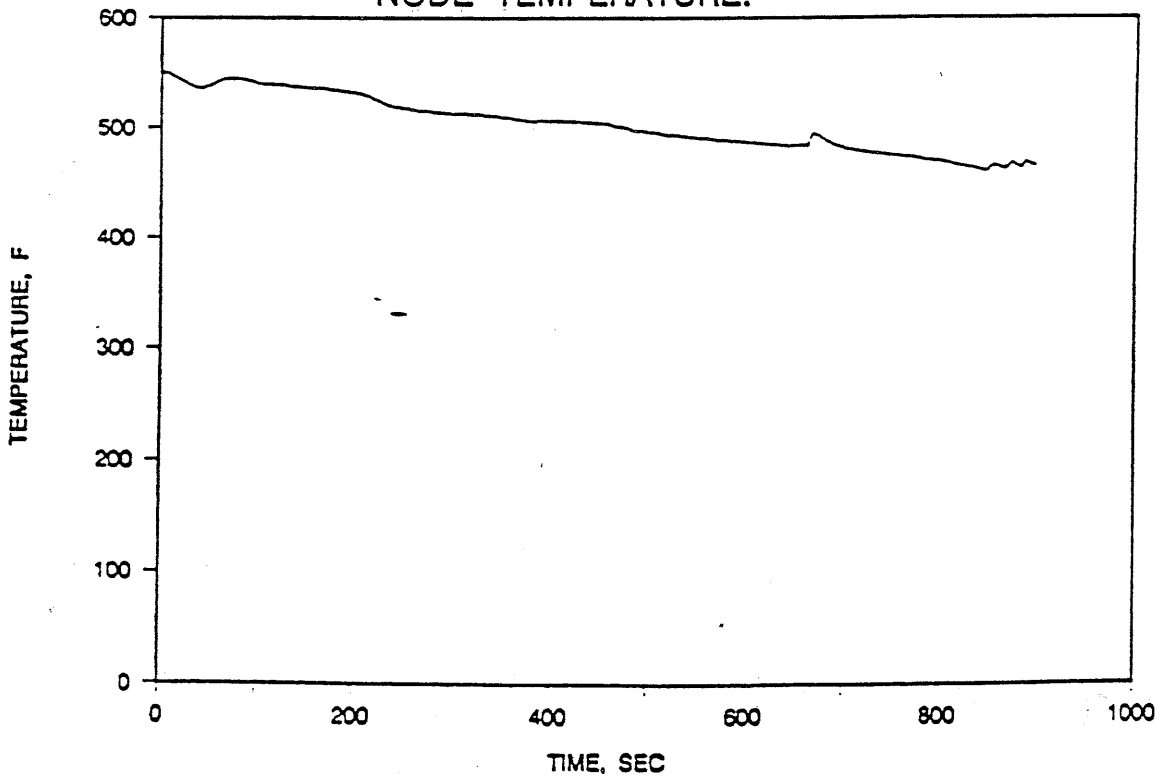


FIGURE 4.4. L-3-5 DOWNCOMER ECC INJECTION
NODE TEMPERATURE.



5. The following questions are related to the analysis of Semiscale Test S-LH-1 provided in response to Question 17.
- a. Provide information to show how well the RELAP5/MOD2-B&W analysis calculated the rod temperatures in the Semiscale core, and discuss what effect the over-prediction of the core collapsed liquid level from 200 s to approximately 300 s had on the core thermal response.
 - b. The faster depressurization in the RELAP5/MOD2-B&W calculation after the loop seal cleared was stated to be due to steam venting. This response is not considered adequate. Because the loop seal cleared in both the test and the calculation, would not steam venting be occurring in both the test and calculation? Additional information is needed to clarify the reason or reasons for the difference between the calculated and measured depressurization rates.
 - c. The nodalization diagram for the Semiscale Test S-LH-1 analysis has more detailed nodalization than that recommended in BAW-10168P for SBLOCA EM model. For example, 16 volumes were used to model the U-tubes on the primary side of the steam generator versus eight in the EM model, and eight nodes in the downcomer versus three in the EM model. Because the peak cladding temperature calculation can be affected by the steam generator nodalization, clarify the effect of the analysis results of the more detailed nodalization used in the S-LH-1 analysis versus the nodalization recommended in BAW-10168P.

Response: B&W presented a benchmark of Semiscale test S-LH-1 as the response to Question 17 of the first round of

questions on BAW-10164. As a result of further investigation into that benchmark and the test results, a revised benchmark has been run. The revision, which uses a tighter match to boundary conditions and recognition of some scale atypicalities, produces results that agree with the experiment far better than the original benchmark. The following response contains both the original and the revised benchmarks and supersedes the response to Question 17 of the first set. For convenience question 17 is quoted below.

17. " The experience with advanced thermal hydraulic computer programs has shown an important sensitivity to modeling of the steam generators when analyzing SBLOCAs. Specifically, the modeling of liquid entrainment, condensation, and hydraulic resistance (i.e., flow regime maps) could significantly depress the mixture level in the core. This phenomenon was observed in Semiscale Test S-UT-8 and later studied in Semiscale Tests S-LH-1 and S-LH-2. Recognizing Semiscale's atypicality, the staff nevertheless believes this phenomenon to be real and, therefore, possible in a full scale reactor. It is for this reason that we request validation of your computer program to predict this phenomenon, should it occur in a full scale reactor. Validation with Semiscale Tests S-LH-1 and S-LH-2 or demonstrating that the phenomenon observed in the Semiscale experiments is calculated to occur in a plant calculation would be acceptable. Use of other integral experiments for validation requires that these experiments simulate the hydraulic behavior observed in the Semiscale tests."

Semiscale S-LH-1 is a 5% break at the pump discharge pipe with a 0.9% core bypass flow from the downcomer to the upper head. The simulation of S-LH-1, using RELAP5/MOD2-B&W, demonstrates the capability of the code to predict SBLOCA phenomena, such as core uncover/recovery, natural circulation including reflux boiling, loop seal clearing, and ECCS performance. The size of the break is such that decay heat removal via the steam generator is provided only briefly, and the steam generators do not play a significant role in mitigating the simulated accident. Numerous benchmarks of Semiscale test series S-NC, that demonstrate the adequacy of RELAP5/MOD2 to predict long-term core cooling by reflux boiling and natural circulation, have been performed by the industry.^{5-1,5-2} The simulations of S-LH-1 presented herein confirm the industry results for RELAP5/MOD2-B&W with particular attention to the larger of the small breaks which form the most severe challenge to the ECCS.

Test Facility

The S-LH-1 test was conducted using the Semiscale MOD-2C facility shown in Figure 5-1. It consisted of a pressure vessel with simulated reactor internals and an external downcomer. The intact loop simulated three unaffected loops of a typical Westinghouse 4-loop PWR, while the broken loop simulated an affected loop in which the break is assumed to occur. The intact loop steam generator contained six inverted U-tubes, and the broken loop steam generator contained two inverted U-tubes. The reactor core simulator was a 5 x 5 bundle with electrically heated rods (23 rods were powered during the test). The upper head region contained a simulated control rod guide tube and two

simulated support columns. The bypass line that extended from the external downcomer to the upper head was used to simulate the core bypass flow. A pressurizer was connected by a surge line to the intact loop hot leg. Both loops had primary coolant circulation pumps. Emergency core coolant from an accumulator and pumped injection system (LPI and HPI) were routed to the loop cold legs. An open loop secondary coolant system was used to control the secondary side pressure with feedwater and steam control valves.

Model Description

The Semiscale MOD-2C RELAP5 base model was originally developed by EG&G for the post-test analysis of experiments S-LH-1 and S-LH-2 (NUREG/CR-4438). The nodalization diagram is shown in Figure 5-2. The model consists of 181 hydrodynamic volumes, 172 junctions, and 256 heat structures. All volume and junction parameters are calculated with nonequilibrium and nonhomogeneous models. Steam generator secondaries, ECC injection, system environmental heat losses, and both vessel and piping external heaters are modelled in detail. The core axial power profile is modelled with twelve stacked heat structures over six two-foot long axial fluid volumes. The upper head region is nodalized to allow for junctions to be connected at the elevations of the top of the control rod guide tube, core bypass line and support columns, and at the elevation of the holes in the guide tube below the upper core support plate.

Changes were made to the original EG&G model to account for and distribute unrecoverable losses due to pipe bends, orifices at the pump discharge pipes, area changes at the steam generator inlet and outlet plenums, and flowmeters in the hot and cold leg pipes. A steady-state calculation was

made with these changes to obtain the initial conditions presented in Table 5-1. The calculated initial conditions compared well with the test conditions except for the secondary side masses and pressures. These were adjusted to achieve the desired primary cold leg temperatures. The calculated pump speeds are slightly higher than the test measurements (8% and 3% for the intact and broken loops, respectively) as a result of higher pump discharge orifice resistances. The following changes that do not affect the steady-state initial conditions were made: the RELAP5/MOD2-B&W core surface heat transfer model was invoked, the leak discharge models were set to those for an evaluation model calculation, and thermal equilibrium was assumed in the core region.

As in the EG&G model, the external heaters were treated mechanistically in RELAP5, and the measured power to the heaters as a function of time was input as a boundary condition. The core decay power and pump coastdown speeds as a function of time were also input to the model. There was limited secondary side steam valve model information available from this experiment. Since the secondary system responses have an impact on the natural circulation and reflux boiling phases of the transient, the secondary side pressure responses from the experiment were used as boundary conditions in the calculation (see Table 5-2).

In order to improve the results several model changes were incorporated into the revised benchmark. The changes, detailed later in the section on Revised Model Changes, were:

- 1) Alteration of the discharge coefficient from 1.0 to 0.7 at a leak inlet void fraction of 70 percent.

- 2) Alteration of upper downcomer modelling to account for the bypass of the intact loop HPI.
- 3) A junction in the simulation of the guide tubes was made homogeneous and the connection of the core bypass to upper head adjusted.
- 4) Rearrangement of the vessel lower head flow paths.
- 5) Reduction of the loop exterior heat losses.
- 6) The secondary side pressure versus time curve was altered slightly.

Results of Base Analysis with a CD of 1.0

The sequence of major events is presented in Table 5-2 for the original and revised analyses. Figures 5-3 through 5-21 show the results of the benchmark calculations. The original results are indicated as dashed lines on all of the figures. The transient was initiated at zero seconds by opening the leak, and thereby causing a flow of subcooled primary fluid out the break, resulting in a rapid system depressurization. A leak discharge coefficient of 1.0 was applied to both the subcooled and saturated choke flow models. Figure 5-3 shows good agreement in the leak flow rate between the base RELAP5 calculation and the experimental data. The primary system pressure response is controlled by the leak flow, and Figure 5-4 shows that the calculated pressure is in good agreement with the experimental result up to 200 seconds. The calculated time to reach the safety injection system (SIS) setpoint, 1827.5 psia in the pressurizer is approximately 3 seconds later

than the experiment, primarily due to a slower draining in the pressurizer. This is caused by a higher overall intact loop resistance. The calculated steady-state pump speed in the intact loop is approximately 8% higher than that of the experiment.

The draining of the steam generator tubes, shown in Figure 5-21, occurred after the pump speed coasted down to zero at 100 seconds. At this point, the primary system entered a reflux condensation cooling mode as evidenced by the counter-current flow shown in Figure 5-21. Figures 5-5 through 5-8 show U-tube liquid levels in both the intact and broken loops. It should be noted that the measured liquid levels using differential pressure cells can lead to considerable error during the pump coastdown period (0 - 100 seconds).⁵⁻³ Both the prediction and the experimental data show that the upflow side of the U-tube consistently drained later than the downflow side due to de-entrainment and reflux condensation on the tube surface.

Following draining of the steam generator U-tubes, a liquid seal was formed in the pump suction of both loops. The seals caused a blockage of steam flow to the break. As a result, the primary system entered a period of manometric level depression in both the downflow side of the pump suction seals and in the core liquid level. To clear the pump suction loop seals, the liquid head imbalance between the downcomer and the core must accrue to the total of the loop seal level plus the liquid holdup, due to reflux condensation, in the upflow side of the U-tubes. As shown in Figures 5-5 and 5-7, the liquid level in the upflow side of the steam generator U-tubes is a significant contributor to the total ΔP that opposes loop seal clearing. The loop seals cleared at 175 seconds and 214 seconds for the intact loop and the broken loop, respectively.

Figures 5-9 through 5-12 show the liquid level in the pump suction pipes. The intact loop seal cleared first, followed by the broken loop, because the primary-to-secondary heat transfer was terminated earlier in the intact loop than in the broken loop. Clearing of the loop seals produces a continuous path to the break for steam generated in the core. The steam conditions at the leak result in lower leak mass flows, but higher volumetric flows. As a result, the primary system begins a rapid depressurization. The base model depressurization rate was faster than was observed in the experiment, in spite of good agreement in discharge mass flow rates between the calculation and the experiment. The effect would be consistent with a model that was discharging a higher quality at a larger volumetric rate than the corresponding experiment. This observation is part of the basis for the alterations made to the model for the second benchmark. It is unfortunate that there are no experimental results available by which the energy discharge rate or the heat loss to the ambient surroundings can be determined. With data of that sort the above hypothesis could be directly confirmed.

One of the important parameters used as an indicator for SBLOCA mitigation is core collapsed liquid level. This is shown in Figure 5-13. As a result of correctly predicting primary system mass inventory and reflux heat transfer, the agreement in the first core level depression between the calculation and the experiment is excellent. After clearing the loop seals, core decay heat continues to boil-off fluid in the core region and, since the HPIS flow alone is not sufficient to makeup for fluid lost out the break, the core liquid level continues to decrease until accumulator actuation is achieved.

Accumulator injection occurred much earlier in the base EM calculation than in the experiment due to the faster depressurization rate. However, the shortened core boil-off period was compensated for by increased flashing. Thus, the second core collapsed liquid level depression was calculated to be nearly the same as the measurement except for its timing. The experiment shows that a more significant and uniform core heat-up occurred during the second depression. The ability of RELAP5 to correctly predict the two distinct core liquid level depressions demonstrates that the code can accurately calculate important thermal-hydraulic system parameters.

Figure 5-14 shows the normalized primary system mass inventory. The mass inventory increased following accumulator injection. The HPIS injection flow rates for both the intact and broken loops are presented in Figure 5-15 and 5-16, respectively. The calculated flow rates are higher than those of the experiment due to the faster depressurization rate predicted by RELAP5 for this base EM model.

Following the completion of the base RELAP5 calculation, the collapsed liquid level was used with the power and pressure time histories to calculate core mixture levels with the FOAM2 code. The resultant mixture levels were input into FRAP-T6 with pressure, decay heat, core mass fluxes from FOAM2, and inlet enthalpy to compute a predicted cladding temperature excursion. The results of the FRAP-T6 calculations are shown in Figures 5-19 and 5-20 for the 8.2 and 10.2 foot core elevations. During both temperature excursions the calculated temperature peaks exceeded the experimental values for both elevations, demonstrating conservatism in the evaluation model steam cooling models.

Revised Model Changes

The first benchmark simulated the test using a leak discharge coefficient of 1.0 for the entire transient. After loop seal clearing, the calculated system depressurization, Figure 5-4, exceeded that of the test due to over-prediction by the Moody choked flow correlation. Based on experimental data, the Moody critical flow model is observed to over-predict two-phase leak flows for qualities greater than 10 percent while under-predicting the flow for lower qualities. To account for this the revised model used dual discharge coefficients, switching between the coefficients at a void fraction of 70 percent.

The RELAP5/MOD2-B&W EM choked flow model has an option to include four discharge coefficients as functions of the leak inlet conditions. Separate coefficients can be used for subcooled flow, during the transition to two-phase flow, during two-phase, and for steam (superheated) flow. In making adjustments to these coefficients it is equally important to maintain their relationships to each other as it is set individual coefficients correctly. Once relative values are determined specific values can be set by comparison to data or through a spectrum approach as is used in licensing. Although experimental data indicates that Moody under-predicts the discharge rates for low quality flow, the data also show that the same discharge coefficient should be applied to Henry-Fauske extended into the subcooled region and Moody at low qualities. Using 1.0 as the base discharge coefficient for extended Henry-Fauske suggests that 1.0 should also be used for the transition regime, a reduction to about 0.7 be used for the two-phase regime, and 1.0 be used under superheated conditions. The

normalized values of discharge coefficients used in the revised model were 1.0, 1.0, 0.7, and 1.0.

The RELAP5/MOD2-B&W EM choked flow model also provides control over the conditions at which to apply the discharge coefficients. The lower bound for the transition regime is set to 1 percent void fraction and the upper bound at 70 percent void fraction. The subcooled coefficient applies whenever the leak inlet void fraction is less than 1 percent. The superheat discharge coefficient is applied whenever the leak inlet enthalpy is greater than or equal to the leak node saturated steam enthalpy. The table that follows shows the coefficients and the switching in chart form.

Once the relative values of the discharge coefficients have been specified, the specific values to be used in a given evaluation can be determined. This can be done through an adjustment of the break area or through the multiplication of each of the discharge coefficients by a constant. In licensing calculations this is done by break area adjustment and is part of the spectrum approach to the identification of the worst case break. In experimental benchmarks this is usually done by adjusting one of the coefficients to match a measured flow and then adjusting the remaining coefficients to maintain their relationships with each other. Based upon the test data for S-LH-1 the subcooled and transition discharge coefficients were set to 1.13. Therefore, the two-phase value became 0.79 ($= 0.7 * 1.13$) and the superheated value 1.13.

Discharge Coefficients Relationships

Regime	Range of Application	Normalized Value	Value used in Revised Model
Subcooled	$\alpha_g < 1\%$	1.0	1.13
Transition	$\alpha_g \geq 1\%$ & $\alpha_g \leq 70\%$	1.0	1.13
Two-phase	$\alpha_g > 70\%$ & $H_{mix} < H_{g,sat}$	0.7	0.79
Superheat	$H_{mix} \geq H_{g,sat}$	1.0	1.13

System depressurization and inventory prediction of the original model were further complicated by a difference between the predicted and experimental break inlet conditions. Following loop seal clearing, the calculated break inlet flow was composed of steam from core boiling and system flashing and the broken loop ECCS liquid. The resultant break quality was between 85 and 90 percent. Evidence from the experiment -- measured break inlet quality, break flow rate, system mass balance, and the reactor vessel level decrease rates -- indicates that the break inlet quality should lie between 70 and 75 percent. Vessel and system mass balances calculated from the test data between 300 and 500 seconds cannot be matched using the intact loop HPI, decay heat, and flashing. The test break density indicated a quality of 70 to 80 percent. The break mass and energy discharges cannot be reasonably matched unless a quality of about 70 percent is used (break energy rate is inferred from the system energy balance and depressurization). On an individual basis the uncertainty of each measurement makes it difficult to be absolutely conclusive about the break inlet quality. However, taken in

combination the evidence is compelling that the break quality averaged about 70 percent and that this was caused by bypassing of most of the intact loop HPI.

The intact loop HPI bypass was probably caused by a combination of the atypically short distance between inlet nozzles and high steam velocities in neighborhood of the broken leg nozzle. The intact cold leg mixture, which may not have been well mixed, transits the top of the downcomer so quickly that there is little time for a separation of steam and water prior to the high velocities at the broken loop nozzle. The result is essentially the entrainment of most of the HPI across the top of the downcomer. A change was made in the cold leg nozzle to downcomer connection for the revised model to essentially force bypass of the intact loop HPI. Noding changes included separation of volume 101 into two volumes (101 & 102) of equal height. The two cold leg nozzle junctions were modelled as one-half the original area and connected as upward oriented junctions to the top of control volume 101. A separate bypass junction (103) with one-half the cold leg nozzle area was connected as a downward oriented junction between the two cold legs. Associated changes were made to the junction connections from 101 to 102 to the rest of the downcomer. The arrangement is depicted in Figure 5-2a.

The reactor vessel upper head region drained too quickly in the original calculation. Phase separation in the guide tube allowed high upward steam flow which promoted draining. The junction between control volumes 183 and 184 was switched to a homogeneous condition. Justification of this switch is rooted in the atypical small size of this connection with the plugged drain holes. This type of model would not be used in plant applications. An associated change, which is currently used in the applications, was the

modelling of the reactor vessel upper head connection of the bypass line. The junction was connected to the top of control volume 192 instead of the bottom of 193 to give a better bypass inlet phase condition.

The connection to the top of control volume 130 represented the Semiscale geometry; however, it allowed the bottom of the downcomer to trap steam during the last portion of the pump coast-down phase. At the end of the simulated pump coastdown the steam trapped in the downcomer was discharged out of the break and the system levels realigned. Moving the connection to the bottom of volume 140 allowed the core to serve as part of the steam discharge path. Plant application models use the revised model type of connection.

A change was made associated with the mechanistic loop heat loss modelling. Based on the mass and energy balance calculations on the core and downcomer during the core boil-off phase, the heat losses were considered to be too large. They were reduced by modelling the exterior heat loss as a heat transfer coefficient versus time. Initially a value of 1 Btu/hr-ft²-s was chosen. This value was decreased by a factor of 100 to reduce the heat loss on the outside of the insulation during the transient.

The secondary side boundary conditions were also modified for the revised prediction. The original base calculation imposed the measured test secondary pressure as a boundary condition. A more appropriate boundary condition would be the primary-to-secondary temperature difference during the saturated phase of the transient. This boundary condition resulted in a slight reduction in the secondary pressure in the 100 to 300 second time frame. It maintained a similar potential for heat transfer in each loop, which is important because this heat transfer has a strong influence on

individual loop seal level depressions. After 300 seconds a smooth linear ramp back to the test pressure was implemented. The imposed secondary pressure boundary conditions are shown in Table 5.2.

Revised Model Results.

The revised, best-estimate, model results are summarized in Table 5-2 and shown in Figures 5-3 through 5-21 as the dotted lines. The new set of discharge coefficients greatly improve the system pressure (Figure 5-4) and liquid mass inventory (Figure 5-14) predictions. The prediction of these parameters was improved primarily by matching the test leak fluid composition during the boil-off period while maintaining the appropriate total discharge. The downcomer bypass noding arrangement provided the mechanism to accurately simulate this behavior. Between 300 and 500 seconds the normalized mass prediction deviates somewhat from the test values. This deviation is partly due to the inventory in the broken loop pump suction piping, not clearing until 600 seconds.

Improvement in the prediction of the upper head level, shown in Figure 5-17, between 50 and 150 seconds helped to redistribute the system inventory such that it was more consistently with test observations. The lower downcomer model changed the steam storage in the lower downcomer; however, the forced bypass model in the nozzle belt region allowed more steam to be stored in the upper downcomer. The level behavior is shown in Figure 5-18. Upon intact loop seal clearing, the test, base, and revised model levels all resided at the cold leg nozzle elevation.

The timing of the intact loop seal clearing was the same as the base case and the test, although the duration and magnitude were slightly less than the previous values. The revised core collapsed level, shown in Figure 5-13, rose above the test data between 180 and 280 seconds. The over-prediction of the level was due to the rapid equalization of the downcomer and core levels. The difference appears to be due to a slight difference in the loop seal behavior. Once the downside of the intact pump suction clears, a steam venting path can be readily established. However, the facility seems to retain a small plug of liquid which acts as a resistance to the steam flow. The resistance remains partially in place until approximately 475 seconds. Its effect can be seen in the differential between the test downcomer and core collapsed levels.

The slight over-prediction of the core collapsed levels from the intact loop seal clearing until 450 seconds had minimal impact on the peak heater rod temperatures. The steam cooling above the mixture level in FRAP-T6 under-predicted the cooling; therefore, the temperature escalation was faster than that observed in the test.

At 500 seconds, the revised prediction was restarted and a path, that included one-tenth of the cold leg nozzle, was connected from the intact leg to the top of control volume 102. This path allowed a portion of the ECCS liquid to enter the downcomer and not be bypassed. The mass and energy balances on the test core region indicate that some of the intact loop ECCS fluid was still being bypassed after accumulator actuation. This path allowed approximately the same, but slightly less, liquid to enter the downcomer than occurred in the test. The system depressurization between 500 and 700 seconds, Figure 5-4, was more rapid than the

test. The rapid depressurization was slowed at approximately 650 seconds due to boiling of small amounts of liquid that had swelled into the hot legs and inlet of the steam generator tubes. Since the depressurization was slowed, the rate of accumulator injection was lower and less steam condensation occurred. The revised calculation reached a pressure equilibrium at 850 seconds, thus halting the accumulator flow. The intact loop HPI was still insufficient to absorb all the core decay heat at this time and a second core boil-off began. The test appeared to be approaching this condition at 1000 seconds.

Conclusions

RELAP5/MOD2-B&W calculated the major events of the Semiscale S-LH-1 transient -- two-phase natural circulation, reflux boiling and liquid holdup, pump suction loop seal clearing, core liquid level depression, ECCS injection and core recovery -- in the proper sequence for both benchmarks provided in this response. Both benchmarks calculated the overall system responses in reasonable agreement with the experimental data. The assumptions and boundary conditions used for the base calculation resulted in a depressurization rate that effectively modeled a larger break. The SBLOCA code package, namely RELAP5/MOD2-B&W, FOAM2, and FRAP-T6, calculated a conservative heater rod surface temperature in both predictions, with the original and revised calculations producing similar peak temperatures. The revised RELAP5/MOD2-B&W calculation was able to closely match the test behavior for S-LH-1 including small scale facility effects.

Although the benchmarks were conducted to demonstrate basic code capabilities, most of the modeling used is

representative of that for evaluation model calculations. The degree of nodalization employed in the benchmarks was higher than required. The detail used in the pressurizer, hot legs, UTSG secondary sides, UTSG primary sides, lower downcomer, and cold legs provides minimal benefit over lesser models. The noding near the bottom of the pump suction downside is required to preserve the proper timing for loop seal clearing. Steam generator noding should be sufficient to determine the total energy transport in or out of the primary system and to differentiate between upside or downside condensation for proper liquid tracking during reflux boiling. The emphasis in component noding should be to model the elevations of liquid traps correctly. Sufficient noding near the break should be provided to place the ECCS injection location properly for the event being studied.

Connections between and within components require careful consideration. Regions of particular importance are the hot and cold leg nozzles, upper head to upper plenum connections, and upper downcomer connections. Junctions will be connected to volumes, that may establish mixture levels, in an orientation that will tend to pass liquid or steam in accordance with the predicted levels. Double flow path modelling will be used for hot and cold leg nozzles. The S-LH-1 benchmark used crossflow junctions for the nozzle areas. Although the crossflow junctions perform similar to double flow paths, double flow path modelling has two advantages. It has the capacity to model liquid-liquid counter-current flows that may develop in the cold leg nozzles, and retains the full complement of momentum terms.

The noding proposed for the SBLOCA evaluations and described in BAW-10168 is sufficient to meet these computational

needs. The benchmarking of Semiscale test S-LH-1, Loft test L-3-5, the Mist test series, and others demonstrate that RELAP5/MOD2-B&W can adequately predict system thermal-hydraulic responses during a SBLOCA with differing levels of detail used in the noding. Further the combination of noding and code packages selected for the small break evaluations produce conservative peak cladding temperature results for SBLOCAs that result in temperature excursions. Therefore, the RELAP5/MOD2-B&W, FRAP-T6-B&W, and FOAM2 computer codes are adequate for calculating SBLOCA fluid conditions and core cladding temperatures.

References

- 5-1. K. P. Ardron and P. C. Hall, "UK Experience with RELAP5/MOD2," Central Electricity Generating Board, Generation Development and Construction Division, Barnwood, Gloucester, UK (Private Communication).
- 5-2. P. Ting, R. Hanson, and R. Jenks, International Code Assessment and Applications Program, NUREG-1270, Vol. 1, March 1987.
- 5-3. G. G. Loomis and J. E. Streit, Results of Semiscale MOD-2C Small-Break (5%) Loss-of Coolant Accident Experiments S-LH-1 and S-LH-2, NUREG/CR-4438, November 1985.

Table 5-1. Comparison of Calculated and Measured Initial Conditions for Semiscale Test S-LH-1.

<u>Parameter</u>	<u>RELAP5</u>	<u>Measured</u>
Pressurizer Pressure, psia	2244.	2244.
Core Power, Kw	2015.	2015.
Pressurizer Liquid Level, inches	155.5	155.6
Cold Leg Fluid Temperature, F		
Intact Loop	552.1	552.2
Broken Loop	555.6	556.7
Primary System Flow Rate, lbm/s		
Intact Loop	15.7	15.6
Broken Loop	5.2	5.2
Core Bypass Flow (% of total core flow)	0.9	1.0
SG Secondary Pressure, psia		
Intact Loop	829.6	859.7
Broken Loop	881.8	857.2
Core ΔT , F	67.8	67.4
SG Secondary Side Mass, lbm		
Intact Loop	421.0	374.8
Broken Loop	94.8	78.0

Table 5-2. Comparison of Calculated and Measured Sequence of Events for Semiscale Test S-LH-1.

<u>Event</u>	<u>Time, seconds</u>		
	<u>Measured</u>	<u>RELAP5 PREDICTIONS</u>	
		<u>BASE</u>	<u>REVISED</u>
Break Opened	0.5	0.0	0.0
Pressurizer at 1827.5 psia (SIS)	14.67	17.65	17.35
Reactor Scram	19.57	22.60	22.30
Pump Coastdown Initiated			
Intact Loop	21.35	24.35	24.05
Broken Loop	20.76	23.75	23.45
Feedwater Off			
Intact Loop	19.67	22.70	22.40
Broken Loop	19.00	22.00	21.70
MSIV Closure			
Intact Loop	22.0	25.00	24.70
Broken Loop	22.0	25.00	24.70
HPIS Initiated			
Intact Loop	41.60	44.60	44.40
Broken Loop	40.98	44.60	44.40
Pressurizer Emptied	33.90	44.00	40.00
Intact Loop Seal Cleared	171.4	175.0	175.0
Broken Loop Seal Cleared	262.3	214.0	605.0

Table 5-2. Comparison of Calculated and Measured Sequence of Events for Semiscale Test S-LH-1 (continued).

<u>Event</u>	<u>Time, seconds</u>		
	<u>Measured</u>	<u>RELAP5 PREDICTIONS</u>	
		<u>BASE</u>	<u>REVISED</u>
Accumulator Injection			
Intact Loop	503.8	324.0	490.0
Broken Loop	501.4	324.0	490.0

SG Secondary Side Pressure Used in the RELAP5 Predictions

<u>BASE RELAP5 SECONDARY PRESSURE</u>			<u>REVISED RELAP5 SECONDARY PRESSURE</u>		
<u>Time</u>	<u>Intact Loop</u>	<u>Broken Loop</u>	<u>Time</u>	<u>Intact Loop</u>	<u>Broken Loop</u>
<u>sec</u>	<u>psia</u>	<u>psia</u>	<u>sec</u>	<u>psia</u>	<u>psia</u>
0	860	858	0	860	858
20	860	888	20	860	888
40	1016	1021	40	1016	1021
60	1000	1010	60	1000	1010
100	995	995	100	995	995
200	989	974	150	977	940
300	958	926	200	958	910
1000	863	700	250	929	890
			300	900	877
			1000	863	700

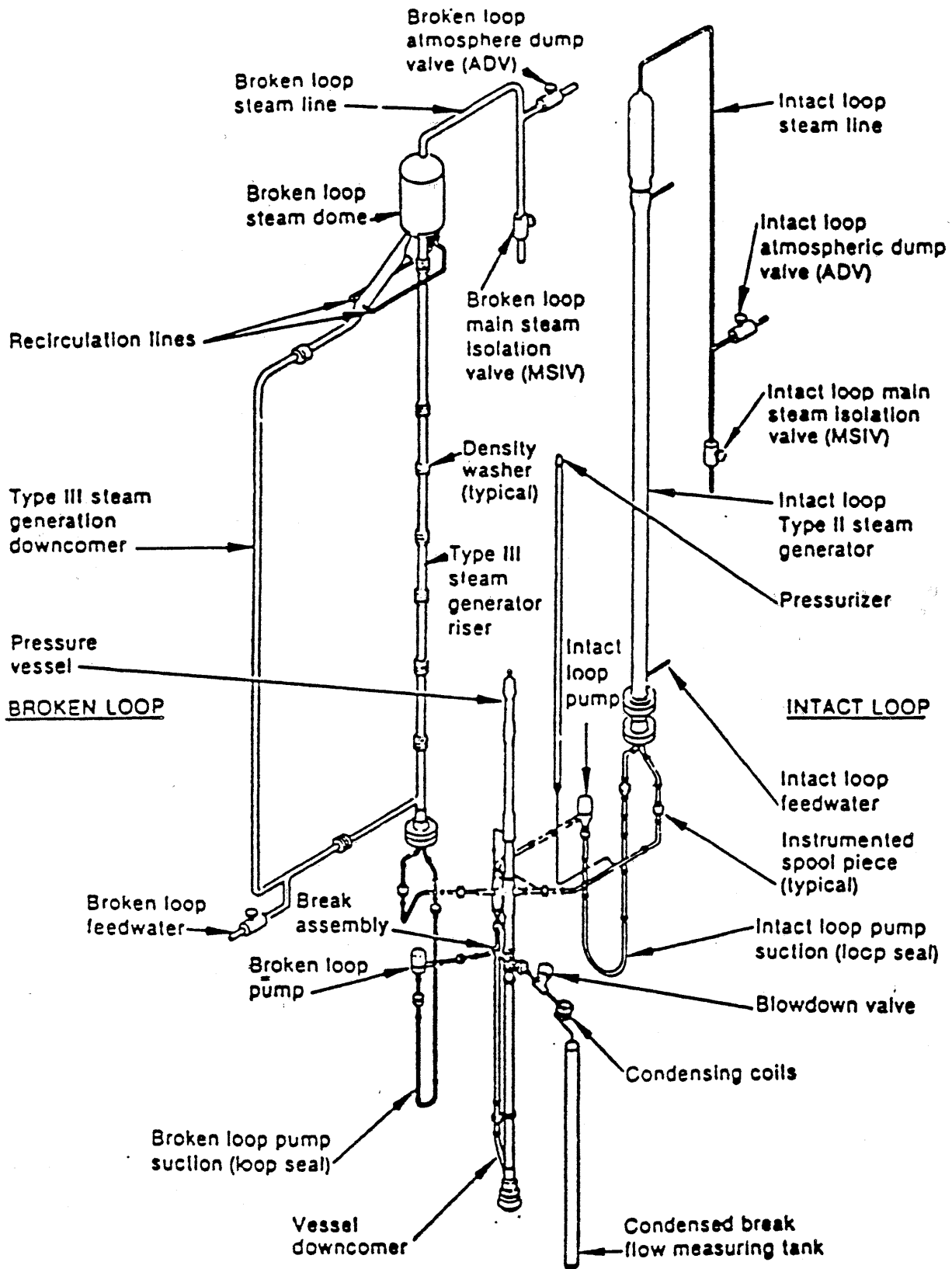


Figure 5-1. Semiscale MOD-2C System Configuration.

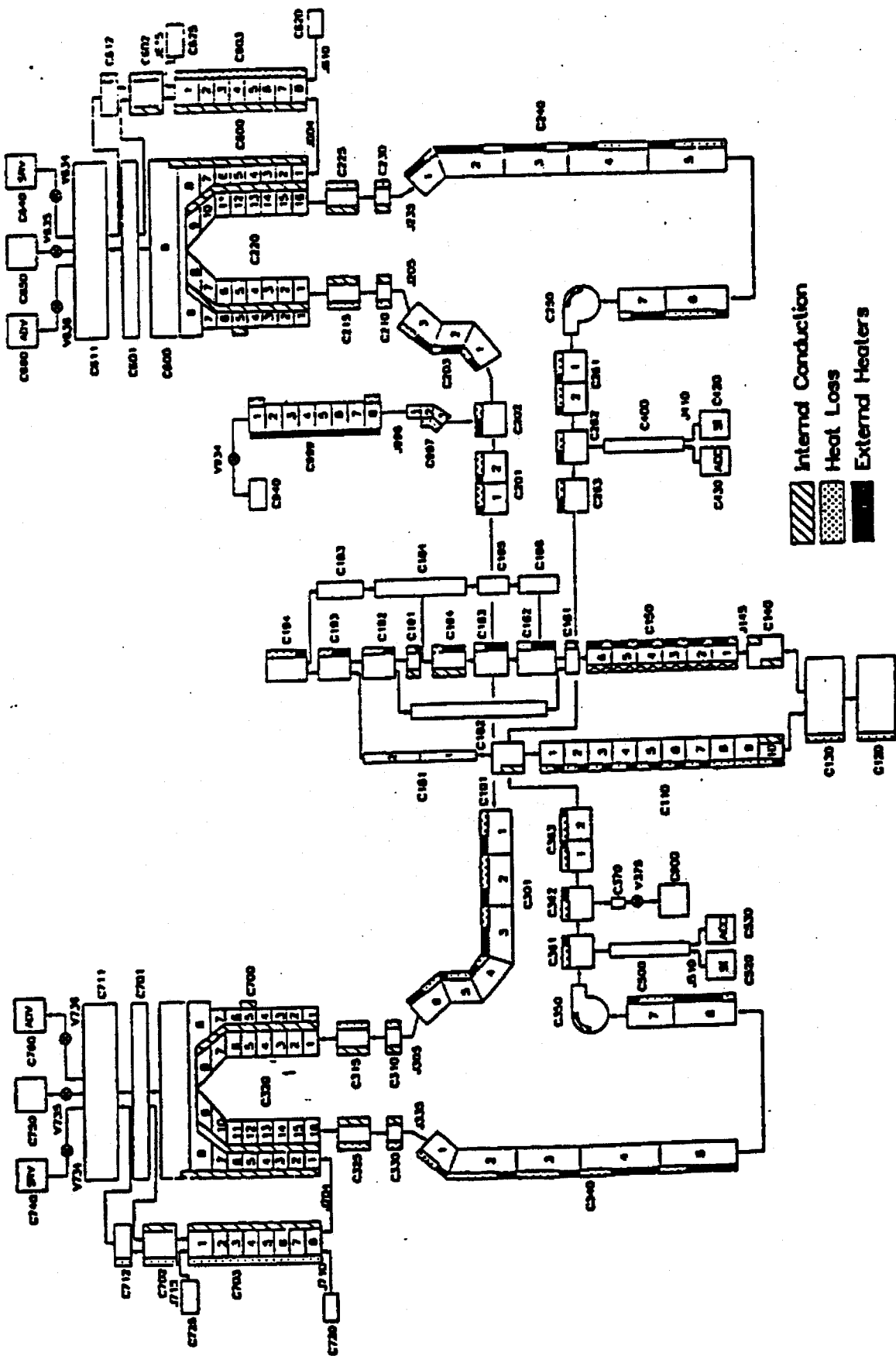


Figure 5-2. Semiscale Test S-LII-1 Base Model Noding Diagram

Figure 5-2a. Semiscale Test S-LH-1 Forced ECCS Bypass Downcomer Noding Diagram.

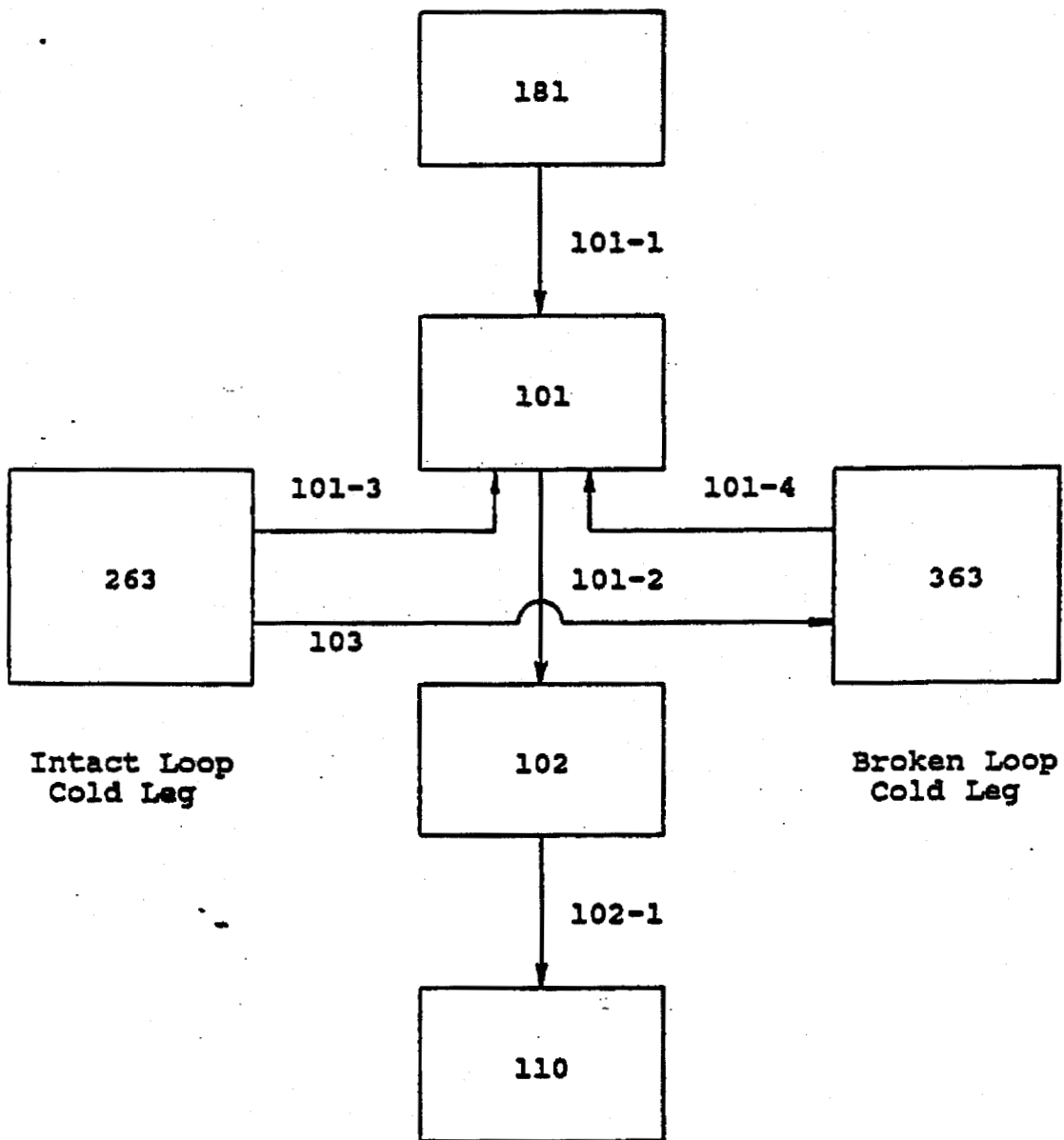


FIGURE 5-3. SEMISCALE TEST S-LH-1; LEAK FLOW RATE.

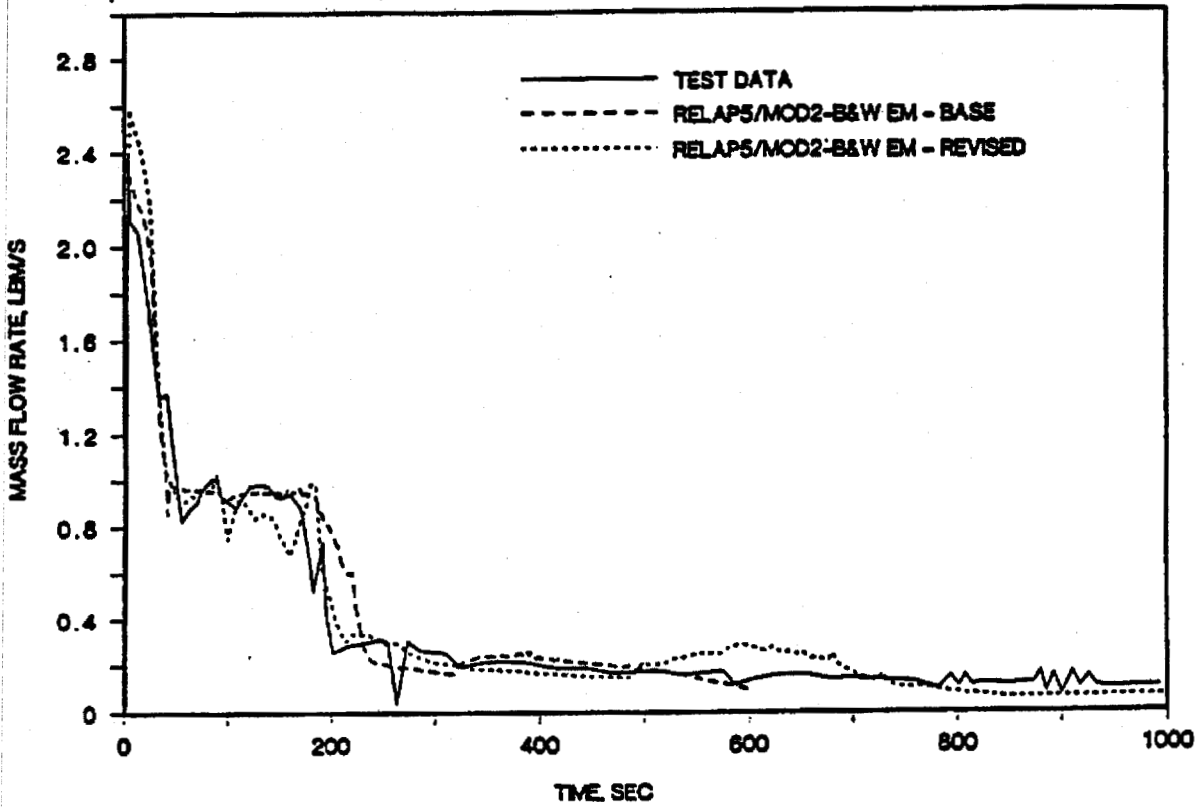


FIGURE 5-4. SEMISCALE TEST S-LH-1; PRIMARY SYSTEM PRESSURE.

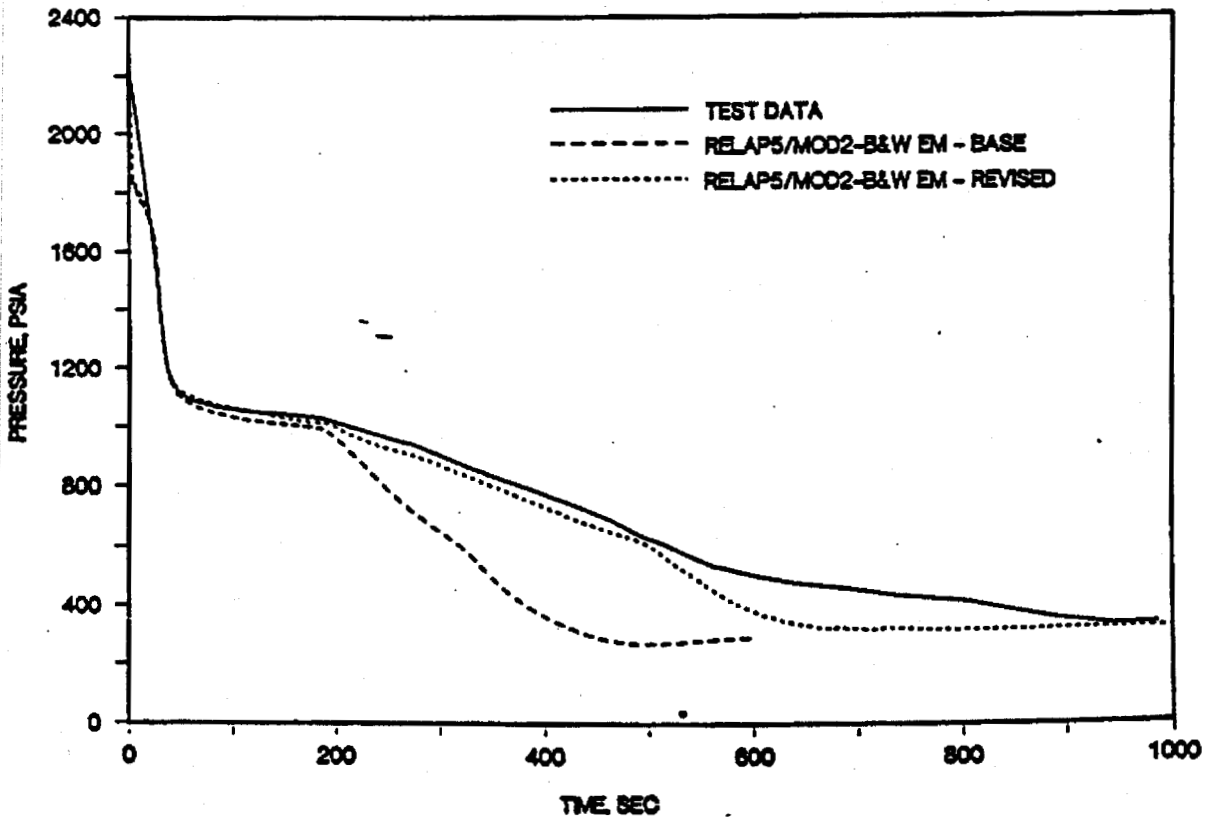


FIGURE 5-5. SEMISCALE TEST S-LH-1; INTACT LOOP STEAM GENERATOR
TUBE LEVEL - UP SIDE.

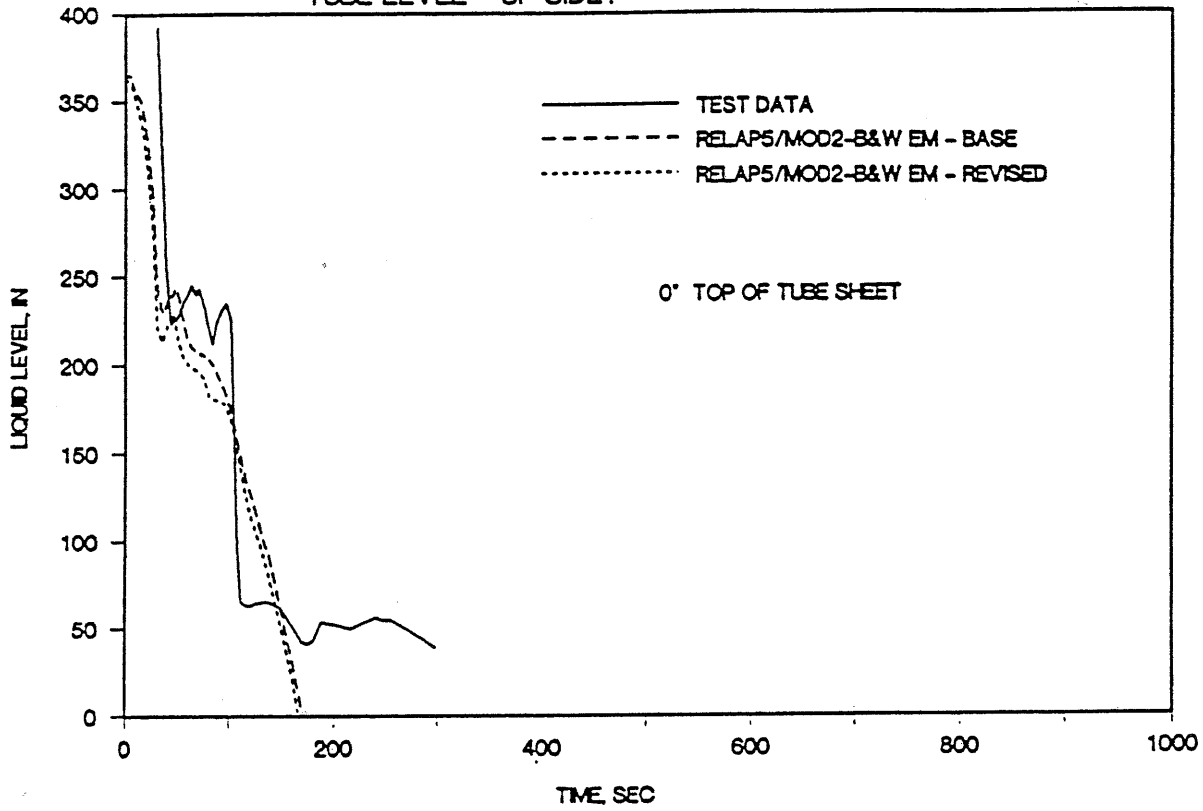


FIGURE 5-6. SEMISCALE TEST S-LH-1; INTACT LOOP STEAM GENERATOR
TUBE LEVEL - DOWN SIDE.

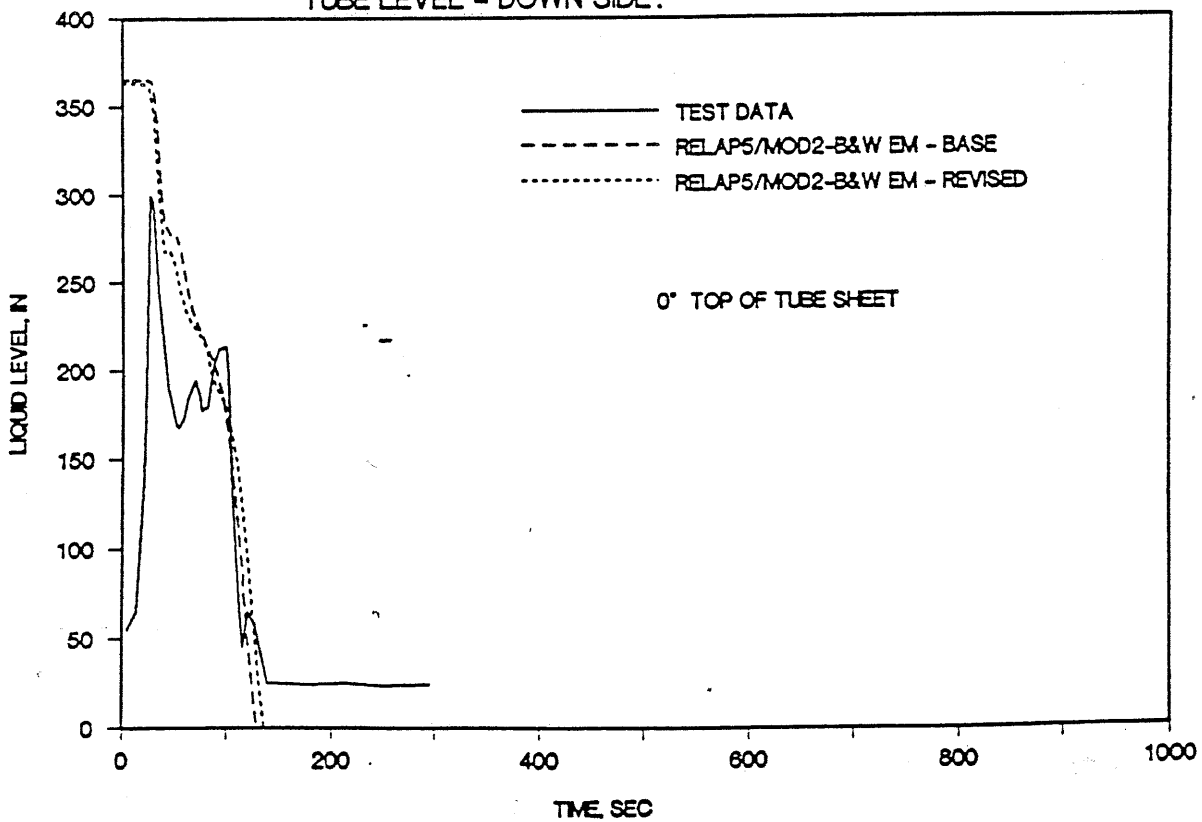


FIGURE 5-7. SEMISCALE TEST S-LH-1; BROKEN LOOP STEAM GENERATOR
TUBE LEVEL - UP SIDE.

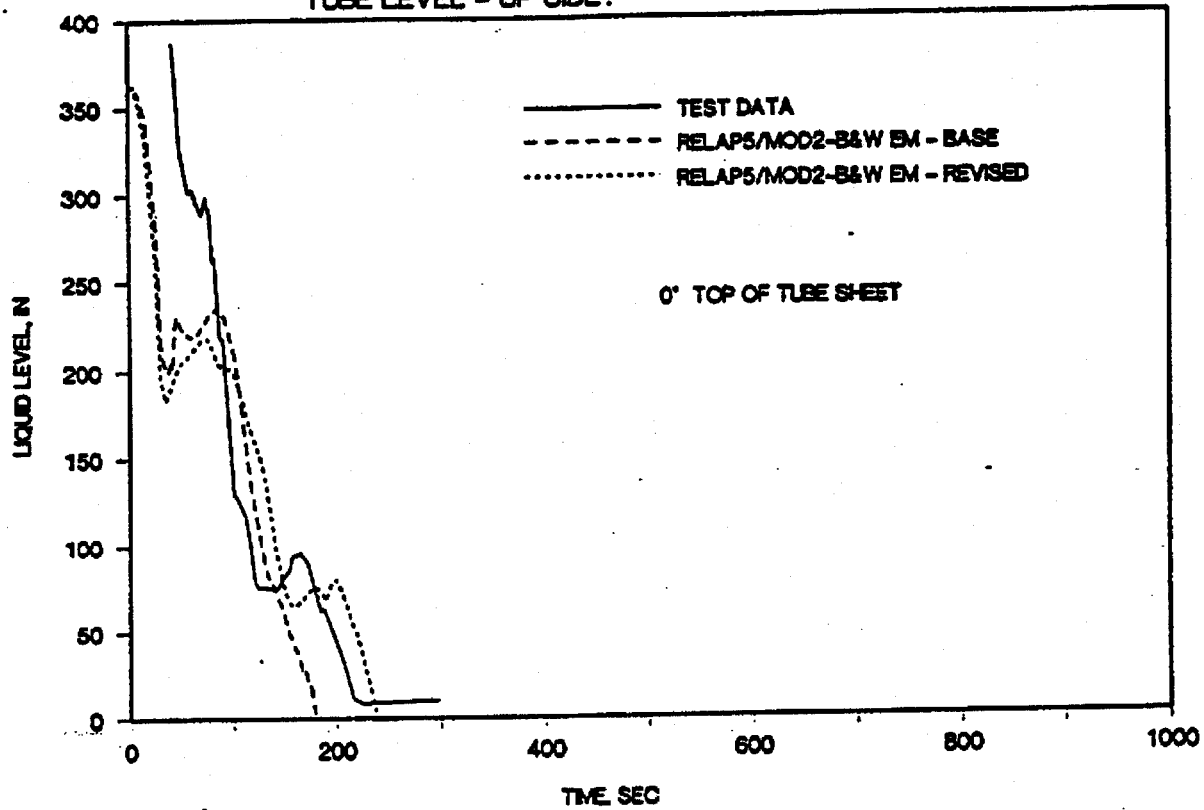


FIGURE 5-8. SEMISCALE TEST S-LH-1; BROKEN LOOP STEAM GENERATOR
TUBE LEVEL - DOWN SIDE.

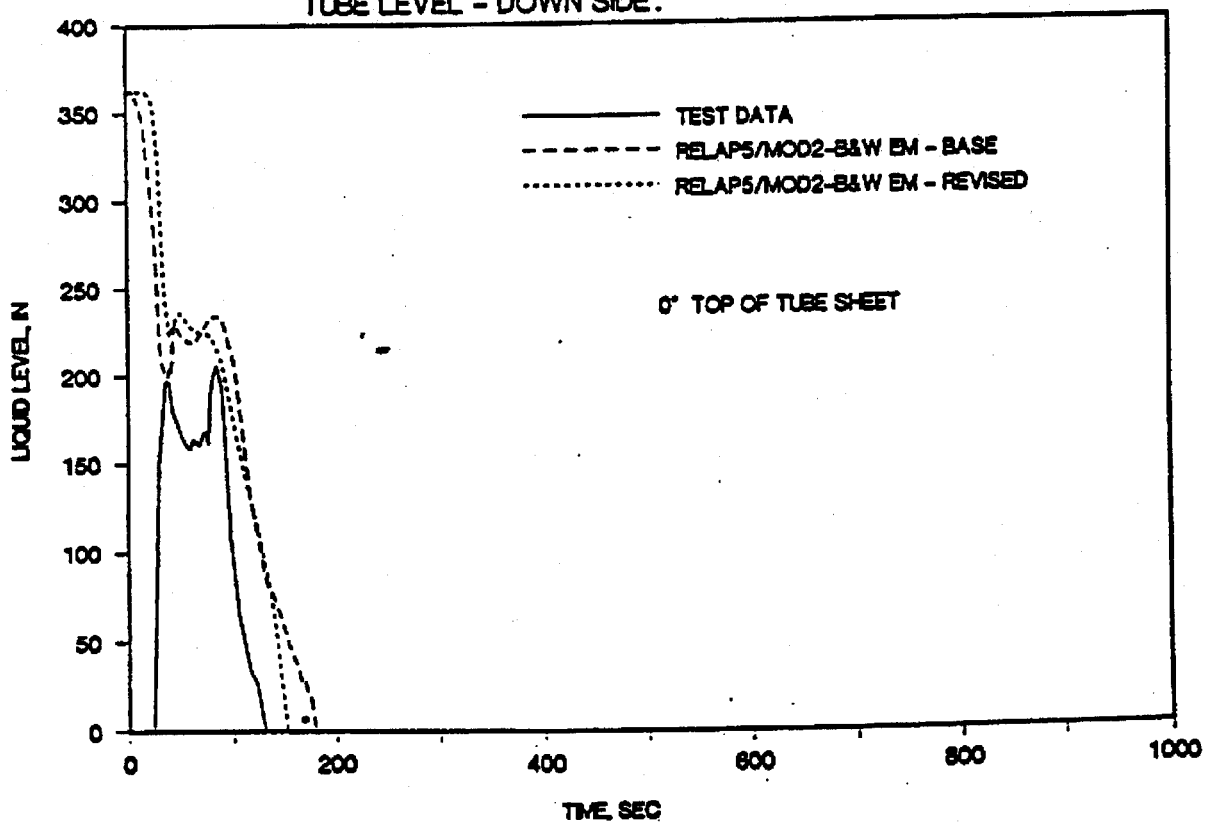


FIGURE 5-9. SEMISCALE TEST S-LH-1; INTACT LOOP PUMP SUCTION LEVEL - DOWN SIDE.

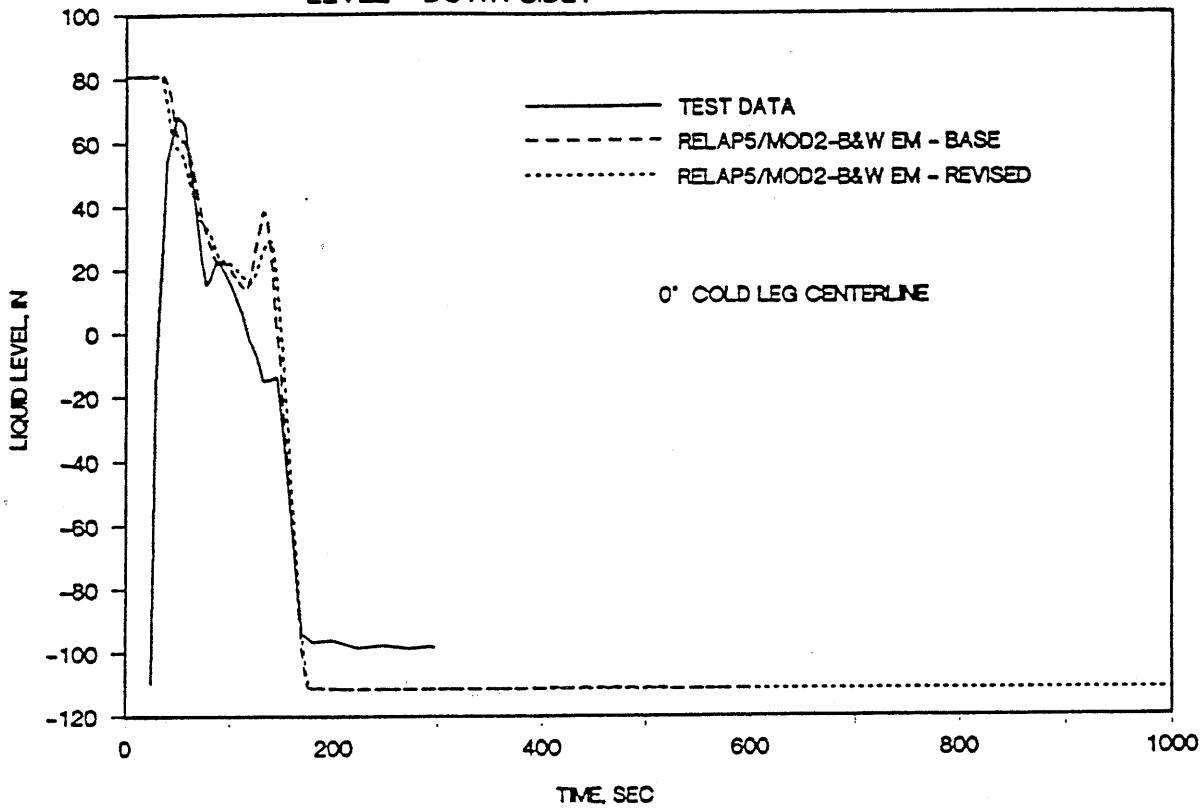


FIGURE 5-10. SEMISCALE TEST S-LH-1; INTACT LOOP PUMP SUCTION LEVEL - UP SIDE.

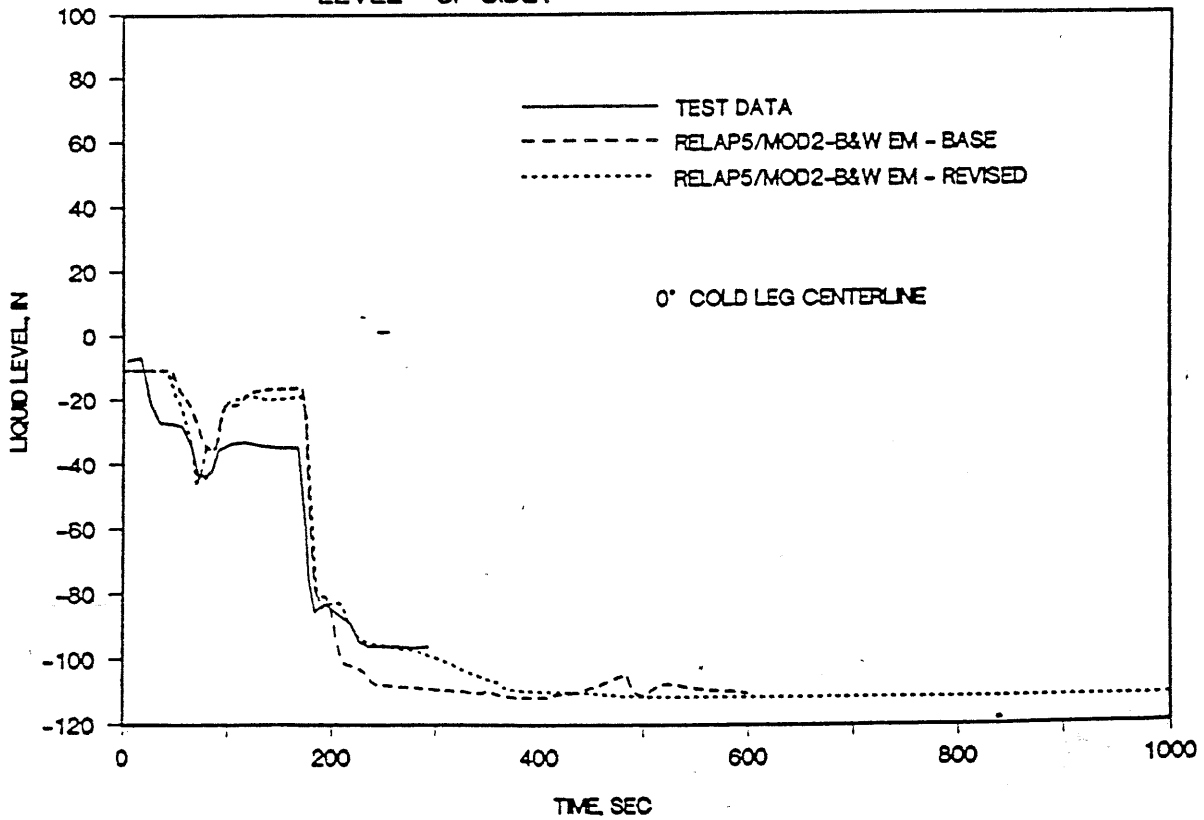


FIGURE 5-11. SEMISCALE TEST S-LH-1; BROKEN LOOP PUMP SUCTION LEVEL - DOWN SIDE.

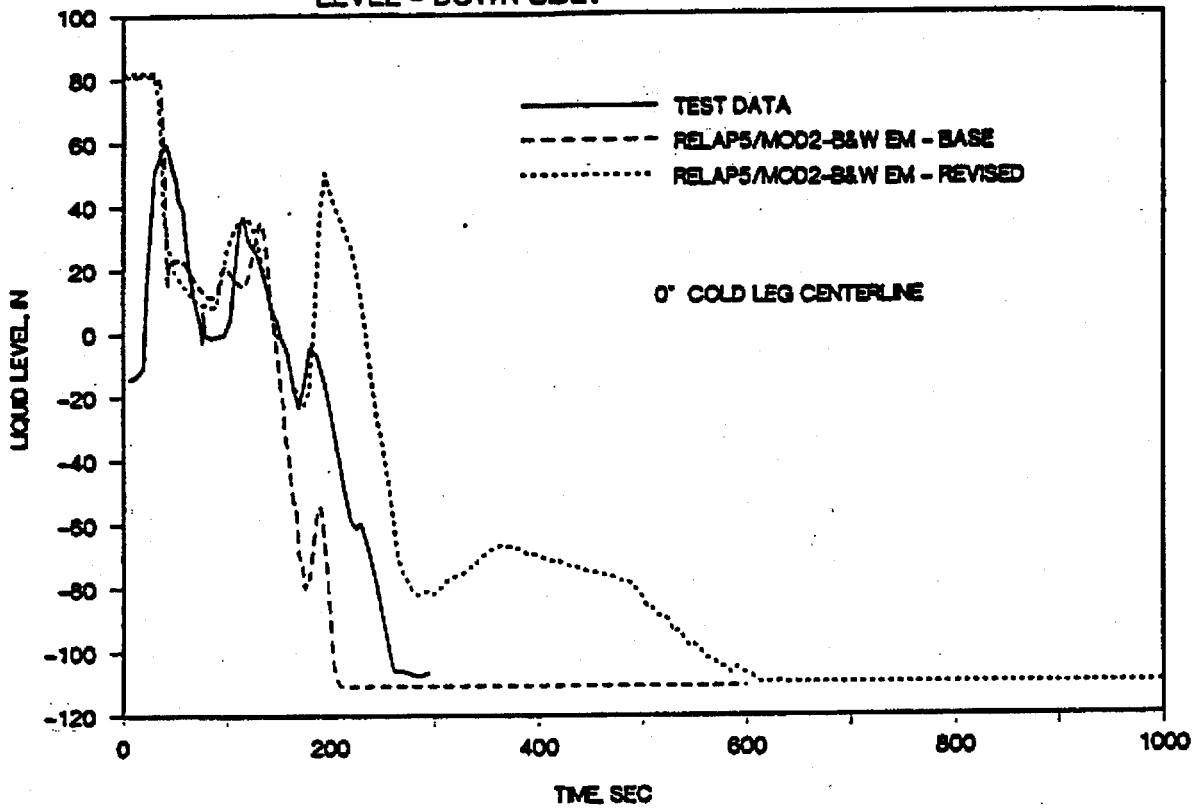


FIGURE 5-12. SEMISCALE TEST S-LH-1; BROKEN LOOP PUMP SUCTION LEVEL - UP SIDE.

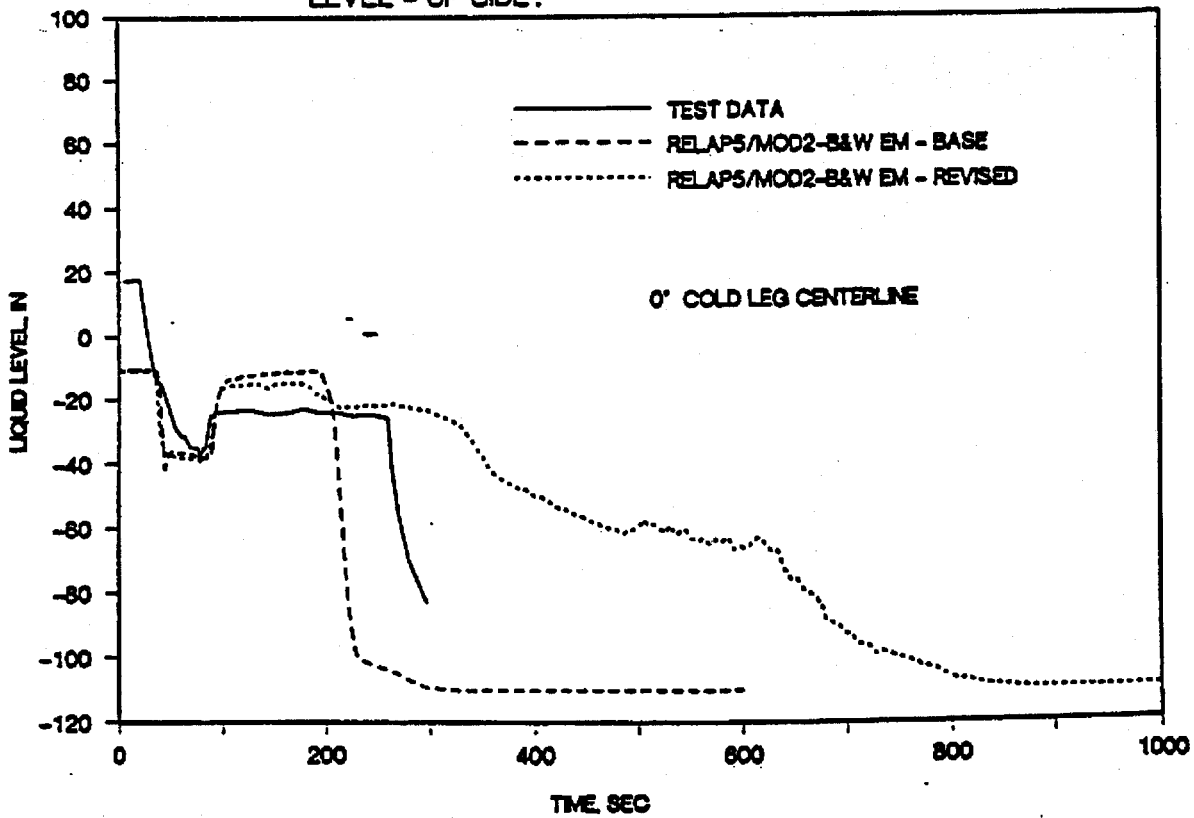


FIGURE 5-13. SEMISCALE TEST S-LH-1; VESSEL LIQUID LEVEL.

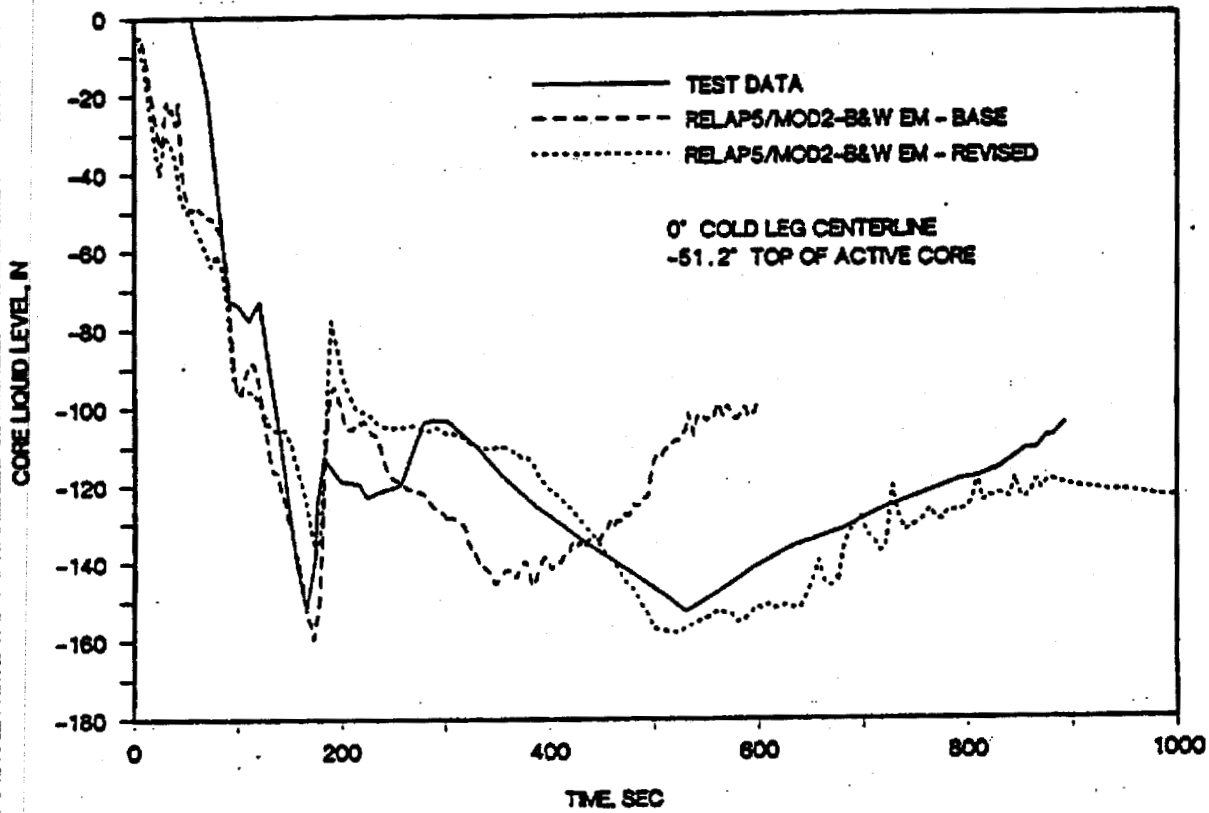


FIGURE 5-14. SEMISCALE TEST S-LH-1; PRIMARY SYSTEM NORMALIZED MASS.

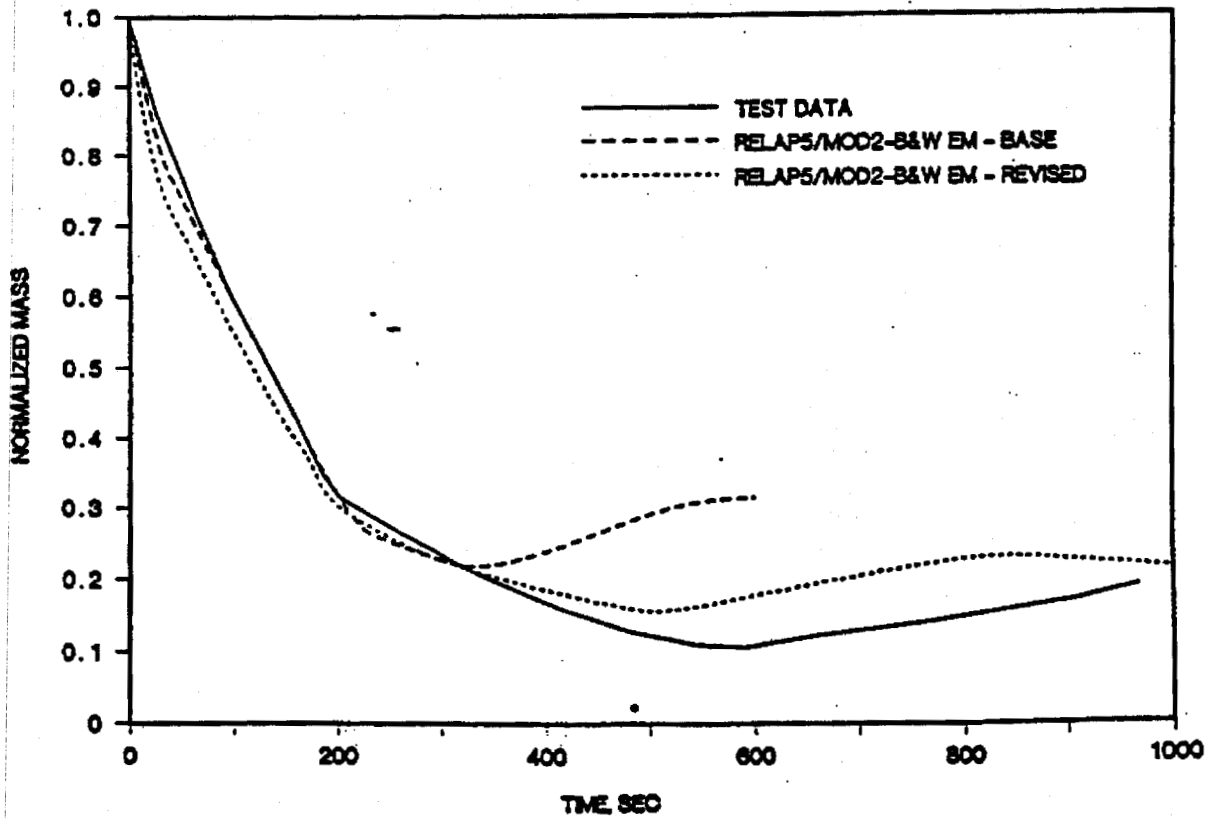


FIGURE 5-15. SEMISCALE TEST S-LH-1; INTACT LOOP ECC FLOW RATE.

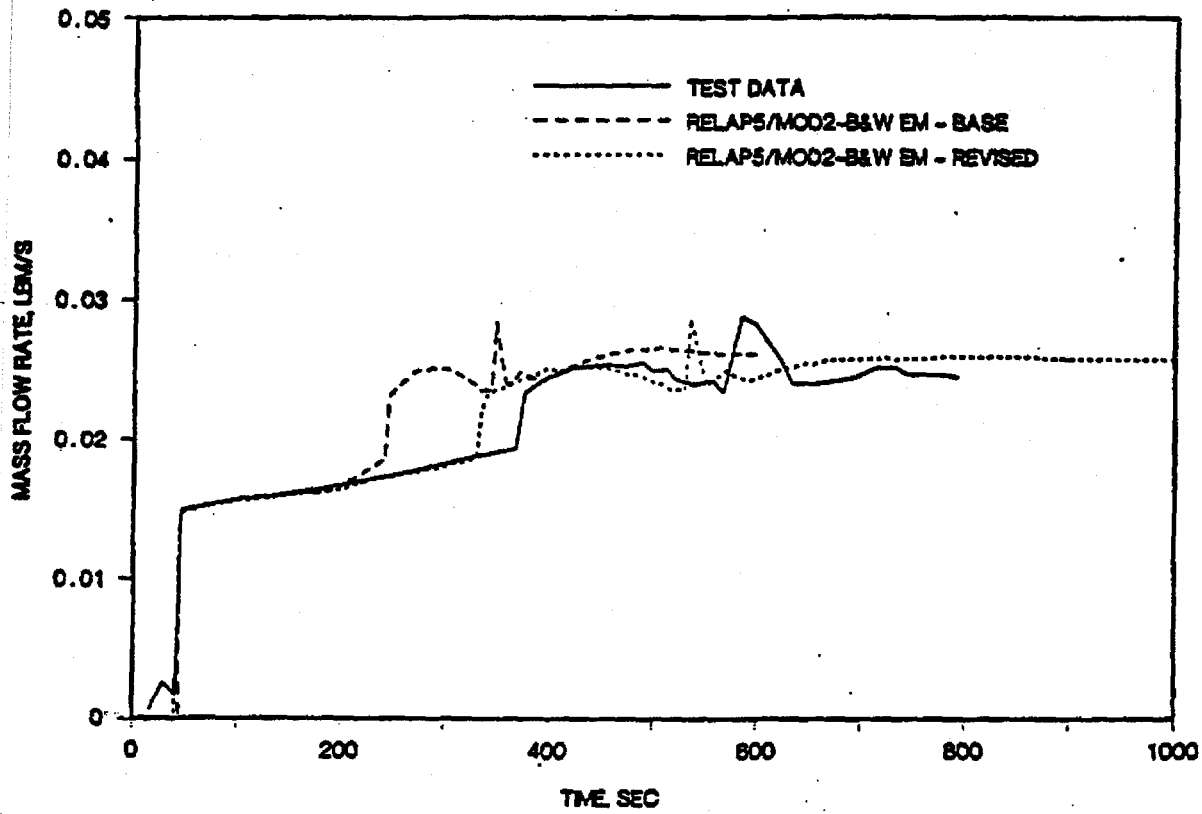


FIGURE 5-16. SEMISCALE TEST S-LH-1; BROKEN LOOP ECC FLOW RATE.

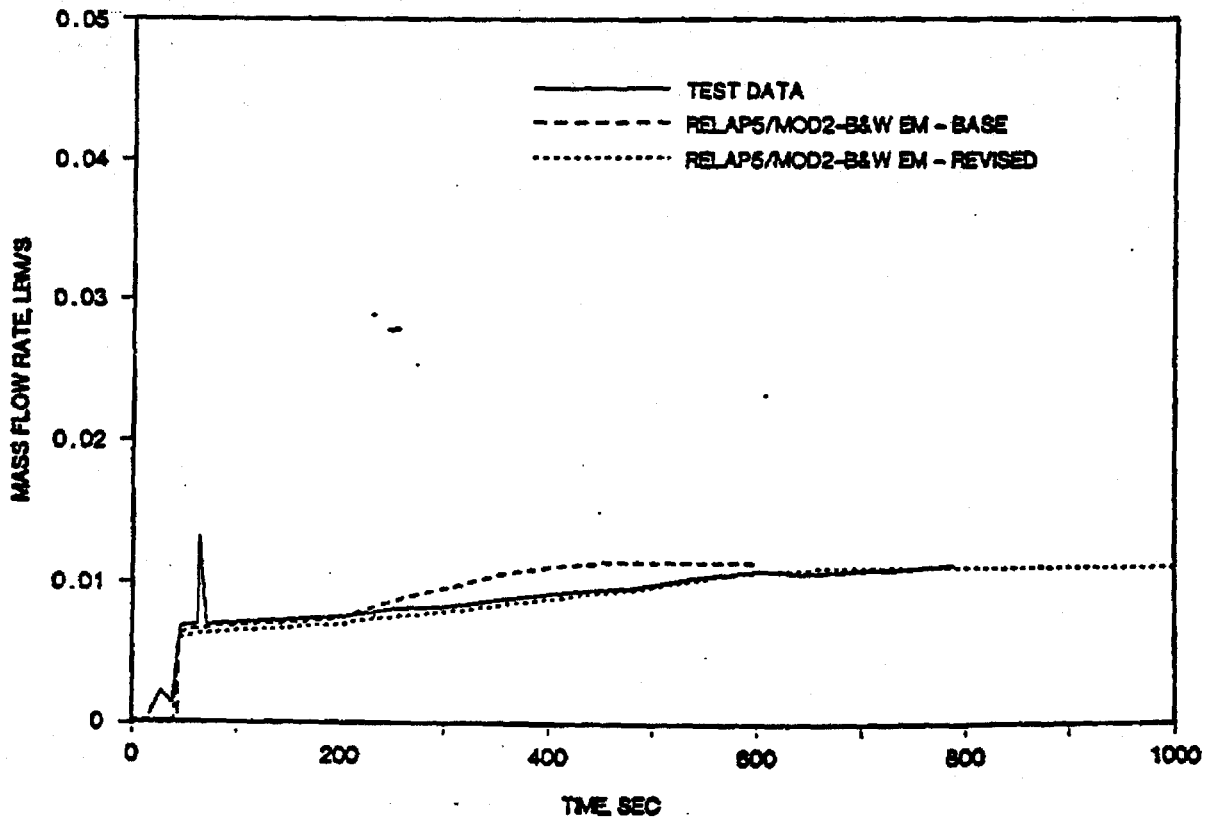


FIGURE 5-17. SEMISCALE TEST S-LH-1; VESSEL UPPER HEAD LIQUID LEVEL.

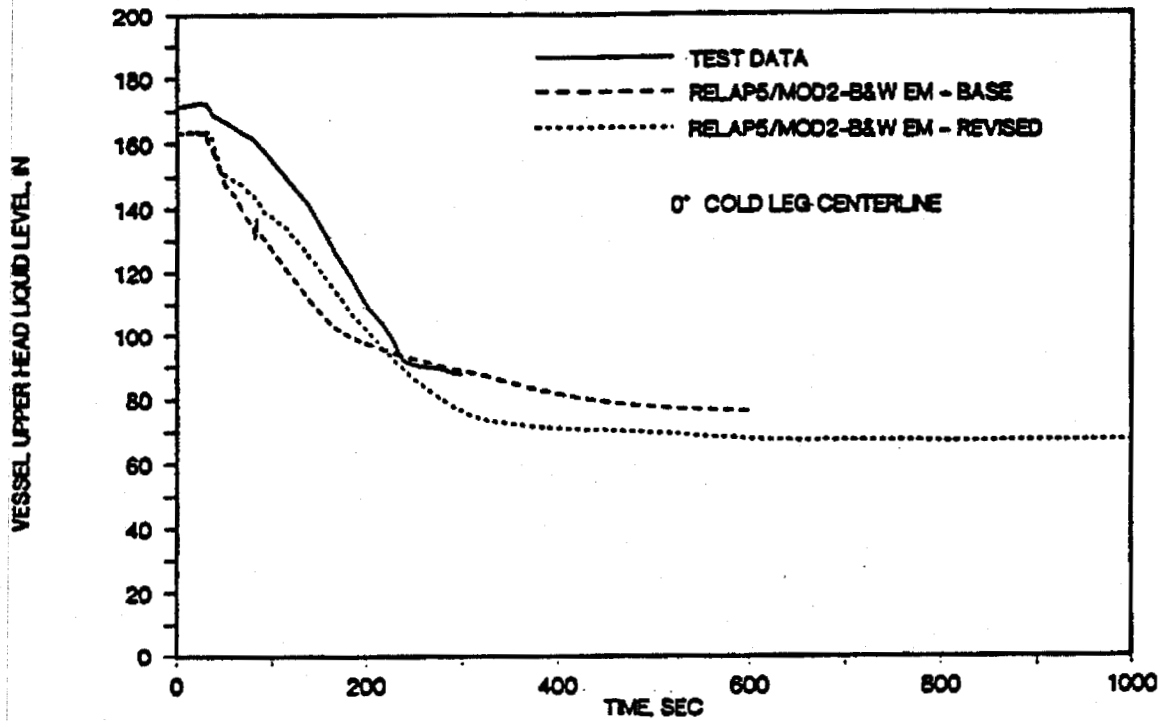


FIGURE 5-18. SEMISCALE TEST S-LH-1; DOWNCOMER LIQUID LEVEL.

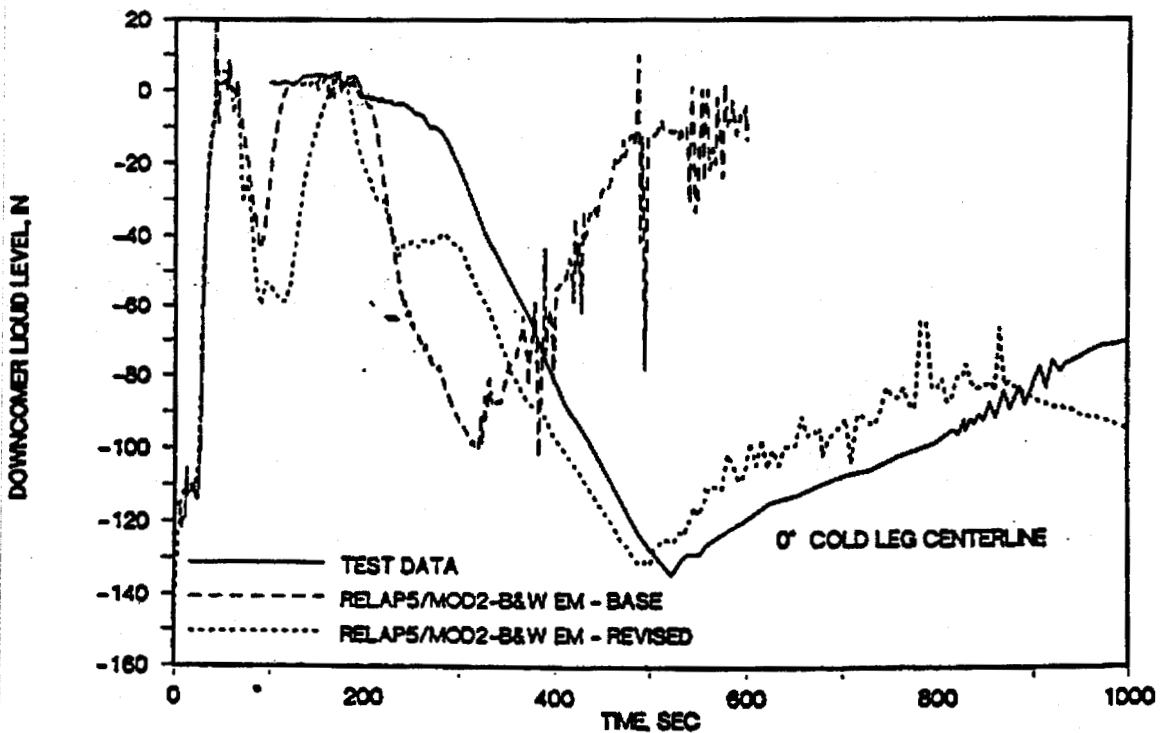


FIGURE 5-19. SEMISCALE TEST S-LH-1; 8 FOOT HEATER ROD SURFACE TEMPERATURE.

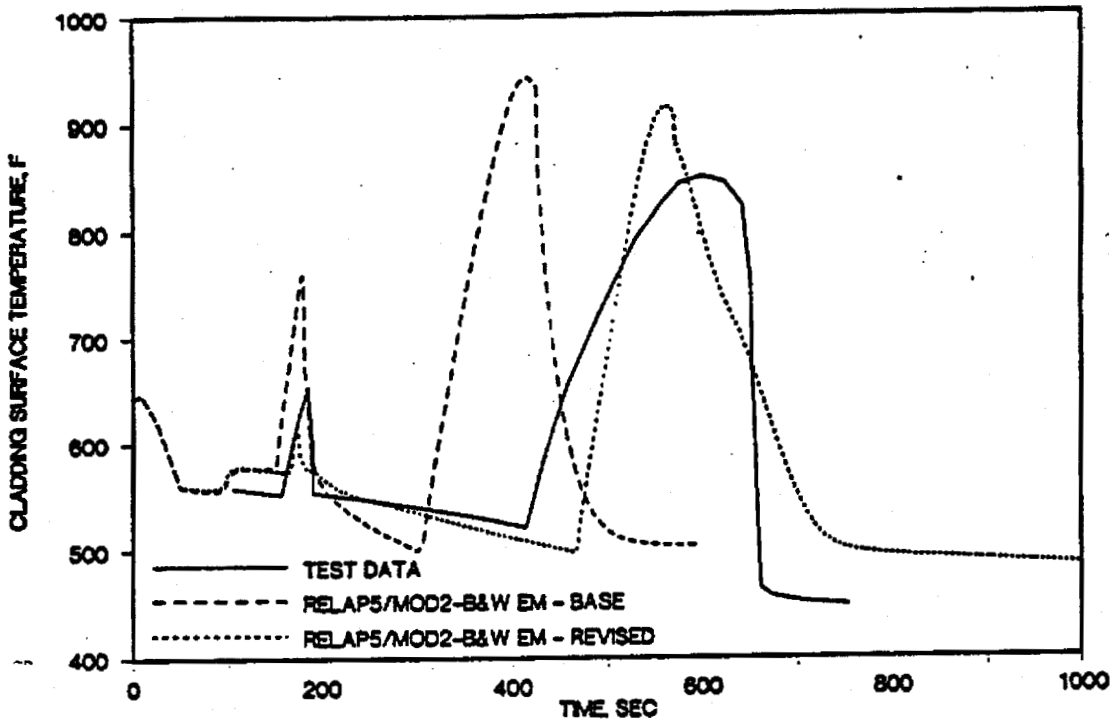


FIGURE 5-20. SEMISCALE TEST S-LH-1; 10 FOOT HEATER ROD SURFACE TEMPERATURE.

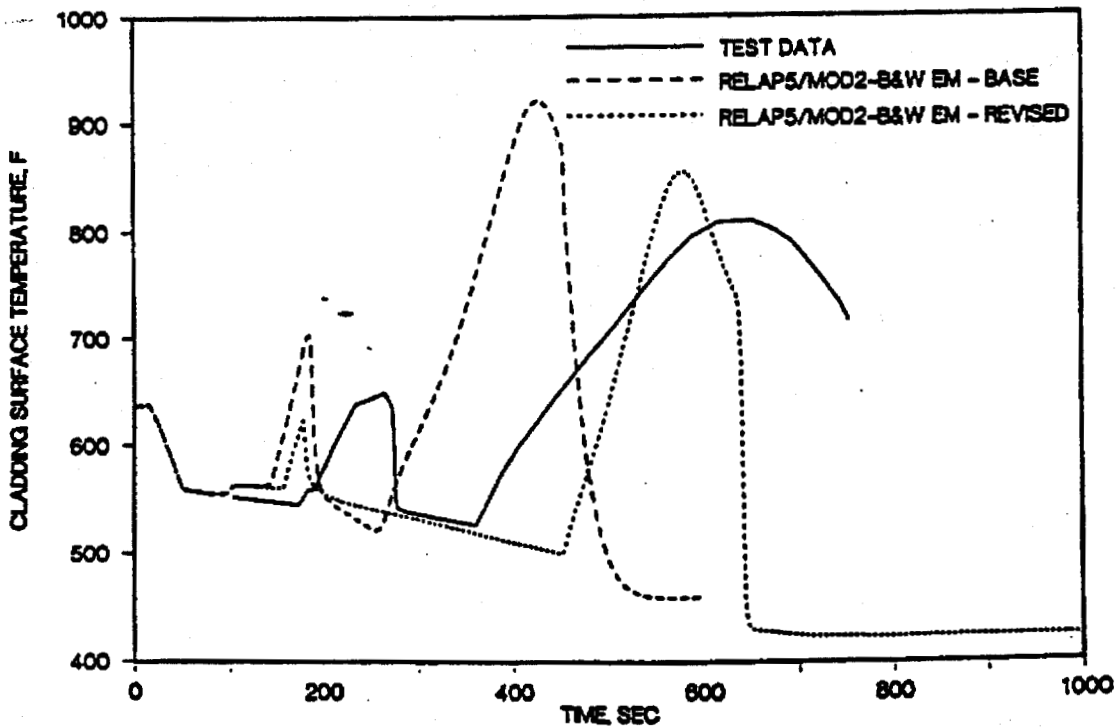
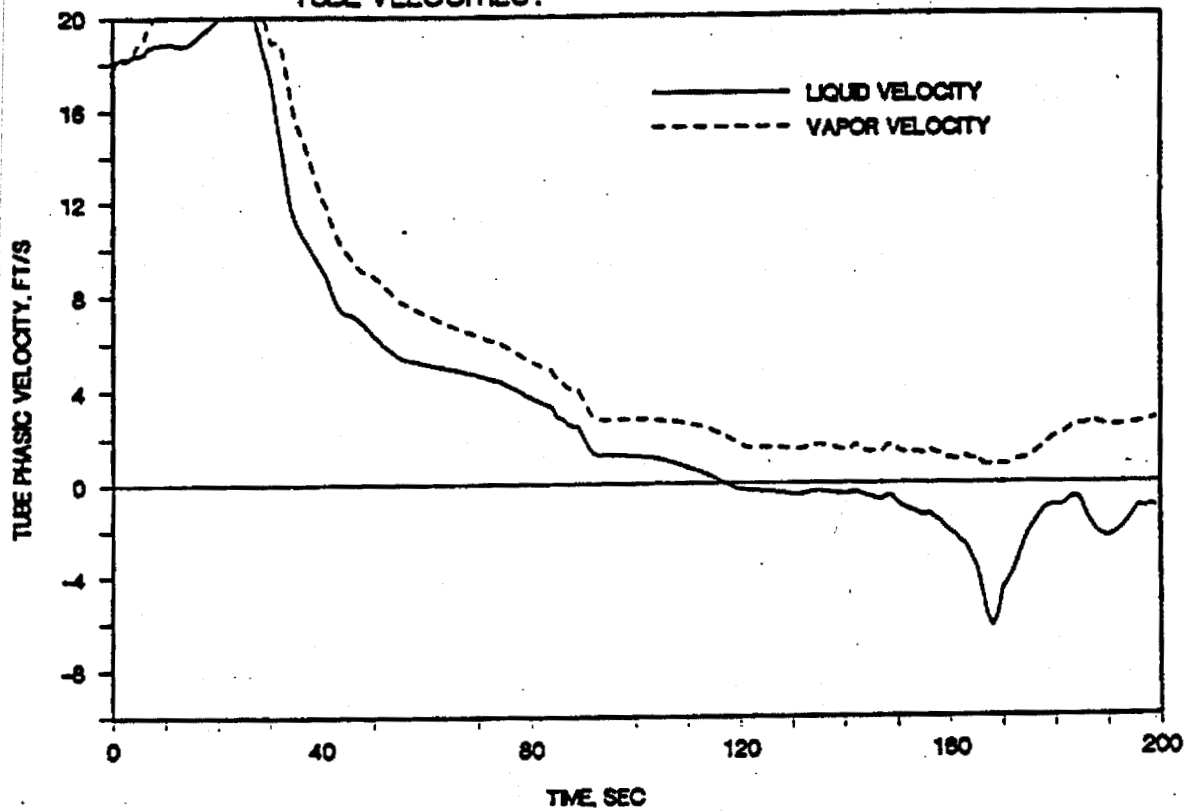


FIGURE 5-21. SEMISCALE TEST S-LH-1; RELAP5/MOD2 BASE CASE CALCULATED TUBE VELOCITIES.



6. Your response to Question 18 stated that an assessment calculation for a 1.0 ft² break, which was selected as a transition point between the large- and small-break LOCA calculations, was not needed because this break size is not the limiting case for either large- or small-break LOCA. Confirm that your plant specific break spectrum analyses will include calculations, with both the large- and small-break LOCA EMs, of a 1.0 ft² break in order to demonstrate compliance with Section C.1.a of Appendix K to 10 CFR 50.

Response: The B&W recirculating steam generator LOCA evaluation model separates small breaks from large breaks at a break area of 1.0 ft². Should the evaluation of a break with that area become necessary as part of a spectrum or partial spectrum submittal for compliance with 10CFR50.46, the evaluation will be performed as both a large break and as a small break. Both results will be reported in the submittal and the deviations between the treatments evaluated and explained.

This page intentionally left blank.

5.3 Safety Evaluation Report of Revision 1

This section contains the safety evaluation report, dated April 18, 1990, issued as a result of NRC review of revision 1 of this topical report. The SER is based on the technical report produced by EG&G, Idaho National Laboratory, as part of the review process; this technical report is included in this section.

This page intentionally left blank.



UNITED STATES
NUCLEAR REGULATORY COMMISSION
WASHINGTON, D. C. 20555

April 18, 1990

Mr. J. H. Taylor, Manager
Licensing Services
B&W Nuclear Technologies
3315 Old Forest Road
P. O. Box 10935
Lynchburg, Virginia 24506-0935

Dear Mr. Taylor:

SUBJECT: ACCEPTANCE FOR REFERENCING OF LICENSING TOPICAL REPORT, BAW-10164P, REVISION 1, "RELAP5/MOD2-B&W, AN ADVANCED COMPUTER PROGRAM FOR LIGHT WATER REACTOR LOCA AND NON-LOCA TRANSIENT ANALYSIS"

We have completed our review of the subject topical report submitted by the Babcock & Wilcox Fuel Company (BWFC), a company of B&W Nuclear Technologies, by a letter of December 28, 1987, and revised by letters of November 2, 1988 and January 30, 1990. We find the report to be acceptable for referencing in license applications to the extent specified and under the limitations delineated in the report and the associated evaluation by the U. S. Nuclear Regulatory Commission (NRC), which is enclosed. The evaluation defines the basis for acceptance of the report.

We do not intend to repeat our review of the matters described in the report when the report appears as a reference in the license applications, except to ensure that the material presented is applicable to the specific plant involved. Our acceptance applies only to the matters described in the report.

In accordance with procedures established in NUREG-0390, NRC requests that BWFC publish accepted versions of this report, proprietary and non-proprietary, within three months of receipt of this letter. The accepted versions shall incorporate this letter and the enclosed evaluation between the title page and the abstract. The accepted versions shall include an "-A" (designating accepted) following the report identification symbol.

Should our criteria or regulations change such that our conclusions about the acceptability of the report are invalidated, we expect BWFC or the applicants referencing the topical report, or both, to revise and resubmit their respective documentation, or to submit justification for the continued effective applicability of the topical report without revision of their respective documentation.

Sincerely,

A handwritten signature in black ink, appearing to read "A. C. Thadani".

Ashok C. Thadani, Director
Division of Systems Technology
Office of Nuclear Reactor Regulation

Enclosures:
's stated

UNITED STATES
NUCLEAR REGULATORY COMMISSION
WASHINGTON, D. C. 20555



ENCLOSURE 1

SAFETY EVALUATION OF THE BABCOCK & WILCOX FUEL COMPANY
TOPICAL REPORT BAW-10164P, REVISION 1,
RELAP5/MOD2-B&W, AN ADVANCED COMPUTER PROGRAM FOR
LIGHT WATER REACTOR LOCA AND NON-LOCA TRANSIENT ANALYSIS

1.0 INTRODUCTION

As part of safety analysis for fuel reloads of the pressurized water reactor (PWR) plants equipped with recirculating steam generators (RSGs), the Babcock & Wilcox Fuel Company (BWFC) developed reload safety analysis methodologies for loss-of-coolant accidents (LOCAs) and non-LOCA transients and accidents. The LOCA evaluation model is described in topical report BAW-10168P, "RSG LOCA" (Ref. 1). The approach for the safety analysis of non-LOCA transients is described in topical report BAW-10169P, "RSG Plant Safety Analysis" (Ref. 2). The system transient analysis code RELAP5/MOD2-B&W is used, complemented with other codes, to perform both LOCA and non-LOCA analyses. The RELAP5/MOD2-B&W code, which is the subject of this review, is described in the report BAW-10164P, Revision 1, submitted and amended by letters of December 28, 1987, November 2, 1988, and January 30, 1990 (Refs. 3, 4, 5),

For a large-break LOCA, the RELAP5/MOD2-B&W code is used to calculate reactor coolant system transients and core thermal hydraulic conditions during the blowdown phase. These calculations are followed by the use of the REFLOD3B and BEACH codes (Refs. 6 and 7) to calculate the refill and reflood responses. For a small-break LOCA (SBLOCA), the entire system response is analyzed with the RELAP5/MOD2-B&W code. If a core uncover is predicted to occur, the FOAM2 code (Ref. 8) is used to calculate the mixture height inside the reactor core. The FRAP-T6-B&W code (Ref. 9) is then used in both large-break and small-break LOCAs to calculate the thermal response and peak cladding temperature (PCT) at the hot fuel rod.

The non-LOCA safety analysis methodology uses the RELAP5/MOD2-B&W code to model and calculate the system responses for each transient. Reactor core power during each transient is calculated using the point kinetics neutronic model in the RELAP5/MOD2-B&W code. The resulting thermal hydraulic conditions of the core calculated using the RELAP5/MOD2-B&W code are used as boundary conditions for another core thermal hydraulic code, such as LYNXT (Ref. 10), to determine the temperature and departure from nucleate boiling ratio (DNBR) of the hot rod.

This safety evaluation addresses only the acceptability of using the RELAP5/MOD2-B&W code with proper details of the reactor system nodding for calculation of transient system response as part of the reload safety analysis of LOCA and non-LOCA transients and accidents. Implementation of the overall transient and accident analyses is addressed in the review of the LOCA evaluation model (EM) topical report BAW-10168P and the non-LOCA safety analysis method report BAW-10169P. Because the RELAP5/MOD2-B&W code is a part of the LOCA EM and the non-LOCA safety analysis, the restrictions imposed on RELAP5/MOD2-B&W will also affect these analyses, and vice versa.

2.0 DESCRIPTION OF RELAP5/MOD2-B&W

The RELAP5/MOD2-B&W code is a BWFC version of the advanced system analysis computer code RELAP5/MOD2. RELAP5/MOD2 was developed by the Idaho National Engineering Laboratory as a best-estimate code to simulate a wide variety of PWR system transients. The code, which is also organized into modules by components and functions, was designed to model the behavior of all major components in the reactor system during accidents ranging from large-break and small-break LOCAs to anticipated operational transients involving the plant control and protection systems. This code supports simulation of the primary system, secondary system, feedwater train, system controls, and core neutronics. Special component models include pumps, valves, heat structures, electric heaters, turbines, separators and accumulators.

The fundamental equations, constitutive models and correlations, and method of solution of RELAP5/MOD2 are described in NUREG/CR-4312 (Ref. 11). The recently published NUREG/CR-5194 (Ref. 12) contains a very detailed description of models and correlations used in the RELAP5/MOD2 code. RELAP5/MOD2-B&W preserves the original models of RELAP5/MOD2. However, new features and models have been added to ensure compliance with the requirements in Appendix K for LOCA ECCS evaluation model to permit licensing LOCA analysis. The more significant features added include:

- (1) The Moody, extended Henry-Fauske, and Murdock-Bauman critical flow models.
- (2) A core heat transfer model
- (3) The return to nucleate boiling and transition boiling lockout logics
- (4) New fuel rod behavior models to represent fuel rod fission gases, rod deformation, fuel-cladding swelling and rupture, gap conductance, and zircaloy-water reaction.

The RELAP5/MOD2-B&W hydrodynamic model is a one-dimensional (axial), transient, two-fluid model used to calculate the flow of a steam-water two-phase mixture. This two-fluid model uses six field equations: 2 phasic-continuity equations, 2 phasic-momentum equations and 2 phasic-energy equations. Therefore, RELAP5/MOD2-B&W is capable of calculating the characteristics of non-homogeneous, non-equilibrium flow. The hydrodynamics model also contains several options for invoking simpler hydrodynamics models, such as homogeneous flow, thermal equilibrium, and frictionless flow models, which can be used independently or in combination. The system model is solved numerically using a semi-implicit finite difference technique. The user can also select an option for solving the system model using a nearly-implicit finite difference technique that allows for violation of the material Courant limit, and is suitable for steady state calculations and for slowly-varying, quasi-steady transient calculations.

The RELAP5/MOD2-B&W code uses a point-kinetics model with six delayed neutron groups to calculate reactor power as a function of time. It contains provisions for fuel temperature, moderator temperature and density reactivity feedback. Other reactivity feedbacks such as those caused by boron concentration changes and tripped-rod reactivity are provided with input tables for generalized reactivity with respect to time.

The constitutive models in the RELAP5/MOD2-B&W code include models for defining flow regimes, and flow-regime-related models for calculating wall friction, interfacial mass transfer, heat transfer, and drag force. A core structure heat transfer model and a fuel pin heat conduction model with dynamic fuel cladding gap conductance model are included. The core heat transfer package can calculate heat transfer coefficients for various heat transfer regimes from single-phase convection, nucleate boiling, to post-critical heat flux (CHF) heat transfers.

Other special features of the RELAP5/MOD2-B&W that are very useful in the thermal-hydraulic analysis of PWRs include dynamic pressure loss models associated with abrupt area change for single-phase and two-phase flows, a centrifugal pump performance model with two-phase degradation effects, choked flow models with treatment for horizontal stratification, nonhomogeneous two-phase flow, counter-current flow models, crossflow junctions, decay heat models, a fine mesh renodalizing scheme for heat conduction, liquid entrainment, a motor valve model, a relief valve model, control system, and trip system.

3.0 STAFF EVALUATION

The staff performed the evaluation of the RELAP5/MOD2-B&W code with technical assistance from Idaho National Engineering Laboratory. A technical evaluation report (TER) regarding the acceptability of the RELAP5/MOD2-B&W code is attached as part of this evaluation. We have reviewed the TER and concurred with the conclusion.

Based on our review, we find that the RELAP5/MOD2-B&W code contains appropriate phenomenological models suitable for calculating both LOCA and non-LOCA transients. Also, the RELAP5/MOD2-B&W code contains nothing that is plant-specific in nature or that would preclude the application of the code to any of the recirculating steam generator plants. Therefore, the RELAP5/MOD2-B&W code can be applied to any of the proposed Westinghouse and Combustion Engineering plants.

BWFC has developed two plant-noding models with the RELAP5/MOD2-B&W code for the analysis of non-LOCA transients and accidents. One is a low-power model for analysis of steamline breaks at low power. The other is a full-power model for analysis of other transients such as a turbine trip, a locked reactor coolant pump rotor, and the uncontrolled withdrawal of a rod cluster control assembly bank, etc. The report BAW-10169P (Ref. 2) describes both models, and also presents the benchmark comparisons between the results of the RELAP5/MOD2-B&W calculations with these models and the results of selected final safety analysis reports (FSARs) of Westinghouse PWR-designed plants for the transients and accidents representing different transient categories to be analyzed in the safety analysis. The comparisons of several important parameters, such as neutron and thermal powers, pressurizer pressure and water level, core inlet and average temperatures, and flow rate, indicated a generally good agreement in the trends of these parameters. This agreement indicates the appropriateness of using the RELAP5/MOD2-B&W code with proper plant noding details to calculate the system responses to the transients. Therefore, it is acceptable to use the RELAP5/MOD2-B&W code for licensing calculations of transient reactor system responses. However, for a complete safety analysis, an approved core thermal hydraulic code and critical heat flux correlation should be used with the RELAP5/MOD2-B&W code. The noding details and inputs should be justified on a plant-specific basis. The choice of constitutive models including the empirical models and correlations should be justified to ensure that their use is within the ranges of applicability.

The RELAP5/MOD2-B&W code also contains the features and models necessary to satisfy the requirements of Appendix K to 10 CFR 50. Therefore, we find this code to be acceptable for use in integral system analyses for the large-break and small-break LOCAs, i.e. the calculation of the system blowdown response for large-break LOCAs and the calculation of the system hydraulic response for small-break LOCAs.

4.0 SUMMARY

The staff has reviewed Topical Report BAW-10164P, Revision 1. Except for the following conditions and restrictions, we find that the RELAP5/MOD2-B&W code is acceptable for calculating the reactor system responses in performing the safety analysis of transients and accidents, including large-break and small-break LOCAs.

- (1) The Chen-Sundaram-Ozkaynak film-boiling correlation in the core heat transfer model and the B&W auxiliary feedwater model for once-through steam generators were not reviewed and, therefore, should not be used in licensing calculations without prior review and approval by the NRC.
- (2) Prerupture cladding swell is not modeled because BWFC indicated that the swell is generally less than 20 percent with insignificant flow diversion effects. The acceptability of neglecting the effects of prerupture swelling is part of the LOCA EM review based on BWFC's analysis of the flow diversion effects. The SER on report BAW-10168P will address the resolution of this matter.
- (3) The built-in kinetics data for decay heat calculations in the RELAP5/MOD2-B&W code are based on the 1973 and 1979 standards of the American Nuclear Society (ANS). Because Appendix K requires the use of a value that is 1.2 times the 1971 ANS standard for decay heat calculation, BWFC should ensure that the decay heat used in licensing LOCA analysis complies with Appendix K.

- (4) The LOCA assessments of the Extended Henry-Fauske and Moody critical flow models were based on the use of the static properties as input to the critical flow tables. The LOCA licensing calculations should be performed accordingly.
- (5) The interphase drag model of the RELAP5/MOD2-B&W code tends to overpredict interphase drag. This overprediction may cause nonconservative predictions of loop seal clearing phenomena in that liquid is cleared even when the steam flow is not sufficiently high to drag the liquid out of the loop seal. Therefore, this model may not accurately calculate the core uncover and the peak cladding temperature (PCT). A resolution requiring a sensitivity study to choose a proper loop seal nodalization that results in the highest PCT calculation will be addressed in the LOCA EM review.
- (6) Even though noncondensable gases are not modeled in the SBLOCA system analysis, BWFC demonstrated negligible effect that all sources of noncondensable gases will have on the overall response of the system for the range of SBLOCAs. However, BWFC noted that a 50 psi increase above the steam generator control pressure of 1150 psia could result from a worst case release of noncondensable gases. The staff believes that this pressure increase generally would not substantially reduce the injection capabilities of the charging and safety injection (SI) systems. However, because the performance characteristics of the SI pumps vary widely in the plants, verification should be made on a plant-specific basis to ensure that a 50 psi pressure increase will not greatly reduce SI flow such that the PCT would increase by more than 50°F. Otherwise, additional information should be provided to justify neglect of noncondensable gases, or the effect of the pressure increase caused by noncondensable gases should be included in the analysis.
- (7) For a complete safety analysis, an approved core thermal hydraulic code and CHF correlation should be used with the RELAP5/MOD2-B&W code. The noding details and inputs should be justified on a plant-specific basis.

The choice of constitutive models including the empirical models and correlations should be justified to ensure their use is within the ranges of applicability.

REFERENCES

1. BAW-10168P, "RSG LOCA - B&W Loss-of-coolant Accident Evaluation Model for Recirculating Steam Generator Plants, Volume I - Large Break, Volume II - Small Break," July 1988.
2. BAW-10169P-A, "RSG Plant Safety Analysis - B&W Safety Analysis Methodology for Recirculating Steam Generator Plants," October 1989.
3. Letter from J. H. Taylor (BWFC) to J. A. Norberg (NRC), "ECCS Methodology for Licensing Catawba and McGuire Reloads," JHT/87-271, December 28, 1987.
4. Letter from J. H. Taylor (BWFC) to J. A. Norberg (NRC), "ECCS Methodology for Licensing Catawba and McGuire Reloads," JHT/88-203, November 2, 1988.
5. Letter from J. H. Taylor (BWFC) to Valeria Wilson (NRC), "RELAP5/MOD2 Topical Report, BAW-10168P (sic. BAW-10164P), JHT/90-8, January 30, 1990.
6. BAW-10171P, Revision 2, "REFLOD3B - Model for Multinode Core Reflood Analysis," February 1989.
7. BAW-10166P, Revision 1, "BEACH - Best Estimate Analysis Core Heat Transfer, A Computer Program For Reflood Heat Transfer During LOCA," December 1988.
8. BAW-10155-P, "FOAM2 - Computer Program to Calculate Core Swell Level and Mass Flow Rate During Small-Break LOCA," October 1987.

9. BAW-10165P, "FRAP-T6-B&W - A Computer Code for Transient Analysis of Light Water Reactor Fuel Rods," October 1987.
10. BAW-10156-A, "LYNXT - Core Transient Thermal-Hydraulic Program," February 1986.
11. NUREG/CR-4312, EGG-2396, "RELAP5/MOD2 Code Manual," Volumes 1 and 2, August 1985.
12. NUREG/CR-5194, EGG-2531, "RELAP5/MOD2 Models and Correlations," August 1988.

EGG-EAST-8695
February 1990

TECHNICAL EVALUATION REPORT

RELAP5/MOD2 - B&W, AN ADVANCED COMPUTER PROGRAM
FOR LIGHT WATER REACTOR LOCA AND NON-LOCA
TRANSIENT ANALYSES

C. P. Fineman

Prepared for the
U.S. NUCLEAR REGULATORY COMMISSION

This page is intentionally left blank.

EGG-EAST-8695

TECHNICAL EVALUATION REPORT
RELAP5/MOD2 - B&W
AN ADVANCED COMPUTER PROGRAM
FOR
LIGHT WATER REACTOR LOCA AND NON-LOCA TRANSIENT ANALYSES

C. P. Fineman

February 1990

Idaho National Engineering Laboratory
EG&G Idaho, Inc.
Idaho Falls, Idaho 83415

Prepared for the
U.S. Nuclear Regulatory Commission
Washington D.C. 20555
Under DOE Contract No. DE-AC07-76ID01570
FIN No. D6030

ABSTRACT

A review was completed of the RELAP5/MOD2 - B&W computer program developed by Babcock & Wilcox (B&W) for performing pressurized water reactor (PWR) loss-of-coolant accident (LOCA) licensing analyses. The review consisted of an evaluation of the RELAP5/MOD2 - B&W computer program as well as the modifications made by B&W to the RELAP5/MOD2, cycle 36.04, computer program from which the licensing version of RELAP5/MOD2 - B&W originated. Integral assessment calculations were reviewed to evaluate the validity and proper implementation of the modifications and added models. The review found that RELAP5/MOD2 - B&W met the requirements of 10CFR50, Appendix K, and NUREG-0737, Item II.K.3.30, and it is recommended the code be accepted for use in PWR licensing analyses on the basis that suggested conditions and requirements are followed. The break sizes for which RELAP5/MOD2 - B&W is recommended for use include both large and small breaks. However, prior to using RELAP5/MOD2 - B&W in LOCA applications, B&W must receive approval of their LOCA evaluation model methodology being reviewed separately.

SUMMARY

This report documents the review and evaluation of the Babcock & Wilcox (B&W) computer program RELAP5/MOD2 - B&W for use in performing pressurized water reactor (PWR) loss-of-coolant accident (LOCA) licensing analyses. RELAP5/MOD2 - B&W is capable of analyzing the steady state and transient thermal-hydraulic response of a light-water reactor. The code has features that allow compliance with the requirements of 10CFR50, Appendix K. RELAP5/MOD2 - B&W is based on RELAP5/MOD2, cycle 36.04, developed at the Idaho National Engineering Laboratory (INEL) under Nuclear Regulatory Commission (NRC) sponsorship. The code was submitted to the Office of Nuclear Reactor Regulation for approval as a licensing method. The Office of Nuclear Reactor Regulation requested assistance from the INEL in reviewing RELAP5/MOD2 - B&W.

The RELAP5/MOD2 - B&W code was reviewed and assessed as well as the model additions and modifications made by B&W to RELAP5/MOD2, cycle 36.04. This review was made using the information provided by B&W in the RELAP5/MOD2 - B&W code manual and in B&W's responses to questions submitted by the NRC to B&W. The code was also reviewed to ensure that known updates and corrections to RELAP5/MOD2, cycle 36.04, were included in RELAP5/MOD2 - B&W by B&W or appropriate justification given if excluded. Finally, the code was reviewed for compliance with NRC requirements.

Based on this review, it is recommended that RELAP5/MOD2 - B&W be accepted for performing PWR licensing analyses provided suggested conditions and requirements are followed. The break sizes for which RELAP5/MOD2 - B&W is recommended for use include both large and small breaks. This is based on the adequate RELAP5/MOD2 - B&W analyses of LOFT Test L3-5, Semiscale Test S-LH-1, and Semiscale Test S-04-6. These represent large and small break experiments. However, prior to using RELAP5/MOD2 - B&W in LOCA applications, B&W must receive approval of their LOCA evaluation model methodology being reviewed separately.

PREFACE

This report was prepared for the U.S. Nuclear Regulatory Commission, Office of Nuclear Reactor Regulation, by EG&G Idaho, Inc., Energy and Systems Technology Group.

CONTENTS

ABSTRACT	ii
SUMMARY	iii
PREFACE	iv
1. INTRODUCTION	1
2. RELAP5/MOD2 - B&W CODE DESCRIPTION AND ASSESSMENT	3
2.1 General Code Overview	3
2.2 Model Description and Assessment	5
2.2.1 Critical Flow Models	5
2.2.2 Core Heat Transfer Models	6
2.2.2.1 Pre-CHF Correlations	6
2.2.2.2 CHF Correlations	7
2.2.2.3 Post-CHF Correlations	8
2.2.3 Heat Transfer Logic Options	10
2.2.4 Fuel Behavior Models	11
2.3 Assessment Calculations	13
2.3.1 LOFT Test L3-5	13
2.3.2 Semiscale Test S-LH-1	15
2.3.3 Semiscale Test S-04-6	18
2.3.4 Assessment Summary	21
2.4 Phenomena Important to PWR SBLOCA	21
2.4.1 Noncondensable Gas	22
2.4.2 Condensation Heat Transfer	25
2.4.3 Natural Circulation	28
2.5 Calculation of S-UT-8 Phenomena	29
2.6 Loop Seal Clearing Phenomena	29
3. COMPLIANCE WITH NRC REQUIREMENTS	31
4. RELAP5/MOD2 CODE UPDATES	33
5. CONCLUSIONS	34
6. REFERENCES	39

This page intentionally left blank.

TECHNICAL EVALUATION REPORT
RELAP5/MOD2 - B&W
AN ADVANCED COMPUTER PROGRAM
FOR
LIGHT WATER REACTOR LOCA AND NON-LOCA TRANSIENT ANALYSES

1. INTRODUCTION

RELAP5/MOD2 - B&W¹ is a computer program developed by Babcock & Wilcox (B&W) for light water reactor (LWR) system thermal-hydraulic analysis. It provides integral analysis capability of the system and core response to normal and off-normal events during steady state and transients. RELAP5/MOD2 - B&W was adapted from RELAP5/MOD2, cycle 36.04,² by B&W for use in recirculating steam generator (RSG) pressurized water reactor (PWR) loss-of-coolant accident (LOCA) analyses, both large break LOCAs (LBLOCAs) and small break LOCAs (SBLOCAs). RELAP5/MOD2 - B&W was submitted to the Nuclear Regulatory Commission (NRC) by B&W for review and acceptance for licensing applications as a method to analyze PWR LOCAs in a manner that conforms to NRC requirements contained in 10CFR50, Appendix K, and other pertinent NRC regulations. RELAP5/MOD2 - B&W will be used by B&W as part of an overall RSG LOCA Evaluation Model (EM) methodology³ being reviewed separately. Application of RELAP5/MOD2 - B&W to LOCA analyses is contingent on the approval of the RSG LOCA EM methodology. RELAP5/MOD2 - B&W is also being reviewed separately for use in analyzing non-LOCA transients; however, the review documented in this report focused on the code's capability to analyze LBLOCAs and SBLOCAs.

The Office of Nuclear Reactor Regulation (NRR) is responsible for the evaluation and review of computer codes and their proposed applications. The Office of Nuclear Reactor Regulation requested the Idaho National Engineering Laboratory (INEL) provide assistance in the review of the RELAP5/MOD2 - B&W computer code. Specifically, the request for assistance included:

1. Evaluation of RELAP5/MOD2 - B&W as a method to analyze the entire PWR break spectrum.

2. Evaluation of RELAP5/MOD2 - B&W for compliance with requirements contained in 10CFR50, Appendix K, and NUREG-0737, Item II.K.3.30.
3. Assurance that corrections to RELAP5/MOD2, cycle 36.04, the base code for RELAP5/MOD2 - B&W were incorporated into RELAP5/MOD2 - B&W.

Related to the above reviews, NRR also requested INEL review and evaluate B&W's responses to NRC questions regarding the loss-of-coolant modeling applications. The questions were those transmitted to B&W by the NRC in References 4 and 5. Babcock & Wilcox's responses to these questions are contained in References 6 to 10.

This technical evaluation report documents the results of the RELAP5/MOD2 - B&W review and assessment for PWR LOCA analyses. Section 2 provides a brief overview of the history of RELAP5/MOD2 - B&W and its development from RELAP5/MOD2, cycle 36.04. This section also discusses B&W's modifications to the RELAP5 base code and B&W's code assessment work. Section 3 reviews the code for compliance with NRC requirements defined in Appendix K to 10CFR50. Section 4 reviews the implementation status in RELAP5/MOD2 - B&W of all documented updates to RELAP5/MOD2, cycle 36.04, generated by the code developers at the INEL. Section 5 summarizes the conclusions reached from this review and the references are listed in Section 6.

2. RELAP5/MOD2 - B&W CODE DESCRIPTION AND ASSESSMENT

This section presents a brief description of RELAP5/MOD2 - B&W and discusses its relationship to the RELAP5/MOD2, cycle 36.04, code from which it was developed. Then, each of the modifications made by B&W are discussed. The results of RELAP5/MOD2 - B&W integral assessment calculations will then be reviewed followed by a discussion of the code's ability to simulate the phenomena important to PWR SBLOCAs. Finally, the code's ability to simulate the type of phenomena observed in Semiscale Test S-UT-8¹¹ and loop seal clearing is discussed.

2.1 General Code Overview

RELAP5/MOD2 - B&W is a LWR reactor system transient simulation code based on a nonequilibrium and nonhomogeneous model for two-phase conditions. A full six equation, two fluid model for the vapor-liquid flow field is used. The code formulation of the hydrodynamic components, power sources, heated structures, trips, and control systems provides a flexible method for modeling LWR systems. RELAP5/MOD2 - B&W includes many general component models from which general systems can be simulated. The component models include pumps, valves, pipes, heat structures, reactor point kinetics, accumulators, and control system components. Special process models are included to account for form losses, abrupt area changes, branches, choked flow, boron tracking, and noncondensable gases.

RELAP5/MOD2 - B&W is based on RELAP5/MOD2, cycle 36.04, which was developed under NRC sponsorship. Babcock & Wilcox decided to maintain the same modeling philosophy in RELAP5/MOD2 - B&W as in the base code. The same formulation of the differential equations for the thermal-hydraulic models, the same basic constitutive relations, code architecture, principle solution techniques, and user convenient features were retained in RELAP5/MOD2 - B&W.

Although RELAP5/MOD2 was specifically developed to include the capability to simulate SBLOCAs and operational transients, the code is fully capable of simulating LBLOCAs as well. The application of RELAP5/MOD2 to a wide variety of thermal-hydraulic problems, including

large and small break LOCAs, indicated the formulation of the differential equations and solution techniques provide numerically stable solutions. With RELAP5/MOD2 - B&W maintaining the same basic approach, it can be concluded that it will also provide numerically stable solutions and, therefore, the general code models and structure are adequate for PWR LOCA analyses.

Babcock & Wilcox's assessment of RELAP5/MOD2 - B&W identified several areas that required changes to RELAP5/MOD2 to meet the EM requirements of Appendix K to 10CFR50. As a result, B&W began a code development program in the following areas:

1. Addition of the Moody, extended Henry-Fauske, and Murdock-Bauman critical flow models.
2. Addition of a core heat transfer model.
3. Addition of logic to prevent a return to nucleate boiling and transition boiling.
4. Addition of new fuel rod behavior models to represent fuel rod fission gases, rod cladding swell and rupture and rupture flow blockage, gap conductance, and zircaloy-water reaction.

The modifications made by B&W and their assessment are presented in more detail in Section 2.2.

One model added by B&W was not reviewed for use in a licensing calculation. This was the B&W auxiliary feedwater model for once through steam generators. Because it is B&W's intent to apply RELAP5/MOD2 - B&W to recirculating steam generator plants, this model was not reviewed at this time.

Also, the built-in reactor kinetics data for decay heat calculations in RELAP5/MOD2 - B&W are based on the American Nuclear Society (ANS) 1973 and 1979 standards, but the user has the option of entering different data. Because Appendix K requires the use of 1.2 times the ANS 1971

standard for decay heat calculations in LOCA licensing analyses, B&W should ensure the decay heat used in licensing analyses complies with Appendix K.

2.2 Model Description and Assessment

2.2.1 Critical Flow Models

RELAP5/MOD2 - B&W includes the original Ransom-Trapp critical flow model found in the RELAP5/MOD2 base code, and B&W added the Moody,¹² Extended Henry-Fauske,¹³ and Murdock-Bauman¹⁴ critical flow models to RELAP5/MOD2 - B&W. The Extended Henry-Fauske (H-F) model can be used to calculate subcooled critical flow, the Moody model calculates two-phase break flow, and the Murdock-Bauman model calculates superheated steam critical flow. Addition of the Moody model allows the code user to meet the Appendix K requirement that two-phase critical flow during a LOCA be calculated with the Moody model at all break locations.

All the models were incorporated as a tables of mass flux versus stagnation enthalpy and pressure. The critical flow tables may be entered with stagnation properties or the static pressure and enthalpy from the donor cell. If the stagnation properties are chosen, they are calculated from the upstream volume static pressure and enthalpy assuming isentropic flow.

To convert the critical mass flux from the critical flow table to the phasic velocities needed by RELAP5/MOD2 - B&W, several options are available. These include a homogeneous (no slip) model, user input constant slip, Moody's slip model, RELAP5 momentum equation slip, and upstream volume equilibrium quality slip.

Assessment on the implementation of these models was provided by the integral assessment calculation for Semiscale large break Test S-04-6 and small break experiments Semiscale Test S-LH-1 and LOFT Test L3-5. In the EM calculations of these tests, subcooled, two-phase, and superheated steam critical flow were calculated using the extended Henry-Fauske, Moody, and Murdock-Bauman models. The options chosen for calculating the critical flow in the LBLOCA assessment were the use of the static properties and

Moody slip was used with the Moody critical flow model. For SBLOCAs, the options chosen for calculating the critical flow were the use of static properties and a slip ratio of one was used with the Moody critical flow model. The calculated results for Test S-04-6 show the extended Henry-Fauske model slightly overpredicted the subcooled discharge and the Moody model, as expected, overpredicted the two-phase discharge. Both the LBLOCA and SBLOCA results indicate the models using these options were implemented correctly. Thus, the critical flow models in RELAP5/MOD2 - B&W discussed above with the listed options for LBLOCA and SBLOCA calculations, respectively, are recommended for use in LOCA licensing calculations.

2.2.2 Core Heat Transfer Models

Babcock & Wilcox added a new core heat transfer package to RELAP5/MOD2 - B&W for use in licensing calculations. The package is designed to meet the evaluation model requirements of Appendix K to 10CFR50 for large and small break analyses. The correlations used in the core model will be discussed in a sequence following the boiling curve: pre-critical heat flux (pre-CHF) correlations, CHF correlations, and post-CHF correlations. Application of the core model in the assessment calculations showed it was adequate to calculate the core heat transfer response as part of the system calculation in the overall RSG LOCA EM.

2.2.2.1 Pre-CHF Correlations. The pre-CHF correlations are divided into three categories: single-phase liquid, subcooled nucleate boiling, and nucleate boiling correlations. The correlations will be discussed in that order.

The Dittus-Boelter¹⁵ and Rohsenow-Choi^{16,17} correlations are used to calculate the single-phase liquid wall to fluid heat transfer in the core. The core heat transfer logic chooses the maximum of the two correlations as the single-phase heat transfer coefficient. This is the same type of logic used in the system heat transfer model (and the RELAP5/MOD2 base code), where the maximum of the Dittus-Boelter, Rohsenow-Choi, and a natural convection correlation is used for the single-phase heat transfer coefficient. The Dittus-Boelter and Rohsenow-Choi correlations are widely used to model single-phase forced

convection heat transfer in reactor transient simulation codes. The use of these correlations in a number of different reactor transient simulation codes has proven them adequate for modeling this type of heat transfer.

Subcooled nucleate boiling heat transfer is modeled using the modified Chen correlation.¹⁸ This is the same correlation used in the system model and the RELAP5 base code. Using the modified Chen correlation to calculate subcooled nucleate boiling in the application of RELAP5/MOD2 and other reactor analysis codes to a variety of problems has proven adequate.

A combination of the Chen,¹⁹ Thom,²⁰ and Shrock-Grossman²¹ correlations is used to calculate the nucleate boiling heat transfer coefficient. The ranges where the correlations are applied are: Chen correlation, pressure less than 750 psia; the Thom correlation, pressure greater than 1000 psia and void fraction less than 0.8; and the Shrock-Grossman correlation, pressure greater than 1000 psia and void fraction greater than 0.9. Linear interpolation is used to connect the correlations. The nucleate boiling correlations and selection logic used in RELAP5/MOD2 - B&W are similar to that used in the THETA1-B²² code previously approved by the NRC,²³ except the Chen correlation replaced the Jens and Lottes correlation.²⁴ Also, for qualities above 0.95, the heat flux is a linear interpolation on quality between the nucleate boiling flux and the single-phase vapor flux. The nucleate boiling heat transfer correlations and logic are adequate for use in RELAP5/MOD2 - B&W.

2.2.2.2 CHF Correlations. The CHF correlations used in RELAP5/MOD2 - B&W are divided into high and low flow categories. The high flow correlations and selection logic will be discussed first followed by the low flow correlations and logic.

The high flow correlations and selection logic, with the exception of one high pressure CHF correlation, are similar to the logic in the previously approved THETA1-B code. The high flow correlations are used if the mass flux is greater than 500,000 lbm/h-ft². For pressures greater than 1500 psia, the user has the option of choosing one of three correlations developed by B&W for use with their fuel. These are the B&W-2²⁵ (B&W 15 x 15 fuel bundles), BWC²⁶ (17 x 17 and zirconium grid

15 x 15 fuel bundles), and BWC MV²⁷ (17 x 17 mixing vane fuel bundles). The B&W-2 correlation is listed in Appendix K and the BWC and BWC MV correlations were approved by the NRC.^{28,29} In the topical report defining B&W's RSG LOCA EM (Reference 3), B&W stated that only the BWC MV correlation will be used in licensing calculations. At pressures below 1300 psia, the Barnett³⁰ or the modified Barnett (Hughes)³¹ CHF correlations are used in the high flow regime. These correlations are listed in Appendix K. Linear interpolation is used to connect the various regions where the individual correlations are applied. The high flow CHF model is considered adequate based on the previous NRC approval of the correlations and logic.

The low flow correlations are used if the mass flux is less than 200,000 lbm/h-ft². The high and low flow regions are connected by linear interpolation on mass flux between the high flow CHF correlation evaluated at its low flow limit and the low flow CHF correlation evaluated at its high flow limit. The low flow CHF value is taken to be the maximum of the MacBeth³² and the Griffith³³ correlations. These correlations and the selection logic are similar to that in the previously approved THETA1-B code. Therefore, the low flow correlations and logic are considered adequate for calculating low flow CHF.

In all regions, there are two additional constraints applied to the CHF calculation. First, a minimum CHF of 90,000 Btu/h-ft² is used. The same minimum CHF value is used in THETA1-B. Second, for void fractions greater than 0.8, the value for CHF is taken as the value of the heat flux calculated using the transition boiling heat transfer coefficient. For the McDonough, Milich, and King transition boiling correlation³⁴ used in RELAP5/MOD2 - B&W, this results in the calculation of a lower CHF value than the use of the CHF correlation alone. Based on the previous NRC approval of the minimum CHF constraint and the fact that the second constraint results in a conservative CHF calculation relative to using only the CHF correlation, these constraints are recommended for acceptance.

2.2.2.3 Post-CHF Correlations. The post-CHF region is divided into transition boiling, film boiling and single-phase vapor plus radiation regimes.

As noted above, the transition boiling heat transfer coefficient is calculated using the McDonough, Milich, and King correlation. This is one of the correlations specifically listed in Appendix K as acceptable for calculating transition boiling heat transfer.

The code user has the option of calculating the film boiling heat transfer coefficient using the maximum of the Condie-Bengston correlation³⁵ and the Rohsenow-Choi correlation or the maximum of the CSO correlation³⁶⁻⁴⁰ and the Rohsenow-Choi correlation. The maximum of the two correlations is used because single-phase forced convection heat transfer, modeled with the Rohsenow-Choi correlation, provides a lower bound on film boiling heat transfer. A comparison of the Condie-Bengston correlation to rod bundle film boiling data in Reference 35 was reviewed to determine the adequacy of the correlation for calculating film boiling heat transfer. The comparison showed the Condie-Bengston correlation tended to be slightly conservative in calculating film boiling data. Therefore, the Condie-Bengston correlation is adequate for film boiling heat transfer. In Reference 7, B&W stated that only the combination of Condie-Bengston and Rohsenow-Choi would be used in EM calculations, and, therefore no assessment of the CSO correlation would be provided. Based on this discussion, the CSO correlation cannot be used in a licensing calculation without additional review and approval by the NRC.

For heat transfer to single-phase vapor, the maximum of the McEligot⁴¹ and the Rohsenow-Choi correlations is used to calculate the convection part of the heat flux. Babcock & Wilcox provided additional information on the assessment of the McEligot correlation in their response to question 8, Reference 7. For Reynolds numbers greater than 10,000, data in Reference 42 verified the adequacy of the McEligot correlation. For Reynolds numbers below 10,000, a comparison of the Dittus-Boelter correlation to data in Reference 35 was discussed by B&W. This comparison showed the Dittus-Boelter correlation adequately calculated the single-phase vapor data down to Reynolds numbers of 2000. Because the McEligot correlation will calculate lower heat transfer coefficients than the Dittus-Boelter correlation, the data in Reference 35 support the adequacy of the McEligot correlation down to Reynolds numbers of 2000. Additional data supporting the use of the McEligot correlation for Reynolds

numbers less than 2000 was provided in by B&W in Reference 71. This data showed the McEligot correlation was adequate to calculate the heat transfer coefficient down to Reynolds numbers of 700 to 800 where the Rohsenow-Choi would then be applied. The radiation heat flux portion of single-phase vapor heat transfer is calculated using the correlation developed by Sun,⁴³ which is the same model used in the RELAP5/MOD2 base code, and is considered adequate.

The heat transfer logic in the post-CHF region selects the heat flux to be the maximum of the transition boiling and film boiling heat fluxes (this is similar to the RELAP5/MOD2 base code) as long as the difference between the wall temperature and the saturation temperature is less than 300°F and the quality is less than 0.95. However, if the transition boiling heat flux is greater than the pre-CHF heat flux, evaluated at the same conditions, then the heat flux is set equal to the film boiling heat flux. Between qualities of 0.95 and 0.999, the heat flux is a linear interpolation on quality between the single-phase vapor and the maximum of the transition or film boiling heat fluxes. When the quality is above 0.999, the heat flux is set equal to the single-phase vapor heat flux. If the wall superheat is greater than 300°F, the same logic is applied except only the film boiling and single-phase vapor correlations are used.

2.2.3 Heat Transfer Logic Options

Appendix K to 10CFR50 requires a code lockout return to nucleate boiling heat transfer once CHF is predicted at an axial fuel rod location during blowdown. Appendix K also requires a lockout regarding the return to transition boiling once the cladding superheat exceeds 300°F during the blowdown phase of a LOCA. These requirements force a degraded heat transfer calculation during the blowdown phase of a LOCA even though local conditions may allow a rewet and a return to nucleate boiling. Babcock & Wilcox added the appropriate heat transfer logic to RELAP5/MOD2 - B&W to allow the user to meet these Appendix K requirements.

The heat transfer logic sets the appropriate flag to true once CHF is exceeded. With this flag set to true, only post-CHF heat transfer correlations are evaluated and used to calculate the heat transfer with one

exception. If the wall temperature is less than the saturation temperature, then single-phase liquid convection or two-phase condensation is allowed by the code. When the wall superheat is greater than 300°F, another flag is set to true, and with this flag true, the code only applies film boiling or convection to steam with the same exception noted above for the nucleate boiling lockout. The exception to the nucleate and transition boiling lockouts discussed above is considered acceptable during the blowdown because, with the wall temperature less than the saturation temperature, the use of the single-phase liquid or two-phase condensation correlations will allow the fluid to heat the cladding.

It should also be noted that B&W does not lockout nucleate boiling in the case where the heat transfer regime changes from nucleate boiling to steam cooling without exceeding CHF. However, should this change in heat transfer result in the wall superheat exceeding 300°F, then return to transition boiling is locked out by the code. The INEL agrees that this logic is in agreement with Appendix K.

2.2.4 Fuel Behavior Models

Fuel behavior models were added to RELAP5/MOD2 - B&W to enable the fuel rod behavior to be calculated during a LOCA. These models include a fuel rod cladding swell and rupture deformation model, a fuel rod gap conductance model, and zircaloy-water reaction. The cladding swell and rupture deformation models are based on NUREG-0630,⁴⁴ which is an acceptable data source.

The gap conductance model in the RELAP5/MOD2 - B&W core model is similar to the model used in FRAP-T6-B&W⁴⁵ and approved for use in B&W licensing applications in Reference 46. The only difference between the RELAP5/MOD2 - B&W and FRAP-T6-B&W models is that RELAP5/MOD2 - B&W uses a simplified form of the FRAP-T6-B&W gap width model. The RELAP5/MOD2 - B&W model calculates a gap width different from FRAP-T6-B&W only when non-concentric rather than concentric fuel pellets are modeled. In a telephone conversation on November 8, 1989, B&W stated the fuel pellet model chosen for use in RELAP5/MOD2 - B&W depends on which model most accurately matches the fuel stored energy calculated by the steady state

fuel code. In addition, B&W stated that comparing the results of two RELAP5/MOD2 - B&W blowdown calculations that used the different fuel pellet models showed the end-of-blowdown conditions were essentially the same (fuel temperatures within about 2°F). Based on this information, the simplified model is considered adequate.

The zircaloy-water reaction model is based on the Baker-Just model⁴⁷ as required by Appendix K.

All these models are described in detail in Section 2.3.2 of the RELAP5/MOD2 - B&W manual.

RELAP5/MOD2 - B&W does not account for prerupture cladding swell in the thermal-hydraulic core flow calculation. Only if the cladding ruptures are the axial friction loss factors adjusted to account for the added flow resistance due to rupture. With respect to rupture, the rods in the hot assembly and the average core are treated the same. Babcock & Wilcox discussed its position on prerupture cladding swell in their response to Question 9, Reference 48, on the RSG LOCA EM. They stated the prerupture flow blockage is small (less than 20%) and results in a smooth area change that will not significantly add to the flow resistance. Babcock and Wilcox referenced data by Hardy⁴⁹ to justify this position. They stated any swelling during blowdown would be located near the high power elevations, and any flow diversion that might occur would be quickly recovered. The INEL reviewed additional data on zircaloy cladding behavior during ballooning and rupture in References 50 and 51. This data supports B&W's argument with respect to cladding behavior. This data showed prerupture cladding swell is limited because once cladding swell exceeded 10 to 20% the cladding rapidly expanded to the point of rupture. However, B&W did not provide analyses, test data, or reference material to support their argument that flow diversion effects for cladding swell of 20% or less are minimal. This must be resolved before neglect of prerupture cladding swell can be accepted. The question on flow diversion is also being considered in the INEL review of the RSG LOCA EM. Therefore, resolution of the concern about flow diversion effects for RELAP5/MOD2 - B&W, will be completed as part of the LOCA EM review. However, should B&W's response to the flow diversion question for the RSG LOCA EM review prove inadequate to

resolve this concern, RELAP5/MOD2 - B&W code changes may be required. Also, B&W would need to justify the acceptability of any licensing analyses where cladding swell exceeded 20% but rupture was not calculated.

2.3 Assessment Calculations

RELAP5/MOD2 - B&W was assessed against a LOFT small break experiment, Test L3-5,⁵² a Semiscale small break experiment, Test S-LH-1,⁵³ and a Semiscale large break experiment, Test S-04-6.⁵⁴ The LOFT small break assessment calculation will be discussed first followed by Semiscale Tests S-LH-1 and S-04-6.

2.3.1 LOFT Small Break L3-5

LOFT L3-5 was a 2.5% small break LOCA experiment with the pumps tripped at the initiation of the experiment. The break was located in the intact loop cold leg between the pumps and the vessel inlet nozzle. The calculation was run as a EM calculation. Therefore, EM models for break flow, core heat transfer, etc. were used. To try and approximate the measured system depressurization rate, a multiplier of 0.6 was used with the Moody two-phase critical flow model.

During the subcooled blowdown, the calculated system pressure decreased more slowly than the measured pressure. However, the calculated pressure decreased more rapidly than the measured pressure as the system approached saturated conditions. The two pressures are compared in Figure 3-2, Reference 9. Because the measured break flow during the subcooled blowdown is not available, it is not clear why the calculated system depressurization was slower than measured. However, B&W attributed the difference in saturated blowdown to differences in the calculated and measured break flows. The comparison of the calculated and measured break flows in Figure 3-1, Reference 9, confirms this as the calculated break flow after 60 s is higher than the data.

The calculated flow in the intact loop hot leg dropped much more rapidly than the measured flow (see Figure G.2-8, Reference 1). This was due to the pump in the RELAP5/MOD2 - B&W calculation coasting down more

rapidly than the pump in the test (Figure G.2-7, Reference 1). According to B&W, the reason for the difference in pump coastdown is not clear. In their response to question 3b, Reference 9, B&W stated the moment of inertia or the frictional torques of the pump and motor used in the analysis would need to be increased or decreased, respectively, by a factor of 4 to 5 in order to match the measured pump coastdown. The reported moment of inertia for the LOFT pump is 0.0001 that of a full-size RCP. Babcock & Wilcox stated this small a value is surprising in light of the LOFT scaling.

This difference between the calculated and measured pump coastdown is not considered critical to the overall analysis. The rest of the system parameters were adequately calculated in spite of the pump coastdown difference. Furthermore, B&W will not analyze SBLOCAs with the pumps running (see response to question 54d on the B&W LOCA EM methodology, Reference 48). In licensing SBLOCA analyses, the RCPs will coastdown early in the analysis and not play a significant part in the system response. Thus, not matching the pump coastdown in L3-5 is considered acceptable.

The flow comparison in Figure G.2-8 also shows that natural circulation was established once the pump coastdown was completed in both the calculation and the test. This occurred at approximately 35 s in the calculation and at 60 s in the test.

As shown in Figure 3-3, Reference 9, the system mass inventory is underpredicted during the entire transient. Before 60 s, this is probably due to overcalculating the break flow; but, the measured break flow during this time was not available. After 60 s, this was due to overpredicting the critical flow. The system mass distribution was adequately calculated as shown by Figures 3-4 and 3-5, Reference 9. The hot leg was calculated to drain at approximately the same time as in the experiment (Figure 3-4), and B&W stated the cold leg drained more rapidly in the calculation than in the test (Figure 3-5) due to the higher break flow.

These comparisons show that RELAP5/MOD2 - B&W was able to satisfactorily calculate the important phenomena in LOFT small break experiment L3-5.

2.3.2 Semiscale Test S-LH-1

Babcock & Wilcox assessed RELAP5/MOD2 - B&W using data from Semiscale Test S-LH-1. This test was chosen because it represented an integral test designed for PWR SBLOCAs where core uncover/recovery was encountered; also, it was a test where steam generator liquid holdup and consequent core uncover were observed. Two assessment calculations were completed for Test S-LH-1 using EM options, a base case calculation using single-phase and two-phase discharge coefficients of 1.0 and a sensitivity calculation where the single- and two-phase discharge coefficients were varied from 1.13 to 0.7. Other model changes were made in the sensitivity study to result in a better comparison between the calculated and measured results. These changes are discussed in more detail below. The base case calculation will be discussed first followed by the sensitivity calculation. All figures for the discussion on the base case and sensitivity calculations for Test S-LH-1 were taken from Reference 9.

For the base case calculation, RELAP5/MOD2 - B&W calculated well the U-tube level response in the intact and broken loop steam generators (Figures 5-5 to 5-8). During the loop seal clearing period, the calculated core level depression matched the test data well (Figure 5-13). As a result of using EM models, the calculated rod heatup, shown in Figures 5-19 and 5-20, exceeded the measured core heatup. The intact loop pump suction seal (Figures 5-9 and 5-10) was calculated to clear at approximately the same time as in the test. In the calculation, the broken loop pump suction seal (Figures 5-11 and 5-12) cleared at the same time as the intact loop seal, and, therefore, about 80 s before the broken loop pump suction seal in the test. Once the loop seals cleared, the fluid in the core began to boil off, and the core began to uncover in the experiment. Less core uncover was calculated than measured as shown in Figure 5-13. Due to the calculation of a more rapid depressurization after 200 s (see Figure 5-4), the accumulator setpoint was reached at 324 s in the calculation as opposed to 500 s in the test. With the early accumulator injection, the system mass inventory (Figure 5-14) and core collapsed level began to increase in the calculation before they did in the test. However, the depth of the second core uncover in the calculation was about the same as in the test, in spite of the early accumulator injection; therefore, the calculated peak

cladding temperature (PCT) exceeded the measured PCT by approximately 90°F due to the use of EM methods (Figures 5-19 and 5-20). The PCT was calculated using the SBLOCA EM methodology described in Reference 3.

Babcock & Wilcox addressed the faster depressurization in the base case calculation by changing the discharge coefficients in the sensitivity calculation discussed below. However, overall, the break flow rate comparison showed the break flow in the base case compared well to the measured flow.

The sensitivity calculation of Semiscale Test S-LH-1 was completed with a model that included a number of input changes. These included:

- a. Different discharge coefficients were used for subcooled (1.13), two-phase (0.79), and superheated steam discharge conditions (1.13).
- b. A special upper downcomer model to force the bypass of the intact loop high pressure safety injection (HPSI) to the broken loop to match the estimated break quality, vessel mass balance, and system mass balance in the test.
- c. Revised heat loss modeling. The system heat loss to the environment was reduced based on core and downcomer mass and energy balances during the core boiloff phase.
- d. The secondary boundary condition was revised to be based on the measured primary to secondary temperature difference rather than the measured secondary pressure.
- e. Changes to several junction connections.

Babcock & Wilcox stated the special upper downcomer model (change b above) was not applicable to full size PWR calculations. The model was required to adequately calculate Test S-LH-1 because the distance between intact and broken loop cold leg nozzles is much smaller in Semiscale than in a full size PWR. This would have the effect of enhancing the

possibility of bypass in Semiscale over a full size PWR and, therefore, required special treatment. Because this geometric difference between the Semiscale system and a full size PWR is real, INEL considers this adequate justification for not applying this model to B&W full size PWR calculations. The INEL notes the other major changes (a and c) are also not directly applicable to a full size PWR. Change a will be covered by the SBLOCA break size spectrum analysis. The heat loss change is only applicable to small scale facilities, where heat loss is a problem, not full size plants.

As a result of the above model changes, the RELAP5/MOD2 - B&W calculated system pressure, core collapsed level, and system mass inventory (Figures 5-4, 5-13, and 5-14) were in much better agreement with the test data during the core boiloff. The steam generator U-tube level response during the loop-seal clearing core level depression was about the same as the base calculation and both compared well to the measured data (Figures 5-5 to 5-8). The core collapsed level during the loop-seal clearing period was calculated to be slightly higher than the base calculation and the data as shown in Figure 5-13. Babcock & Wilcox attributed this to increased draining from the hot leg into the core during the reflux cooling period in the revised calculation (Reference 55). However, the core level was depressed below the top of the core during this period. The intact loop pump suction cleared first in the test and revised calculation and at approximately at the same time (Figures 5-9 and 5-10). The broken loop loop-seal cleared much later in the revised calculation than in the test (605 s versus 262 s) and the base calculation (605 s versus 180 s) as shown in Figures 5-11 and 5-12. Babcock & Wilcox attributed this to differences in broken loop steam generator heat transfer (Reference 55). The RELAP5/MOD2 - B&W output was used by B&W in a rod heatup calculation using the SBLOCA EM methodology mentioned above. This data showed the PCT in the revised calculation was approximately 65°F higher than the measured PCT (see Figure 5-19).

Overall, there are a number of differences between the calculated and measured results presented by B&W. However, because B&W's SBLOCA methodology is based on Appendix K and not best estimate calculations and because the overall method conservatively calculated the PCT, B&W has

demonstrated that RELAP5/MOD2 - B&W was able to adequately calculate the Semiscale system response to Test S-LH-1 based on the code's intended application.

2.3.3 Semiscale Test S-04-6

Semiscale Test S-04-6, was a large break LOCA experiment (200% double-ended offset shear cold leg break) conducted in the Semiscale Mod-1 test facility. Babcock & Wilcox performed two calculations for this assessment, a best estimate, base case calculation using RELAP5/MOD2, cycle 36.04, and a calculation using the options that would be used in an EM licensing calculation. The figures for the Test S-04-6 discussion were taken from Reference 7.

The pressure near the vessel side of the break for the two calculations is compared to the test data in Figure 12.4. This comparison shows the fastest depressurization was calculated by the EM calculation. This was expected because the EM models maximize the system mass depletion, and this maximizes the depressurization rate. The break flow comparison in Figure 12.14 shows that the calculated EM break flow was in fact larger than the RELAP5/MOD2 or the measured break flows from 5 to 15 s.

RELAP5/MOD2 also calculated a faster depressurization than the test data. The biggest difference in the RELAP5/MOD2 and measured depressurization rates occurred during the first 3 to 5 s and was due to the calculated subcooled break flow being greater than the measured break flow. However, once the the calculated and the test break flow transition to two-phase conditions, the calculated break flow agrees very well with the measured break flow. As a result, the depressurization in the RELAP5/MOD2 calculation after 5 s follows the trends of the data fairly well.

The oscillations in all the break flows after 15 s in Figure 12.14 were due to slugs of subcooled emergency core cooling system (ECCS) water moving from the cold leg to the break.

The comparisons of the calculated and measured mass flow rates in the intact loop cold leg and vessel showed good agreement. However, the calculated flow in the intact loop hot leg for both the best estimate and EM calculations underpredicted the measured flow during the first 10 s. Babcock & Wilcox stated (Reference 9, question 2c) this was due to overpredicting the pump side break flow which biased the vessel outlet flow to the broken loop. This caused the intact loop hot leg flow to be underpredicted. However, the calculated and measured intact loop cold leg flows compare well because the intact loop pump drained the pressurizer more rapidly in the calculation than in the experiment.

Comparison of measured and calculated densities at the two break locations and the core inlet showed some differences. At the core inlet, B&W stated (Reference 7, question 12) the two calculated densities were higher than the measured data due to lower heat transfer. At the vessel side of the break (Figure 12.23), the density calculated by the EM analysis overpredicted the density decrease as the cold leg transitions to two-phase conditions, but the EM calculated density increased so that the calculated and measured density compared well after 5 s. The best estimate calculation underpredicted the data from 3 to 10 s. No explanation was given for this difference. At the pump side of the break, according to B&W, the two calculated densities were different than the measured density due to differences between the calculated and measured pressures near this side of the break (Reference 7).

Babcock & Wilcox also compared the calculated and measured fluid temperatures in the system. These comparisons show differences consistent with the pressure differences found in Figure 12.4. For most of the comparisons, the calculated and measured liquid and vapor temperatures follow the system saturation temperature. At the core inlet and in the upper plenum, superheated steam was calculated and measured in the test; however, the amount of superheat was underpredicted by both calculations. This difference is at least partly attributable to the higher calculated rod temperatures in both calculations as discussed below.

Comparison of the EM calculated rod temperature for the high power rod hot spot to the best estimate calculation and the test data, shows the PCT

was significantly overpredicted by the EM model (Figure 12.33). The EM calculated PCT was approximately 1480°F, the best estimate PCT was 1210°F, and the hot rod PCT in the test was 1150°F. This difference was due to the early CHF calculated by the EM model compared to the best estimate calculation and the test data.

For the average power rods, the EM calculated rod temperature for the hot spot was also higher than the best estimate calculation and the test data (Figure 12.32) but the difference was not as great as for the high power rods. This difference was also due to the early CHF calculated by the EM model compared to the best estimate calculation and the test data. This overprediction of the temperatures in the average core is not considered a problem because B&W indicated in a telephone conversation on November 16, 1989 that the limiting PCT for the plants to be analyzed occurs during reflood. In this case, the overprediction of rod temperatures at the end-of-blowdown (EOB) is conservative because it increases the amount of energy to remove from the rods during reflood. However, should the limiting PCT be calculated during blowdown or a blowdown rupture occur, then B&W should verify that overpredicting average core temperatures, through its influence on core hydraulics, does not adversely affect the hot rod PCT calculation.

The highest temperature in Figure 12.32 is the temperature measured on Rod D8-27. This temperature on an average rod exceeded the highest temperature measured on the high power rods and about equaled the peak calculated hot rod temperature in the EM analysis. The similarity between the temperature response of rod D8-27 and the EM hot rod was due to the early CHF of the rod in the experiment and the EM hot rod. For the other rod temperatures in these figures, both calculated and measured, delayed CHF resulted in greater energy removal and lower rod temperatures.

Comparison of the EM and RELAP5/MOD2, Cycle 36.04, calculations showed slightly better cooling in the EM calculation after 12 s. Babcock & Wilcox stated (Reference 9, question 2f) this difference was due to the calculation of higher reverse core flow in the EM case as compared to the Cycle 36.04 case. As a result, the EM analysis calculated a higher heat transfer coefficient. The higher heat transfer coefficient

combined with the higher cladding temperatures of the EM analysis to result in a higher calculated heat flux and better cooling of the cladding relative to the Cycle 36.04 case.

In response to a question on how the PCT calculated by RELAP5/MOD2 - B&W would compare to the measured PCT if the calculated pressure more accurately matched the test data (question 2a, Reference 9), B&W provided the results of an analysis of Test S-04-6 where a discharge coefficient of 0.4 was used for two-phase critical flow. The calculated pressure for this analysis matched the test pressure much more closely than the analyses discussed above. A comparison of hot rod cladding temperatures showed the PCT for this calculation was less than the PCT for the earlier EM calculation, but it was still considerably higher than the measured hot rod PCT.

The data presented by B&W indicates RELAP5/MOD2 - B&W adequately calculates the phenomena associated with large break LOCAs. Conservative blowdown PCTs and end of blowdown temperatures were calculated with the EM model. The use of EM models resulted in the end-of-blowdown being calculated at approximately 18 s in the EM analysis versus 37 s in the test.

2.3.4 Assessment Summary

Based on the assessment results presented by B&W, RELAP5/MOD2 - B&W was able to adequately calculate the system response to both large and small break LOCAs. The comparisons also showed the code was able to calculate vapor superheat. Therefore, it is recommended the code be accepted for integral systems large and small break LOCA licensing analyses.

2.4 Phenomena Important to PWR SBLOCA

In this section, the code's ability to simulate the important phenomena during a PWR SBLOCA will be discussed. This includes its ability to represent a noncondensable gas; condensation heat transfer; and single-phase, two-phase, and reflux natural circulation.

2.4.1 Noncondensable Gas

The RELAP5/MOD2 - B&W hydrodynamic model has the capability to model the presence of a noncondensable gas along with the vapor and liquid phases of water. The noncondensable model in RELAP5/MOD2 - B&W is the same one used in RELAP5/MOD2 and discussed in Reference 2. However, B&W did not assess the noncondensable gas model in the code for the reasons discussed below.

Babcock & Wilcox stated (response to question 4b, Reference 10) that they would not include noncondensibles in their calculations because of the expected negligible effect on SBLOCAs. They stated the volume of noncondensable gases which can be trapped in the primary system during a SBLOCA is too small to impact overall system results. The following potential sources of noncondensable gases were included in B&W's analysis for breaks where the steam generators are needed for core cooling:

(1) gases dissolved in the primary coolant system and pressurizer, the charging system, and the refueling water; (2) fission and fill gas in fuel rods; (3) gases generated by the radiolytic decomposition of injected water; and (4) hydrogen released from metal-water reaction. Sources excluded by B&W included the nitrogen dissolved in the accumulator water and nitrogen cover gas in the accumulators. However, these are potential sources of noncondensable gas only for the larger SBLOCAs where the steam generators become a heat source. Babcock & Wilcox considered these sources for the larger SBLOCAs. Considering the first three sources above, B&W calculated the maximum amount of noncondensable released would be 117 ft³ at 1150 psia and 562°F. This amounts to 29 ft³ per steam generator or 5.7% of the steam generator tube volume/steam generator (assuming 10% tube plugging). Considering the first three sources plus hydrogen generated by 1% core wide oxidation, B&W calculated the maximum amount of noncondensable released would be 231 ft³ at 1150 psia and 562°F. This amounts to 58 ft³ per steam generator or 11% of the steam generator tube volume/steam generator (assuming 10% tube plugging).

Babcock & Wilcox divided SBLOCAs into two categories: those that rely on the steam generators for heat removal and those where the primary system depressurized to below the the secondary pressure. The applicable sources

of noncondensibles and their potential effects on the two SBLOCA categories are discussed below.

For smaller small breaks, noncondensable gases could have a significant effect because the system pressure is above the accumulator setpoint for a long time. For these break sizes, the steam generators must be maintained as a heat sink because energy removal through the break is insufficient to maintain the primary system pressure below the HPSI shutoff head. During the single- and two-phase natural circulation portions of this size SBLOCA, B&W included the amount of noncondensibles added to the primary system from sources 1, 2, and 3. Metal-water reaction was not included as a source because the core is covered by a single- or two-phase mixture in these modes of natural circulation. The worst case assumption for these modes of natural circulation is that all the noncondensable gases collect in the tube region. If the noncondensibles were pushed to the downflow side of the generator, the driving force for natural circulation would be reduced. However, the lower flow would cause greater heating of the fluid on the hot side that would compensate for the loss of cold side driving head. The system would settle into a slightly different condition but able to remove decay heat because the degradation in steam generator heat transfer in this situation is small.

For the reflux mode of cooling, B&W referred to Semiscale tests⁵⁶ and single-tube tests⁵⁷ that studied the effects of noncondensibles on reflux cooling. According to the Semiscale tests, up to 5% of the tube volume could be occupied by noncondensibles without seriously affecting reflux cooling. Therefore, for SBLOCAs without significant metal-water reaction (i.e., only sources 1 - 3 above are included), the Semiscale tests indicate no effect on steam generator performance. If all four sources are included, B&W calculated 11% of the tube volume could be occupied by noncondensibles at 1150 psia and 562°F. With this tube volume occupied by noncondensable gases, B&W concluded the effect of noncondensable gases is a reduction in condensation heat transfer due to reduced steam generator heat transfer area. However, the net result would be to stabilize at a slightly higher primary pressure (50 psi) than for the case without noncondensibles. Babcock & Wilcox noted this 50 psi increase above the steam generator control pressure of 1150 psia would not substantially

reduce the injection capabilities of the charging and safety injection (SI) systems. However, the performance characteristics of SI pumps vary widely in the plants the B&W LOCA EM will be used to analyze. Therefore, B&W should verify on a plant specific basis that neglecting the 50 psi pressure increase in the calculations will not reduce SI flow such that the PCT increases by more than 50°F. If the PCT should change by more than 50°F, additional information would be needed to justify continued neglect of noncondensibles in the analysis.

Therefore, for those SBLOCAs that rely on steam generator heat transfer for energy removal, the effect of noncondensibles are minimal and need not be considered directly in the analysis except as noted above.

For the larger breaks that depressurize to the accumulator setpoint, B&W noted that any effect of noncondensable gases present in the system would occur when the steam generators are a heat source and not relied on for heat removal. Therefore, the effects of noncondensable gases on these heat removal processes need not be considered (Reference 10, question 4b). The INEL notes this would include all possible sources of noncondensable gases (sources 1 to 4 and nitrogen dissolved in the accumulator water and nitrogen cover gas). Babcock & Wilcox (Reference 10, question 4b) considered the potential effects of releasing the accumulator nitrogen cover gas at a time when the system pressure stabilizes at a pressure just below the low pressure injection (LPI) pump dead head pressure. If the accumulators were to release the nitrogen at a critical time, increasing the system pressure and shutting off the LPI flow, the event severity could be increased. To account for this possibility, B&W noted that the charging and SI system have reached runout flow at 200 psia and that they are capable of removing all decay heat after 300 s (for a 3500 MW_t plant). Therefore, SBLOCAs that take longer than 300 s to depressurize to 200 psia do not require LPI injection to mitigate the event. For breaks that do not depressurize below 140 psia, B&W stated that accumulator gas discharge will not occur while the LPI is required for core cooling. For breaks that depressurize below 140 psia, B&W stated that there is sufficient break flow to vent the nitrogen and still remove core decay heat. Therefore, the system depressurization may be slowed but the system would not repressurize and LPI flow is unaffected.

Therefore, for those SBLOCAs that do not rely on steam generator heat transfer for energy removal, the effect of noncondensibles are minimal and need not be considered directly in the analysis.

The INEL reviewed B&W's work and agrees with its conclusion that the effect of noncondensable gases from sources 1 to 4 will be small on the class of breaks where they apply. Therefore, not including noncondensibles from these sources in RELAP5/MOD2 - B&W analyses is considered acceptable. Babcock & Wilcox noted that, for larger SBLOCAs where the steam generators become a heat source, the effects of noncondensable gases from whatever source need not be considered in the analysis. Finally, B&W showed the nitrogen cover gas in the accumulators will not impact larger SBLOCAs by increasing the system pressure enough to shut off LPI flow. Therefore, the effects of noncondensibles can be neglected, except where the noncondensable gases could cause a change in PCT greater than 50°F, in RELAP5/MOD2 - B&W SBLOCA EM analyses. However, it should be noted that the system volume occupied by noncondensable gases would increase as the system pressure and temperature decreased while the plant was cooled to shutdown cooling conditions. At 300 psia and 300°F, the noncondensable gas volumes discussed by B&W, 117 and 231 ft³, would increase to approximately 330 and 655 ft³, respectively. With the noncondensable occupying this much of the primary system, the effects of noncondensable gases on steam generator heat removal during the long term cooling analysis would need to be considered. As such, the assumptions regarding noncondensable gases for the short term are not applicable to the post-LOCA long term cooling analysis. Additional justification is required for the application of RELAP5/MOD2 - B&W to long term cooling analyses or the effects of noncondensable gases directly accounted for in the long term cooling analysis.

2.4.2 Condensation Heat Transfer

One of the areas of concern in modeling SBLOCAs that was identified in NUREG-0737, Item II.K.3.30, was the ability to accurately calculate condensation heat transfer rates. The need to confirm this feature of the small break model against applicable experimental data was recognized.

The condensation/vaporization models in RELAP5/MOD2 - B&W are identical to the models used in RELAP5/MOD2. These models are discussed in Section 2.1.3.4 of Reference 1. In assessing these models, B&W (Reference 10, question 4d) referred to a detailed review of the correlations and models in RELAP5/MOD2 performed by the INEL.⁵⁸ With respect to the interphase mass transfer models used to calculate condensation and vaporization, the INEL review in Reference 58 noted this was an area of active research, and the code models were an approximate representation of current understanding. While many of the models were considered ad hoc because better information was not available or because the information available is difficult to implement in the code, the INEL review in Reference 58 concluded the models were a reasonable, if incomplete, engineering approximation to interfacial heat transfer.

Babcock & Wilcox discussed (Reference 10, question 4d) RELAP5/MOD2 - B&W's ability to calculate vapor superheat. In the core, B&W noted the code's ability to calculate vapor superheat depends on both the wall heat transfer and interphase heat transfer. The wall heat transfer in the RELAP5/MOD2 - B&W core heat transfer model was reviewed in Section 2.2.2 and found acceptable. A paper by Lin et. al.,⁵⁹ was referenced by B&W to discuss the post-CHF interphase heat and mass transfer models. This paper showed RELAP5/MOD2 overpredicted the vapor superheat in high quality tests and underpredicted it in low quality tests. However, the paper also noted that some of the reported data for the low quality test may not have been accurately measured.

The assessment of RELAP5/MOD2 - B&W by B&W included an analysis of Semiscale large break Test S-04-6. This calculation (Reference 7, question 12) showed the code was able to calculate vapor superheat in the core during the last part of the blowdown. The amount of vapor superheat was less than the data, but this is at least partly attributable to the fact the calculated rod temperatures were considerably higher than the data. This means more energy remained in the rods in the calculation and less energy was available to heat the fluid.

In their response to question 4d, Reference 10, B&W noted that even if RELAP5/MOD2 - B&W does not calculate vapor superheat correctly, this will

have little impact on the calculation of the PCT. This is because in the B&W SBLOCA EM methodology only the core collapsed liquid level from RELAP5/MOD2 - B&W is used in the PCT calculation. This level is passed to FOAM2 for the calculation of mixture level and steaming rate. These parameters are then passed to FRAP-T6-B&W for the PCT calculation. In FRAP-T6-B&W, only steam cooling is allowed above the mixture level. This eliminates any cooling due to entrainment of liquid from the two-phase mixture in the core. Babcock & Wilcox provided an assessment of the overall SBLOCA EM methodology in their response to question 5, Reference 9. This assessment showed that the B&W methodology overpredicted the PCT in Semiscale small break Test S-LH-1 by approximately 65 to 90°F. Based on these considerations, the vaporization model in RELAP5/MOD2 - B&W is considered adequate.

The condensation model in RELAP5/MOD2 - B&W is also the same as the RELAP5/MOD2 base code. Developmental assessment of RELAP5/MOD2⁶⁰ was one of the references given by B&W (Reference 10, question 4d) to demonstrate the acceptability of the condensation models in RELAP5/MOD2 - B&W. These assessments using data by Bankoff⁶¹ and Aoki⁶² were reviewed and showed the condensation model provided reasonable results. Babcock & Wilcox stated their assessment work on LOFT Test L3-5 and Semiscale Tests S-04-6 and S-LH-1 also verified the adequacy of the condensation models in the code. The assessment calculation for Semiscale Test S-04-6 does not show unphysical behavior in the loop flow and cold leg pressure and temperatures during the accumulator injection period (see Figures 12.18, 12.19, 12.6, and 12.29, Reference 7). Similar observations were made by B&W for the SBLOCA assessments using Semiscale Test S-LH-1 and LOFT Test L3-5 (Figures 4.1 to 4.4, Reference 10). Therefore, the INEL considers the condensation model adequate for modeling ECC induced condensation.

With respect to the condensation that could occur on the primary side of the steam generator U-tubes, B&W (Reference 10, question 4d) referred to a study by Nithianandan, et al.,⁶³ that evaluated the code's ability to model surface condensation. This study used data from B&W single tube experiments and Massachusetts Institute of Technology pressurizer tests. The study concluded the surface condensation model was adequate. The study was reviewed and INEL agrees with the conclusions of the paper. This

indicates the code simulation of the condensation heat transfer in the steam generator U-tubes was adequate.

Based on the information provided by B&W, the condensation model in RELAP5/MOD2 - B&W is adequate for modeling RSG plant SBLOCAs.

2.4.3 Natural Circulation

NUREG-0737, Item II.K.3.30, also identified the need to experimentally and analytically verify the various modes of single-phase and two-phase natural circulation predicted to occur in each vendor's reactor during a SBLOCA.

To demonstrate RELAP5/MOD2 - B&W's ability to calculate natural circulation, B&W compared the calculated flow to the flow from integral experiments where the pumps were tripped. This included LOFT Test L3-5 and MIST data for single-phase natural circulation and Semiscale Test S-LH-1 for two-phase and reflux natural circulation (Reference 10, question 4c). For LOFT Test L3-5, the RELAP5/MOD2 - B&W model underpredicted the measured flow rate for the first 200 s during which single-phase natural circulation occurred. MIST data showed the code adequately calculated single-phase natural circulation.

For Semiscale Test S-LH-1, B&W noted the code was able to calculate two-phase and reflux natural circulation based on a comparison of the calculated liquid and vapor velocities in the U-tubes. In the calculation, B&W stated two-phase natural circulation began at approximately 80 s (at the end of pump coastdown) and lasted until approximately 120 s when countercurrent liquid and vapor velocities were calculated; reflux cooling began at that time. Although separate liquid and vapor velocities were not measured in the test, B&W presented test data to indicate that two-phase natural circulation and reflux cooling occurred in the test during the same time frames as the calculation. Babcock & Wilcox also concluded, based on the good system pressure and break flow comparisons during this time that the code adequately calculated the heat removal associated with two-phase natural circulation and reflux cooling; therefore, the natural circulation calculation was also good.

RELAP5/MOD2 - B&W was able to conservatively or adequately calculate single-phase natural circulation. Babcock & Wilcox also demonstrated the code calculated two-phase and reflux natural circulation under appropriate conditions and at times consistent with those where indirect evidence indicated two-phase and reflux natural circulation were occurring in Semiscale Test S-LH-1. These considerations indicate the code models are adequate to simulate natural circulation during RSG plant SBLOCAs.

2.5 Calculation of S-UT-8 Phenomena

Question 17 of Reference 4 requested B&W to validate the ability of RELAP5/MOD2 - B&W to calculate phenomena similar to that observed during Semiscale Test S-UT-8 and studied in later Semiscale experiments S-LH-1 and S-LH-2 (Reference 53). This included liquid holdup in the upside of the steam generator U-tubes and consequent core level depression. To demonstrate the codes's ability to calculate these phenomena, B&W analyzed Semiscale Test S-LH-1 as discussed in Section 2.3.2 of this report. The results of the Semiscale Test S-LH-1 assessment indicated RELAP5/MOD2 - B&W has the capability to calculate liquid holdup phenomena adequately.

2.6 Loop Seal Clearing Phenomena

The RELAP5/MOD2 interphase drag model tends to overpredict interphase drag. The RELAP5/MOD2 interphase drag model was retained unchanged in RELAP5/MOD2 - B&W. While this resulted in the adequate calculation of steam generator liquid holdup phenomena as discussed above, it is nonconservative for loop seal clearing phenomena. This is because the high drag tends to clear the loop seal of all liquid even in cases where the steam flow is not high enough to entrain the liquid and carry it out of the loop seal. As a result, core uncover and the PCT may not be accurately calculated in cases where the code predicts the loop seal cleared of liquid when liquid should have been retained.

Babcock & Wilcox noted that RELAP5/MOD2 - B&W tended to overpredicted level swell phenomena in the core in their response to question 59, Reference 48. This discussion defined the quiet water level passed to the FOAM2 code when core uncover is predicted. Babcock & Wilcox noted

RELAP5/MOD2 - B&W conservatively overpredicted frothing and resulted in too much liquid being carried from the core into the upper plenum, hot legs, and steam generator tube upflow. Therefore, B&W wanted to include this non-core liquid in the quiet water level passed to FOAM2. The INEL notes the same code models involved in the overprediction of frothing in the core will result in the inaccurate calculation of loop seal clearing.

A Finnish assessment of RELAP5/MOD2 against data taken in a full scale loop seal test facility showed the code calculated too much liquid being carried out of the loop seal.⁶⁴

W. Weaver, INEL, indicated that the Finns also assessed RELAP5/MOD3 against the loop seal clearing tests with only slight improvement. The RELAP5/MOD3 interphase drag models are being modified with the intent to better calculate the loop seal clearing tests.⁶⁵

Experimental evidence for partial loop seal clearing was observed in Semiscale small break Tests S-UT-8 and S-07-10D.⁶⁶ In addition, partial loop seal clearing, as well as, cyclic loop seal clearing followed by loop seal refill have been observed in some of the small break experiments conducted in the Japan Atomic Energy Research Institute's ROSA-IV Program Large Scale Test Facility (LSTF).⁶⁷⁻⁶⁹

The overprediction of drag can be addressed by both model changes and nodalization. The INEL believes that adequate nodalization of the loop seal can overcome this interphase drag model problem. Therefore, this problem will be resolved by requiring B&W to perform a loop seal nodalization sensitivity study as part of the review of the RSG LOCA EM. This study should show that the loop seal nodalization chosen by B&W for use in LOCA licensing calculations results in the highest PCT and that liquid is retained in the loop seal when steam flow conditions would result in liquid retention. Alternately, B&W could provide evidence to demonstrate RELAP5/MOD2 - B&W correctly calculates loop seal phenomena, including cases where liquid was retained in the loop seal for low steam flow conditions. However, should these approaches prove inadequate to resolve this concern, RELAP5/MOD2 - B&W code changes may be required along with assessing the code against several loop seal separate effect tests.

3. COMPLIANCE WITH NRC REQUIREMENTS

Appendix K to 10CFR50 specifies the required and acceptable features of any model used for LOCA licensing analyses. Additional NRC requirements also apply. No attempt will be made to try and address all of B&W's responses in this section, but those responses having a bearing on this licensing assessment or areas of potential concern will be addressed.

All requirements related to simulating the metal-water reaction were met. Babcock & Wilcox incorporated the Baker-Just model into RELAP5/MOD2 - B&W. The code has the capability to prevent the ruptured node from being less than 3 inches in length.

The fuel rod behavior requirements were met by incorporating fuel rod behavior models into the code. This included a dynamic gap conductance model and cladding swell and rupture models based on data from NUREG-0630.

The Moody Critical Flow model was incorporated into RELAP5/MOD2 - B&W. Therefore, it is available for the code user to meet the Appendix K requirement to calculate two-phase critical flow with this model. Appendix K also requires the break size and discharge coefficients be varied to determine the limiting break size, i.e. the break size yielding the highest PCT. The code is capable of varying both the break size and the discharge coefficient.

For LBLOCAs, Appendix K requires the ECC injected into the inlet lines or the reactor vessel during the bypass period be subtracted from the vessel inventory. In the RSG LOCA EM, B&W defined the end of bypass to be the same as the end of blowdown. During the blowdown period, when RELAP5/MOD2 - B&W is used to calculate the system response, ECC bypass is modeled by removing from the inlet annulus node the smaller of 110% of the ECC flow or 99% of all liquid residing in the inlet annulus node. Therefore, the code is capable of meeting this requirement.

To meet the CHF and core heat transfer requirements of Appendix K, B&W added a new core heat transfer algorithm. The algorithm uses Appendix K

recommended CHF and heat transfer correlations, correlations that were previously approved by the NRC, or widely used and accepted correlations.

The post-CHF heat transfer requirements of Appendix K specify return to nucleate boiling be locked out once CHF has occurred during blowdown and a return to transition boiling be locked out if cladding superheat exceeds 300°F during blowdown. Babcock & Wilcox added the appropriate logic to RELAP5/MOD2 - B&W to meet these requirements.

The centrifugal pump model in RELAP5/MOD2 - B&W is the same model used in RELAP5/MOD2. The RELAP5/MOD2 model has proven adequate for a wide variety of transients. The pump homologous curves used in the plant models were discussed in B&W's response to question 14 in Reference 48. The information provided showed the homologous curves to be used in the plant models are based on acceptable data sources.

The Appendix K requirement relating to the thermal-hydraulic interaction between the steam and the ECC water is met. This is because RELAP5/MOD2 - B&W is a two-fluid thermal-hydraulic code with the capability to treat the steam/ECC water interaction included in the basic fluid models. Analysis of LBLOCA and SBLOCA experiments by B&W and analysis of separate effects experiments referenced by B&W indicate these models adequately represent the steam/ECC water interaction.

Appendix K requires the effect of the compressed gas in the accumulator on the reflood rate be considered in LOCA licensing analyses. Because RELAP5/MOD2 - B&W is only used to calculate the blowdown portion of the LOCA, this requirement does not apply. For SBLOCAs, the code does not include models to calculate reflood heat transfer. However, the Appendix K requirement to include acceptable reflood heat transfer models only applies to computer programs used to analyze large break LOCA reflood conditions.

4. RELAP5/MOD2 CODE UPDATES

RELAP5/MOD2 - B&W was developed from the publicly released RELAP5/MOD2, cycle 36.04, code. During the development of RELAP5/MOD2 - B&W, RELAP5/MOD2 was updated to correct errors or to add model improvements. This resulted in the creation of cycles 36.05 and 36.06, where cycle 36.06 was the latest released version of the code. Approval of RELAP5/MOD2 - B&W included a review of the status of these updates.

In response to a question on the status of these updates in RELAP5/MOD2 - B&W, B&W stated (question 45, Reference 48) that all of the cycle 36.05 updates were incorporated into the code. The cycle 36.06 updates were not incorporated into RELAP5/MOD2 - B&W because those updates were specific to the CRAY version of RELAP5/MOD2; therefore, they are not applicable to RELAP5/MOD2 - B&W.

Therefore, RELAP5/MOD2 - B&W contains the error corrections from RELAP5/MOD2, cycles 36.05 and 36.06, that are applicable to the code. This ensures that known errors were corrected.

5. CONCLUSIONS

The RELAP5/MOD2 - B&W submittal by B&W was reviewed to determine the code's acceptability for use in PWR LBLOCA and SBLOCA licensing analyses. Based on this review, it is recommended the code be approved for use in LOCA licensing analyses with the following comments and restrictions:

1. Application of RELAP5/MOD2 - B&W to LOCA analyses is dependent on the approval of the B&W LOCA EM methodology being reviewed separately.
2. It is recommended that RELAP5/MOD2 - B&W be approved for use in integral systems LOCA licensing analyses. For LBLOCAs, this includes the calculation of the system blowdown response. For SBLOCAs, this includes the calculation of the system hydraulic response. The calculation of peak cladding temperature for LOCAs will be performed with BEACH⁷⁰ and FRAP-T6-B&W which were reviewed separately. It is recommended RELAP5/MOD2 - B&W be used to analyze the full spectrum of large and small breaks.
3. Babcock & Wilcox will not model noncondensable gases in its SBLOCA system analyses. They demonstrated that the effect on the overall system response from all sources of noncondensable will be negligible for the range of SBLOCAs they intend to apply the methods. However, B&W noted a 50 psi increase above the steam generator control pressure of 1150 psia could result from a worst case noncondensable release. Babcock & Wilcox also stated this would not substantially reduce the injection capabilities of the charging and SI systems. However, the performance characteristics of SI pumps vary widely in the plants the B&W LOCA EM will be used to analyze. Therefore, B&W should verify on a plant specific basis that neglecting the 50 psi pressure increase (resulting from noncondensable gas build up in the steam generator) in the calculations will not reduce SI flow such that the PCT would increase by more than 50°F. If the PCT should change by more than 50°F, additional information would be needed to justify continued neglect of noncondensables in the analysis. Babcock & Wilcox could analyze a pressure increase less than 50 psi if the smaller increase can be justified from the plant specific analysis.

4: The four modifications reviewed in Section 2.2 of this report are recommended for acceptance for use in LOCA licensing analyses with the following limitations:

- a. Babcock & Wilcox stated the CSO film boiling correlation added to the code in the core heat transfer model will not be used for licensing applications. Therefore, the CSO correlation was not reviewed and the correlation cannot be used in a licensing calculation without additional review and approval by the NRC.
- b. Based on information provided by B&W and additional information reviewed by INEL, prerupture cladding swell is limited because, once cladding swell exceeds 10 to 20%, the cladding rapidly expands to the point of rupture. However, B&W did not provide analyses, test data, or reference material to support their argument that flow diversion effects for cladding swell of 20% or less are minimal. This must be resolved before neglect of prerupture cladding swell can be accepted. The question on flow diversion is also being considered in the INEL review of the RSG LOCA EM. Therefore, resolution of the concern about flow diversion effects for RELAP5/MOD2 - B&W, will be completed as part of the LOCA EM review. However, should B&W's response to the flow diversion question for the RSG LOCA EM review prove inadequate to resolve this concern, RELAP5/MOD2 - B&W code changes may be required. Also, B&W would need to justify the acceptability of any licensing analyses where cladding swell exceeded 20% but rupture was not calculated.
- c. The LBLOCA assessments of the Extended Henry-Fauske and Moody critical flow models added to the code were based on the use of the static properties as input to the critical flow tables and use of Moody slip with the Moody model. The SBLOCA assessments of the same models were based on the use of the static properties as input to the critical flow tables and use of a slip ratio of one with the Moody model. These options must be used in large and small break LOCA licensing calculations, respectively, unless other options are justified in the plant specific submittal.

5. Babcock & Wilcox intends to apply RELAP5/MOD2 - B&W to a variety of Westinghouse three- and four-loop plants and Combustion Engineering (CE) three- and four-loop plants. The review found the code was not plant specific in nature. Therefore, RELAP5/MOD2 - B&W can be applied to any of the proposed Westinghouse and CE plants.

6. The RELAP5/MOD2 interphase drag model tends to overpredict interphase drag. The RELAP5/MOD2 interphase drag model was retained unchanged in RELAP5/MOD2 - B&W. This is nonconservative for loop seal clearing phenomena because the high drag tends to clear the loop seal of all liquid even in cases where the steam flow is not high enough to entrain the liquid and carry it out of the loop seal. As a result, core uncover and the PCT may not be accurately calculated in cases where the code predicts the loop seal cleared of liquid when liquid should have been retained. This overprediction of drag can be addressed by both model changes and nodalization. The INEL believes that adequate nodalization of the loop seal can overcome the shortcomings of the interphase drag model. Therefore, this problem will be resolved by requiring B&W to perform a loop seal nodalization study as part of the review of the RSG LOCA EM. This study should show that the loop seal nodalization chosen by B&W for use in LOCA licensing calculations results in the highest PCT and that liquid is retained in the loop seal when steam flow conditions would result in liquid retention. Alternately, B&W could provide evidence to demonstrate RELAP5/MOD2 - B&W correctly calculates loop seal phenomena, including cases where liquid was retained in the loop seal for low steam flow conditions. However, should these approaches prove inadequate to resolve this concern, RELAP5/MOD2 - B&W code changes and benchmarking may be required.

7. RELAP5/MOD2 - B&W overpredicted the average core cladding temperatures in the Test S-04-6 assessment calculation. This is not considered a problem because B&W indicated in a telephone conversation on November 16, 1989 that the limiting PCT for the plants to be analyzed occurs during reflood. In this case, the overprediction of rod temperatures at the EOB is conservative because it increases the amount of energy to remove from the rods during reflood. However,

should the limiting PCT be calculated during blowdown or a blowdown rupture occur, then B&W should verify that overpredicting average core cladding temperatures, through its influence on core hydraulics, does not non-conservatively affect the hot rod PCT calculation.

8. The B&W auxiliary feedwater model for once through steam generators, added to the RELAP5/MOD2 base code by B&W, was not reviewed for use in licensing calculations. Because it is B&W's intent to apply RELAP5/MOD2 - B&W to recirculating steam generator plants, this model was not reviewed at this time.
9. The built-in reactor kinetics data for decay heat calculations in RELAP5/MOD2 - B&W are based on the ANS 1973 and 1979 standards. Because Appendix K requires the use of 1.2 times the ANS 1971 standard for decay heat calculations in LOCA licensing analyses, B&W should ensure the decay heat used in licensing analyses complies with Appendix K.
10. While B&W showed the effects of noncondensable gases would be small at primary system pressures of 1150 to 1200 psia, the system volume occupied by noncondensable gases would increase as the plant was cooled to shutdown cooling conditions. At 300 psia and 300°F, the noncondensable gas volumes discussed by B&W, 117 and 231 ft³, would increase to approximately 330 and 655 ft³. With this increased volume of the primary system occupied by noncondensable gases, the effects of noncondensable gases on the long term cooling analysis would need to be considered. As such, the assumptions regarding noncondensable gases for the short term are not applicable to the post-LOCA long term cooling analysis. Additional justification is required for the application of RELAP5/MOD2 - B&W to long term cooling analyses or the effects of noncondensable gases directly accounted for in the long term cooling analysis.

11. In Reference 72, B&W supplied information on an error correction for the RELAP5/MOD2 - B&W calculation of the rupture K factor. The change was reviewed and the INEL agrees with B&W on the need for the correction. With the change, the code correctly calculates the rupture K factor.

6. REFERENCES

1. RELAP5/MOD2 - B&W: An Advanced Computer Program for Light Water Reactor LOCA and Non-LOCA Transient Analysis, BAW-10164P, Rev. 1, Babcock & Wilcox Nuclear Power Group, October 1988.
2. V. H. Ransom, et al., RELAP5/MOD2 Code Manual, NUREG/CR-4312, EGG-2396, August 1985.
3. B&W Loss-of-Coolant Accident Evaluation Model for Recirculating Steam Generator Plants, BAW-10168P, Rev. 1, Babcock & Wilcox Nuclear Power Group, September 1989.
4. W. Hodges, NRC, ltr to J. H. Taylor, B&W, "Request for Additional Information Regarding BAW-10164P, RELAP5/MOD2 - B&W," March 31, 1988.
5. W. Hodges, NRC, ltr to J. H. Taylor, B&W, "Request for Additional Information Regarding BAW-10164P, RELAP5/MOD2 - B&W," March 23, 1988.
6. J. H. Taylor, B&W, ltr to J. A. Norberg, NRC, "RELAP5/MOD2 - B&W Topical Report BAW-10164P," JHT/88-153, August 15, 1988.
7. J. H. Taylor, B&W, ltr to J. A. Norberg, NRC, "RELAP5/MOD2 - B&W Topical Report BAW-10164P," JHT/88-215, November 23, 1988.
8. J. H. Taylor, B&W, ltr to J. A. Norberg, NRC, "RELAP5/MOD2 - B&W Topical Report BAW-10164P," JHT/88-231, December 23, 1988.
9. J. H. Taylor, B&W, ltr to J. A. Norberg, NRC, "RELAP5/MOD2 - B&W Topical Report, BAW-10164P," JHT/89-95, May 11, 1989.
10. J. H. Taylor, B&W, ltr to J. A. Norberg, NRC, "RELAP5/MOD2 - B&W Topical Report BAW-10164P," JHT/89-149, July 20, 1989.
11. G. G. Loomis, "Semiscale Liquid Hold-Up Investigations: A Comparison of Results From Small Break LOCA Tests Performed in the Semiscale MOD-2A and MOD-2C Facilities," 13th Water Reactor Safety Information Meeting, Gaithersburg, MD, October 22-25, 1985.
12. F. J. Moody, "Maximum Flow Rate of a Single-Component, Two-Phase Mixture," ASME Paper 64-HT-35, 1964.
13. R. E. Henry and H. K. Fauske, "The Two-Phase Critical Flow of One-Component Mixtures in Nozzles, Orifices, and Short Tubes," ASME Journal of Heat Transfer, 93, Series C, No. 2, 179, May 1971.
14. J. W. Murdock and J. M. Bauman, "The Critical Flow Function for Superheated Steam," Journal of Basic Engineering, Transactions of ASME, September 1964.
15. F. W. Dittus and L. M. K. Boelter, "Heat Transfer in Automobile Radiators of the Tubular Type," Publications in Engineering, University of California, Berkeley, 2, pp. 443-461, 1930.

16. W. M. Rohsenow and H. Y. Choi, Heat, Mass, and Momentum Transfer, Prentice-Hall, Inc., 1961, p. 166.
17. J. M. Delhaye, M. Giot, and M. L. Reithmuller, Thermohydraulics of Two-Phase Systems for Industrial Design and Nuclear Engineering, Hemisphere Publishing Corporation, 1981, pp. 261-262.
18. J. G. Collier, Convection Boiling and Condensation, London: McGraw-Hill Book Company, Inc., 1972.
19. J. C. Chen, "A Correlation for Boiling Heat Transfer to Saturated Fluid in Convective Flow," Process Design Development, 5, 1966, pp. 322-327.
20. J. R. S. Thom, et al., "Boiling in Subcooled Water During Flow Up Heated Tubes or Annuli," Proceeding of Institute of Mechanical Engineers, 3C180, 1966.
21. V. H. Schrock and L. M. Grossman, Forced Convection Boiling Studies, Final Report on Forced Convection Vaporization Project, TID-14632, 1959.
22. Babcock & Wilcox Revisions to THETA1-B, A Computer Program for Nuclear Reactor Core Thermal Analysis (IN-1445) - Revision 3, BAW-10094, Rev. 3, February 1981.
23. C. O. Thomas, NRC, ltr to J. H. Taylor, B&W, "Acceptance for Referencing of Licensing Topical Report BAW-10094, Revision 3, Babcock & Wilcox Revisions to THETA1-B, A Computer Program for Nuclear Reactor Core Thermal Analysis (IN-1445)," May 1985.
24. W. H. Jens and P. A. Lottes, Analysis of Heat Transfer, Burnout, Pressure Drop, and Density Data for High-Pressure Water, ANL-4627, May 1951.
25. Correlation of Critical Heat Flux in a Bundle Cooled by Pressurized Water, BAW-10000, March 1970.
26. R. H. Wilson, D. A. Farnsworth, and R. H. Stoudt, BWC Correlation of Critical Heat Flux, BAW-10143-A, Babcock & Wilcox, April 1985.
27. D. A. Farnsworth and G. A. Meyer, BWCMV Correlation of Critical Heat Flux in Mixing Vane Grid Fuel Assemblies, BAW-10159P, Babcock & Wilcox, May 1986.
28. C. O. Thomas, NRC, ltr to J. H. Taylor, "Acceptance for Referencing of Licensing Topical Report BAW-10143P, Parts 1 and 2," June 1, 1984.
29. A. Thadani, NRC, ltr to J. H. Taylor, "Acceptance for Referencing of Licensing Topical Report BAW-10159P, BWCMV Correlation of CHF in Mixing Vane Grid Fuel Assemblies, May 1986," February 17, 1989.

30. P. G. Barnett, A Correlation of Burnout Data for Uniformly Heated Annuli and Its Use for Predicting Burnout in Uniformly Heated Rod Bundles, AEEW-R463, September 1966.
31. E. D. Hughes, A Correlation of Rod Bundle Critical Heat Flux for Water in the Pressure Range 150 to 725 psia, IN-1412, July 1970.
32. R. V. Macbeth, Burn-out Analysis Part 4: Application of a Local Conditions Hypothesis to World Data for Uniformly Heated Round Tubes and Rectangular Channels, AEEW-R267, August 1963.
33. C. T. Avedisian, Critical Heat Flux in Countercurrent Flow, M. S. Thesis Massachusetts Institute of Technology, 1974.
34. J. B. McDonough, W. Milich, and E. C. King, Partial Film Boiling with Water at 2000 psia in a Round Tube, Technical Report 62, MSA Research Corporation, 1958.
35. G. L. Yoder, Rod Bundle Film Boiling and Steam Cooling Data Base and Correlation Evaluation, NUREG/CR-4394, ORNL/TM-9628, August 1986.
36. J. C. Chen, R. K. Sundaram, and F. T. Ozkaynak, A Phenomenological Correlation for Post-CHF Heat Transfer, NUREG-0237, June 1977.
37. S. W. Webb and J. C. Chen, Assessment of Post-Critical Heat Flux Models with Lehigh Nonequilibrium Data, NUREG/CR-4353, April 1986.
38. S. W. Webb and J. C. Chen, "Inferring Nonequilibrium Vapor Conditions in Convective Film Boiling," Second International Topical Meeting on Nuclear Reactor Thermal-Hydraulics, Santa Barbara, California, January 11-14, 1983, Thermal-Hydraulics of Nuclear Reactors, Volume 1, pp. 326-334.
39. S. W. Webb and J. C. Chen, "A Two-Region Vapor Generation Rate Model for Convective Film Boiling," First International Workshop on Fundamental Aspects of Post-Dryout Heat Transfer, Salt Lake City, Utah, April 2-4, 1984, pp. 485-508.
40. J. C. Chen, R. K. Sundaram, and K. L. Chen, Analysis of Babcock & Wilcox Data on Film Boiling Heat Transfer, Report TS-811, Lehigh University, March 1, 1981.
41. D. M. McEligot, L. W. Ormond, and H. C. Perkins, "Internal Low Reynolds Number Turbulent and Transitional Gas Flow with Heat Transfer," Journal of Heat Transfer, 88, 1966, p. 239.
42. H. Kumamaru, et al., "Investigation of Uncovered-Bundle Heat Transfer Under High-Pressure Boil-Off Conditions," Nuclear Engineering and Design, 96, 1986, pp. 81-94.
43. K. H. Sun, J. M. Gonzalez, and C. L. Tien, "Calculation of Combined Radiation and Convection Heat Transfer in Rod Bundles Under Emergency Cooling Conditions," Journal of Heat Transfer, Transactions of ASME, 98, 1976, p. 414.

44. D. A. Powers and R. O. Meyer, Cladding Swelling Models for LOCA Analysis, NUREG-0630, April 1980.
45. J. H. Jones, FRAP-T6-B&W -- A Computer Code for the Transient Analysis of Light Water Reactor Fuel Rods, BAW-10165P, Rev. 1, October 1988.
46. A. Thadani, NRC, ltr to J. H. Taylor, B&W, "Acceptance for Referencing of Licensing Topical Report BAW-10165P, FRAP-T6-B&W - A Computer Code for the Transient Analysis of Light Water Reactor Fuel Rods," May 19, 1989.
47. L. Baker and L. C. Just, Studies of Metal-Water Reactions at High Temperatures, III. Experimental and Theoretical Studies of the Zirconium-Water Reaction, ANL-6548, May 1962.
48. J. H. Taylor, B&W, ltr to J. A. Norberg, NRC, "RSG LOCA Topical Report, BAW-10168P," JHT/89-66, March 31, 1989.
49. D. G. Hardy, "High-Temperature Rupture Behavior of Zircaloy Tubing," CONF-730304, USAEC/TIC, Water-Reactor Safety, March 1973.
50. H. M. Chung, et al., "III. Mechanical Properties of Zircaloy Containing Oxygen," Light-Water-Reactor Safety Research Program: Quarterly Progress Report, January - March 1976, ANL-76-49, pp. 34-59.
51. F. J. Erbacher and S. Leistikow, "Zircaloy Fuel Cladding Behavior in a Loss-of-Coolant Accident: A Review," ASTM STP 939, 1987, pp. 451-488.
52. L. T. L. Dao and J. M. Carpenter, Experimental Data Report for LOFT Nuclear Small Break Experiment L3-5/L3-5A, NUREG/CR-1695, EGG-2060, November 1980.
53. G. G. Loomis and J. E. Streit, Results of Semiscale Mod-2C Small Break (5%) Loss-of-Coolant Accident Experiments S-LH-1 and S-LH-2, NUREG/CR-4438, EGG-2424, November 1985.
54. H. S. Crapo, et al., Experimental Data Report for Semiscale MOD-1 Tests S-04-5 and S-04-6 (Baseline ECC Tests), TREE-NUREG-1045, January 1977.
55. Personal communication with J. Klingenfus, B&W, June 21 and 27, 1989.
56. G. G. Loomis, Summary of the Semiscale Program (1965-1986), NUREG/CR-4945, EGG-2509, July 1987, pp. 196-199.
57. D. Hein, R. Rippel, and P. Weiss, "The Distribution of Gas in a U-Tube Heat Exchanger and its Influence on the Condensation Process," International Heat Transfer Conference, Munich, Germany, September 1982.
58. R. A. Dimenna, et al., RELAP5/MOD2 Models and Correlations, NUREG/CR-5194, EGG-2581, August 1988.

59. J. C. Lin, et al., "RELAP5/MOD2 Post-CHF Heat and Mass Transfer Models," International Workshop on Fundamental Aspects of Post-Dryout Heat Transfer, Salt Lake City, Utah, April 1-4, 1984.
60. V. H. Ransom, et al., RELAP5/MOD2 Code Manual, Volume 3: Developmental Assessment Problems, EGG-TFM-7952, December 1987..
61. I. S. Lim, et al., Concurrent Steam/Water Flow in a Horizontal Channel, NUREG/CF-2289, August 1981.
62. S. Aoki, et al., "Direct Contact Condensation of Flowing Steam onto Injected Water," Sixth International Heat Transfer Conference, Toronto, Canada, August 7-11, 1978, Hemisphere Publishing Corporation, Washington, D.C., 1978, paper NRR19, pp. 107-112.
63. C. K. Nithianandan, et al., "RELAP5/MOD2 Models for Surface Condensation in the Presence of Noncondensable Gases," Eighth International Heat Transfer Conference, San Francisco, California, 1986, Hemisphere Publishing Corporation, pp. 1627-1633.
64. P. Vuorio and H. Tuomisto, "Assessment of RELAP5 and SMABRE Phase Separation Models Against Full-Scale Loop Seal Experiments," Third International Topical Meeting on Nuclear Power Plant Thermal Hydraulics and Operation, Seoul, Korea, November 14-17, 1988.
65. Private communication with W. Weaver, INEL.
66. Experimental Data Report for Semiscale MOD-3 Small Break Test S-07-10D (Baseline Test Series), NUREG/CR-1641, EGG-2065, December 1980.
67. Y. Kukita, et al., "Intentional Coolant System Depressurization: Experimental Studies in the ROSA-III and ROSA-IV Programs," CSNI Specialist Meeting on Intentional Coolant System Depressurization, Garching, Federal Republic of Germany, June 12-14, 1989.
68. K. Tasaka, et al., "The Results of 0.5% Small Break LOCA in ROSA-IV LSTF Break Location Parameter Test Series," Proceeding of the 15th Water Reactor Safety Information Meeting, Gaithersburg, MD, 1987.
69. K. Tasaka, et al., "Loop Seal Clearing and Refilling During a PWR Small Break LOCA," Proceeding of the 16th Water Reactor Safety Information Meeting, Gaithersburg, MD, October 24-27, 1988.
70. BEACH: Best Estimate Analysis Core Heat Transfer, A Computer Program for Reflood Heat Transfer During LOCA, BAW-10166P, Rev. 2, Babcock & Wilcox Nuclear Power Group, September 1989.
71. J. H. Taylor, B&W, ltr to V. Wilson, NRC, "RELAP5/MOD2 Topical Report, BAW-10164P," JHT/90-9, January 30, 1990.
72. J. H. Taylor, B&W, ltr to V. Wilson, NRC, "RELAP5/MOD2 Topical Report, BAW-10164P," JHT/90-8, January 30, 1990.

5.4 Responses to Request for Additional Information on Revision 2

This section contains questions transmitted to BWNT by R. C. Jones of the NRC in his letter of October 1993, and responses transmitted by BWNT to the NRC in a letter from J. H. Taylor (JHT/93-279) dated November 16, 1996.

BWNT Response to NRC's Request for Additional Information on BAW-10164, Revision 2, August 1992

Question 1 - Page 2.1-52.3

Please explain any differences between the interphasic friction model for slug flow (equation 2.1.3-30.7, p. 2.1-52.3) used in RELAP5/MOD2 B&W and BEACH. In particular, the multiplier on the Taylor bubble term appears to be different. Also, is smoothing of drag for the junction performed differently? Give the physical basis for any differences in the models.

Response: The interphase friction model for slug flow, given by Equation 2.1.3-30.7 on page 2.1-52.3 of the RELAP5 topical report (BAW-10164, Revision 2, August 1992) is the same as Equation 2.1.3-33 on page 2.1-34 of the currently-approved BEACH topical report (BAW-10166, Revision 3, October 1990). As stated on page 2.1-52.3 of the RELAP5, Revision 2, report, the Taylor bubble multiplier, C_{wsl} , is set equal to one. Accordingly, the multiplier was set to one in the ORNL (Appendix H) and ROSA-IV (Appendix J) benchmarks.

In Revision 4 of the BEACH topical report, a multiplier, $C_{o_{sl}}$, was added to the Taylor bubble term in Equation 2.1.3-33 on page 2.1-35. Its value is set to 0.25 when the "NEWQUEN" option, which selects the BEACH, Revision 4, reflood options, is selected. BEACH predicted the proper void distribution below the quench front with this constant value, 0.25, for the reflood tests described in Revision 4 of the topical. On the other hand, the ORNL benchmarks show that RELAP5, with C_{wsl} set to one, predicts the proper core void distribution for SBLOCA conditions.

In RELAP5, Revision 2 (and retained in Revision 3), an option was added to the Wilson drag model to modify the base RELAP5 drag smoothing in user-specified junctions (see pages 2.1-52.3 and 2.1-52.4). Exercising the RELAP5, Revision 2, option effectively removes base RELAP5 smoothing from user-selected junctions. At present, the option is only used in SBLOCA applications.

During SBLOCA transients, when the mixture level is in the upper plenum (during the hot leg draining period and the period preceding core uncover), RELAP5, using the Revision 2 option, predicted the expected void distribution in the upper core and plenum regions, including the discontinuous void behavior at the core-upper plenum boundary. With the base RELAP5 smoothing method, the code tended to flatten the void profile in the upper core region as shown in Figure 2.1.3-3.1 on page 2.1-52.4. When the mixture level is within the core region, RELAP5 calculated the proper void distribution with the base smoothing method. The RELAP5, Revision 2, option is recommended for use in the core-upper plenum interface junctions and in upper plenum junctions for SBLOCA applications. The option is considered part of the SBLOCA evaluation model, BAW-10168, Revision 2, Volume II, October 1992.

Question 2 - Appendix H

In Appendix H, Figure H.1, the outlet junction from the core is labeled as a BRANCH component, but no volume is associated with the component. In RELAP5 MOD2, the BRANCH component has a volume. Has this been changed in RELAP5 MOD2 B&W? Also, please explain the junction shown entering the time dependent volume representing the lower plenum.

Response: There has been no change in RELAP5/MOD2 with respect to designation of BRANCH components as volumes. Figure H.1 is unclear; a revised figure showing this component as a volume is given below. The junction entering the time-dependent volume is not in the model. This has also been corrected in the attached figure.

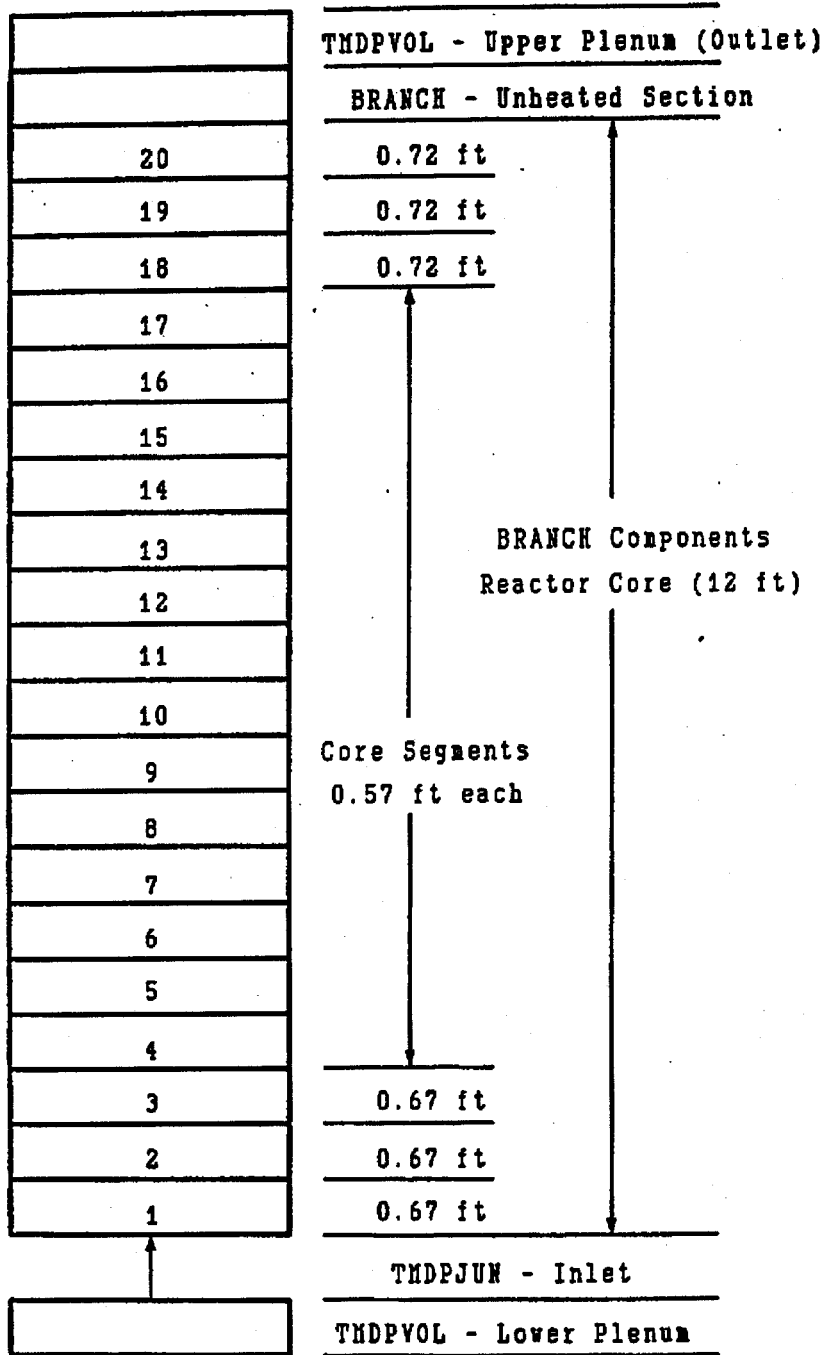


Figure H.1. RELAP5 Model of Hypothetical Reactor Core.

Question 3 - Appendix H, Figures H.28 to H.33

In Figures H.28 through H.33 the vapor temperature is consistently overpredicted by RELAP5 MOD2 B&W. Yet if it were not for the dip in surface temperature caused by the grid effect, the surface temperature would be underpredicted for experiments 3.09.10 i, j, l, and m. This would seem to indicate that the heat transfer coefficient to the vapor predicted by RELAP5 is high and non-conservative. If the vapor temperature were predicted correctly, the fuel surface temperature would be underpredicted. Please discuss the comparisons to the test data and show that these comparisons do not depend on systematically underpredicting the vapor temperature.

Response: The ORNL tests in Appendix H are quasi-steady or steady-state experiments. As such, the energy transfer to the fluid is equal to the decay heat in the test rods, so the heat transfer to the vapor will be the same irrespective of the decrease in the clad temperature at the grid location. Therefore, surface temperatures at locations removed from the grid site are not perturbed by the presence of the grid for tests 3.09.10i, j, l, and m.

The heat transfer coefficient for single-phase vapor is computed using the McEligot-plus-radiation correlation set for both large and small break LOCA. Its use is documented in the approved BWNT evaluation model (BAW-10168, Revision 1, September 1989). The correlation and its implementation are detailed in the approved RELAP5 and FRAP-T6 code topical reports, BAW-10164, Revision 1, October 1988 and BAW-10165, Revision 1, October 1988, respectively. Additional discussion is also presented in the response to Question 8 on the RELAP5 topical report (see BAW-10164, Revision 2, August 1992, pages 5-22 and 5-23), and in the Technical Evaluation Report (TER) for the approved RELAP5 report (see BAW-10164, Revision 2, August 1992, pages 5-219 and 5-220). The response to Question 8 and the TER both document the widely accepted use of the McEligot-plus-radiation correlation set for the calculation of steam cooling in LOCA applications.

The accurate measurement of vapor temperature, using thermocouples in the presence of unheated structures, is difficult at best. ORNL used two methods to obtain vapor temperatures. The first method

consisted of a numerical averaging of the fluid thermocouple measurements within the test assembly. The thermocouples were mounted on four unheated rods used to simulate guide tubes. Because of the proximity of the thermocouples to unheated walls, the measured vapor temperatures were necessarily lower than those next to the hot rods in the test assembly. The second method comprised an energy balance based on assembly power distribution. The method used the bundle thermocouples mounted downstream of the test assembly as an exit condition. Again, thermocouple placement was next to an unheated structure, the top of the test assembly. It is unclear which method was used in the ORNL report³¹, but either would tend to substantially underpredict the vapor temperature surrounding the hot pin. Experimental vapor temperatures around the hot rod would be expected to be substantially the same as those predicted by RELAP5.

Based on the discussion above, BWNT believes that RELAP5-predicted vapor temperatures are appropriate for use in SBLOCA applications. Furthermore, from the ROSA-IV benchmark, comparisons of the predicted and experimental clad heatup rates during the core boildown period (see BAW-10164, Revision 2, August 1992, Figures J.34 through J.36), confirms that the McEligot-plus-radiation correlation set is properly implemented and suitable for use in SBLOCA licensing calculations.

³¹ Anklam, T. M., et al., "Experimental Investigations of Uncovered-Bundle Heat Transfer and Two-Phase Mixture-Level Swell under High-Pressure Low Heat-Flux Conditions," NUREG/CR-2456, ORNL-5848, March 1982.

Question 4 - Table H.2

The column headings for the pressure and the power density appear to be reversed. Please review this table and make the necessary corrections.

Response: The pressure and power density headings in Table H.2 were indeed inadvertently reversed. The corrected table is given below.

Table H.2. ORNL Thermohydraulics Test Facility (THTF) Benchmark Cases.

Case	Experiment	Power Density (kw/ft)	Pressure (psia)	Mass Flux (lbm/hr/ft ²)
13	3.09.10i	0.68	650	21943.9
14	3.09.10j	0.33	610	9333.4
15	3.09.10k	0.10	580	2306.5
16	3.09.10l	0.66	1090	21461.4
17	3.09.10m	0.31	1010	9313.0
18	3.09.10n	0.14	1030	3395.2
19	3.09.10aa	0.39	590	14938.7
20	3.09.10bb	0.20	560	6961.9
21	3.09.10cc	0.10	520	3706.1
22	3.09.10dd	0.39	1170	14615.7
23	3.09.10ee	0.19	1120	8111.9
24	3.09.10ff	0.08	1090	3561.1

Question 5 - Pages 2.3-83 and I-5

The equation used to compute the critical heat flux stated in Section 2.3.3, Equation 2.3.3-41.1 (q_{crit}) is different than that given by Equation I-1 in Appendix I (CHF). Differences are noted in the a_3x_3 and a_4x_2 terms of Equation 2.3.3-41.1. In addition, the Tong correction factor is missing from Equation 2.3.3-41.1. Please reconcile these differences.

Response: Equation I-1 contains typographical errors; the "ax" terms should be identical to those in Equation 2.3.3-41.1. Equation I-1 should read:

$$CHF = \frac{FLS(a_0 + a_1x_1 + a_2x_2 + a_3x_3 + a_4x_1^2 + a_5x_2^2 + a_6x_3|x_3| + a_7x_1x_2 + a_8x_1x_3 + a_9x_2x_3 + a_{10}x_1^3 + a_{11}x_2^3 + a_{12}x_3^3 + a_{13}x_1x_2x_3)}{F}$$

The Tong factor is not missing from Equation 2.3.3-41.1; it has been set equal to one as stated on the top of page I-6. Implementation of the Tong factor in this manner was previously approved for the BWCMV CHF correlation as documented in both the RELAP5 and FRAP-T6 approved topical reports, BAW-10164, Revision 1, October 1988 and BAW-10165, Revision 1, October 1988, respectively.

Question 6 - Pages 2.3-83 and I-5

The equation used to compute the spacer grid factor stated as part of Equation 2.3.3-41 is different than that given by Equation I-2 in Appendix I. Differences are noted in the C_4LS and C_5L^2 terms in Equation 2.3.3-41. Please reconcile these differences.

Response: Equation I-2 contains typographical errors; it should be identical to the "FLS" term in Equation 2.3.3-41. Equation I-2 should read:

$$FLS = C_1 + C_2L + C_3S + C_4LS + C_5L^2 + C_6S^2.$$

Question 7 - Pages 2.3-83.1 and I-5

There appears to be a problem with units reconciliation for the X_1 and X_2 terms on pages 2.3-83.1 and I-5. Substituting the English to SI Conversion Factors from Table 2.3.3-1 yields the following:

$$X_1 = e \left[\frac{P(\text{psia})}{1000 \times 6894.757 \frac{\text{Pa}}{\text{psia}}} \right]$$

$$X_2 = \frac{G(\text{lb/hr-ft}^2)}{10^6 \times 1.356 \times 10^{-3} \frac{\text{kg/m}^2\text{-s}}{\text{lbm/hr-ft}^2}}$$

Note that the English pressure and flow units do not cancel. Please recheck these equations. Also, please explain the factors of 1000 and 10^6 in these equations.

Response: On pages 2.3-83.1 and I-5, the units for pressure, P, and mass flux, G, in the BWUMV CHF correlation are incorrectly stated as psia and lbm/hr-ft², respectively. The correct unit for pressure is Pa and kg/s-m² for mass flux. The 1000 factor in the X₁ equation is a pressure normalization factor having units of psia. The 10⁶ factor in the X₂ equation is a mass flux normalization factor having units of lbm/hr-ft². Both X₁ and X₂ are non-dimensional quantities.

Question 8 - Appendix J

Please describe the modeling which alters the geometry of the steam generator outlet piping by modifying the vertical angle from 50 degrees to 14 degrees in more detail. Does this affect the volume, length or flow area of any component? Is this modification necessary to model reflux boiling?

Response: This modeling change was made to implement the RELAP5 horizontal stratification model which considers stratified conditions in horizontal components with an inclination angle less than 15 degrees. To facilitate drain-back during the loop draining/reflux cooling phases of an SBLOCA transient, the steam generator inlet piping components (volumes 208-2 and 408-2) were changed to horizontal components with inclination angles of 14 degrees. The reduction in vertical elevation due to the inclination angle change is compensated for in the steam generator inlet plenum (volumes 212 and 412) such that the total elevation change from the hot leg piping to the bottom of the steam generator tube sheet is preserved. This also preserves the overall system hydrostatic head, which is an important first-order effect in SBLOCA transients. Thus, the model change does not alter the transient characteristics of the SBLOCA. The other component geometries such as volume, volume length, volume flow area, and flow resistance are not altered. The modification prevents excessive liquid holdup in the upflow side of the steam generator,

and is necessary to properly simulate reflux boiling and tube draining as demonstrated in the results of the benchmark analysis.

Question 9 - Appendix J

On page J-7, it is stated that the non-equilibrium model is used, except in the core region. We understood that in RELAP5 MOD2, equilibrium nodes cannot be connected to non-equilibrium nodes. Has the code been altered to allow this modeling approach? If so, please give the details of this code change.

Response: RELAP5 has not been modified. Since its release, MOD2 has been fully capable of connecting equilibrium and non-equilibrium nodes. The ROSA-IV facility was benchmarked using equilibrium core nodes so as to replicate BWNT's currently approved SBLOCA EM core modeling (BAW-10168, Revision 1, Volume II, September 1989). Equilibrium core noding is also used in the approved LBLOCA evaluation model (BAW-10168, Revision 1, Volume I, September 1989), and is retained in recent SBLOCA and LBLOCA revisions to the evaluation model, BAW-10168, Revision 2, October 1992 and BAW-10168, Revision 3, October 1993, respectively.

Question 10 - Appendix J

In the Appendix J benchmark, the accumulator flow is stated to be (page J-11) "conservatively less than that of the experiment". Is this a result of the code prediction or was the accumulator modeled to achieve this result? With accumulator injection significantly less than that of the test, how does the benchmark demonstrate that the predictions of key variables, such as fuel surface temperature, are accurate? If the actual accumulator flow were used, this could result in the prediction of additional cooling and lower fuel temperatures.

Response: The accumulator was not modeled to underpredict its flow rate. BWNT experience with SBLOCA analysis has shown the need to increase accumulator line resistances, typically by factors up to 100, to mitigate high initial accumulator flow induced instabilities--flow oscillations and unphysical thermalhydraulic

behavior--in volumes downstream of the injection location. The added resistance, however, does not impact accumulator performance during the core uncover period--the period of interest--since, in general for SBLOCA, the pressure drop between accumulator and reactor coolant system remains small, 4 psi for the ROSA-IV benchmark during the cladding temperature excursions. A case with unaltered line resistance shows accumulator flows being oscillatory but on average comparable to the benchmark case (increased resistance) during the period of interest (see Figure 10-1, attached herein); Figure 10-2 demonstrates the lack of impact on clad temperature heatup. The resistance change has no consequential effect on peak cladding temperature.

In the ROSA-IV benchmark, accumulator injection is not substantially underpredicted during the important core uncover period. Major events and system response are calculated in good agreement with the experiment. Slopes on clad temperature curves (Figures J.35 and J.36) are properly predicted, demonstrating appropriate heat transfer during core boil-off. There is no concern regarding the predicted accuracy of key variables.

Use of actual accumulator flow would not cause the clad temperature to be underpredicted. The benchmark shows cladding temperatures begin to rise with the onset of the second core uncover period, at approximately 320 seconds as shown in Figures J.20, J.35 and J.36. Accumulator injection, however, does not start until about 430 seconds, by which time the predicted cladding temperatures have almost peaked and are already above those of the experimental data. Integrated accumulator flow, a more appropriate measure for SBLOCA, is also reasonably predicted at approximately 550 seconds, by which time all clad temperature excursions have been quenched and core recovery assured (see Figure J.29).

Therefore, the use of actual accumulator flow or one from a line with resistance factors from 1 to 100 will not result in underpredicting clad temperatures. The conclusions stated in Appendix J remain valid and unchanged. The ROSA-IV integral system benchmark demonstrates the appropriateness of RELAP5 for use in SBLOCA applications.

FIGURE 10-1. INTACT LOOP ACCUMULATOR FLOW RATE.

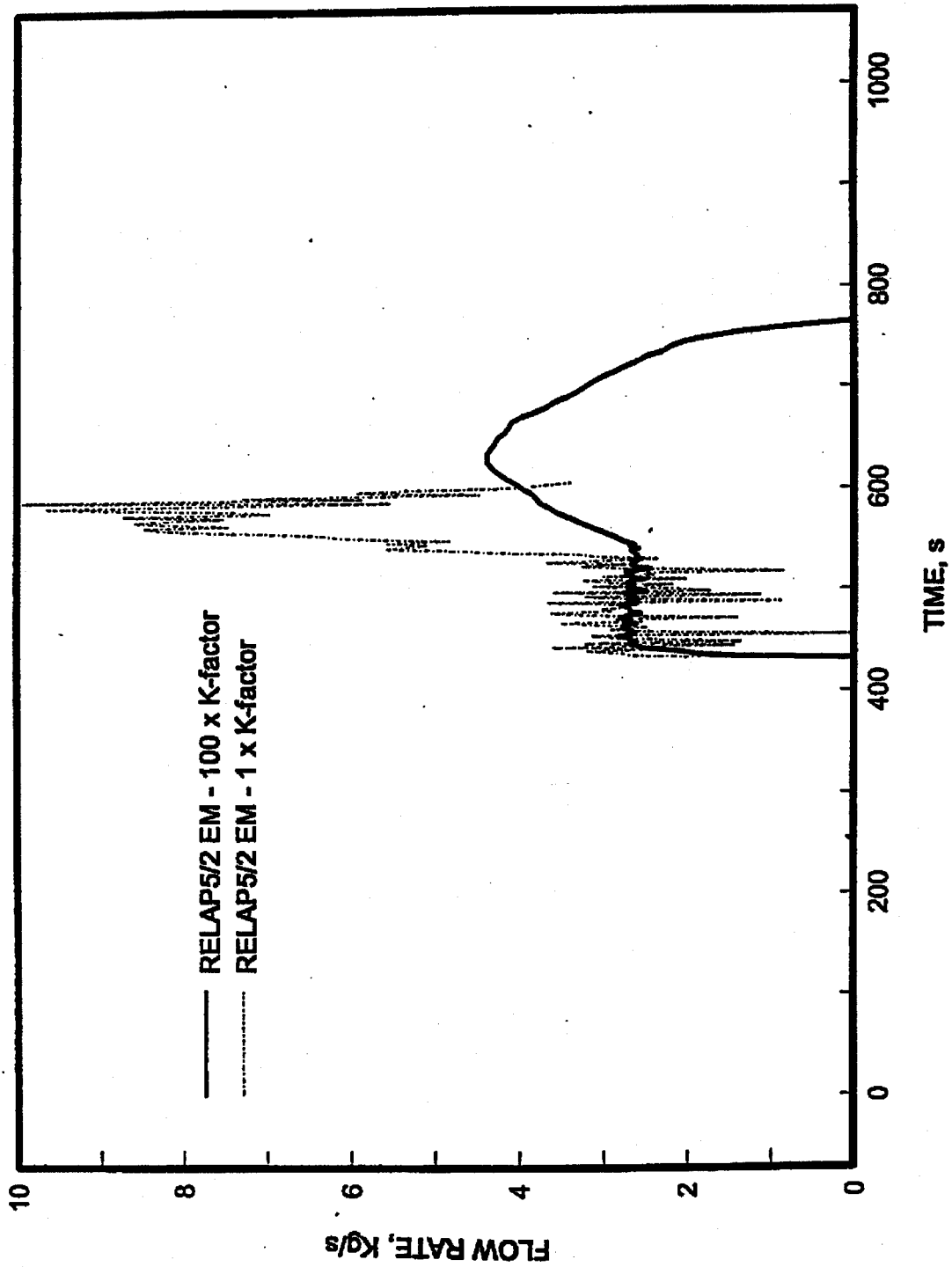
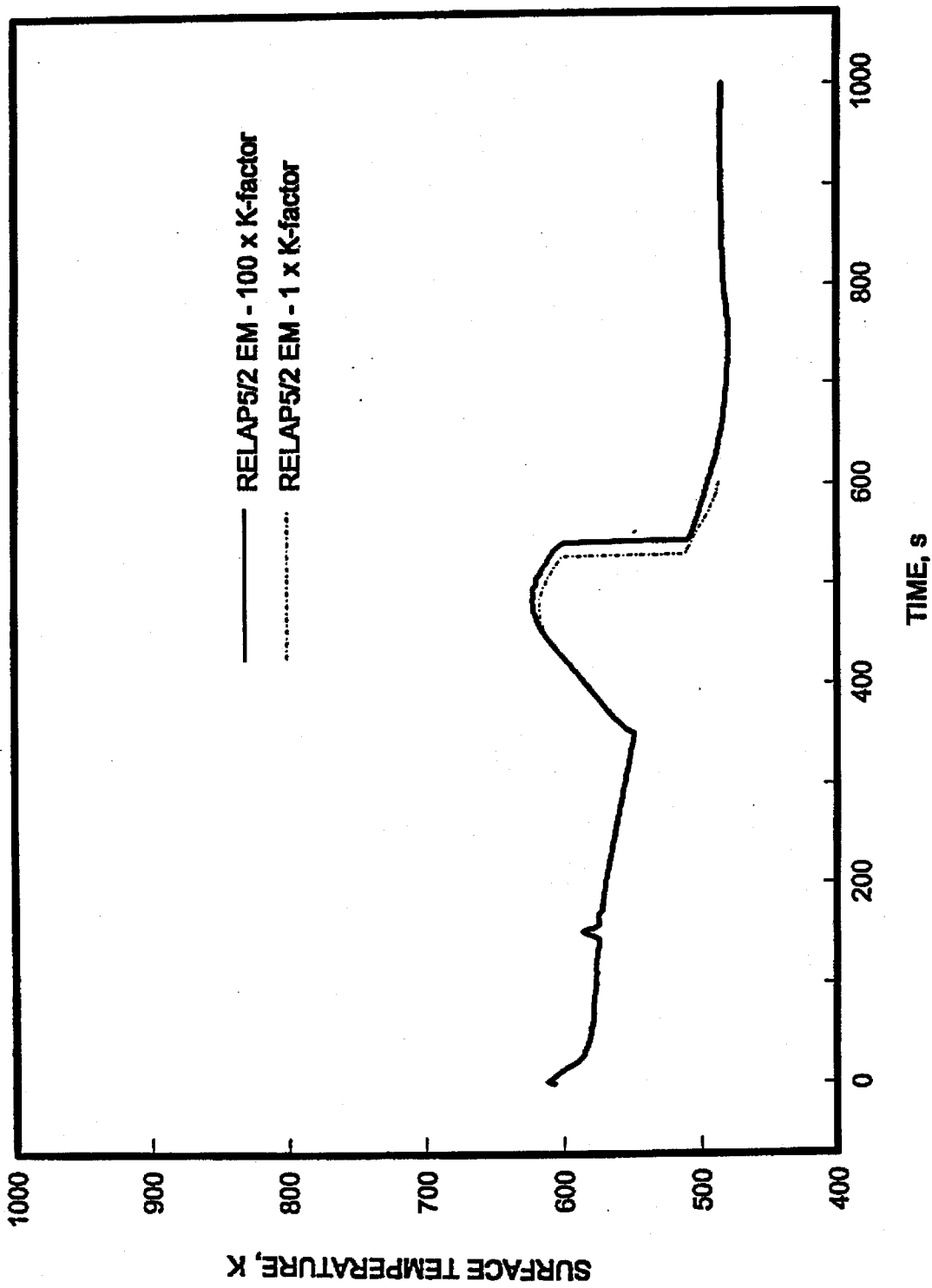


FIGURE 10-2. HOT ROD SURFACE TEMPERATURE - ELEV 3.61 M.



Question 11

No question 11 was transmitted in the request for additional information on BAW-10164, Revision 2, August 1992.

Question 12 - Appendix J

On page J-8, reference is made to Table 2. Should this be Table J.2?

Response: The reference table on page J-8 should be Table J.2.

5.5 Responses to Request for Additional Information on Revision 3

This section contains questions transmitted to BWNT by R. C. Jones of the NRC in his letter of October 1993, and responses transmitted by BWNT to the NRC in a letter from J. H. Taylor (JHT/94-7) dated January 21, 1993 [4].

Requests for Additional Information

BAW-10164P, Revision 3

**"RELAP5/MOD2-B&W, An Advanced Computer Program for
Light Water Reactor LOCA and Non-LOCA Transient Analysis"**

Question 1 - General

Please clarify the intended usage of the changes made in Revision 3 of the Topical Report. In particular, will any of the new or revised features added to RELAP5/MOD2-B&W be used for Appendix K analysis?

Response

The transmittal letter for Revision 3 summarizes the code modifications specifically added for EM calculations. These can be divided into three general categories: (1) OTSG modeling improvements, (2) EM fuel pin modeling improvements, and (3) fuel rod surface heat transfer modifications. Each of the options discussed in this response is intended for EM use.

The OTSG or IEOTSG model improvements include the BWNT slug-drag and annular mist models, a new secondary side CHF correlation, and a smoothing of the Chen nucleate boiling S_f factor based on void fraction. These changes improve predictions of secondary side steady-state void distributions and liquid inventories, improve transient dry-out predictions, and smooth the heat transfer calculated at near dry-out conditions. The slug-drag model will also be used on the primary side (inside the SG tubes) for SBLOCA applications on B&W-designed plants.

RELAP5/MOD2-B&W will be used to calculate the system thermal-hydraulic and fuel pin thermal response during the blowdown phase

of both large and small break LOCAs. The EM pin model changes improve the internal pin pressure calculations by adding a fuel pin thermal-expansion model in the axial direction. An option to allow fuel-clad mechanical contact for high burnup conditions enables the full range of fuel pin time-in-life conditions to be analyzed. An implicit solution of the Baker-Just metal-water reaction model was added to improve the numerical simulation for applications with blowdown ruptures. The fuel pin axial expansion, closed gap conductance, and implicit metal-water reaction models were formulated based on the NRC-approved FRAP-T6-B&W (BAW-10165) fuel pin performance models.

In addition to these model improvements, several optional conveniences were added to facilitate user input and output requirements. The input options included an automated steady-state fuel pin temperature iteration for matching the fuel pin stored energy specified from the NRC-approved TACO3 (BAW-10162) calculations and an automated BEACH droplet break-up and convective enhancement parameter calculation. For interpretation of calculated results, peak cladding temperature (PCT), time of PCT, location of PCT, maximum local oxidation, location of the maximum oxidation, and channel average oxidation edits were added to the code output.

The fuel pin surface heat transfer model was modified by the addition of a filtered mass flux option to meet Appendix K requirements. An option to increase the surface heat transfer area to account for blowdown pin rupture in the film boiling and steam-plus-radiation heat transfer modes was also added. All of the Revision 3 modifications are intended for use in Appendix K licensing analyses.

Question 2 - Page 2.1-52.4

B&W states that the modifications made to the INEL slug flow regime interphase drag model were developed from numerous benchmarks. However, no further information is given on these benchmarks beyond the calculations in Appendices K and L. Please provide additional information on the benchmarks used to develop this model. Were other benchmarks used?

Response

The BWNT modification of the INEL drag model was formulated by benchmark comparisons completed with the developmental code version. RELAP5/MOD2-B&W results were compared against results obtained with the NRC-approved FOAM2 code (BAW-10064), which uses the Wilson Bubble Rise model. The modifications were further verified by the separate-effects benchmarks to the GE Level Swell Test 1004-3, the Christensen subcooled boiling tests, and the ORNL bundle dryout tests. The results of these benchmarks, which were documented in the developmental assessment, showed good agreement with the experimental data. (The response to Question 14 presents additional ORNL benchmark results performed with Version 19.0.) The BWNT modification was then used in the Version 14.0 benchmarks against steady-state and transient 19-tube OTSG and IEOTSG test data. These steam generator secondary side benchmarks concluded that the default BWNT slug-drag model should be used with the addition of a 0.19 overall multiplier on the annular mist flow regime as shown on page 2.1-53 of the topical report. The OTSG benchmarks were provided in Appendix K. A final integral system benchmark against MIST test 320201 was provided in Appendix L. This benchmark provided drag comparisons in the core, steam generator primary tube regions, and steam generator secondary tube bundle (with the 0.19 annular mist multiplier).

Question 3 - Pages 2.1-52, 2.1-52.4, and 2.1-52.5

With the publication of Revision 3 of BAW-10164P, there are now three separate models for determining the interphase drag in the slug flow regime which are: 1) the base INEL model, 2) the Wilson drag model, and 3) the B&W modified slug-drag model. The user has the option for selecting which of these models will be used for a given calculation. Please discuss how the user will select from among these models for a given analysis.

Response

The selection of the drag model is controlled by the evaluation model. For LBLOCA blowdown applications on RSG and B&W-designed plants, the base INEL drag model is used for all primary components. Both large and small LOCA models on B&W-designed plants use the default BWNT slug-drag model in the secondary tube bundle region with a 0.19 overall multiplier on the annular mist flow regime (see page 2.1-53). For SBLOCA applications in RSG plants, the Wilson drag model option is used for the reactor vessel core, upper plenum, and all vertical components. The B&W-designed plants use the Wilson drag model in the core and upper plenum. The default BWNT slug-drag model is used inside the steam generator tubes for small LOCA applications. The default coefficients with the 0.19 multiplier on the annular mist regime are used for OTSG and IEOTSG secondary side applications. Both the B&W-designed plant EM and the RSG plant EM deactivate the Wilson void fraction smoothing option in the RV upper plenum.

Question 4 - Page 2.3.37

On Table 2.3.2-2, please explain why ϵ_{TC} at 1073 K has been changed from 5.22E-3 to 5.14E-3.

Response

The code topical report was in error prior to Revision 3 in reporting the value of the radial strain function, ϵ_{TC} , as 5.22E-3 at 1073 K. The internal code values have always been 5.1395E-3 at 1073.15 K and 5.22E-3 at 1083.15 K. These values are consistent with the MATPRO-Version 11 correlation set (Reference 119 of the topical report).

Question 5 - Page 2.3-46

The quantity β^2 is the fraction of flow area unblocked, not blocked as stated here. Please review and correct this definition.

Response

The quantity β^2 is the fraction of the flow area unblocked. The code formulation is consistent with the correct definition and hence needs no modification. The code topical report text is incorrect and needs to be revised to provide the correct definition.

Additional Typographical Correction: A typographical error was discovered in Equation 2.3.2-20 on page 2.3-36. The equation should have been cast:

$$u_{TC} = (r_{N_{HS}+1} + r_{N_f+2}) \epsilon_{TC} / 2 . \quad 2.3.2-20$$

↑

A plus (+) sign has replaced a minus (-) sign in the above equation at the location indicated by the vertical arrow (↑).

Question 6 - Pages 2.3-37 to 2.3-57

Please describe the qualifications of the clad and fuel axial strain model. Is this model adapted from a previously approved fuel performance code? If so, please describe any differences between this model and the previously approved model.

Response

The clad and fuel axial strain model of RELAP5/MOD2-B&W is used for transient upper pin plenum internal gas volume calculations. The addition of this model improves the predicted internal pin pressure response during the LOCA. The model provides the change in plenum volume term, ΔV_{P_u} , of Equations 2.3.2-51.1 or 2.3.2-51.3 due to changes in fuel rod temperatures from hot initial conditions. This model is comparable to the previously approved fuel performance code FRAP-T6-B&W (BAW-10165, Reference 148 of the RELAP5/MOD2-B&W topical report) with the minor differences outlined below.

The RELAP5/MOD2-B&W model uses the inside clad radius, r_{ic_u} , in calculating the volume change term where as FRAP-T6 uses the fuel pellet radius. Both codes calculate the change in gas plenum length, ΔL_{cf} , as given in Equation 2.3.2-51.4. RELAP5/MOD2-B&W, however, accounts only for the thermal axial strain whereas FRAP-T6 accounts for both thermal and mechanical axial strains. The default thermal material properties ϵ_{ATC} and ϵ_{ATF} of Equations 2.3.2-51.5 and 2.3.2-51.6, respectively, are identical in both codes. RELAP5/MOD2-B&W uses the fuel volume-averaged temperature to calculate the fuel thermal expansion values for each segment, whereas FRAP-T6 uses the fuel temperature value at dish radius locations for the calculation of the thermal expansion function. Also, FRAP-T6 has a term to account for the effect of plutonium content on ϵ_{ATF} .

These differences between the FRAP-T6 models and the RELAP5/MOD2-B&W models are minimal. The FRAP-T6 models are more detailed and complex because it is a fuel pin performance code. The models

extracted from FRAP-T6 for use in RELAP5/MOD2-B&W are LOCA-specific. That is, those parameters which may produce significant effects during the course of a LOCA transient have been integrated into the RELAP5/MOD2-B&W code.

Question 7 - Page 2.3-52

Table 2.3.2-2 referred to on page 2.3-52 could not be located. Please provide a copy.

Response

The requested Table 2.3.2-2 can be found on page 2.3-37 of the topical report and was transmitted to the NRC with the Revision 3 submittal. Question 4 identifies a change unique to the Revision 3 table; therefore that page should have been in the submittal. Nonetheless, a copy of the page is attached with the transmittal of this response.

Question 8 - Appendix K

The feedwater temperature is an important determinant of boiling length. Please clarify where the feedwater temperature is measured. Is the measurement before or after the steam aspiration?

Please describe the modeling of the steam aspiration process. It would seem that node 619 should be at a higher pressure than node 634. If this is so, how does the steam flow against the pressure gradient? How do you assure that the amount of steam flow predicted by the code is correct?

Response

The feedwater temperature was measured with a thermocouple located approximately 3 ft upstream of the aspirator mixer box for the OTSG tests. Therefore, the temperature was measured before mixing occurred with the aspirator flow.

The purpose of the aspirator path is to mix steam with the feedwater to preheat the water to saturation before it enters the tube bundle. Therefore, the feedwater temperature and flow control the aspirator flow. The feedwater and aspirator mixture determine the lower tube bundle flow rate, which directly influences the heat transfer and boiling length.

The pressure gradient that sustains the steam aspiration flow is created by the tube bundle-to-downcomer manometric balance. High boiling contributions in the mixture region lead to steam binding in the upper regions, and result in a bundle collapsed liquid level that remains below the downcomer level. The steam condensation on the subcooled feedwater injected into the top of the downcomer causes a local depressurization, which augments the aspiration flows.

The aspiration process is self-limiting. If too little steam is aspirated, the subcooled downcomer fluid condenses all of the steam creating additional local depressurization that increases the differential pressure across the aspirator. This

differential pressure increase leads to a corresponding increase in aspirator flow. Conversely, if too much steam is aspirated, the downcomer fluid saturates and cannot condense all of the steam. The pressure at the top of the downcomer increases such that the aspirator flow declines. Therefore, the steam aspiration process is self-limiting both in operation and in code applications. The confirmation of the code model is best shown by benchmarks against the 19-tube ARC steady-state and transient tests contained in Appendix K of BAW-10164.

Question 9 - Appendix K

No plots are given comparing the RELAP5/MOD2-B&W results for the steam generator secondary level or mass to the OTSG-LOFW data in Appendix K. Please provide these plots.

Response

For two-phase, high flow applications (where flow losses are high), such as those observed in this OTSG benchmark, the determination of the experimental collapsed level is difficult at best, even during steady-state conditions. Under highly transient conditions, the calculation of collapsed levels is nearly impossible, without recourse to a code calculation that must be presumed accurate. Therefore, no transient collapsed levels or mass inventories were reported with the test results.

To provide information approximating what is requested, the comparison of the steady-state and transient total boiler differential pressures are supplied in Table 9-1 and Figure 9-1, respectively. The calculated steady-state differential was slightly higher than the measured value. This difference was attributed to and consistent with the initial steam flow comparison. The transient boiler pressure differential also reflected the higher steam flow rate calculated during the early portion of the benchmark. The calculated value was filtered to smooth oscillations. The filter used a centered five-point moving mesh averaging technique to smooth the oscillations in the differential pressure curve, given an edit frequency of one point per second.

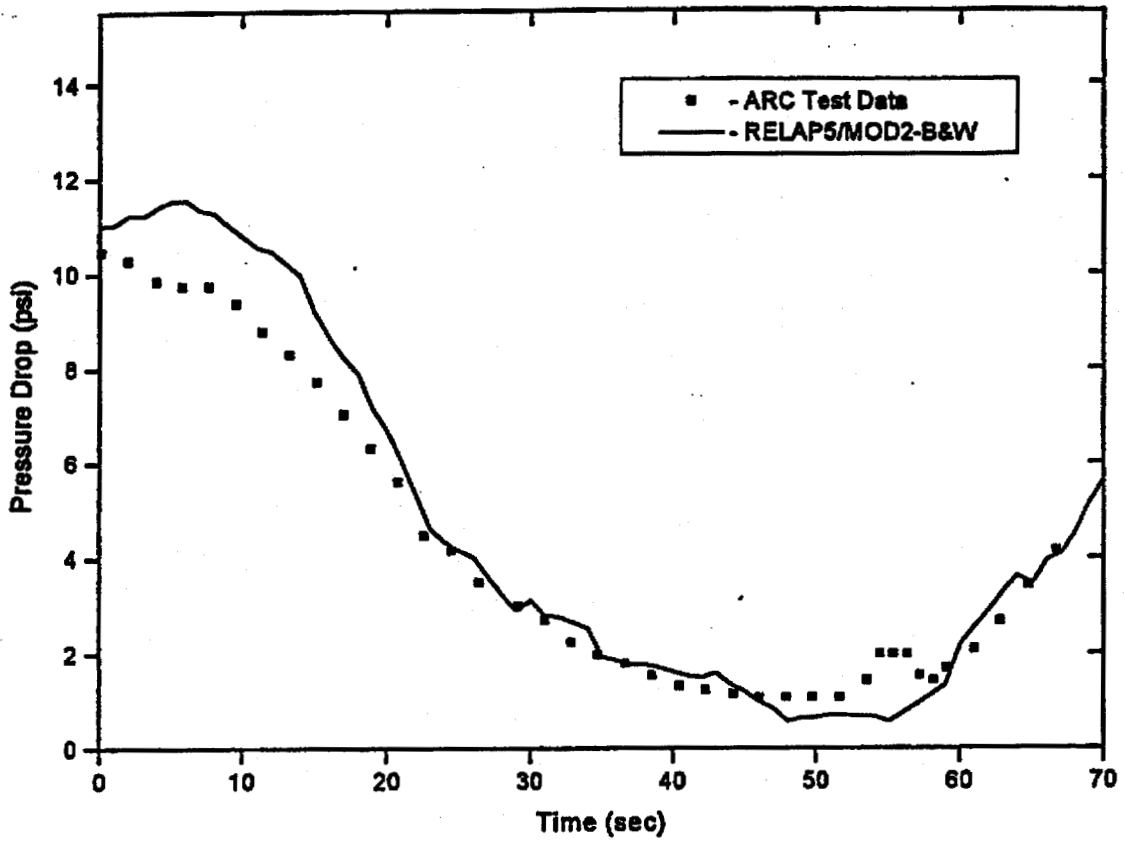
The initial steady-state comparison of the RELAP5/MOD2-B&W mass inventory versus the value calculated from the test data is provided in Table 9-1. The facility initial secondary mass inventory was generated by adding the dry secondary steam mass to the integrated difference in the experimentally-measured steam flow minus the feedwater flow during the loss-of-feedwater

portion of the test. This integrated value was compared against the total inventory from the RELAP5/MOD2-B&W steady-state calculation. Approximately 7 lbm of steam was computed to remain in the dry secondary side prior to the beginning of refill.

Table 9-1. Additional Steady-State Parameters for the 19-Tube Model OTSG LOFW Test.

	<u>Model OTSG</u>	<u>RELAP5/MOD2-B&W</u>
Secondary Total Inventory, lbm	57.0	55.1
Total Boiler ΔP, psid	10.2	11.0

FIGURE 9-1. OTSG LOFW Benchmark Boiler Region Differential Pressure Comparison.



Question 10 - Appendix L, Page L-13

On Table L.1, why is the core power input to the RELAP5 model two percent higher than that used in the test? Please explain the effect of this difference on the benchmark results.

Response

Table L.1 is in error. This table reflects the typical test steady-state conditions that were used as target values from which to initialize the post-test prediction model. Attached is a revised Table L.1 listing the actual initial conditions from Test 320201. These actual test conditions are much closer to the MIST RELAP5/MOD2-B&W initialization values.

The difference in the initial core power is much smaller with the corrected table. Nonetheless, it differs, and the difference relates to MIST operation and post-test benchmarking method. The initial power represents a 3.5 percent scaled core power (where full power is 2700 MW based on a 1/817 scale factor) with an additional 0.4 percent to offset the uncompensated loop heat losses. After break initiation, the power was held at the steady-state value until a MIST operator activated the core decay heat ramp. The total power supplied to the core heaters was controlled by a programmed curve set to match the 1971 ANS decay heat curve with a 1.2 multiplier. This curve was independent of the initial MIST test value other than the intersection point. The activation of the ramp, which occurred upon hot leg saturation (within one minute of the break opening for this test), assured that the calculated and test core power fractions were similar. Thus, the integrated difference in the transient power was quickly minimized. The effect on transient results was therefore negligible or inconsequential.

The initial steady-state values do not exactly match the test data because of the method agreed upon for the MIST post-test prediction analyses. The main goal of this method was to obtain

"unadjusted" post-test prediction results to assess and verify the code formulation via use of the "frozen" input model. Changes in the input model were reserved for cases in which test initial conditions or control functions differed significantly from those specified in the base input model. Any adjustment of the post-test prediction model required justification and documentation. Therefore, many parameters were reviewed prior to performing a code calculation to determine the possible effects on results, given the noted deviations. Differences in the initial parameters listed in the corrected Table L.1 were categorized as having insignificant effects and therefore were not changed for the prediction. In the test initial conditions, the pressurizer surge line and lower pressurizer liquid temperatures were examples of deviations from the RELAP5/MOD2-B&W model that were considered significant. The temperatures controlled the timing of the loss of natural circulation and in turn affected the secondary side pressure response. The secondary response was quite important for this transient, since it controlled the timing of the steam generator reverse heat transfer that activated the secondary side blowdown.

Table L.1. Comparison of MIST Initial Conditions to RELAP5/MOD2-B&W Values.

<u>Parameter, Units</u>	<u>MIST Test 320201 Value</u>	<u>RELAP5/MOD2-B&W Value</u>
Primary Pressure, psia	1733.2	1726.5
Secondary Pressure, psia	1013.9/1014.1	1010.0
Core Exit Temperature, F	592.	593.4
SG Exit Temperature, F	549.	550.3
Core Exit Subcooling, F	23.6	22.0
Core Power to Fluid, Btu/s	119.0	119.5
Pressurizer Level, ft	4.9	5.0
SG Secondary Level, ft	4.7/5.0	5.0
Core Flow Rate, lbm/s	1.86	1.86

Question 11 - Appendix L, Page L-13

On Table L-2, please explain the large difference in the time of hot leg U-bend voiding between versions 5.0 and 14.0 predictions. In particular, describe the change in which loop hot leg U-bend voids first, and the large difference in time of occurrence between the test data and predictions. Also, page -v- states that SBLOCA modifications were made in code version 18.0, yet page L-11 states that the models in version 14.0 are identical to those in version 19.0. Why was an earlier version, 14.0, used for this benchmark? Are there actually no differences in the models, compared to version 19.0?

Response

The differences between the natural circulation flow interruption predictions for Versions 5.0 and 14.0 are attributable to differences in the pressurizer and surge line initial temperature conditions. The fluid temperature in the bottom of the pressurizer was lower than the saturation temperature due to surge line heat losses and insurges that occurred during the steady-state period. In the Version 14.0 benchmark, the pressurizer fluid temperature was changed to match the actual test data. The colder fluid caused a variation in the hot leg A flashing rates between the two benchmarks. In the Version 5.0 prediction, the pressurizer fluid temperature was saturated, and additional flashing occurred. Thus, the interruption of the loop A flow occurred later than that calculated by the Version 14.0 benchmark.

A difference in the hot leg B interruption time was also reported. This variation was also related to the change in the pressurizer fluid state. The subcooled liquid reduced the flashing rate in the pressurizer, causing a faster RCS depressurization. The faster depressurization allowed the liquid in the B loop hot leg to saturate, flash, and interrupt sooner because of the collection of steam in the hot leg U-bend region.

The test time reported for interruption of natural circulation was erroneously given as the onset of voiding in the hot leg U-bend region. The loss of circulation should have been reported as

between 60 and 120 seconds in both hot legs. The interruption time cannot be further resolved, given the scales of the available data plots. The true variation in the timing between the test and prediction is therefore small. The adjustment of the pressurizer liquid temperature improved the predicted RCS initial pressure response as well as the predicted loop flow and primary-to-secondary heat transfer interruption. The integrated effect was observed by the excellent agreement of the secondary side pressures shown in Figure L-4.

During the review of Table L.2, a difference was also noted in reported time of the operator actions to activate HPI, AFW, and the core power ramp. These operator actions were performed between 35 and 55 seconds in the test, not 30 to 42 seconds as previously reported in Table L.2. A revised Table L.2 is provided with the two indicated corrections.

This benchmark was included specifically to validate the BWNT slug-drag model. All of the SBLOCA modifications referred to in Version 18.0 and 19.0 are optional, user-activated models that were not available in Version 14.0 of the code. None of these modifications included changes to the BWNT slug-drag model. This benchmark, performed using Version 19.0 of the code, with the Version 14.0 input model, would reproduce the same results (since none of the new optional code models were activated). Therefore, it was appropriate to present the Version 14.0 benchmark results as those representative of Version 19.0 results.

Table L.2. Sequence of Events.

<u>Event</u>	<u>MIST Observation Seconds</u>	<u>Ver 5.0 Prediction Seconds</u>	<u>Ver 14.0 Prediction Seconds</u>
Leak opened	0	0	0
Primary saturates	12	31	34
Pzr level reaches one foot (HPI, AFW, and DH ramp started)	35-55	60	57
Hot leg U-bend voiding interrupts natural circ. (Loop A/Loop B)	60 to 120 (both)	85/130	130/90
High elev BCM begins (Loop A/Loop B)	170/175	180/185	180/180
Break saturates	190	130	140
Secondary refilled and AFW shutoff (SG A/SG B)	480/480	490/440	480/480
Primary and secondary pressures equalize	1560	1500	1650
Secondary blowdown	1710	1500	1650
CFT injection begins	1920	1680	1800

Question 12 - Appendix L, Page L-6

Page L-6 states that the revised slug drag model was implemented in the core and the shell side of the steam generator. Please confirm that the model used in Appendix L used the B&W modified slug-drag model referred to on page 2-52. Also, please confirm that the default coefficients presented on pages 2.1-52.4 and 2.1-52.5 are used in the benchmarks presented in Appendix L.

Response

The input model for Appendix L used the BWNT slug-drag model with the default coefficients, outlined on page 2.1-52.5, for the core and primary tube regions. The secondary side of the steam generator tube bundle region used the default BWNT slug-drag model with an overall multiplier on the annular mist drag of 0.19.

Question 13 - Figures L-5 and L-6

Figures L-5 and L-6 present the collapsed liquid level in feet. Page L-7 infers that the reference level for the steam generator is the lower tube sheet. The reference level for the reactor vessel is not stated. Please provide the reference location for the reactor vessel and confirm that the reference level for the steam generator secondary is the lower tube sheet.

Response

In the MIST facility all collapsed level comparisons were referenced to the same datum (0.0 ft), which is the elevation of the upper face of the lower tube sheet in the steam generator. In the RELAP5/MOD2-B&W model, the bottom of the reactor vessel is located at 0.848 ft, the core is located between 4.74 ft and 16.74 ft, and the centerlines of the hot and cold leg RV nozzle connections are at 21.25 ft.

Question 14 - Page L-6

In addition to use of the revised interphase drag model in the slug flow regime, the number of volumes in the core region was increased from 3 to 20. The reason given for this change is that greater detail is needed to maintain consistency with the revised models. Presumably, this choice of nodalization results in the good agreement in the collapsed liquid level between the RELAP5/MOD2-B&W code and the MIST data. Use of 20 control volumes in the core obviously provides more detail on the axial flow profile in the core as compared to 3 control volumes. The question arises as to how much of the improved predictions is due to the modeling changes as compared to just increasing the nodal detail using the original RELAP5/MOD2 models.

Please discuss the implications of increasing the number of core volumes from 3 to 20 focusing on the degree of improvement resulting from the use of the new models as compared to just increasing the number of core nodes. Please include a sensitivity evaluation using the original RELAP5/MOD2 interphase drag models with the revised models.

Response

It is known that the INEL slug flow regime drag model overpredicts the interphasic drag in heated regions with small hydraulic diameters. Increased nodalization was the first undocumented attempt by BWNT to improve the core void distribution during the critical phase of plant SBLOCA analyses. The core void distribution was not significantly changed, even with big increases in the number of control volumes. The predictions consistently indicated high interphasic drag that yielded excessive two-phase level swell. The high level swell was not conservative for core cooling calculations. Therefore, the INEL model was considered inappropriate for SBLOCA licensing calculations that could predict clad heatup.

To confirm these findings and address the stated request for a sensitivity study, several benchmarks of test 3.09.10j from the ORNL Thermal-Hydraulics Test Facility were performed. This test is discussed in Appendix H of the RELAP5/MOD2-B&W code topical report. Selection of this test was made because of its similarity to the conditions at the minimum core inventory time of the typical, most-

limiting SBLOCA transient. Since this limiting SBLOCA has a small break area, the RCS depressurization rate is slow. Core recovering is nearly initiated with HPI flow at the approximate time that the RCS reaches the CFT fill pressure. The 0.05-ft² to 0.10-ft² break range is expected to produce this limiting condition between 20 and 40 minutes into the transient. The approximate core power is 2 percent of a maximum 17 kW/ft, which equals 0.34 kW/ft. This power level, and RCS pressure of approximately 600 psia, are the conditions characteristic of the most-limiting core mixture level encountered during the spectrum of SBLOCA analyses. Therefore, this test provides the most critical conditions for core level swell comparisons.

The first benchmark analysis used the Case 14 model from Appendix H and the INEL slug-drag model with a 24-volume representation. The predicted void distribution is shown in Figure 14-1. The second benchmark also used the INEL drag model with the 24-volume model combined into 4 equal-sized volumes. The curves indicate that the void distribution is poorly predicted by both the 4- and 24-volume models. The increased noding detail did little to improve the prediction because the interphase drag was excessive.

The same two benchmarks were performed using the default BWNT slug-drag model. Figure 14-2 gives the results for both the 4- and 24-volume analyses. As expected, good agreement was obtained with both models. The revised interphase drag was key in the improved behavior. The increased noding detail gives better resolution of the mixture height, but does little to the pool region void distribution.

Figure 14-3 gives the 24-volume model results for the base INEL drag option, default BWNT slug-drag option, and the default Wilson slug-drag option. The BWNT slug-drag and the Wilson drag results both provide good agreement to the experimental data. The quality of the predictions indicate that either model would be acceptable for core drag predictions.

The formulation of the BWNT slug-drag model was based on a 20 axial volume core region. The discretization was identical to that used for the large break BEACH analyses (BAW-10168). This model was selected for consistency between large and small break methods as well as to better resolve the core mixture level for transients that may predict cladding heatup. Three or four axial volumes would be adequate for cases in which the core does not undergo a heatup. In the event, however, that the mixture level does descend into the core region, the mixture height is resolved to within approximately 0.6 ft with the use of the 20-volume model.

Although the BWNT slug-drag modifications were developed with a finely noded core region, the model has been shown to improve the phase separation in a coarsely-noded core or in steam generator secondary side bundles. This marked improvement demonstrates that it is not the number or the size of control volumes, rather it is the interphasic drag model, that is key to predicting proper phase separation in heated regions with small hydraulic diameters.

FIGURE 14-1. RELAP5/MOD2-B&W Predictions of ORNL Test 3.09.10j: 0.33 KW/ft, 610 psia.

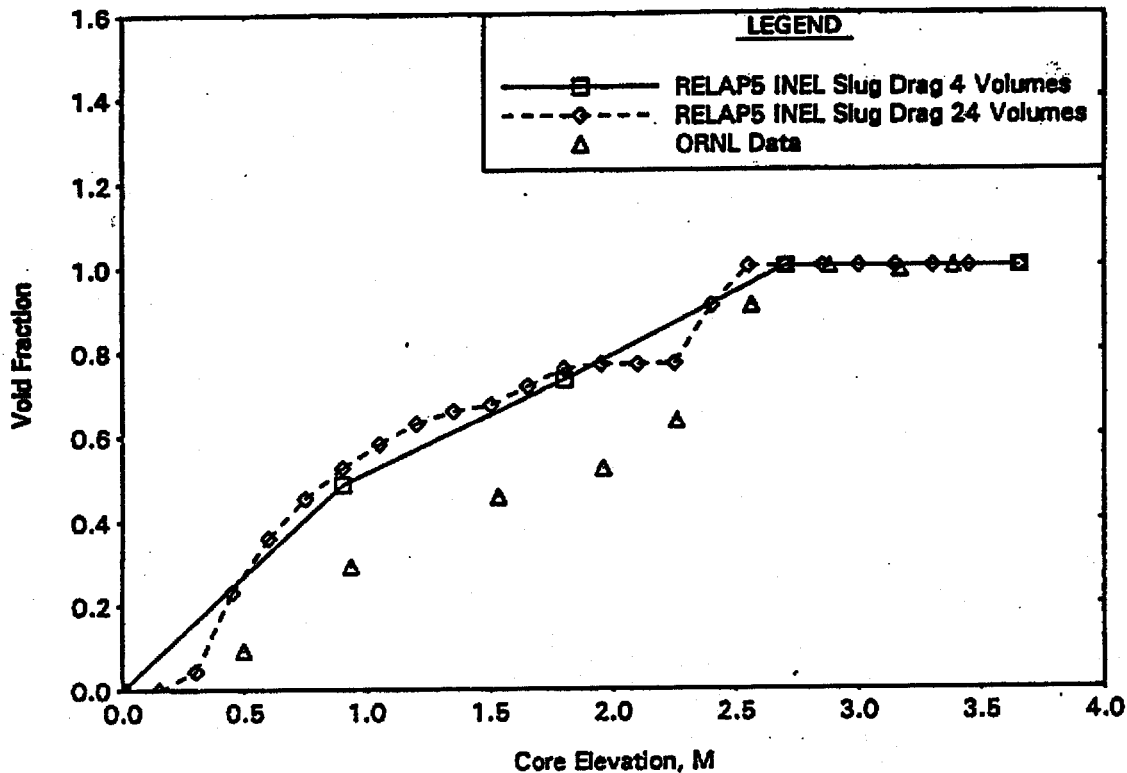


FIGURE 14-2. RELAP5/MOD2-B&W Predictions of ORNL Test 3.09.10j: 0.33 KW/ft, 610 psia.

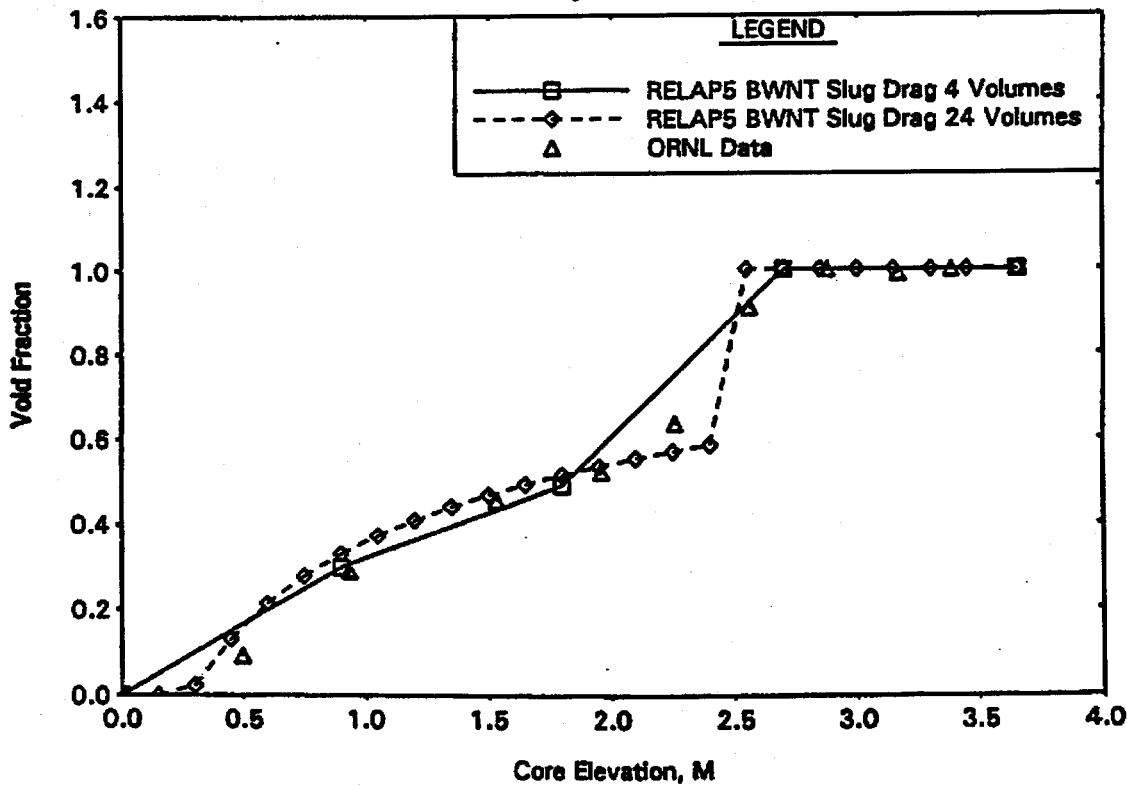
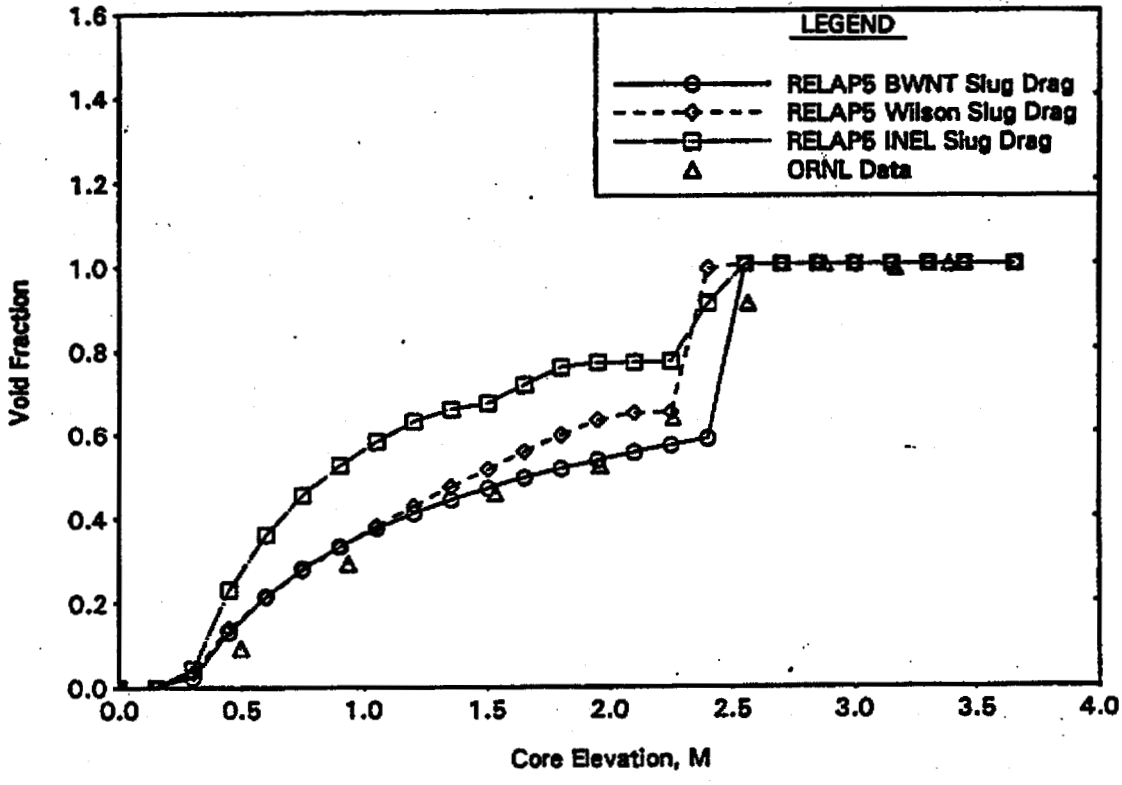


FIGURE 14-3. RELAP5/MOD2-B&W Predictions with the BWNT, Wilson, and INEL Slug Drag Using the 24 Volume Core Model.



Question 15 - Page L-6

The revised interphase drag model is used to model the secondary side of the steam generator. The number of control volumes used to model the secondary side is not stated in the text. However, Figure L-2 indicates that there are 9 control volumes used on the secondary. If this assertion is true, then the height of each control volume representing the steam generator is much greater than those used in the reactor core.

Please discuss the nodalization of the steam generator system given the apparent need for greater detail in the core region in order to predict the collapsed liquid level as discussed in Question 2.

Response

The control volume heights below the steam generator aspirator elevation are 6.4 ft, and those in the MIST core are 0.6 ft. The effectiveness of the BWNT slug-drag model is not dependent upon the volume heights or number of volumes as indicated in the response to Question 14. Benchmarks with the ARC OTSG data, given in Appendix K, indicate that this level of detail is adequate to predict the governing phenomena in the steam generator. The location of the boiling and transition regions in the OTSG are known in sufficient detail to address level variations. The BWNT slug-drag model improves the void distribution profile and the associated inventory prediction, and as a consequence, the transient primary-to-secondary heat transfer is more accurately calculated. Better predictions of secondary heat transfer improve the accuracy of primary system response predictions.

Question 16 - Appendix L

One of the key variables to be predicted is the fuel surface temperature. No comparison of predictions to test data are shown in the benchmark in Appendix L. Please provide this comparison or explain why such a comparison is inappropriate.

Response

Fuel temperature is an important parameter in SBLOCA analyses but for this particular benchmark the mixture level remained continuously above the top of the core in the analysis as well as in the test. The minimum vessel mixture level was located at the hot leg nozzle elevation. As a result, nucleate boiling removed the fuel stored energy and decay heat contributions after core fluid saturation. The high heat transfer coefficients associated with the nucleate boiling regime maintained the pin surface temperatures within several degrees of the fluid saturation temperature. Since no surface temperature excursions were observed in the test or in the analysis, no comparison of the temperature predictions to the test data were given.

Attachment for Question 7

The following page is a copy of page 2.3-37 containing Table 2.3.2-2.

The radial strain function is defined by either a user input cubic fit

$$\epsilon_{TC} = C_1 T^3 + C_2 T^2 + C_3 T + C_4 , \quad 2.3.2-21$$

or a built in code correlation set¹¹⁹

$$\epsilon_{TC} = -2.0731 \cdot 10^{-3} + 6.721 \cdot 10^{-6} T_C \quad 2.3.2-22$$

for $T_C < 1073K$ (α phase), and

$$\epsilon_{TC} = -9.4495 \cdot 10^{-3} + 9.7 \cdot 10^{-6} T_C \quad 2.3.2-23$$

for $T_C > 1273K$ (β phase), where T_C is the average cladding temperature (K). In the α phase to β phase transition zone, $1073K < T_C < 1273K$, a table lookup is used. Some selected values are listed in Table 2.3.2-2.

Table 2.3.2-2. Thermal Strain of Zircaloy for $1073 K < T < 1273 K$.

<u>T(K)</u>	<u>Radial Strain</u> ϵ_{TC}	<u>Axial Strain</u> ϵ_{ATC}
1073.	$5.14 \cdot 10^{-3}$	$3.53 \cdot 10^{-3}$
1093.	$5.25 \cdot 10^{-3}$	$3.50 \cdot 10^{-3}$
1103.	$5.28 \cdot 10^{-3}$	$3.46 \cdot 10^{-3}$
1123.	$5.24 \cdot 10^{-3}$	$3.33 \cdot 10^{-3}$
1143.	$5.15 \cdot 10^{-3}$	$3.07 \cdot 10^{-3}$
1183.	$4.45 \cdot 10^{-3}$	$1.50 \cdot 10^{-3}$
1223.	$2.97 \cdot 10^{-3}$	$1.10 \cdot 10^{-3}$
1273.	$2.90 \cdot 10^{-3}$	$1.40 \cdot 10^{-3}$

5.6 Supplemental Information on Revisions 2 and 3

This section contains supplemental information transmitted by BWNT to the NRC in a letter from J. H. Taylor (JHT/94-146) dated September 20, 1994.

Supplemental Information for BAW-10164

RELAP5/MOD2-B&W Revision 2 and 3

1. Given that RELAP5/MOD2-B&W has a two-fluid, six equation formulation, why are equilibrium control volumes used in the core region for RELAP5/MOD2-B&W LOCA analyses?

Response: The EM core heat transfer package used for fuel pin surface heat transfer uses nucleate, transition, and film boiling correlations that were formulated based on equilibrium fluid state conditions. Use of the RELAP5/MOD2-B&W nonequilibrium control volume option can, under certain blowdown conditions, result in higher surface heat transfer than would be calculated with equilibrium fluid conditions. This heat removal is not consistent with the formulation of the correlations and can be nonconservative from a peak cladding temperature perspective. Therefore, equilibrium control volumes are selected for use in the core region to provide appropriate boundary conditions for application of the EM core heat transfer correlations in RELAP5/MOD2-B&W. This approach is consistent with that used in the approved evaluation model, BAW-10168P Revision 1.

2. There are a number of additional user input options included in the revision 2 and 3 submittals to RELAP5/MOD2-B&W. Please identify those options that will be used in evaluation model calculations.

Response: The review of RELAP5/MOD2-B&W revisions is somewhat complicated because the impact on EM calculations of the new options are provided under separate cover. The new code options have been qualified by separate effects benchmarks and calculations. Description of the EM options is not presented in the RELAP5/MOD2-B&W code topical report, since two separate evaluation models reference the latest revisions to the code. The OTSG LOCA EM is contained in BAW-10192P and the RSG LOCA EM is contained in BAW-10168P Revisions 2 and 3. Section 9.0 of the large and small LOCA volumes of each EM is titled "Required Documentation." This section identifies the computer codes used in the EM and lists specific code options controlled by the EM. Also included is a table listing the generic and prescribed code inputs used in each EM. These EM tables are the appropriate locations to provide the necessary user input option control.

3. The BWNT small break LOCA (SBLOCA) evaluation models were revised to use the BWUMV critical heat flux correlation. The correlation is presented in Appendix I of the RELAP5/MOD2-B&W topical report, BAW-10164 Revision 2. Please clarify the value used for the Tong factor and provide justification for use in RELAP5/MOD2-B&W.

Response: The BWUMV correlation is a steady-state, local-condition critical heat flux correlation adapted from the NRC-approved BWCVM (Ref. 1) correlation. The correlation includes the non-uniform Tong factor. The Tong factor, with a value generally greater than one, accounts for non-uniformity in the power shape of the test section. The factor is required when comparing the correlation with steady-state data. As such, the measured-to-predicted comparisons in Appendix I are based on steady-state experiments, and therefore use the Tong factor.

For LOCA analysis, however, BWNT's established practice is to reduce transient CHF conservatism by setting the value of the Tong factor to 1.0. The measured-to-predicted comparisons and statistics in Appendix I demonstrate that the BWUMV correlation is properly formulated and appropriate for steady-state CHF prediction. Setting the Tong factor to 1.0 in transient analysis is a practice applied to all previous CHF correlations including BWCVM. This technique has been approved in all previous LOCA evaluation models, dating back to 1971. Support for the position is primarily based on experiments that do not indicate that fuel pins will experience CHF during the flow coastdown phase of the SBLOCA transient.

Secondarily, it is generally recognized that steady-state CHF correlations under predict transient CHF when CHF is based on local conditions. The following is a summary of supporting references.

Few authors make direct statements on the conservatism of applying steady-state correlations to transient situations. It is common for the author to present the information but leave its

interpretation to the reader. Also, much of the reference material addresses only large LOCA conditions or extreme transients, since the experimental base for SBLOCA indicates no departures from nucleate boiling.

A survey by Leung (Ref. 2) interprets the observations of various investigators. Section III.B of the survey is mostly appropriate for larger breaks, while Section III.A, flow reduction transients, is reasonably characteristic of SBLOCAs. A review of the works by Schrock (page 25), Maxon and Edwards (page 25), Shiralka et al. (page 27), Letourneau and Green (page 27), Smirnov, Griffith et al., Redfield et al., Cermak et al., Lawson, Morgan et al., and Hicken et al. all confirm the conservatism of transient CHF predictions with steady-state correlations. The evidence presented continues throughout Section III of Leung's work.

Other authors, Tong and Weisman (Section 4.3.2.8 of Ref. 3), Collier (Section 9.6.2 of Ref. 4), Khater and Raithby (Chapter 3 of Ref. 5), McIntyre and Merilo (Ref. 6), and Vojtec (Ref. 7) also substantiate the generally held opinion that the prediction of CHF by steady-state correlations during a transient is highly conservative.

The observation that CHF does not occur during the SBLOCA coastdown period derives from integral system tests. Such tests consistently demonstrate that CHF does not occur for SBLOCA. Across the range of SBLOCA integral system tests--Semiscale, LOBI, ROSA, MIST, and LOFT (Ref. 8-13)--no observations of temperature excursions during the flow coastdown phase were made. In these reference tests, none of the cladding temperature excursions was initiated prior to loop seal clearing.

In conclusion three points were made in support of setting the Tong factor to one for SBLOCA CHF calculations.

- The transient application of steady-state CHF correlations with the Tong factor set to one was approved in all previous BWNT evaluation models. Only the CHF correlation, not its method of implementation, is being changed (BWC MV to BWUMV) in this SBLOCA revision to the RELAP5 topical report
- There is broad consensus in the literature that the use of steady-state, local-condition CHF correlations for transient predictions is conservative. Thus, the reduction of conservatism in the SBLOCA evaluation model, through setting the Tong factor to one is appropriate.
- The experimental record for SBLOCA shows that CHF does not occur during the flow coastdown phase of the transient.

Therefore, it is justifiable for BWNT to continue its standard practice of setting the Tong factor equal to one for the prediction of CHF during SBLOCA transients.

References for Supplemental Question 3

1. BAW-10159, "BWC MV Correlation of Critical Heat Flux in Mixing Vane Grid Fuel Assemblies," B&W Fuel Company, July 1990.
2. Leung, J. C. M., NUREG/CR-0056, ANL-78-39, Critical Heat Flux Under Transient Conditions: A Literature Survey, June 1978.
3. Tong, L. S. and J. Weisman, "Thermal Analysis of Pressurized Water Reactors," Second Edition, Published by American Nuclear Society, 1979.
4. Collier, J. G., "Convective Boiling and Condensation," Second Edition, McGraw-Hill, 1981.

5. Khater and Raithby, EPRI NP-1792, Full-Scale Controlled Transient Heat Transfer Tests--Analysis Using the FAST Prediction Method, April 1981.
6. McIntyre and Merilo, Controlled Transient CHF Tests in a 5x5 Rod Bundle Under Loss-of-Coolant Accident Conditions, Seventh International Heat Transfer Conference, Munich, Germany, 1982.
7. Vojtec, Investigation of Transient Heat Flux Phenomena and Forced Convection Film Boiling Heat Transfer, Seventh International Heat Transfer Conference, Munich, Germany, 1982.
8. Kmetyk, L. N., "TRAC-PF1/MOD1 Independent Assessment: Semiscale MOD-2A Intermediate Break Test S-IB-3," NUREG/CR-4465, February 1986.
9. Duffield, J. S. and I. Shepherd, "Experience with CATHARE at J. R. C. ISPRA," CATHARE International Seminar, Grenoble, France, May 1988.
10. Barre and Bernard, "The CATHARE Code Strategy and Assessment," Nuclear Engineering and Design 124, 1990.
11. Koizumi, Y., et al., "Temporary Core Liquid Level Depression During A Cold-Leg Small-Break Loss-of-Coolant Accident: The Effect of Break Size and Power Level," Nuclear Technology, Vol. 96, December 1991.
12. Tasaka, K., et al., "The Results of the ROSA-IV LSTF Small-Break LOCA Experiments," Thirteenth Water Reactor Safety Research Meeting, NUREG/CP-0072, Volume 4, February 1986.
13. "Multiloop Integral System Test (MIST): Final Report," NUREG/CR-5395.
14. Jarrell, D. B. and J. M. Divine, "Experiment Data report for LOFT Intermediate Break Experiment L5-1 and Severe Core Transient Experiment L8-2," NUREG/CR-2398, EGG-2136, November 1981.

4. Figure I-6 of BAW-10164 (RELAP5/MOD2-B&W) gives the measured-to-predicted CHF ratios for the BWUMV correlation as a function of mass flux. The number of test points with mass fluxes below 1.25 mlbm/hr-ft² appears to be inconsistent with the sum of points given in Table I-3 and Appendix B of BAW-10159 (BWC MV). Please clarify the apparent differences in number of test points versus the number of data points included on that figure. Also, please provide confirmation of the applicable parameter range over which the BWUMV correlation is used in RELAP5/MOD2-B&W SBLOCA applications.

Response: Figure I-6 contains 77 calculated points for mass fluxes less than 1.25 Mlbm/hr-ft². The points are comprised of 22 test points from Table I.3 of BAW-10164 Appendix I, 20 test points from BAW-10159 Appendix B, and 35 test points from Table Q1-1 in BAW-10159 Appendix F. The points from Appendix F were considered annular flow points (qualities near 22 percent or above) for BWC MV. The form of the BWC MV CHF equation is a linear function of quality that is invalid for high qualities, which makes annular flow data inappropriate. These points are, on the other hand, appropriate for use in the BWUMV form of the correlation, which extends the quality range to 67 percent. Therefore, these points were included in the data base used to validate the BWUMV correlation.

The thermal-hydraulic parameter ranges used for the BWUMV correlation as implemented in RELAP5/MOD2-B&W are listed as:

$$\begin{aligned} 1300 \text{ psia} &\leq \text{Pressure} \leq 2455 \text{ psia} \\ 0.5 \text{ Mlbm/hr-ft}^2 &\leq \text{Mass Flux} \leq 3.871 \text{ Mlbm/hr-ft}^2. \end{aligned}$$

No upper limit on flow or pressure is included in RELAP5/MOD2-B&W. However, SBLOCA EM applications will not result in state conditions that exceed these values. Also, the quality is not explicitly limited in RELAP5/MOD2-B&W, however, in typical SBLOCA analyses the quality will not exceed the BWUMV limit unless it is due to dryout from core uncovering. Under these conditions CHF is unimportant. Additionally, should core uncovering occur, it

is typically at pressures below the minimum BWUMV pressure limit such that the correlation is not used.

5. Only one MIST benchmark is provided in Revision 3 of BAW-10164. Have any additional benchmarks been performed to qualify the RELAP5/MOD2-B&W system predictions for B&W-designed plants?

Response: The RELAP5/MOD2 code was developed by EG&G, Idaho for predicting the system thermal-hydraulic behavior of a PWR during transient conditions such as a loss-of-coolant-accident (LOCA), particularly SBLOCA. The code has been benchmarked against many tests conducted in the U.S. and internationally. These benchmarks, in general, have confirmed that RELAP5/MOD2 is capable of simulating important system responses including system depressurization and flashing, break mass discharges, two-phase flow phenomena, core heat transfer, and system voiding. Most integral test facilities were scaled to a 4-loop recirculating steam generator (RSG) type reactor design. To provide integral system thermal-hydraulic data on B&W-designed plants, the NRC, BWNT, the B&W Owners Group, and EPRI jointly funded the design, construction, and testing of the Multiloop Integral System Test (MIST) facility. This scaled facility was designed to simulate prototypical SBLOCA phenomena for code benchmarking. The facility contained the unique features of the B&W-designed NSSS with two hot legs, four cold legs, once-through steam generators (OTSGs), and reactor vessel vent valves (RVVVs).

Pretest predictions and posttest predictions (Ref. 1-6) with a frozen input model were performed with RELAP5/MOD2-B&W to verify the simulations of the system responses during SBLOCA and SGTR events. The results consistently showed that the overall code RCS predictions were reasonably accurate. One deficiency that was repeatedly observed in all the predictions was underprediction of the core collapsed level. The source of the problem was high interphasic drag in the slug flow regime, which resulted in retention of too much steam within the two-phase mixture in the vessel. The excessive level swell affected the

core collapsed level predictions but did not have any significant effect on the remainder of the RCS response. Only heated regions with small hydraulic diameters revealed the excessive level swell. For certain tests, prediction of secondary side behavior (a heated region with small hydraulic diameter) also exhibited excessive level swell.

The code versions used for these MIST benchmarks did not have the Wilson or B&W slug-drag model improvements. The drag model changes were the only significant code modifications that would now be used for MIST predictions. A MIST benchmark was chosen to confirm that the overall RCS results would not be appreciably changed between the old version and new version when the new slug flow regimes models were used. That benchmark was also chosen to confirm the improvement in the calculated core and secondary side collapsed levels. Therefore, the benchmark to MIST Test 320201, a scaled 50 cm² break in the CLPD, was reanalyzed with the new drag models, and the results were included in Appendix L of BAW-10164. The overall RCS response was quite similar to the earlier calculations. As expected, the core and steam generator secondary side collapsed levels were greatly improved by the drag model change.

Investigation of the other MIST benchmarks referenced on page L-3 of Revision 3 of BAW-10164 led to the conclusion that under comparable boundary conditions the code predictions were reasonably correct except for the core or steam generator level swells due to high interphasic drag in the slug flow regime. For the scaled 10 cm² breaks or larger with pumps tripped (Tests 3109AA¹, 3105AA⁶, 320302¹, 320503¹, 320604³, 3404AA⁵, 3406AA¹, 350101⁴, and 3601AA²) the core region collapsed liquid level was underpredicted by about 1.2 to 3.3 ft. It should be noted that the level mismatch was fairly constant, especially when differences in depressurization rates were considered between the test and prediction. Reanalysis of these cases with Version 19 of RELAP5/MOD2-B&W would greatly improve the core level with

little change in overall RCS response as noted in the benchmark of Test 320201. Revised benchmarks of these MIST tests with the new drag models is not warranted, however, since no new evidence would be provided to substantiate the RELAP5/MOD2-B&W models for SBLOCA applications.

The revised benchmark of Test 320201 along with other benchmarks (GE level swell test 100-4, Christensen subcooled boiling tests, 19-tube OTSG benchmarks, ORNL bundle dryout tests, and the comparison against the NRC-approved FOAM2 code) provide ample justification for the use of RELAP5/MOD2-B&W Version 19 in SBLOCA EM applications. Accurate RCS SBLOCA response for both OTSG plants and RSG plants has been demonstrated. The drag model changes improve the core level swell predictions, such that conservative predictions of cladding temperature excursions will be calculated during periods in which the core mixture level is within the heated core region.

References for supplemental question 5:

1. J. A. Klingenfus and M. V. Parece, "RELAP5/MOD2 MIST Analysis Comparisons," Multiloop Integral System Test (MIST): Final Report, Vol. 10, NUREG/CR-5395, December 1989.
2. C. A. Schamp and J. A. Klingenfus, "RELAP5/MOD2 MIST Post-Test Benchmark of MIST TEST 3601AA - ATOG With Pumps Available," BAW-2033, 77-1171774-00, December 1988.
3. M. K. Smith and M. V. Parece, "RELAP5/MOD2 MIST Post-Test Benchmark of Test No. 320604 - 10 CM² Pump Discharge Break," BAW-2029, 77-1171643-00, December 1988.
4. M. B. McGuirk and M. V. Parece, "RELAP5/MOD2 MIST Post-Test Benchmark of Test No. 350101 - 10 CM² Primary System Break With High Point Vents," BAW-2032, 77-1168638-00, December 1988.
5. J. C. Seals and P. W. Ploch, "RELAP5/MOD2 MIST Post-Test Benchmark of Test No. 3404AA - Double-Ended Rupture of 10 Steam Generator Tubes," BAW-2031, 77-1171708-00, February 1989.

6. M. K. Smith and M. V. Parece, "RELAP5/MOD2 MIST Post-Test Benchmark of Test No. 3105AA - 10 CM² Pump Discharge Break," BAW-2030, 77-1171703-00, December 1988.

6. The B&W high auxiliary feedwater (AFW) model was not reviewed in the original release of BAW-10164 because the model was not used for applications on RSG plants. BWNT requested that this model be reviewed and approved for use in applications on B&W-designed plants. Please provide benchmarks or other supporting information justifying the use of this model in LOCA applications.

Response: The B&W high AFW model was originally developed for use in the AUX code, which calculated the dynamic interaction of the RCS and emergency feedwater system. It was later incorporated into the CRAFT2 code (Ref. 6-1). The NRC reviewed and approved the code model for use on B&W-designed plant EM applications in Reference 6-2. This approved model was later incorporated into RELAP5/MOD2-B&W with some minor calculational improvements.

The CRAFT2 SER summarizes the documentation used to quantify the high AFW tube wetting and heat transfer models. These included AUX benchmarks to plant data, Oconee-1 natural circulation tube wetting data, and ARC flow visualization data. It concludes that the high AFW model has been adequately verified against both separate-effects and integral system test data such that it is acceptable for use in SBLOCA EM applications.

The RELAP5/MOD2-B&W high AFW model consists of an AFW tube wetting model and a wetted tube heat transfer model. The tube wetting model is unchanged from the approved CRAFT2 model. The CRAFT2 heat transfer model has undergone some minor changes and improvements. The most significant change was a restriction of the Drew falling film heat transfer coefficient for subcooled AFW liquid heat transfer. For saturated liquid, the Chen nucleate boiling correlation was used to calculate the heat transfer coefficient for the wetted tubes. The steam heat transfer on the dry tubes was calculated based on the Dittus-Boelter correlation with a steam only Reynolds and Prandtl numbers.

The benchmark that best confirms the performance of the revised heat transfer model was performed as a part of the RELAP5/MOD2-B&W code certification effort. The benchmark is against test data from the MIST facility during steady-state conditions with high AFW injection. Figure 6-1 shows a cross-section of the MIST steam generator, including the tube designations. The AFW enters into the tube bundle approximately 50 feet from the lower tube sheet. Figure 6-2 shows a noding diagram of the RELAP5/MOD2 steam generator model used in the benchmark. The model arrangement above the aspirator is identical to models used in the SBLOCA EM. The primary tube region was separated into two regions. AFW was injected directly onto Tube J. Tubes H, J, and K were included in the AFW wetted region modeled by pipe Component 150. The remaining 16 tubes were included in the dry region modeled by pipe Component 140. Figure 6-3 shows the measured primary side temperature distributions and those predicted by the two channel RELAP5/MOD2 model. The comparisons are excellent. Because this was a separate-effects steady-state test, the heat transfer coefficients were easily quantified and justified.

The transient-effects modeling of the B&W high AFW model were supported by every MIST test benchmark. The tests began in a steady-state natural circulation condition with high AFW injection. After break initiation, the transient steam generator heat removal from the AFW was very important to the overall behavior of both the primary and secondary sides. The quality of these comparisons confirms the validity of the entire high AFW computer model in numerous integral system benchmarks. This model will be used similarly for typical plant SBLOCA applications. In these analyses, this AFW model will affect the steam generator heat removal and provide the appropriate influence on the RCS system responses.

In summary, RELAP5/MOD2-B&W uses an improved form of the high AFW model that was approved for EM use in the CRAFT2 code. The

additional separate effects and integral system benchmarks further confirm the validity of the revised model and its appropriateness for use in SBLOCA applications. BWNT believes that, based on the previous NRC-approval and these new benchmarks, ample justification is provided for approving use of this model for B&W-designed plant SBLOCA applications with the RELAP5/MOD2-B&W code.

References for Question 6

- 6-1. J. J. Cudlin, et al., "CRAFT2 - FORTRAN Program for Digital Simulation of a Multinode Reactor Plant During Loss of Coolant," BAW-10092A, Rev. 3, July, 1985.

- 6-2. "Safety Evaluation Report for the Babcock and Wilcox Owners Group Small Break Loss-of-Coolant Accident Evaluation Model, CRAFT2 (Rev. 3) (BAW-10192P, Rev. 3 and BAW-10154)," 5/10/85, (Included in Ref. 6-1)

Figure 6-1. MIST STEAM GENERATOR CROSS-SECTION.

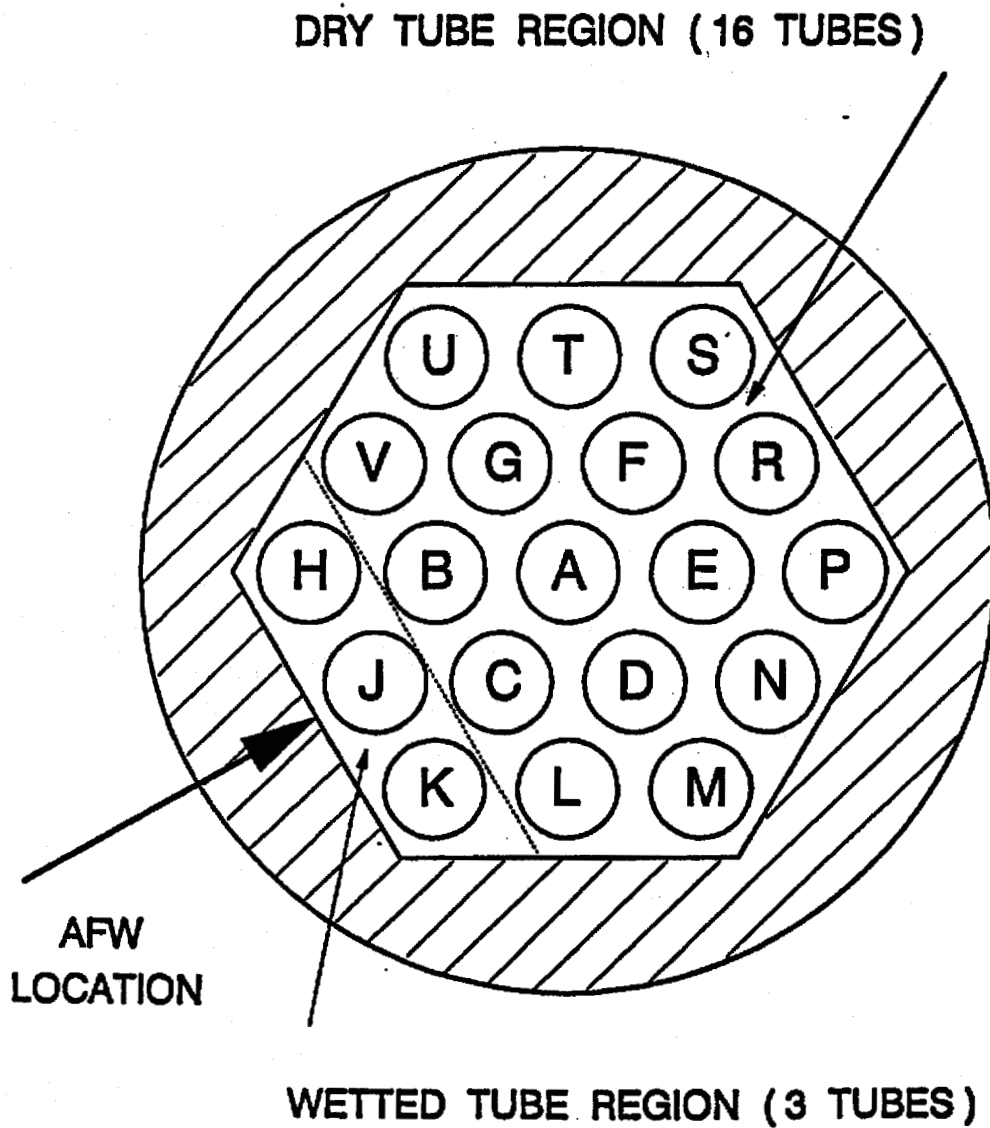


Figure 6-2. MIST STEAM GENERATOR NODING ARRANGEMENT.

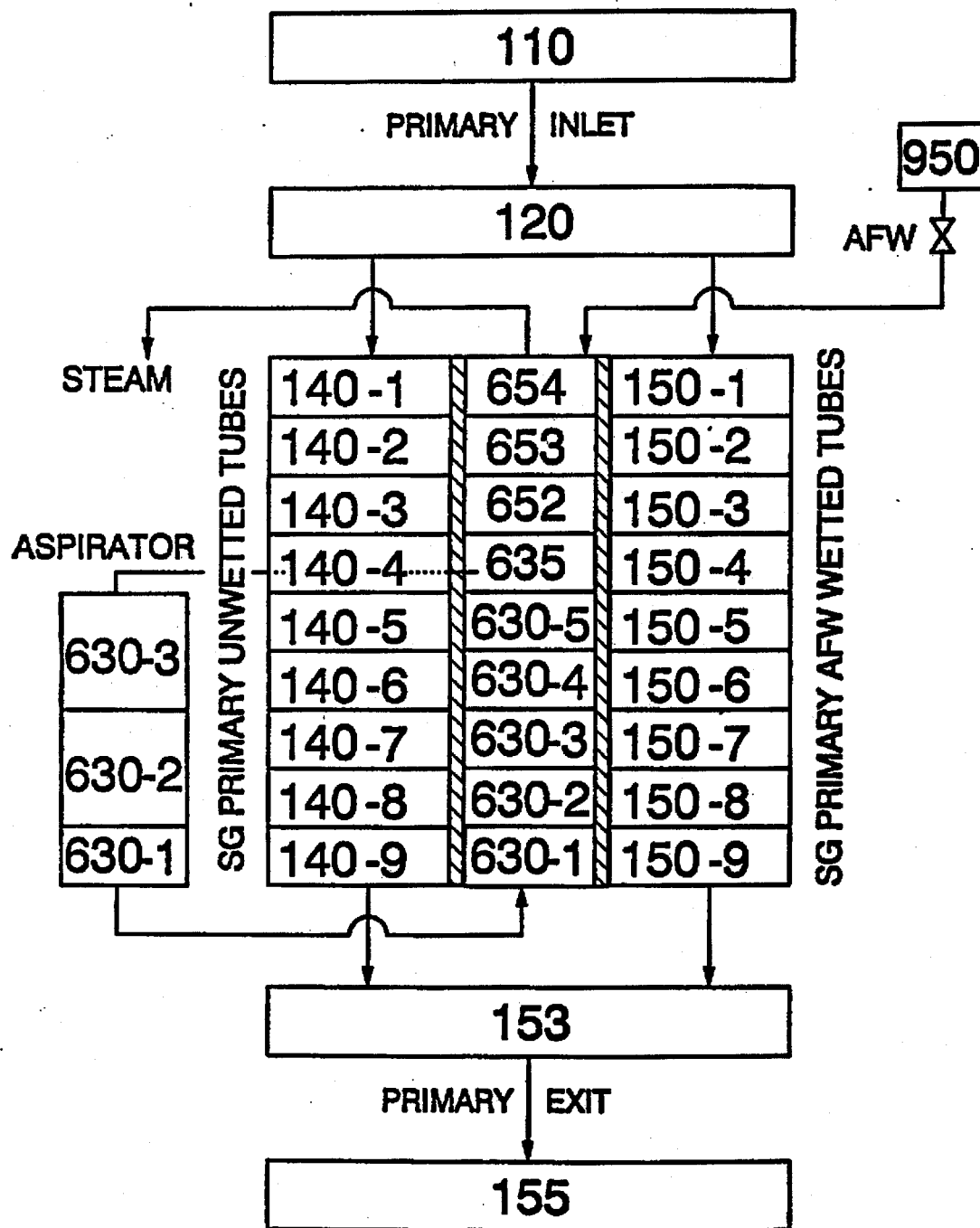
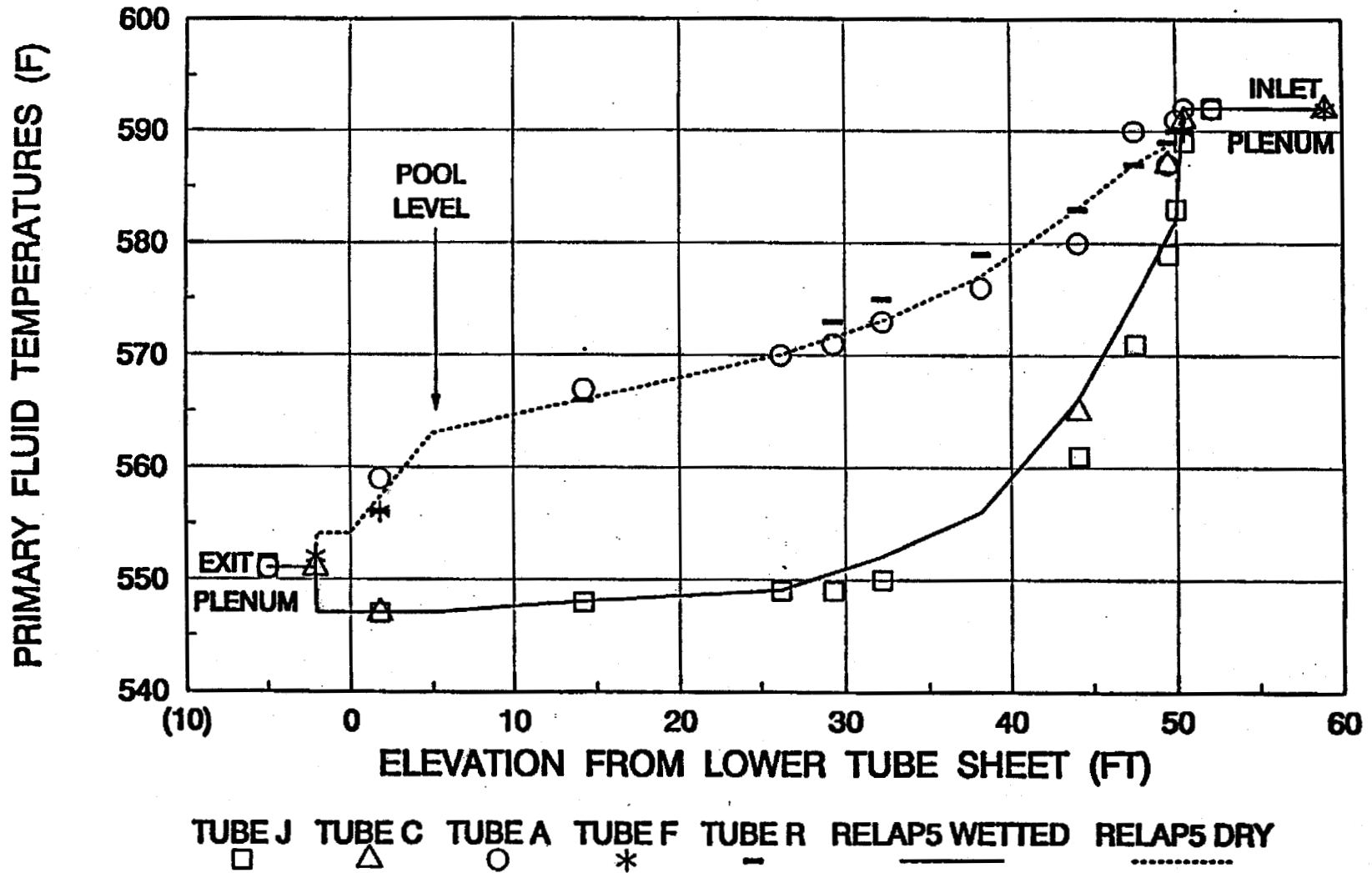


FIGURE 6-3. MIST MEASURED VS PREDICTED PRIMARY TEMPERATURES.



5-318
18

7. The MIST SBLOCA benchmarks provided in previous references did not show fuel temperature excursions. Please give references that justify conservative cladding temperature calculations during periods with fuel temperature excursions.

Response: For all of the MIST tests in which the reactor coolant pumps were not operating, none showed fuel temperature excursions. Therefore, combinations of test benchmarks must be used to support the conservatism of fuel temperature calculations for B&W-designed plants. There are four phenomena that govern the cladding temperature response: (1) the reactor coolant system (RCS) pressure response; (2) the RCS liquid inventory and distribution; (3) the core liquid inventory and mixture level during the core boildown phase, and (4) the core heat transfer above the mixture level during the boildown phase.

The MIST tests provided typical OTSG-plant RCS pressure and inventory responses for code benchmarks, directly addressing the first two phenomena. Good comparisons were obtained in the numerous RELAP5/MOD2-B&W benchmarks given as references in supplemental Question 5. These comparisons demonstrated that the code models, with typical plant nodalization, reproduced the key test thermal-hydraulic behavior for a large number of transients. Good representation of the RCS behavior provides the appropriate forcing functions for liquid inventory distribution, flashing contributions, leak phase determination, HPI flow, and overall transient progression.

Benchmarks of the MIST tests assure that the transient liquid inventory is appropriately calculated. Because the range of MIST experiments does not include cases for which the core mixture level falls into the active region, MIST is not the best benchmark for the core mixture level calculation. The core mixture level calculation during the core boildown phase is best benchmarked by the stand-alone FOAM2 and ORNL benchmarks provided in Appendix H of BAW-10164. The range of core and fuel assembly

geometries to which RELAP5/MOD2-B&W has been benchmarked is extended through the FOAM2 benchmarks to include fuel for boiling water reactors (the GE tests), for Japanese reactors (the Hitachi tests), for Westinghouse reactor designs (the Westinghouse tests), and for B&W-designed plants (the B&W tests). The benchmarks confirm both that the RELAP5/MOD2-B&W code correctly determines the mixture level in a prototypical core region and that it does so over a wide range of core and fuel assembly geometries. The ORNL benchmarks also provide comparisons and confirmation of the cladding surface temperature predictions (see Figures H.28 through H.33).

The MIST benchmarks showed accurate prediction of the RCS pressure and liquid inventory during the loop-draining phase. Good predictions of these parameters assure that the SBLOCA will enter the core boildown phase at the appropriate transient time and with the appropriate reactor vessel liquid inventory. The core boildown is then governed by the ECCS injection and core decay heat rates.

Since the mixture level has been shown to be correctly calculated (Appendix H), the determination of the heat transfer for portions of the fuel rods cooled by mixture and by steam must also be correct. The fuel pin heatup is controlled by integrated fuel pin heat addition above the mixture level and by the core steaming rate below the mixture level. Heat transfer below the mixture has repeatedly been shown to be sufficient to maintain the cladding within a few degrees of the coolant saturation temperature. Thus, except for the movement of mixture level, the core steaming rate is a straightforward function of the decay heating rate. Above the mixture, the cladding temperature is controlled by conduction and radiation heat transfer to vapor and by the vapor superheat. For a given cladding temperature excursion, the majority of the heat removal is attributed to the superheating of the vapor and only a small portion (estimated to

be approximately one-quarter) is due directly to other heat transfer mechanisms.

The calculational approach used in RELAP5/MOD2-B&W for the determination of vapor temperature and cladding heat transfer coefficient is straightforward and widely accepted for core boildown conditions. Two examples of temperature excursions during integral system benchmarks are contained in the RELAP5/MOD2-B&W topical BAW-10164, Revision 2. Appendix J contains an SBLOCA benchmark of a ROSA test. Conservative cladding temperatures were shown during the long-term core boildown phase of that transient. Section 5 of this topical (responses to questions) contains a benchmark of Semiscale S-LH-1 beginning on page 5-153. The calculated cladding temperatures given on page 5-187 were conservative compared to the test data. The Technical Evaluation Report (TER) for BAW-10164, Revision 2, (page 5-227 and 5-228) acknowledges this conservatism.

These benchmarks collectively demonstrate that the RELAP5/MOD2-B&W code, with typical plant input models, produces best-estimate RCS thermal-hydraulic responses during SBLOCA transient benchmarks for OTSG and RSG plants. Separate-effects core level swell benchmarks confirm the mixture level calculations and steam cooling tests in conjunction with integral system tests, ROSA and Semiscale, confirm the accuracy of the calculated cladding heatup. These models are ultimately coupled with key conservatisms in the SBLOCA plant analyses. The most important of the conservatisms is the 10CFR50 Appendix K requirement that core decay heat be calculated as 120 percent of ANS 1971 standard. This decay heat (1.2 X ANS 1971 is approximately 35 percent above current best-estimate values) causes significantly more core boiloff, such that core heatup begins much earlier than is realistic. The heatup generally lasts longer, and more ECCS is required to match and exceed the core boiloff rate. The early timing of the heatup and the longer heatup period ensure that conservative cladding temperatures will be calculated.

B&W designed NSSs provide one feature not found in other PWRs. The reactor vessel vent valves (RVVVs) are unique to B&W-designed plants. The RVVVs swing open to provide a direct path for venting of core steam to a cold leg break location. Their design and performance preclude the need for the cold leg pump suction to be cleared of water for system steam production to be vented to cold leg breaks. Thus, the core liquid inventory reduction and attendant cladding temperature increase required to accomplish loop seal clearing in other PWR designs is eliminated.

The RVVVs are not significant to SBLOCA predictions other than in their function to control the pressure difference between the reactor vessel downcomer and core, and the prevention of the need for loop seal clearing. This function is important, but it does not relate directly to the cladding temperature calculation. The only relationship is through the reactor vessel liquid inventory predictions. The ability of the RELAP5/MOD2-B&W to appropriately model the RVVV influence on system inventory has been adequately benchmarked in the MIST test series. Therefore, further justification of the RVVV performance during an SBLOCA core boildown phase in which it plays a secondary role is not warranted.

The cladding temperature excursion during SBLOCA in current PWR designs is brought about and governed by the same physical processes, regardless of the particular PWR design. BWNT has provided appropriate benchmarks of the ability of RELAP5/MOD2-B&W to simulate these mechanisms. The unique features of the B&W design that effect SBLOCA, the RVVVs and once-through steam generators, have been tested and benchmarked to a test facility that includes a direct modeling of the devices during the SBLOCA phases within which they act to produce differences between the B&W design and other NSS designs. There is, therefore, no need for the inclusion of a core uncovering test specific to the B&W design in the SBLOCA benchmark matrix.

8. Information provided in Supplemental Question 3 stated that a Tong factor of one has been used in LOCA applications since 1971. Please provide a previously-approved reference that explicitly states this licensing position.

Response: BWNT has two examples of NRC-approved LOCA evaluation models that explicitly state how the Tong factor is used. The first EM is for B&W-designed plants (BAW-10104, Rev. 5). THETA1-B (BAW-10094A, Rev. 3) is the core thermal analysis code used in this EM. It states in the first paragraph on page 21 of BAW-10094:

"A nonuniform flux factor is combined with the Westinghouse W-3, the Babcock & Wilcox B&W-2 and BWC CHF correlations for steady state calculations. However, since the flux factor was not developed for accelerating and decelerating flow situations it is not used during transient computations."

The second EM is for RSG plants (BAW-10168, Rev. 1). FRAP-T6 (BAW-10165, Rev. 1) is the core thermal analysis code used in this EM. It states on page 2.1-37 for the B&W-2 CHF correlation (Equation 2.1.4-30 gives the Tong factor):

" F_{BW2} = nonuniform axial power shape factor, (optionally used only for steady-state calculations),"

The BWC (Equation 2.1.4-32), BWC MV (Equation 2.1.4-34), and W-3 (Equation 2.1.4-35) CHF sections contain similar statements to the one shown above, indicating that the Tong factor is not used for transient applications.

9. Equation 2.1.3-30.6 contains a user-specified coefficient, C_{vB} . What value is used for this coefficient?

Response: Equation 2.1.3-30.6 is

$$v_{bub} = C_{vB} \Delta v .$$

A value of 1.0 is used for C_{vB} in all EM SBLOCA applications. This input was originally included to permit sensitivity studies, but it has never been used in any reported application.

During the review of this question, a typographic error was noted in Equation 2.1.3-30.7. The last term in that equation is Δv^2 . This term should have been v_{bub}^2 from Equation 2.1.3-30.6. However, since C_{vB} is always 1.0, the equation is correct as used in the EM applications.

5.7 Revisions 2 and 3 SER

This section contains the SER/TER transmitted to BWNT by G. M. Holahan of the NRC in his letter of March 14, 1995.

Rev. 3
7/96

This page intentionally left blank.



UNITED STATES
NUCLEAR REGULATORY COMMISSION

WASHINGTON, D.C. 20555-0001

March 14, 1995

Mr. J.H. Taylor, Manager
Licensing Services
B&W Nuclear Technologies
3315 Old Forrest Road
P.O.Box 10935
Lynchburg, VA 24506-0935

Dear Mr. Taylor:

SUBJECT: ACCEPTANCE FOR REFERENCING OF TOPICAL REPORT, BAW-10164P, REVISIONS 2 AND 3, "AN ADVANCED COMPUTER PROGRAM FOR LIGHT-WATER REACTOR LOCA AND NON-LOCA TRANSIENT ANALYSIS"

The NRC staff has reviewed the topical report BAW-10164P, Revisions 2 and 3, which describe a RELAP5 based computer program for PWR LOCA and non-LOCA transient analysis. Revision 2 was intended for small break LOCA applications and Revision 3 included enhancements to the evaluation model for fuel pin heat transfer, and benchmarks extending application of the code to the once through steam generator plants. In addition to the benchmarks provided in the approved Revision 1 of the code, Revisions 2 and 3 provided comparisons to the ROSA-IV, THTF and the MIST experimental data. The RELAP5 based computer program provides predictions of the physical phenomena which are important during a small break LOCA.

The staff finds BAW-10164P, Revisions 2 and 3 to be acceptable for referencing in LOCA and non-LOCA PWR licensing actions to the extent specified, and under the limitations stated in BAW-10164P, Revisions 2 and 3 and the associated U.S. Nuclear Regulatory Commission safety evaluation report which defines the basis for accepting this topical report.

If the staff's criteria or regulations change so that its conclusions about the acceptability of the report are invalidated, B&W Nuclear Technologies should revise and resubmit their respective documentation or submit justification for the continued effective applicability of the topical report without revising their respective documentation.

The staff was assisted in this review by SCIENTECH, Inc. under contract No. NRC-03-093-031, JCN No. E-2095, Task Order No. 2.

James H. Taylor

-2-

Our safety evaluation (Enclosure 1) is based on the SCIENTECH, Inc. technical evaluation report SCIE-NRC-224-94 which is in Enclosure 2.

Sincerely,



Gary M. Holahan, Director
Division of Systems Safety and Analysis
Office of Nuclear Reactor Regulation

Enclosures:
As stated



UNITED STATES
NUCLEAR REGULATORY COMMISSION
WASHINGTON, D.C. 20555-0001

ATTACHMENT 1

SAFETY EVALUATION BY THE OFFICE OF NUCLEAR REACTOR REGULATION
BAW-10164P, REVISIONS 2 AND 3, "AN ADVANCED COMPUTER PROGRAM
FOR LIGHT WATER REACTOR LOCA AND NON-LOCA TRANSIENT ANALYSIS"

B&W NUCLEAR TECHNOLOGIES

1.0 INTRODUCTION

By letter dated September 18, 1992, the B&W Nuclear Technologies Company submitted the topical report BAW-10164P, Revisions 2 and 3 for NRC review. The report describes a pressurized water reactor (PWR) thermal-hydraulics transient analysis code for LOCA and non-LOCA transients analysis based on the RELAP5/MOD2 code.

RELAP5/MOD2-B&W is a B&W Nuclear Technologies (BWNT) adaptation of the Idaho National Engineering Laboratory (INEL) RELAP5/MOD2⁽¹⁾ code used for PWR licensing and best estimate thermal hydraulics transient analysis. RELAP5/MOD2 was developed by INEL as a best-estimate computer code for light water reactor transient analysis. B&W Nuclear Technologies has added features to permit use of the RELAP5/MOD2-B&W code for ECCS evaluation model (EM) calculations. The previous revision of the RELAP5-B&W code, Revision 1⁽²⁾, was approved for use in the analysis of small break and large break LOCAs⁽³⁾ (SBLOCA and LBLOCA) for recirculating steam generator plants.

Revision 2 of BAW-10164P⁽⁵⁾ describes updates for use in performing small break LOCA analysis. These updates include an additional critical heat flux (CHF) correlation referred to as

BWUMV, addition of the Wilson model for determining interphase drag, addition of a counter-current flow limiting (CCFL) model and correction of minor code errors. Benchmarks are included in Revision 2 to specifically address the Wilson interphase drag model and the small break LOCA EM model. The SBLOCA benchmark is against experimental data from the ROSA-IV large scale test facility.

In addition to the correction of minor errors, Revision 3 of BAW-10164P⁽⁶⁾ includes enhancements to the EM fuel pin model, EM heat transfer model, and models to support use of the code for analysis of once through steam generator (OTSG) plants. These models include the Becker CHF correlation, further modifications to the slug-drag model, the high auxiliary feedwater model and the Chen nucleate boiling heat transfer coefficient void ramp. Benchmarks against model 19-tube OTSG data and against SBLOCA test data from the MIST facility, which has simulated OTSGs, are included. The modifications to the approved licensing model proposed in References 4 and 5 are the subject of the review and evaluation documented in this report.

2. SUMMARY OF THE TOPICAL REPORT

BAW-10164P Revisions 2 and 3 present best estimate and licensing type calculation for PWRs. Simulation methods are presented for large and small break LOCAs as well as operational transients such as anticipated transients without scram, loss of off-site power, loss of feedwater, and loss of flow. The solution is based on a two energy equation scheme, a two step numerical option, a gap conductance model, constitutive models and control system models. Control system and secondary system components have been added to permit modeling of plant controls, turbines, condensers, and secondary feedwater conditioning systems. Benchmark comparison of code predictions to integral system test

results are also presented.

Revision 2 deals mainly with the small break LOCA. Revision 3 includes enhancements to the evaluation model for fuel pin heat transfer modelling to extend the code applicability to the once through steam generators.

3.0 EVALUATION

Review and evaluation of the RELAP5/MOD2-B&W code includes Revision 2 and Revision 3 of BAW-10164P. Revision 2 provides additional models specifically intended for SBLOCA applications. Revision 3 includes enhancements to the EM fuel pin and heat transfer model, additions and benchmarks which extend application of the code to the once through steam generator plants. An initial review of Revisions 2 and 3 led to generation of Requests for Additional Information^(8,9). Supplemental information was also submitted by BWNT during the review process⁽¹⁰⁾. Each of the model additions or modifications is discussed and evaluated in the following sections.

3.1 BAW-10164P, Revision 2

3.1.1 Model Changes for the Slug Flow Regime

BWNT added an option for determining the Taylor bubble interphase drag during slug flow based on the Wilson drag model. The Wilson drag model is based on the Wilson bubble rise velocity in a vertical pipe. BWNT applied the Wilson drag model for reflood applications using the BEACH program and is now applying the model for non-reflood applications in RELAP5/MOD2-B&W. These changes are discussed on pages 2.1-51 to 2.1-54 of BAW-10164P. Benchmarks are provided in Appendix H.

In implementing the Wilson drag model for RELAP5/MOD2, BWNT derived an expression for the interphasic friction for Taylor bubbles. Flow was assumed to be in a quasi-steady state. The derivation of this expression was checked. The formulation was determined to be correct. BWNT also incorporated improvements to match the bubble rise data at higher void fractions. An apparent difference between the interphase friction model for slug flow used in RELAP5/MOD2 B&W compared to that used in the BEACH⁽⁷⁾ program was questioned. BEACH uses the same Wilson drag model with a different multiplier, on the Taylor bubble term. BWNT responded that the different multipliers were selected based on comparisons to reflood benchmarks in the case of BEACH and small break LOCA benchmarks in the case of RELAP5/MOD2-B&W.

An option to remove smoothing in selected junctions, (not used in BEACH), was added to RELAP5/MOD2-B&W. This option allows smoothing to be bypassed. Since discontinuous void distributions may occur during a small break LOCA, use of this option for small break calculations may be appropriate.

Benchmarks were performed by BWNT using the Wilson drag model against results obtained from the NRC-approved computer code FOAM2⁽¹¹⁾ and with small break LOCA experiments performed at the Thermal Hydraulic Test Facility (THTF) at the Oak Ridge National Laboratory. These benchmarks are presented in Appendix H to BAW-10164P.

The FOAM2 program, developed by BWNT and previously approved by the NRC, is used to determine whether the water content of a reactor core is sufficient to cover the core with a combination of liquid and two phase mixture based on a given core void distribution. If it is determined that the core is uncovered, FOAM2 calculates the two-phase swell level and steaming rate. The FOAM2 program utilizes the Wilson bubble rise correlation to

directly calculate the core void distribution. The Wilson bubble velocity correlation used in FOAM2 is somewhat different from that used in RELAP5/MOD2-B&W since it does not include the changes made by BWNT to better match the bubble rise data at higher void fractions. BWNT stated that the core void distribution results calculated by RELAP5/MOD2 B&W and FOAM2 should be similar except potentially at higher void fractions because of differences in the formulation of the Wilson model. The benchmarks show that RELAP5/MOD2-B&W predicts void distributions which are comparable to FOAM2 predictions.

Calculations using FOAM2 were performed for reactor powers of 1.5, 2.5, and 5.0 percent of full power. System pressures ranging from 100 to 1600 psia were included in the analysis. BWNT presented plots of core void fraction vs. core elevation comparing the RELAP5/MOD2-B&W results and the FOAM2 results. These plots show acceptable agreement between RELAP5/MOD2-B&W and FOAM2, with RELAP5/MOD2-B&W showing very slightly different results at high void fractions.

The RELAP5/MOD2-B&W code predictions were compared to THTF test results for a range of pressures (520 to 1170 psia), power densities (0.08 to 0.68 kw/ft), and mass flux (3395 to 21943 lbm/hr-ft²). BWNT presented plots of the results of core void fraction vs. core elevation as well as rod surface and vapor temperature vs. core elevation comparing the RELAP5/MOD2-B&W results and the THTF test results. In general, the void fractions predicted by RELAP5/MOD2-B&W are somewhat higher than the THTF results. Additionally, RELAP5/MOD2-B&W generally overpredicts the vapor and surface temperature relative to the THTF tests. There is a dip in surface temperature in the THTF tests at the core elevation of 11 feet. BWNT attributes the dip to grid effects on the heat transfer rate which are not accounted for in the RELAP5/MOD2-B&W model. The dip in surface temperature

caused by the grid effect, was questioned. The surface temperature would be underpredicted for THTF tests 3.09.10 i, j, l, and m. Underprediction of the surface temperature could indicate that the heat transfer coefficient to the vapor is high and non-conservative. It was requested that BWNT discuss the comparisons between RELAP5/MOD2-B&W and the THTF tests and show that the comparisons do not rely on systematic underprediction of the vapor temperature. In their response, BWNT indicated that the heat transfer coefficient for single phase vapor is computed using the McEligot-plus radiation correlation set. BWNT pointed out that use of the correlation is widely accepted and was reviewed and accepted in previous submittals of RELAP5 and FRAP-T6 topical reports. BWNT also noted that the measurement of vapor temperature is low because the thermocouples were mounted on the unheated rods used to simulate guide tubes. Actual temperatures measured at THTF would be higher and more in agreement with RELAP5/MOD2-B&W. The BWNT response was deemed satisfactory. This benchmark shows that use of the Wilson model for interphase drag produces reasonably accurate predictions of SBLOCA experimental data.

3.1.2 Model Changes for the Annular Mist Flow Regime

BWNT has added an option to RELAP5/MOD2-B&W to include calculation of the overall drag computed for control volumes in an annular mist flow regime. This change is used in the OTSG and MIST benchmarks discussed in Sections 3.2.7 and 3.2.8 of this evaluation.

3.1.3 Counter-Current Flow Limiting Model

BWNT added optional counter-current flow limiting (CCFL) models which are intended for use in predicting flows at the steam generator U-tube inlets and steam generator plenum inlets during the reflux condensation period of a SBLOCA. Addition of the CCFL

model is described on pages 2.1-133 to 2.1-133.3 of BAW-10164P.

The CCFL model modifications, consisting of a correlation for flooding in vertical tubes, are included in the form of a general relationship between the dimensionless vapor flux, j_g^* and the dimensionless liquid flux, j_f^* . The relationship is implemented in the code in a manner similar to the implementation in RELAP5/MOD3. Different values of the correlation parameters are used at the U-tube inlets and at the steam generator plenum inlet. This model was benchmarked against ROSA-IV small break LOCA data in Appendix J of the Topical Report. Flow predictions were in reasonable agreement with the test data. Therefore, the use of the CCFL model at the steam generator plenum and tube inlet, with the parameters used in the benchmark, is acceptable for the analysis of SBLOCAs in recirculating steam generators. As demonstrated by the fact that different correlation parameters are required at the inlet plenum and the tubes, CCFL is very geometry specific. Other uses of the CCFL model will require that the model be validated for that application.

3.1.4 Condensation Heat Transfer Correlation Modifications

Modifications were made to the condensation heat transfer correlation for vertical or horizontal surfaces. These changes are discussed on pages 2.2-31 and 2.2-32 of BAW-10164P.

The Nusselt laminar film correlations for a horizontal surface and for a vertical surface are used in RELAP5/MOD2-B&W. For condensation on a horizontal surface, laminar film condensation in a horizontal tube is assumed. Comparing the formulation given in Collier⁽¹²⁾ against that given by BWNT for condensation within a horizontal tube shows that BWNT did not include the equation developed by Rohsenow for the modified latent heat of vaporization. Omission of this equation will have a small effect

for the heat transfer coefficient result. The expression for a vertical surface was found to be in agreement with Collier.

3.1.5 Changes to the Metal-Water Reaction (Swelled Radius) Model

When a fuel rod swells the radius and hence the surface area of the rod will increase in the swelled region. The rate of heat generation and the molar production rate of hydrogen are proportional to the exposed surface area of the clad. These models have been modified by BWNT as described in Section 2.3.2.4 of BAW-10164P to increase the surface area in proportion to the ratio of the swelled clad radius to the cold clad radius. This increase in area is applied to both the clad inside and outside surfaces. Consideration of the increase in clad radius in the swelled region is appropriate and conservative. Both the energy generation rate and the rate of hydrogen production will increase when this model is used compared to the constant surface area model. This model satisfies the requirements of Appendix K and is acceptable for ECCS EM calculations.

3.1.6 Core Heat Transfer Selection Model Modifications

BWNT installed a separate heat transfer option for use in SBLOCA analysis. The changes are discussed on pages 2.3-60 to 2.3-61.2, 2.3-64, 2.3-67, 2.3-83, and 2.3-84 of BAW-10164P. The changes to the switching logic for SBLOCA include the removal of Appendix K restrictions regarding no return to nucleate boiling and the lock into film boiling after the wall superheat exceeds 300° F. The switching logic is unchanged for LBLOCA. BWNT stated that the no return to nucleate boiling and the lock into film boiling restrictions of Appendix K are not applicable to SBLOCA. This assertion is acceptable. While the acceptance criteria of 10 CFR 50.46 apply to LBLOCA, the possible core heatup scenarios following a SBLOCA are varied and more complex than those for the

LBLOCA. The use of a reflood heat transfer model lockout of return to nucleate boiling and prediction of quenching is inappropriate for the small break.

An option to allow use of the BWUMV critical heat flux correlation can be selected by the user depending on the fuel design being evaluated. This correlation is used only at pressures greater than 1300 psia at mass fluxes greater than 500,000 lbm/hr-ft² in the core heat transfer selection logic in RELAP5/MOD2-B&W. The BWUMV correlation is reviewed in the next section.

3.1.7 BWUMV Critical Heat Flux Correlation

The BWUMV (B&W Universal Mixing Vane) critical heat flux correlation was developed for the analysis of SBLOCA. The development of the BWUMV correlation is presented in Appendix I to BAW-10164P. BWNT developed this correlation from the database for the previously approved BWCUMV correlation⁽¹³⁾ with additional mid-flow regime data from three Westinghouse tests.

BWUMV utilizes a third order polynomial fit using three independent variables based on pressure (P), mass flux (G), and quality (X_{eth}). Typographical errors in the CHF equation, units conversion errors, and the FLS equation, were questioned. The responses with the corrected equations and units are provided in Reference 8.

The number of data points and their distribution in the mass flux range below 0.95×10^6 lb/hr-ft² was questioned. BWNT indicated in their response that the total number of data points with mass fluxes below 1.25×10^6 lb/hr-ft² is 77. In addition to the 22 points from Table I.3 of Appendix I, 20 points are from the data presented in Appendix B of BAW-10159 and 35 test points are from

the data presented in Appendix F of BAW-10159. Of these 77 points, a total of 32 points were measured at a local mass flux of between 0.4×10^6 and 1.0×10^6 lb/hr-ft². This total is comparable to the number of points at the lower end of the flow range of the BWCMV correlation.

In evaluating the distribution of points about the measured/predicted ratio for pressure and mass flux, it is noted that the data clustered about 750 psia and 1000 psia on Figure I.5 are not uniformly distributed about the mean value of 1.0. It appears that 10 of the 11 points measured at 750 psia are below the mean and 10 of the 12 points measured at 1000 psia are above the mean. Because of this bias and because of the small number of points, we believe that the BWUMV results are biased at pressures of 750 and 1000 psia. It is recognized that this bias does not affect BWUMV predictions above 1300 psia. However, BWNT did conclude in Appendix I to BAW-10164P that the BWUMV correlation is applicable to CHF calculations for pressures and flow rates above 750 psia. Given the apparent bias in the data points at 750 and 1000 psia, the BWUMV correlation should not be used for CHF calculations at pressures below 1300 psia.

Numerical checks of the BWUMV correlation were performed. These calculations were done to determine how well the BWUMV correlation reproduces predicted results, to determine the behavior of the BWUMV correlation over a range of pressure, flow rate and quality, and to compare the BWUMV to the BWCMV correlation since they were developed from the same database for the most part.

In general, the numerical checks show that the BWUMV and the BWCMV correlations are in agreement within the statistical uncertainty band. Some differences in the results are noted in cases where the flow is varied over the BWCMV range of validity.

These differences are more significant when the pressure is at 1500 and 1800 psia. Evaluations performed where the pressure is varied over the BWCMV range of validity also show some difference between the two correlations.

The statement is made in Appendix I that the Tong factor is set equal to one in the RELAP5/MOD2 B&W implementation of BWUMV. In discussions with BWNT they stated that the Tong factor is included in the development of the BWUMV correlation. It is during the SBLOCA transient analysis that the Tong factor is set equal to 1. BWNT also indicated that their standard practice is to set the Tong factor equal to 1 for LOCA analysis and indicated several references where this practice has been previously approved.

Based on this review, it is concluded that the BWUMV correlation is acceptable for used in RELAP5/MOD2 B&W subject to the restriction that the correlation should not be used below pressures of 1300 psia.

3.1.8 SBLOCA EM Benchmark

BWNT performed a benchmark using RELAP5/MOD2 B&W against a SBLOCA experiment performed at the ROSA-IV facility in 1988. The ROSA-IV facility simulates a recirculating steam generator plant. The results of this benchmark are presented in Appendix J to BAW-10164P. It is important to note that this is not the only benchmark of RELAP5/MOD2-B&W for a SBLOCA. As noted in appendix J, the peak clad temperatures during the experiment are not significant relative to the acceptance criteria. Benchmarks against LOFT and Semiscale SBLOCA data, presented in Section 5 of BAW-10164, provide additional coverage of SBLOCA phenomenology, including clad temperature prediction. This benchmark serves to show that the additional models for SBLOCA, such as CCFL and Wilson drag, are performing correctly and will adequately predict

test data.

The RELAP5/MOD2-B&W model for ROSA-IV, and other benchmarks and applications models, use equilibrium thermodynamics nodes in the core region and non-equilibrium nodes in the remainder of the system. Since the RELAP5/MOD2 Code Manual specifically states that equilibrium nodes cannot be connected to non-equilibrium nodes, BWNT was questioned on node connectivity. In their response BWNT stated that RELAP5/MOD2 has always been fully capable of connecting equilibrium and non-equilibrium nodes, and that this is consistent with the approved EM core modeling. This was confirmed by INEL (the RELAP5 code development organization), that the equilibrium option is obtained using the same basic equations with the interphase heat transfer coefficient set to a very high value. This assures that sufficient heat transfer will occur to keep both phases at saturation conditions. Contrary to the statements in the code manual, it is possible to connect equilibrium and non-equilibrium nodes without adversely affecting the calculational algorithms. BWNT uses equilibrium nodes in the core region to obtain saturation fluid temperature as the boundary condition for the core heat transfer correlations, which were developed on this basis.

When modeling complex systems, it is sometimes necessary to slightly modify the representation to compensate for code model limitations. BWNT used two such modifications in their representation of the ROSA-IV facility. First, the friction factor for the accumulator injection line was increased by a factor of 100 above the nominal value, to eliminate unrealistic injection flow oscillations. Also, the angle of the inlet pipe to the steam generator plenum was decreased to less than 15 degrees to permit use of the horizontal pipe stratification model. BWNT provided justification for these model modifications. In both cases, the BWNT responses adequately explained the need for modifications to overcome code

limitations.

BWNT performed a time step sensitivity study which demonstrated that the 0.05 second time step used for the calculations was adequate.

Results of the calculations showed that the basic thermal-hydraulic phenomena which occurred during the SBLOCA were predicted with reasonable accuracy. Key events were predicted to occur in essentially the correct sequence. Differential pressures in the core and recirculation loops, key determinants of the flows, were adequately predicted. This benchmark further demonstrates that the RELAP5/MOD2-B&W computer program is capable of predicting the important thermal-hydraulic phenomena which occur during a SBLOCA in a recirculating steam generator plant.

3.2 BAW-10164P, Revision 3

3.2.1 Revision to the Slug Flow Drag Model

BWNT incorporated a third option for evaluating the Taylor bubble interphase drag in slug flow. The three models now available are the base INEL model, the Wilson drag model submitted with Revision 2 of BAW-10164P, and the B&W modified slug-drag model, as described on pages 2.1-52.4 and 2.1-52.5 of Revision 3 of BAW-10164P. (The Wilson drag model was reviewed in Section 3.1.1 above).

In the B&W modified slug-drag model, adjustments are made to the interphase friction terms through the use of empirically derived coefficients. BWNT states that these adjustments were based on numerous benchmarks. BWNT listed the benchmarks used which included those documented in Appendices K and L to BAW-10164P. These benchmarks are discussed in Sections 3.2.7 and 3.2.8 of this evaluation.

3.2.2 Modifications to the Chen Heat Transfer Coefficient

The saturated nucleate boiling heat transfer coefficients used in RELAP5/MOD2-B&W are calculated using the Chen heat transfer correlation to model the boiling component of the heat transfer coefficient. The Chen heat transfer correlation employs a nucleate boiling suppression factor S . S was modified by including a multiplicative weighing factor to force S , and the boiling heat transfer coefficient to zero as the steam void fraction approaches one. B&W notes that this ramp is needed for once-through steam generator applications to preclude sharp increases in S that result in disproportionately high overall heat transfer as the void fraction approaches one.

3.2.3 Incorporation of the Becker CHF Model

The Becker CHF correlation for rod bundles is incorporated into RELAP5/MOD2-B&W as described in Section 2.2.2.2 of Revision 3 of BAW-10164P. BWNT states that this correlation was used to obtain better predictions of secondary side heat transfer relative to the Biasi-Zuber correlation used in RELAP5/MOD2 at power levels below 80 percent of full power. The Becker CHF correlation is used up to a pressure of 90 bar (1306 psia). Linear interpolation between the Becker and Biasi-Zuber correlations is performed between 80 and 90 psia to obtain a smooth transition between the two correlations.

Benchmarks comparing results of RELAP5/MOD2-B&W to OTSG test data are presented in Appendix K of BAW-10164P and are discussed in Section 3.2.7 of this SER. These benchmarks show good agreement between RELAP5/MOD2-B&W results using the Becker CHF correlation and the OTSG test data as discussed in Section 3.2.7.

3.2.4 EM Pin Model Modifications

BWNT enhanced the fuel pin model in RELAP5/MOD2-B&W by adding features which had previously been approved for use in the FRAP-T6-B&W⁽¹⁴⁾ and TACO3⁽¹⁵⁾ computer programs. These changes are discussed in Section 2.3.2 of Revision 3 of BAW-10164P. There are three basic areas in which the fuel pin model provides calculations: dynamic fuel/clad gap conductance, fuel rod swelling, and rupture based on the NUREG-0630⁽¹⁶⁾ approach and clad metal-water reaction. Enhancements in Revision 3 include addition of a closed gap contribution to gap conductance to allow modeling of high burnup cases, fuel pin axial expansion, automated clad rupture calculation, implicit metal-water reaction option and automated steady-state gap multiplier option.

The RELAP5/MOD2-B&W enhanced fuel pin model has some differences compared to the previously approved models in FRAP-T6-B&W and TACO3. These are due to the less detailed nature of the model used in RELAP5/MOD2-B&W compared to the fuel performance codes.

The previously approved gap conductance model allowed for modeling of a non concentric fuel stack within the clad, but did not include a contact conductance term in the calculation of total gap conductance. The option to include a contact resistance contribution has been added based upon the model presently used in the TACO3 computer program. Since Appendix K does not prohibit the use of contact resistance, this model is acceptable for cases of high burnup fuel with a closed gap.

The gap gas pressure is used to determine the amount of clad swelling and rupture. One of the variables which determines the gap gas pressure is the amount of volume available for the gas to occupy. A portion of this volume is located in the gas plenum at the top of each fuel rod. When the clad and fuel expand axially

at different rates the volume of the plenum will change. The axial expansion model accounts for this change in plenum volume due to differential thermal expansion of the fuel and clad from the cold condition. Thermal strain correlations from MATPRO⁽¹⁷⁾, or user input fits, are used to determine the amount of fuel and clad axial expansion. Including the effects of axial fuel rod expansion on plenum volume is appropriate for a best-estimate calculation, and is acceptable for Appendix K to 10 CFR 50 LOCA analysis, which does not prohibit including this model. Only minimal differences exist between the enhanced fuel pin model and the FRAP-T6-B&W model. The enhanced model is acceptable for use in ECCS evaluation model calculations.

Addition of an automated clad rupture model introduces heat transfer enhancement downstream of a rupture location. The model used for this option has been previously approved for use in the BEACH computer program. This option automates the calculation of rupture location for use in BEACH. Use of this model in RELAP5/MOD2-B&W is consistent with the Appendix K to 10 CFR 50 approved model and is, therefore, acceptable.

An implicit formulation of the Baker-Just metal water reaction model has been implemented in RELAP5/MOD2-B&W. The model is the same as that which is used in the FRAP-T6-B&W computer code. Appendix K to 10 CFR 50 requires use of the Baker-Just model but does not specify the numerical solution technique to be used. The implicit solution will improve accuracy for calculations which use a larger time step. Use of this option is acceptable for compliance with Appendix K to 10 CFR 50.

Initialization of the RELAP5/MOD2-B&W model must comply with Appendix K to 10 CFR 50 in the sense that initial stored energy in the fuel must be conservatively specified. This is done by adjusting the fuel clad gap conductance to obtain the desired

value of volume average fuel temperature. In earlier versions of the program a user specified multiplier on the gas conductance term of the gap conductance was provided to permit adjustment and matching of volume average fuel temperature. This required that an iterative process be performed by the user. An option has been added to automate this iteration process. The user can specify the desired volume average fuel temperature, rather than the multiplier on the gas conductance term, and the code will iterate to determine the gas conductance multiplier. This is a user convenience feature which is acceptable for ECCS evaluation model calculations.

3.2.5 EM Heat Transfer Model Modifications

BWNT incorporated a filtered flow option to be used with the core heat transfer model. This option was added to facilitate addressing the Appendix K to 10 CFR 50 requirement to eliminate any calculated rapid flow oscillations with a period of less than 0.1 seconds during the LBLOCA blowdown phase. This requirement is mandated because rapid flow oscillations can cause overprediction of the amount of energy removed from the core which would cause peak clad temperature to be underpredicted. The method, described in Section 2.3.3 of BAW-10164P, is consistent with the requirements of Appendix K to 10 CFR 50.

3.2.6 Post-CHF Model Modifications

User defined correction factors were added to the equation used to determine the total wall-to-fluid heat flux due to transition boiling as shown on page 2.3-86 of Revision 3 to BAW-10164P. These constants are defined as C_{1TR} and C_{1TR1} which have a default value of 1.0. BWNT did not identify any benchmarks that used values other than 1.0 for these correction factors.

A user option was added to allow adjustment of the surface heat transfer coefficient following cladding rupture of a fuel pin on page 2.3-89 of Revision 3 to BAW-10164P. If this option is invoked, the heat flux in a ruptured segment single heat structure is multiplied by the ratio of the ruptured to cold outside cladding radius. The heat flux is then computed using the increased surface area resulting from clad swelling and rupture. This change is physically realistic and does not violate Appendix K requirements. It is, therefore, acceptable.

3.2.7 OTSG Benchmarks

BWNT performed two benchmarks of the RELAP5/MOD2-B&W code to demonstrate the adequacy of the OTSG modelling. These benchmarks are discussed in Appendix K to BAW-10164P. The first set of benchmarks are comparisons to steady-state tests performed in 1969 to demonstrate the ability of the code to predict the shell side nucleate boiling length at various power levels. The second benchmark is a comparison to a loss of feedwater flow test performed in 1977 to demonstrate the ability of the code to predict boil-down and refill of a OTSG.

The tests were performed at the Alliance Research Center (ARC) Nuclear Steam Generator Test Facility. This facility provided the capability of testing steam generators at full system pressure and temperature conditions. The primary side of the test loop consisted of a gas-fired furnace to simulate reactor heat input into the primary fluid, a pressurizer, flow control valves, flow measuring elements, and a water conditioning system. The secondary system was a closed circuit test loop consisting of steam flow control valves, steam flow measuring equipment, feedwater heaters, back pressure control valves, a flash tank, circulating pumps, feedwater control valves, feedwater flow measuring equipment, feedwater flow bypass valves, and a water conditioning system.

The model steam generator used for these benchmarks, referred to as the 19-tube OTSG, is a single pass, counterflow, tube and shell heat exchanger. The tube bundle consisted of 19 full length tubes, each 5/8 inch diameter, spaced on a triangular pitch on 7/8 inch centers. Primary inlet flow entered at the top of the steam generator, flowed downward through the tube bundle and exited at the bottom. Secondary feedwater flow entered the tube bundle at the bottom, was boiled as it passed by the outside of the tube bundle, and exited at the top. The feedwater was raised to saturation conditions by mixing the water with steam from the tube region via a steam bleed pipe connected from the secondary side of the generator to the steam/feedwater mixer. A question on where the feedwater temperature is measured was raised. BWNT stated that the feedwater temperature is measured with a thermocouple located approximately three feet upstream of the steam/feedwater mixer.

In the steady state tests, boiling length (dryout location) was determined from primary tube and secondary side thermocouples for a range from 0 to 100 percent of the full scaled power consistent with a 2700 MWth plant. The loss of feedwater flow test initialized to full scaled power consistent with a 2772 MWth plant. The test was initiated by the simultaneous trip of the feedwater pump and closure of the feedwater isolation valve. The steam generator was allowed to boil dry and then the feedwater was restarted. Secondary steam flow and temperature and primary outlet temperature were measured during the test.

The RELAP5/MOD2-B&W model utilized 11 axial control volumes in the primary tube region and in the secondary shell region. Primary to secondary heat transfer was modelled using eleven heat structures between the primary and secondary sides. The external downcomer was modeled with five axial control volumes that represented the piping from the steam/feedwater mixing region to the tube bundle inlet. Feedwater aspiration was provided by a

single junction component that connected the tube bundle region to the external downcomer. A junction connection between the shell side of the heat exchanger and the control volume representing the steam/water mixer is included in the model. Time dependent volume and time dependent junction components were used to set inlet flowrate and temperature of the primary and secondary side coolant.

A question on the modeling of the steam/feedwater mixing or aspiration process, addressed the relative pressures between the control volume representing the mixer and the volume representing the source of aspiration steam from the secondary to the mixer. Assuming a normal flow junction connecting these volumes, the pressure in the secondary must be higher than the mixer in order to provide steam flow to the mixer. BWNT responded that the bundle collapsed liquid level remains below the downcomer level (presumably below the level of the steam/feedwater mixer) during the tests. As a result the pressure gradient that sustains the steam flow from the secondary is maintained by manometric effects. BWNT also noted that this process is self-governing due to changes in the pressure gradient as the downcomer fluid approaches saturation.

BWNT employed some of the features incorporated into RELAP5/MOD2-B&W for the 19-tube OTSG benchmark. These features are summarized below:

- * The Becker critical heat flux correlation, discussed in Section 3.2.3, are used on the shell side of the tube heat structure,
- * The multipliers defined by the B&W modified slug-drag model and the annular mist model are used, and
- * A linear ramp was applied to the Chen boiling suppression

factor. This adjustment to the suppression factor was discussed in Section 3.2.2.

The first set of results for the steady state benchmark compared the boiling lengths predicted by RELAP5/MOD2-B&W to those measured during the 19-tube OTSG tests. BWNT presented tabulated results and a plot comparing the boiling length above the lower tube sheet predicted by RELAP5/MOD2-B&W to the 19-tube OTSG tests at power levels ranging from 20 to 100 percent of the scaled power levels relative to a 2700 MWth plant. The results show that the boiling lengths predicted by RELAP5/MOD2-B&W are in good agreement with the test data. In contrast, results from RELAP5/MOD2 Cycle 36.05 also shown on these plots, differ significantly from the test data below 80 percent scaled power. BWNT attributes this agreement in the boiling length results between RELAP5/MOD2-B&W and the 19-tube OTSG test to the use of the Becker critical heat flux correlation.

For the LOFW benchmark, BWNT presented comparison plots between RELAP5/MOD2-B&W and 19-tube OTSG data for steam flow rate and the primary outlet temperature after the initiation of the LOFW transient. Plots of the primary and secondary system fluid temperatures prior to the initiation of the LOFW test are also presented to show initial conditions. The plots of steam flow rate and primary outlet temperature show that the magnitude and trend of the results are in good agreement between RELAP5/MOD2-B&W and the 19-tube OTSG test.

BWNT was requested to provide comparison plots between RELAP5/MOD2-B&W and 19-tube OTSG data comparing steam generator secondary level or mass. In their response, BWNT noted that determination of collapsed liquid level is difficult to obtain under two phase high flow conditions. BWNT did provide comparisons of the steady state and transient differential pressure in the boiler. The response of BWNT to this question

was reviewed and found adequate.

3.2.8 MIST Benchmarks

As part of their evaluation of the Revision 3 modifications to the RELAP5/MOD2-B&W code, BWNT included an integral system benchmark of a SBLOCA for a simulated reactor system using OTSGs. BWNT included this benchmark as a further check of the modifications made to reduce interphase drag in the slug flow regime (Wilson bubble rise model) and in the annular flow regimes.

The integral system benchmark was performed using data from the Multi-Loop Integral System Test (MIST) facility which is a scale model of a B&W lowered-loop 177 fuel assembly pressurized water reactor. The MIST facility is designed to operate at pressures and temperatures typical of an operating B&W plant. The MIST facility consists of two 19-tube once-through steam generators, a reactor vessel with a heated core and external downcomer, pressurizer with a power operated relief valve, two hot legs and four cold legs. Further information on facility scaling and instrumentation is found in Appendix L to BAW-10164P.

BWNT notes in Appendix L to BAW-10164P, that a number of pre- and post-test predictions have been made for MIST tests using the RELAP5/MOD2 code as a part of the MIST program. These predictions were made with earlier versions of the code, which did not include the recent modifications. The benchmark presented in Appendix L includes a comparison of experimental data with RELAP5/MOD2 results obtained with both the current and earlier versions of the code. This allows an evaluation of the effects of the recent model changes, in particular upon the prediction of collapsed liquid level in the reactor vessel and steam generator secondary. The results show that the code modifications clearly improve the collapsed liquid level

predictions.

The RELAP5/MOD2-B&W model simulates the MIST reactor vessel, downcomer, hot and cold legs, OTSGs, reactor coolant pumps, and other major components. A double flow path connection to the external reactor vessel downcomer is used in this model so that countercurrent two-phase flow can be predicted. The steam generator modelling employs two radial regions to account for tubes directly wetted by auxiliary feedwater (AFW) injection on the shell side of the steam generator. The other region represents the 16 tubes in contact with secondary steam. BWNT notes in their response that the BWNT modified slug-drag model was employed in the core and primary tube region. For the secondary side of the steam generator tube region, the BWNT slug-drag model is used on the annular mist drag.

In the RELAP5/MOD2-B&W model, the core region was modified so that twenty control volumes represent the full height core. BWNT states that this nodding is necessary for consistency with the revised models. BWNT was requested to discuss the implications of increasing the number of core volumes focusing on the degree of improvement resulting from the use of the new interphase drag model as compared to just increasing the number of core nodes.

BWNT performed a nodding sensitivity study based on ORNL THTF Test 3.09.10j discussed in Appendix H to BAW-10164P. In this study, BWNT ran cases using 4 and 24 nodes in the core region using both the INEL drag model and the BWNT slug-drag model. Plots presented by BWNT show good agreement between the RELAP5/MOD2-B&W results using the BWNT slug-drag model for both the 4 and 24 node core models and the THTF data. The results from the INEL model show poor agreement with the THTF data. BWNT notes in their response that the INEL model is known to overpredict the interphase drag in heated regions with small hydraulic diameters. In this context, the BWNT response

regarding the nodalization of the steam generator secondary was reviewed and is acceptable.

MIST test 320201, used for the RELAP5/MOD2-B&W benchmark, simulated a scaled 50 cm² pump discharge break. This is reported by BWNT to be the most limiting small break size for B&W designed plants. The MIST facility was initialized in natural circulation mode with the core power scaled to 3.5 percent for this test. BWNT noted that since the MIST facility was capable of only ten percent full-scaled power operation, the facility was initialized to conditions corresponding to 145 seconds after trip. Other initial conditions include primary system pressure corresponding to 22 °F core exit subcooling, pressurizer level of 5 feet above the bottom of the pressurizer, steam generator pressure of 1010 psia, and a steam generator secondary level controlled to five feet above the lower tube sheet by throttling high elevation AFW injection.

The MIST test was initiated by turning off the pressurizer heaters and opening the leak. When the pressurizer level reached one foot, full high pressure injection flow was started and steam generator secondary refill using full capacity AFW was initiated.

BWNT presented comparison plots between RELAP5/MOD2-B&W and MIST for primary pressure, secondary pressure, reactor vessel liquid level and secondary liquid level. A tabulation of the timing of key events is presented in Table L.2 of BAW-10164P. Additional information was provided on the elevation of the steam generators and reactor vessel at the MIST facility. The results for BWNT Versions 5 and 14 of RELAP5/MOD2-B&W are presented. The main difference in these code versions is that Version 14 utilizes the revised interphase drag models.

In general, there is good agreement between the RELAP5/MOD2-B&W

Version 14 results and the MIST data. BWNT noted that the improved prediction of reactor vessel and secondary liquid levels is due to the revised slug drag model. The large difference in timing of the hot leg voiding between Revisions 5 and 14 of RELAP5/MOD2-B&W was questioned. BWNT attributed this to differences in the initial temperature conditions in the pressurizer and surge line used in the Revision 5 and Revision 14 calculations. BWNT also revised Table L.2 which corrects the reported time of operator actions.

In reviewing the MIST benchmark, it is noted that no fuel rod temperature excursion occurred during this test. This issue was discussed with BWNT. BWNT responded that the mixture level in the vessel remained above the core during the test, resulting in removal of the stored energy in the fuel by nucleate boiling. In view of this lack of core uncover, BWNT noted that MIST is not the best benchmark for the core mixture level calculation. The stand-alone FOAM2 and ORNL benchmarks presented in Appendix H to BAW-10164P were provided to better address the code's predictive capability.

MIST benchmarks address the capability to predict system pressure, liquid inventory and liquid distribution. In this respect, the MIST test 320201 benchmark demonstrates that the modifications made to the code improve its predictive capability in these areas. When considered along with the other benchmarks, including additional MIST benchmarks, BWNT has demonstrated that RELAP5/MOD2 B&W is capable of adequately predicting the system response for an OTSG plant.

In discussing cladding temperature during an SBLOCA, BWNT argues that the cladding temperature excursion during SBLOCA is governed by the same physical processes for all current PWR designs. During core boildown, the vapor temperature and fuel cladding heat transfer are dependent upon local mechanisms and not upon

integral system parameters. Therefore, heatup during core boiloff depends upon the core geometry, but not the integral system geometry. Benchmarks against ROSA-IV, ORNL and Semiscale test data are hence acceptable for demonstrating that RELAP5/MOD2-B&W is capable of adequately predicting fuel clad temperatures during this heatup phase.

3.3 High Auxiliary Feedwater Model

BWNT developed the high auxiliary feedwater model to calculate the B&W OTSG heat transfer correctly during auxiliary feedwater injection from high elevation locations. This model was included in the Revision 1 submittal but was not reviewed because B&W did not intend to use RELAP5/MOD2-B&W for OTSG analysis at that time as noted in Section 5 of the Revision 1 safety evaluation report. BWNT requested a review of this model and has provided additional information to support this request.

The high auxiliary feedwater model was reviewed as part of the CRAFT2 code Topical Report transmittal in 1985. This report included several benchmarks against plant and experimental data. BWNT has made some modifications to the heat transfer models since that time. Therefore, an additional RELAP5/MOD2-B&W benchmark of the revised heat transfer models against test data from the MIST facility was provided by BWNT. Included is a plot comparing RELAP5/MOD2 predicted primary side temperature as a function of elevation above the tube sheet against steady-state MIST measurements. This plot shows good agreement between the RELAP5/MOD2 B&W predictions and the MIST measurements along the length of the steam generator tubes. The steady-state nature of this test allowed the calculated heat transfer coefficients used in the model to be justified. The high AFW model was also used for the additional MIST benchmarks performed by BWNT. These serve to demonstrate the adequacy of the model for transient applications.

Based upon the discussions and benchmarks provided by BWNT, it is concluded that the revisions to the high auxiliary feedwater model have not changed significantly from the model previously accepted. Therefore, we find it acceptable for use in SBLOCA analysis.

3.4 Parameters Used in RELAP5/MOD2-B&W Benchmarks

BWNT has incorporated a number of user specified input parameters in RELAP5/MOD2-B&W. The value of these parameters used in the RELAP5/MOD2 B&W benchmarks are listed in Table 1 of this evaluation. The values of these parameters were selected to improve the agreement between RELAP5/MOD2-B&W and the FOAM2, THTF, OTSG, and MIST benchmark data. The values of the user specified parameters listed in Table 1 are the only acceptable values for LOCA licensing calculations.

One of the motivations driving the initial development of the RELAP5 code was the need to eliminate user choice of modeling options and input dials. When an analysis is performed with RELAP5, one can be certain of what models and fitting parameters are used. The addition of numerous options and dials by BWNT is contrary to this characteristic of RELAP5. The last condition listed above is intended to eliminate the use of user specified dials in keeping with the intent of the RELAP5 approach.

Table 1
Summary of User Specified Parameters Used in the
RELAP5/MOD 2-B&W Benchmarks

Parameter	Description	Page Where Parameter Is Described	Affected Benchmark
C_{wb}	Multiplier on bubble velocity in the Wilson Bubble Rise Model	2.1-52.3 (Revision 2)	FOAM2 code, ORNL THTF tests (Appendix H)
C_{wsl}	Multiplier on the interphase drag predicted for slug flow	2.1-52.3 (Revision 2)	FOAM2 code, ORNL THTF tests (Appendix H)
xms	Multiplier on the interphase drag computed for annular mist flow	2.1-53 (Revision 2)	OTSG benchmarks (Appendix K), MIST benchmarks (Appendix L)
xsg	High void fraction slug coefficient	2.1-52.5 (Revision 3)	OTSG benchmarks (Appendix K), MIST benchmarks (Appendix L)

5-356

Table 1
Summary of User Specified Parameters Used in the
RELAP5/MOD 2-B&W Benchmarks

Parameter	Description	Page Where Parameter Is Described	Affected Benchmark
α_s	Low end of void fraction for adjustment	2.1-52.5 (Revision 3)	OTSG benchmarks (Appendix K), MIST benchmarks (Appendix L)
α_{eh}	High end of void fraction for adjustment	2.1-52.5 (Revision 3)	OTSG benchmarks (Appendix K), MIST benchmarks (Appendix L)
xslg	Slope of drag pressure term	2.1-52.5 (Revision 3)	OTSG benchmarks (Appendix K), MIST benchmarks (Appendix L)
cxslg	x-intercept for pressure term	2.1-52.5 (Revision 3)	OTSG benchmarks (Appendix K), MIST benchmarks (Appendix L)

Table 1
Summary of User Specified Parameters Used in the
RELAP5/MOD 2-B&W Benchmarks

Parameter	Description	Page Where Parameter Is Described	Affected Benchmark
α_{gr}	Void fraction at which to begin the S ramp	2.2-22 (Revision 3)	OTSG benchmarks (Appendix K)
$C1_{TR}$ $C1_{TRI}$	User multiplicative constants used in the equation to determine wall-to-fluid heat flux during transition boiling.	2.3-86 (Revision 3)	

4.0 COMPLIANCE WITH NRC REQUIREMENTS

Appendix K to 10-CFR-50 specifies required and acceptable features of ECCS evaluation models. Previous revisions of the RELAP5/MOD2-B&W program, through Rev. 1, have been reviewed and found to satisfy the requirements of Appendix K when used with the approved B&W ECCS methodology, subject to any restrictions cited in the SER.

The modifications documented in Revisions 2 and 3 of BAW-10164P do not affect compliance with any of the required features of Appendix K. Modifications of the fuel pin model are such that the requirements of Appendix K continue to be satisfied. Inclusion of a contact conductance term in the calculation of fuel clad gap conductance does not affect compliance with Appendix K which states that "thermal conductance of the gap between the UO₂ and the cladding shall be evaluated as a function of the burnup, taking into consideration fuel densification and expansion, the composition and pressure of the gases within the fuel rod, the initial cold gap dimension with its tolerances, and cladding creep." Section B of Appendix K also specifies that "The gap conductance shall be varied in accordance with changes in gap dimensions and any other applicable variables."

Inclusion of axial thermal expansion of the cladding and fuel in the gas plenum volume calculation also does not affect compliance with Appendix K. The plenum volume is used in the calculation of internal rod pressure which is a key determinant of the amount of swelling and rupture. Appendix K requires that "the swelling and rupture calculations shall be based on applicable data in such a way that the degree of swelling and incidence of rupture are not underestimated." Calculation of gas gap pressure using plenum volume which accounts for axial thermal expansion of the fuel and cladding improves accuracy and should not result in underestimating the pressure or the incidence of swelling and

rupture.

Appendix K specifies that the Baker-Just model be used to calculate the metal-water reaction rate, but does not specify the solution method. Therefore, the implicit solution technique is acceptable, given that it yields a mathematically correct solution of the required equation. Appendix K also requires that "The degree of swelling and rupture shall be taken into account in calculations of gap conductance, cladding oxidation and embrittlement, and hydrogen generation." The "swelled radius" modification to the metal-water reaction model accounts for the increase in clad radius, and hence surface area, due to swelling. This model change affects the hydrogen generation and cladding oxidation, and is in compliance with the Appendix K requirements listed above. The iterative technique for determining a multiplier on gap conductance which yields a desired initial stored energy is a user convenience feature which does not affect the previously approved model.

Section C.4.e of Appendix K to 10 CFR 50 states: "After CHF is first predicted at an axial fuel rod location during blowdown, the calculation shall not use nucleate boiling heat transfer correlations at that location subsequently during the blowdown even if the calculated local fluid and surface conditions would apparently justify the reestablishment of nucleate boiling. Heat transfer assumptions characteristic of return to nucleate boiling (rewetting) shall be permitted when justified by the calculated local fluid conditions during the reflood portion of a LOCA." The core heat transfer selection model modifications assure that no return to nucleate boiling will occur before the end of blowdown for the large break LOCA. Since the definitions of blowdown and reflood are inappropriate for SBLOCA, it is acceptable to bypass this "no return to nucleate boiling" requirement in that case. The modification is therefore in compliance for LBLOCA analysis, and acceptable for the SBLOCA

analysis where the requirement is inappropriate.

CHF correlations acceptable for use in LOCA analysis are listed in Sections C.4.b and d. Section C.4.a states that "Correlations developed from appropriate steady-state and transient-state experimental data are acceptable for use in predicting the critical heat flux (CHF) during LOCA transients. The computer programs in which these correlations are used shall contain suitable checks to assure that the physical parameters are within the range of parameters specified for use of the correlation by their respective authors". As discussed in Section 2.1.7 of this report, the BWUMV CHF correlation has been developed using appropriate experimental data for fuel with mixing vanes. The correlation is therefore acceptable for use within the ranges of parameters specified. It is noted that BWNT requested that the correlation be approved for pressures down to 750 psia. Based upon the data comparison provided by BWNT, the staff concludes that the correlation is acceptable down to pressures of 1300 psia and mass fluxes of 500,000 lb/hr-ft². Checks which restrict use of the correlation to this range must be included in RELAP5/MOD2-B&W for the code to be acceptable.

Benchmarks against calculations of the approved computer program FOAM2 and THTF experimental test data have shown that addition of the Wilson drag model improves predictions of void distribution in the core region. Appendix K does not list specific requirements in this area. The modification, which improves modeling accuracy, is therefore acceptable. A number of the other code enhancements fall into this same category. They cover areas where Appendix K does not specify required features. These include the annular mist flow regime overall drag multiplier, condensation heat transfer correlation modifications, Wilson slug flow drag model, and the CCFL model. Appropriate justification has been provided to show that these enhancements improve

modeling accuracy.

5.0 CONCLUSIONS AND LIMITATIONS

Modifications made to RELAP5/MOD2-B&W as described in Revisions 2 and 3 of BAW-10164P have been reviewed and evaluated. Based on the benchmarks presented, the staff finds that the models described in version 19 of RELAP5/MOD2-B&W to be acceptable for LOCA and non-LOCA analysis for PWRs with recirculating and OTSGs subject to the following limitations:

- * Use of the Wallis and UPTF parameters at the tube bundle and steam generator plenum inlet are acceptable. The parameters used in the CCFL model for any other application must be validated, and the validation reviewed and approved by the staff for that application (see section 3.1.3 of this evaluation).
- * The BWUMV correlation is limited to pressures above 1300 psia.
- * For large break LOCA ECCS evaluation model calculations, form losses due to ruptured cladding should not be excluded using the user option described in Section 3.2.4 of this evaluation.
- * The value of the user specified parameters listed in Table 1 of this evaluation (i.e. those used for the benchmark calculations) are the only acceptable values for LOCA licensing calculations.

Table 2 lists typographical errors that were found during the course of this review. Correction of these errors should be incorporated into the approved version of BAW-10164P. The automated blockage droplet breakup calculation, the implicit formulation of the Baker-Just metal water reaction model and the fuel rod Evaluation Model improvements referred to in Section 5 of the BEACH safety evaluation report⁽¹⁸⁾ were reviewed in this evaluation and found acceptable. Contingency 4 given in Section 5 of the BEACH safety evaluation report is no longer applicable. That contingency states: "Use of the automated blockage droplet breakup calculation, implicit formulation of the Baker-Just metal

water reaction model and the fuel rod Evaluation Model (EM) improvements should be made contingent upon their approval in Revision 3 of BAW-10164P, which describes these updates."

Table 2
Summary of Changes That Should Be Made To The
Approved Version of BAW-10164, Revision 2 and 3

Affected Report Revision and Section	Change Summary
Revision 2, Appendix H, Figure H.1	Correction to Figure H.1 in response to Question 2 of the Revision 2 RAI
Revision 2, Appendix H, Table H.2	Correction to Table H.2 in response to Question 4 of the Revision 2 RAI
Revision 2, Section 2.3.3 and Appendix I	Correction to Equation I-1, I-2 and pressure and mass flux units in response to Questions 5, 6, and 7 of the Revision 2 RAI
Revision 2, Appendix I, Table I.3	Duplication in point numbers in Test 160 (point 789) and Test 164 (points 2060 and 2065) should be corrected or clarified.
Revision 2, Appendix J, Page J-8	Reference to Table 2 should be Table J.2 per Question 11 of the Revision 2 TER
Revision 3, Section 2.3.2	Correction of ϵ_{TC} value on Table 2.3.2-2 in response to Question 4 to the Revision 3 RAI.
Revision 3, Page 2.3-46	Correction to β^2 definition in text in response to Question 5 of the Revision 3 RAI. Other correction noted by BWNT on Page 2.3-36 should also be included.
Revision 3, Appendix L, Table L.1	Revision to Table L.1 in response to Question 10 of the Revision 3 RAI.
Revision 3, Appendix L, Table L.2	Revision to Table L.2 in response to Question 11 of the Revision 3 RAI.

5.0 REFERENCES

1. Ransom, V. H., et. al., RELAP5/MOD2 Code Manual -- Volume 1: Code Structures, System Models and Solution Methods and Volume 2: Users Guide and Input Requirements, NUREG/CR-4312 - Volume 1, August, 1985 and NUREG/CR-4312 - Volume 2, December 1985.
2. B&W Nuclear Technologies, RELAP5/MOD2-B&W -- An Advanced Computer Program for Light Water Reactor LOCA and non-LOCA Transient Analysis, BAW-10164P, Revision 1, October 1988.
3. Letter from A. C. Thadani (USNRC) to J. H. Taylor (B&W Nuclear Technologies), Acceptance for Referencing of Topical Report BAW-10164P, Revision 1, RELAP5/MOD2-B&W, An Advanced Computer Program for Light Water Reactor LOCA and Non-LOCA Transient Analysis, April 18, 1990.
4. Code of Federal Regulations, ECCS Evaluation Models, Chapter 10, Part 50, Appendix K
5. B&W Nuclear Technologies, RELAP5/MOD2-B&W -- An Advanced Computer Program for Light Water Reactor LOCA and Non-LOCA Transient Analysis, BAW-10164P, Revision 2, August 1992.
6. B&W Nuclear Technologies, RELAP5/MOD2-B&W -- An Advanced Computer Program for Light Water Reactor LOCA and non-LOCA Transient Analysis, BAW-10164P, Revision 3, October 1992.
7. Letter from J. H. Taylor (B&W Nuclear Technologies) to R. C. Jones (USNRC) BEACH Topical Report BAW-10166P, JHT/93-214, August 31, 1993.
8. Letter from J.H. Taylor (B&W Nuclear Technologies), Response to NRC's Request for Additional Information on BAW-10164, Revision 2, August, 1992; RELAP5/MOD2-B&W, An Advanced Computer Program for Light Water Reactor LOCA and NON-LOCA Transient Analysis, JHT/93-279, November 16, 1993
9. Letter from J.H. Taylor (B&W Nuclear Technologies), Response to NRC's Request for Additional Information on BAW-10164, Revision 3, October, 1992; RELAP5/MOD2-B&W, An Advanced Computer Program for Light Water Reactor LOCA and NON-LOCA Transient Analysis, JHT/94-7, January 21, 1994
10. Letter from J.H. Taylor (B&W Nuclear Technologies), Response to NRC's Supplemental Request for Additional Information on BAW-10164, Revision 2, August, 1992; RELAP5/MOD2-B&W, An Advanced Computer Program for Light Water Reactor LOCA and NON-LOCA Transient Analysis, JHT/94-146, September 20, 1994.

This page intentionally left blank.

5-364.2

Rev. 4
9/99

11. B&W Nuclear Technologies, FOAM2 -- Computer Program to Calculate Core Swell Level and Mass Flow Rate During Small Break LOCA, BAW-10155A, October 1990.
12. Collier, John G., Convective Boiling and Condensation, Mc-Graw-Hill International Book Company, 2nd. edition, 1972
13. B&W Fuel Company, Correlation of Critical Heat Flux in Mixing Vane Grid Fuel Assemblies, BAW-10159P-A, July 1990
14. B&W Nuclear Technologies, FRAP-T6-B&W - A Computer Code for the Transient Analysis of Light Water Reactor Fuel Rods, BAW-10165P, October 1988.
15. B&W Nuclear Technologies, TACO3 - Fuel Pin Thermal Analysis Computer Code, BAW-10162P-A, October 1989.
16. D.A. Powers and R.O. Meyers, Cladding Swelling and Rupture Models for LOCA Analysis, NUREG-0630, April, 1980
17. D.L. Hagrman, et. al., MATPRO - Version 11 (Revision 2), NUREG/CR-4079, August 1981
18. D.A. Prelewicz, Technical Evaluation Report - BEACH - Best Estimate Analysis Core Heat Transfer, A Computer Program for Reflood Heat Transfer During LOCA, BAW-10166P, Revision 4, SCIENTECH, Inc., SCIE-NRC-219-93, November, 1993

ATTACHMENT 2

SCIE-NRC-224-94
Revision 1

**TECHNICAL EVALUATION REPORT
(Non-Proprietary Version)**

- RELAP5/MOD2-B&W -

**An Advanced Computer Program for Light Water
Reactor LOCA and Non-LOCA Transient Analysis
BAW-10164P, Revisions 2 and 3**

**W. C. Arcier
D. A. Prelewicz**

Prepared for

**U. S. Nuclear Regulatory Commission
Washington, D. C. 20555**

March 1995

**SCIENTECH, Inc.
11140 Rockville Pike, Suite 500
Rockville, Maryland 20852**

**TECHNICAL EVALUATION REPORT
(Non-Proprietary Version)
- RELAP5/MOD2-B&W -
An Advanced Computer Program for Light Water
Reactor LOCA and Non-LOCA Transient Analysis
BAW-10164P, Revisions 2 and 3**

1.0 INTRODUCTION

By letter dated September 18, 1992, the B&W Nuclear Technologies Company submitted the topical report BAW-10164P, Revisions 2 and 3 for NRC review. The report describes a pressurized water reactor (PWR) thermal-hydraulics transient analysis code for LOCA and non-LOCA transients analysis based on the RELAP5/MOD2 code.

RELAP5/MOD2-B&W is a B&W Nuclear Technologies (BWNT) adaptation of the Idaho National Engineering Laboratory (INEL) RELAP5/MOD2⁽¹⁾ code used for PWR licensing and best estimate thermal hydraulics transient analysis. RELAP5/MOD2 was developed by INEL as a best-estimate computer code for light water reactor transient analysis. B&W Nuclear Technologies has added features to permit use of the RELAP5/MOD2-B&W code for ECCS evaluation model (EM) calculations. The previous revision of the RELAP5-B&W code, Revision 1⁽²⁾, was approved for use in the analysis of small break and large break LOCAs⁽³⁾ (SBLOCA and LBLOCA) for recirculating steam generator plants.

Revision 2 of BAW-10164P⁽⁴⁾ describes updates for use in performing small break LOCA analysis. These updates include an additional critical heat flux (CHF) correlation referred to as BWUMV, addition of the Wilson model for determining interphase drag, addition of a counter-current flow limiting (CCFL) model and correction of minor code errors. Benchmarks are included in Revision 2 to specifically address the Wilson interphase drag model and the small break LOCA EM model. The

SBLOCA benchmark is against experimental data from the ROSA-IV large scale test facility.

In addition to the correction of minor errors, Revision 3 of BAW-10164P⁽⁶⁾ includes enhancements to the EM fuel pin model, EM heat transfer model, and models to support use of the code for analysis of once through steam generator (OTSG) plants. These models include the Becker CHF correlation, further modifications to the slug-drag model, the high auxiliary feedwater model and the Chen nucleate boiling heat transfer coefficient void ramp. Benchmarks against model 19-tube OTSG data and against SBLOCA test data from the MIST facility, which has simulated OTSGs, are included. The modifications to the approved licensing model proposed in References 4 and 5 are the subject of the review and evaluation documented in this report.

2. SUMMARY OF THE TOPICAL REPORT

BAW-10164P Revisions 2 and 3 present best estimate and licensing type calculation for PWRs. Simulation methods are presented for large and small break LOCAs as well as operational transients such as anticipated transients without scram, loss of off-site power, loss of feedwater, and loss of flow. The solution is based on a two energy equation scheme, a two step numerical option, a gap conductance model, constitutive models and control system models. Control system and secondary system components have been added to permit modeling of plant controls, turbines, condensers, and secondary feedwater conditioning systems. Benchmark comparison of code predictions to integral system test results are also presented.

Revision 2 deals mainly with the small break LOCA. Revision 3 includes enhancements to the evaluation model for fuel pin heat transfer modelling to extent the code applicability to the once through steam generators.

3.0 EVALUATION

Review and evaluation of the RELAP5/MOD2-B&W code includes Revision 2 and Revision 3 of BAW-10164P. Revision 2 provides additional models specifically intended for SBLOCA applications. Revision 3 includes enhancements to the EM fuel pin and heat transfer model, additions and benchmarks which extend application of the code to the once through steam generator plants. An initial review of Revisions 2 and 3 led to generation of Requests for Additional Information^(8,9). Supplemental information was also submitted by BWNT during the review process⁽¹⁰⁾. Each of the model additions or modifications is discussed and evaluated in the following sections.

3.1 BAW-10164P, Revision 2

3.1.1 Model Changes for the Slug Flow Regime

BWNT added an option for determining the Taylor bubble interphase drag during slug flow based on the Wilson drag model. The Wilson drag model is based on the Wilson bubble rise velocity in a vertical pipe. BWNT applied the Wilson drag model for reflood applications using the BEACH program and is now applying the model for non-reflood applications in RELAP5/MOD2-B&W. These changes are discussed on pages 2.1-51 to 2.1-54 of BAW-10164P. Benchmarks are provided in Appendix H.

In implementing the Wilson drag model for RELAP5/MOD2, BWNT derived an expression for the interphasic friction for Taylor bubbles. Flow was assumed to be in a quasi-steady state. The derivation of this expression was checked. The formulation was determined to be correct. BWNT also incorporated improvements to match the bubble rise data at higher void fractions. An apparent difference between the interphase friction model for slug flow used in RELAP5/MOD2 B&W compared to that used in the BEACH⁽⁷⁾ program was questioned. BEACH uses the same Wilson

drag model with a different multiplier, on the Taylor bubble term. BWNT responded that the different multipliers were selected based on comparisons to reflood benchmarks in the case of BEACH and small break LOCA benchmarks in the case of RELAP5/MOD2-B&W.

An option to remove smoothing in selected junctions, (not used in BEACH), was added to RELAP5/MOD2-B&W. This option allows smoothing to be bypassed. Since discontinuous void distributions may occur during a small break LOCA, use of this option for small break calculations may be appropriate.

Benchmarks were performed by BWNT using the Wilson drag model against results obtained from the NRC-approved computer code FOAM2⁽¹⁾ and with small break LOCA experiments performed at the Thermal Hydraulic Test Facility (THTF) at the Oak Ridge National Laboratory. These benchmarks are presented in Appendix H to BAW-10164P.

The FOAM2 program, developed by BWNT and previously approved by the NRC, is used to determine whether the water content of a reactor core is sufficient to cover the core with a combination of liquid and two phase mixture based on a given core void distribution. If it is determined that the core is uncovered, FOAM2 calculates the two-phase swell level and steaming rate. The FOAM2 program utilizes the Wilson bubble rise correlation to directly calculate the core void distribution. The Wilson bubble velocity correlation used in FOAM2 is somewhat different from that used in RELAP5/MOD2-B&W since it does not include the changes made by BWNT to better match the bubble rise data at higher void fractions. BWNT stated that the core void distribution results calculated by RELAP5/MOD2 B&W and FOAM2 should be similar except potentially at higher void fractions because of differences in the formulation of the Wilson model. The benchmarks show that RELAP5/MOD2-B&W predicts void distributions which are comparable to FOAM2 predictions.

Calculations using FOAM2 were performed for reactor powers of 1.5, 2.5, and 5.0 percent of full power. System pressures ranging from 100 to 1600 psia were included in the analysis. BWNT presented plots of core void fraction vs. core elevation comparing the RELAP5/MOD2-B&W results and the FOAM2 results. These plots show acceptable agreement between RELAP5/MOD2-B&W and FOAM2, with RELAP5/MOD2-B&W showing very slightly different results at high void fractions.

The RELAP5/MOD2-B&W code predictions were compared to THTF test results for a range of pressures (520 to 1170 psia), power densities (0.08 to 0.68 kw/ft), and mass flux (3395 to 21943 lbm/hr-ft²). BWNT presented plots of the results of core void fraction vs. core elevation as well as rod surface and vapor temperature vs. core elevation comparing the RELAP5/MOD2-B&W results and the THTF test results. In general, the void fractions predicted by RELAP5/MOD2-B&W are somewhat higher than the THTF results. Additionally, RELAP5/MOD2-B&W generally overpredicts the vapor and surface temperature relative to the THTF tests. There is a dip in surface temperature in the THTF tests at the core elevation of 11 feet. BWNT attributes the dip to grid effects on the heat transfer rate which are not accounted for in the RELAP5/MOD2-B&W model. The dip in surface temperature caused by the grid effect, was questioned. The surface temperature would be underpredicted for THTF tests 3.09.10 i, j, l, and m. Underprediction of the surface temperature could indicate that the heat transfer coefficient to the vapor is high and non-conservative. It was requested that BWNT discuss the comparisons between RELAP5/MOD2-B&W and the THTF tests and show that the comparisons do not rely on systematic underprediction of the vapor temperature. In their response, BWNT indicated that the heat transfer coefficient for single phase vapor is computed using the McEligot-plus radiation correlation set. BWNT pointed out that use of the correlation is widely accepted and was reviewed and accepted in previous submittals of RELAP5 and FRAP-T6 topical reports. BWNT also noted that the measurement of vapor temperature is low because the thermocouples were mounted on the unheated rods used to simulate guide tubes. Actual temperatures measured at THTF would be higher and more in agreement with

RELAP5/MOD2-B&W. The BWNT response was deemed satisfactory. This benchmark shows that use of the Wilson model for interphase drag produces reasonably accurate predictions of SBLOCA experimental data.

3.1.2 Model Changes for the Annular Mist Flow Regime

BWNT has added an option to RELAP5/MOD2-B&W to include calculation of the overall drag computed for control volumes in an annular mist flow regime. This change is used in the OTSG and MIST benchmarks discussed in Sections 3.2.7 and 3.2.8 of this evaluation.

3.1.3 Counter-Current Flow Limiting Model

BWNT added optional counter-current flow limiting (CCFL) models which are intended for use in predicting flows at the steam generator U-tube inlets and steam generator plenum inlets during the reflux condensation period of a SBLOCA. Addition of the CCFL model is described on pages 2.1-133 to 2.1-133.3 of BAW-10164P.

The CCFL model modifications, consisting of a correlation for flooding in vertical tubes, are included in the form of a general relationship between the dimensionless vapor flux, j_v^* and the dimensionless liquid flux, j_l^* . The relationship is implemented in the code in a manner similar to the implementation in RELAP5/MOD3. Different values of the correlation parameters are used at the U-tube inlets and at the steam generator plenum inlet. This model was benchmarked against ROSA-IV small break LOCA data in Appendix J of the Topical Report. Flow predictions were in reasonable agreement with the test data. Therefore, the use of the CCFL model at the steam generator plenum and tube inlet, with the parameters used in the benchmark, is acceptable for the analysis of SBLOCAs in recirculating steam generators. As demonstrated by the fact that different correlation parameters are required at the inlet

plenum and the tubes, CCFL is very geometry specific. Other uses of the CCFL model will require that the model be validated for that application.

3.1.4 Condensation Heat Transfer Correlation Modifications

Modifications were made to the condensation heat transfer correlation for vertical or horizontal surfaces. These changes are discussed on pages 2.2-31 and 2.2-32 of BAW-10164P.

The Nusselt laminar film correlations for a horizontal surface and for a vertical surface are used in RELAP5/MOD2-B&W. For condensation on a horizontal surface, laminar film condensation in a horizontal tube is assumed. Comparing the formulation given in Collier⁽¹²⁾ against that given by BWNT for condensation within a horizontal tube shows that BWNT did not include the equation developed by Rohsenow for the modified latent heat of vaporization. Omission of this equation will have a small effect for the heat transfer coefficient result. The expression for a vertical surface was found to be in agreement with Collier.

3.1.5 Changes to the Metal-Water Reaction (Swelled Radius) Model

When a fuel rod swells the radius and hence the surface area of the rod will increase in the swelled region. The rate of heat generation and the molar production rate of hydrogen are proportional to the exposed surface area of the clad. These models have been modified by BWNT as described in Section 2.3.2.4 of BAW-10164P to increase the surface area in proportion to the ratio of the swelled clad radius to the cold clad radius. This increase in area is applied to both the clad inside and outside surfaces. Consideration of the increase in clad radius in the swelled region is appropriate and conservative. Both the energy generation rate and the rate of hydrogen production will increase when this model is used compared to the constant

surface area model. This model satisfies the requirements of Appendix K and is acceptable for ECCS EM calculations.

3.1.6 Core Heat Transfer Selection Model Modifications

BWNT installed a separate heat transfer option for use in SBLOCA analysis. The changes are discussed on pages 2.3-60 to 2.3-61.2, 2.3-64, 2.3-67, 2.3-83, and 2.3-84 of BAW-10164P. The changes to the switching logic for SBLOCA include the removal of Appendix K restrictions regarding no return to nucleate boiling and the lock into film boiling after the wall superheat exceeds 300° F. The switching logic is unchanged for LBLOCA. BWNT stated that the no return to nucleate boiling and the lock into film boiling restrictions of Appendix K are not applicable to SBLOCA. This assertion is acceptable. While the acceptance criteria of 10 CFR 50.46 apply to LBLOCA, the possible core heatup scenarios following a SBLOCA are varied and more complex than those for the LBLOCA. The use of a reflood heat transfer model lockout of return to nucleate boiling and prediction of quenching is inappropriate for the small break.

An option to allow use of the BWUMV critical heat flux correlation can be selected by the user depending on the fuel design being evaluated. This correlation is used only at pressures greater than 1300 psia at mass fluxes greater than 500,000 lbm/hr-ft² in the core heat transfer selection logic in RELAP5/MOD2-B&W. The BWUMV correlation is reviewed in the next section.

3.1.7 BWUMV Critical Heat Flux Correlation

The BWUMV (B&W Universal Mixing Vane) critical heat flux correlation was developed for the analysis of SBLOCA. The development of the BWUMV correlation is presented in Appendix I to BAW-10164P. BWNT developed this correlation from the database for the previously approved BWCMV correlation⁽¹³⁾ with additional mid-flow regime data from three Westinghouse tests.

BWUMV utilizes a third order polynomial fit using three independent variables based on pressure (P), mass flux (G), and quality (X_{CHF}). Typographical errors in the CHF equation, units conversion errors, and the FLS equation, were questioned. The responses with the corrected equations and units are provided in Reference 8.

The number of data points and their distribution in the mass flux range below 0.95×10^6 lb/hr-ft² was questioned. BWNT indicated in their response that the total number of data points with mass fluxes below 1.25×10^6 lb/hr-ft² is 77. In addition to the 22 points from Table I.3 of Appendix I, 20 points are from the data presented in Appendix B of BAW-10159 and 35 test points are from the data presented in Appendix F of BAW-10159. Of these 77 points, a total of 32 points were measured at a local mass flux of between 0.4×10^6 and 1.0×10^6 lb/hr-ft². This total is comparable to the number of points at the lower end of the flow range of the BWCMV correlation.

In evaluating the distribution of points about the measured/predicted ratio for pressure and mass flux, it is noted that the data clustered about 750 psia and 1000 psia on Figure I.5 are not uniformly distributed about the mean value of 1.0. It appears that 10 of the 11 points measured at 750 psia are below the mean and 10 of the 12 points measured at 1000 psia are above the mean. Because of this bias and because of the small number of points, we believe that the BWUMV results are biased at pressures of 750 and 1000 psia. It is recognized that this bias does not affect BWUMV predictions above 1300 psia. However, BWNT did conclude in Appendix I to BAW-10164P that the BWUMV correlation is applicable to CHF calculations for pressures and flow rates above 750 psia. Given the apparent bias in the data points at 750 and 1000 psia, the BWUMV correlation should not be used for CHF calculations at pressures below 1300 psia.

Numerical checks of the BWUMV correlation were performed. These calculations were done to determine how well the BWUMV correlation reproduces predicted results, to determine the behavior of the BWUMV correlation over a range of pressure,

flow rate and quality, and to compare the BWUMV to the BWCMV correlation since they were developed from the same database for the most part.

In general, the numerical checks show that the BWUMV and the BWCMV correlations are in agreement within the statistical uncertainty band. Some differences in the results are noted in cases where the flow is varied over the BWCMV range of validity. These differences are more significant when the pressure is at 1500 and 1800 psia. Evaluations performed where the pressure is varied over the BWCMV range of validity also show some difference between the two correlations.

The statement is made in Appendix I that the Tong factor is set equal to one in the RELAP5/MOD2 B&W implementation of BWUMV. In discussions with BWNT they stated that the Tong factor is included in the development of the BWUMV correlation. It is during the SBLOCA transient analysis that the Tong factor is set equal to 1. BWNT also indicated that their standard practice is to set the Tong factor equal to 1 for LOCA analysis and indicated several references where this practice has been previously approved.

Based on this review, it is concluded that the BWUMV correlation is acceptable for used in RELAP5/MOD2 B&W subject to the restriction that the correlation should not be used below pressures of 1300 psia.

3.1.8 SBLOCA EM Benchmark

BWNT performed a benchmark using RELAP5/MOD2 B&W against a SBLOCA experiment performed at the ROSA-IV facility in 1988. The ROSA-IV facility simulates a recirculating steam generator plant. The results of this benchmark are presented in Appendix J to BAW-10164P. It is important to note that this is not the only benchmark of RELAP5/MOD2-B&W for a SBLOCA. As noted in appendix J, the peak clad temperatures during the experiment are not significant relative to the acceptance

criteria. Benchmarks against LOFT and Semiscale SBLOCA data, presented in Section 5 of BAW-10164, provide additional coverage of SBLOCA phenomenology, including clad temperature prediction. This benchmark serves to show that the additional models for SBLOCA, such as CCFL and Wilson drag, are performing correctly and will adequately predict test data.

The RELAP5/MOD2-B&W model for ROSA-IV, and other benchmarks and applications models, use equilibrium thermodynamics nodes in the core region and non-equilibrium nodes in the remainder of the system. Since the RELAP5/MOD2 Code Manual specifically states that equilibrium nodes cannot be connected to non-equilibrium nodes, BWNT was questioned on node connectivity. In their response BWNT stated that RELAP5/MOD2 has always been fully capable of connecting equilibrium and non-equilibrium nodes, and that this is consistent with the approved EM core modeling. This was confirmed by INEL (the RELAP5 code development organization), that the equilibrium option is obtained using the same basic equations with the interphase heat transfer coefficient set to a very high value. This assures that sufficient heat transfer will occur to keep both phases at saturation conditions. Contrary to the statements in the code manual, it is possible to connect equilibrium and non-equilibrium nodes without adversely affecting the calculational algorithms. BWNT uses equilibrium nodes in the core region to obtain saturation fluid temperature as the boundary condition for the core heat transfer correlations, which were developed on this basis.

When modeling complex systems, it is sometimes necessary to slightly modify the representation to compensate for code model limitations. BWNT used two such modifications in their representation of the ROSA-IV facility. First, the friction factor for the accumulator injection line was increased by a factor of 100 above the nominal value, to eliminate unrealistic injection flow oscillations. Also, the angle of the inlet pipe to the steam generator plenum was decreased to less than 15 degrees to permit use of the horizontal pipe stratification model. BWNT provided justification for these

model modifications. In both cases, the BWNT responses adequately explained the need for modifications to overcome code limitations.

BWNT performed a time step sensitivity study which demonstrated that the 0.05 second time step used for the calculations was adequate.

Results of the calculations showed that the basic thermal-hydraulic phenomena which occurred during the SBLOCA were predicted with reasonable accuracy. Key events were predicted to occur in essentially the correct sequence. Differential pressures in the core and recirculation loops, key determinants of the flows, were adequately predicted. This benchmark further demonstrates that the RELAP5/MOD2-B&W computer program is capable of predicting the important thermal-hydraulic phenomena which occur during a SBLOCA in a recirculating steam generator plant.

3.2 BAW-10164P, Revision 3

3.2.1 Revision to the Slug Flow Drag Model

BWNT incorporated a third option for evaluating the Taylor bubble interphase drag in slug flow. The three models now available are the base INEL model, the Wilson drag model submitted with Revision 2 of BAW-10164P, and the B&W modified slug-drag model, as described on pages 2.1-52.4 and 2.1-52.5 of Revision 3 of BAW-10164P. (The Wilson drag model was reviewed in Section 3.1.1 above).

In the B&W modified slug-drag model, adjustments are made to the interphase friction terms through the use of empirically derived coefficients. BWNT states that these adjustments were based on numerous benchmarks. BWNT listed the benchmarks used which included those documented in Appendices K and L to BAW-10164P. These benchmarks are discussed in Sections 3.2.7 and 3.2.8 of this evaluation.

3.2.2 Modifications to the Chen Heat Transfer Coefficient

The saturated nucleate boiling heat transfer coefficients used in RELAP5/MOD2-B&W are calculated using the Chen heat transfer correlation to model the boiling component of the heat transfer coefficient. The Chen heat transfer correlation employs a nucleate boiling suppression factor S . S was modified by including a multiplicative weighing factor to force S , and the boiling heat transfer coefficient to zero as the steam void fraction approaches one. B&W notes that this ramp is needed for once-through steam generator applications to preclude sharp increases in S that result in disproportionately high overall heat transfer as the void fraction approaches one.

3.2.3 Incorporation of the Becker CHF Model

The Becker CHF correlation for rod bundles is incorporated into RELAP5/MOD2-B&W as described in Section 2.2.2.2 of Revision 3 of BAW-10164P. BWNT states that this correlation was used to obtain better predictions of secondary side heat transfer relative to the Biasi-Zuber correlation used in RELAP5/MOD2 at power levels below 80 percent of full power. The Becker CHF correlation is used up to a pressure of 90 bar (1306 psia). Linear interpolation between the Becker and Biasi-Zuber correlations is performed between 80 and 90 psia to obtain a smooth transition between the two correlations.

Benchmarks comparing results of RELAP5/MOD2-B&W to OTSG test data are presented in Appendix K of BAW-10164P and are discussed in Section 3.2.7 of this SER. These benchmarks show good agreement between RELAP5/MOD2-B&W results using the Becker CHF correlation and the OTSG test data as discussed in Section 3.2.7.

3.2.4 EM Pin Model Modifications

BWNT enhanced the fuel pin model in RELAP5/MOD2-B&W by adding features which had previously been approved for use in the FRAP-T6-B&W⁽¹⁴⁾ and TACO3⁽¹⁵⁾ computer programs. These changes are discussed in Section 2.3.2 of Revision 3 of BAW-10164P. There are three basic areas in which the fuel pin model provides calculations: dynamic fuel/clad gap conductance, fuel rod swelling, and rupture based on the NUREG-0630⁽¹⁶⁾ approach and clad metal-water reaction. Enhancements in Revision 3 include addition of a closed gap contribution to gap conductance to allow modeling of high burnup cases, fuel pin axial expansion, automated clad rupture calculation, implicit metal-water reaction option and automated steady-state gap multiplier option.

The RELAP5/MOD2-B&W enhanced fuel pin model has some differences compared to the previously approved models in FRAP-T6-B&W and TACO3. These are due to the less detailed nature of the model used in RELAP5/MOD2-B&W compared to the fuel performance codes.

The previously approved gap conductance model allowed for modeling of a non concentric fuel stack within the clad, but did not include a contact conductance term in the calculation of total gap conductance. The option to include a contact resistance contribution has been added based upon the model presently used in the TACO3 computer program. Since Appendix K does not prohibit the use of contact resistance, this model is acceptable for cases of high burnup fuel with a closed gap.

The gap gas pressure is used to determine the amount of clad swelling and rupture. One of the variables which determines the gap gas pressure is the amount of volume available for the gas to occupy. A portion of this volume is located in the gas plenum at the top of each fuel rod. When the clad and fuel expand axially at different rates the volume of the plenum will change. The axial expansion model accounts for this

change in plenum volume due to differential thermal expansion of the fuel and clad from the cold condition. Thermal strain correlations from MATPRO⁽¹⁷⁾, or user input fits, are used to determine the amount of fuel and clad axial expansion. Including the effects of axial fuel rod expansion on plenum volume is appropriate for a best-estimate calculation, and is acceptable for Appendix K to 10 CFR 50 LOCA analysis, which does not prohibit including this model. Only minimal differences exist between the enhanced fuel pin model and the FRAP-T6-B&W model. The enhanced model is acceptable for use in ECCS evaluation model calculations.

Addition of an automated clad rupture model introduces heat transfer enhancement downstream of a rupture location. The model used for this option has been previously approved for use in the BEACH computer program. This option automates the calculation of rupture location for use in BEACH. Use of this model in RELAP5/MOD2-B&W is consistent with the Appendix K to 10 CFR 50 approved model and is, therefore, acceptable.

An implicit formulation of the Baker-Just metal water reaction model has been implemented in RELAP5/MOD2-B&W. The model is the same as that which is used in the FRAP-T6-B&W computer code. Appendix K to 10 CFR 50 requires use of the Baker-Just model but does not specify the numerical solution technique to be used. The implicit solution will improve accuracy for calculations which use a larger time step. Use of this option is acceptable for compliance with Appendix K to 10 CFR 50.

Initialization of the RELAP5/MOD2-B&W model must comply with Appendix K to 10 CFR 50 in the sense that initial stored energy in the fuel must be conservatively specified. This is done by adjusting the fuel clad gap conductance to obtain the desired value of volume average fuel temperature. In earlier versions of the program a user specified multiplier on the gas conductance term of the gap conductance was provided to permit adjustment and matching of volume average fuel temperature. This required that an iterative process be performed by the user. An option has been

added to automate this iteration process. The user can specify the desired volume average fuel temperature, rather than the multiplier on the gas conductance term, and the code will iterate to determine the gas conductance multiplier. This is a user convenience feature which is acceptable for ECCS evaluation model calculations.

3.2.5 EM Heat Transfer Model Modifications

BWNT incorporated a filtered flow option to be used with the core heat transfer model. This option was added to facilitate addressing the Appendix K to 10 CFR 50 requirement to eliminate any calculated rapid flow oscillations with a period of less than 0.1 seconds during the LBLOCA blowdown phase. This requirement is mandated because rapid flow oscillations can cause overprediction of the amount of energy removed from the core which would cause peak clad temperature to be underpredicted. The method, described in Section 2.3.3 of BAW-10164P, is consistent with the requirements of Appendix K to 10 CFR 50.

3.2.6 Post-CHF Model Modifications

User defined correction factors were added to the equation used to determine the total wall-to-fluid heat flux due to transition boiling as shown on page 2.3-86 of Revision 3 to BAW-10164P. These constants are defined as $C_{1_{TR}}$ and $C_{1_{TR1}}$ which have a default value of 1.0. BWNT did not identify any benchmarks that used values other than 1.0 for these correction factors.

A user option was added to allow adjustment of the surface heat transfer coefficient following cladding rupture of a fuel pin on page 2.3-89 of Revision 3 to BAW-10164P. If this option is invoked, the heat flux in a ruptured segment single heat structure is multiplied by the ratio of the ruptured to cold outside cladding radius. The heat flux is then computed using the increased surface area resulting from clad swelling and

rupture. This change is physically realistic and does not violate Appendix K requirements. It is, therefore, acceptable.

3.2.7 OTSG Benchmarks

BWNT performed two benchmarks of the RELAP5/MOD2-B&W code to demonstrate the adequacy of the OTSG modelling. These benchmarks are discussed in Appendix K to BAW-10164P. The first set of benchmarks are comparisons to steady-state tests performed in 1969 to demonstrate the ability of the code to predict the shell side nucleate boiling length at various power levels. The second benchmark is a comparison to a loss of feedwater flow test performed in 1977 to demonstrate the ability of the code to predict boil-down and refill of a OTSG.

The tests were performed at the Alliance Research Center (ARC) Nuclear Steam Generator Test Facility. This facility provided the capability of testing steam generators at full system pressure and temperature conditions. The primary side of the test loop consisted of a gas-fired furnace to simulate reactor heat input into the primary fluid, a pressurizer, flow control valves, flow measuring elements, and a water conditioning system. The secondary system was a closed circuit test loop consisting of steam flow control valves, steam flow measuring equipment, feedwater heaters, back pressure control valves, a flash tank, circulating pumps, feedwater control valves, feedwater flow measuring equipment, feedwater flow bypass valves, and a water conditioning system.

The model steam generator used for these benchmarks, referred to as the 19-tube OTSG, is a single pass, counterflow, tube and shell heat exchanger. The tube bundle consisted of 19 full length tubes, each 5/8 inch diameter, spaced on a triangular pitch on 7/8 inch centers. Primary inlet flow entered at the top of the steam generator, flowed downward through the tube bundle and exited at the bottom. Secondary feedwater flow entered the tube bundle at the bottom, was boiled as it passed by the

outside of the tube bundle, and exited at the top. The feedwater was raised to saturation conditions by mixing the water with steam from the tube region via a steam bleed pipe connected from the secondary side of the generator to the steam/feedwater mixer. A question on where the feedwater temperature is measured was raised. BWNT stated that the feedwater temperature is measured with a thermocouple located approximately three feet upstream of the steam/feedwater mixer.

In the steady state tests, boiling length (dryout location) was determined from primary tube and secondary side thermocouples for a range from 0 to 100 percent of the full scaled power consistent with a 2700 MWth plant. The loss of feedwater flow test initialized to full scaled power consistent with a 2772 MWth plant. The test was initiated by the simultaneous trip of the feedwater pump and closure of the feedwater isolation valve. The steam generator was allowed to boil dry and then the feedwater was restarted. Secondary steam flow and temperature and primary outlet temperature were measured during the test.

The RELAP5/MOD2-B&W model utilized 11 axial control volumes in the primary tube region and in the secondary shell region. Primary to secondary heat transfer was modelled using eleven heat structures between the primary and secondary sides. The external downcomer was modeled with five axial control volumes that represented the piping from the steam/feedwater mixing region to the tube bundle inlet. Feedwater aspiration was provided by a single junction component that connected the tube bundle region to the external downcomer. A junction connection between the shell side of the heat exchanger and the control volume representing the steam/water mixer is included in the model. Time dependent volume and time dependent junction components were used to set inlet flowrate and temperature of the primary and secondary side coolant.

A question on the modeling of the steam/feedwater mixing or aspiration process, addressed the relative pressures between the control volume representing the mixer

and the volume representing the source of aspiration steam from the secondary to the mixer. Assuming a normal flow junction connecting these volumes, the pressure in the secondary must be higher than the mixer in order to provide steam flow to the mixer. BWNT responded that the bundle collapsed liquid level remains below the downcomer level (presumably below the level of the steam/feedwater mixer) during the tests. As a result the pressure gradient that sustains the steam flow from the secondary is maintained by manometric effects. BWNT also noted that this process is self-governing due to changes in the pressure gradient as the downcomer fluid approaches saturation.

BWNT employed some of the features incorporated into RELAP5/MOD2-B&W for the 19-tube OTSG benchmark. These features are summarized below:

- o The Becker critical heat flux correlation, discussed in Section 3.2.3, are used on the shell side of the tube heat structure,
- o The multipliers defined by the B&W modified slug-drag model and the annular mist model are used, and
- o A linear ramp was applied to the Chen boiling suppression factor. This adjustment to the suppression factor was discussed in Section 3.2.2.

The first set of results for the steady state benchmark compared the boiling lengths predicted by RELAP5/MOD2-B&W to those measured during the 19-tube OTSG tests. BWNT presented tabulated results and a plot comparing the boiling length above the lower tube sheet predicted by RELAP5/MOD2-B&W to the 19-tube OTSG tests at power levels ranging from 20 to 100 percent of the scaled power levels relative to a 2700 MWth plant. The results show that the boiling lengths predicted by RELAP5/MOD2-B&W are in good agreement with the test data. In contrast, results from RELAP5/MOD2 Cycle 36.05 also shown on these plots, differ significantly from the test data below 80 percent scaled power. BWNT attributes this agreement in the

boiling length results between RELAP5/MOD2-B&W and the 19-tube OTSG test to the use of the Becker critical heat flux correlation.

For the LOFW benchmark, BWNT presented comparison plots between RELAP5/MOD2-B&W and 19-tube OTSG data for steam flow rate and the primary outlet temperature after the initiation of the LOFW transient. Plots of the primary and secondary system fluid temperatures prior to the initiation of the LOFW test are also presented to show initial conditions. The plots of steam flow rate and primary outlet temperature show that the magnitude and trend of the results are in good agreement between RELAP5/MOD2-B&W and the 19-tube OTSG test.

BWNT was requested to provide comparison plots between RELAP5/MOD2-B&W and 19-tube OTSG data comparing steam generator secondary level or mass. In their response, BWNT noted that determination of collapsed liquid level is difficult to obtain under two phase high flow conditions. BWNT did provide comparisons of the steady state and transient differential pressure in the boiler. The response of BWNT to this question was reviewed and found adequate.

3.2.8 MIST Benchmarks

As part of their evaluation of the Revision 3 modifications to the RELAP5/MOD2-B&W code, BWNT included an integral system benchmark of a SBLOCA for a simulated reactor system using OTSGs. BWNT included this benchmark as a further check of the modifications made to reduce interphase drag in the slug flow regime (Wilson bubble rise model) and in the annular flow regimes.

The integral system benchmark was performed using data from the Multi-Loop Integral System Test (MIST) facility which is a scale model of a B&W lowered-loop 177 fuel assembly pressurized water reactor. The MIST facility is designed to operate at pressures and temperatures typical of an operating B&W plant. The MIST facility

consists of two 19-tube once-through steam generators, a reactor vessel with a heated core and external downcomer, pressurizer with a power operated relief valve, two hot legs and four cold legs. Further information on facility scaling and instrumentation is found in Appendix L to BAW-10164P.

BWNT notes in Appendix L to BAW-10164P, that a number of pre- and post-test predictions have been made for MIST tests using the RELAP5/MOD2 code as a part of the MIST program. These predictions were made with earlier versions of the code, which did not include the recent modifications. The benchmark presented in Appendix L includes a comparison of experimental data with RELAP5/MOD2 results obtained with both the current and earlier versions of the code. This allows an evaluation of the effects of the recent model changes, in particular upon the prediction of collapsed liquid level in the reactor vessel and steam generator secondary. The results show that the code modifications clearly improve the collapsed liquid level predictions.

The RELAP5/MOD2-B&W model simulates the MIST reactor vessel, downcomer, hot and cold legs, OTSGs, reactor coolant pumps, and other major components. A double flow path connection to the external reactor vessel downcomer is used in this model so that countercurrent two-phase flow can be predicted. The steam generator modelling employs two radial regions to account for tubes directly wetted by auxiliary feedwater (AFW) injection on the shell side of the steam generator. The other region represents the 16 tubes in contact with secondary steam. BWNT notes in their response that the BWNT modified slug-drag model was employed in the core and primary tube region. For the secondary side of the steam generator tube region, the BWNT slug-drag model is used on the annular mist drag.

In the RELAP5/MOD2-B&W model, the core region was modified so that twenty control volumes represent the full height core. BWNT states that this noding is necessary for consistency with the revised models. BWNT was requested to discuss the implications of increasing the number of core volumes focusing on the degree of

improvement resulting from the use of the new interphase drag model as compared to just increasing the number of core nodes.

BWNT performed a noding sensitivity study based on ORNL THTF Test 3.09.10j discussed in Appendix H to BAW-10164P. In this study, BWNT ran cases using 4 and 24 nodes in the core region using both the INEL drag model and the BWNT slug-drag model. Plots presented by BWNT show good agreement between the RELAP5/MOD2-B&W results using the BWNT slug-drag model for both the 4 and 24 node core models and the THTF data. The results from the INEL model show poor agreement with the THTF data. BWNT notes in their response that the INEL model is known to overpredict the interphase drag in heated regions with small hydraulic diameters. In this context, the BWNT response regarding the nodalization of the steam generator secondary was reviewed and is acceptable.

MIST test 320201, used for the RELAP5/MOD2-B&W benchmark, simulated a scaled 50 cm² pump discharge break. This is reported by BWNT to be the most limiting small break size for B&W designed plants. The MIST facility was initialized in natural circulation mode with the core power scaled to 3.5 percent for this test. BWNT noted that since the MIST facility was capable of only ten percent full-scaled power operation, the facility was initialized to conditions corresponding to 145 seconds after trip. Other initial conditions include primary system pressure corresponding to 22° F core exit subcooling, pressurizer level of 5 feet above the bottom of the pressurizer, steam generator pressure of 1010 psia, and a steam generator secondary level controlled to five feet above the lower tube sheet by throttling high elevation AFW injection.

The MIST test was initiated by turning off the pressurizer heaters and opening the leak. When the pressurizer level reached one foot, full high pressure injection flow was started and steam generator secondary refill using full capacity AFW was initiated.

BWNT presented comparison plots between RELAP5/MOD2-B&W and MIST for primary pressure, secondary pressure, reactor vessel liquid level and secondary liquid level. A tabulation of the timing of key events is presented in Table L.2 of BAW-10164P. Additional information was provided on the elevation of the steam generators and reactor vessel at the MIST facility. The results for BWNT Versions 5 and 14 of RELAP5/MOD2-B&W are presented. The main difference in these code versions is that Version 14 utilizes the revised interphase drag models.

In general, there is good agreement between the RELAP5/MOD2-B&W Version 14 results and the MIST data. BWNT noted that the improved prediction of reactor vessel and secondary liquid levels is due to the revised slug drag model. The large difference in timing of the hot leg voiding between Revisions 5 and 14 of RELAP5/MOD2-B&W was questioned. BWNT attributed this to differences in the initial temperature conditions in the pressurizer and surge line used in the Revision 5 and Revision 14 calculations. BWNT also revised Table L.2 which corrects the reported time of operator actions.

In reviewing the MIST benchmark, it is noted that no fuel rod temperature excursion occurred during this test. This issue was discussed with BWNT. BWNT responded that the mixture level in the vessel remained above the core during the test, resulting in removal of the stored energy in the fuel by nucleate boiling. In view of this lack of core uncover, BWNT noted that MIST is not the best benchmark for the core mixture level calculation. The stand-alone FOAM2 and ORNL benchmarks presented in Appendix H to BAW-10164P were provided to better address the code's predictive capability.

MIST benchmarks address the capability to predict system pressure, liquid inventory and liquid distribution. In this respect, the MIST test 320201 benchmark demonstrates that the modifications made to the code improve its predictive capability in these areas. When considered along with the other benchmarks, including additional MIST

benchmarks, BWNT has demonstrated that RELAP5/MOD2 B&W is capable of adequately predicting the system response for an OTSG plant.

In discussing cladding temperature during an SBLOCA, BWNT argues that the cladding temperature excursion during SBLOCA is governed by the same physical processes for all current PWR designs. During core boildown, the vapor temperature and fuel cladding heat transfer are dependent upon local mechanisms and not upon integral system parameters. Therefore, heatup during core boiloff depends upon the core geometry, but not the integral system geometry. Benchmarks against ROSA-IV, ORNL and Semiscale test data are hence acceptable for demonstrating that RELAP5/MOD2-B&W is capable of adequately predicting fuel clad temperatures during this heatup phase.

3.3 High Auxiliary Feedwater Model

BWNT developed the high auxiliary feedwater model to calculate the B&W OTSG heat transfer correctly during auxiliary feedwater injection from high elevation locations. This model was included in the Revision 1 submittal but was not reviewed because B&W did not intend to use RELAP5/MOD2-B&W for OTSG analysis at that time as noted in Section 5 of the Revision 1 safety evaluation report. BWNT requested a review of this model and has provided additional information to support this request.

The high auxiliary feedwater model was reviewed as part of the CRAFT2 code Topical Report transmittal in 1985. This report included several benchmarks against plant and experimental data. BWNT has made some modifications to the heat transfer models since that time. Therefore, an additional RELAP5/MOD2-B&W benchmark of the revised heat transfer models against test data from the MIST facility was provided by BWNT. Included is a plot comparing RELAP5/MOD2 predicted primary side temperature as a function of elevation above the tube sheet against steady-state MIST measurements. This plot shows good agreement between the RELAP5/MOD2 B&W

predictions and the MIST measurements along the length of the steam generator tubes. The steady-state nature of this test allowed the calculated heat transfer coefficients used in the model to be justified. The high AFW model was also used for the additional MIST benchmarks performed by BWNT. These serve to demonstrate the adequacy of the model for transient applications.

Based upon the discussions and benchmarks provided by BWNT, it is concluded that the revisions to the high auxiliary feedwater model have not changed significantly from the model previously accepted. Therefore, we find it acceptable for use in SBLOCA analysis.

3.4 Parameters Used in RELAP5/MOD2-B&W Benchmarks

BWNT has incorporated a number of user specified input parameters in RELAP5/MOD2-B&W. The value of these parameters used in the RELAP5/MOD2 B&W benchmarks are listed in Table 1 of this evaluation. The values of these parameters were selected to improve the agreement between RELAP5/MOD2-B&W and the FOAM2, THTF, OTSG, and MIST benchmark data. The values of the user specified parameters listed in Table 1 are the only acceptable values for LOCA licensing calculations.

One of the motivations driving the initial development of the RELAP5 code was the need to eliminate user choice of modeling options and input dials. When an analysis is performed with RELAP5, one can be certain of what models and fitting parameters are used. The addition of numerous options and dials by BWNT is contrary to this characteristic of RELAP5. The last condition listed above is intended to eliminate the use of user specified dials in keeping with the intent of the RELAP5 approach.

Table 1
 Summary of User Specified Parameters Used in the
 RELAP5/MOD 2-B&W Benchmarks

Parameter	Description	Page Where Parameter Is Described	Affected Benchmark
C_{WB}	Multiplier on bubble velocity in the Wilson Bubble Rise Model.	2.1-52.3 (Revision 2)	FOAM2 code, ORNL THTF tests (Appendix H)
C_{WSL}	Multiplier on the interphase drag predicted for slug flow	2.1-52.3 (Revision 2)	FOAM2 code, ORNL THTF tests (Appendix H)
xms	Multiplier on the interphase drag computed for annular mist flow	2.1-53 (Revision 2)	OTSG benchmarks (Appendix K), MIST benchmarks (Appendix L)
xsg	High void fraction slug coefficient	2.1-52.5 (Revision 3)	OTSG benchmarks (Appendix K), MIST benchmarks (Appendix L)

Table 1
Summary of User Specified Parameters Used in the
RELAP5/MOD 2-B&W Benchmarks

Parameter	Description	Page Where Parameter Is Described	Affected Benchmark
α_s	Low end of void fraction for adjustment	2.1-52.5 (Revision 3)	OTSG benchmarks (Appendix K), MIST benchmarks (Appendix L)
α_{sh}	High end of void fraction for adjustment	2.1-52.5 (Revision 3)	OTSG benchmarks (Appendix K), MIST benchmarks (Appendix L)
xslg	Slope of drag pressure term	2.1-52.5 (Revision 3)	OTSG benchmarks (Appendix K), MIST benchmarks (Appendix L)
cxslg	x-intercept for pressure term	2.1-52.5 (Revision 3)	OTSG benchmarks (Appendix K), MIST benchmarks (Appendix L)

5-393

Table 1
Summary of User Specified Parameters Used in the
RELAP5/MOD 2-B&W Benchmarks

Parameter	Description	Page Where Parameter Is Described	Affected Benchmark
α_{gr}	Void fraction at which to begin the S ramp	2.2-22 (Revision 3)	OTSG benchmarks (Appendix K)
C1 _{TR} , C1 _{TR1}	User multiplicative constants used in the equation to determine wall-to-fluid heat flux during transition boiling.	2.3-86 (Revision 3)	

S-394

4.0 COMPLIANCE WITH NRC REQUIREMENTS

Appendix K to 10-CFR-50 specifies required and acceptable features of ECCS evaluation models. Previous revisions of the RELAP5/MOD2-B&W program, through Rev. 1, have been reviewed and found to satisfy the requirements of Appendix K when used with the approved B&W ECCS methodology, subject to any restrictions cited in the SER.

The modifications documented in Revisions 2 and 3 of BAW-10164P do not affect compliance with any of the required features of Appendix K. Modifications of the fuel pin model are such that the requirements of Appendix K continue to be satisfied. Inclusion of a contact conductance term in the calculation of fuel clad gap conductance does not affect compliance with Appendix K which states that "thermal conductance of the gap between the UO_2 and the cladding shall be evaluated as a function of the burnup, taking into consideration fuel densification and expansion, the composition and pressure of the gases within the fuel rod, the initial cold gap dimension with its tolerances, and cladding creep." Section B of Appendix K also specifies that "The gap conductance shall be varied in accordance with changes in gap dimensions and any other applicable variables."

Inclusion of axial thermal expansion of the cladding and fuel in the gas plenum volume calculation also does not affect compliance with Appendix K. The plenum volume is used in the calculation of internal rod pressure which is a key determinant of the amount of swelling and rupture. Appendix K requires that "the swelling and rupture calculations shall be based on applicable data in such a way that the degree of swelling and incidence of rupture are not underestimated." Calculation of gas gap pressure using plenum volume which accounts for axial thermal expansion of the fuel and cladding improves accuracy and should not result in underestimating the pressure or the incidence of swelling and rupture.

Appendix K specifies that the Baker-Just model be used to calculate the metal-water reaction rate, but does not specify the solution method. Therefore, the implicit solution technique is acceptable, given that it yields a mathematically correct solution of the required equation. Appendix K also requires that "The degree of swelling and rupture shall be taken into account in calculations of gap conductance, cladding oxidation and embrittlement, and hydrogen generation." The "swelled radius" modification to the metal-water reaction model accounts for the increase in clad radius, and hence surface area, due to swelling. This model change affects the hydrogen generation and cladding oxidation, and is in compliance with the Appendix K requirements listed above. The iterative technique for determining a multiplier on gap conductance which yields a desired initial stored energy is a user convenience feature which does not affect the previously approved model.

Section C.4.e of Appendix K to 10 CFR 50 states: "After CHF is first predicted at an axial fuel rod location during blowdown, the calculation shall not use nucleate boiling heat transfer correlations at that location subsequently during the blowdown even if the calculated local fluid and surface conditions would apparently justify the reestablishment of nucleate boiling. Heat transfer assumptions characteristic of return to nucleate boiling (rewetting) shall be permitted when justified by the calculated local fluid conditions during the reflood portion of a LOCA." The core heat transfer selection model modifications assure that no return to nucleate boiling will occur before the end of blowdown for the large break LOCA. Since the definitions of blowdown and reflood are inappropriate for SBLOCA, it is acceptable to bypass this "no return to nucleate boiling" requirement in that case. The modification is therefore in compliance for LBLOCA analysis, and acceptable for the SBLOCA analysis where the requirement is inappropriate.

CHF correlations acceptable for use in LOCA analysis are listed in Sections C.4.b and d. Section C.4.a states that "Correlations developed from appropriate steady-state and transient-state experimental data are acceptable for use in predicting the critical

heat flux (CHF) during LOCA transients. The computer programs in which these correlations are used shall contain suitable checks to assure that the physical parameters are within the range of parameters specified for use of the correlation by their respective authors". As discussed in Section 2.1.7 of this report, the BWUMV CHF correlation has been developed using appropriate experimental data for fuel with mixing vanes. The correlation is therefore acceptable for use within the ranges of parameters specified. It is noted that BWNT requested that the correlation be approved for pressures down to 750 psia. Based upon the data comparison provided by BWNT, the staff concludes that the correlation is acceptable down to pressures of 1300 psia and mass fluxes of 500,000 lb/hr-ft². Checks which restrict use of the correlation to this range must be included in RELAP5/MOD2-B&W for the code to be acceptable.

Benchmarks against calculations of the approved computer program FOAM2 and THTF experimental test data have shown that addition of the Wilson drag model improves predictions of void distribution in the core region. Appendix K does not list specific requirements in this area. The modification, which improves modeling accuracy, is therefore acceptable. A number of the other code enhancements fall into this same category. They cover areas where Appendix K does not specify required features. These include the annular mist flow regime overall drag multiplier, condensation heat transfer correlation modifications, Wilson slug flow drag model, and the CCFL model. Appropriate justification has been provided to show that these enhancements improve modeling accuracy.

5.0 CONCLUSIONS AND LIMITATIONS

Modifications made to RELAP5/MOD2-B&W as described in Revisions 2 and 3 of BAW-10164P have been reviewed and evaluated. Based on the benchmarks presented, the staff finds that the models described in version 19 of RELAP5/MOD2-B&W to be acceptable for LOCA and non-LOCA analysis for PWRs with recirculating and OTSGs subject to the following limitations:

- o Use of the Wallis and UPTF parameters at the tube bundle and steam generator plenum inlet are acceptable. The parameters used in the CCFL model for any other application must be validated, and the validation reviewed and approved by the staff for that application (see section 3.1.3 of this evaluation).
- o The BWUMV correlation is limited to pressures above 1300 psia.
- o For large break LOCA ECCS evaluation model calculations, form losses due to ruptured cladding should not be excluded using the user option described in Section 3.2.4 of this evaluation.
- o The value of the user specified parameters listed in Table 1 of this evaluation (i.e. those used for the benchmark calculations) are the only acceptable values for LOCA licensing calculations.

Table 2 lists typographical errors that were found during the course of this review. Correction of these errors should be incorporated into the approved version of BAW-10164P. The automated blockage droplet breakup calculation, the implicit formulation of the Baker-Just metal water reaction model and the fuel rod Evaluation Model improvements referred to in Section 5 of the BEACH safety evaluation report⁽¹⁸⁾ were reviewed in this evaluation and found acceptable. Contingency 4 given in Section 5 of the BEACH safety evaluation report is no longer applicable. That contingency states: "Use of the automated blockage droplet breakup calculation, implicit formulation of the Baker-Just metal water reaction model and the fuel rod Evaluation Model (EM)

Improvements should be made contingent upon their approval in Revision 3 of BAW-10164P, which describes these updates."

Table 2
Summary of Changes That Should Be Made To The
Approved Version of BAW-10164, Revision 2 and 3

Affected Report Revision and Section	Change Summary
Revision 2, Appendix H, Figure H.1	Correction to Figure H.1 in response to Question 2 of the Revision 2 RAI
Revision 2, Appendix H, Table H.2	Correction to Table H.2 in response to Question 4 of the Revision 2 RAI
Revision 2, Section 2.3.3 and Appendix I	Correction to Equation I-1, I-2 and pressure and mass flux units in response to Questions 5, 6, and 7 of the Revision 2 RAI
Revision 2, Appendix I, Table I.3	Duplication in point numbers in Test 160 (point 789) and Test 164 (points 2060 and 2065) should be corrected or clarified.
Revision 2, Appendix J, Page J-8	Reference to Table 2 should be Table J.2 per Question 11 of the Revision 2 TER
Revision 3, Section 2.3.2	Correction of ϵ_{TC} value on Table 2.3.2-2 in response to Question 4 to the Revision 3 RAI.
Revision 3, Page 2.3-46	Correction to β^2 definition in text in response to Question 5 of the Revision 3 RAI. Other correction noted by BWNT on Page 2.3-36 should also be included.
Revision 3, Appendix L, Table L.1	Revision to Table L.1 in response to Question 10 of the Revision 3 RAI.
Revision 3, Appendix L, Table L.2	Revision to Table L.2 in response to Question 11 of the Revision 3 RAI.

5.0 REFERENCES

1. Ransom, V. H., et. al., RELAP5/MOD2 Code Manual -- Volume 1: Code Structures, System Models and Solution Methods and Volume 2: Users Guide and Input Requirements, NUREG/CR-4312 - Volume 1, August, 1985 and NUREG/CR-4312 - Volume 2, December 1985.
2. B&W Nuclear Technologies, RELAP5/MOD2-B&W -- An Advanced Computer Program for Light Water Reactor LOCA and non-LOCA Transient Analysis, BAW-10164P, Revision 1, October 1988.
3. Letter from A. C. Thadani (USNRC) to J. H. Taylor (B&W Nuclear Technologies), Acceptance for Referencing of Topical Report BAW-10164P, Revision 1, RELAP5/MOD2-B&W, An Advanced Computer Program for Light Water Reactor LOCA and Non-LOCA Transient Analysis, April 18, 1990.
4. Code of Federal Regulations, ECCS Evaluation Models, Chapter 10, Part 50, Appendix K
5. B&W Nuclear Technologies, RELAP5/MOD2-B&W -- An Advanced Computer Program for Light Water Reactor LOCA and Non-LOCA Transient Analysis, BAW-10164P, Revision 2, August 1992.
6. B&W Nuclear Technologies, RELAP5/MOD2-B&W -- An Advanced Computer Program for Light Water Reactor LOCA and non-LOCA Transient Analysis, BAW-10164P, Revision 3, October 1992.
7. Letter from J. H. Taylor (B&W Nuclear Technologies) to R. C. Jones (USNRC), BEACH Topical Report BAW-10166P, JHT/93-214, August 31, 1993.
8. Letter from J.H. Taylor (B&W Nuclear Technologies), Response to NRC's Request for Additional Information on BAW-10164, Revision 2, August, 1992; RELAP5/MOD2-B&W, An Advanced Computer Program for Light Water Reactor LOCA and NON-LOCA Transient Analysis, JHT/93-279, November 16, 1993
9. Letter from J.H. Taylor (B&W Nuclear Technologies), Response to NRC's Request for Additional Information on BAW-10164, Revision 3, October, 1992; RELAP5/MOD2-B&W, An Advanced Computer Program for Light Water Reactor LOCA and NON-LOCA Transient Analysis, JHT/94-7, January 21, 1994

10. Letter from J.H. Taylor (B&W Nuclear Technologies), Response to NRC's Supplemental Request for Additional Information on BAW-10164, Revision 2, August, 1992; RELAP5/MOD2-B&W, An Advanced Computer Program for Light Water Reactor LOCA and Non-LOCA Transient Analysis, JHT/94-146, September 20, 1994.
11. B&W Nuclear Technologies, FOAM2 -- Computer Program to Calculate Core Swell Level and Mass Flow Rate During Small Break LOCA, BAW-10155A, October 1990.
12. Collier, John G., Convective Boiling and Condensation, Mc-Graw-Hill International Book Company, 2nd. edition, 1972
13. B&W Fuel Company, Correlation of Critical Heat Flux in Mixing Vane Grid Fuel Assemblies, BAW-10159P-A, July 1990
14. B&W Nuclear Technologies, FRAP-T6-B&W - A Computer Code for the Transient Analysis of Light Water Reactor Fuel Rods, BAW-10165P, October 1988.
15. B&W Nuclear Technologies, TACO3 - Fuel Pin Thermal Analysis Computer Code, BAW-10162P-A, October 1989.
16. D.A. Powers and R.O. Meyers, Cladding Swelling and Rupture Models for LOCA Analysis, NUREG-0630, April, 1980
17. D.L. Hagrman, et. al., MATPRO - Version 11 (Revision 2), NUREG/CR-4079, August 1981
18. D.A. Prelewicz, Technical Evaluation Report - BEACH - Best Estimate Analysis Core Heat Transfer. A Computer Program for Reflood Heat Transfer During LOCA, BAW-10166P, Revision 4, SCIENTECH, Inc., SCIE-NRC-219-93, November, 1993

5.0 LICENSING DOCUMENTS

This section contains documents generated as a result of U.S. Nuclear Regulatory Commission (NRC) review of previous versions of this topical report. Sections 5.1 and 5.2 contain responses to rounds one and two questions, respectively, for revision 1 of this report. These documents were previously issued in the approved proprietary and non-proprietary versions as appendices H and I. Section 5.3 contains the Safety Evaluation Report (SER) issued for revision 1.

Section 5.4 and 5.5 contain responses to NRC questions on revisions 2 and 3, respectively, of this report. Section 5.6 contain supplemental information to revisions 2 and 3. Section 5.7 contains the SER issued for revisions 2 and 3. Section 5.8 contains responses to NRC questions on revision 4. Section 5.9 contains the SER issued for revision 4. Finally, Section 5.10 contains the pages removed or replaced from revision 3 to create revision 4 and Section 5.11 contains pages that were replaced due to SER direction and typographical errors.

FRAMATOME COGEMA FUELS

September 24, 1999
GR99-194.doc

U. S. Nuclear Regulatory Commission
ATTN: Document Control Desk
Washington, D. C. 20555

References:

1. J. L. Birmingham, NRC, to C. F. McPhatter, Framatome Cogema Fuels, Request for Additional Information for Topical report BAW-10227P, "Evaluation of Advanced Cladding and Structural Material (M5) in PWR Reactor Fuel," October 26, 1998.
2. J. L. Birmingham, NRC, to C. F. McPhatter, Framatome Cogema Fuels, Request for Additional Information for Topical report BAW-10227P, "Evaluation of Advanced Cladding and Structural Material (M5) in PWR Reactor Fuel," January 29, 1999.
3. T. A. Coleman to U.S. NRC Document Control Desk, GR99-031.doc, February 5, 1999.
4. T. A. Coleman to U.S. NRC Document Control Desk, GR99-089.doc, April 23, 1999.
5. T. A. Coleman to U.S. NRC Document Control Desk, GR99-156.doc, July 29, 1999.

Gentlemen:

References 1 and 2 contain NRC requests for additional information (RAIs) on topical report BAW-10227P. FCF has provided responses to the RAIs in references 3, 4 and 5. In addition to references 1 and 2, the contract reviewer for BAW-10227P has verbally provided requests for information in numerous telecons that have taken place since mid-July. FCF has informally provided all the requested information via Fax, Email, and FedEx. The purpose of this letter is to provide a formal record of those transmittals.

In accordance with 10 CFR 2.790, FCF requests that these responses be considered proprietary and withheld from public disclosure. Attachment 1 is the FCF proprietary version of the responses. Attachment 2 is the affidavit identifying the criteria for the proprietary request. Attachment 3 is the non-proprietary version of the responses.

These responses will be incorporated into the NRC-approved version of BAW-10227P as Appendix K. K.1 is the response to verbal RAIs on the original response to question 2. K.2 is the response to verbal RAIs on the original response to question 5. K.3 is the response to the verbal RAIs on the original response to question 12. K.4 is the response to the verbal RAIs on the original response to question 14. K.5 is the response to the verbal RAIs on the original response on question 19. K.6 is a supplemental addition to Enclosure 1 of the April 23 responses (reference 4). K.7 provides FCF's plans for post irradiation examinations (PIEs) of fuel with M5 cladding.

All the enclosed information has already been provided to the NRC contract reviewer. It has been reviewed and the NRC has concluded that there no outstanding technical issues on BAW-10227P. Since additional review is not required, the NRC is requested to issue the SER for BAW-10227P by October 15, 1999.

Very truly yours,



T. A. Coleman, Vice President
Government Relations

cc: J. S. Wermiel, NRC
S. L. Wu, NRC
M. A. Schoppman
R. N. Edwards
C. E. Beyer, PNL
20A13 File/Records Management

Attachment 1

The FCF proprietary version of responses to NRC requests for additional information (RAI) has not been included in this report. Please see BAW-10227P-A, "Evaluation of Advanced Cladding and Structural Material (M5) in PWR Reactor Fuels", pages k-1 - k-39.

Rev. 4
9/99

K.8 Additional Change Pages for BAW-10164

The April 23, 1999 response to request for additional information included documentation of several changes to RELAP5 that were required to allow the input of M5 data. These changes replaced Zircaloy appropriate correlations that had been incorporated directly in the coding with input tables to allow the use of M5 correlations and data. At that time, Framatome had not proposed any change to the Chapman cladding stress versus rupture temperature correlation. Section K.5 of this submittal alters the coefficients of the Chapman correlation to better represent the M5 alloy. This requires the incorporation of input values for the cladding stress versus rupture temperature correlation coefficients. The change page documentation for BAW-10164 in Enclosure 1 accomplishes those changes. In addition Framatome Technologies Incorporated (FTI) would like to have only one revision level to BAW-10164 for M5 application. Therefore, all of the BAW-10164 change pages submitted in April have been re-dated to September and are included in Enclosure 1. Enclosure 1 is thus a complete record of the required changes and Framatome requests the approval for these changes to BAW-10164.

Beginning of Enclosure 1

LISTING OF CHANGES IMPLEMENTED IN REVISION 4 OF RELAP5/MOD2-B&W TOPICAL REPORT

<u>Page</u>	<u>Type/Change</u>	<u>Item</u>	<u>Reason</u>
--	Revision	Title page	Revision & Date
i-ii	Revision	Abstract	Revision & Date
v	Addition	Revision Record	New topical version
xii	Revision	Table/Contents, etc.	New revisions
1-1	Addition	Introduction	Zirconium-based alloy clad
2.1-126 to 2.1-126.2	Addition	Void-Dependent Cross-flow	New code option
2.3-25 to 2.3-28	Addition	EM Pin Model Changes	Zirconium-based alloy clad
2.3-33	Addition	EM Pin Model Changes	Zirconium-based alloy clad
2.3-35 to 2.3-37	Addition	EM Pin Model Changes	Zirconium-based alloy clad
2.3-39 to 2.3-41	Addition	EM Pin Model Changes	Zirconium-based alloy clad
2.3-45 to 2.3-46.2.2	Addition	EM Pin Model Changes	Zirconium-based alloy clad
2.3-52	Correction	EM Pin Model	Zirconium-based alloy clad
2.3-55	Addition	Steady-State EM Pin Model	Fuel temperature convergence
5-364.1 to 5-364.2	Correction	Missing SER Page	Include missing page

(NOTE: Pages 2.1-126.1, 2.1-126.2, 2.3-27.1, 2.3-27.2, 2.3-46.2.1, 2.3-46.2.2, 5-364.1, and 5-364.2 were added in Revision 4)

This page is intentionally left blank.

BAW-10164P
Topical Report
Revision 4
September 1999

- RELAP5/MOD2-B&W -
An Advanced Computer Program for
Light Water Reactor LOCA and Non-LOCA
Transient Analysis

Framatome Technologies Inc.
P. O. Box 10935
Lynchburg, Virginia 24506

This page is intentionally left blank.

Framatome Technologies Inc.
Lynchburg, Virginia

Topical Report BAW-10164P
Revision 4
September 1999

RELAP5/MOD2-B&W

An Advanced Computer Program for
Light Water Reactor LOCA and Non-LOCA
Transient Analysis

Key Words: RELAP5/MOD2, LOCA, Transient, Water Reactors

Abstract

This document describes the physical solution technique used by the RELAP5/MOD2-B&W computer code. RELAP5/MOD2-B&W is a Framatome Technologies Incorporated (previously known as and referred to in the text as B&W or B&W Nuclear Technologies) adaption of the Idaho National Engineering Laboratory RELAP5/MOD2. The code developed for best estimate transient simulation of pressurized water reactors has been modified to include models required for licensing analysis of zircaloy or zirconium-based alloy fuel assemblies. Modeling capabilities are simulation of large and small break loss-of-coolant accidents, as well as operational transients such as anticipated transient without SCRAM, loss-of-offsite power, loss of feedwater, and loss of flow. The solution technique contains two energy equations, a two-step numerics option, a gap conductance model, constitutive models, and component and control system models. Control system and secondary system components have been added to permit modeling of plant controls, turbines, condensers, and secondary feedwater conditioning systems. Some discussion of the numerical techniques is presented. Benchmark comparison of code

Rev. 4
9/99

predictions to integral system test results are presented in an appendix.

Rev. 4
9/99

This page is intentionally left blank.

Topical Revision Record

<u>Documentation</u> <u>Revision</u>	<u>Description</u>	<u>Program</u> <u>Change?</u>	<u>Program</u> <u>Version</u>
0	Original issue	_____	8.0
1	Typographical corrections Replace CSO correlation with Condie-Bengston IV.	yes	10.0
2	SBLOCA modifications Miscellaneous corrections	yes	18.0
3	EM Pin Enhancements Filtered Flows for Hot Channel Heat Transfer Rupture Area Enhancement for Surface Heat Transfer OTSG Improvements and Benchmarks using the Becker CHF, Slug Drag, and Chen Void Ramp	yes	19.0
4	Zirconium-based alloy pin model changes Option for multiple pin channels in a single core fluid channel Void-dependent core cross flow option Zirconium-based alloy rupture temperature	yes	24.0

Rev. 4
9/99

This page is intentionally left blank.

LIST OF FIGURES (Cont'd)

Figure	Page
2.1.3-5. Two Vertical Vapor/Liquid Volumes	2.1-87
2.1.4-1. Equilibrium Speed of Sound as a Function of Void Fraction and Virtual Mass Coefficient . . .	2.1-95
2.1.4-2. Coefficient of Relative Mach Number for Thermal Equilibrium Flow as a Function of Void Fraction and Virtual Mass Coefficient . . .	2.1-96
2.1.4-3. Subcooled Choking Process	2.1-98
2.1.4-4. Orifice at Abrupt Area Change	2.1-114
2.1.4-5. Schematic Flow of Two-Phase Mixture at Abrupt Area Change	2.1-117
2.1.4-6. Simplified Tee Crossflow	2.1-124
2.1.4-7. Modeling of Crossflows or Leak	2.1-125
2.1.4-8. Leak Flow Modeling	2.1-127
2.1.4-9. One-dimensional Branch	2.1-130
2.1.4-10. Gravity Effects on a Tee	2.1-132
2.1.4-11. Volumes and Junction Configurations Available for CCFL Model	2.1-133.1
2.1.5-1. Typical Separator Volume and Junctions	2.1-135
2.1.5-2. Vapor Outflow Void Donoring	2.1-136
2.1.5-3. Liquid Fallback Void Donoring	2.1-136
2.1.5-4. Typical Pump Characteristic Four- Quadrant Curves	2.1-141
2.1.5-5. Typical Pump Homologous Head Curves	2.1-142
2.1.5-6. Typical Pump Homologous Torque Curves	2.1-143
2.1.5-7. Single-Phase Homologous Head Curves for 1-1/2 Loop MOD1 Semiscale Pumps	2.1-145
2.1.5-8. Fully Degraded Two-Phase Homologous Head Curves for 1-1/2 Loop MOD1 Semiscale Pumps . . .	2.1-146
2.1.5-9. Torque Versus Speed, Type 93A Pump Motor . . .	2.1-152

LIST OF FIGURES (Cont'd)

Figure	Page
2.1.5-10. Schematic of a Typical Relief Valve in the Closed Position	2.1-162
2.1.5-11. Schematic of a Typical Relief Valve in the Partially Open Position	2.1-163
2.1.5-12. Schematic of a Typical Relief Valve in the Fully Open Position	2.1-163
2.1.5-13. Typical Accumulator	2.1-170
2.2.1-1. Mesh Point Layout	2.2-3
2.2.1-2. Typical Mesh Points	2.2-4
2.2.1-3. Boundary Mesh Points	2.2-5
2.2.2-1. Logic Chart for System Wall Heat Transfer Regime Selection	2.2-34
2.3.2-1. Gap Conductance Options	2.3-27.1
2.3.2-2. Fuel Pin Representation	2.3-34
2.3.2-3. Fuel Pin Swell and Rupture Logic and Calculation Diagram	2.3-48
2.3.3-1. Core Model Heat Transfer Selection Logic	
a) Main Driver for EM Heat Transfer	2.3-62
b) Driver Routine for Pre-CHF and CHF Correlations	2.3-63
c) Driver Routine for CHF Correlations	2.3-64
d) Driver Routine for Post-CHF Correlations	2.3-65
3.1-1. RELAP5 Top Level Structure	3.1-1
3.2-1. Transient (Steady-State) Structure	3.2-1
G.1-1. Semiscale MOD1 Test Facility - Cold Leg Break Configuration	G-14
G.1-2. Semiscale MOD1 Rod Locations for Test S-04-6	G-15

1. INTRODUCTION

RELAP5/MOD2 is an advanced system analysis computer code designed to analyze a variety of thermal-hydraulic transients in light water reactor systems. It is the latest of the RELAP series of codes, developed by the Idaho National Engineering Laboratory (INEL) under the NRC Advanced Code Program. RELAP5/MOD2 is advanced over its predecessors by its six-equation, full nonequilibrium two-fluid model for the vapor-liquid flow field and partially implicit numerical integration scheme for more rapid execution. As a system code, it provides simulation capabilities for the reactor primary coolant system, secondary system, feedwater trains, control systems, and core neutronics. Special component models include pumps, valves, heat structures, electric heaters, turbines, separators, and accumulators. Code applications include the full range of safety evaluation transients, loss-of-coolant accidents (LOCAs), and operating events.

RELAP5/MOD2 has been adopted and modified by B&W for licensing and best estimate analyses of PWR transients in both the LOCA and non-LOCA categories. RELAP5/MOD2-B&W retains virtually all of the features of the original RELAP5/MOD2. Certain modifications have been made either to add to the predictive capabilities of the constitutive models or to improve code execution. More significant, however, are the B&W additions to RELAP5/MOD2 of models and features to meet the 10CFR50 Appendix K requirements for ECCS evaluation models. The Appendix K modifications are concentrated in the following areas: (1) critical flow and break discharge, (2) fuel pin heat transfer correlations and switching, and (3) fuel clad swelling and rupture for both zircaloy and zirconium-based alloy cladding types.

This report describes the physical models, formulation, and structure of the B&W version of RELAP5/MOD2 as it will be applied to ECCS and system safety analyses. It has been prepared as a stand-alone document; therefore substantial portions of the text that describe the formulation and numerics have been taken directly from original public domain reports, particularly NUREG/CR-4312¹. Chapter 2 presents the method of solution in a series of subsections, beginning with the basic hydrodynamic solution including the field equations, state equations, and constitutive models in section 2.1. Certain special process models, which require some modification of the basic hydrodynamic approach, and component models are also described. The general solution for heat structures is discussed in section 2.2. Because of the importance of the reactor core and the thermal and hydraulic interaction between the core region and the rest of the system, a separate section is dedicated to core modeling. Contained in section 2.3 are the reactor kinetics solution, the core heat structure model, and the modeling for fuel rod rupture and its consequences. Auxiliary equipment and other boundary conditions are discussed in section 2.4 and reactor control and trip function techniques in section 2.5. Chapter 3 provides an overview of the code structure, numerical solution technique, method and order of advancement, and initialization. Time step limitation and error control are presented in section 3.3.

The INEL versions of RELAP5/MOD2 contain certain solution techniques, correlations, and physical models that have not been selected for use by B&W. These options have been left intact in the coding of the B&W version, but descriptions have not been included in the main body of this report. Appendix A contains a list of those options that remain in the RELAP5/MOD2 programming but are not used by B&W and not submitted for review. A brief description of each along with a reference to an appropriate full discussion is provided in the appendix. Appendix B defines the nomenclature used throughout this report. Appendix G documents

$v_{J,3}$ not be included in the volume average (axial) velocity calculation for cell L.

The second area of numerical modification relates to the reduced form of the momentum equations to be used at a crossflow junction. In crossflow junctions, the cross product momentum flux terms are neglected, that is, there is no x-direction transport of momentum due to the y velocity.

For the case of a small crossflow junction between two axial-flow streams (J_2 in Figure 2.1.4-7) all the geometric input (AVOL, DX, DZ) for both of the volumes relates to the axial flow direction as does the wall drag and code calculated form losses. Since the crossflow has a different flow geometry and resistance (for example, crossflow resistance in a rod bundle) the friction and form losses must be user input and must be appropriate for the crossflow direction geometry. For crossflow junctions the user input form losses should include all crossflow resistance (form losses and wall drag). The normal terms representing wall drag and abrupt area change losses are not included in the formulation of the momentum equation at a crossflow junction as these refer to the axial properties of the K and L volumes.

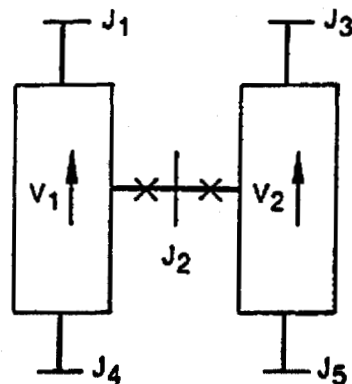


Figure 2.1.4-7. Modeling of Crossflows or Leak.

Since the connecting K and L volumes are assumed to be predominately axial-flow volumes, the crossflow junction momentum flux (related to the axial volume velocity in K and L) is neglected along with the associated numerical viscous term. In addition, the horizontal stratified pressure gradient is neglected.

All lengths and elevation changes in the one-dimensional representation are based upon the axial geometry of the K and L volumes and the crossflow junction is assumed to be perpendicular to the axial direction and of zero elevation change, thus, no gravity force term is included.

The resulting vapor momentum finite difference equation for a crossflow junction is

$$\begin{aligned} & \left(\alpha_g \rho_g \right)_j^n \left(v_g^{n+1} - v_g^n \right)_j \Delta x_j = - \alpha_{g,j}^n (P_L - P_K)^{n+1} \Delta t \\ & - \left(\alpha_g \rho_g \right)_j^n HLOSSG_j^n v_{g,j}^{n+1} \Delta t \\ & - \left(\alpha_g \rho_g \right)_j^n FIG_j^n \left(v_{g,j}^{n+1} - v_{f,j}^{n+1} \right) \Delta x_j \Delta t \end{aligned}$$

+ ADDED MASS + MASS TRANSFER MOMENTUM.

2.1.4-72

A similar equation can be written for the liquid phase. In Equation 2.1.4-72, $HLOSSG_j^n$ contains only the user-input crossflow resistance. The Δx_j term that is used to estimate the inertial length associated with crossflow is defined using the diameters of volumes K and L,

$$\Delta x_j = \frac{1}{2} [D(K) + D(L)] .$$

2.1.4-73

A special void-dependent form loss option of the full crossflow model has been added for certain multi-core channel applications. This option allows the user to alter the input constant form loss coefficient based on the void fraction in the upstream volume. The specific applications are possibly multi-channel core analyses such as SBLOCA scenarios with significant core uncovering or future multi-channel BEACH reflooding calculations. This model allows the regions of the core covered by a two-phase mixture or pool to have a resistance that is different from that in the uncovered or steam region. The crossflow resistance changes can alter the volume-average axial velocities that are used to determine the core surface heat transfer. Any cross flow is excluded from the volume average velocity used for heat transfer.

The model uses the input form loss coefficients whenever the upstream steam void fraction is less than a user-supplied minimum void fraction value given as $\alpha_{\min-Kcross}$. The model allows user input of a forward, $M_{K-forward}$, and reverse, $M_{K-reverse}$, crossflow resistance multiplier when the upstream steam void fraction is greater than the maximum user-input void fraction, $\alpha_{\max-Kcross}$. Linear interpolation is used to determine the multiplicative factor when the void fraction is between minimum and maximum input void fractions as indicated in the following equations. For the forward flow direction (from Volume K to Volume L),

If	$\alpha_g(K) < \alpha_{\min-Kcross}$	$K_{jun} = K_{jun \text{ forward}}$
If	$\alpha_{\max-Kcross} \leq \alpha_g(K)$	$K_{jun} = K_{jun \text{ forward}} * M_{K-forward}$
If	$\alpha_{\min-Kcross} \leq \alpha_g(K) < \alpha_{\max-Kcross}$	$K_{jun} = K_{jun \text{ forward}} * M_{Kf \text{ interp}}$

2.1.4-73.1

where

$$M_{kf \text{ interp}} = 1 - (1 - M_{K\text{-forward}}) * [\alpha_{\min\text{-Kcross}} - \alpha_g(K)] / (\alpha_{\min\text{-Kcross}} - \alpha_{\max\text{-Kcross}})$$

and $K_{\text{jun forward}}$ is the user-supplied forward loss coefficient specified in this junction input.

The equation for the reverse flow direction (from Volume L to Volume K) is similar.

If $\alpha_g(L) < \alpha_{\min\text{-Kcross}}$	$K_{\text{jun}} = K_{\text{jun reverse}}$
If $\alpha_{\max\text{-Kcross}} \leq \alpha_g(L)$	$K_{\text{jun}} = K_{\text{jun reverse}} * M_{K\text{-reverse}}$
If $\alpha_{\min\text{-Kcross}} \leq \alpha_g(L) < \alpha_{\max\text{-Kcross}}$	$K_{\text{jun}} = K_{\text{jun reverse}} * M_{Kf \text{ interp}}$

2.1.4-73.2

where

$$M_{Kr \text{ interp}} = 1 - (1 - M_{K\text{-reverse}}) * [\alpha_{\min\text{-Kcross}} - \alpha_g(L)] / (\alpha_{\min\text{-Kcross}} - \alpha_{\max\text{-Kcross}})$$

and $K_{\text{jun reverse}}$ is the user-supplied reverse loss coefficient specified in this junction input.

The code performs several input checks to ensure that the user input will not cause code failures. These checks include tests to see if the input form loss multipliers are greater than zero. The minimum void fraction must be greater than zero and less than the maximum void fraction input. The maximum void fraction must be less than or equal to one.

The crossflow option can be used with the crossflow junction perpendicular to the axial flow in Volume L (or K) but parallel

2.3.2. Core Heat Structure Model

The ordinary RELAP5 heat structures are general in nature and can be used for modeling core fuel pins; however, licensing calculations require special treatment of the fuel pin heat transfer. To accommodate these requirements, two additional models, commonly referred to as the EM (Evaluation Model) pin and core surface heat transfer models, were added to the code. The EM pin model calculates dynamic fuel-clad gap conductance, fuel rod swell and rupture using either NUREG-0630¹¹⁷ or user input options (for modeling M5 cladding or other zirconium-based alloy cladding material types), and cladding metal-water reaction. The core fuel pin surface heat transfer is calculated with a flow regime-dependent set of correlations that include restrictions on which correlations can be selected per NRC licensing requirements. These new models are independent and mutually exclusive of the original system heat transfer model (described in section 2.2.2) and the existing simple gap conductance model¹¹⁸ (referenced in Appendix A). The new models are explicitly coupled to the solution scheme through the modification of the gap conductance term, addition of fluid hydraulic resistance upon rupture, deposition of metal-water reaction energy in the clad, and determination of fuel pin surface heat transfer. The new EM pin model calculations are described in this section, while the EM heat transfer description is contained in section 2.3.3.

The EM pin model consists of three basic parts:

1. Dynamic fuel-clad gap conductance,
2. Fuel rod swell and rupture using NUREG-0630 or user specified swell and rupture options, and
3. Clad metal-water reaction,

which couple explicitly to the heat structure solution scheme or add fluid hydraulic resistance upon rupture. The model may be executed either in a steady-state initialization or transient mode determined by user input.

The pin calculations are performed on single fuel rod which represent the average behavior of a large number of rods. Each rod (also termed channel) can be broken into up to ninety heat structures, each having an associated pin segment. The gap conductance, deformation mode, and metal-water reaction are determined for each individual segment based on the channel specific pin pressure.

The changes to the EM pin model included in Version 21 and later code versions are:

1. User options to model zircaloy and/or M5 cladding (or other zirconium-based alloy material types) in the same problem,
2. User options to specify the pin channel as a primary or supplemental channel for additive form loss and BEACH droplet breakup calculations upon pin rupture, and
3. Integration of the NRC SER limitation (BEACH code-BAW-10166, Rev. 2 dated 8/13/90) for use of a maximum flow blockage of 60 percent in the ruptured cladding droplet breakup calculations.

The option to allow zirconium-based alloy cladding types requires user input to identify which pin channels are zircaloy and which are not. The zirconium-based alloy cladding also requires additional user input to specify the material properties necessary to calculate the transient cladding swell and rupture behavior.

The supplemental pin capability was added to improve the calculational methods that require modeling of multiple EM pin channels within a single hydrodynamic fluid channel (i.e., an assembly or a group of assemblies) for LOCA applications. The relationship between the supplemental pin and the remainder of the pins in a common fluid channel is one in which the supplemental pin swell and rupture will not define the rupture flow blockage for the entire channel. Rather it will define a local effect that should not be used in determination of the channel droplet breakup parameters and the additive form loss due to rupture. These parameters should be controlled by the larger group of pins (i.e. primary channel) and not the smaller grouping (i.e. supplemental channel). The supplemental rod modeling is particularly useful for gadolinia or lead test pin (M5) analyses. It may also be used in future EM revisions for hot pin applications, in which the hot pin has a higher radial peak or a different initial fuel temperature.

2.3.2.1. Transient Dynamic Fuel-Clad Gap Conductance

The RELAP5 heat structure conduction scheme uses cold, unstressed geometrical dimensions for its solution technique. The dynamic gap conductance, h_{gap} , is calculated from hot stressed conditions from which an effective gap thermal conductivity, \bar{K}_{gap} , based on cold gap size, $\tau_{g_{cold}}$, is determined for each pin segment.

$$\bar{K}_{gap} = h_{gap} \cdot \tau_{g_{cold}}$$

2.3.2-1

The gap conductance is determined by calculating the gap gas conductivity, temperature jump gap distance, radiation component, and dynamic fuel-clad gap from the deformation models. An

additive fuel-clad contact conductance term has also been included as an option to simulate the closed gap contribution for high fuel rod burn-up applications. Two options are provided to calculate the conductance. The first option assumes that the fuel pellet is concentric within the clad, while the second option assumes the fuel pellet is non-concentric within the clad as illustrated in Figure 2.3.2-1.

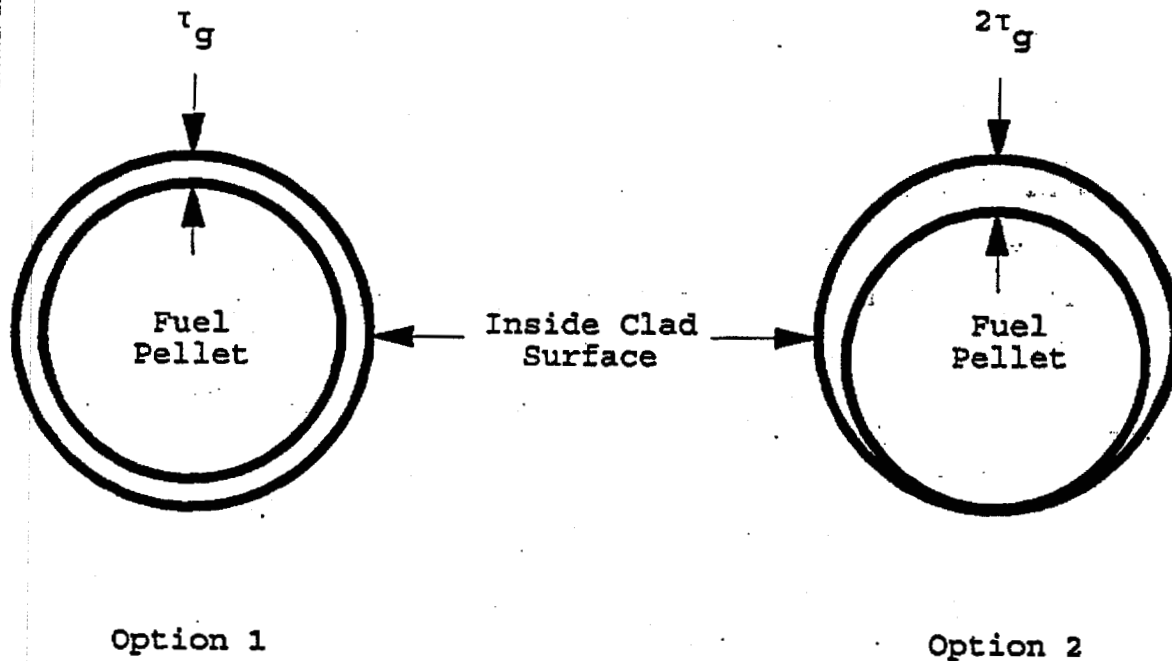


Figure 2.3.2-1. Gap Conductance Options.

Eight half-symmetrical azimuthal sections are used for determining the overall conductance for the second option without calculating an azimuthal temperature gradient. The total gap conductance is determined by

$$h_{\text{gap}} = M_g h_{\text{gap gas}} + h_{\text{rad}} + h_{\text{fcc}} \quad 2.3.2-2$$

with

h_{gap} = conductance through gap gas ($\text{w/m}^2\text{-K}$),

M_g = user input multiplier used to acquire correct initial temperature within fuel,

$h_{\text{gap gas}}$ = gap gas conductance contribution ($\text{w/m}^2\text{-K}$),

h_{rad} = conductance due to radiation contribution from fuel to clad ($\text{w/m}^2\text{-K}$), and

h_{fcc} = gap contact conductance contribution due to fuel-cladding mechanical interaction ($\text{w/m}^2\text{-K}$).

The radiation gap conductance contribution is calculated by

$$h_{\text{rad}} = \frac{\sigma}{\frac{1}{e_f} + \frac{r_f}{r_{ic}} \left(\frac{1}{e_c} - 1 \right)} \left[\frac{T_{fs}^4 - T_{ics}^4}{T_{fs} - T_{ics}} \right]$$

$$= \frac{\sigma (T_{fs}^2 + T_{ics}^2) (T_{fs} + T_{ics})}{\frac{1}{e_f} + \frac{r_f}{r_{ic}} \left(\frac{1}{e_c} - 1 \right)},$$

2.3.2-2.1

where

σ = Stefan-Boltzmann constant,

= 5.6697×10^{-8} (w/m²-K⁴),

e_f = emissivity of fuel surface,

e_c = emissivity of clad-inside surface,

T_{fs} = fuel outside surface temperature (K), and

T_{ics} = clad-inside surface temperature (K).

$$\begin{aligned}
C_1 &= 1.0 \cdot 10^{-5} \text{ (K}^{-1}\text{)}, \\
C_2 &= -3.0 \cdot 10^{-3}, \\
C_3 &= 4.0 \cdot 10^{-2}, \text{ and} \\
C_4 &= -5.0 \cdot 10^3 \text{ (K)}.
\end{aligned}$$

The fuel is defined by the first material type specified in the heat structure input, with the next material type being the gap and the third the clad as shown in Figure 2.3.2-2. Any deviation from the geometry will result in an error or misinterpretation of the information by the pin model. The gap can only be one mesh interval wide, while fuel or clad must be greater than or equal to one mesh interval. Currently no provisions are made for annular fuel pellets.

The calculation of the inside clad radius is not as straightforward as the fuel outside radius. Seven different calculational modes are required to cover the possible clad conditions. They are defined as:

1. Elastic and thermal expansion within an unruptured channel,
2. Elastic and thermal expansion within 166.7K (300°F) of the clad rupture temperature within an unruptured channel,
3. Plastic deformation within an unruptured channel,
4. Elastic thermal expansion within a ruptured channel,
5. Plastic deformation in a ruptured channel,
6. Ruptured segment, and
7. Fuel-cladding mechanical iteration (closed gap).

Each mode is related to the NUREG-0630 calculated rupture temperature for zircaloy cladding by the equation:

$$T_{\text{rupt}} = 4233 - \frac{20.4\sigma_h}{1 + H} - \frac{(8.51 \cdot 10^6)\sigma_h}{100(1 + H) + 2790\sigma_h}, \quad 2.3.2-17$$

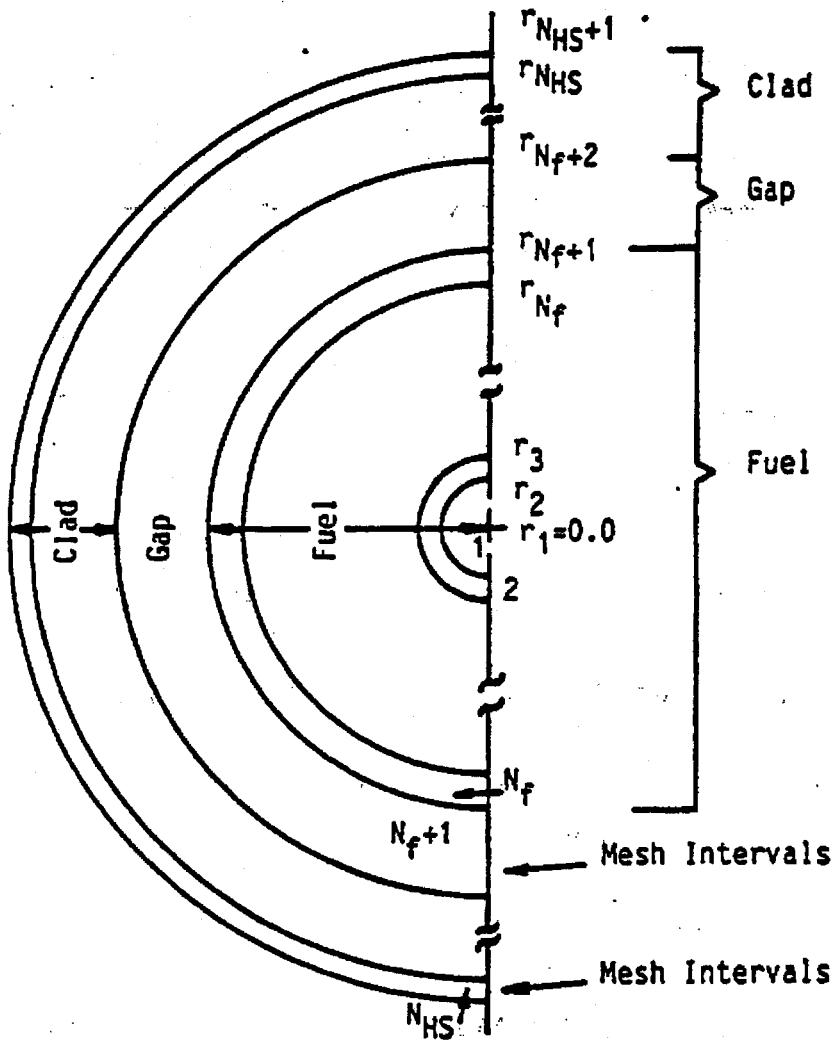


Figure 2.3.2-2. Fuel Pin Representation.

where

T_{rupt} = cladding rupture temperature (K),

σ_h = clad hoop stress (kpsi), and

H = dimensionless clad heating ramp rate, $0 \leq H \leq 1$.

The rupture temperature for other zirconium-based alloys is calculated by the following equation:

$$T_{rupt} = a1 - \frac{a2(\sigma_h - a7)}{a4 + H} - \frac{a3(\sigma_h - a7)}{a5(a4 + H) + a6(\sigma_h - a7)} \quad 2.3.2-17a$$

where $a1$ through $a7$ are user-specified input constants. The clad hoop stress for any pin segment in either equation is given by

$$\sigma_h = C_p (P_g r_{ic_cold} - P_f r_{oc_cold}) / (r_{oc_cold} - r_{ic_cold}), \quad 2.3.2-18$$

with

r_{ic_cold} = cold unstressed inside clad radius (m),

r_{oc_cold} = cold unstressed outside clad radius (m),

P_g = internal fuel rod pin pressure for that channel (Pa), and

P_f = external fluid pressure of the right-hand side heat structure associated volume (Pa).

$$C_p = 1 / 6.894757 \times 10^6$$

The heating rate can be either a user input constant or one of three additional transient-dependent algorithms discussed in detail later in this section.

At the beginning of each new time step following a successful RELAP5 time step advancement, the hoop stress and normalized heating ramp rate are computed for each pin segment. The clad average temperature is also known at this time. If the clad

average temperature is greater than the rupture temperature, then rupture occurs. Should the segment still be elastic and the rupture minus the clad temperature is less than 166.7K (300 F), then the segment stays elastic. Between these two temperatures the clad can be either elastic or plastic depending upon this temperature difference and the burst strain as described in the following paragraphs for ruptured or unruptured channels.

Mode 1: Unruptured Elastic and Thermal Deformation

Within an unruptured channel, the clad is considered purely elastic if it has never gone plastic, ruptured, or the temperature difference between rupture and clad average temperatures is less than 166.7 K (300 F). The inside clad radius for this pure elastic mode is determined by

$$r_{ic} = r_{ic_{cold}} + u_{TC} + u_{CC} + u_e , \quad 2.3.2-19$$

where

u_{TC} = clad radial displacement due to thermal expansion (m),
(m),

u_{CC} = clad radius over-specification factor (m), determined during pin transient initiation, and

u_e = clad radial displacement due to elastic deformation (m).

The clad thermal expansion is determined similarly to that for the fuel.

$$u_{TC} = (r_{N_{HS}+1} - r_{N_f+2}) e_{TC} / 2 , \quad 2.3.2-20$$

with N_{HS} = total number of mesh intervals in the heat structure,

r_n = heat structure radius at the inside of mesh interval n or outside of n-1 (m), and

e_{TC} = radial strain function defining fuel thermal expansion as a function of clad average temperature.

The radial strain function is defined by either a user input table as a function of cladding temperature for zirconium-based material types other than zircaloy or a built in code correlation set for zircaloy cladding¹¹⁹ consisting of

$$\epsilon_{TC} = -2.0731 \cdot 10^{-3} + 6.721 \cdot 10^{-6} T_C \quad 2.3.2-22$$

for $T_C \leq 1073.15$ K (α phase), and

$$\epsilon_{TC} = -9.4495 \cdot 10^{-3} + 9.7 \cdot 10^{-6} T_C \quad 2.3.2-23$$

for $T_C \geq 1273.15$ K (β phase), where T_C is the average cladding temperature (K). In the α phase to β phase transition zone, 1073.15 K $< T_C < 1273.15$ K, a table lookup is used. Some selected values are listed in Table 2.3.2-2.

Table 2.3.2-2. Thermal Strain of Zircaloy for 1073.15 K $< T < 1273.15$ K.

T(K)	Radial Strain	Axial Strain
	ϵ_{TC}	ϵ_{ATC}
1073.15	$5.14 \cdot 10^{-3}$	$3.53 \cdot 10^{-3}$
1093.15	$5.25 \cdot 10^{-3}$	$3.50 \cdot 10^{-3}$
1103.15	$5.28 \cdot 10^{-3}$	$3.46 \cdot 10^{-3}$
1123.15	$5.24 \cdot 10^{-3}$	$3.33 \cdot 10^{-3}$
1143.15	$5.15 \cdot 10^{-3}$	$3.07 \cdot 10^{-3}$
1183.15	$4.45 \cdot 10^{-3}$	$1.50 \cdot 10^{-3}$
1223.15	$2.97 \cdot 10^{-3}$	$1.10 \cdot 10^{-3}$
1273.15	$2.90 \cdot 10^{-3}$	$1.40 \cdot 10^{-3}$

The average clad temperature is calculated via a volume weighted average.

$$\bar{T}_C = \sum_{n=N_f+2}^{N_{HS}} \frac{(r_{n+1}^2 - r_n^2)}{(r_{N_{HS}+1}^2 - r_{N_f+2}^2)} \left[\frac{(T_{n+1} + T_n)}{2} \right]. \quad 2.3.2-24$$

The maximum clad average temperature is calculated for each EM pin channel and written at each major edit and at the end of each case. The segment number and time of the peak cladding temperature is also specified. The fuel volume weighted average temperature, \bar{T}_f , is calculated similarly to the cladding.

$$\bar{T}_f = \sum_{n=1}^{N_f} \frac{(r_{n+1}^2 - r_n^2)}{(r_{N_f+1}^2 - r_1^2)} \left[\frac{(T_{n+1} + T_n)}{2} \right]. \quad 2.3.2-25$$

The elastic deformation, u_e , is calculated by

$$u_e = \left[\frac{r_{N_{HS}+1} + r_{N_f+2}}{2} \right] \left[\frac{\sigma_h - \nu \sigma_z}{E} \right], \quad 2.3.2-26$$

where

E = Young's modulus for clad (Pa),

σ_h = segment clad hoop stress (Pa),

σ_z = channel clad axial stress (Pa), and

ν = Poisson's ratio for clad (dimensionless).

The channel axial stress is the same for all segments in the channel and is determined by

$$\sigma_z = \frac{P_g r_{ic_cold}^2 - P_f r_{oc_cold}^2}{r_{oc_cold}^2 - r_{ic_cold}^2}. \quad 2.3.2-27$$

Young's modulus is given either by the code for zircaloy cladding as

$$E = \begin{cases} 1.088 \cdot 10^{11} - 5.475 \cdot 10^7 T_c; & \text{for } 1090K \geq T_c \\ 1.017 \cdot 10^{11} - 4.827 \cdot 10^7 T_c; & \text{for } 1240K \geq T_c > 1090K \\ 9.21 \cdot 10^{10} - 4.05 \cdot 10^7 T_c; & \text{for } 2027K \geq T_c > 1240K \\ 1.0 \cdot 10^{10} & ; \text{ for } T_c > 2027K, \end{cases}$$

2.3.2-28

or by a user-specified cubic equation that can be used for zirconium-based alloy cladding

$$E = C_1 T_c^3 + C_2 T_c^2 + C_3 T_c + C_4 . \quad 2.3.2-29$$

Poisson's ratio is a constant which is defined as 0.30 for zircaloy by the code, however, the user can over-ride this value for zirconium-based alloy cladding types.

The normalized heating ramp rate for the elastic mode is determined by one of two methods. The code calculates an instantaneous heating rate for one method, while the other method sets the rate to a normalized user-input value between 0 and 1. The calculated heating rate is normalized via a constant value, H_{Rnorm} , of 28 K/s for zircaloy cladding or a user input for other zirconium-based alloy cladding materials.

$$H = \left\{ \frac{dT_c}{dt} \right\} / H_{Rnorm} \\ = \left\{ \frac{T_c^n - T_c^{n-1}}{t^n - t^{n-1}} \right\} / H_{Rnorm} \quad 2.3.2-30$$

The normalized heating rate is always limited to values between 0 and 1 or $(0 \text{ K/s} / H_{Rnorm}) \leq H \leq (28 \text{ K/s} / H_{Rnorm} = 1)$ for zircaloy cladding and between $(H_{slow \text{ input}} / H_{Rnorm}) \leq H \leq (H_{fast \text{ input}} / H_{Rnorm})$ for

other zirconium-based alloy cladding types. This limit is applied to H prior to using it in any subsequent checking or calculations. The superscripts reflect the current time, n, and old time, n-1, values. The zirconium-based alloy slow or fast ramp rate divided by the normalized rate is still limited between 0 and 1, but they do not have to be equal to 0 or 1. Values greater than 0 or less than 1 activate the slow or fast ramp curves at different normalized heating rates.

Mode 2: Unruptured Elastic and Thermal Deformation Within 166.7K (300 F) of the Rupture Temperature

When the clad average temperature is within 166.7K (300 F) of the rupture temperature, the elastic inside clad radius is calculated as shown in Mode 1. This radius is compared against the plastic inside clad radius calculated in Mode 3. If the elastic radius is greater than the plastic radius, then Mode 2 is retained and the inside clad radius is set to the elastic radius. If not, the clad becomes plastic (Mode 3) and the plastic clad calculations are used. An informative message is printed when a segment first becomes plastic. No return to elastic Modes (1 or 2) is permitted once the clad becomes plastic.

$$r_{ic} = \text{MAX}(r_{ic_{\text{elastic}}}, r_{ic_{\text{plastic}}}) . \quad 2.3.2-31$$

If $r_{ic_{\text{elastic}}} \geq r_{ic_{\text{plastic}}}$, Mode = 2 .

If $r_{ic_{\text{elastic}}} < r_{ic_{\text{plastic}}}$, Mode = 3 .

Mode 3: Unruptured Plastic Deformation

The unruptured plastic deformation is determined by the plastic strain, e_p .

$$r_{ic} = r_{ic_{\text{cold}}} (1 + e_p), \quad 2.3.2-32$$

with

$$e_p = e_{cps} \exp[-0.02754(T_{rupt} - T_c)], \quad 2.3.2-33$$

where e_{cps} is $0.2 * e_b$ (e_b is the burst strain) based on NUREG-0630 for maximum cladding plastic strain and on user input tables for zirconium-based alloy cladding. The plastic strain or burst strain is determined by a double interpolation, relative to H and T_{rupt} in the user input or default NUREG-0630 burst strain Tables 2.3.2-3 and 2.3.2-4. The plastic strain behaves as a ratchet. Once a given plastic strain is reached, no decrease in its value is allowed. In other words, for plastic mode calculations

$$r_{ic} = \text{MAX}(r_{ic}^n, r_{ic}^{n-1}), \quad 2.3.2-34$$

where the superscripts refer to the current and old time values.

If the plastic mode is selected, the normalized heating ramp rate is calculated from any of three user options: user input constant, average ramp rate, or plastic weighted ramp rate. The normalized average ramp rate is calculated from

$$H = \left\{ \frac{T_c^n - T_c^p}{t^n - t^p} \right\} / H_{Rnorm}, \quad 2.3.2-35$$

where

t = time (s),

n = superscript defining the current time, and

p = superscript defining the time in which the clad first went plastic.

The normalized plastic weighted ramp is calculated by

$$H = \left[\frac{\int_{t^p}^{t^n} W(T) \left\{ \frac{dT_c}{dt} \right\} dt}{\int_{t^p}^{t^n} W(T) dt} \right] / H_{Rnorm} \quad 2.3.2-36$$

Table 2.3.2-3. NUREG-0630 Slow-Ramp Correlations for Burst Strain and Flow Blockage.

<u>Rupture temperature, C</u>	<u>≤10 C/S burst strain, %</u>	<u>≤10 C/S flow blockage, %</u>
600	10	6.5
625	11	7.0
650	13	8.4
675	20	13.8
700	45	33.5
725	67	52.5
750	82	65.8
775	89	71.0
800	90	71.5
825	89	71.0
850	82	65.8
875	67	52.5
900	48	35.7
925	28	20.0
950	25	18.0
975	28	20.0
1000	33	24.1
1025	35	25.7
1050	33	24.1
1075	25	18.0
1100	14	9.2
1125	11	7.0
1150	10	6.5
1175	10	6.5
1200	10	6.5

nodding options) chosen by the user. The fine mesh nodding option computes the inside radius as

$$r_{ic} = r_{ic_{cold}} (1 + \epsilon_B) .$$

2.3.2-39

With this option, the gap conductance is calculated as though there is steam in the gap. The steam thermal conductivity is evaluated at the gap temperature and used with the hot gap size to compute the conductance. This option also calculates inside metal-water reaction for the ruptured segment.

The coarse mesh nodding option computes the inside clad radius as

$$r_{ic} = r_{ic_{cold}} (1 + \epsilon_{cps}) .$$

2.3.2-40

This option uses the regular gap gas conductance and does not consider inside metal-water reaction. It is intended for use nominally when the expected rupture length is small when compared to the total segment length. The microscopic effects at the rupture site considered with the fine mesh option are expected to be negligible when compared to the longer segment behavior. With the coarse mesh option, the overall behavior will be more closely controlled by the entire segment rather than just the rupture site conditions.

Within the ruptured channel various calculations are modified at the time of rupture. Each segment within that channel undergoes a mode change. The pin pressure becomes that of the hydrodynamic volume associated with the ruptured segment. An additive form loss coefficient is calculated at rupture based on the clad flow blockage by a simple expression for an abrupt contraction-expansion.

$$K_{\text{add}} = \frac{0.5(1 - \beta^2) + (1 - \beta^2)^2}{(\beta^2)^2},$$

2.3.2-41

where

$$\begin{aligned} \beta^2 &= \text{fraction of the channel flow area blocked,} \\ &= (1.0 - A_{\text{blocked}}/A_{\text{channel}}). \end{aligned}$$

The flow blockage is obtained via a double table interpolation relative to the normalized heating ramp rate and rupture temperature similarly to the clad burst strain. The table is either user supplied or default NUREG-0630 values listed in Tables 2.3.2-3 and 2.3.2-4. The additive value of the loss coefficient is edited at the time of rupture. The flow blockage loss coefficient is added automatically to the problem for a primary pin channel unless the user overrides via a new optional input. If added, the form loss is applied to the forward flow direction for the inlet (bottom) junction and the reverse flow direction for the exit (top) junction attached to the volume in which the clad ruptured. The user option to exclude this form loss addition from the junctions has been included for supplemental pin channels or for certain non-licensing sensitivity studies with multiple cross-connected channels.

Another option has been added to the EM Pin model to help minimize user burden when running EM reflooding heat transfer analyses with BEACH (BAW-10166 Section 2.1.3.8.4). This user-controlled option automatically includes code-calculated pin rupture, droplet break-up (up to 60 percent blockage) for primary pin channels and convective enhancement adjustments for primary or supplemental pin channels. The input grid parameters are modified with the ruptured values and will be retained for use in the reflooding heat transfer calculations. This model is optional and requires input to activate the calculations. If no input is specified the default is that no rupture enhancements will be calculated and no droplet

breakup calculations will be performed for any supplemental pin channels.

When this option is activated, Equations 2.3.2-41.1 through 2.3.2-41.4 will be calculated following cladding rupture for primary pin channels, only. The first calculation performed determines the midpoint elevation of ruptured segment, referenced from the bottom of the pin channel (which coincides with the bottom of the heat structure geometry or reflood stack). This midpoint elevation, Z_{grid} , is the location where the new "grid" is inserted. This elevation is used to determine the droplet break-up effects for the ruptured segment.

$$Z_{grid} = 0.5 \cdot \Delta Z_{rupt\ seg} + \sum_{j=1}^{rupt\ seg-1} \Delta Z_{seg_j}, \quad 2.3.2-41.1$$

where

ΔZ_{seg} = elevation change of pin segment.

The second set of calculations is to calculate rupture droplet breakup efficiency. These calculations are identical to those described in Sections 2.1.3.7. and 2.1.3.8. of Reference 123. The rupture atomization factor, η_{etamax} , is calculated as

$$\eta_{etamax} = \frac{1}{[1 + \{(n^{1/3} - 1) \cdot \min(0.60, \epsilon_{fb})\}]}, \quad 2.3.2-41.2$$

where

n = number of equal size droplets resulting from the split-up of the larger droplets,

ϵ_{fb} = flow blockage fraction (limited to a maximum of 0.60).

The increase in the droplet surface area from that used for interface heat transfer is defined in Equation 2.1.3-105¹²³ as

$$\Delta a_{gf} = C_{\max DB} \theta a_{gf}$$

The proportionality constant, $C_{\max DB}$, is determined from the constant, C_1 , the rupture flow blockage fraction (limited to a maximum of 0.60), and the length of the ruptured segment.

$$C_{\max DB} = \frac{C_1 \cdot \min(0.6, e_{fb})}{\Delta Z_{\text{rupt seg}}} \quad 2.3.2-41.3$$

The velocity of the fluid at the ruptured location increases because of the flow area reduction. The physical area in the code calculations is not modified, but a velocity multiplier, used for determining the droplet Weber number, is calculated from

$$\text{VELMULT} = \frac{1}{1 - \min(0.6, e_{fb})} \quad 2.3.2-41.4$$

The cladding rupture results in an increase in the pin outside heat transfer surface area. The increase in area is not directly included in the conduction solution in the code calculations. It is accounted for by using the rupture convective enhancement factor and applying it to the grid wall heat transfer enhancement factor, F_{gf} , for primary or supplemental channels. The rupture enhancement, M_{RAR} , is a multiplicative contribution determined by

$$M_{RAR} = \text{Rupture Area Ratio}$$

$$= \frac{2\pi r_{\text{rupt oc}} L}{2\pi r_{\text{oc cold}} L} = \frac{r_{\text{rupt oc}}}{r_{\text{oc cold}}} \quad 2.3.2-41.5$$

where

$r_{rupt_{oc}}$ = outside clad radius of the ruptured node given by

$$= r_{ic} + \left[r_{oc_{cold}} - r_{ic_{cold}} \right] \left[r_{ic_{cold}} / r_{ic} \right]. \quad 2.3.2-41.6$$

The total wall heat transfer convective factor then becomes

$$F_{gg_{tot}} = F_{gg_{grid}} \cdot M_{RAR}. \quad 2.3.2-41.7$$

These droplet break-up and convective enhancement terms are optionally calculated and edited at rupture by the EM pin model.

This page intentionally blank.

r_{iC_1} = inside clad radius of the top pin segment (m), and

ΔL_p = change in gas plenum length (m).

The change in gas plenum length is calculated from the net change in the fuel and clad stack lengths due to axial thermal expansions as follows. Let

ΔL_{cf} = change in gas plenum length from cold condition (m),
2.3.2-51.4

where

ΔL_c = total axial thermal expansion of clad from cold condition (m),

$$= \sum_{j=1}^{\# \text{ seg}} (L_j \epsilon_{ATC_j}) , \text{ and}$$
 2.3.2-51.5

ΔL_f = total axial thermal expansion of fuel from cold condition (m),

$$= \sum_{j=1}^{\# \text{ seg}} (L_j \epsilon_{ATF_j}) .$$
 2.3.2-51.6

Then

ΔL_p = change in gas plenum length from hot initial condition (m),
$$= \Delta L_{cf} - \Delta L_{cf}^0 ,$$
 2.3.2-51.7

where

ΔL_{cf}^0 = initial over-specification in gas plenum length (m), determined during pin transient initiation,

L_j = axial length of the jth segment (m),

ϵ_{ATF} = fuel strain function of Equation 2.3.2-15, evaluated at fuel volume weighted average temperature \bar{T}_f of Equation 2.3.2-25, (dimensionless), and

ϵ_{ATC} = axial strain function defining clad axial thermal expansion as a function of clad volume average temperature, (dimensionless).

The axial strain for the cladding is defined by either a user-input table versus cladding temperature for zirconium-based alloy cladding (Note: This table replaces the cubic fit from Rev. 3 Eqn 2.3.2-51.8.) or a built in code correlation set for zircaloy cladding¹¹⁹

$$\begin{aligned}\epsilon_{ATC} &= -2.506 \times 10^{-5} + (T_C - 273.15) 4.441 \times 10^{-6} \\ &= -1.2381 \times 10^{-3} + 4.441 \times 10^{-6} T_C\end{aligned}\quad 2.3.2-51.9$$

for $T_C \leq 1073.15$ K (α phase), or

$$\begin{aligned}\epsilon_{ATC} &= -8.3 \times 10^{-3} + (T_C - 273.15) 9.7 \times 10^{-6} \\ &= -1.0950 \times 10^{-2} + 9.7 \times 10^{-6} T_C\end{aligned}\quad 2.3.2-51.10$$

for $T_C \geq 1273.15$ K (β phase), where T_C is the volume average cladding temperature (K) of Equation 2.3.2-24. In the α phase to β phase transition zone, 1073.15 K $< T_C < 1273.15$ K, a table lookup is used. Some selected values are listed in Table 2.3.2-2.

Using the assumption that both the slope of the fuel mesh point temperatures and the overall gap conductance will not change significantly, the last gap multiplier (1.0 for the first iteration) can be adjusted via a ratio to give a new multiplier,

$$M_g^{n+1} = \frac{\Delta T_{\text{gap}}}{(\Delta T_{\text{gap}} + \Delta \bar{T}_f)} M_g^n \quad 2.3.2-52.3$$

After calculation of the new gap multiplier, another conduction solution iteration step is taken. The fuel volume average temperature differential is recalculated via Equation 2.3.2-52.1. If the absolute value is greater than 2 K, then another iteration step is taken after recalculating a new multiplier via Equations 2.3.2-52.2 and 2.3.2-52.3. If the absolute value is less than 2 K, then the iteration has converged and the last multiplier calculated is edited and used during the steady-state and transient EM pin calculations. Up to twenty-one iterations are allowed. If convergence is not obtained in twenty-one iterations, then the code will stop at the end of the initialization process and appropriate failure messages will be edited. Failure of the iteration to converge is generally related to poor estimates given for the initial mesh point temperature distribution. An improved estimate will normally allow the iteration to converge properly. If convergence is still a problem, user specification of the multiplier is also available.

At the completion of the EM pin steady-state calculations (i.e., after EM pin steady-state trip becomes true or during the first time step if there is no trip) several calculations are required to initiate the pin transient calculations. The user-supplied cold unstressed pin geometry input via the heat structure cards is elastically expanded using the final code calculated temperature and mechanical stresses.

$$r_{fo} = r_{fcold} + u_{TF}$$

2.3.2-53

and

$$r_{ico} = r_{icold} + u_{TC} + u_e + u_{fcc}$$

2.3.2-54

with

r_{fo} = thermally expanded outside fuel radius (m),

r_{ico} = thermally and mechanically expanded inside clad radius (m),

u_e = elastic deformation due to mechanical stresses (m),
and

u_{fcc} = elastic deformation from gap mechanical contact (m).
This term is calculated from the user supplied input contact pressure and cladding radii during the initialization.

$$u_{fcc} = \frac{P_{fcc} \cdot r_{ic}}{E_c} \left\{ \left[\frac{r_{oc}^2 + r_{ic}^2}{r_{oc}^2 - r_{ic}^2} \right] + \nu_c + \frac{E_c}{E_f} (1 - \nu_f) \right\}$$

2.3.2-54.1

The calculated radii are compared against the input values by

$$u_{FC} = r_{finput} - r_{fo}$$

2.3.2-55

$$u_{CC} = r_{icinput} - r_{ico}$$

2.3.2-56

and

$$u_{cg} = \begin{cases} 0.0 & \text{for } P_{fccinput} = 0.0 \\ r_{icinput} - r_{finput} & \text{for } P_{fccinput} > 0.0 \end{cases}$$

2.3.2-56.1

5.0 REFERENCES

1. Ransom, V. H., et. al., RELAP5/MOD2 Code Manual -- Volume 1: Code Structures, System Models and Solution Methods and Volume 2: Users Guide and Input Requirements, NUREG/CR-4312 - Volume 1, August, 1985 and NUREG/CR-4312 - Volume 2, December 1985.
2. B&W Nuclear Technologies, RELAP5/MOD2-B&W -- An Advanced Computer Program for Light Water Reactor LOCA and non-LOCA Transient Analysis, BAW-10164P, Revision 1, October 1988.
3. Letter from A. C. Thadani (USNRC) to J. H. Taylor (B&W Nuclear Technologies), Acceptance for Referencing of Topical Report BAW-10164P, Revision 1, RELAP5/MOD2-B&W, An Advanced Computer Program for Light Water Reactor LOCA and Non-LOCA Transient Analysis, April 18, 1990.
4. Code of Federal Regulations, ECCS Evaluation Models, Chapter 10, Part 50, Appendix K
5. B&W Nuclear Technologies, RELAP5/MOD2-B&W -- An Advanced Computer Program for Light Water Reactor LOCA and Non-LOCA Transient Analysis, BAW-10164P, Revision 2, August 1992.
6. B&W Nuclear Technologies, RELAP5/MOD2-B&W -- An Advanced Computer Program for Light Water Reactor LOCA and non-LOCA Transient Analysis, BAW-10164P, Revision 3, October 1992.
7. Letter from J. H. Taylor (B&W Nuclear Technologies) to R. C. Jones (USNRC) BEACH Topical Report BAW-10166P, JHT/93-214, August 31, 1993.
8. Letter from J.H. Taylor (B&W Nuclear Technologies), Response to NRC's Request for Additional Information on BAW-10164, Revision 2, August, 1992; RELAP5/MOD2-B&W, An Advanced Computer Program for Light Water Reactor LOCA and NON-LOCA Transient Analysis, JHT/93-279, November 16, 1993
9. Letter from J.H. Taylor (B&W Nuclear Technologies), Response to NRC's Request for Additional Information on BAW-10164, Revision 3, October, 1992; RELAP5/MOD2-B&W, An Advanced Computer Program for Light Water Reactor LOCA and NON-LOCA Transient Analysis, JHT/94-7, January 21, 1994
10. Letter from J.H. Taylor (B&W Nuclear Technologies), Response to NRC's Supplemental Request for Additional Information on BAW-10164, Revision 2, August, 1992; RELAP5/MOD2-B&W, An Advanced Computer Program for Light Water Reactor LOCA and NON-LOCA Transient Analysis, JHT/94-146, September 20, 1994.

This page intentionally left blank.

5-364.2

5-453

**Rev. 4
9/99**

Attachment 2

This page is intentionally left blank.

AFFIDAVIT OF THOMAS A. COLEMAN

- A. My name is Thomas A. Coleman. I am Vice President of Government Relations for Framatome Cogema Fuels (FCF). Therefore, I am authorized to execute this Affidavit.
- B. I am familiar with the criteria applied by FCF to determine whether certain information of FCF is proprietary and I am familiar with the procedures established within FCF to ensure the proper application of these criteria.
- C. In determining whether an FCF document is to be classified as proprietary information, an initial determination is made by the Unit Manager, who is responsible for originating the document, as to whether it falls within the criteria set forth in Paragraph D hereof. If the information falls within any one of these criteria, it is classified as proprietary by the originating Unit Manager. This initial determination is reviewed by the cognizant Section Manager. If the document is designated as proprietary, it is reviewed again by personnel and other management within FCF as designated by the Vice President of Government Relations to assure that the regulatory requirements of 10 CFR Section 2.790 are met.
- D. The following information is provided to demonstrate that the provisions of 10 CFR Section 2.790 of the Commission's regulations have been considered:
- (i) The information has been held in confidence by FCF. Copies of the document are clearly identified as proprietary. In addition, whenever FCF transmits the information to a customer, customer's agent, potential customer or regulatory agency, the transmittal requests the recipient to hold the information as proprietary. Also, in order to strictly limit any potential or actual customer's use of proprietary information, the substance of the following provision is included in all agreements entered into by FCF, and an equivalent version of the proprietary provision is included in all of FCF's proposals:

AFFIDAVIT OF THOMAS A. COLEMAN (Cont'd.)

"Any proprietary information concerning Company's or its Supplier's products or manufacturing processes which is so designated by Company or its Suppliers and disclosed to Purchaser incident to the performance of such contract shall remain the property of Company or its Suppliers and is disclosed in confidence, and Purchaser shall not publish or otherwise disclose it to others without the written approval of Company, and no rights, implied or otherwise, are granted to produce or have produced any products or to practice or cause to be practiced any manufacturing processes covered thereby.

Notwithstanding the above, Purchaser may provide the NRC or any other regulatory agency with any such proprietary information as the NRC or such other agency may require; provided, however, that Purchaser shall first give Company written notice of such proposed disclosure and Company shall have the right to amend such proprietary information so as to make it non-proprietary. In the event that Company cannot amend such proprietary information, Purchaser shall, prior to disclosing such information, use its best efforts to obtain a commitment from NRC or such other agency to have such information withheld from public inspection.

Company shall be given the right to participate in pursuit of such confidential treatment."

AFFIDAVIT OF THOMAS A. COLEMAN (Cont'd.)

(ii) The following criteria are customarily applied by FCF in a rational decision process to determine whether the information should be classified as proprietary. Information may be classified as proprietary if one or more of the following criteria are met:

- a. Information reveals cost or price information, commercial strategies, production capabilities, or budget levels of FCF, its customers or suppliers:
- b. The information reveals data or material concerning FCF research or development plans or programs of present or potential competitive advantage to FCF.
- c. The use of the information by a competitor would decrease his expenditures, in time or resources, in designing, producing or marketing a similar product.
- d. The information consists of test data or other similar data concerning a process, method or component, the application of which results in a competitive advantage to FCF.
- e. The information reveals special aspects of a process, method, component or the like, the exclusive use of which results in a competitive advantage to FCF.
- f. The information contains ideas for which patent protection may be sought.

AFFIDAVIT OF THOMAS A. COLEMAN (Cont'd.)

The document(s) listed on Exhibit "A", which is attached hereto and made a part hereof, has been evaluated in accordance with normal FCF procedures with respect to classification and has been found to contain information which falls within one or more of the criteria enumerated above. Exhibit "B", which is attached hereto and made a part hereof, specifically identifies the criteria applicable to the document(s) listed in Exhibit "A".

- (iii) The document(s) listed in Exhibit "A", which has been made available to the United States Nuclear Regulatory Commission was made available in confidence with a request that the document(s) and the information contained therein be withheld from public disclosure.
- (iv) The information is not available in the open literature and to the best of our knowledge is not known by Combustion Engineering, Siemens, General Electric, Westinghouse or other current or potential domestic or foreign competitors of Framatome Cogema Fuels.
- (v) Specific information with regard to whether public disclosure of the information is likely to cause harm to the competitive position of FCF, taking into account the value of the information to FCF; the amount of effort or money expended by FCF developing the information; and the ease or difficulty with which the information could be properly duplicated by others is given in Exhibit "B".

I have personally reviewed the document(s) listed on Exhibit "A" and have found that it is considered proprietary by FCF because it contains information which falls within one or more of the criteria enumerated in Paragraph D, and it is information which is customarily held in confidence and protected as proprietary information by FCF. This report comprises information utilized by FCF in its business which afford FCF an

AFFIDAVIT OF THOMAS A. COLEMAN (Cont'd.)

opportunity to obtain a competitive advantage over those who may wish to know or use the information contained in the document(s).

TH Coleman

THOMAS A. COLEMAN

State of Virginia)

) SS. Lynchburg

City of Lynchburg)

Thomas A. Coleman, being duly sworn, on his oath deposes and says that he is the person who subscribed his name to the foregoing statement, and that the matters and facts set forth in the statement are true.

TH Coleman

THOMAS A. COLEMAN

Subscribed and sworn before me
this 27th day of Sept. 1999.

Brenda C. Cardona
Notary Public in and for the City
of Lynchburg, State of Virginia.

My Commission Expires July 31, 2003

EXHIBITS A & B

EXHIBIT A

Responses to NRC Requests for Additional Information on Topical Report
BAW-10227P, "Evaluation of Advanced Cladding and Structural Material (M5) in PWR
Reactor Fuel," dated October 26, 1998 and January 29, 1999.

EXHIBIT B

The above listed document contains information that is considered Proprietary in
accordance with Criteria b, c, d, and e of the attached affidavit.

Attachment 3

The FCF non-proprietary version of responses to NRC requests for additional information (RAI) has not been included in this report. Please see BAW-10227-A, "Evaluation of Advanced Cladding and Structural Material (M5) in PWR Reactor Fuels", pages k-1 - k-39 and enclosure 1 to that section. There is no proprietary information in the submitted change pages to BAW-10164. Therefore, the pages are identical to those shown in attachment 1.

Rev. 4
9/99

February 29, 2000
FTI-00-551

Document Control Desk
U. S. Nuclear Regulatory Commission
Washington, DC 20555-0001

Subject: Modeling Refinements to Framatome Technologies' RELAPS-Based, Large Break LOCA Evaluation Models—BAW-10168 for Non-B&W-Designed, Recirculating Steam Generator Plants and BAW-10192 for B&W-Designed, Once-Through Steam Generator Plants.

Gentlemen:

Framatome Technologies Incorporated (FTI) maintains two NRC-approved large break loss-of-coolant accident (LBLOCA) evaluation models (EMs) to demonstrate compliance with the requirements of 10CFR50.46. The EM described in BAW-10168P-A, Revision 3, December 1996 applies to plant designs incorporating recirculating steam generators (RSGs) and the EM described in BAW-10192P-A, Revision 0, June 1998 is applied to the B&W NSS design. FTI is refining the modeling of the hot rod/hot assembly in its LBLOCA EMs to improve the simulation of the LOCA cooling process. The refinements apply equally to LBLOCA licensing calculations performed with the RSG and the B&W EMs.

FTI's existing LBLOCA evaluations do not resolve the difference between the hot rod within the hot fuel assembly and the hot fuel assembly. Without such differentiation, it becomes necessary to apply all fuel temperature uncertainties and margins considered appropriate to the hot rod to the entire hot assembly. This places an undue burden on the calculation of the coolant properties within the hot assembly. To reduce this effect and remove over-conservatism from the evaluations, the heat structure simulating the hot rod/hot assembly is being split, one structure for the hot assembly and one for the hot rod. The refinement allows for the application of more realistic, steady state, volume-averaged, fuel temperature, uncertainty factors.

Future LBLOCA analyses will be performed in the following manner:

The average core heat structure will be initialized with no uncertainty. The hot assembly heat structure will be initialized at a statistical-based, uncertainty providing 95 percent confidence in 95 percent of all instances that the average fuel temperature in the assembly is bounded. The maximum 95/95, fuel temperature uncertainty will be imposed only on the hot rod heat structure. [Note that a correction to TACO3 predictions at high burnup will still be applied.]

This approach to the simulation of the thermal evolution of the peak cladding temperature is consistent with generally accepted industry practice and does not, in Framatome Technologies' opinion, comprise a change or revision to the existing approved LBLOCA EMs. Rather, the change in simulation can be accomplished under the dictates of the existing EMs because it lies within the modeling prerogatives retained by FTI.

The heat structure refinements affect the RELAP5 and BEACH (a set of subroutines within the RELAP5 computer code) simulations because they involve the prediction of hot rod cladding temperatures. REFL0D3B is unaffected because only the average core is included in the calculation scheme. Computer code updates were incorporated, as a user convenience, into RELAP5/MOD2-B&W Version 24.0HP, including its BEACH subroutines. They were submitted to the NRC as Revision 4 of the RELAP5/MOD2-B&W topical in April 1998 and replaced in toto in September 1998. The submittal was part of the RELAP5/MOD2-B&W M5 advanced clad implementation package.

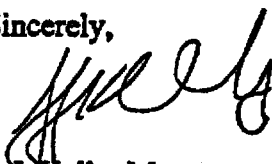
Currently, these refinements are not being considered for application to FTI's small break LOCA methods. Framatome Technologies will continue to apply the TACO3-based, hot rod, volume-averaged, fuel temperature, uncertainty factor to all fuel assemblies in its small break LOCA evaluation models.

The attached material is presented to continue close communications with the NRC regarding the status of Framatome Technologies' LOCA licensing applications and modeling techniques. If the NRC disagrees with or is concerned over Framatome Technologies' large break LOCA refinements, an expeditious response to this letter is requested.

Framatome Technologies intends to apply these refined modeling techniques in future large break LOCA analyses. The first application is scheduled for the TVA Sequoyah plants starting in August 2000. Framatome, also requests the approval of the RELAP5/MOD2-B&W changes included in the proposed Revision 4 to BAW010164 by August 2000. Framatome requests that the NRC inform us, by May 2000, of any disagreement with our position on the implementation of these heat structure refinements.

The attachment is considered non-proprietary to Framatome Technologies. If you require additional information, please contact John Biller at 804/832-2600 or John Klingenfus at 804/832-3294.

Sincerely,



J. J. Kelly, Manager
B&W Owners Group Services

/bcc

w/ Attachment

cc: Stewart N. Bailey/NRC
L. Lois/NRC
F. R. Orr/NRC
D. M. Lafever/TVA-SQN
J. R. Biller/FTI/OF53
B. M. Dunn/FTI/OF53
J. A. Klingenfus/FTI/OF53
R. J. Schomaker/FTI-BWOG/OF59
M. A. Schoppman/FTG/MD82

w/o Attachment

J. B. Andrews/FCF/OF19
A. B. Copey/FCF/OF19
J. J. Cudlin/FTI/OF53
G. E. Hanson/FCF/OF19
G. A. Meyer/FCF/OF13

bc: R. J. Lowe, OF53
M. L. Miller, OF53
C. K. Nithianandan, OF53
D. R. Page, OF53
J. R. Paljug, OF49
M. V. Parece, OF49
J. C. Seals, OF53
N. H. Shah, OF53
D. A. Wesley, OF19
G. J. Wissinger, OF53

Attachment

I. Introduction

Framatome Technologies Incorporated (FTI) maintains two NRC approved large break loss-of-coolant accident (LBLOCA) evaluation models (EMs) to demonstrate compliance with the requirements of 10CFR50.46. The EM described in BAW-10168P-A, Revision 3, December 1996 ⁽¹⁾ applies to plant designs incorporating recirculating steam generators (RSGs) and the EM described in BAW-10192P-A, Revision 0, June 1998 ⁽²⁾ is applied to the B&W NSS design. FTI is refining the modeling of the hot rod/hot assembly in our LBLOCA EMs to improve the simulation of the LOCA cooling process. The refinements apply equally to LBLOCA licensing calculations performed with the RSG and the B&W EMs.

FTI's existing LBLOCA evaluations do not resolve the difference between the hot rod within the hot fuel assembly and the hot fuel assembly. Without such differentiation, it becomes necessary to apply all uncertainties and margins considered appropriate to the hot rod to the entire hot assembly. This places an undue burden on the calculation of the coolant properties within the hot assembly. To reduce this effect and remove over-conservatism in the evaluations, the heat structure simulating the hot rod/hot assembly is being split, one structure for the hot assembly and one for the hot rod. This approach does not, in Framatome Technologies' opinion, comprise a change or revision to the existing approved LBLOCA EMs. Rather, the change in simulation can be accomplished under the dictates of the existing EMs because it lies within the modeling prerogatives retained by FTI.

Both the RSG and the B&W LBLOCA evaluation models are composed of three (3), NRC-approved computer codes:

- RELAP5/MOD2-B&W ⁽³⁾, which is used to compute the system thermal-hydraulic response during blowdown including hot rod/hot assembly temperatures.
- REFLOD3B ⁽⁴⁾, which predicts the refill/reflood system thermal-hydraulic response.
- BEACH ⁽⁵⁾, which comprises a set of subroutines within the RELAP5 code used to calculate hot rod/hot assembly refill and reflood thermal behavior.

Figure 1 shows the basic interface between these three (3) codes. The heat structure refinements affect the RELAP5 and BEACH simulations because they involve the prediction of hot rod cladding temperatures. Because only the average core is included in the calculation scheme, REFLOD3B is unaffected. Figures 2a and 2b show representative blowdown (RELAP5)/refill-reflood (BEACH) core noding schemes. [Note that for simplicity the blowdown crossflow junctions are not shown in Figures 2a and 2b. During blowdown, each elevation-pair of hot and average core nodes is cross-connected. At the start of refill—the BEACH calculation—the blowdown crossflow junctions are deleted from the problem. The use of and the deletion of crossflow junctions in the LBLOCA simulation is unchanged by the refinements discussed herein.] For the current simulations, the average core and the hot channel each connect to a single heat structure. The heat structure for the hot channel represents one complete fuel assembly (the hot assembly plus the hot rod) with

maximum uncertainties and margins applied to all rods. All rods are driven at the maximum allowable peaking. The heat structure in the average core represents all core fuel assemblies less the one hot channel assembly.

Core heat structures are initialized using steady state, volume-averaged, fuel temperature inputs calculated by the TACO3 fuel code ⁽⁶⁾. While not required by the EMs ^(1,2), the TACO3-specified "hot rod" uncertainty factor (1.115) has usually been applied to both the hot assembly heat structure and the average core heat structure. This provides a conservative overestimation of the initial core stored energy. Some current analyses have removed the hot rod uncertainty factor from the average core heat structure but in all current calculations the full factor is applied to the hot assembly heat structure. This practice substantially overestimates the initial enthalpy of the heat structures. Of particular importance is the overestimation of the enthalpy in the hot assembly and its resultant impact on the coolant properties during blowdown, refill, and reflood. In future LBLOCA analyses, FTI will impose the following conservatism:

The average core heat structure will be initialized with no uncertainty. The hot assembly heat structure will be initialized at a statistical-based, uncertainty providing 95 percent confidence in 95 percent of all instances that the average fuel temperature in the assembly is bounded. The maximum 95/95, fuel temperature uncertainty will be imposed only on the hot rod heat structure. [Note that a correction to TACO3 predictions at high burnup will still be applied.]

To accomplish this, it is necessary to resolve the heat structure modeling of the hot rod/assembly from one to two heat structures with a shared coolant channel. One structure simulates the hot rod of the hot assembly and the other the hot assembly less the hot rod. Figure 2c illustrates the resulting coolant channel heat structure scheme. The maximum fuel temperature uncertainty is used to initialize the hot rod heat structure and an appropriately conservative fuel temperature uncertainty is used for the hot assembly heat structure. The following sections describe minor RELAP5 code adjustments necessary for multiple heat structure modeling, specific parameter derivations and assignments between the multiple heat structures, and comparative results of the revised modeling for both the B&W and the RSG EMs.

II. RELAP5/MOD-B&W Modifications

For any given core fluid channel, a wide range of reasons exists for use of multiple heat structure capabilities—that is, supplemental rods. Simulation of fuel rod differences within an assembly or a group of fuel assemblies is the essential reason. The capability is particularly useful in modeling gadolinium rods, lead test rods, or in the quantification of peaking or initial enthalpy differences between rods. RELAP5/MOD2-B&W ⁽³⁾, including its BEACH ⁽⁵⁾ subroutines, has the general ability to model multiple heat structures per coolant channel. However, the code was updated to facilitate proper simulation of bundle and individual rod parameters within the confines of a LBLOCA calculation. It becomes important, in a multiple heat structure environment, to distinguish between characteristics created by and important to individual rods and those created by the fuel assembly as a

whole. Updates were incorporated, as a user convenience, into RELAP5/MOD2-B&W Version 24.0HP, including its BEACH subroutines. They were submitted to the NRC as Revision 4 of the RELAP5/MOD2-B&W topical in April 1998. The submittal was part of the RELAP5/MOD2-B&W M5 advanced clad implementation package. (These changes have nothing to do with the M5 cladding but that submittal was convenient and timely.) The changes were replaced in toto in September 1998 because an additional code upgrade required by the M5 cladding had been recognized. The following is a brief discussion of the RELAP5/BEACH upgrades incorporated in Version 24.0HP to support multiple heat structure simulation.

The occurrence of rupture, being dependent on cladding temperature and internal rod pressure, is a heat structure calculation. The effect of rupture, however, may be on individual rods or through an impact on the coolant channel and, hence, on all heat structures within the channel. Therefore, the effects of rupture must be properly sorted and related to the appropriate causative heat structure. The cladding strain and heat transfer area prior to or after rupture, to the extent that they are included in the LOCA calculations, are individual rod- or rod group-related and should be determined from the individual heat structure status. RELAP5/MOD2-B&W has always associated the calculation of these parameters with individual heat structures and that is unchanged. The rupture-induced droplet breakup model, the resultant inter-phase heat transfer parameters, and the rupture flow resistance factor are assembly effects and should be queued to the assembly regardless of the status of individual rods or any other supplemental rods. Accordingly, the hot pin rupture location is hot assembly-based. Within the RELAP5/MOD2-B&W and BEACH rod models, the quench front and incipient boiling locations are determined by the heat structure routines. These parameters are rod- or rod group-related and should be determined from the status of an individual heat structure.

With Version 24.0HP of RELAP5/MOD2-B&W and its BEACH options, a user option specifies each rod or rod group as primary or supplemental. This allows form loss, rupture-induced droplet breakup (BEACH), and quench front and incipient boiling location calculations to be performed based on the appropriate heat structure. Thus, even after an individual rod ruptures, rupture-induced droplet breakup cooling will be based on the specified primary bundle, heat structure prediction of rupture.

The RELAP5/MOD2-B&W and BEACH updates in Version 24.0HP allow each heat structure to have an individual material makeup. One heat structure, for example, could represent Zircaloy-4 fuel rods while a second heat structure in the same fluid channel could represent a set of gadolinium fuel rods or perhaps clad with an advanced material. An "IF" check has also been added to automate compliance with the NRC-imposed limitation on the amount of blockage that can be used in the rupture-induced droplet breakup model. Regardless of the amount of coolant channel blockage calculated, no more than a 60 percent channel blockage will be used in the droplet breakup calculations.

III. Steady State, Volume-Averaged, Fuel Temperature Distribution

The reason for making these refinements in the modeling of the hot rod/hot assembly is to mechanistically incorporate into the solution differences between the two regions in the LOCA predictions. One of these differences occurs in the amount of uncertainty to be used in the initialization of the fuel pellet enthalpy. The large break LOCA evaluation models ^(1,2) indirectly specify the value of the fuel temperature uncertainty factor through reference to an approved fuel code, TACO3 ⁽⁶⁾ (BAW-10162P-A). TACO3 provides essentially a best estimate prediction of the fuel pellet steady state temperature. To assure conservatism in the LOCA initialization, the predicted fuel temperature is increased by the published TACO3 uncertainty providing 95 percent confidence in 95 percent of all instances that the temperature is not underpredicted. The TACO3 topical report specifies an 11.5 percent uncertainty value for the hot spot. The topical report also demonstrates that the average channel uncertainty is zero, and provides data necessary to determine an appropriate hot assembly uncertainty factor. For exposures above 40 GWd/mtU, a bias is added to TACO3 temperature predictions in accordance with the extended burnup topical report ⁽⁸⁾.

A probabilistic analysis was performed for the immediate vicinity of the hot rod. Based on the TACO3 uncertainty distribution function, a three-percent value was found to assure with a 95/95 percent confidence that the average fuel temperature within this region was bounded. For convenience and ease of application, past evaluations applied the full TACO3 uncertainty to the entire hot assembly and average core. This practice is not specified or required by TACO3 ⁽⁶⁾ nor is it specified or required by either LBLOCA EM ^(1,2). FTI's prior use of a single, large uncertainty factor (1.115) was a self-imposed conservatism that is now being removed. Discussions of the development of appropriate fuel assembly uncertainties and representative evaluations of the impact for both B&W-designed and RSG plants follow.

1. Fuel Temperature Uncertainty for the Average Core

The recommended uncertainty factor to use for the TACO3 ⁽⁶⁾, LOCA fuel temperature predictions is one (1) for exposures below 40 GWd/mtU. The value is based on probabilistic analysis (the results of which are documented in Reference 6) performed with TACO3-predicted fuel temperatures. The probabilistic analysis, based on a sample size of over 700, yielded a mean measured-to-predicted fuel temperature quotient of 1.00. (Note that an average channel in either evaluation model easily comprises more than 20,000 fuel rods.) Furthermore, no significant bias was observed with respect to temperature, power, or burnup. Therefore, nearly half of the TACO3 temperature predictions were less than measurements and half were greater than measurements. In essence, TACO3 predictions are best estimate. It follows directly that the mean measured-to-predicted quotient of 1.00 should be applied to core average channel temperature predictions. Again, for exposures above 40 GWd/mtU, a bias is added to TACO3 temperature predictions in accordance with the extended burnup topical report ⁽⁸⁾.

While not explicitly stated, the recommended fuel temperature, uncertainty factor in the NRC-approved, TACO3 topical report was formulated to apply within hot rods only. Figure I-4 in the topical report illustrates this point. The LOCA rod average linear heat rates in this figure correspond to typical hot rod F_Q 's. An average channel fuel temperature uncertainty factor of one (1), therefore, is appropriate and consistent with the intent and approval of the fuel temperature probabilistic predictions and with the LOCA applications uncertainty factor presented in the TACO3 topical report. Average channel modeling remains unchanged. Only an overt and unnecessary input conservatism is being removed.

2. Fuel Temperature Uncertainty for the Hot Assembly

As discussed in Section II, FTI increased the hot channel heat structure detail—a switch from one to multiple heat structures. The large break LOCA hot channel (in both evaluation models) comprises a single fuel assembly, all rods of which are driven at the maximum allowable peaking. In the evaluation of homogeneous fuel assemblies, one heat structure represents the hot rod and a second hot channel heat structure represents the remainder of the hot assembly. Both heat structures are coupled to a single coolant channel representing the hot channel. If the assembly is not homogeneous—a gadolinium or MOX application, for example—an individual heat structure is used to represent each of the hot rods (or rod groups) to be evaluated and another structure represents the remainder of the hot assembly. Again all of these heat structures are coupled to a single coolant channel representing the hot channel.

Using the measured-to-predicted data in the TACO3⁽⁶⁾ topical report, a probabilistic analysis was performed to determine the appropriate initial fuel enthalpy (fuel temperature) uncertainty factor for application to the rods (the hot assembly rods) surrounding the hot rod. For the purpose of this discussion, the term hot spot will be used as the location on the hot rod that will eventually produce or be the location of the peak cladding temperature. The probabilistic evaluation proceeded in three steps:

1. Determination of the region within the hot assembly that drives interactions (heat transfer) with the hot spot and generation of a large number of randomly distributed sets of fuel pellet enthalpy uncertainties within that region.
2. Determination and assignment of importance factors for each individual pellet and computation of the average weighted uncertainty for each set.
3. Ordering of the sets to determine the probability distribution of the average uncertainty within the region.

The premise of the separate heat structures is that certain aspects of the heat transfer process occurring at the hot spot are not controlled by hot spot conditions but rather by surrounding conditions. Locally the interaction or coupling between the hot spot and its surroundings is through heat transfer to the coolant and the physical state of the coolant. Although the hot spot influences the coolant state, preconditioning and mixing within the

entire hot assembly is far more influential. In this conditioning, however, the fuel in immediate proximity to the hot spot dominates. A proper determination of the drivers for the coolant conditions at the hot spot would reflect the varying influence of the fuel surrounding the hot spot, making remote fuel of low importance and nearby fuel of higher importance. To conservatively specify the region of influence, FTI uses only the fuel pellets within the hot rod, within the rods in contact with the four coolant subchannels directly associated with the hot rod, and within the same grid span as the hot spot. Weighting factors for each rod are determined in accordance with their association with the four subchannels. Because the average uncertainty of a group will vary inversely with the membership count of the group, this limitation will overpredict the uncertainty. This uncertainty, in the FTI approach, is then assigned to the entire hot assembly, excepting the supplemental rods, to assure a conservative representation of the coolant drivers near the hot spot.

Following the determination of the region, a series of possible uncertainty distributions is assembled by randomly assigning an enthalpy uncertainty to each fuel pellet in accordance with the TACO3 uncertainty distribution function. Each set represents a physically possible distribution of the fuel steady state enthalpies within the region but there is no assurance of conservatism. Weighting factors for the contribution of each pellet are then assigned according to the dominant physical process for the coupling. There are two of these. During periods of flow, the coupling is via convective heat transfer and the importance is assigned in accord with the individual pellet influence on the coolant temperature. During stagnant conditions, the coupling is via radiation heat transfer and the importance is assigned via the influence of pellets on cladding temperatures and the corresponding view factors. For flow periods, the region is limited to only one half of the grid span and all pellets within the region contribute according to their association with the hot subchannel. This includes the pellets in the hot rod that are assigned an importance of 1.0. For the regional uncertainty, the pellets in the hot rod below the hot spot are assigned uncertainties according to the TACO3 uncertainty distribution but those at the hot spot are forced to the TACO3 95/95 percent confidence level. For stagnant periods, none of the pellets within the hot rod are included because there is no axial radiation within a rod. However, the entire grid span is allowed because the heat transfer process is unrelated to direction. The importance factors are determined from the view factor relating the hot spot to the clad surrounding each pellet.

With the appropriate weighting factors assigned to each pellet, the average uncertainty of each set is computed. The resulting array of average uncertainties is ordered and the average uncertainty that bounds 95 percent of the values in the array (in 95 percent of all instances) is determined. If the fuel temperature uncertainty for the hot bundle heat structure is set to a value equal to or greater than this 95/95 percent bound, the fuel temperature impact of the hot assembly modeling will be suitably bounding for the LOCA calculation. For the TACO3 uncertainty distribution, the computed 95/95 percent confidence uncertainty value for flowing conditions was determined to be 2.1 percent. For stagnant conditions, the value was determined to be 2.6 percent. Within the FTI LOCA evaluations a fuel temperature uncertainty of 3 percent will be assigned for the heat structure modeling the hot assembly when the bundle exposure is up to 40

GWd/mtU and the fuel temperature prediction is generated by TACO3. Above 40 GWd/mtU, the uncertainty will be linearly increased in accordance with the extended burnup topical report ⁽⁸⁾.

3. Fuel Temperature Uncertainty for the Hot Rod

The recommended fuel temperature uncertainty factor presented in the NRC-approved, TACO3 topical report was formulated for the hot spot. The TACO3-recommended uncertainty factor, 11.5 percent, will continue to be applied to the simulation of the entire hot rod for rod average burnups up to 40 GWd/mtU. For rod average burnups above 40 GWd/mtU, the uncertainty is increased in accordance with the extended burnup topical report ⁽⁸⁾. By preserving the application of the recommended pellet uncertainty factor to the entire hot rod, the appropriate initial fuel enthalpy will have been applied at the location of peak cladding temperature regardless of where in the hot rod that temperature occurs.

IV. Heat Transfer During Refill

The RSG- and B&W-designed EMs present slightly differing interpretations as to heat transfer from the reactor core during the refill period. Previously, this phase of the accident was mostly termed the adiabatic heatup period because minimal heat transfer from the core was possible and most evaluation models simply chose not to model any. There is actually no requirement in the regulation to restrict heat transfer during this period, other than application of the reflood restriction on convective heat transfer to steam cooling models. Recently, radiation models have been approved within the industry for heat transfer during refill/reflood. These models do not allow large amounts of heat transport, but over the course of refill small contributions accumulate and are significant. The RSG EM implies that this period is modeled as adiabatic. The B&W-design EM more correctly describes the period as nearly adiabatic. In fact, in Revision 3 of the RSG evaluation model, when RELAP5/MOD2-B&W replaced FRAP-T6-B&W for the calculation of the hot spot temperature during blowdown and the application of BEACH was expanded to initiate at the end of blowdown, heat transfer to the stagnant steam resident within the core was included. For the BEACH application, it was possible to input zero incoming flow but it was not possible to eliminate the resident steam. Therefore, for the last several years a description of nearly or essentially adiabatic is more appropriate. The NRC understood this when the FRAP-T6-B&W replacement was approved for the RSG EM.

When all rods in the hot bundle are identical, as with the previous LOCA implementations, the slight amount of heat transfer possible to the resident steam is divided equally between each rod in the assembly and the heat flow to the resident steam has an insignificant effect on an individual rod. However, when most of the rods within the hot assembly are initialized such that they will have lower temperatures than the hot rod during refill, the potential for heat transfer from the hot rod is increased and the result is noticeable. The effect is created because only about 0.5 percent of the energy transmitted to the steam is from the hot rod. Thus the steam maintains the temperature of

the hot bundle heat structure creating a temperature difference to the hot rod that leads to the transport of significant energy. To assure that this energy is not an over prediction of the actual available heat transport, the energy transfer was compared to what could have been transported by rod-to-rod radiation. The amount of energy released to the resident steam from the hot spot by the FTI model during refill amounts to approximately 2.5 percent of the decay heat rate at the hot spot. Rod-to-rod radiation would allow the transport of approximately 5 percent of the hot spot decay heat to surrounding rods. Thus, during the refill period, the heat transfer allowed by FTI's modeling remains conservative by a factor of two (2).

V. Comparisons

This section presents the results of cases that were used to assess the impact of updating from one to two hot channel heat structures and, more importantly, that of reducing the uncertainty factors. Results are shown for both B&W lowered-loop and RSG plants. Expectations for the B&W raised-loop design would fall between the results for the above mentioned plant types. The initial comparison cases are based on a uniform uncertainty of 11.5 percent. They demonstrate that the addition of a second heat structure in the hot channel has no effect of any significance whatsoever on case results. Minor noted differences result from normal computer code numerical issues—round off. The comparisons confirm proper RELAP5 implementation and no impact on prior licensing calculations.

The final comparison cases show the predictive changes achieved by reducing the self-imposed conservatism on the steady state, volume-averaged, fuel temperature, uncertainty factors. Factors of 1.0, 1.03, and 1.115 were applied to the average core, the hot assembly, and the hot rod, respectively. Primarily, the final comparison cases are discussed below.

1. Once-Through Steam Generator Plants

B&W-designed plants would be expected to show a greater sensitivity to reductions in initial stored energy than would U-tube steam generator plants. Experience indicates that the peak-clad temperature for once-through steam generator plants (notably the lowered-loop design) generally occurs late in or immediately following the end of the refill period. The refill period is the period required for the ECCS to completely fill the depleted inventory of the reactor vessel lower head and lower plenum. Since B&W plants peak early in the transient, the large break LOCA is substantially influenced by stored energy. (On the other hand, U-tube plants generally peak well past the end of the refill period. Accordingly, recirculating steam generator plants are largely controlled by decay heat and are less influenced by initial stored energy levels.)

The large break LOCA plant model used for TMI-1 nuclear plant reload licensing application was selected for the multiple core heat structure evaluation. The axial peak power at the 2.5-ft level yields the limiting PCT based on the currently licensed axial power limit (K_2). The plant configuration is presented in Table 1. The evaluation of cladding temperature transients is performed with three computer codes, interconnected as depicted

in Figure 1. The computer code models are consistent with the EM described in Reference 2. The core is radially divided into two fluid channels, hot and average fluid channels as shown in Figure 2a. Each channel consists of 22 axial volumes, numbered 325 through 346 and 425 through 446 for the hot and average fluid channels respectively. The bottom and top volumes (325 and 346 and 425 and 446) in each channel are unheated core volumes. The active core regions for the hot and average fluid channels are volumes 326 through 345 (heat structures 2 through 21) and volumes 426 through 445 respectively. The RELAP5/MOD2-B&W code ⁽³⁾ is used to predict the reactor coolant system thermal-hydraulic transients during the blowdown and post-blowdown core thermal analysis (BEACH). The REFLOD3B code ⁽⁴⁾ is used to generate post-blowdown hydraulic boundary conditions to be used in the core thermal analysis with the BEACH code. The initial volume-averaged fuel temperatures are calculated by the TACO3 code ⁽⁶⁾, and are adjusted to account for uncertainties for LOCA application. The following three analyses were performed to evaluate the effects of the uncertainty on the PCT.

- Case 1 (Base EM): The current licensing model has two core heat structures, one representing the hottest assembly, and the other representing the remaining 176 assemblies. The volume-averaged fuel temperatures for both heat structures have 11.5 percent uncertainty added.
- Case 2: This is Case 1 with three core heat structures. The base EM hot assembly heat structure is split into two heat structures within the hot fluid channel, one representing one (1) hot rod and the other representing the remaining 207-rod hot assembly. The temperature uncertainty remains at 11.5 percent. The average heat structure remains unchanged.
- Case 3: This is Case 2 with reduced uncertainty in the hot and average assembly heat structures. The uncertainty in the 207-rod hot assembly heat structure in Case 2 is reduced from 11.5 to 3 percent. The uncertainty for the average assembly heat structure is reduced from 11.5 to 0 percent. The hot rod heat structure remains unchanged.

The results of the B&W reduced uncertainty case are compared to the unreduced uncertainty case in Table 2 and in Figures 3 through 7. Both cases use three (3) core heat structures, one (1) in the average fluid channel, and two (2) in the hot fluid channel.

The results of the evaluation are summarized in Table 2. The peak cladding temperatures for the hot rod unruptured (node 6) and ruptured (node 7) nodes are presented in Figures 3 and 4, respectively. The cladding burst occurred near the end of blowdown due to the high peak power (16.8 kw/ft) and the low core downflow during blowdown. A brief period of enhanced local cooling following the rupture was observed. However, this is more than offset by energy addition from the metal-water reaction during the subsequent refill period. Thus, the heatup rate at the ruptured node is substantially greater than unruptured locations. In addition, high flooding rates during the early phase of the reflood transient are sufficient to provide cladding temperature turnaround a few seconds after the start of reflood. Thus, the ruptured node PCT becomes limiting. The hot spot (node 7) mass flow rate during the

blowdown in Figure 5 is relatively insensitive to the core stored energy. Figure 6 shows slightly higher flooding rates for Case 3 during the early phase of the reflood transient. The hot spot vapor temperature plots in Figure 7 show that the Case 3 vapor temperature is generally lower than those of Cases 1 and 2 due to lower energy deposition in the hot channel.

The results of Cases 1 (base EM) and 2 confirm that the multiple-core heat structure model is properly implemented in the RELAP5/MOD2 code. The clad rupture occurred at node 7 for both the hot rod and hot assembly heat structures. Case 3 with the lower hot channel fluid temperature and higher flooding rate results in a lower heatup rate. The PCT for Case 3 decreased by more than 150 F below the base EM case. The PCTs for the base EM and the revised EM (Case 3) with the reduced uncertainties are 2055 F and 1904 F respectively. Both values are substantially below 10CFR50.46 limits.

2. U-Tube Steam Generator Plants

The large break LOCA plant model used for the Sequoyah nuclear plant reload licensing application was selected for the multiple core heat structure evaluation. The axial peak power at the 9.7-ft level yields the limiting PCT based on the current licensed axial power limit (K_2). The plant configuration is presented in Table 3. The evaluation of cladding temperature transients is performed with three computer codes. Their connectivity is depicted in Figure 1. The computer code models are consistent with the EM described in Reference 1. The core is radially divided into two fluid channels, hot and average fluid channels as shown in Figure 2b. Each channel consists of 20 axial volumes, numbered 326 through 345 and 426 through 445 for the hot and average fluid channels respectively. The RELAP5/MOD2-B&W code ⁽³⁾ is used to predict the reactor coolant system thermal-hydraulic transients during the blowdown and post-blowdown core thermal response (BEACH). The REFLOD3B code ⁽⁴⁾ is used to generate post-blowdown hydraulic boundary conditions to be used in the core thermal analysis. The initial volume-averaged fuel temperatures are calculated by the TACO3 code ⁽⁶⁾, and are adjusted to account for uncertainties for LOCA application. The following three analyses were performed to evaluate the effects of initial fuel temperature uncertainty on PCT.

- **Case 1 (Base EM):** The current licensing model has two core heat structures, one representing the hot assembly and the other representing the remaining 192 assemblies. The volume-averaged fuel temperatures for both heat structures have 11.5 percent uncertainty added.
- **Case 2:** This is Case 1 with three core heat structures. The base EM hot assembly heat structure is split into two (2) heat structures within the hot fluid channel, one representing one (1) hot rod and the other representing the remaining 263 rods in the hot assembly. The temperature uncertainty remains at 11.5 percent. The average heat structure remains unchanged.

- **Case 3:** This is Case 2 with reduced uncertainty in the hot and average assembly heat structures. The uncertainty on the 263 rods in the hot assembly heat structure in Case 2 is reduced from 11.5 to 3 percent. The uncertainty for the average assembly heat structure is reduced from 11.5 to 0 percent. The hot rod heat structure remains unchanged at 11.5 percent.

The results of the evaluation are summarized in Table 4. The peak cladding temperatures for the hot rod unruptured (node 15) and ruptured (node 17) nodes are presented in Figures 8 and 9 respectively. In RSG plants with lower peak power (12.43 kw/ft), clad burst occurs during reflood and rupture-induced local cooling reduces rupture node heatup. For the unruptured node, clad temperature turnaround occurs later due to low flooding rates. Thus, the unruptured node yields the limiting PCT. The hot spot (node 15) mass flow rate during blowdown (Figure 10) is relatively insensitive to the core stored energy. Figure 11 shows slightly higher flooding rates for Case 3 during the early phase of the reflood transient (80 seconds). The hot spot vapor temperature curves in Figure 12 show that the Case 3 vapor temperature is generally lower than those in Cases 1 and 2. This is due to a lower energy deposit in the hot channel. The combined effects of lower hot channel energy and higher flooding rate in Case 3 produce a lower PCT. The effects of lower hot channel energy and higher flooding rate on the PCT in Case 3 are less pronounced than in the OTSG study due to a longer temperature turnaround time. The Case 3 PCT is 60 F less than the base EM case.

Again, the results of Cases 1 (base EM) and 2 confirm that the multiple-core heat structure model is properly implemented in the RELAP5/MOD2 code. The PCTs for the current EM (Case 1) and the revised EM (Case 3) with reduced uncertainty are 2159 F and 2098 F respectively. Both PCT values are below 10CFR50.46 limits.

VI. Conclusions

Framatome Technologies is refining the modeling of the hot rod/hot assembly in its LBLOCA EMs by separating these regions into separate heat structures. The refinements apply equally to LBLOCA licensing calculations performed with the RSG and B&W EMs. The changes affect the modeling in RELAP5 (including BEACH) and do not affect REFLOD3B modeling or usage.

First, additional modeling detail was added to the hot fluid channel. The hot channel contains two (2) heat structures, one representing the hot rod and one representing the hot assembly (less the one hot rod). Previously only one (1) heat structure was modeled in the hot fluid channel. Hot channel fluid conditions drive both heat structures and both structures are initialized at the same maximum allowable peaking or kilowatts per foot. The evaluation model results are not affected by the insertion of additional hot channel modeling detail. However, the modeling refinement allows the incorporation and simulation of differences between the hot rod and the remainder of the hot rods in the hot bundle that can affect the results of EM calculations. The added detail is appropriate for inclusion in future large break LOCA analyses and the continued licensing validity of the evaluation models is demonstrated and retained.

Secondly, unwarranted conservatism in the specification of volume-averaged fuel temperature uncertainties was removed. Previously, the TACO3-specified "hot rod" uncertainty factor was applied to all core fuel rods, substantially overestimating the initial core stored energy. Neither evaluation model ^(1,2) imposed the conservatism, nor was it required by TACO3 ⁽⁶⁾. The recommended uncertainty specified in the TACO3 topical report was formulated for hot rods. Essentially the over conservatism is self-imposed and subject to removal without affecting the licensing basis of the large break LOCA evaluation models. Based on work reported in the TACO3 topical report, no volume-averaged fuel temperature uncertainty will be applied to the average core heat structure (a standard industry practice), and a three (3) percent uncertainty on TACO3 was justified and will be applied to the hot assembly heat structure. The TACO3-specified uncertainty will continue to be applied to the hot rod.

[Note: The future will likely hold changes to fuel code technology—the replacement of TACO3 with an improved code, COPERNIC ⁽⁷⁾, for example. Under such circumstances, fuel temperature uncertainty factors—appropriate to the new technology—for the average core, hot rod, and hot assembly heat structures will be developed. The uncertainty factors would be used in LBLOCA analyses based on the advanced fuel code. Framatome Technologies would inform the NRC of such a change.]

Comparison cases demonstrate the impact of reverting to normal industry volume-averaged fuel temperature uncertainties. Clad temperature reductions in the representative B&W plant case are substantial. This results from the transient being largely dominated by the initial stored energy. The PCT, normally occurring immediately after the end of refill, is substantially reduced. The U-tube steam generator plants generally experience a late transient peak, well after the end of the refill period. These plant transients are largely dominated by decay heat and show less impact to a reduction in initial core stored energy.

The unwarranted conservatism in setting the initial core stored energy will be removed in the next applications of either of the LBLOCA EMs. This refinement is considered to lie within the confines of the existing EMs and does not comprise a change to the EMs. The applicability and NRC licensing status of the EMs are not perturbed and the EMs incorporating the refinements remain valid for use in LBLOCA licensing applications.

VI. References

1. BAW-10168P-A, "RSG LOCA, BWNT Loss-of-Coolant Accident Evaluation Model for Recirculating Steam Generator Plants," Revision 3, December 1996.
2. BAW-10192P-A, "BWNT LOCA, BWNT Loss-of-Coolant Accident Evaluation Model for Once-Through Steam Generator Plants," Revision 0, June 1998.
3. BAW-10164P-A, "RELAP5/MOD2-B&W, An Advanced Computer Program for Light Water Reactor LOCA and Non-LOCA Transient Analysis," Revision 3, July 1996.
4. BAW-10171P-A, "REFLOD3B, Model for Multinode Core Reflooding Analysis," Revision 3, December 1995.
5. BAW-10166P-A, "BEACH, Best Estimate Analysis Core Heat Transfer, A Computer Program for Reflood Heat Transfer During LOCA," Revision 4, February 1996.
6. BAW-10162P-A, "TACO3, Fuel Rod Thermal Analysis Computer Code," Revision 0, November 1989.
7. BAW-10231P, "COPERNIC Fuel Rod Design Computer Code," Revision 0, September 1999.
8. BAW-10186P-A, "Extended Burnup Evaluation," Revision 0, June 1997.

Table 1. Initial Conditions for OTSG LBLOCA—2.5-ft Axial Peak.

Parameters

Reactor Core Power (102 %), MWt	2827.4
Peak Linear Power, kw/ft	16.8
Total Peaking Factor, F_q	2.625
Radial Peaking Factor, $F_{\Delta H}$	1.544
Fuel Assembly	15 x 15 Mark-B9
Number Of Fuel Assemblies	177
Thermal Design Flow, lbm/hr	133.9×10^6
Bypass Flow, percentage	7.5
RCS Average Temperature, F	579.0
Pressurizer Pressure, psia	2199.0
Pressurizer Level, in	220.0
Steam Generator Tube Plugging, percentage	20.0
Accumulator Water Volume, ft ³ /tank	985.0
Accumulator Gas Pressure, psia	580.0

Table 2. Summary of Results for OTSG LBLOCA—2.5-ft Axial Peak.

<u>Parameters</u>	<u>Base EM</u>	<u>Case 2</u>	<u>Case 3</u>
End of Blowdown, s	20.71	20.69	20.72
Beginning of Core Recovery, s	27.45	27.43	27.40
Hot Rod PCT, F	N/A*	2050	1904
Hot Rod PCT Node	N/A*	7	7
Hot Rod PCT Time, s	N/A*	30.7	28.1
Hot Assembly PCT, F	2055	2050	1787
Hot Assembly PCT Node	7	7	7
Hot Assembly PCT Time, s	30.8	30.7	28.1
Average Assembly PCT, F	1447	1447	1327
Average Assembly PCT Node	8	8	8
Average Assembly PCT Time, s	7.4	7.4	35.9
Hot Rod Rupture Node	N/A*	7	7
Hot Rod Rupture Time, s	N/A*	17.95	18.4
Hot Rod Rupture Node PCT, F	N/A*	2050	1904
Hot Assembly Rupture Node	7	7	7
Hot Assembly Rupture Time, s	17.9	17.95	20.2
Hot Assembly Rupture Node PCT, F	2055	2050	1787

* Note this model does not distinguish between the hot rod and the hot assembly, as such the hot rod PCT is the hot assembly PCT.

Table 3. Initial Conditions for RSG LBLOCA—9.7-ft Axial Peak.

Parameters

Reactor Core Power (102 %), MWt	3479.2
Peak Linear Power, kw/ft	12.43
Total Peaking Factor, F_q	2.3
Radial Peaking Factor, $F_{\Delta H}$	1.471
Fuel Assembly	17 x 17 Mark-BW
Number Of Fuel Assemblies	193
Thermal Design Flow, gpm	348,000
Bypass Flow, percentage	7.0
RCS Average Temperature, F	578.2
Pressurizer Pressure, psia	2250
Pressurizer Level, percentage	60
Steam Generator Tube Plugging, percentage	15
Accumulator Water Volume, ft ³ /tank	1095
Accumulator Gas Pressure, psia	614.7

Table 4. Summary of Results for RSG LBLOCA—9.7-ft Axial Peak.

<u>Parameters</u>	<u>Base EM</u>	<u>Case 2</u>	<u>Case 3</u>
End of Blowdown, s	25.69	25.69	25.76
Beginning of Core Recovery, s	46.92	46.92	46.10
Hot Rod PCT, F	N/A*	2171	2098
Hot Rod PCT Node	N/A*	15	15
Hot Rod PCT Time, s	N/A*	119.1	130.9
Hot Assembly PCT, F	2159	2173	2090
Hot Assembly PCT Node	15	15	15
Hot Assembly PCT Time, s	118.6	119.1	152.7
Average Assembly PCT, F	1653	1654	1657
Average Assembly PCT Node	15	15	17
Average Assembly PCT Time, s	122.8	123.5	122.6
Hot Rod Rupture Node	N/A*	17	17
Hot Rod Rupture Time, s	N/A*	56.7	59.5
Hot Rod Rupture Node PCT, F	N/A*	2025	1745
Hot Assembly Rupture Node	17	17	17
Hot Assembly Rupture Time, s	56.7	56.7	60.8
Hot Assembly Rupture Node PCT, F	2016	2029	1736

* Note this model does not distinguish between the hot rod and the hot assembly, as such the hot rod PCT is the hot assembly PCT.

FIGURE 1. LBLOCA EM Computer Code Interface.

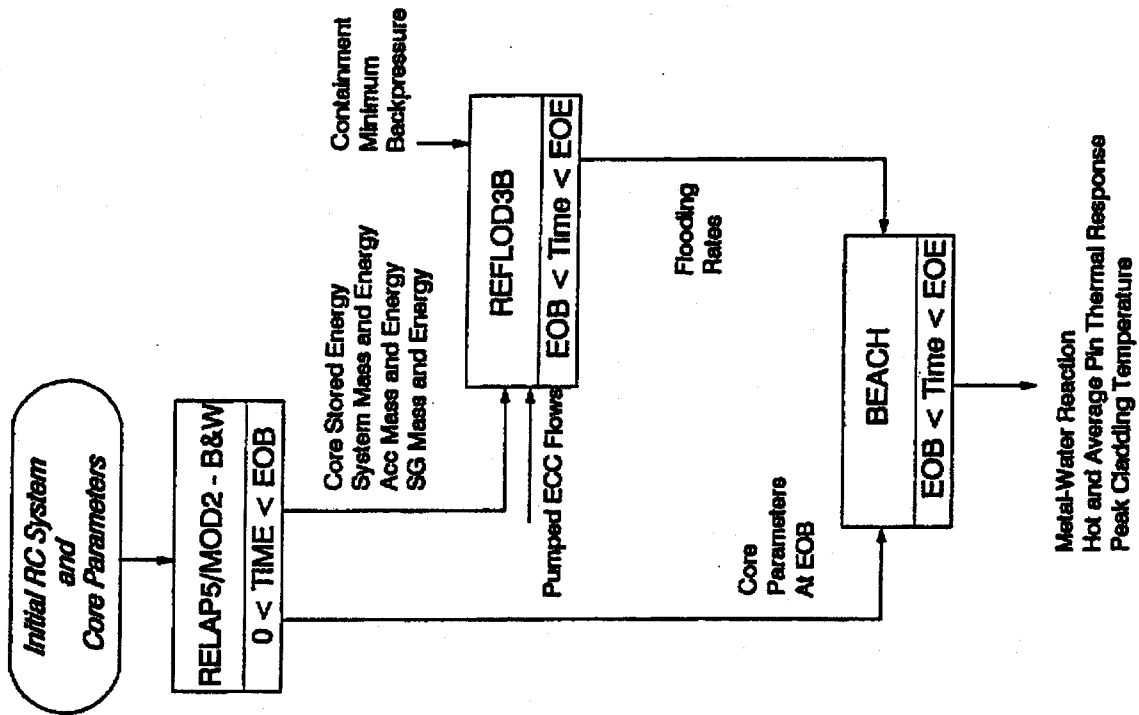
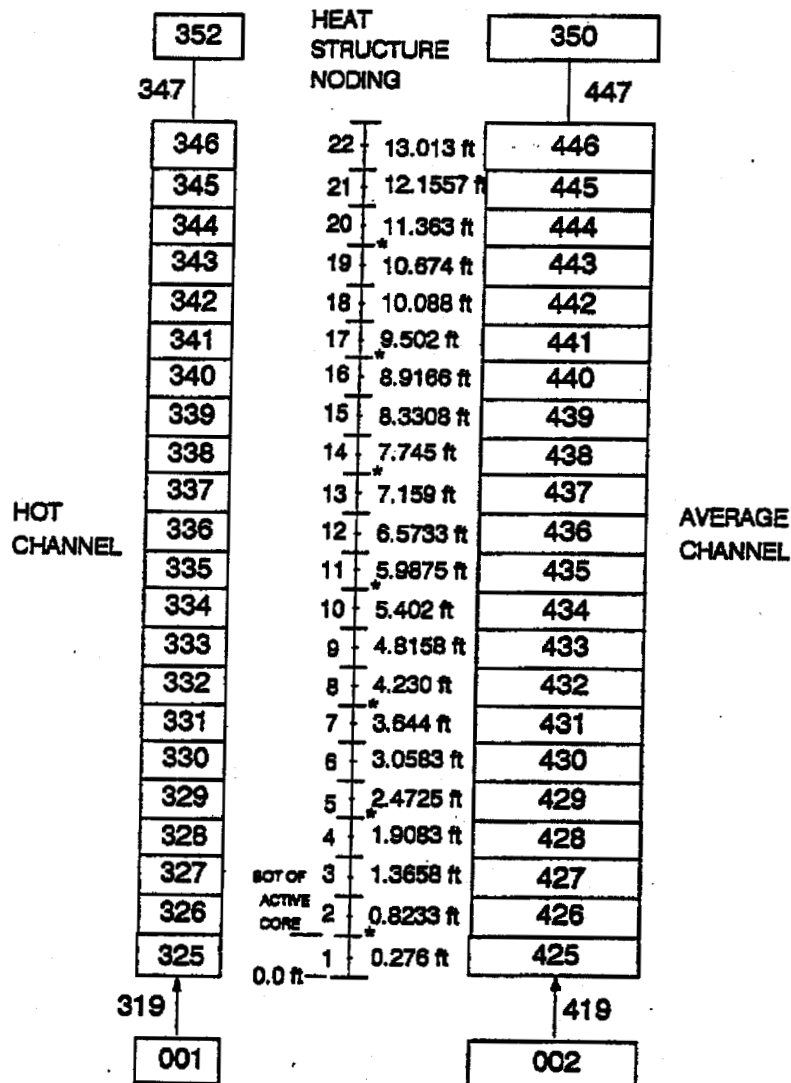


FIGURE 2a. RELAP5-BEACH Core Noding Arrangement For OTSG.



* GRID LOCATION

FIGURE 2b. RELAP5-BEACH Core Noding Arrangement For RSG.

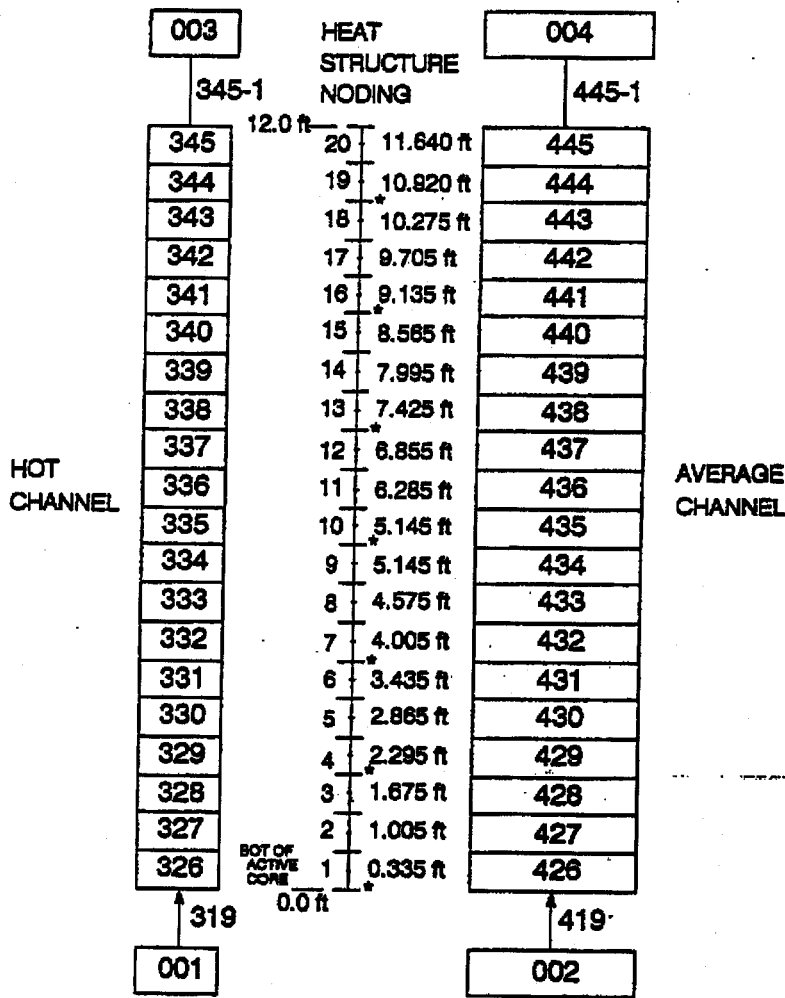


FIGURE 2c. Representative RELAP5-BEACH Core Heat Structure Arrangement.

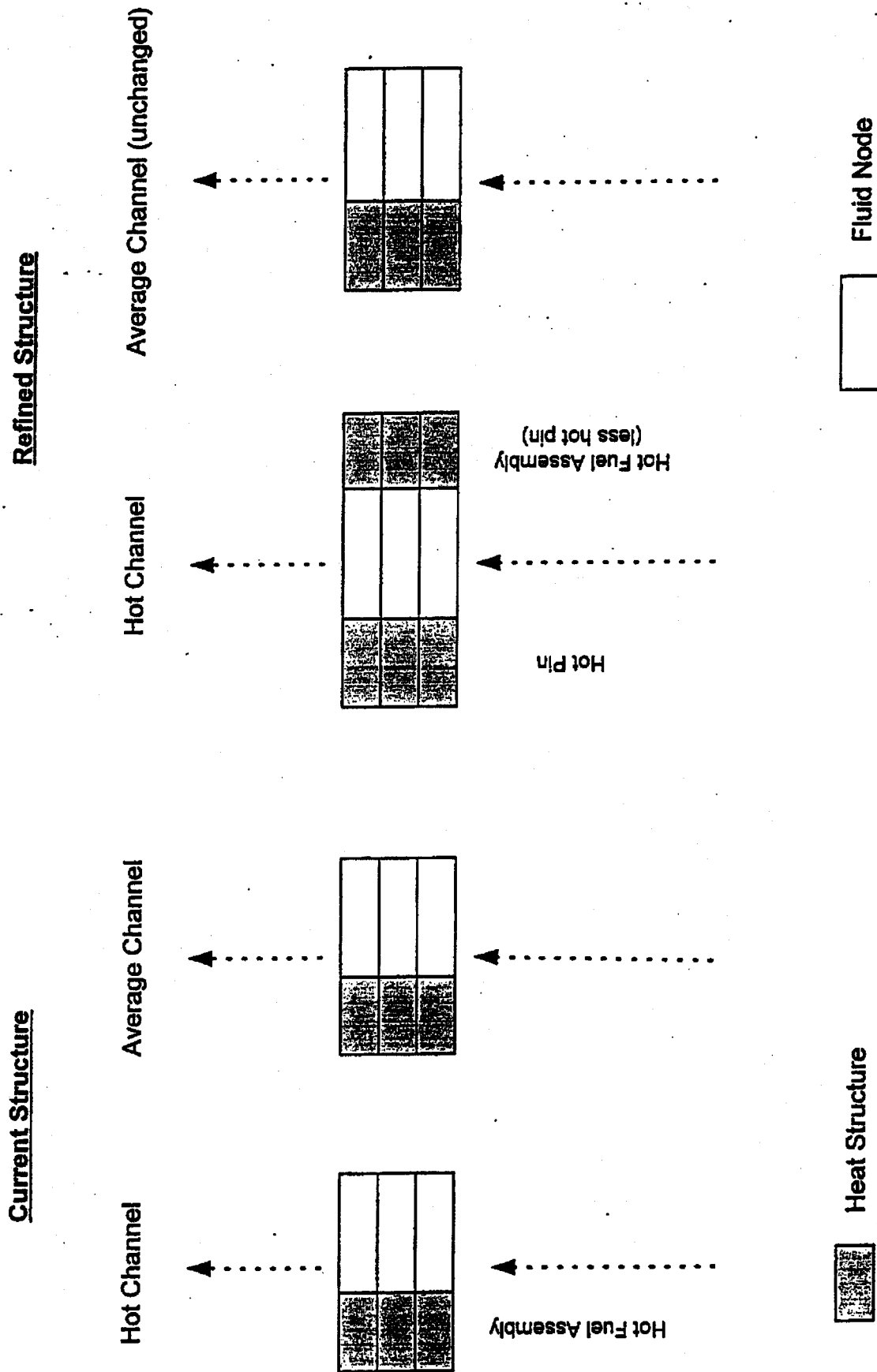


FIGURE 3. OTSG Unruptured Node PCT
2.5-ft Axial Peak.

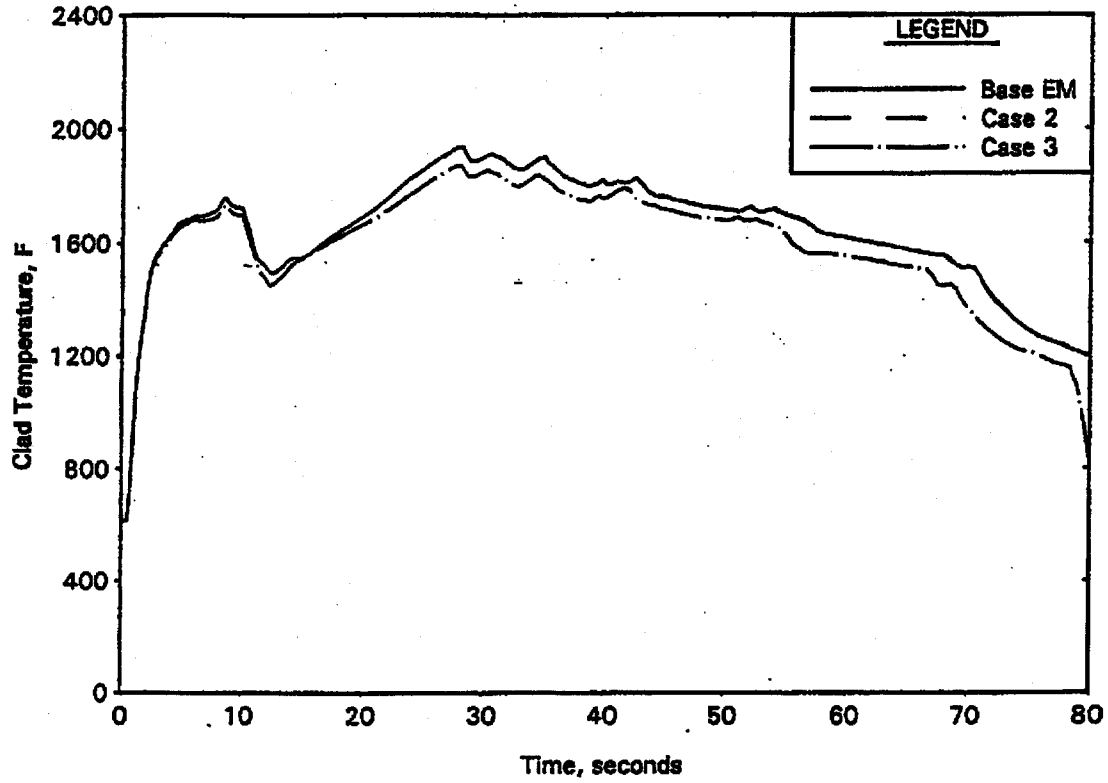


FIGURE 4. OTSG Ruptured Node PCT
2.5-ft Axial Peak.

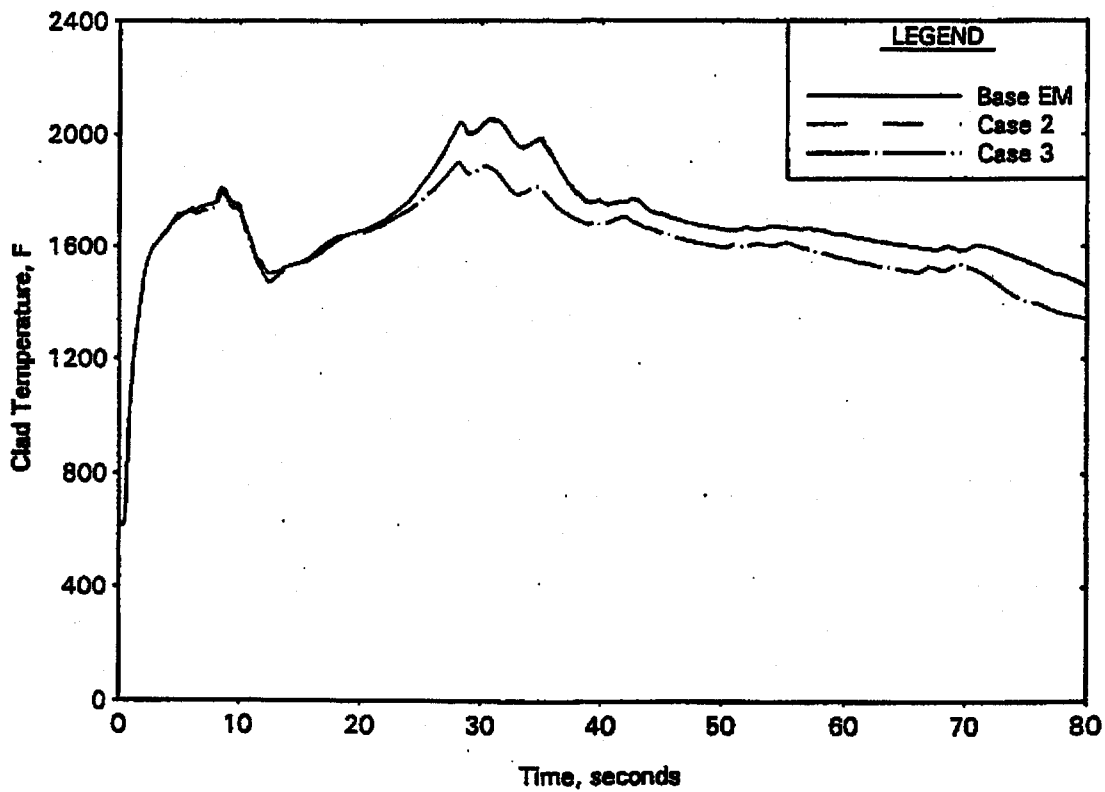


FIGURE 5. OTSG Blowdown Hot Channel Flow At PCT Location
2.5-ft Axial Peak.

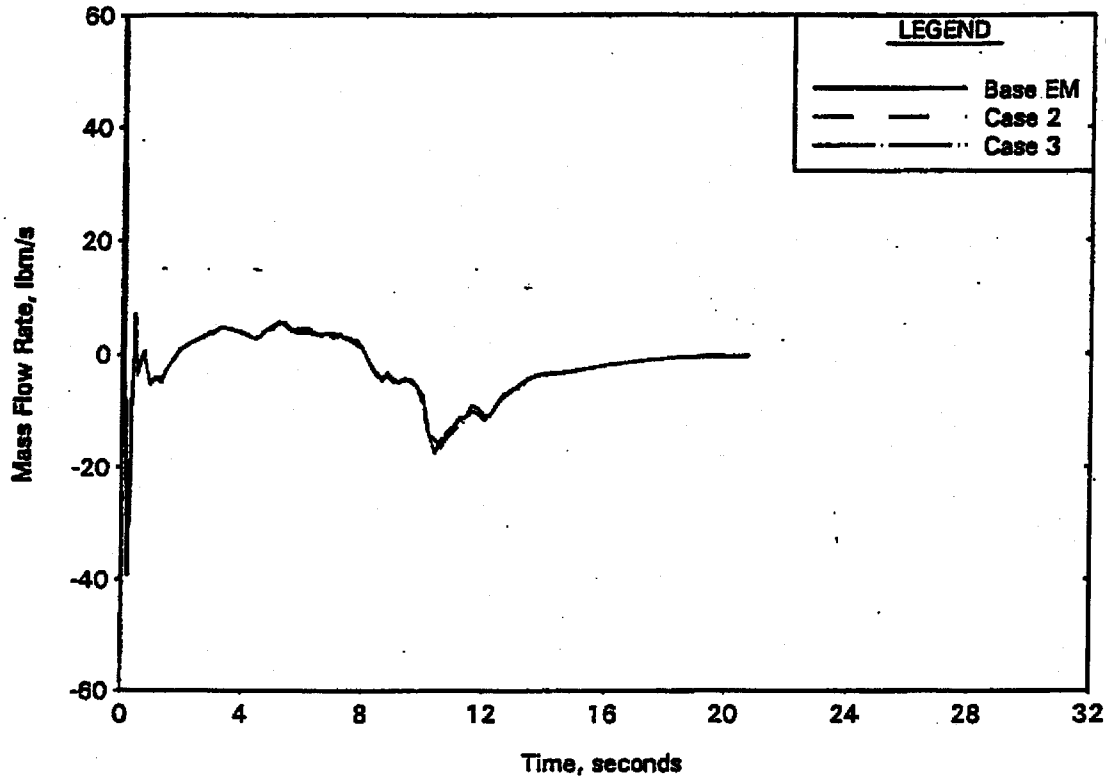


FIGURE 6. OTSG Core Flooding Rate
2.5-ft Axial Peak.

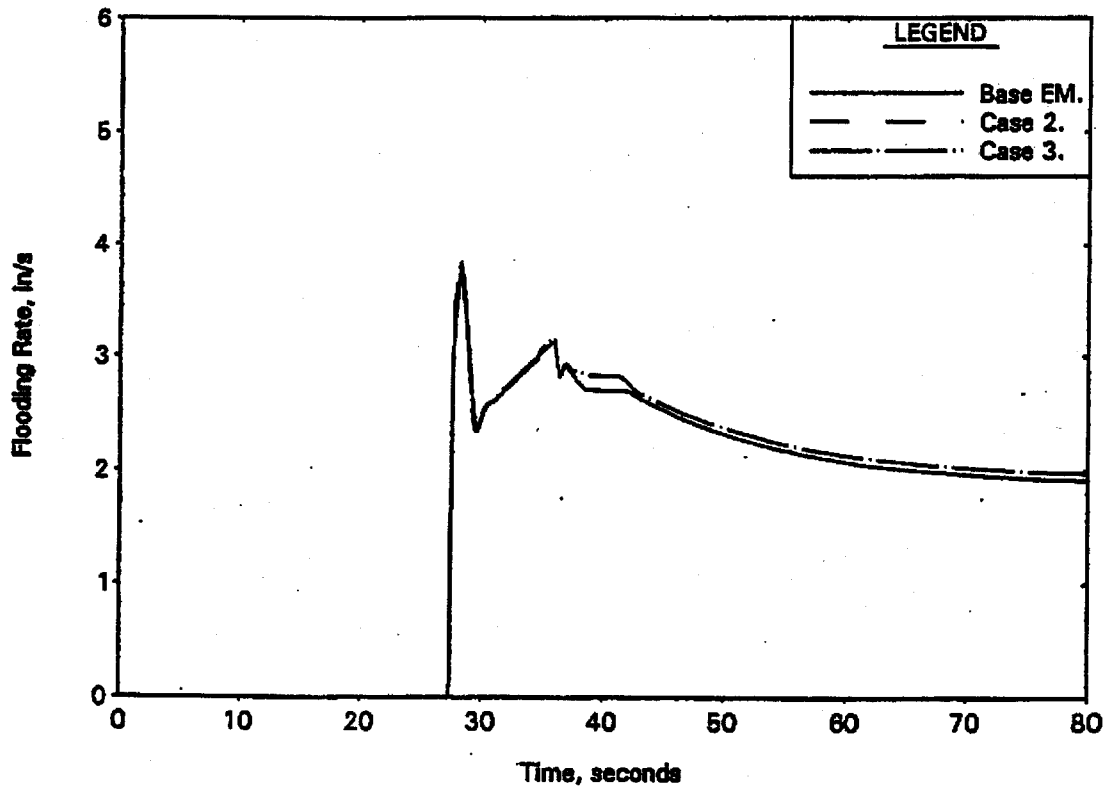


FIGURE 7. OTSG Hot Spot Vapor Temperature
2.5-ft Axial Peak.

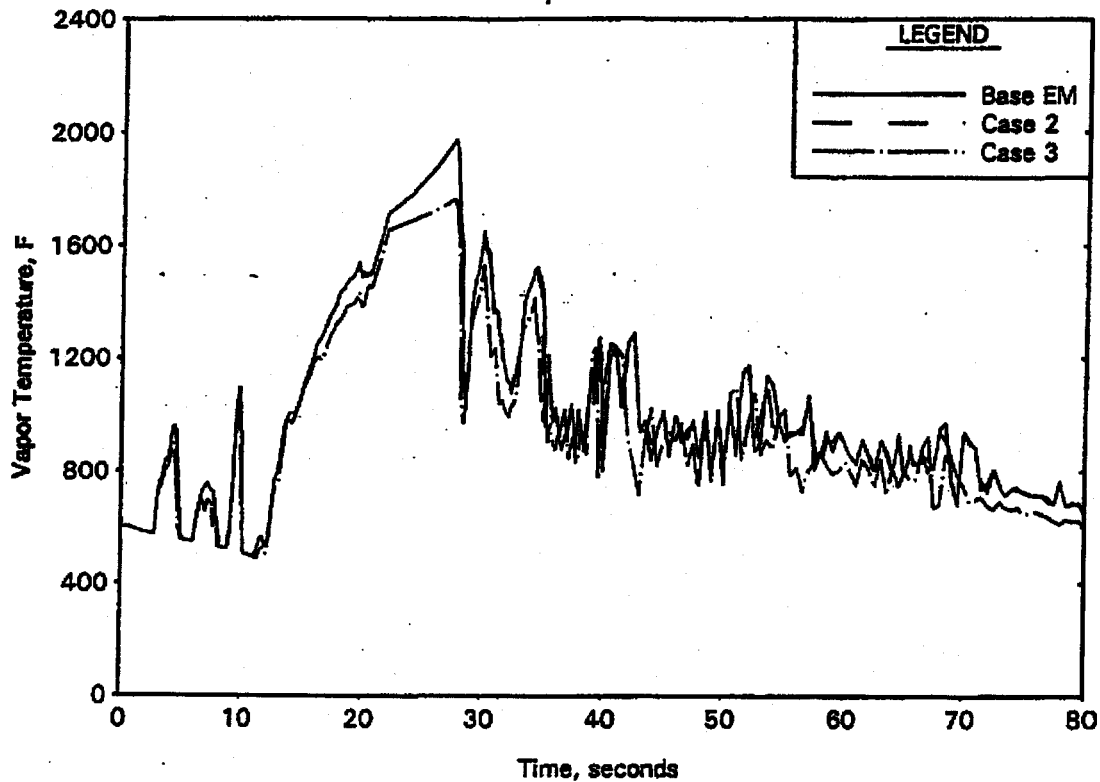


FIGURE 8. RSG Unruptured Node PCT-Node 15
9.7-ft Axial Peak.

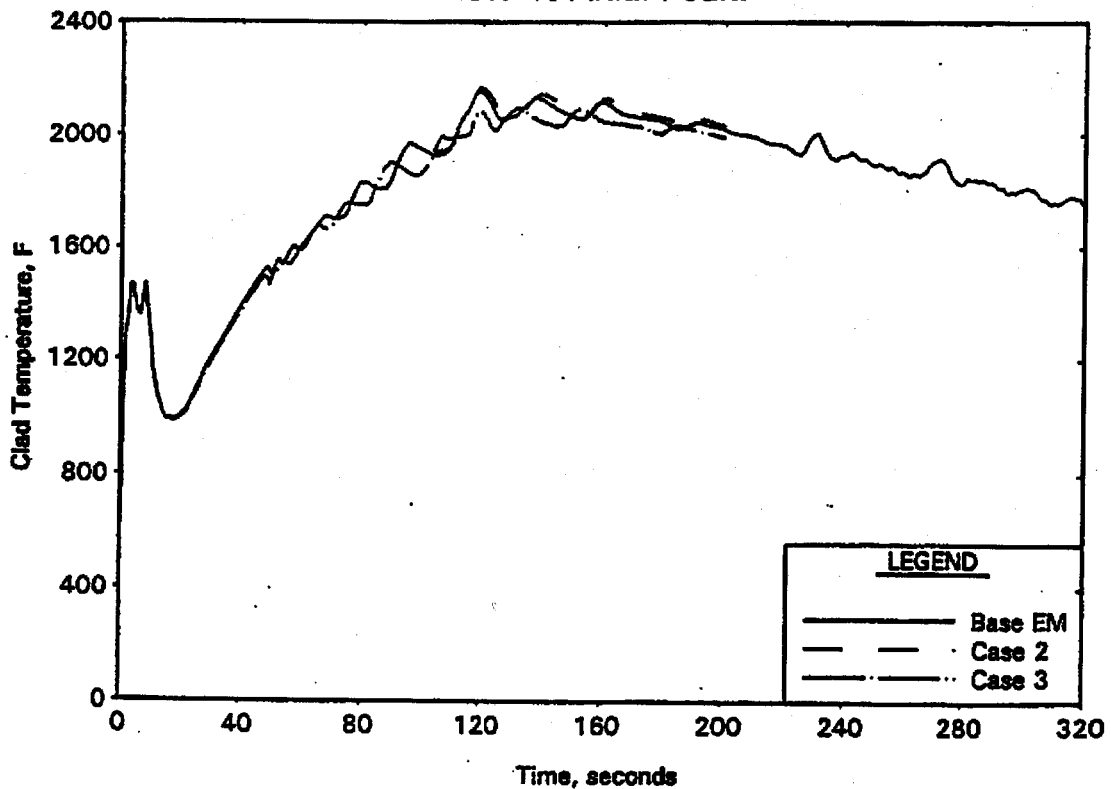


FIGURE 9. RSG Ruptured Node PCT-Node 17
9.7-ft Axial Peak.

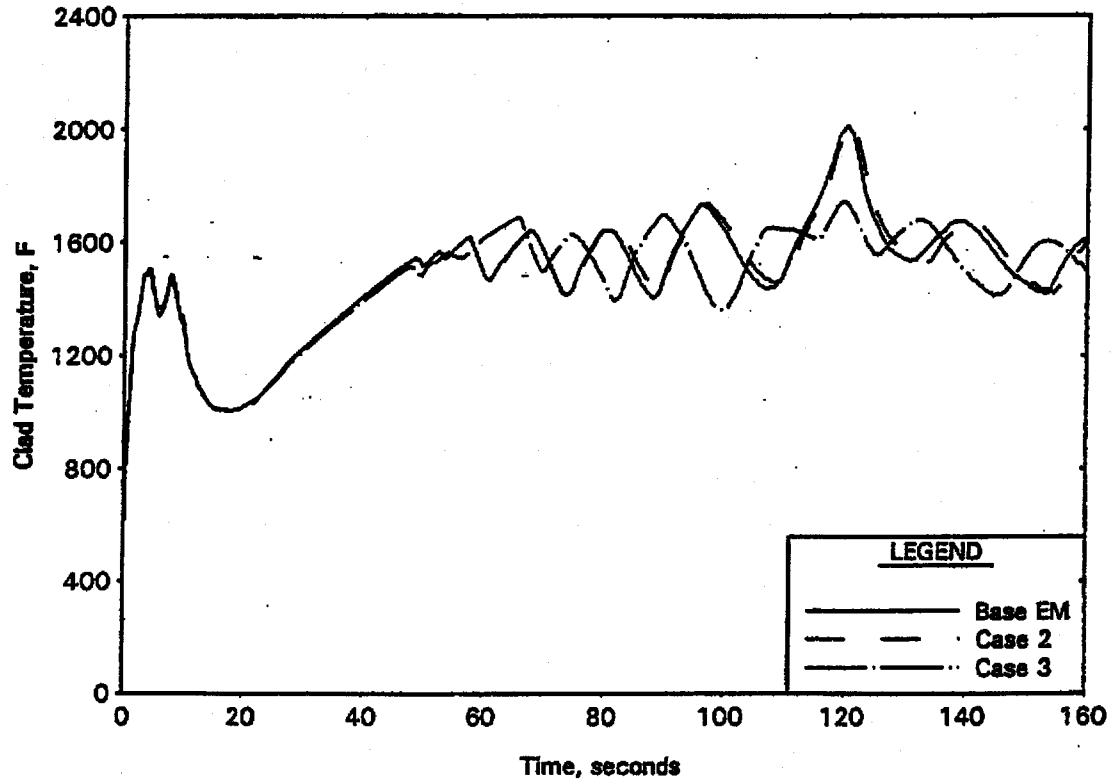


FIGURE 10. RSG Blowdown Hot Channel Flow At PCT Location
9.7-ft Axial Peak.

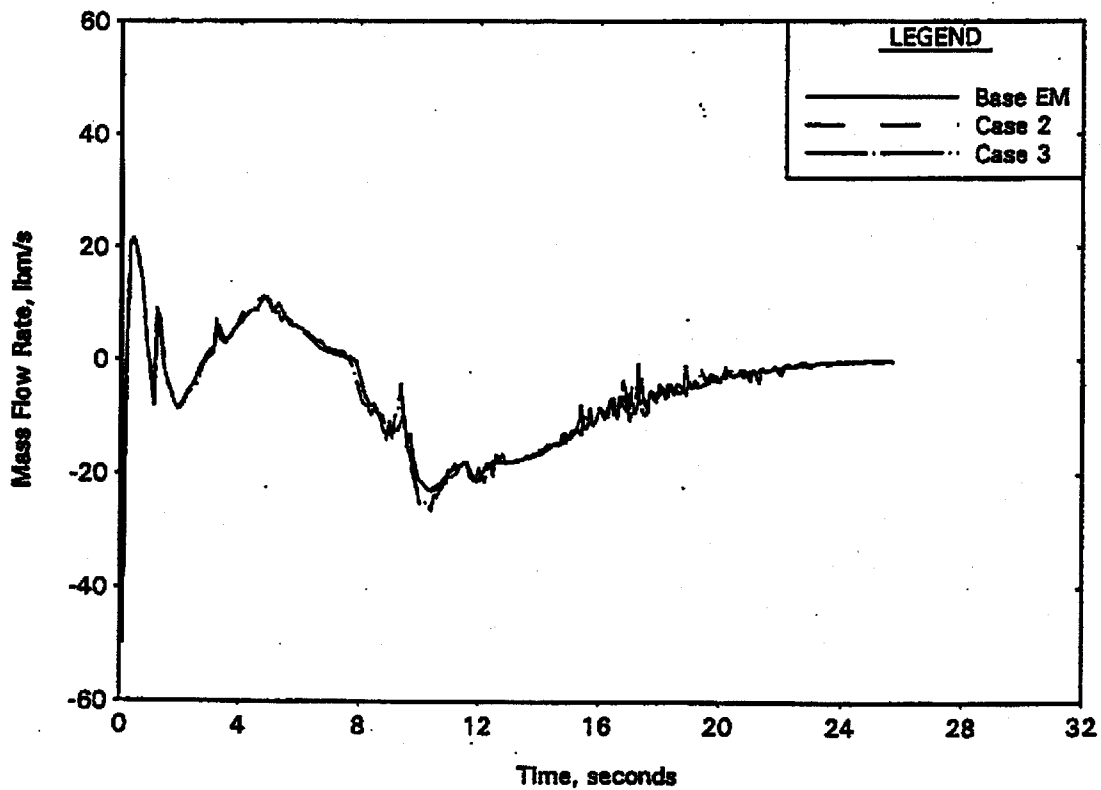


FIGURE 11. RSG Core Flooding Rate
9.7-ft Axial Peak.

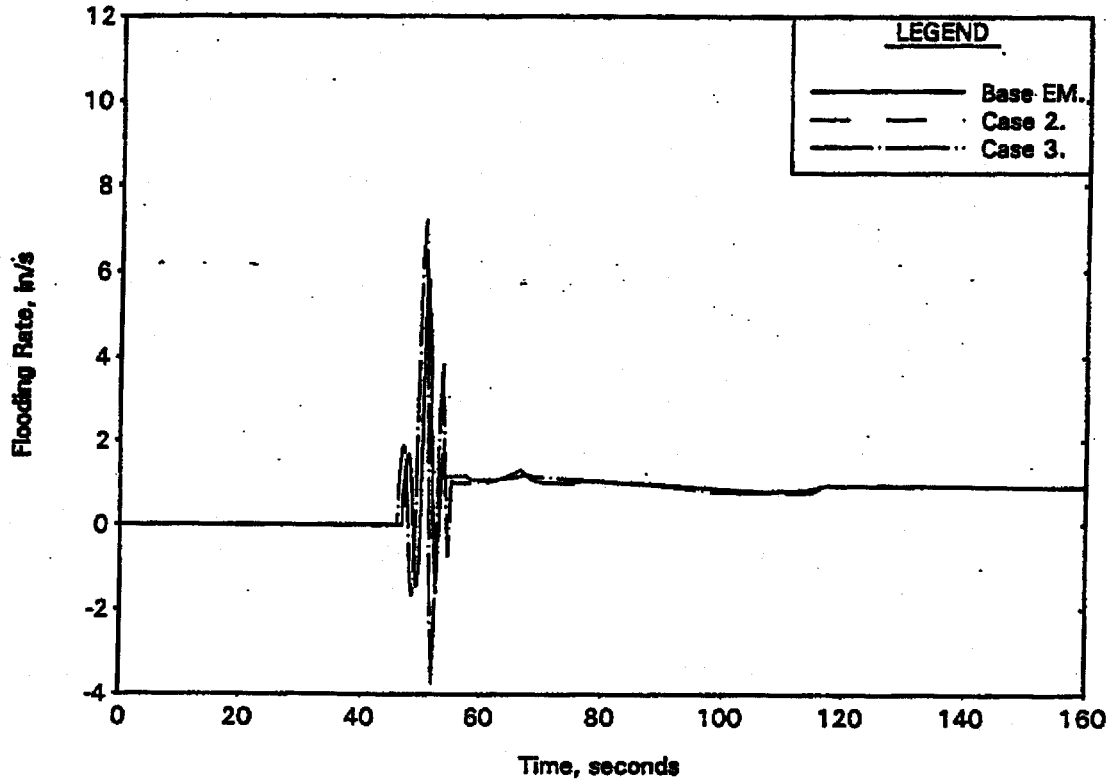
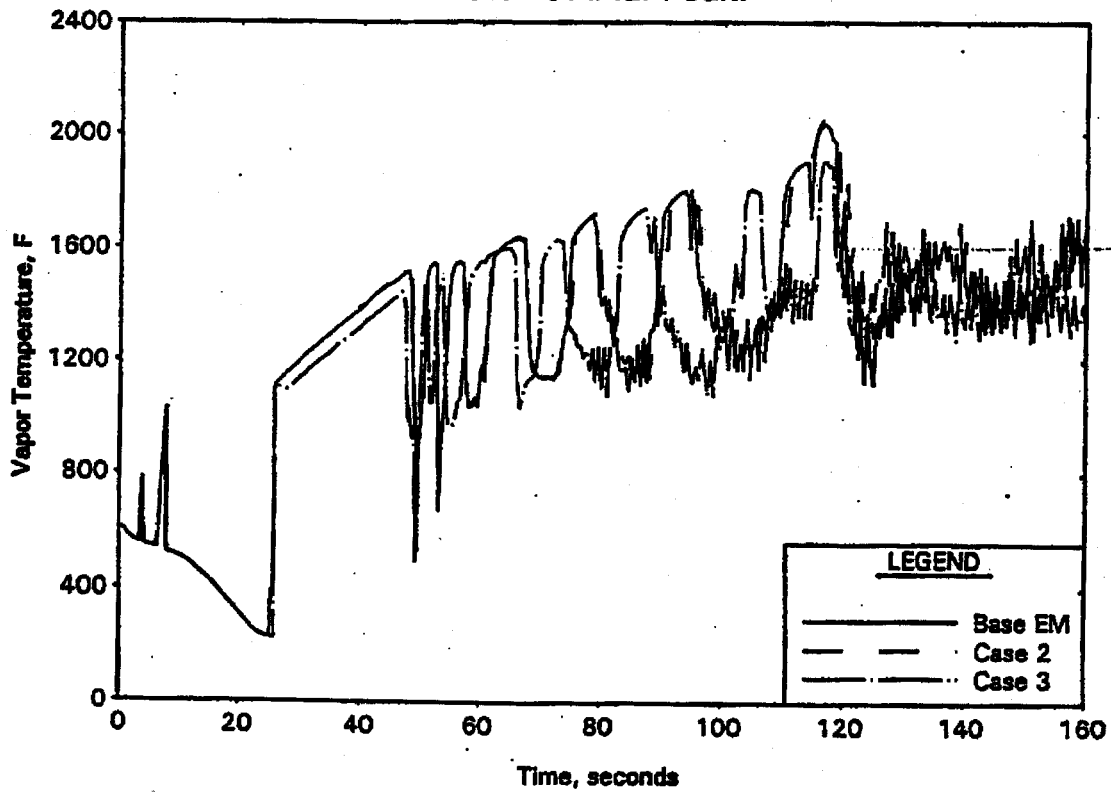


FIGURE 12. RSG Hot Spot (Node 15) Vapor Temperature
9.7-ft Axial Peak.



September 5, 2000
FTI-00-2225

Document Control Desk
U. S. Nuclear Regulatory Commission
Washington, DC 20555-0001

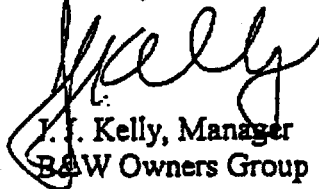
Subject: Additional Information on Modeling Updates to Framatome Technologies'
RELAP5-Based, Large Break LOCA Evaluation Models - BAW-10168 for Non-
B&W-Designed, Recirculating Steam Generator Plants and BAW-10192 for
B&W-Designed, Once-Through Steam Generator Plants

Gentlemen:

On February 29, 2000, Framatome Technologies submitted modeling updates on its large break LOCA evaluation models - BAW-10168P-A, Revision 3, December 1996 and BAW-10192P-A, Revision 0, June 1998. In discussions concerning the change in the determination of the hot assembly initial fuel temperature, the NRC staff indicated that it would be desirable if additional detail were provided on the calculation. The attachment includes such information for use in the NRC's review of our submittals.

The attachment is considered Non-Proprietary to Framatome Technologies. If you require additional information, please contact John Biller at 804/832-2600 or John Klingenfus at 804/832-3294.

Sincerely,



J. F. Kelly, Manager
BAW Owners Group Services

Attachment

cc:

S. N. Bailey	-	Nuclear Regulatory Commission
L. Lois/NRC	-	Nuclear Regulatory Commission
F. R. Orr/NRC	-	Nuclear Regulatory Commission
J. R. Biller	-	Framatome Technologies/OF53
B. M. Dunn	-	Framatome Technologies/OF53
C. K. Nithianandan	-	Framatome Technologies/OF53
J. A. Klingenfus	-	Framatome Technologies/OF53
R. N. Edwards	-	Framatome Technologies/MD82
M. A. Schoppman	-	Framatome Technologies/MD82

Attachment

Introduction

The representation of the hot fuel assembly under the Framatome LOCA evaluation models (EMs) is being refined to include better represent the cooling mechanisms acting at the hot spot. During conditions of moderate to high flows the representation of the vapor temperatures at the hot spot is being improved. Further, the adiabatic period during lower head/lower plenum refill is being replaced with an approximation of the convective and radiation heat transfer processes present during the phase. Separating the hot spot and the hot assembly, allowing heat transfer during the refill phase, and probabilistically distributing the initial fuel pellet temperatures achieve these changes.

One of the parameters that can be changed between the hot spot (the location that will eventually produce the peak cladding temperature (PCT)) and the hot assembly is the initial fuel temperature. The base uncertainty in TACO3 predictions (that applicable for exposures below 40 GWd/mtU) is obtained by benchmarking a large number of unrelated tests. There is no apparent dependency between the predicted to measured uncertainty values and particular code correlations or input parameters. (Above 40 GWd/mtU a dependency does exist and the addition of a bias is required.) Therefore, the base uncertainty applies at the pellet level and the actual to predicted temperature ratios for the fuel pellets in the immediate environment of the hot spot should be distributed according to the probability density function of the uncertainty of the prediction. For the hot spot, the initial fuel temperature should continue to be the temperature predicted by TACO3 plus the uncertainty needed to provide 95 % confidence that the modeled temperature overpredicts 95 % of the data. For TACO3, up to burnup exposures of 40 GWd/mtU, that means 111.5 % of the TACO3 prediction. For the hot assembly, however, the only requirement is that the fluid conditions, which provide cooling for the hot spot, are reasonably conservative.

If the hot pin and the remainder of the hot assembly are separated and the hot assembly fluid conditions used to cool the hot pin, the hot spot parameters can be separated from the determination of the coolant conditions. This is the refinement for the next applications of the Framatome EMs.

Current Modeling Approach and Required Revision

Currently Framatome models the hot fuel assembly and hot pin as one entity. This necessitates treating the entire hot assembly with all of the conservatisms required to assure that the hot pin or hot spot is not under-predicted. The result is a significant overprediction of the severity of the environs of the hot spot. By separating the hot pin from the hot assembly it is possible to reduce the conservatisms imposed by the hot pin environs while maintaining a conservative solution.

Convective and radiative processes govern heat transfer from the hot spot. During accident phases with relative high flow, the convective processes are dominant and primary attention is required to determine the incoming flow, its characteristics, and the convective coefficient. During accident phases with no or very low core flow, radiation to the immediate environs of the hot spot will dominate the solution. At these times, the combined heat capacity of the environs along with the radiative coefficient must be considered to assure an appropriate solution. The separation of hot spot and hot assembly assures appropriate conservatism by modeling the hot assembly such that:

1. The coolant conditions within the immediate surroundings of the hot spot during flow periods are conservatively predicted using initial fuel pellet temperatures that are at approximately the 95%/95% one sided upper tolerance limit, and
2. During stagnant conditions, the heat removal achieved by the separated model is an underprediction of that which would occur via the combined radiative and convective processes.

Under the new model the hot pin will be a separate heat structure that shares a coolant channel with the hot fuel assembly heat structure. The hot fuel assembly is comprised of all fuel pins within the hot assembly except the hot fuel pin(s). The hot pin, as implied, is comprised of one fuel pin. In some applications, MOX or gadolinium, it is anticipated that there could be more than one hot pin heat structures. Because the effect of axial heat conduction between fuel pellets in a fuel pin is small; the entire hot pin is modeled with the initial fuel temperatures applicable to the hot spot without serious over-prediction of consequences. That allows the simulation of a continuum of possible positions along the hot pin for the hot spot with a single model and computer run. Therefore, for TACO3 based evaluations, 11.5 % is added to the predicted fuel temperature for all pellets in the hot pin when the hot pin exposure is less than 40 GWd/mtU.

The initial fuel temperature within the hot assembly pellets is determined by probabilistically distributing the fuel pellet temperature prediction uncertainty throughout the immediate environs of the hot pin and determining the conservative effective average uncertainty at a 95 % confidence level. This average uncertainty is then assigned to the entire hot assembly. The result is that the hot assembly evolves in a fashion representative of the hot pin environs. This creates an over-prediction of the average fuel temperatures within the hot assembly but a reasonable representation of the hot pin coolant condition when flow is present.

The coolant heat capacity, however, is that of the entire assembly at the elevation of the hot spot and substantially larger than the region of the assembly near the hot spot. If coolant is flowing and the rise in temperature along the length of the hot spot not significant, the oversized heat capacity is not an issue. During relatively stagnant periods, vessel refill, the cladding temperatures limit the increases in vapor temperatures and the vapor heat capacity is significant in determining the vapor energy absorption. However, under these conditions, radiative heat transfer to the hot spot environs dominates energy transport away from the hot spot. This transfer mechanism occurs to the coolant and directly to the surrounding fuel pins with the surrounding pins being the far more important heat sink. The use of the entire hot assembly vapor heat capacity and the RELAPS/MOD2-B&W steam heat transfer modeling allows less than one half of the energy flow from the hot spot then would result from radiation to surrounding pins. Therefore, so long as a true pin-to-pin radiation model is not incorporated into the EMs, the use of the hot assembly vapor as a heat sink for the hot spot during refill will be conservative.

Demonstration of Fuel Temperature Distributions and Effects

To determine the appropriate fuel temperature distributions and assure a conservative prediction during refill, the following steps are required:

Fuel Temperature Distribution:

1. Determine the number and position of fuel pins and pellets, which effectively control the hot pin fluid conditions.

2. Determine a probability density function for the uncertainty of the TACO3 fuel temperature prediction.
3. Determine, with 95 % confidence, the average uncertainty for the fuel pins and pellets identified.
4. Combine this uncertainty with the hot spot uncertainty to obtain the appropriate uncertainty for the region of the hot assembly surrounding the hot spot.

Refill Heat Transfer Comparison:

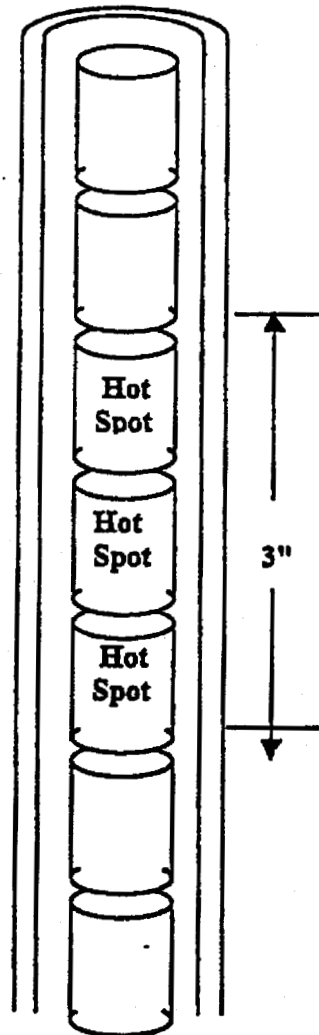
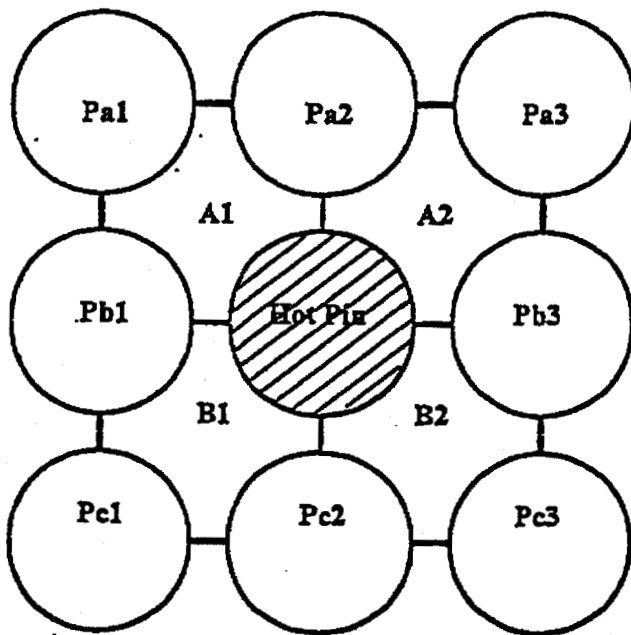
1. Determine the view factors for radiative heat transfer between the hot pellet and the surrounding fuel pins/pellets.
2. Probabilistically distribute the fuel pellet initial temperature uncertainty within the significant view factor positions.
3. Determine the 95 % confidence limit for average fuel temperature uncertainty.
4. Compare the resultant radiative energy transport to the average energy removal from the hot spot with the refined model.

Fuel Temperature Distribution - Based on Flow in Assembly

Determination of the number and position of fuel pellets that control the hot pin fluid conditions

As discussed, the modeling approach will consist of a hot pin (hot spot), modeled as a separate heat structure surrounded by the remainder of the hot assembly. Because the FTI evaluation models (RELAP5) do not consider rod-to-rod radiative heat transfer, the coupling between the hot assembly and the hot spot is through the fluid conditions at which heat transfer takes place. Further, because the hot assembly heat structure and fluid nodes, not a sub-region of the hot assembly, will be used to provide the coolant conditions for the hot spot, the hot assembly must be modeled to achieve fluid conditions representative of those with which the hot spot will be cooled. Therefore, it is necessary to establish the region of the fuel assembly around the hot spot within which the heat transfer takes place. Only pins and pellets within this region can be expected to influence the fluid condition surrounding the hot spot sufficiently to warrant inclusion in the determination of those conditions.

The following diagram of fuel assembly lattice positions is useful:



Considering the hot pin in the above drawing, the four fluid sub-channels A1, A2, B1, and B2

provide direct cooling. Realistically, the fluid sub-channels just removed from these four can be expected to mix well with the four and also be part of the cooling region. However, because expansion of the region would only lower the value of the resultant upper tolerance limit of the region uncertainty, the present calculation conservatively considers only the four sub-channels in contact with the hot pin. The pins that most govern the fluid conditions within these four sub-channels form a 9-pin array of the hot pin and its neighbors. Within the array the hot pin is fully involved, the laterally adjacent pins are only 1/2 exposed to the four flow sub-channels, and the diagonal pins only 1/4. Therefore, weighting factors, as given in the diagram below, have been assigned to the pins in determining the relative influence on the four fluid sub-channels.

1/4	1/2	1/4
1/2		1/2
1/4	1/2	1/4

Axially the cooling region will be limited to within a structural grid span which, for the purposes of this calculation, will be taken as approximately 1.5 feet (18 inches) in length. Further, only one half of that span plus one half of the length of the hot spot will be considered. This places the hot spot in the middle of the span that is a reasonable assumption and simplifies consideration of reverse flow situations. Theoretically the hot spot could be considered as having the height of one pellet (that in fact is done in establishing radiation cooling in the next section). However, a characteristic length of 3 inches, taken from the 10CFR50.46 Appendix K minimum rupture length definition, has frequently been applied within LOCA evaluations. Although 10CFR50.46 would probably not force a 3 inch height, such a length is not unreasonable. If the hot spot were not centered or if mid-span mixing grids (MSMGs) were incorporated, the hot spot would either see a larger number of pellets controlling the fluid temperature (high hot spot) or be closer to a mixer that would bring in coolant from other sub-channels (hot spot low, reverse flow hot spot high, or any MSMG application). In each case the effective mixing zone is increased, therefore, a half grid span mixing length, 10.5 inches ($15/2 + 3$), is acceptable or all hot spot positions and for MSMG assemblies.

The pellet height will be taken as 1/2 inch. Actual pellets vary in height from slightly greater than 0.4 inches to less than 0.5 inches. As will be shown in Section 4, the solution is not greatly affected by the actual length of the pellet and the approximation of a larger pellet height is reasonable and convenient. For the two grid span types considered, the following table provides the sets and weighting factors.

Number of pellets within each pin in region	21
Number of pellets within the Hot Spot	6
Number of pellets in Hot Pin to be probabilistically distributed	15
Number of pellets in at weighting factor of 1 and maximum uncertainty (11.5%)	6
Number of statistical pellets at weighting factor of 1	15
Number of statistical pellets at weighting factor of 1/2	84
Number of statistical pellets at weighting factor of 1/4	84

Thus, the set for which the fuel temperature uncertainty is to be determined comprises 15 pellets at full weighting, 84 pellets at 1/2 weighting, 84 pellets at 1/4 weighting, and 6 pellets forced to the TACO3 11.5 % uncertainty.

A recognized conservatism of the approach is that the existence of control rod guide tubes and the instrument tubes is ignored. Only a few of the 9 pin sets within the assembly do not include an instrument tube or a guide tube and none would be free of the influence of one of these. However, no guide tube or instrument tube is included for the evaluation.

Determination, with 95 % confidence, of the average uncertainty for the fuel pellets within the region surrounding the hot spot

To determine the average uncertainty for the group of pellets presented in Section 2.1 an EXCEL Workbook was created to randomly determine the uncertainty of each pellet in accordance with the TACO3 uncertainty distribution. By collecting groups of 15, 84, and 84 such pellets, a single possible set of uncertainties for the surrounding region is determined. The average uncertainty of each set is then determined through application of the weighting factors and the result stored in an array. The process is repeated 50,000 times with the average uncertainty of each set added to the array to give a large number of samples. The array is then ordered and the uncertainty values at selected percentage positions within the array reported. The value at the 95 % position is the uncertainty that bounds 95 % of the results and will be used to determine the average fuel temperature for the environs of the hot spot.

The result for the pellet distribution selection is that approximately 95 percent of the time the average uncertainty for fuel pellets in the environs surrounding the hot spot will be bounded by an uncertainty of 1.4 % including the TACO3 .5 % bias.

**Combination of surrounding pellet uncertainty with the hot spot 95 percent uncertainty
(Gives the appropriate uncertainty for the hot spot/hot pin region)**

The average uncertainty for the pellets in the region surrounding the hot spot was determined to be 1.4 percent. However, the region which determines the coolant properties by which the hot spot is cooled should also include the hot spot. These pellets will be considered to be at the upper 95%/95% tolerance level (11.5 %) for the TACO3 measured to predicted ratio. Combining these uncertainties and averaging gives a hot spot region initial fuel temperature uncertainty of:

$$\text{Hot Spot Region FTU} = \left[\frac{6 \cdot 1.115 + 78 \cdot 1.014}{84} \right] = 1.021$$

Thus, if the entire hot fuel assembly is initialized with an uncertainty of 2.1 percent, the fluid conditions, to the extent that they are influenced by the fuel pin thermal response, will be representative of the region immediately surrounding the hot spot during LOCA phases wherein flow induced cooling is significant (blowdown and reflood).

Refill Heat Transfer Comparison - Very Low Flow Conditions

For the proposed model, the hot pin and the hot assembly will be simulated at the same normalized power. Because both regions are cooled by the same coolant, the only difference between these regions then is comprised of the initial fuel temperature. From experience the difference in fuel temperatures during refill between pins initialized at different temperatures is about half the initial difference. A similar difference can be expected across the fuel pellet to its outer surface and within the cladding. Therefore, an approximate evaluation of the amount of energy transport possible by radiant heat transfer can be made based on the initial fuel temperatures for pellets within a region.

The first step in specifying the radiative heat transfer is to determine to what pins and pellets radiative heat transfer can take place and the relative importance of each. The next step is to probabilistically distribute pellets to these locations, generate a large number of possible distributions and compute the average effective fuel temperature uncertainty. The final step is to use the expected temperature differences in the radiative heat transfer model to compute a representative energy transport.

Determine the view factors for radiative heat transfer between the hot pellet and the surrounding fuel pins/pellets

An examination of the earlier diagram shows that direct radiative heat transfer from the hot pin can only take place to the pins in the immediate surrounding ring and selected pins of the next outer ring. Within the half quadrant formed by the hot pin (Pb2), Pb3 and Pa3, only a small window is available to pass radiant energy on to the next outer most pin lattice. Pa4 will intercept radiation passing through this window. Thus, it is only necessary to evaluate view factors for the pins at lattice points Pa3, Pb3, and Pa4 and apply symmetry around the hot pin. The following diagrams show the planner view angles occupied by each of these lattice points for both the Mark-B (15x15) assembly and the Mark-BW (17x17) assemblies. Although representative dimensions have been used, the dimensions do vary slightly within the design covered. However, as can be seen there is negligible difference between the view factors of the 15x15 and 17x17 assemblies and no significant difference is expected for the small dimensional changes possible from one design to another.

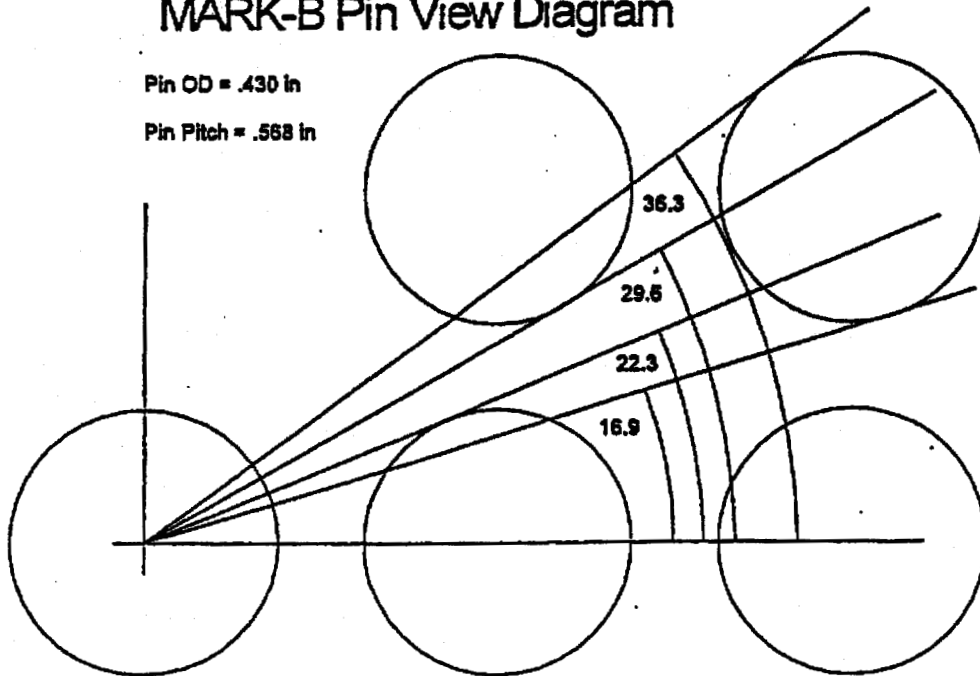
Using the Mark-BW assembly as the base, the three pins occupy the following view angles from the center of the hot pin within the half quadrant: the adjacent pin occupies 22.4°, the diagonal pin in the close ring 15.4°, and the diagonal pin in the far ring 7.2°. From these angles and the distance of the pin from the center of the hot spot, the base of the area occluded by a pin segment can be calculated. When the base is combined with the height of a pin segment and the resultant area projected to a sphere, the fraction of sphere area or the solid angle occupied by a given segment can be calculated. This sphere fraction or solid angle gives the relative importance of the segment within the radiative process.

To facilitate the calculations an occlusion factor defined as the portion of the pin seen by the hot spot is defined for each pin position. For the adjacent and the diagonal pins the factor is 1. For the diagonal pin in the far ring the factor is $7.2/(36.2-16.9) = 0.373$.

MARK-B Pin View Diagram

Pin OD = .430 in

Pin Pitch = .568 in

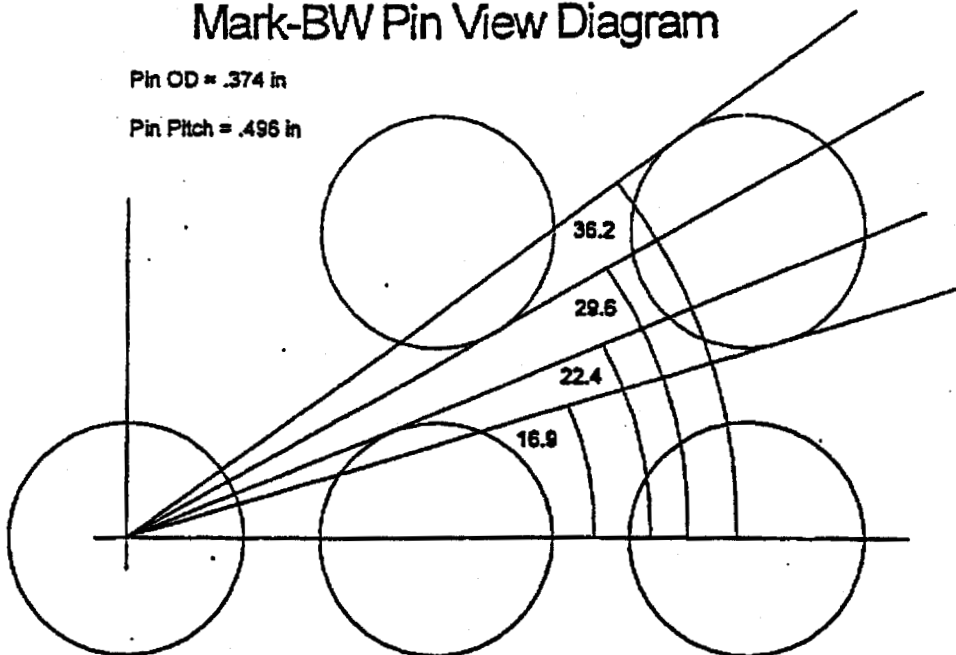


Dimensions from Reference 8, pages 5 and 11.

Mark-BW Pin View Diagram

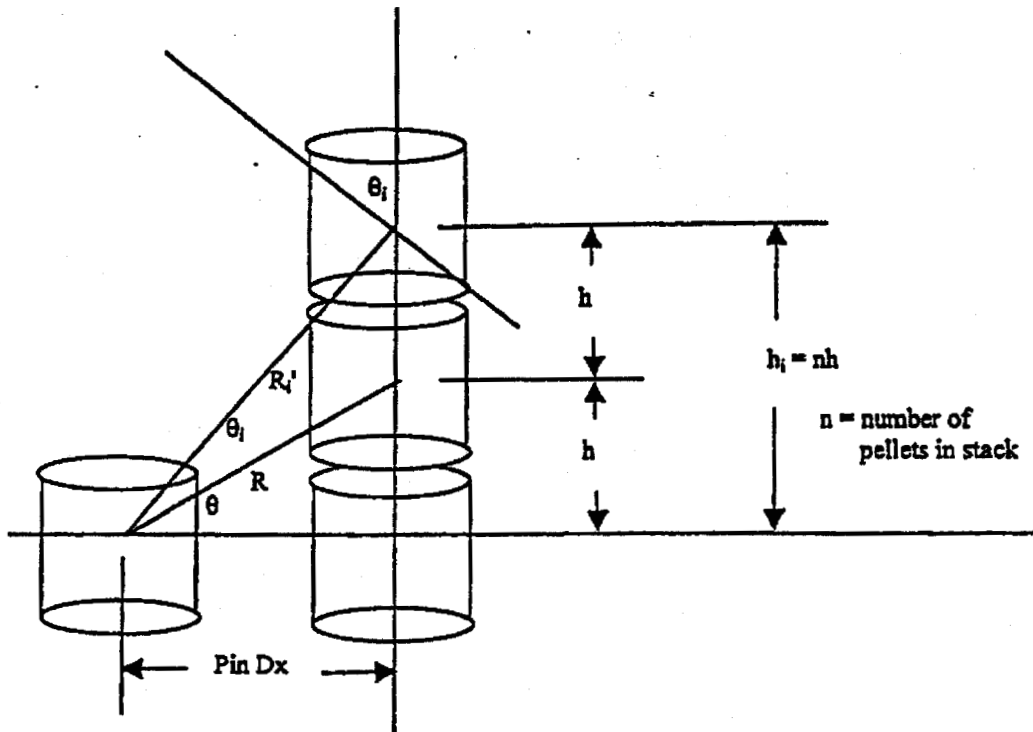
Pin OD = .374 in

Pin Pitch = .496 in



Dimensions from Reference 9, page 24.

The pin segments considered are one pellet in height because the fuel temperature uncertainty is assigned pellet by pellet. For convenience the pellet height is taken as 0.5 inches. Actual heights range between 0.4 and 0.5 inches. Using 0.5 minimizes the number of pellet segments to consider and increases, just slightly, the average uncertainty of the resulting sets. The height of each segment can be determined from the following diagram.



For radiation heat transfer, the pellet stacks run above and below the hot spot location because there is no preferential radiation direction. For the evaluation only one pellet is considered and the view areas or factor are evaluated as if radiation emitted from the center of that pellet. A more accurate determination would involve integration over the surface of the initiating pellet or pellets and, because the energy will be transported uniformly to the surface of the hot pin, not alter the results beyond the margins achieved. The area of sink is taken at the center line of each pellet and then projected onto a sphere at that radius. The solid angle or sphere surface fraction is computed from the projected area and a sphere area at the calculated radius (actually the calculation takes credit for symmetry and works on a hemisphere).

$$R_i = (\text{Pin } Dx^2 + h_i^2)^{0.5}$$

$$\text{Cos } \theta_i = \text{Pin } Dx / R_i$$

$$\text{Area of Segment} = h \cdot \text{Pin Diameter}$$

$$\text{Projected Area seen by the hot spot @ } R_i = \text{Cos } \theta_i \cdot \text{Area of Segment} \cdot \text{Occlusion Factor}$$

$$\text{Sphere Area @ } R_i = 4 \cdot \pi \cdot R_i^2$$

Fraction of Sphere @ R_i = Relative View Factor = Projected Area @ R_i / Sphere Area @ R_i

This development has been placed in the XL workbook. Each of the 3 pin positions are evaluated separately and then combined in a summary sheet. The summary sheet also contains the grouping and averaging of the number of segments and their individual importance factors into 8 groups. Two of these groups have no members for the configurations studied herein and the group with the lowest importance is arbitrarily assigned a 0.0 average importance.

Applicability to Other Hot Spot Locations and to MSMG Designs

The evaluation performed places the hot spot in the middle of a normal grid span. If the hot spot is located above or the mid-plane of a grid span or if MSMGs were present the view of some of the fuel locations credited in this evaluation would be occluded by the closer grid or the MSMG. As will be shown only the very close neighbor pin positions are significant in determining the radiation heat transfer. Therefore, even if these locations were removed from the evaluation the result would not change appreciably. Further, the view would still be present except that it would now be occupied by an unheated structure, some kind of grid. This would undoubtedly result in an effective increase in radiative heat transport. Therefore, the central position is acceptable for the demonstration for all hot spot positions or for application to an MSMG design.

Probabilistically distribute the fuel pellet initial temperature uncertainty within the significant view factor positions

The relative importance for the pin segments that receive radiation from the hot pellet are:

Group	Number of Pin Segments/Pellets	Relative Importance
1	4	.0605
2	12	.0242
3	8	.0163
4	24	.0052
5	24	.0030

The group numbers have been revised to be consecutive. These groups are now assigned fuel temperature uncertainties randomly in accordance with the TACO3 uncertainty distribution to achieve a 95 % confidence limit the set average uncertainty. The pin segments that will receive radiation from the hot spot are evaluated and the hot spot is not a member of that group. Using the above table for input and setting the forced (hot spot) pellets to 0, the 95 % confidence level for the set average is 2.5 % fuel temperature uncertainty.

For the evaluations conducted herein, the fuel temperature uncertainty for all receptor regions will be considered

2.5 % (note that in the LOCA calculations a 3 % uncertainty is used for conservatism.)

Note should be made that some of the possible receptors, 520 of them, are not included. These receptors, however, have a low average uncertainty and if included would only decrease the uncertainty. Also the evaluation conducted is only for one pellet as the source while the hot spot is treated as 6 pellets. Each of these 6 will have a replication of the sink evaluated here in and

thus the same uncertainty result can be applied.

Compare the resultant radiative energy transport to the average energy removal from the hot spot with the revised model

To demonstrate that the model as implemented achieves a conservative solution during refill the heat flux actually achieved for a representative calculation is herein compared to that which would have been achieved with radiation heat transfer.

The following is a simplified equations for radiant heat transfer.

$$q = 0.172 \cdot A \cdot \left[\left(\frac{T_s}{100} \right)^4 - \left(\frac{T_r}{100} \right)^4 \right] \cdot e \cdot F_a \quad \text{and}$$

$$e = \frac{1}{\frac{1}{e_s} + \frac{1}{e_r} - 1} \quad ;$$

where	q	= heat flow from interior object, Btu/hr	
	A	= Area of source for an enclosed body	
	T _s	= Source temperature, R	
	T _r	= receptor temperature, R	
	e _s	= emissivity of source	
	e _r	= emissivity of receptor	
	F _a	= Geometric factor	= 1 for enclosed bodies

Within the core e_s = e_r ≈ 0.7 e = 0.54.

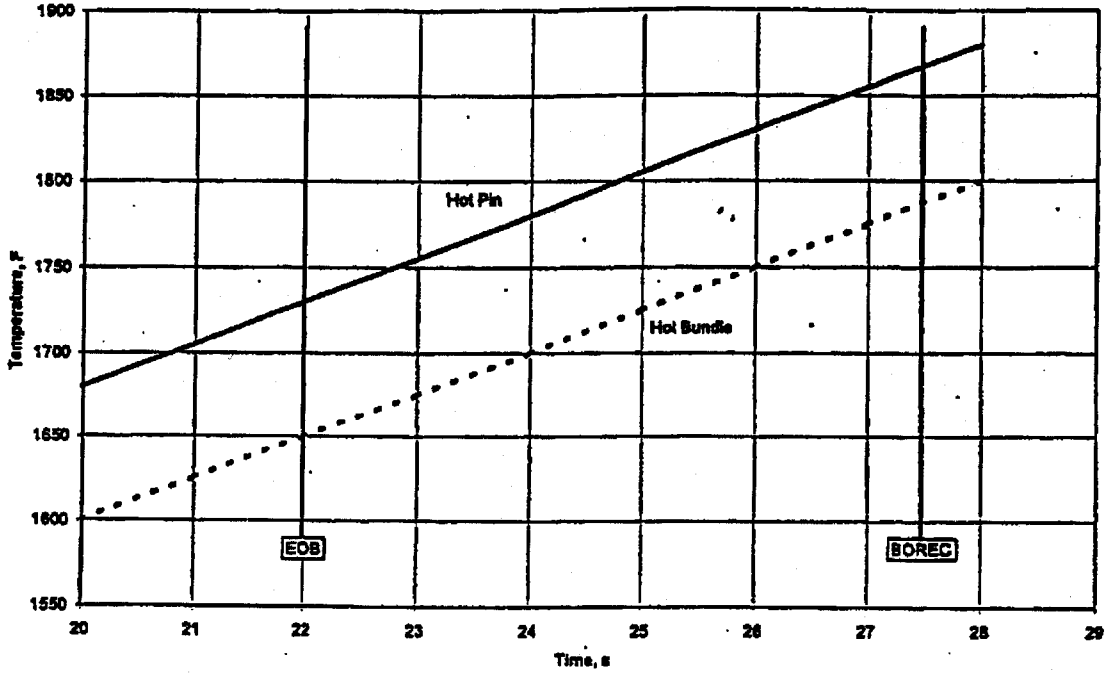
As in the determination of importance, we will assume a pellet height of 0.5 in, but because the reference run to which we will compare heat exchange is for a 15x15 design we will use the Mark-B pin diameter of 0.43 in.

The area of source "A" is therefore becomes 0.675 in² or 0.00469 ft².

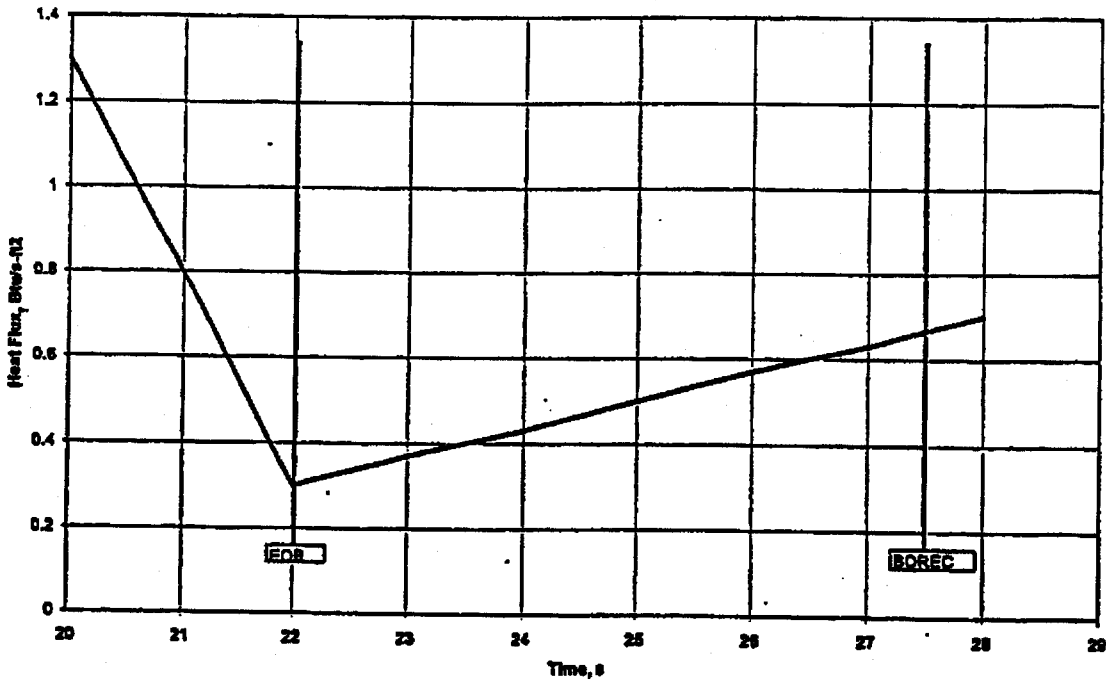
The following calculation was conducted with the proposed RELAP5 standalone hot pin model transferring energy to a hot bundle controlled fluid channel. The fuel temperature initialization of the hot bundle included 3 % uncertainty. The following figures provide the hot pin temperature and heat flux extracted from case "FDAF WJGF" at the position of the peak cladding temperature, level 6. Refill for this case was between 22 and 27.5 seconds.

Figures from "refill_radiation.xls"

Hot Pin & Hot Bundle Temperatures



Heat Flux from Hot Pin



From this data and the prior equations a workbook comparing the heat flow achieved during refill and that which would have been possible with a radiation heat transfer model was constructed. The output shows that heat fluxes achieved were conservative by a factor of 2 during refill.

radiation.xls Jennings worksheet

Radiation Heat Transfer Calculation

The data in columns a, b, d, l is from 32-5003556-00

Data Source

- Tsource Simplified characterization of hot bundle temperature transient on page 217 of 32-5003556-00
- Tsink Simplified characterization of hot rod temperature transient on page 207 of 32-5003556-00
- Heat Flux Simplified characterization of heat flux transient taken from plot of FDAFWJGF in 32-5003556-00
This plot is not recorded in 32-5003556-02 and is therefore reproduced herein as Figure 2

Length of Source	0.5 in	Diameter of Source	0.43 in	FA	1
Area of Source	0.675 in ²	Effective Emissivity	0.00489 ft ²	EOB	22 s
Emissivity	0.7		0.538	BOCR	27.5 s

Time s	Tsource, T _s		Tsink, T _r		$(T_s/100)^4 - (T_r/100)^4$	Radiation		Model		Ratio Model/Radiation
	F	R	F	R		Q _r Btu/Hr	Q _r Btu/s	Heat Flux Btu/s-ft ²	Q	
20	1680	2140	1600	2060	29646	12.9	0.00358	1.3	0.00610	1.704501
21	1705	2155	1625	2085	30717	13.3	0.00371	0.8	0.00375	1.012345
22	1730	2190	1650	2110	31814	13.8	0.00384	0.3	0.00141	0.366543
23	1755	2215	1675	2135	32936	14.3	0.00397	0.37	0.00174	0.438663
24	1780	2240	1700	2160	34085	14.8	0.00411	0.43	0.00202	0.490373
25	1805	2265	1725	2185	35260	15.3	0.00425	0.5	0.00235	0.5512
26	1830	2290	1750	2210	36462	15.8	0.00440	0.57	0.00267	0.607658
27	1855	2315	1775	2235	37690	16.4	0.00455	0.63	0.00296	0.649728
28	1880	2340	1800	2260	38946	16.9	0.00470	0.7	0.00328	0.698639

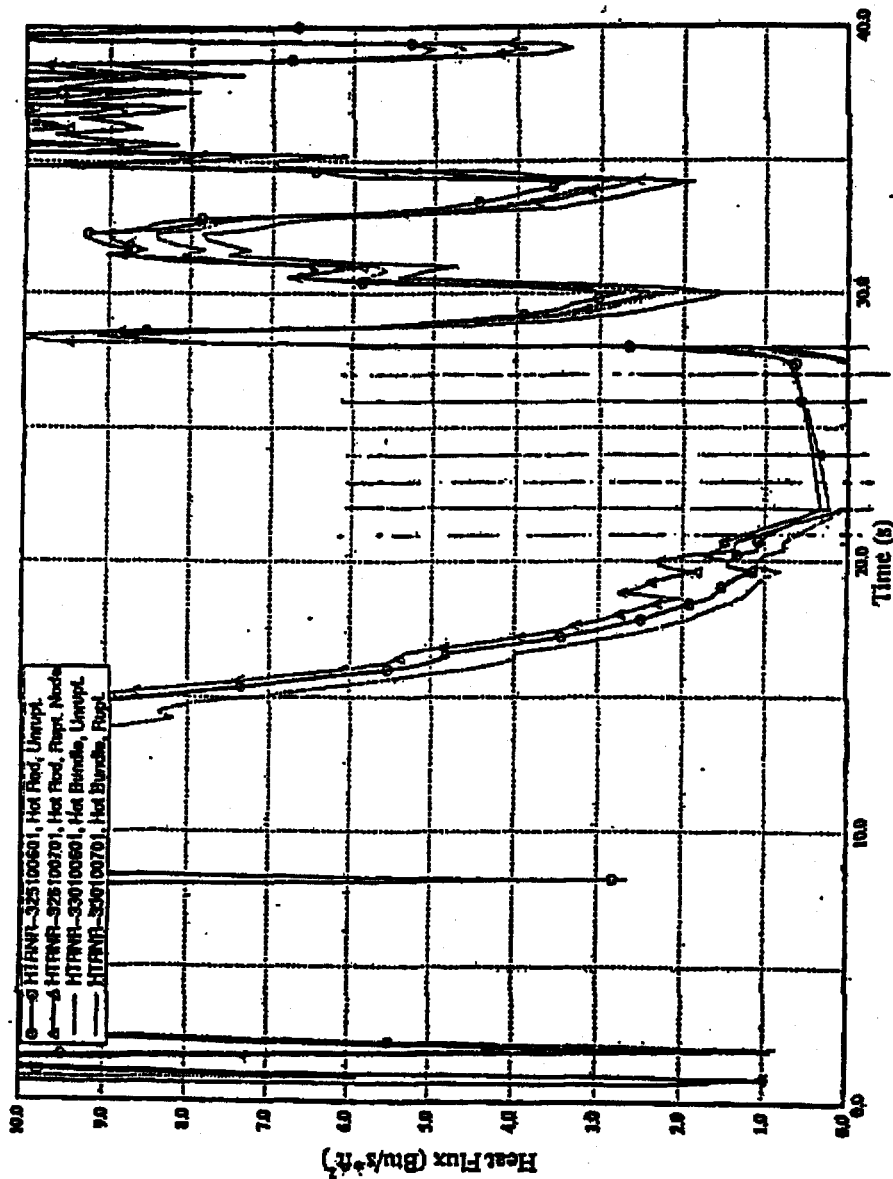
Average Net Hot Pellet Loss During Refill 22 - 27 s 0.004188

Plant Power	2772 MWT	Plant	2627856.0 Btu/s
Relative Power EOB	0.05	@ EOB	131392.8 Btu/s
# of FA	177	per FA	742.3 Btu/s
# of pins/FA	208	per pin	3.568905 Btu/s
Length of each pin	12		
# of segments in pin	288	per segment	0.012392 Btu/s
Local Peaking	2.5	peak segment	0.030980 Btu/s
Average Heat to sink	0.004188	Average heat to sink	0.00419 Btu/s
# sink pellets/source	3	To each sink pellet	0.00140

Ratio Radiation heat to generated heat 0.045

One item of concern is the effect that the real, radiative, heat flux would have on the temperatures of the hot bundle pins if the transfer actually took place. This would only be a concern if the radiation heat load was significant relative to other heat loads. At the bottom of the worksheet a comparison between radiation heat load on the sink pins to decay heat energy is made. This comparison shows that the radiation load is only about 5 % of the decay heat and from the model half of that 5 % was present. Therefore, the comparison is valid and the use of the standalone hot pin model is a conservative approximation of the heat transfer to be expected from the hot spot during the refill or other low flow periods.

Hot Rod Hot Spot Heat Flux from FDAFWJGF.



FDAFWJGF

RELAP5MOD2.8AW Ver. 2.3.0/HT

Conclusions

The FTI LOCA evaluation models are being upgraded to use a two region approach to determination of the heat transfer processes around the hot spot. The hot bundle is modeled as a heat structure with an associated coolant channel. The hot pin is modeled as a separate heat structure that uses the hot bundle coolant channel as its heat sink. This allows a more accurate determination of the coolant conditions for the hot pin. This calculation was to determine what the appropriate fuel temperature uncertainty was for the initialization of the hot bundle fuel. The method was to randomly distribute the fuel temperature uncertainty within the effective regions of the hot bundle according to the uncertainty distribution curve for the fuel temperature prediction, TACO3 code. 50,000 sets of such distributions were generated and sorted in order. The final distribution used was that which bounded 95 % of those sets. This provides assurance that the fluid temperatures achieved in the hot bundle are appropriately conservative for the evaluation of peak cladding temperature as far as the initialization of fuel temperature is concerned.

Heat transfer from the hot spot is governed by either convective transfer or radiant transfer during the course of an accident.

For convective heat transfer conditions a fuel temperature uncertainty of 2.1% for the hot bundle initialization is appropriate.

For radiative heat transfer a fuel temperature uncertainty of 2.5% for the hot bundle initialization is appropriate.

For pin average burnups below 40 GWd/mtU, the proposed model will use an uncertainty of 3 % to initialize the fuel temperature in the hot bundle and is therefore conservative beyond the 95 % level used to determine the appropriate values for initialization.

For pin average burnups greater than 40 GWd/mtU but less than 65 GWd/mtU, a bias will be added to both the hot pin and the hot bundle temperatures in accordance with the approval of TACO3 for those burnups.

March 23, 2001
FANP-01-915

Document Control Desk
U. S. Nuclear Regulatory Commission
Washington, DC 20555-0001

Subject: Additional Information on Use of the Void-Dependent Cross-Flow Model
Implemented in RELAP5/MOD2-B&W Code (BAW-10164, Rev. 4 P) for B&W-
Plant SBLOCA Applications Performed Using the BWNT LOCA EM (BAW-
10192PA)

Gentlemen:

The attached response addresses a verbal request for additional information from Frank Orr of the Nuclear Regulatory Commission. It was prepared to clarify use of a code automation feature in the new RELAP5/MOD2-B&W code topical revision (BAW-10164 Revision 4). This material clarifies the development and future use of the RELAP5/MOD2 void-dependent cross-flow model for SBLOCA applications performed for the B&W-designed plants in accordance with the BWNT LOCA Evaluation Model (EM) (BAW-10192 PA). This new code model automates the user implementation of the core cross-flow modeling approach used in this NRC-approved LOCA EM topical.

Some of the material in the attachment is considered Proprietary to Framatome ANP (FRA-ANP) as sworn by me as Vice President, Engineering and Licensing, FRA-ANP, presented as an enclosure within this submittal. All the proprietary material, which is enclosed in [brackets], is classified as categories "c" and "e" based on the FRA-ANP proprietary criteria given in the enclosure.

If clarification of any of the provided information is needed, please contact John Klingenfus at (804) 832-3294.

Very truly yours



R. W. Ganthner
Vice President
Engineering and Licensing

cc: Frank Orr/NRC
John Klingenfus, OF53
R. J. Schomaker, OF57
J. R. Biller, OF53

AFFIDAVIT OF RAYMOND W. GANTHNER

- A. My name is Raymond W. Ganthner. I am Vice-President of Engineering & Licensing for Framatome ANP, Inc. (FRA-ANP), and as such, I am authorized to execute this Affidavit.
- B. I am familiar with the criteria applied by FRA-ANP to determine whether certain information of FRA-ANP is proprietary and I am familiar with the procedures established within FRA-ANP to ensure the proper application of these criteria.
- C. In determining whether an FRA-ANP document is to be classified as proprietary information, an initial determination is made by the Unit Manager, who is responsible for originating the document, as to whether it falls within the criteria set forth in Paragraph D hereof. If the information falls within any one of these criteria, it is classified as proprietary by the originating Unit Manager. This initial determination is reviewed by the cognizant Section Manager. If the document is designated as proprietary, it is reviewed again by me to assure that the regulatory requirements of 10 CFR Section 2.790 are met.
- D. The following information is provided to demonstrate that the provisions of 10 CFR Section 2.790 of the Commission's regulations have been considered:
- (i) The information has been held in confidence by FRA-ANP. Copies of the document are clearly identified as proprietary. In addition, whenever FRA-ANP transmits the information to a customer, customer's agent, potential customer or regulatory agency, the transmittal requests the recipient to hold the information as proprietary. Also, in order to strictly limit any potential or actual customer's use of proprietary information, the substance of the following provision is included in all agreements entered into by FRA-ANP, and an equivalent version of the proprietary provision is included in all of FRA-ANP's proposals:

AFFIDAVIT OF RAYMOND W. GANTHNER (Cont'd.)

"Any proprietary information concerning Company's or its Supplier's products or manufacturing processes which is so designated by Company or its Suppliers and disclosed to Purchaser incident to the performance of such contract shall remain the property of Company or its Suppliers and is disclosed in confidence, and Purchaser shall not publish or otherwise disclose it to others without the written approval of Company, and no rights, implied or otherwise, are granted to produce or have produced any products or to practice or cause to be practiced any manufacturing processes covered thereby.

Notwithstanding the above, Purchaser may provide the NRC or any other regulatory agency with any such proprietary information as the NRC or such other agency may require; provided, however, that Purchaser shall first give Company written notice of such proposed disclosure and Company shall have the right to amend such proprietary information so as to make it non-proprietary. In the event that Company cannot amend such proprietary information, Purchaser shall prior to disclosing such information, use its best efforts to obtain a commitment from NRC or such other agency to have such information withheld from public inspection.

Company shall be given the right to participate in pursuit of such confidential treatment."

AFFIDAVIT OF RAYMOND W. GANTHNER (Cont'd.)

- (ii) The following criteria are customarily applied by FRA-ANP in a rational decision process to determine whether the information should be classified as proprietary. Information may be classified as proprietary if one or more of the following criteria are met:
- a. Information reveals cost or price information, commercial strategies, production capabilities, or budget levels of FRA-ANP, its customers or suppliers.
 - b. The information reveals data or material concerning FRA-ANP research or development plans or programs of present or potential competitive advantage to FRA-ANP.
 - c. The use of the information by a competitor would decrease his expenditures, in time or resources, in designing, producing or marketing a similar product.
 - d. The information consists of test data or other similar data concerning a process, method or component, the application of which results in a competitive advantage to FRA-ANP.
 - e. The information reveals special aspects of a process, method, component or the like, the exclusive use of which results in a competitive advantage to FRA-ANP.
 - f. The information contains ideas for which patent protection may be sought.

AFFIDAVIT OF RAYMOND W. GANTNER (Cont'd.)

The document(s) listed on Exhibit "A", which is attached hereto and made a part hereof, has been evaluated in accordance with normal FRA-ANP procedures with respect to classification and has been found to contain information which falls within one or more of the criteria enumerated above. Exhibit "B", which is attached hereto and made a part hereof, specifically identifies the criteria applicable to the document(s) listed in Exhibit "A".

- (iii) The document(s) listed in Exhibit "A", which has been made available to the United States Nuclear Regulatory Commission was made available in confidence with a request that the document(s) and the information contained therein be withheld from public disclosure.
- (iv) The information is not available in the open literature and to the best of our knowledge is not known by General Electric, Westinghouse-CE, or other current or potential domestic or foreign competitors of FRA-ANP.
- (v) Specific information with regard to whether public disclosure of the information is likely to cause harm to the competitive position of FRA-ANP, taking into account the value of the information to FRA-ANP; the amount of effort or money expended by FRA-ANP developing the information; and the ease or difficulty with which the information could be properly duplicated by others is given in Exhibit "B".

E. I have personally reviewed the document(s) listed on Exhibit "A" and have found that it is considered proprietary by FRA-ANP because it contains information which falls within one or more of the criteria enumerated in Paragraph D, and it is information which is customarily held in confidence and protected as proprietary information by FRA-ANP. This report

AFFIDAVIT OF RAYMOND W. GANTHNER (Cont'd.)

comprises information utilized by FRA-ANP in its business which affords FRA-ANP an opportunity to obtain a competitive advantage over those who may wish to know or use the information contained in the document(s).



RAYMOND W. GANTHNER

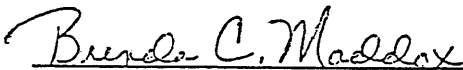
State of Virginia)) SS. Lynchburg
City of Lynchburg)

Raymond W. Ganthner, being duly sworn, on his oath deposes and says that he is the person who subscribed his name to the foregoing statement, and that the matters and facts set forth in the statement are true.



RAYMOND W. GANTHNER

Subscribed and sworn before me
this 23rd day of March 2001.



Notary Public in and for the City
of Lynchburg, State of Virginia.

*It was commissioned a notary public
as Brenda C. Cardona.*

My Commission Expires July 31, 2003

EXHIBITS A & B

EXHIBIT A

Response to a Verbal Request for Additional Information on Use of the Void-Dependent Cross-Flow Model Implemented in RELAP5/MOD2-B&W Code (BAW-10164, Rev. 4P) for B&W-Plant SBLOCA Applications Performed Using the BWNT LOCA EM (BAW-10192PA).

EXHIBIT B

The above listed document contains information, which is considered Proprietary in accordance with Criteria c and e of the attached affidavit.

Attachment

**Response to a Verbal Request for Additional Information
on the RELAP5/MOD2-B&W Void-Dependent Core Cross-Flow Model
Used in B&W-Plant SBLOCA Applications**

Table of Contents

1.	<i>Background and Introduction</i>	2
2.	<i>Void-Dependent Cross-Flow Model</i>	3
3.	<i>Summary and Conclusion</i>	6

List of References

1. FTI Topical Report BAW-10192PA-00, "BWNT LOCA – BWNT Loss-of-Coolant Accident Evaluation Model for Once-Through Steam Generator Plants", June 1998.
2. FTI Topical Report BAW-10164PA-03, "RELAP5/MOD2-B&W An Advanced Computer Program for Light Water Reactor LOCA and Non-LOCA Transient Analysis," July 1996.
3. FCF Topical Report BAW-10227P-A, "Evaluation of Advanced Cladding and Structural Material (M5) in PWR Reactor Fuel," February 2000.

1. Background and Introduction

Framatome Advanced Nuclear Power (FRA-ANP), previously Framatome Technologies Inc., has used the BWNT LOCA Evaluation Model (EM) documented in BAW-10192P-A (Reference 1) for small break loss of coolant accident (SBLOCA) licensing analyses for the B&W-designed 177-fuel assembly lowered-loop (177-FA LL) and raised-loop (177-FA RL) plants. These analyses have been performed in accordance with the EM descriptions and they have complied with the EM and code limitations and restrictions imposed via the NRC safety evaluation reports (SERs). During the course of analysis, FRA-ANP has discovered that the SBLOCA core cross-flow form loss modeling requirements are cumbersome for the analysts to use when analyzing the spectrum of SBLOCA transients with core uncovering. FRA-ANP has remedied these problems by standardizing the current EM cross-flow implementation methods via RELAP5/MOD2-B&W code automation improvements. The extent of the FRA-ANP code improvements and plans for using this improved implementation are provided to the NRC through this documentation.

The EM describes the philosophy and physical cross-flow modeling approach used in SBLOCA analyses (Reference 1, Volume II, Section A.4). A high cross-flow resistance is used in the pool region to stabilize the void gradients or mixture levels between the hot and average channels. This pool void gradient results in a slightly higher hot channel

mixture level than that of the average core. Above the mixture level, the cross-flow resistance from the hot-to-average channel is conservatively reduced to allow steam flow diversion out of the hot channel. The average-to-hot channel resistance is increased in the steam region to restrict the flow of cooler steam from the average channel. The cross-flow resistance model that represents this stated approach is shown as the "Base Case" model in Table A-3 of the SBLOCA EM (Reference 1). Demonstration cases provided characteristic behavior when this segmented flow resistance model is used with low resistances in the upper core region and a high resistance in the lower core or pool region. Section A.4 of the SBLOCA EM (Volume II) states that the discontinuity in the resistances must be near or below the elevation of the minimum core mixture level obtained in the analysis. If the user specifies the transition elevation between the wrong two volumes, then an iteration on the cross-flow resistance input model might be required. This iteration is both burdensome to the user and it can introduce a variation of roughly +/- 40 F in the maximum peak clad temperature (PCT) prediction related to the degree of conservatism that the user imposed via specification of the elevation of the cross-flow resistance step change. This type of variation has been noted in SBLOCA analyses with limiting PCTs in the 1300 to 1450 F range for B&W-designed plants.

FRA-ANP reviewed the EM modeling philosophy and devised a simple code model that could be made responsive to the SBLOCA cross-flow resistance model requirements and change dynamically with the actual mixture levels. This variable resistance model will eliminate any potential user iteration associated with the specification of the fixed cross-flow resistance change. This standardization of the resistance modeling will also eliminate any PCT variations associated with the user's specification of the fixed-resistance transition elevation.

The new RELAP5/MOD2-B&W code (Reference 2) cross-flow model option alters the cross-flow resistance based on the local volume upstream conditions. At void fractions less than the pool region cutoff, the high cross-flow loss coefficients are used. At void fractions greater than the steam region cutoff, the low form loss coefficients are used. A smoothing region with linear interpolation between the two cutoff values is included to smooth the transition between the two resistance factors. This improved implementation method remains consistent with current EM discussions, therefore it is not considered to be an EM change. Nonetheless, FRA-ANP has notified the NRC of the implementation method differences, because of the slight alteration of the interpolation region and code automation of the cross-flow resistance model. The RELAP5/MOD2-B&W cross-flow code formulation changes were included in the documentation provided in the Revision 4 code updates supplied with the M5 licensing documentation in Appendix K of Reference 3. That information, with the void fractions at which the transitions occur, clearly defines the model that Framatome ANP will use in BAW-10192 SBLOCA EM applications.

2. Void-Dependent Cross-Flow Model

The basic principles described in Section A.4 of the SBLOCA EM volume describe a relationship between the cross-flow form loss and the upstream fluid conditions. If the upstream fluid is representative of the pool region (i.e. below the mixture level), then the

resistance should be high. Use of the higher pool resistance supports the variations in the mixture region void fraction related to power differences between the hot and average channels. These resistances are reduced [c, e] above the top of the mixture region to allow for steam flow diversion out of the hot channel. The steam region resistance factor from the average-to-hot channel is increased [c, e] to restrict steam flow from the average-to-hot channel. The pool or steam region can be defined within the code via use of an upstream volume void fraction. Based on simple changes in code logic, the cross-flow resistance was modified based on the upstream void fraction for any junction that is designated as a void-dependent cross-flow junction.

The new code option allows the user to specify the core cross-flow junctions as void-dependent cross-flow paths via a specialized flag on the junction-input cards. The user also provides the void fractions that define the steam region and the pool region. The pool region cross-flow resistance is specified for the junctions. If the upstream volume void fraction is below the pool region void fraction, then the high void fraction form loss factor [c, e] is unmodified. If the upstream volume void fraction is above the steam region void fraction, then the hot-to-average pool resistance is reduced [c,e] to the steam form loss [c, e] for the hot-to-average resistance. A lower multiplicative factor [c, e] is used to adjust the pool resistance value to the average-to-hot steam form loss [c, e]. All of these form loss coefficients are unmodified from the original fixed cross-flow EM modeling concepts. The only difference with the void-dependent model implementation is that a smoothing integral is used when the void fraction falls between the pool and steam void fractions. A linear interpolation on upstream void fraction will be used to define the multiplicative adjustments for both the forward and reverse form loss coefficients under these conditions.

This new code option forces the cross-flow resistance to be similar to that described in the EM at the time of minimum core inventory. It has the added benefit of providing a smooth transition from the higher pool region resistance to that of the steam region both during both the uncovering and refill phases. Without this new code option, the user was limited to a fixed cross-flow resistance specification at a predefined core elevation. This fixed modeling could be modified via code restarts in the transient, although this approach provides another way that the user can affect the overall calculation of PCT.

The new void-dependent user-input options for the pool void fraction cutoff value are obtained by observing the maximum pool-region void fraction in the worst break size range for the SBLOCA spectrum analyses. Generally, the highest PCT is predicted for B&W-plant analyses when the break size is between 0.024 and 0.15 ft². The highest core void fractions in the pool regions vary [c, e] for these break sizes, with the void fraction increasing with break size. The pool-region cutoff void fraction [c, e] will cover all of these break sizes and should be reasonable for the typically non-limiting analyses at larger break sizes. In fact, its use on the largest SBLOCAs will likely reduce the cross-flow over the entire channel, causing the PCTs to increase slightly for these break sizes. These breaks should remain non-limiting, however, because the uncovering duration is short.

The steam-region void-fraction cutoff should be set close to 1.0 during the core-uncovering phase. Consideration of the refill phase suggests that the steam-region void-fraction cutoff should be slightly less than 1.0 to prevent an increase in the resistance before there is a mixture level re-established in the volume. Accordingly, a void fraction [c, e] was selected as a reasonable value that is appropriate for both the initial uncovering and refill periods for all SBLOCA transients.

In equation form, the form losses are defined for the positive flow direction (forward flow) from the average channel to the hot channel (i.e. Volume K is the average channel volume, Volume L is the hot channel volume).

Void fraction Check		Form Loss Factor	For Flow From
$\alpha_g(K) \leq \alpha_{pool}$	Then,	$K_{forward} = K_{forward\ input}$ [c, e]	average-to-hot
$\alpha_g(L) \leq \alpha_{pool}$	Then,	$K_{reverse} = K_{reverse\ input}$ [c, e]	hot-to-average
$\alpha_g(K) \geq \alpha_{stm}$	Then,	$K_{forward} = K_{forward\ input} * M_{forward-stm}$ [c, e]	average-to-hot
$\alpha_g(L) \geq \alpha_{stm}$	Then	$K_{reverse} = K_{reverse\ input} * M_{reverse-stm}$ [c, e]	hot-to-average
$\alpha_{pool} \leq \alpha_g(K) \leq \alpha_{stm}$	Then,	$K_{forward} = K_{forward\ input} * M_{forward-stm}^{Interpolated}$	average-to-hot
$\alpha_{pool} \leq \alpha_g(L) \leq \alpha_{stm}$	Then,	$K_{reverse} = K_{reverse\ input} * M_{reverse-stm}^{Interpolated}$	hot-to-average

where

$$M_{forward-stm}^{Interpolated} = 1 - (1 - M_{forward-stm}) * \left[\frac{\alpha_{pool} - \alpha_g(K)}{\alpha_{pool} - \alpha_{stm}} \right],$$

$$M_{reverse-stm}^{Interpolated} = 1 - (1 - M_{reverse-stm}) * \left[\frac{\alpha_{pool} - \alpha_g(L)}{\alpha_{pool} - \alpha_{stm}} \right],$$

[c, e] (average-to-hot)

[c, e] (hot-to-average)

[c, e]

[c, e]

3. Summary and Conclusion

The void-dependent cross-flow option implemented in RELAP5/MOD2-B&W Revision 4 standardizes the SBLOCA cross-flow modeling approach used in BAW-10192PA. It is an improved code implementation that was developed from the original EM methods with a resistance model that responds mechanistically to the actual core mixture level. It preserves the three major conservatisms that were targeted or imposed by the EM cross-flow model selections. These conservatisms entailed (1) limiting the difference in the hot and average mixture levels to roughly one volume height or less, (2) forcing a low cross-flow resistance in the uncovered or steam region to maximize flow diversion out of the hot channel, and (3) restricting the average-to-hot channel steam region flow. These three conservatisms are preserved with the new void-dependent model.

A small set of limiting SBLOCA plant cases have been run with the new void-dependent cross-flow option, and these have been compared with the original fixed-resistance method application results. The PCTs have increased in some cases and decreased in others, but the general variation in PCTs is primarily influenced by the degree of conservatism imposed by the user-specified fixed cross-flow resistance step change location in the original application. The representative plant cases examined showed that the void-dependent cross-flow model PCT falls within the PCT range that can be produced by different user-selected locations of the fixed cross-flow resistance model. Therefore, based on this examination of these current SBLOCA application cases, FRA-ANP has concluded that this new void-dependent standardization will not provide any significant increase or decrease in the BAW-10192PA calculated SBLOCA PCTs for limiting SBLOCA analyses performed with a loss of offsite power (LOOP). Therefore, the void-dependent model will be included in future B&W-designed EM applications performed with Reference 1.

The new model has the added benefit in that it is responsive to faster transients with dynamic mixture level transitions and applications such as those with manual reactor coolant pump trip within the first several minutes after loss of subcooling margin. These applications, which are being performed as a result of Preliminary Safety Concern (PSC) 2-00, were not considered when the fixed resistance model was developed. The void dependent cross-flow model is well suited for applications such as these; therefore it was used for the PSC 2-00 analyses that will be submitted to the NRC in April, 2001.

The void-dependent cross-flow model with the inputs prescribed in this letter represents an automated form of the fixed core cross-flow resistance model that the NRC approved for use for SBLOCA applications with BAW-10192PA. The automated model retains the prescribed EM conservatisms from the original SBLOCA EM approach and standardizes the PCT predictions for LOOP or no LOOP transients for B&W-designed plants. Therefore, FRA-ANP intends to use the void-dependent model in all future SBLOCA applications performed with the BAW-10192PA EM.

This page is intentionally left blank.



June 15, 2001
NRC:01:026

Document Control Desk
ATTN: Chief, Planning, Program and Management Support Branch
U.S. Nuclear Regulatory Commission
Washington, D.C. 20555-0001

NRC Review and Approval of BAW-10164P Revision 4, RELAP5/MOD2-B&W, An Advanced Computer Program for Light Water Reactor LOCA and Non-LOCA Transient Analysis

Framatome ANP (FRA-ANP) Lynchburg maintains two NRC-approved large break loss-of-coolant accident (LBLOCA) evaluation models (EMs). The EM described in BAW-10168P-A, Revision 3, December 1996, applies to recirculating steam generator (RSG) plants and the EM described in BAW-10192P-A, Revision 0, June 1998, is applied to B&W plants. These EMs use the RELAP5 code described in BAW-10164P-A Revision 3.

The EMs are being modified as described in the attachment. The modifications have been under review by the NRC for the past year. The purpose of the attachment to this letter is to summarize the changes and the documentation provided to the NRC to support the changes. A copy of this letter and the enclosures has been provided directly to those on distribution.

The NRC has been requested to approve these changes by issuance of a Safety Evaluation for the report BAW-10164 Revision 4. Framatome ANP would appreciate completion of the NRC review of these changes and the issuance of the Safety Evaluation by July 31, 2001.

Framatome ANP considers some of the information contained in the attachment and enclosures to this letter to be proprietary. The proprietary information in the attachment is enclosed within brackets []. As required by 10 CFR 2.790(b) an affidavit is enclosed to support the withholding of this information from public disclosure.

Very truly yours,

James F. Mallay, Director
Regulatory Affairs

Enclosure

cc: F. M. Akstulewicz (w/enclosures)
S. N. Bailey (w/enclosures)
F. Orr (w/enclosures)

Framatome ANP Richland, Inc.

2101 Horn Rapids Road
Richland, WA 99352

Tel: (509) 375-8100
Fax: (509) 375-8402

The modeling changes are 1) subdivision of the hot bundle modeling and hot pin versus hot bundle fuel temperature uncertainty, 2) void dependent cross flow model for small breaks, and 3) implementation of the BEACH blockage limitation.

Subdivision of the Hot Bundle Modeling and Hot Pin versus Hot Bundle Fuel Temperature Uncertainty

The modeling of the hot rod/hot assembly is broken into two heat structures to improve the simulation of the LOCA cooling process. The changes apply to the large break LOCA EMs for both RSG and the B&W plants.

References 1, 2, and 3 were provided to the NRC to describe this modification. The previously provided references are enclosed with this letter to facilitate the NRC review. A copy of these references has been provided directly to Frank Akstulewicz.

RELAP5 Changes for This Modification

In order to model the hot pin and the hot assembly as separate heat structures, an option was added to RELAP5/MOD2-B&W to specify the pin channel (rod) as a primary or supplemental channel. The supplemental pin capability allows multiple pin channels within a single hydrodynamic fluid channel (i.e., a fuel assembly, for example). The changes to RELAP5/MOD2-B&W are documented in Revision 4 of RELAP5/MOD2-B&W topical report (Reference 1) on the following pages.

Page 2.3-26, Item 2

Page 2.3-27

Pages 2.3-46, 2.3-46.1 and 2.3-46.2

All changes are identified with a vertical line in the left or right margin

Further discussion of these changes is given in Section II of Reference 2.

Reactor Modeling Changes

These changes are documented in Reference 2, which describes the application of this model in the RSG and B&W plant EMs. Reference 2 describes the division of the heat structures simulating the hot rod and hot assembly, the calculation of steady state volume averaged fuel temperatures for each, and the sensitivity of the changes for both RSG and B&W designs.

The average core heat structure will be initialized with no uncertainty. The hot assembly heat structure will be initialized at a statistical-based uncertainty providing 95 percent confidence in 95 percent of all instances that the average fuel temperature in the assembly is bounded. The maximum 95/95, fuel temperature uncertainty will be imposed only on the hot rod heat structure. (Note that a correction to TACO3 predictions at high burnup will still be applied.)

Additional supporting information describing the calculation of the initial fuel temperature within the hot assembly was provided in Reference 3.

Void-Dependant Cross Flow Model for Small Breaks

The cross flow resistance model used within the core simulation for small break evaluations of B&W-designed plants is automated. The changes apply only to the small break LOCA EMs for the B&W plants.

This revised model is described in more detail in Reference 4. The change is also described briefly in BAW-10164P Revision 4 (Reference 1). A copy of the previously provided Reference 4 is enclosed with this letter to facilitate the review.

RELAP5 Changes for This Modification

The void-dependant cross flow model is an automation of the procedure outlined in Section A.4 of the BWNT LOCA evaluation model BAW-10192P-A, Revision 0, June 1998. Different cross flow resistances are required above and below the mixture height for the proper simulation of small break core uncovering. The current procedure is manual alteration of the resistances during the transient using code restarts. The automation divides the core region into three segments: a mixture region where the void fraction is less than the user input value $\alpha_{min-Kcross}$; a steam or in the misty region where the void fraction is larger than the user input value $\alpha_{max-Kcross}$; and a transition zone where the void fraction is between the two user input values. User input values for the K-factors and multipliers are selected so that the resulting form loss coefficients in the mixture region and in the steam or misty region will be the same as those specified in BAW-10192. In the transition zone, linear interpolation is used to calculate the form loss coefficients. A void fraction of [c,e] typically represents the slug-to-annular flow transition boundary and therefore it is used as $\alpha_{min-Kcross}$. A void fraction of about [c,e] is a reasonable value for the lower boundary of the mist flow regime and therefore it is used as $\alpha_{max-Kcross}$. The changes to RELAP5/MOD2-B&W are documented in Revision 4 of the RELAP5/MOD2-B&W topical report (Reference 1) on the following pages.

Pages 2.1-126.1 and 2.1-126.2

All changes are identified with a vertical line in the left or right margin.

Reactor Modeling Changes

No changes to the reactor modeling are required because this is an automation of a technique already described in the approved BWNT LOCA evaluation model, BAW-10192. Although the modeling is general in its applicability, Framatome ANP only intends to apply it within the BWNT evaluation model for small breaks.

Implementation of the BEACH Blockage Limitation

The third change is the implementation of an SER limitation on the amount of blockage that can be credited in evaluating rupture induced cooling effects. The SER for the BEACH topical report

Revision 2 (this SER is documented on pages 5-226 through 5-230 of BAW-10166P-A, Revision 4, February 1996) limits the credited blockage to 60 percent of the flow channel. This limitation was previously verified by the user. The code logic that calculates rupture induced cooling effects was modified by limiting the maximum value of the credited blockage to 60 percent to assure implementation of the limit.

This modification is described in Reference 1.

RELAP5 Changes for This Modification

The logic changes to implement the limitation automatically are described in Revision 4 of the RELAP5/MOD2-B&W topical report (Reference 1) on the following pages.

Pages 2.1-126.1 and 2.1-126.2

All changes are identified with a vertical line in the left or right margin.

- Ref.: 1. BAW-10164P Revision 4, *RELAP5/MOD2-B&W An Advanced Computer Program for Light Water Reactor LOCA and Non-LOCA Transient Analysis*, September 1999. This reference was provided with the letter GR99-194.doc, September 24, 1999.
- Ref.: 2. Letter, J. J. Kelley (Framatome Technologies) to Document Control Desk (NRC), "Modeling Refinements to Framatome Technologies' RELAP-5 Based, Large Break LOCA Evaluation Models-BAW-10168 for Non-B&W-Designed, Recirculating Steam Generator Plants and BAW-10192 for B&W-Designed, Once-Through Steam Generator Plants," FTI-00-551, February 29, 2000.
- Ref.: 3. Letter, J. J. Kelley (Framatome Technologies) to Document Control Desk (NRC), "Additional Information on Modeling Updates to Framatome Technologies' RELAP-5 Based, Large Break LOCA Evaluation Models-BAW-10168 for Non-B&W-Designed, Recirculating Steam Generator Plants and BAW-10192 for B&W-Designed, Once-Through Steam Generator Plants," FTI-00-2225, September 5, 2000.
- Ref.: 4. Letter, R. W. Ganthner (Framatome Technologies) to Document Control Desk (NRC), "Additional Information on Use of the Void-Dependent Cross-Flow Model Implemented in RELAP5/MOD2-B&W Code (BAW-10164, Rev. 4 P) for B&W-Plant SBLOCA Applications Performed Using the BWNT LOCA EM (BAW-10192PA), FANP-01-915, March 23, 2001.

6. The following criteria are customarily applied by FRA-ANP to determine whether information should be classified as proprietary:

- (a) The information reveals details of FRA-ANP's research and development plans and programs or their results.
- (b) Use of the information by a competitor would permit the competitor to significantly reduce its expenditures, in time or resources, to design, produce, or market a similar product or service.
- (c) The information includes test data or analytical techniques concerning a process, methodology, or component, the application of which results in a competitive advantage for FRA-ANP.
- (d) The information reveals certain distinguishing aspects of a process, methodology, or component, the exclusive use of which provides a competitive advantage for FRA-ANP in product optimization or marketability.
- (e) The information is vital to a competitive advantage held by FRA-ANP, would be helpful to competitors to FRA-ANP, and would likely cause substantial harm to the competitive position of FRA-ANP.

7. In accordance with FRA-ANP's policies governing the protection and control of information, proprietary information contained in this Document has been made available, on a limited basis, to others outside FRA-ANP only as required and under suitable agreement providing for nondisclosure and limited use of the information.

8. FRA-ANP policy requires that proprietary information be kept in a secured file or area and distributed on a need-to-know basis.

9. The foregoing statements are true and correct to the best of my knowledge,
information, and belief.

John S. Holm

SUBSCRIBED before me this 15th
day of June, 2001.

Valerie W. Smith

Valerie W. Smith
NOTARY PUBLIC, STATE OF WASHINGTON
MY COMMISSION EXPIRES: 10/10/04



Note on Attachments

References 1, 2, 3, and 4 were provided to the NRC as part of the letter dated June 15, 2001. Each of these references were also submitted individually and have been included in this document on pages 5-404 through 5-462, 5-463 through 5-493, 5-494 through 5-510, and 5-511 through 5-524 respectively.

Rev. 4
9/99

5.9 Revision 4 SER

This section contains the SER transmitted to FRA-ANP by Leslie W. Barnett of the NRC in their letter dated April 9, 2002.

Rev. 4
9/99



**UNITED STATES
NUCLEAR REGULATORY COMMISSION**

WASHINGTON, D.C. 20555-0001

April 9, 2002

Mr. James F. Mallay
Director, Regulatory Affairs
Framatome ANP, Richland, Inc.
2101 Horn Rapids Road
Richland, WA 99352

SUBJECT: SAFETY EVALUATION OF FRAMATOME TECHNOLOGIES TOPICAL REPORT BAW-10164P REVISION 4, "RELAP5/MOD2-B&W, AN ADVANCED COMPUTER PROGRAM FOR LIGHT WATER REACTOR LOCA AND NON-LOCA TRANSIENT ANALYSES" (TAC NOS. MA8485 AND MA8468)

Dear Mr. Mallay:

By letters dated September 24, 1999 and February 29, 2000, Framatome submitted BAW-10164P, Revision 4, "RELAP5/MOD2-B&W, An Advanced Computer Program for Light Water Reactor LOCA and Non-LOCA Transient Analyses," for review by the NRC staff. By letters dated September 5, 2000, March 23, 2001, and June 15, 2001, Framatome provided additional information.

Framatome proposed the following changes to BAW-10164P-A (as Revision 4) and refinements to the loss of coolant accident (LOCA) evaluation models (EMs):

1. A change that will model the hot channel modeling to treat the hot pin and the hot assembly as two heat structures for large break LOCA (LBLOCA) evaluations of recirculating steam generator (RSG) and once through steam generator (OTSG) plants.
2. A change to the initial fuel stored energy uncertainty that will apply a lower uncertainty in the initial fuel stored energy, derived from TACO3, to the hot assembly and core average heat structures for LBLOCA evaluations of RSG and OTSG plants.
3. A change to automate the void-dependent cross-flow model and to interpolate the inter-channel void-dependent cross-flow for small break LOCA (SBLOCA) evaluations for OTSG plants, and
4. Automation of the core heat BEACH blockage limitation that will automate flow-blockage limit in BEACH, used for LBLOCA and SBLOCA analyses of RSG and OTSG plants.

The staff has completed its review of the subject topical report (TR) and finds it is acceptable for referencing in licensing applications to the extent specified and under the limitations delineated in the report and in the associated safety evaluation (SE). The SE defines the basis for acceptance of the report.

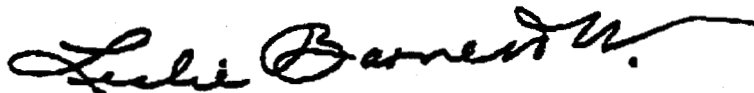
Pursuant to 10 CFR 2.790, we have determined that the enclosed SE does not contain proprietary information. However, we will delay placing the SE in the public document room for a period of 10 working days from the date of this letter to provide you with the opportunity to comment on the proprietary aspects only. If you believe that any information in the enclosure is proprietary, please identify such information line by line and define the basis pursuant to the criteria of 10 CFR 2.790.

We do not intend to repeat our review of the matters described in the subject report, and found acceptable, when the report appears as a reference in license applications, except to ensure that the material presented applies to the specific plant involved. Our acceptance applies only to matters approved in the report.

In accordance with the guidance provided in NUREG-0390, we request that Framatome publish an accepted version of this TR within 3 months of receipt of this letter. The accepted version shall incorporate this letter and the enclosed safety evaluation between the title page and the abstract. It must be well indexed such that information is readily located. Also, it must contain in appendices historical review information, such as questions and accepted responses, and original report pages that were replaced. The accepted version shall include an "-A" (designated accepted) following the report identification symbol.

Should our criteria or regulations change so that our conclusions as to the acceptability of the report are invalidated, Framatome and/or the applicants referencing the TR will be expected to revise and resubmit their respective documentation, or submit justification for the continued applicability of the TR without revision of their respective documentation.

Sincerely,



Leslie W. Barnett, Acting Director
Project Directorate IV
Division of Licensing Project Management
Office of Nuclear Reactor Regulation

Project No. 693

Enclosure: Safety Evaluation



UNITED STATES
NUCLEAR REGULATORY COMMISSION
WASHINGTON, D.C. 20555-0001

SAFETY EVALUATION BY THE OFFICE OF NUCLEAR REACTOR REGULATION

TOPICAL REPORT BAW-10164P, REVISION 4, "RELAP5/MOD2-B&W,

AN ADVANCED COMPUTER PROGRAM

FOR LIGHT WATER REACTOR LOCA AND NON-LOCA TRANSIENT ANALYSES"

PROJECT NO. 693

1.0 INTRODUCTION

Framatome ANP proposed several changes to its loss-of-coolant accident (LOCA) evaluation models (EMs) and methodologies in letters dated September 24, 1999 and February 29, 2000. Framatome provided additional information by letters dated September 5, 2000, March 23, 2001, and June 15, 2001.

Framatome ANP maintains several LOCA EMs to cover the conditions of small break LOCAs (SBLOCAs) and large break LOCAs (LBLOCAs) in once-through steam generator (OTSG) plants and recirculating steam generator (RSG) plants. The LOCA EMs are described in several Framatome topical reports, including the following:

BAW-10168P-A, "RSG LOCA, BWNT Loss-of Coolant Accident Evaluation Model for Recirculating Steam Generator Plants," Revision 3, December 1996.

BAW-10192P-A, "BWNT LOCA, BWNT Loss of Coolant Accident Evaluation Model for Once-Through Steam Generator Plants," Revision 0, June 1998.

BAW-10164P-A, "RELAP5/MOD2-B&W, An Advanced Computer Program for Light Water Reactor LOCA and Non-LOCA Transient Analyses," Revision 3, July 1996.

BAW-10166P-A, "BEACH, Best Estimate Analysis Core Heat Transfer, A Computer Program for Reflood Heat Transfer During LOCA," Revision 4, February 1996.

BAW-10162P-A, "TACO3, Fuel Rod Thermal Analysis Computer Code," Revision 0, November 1989.

Framatome proposed the following changes to BAW-10164P-A (as Revision 4) and refinements to the LOCA EMs:

1. A change that will model the hot channel modeling to treat the hot pin and the hot assembly as two heat structures for LBLOCA evaluations of RSG and OTSG plants.

2. A change to the initial fuel stored energy uncertainty that will apply a lower uncertainty in the initial fuel stored energy, derived from TACO3, to the hot assembly and core average heat structures for LBLOCA evaluations of RSG and OTSG plants,
3. A change to automate the void dependent crossflow model and to interpolate the inter-channel void-dependent cross-flow for SBLOCA evaluations for OTSG plants, and
4. Automation of the core heat BEACH blockage limitation that will automate flow-blockage limit in BEACH, used for LBLOCA and SBLOCA analyses of RSG and OTSG plants.

2.0 STAFF EVALUATION

The staff reviewed the above proposed changes for acceptability in the context of the previously approved LOCA EMs listed above (e.g., Revision 3 to BAW-10164P-A, Revision 3 to BAW-10168P-A, and Revision 0 to BAW-10192P-A). These EMs will use the RELAP 5 code described in BAW-10164P, Revision 4.

The staff's review of the changes to the hot channel modeling, fuel initial stored energy uncertainty, cross-flow modeling, and flow blockage limit automation, in the context of the previously approved LOCA EMs, is presented below.

2.1 Changes to the Hot Channel Modeling in the LBLOCA Methodology

By letters dated September 24, 1999, and February 29, 2000, Framatome described the changes to the hot assembly modeling. Additional information was provided in letters dated September 5, 2000, March 23, 2001, and June 15, 2001. The changed modeling applies to the RELAP5/MOD2-B&W LBLOCA EMs for OTSG (BAW-10192P-A, Revision 0) and RSG (BAW-10168P-A, Revision 3) plants. The principal amended changes are: (a) replacing the hot rod/hot assembly channel with one channel containing two heated surfaces, one representing the hot rod and the other representing the other rods in the hot assembly, and (b) using the fuel initial stored energy uncertainty, and corresponding initial fuel rod conditions, as discussed in Section 2.2.

Currently, the Framatome model for peak cladding temperature (PCT) calculations does not differentiate between the hot fuel assembly and the hottest pin. This modeling scheme causes the entire hot assembly to incorporate all of the conservatism required for the hot pin or hot spot to assure that the hot pin or hot spots are not under predicted. In the present model, Framatome assumes that the hot assembly consists of all hot rods at the peak rod power and peaking factors, and at the hottest rod initial temperature (stored energy) uncertainty. Framatome contends that this model results in a significant overprediction of the severity of the hot pin or hot spot conditions, and a very conservative prediction of the PCT. Framatome also contends that this conservative modeling did not represent the actual physical phenomenon in that there are cooling mechanisms affecting the hot spot. Framatome contends that these cooling mechanisms include convective heat transfer when there is high coolant flow, and a radiative heat transfer process to the immediate surroundings of the hot spot during low coolant flow. The cooling mechanisms govern heat transfer between the hot spot and the hot fuel assembly.

Therefore, Framatome proposed a new model which separates hot pin and hot spots from the hot fuel assembly. In the proposed model, the power of the rods in the core is assumed to be the same as in the present model, with all rods in the hot assembly at the same limiting power. However, in the proposed version, the initial conditions of temperature uncertainties for the fuel rods in the hot assembly are changed based on TACO3 calculations. The hottest rod uncertainty remains the same as assumed in the present model. The remainder of the rods in the hot assembly have an initial temperature uncertainty, derived from TACO3 calculations, statistically based on the fuel rods immediately surrounding the hottest rod. This lowers the temperature uncertainty assumption for all the fuel rods in the hot assembly except for the hottest rod. In addition, the average core heat structure will be initialized with no uncertainty, consistent with the above statistical approach. The fuel temperature uncertainty is discussed in more detail in Section 2.2 of this safety evaluation. The rest of the rods in the core are modeled the same as in the present model.

The changes would not affect the hot rod directly. The hot rod would be represented the same as it is in the present model. However, the changes to the initial conditions including the stored energy of the other rods, would in turn change the transient effects of the other rods. The transient effects of the other rods would affect the transient coolant conditions of the hot channel, and thereby affect the transient behavior of the hot rod. The overall result of the reduced conservatism of the non-hot rod initial conditions is a lowering of the calculated peak cladding temperature.

The staff concludes that the change to two heat surfaces in the hot channel and the changes in assumed initial fuel temperature uncertainty are acceptable because the methodology continues to assume that all the fuel rods in the hot assembly are at the same limiting power and peaking factors as the hottest rod. The staff expects the assumed power level in the hot assembly to be sufficiently conservative such that the EM, using the initial fuel temperature uncertainty discussed below, will provide conservative results.

In summary, the staff concludes that the hot channel modeling changes are acceptable for the proposed version of the methodology because the Framatome assumption that all the hot assembly fuel rods are at the hottest rod's power assures that the methodology will continue to be conservative when changes reducing the conservatism of the initial fuel temperature uncertainty are included.

2.2 Changes to Initial Fuel Stored Energy Uncertainty

By letter dated February 29, 2000, Framatome proposed changes to the uncertainty applied to the fuel initial stored energy. As previously discussed, the current Framatome model for PCT does not differentiate between the hot fuel assembly and the hottest pin. This modeling scheme causes the entire hot assembly to incorporate all of the conservatisms required for the hot pin or hot spot to assure that the hot pin or hot spot is not underpredicted. As a result, in the current EM, Framatome applies an uncertainty that is applicable to the hot spot to the entire hot assembly and hot pin. The stored energy in the fuel is derived from the approved TACO3 fuel performance code.

Framatome's proposed new model includes a hot pin modeled as a separate heat structure that shares a coolant channel with the hot fuel assembly. The hot fuel assembly is comprised of all fuel pins within the hot assembly except the hot pin. For the hot pin, Framatome will use an initial fuel temperature uncertainty of 11.5 percent, which is based on the hot spot. This is the same uncertainty value as is used for the hot rod/assembly in the current model. Thus, the stored energy for the hot pin is identical for both current and proposed models. The staff considers this approach acceptable.

The initial fuel temperature uncertainty for the hot fuel assembly is determined by a probability distribution of the fuel pellet temperature predictions such that the temperature is overpredicted 95 percent of the time at the 95 percent confidence level. To deduce the average fuel temperature uncertainty for the hot fuel assembly, Framatome described a flow channel that shows a hot pin surrounded by eight fuel pins to form four subchannels. Framatome contended that only pins and pellets within these subchannels can be expected to affect the heat transfer from the hot spot. This approach effectively shields the hot pin from influence by those pins outside the channel, thereby conservatively predicting fuel temperature uncertainty. Framatome assigned weighting factors for those eight pins surrounding the hot pin that contribute heat to the subchannels. These weighting factors are based on a conservative geometrical consideration that maximizes the heat added to the subchannels. Framatome notes that there is an additional conservatism because the control rod guide tubes and instrument tubes are not considered in the hot fuel assembly. To determine the average uncertainty for the fuel pellets surrounding the hot pin, Framatome applied a statistical method to randomly determine the uncertainty of each pellet, according to the TACO3 uncertainty distribution, and considered the applicable heat transfer mechanisms at the hot spot. This process was repeated until a 95/95 confidence level was reached. The result showed that the average uncertainty for the hot fuel assembly is 2.1 percent for conditions with coolant flow and 2.3 percent for conditions without coolant flow. For conservatism, Framatome will assign an average uncertainty of 3 percent for the hot assembly. Based on this average uncertainty, Framatome can calculate the stored energy for the hot fuel assembly. The staff agrees with this approach.

Similar to the calculation of hot assembly uncertainty, Framatome evaluated the average uncertainty to be applied to the average core heat structure. Framatome determined that, core wide, the average uncertainty is zero (e.g., no bias in the TACO3 results). Framatome noted, however, that a correction to the TACO3 results is applied for high burnup fuel (greater than 40 GWd/mtU), consistent with the high burnup Topical Report, BAW-10186P-A, "Extended Burnup Evaluation," Revision 0, June 1997.

The staff has reviewed Framatome's proposed stored energy model for hot pin, hot fuel assembly, and average core heat structures. Based on the approved TACO3 code and conservative approach in the modeling and statistical method, the staff finds the proposed changes to be acceptable.

2.3 Changes to Void-Dependent Cross-Flow Model

Framatome proposed to change its small break LOCA analysis methodology as described in their September 24, 1999, letter. The staff also consulted BAW-10192P-A, Volume 2, which described the previous SBLOCA methodology for B&W designs. The previous methodology provides coefficients controlling cross-flow in the core between the hot channel and the average channel in both directions for both below the water surface and the steam space above the water surface. The values of the coefficients used in the approved model were determined by analytical sensitivity studies to assure relative conservatism and consistent calculated behavior. No formal comparisons to test data were performed. The time-dependent variance of the fluid condition at any given level determines the values of these coefficients at that level. In the present methodology, coefficient values were entered by the analyst in an iterative process of interpretation of the calculated time- and level-dependent fluid conditions.

The existing core cross-flow model provides flow coefficients between the hot channel and the average channel. The coefficients are fixed-valued, but specific to the flow location (above and below the water surface) and the flow direction (out of the hot channel or into the hot channel from the average channel). In the previous model, the values of the time-dependent coefficient values were determined by the analyst's assessment of the time variance of fluid conditions in the channels. The specific values were initially checked against large break data, and then tuned with sensitivity studies to give qualitatively credible results and identify the bounding case of those studied. This was considered by the staff in its previous review and approval of the model.

The proposed model change adds a void-dependent transition zone (which varies in elevation with the time-dependent change in core water level) to interpolate the coefficients, providing greater continuity to the calculations. In the updated methodology, the interpretation of time- and level-dependent fluid condition is automated, avoiding the possible inconsistencies introduced by different interpretations between analysts.

In a letter dated March 23, 2001, Framatome stated that it examined the relative effect of this change for a limited number of cases that they considered representative. In comparisons of results using the previous model and results using the proposed model, the calculated results using the proposed model are consistent and fall within the range of variance between different analysts using the previous model. This demonstrates that, for SBLOCA analyses representative of B&W-design licensing cases, use of the proposed model yields results within the range of results using the previously approved model.

The staff concludes that the proposed treatment of cross-flow is acceptable for the proposed version of the SBLOCA methodology because the proposed automated cross-flow model provided more consistent results than the previously approved analyst-controlled model, and because the results using the proposed model fell within the range of variance of the results using the previously approved analyst-controlled model in comparisons performed by Framatome.

Future changes to the Framatome SBLOCA methodology could significantly affect either the form of the cross-flow model or the cross-flow coefficient values. Because the staff only considered the proposed cross-flow model within the context of the Framatome SBLOCA

methodology as it is presently configured, and for scenarios represented in a limited sensitivity study, future modifications of the SBLOCA methodologies could compromise any conservatism remaining in the methodology. The staff will in future reviews of SBLOCA model changes, request additional empirical data comparisons supporting the cross-flow model discussed in this safety evaluation to confirm that sufficient conservatism remains in the future methodologies in accordance with 10 CFR Part 50, Appendix K.

Plant design and fuel differences, and discovered errors or changes, could affect the results, both quantitative and qualitative, due to the form of the cross-flow model or the cross-flow coefficient values. Differences in the results could indicate different compensatory or remedial actions. Deviations from the versions of the LOCA methodologies containing the cross-flow model discussed in this safety evaluation are subject to the requirements of 10 CFR 50.46.

2.4 Automation of BEACH Blockage Limitation

The approved version of the BEACH methodology contains a credited flow blockage limitation of 60 percent, which is implemented by the analyst inspecting the analytical results. In the September 24, 1999, letter, Framatome proposed to automate this limit in the BEACH coding. This automation is more convenient, and makes implementation of the limitation and calculated results more reliable and consistent. For these reasons, the staff finds this change acceptable.

3.0 CONCLUSIONS

Based on reviews discussed in Section 2, the staff finds the following Framatome proposed methodology changes (BAW-10164P, Revision 4) acceptable within the stated terms and limitations:

1. A change that will model the hot channel modeling to treat the hot pin and the hot assembly as two heat structures for LBLOCA evaluations of RSG and OTSG plants.
2. A change to the initial fuel stored energy uncertainty that will apply a lower uncertainty in the initial fuel stored energy, derived from TACO3, to the hot assembly and core average heat structures for LBLOCA evaluations of RSG and OTSG plants.
3. A change to automate the void dependent crossflow model and to interpolate the inter-channel void-dependent cross-flow for SBLOCA evaluations for OTSG plants.
4. Automation of the core heat BEACH blockage limitation that will automate the flow-blockage limit in BEACH, used for LBLOCA and SBLOCA analyses of RSG and OTSG plants.

For reasons discussed in Section 2, in its review of future changes to the LBLOCA and SBLOCA methodologies beyond the context discussed in this safety evaluation, the staff will closely examine the impacts of the proposed changes with respect to the TACO3 stored energy model, the hot channel modeling changes, and the cross-flow model discussed in this safety evaluation.

As discussed in Section 2, the methodology changes addressed in this safety evaluation are significant. They involve both LBLOCA and SBLOCA, and a variety of plant designs, including recirculating steam generator and once-through steam generator designs. The methodology changes would likely affect the various plant designs differently. Identified errors and changes, and compensatory and remedial actions could be different between the plants. Deviations from the versions of the LOCA methodologies containing the items discussed in this safety evaluation (BAW-10164P, Revision 4) are subject to the requirements of 10 CFR 50.46.

Principal Contributor: F. Orr

Date: April 9, 2002

5.10 Pages removed for Revision 4

The following pages have been replaced in revision 3 to create revision 4.

Rev. 4
9/99

BAW-10164-A
Topical Report
Revision 3
October 1996

- RELAP5/MOD2-B&W -

**An Advanced Computer Program for
Light Water Reactor LOCA and Non-LOCA
Transient Analysis**

B&W Nuclear Technologies
P. O. Box 10935
Lynchburg, Virginia 24506

B&W Nuclear Technologies
Lynchburg, Virginia

Topical Report BAW-10164-A
Revision 3
October 1996

RELAP5/MOD2-B&W

An Advanced Computer Program for
Light Water Reactor LOCA and Non-LOCA
Transient Analysis

Key Words: RELAP5/MOD2, LOCA, Transient, Water Reactors

Abstract

This document describes the physical solution technique used by the RELAP5/MOD2-B&W computer code. RELAP5/MOD2-B&W is a B&W Nuclear Technologies adaption of the Idaho National Engineering Laboratory RELAP5/MOD2. The code developed for best estimate transient simulation of pressurized water reactors has been modified to include models required for licensing analysis. Modeling capabilities are simulation of large and small break loss-of-coolant accidents, as well as operational transients such as anticipated transient without SCRAM, loss-of-offsite power, loss of feedwater, and loss of flow. The solution technique contains two energy equations, a two-step numerics option, a gap conductance model, constitutive models, and component and control system models. Control system and secondary system components have been added to permit modeling of plant controls, turbines, condensers, and secondary feedwater conditioning systems. Some discussion of the numerical techniques is presented. Benchmark comparison of code predictions to integral system test results are presented in an appendix.

Rev. 3

This page is intentionally left blank.

Topical Revision Record

<u>Documentation Revision</u>	<u>Description</u>	<u>Program Change?</u>	<u>Program Version</u>
0	Original issue	—	8.0
1	Typographical corrections Replace CSO correlation with Condie-Bengston IV	yes	10.0
2	SBLOCA modifications Miscellaneous corrections	yes	18.0
3	EM Pin Enhancements Filtered Flows for Hot Channel Heat Transfer Rupture Area Enhancement for Surface Heat Transfer OTSG Improvements and Benchmarks using the Becker CHF, Slug Drag, and Chen Void Ramp	yes	19.0

TABLE OF CONTENTS (cont'd)

4. REFERENCES	4-1
5. LICENSING DOCUMENTS	5-1
5.1 Responses to Revision 1 Questions: Round 1	5-3
5.2 Responses to Revision 1 Questions: Round 2	5-101
5.3 Revision 1 Safety Evaluation Report (SER)	5-191
5.4 Responses to Revision 2 Questions	5-254
5.5 Responses to Revision 3 Questions	5-268
5.6 Supplemental Information to Revisions 2 and 3	5-300
5.7 Revisions 2 and 3 SER	5-325

LIST OF FIGURES (Cont'd)

Figure	Page
2.1.5-10. Schematic of a Typical Relief Valve in the Closed Position	2.1-162
2.1.5-11. Schematic of a Typical Relief Valve in the Partially Open Position	2.1-163
2.1.5-12. Schematic of a Typical Relief Valve in the Fully Open Position	2.1-163
2.1.5-13. Typical Accumulator	2.1-170
2.2.1-1. Mesh Point Layout	2.2-3
2.2.1-2. Typical Mesh Points	2.2-4
2.2.1-3. Boundary Mesh Points	2.2-5
2.2.2-1. Logic Chart for System Wall Heat Transfer Regime Selection	2.2-34
2.3.2-1. Gap Conductance Options	2.3-27
2.3.2-2. Fuel Pin Representation	2.3-34
2.3.2-3. Fuel Pin Swell and Rupture Logic and Calculation Diagram	2.3-48
2.3.3-1. Core Model Heat Transfer Selection Logic	
a) Main Driver for EM Heat Transfer	2.3-62
b) Driver Routine for Pre-CHF and CHF Correlations	2.3-63
c) Driver Routine for CHF Correlations	2.3-64
d) Driver Routine for Post-CHF Correlations	2.3-65
3.1-1. RELAP5 Top Level Structure	3.1-1
3.2-1. Transient (Steady-State) Structure	3.2-1
G.1-1. Semiscale MOD1 Test Facility - Cold Leg Break Configuration	G-14
G.1-2. Semiscale MOD1 Rod Locations for Test S-04-6	G-15

1. INTRODUCTION

RELAP5/MOD2 is an advanced system analysis computer code designed to analyze a variety of thermal-hydraulic transients in light water reactor systems. It is the latest of the RELAP series of codes, developed by the Idaho National Engineering Laboratory (INEL) under the NRC Advanced Code Program. RELAP5/MOD2 is advanced over its predecessors by its six-equation, full nonequilibrium two-fluid model for the vapor-liquid flow field and partially implicit numerical integration scheme for more rapid execution. As a system code, it provides simulation capabilities for the reactor primary coolant system, secondary system, feedwater trains, control systems, and core neutronics. Special component models include pumps, valves, heat structures, electric heaters, turbines, separators, and accumulators. Code applications include the full range of safety evaluation transients, loss-of-coolant accidents (LOCAs), and operating events.

RELAP5/MOD2 has been adopted and modified by B&W for licensing and best estimate analyses of PWR transients in both the LOCA and non-LOCA categories. RELAP5/MOD2-B&W retains virtually all of the features of the original RELAP5/MOD2. Certain modifications have been made either to add to the predictive capabilities of the constitutive models or to improve code execution. More significant, however, are the B&W additions to RELAP5/MOD2 of models and features to meet the 10CFR50 Appendix K requirements for ECCS evaluation models. The Appendix K modifications are concentrated in the following areas: (1) critical flow and break discharge, (2) fuel pin heat transfer correlations and switching, and (3) fuel clad swelling and rupture.

Since the connecting K and L volumes are assumed to be predominately axial-flow volumes, the crossflow junction momentum flux (related to the axial volume velocity in K and L) is neglected along with the associated numerical viscous term. In addition, the horizontal stratified pressure gradient is neglected.

All lengths and elevation changes in the one-dimensional representation are based upon the axial geometry of the K and L volumes and the crossflow junction is assumed to be perpendicular to the axial direction and of zero elevation change, thus, no gravity force term is included.

The resulting vapor momentum finite difference equation for a crossflow junction is

$$\begin{aligned}
 & \left[\alpha_{g'} \rho_g \right]_j^n \left[v_{g,j}^{n+1} - v_{g,j}^n \right] \Delta x_j = - \alpha_{g,j}^n (P_L - P_K)^{n+1} \Delta t \\
 & - \left[\alpha_{g'} \rho_g \right]_j^n HLOSSG_j^n v_{g,j}^{n+1} \Delta t \\
 & - \left[\alpha_{g'} \rho_g \right]_j^n FIG_j^n \left[v_{g,j}^{n+1} - v_{f,j}^{n+1} \right] \Delta x_j \Delta t \\
 & + \text{ADDED MASS} + \text{MASS TRANSFER MOMENTUM} . \qquad 2.1.4-72
 \end{aligned}$$

A similar equation can be written for the liquid phase. In Equation 2.1.4-72, $HLOSSG_j^n$ contains only the user input crossflow resistance. The Δx_j term that is used to estimate the inertial length associated with crossflow is defined using the diameters of volumes K and L,

$$\Delta x_j = \frac{1}{2} [D(K) + D(L)] \qquad 2.1.4-73$$

The crossflow option can be used with the crossflow junction perpendicular to the axial flow in volume L (or K) but parallel

2.3.2. Core Heat Structure Model

The ordinary RELAP5 heat structures are general in nature and can be used for modeling core fuel pins; however, licensing calculations require special treatment of the fuel pin heat transfer. To accommodate these requirements, two additional models, commonly referred to as the EM (Evaluation Model) pin and core surface heat transfer model were added to the code. The EM pin model calculates dynamic fuel-clad gap conductance, fuel rod swell and rupture using NUREG-0630¹¹⁷ options, and cladding metal-water reaction. The core fuel pin surface heat transfer is calculated with a flow regime-dependent set of correlations that include restrictions on which correlations can be selected per NRC licensing requirements. These new models are independent and mutually exclusive of the original system heat transfer model (described in section 2.2.2) and the existing simple gap conductance model¹¹⁸ (referenced in Appendix A). The new models are explicitly coupled to the solution scheme through the modification of the gap conductance term, addition of fluid hydraulic resistance upon rupture, deposition of metal-water reaction energy in the clad, and determination of fuel pin surface heat transfer. The new EM pin model calculations are described in this section, while the EM heat transfer description is contained in section 2.3.3.

The EM pin model consists of three basic parts:

1. Dynamic fuel-clad gap conductance,
2. Fuel rod swell and rupture using NUREG-0630 options, and
3. Clad metal-water reaction,

which couple explicitly to the heat structure solution scheme or add fluid hydraulic resistance upon rupture. The model may be executed either in a steady-state initialization or transient mode determined by user input.

The pin calculations are performed on single fuel rod which represent the average behavior of a large number of rods. Each rod (also termed channel) can be broken into up to ninety heat structures, each having an associated pin segment. The gap conductance, deformation mode, and metal-water reaction are determined for each individual segment based on the channel specific pin pressure.

2.3.2.1. Transient Dynamic Fuel-Clad Gap Conductance

The RELAP5 heat structure conduction scheme uses cold, unstressed geometrical dimensions for its solution technique. The dynamic gap conductance, h_{gap} , is calculated from hot stressed conditions from which an effective gap thermal conductivity, \bar{K}_{gap} , based on cold gap size, $r_{g_{\text{cold}}}$, is determined for each pin segment.

$$\bar{K}_{\text{gap}} = h_{\text{gap}} \cdot r_{g_{\text{cold}}}$$

2.3.2-1

The gap conductance is determined by calculating the gap gas conductivity, temperature jump gap distance, radiation component, and dynamic fuel-clad gap from the deformation models. An additive fuel-clad contact conductance term has also been included as an option to simulate the closed gap contribution for high fuel rod burn-up applications. Two options are provided to calculate the conductance. The first option assumes that the fuel pellet is concentric within the clad, while the second option assumes the fuel pellet is non-concentric within the clad as illustrated in Figure 2.3.2-1.

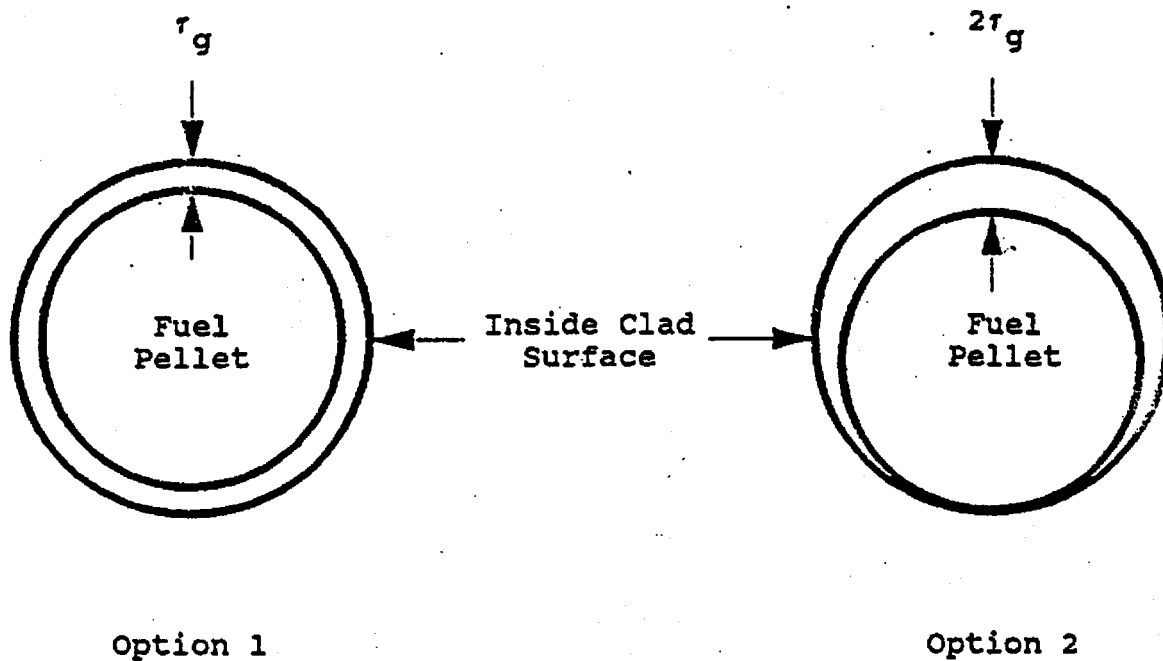


Figure 2.3.2-1. Gap Conductance Options.

Eight half-symmetrical azimuthal sections are used for determining the overall conductance for the second option without calculating an azimuthal temperature gradient. The total gap conductance is determined by

$$h_{\text{gap}} = M_g h_{\text{gap gas}} + h_{\text{rad}} + h_{\text{fcc}} \quad 2.3.2-2$$

with

h_{gap} = conductance through gap gas ($\text{w/m}^2\text{-K}$),

M_g = user input multiplier used to acquire correct initial temperature within fuel,

$h_{\text{gap gas}}$ = gap gas conductance contribution ($\text{w/m}^2\text{-K}$),

h_{rad} = conductance due to radiation contribution from fuel to clad ($\text{w/m}^2\text{-K}$), and

h_{fcc} = gap contact conductance contribution due to fuel-cladding mechanical interaction ($\text{w/m}^2\text{-K}$).

The radiation gap conductance contribution is calculated by

$$h_{\text{rad}} = \frac{\sigma}{\frac{1}{e_f} + \frac{r_f}{r_{ic}} \left(\frac{1}{e_c} - 1 \right)} \left[\frac{T_{fs}^4 - T_{ics}^4}{T_{fs} - T_{ics}} \right]$$

$$= \frac{\sigma(T_{fs}^2 + T_{ics}^2)(T_{fs} + T_{ics})}{\frac{1}{e_f} + \frac{r_f}{r_{ic}} \left(\frac{1}{e_c} - 1 \right)},$$

2.3.2-2.1

where

σ = Stefan-Boltzmann constant,

= 5.6697×10^{-8} ($\text{w/m}^2\text{-K}^4$),

e_f = emissivity of fuel surface,

e_c = emissivity of clad-inside surface,

T_{fs} = fuel outside surface temperature (K), and

T_{ics} = clad-inside surface temperature (K).

$$\begin{aligned}
C_1 &= 1.0 \cdot 10^{-5} \text{ (K}^{-1}\text{)}, \\
C_2 &= -3.0 \cdot 10^{-3}, \\
C_3 &= 4.0 \cdot 10^{-2}, \text{ and} \\
C_4 &= -5.0 \cdot 10^3 \text{ (K)}.
\end{aligned}$$

The fuel is defined by the first material type specified in the heat structure input, with the next material type being the gap and the third the clad as shown in Figure 2.3.2-2. Any deviation from the geometry will result in an error or misinterpretation of the information by the pin model. The gap can only be one mesh interval wide, while fuel or clad must be greater than or equal to one mesh interval. Currently no provisions are made for annular fuel pellets.

The calculation of the inside clad radius is not as straightforward as the fuel outside radius. Seven different calculational modes are required to cover the possible clad conditions. They are defined as:

1. Elastic and thermal expansion within an unruptured channel,
2. Elastic and thermal expansion within 166.7K (300°F) of the clad rupture temperature within an unruptured channel,
3. Plastic deformation within an unruptured channel,
4. Elastic thermal expansion within a ruptured channel,
5. Plastic deformation in a ruptured channel,
6. Ruptured segment, and
7. Fuel-cladding mechanical iteration (closed gap).

Each mode is related to the NUREG-0630 calculated rupture temperature.

$$T_{\text{rupt}} = 4233 - \frac{20.4\sigma_h}{1 + H} - \frac{(8.51 \cdot 10^6)\sigma_h}{100(1 + H) + 2790\sigma_h} \quad 2.3.2-17$$

where

T_{rupt} = NUREG-0630 rupture temperature (K),

σ_h = clad hoop stress (kpsi), and

H = dimensionless clad heating ramp rate, $0 \leq H \leq 1$.

The clad hoop stress for any pin segment is given by

$$\sigma_h = C_p (P_g r_{ic_cold} - P_f r_{oc_cold}) / (r_{oc_cold} - r_{ic_cold}), \quad 2.3.2-18$$

with

r_{ic_cold} = cold unstressed inside clad radius (m),

r_{oc_cold} = cold unstressed outside clad radius (m),

P_g = internal fuel rod pin pressure for that channel (Pa), and

P_f = external fluid pressure of the right-hand side heat structure associated volume (Pa).

$C_p = 1 / 6.894757 \times 10^6$

The heating rate can be either a user input constant or one of three additional transient-dependent algorithms discussed in detail later in this section.

At the beginning of each new time step following a successful RELAP5 time step advancement, the hoop stress and normalized heating ramp rate are computed for each pin segment. The clad average temperature is also known at this time. If the clad average temperature is greater than the rupture temperature, then rupture occurs. Should the segment still be elastic and the rupture minus the clad temperature is less than 166.7K (300 F), then the segment stays elastic. Between these two temperatures the clad can be either elastic or plastic depending upon this

temperature difference and the burst strain as described in the following paragraphs for ruptured or unruptured channels.

Mode 1: Unruptured Elastic and Thermal Deformation

Within an unruptured channel, the clad is considered purely elastic if it has never gone plastic, ruptured, or the temperature difference between rupture and clad average temperatures is less than 166.7 K (300 F). The inside clad radius for this pure elastic mode is determined by

$$r_{ic} = r_{ic_{cold}} + u_{TC} + u_{CC} + u_e, \quad 2.3.2-19$$

where

u_{TC} = clad radial displacement due to thermal expansion (m),

u_{CC} = clad radius over-specification factor (m), determined during pin transient initiation, and

u_e = clad radial displacement due to elastic deformation (m).

The clad thermal expansion is determined similarly to that for the fuel.

$$u_{TC} = (r_{N_{HS}+1} - r_{N_f+2}) \epsilon_{TC} / 2, \quad 2.3.2-20$$

with

N_{HS} = total number of mesh intervals in the heat structure,

r_n = heat structure radius at the inside of mesh interval n or outside of n-1 (m), and

ϵ_{TC} = radial strain function defining fuel thermal expansion as a function of clad average temperature.

The radial strain function is defined by either a user input cubic fit

$$\epsilon_{TC} = C_1 T^3 + C_2 T^2 + C_3 T + C_4 , \quad 2.3.2-21$$

or a built in code correlation set¹¹⁹

$$\epsilon_{TC} = -2.0731 \cdot 10^{-3} + 6.721 \cdot 10^{-6} T_C \quad 2.3.2-22$$

for $T_C < 1073K$ (α phase), and

$$\epsilon_{TC} = -9.4495 \cdot 10^{-3} + 9.7 \cdot 10^{-6} T_C \quad 2.3.2-23$$

for $T_C > 1273K$ (β phase), where T_C is the average cladding temperature (K). In the α phase to β phase transition zone, $1073K < T_C < 1273K$, a table lookup is used. Some selected values are listed in Table 2.3.2-2.

Table 2.3.2-2. Thermal Strain of Zircaloy for $1073 K < T < 1273 K$.

<u>T(K)</u>	Radial Strain	Axial Strain
	ϵ_{TC}	ϵ_{ATC}
1073.	$5.14 \cdot 10^{-3}$	$3.53 \cdot 10^{-3}$
1093.	$5.25 \cdot 10^{-3}$	$3.50 \cdot 10^{-3}$
1103.	$5.28 \cdot 10^{-3}$	$3.46 \cdot 10^{-3}$
1123.	$5.24 \cdot 10^{-3}$	$3.33 \cdot 10^{-3}$
1143.	$5.15 \cdot 10^{-3}$	$3.07 \cdot 10^{-3}$
1183.	$4.45 \cdot 10^{-3}$	$1.50 \cdot 10^{-3}$
1223.	$2.97 \cdot 10^{-3}$	$1.10 \cdot 10^{-3}$
1273.	$2.90 \cdot 10^{-3}$	$1.40 \cdot 10^{-3}$

Young's modulus is given either by the code for zircaloy cladding as

$$E = \begin{cases} 1.088 \cdot 10^{11} - 5.475 \cdot 10^7 T_c & 1090K \geq T_c \\ 1.017 \cdot 10^{11} - 4.827 \cdot 10^7 T_c & 1240K \geq T_c > 1090K \\ 9.21 \cdot 10^{10} - 4.05 \cdot 10^7 T_c & 2027K \geq T_c > 1240K \\ 1.0 \cdot 10^{10} & T_c > 2027K, \end{cases}$$

2.3.2-28

or by a user specified cubic equation

$$E = C_1 T_c^3 + C_2 T_c^2 + C_3 T_c + C_4 . \quad 2.3.2-29$$

Poisson's ratio is a constant which is defined as 0.30 for zircaloy by the code, however, the user can over-ride this value.

The normalized heating ramp rate for the elastic mode is determined by one of two methods. One method calculates an instantaneous heating rate and normalizes it with respect to a rate of 28K/s.

$$H = \left(\frac{dT_c}{dt} \right) / 28.0$$

$$= \left(\frac{T_c^n - T_c^{n-1}}{\Delta t} \right) / 28.0 . \quad 2.3.2-30$$

The normalized value is then limited to $0 \leq H \leq 1$ before using it for subsequent checking and calculations. The superscripts reflect the current and old time values. The second method defines the normalized heating rate as a constant between 0 and 1 based on user input.

Mode 2: Unruptured Elastic and Thermal Deformation Within 166.7K (300 F) of the Rupture Temperature

When the clad average temperature is within 166.7K (300 F) of the rupture temperature, the elastic inside clad radius is calculated as shown in Mode 1. This radius is compared against the plastic inside clad radius calculated in Mode 3. If the elastic radius is greater than the plastic radius, then Mode 2 is retained and the inside clad radius is set to the elastic radius. If not, the clad becomes plastic (Mode 3) and the plastic clad calculations are used. An informative message is printed when a segment first becomes plastic. No return to elastic Modes (1 or 2) is permitted once the clad becomes plastic.

$$r_{ic} = \text{MAX}(r_{ic_{\text{elastic}}}, r_{ic_{\text{plastic}}}) \quad 2.3.2-31$$

$$\text{If } r_{ic_{\text{elastic}}} \geq r_{ic_{\text{plastic}}}, \quad \text{Mode} = 2 .$$

$$\text{If } r_{ic_{\text{elastic}}} < r_{ic_{\text{plastic}}}, \quad \text{Mode} = 3 .$$

Mode 3: Unruptured Plastic Deformation

The unruptured plastic deformation is determined by the plastic strain, ϵ_p .

$$r_{ic} = r_{ic_{\text{cold}}} (1 + \epsilon_p), \quad 2.3.2-32$$

with

$$\epsilon_p = 0.2 \epsilon_B \exp[-0.02754(T_{\text{rupt}} - T_C)], \quad 2.3.2-33$$

where ϵ_B is the clad burst strain determined by a double interpolation relative to H and T_{rupt} in the user input or default NUREG-0630 burst strain Tables 2.3.2-3 and 2.3.2-4. The

plastic strain behaves as a ratchet. Once a given plastic strain is reached, no decrease in its value is allowed. In other words, for plastic mode calculations

$$r_{ic} = \text{MAX}(r_{ic}^n, r_{ic}^{n-1}), \quad 2.3.2-34$$

where the superscripts refer to the current and old time values.

If the plastic mode is selected, the normalized heating ramp rate is calculated from any of three user options: user input constant, average ramp rate, or plastic weighted ramp rate. The normalized average ramp rate is calculated from

$$H = \left[\frac{T_c^n - T_c^p}{t^n - t^p} \right] / 28.0, \quad 2.3.2-35$$

where

t = time (s),

n = superscript defining the current time, and

p = superscript defining the time in which the clad first went plastic.

The normalized plastic weighted ramp is calculated by

$$H = \left[\frac{\int_{t^p}^{t^n} W(T) \left(\frac{dT_c}{dt} \right) dt}{\int_{t^p}^{t^n} W(T) dt} \right] / 28.0, \quad 2.3.2-36$$

noding options) chosen by the user. The fine mesh noding option computes the inside radius as

$$r_{ic} = r_{ic_{cold}} (1 + \epsilon_B) . \quad 2.3.2-39$$

With this option, the gap conductance is calculated as though there is steam in the gap. The steam thermal conductivity is evaluated at the gap temperature and used with the hot gap size to compute the conductance. This option also calculates inside metal-water reaction for the ruptured segment.

The coarse mesh noding option computes the inside clad radius as

$$r_{ic} = r_{ic_{cold}} (1 + 0.2 \epsilon_B) . \quad 2.3.2-40$$

This option uses the regular gap gas conductance and does not consider inside metal-water reaction. It is intended for use nominally when the expected rupture length is small when compared to the total segment length. The microscopic effects at the rupture site considered with the fine mesh option are expected to be negligible when compared to the longer segment behavior. With the coarse mesh option, the overall behavior will be more closely controlled by the entire segment rather than just the rupture site conditions.

Within the ruptured channel various calculations are modified at the time of rupture. Each segment within that channel undergoes a mode change. The pin pressure becomes that of the hydrodynamic volume associated with the ruptured segment. An additive form loss coefficient is calculated at rupture based on the clad flow blockage by a simple expression for an abrupt contraction-expansion.

$$K_{add} = \frac{0.5(1 - \beta^2) + (1 - \beta^2)^2}{(\beta^2)^2} , \quad 2.3.2-41$$

where

$$\beta^2 = \text{fraction of the channel flow area blocked,} \\ = (1.0 - A_{\text{blocked}}/A_{\text{channel}}).$$

The flow blockage is obtained via a double table interpolation relative to the normalized heating ramp rate and rupture temperature similarly to the clad burst strain. The table is either user supplied or default NUREG-0630 values listed in Tables 2.3.2-3 and 2.3.2-4. The additive value of the loss coefficient is edited at the time of rupture. The flow blockage loss coefficient is added automatically to the problem unless the user overrides via a new optional input. If added, the form loss is applied to the forward flow direction for the inlet (bottom) junction and the reverse flow direction for the exit (top) junction attached to the volume in which the clad ruptured. The user option to exclude this form loss addition from the junctions has been included for certain non-licensing specialized applications (such as in models that use a single fluid channel in the core with multiple radial heat structure channels).

Another option has been added to the EM Pin model help to minimize user burden when running EM reflooding heat transfer analyses with BEACH (BAW-10166 Section 2.1.3.8.4). This user-controlled option automatically includes code-calculated pin rupture, droplet break-up and convective enhancement adjustments. The input grid parameters are modified with the ruptured values and will be retained for use in the reflooding heat transfer calculations. This model is optional and requires input to activate the calculations. If no input is specified the default is that no rupture enhancements will be calculated.

When this option is selected several sets of calculations will be performed following cladding rupture. The first calculation

performed determines the midpoint elevation of ruptured segment, referenced from the bottom of the pin channel (which coincides with the bottom of the heat structure geometry or reflod stack). This midpoint elevation, Z_{grid} , is the location where the new "grid" is inserted. This elevation is used to determine the droplet break-up effects for the ruptured segment.

$$Z_{grid} = 0.5 \cdot \Delta Z_{rupt\ seg} + \sum_{j=1}^{rupt\ seg-1} \Delta Z_{seg\ j}, \quad 2.3.2-41.1$$

where

ΔZ_{seg} = elevation change of pin segment.

The second set of calculations is to calculate rupture droplet breakup efficiency. These calculations are identical to those described in Sections 2.1.3.7. and 2.1.3.8. of Reference 123. The rupture atomization factor, η_{etamax} , is calculated as

$$\eta_{etamax} = \frac{1}{[1 + (n^{1/3} - 1)\epsilon_b]}, \quad 2.3.2-41.2$$

where

n = number of equal size droplets resulting from the split-up of the larger droplets,

b, c, d, e

ϵ_b = flow blockage fraction.

The increase in the droplet surface area from that used for interface heat transfer is defined in Equation 2.1.3-105¹²³ as

$$\Delta a_{gf} = C_{maxDB} \Theta a_{gf}.$$

The proportionality constant, C_{maxDB} , is determined from the constant, C_1 , the rupture flow blockage fraction, and the length of the ruptured segment.

$$C_{maxDB} = \frac{C_1 \epsilon_b}{\Delta Z_{rupt\ seg}}. \quad 2.3.2-41.3$$

[b,c,d,e]

The velocity of the fluid at the ruptured location increases because of the flow area reduction. The physical area in the code calculations is not modified, but a velocity multiplier, used for determining the droplet Weber number, is calculated from

$$\text{VELMULT} = \frac{1}{1 - \epsilon_b} \quad . \quad 2.3.2-41.4$$

The cladding rupture results in an increase in the pin outside heat transfer surface area. The increase in area is not directly included in the conduction solution in the code calculations. It is accounted for by using the rupture convective enhancement factor and applying it to the grid wall heat transfer enhancement factor, F_{gg} . The rupture enhancement, M_{RAR} , is a multiplicative contribution determined by

$$\begin{aligned} M_{RAR} &= \text{Rupture Area Ratio} \\ &= \frac{2\pi r_{\text{rupt}_{oc}} L}{2\pi r_{oc_{\text{cold}}} L} = \frac{r_{\text{rupt}_{oc}}}{r_{oc_{\text{cold}}}} \quad , \quad 2.3.2-41.5 \end{aligned}$$

where:

$$\begin{aligned} r_{\text{rupt}_{oc}} &= \text{outside clad radius of the ruptured node given by} \\ &= r_{ic} + [r_{oc_{\text{cold}}} - r_{ic_{\text{cold}}}] [r_{ic_{\text{cold}}} / r_{ic}]. \quad 2.3.2-41.6 \end{aligned}$$

The total wall heat transfer convective factor then becomes

$$F_{gg_{\text{tot}}} = F_{gg_{\text{grid}}} \cdot M_{RAR} \quad . \quad 2.3.2-41.7$$

These droplet break-up and convective enhancement terms are optionally calculated and edited at rupture by the EM pin model.

L_j = axial length of the jth segment (m),

ϵ_{ATF} = fuel strain function of Equation 2.3.2-15, evaluated at fuel volume weighted average temperature \bar{T}_f of Equation 2.3.2-25, (dimensionless), and

ϵ_{ATC} = axial strain function defining clad axial thermal expansion as a function of clad volume average temperature, (dimensionless).

The axial strain function for clad is defined by either a user input cubic fit

$$\epsilon_{ATC} = C_1 T^3 + C_2 T^2 + C_3 T + C_4 \quad 2.3.2-51.8$$

or a built in code correlation set¹¹⁹

$$\begin{aligned} \epsilon_{ATC} &= -2.506 \times 10^{-5} + (T_C - 273.15) 4.441 \times 10^{-6} \\ &= -1.2381 \times 10^{-3} + 4.441 \times 10^{-6} T_C \end{aligned} \quad 2.3.2-51.9$$

for $T_C < 1073.15K$ (α phase), and

$$\begin{aligned} \epsilon_{ATC} &= -8.3 \times 10^{-3} + (T_C - 273.15) 9.7 \times 10^{-6} \\ &= -1.0950 \times 10^{-2} + 9.7 \times 10^{-6} T_C \end{aligned} \quad 2.3.2-51.10$$

for $T_C \geq 1273K$ (β phase), where T_C is the volume average cladding temperature (K) of Equation 2.3.2-24. In the α phase to β phase transition zone, $1073K < T_C < 1273K$, a table lookup is used. Some selected values are listed in Table 2.3.2-2.

Using the assumption that both the slope of the fuel mesh point temperatures and the overall gap conductance will not change significantly, the last gap multiplier (1.0 for the first iteration) can be adjusted via a ratio to give a new multiplier,

$$M_g^{\eta+1} = \frac{\Delta T_{\text{gap}}}{(\Delta T_{\text{gap}} + \Delta \bar{T}_f)} M_g^{\eta} \quad . \quad 2.3.2-52.3$$

After calculation of the new gap multiplier, another conduction solution iteration step is taken. The fuel volume average temperature differential is recalculated via Equation 2.3.2-52.1. If the absolute value is greater than 2 K, then another iteration step is taken after recalculating a new multiplier via Equations 2.3.2-52.2 and 2.3.2-52.3. If the absolute value is less than 2 K, then the iteration has converged and the last multiplier calculated is edited and used during the steady-state and transient EM pin calculations. Up to six iterations are allowed. If convergence is not obtained in six iterations, then the code will stop at the end of the initialization process and appropriate failure messages will be edited. Failure of the iteration to converge is generally related to poor estimates given for the initial mesh point temperature distribution. An improved estimate will normally allow the iteration to converge properly. If convergence is still a problem, user specification of the multiplier is also available.

At the completion of the EM pin steady-state calculations (i.e., after EM pin steady-state trip becomes true or during the first time step if there is no trip) several calculations are required to initiate the pin transient calculations. The user-supplied cold unstressed pin geometry input via the heat structure cards is elastically expanded using the final code calculated temperature and mechanical stresses.

5.0 LICENSING DOCUMENTS

This section contains documents generated as a result of U.S. Nuclear Regulatory Commission (NRC) review of previous versions of this topical report. Sections 5.1 and 5.2 contains responses to rounds one and two questions, respectively, for revision 1 of this report. These documents were previously issued in the approved proprietary and non-proprietary versions as appendices H and I. Section 5.3 contains the Safety Evaluation Report (SER) issued for revision 1.

Sections 5.4 and 5.5 contain responses to NRC questions on revisions 2 and 3, respectively, of this report. Section 5.6 contains supplemental information to revisions 2 and 3. Section 5.7 contains the SER issued for revisions 2 and 3.

Rev. 3

7/96

5.11 SER Directed Changes and Typographical Corrections

The SER for Revisions 2 and 3 of the RELAP5/MOD2-B&W topical requested that changes be made to portions of the text based on typographical changes identified in the RAIs. These changes were not incorporated in the approved version of Revision 3 per the SER direction. They are being included in the Approved Revision 4 Topical to ensure that the incorrect information given previously is not used in completing future analyses, references, or evaluations.

Some of the incorrect material was crossed out while other simple typos were fixed. Underlined, italicized text was added to denote the corrections or to direct the reader to the corrected information provided based on the response to the RAI. The information is marked in the margin with a change bar and a letter "t" to denote the requested typographical corrections identified in the Revision 2 & 3 SER Table 2. These SER directed changes were located on pages 2.3-36, 2.3-46, 2.3-83.1, H-6, H-7, I-5, I-11, I-12, J-8, and L-13.

In addition, two typographical errors have been discovered in two other text descriptions versus what is contained in the actual code formulation. The first error is in the two-phase head degradation table (first HAD head degradation point) on page 2.1-149. The topical has the incorrect sign for the head difference given in Subroutine RPUMP. The second error is in the steam heat transfer coefficient Equation 2.2.2-76 in the B&W high AFW model on page 2.2-40. The equation was corrected to match the correct formulation used in Subroutine HTFILM. These two errors could result in inappropriate code input to analyses or incorrect hand calculations based on the equation given. Therefore, corrected information has been provided in the approved topical version by replacing these two pages. The incorrect material was replaced with underlined, italicized text to indicate the corrected information. The information is marked in the margin with a change bar and a letter "s" to denote the supplemental typographical correction.

Each of the replaced pages (12 in all) with the incorrect information are attached following this page. These pages

Rev. 4
9/99

have been updated with the correct information in the main body of the Revision 4 topical text.

Rev. 4
9/99

Table 2.1.5-1. Semiscale Dimensionless Head Ratio Difference (single-phase minus two-phase) Data.

$$x = \frac{v}{\alpha} \quad \text{or} \quad \frac{\alpha}{v}$$

$$y = \frac{h}{\alpha^2} \left|_{1\phi} \quad - \quad \frac{h}{\alpha^2} \right|_{2\phi} \quad - \quad \text{or} \quad \frac{h}{v^2} \left|_{1\phi} \quad - \quad \frac{h}{v^2} \right|_{2\phi}$$

Curve Type	x	y	Curve Type	x	y
1 (HAN)	0.00	0.00	4 (HVD)	-1.00	-1.16
	0.10	0.83		-0.90	-0.78
	0.20	1.09		-0.80	-0.50
	0.50	1.02		-0.70	-0.31
	0.70	1.01		-0.60	-0.17
	0.90	0.94		-0.50	-0.08
	1.00	1.00		-0.35	0.00
2 (HVN)	0.00	0.00	-0.20	0.05	
	0.10	-0.04	-0.10	0.08	
	0.20	0.00	0.00	0.11	
	0.30	0.10	5 (HAT)	0.00	0.00
	0.40	0.21		0.20	-0.34
	0.80	0.67		0.40	-0.65
	0.90	0.80		0.60	-0.95
1.00	1.00	0.80	-1.19		
3 (HAD)	-1.00	1.16	1.00	-1.47	
	-0.90	-1.24	6 (HVT)	0.00	0.11
	-0.80	-1.77		0.10	0.13
	-0.70	-2.36		0.25	0.15
	-0.60	-2.79		0.40	0.13
	-0.50	-2.91		0.50	0.07
	-0.40	-2.67		0.60	-0.04
	-0.25	-1.69		0.70	-0.23
	-0.10	-0.50		0.80	-0.51
	0.00	0.00		0.90	-0.91
		1.00		-1.47	
		7 (HAR)	-1.00	0.00	
			0.00	0.00	
		8 (HVR)	-1.00	0.00	
			0.00	0.00	

For $(T_{\text{sat}} - 4.0) < T_l < T_{\text{sat}}$,

$$\Gamma_{\text{wf}} = \Gamma_{\text{wChen}} - [(\Gamma_{\text{wChen}} - 0.0)(T_{\text{sat}} - T_l)/4.0] \quad 2.2.2-73$$

and

$$\Gamma_{\text{wg}} = 0.0 \quad 2.2.2-74$$

In the cases where $(T_{\text{sat}} - 4.0) > T_l$, there is an additional limit applied to Γ_{wf} . If Γ_{wf} calculated by Equations 2.2.2-70 or 2.2.2-72 exceeds 80% of the liquid available for boiling within a control volume, then the wetted area is reduced accordingly to give a value which can only equal 80%. This limit avoids the possibility of introducing an artificial mass error by vaporizing more liquid than is available.

Average Heat Flux and Heat Transfer Coefficients

The average values of heat flux and heat transfer coefficients are calculated as follows

$$h_{\text{fff}} = h_l A_{\text{wet}}/A_{\text{slab}} \quad 2.2.2-75$$

$$h_{\text{ffg}} = h_g A_{\text{wet}}/A_{\text{slab}} \quad 2.2.2-76$$

$$h_{\text{ff}} = h_{\text{fff}} + h_{\text{ffg}} \quad 2.2.2-77$$

$$q_{\text{fff}} = h_{\text{fff}}(T_w - T_l) \quad 2.2.2-78$$

$$q_{\text{ffg}} = h_{\text{ffg}}(T_w - T_g) \quad \text{and} \quad 2.2.2-79$$

$$q_{\text{ff}} = q_{\text{fff}} + q_{\text{ffg}} \quad 2.2.2-80$$

temperature difference and the burst strain as described in the following paragraphs for ruptured or unruptured channels.

Mode 1: Unruptured Elastic and Thermal Deformation

Within an unruptured channel, the clad is considered purely elastic if it has never gone plastic, ruptured, or the temperature difference between rupture and clad average temperatures is less than 166.7 K (300 F). The inside clad radius for this pure elastic mode is determined by

$$r_{ic} = r_{ic_{cold}} + u_{TC} + u_{CC} + u_e, \quad 2.3.2-19$$

where

u_{TC} = clad radial displacement due to thermal expansion (m),

u_{CC} = clad radius over-specification factor (m), determined during pin transient initiation, and

u_e = clad radial displacement due to elastic deformation (m).

The clad thermal expansion is determined similarly to that for the fuel.

$$u_{TC} = (r_{N_{HS}+1} - r_{N_f+2}) \epsilon_{TC} / 2, \quad 2.3.2-20$$

with

N_{HS} = total number of mesh intervals in the heat structure,

r_n = heat structure radius at the inside of mesh interval n or outside of n-1 (m), and

ϵ_{TC} = radial strain function defining fuel thermal expansion as a function of clad average temperature.

where

$$\beta^2 = \text{fraction of the channel flow area blocked,} \\ = (1.0 - A_{\text{blocked}}/A_{\text{channel}}).$$

The flow blockage is obtained via a double table interpolation relative to the normalized heating ramp rate and rupture temperature similarly to the clad burst strain. The table is either user supplied or default NUREG-0630 values listed in Tables 2.3.2-3 and 2.3.2-4. The additive value of the loss coefficient is edited at the time of rupture. The flow blockage loss coefficient is added automatically to the problem unless the user overrides via a new optional input. If added, the form loss is applied to the forward flow direction for the inlet (bottom) junction and the reverse flow direction for the exit (top) junction attached to the volume in which the clad ruptured. The user option to exclude this form loss addition from the junctions has been included for certain non-licensing specialized applications (such as in models that use a single fluid channel in the core with multiple radial heat structure channels).

Another option has been added to the EM Pin model help to minimize user burden when running EM reflooding heat transfer analyses with BEACH (BAW-10166 Section 2.1.3.8.4). This user-controlled option automatically includes code-calculated pin rupture, droplet break-up and convective enhancement adjustments. The input grid parameters are modified with the ruptured values and will be retained for use in the reflooding heat transfer calculations. This model is optional and requires input to activate the calculations. If no input is specified the default is that no rupture enhancements will be calculated.

When this option is selected several sets of calculations will be performed following cladding rupture. The first calculation

**Table H.2. ORNL Thermohydraulics Test Facility (THTF)
Benchmark Cases.**

Case	Experiment	Pressure (psia)	Power Density (kw/ft)	Mass Flux (lbm/hr/ft ²)
13	3.09.10i	0.68	650	21943.9
14	3.09.10j	0.33	610	9333.4
15	3.09.10k	0.10	580	2306.5
16	3.09.10l	0.66	1090	21461.4
17	3.09.10m	0.31	1010	9313.0
18	3.09.10n	0.14	1030	3395.2
19	3.09.10aa	0.39	590	14938.7
20	3.09.10bb	0.20	560	6961.9
21	3.09.10cc	0.10	520	3706.1
22	3.09.10dd	0.39	1170	14615.7
23	3.09.10ee	0.19	1120	8111.9
24	3.09.10ff	0.08	1090	3561.1

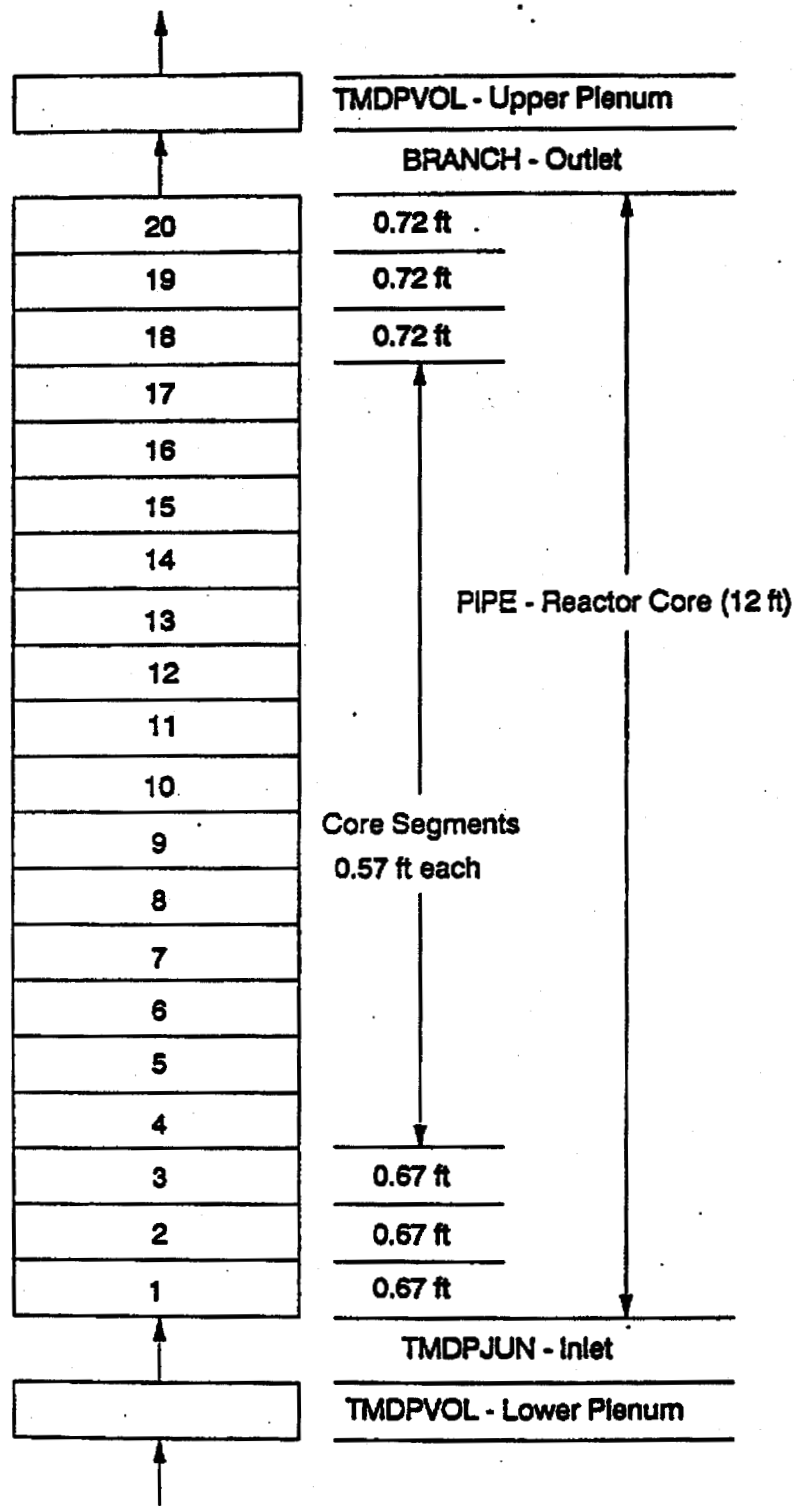


Figure H.1. RELAP5 Model of Hypothetical Reactor Core.

I.2.1. Correlation Form

The critical heat flux was assumed to depend on three parameters:

$$\begin{aligned}x_1 &= \exp[P / (1000 \cdot C1_p)], \\x_2 &= G / (10^6 \cdot C1_{MF}), \text{ and} \\x_3 &= X_{eth}.\end{aligned}$$

where P is the system pressure in psia, G is the mass flux in lbm/hr/ft², X_{eth} is the quality at CHF, and C1_p and C1_{MF} are the English-to-metric conversion factors for pressure and mass flux, respectively.

Based on the work of Farnsworth¹⁴², a general polynomial form was assumed:

$$\begin{aligned}\text{CHF} = \text{FLS} & (a_0 + a_1x_1 + a_2x_2 + a_3x_3^2 + a_4x_1^2 + a_5x_2 + a_6x_3|x_3| \\ & a_7x_1x_2 + a_8x_1x_3 + a_9x_2x_3 + a_{10}x_1^3 + a_{11}x_2^3 + a_{12}x_3^3 + \\ & a_{13}x_1x_2x_3) / F,\end{aligned} \tag{I-1}$$

where FLS is the bundle specific multiplier used in BWC MV and is defined by

$$\text{FLS} = C_1 + C_2L + C_3S + C_4L^2 + C_5LS + C_6S^2, \tag{I-2}$$

in which

- L = heated length,
- S = spacer grid spacing, and
- C₁ = empirically determined coefficients.

Table I.3. Calculated Local Condition Values.

	Point	Pressure psia	Mass Flux lbm/hr/ft ²	Heat Flux btu/hr/ft ²	Quality
Test 121					
	430	2015	405308	370043	0.2556
	431	2015	721925	461763	0.0969
	432	2015	704141	521065	0.0664
	433	2015	916371	521065	0.0664
Test 160					
	786	2115	527956	287300	0.3641
	787	2385	531861	282880	0.3157
	788	1805	541406	311610	0.3265
	789	1515	519832	373490	0.5620
	789	1515	513721	373490	0.6653
	790	2115	532879	335920	0.3127
	791	2405	519639	329290	0.2604
	792	1800	531920	370175	0.4239
	793	1815	516979	397800	0.4586
	794	2075	508498	349180	0.3110
Test 164					
	2055	1000	2554047	601121	0.2000
	2056	1000	3018628	682772	0.1931
	2057	1000	1588414	363385	0.3162
	2058	1000	2035850	647578	0.2044
	2059	1005	2518548	709520	0.1634
	2060	1005	3030165	751754	0.1683
	2060	1005	3050214	611714	0.1980
	2061	1005	1103392	348591	0.4161
	2062	1010	1575738	404069	0.3199
	2063	760	1879028	372631	0.3371
	2064	760	2634649	444754	0.2812
	2065	765	3096974	713744	0.2090

Table I.3 (continued). Calculated Local Condition Values.

	Point	Pressure psia	Mass Flux lbm/hr/ft ²	Heat Flux btu/hr/ft ²	Quality
Test 164 (continued)					
	2065	765	3147021	468794	0.2528
	2066	755	1617322	374481	0.3567
	2067	750	2115662	392049	0.3122
	2068	750	1627688	338420	0.3935
	2069	745	1026514	327324	0.4569
	2070	750	1049376	347666	0.4291
	2071	1005	2120543	578597	0.2326
	2072	995	1044837	307906	0.4731
	2073	1005	558151	281092	0.6404
	2074	1000	547973	239483	0.5657
	2075	760	538561	378692	0.4393
	2076	755	545706	232086	0.6060

9

Counter current flow limiting (CCFL) is applied to the junctions at the steam generator plenum and tube inlets. The Wallis correlation from Reference 145 is used in the steam generator tube inlet junction, and the CCFL correlation based on the UPTF data from Reference 146 is used in the steam generator plenum inlet junction. The results of the CCFL calculation will be discussed later. The SBLOCA EM heat transfer model is used for the core heat transfer calculation. This model uses the BWUMV CHF correlation to calculate DNB, and permits return to nucleate boiling when rewetting is calculated during the post-DNB period.

A discharge coefficient of 1.1 is used for subcooled flow and two-phase flow up to 70 percent void fraction, and the two-phase coefficient is reduced to 0.77 for void fraction greater than 70 percent. These relative values were used to match a measured flow, and are consistent with the relationship of discharge coefficients with respect to void fraction discussed in Volume 2 Section 4.3.2.3 of BAW-10168, Revision 2.

Results of the Benchmark

The steady-state initial conditions for the benchmark are presented along with the test conditions in Table 2. To demonstrate model stability relative to time advancement, the EM model was run with a time step advancement of 0.05 seconds (base case) and with a reduced time step of 0.005 seconds. Figures 6 through 10 show the results of the time step study, and confirm that the reduced time step advancement does not change the results. A comparison of the results of the base case (RELAP5/MOD2 EM) with the experimental data identified with instrumentation tag names listed in Reference 142 is presented in Table J.3 and Figures J.11 through J.36 below.

The calculated sequence of major events are presented along with the test data in Table J.3. Due to a facility power limitation,

Table L.1. Comparison of MIST Initial Conditions to RELAP5/MOD2-B&W Values.

<u>Parameter, Units</u>	<u>MIST Value</u>	<u>RELAP5/MOD2-B&W Value</u>
Primary Pressure, psia	1730.0	1726.5
Secondary Pressure, psia	1010.0	1010.0
Core Exit Temperature, F	592.0	593.4
SG Exit Temperature, F	551.0	550.3
Core Exit Subcooling, F	22.0	22.0
Core Power, Btu/s	117.0	119.5
Pressurizer Level, ft	5.0	5.0
SG Secondary Level, ft	4.8	5.0
Core Flow Rate, lbm/s	1.86	1.86

Table L.2. Sequence of Events.

<u>Event</u>	<u>MIST Observation Seconds</u>	<u>Ver 5.0 Prediction Seconds</u>	<u>Ver 14.0 Prediction Seconds</u>
Leak opened	0	0	0
Primary saturates	12	31	34
Pzr level reaches one foot (HPI, AFW, and DH ramp started)	30-42	60	57
Hot leg U-bend voiding interrupts natural circ. (Loop A/Loop B)	54/42	85/130	130/90
High elev BCM begins (Loop A/Loop B)	170/175	180/185	180/180
Break saturates	190	130	140
Secondary refilled and AFW shutoff (SG A/SG B)	480/480	490/440	480/480
Primary and secondary pressures equalize	1560	1500	1650
Secondary blowdown	1710	1500	1650
CFT injection begins	1920	1680	1800

This page is intentionally left blank.

APPENDIX A

RELAP5/MOD2 MODELS NOT
EMPLOYED IN EVALUATIONS

Several special component and constitutive models are included within RELAP5/MOD2-B&W which will not be used for evaluation model calculations. These models include: reflood heat transfer, noncondensable gas heat transfer degradation, the original INEL simple gap conductance model, jet mixing, and the turbine component. These sections will not be described within this report; however, a reference back to the original INEL release of RELAP5/MOD2 code manual¹ will be given for completeness.

The reflood heat transfer option will not be used in the RELAP5 evaluation model calculations. It is described in sections 3.1.3.6, 3.2.8, and 3.2.9 of Reference 1. The reflood portion of the LBLOCA transient will be performed by the BEACH code¹²³, a derivative of RELAP5/MOD2.

Two noncondensable gas heat transfer degradation models are available within RELAP5/MOD2-B&W. An original INEL model and a new mechanistic model option added by B&W are formulated within the code. A complete description of the INEL model can be found in Reference 1.

A new detailed gap conductance model which included clad swell and rupture calculations as well as metal water reaction calculations was added for evaluation model calculations. The original simple gap conductance model described in section 3.2.10 of Reference 1 will therefore not be used.

The turbine and jet mixer special component models will not be used for licensing calculations. A complete description of these models is found in Reference 1 sections 3.1.5.5 and 3.1.5.3.

APPENDIX B

LIST OF SYMBOLS

(Variables which are not dimensioned have SI units)

- A Cross-sectional area (m^2), coefficient matrix in hydrodynamics, coefficient in pressure and velocity equations
- A_1 Coefficient in heat conduction equation at boundaries
- A_L Surge line cross sectional area (m^2)
- A_t Throat area (m^2)
- a Speed of sound (m/s), interfacial area per unit volume (m^{-1}), coefficient in gap conductance, coefficient in heat conduction equation, absorption coefficient
- B Coefficient matrix, drag coefficient, coefficient in pressure and velocity equations
- B_1 Coefficient in heat conduction equation at boundaries
- b Coefficient in heat conduction equation, source vector in hydrodynamics
- B_x Body force in x-coordinate direction (m/s^2)
- B_y Body force in y-coordinate direction (m/s^2)
- C Coefficient of virtual mass, general vector function, coefficient in pressure, and velocity equations, delay neutron precursors in reactor kinetics, concentration

C_o	Coefficient in noncondensable energy equation (J/kg-K)
C_d	Drag coefficient
C_g	Dimensional constant in correlation for Γ_g
C_p	Specific heat at constant pressure (J/kg-K)
C_v	Specific heat at constant volume (J/kg-K)
c	Coefficient in heat conduction equation, coefficient in new time volume-average velocity equation
D	Coefficient of relative Mach number, diffusivity, diameter (m), heat conduction boundary condition matrix, coefficient in pressure and velocity equations
D_o	Coefficient in noncondensable energy equation (J/kg-K ²)
D_1	Coefficient of heat conduction equation at boundaries
d	Coefficient in heat conduction equation, droplet diameter (m)
DISS	Energy dissipation function (w/m ³)
E	Total energy ($U + v^2/2$) (J/kg), emissivity, Young's modulus, term in iterative heat conduction algorithm, coefficient in pressure equation

e	Interfacial roughness
Eu	Euler number
F	Term in iterative heat conduction algorithm, gray-body factor with subscript, frictional loss coefficient, vertical stratification factor
FIF, FIG	Interphase drag coefficients (liquid, vapor) (s^{-1})
FI	Interphase drag coefficient ($m^3/kg-s$)
FWF, FWG	Wall drag coefficients (liquid, vapor) (s^{-1})
f	Interphase friction factor, vector for liquid velocities in hydrodynamics, delayed neutron fraction
G_{head}	Pressure drop across valve due to gravity (Pa)
G	Mass velocity (kg/s), shear stress, gradient, coefficient in heat conduction, vector quantity, fraction of delayed neutrons in reactor kinetics
G_c	Dynamic pressure for valve (Pa)
Gr	Grashof number
g	Gravitational constant (m/s^2), temperature jump distance (m), vector for vapor velocities in hydrodynamics
$g_{z,g}$	Acceleration due to gravity (m/s^2)

H	Elevation (m), volumetric heat transfer coefficient ($w/K\text{-m}^3$), head (m), clad non-dimensional heating ramp rate
HLOSSF	Form or frictional losses (liquid) (m/s)
HLOSSG	Form or frictional losses (vapor) (m/s)
h	Specific enthalpy (J/kg), heat transfer coefficient ($w/m^2\text{-K}$), energy transfer coefficient for Γ_g , head ratio
h_L	Dynamic head loss (m)
I	Identity matrix, moment of inertia ($N\text{-m}\text{-s}^2$)
J	Junction velocity (m/s)
K	Energy form loss coefficient, metal-water rate constant ($g^2/cm^4\text{-s}$)
k	Thermal conductivity ($w/m\text{-K}$)
k_B	Boltzmann constant
k_s	Spring constant
L	Length, limit function
L_L	Surge line length (m)
ll	Liquid level (m)
M	Mach number, molecular weight, pump two-phase multiplier, mass transfer rate, mass (kg)

N	Number of system nodes, number density ($\#/m^3$), pump speed (rad/s)
Nu	Nusselt number
n	Unit vector, order of equation system, moles of gap gas (kg mole)
P_{Br}	Valve closing back pressure (Pa)
P	Pressure (Pa), reactor power (w), channel perimeter (m), turbine power (J/s)
P_D	Nitrogen pressure in dome (Pa)
P_f	Relates reactor power to heat generation rate in heat structures, immediate fission power (MeV/s)
P_o	Atmospheric pressure (Pa)
p	Wetted perimeter (m), particle probability function
PCV	Specified pressure required to close a valve (Pa)
Pr	Prandtl number
Q	Volumetric heat addition rate (w/m^3), space dependent function, volumetric flow rate (m^3/s)
Q_D	Total heat transfer to vapor dome (w)
Q_f	Immediate fission energy per fission (MeV)
q	Heat transfer rate (w), heat flux (w/m^2)

q_t	Specified time dependent, space dependent factor in the source term of heat conduction
R	Reynolds number, radius (m), surface roughness in gap conductance, radiation resistance term, gas constant (cal/gmole-K)
Re	Reynolds number
Re_p	The particle Reynolds number
R_n, R_s	Universal gas constants (noncondensable, steam) (N-m/kg-K)
r	Reaction fraction for turbine
S	Chen's boiling suppression factor, stress gradient, specific entropy (J/kg-K), shape factor, real constant, source term in heat conduction or reactor kinetics (w)
s	Surface, Laplace transform variable
T	Temperature (K), trip
T_c	Critical temperature (K)
T_R	Reduced temperature (K)
T_t	Specified time dependent function in heat conduction
t	Time (s)

U	Specific internal energy (J/kg), vector of dependent variables
u	Radial displacement in gap conductance (m)
V	Volume (m^3), specific volume (m^3/kg), control quantity
V _v	Volume of noncondensable in accumulator dome (m^3)
VFDP, VGDP	Coefficient for pressure change in momentum equations (liquid, vapor) (m/s-Pa)
VIS	Numerical viscosity terms in momentum equations (m^2/s^2)
VIS _F , VIS _G	Numerical viscosity terms in momentum equations (liquid, vapor) (m^2/s^2)
VUNDER, VOVER	Separator model parameters (liquid, vapor)
v	Mixture velocity (m/s), phasic velocity (m/s), flow ratio, liquid surge line velocity (m/s)
v _c	Choking velocity (m/s)
W	Weight of valve disk, weighting function in reactor kinetics, relaxation parameter in heat conduction, shaft work per unit mass flow rate
W _{crit}	Critical Weber number
We	Weber number

w	Humidity ratio
X	Static quality, mass fraction, conversion from MeV/s to watts
x	Spatial coordinate (m), vector of hydrodynamic variables
Y	Control variable
Z	Two-phase friction correlation factor, function in reactor kinetics
z	Elevation change coordinate (m)
Symbols	
α	Void fraction, subscripted volume fraction, angular acceleration (rad/s ²), coefficient for least squares fit, speed ratio
β	Coefficient of isobaric thermal expansion (K ⁻¹), effective delayed neutron fraction in reactor kinetics
Γ	Volumetric mass exchange rate (kg/m ³ -s)
ΔP_f	Dynamic pressure loss (Pa)
ΔP_s	Increment in steam pressure (Pa)
ΔV_s	Increment in specific volume of steam (m ³ /kg)
Δt	Increment in time variable (s)

Δt_c	Courant time step (s)
Δx	Increment in spatial variable (m)
β	Area ratio, truncation error measure, film thickness (m), impulse function, Deryagin number
ϵ	Coefficient, strain function, emissivity, tabular function of area ratio, surface roughness, wall vapor generation/condensation flag
ζ	Diffusion coefficient, multiplier or horizontal stratification terms the right side of heat conduction equation in finite difference form
η	Efficiency, bulk/saturation enthalpy flag
θ	Relaxation time in correlation for Q, angular position (rad)
κ	Coefficient of isothermal compressibility (Pa^{-1})
Λ	Prompt neutron generation time, Baroczy dimensionless property index
λ	Eigenvalue, interface velocity parameter, friction factor, decay constant in reactor kinetics
μ	Viscosity (kg/m-s)
ν	Kinematic viscosity (m^2/s), Poisson's ratio
ξ	Exponential function, RMS precision
π	3.141592654

ρ	Density (kg/m^3), reactivity in reactor kinetics (dollars)
Σ_f	Fission cross section
Σ'	Depressurization rate (Pa/s)
σ	Surface tension (J/m^2), stress, flag used in heat conduction equations to indicate transient or steady state
r	Shear stresses (N), torque (N-m), fuel-clad gap (m)
ϕ	Donored property, Lockhart-Martinelli two-phase parameter, neutron flux in reactor kinetics, angle of inclination of valve assembly
x	Lockhart-Martinelli parameter
ψ	Coefficient, fission rate (#/s)
ω	Angular velocity (rad/s), function variable in reactor kinetics

Subscripts

a	Average value
B	Boron, dissolved solid
b	Bubble
CHF	Value at critical heat flux

c	Vena contracta, continuous phase, cladding, critical property, cross section
cm	Cladding midpoint
con	Condensation
cr	Critical property or condition
D	Drive line, vapor dome
d	Droplet, delay in control component
e	Thermodynamic equilibrium, equivalent quality in hydraulic volumes, value ring exit, elastic deformation
exp	Used to indicate explicit velocities in choking
F	Wall friction, fuel
FB, FBB	Film boiling, Bromley film boiling
f	Liquid phase
fg	Phasic difference (i.e., vapor term-liquid term)
fp	Onset of vapor pull-through
fr	Frictional
g	Vapor phase, gap
ge	Incipient liquid entrainment

H	Head
HE	Homogeneous equilibrium
HF	Homogeneous frozen
hy	Hydraulic
I	Interface, delayed neutron group index
IB	Incipience of boiling
i	Inlet, interface
j, j+1, j-1	Spatial noding indices, junctions
K	Spatial noding indices, volumes
L	Spatial noding index, volumes, laminar
l	Left boundary in heat conduction
M	Rightmost boundary in heat conduction
m	Mixture property, motor, mesh point
NB	Nucleate boiling
n	Noncondensable component of vapor phase
o	Reference value
R	Rated values

r Relative Mach number, right boundary in heat conduction

S Suction region

s Steam component of vapor phase

sat Saturated quantity

T Point of minimum area, turbulent

TB Transition film boiling

t Turbulent, tangential

tt Fully turbulent

up Upstream quantity

v Mass mean Mach number, vapor quantity, valve

w Wall, water

wall Wall of tank

wg, wf Wall to vapor, wall to liquid

1 Upstream station, multiple junction index, vector index

1 ϕ Single-phase value

2 Downstream station, multiple junction index, vector index

2ϕ Two-phase value

r Torque

\cdot Vector

\equiv Matrix

Superscripts

b Boundary gradient weight factor in heat conduction, vector quantities

exp Old time terms in velocity equation

I Imaginary part of complex number

$m-1, m, m+1$ Mesh points in heat conduction finite difference equation or mean value

$n, n+1$ Time level index

$n + 1/2$ An average of quantities with superscripts n and $n + 1$

o Initial value

R Real part of complex number

r Right boundary in heat conduction

s Saturation property, space gradient weight factor in heat conduction

v Volume gradient weight factor in heat conduction

w	Wall
1	Vector index, coefficient in velocity equation
2	Vector index
*	Total derivative of a saturation property with respect to pressure, local variable, bulk/saturation property
'	Derivative
-	Vector, average quantity
.	Donored quantity
-	Unit momentum for mass exchange, intermediate time variable
^	Linearized quantity, quality based on total mixture mass

APPENDIX C
EM CRITICAL FLOW TABLES

The new evaluation model choked flow tables are listed in tabular form in this Appendix. They are listed in the following sections:

- C.1 Moody Critical Flow Table.
- C.2 Extended Henry-Fauske Critical Flow Table.
- C.3 Homogeneous Equilibrium Critical Flow Table.
- C.4 Murdock-Bauman Critical Flow Table.

C.1 MOODY CRITICAL FLOW TABLE

GXX(1) = STAGNATION PRESSURE (PSIA)
 GXX(EVEN) = MAXIMUM FLOW RATE (LBM/FT**2-SEC)
 GXX(ODD) = STAGNATION ENTHALPY (BTU/LB)

NG = NUMBER OF PAIRS OF FLOW AND ENTHALPY VALUES PER PRESSURE
 NPI = NUMBER OF PRESSURE VALUES

DATA NG, NPI / 17, 21 /

DATA G01 / 1.0EO, 214.71EO, 69.733EO, 20.11EO, 173.340EO,
 1 10.95EO, 276.948EO, 7.54EO, 380.555EO, 5.76EO, 484.163EO,
 2 4.65EO, 587.771EO, 3.91EO, 691.378EO, 3.37EO, 794.986EO,
 3 2.96EO, 898.593EO, 2.64EO, 1002.201EO, 2.38EO, 1105.809EO,
 4 2.50EO, 1112.678EO, 2.00EO, 1238.828EO, 1.80EO, 1369.999EO,
 5 1.60EO, 1507.606EO, 1.40EO, 1652.162EO, 1.30EO, 1803.545EO/

DATA G02 / 5.0EO, 527.49EO, 130.196EO, 90.72EO, 230.286EO,
 1 50.86EO, 330.376EO, 35.44EO, 430.465EO, 27.21EO, 530.555EO,
 2 22.09EO, 630.645EO, 18.60EO, 730.734EO, 16.06EO, 830.824EO,
 3 14.13EO, 930.913EO, 12.62EO, 1031.003EO, 11.39EO, 1131.093EO,
 4 11.70EO, 1142.565EO, 9.80EO, 1264.479EO, 8.60EO, 1390.263EO,
 5 7.70EO, 1521.800EO, 7.10EO, 1659.584EO, 6.60EO, 1803.492EO/

DATA G03 / 10.0EO, 767.75EO, 161.261EO, 171.18EO, 259.470EO,
 1 97.76EO, 357.678EO, 68.64EO, 455.887EO, 52.93EO, 554.096EO,
 2 43.09EO, 652.305EO, 36.34EO, 750.513EO, 31.42EO, 848.722EO,
 3 27.67EO, 946.931EO, 24.73EO, 1045.140EO, 22.35EO, 1143.348EO,
 4 22.90EO, 1157.466EO, 19.30EO, 1277.542EO, 17.10EO, 1400.619EO,
 5 15.40EO, 1529.045EO, 14.20EO, 1663.351EO, 13.10EO, 1803.425EO/

DATA G04 / 14.7EO, 943.01EO, 180.179EO, 242.34EO, 277.210EO,
 1 140.17EO, 374.240EO, 98.93EO, 471.270EO, 76.51EO, 568.300EO,
 2 62.40EO, 665.331EO, 52.69EO, 762.361EO, 45.60EO, 859.391EO,
 3 40.19EO, 956.421EO, 35.93EO, 1053.452EO, 32.49EO, 1150.482EO,
 4 33.10EO, 1166.377EO, 28.20EO, 1258.449EO, 24.90EO, 1406.903EO,
 5 22.60EO, 1533.437EO, 20.80EO, 1665.624EO, 19.30EO, 1803.363EO/

DATA G05 / 50.0EO, 1787.76EO, 250.212EO, 706.24EO, 342.600EO,
 1 432.14EO, 434.988EO, 312.25EO, 527.376EO, 244.68EO, 619.764EO,
 2 201.24EO, 712.153EO, 170.93EO, 804.541EO, 148.58EO, 896.929EO,
 3 131.40EO, 989.317EO, 117.79EO, 1081.705EO, 106.74EO, 1174.093EO,
 4 107.50EO, 1196.581EO, 92.90EO, 1312.998EO, 83.20EO, 1428.913EO,
 5 76.00EO, 1548.789EO, 70.40EO, 1673.458EO, 65.80EO, 1802.893EO/

DATA G06 / 100.0EO, 2546.50EO, 298.538EO, 1252.95EO, 387.401EO,
 1 802.83EO, 476.264EO, 591.90EO, 565.127EO, 469.15EO, 653.989EO,
 2 388.73EO, 742.852EO, 331.92EO, 831.715EO, 289.63EO, 920.578EO,
 3 256.92EO, 1009.440EO, 230.86EO, 1098.303EO, 209.60EO, 1187.166EO,
 4 209.20EO, 1214.890EO, 182.30EO, 1330.371EO, 164.50EO, 1442.897EO,
 5 151.10EO, 1558.489EO, 140.30EO, 1678.248EO, 131.60EO, 1802.229EO/

DATA G07 / 200.0EO, 3608.16EO, 355.506EO, 2153.39EO, 439.789EO,
 1 1463.65EO, 524.071EO, 1108.91EO, 608.354EO, 893.05EO, 692.637EO,
 2 747.78EO, 776.920EO, 643.27EO, 861.202EO, 564.45EO, 945.485EO,
 3 502.88EO, 1029.768EO, 453.44EO, 1114.051EO, 412.87EO, 1198.334EO,
 4 407.00EO, 1234.101EO, 357.60EO, 1349.174EO, 325.00EO, 1458.103EO,
 5 300.00EO, 1568.929EO, 279.90EO, 1683.135EO, 263.30EO, 1800.900EO/

DATA G08 / 400.0EO, 5084.55EO, 424.167EO, 3560.62EO, 502.210EO,
 1 2601.91EO, 580.252EO, 2044.87EO, 658.294EO, 1683.97EO, 736.337EO,
 2 1413.45EO, 814.379EO, 1244.89EO, 892.421EO, 1101.42EO, 970.464EO,
 3 987.66EO, 1048.506EO, 895.23EO, 1126.548EO, 818.64EO, 1204.591EO,
 4 792.40EO, 1253.154EO, 701.20EO, 1368.603EO, 641.80EO, 1473.887EO,
 5 595.90EO, 1579.509EO, 558.50EO, 1687.509EO, 527.30EO, 1798.245EO/

DATA G09 / 600.0EO, 6192.24EO, 471.697EO, 4682.13EO, 544.893EO,
 1 3588.84EO, 618.089EO, 2897.01EO, 691.285EO, 2426.85EO, 764.481EO,
 2 2087.61EO, 837.677EO, 1831.53EO, 910.873EO, 1631.43EO, 984.069EO,
 3 1470.77EO, 1057.265EO, 1338.95EO, 1130.461EO, 1228.83EO, 1203.657EO,
 4 1172.40EO, 1262.896EO, 1040.80EO, 1379.241EO, 956.20EO, 1482.588EO,
 5 890.60EO, 1585.098EO, 837.00EO, 1689.262EO, 792.00EO, 1795.591EO/

DATA G10 / 800.0EO, 7103.30EO, 509.811EO, 5630.54EO, 578.769EO,
 1 4472.42EO, 647.726EO, 3689.49EO, 716.684EO, 3135.77EO, 785.641EO,
 2 2725.47EO, 854.599EO, 2409.78EO, 923.557EO, 2159.53EO, 992.514EO,
 3 1956.33EO, 1061.472EO, 1788.08EO, 1130.429EO, 1646.48EO, 1199.387EO,
 4 1550.10EO, 1268.822EO, 1378.50EO, 1386.128EO, 1269.40EO, 1488.245EO,
 5 1184.90EO, 1588.533EO, 1115.70EO, 1689.882EO, 1057.40EO, 1792.940EO/

DATA G11 / 1000.0EO, 7883.70EO, 542.551EO, 6458.25EO, 607.589EO,
 1 5277.33EO, 672.628EO, 4434.96EO, 737.666EO, 3818.11EO, 802.705EO,
 2 3349.91EO, 867.743EO, 2983.26EO, 932.782EO, 2688.66EO, 997.820EO,
 3 2446.89EO, 1062.859EO, 2244.95EO, 1127.898EO, 2073.79EO, 1192.936EO,
 4 1928.00EO, 1272.169EO, 1715.80EO, 1390.601EO, 1582.30EO, 1491.960EO,
 5 1479.30EO, 1590.602EO, 1394.80EO, 1689.784EO, 1323.60EO, 1790.290EO/

DATA G12 / 1200.0EO, 8566.61EO, 571.853EO, 7194.59EO, 633.149EO,
 1 6018.53EO, 694.445EO, 5141.21EO, 755.741EO, 4478.45EO, 817.037EO,
 2 3964.05EO, 878.333EO, 3554.43EO, 939.629EO, 3221.01EO, 1000.925EO,
 3 2944.51EO, 1062.221EO, 2711.61EO, 1123.517EO, 2512.78EO, 1184.813EO,
 4 2306.00EO, 1274.362EO, 2052.90EO, 1393.811EO, 1895.20EO, 1494.624EO,
 5 1773.90EO, 1591.920EO, 1674.40EO, 1689.289EO, 1590.60EO, 1787.642EO/

DATA G13 / 1400.0EO, 9171.02EO, 598.830EO, 7857.52EO, 656.477EO,
 1 6705.77EO, 714.125EO, 5813.30EO, 771.773EO, 5119.72EO, 829.420EO,
 2 4569.95EO, 887.068EO, 4125.04EO, 944.716EO, 3758.28EO, 1002.364EO,
 3 3450.98EO, 1060.011EO, 3189.90EO, 1117.659EO, 2965.42EO, 1175.307EO,
 4 2684.80EO, 1275.682EO, 2390.20EO, 1396.083EO, 2208.30EO, 1496.504EO,
 5 2068.80EO, 1592.681EO, 1954.50EO, 1688.499EO, 1858.30EO, 1784.994EO/

DATA G14 / 1600.0EO, 9708.52EO, 624.202EO, 8458.62EO, 678.235EO,
 1 7345.72EO, 732.268EO, 6454.71EO, 786.300EO, 5743.98EO, 840.333EO,
 2 5169.19EO, 894.366EO, 4696.66EO, 948.399EO, 4302.13EO, 1002.431EO,

3 3968.12E0,1056.464E0, 3681.89E0,1110.497E0, 3433.97E0,1164.530E0,
 4 3067.10E0,1275.712E0, 2729.00E0,1397.285E0, 2522.30E0,1497.542E0,
 5 2364.50E0,1592.855E0, 2235.40E0,1687.403E0, 2126.80E0,1782.347E0/

DATA G15 / 1800.0E0,10186.24E0, 648.490E0, 9005.71E0, 698.875E0,
 1 7943.45E0, 749.258E0, 7068.47E0, 799.642E0, 6353.40E0, 850.027E0,
 2 5763.77E0, 900.411E0, 5271.40E0, 950.795E0, 4855.02E0,1001.179E0,
 3 4498.77E0,1051.564E0, 4190.73E0,1101.948E0, 3921.87E0,1152.332E0,
 4 3448.60E0,1275.998E0, 3067.70E0,1398.372E0, 2836.40E0,1498.413E0,
 5 2660.50E0,1592.891E0, 2516.90E0,1686.228E0, 2396.00E0,1779.701E0/

DATA G16 / 2000.0E0,10608.22E0, 672.111E0, 9504.17E0, 718.734E0,
 1 8503.14E0, 765.356E0, 7657.68E0, 811.979E0, 6950.77E0, 858.601E0,
 2 6356.68E0, 905.224E0, 5852.74E0, 951.846E0, 5420.97E0, 998.468E0,
 3 5047.45E0,1045.091E0, 4721.42E0,1091.713E0, 4434.55E0,1138.336E0,
 4 3833.80E0,1257.411E0, 3408.30E0,1398.751E0, 3151.70E0,1498.725E0,
 5 2957.50E0,1592.538E0, 2799.20E0,1684.851E0, 2666.10E0,1777.056E0/

DATA G17 / 2200.0E0,10975.67E0, 695.462E0, 9956.80E0, 738.132E0,
 1 9027.41E0, 780.802E0, 8224.65E0, 823.471E0, 7538.67E0, 866.141E0,
 2 6951.18E0, 908.811E0, 6444.80E0, 951.481E0, 6004.98E0, 994.150E0,
 3 5620.04E0,1036.820E0, 5280.64E0,1079.490E0, 4979.37E0,1122.159E0,
 4 4220.10E0,1274.756E0, 3749.80E0,1398.911E0, 3467.80E0,1498.821E0,
 5 3255.10E0,1592.023E0, 3082.30E0,1683.386E0, 2937.10E0,1774.411E0/

DATA G18 / 2400.0E0,11209.60E0, 718.953E0,10316.18E0, 757.431E0,
 1 9486.43E0, 795.909E0, 8750.33E0, 834.387E0, 8105.54E0, 872.866E0,
 2 7541.38E0, 911.344E0, 7046.15E0, 949.822E0, 6609.24E0, 988.300E0,
 3 6221.66E0,1026.779E0, 5875.90E0,1065.257E0, 5565.81E0,1103.735E0,
 4 4619.20E0,1271.798E0, 4096.70E0,1397.651E0, 3787.00E0,1497.913E0,
 5 3554.70E0,1590.843E0, 3366.60E0,1681.584E0, 3208.80E0,1771.765E0/

DATA G19 / 2600.0E0,11428.29E0, 744.475E0,10644.57E0, 778.232E0,
 1 9914.50E0, 811.988E0, 9254.60E0, 845.745E0, 8664.25E0, 879.502E0,
 2 8137.27E0, 913.259E0, 7666.18E0, 947.016E0, 7243.77E0, 980.772E0,
 3 6863.58E0,1014.529E0, 6520.03E0,1048.286E0, 6208.34E0,1082.043E0,
 4 5012.40E0,1270.621E0, 4441.80E0,1397.239E0, 4105.40E0,1497.515E0,
 5 3854.20E0,1589.972E0, 3651.40E0,1679.930E0, 3481.50E0,1769.120E0/

DATA G20 / 2800.0E0,11589.07E0, 770.686E0,10931.29E0, 799.200E0,
 110314.45E0, 827.715E0, 9746.45E0, 856.230E0, 9227.42E0, 884.745E0,
 2 8754.35E0, 913.260E0, 8323.15E0, 941.774E0, 7929.53E0, 970.289E0,
 3 7569.46E0, 998.804E0, 7239.24E0,1027.319E0, 6935.60E0,1055.834E0,
 4 5411.00E0,1269.067E0, 4789.20E0,1396.501E0, 4425.40E0,1496.853E0,
 5 4154.90E0,1588.914E0, 3937.10E0,1678.177E0, 3755.00E0,1766.475E0/

DATA G21 / 3000.0E0,11604.42E0, 801.845E0,11109.66E0, 823.687E0,
 110640.97E0, 845.529E0,10200.60E0, 867.371E0, 9788.61E0, 889.213E0,
 2 9403.93E0, 911.055E0, 9044.98E0, 932.898E0, 8709.95E0, 954.740E0,
 3 8397.01E0, 976.582E0, 8104.38E0, 998.424E0, 7830.38E0,1020.266E0;
 4 5816.40E0,1267.043E0, 5139.50E0,1395.404E0, 4747.10E0,1495.908E0,
 5 4456.80E0,1587.660E0, 4223.80E0,1676.323E0, 4029.40E0,1763.830E0/

C.2 EXTENDED HENRY-FAUSKE CRITICAL FLOW TABLE

PE(1,I) = STAGNATION PRESSURE (PSIA)
 PE(EVEN,I) = MAXIMUM FLOW RATE (LB/FT**2-SEC)
 PE(ODD,I) = STAGNATION ENTHALPY (BTU/LB)

NPHE = NUMBER OF PRESSURE VALUES
 NHHE = NUMBER OF PAIRS OF ENTHALPY AND FLOW VALUES PER PRESSURE

DATA NHHE, NPHE / 11, 16 /

DATA PE01 / 10.0, 2293.0, 64.630, 2255.0, 74.271,					
1	2204.0,	83.914,	2140.0,	93.560,	2059.0, 103.210,
2	1955.0,	112.866,	1820.0,	122.527,	1647.0, 132.195,
3	1415.0,	141.871,	1108.0,	151.556,	768.0, 161.261/
DATA PE02 / 14.7, 2788.0, 74.023, 2744.0, 84.605,					
1	2684.0,	95.190,	2609.0,	105.780,	2512.0, 116.377,
2	2388.0,	126.981,	2227.0,	137.594,	2014.0, 148.217,
3	1735.0,	158.852,	1369.0,	169.501,	943.0, 180.179/
DATA PE03 / 50.0, 5174.0, 108.576, 5094.0, 122.624,					
1	4989.0,	136.686,	4853.0,	150.766,	4679.0, 164.868,
2	4449.0,	178.996,	4156.0,	193.154,	3771.0, 207.349,
3	3273.0,	221.585,	2646.0,	235.869,	1787.8, 250.212/
DATA PE04 / 100.0, 7314.0, 131.690, 7203.0, 148.066,					
1	7059.0,	164.470,	6870.0,	180.909,	6624.0, 197.390,
2	6304.0,	213.922,	5895.0,	230.515,	5361.0, 247.176,
3	4691.0,	263.917,	3853.0,	280.749,	2546.5, 298.538/
DATA PE05 / 200.0, 10316.0, 159.379, 10157.0, 178.555,					
1	9940.0,	197.788,	9668.0,	217.089,	9303.0, 236.474,
2	8846.0,	255.958,	8256.0,	275.557,	7513.0, 295.289,
3	6567.0,	315.174,	5460.0,	335.236,	3608.2, 355.506/
DATA PE06 / 400.0, 14530.0, 191.387, 14278.0, 213.823,					
1	13967.0,	236.367,	13556.0,	259.042,	13043.0, 281.874,
2	12377.0,	304.892,	11537.0,	328.128,	10496.0, 351.621,
3	9199.0,	375.416,	7708.0,	399.574,	5084.6, 424.167/
DATA PE07 / 600.0, 17719.0, 212.798, 17412.0, 237.429,					
1	17020.0,	262.216,	16499.0,	287.192,	15845.0, 312.394,
2	15027.0,	337.865,	13996.0,	363.658,	12730.0, 389.838,
3	11153.0,	416.489,	9378.0,	443.724,	6192.2, 471.697/
DATA PE08 / 800.0, 20397.0, 229.413, 20026.0, 255.753,					
1	19544.0,	282.295,	18943.0,	309.081,	18176.0, 336.159,
2	17231.0,	363.591,	16028.0,	391.452,	14557.0, 419.842,
3	12758.0,	448.894,	10734.0,	478.793,	7103.3, 509.811/

DATA PE09 /	1000.0,	22751.0,	243.188,	22316.0,	270.943,
1	21779.0,	298.941,	21080.0,	327.236,	20219.0,
2	19140.0,	384.982,	17782.0,	414.616,	16138.0,
3	14147.0,	476.119,	11891.0,	508.470,	7883.7,
					542.551/

DATA PE10 /	1200.0,	24864.0,	255.011,	24372.0,	283.995,
1	23760.0,	313.263,	23001.0,	342.879,	22039.0,
2	20839.0,	403.484,	19364.0,	434.707,	17546.0,
3	15369.0,	499.957,	12891.0,	534.672,	8566.6,
					571.853/

DATA PE11 /	1400.0,	26793.0,	265.587,	26256.0,	295.666,
1	25596.0,	326.069,	24745.0,	356.869,	23706.0,
2	22400.0,	420.065,	20806.0,	452.751,	18847.0,
3	16460.0,	521.548,	13753.0,	558.615,	9171.0,
					598.830/

DATA PE12 /	1600.0,	28582.0,	275.051,	28009.0,	306.109,
1	27278.0,	337.529,	26357.0,	369.396,	25230.0,
2	23832.0,	434.945,	22100.0,	468.978,	20014.0,
3	17468.0,	541.136,	14547.0,	580.548,	9708.5,
					624.202/

DATA PE13 /	1800.0,	30263.0,	283.684,	29633.0,	315.637,
1	28856.0,	347.990,	27868.0,	380.836,	26676.0,
2	25180.0,	448.564,	23329.0,	483.862,	21090.0,
3	18388.0,	559.264,	15234.0,	601.066,	10186.3,
					648.990/

DATA PE14 /	2000.0,	31856.0,	291.617,	31201.0,	324.390,
1	30358.0,	357.598,	29294.0,	391.347,	28034.0,
2	26436.0,	461.098,	24486.0,	497.583,	22124.0,
3	19264.0,	576.119,	15855.0,	620.360,	10608.2,
					672.111/

DATA PE15 /	2200.0,	33369.0,	298.970,	32664.0,	332.498,
1	31782.0,	366.495,	30655.0,	401.079,	29295.0,
2	27643.0,	472.715,	25603.0,	510.319,	23115.0,
3	20073.0,	591.888,	16430.0,	638.625,	10975.7,
					695.462/

DATA PE16 /	2400.0,	34803.0,	305.833,	34045.0,	340.062,
1	33104.0,	374.792,	31947.0,	410.154,	30531.0,
2	28787.0,	483.557,	26642.0,	522.220,	24030.0,
3	20862.0,	606.736,	16975.0,	656.028,	11209.6,
					718.953/

C.3 HOMOGENEOUS EQUILIBRIUM MODEL CRITICAL FLOW TABLES

TXX(1) = STAGNATION PRESSURE (PSIA)
 TXX(EVEN) = CRITICAL FLOW RATE (LBM/SEC-FT2)
 TXX(ODD) = STAGNATION ENTHALPY (BTU/LBM)

NGHT = NUMBER OF PAIRS OF FLOW RATE AND ENTHALPY VALUES PER PRESSURE

NPT = NUMBER OF PRESSURE VALUES

DATA NGHT, NPT / 27,21 /

DATA T01 /

					1.0EO,
1	716.13EO,	8.030EO,	711.91EO,	18.057EO,	658.45EO, 28.062EO,
2	681.49EO,	38.054EO,	535.31EO,	48.038EO,	447.12EO, 58.019EO,
3	442.29EO,	67.999EO,	20.41EO,	69.733EO,	6.75EO, 173.340EO,
4	5.02EO,	276.948EO,	4.17EO,	380.555EO,	3.65EO, 484.163EO,
5	3.29EO,	587.771EO,	3.01EO,	691.378EO,	2.80EO, 794.986EO,
6	2.62EO,	898.594EO,	2.48EO,	1002.201EO,	2.35EO, 1105.809EO,
7	2.35EO,	1114.029EO,	2.18EO,	1186.541EO,	1.97EO, 1260.427EO,
8	1.81EO,	1336.135EO,	1.67EO,	1423.810EO,	1.55EO, 1514.346EO,
9	1.46EO,	1607.840EO,	1.38EO,	1704.280EO,	1.31EO, 1803.545EO/

DATA T02 /

					5.0EO,
1	1681.25EO,	8.042EO,	1665.45EO,	38.065EO,	1579.07EO, 68.010EO,
2	1378.69EO,	87.975EO,	1162.01EO,	107.955EO,	852.83EO, 117.953EO,
3	385.75EO,	127.958EO,	83.89EO,	130.196EO,	31.49EO, 230.286EO,
4	23.69EO,	330.376EO,	19.80EO,	430.465EO,	17.36EO, 530.555EO,
5	15.65EO,	630.645EO,	14.36EO,	730.734EO,	13.35EO, 830.824EO,
6	12.52EO,	930.914EO,	11.83EO,	1031.003EO,	11.25EO, 1131.093EO,
7	11.22EO,	1139.325EO,	10.47EO,	1213.338EO,	9.53EO, 1288.228EO,
8	8.80EO,	1364.831EO,	8.20EO,	1443.519EO,	7.71EO, 1524.467EO,
9	7.30EO,	1607.747EO,	6.90EO,	1704.209EO,	6.56EO, 1803.492EO/

DATA T03 /

					10.0EO,
1	2391.40EO,	8.057EO,	2236.70EO,	78.004EO,	2047.90EO, 107.967EO,
2	1724.77EO,	127.970EO,	1505.41EO,	137.983EO,	1192.82EO, 148.006EO,
3	659.12EO,	158.038EO,	151.52EO,	161.261EO,	60.84EO, 259.470EO,
4	46.07EO,	357.678EO,	38.62EO,	455.887EO,	33.92EO, 554.096EO,
5	30.60EO,	652.305EO,	28.10EO,	750.513EO,	26.13EO, 848.722EO,
6	24.53EO,	946.931EO,	23.18EO,	1045.140EO,	22.04EO, 1143.348EO,
7	22.01EO,	1146.574EO,	20.69EO,	1221.805EO,	18.86EO, 1297.280EO,
8	17.44EO,	1374.284EO,	16.28EO,	1453.321EO,	15.32EO, 1534.604EO,
9	14.50EO,	1618.208EO,	13.80EO,	1704.121EO,	13.12EO, 1803.425EO/

DATA T04 /

					14.7EO,
1	2904.72EO,	8.071EO,	2774.33EO,	78.016EO,	2495.47EO, 117.977EO,
2	2216.69EO,	137.995EO,	1750.08EO,	158.049EO,	1384.01EO, 168.094EO,
3	789.99EO,	178.152EO,	209.49EO,	180.179EO,	87.60EO, 277.210EO,
4	66.61EO,	374.240EO,	55.94EO,	471.270EO,	49.19EO, 568.300EO,
5	44.41EO,	665.331EO,	40.80EO,	762.361EO,	37.95EO, 859.391EO,

6	35.63EO, 956.421EO,	33.68EO, 1053.452EO,	32.03EO, 1150.482EO,
7	31.98EO, 1154.345EO,	30.06EO, 1230.480EO,	27.45EO, 1306.438EO,
8	25.40EO, 1383.809EO,	23.74EO, 1463.184EO,	22.36EO, 1544.795EO,
9	21.18EO, 1628.719EO,	20.17EO, 1714.939EO,	19.28EO, 1803.363EO/

DATA T05 /				50.0EO,
1	5371.63EO, 8.175EO,	5190.51EO, 108.067EO,	4775.18EO, 158.130EO,	
2	4009.67EO, 198.393EO,	3318.03EO, 218.632EO,	2105.91EO, 238.966EO,	
3	703.71EO, 249.174EO,	571.57EO, 250.212EO,	389.44EO, 277.928EO,	
4	267.62EO, 351.839EO,	192.22EO, 490.421EO,	159.83EO, 619.764EO,	
5	144.72EO, 712.153EO,	133.23EO, 804.541EO,	124.11EO, 896.929EO,	
6	116.64EO, 989.317EO,	110.38EO, 1081.705EO,	105.03EO, 1174.093EO,	
7	104.66EO, 1184.119EO,	99.07EO, 1254.716EO,	91.70EO, 1323.151EO,	
8	85.78EO, 1391.904EO,	80.85EO, 1461.887EO,	76.11EO, 1543.804EO,	
9	72.09EO, 1627.948EO,	68.62EO, 1714.337EO,	65.60EO, 1802.694EO/	

DATA T06 /				100.0EO,
1	7600.63EO, 8.324EO,	7337.38EO, 128.187EO,	6764.11EO, 188.413EO,	
2	5606.26EO, 239.065EO,	4208.59EO, 269.774EO,	3474.36EO, 280.078EO,	
3	2333.70EO, 290.420EO,	989.42EO, 298.538EO,	721.04EO, 325.197EO,	
4	564.01EO, 369.629EO,	412.34EO, 476.264EO,	329.23EO, 609.558EO,	
5	282.31EO, 742.852EO,	260.32EO, 831.715EO,	242.80EO, 920.578EO,	
6	228.41EO, 1009.440EO,	216.31EO, 1098.303EO,	205.95EO, 1187.166EO,	
7	205.33EO, 1194.192EO,	194.62EO, 1269.141EO,	180.35EO, 1339.551EO,	
8	168.93EO, 1409.519EO,	159.42EO, 1480.449EO,	151.30EO, 1552.838EO,	
9	144.28EO, 1626.855EO,	137.31EO, 1713.484EO,	131.25EO, 1802.229EO/	

DATA T07 /				200.0EO,
1	110751.06EO, 8.620EO,	10327.76EO, 158.476EO,	9241.84EO, 239.264EO,	
2	8058.31EO, 280.257EO,	5812.39EO, 321.858EO,	3688.74EO, 342.949EO,	
3	1759.85EO, 353.581EO,	1685.31EO, 355.506EO,	1515.39EO, 363.934EO,	
4	1139.95EO, 406.075EO,	940.63EO, 456.645EO,	778.11EO, 532.500EO,	
5	631.88EO, 658.924EO,	528.84EO, 819.061EO,	475.74EO, 945.485EO,	
6	448.14EO, 1029.768EO,	424.86EO, 1114.051EO,	404.87EO, 1198.334EO,	
7	402.87EO, 1210.131EO,	384.10EO, 1280.034EO,	355.73EO, 1353.710EO,	
8	333.37EO, 1425.503EO,	314.79EO, 1497.762EO,	298.97EO, 1571.261EO,	
9	285.28EO, 1646.255EO,	273.29EO, 1722.810EO,	262.69EO, 1800.900EO/	

DATA T08 /				400.0EO,
1	115203.90EO, 9.212EO,	14540.28EO, 189.071EO,	13309.29EO, 270.329EO,	
2	211259.93EO, 332.672EO,	8740.94EO, 375.266EO,	5255.00EO, 407.962EO,	
3	3105.55EO, 419.039EO,	2818.39EO, 424.168EO,	2475.99EO, 439.776EO,	
4	2091.97EO, 470.993EO,	1858.15EO, 502.210EO,	1539.99EO, 572.448EO,	
5	1347.66EO, 642.686EO,	1155.65EO, 751.945EO,	1013.44EO, 876.813EO,	
6	935.86EO, 970.464EO,	860.17EO, 1087.527EO,	800.37EO, 1204.591EO,	
7	795.86EO, 1216.493EO,	775.13EO, 1271.230EO,	720.21EO, 1341.438EO,	
8	672.03EO, 1417.029EO,	633.05EO, 1491.300EO,	600.27EO, 1566.139EO,	
9	572.15EO, 1642.145EO,	547.66EO, 1719.505EO,	526.11EO, 1798.245EO/	

DATA T09 /				600.0EO,
1	118618.66EO, 9.803EO,	18103.35EO, 169.421EO,	16833.40EO, 270.700EO,	
2	214751.27EO, 343.512EO,	11204.24EO, 408.123EO,	7987.71EO, 441.582EO,	

3 4173.67EO, 464.48EO, 3768.85EO, 471.697EO, 3048.55EO, 508.295EO,
 4 2660.54EO, 544.893EO, 2206.12EO, 618.089EO, 1847.98EO, 720.564EO,
 5 1598.54EO, 837.677EO, 1486.45EO, 910.873EO, 1395.25EO, 984.069EO,
 6 1319.13EO, 1057.265EO, 1254.32EO, 1130.461EO, 1198.26EO, 1203.657EO,
 7 1190.77EO, 1215.928EO, 1173.16EO, 1262.896EO, 1082.18EO, 1340.030EO,
 8 1016.37EO, 1408.262EO, 954.91EO, 1484.762EO, 903.95EO, 1560.997EO,
 9 860.60EO, 1638.031EO, 823.13EO, 1716.199EO, 790.29EO, 1795.591EO/

DATA T10 / 800.0EO,
 121495.90EO, 10.393EO, 20695.34EO, 200.012EO, 19081.41EO, 301.983EO,
 216623.91EO, 375.727EO, 13495.09EO, 430.431EO, 9141.10EO, 476.098EO,
 3 5199.07EO, 499.841EO, 4606.04EO, 509.811EO, 4101.00EO, 530.499EO,
 4 3572.38EO, 564.977EO, 3163.63EO, 606.352EO, 2724.61EO, 675.310EO,
 5 2320.01EO, 778.746EO, 1974.80EO, 923.557EO, 1857.32EO, 992.514EO,
 6 1758.77EO, 1061.472EO, 1674.52EO, 1130.429EO, 1601.39EO, 1199.387EO,
 7 1599.58EO, 1201.250EO, 1575.19EO, 1255.513EO, 1444.57EO, 1339.288EO,
 8 1353.25EO, 1410.638EO, 1280.53EO, 1478.126EO, 1210.09EO, 1555.829EO,
 9 1150.71EO, 1633.910EO, 1099.71EO, 1712.893EO, 1055.23EO, 1792.940EO/

DATA T11 / 1000.0EO,
 124029.48EO, 10.981EO, 23096.00EO, 210.517EO, 20845.04EO, 333.571EO,
 217336.14EO, 419.454EO, 13305.23EO, 476.061EO, 9253.32EO, 511.794EO,
 3 5593.07EO, 536.693EO, 5360.70EO, 542.551EO, 4399.43EO, 588.078EO,
 4 3734.83EO, 646.612EO, 3169.41EO, 731.162EO, 2854.64EO, 802.705EO,
 5 2638.81EO, 867.743EO, 2466.26EO, 932.782EO, 2324.07EO, 997.821EO,
 6 2204.17EO, 1062.859EO, 2101.26EO, 1127.898EO, 2011.64EO, 1192.936EO,
 7 1992.55EO, 1210.394EO, 1947.82EO, 1266.456EO, 1784.28EO, 1352.309EO,
 8 1671.66EO, 1425.265EO, 1582.13EO, 1494.115EO, 1507.04EO, 1561.913EO,
 9 1442.48EO, 1629.779EO, 1377.37EO, 1709.586EO, 1320.92EO, 1790.290EO/

DATA T12 / 1200.0EO,
 126318.85EO, 11.569EO, 25241.12EO, 221.027EO, 23173.53EO, 333.875EO,
 220471.70EO, 408.632EO, 16445.88EO, 476.035EO, 11934.79EO, 523.846EO,
 3 6472.79EO, 562.204EO, 6049.68EO, 571.853EO, 5568.88EO, 590.242EO,
 4 5097.52EO, 614.760EO, 4519.85EO, 657.667EO, 4112.88EO, 700.575EO,
 5 3622.62EO, 774.130EO, 3230.02EO, 859.944EO, 2926.91EO, 951.888EO,
 6 2724.25EO, 1031.573EO, 2536.18EO, 1123.517EO, 2430.66EO, 1184.813EO,
 7 2407.37EO, 1201.318EO, 2347.06EO, 1263.089EO, 2139.70EO, 1353.651EO,
 8 2001.03EO, 1428.978EO, 1892.11EO, 1499.365EO, 1801.41EO, 1568.314EO,
 9 1723.77EO, 1637.122EO, 1656.18EO, 1706.277EO, 1587.34EO, 1787.642EO/

DATA T13 / 1400.0EO,
 128423.09EO, 12.156EO, 27421.06EO, 211.368EO, 25287.74EO, 334.181EO,
 222242.52EO, 419.757EO, 17361.80EO, 499.447EO, 12557.47EO, 548.676EO,
 3 7095.83EO, 588.776EO, 6683.12EO, 598.830EO, 5658.27EO, 644.948EO,
 4 4962.20EO, 696.831EO, 4439.64EO, 754.478EO, 3963.13EO, 829.421EO,
 5 3688.03EO, 887.068EO, 3464.35EO, 944.716EO, 3277.60EO, 1002.364EO,
 6 3118.52EO, 1060.011EO, 2980.82EO, 1117.659EO, 2860.05EO, 1175.307EO,
 7 2827.79EO, 1194.086EO, 2787.21EO, 1241.299EO, 2526.46EO, 1341.691EO,
 8 2352.10EO, 1420.820EO, 2218.97EO, 1493.200EO, 2109.54EO, 1563.395EO,
 9 2016.60EO, 1633.103EO, 1936.14EO, 1702.966EO, 1854.56EO, 1784.994EO/

DATA T14 / 1600.0EO,
 130380.68EO, 12.741EO, 29111.17EO, 231.954EO, 26342.19EO, 366.053EO,
 222067.79EO, 464.563EO, 15699.63EO, 548.276EO, 8599.02EO, 602.066EO,
 3 7531.45EO, 616.772EO, 7267.39EO, 624.202EO, 6283.48EO, 667.428EO,
 4 5642.15EO, 710.654EO, 4937.82EO, 780.897EO, 4517.75EO, 840.333EO,
 5 4218.70EO, 894.366EO, 3973.36EO, 948.399EO, 3767.13EO, 1002.431EO,
 6 3590.46EO, 1056.464EO, 3436.84EO, 1110.497EO, 3301.60EO, 1164.530EO,
 7 3252.42EO, 1189.014EO, 3203.28EO, 1239.587EO, 2882.68EO, 1344.071EO,
 8 2679.74EO, 1425.221EO, 2526.18EO, 1498.984EO, 2400.68EO, 1570.241EO,
 9 2294.50EO, 1640.826EO, 2202.85EO, 1711.435EO, 2122.55EO, 1782.348EO/

DATA T15 / 1800.0EO,
 132218.38EO, 13.326EO, 30781.42EO, 242.471EO, 27490.19EO, 387.615EO,
 222773.30EO, 487.560EO, 15821.59EO, 573.754EO, 8589.41EO, 630.734EO,
 3 7857.19EO, 646.795EO, 7806.53EO, 648.490EO, 6876.29EO, 688.797EO,
 4 6044.93EO, 744.220EO, 5470.07EO, 799.642EO, 5073.59EO, 850.027EO,
 5 4754.88EO, 900.411EO, 4490.93EO, 950.795EO, 4267.42EO, 1001.179EO,
 6 4074.81EO, 1051.564EO, 3906.50EO, 1101.948EO, 3757.71EO, 1152.332EO,
 7 3680.50EO, 1186.215EO, 3618.59EO, 1239.460EO, 3394.22EO, 1298.836EO,
 8 3109.78EO, 1390.193EO, 2912.11EO, 1468.170EO, 2756.26EO, 1541.440EO,
 9 2626.84EO, 1613.133EO, 2499.56EO, 1696.332EO, 2391.32EO, 1779.701EO/

DATA T16 / 2000.0EO,
 133955.66EO, 13.909EO, 32613.64EO, 232.777EO, 29236.62EO, 387.847EO,
 224722.20EO, 487.530EO, 18371.14EO, 573.194EO, 9715.11EO, 645.003EO,
 3 8655.25EO, 661.733EO, 8302.92EO, 672.111EO, 7264.52EO, 718.734EO,
 4 6562.68EO, 765.356EO, 6041.26EO, 811.979EO, 5631.87EO, 858.601EO,
 5 5298.39EO, 905.224EO, 5019.40EO, 951.846EO, 4781.25EO, 998.469EO,
 6 4574.70EO, 1045.091EO, 4393.22EO, 1091.713EO, 4232.05EO, 1138.336EO,
 7 4201.10EO, 1148.283EO, 4112.19EO, 1185.706EO, 4021.18EO, 1240.893EO,
 8 3584.17EO, 1351.059EO, 3324.89EO, 1435.455EO, 3102.61EO, 1523.952EO,
 9 2927.42EO, 1608.933EO, 2783.04EO, 1693.009EO, 2660.89EO, 1777.056EO/

DATA T17 / 2200.0EO,
 135607.23EO, 14.492EO, 34096.21EO, 243.279EO, 30883.91EO, 388.082EO,
 226527.79EO, 487.510EO, 19443.82EO, 585.859EO, 10853.33EO, 659.615EO,
 3 9433.73EO, 677.129EO, 8756.94EO, 695.462EO, 7803.37EO, 738.132EO,
 4 7126.33EO, 780.802EO, 6608.61EO, 823.471EO, 6194.12EO, 866.141EO,
 5 5851.60EO, 908.811EO, 5561.87EO, 951.481EO, 5312.35EO, 994.150EO,
 6 5094.36EO, 1036.820EO, 4901.66EO, 1079.490EO, 4729.64EO, 1122.159EO,
 7 4637.43EO, 1149.415EO, 4548.59EO, 1187.522EO, 4510.73EO, 1218.025EO,
 8 3988.37EO, 1339.694EO, 3683.13EO, 1427.787EO, 3428.14EO, 1518.459EO,
 9 3229.88EO, 1604.716EO, 3067.72EO, 1689.682EO, 2931.24EO, 1774.411EO/

DATA T18 / 2400.0EO,
 137184.51EO, 15.073EO, 35898.96EO, 223.542EO, 32783.10EO, 377.694EO,
 226889.76EO, 510.759EO, 19090.97EO, 612.528EO, 10166.01EO, 693.052EO,
 3 9303.38EO, 714.054EO, 9076.25EO, 718.953EO, 8262.73EO, 757.431EO,
 4 7645.11EO, 795.909EO, 7153.80EO, 834.387EO, 6749.86EO, 872.866EO,
 5 6409.55EO, 911.344EO, 6117.39EO, 949.822EO, 5862.79EO, 988.300EO,
 6 5638.20EO, 1026.779EO, 5438.06EO, 1065.257EO, 5258.18EO, 1103.735EO,
 7 5075.29EO, 1153.449EO, 4935.95EO, 1222.206EO, 4672.68EO, 1270.727EO,

8 4333.15E0,1344.672E0, 3999.72E0,1433.843E0, 3756.82E0,1512.909E0,
 9 3534.24E0,1600.480E0, 3353.62E0,1686.350E0, 3202.40E0,1771.765E0/

DATA T19 / 2600.0E0,
 138696.59E0, 15.653E0,36813.83E0, 264.310E0,33210.24E0, 409.968E0,
 227825.36E0, 522.481E0,19896.25E0, 625.813E0,10829.86E0, 709.590E0,
 3 9699.24E0, 733.410E0, 9407.96E0, 744.475E0, 8710.29E0, 778.232E0,
 4 8155.16E0, 811.988E0, 7698.71E0, 845.745E0, 7314.08E0, 879.502E0,
 5 6983.79E0, 913.259E0, 6695.85E0, 947.016E0, 6441.74E0, 980.772E0,
 6 6215.19E0,1014.529E0, 6011.47E0,1048.286E0, 5826.93E0,1082.043E0,
 7 5703.57E0,1107.711E0, 5518.77E0,1160.241E0, 5446.62E0,1197.675E0,
 8 5320.20E0,1227.844E0, 4834.08E0,1315.521E0, 4474.94E0,1397.239E0,
 9 4129.57E0,1494.237E0, 3750.08E0,1633.563E0, 3474.36E0,1769.120E0/

DATA T20 / 2800.0E0,
 140150.85E0, 16.232E0,38230.31E0, 264.699E0,34648.04E0, 410.174E0,
 228674.42E0, 534.279E0,20589.80E0, 639.301E0,11213.02E0, 727.621E0,
 310138.64E0, 753.572E0, 9699.30E0, 770.686E0, 9126.99E0, 799.200E0,
 4 8649.96E0, 827.715E0, 8243.83E0, 856.230E0, 7892.20E0, 884.745E0,
 5 7583.59E0, 913.260E0, 7309.70E0, 941.774E0, 7064.33E0, 970.289E0,
 6 6842.75E0, 998.804E0, 6641.28E0,1027.319E0, 6457.00E0,1055.834E0,
 7 6124.36E0,1121.221E0, 5885.61E0,1205.299E0, 5392.81E0,1282.213E0,
 8 4929.99E0,1372.797E0, 4567.09E0,1461.125E0, 4297.59E0,1540.859E0,
 9 4081.41E0,1617.173E0, 3901.13E0,1692.106E0, 3747.13E0,1766.475E0/

DATA T21 / 3000.0E0,
 141553.34E0, 16.811E0,39752.96E0, 254.984E0,36393.30E0, 399.685E0,
 230895.16E0, 522.232E0,22518.30E0, 638.147E0,11703.88E0, 745.797E0,
 310519.37E0, 775.147E0, 9873.87E0, 801.845E0, 9458.94E0, 823.687E0,
 4 9094.64E0, 845.529E0, 8771.22E0, 867.371E0, 8481.36E0, 889.213E0,
 5 8219.52E0, 911.055E0, 7981.34E0, 932.898E0, 7763.38E0, 954.740E0,
 6 7562.87E0, 976.582E0, 7377.56E0, 998.424E0, 7205.58E0,1020.266E0,
 7 6928.15E0,1060.464E0, 6563.23E0,1135.614E0, 6448.04E0,1179.815E0,
 8 5515.02E0,1328.310E0, 5042.64E0,1425.647E0, 4714.22E0,1509.351E0,
 9 4459.17E0,1587.660E0, 4218.81E0,1676.323E0, 4020.72E0,1763.830E0/

C.4 MURDOCK-BAUMAN CRITICAL FLOW TABLE FOR SUPERHEATED VAPOR

GXX(1) = STAGNATION PRESSURE (PSIA)
 GXX(EVEN) = CRITICAL FLOW RATE (LB/FT**2-SEC)
 GXX(ODD) = STAGNATION ENTHALPY (BTU/LB)

NHB = NUMBER OF PAIRS OF ENTHALPY AND FLOW VALUES PER PRESSURE
 NPB = NUMBER OF PRESSURE VALUES

DATA NHB,NPB /7,21/

DATA G01 /	1.0EO,	2.38EO,1105.809EO,	2.35EO,1141.101EO,
1	1.97EO,1262.297EO,	1.72EO,1388.407EO,	1.55EO,1520.487EO,
2	1.42EO,1658.914EO,	1.31EO,1803.546EO/	
DATA G02 /	5.0EO,	11.39EO,1131.093EO,	11.24EO,1166.678EO,
1	9.79EO,1265.265EO,	8.59EO,1390.877EO,	7.73EO,1522.229EO,
2	7.08EO,1659.809EO,	6.55EO,1803.492EO/	
DATA G03 /	10.0EO,	22.35EO,1143.348EO,	22.03EO,1179.286EO,
1	19.50EO,1269.014EO,	17.14EO,1393.975EO,	15.44EO,1524.411EO,
2	14.15EO,1660.929EO,	13.11EO,1803.426EO/	
DATA G04 /	14.7EO,	32.49EO,1150.482EO,	31.99EO,1186.845EO,
1	28.54EO,1272.574EO,	25.13EO,1396.898EO,	22.67EO,1526.466EO,
2	20.78EO,1661.983EO,	19.27EO,1803.363EO/	
DATA G05 /	50.0EO,	106.74EO,1174.093EO,	104.68EO,1213.137EO,
1	94.06EO,1300.260EO,	83.80EO,1419.135EO,	76.25EO,1542.013EO,
2	70.36EO,1669.933EO,	65.55EO,1802.894EO/	
DATA G06 /	100.0EO,	209.60EO,1187.166EO,	204.53EO,1230.033EO,
1	180.06EO,1341.546EO,	163.13EO,1451.412EO,	150.18EO,1564.360EO,
2	139.82EO,1681.289EO,	131.15EO,1802.229EO/	
DATA G07 /	200.0EO,	412.87EO,1198.334EO,	401.31EO,1244.107EO,
1	357.56EO,1349.071EO,	324.65EO,1458.026EO,	299.54EO,1568.876EO,
2	279.41EO,1683.108EO,	262.51EO,1800.901EO/	
DATA G08 /	400.0EO,	818.64EO,1204.591EO,	790.41EO,1256.322EO,
1	703.94EO,1366.109EO,	642.58EO,1472.057EO,	595.71EO,1578.268EO,
2	557.86EO,1686.873EO,	525.85EO,1798.245EO/	
DATA G09 /	600.0EO,	1228.83EO,1203.657EO,	1178.21EO,1261.308EO,
1	1045.74EO,1376.982EO,	957.72EO,1480.958EO,	890.56EO,1584.001EO,
2	836.07EO,1688.703EO,	789.92EO,1795.592EO/	
DATA G10 /	800.0EO,	1646.48EO,1199.387EO,	1567.52EO,1262.925EO,
1	1390.36EO,1380.495EO,	1274.14EO,1484.244EO,	1186.07EO,1585.860EO,
2	1114.88EO,1688.525EO,	1054.63EO,1792.941EO/	
DATA G11 /	1000.0EO,	2073.79EO,1192.936EO,	1960.40EO,1262.293EO,
1	1731.88EO,1384.776EO,	1588.70EO,1487.875EO,	1480.61EO,1587.889EO,
2	1393.68EO,1688.413EO,	1320.03EO,1790.291EO/	
DATA G12 /	1200.0EO,	2512.78EO,1184.813EO,	2357.14EO,1260.858EO,
1	2082.05EO,1383.259EO,	1907.73EO,1487.326EO,	1778.05EO,1587.107EO,
2	1674.23EO,1686.865EO,	1586.33EO,1787.642EO/	
DATA G13 /	1400.0EO,	2965.42EO,1175.307EO,	2760.30EO,1257.989EO,
1	2432.47EO,1382.074EO,	2226.80EO,1489.933EO,	2075.80EO,1586.409EO,
2	1955.33EO,1685.352EO,	1853.38EO,1784.995EO/	

DATA G14 / 1600.0EO, 3433.97EO, 1164.53EO, 3170.87EO, 1253.837EO,
1 2782.86EO, 1381.242EO, 2545.77EO, 1486.701EO, 2375.82EO, 1585.793EO,
2 2236.96EO, 1683.872EO, 2121.17EO, 1782.348EO/
DATA G15 / 1800.0EO, 3921.87EO, 1152.332EO, 3591.34EO, 1248.253EO,
1 3132.78EO, 1380.778EO, 2864.44EO, 1486.632EO, 2672.07EO, 1585.260EO,
2 2519.08EO, 1682.426EO, 2389.71EO, 1779.702EO/
DATA G16 / 2000.0EO, 4434.55EO, 1138.336EO, 4025.84EO, 1240.864EO,
1 3481.81EO, 1380.692EO, 3182.73EO, 1486.729EO, 2970.49EO, 1584.810EO,
2 2801.69EO, 1681.012EO, 2658.99EO, 1777.056EO/
DATA G17 / 2200.0EO, 4979.37EO, 1122.159EO, 4471.88EO, 1233.895EO,
1 3840.73EO, 1378.038EO, 3505.97EO, 1485.080EO, 3271.12EO, 1583.219EO,
2 3085.68EO, 1679.026EO, 2930.18EO, 1774.411EO/
DATA G18 / 2400.0EO, 5565.81EO, 1103.735EO, 4921.76EO, 1227.612EO,
1 4200.33EO, 1375.616EO, 3829.65EO, 1483.534EO, 3572.20EO, 1581.681EO,
2 3370.29EO, 1677.062EO, 3202.31EO, 1771.766EO/
DATA G19 / 2600.0EO, 6208.34EO, 1082.043EO, 5373.43EO, 1222.124EO,
1 4560.22EO, 1373.439EO, 4153.64EO, 1482.096EO, 3873.69EO, 1580.196EO,
2 3655.51EO, 1675.119EO, 3475.38EO, 1769.121EO/
DATA G20 / 2800.0EO, 6935.60EO, 1055.834EO, 5824.61EO, 1217.519EO,
1 4919.99EO, 1371.516EO, 4477.81EO, 1480.770EO, 4175.53EO, 1578.765EO,
2 3941.31EO, 1673.198EO, 3749.39EO, 1766.476EO/
DATA G21 / 3000.0EO, 7830.38EO, 1020.266EO, 6273.03EO, 1213.858EO,
1 5279.13EO, 1369.856EO, 4802.02EO, 1479.560EO, 4477.62EO, 1577.390EO,
2 4227.69EO, 1671.299EO, 4024.33EO, 1763.831EO/

DATA PM(25,17),PM(26,17),PM(27,17),PM(28,17),PM(29,17),PM(30,17),
 1 PM(31,17),PM(32,17),PM(33,17),PM(34,17),PM(35,17),PM(36,17),
 2 PM(37,17),PM(38,17),PM(39,17),PM(40,17),PM(41,17),PM(42,17),
 3 PM(43,17),PM(44,17),PM(45,17),PM(46,17),PM(47,17),PM(48,17)/
 4 0.68143584E 03, 0.11157809E 05, 0.68609809E 03, 0.10765562E 05,
 5 0.69076033E 03, 0.10467344E 05, 0.69542258E 03, 0.10284563E 05,
 6 0.70008482E 03, 0.10275959E 05, 0.70474707E 03, 0.10180133E 05,
 7 0.70940931E 03, 0.10112706E 05, 0.71407156E 03, 0.10047270E 05,
 8 0.71873380E 03, 0.89878104E 04, 0.76535625E 03, 0.78172752E 04,
 9 0.81197870E 03, 0.69030697E 04, 0.85860115E 03, 0.62502254E 04/

DATA PM(49,17),PM(50,17),PM(51,17),PM(52,17),PM(53,17),PM(54,17),
 1 PM(55,17),PM(56,17),PM(57,17),PM(58,17),PM(59,17)/
 2 0.90522360E 03, 0.57611957E 04, 0.95184605E 03, 0.53897722E 04,
 3 0.99846850E 03, 0.50810573E 04, 0.10450909E 04, 0.48154370E 04,
 4 0.10917134E 04, 0.45892802E 04, 0.11378696E 04/

DATA PM(1,18),PM(2,18),PM(3,18),PM(4,18),PM(5,18),PM(6,18),
 1 PM(7,18),PM(8,18),PM(9,18),PM(10,18),PM(11,18),PM(12,18),
 2 PM(13,18),PM(14,18),PM(15,18),PM(16,18),PM(17,18),PM(18,18),
 3 PM(19,18),PM(20,18),PM(21,18),PM(22,18),PM(23,18),PM(24,18)/
 4 0.22000000E 04, 0.12813458E 05, 0.69546232E 03, 0.12797706E 05,
 5 0.69588902E 03, 0.12737513E 05, 0.69631572E 03, 0.12703856E 05,
 6 0.69674241E 03, 0.12670456E 05, 0.69716911E 03, 0.12612354E 05,
 7 0.69759581E 03, 0.12579734E 05, 0.69802250E 03, 0.12547358E 05,
 8 0.69844920E 03, 0.12515223E 05, 0.69887590E 03, 0.12459599E 05,
 9 0.69930260E 03, 0.12428195E 05, 0.69972929E 03, 0.12063798E 05/

DATA PM(25,18),PM(26,18),PM(27,18),PM(28,18),PM(29,18),PM(30,18),
 1 PM(31,18),PM(32,18),PM(33,18),PM(34,18),PM(35,18),PM(36,18),
 2 PM(37,18),PM(38,18),PM(39,18),PM(40,18),PM(41,18),PM(42,18),
 3 PM(43,18),PM(44,18),PM(45,18),PM(46,18),PM(47,18),PM(48,18)/
 4 0.70399626E 03, 0.11751453E 05, 0.70826323E 03, 0.11464110E 05,
 5 0.71253020E 03, 0.11375772E 05, 0.71679717E 03, 0.11364155E 05,
 6 0.72106414E 03, 0.11429088E 05, 0.72533111E 03, 0.11397517E 05,
 7 0.72959808E 03, 0.11351836E 05, 0.73386505E 03, 0.11291398E 05,
 8 0.73813202E 03, 0.10144490E 05, 0.78080172E 03, 0.84951054E 04,
 9 0.82347142E 03, 0.74811964E 04, 0.86614112E 03, 0.68680311E 04/

DATA PM(49,18),PM(50,18),PM(51,18),PM(52,18),PM(53,18),PM(54,18),
 1 PM(55,18),PM(56,18),PM(57,18),PM(58,18),PM(59,18)/
 2 0.90881083E 03, 0.64129876E 04, 0.95148053E 03, 0.60360975E 04,
 3 0.99415023E 03, 0.57181600E 04, 0.10368199E 04, 0.54250196E 04,
 4 0.10794896E 04, 0.51763832E 04, 0.11217326E 04/

C.3 HOMOGENEOUS EQUILIBRIUM MODEL CRITICAL FLOW TABLES

TXX(1) = STAGNATION PRESSURE (PSIA)
 TXX(EVEN) = CRITICAL FLOW RATE (LBM/SEC-FT2)
 TXX(ODD) = STAGNATION ENTHALPY (BTU/LBM)

NGHT = NUMBER OF PAIRS OF FLOW RATE AND ENTHALPY VALUES PER PRESSURE

NPT = NUMBER OF PRESSURE VALUES

DATA NGHT, NPT / 27,21 /

DATA T01 / 1.0EO,

1	716.13EO,	8.030EO,	711.91EO,	18.057EO,	658.45EO,	28.062EO,
2	681.49EO,	38.054EO,	535.31EO,	48.038EO,	447.12EO,	58.019EO,
3	442.29EO,	67.999EO,	20.41EO,	69.733EO,	6.75EO,	173.34EO,
4	5.02EO,	276.948EO,	4.17EO,	380.555EO,	3.65EO,	484.163EO,
5	3.29EO,	587.771EO,	3.01EO,	691.378EO,	2.80EO,	794.986EO,
6	2.62EO,	898.594EO,	2.48EO,	1002.201EO,	2.35EO,	1105.809EO,
7	2.35EO,	1114.029EO,	2.18EO,	1186.541EO,	1.97EO,	1260.427EO,
8	1.81EO,	1336.135EO,	1.67EO,	1423.810EO,	1.55EO,	1514.346EO,
9	1.46EO,	1607.840EO,	1.38EO,	1704.280EO,	1.31EO,	1803.545EO,

DATA T02 / 5.0EO,

1	1681.25EO,	8.042EO,	1665.45EO,	38.065EO,	1579.07EO,	68.010EO,
2	1378.69EO,	87.975EO,	1162.01EO,	107.955EO,	852.83EO,	117.953EO,
3	385.75EO,	127.958EO,	83.89EO,	130.196EO,	31.49EO,	230.286EO,
4	23.69EO,	330.376EO,	19.80EO,	430.465EO,	17.36EO,	530.555EO,
5	15.65EO,	630.645EO,	14.36EO,	730.734EO,	13.35EO,	830.824EO,
6	12.52EO,	930.914EO,	11.83EO,	1031.003EO,	11.25EO,	1131.093EO,
7	11.22EO,	1139.325EO,	10.47EO,	1213.338EO,	9.53EO,	1288.228EO,
8	8.80EO,	1364.831EO,	8.20EO,	1443.519EO,	7.71EO,	1524.467EO,
9	7.30EO,	1607.747EO,	6.90EO,	1704.209EO,	6.56EO,	1803.492EO,

DATA T03 / 10.0EO,

1	2391.40EO,	8.057EO,	2236.70EO,	78.004EO,	2047.90EO,	107.967EO,
2	1724.77EO,	127.970EO,	1505.41EO,	137.983EO,	1192.82EO,	148.006EO,
3	659.12EO,	158.038EO,	151.52EO,	161.261EO,	60.84EO,	259.470EO,
4	46.07EO,	357.678EO,	38.62EO,	455.887EO,	33.92EO,	554.096EO,
5	30.60EO,	652.305EO,	28.10EO,	750.513EO,	26.13EO,	848.722EO,
6	24.53EO,	946.931EO,	23.18EO,	1045.140EO,	22.04EO,	1143.348EO,
7	22.01EO,	1146.574EO,	20.69EO,	1221.805EO,	18.86EO,	1297.280EO,
8	17.44EO,	1374.284EO,	16.28EO,	1453.321EO,	15.32EO,	1534.604EO,
9	14.50EO,	1618.208EO,	13.80EO,	1704.121EO,	13.12EO,	1803.425EO,

DATA T04 / 14.7EO,

1	2904.72EO,	8.071EO,	2774.33EO,	78.016EO,	2495.47EO,	117.977EO,
2	2216.69EO,	137.995EO,	1750.08EO,	158.049EO,	1384.01EO,	168.094EO,
3	789.99EO,	178.152EO,	209.49EO,	180.179EO,	87.60EO,	277.210EO,
4	66.61EO,	374.240EO,	55.94EO,	471.270EO,	49.19EO,	568.300EO,
5	44.41EO,	665.331EO,	40.80EO,	762.361EO,	37.95EO,	859.391EO,

6	35.63E0,	956.421E0,	33.68E0,	1053.452E0,	32.03E0,	1150.482E0,
7	31.98E0,	1154.345E0,	30.06E0,	1230.480E0,	27.45E0,	1306.438E0,
8	25.40E0,	1383.809E0,	23.74E0,	1463.184E0,	22.36E0,	1544.795E0,
9	21.18E0,	1628.719E0,	20.17E0,	1714.939E0,	19.28E0,	1803.363E0/

DATA T05 /						50.0E0,
1	5371.63E0,	8.175E0,	5190.51E0,	108.067E0,	4775.18E0,	158.130E0,
2	4009.67E0,	198.393E0,	3318.03E0,	218.632E0,	2105.91E0,	238.966E0,
3	703.71E0,	249.174E0,	571.57E0,	250.212E0,	389.44E0,	277.928E0,
4	267.62E0,	351.839E0,	192.22E0,	490.421E0,	159.83E0,	619.764E0,
5	144.72E0,	712.153E0,	133.23E0,	804.541E0,	124.11E0,	896.929E0,
6	116.64E0,	989.317E0,	110.38E0,	1081.705E0,	105.03E0,	1174.093E0,
7	104.66E0,	1184.119E0,	99.07E0,	1254.716E0,	91.70E0,	1323.151E0,
8	85.78E0,	1391.904E0,	80.85E0,	1461.887E0,	76.11E0,	1543.804E0,
9	72.09E0,	1627.948E0,	68.62E0,	1714.337E0,	65.60E0,	1802.894E0/

DATA T06 /						100.0E0,
1	7600.63E0,	8.324E0,	7337.38E0,	128.187E0,	6764.11E0,	188.413E0,
2	5606.26E0,	239.065E0,	4208.59E0,	269.774E0,	3474.36E0,	280.078E0,
3	2333.70E0,	290.420E0,	989.42E0,	298.538E0,	721.04E0,	325.197E0,
4	564.01E0,	369.629E0,	412.34E0,	476.264E0,	329.23E0,	609.558E0,
5	282.31E0,	742.852E0,	260.32E0,	831.715E0,	242.80E0,	920.578E0,
6	228.41E0,	1009.440E0,	216.31E0,	1098.303E0,	205.95E0,	1187.166E0,
7	205.33E0,	1194.192E0,	194.62E0,	1269.141E0,	180.35E0,	1339.551E0,
8	168.93E0,	1409.519E0,	159.42E0,	1480.449E0,	151.30E0,	1552.838E0,
9	144.28E0,	1626.855E0,	137.31E0,	1713.484E0,	131.25E0,	1802.229E0/

DATA T07 /						200.0E0,
1	110751.06E0,	8.620E0,	10327.76E0,	158.476E0,	9241.84E0,	239.264E0,
2	8058.31E0,	280.257E0,	5812.39E0,	321.858E0,	3688.74E0,	342.949E0,
3	1759.85E0,	353.581E0,	1685.31E0,	355.506E0,	1515.39E0,	363.934E0,
4	1139.95E0,	406.075E0,	940.63E0,	456.645E0,	778.11E0,	532.500E0,
5	631.88E0,	658.924E0,	528.84E0,	819.061E0,	475.74E0,	945.485E0,
6	448.14E0,	1029.768E0,	424.86E0,	1114.051E0,	404.87E0,	1198.334E0,
7	402.87E0,	1210.131E0,	384.10E0,	1280.034E0,	355.73E0,	1353.710E0,
8	333.37E0,	1425.503E0,	314.79E0,	1497.762E0,	298.97E0,	1571.261E0,
9	285.28E0,	1646.255E0,	273.29E0,	1722.810E0,	262.69E0,	1800.900E0/

DATA T08 /						400.0E0,
1	115203.90E0,	9.212E0,	14540.28E0,	189.071E0,	13309.29E0,	270.329E0,
2	211259.93E0,	332.672E0,	8740.94E0,	375.266E0,	5255.00E0,	407.962E0,
3	3105.55E0,	419.039E0,	2818.39E0,	424.168E0,	2475.99E0,	439.776E0,
4	2091.97E0,	470.993E0,	1858.15E0,	502.210E0,	1539.99E0,	572.448E0,
5	1347.66E0,	642.686E0,	1155.65E0,	751.945E0,	1013.44E0,	876.813E0,
6	935.86E0,	970.464E0,	860.17E0,	1087.527E0,	800.37E0,	1204.591E0,
7	795.86E0,	1216.493E0,	775.13E0,	1271.230E0,	720.21E0,	1341.438E0,
8	672.03E0,	1417.029E0,	633.05E0,	1491.300E0,	600.27E0,	1566.139E0,
9	572.15E0,	1642.145E0,	547.66E0,	1719.505E0,	526.11E0,	1798.245E0/

DATA T09 /						600.0E0,
1	118618.66E0,	9.803E0,	18103.35E0,	169.421E0,	16833.40E0,	270.700E0,
2	214751.27E0,	343.512E0,	11204.24E0,	408.123E0,	7987.71E0,	441.582E0,

3	4173.67E0,	464.480E0,	3768.85E0,	471.697E0,	3048.55E0,	508.295E0,
4	2660.54E0,	544.893E0,	2206.12E0,	618.089E0,	1847.98E0,	720.564E0,
5	1598.54E0,	837.677E0,	1486.45E0,	910.873E0,	1395.25E0,	984.069E0,
6	1319.13E0,	1057.265E0,	1254.32E0,	1130.461E0,	1198.26E0,	1203.657E0,
7	1190.77E0,	1215.928E0,	1173.16E0,	1262.896E0,	1082.18E0,	1340.030E0,
8	1016.37E0,	1408.262E0,	954.91E0,	1484.762E0,	903.95E0,	1560.997E0,
9	860.60E0,	1638.031E0,	823.13E0,	1716.199E0,	790.29E0,	1795.591E0/

	DATA T10 /					800.0E0,
121495.90E0,	10.393E0,	20695.34E0,	200.012E0,	19081.41E0,	301.983E0,	
216623.91E0,	375.727E0,	13495.09E0,	430.431E0,	9141.10E0,	476.098E0,	
3 5199.07E0,	499.841E0,	4606.04E0,	509.811E0,	4101.00E0,	530.499E0,	
4 3572.38E0,	564.977E0,	3163.63E0,	606.352E0,	2724.61E0,	675.310E0,	
5 2320.01E0,	778.746E0,	1974.80E0,	923.557E0,	1857.32E0,	992.514E0,	
6 1758.77E0,	1061.472E0,	1674.52E0,	1130.429E0,	1601.39E0,	1199.387E0,	
7 1599.58E0,	1201.250E0,	1575.19E0,	1255.513E0,	1444.57E0,	1339.288E0,	
8 1353.25E0,	1410.638E0,	1280.53E0,	1478.126E0,	1210.09E0,	1555.829E0,	
9 1150.71E0,	1633.910E0,	1099.71E0,	1712.893E0,	1055.23E0,	1792.940E0/	

	DATA T11 /					1000.0E0,
124029.48E0,	10.981E0,	23096.00E0,	210.517E0,	20845.04E0,	333.571E0,	
217336.14E0,	419.454E0,	13305.23E0,	476.061E0,	9253.32E0,	511.794E0,	
3 5593.07E0,	536.693E0,	5360.70E0,	542.551E0,	4399.43E0,	588.078E0,	
4 3734.83E0,	646.612E0,	3169.41E0,	731.162E0,	2854.64E0,	802.705E0,	
5 2638.81E0,	867.743E0,	2466.26E0,	932.782E0,	2324.07E0,	997.821E0,	
6 2204.17E0,	1062.859E0,	2101.26E0,	1127.898E0,	2011.64E0,	1192.936E0,	
7 1992.55E0,	1210.394E0,	1947.82E0,	1266.456E0,	1784.28E0,	1352.309E0,	
8 1671.66E0,	1425.265E0,	1582.13E0,	1494.115E0,	1507.04E0,	1561.913E0,	
9 1442.48E0,	1629.779E0,	1377.37E0,	1709.586E0,	1320.92E0,	1790.290E0/	

	DATA T12 /					1200.0E0,
126318.85E0,	11.569E0,	25241.12E0,	221.027E0,	23173.53E0,	333.875E0,	
220471.70E0,	408.632E0,	16445.88E0,	476.035E0,	11934.79E0,	523.846E0,	
3 6472.79E0,	562.204E0,	6049.68E0,	571.853E0,	5568.88E0,	590.242E0,	
4 5097.52E0,	614.760E0,	4519.85E0,	657.667E0,	4112.88E0,	700.575E0,	
5 3622.62E0,	774.130E0,	3230.02E0,	859.944E0,	2926.91E0,	951.888E0,	
6 2724.25E0,	1031.573E0,	2536.18E0,	1123.517E0,	2430.66E0,	1184.813E0,	
7 2407.37E0,	1201.318E0,	2347.06E0,	1263.089E0,	2139.70E0,	1353.651E0,	
8 2001.03E0,	1428.978E0,	1892.11E0,	1499.365E0,	1801.41E0,	1568.314E0,	
9 1723.77E0,	1637.122E0,	1656.18E0,	1706.277E0,	1587.34E0,	1787.642E0/	

	DATA T13 /					1400.0E0,
128423.09E0,	12.156E0,	27421.06E0,	211.368E0,	25287.74E0,	334.181E0,	
222242.52E0,	419.757E0,	17361.80E0,	499.447E0,	12557.47E0,	548.676E0,	
3 7095.83E0,	588.776E0,	6683.12E0,	598.830E0,	5658.27E0,	644.948E0,	
4 4962.20E0,	696.831E0,	4439.64E0,	754.478E0,	3963.13E0,	829.421E0,	
5 3688.03E0,	887.068E0,	3464.35E0,	944.716E0,	3277.60E0,	1002.364E0,	
6 3118.52E0,	1060.011E0,	2980.82E0,	1117.659E0,	2860.05E0,	1175.307E0,	
7 2827.79E0,	1194.086E0,	2787.21E0,	1241.299E0,	2526.46E0,	1341.691E0,	
8 2352.10E0,	1420.820E0,	2218.97E0,	1493.200E0,	2109.54E0,	1563.395E0,	
9 2016.60E0,	1633.103E0,	1936.14E0,	1702.966E0,	1854.56E0,	1784.994E0/	

DATA T14 / 1600.0EO,
 130380.68EO, 12.741EO, 29111.17EO, 231.954EO, 26342.19EO, 366.053EO,
 222067.79EO, 464.563EO, 15699.63EO, 548.276EO, 8599.02EO, 602.066EO,
 3 7531.45EO, 616.772EO, 7267.39EO, 624.202EO, 6283.48EO, 667.428EO,
 4 5642.15EO, 710.654EO, 4937.82EO, 780.897EO, 4517.75EO, 840.333EO,
 5 4218.70EO, 894.366EO, 3973.36EO, 948.399EO, 3767.13EO, 1002.431EO,
 6 3590.46EO, 1056.464EO, 3436.84EO, 1110.497EO, 3301.60EO, 1164.530EO,
 7 3252.42EO, 1189.014EO, 3203.28EO, 1239.587EO, 2882.68EO, 1344.071EO,
 8 2679.74EO, 1425.221EO, 2526.18EO, 1498.984EO, 2400.68EO, 1570.241EO,
 9 2294.50EO, 1640.826EO, 2202.85EO, 1711.435EO, 2122.55EO, 1782.348EO/

DATA T15 / 1800.0EO,
 132218.38EO, 13.326EO, 30781.42EO, 242.471EO, 27490.19EO, 387.615EO,
 222773.30EO, 487.560EO, 15821.59EO, 573.754EO, 8589.41EO, 630.734EO,
 3 7857.19EO, 646.795EO, 7806.53EO, 648.490EO, 6876.29EO, 688.797EO,
 4 6044.93EO, 744.220EO, 5470.07EO, 799.642EO, 5073.59EO, 850.027EO,
 5 4754.88EO, 900.411EO, 4490.93EO, 950.795EO, 4267.42EO, 1001.179EO,
 6 4074.81EO, 1051.564EO, 3906.50EO, 1101.948EO, 3757.71EO, 1152.332EO,
 7 3680.50EO, 1186.215EO, 3618.59EO, 1239.460EO, 3394.22EO, 1298.836EO,
 8 3109.78EO, 1390.193EO, 2912.11EO, 1468.170EO, 2756.26EO, 1541.440EO,
 9 2626.84EO, 1613.133EO, 2499.56EO, 1696.332EO, 2391.32EO, 1779.701EO/

DATA T16 / 2000.0EO,
 133955.66EO, 13.909EO, 32613.64EO, 232.777EO, 29236.62EO, 387.847EO,
 224722.20EO, 487.530EO, 18371.14EO, 573.194EO, 9715.11EO, 645.003EO,
 3 8655.25EO, 661.733EO, 8302.92EO, 672.111EO, 7264.52EO, 718.734EO,
 4 6562.68EO, 765.356EO, 6041.26EO, 811.979EO, 5631.87EO, 858.601EO,
 5 5298.39EO, 905.224EO, 5019.40EO, 951.846EO, 4781.25EO, 998.469EO,
 6 4574.70EO, 1045.091EO, 4393.22EO, 1091.713EO, 4232.05EO, 1138.336EO,
 7 4201.10EO, 1148.283EO, 4112.19EO, 1185.706EO, 4021.18EO, 1240.893EO,
 8 3584.17EO, 1351.059EO, 3324.89EO, 1435.455EO, 3102.61EO, 1523.952EO,
 9 2927.42EO, 1608.933EO, 2783.04EO, 1693.009EO, 2660.89EO, 1777.056EO/

DATA T17 / 2200.0EO,
 135607.23EO, 14.492EO, 34096.21EO, 243.279EO, 30883.91EO, 388.082EO,
 226527.79EO, 487.510EO, 19443.82EO, 585.859EO, 10853.33EO, 659.615EO,
 3 9433.73EO, 677.129EO, 8756.94EO, 695.462EO, 7803.37EO, 738.132EO,
 4 7126.33EO, 780.802EO, 6608.61EO, 823.471EO, 6194.12EO, 866.141EO,
 5 5851.60EO, 908.811EO, 5561.87EO, 951.481EO, 5312.35EO, 994.150EO,
 6 5094.36EO, 1036.820EO, 4901.66EO, 1079.490EO, 4729.64EO, 1122.159EO,
 7 4637.43EO, 1149.415EO, 4548.59EO, 1187.522EO, 4510.73EO, 1218.025EO,
 8 3988.37EO, 1339.694EO, 3683.13EO, 1427.787EO, 3428.14EO, 1518.459EO,
 9 3229.88EO, 1604.716EO, 3067.72EO, 1689.682EO, 2931.24EO, 1774.411EO/

DATA T18 / 2400.0EO,
 137184.51EO, 15.073EO, 35898.96EO, 223.542EO, 32783.10EO, 377.694EO,
 226889.76EO, 510.759EO, 19090.97EO, 612.528EO, 10166.01EO, 693.052EO,
 3 9303.38EO, 714.054EO, 9076.25EO, 718.953EO, 8262.73EO, 757.431EO,
 4 7645.11EO, 795.909EO, 7153.80EO, 834.387EO, 6749.86EO, 872.866EO,
 5 6409.55EO, 911.344EO, 6117.39EO, 949.822EO, 5862.79EO, 988.300EO,
 6 5638.20EO, 1026.779EO, 5438.06EO, 1065.257EO, 5258.18EO, 1103.735EO,
 7 5075.29EO, 1153.449EO, 4935.95EO, 1222.206EO, 4672.68EO, 1270.727EO,

8 4333.15E0,1344.672E0, 3999.72E0,1433.843E0, 3756.82E0,1512.909E0,
9 3534.24E0,1600.480E0, 3353.62E0,1686.350E0, 3202.40E0,1771.765E0/

DATA T19 / 2600.0E0,
138696.59E0, 15.653E0,36813.83E0, 264.310E0,33210.24E0, 409.968E0,
227825.36E0, 522.481E0,19896.25E0, 625.813E0,10829.86E0, 709.590E0,
3 9699.24E0, 733.410E0, 9407.96E0, 744.475E0, 8710.29E0, 778.232E0,
4 8155.16E0, 811.988E0, 7698.71E0, 845.745E0, 7314.08E0, 879.502E0,
5 6983.79E0, 913.259E0, 6695.85E0, 947.016E0, 6441.74E0, 980.772E0,
6 6215.19E0,1014.529E0, 6011.47E0,1048.286E0, 5826.93E0,1082.043E0,
7 5703.57E0,1107.711E0, 5518.77E0,1160.241E0, 5446.62E0,1197.675E0,
8 5320.20E0,1227.844E0, 4834.08E0,1315.521E0, 4474.94E0,1397.239E0,
9 4129.57E0,1494.237E0, 3750.08E0,1633.563E0, 3474.36E0,1769.120E0/

DATA T20 / 2800.0E0,
140150.85E0, 16.232E0,38230.31E0, 264.699E0,34648.04E0, 410.174E0,
228674.42E0, 534.279E0,20589.80E0, 639.301E0,11213.02E0, 727.621E0,
310138.64E0, 753.572E0, 9699.30E0, 770.686E0, 9126.99E0, 799.200E0,
4 8649.96E0, 827.715E0, 8243.83E0, 856.230E0, 7892.20E0, 884.745E0,
5 7583.59E0, 913.260E0, 7309.70E0, 941.774E0, 7064.33E0, 970.289E0,
6 6842.75E0, 998.804E0, 6641.28E0,1027.319E0, 6457.00E0,1055.834E0,
7 6124.36E0,1121.221E0, 5885.61E0,1205.299E0, 5392.81E0,1282.213E0,
8 4929.99E0,1372.797E0, 4567.09E0,1461.125E0, 4297.59E0,1540.859E0,
9 4081.41E0,1617.173E0, 3901.13E0,1692.106E0, 3747.13E0,1766.475E0/

DATA T21 / 3000.0E0,
141553.34E0, 16.811E0,39752.96E0, 254.984E0,36393.30E0, 399.685E0,
230895.16E0, 522.232E0,22518.30E0, 638.147E0,11703.88E0, 745.797E0,
310519.37E0, 775.147E0, 9873.87E0, 801.845E0, 9458.94E0, 823.687E0,
4 9094.64E0, 845.529E0, 8771.22E0, 867.371E0, 8481.36E0, 889.213E0,
5 8219.52E0, 911.055E0, 7981.34E0, 932.898E0, 7763.38E0, 954.740E0,
6 7562.87E0, 976.582E0, 7377.56E0, 998.424E0, 7205.58E0,1020.266E0,
7 6928.15E0,1060.464E0, 6563.23E0,1135.614E0, 6448.04E0,1179.815E0,
8 5515.02E0,1328.310E0, 5042.64E0,1425.647E0, 4714.22E0,1509.351E0,
9 4459.17E0,1587.660E0, 4218.81E0,1676.323E0, 4020.72E0,1763.830E0/

C.4 MURDOCK-BAUMAN CRITICAL FLOW TABLE FOR SUPERHEATED VAPOR

GXX(1) = STAGNATION PRESSURE (PSIA)
 GXX(EVEN) = CRITICAL FLOW RATE (LB/FT**2-SEC)
 GXX(ODD) = STAGNATION ENTHALPY (BTU/LB)

NHB = NUMBER OF PAIRS OF ENTHALPY AND FLOW VALUES PER PRESSURE
 NPB = NUMBER OF PRESSURE VALUES

DATA NHB,NPB /7,21/

DATA G01 /	1.0E0,	2.38E0,1105.809E0,	2.35E0,1141.101E0,
1	1.97E0,1262.297E0,	1.72E0,1388.407E0,	1.55E0,1520.487E0,
2	1.42E0,1658.914E0,	1.31E0,1803.546E0/	
DATA G02 /	5.0E0,	11.39E0,1131.093E0,	11.24E0,1166.678E0,
1	9.79E0,1265.265E0,	8.59E0,1390.877E0,	7.73E0,1522.229E0,
2	7.08E0,1659.809E0,	6.55E0,1803.492E0/	
DATA G03 /	10.0E0,	22.35E0,1143.348E0,	22.03E0,1179.286E0,
1	19.50E0,1269.014E0,	17.14E0,1393.975E0,	15.44E0,1524.411E0,
2	14.15E0,1660.929E0,	13.11E0,1803.426E0/	
DATA G04 /	14.7E0,	32.49E0,1150.482E0,	31.99E0,1186.845E0,
1	28.54E0,1272.574E0,	25.13E0,1396.898E0,	22.67E0,1526.466E0,
2	20.78E0,1661.983E0,	19.27E0,1803.363E0/	
DATA G05 /	50.0E0,	106.74E0,1174.093E0,	104.68E0,1213.137E0,
1	94.06E0,1300.260E0,	83.80E0,1419.135E0,	76.25E0,1542.013E0,
2	70.36E0,1669.933E0,	65.55E0,1802.894E0/	
DATA G06 /	100.0E0,	209.60E0,1187.166E0,	204.53E0,1230.033E0,
1	180.06E0,1341.546E0,	163.13E0,1451.412E0,	150.18E0,1564.360E0,
2	139.82E0,1681.289E0,	131.15E0,1802.229E0/	
DATA G07 /	200.0E0,	412.87E0,1198.334E0,	401.31E0,1244.107E0,
1	357.56E0,1349.071E0,	324.65E0,1458.026E0,	299.54E0,1568.876E0,
2	279.41E0,1683.108E0,	262.51E0,1800.901E0/	
DATA G08 /	400.0E0,	818.64E0,1204.591E0,	790.41E0,1256.322E0,
1	703.94E0,1366.109E0,	642.58E0,1472.057E0,	595.71E0,1578.268E0,
2	557.86E0,1686.873E0,	525.85E0,1798.245E0/	
DATA G09 /	600.0E0,	1228.83E0,1203.657E0,	1178.21E0,1261.308E0,
1	1045.74E0,1376.982E0,	957.72E0,1480.958E0,	890.56E0,1584.001E0,
2	836.07E0,1688.703E0,	789.92E0,1795.592E0/	
DATA G10 /	800.0E0,	1646.48E0,1199.387E0,	1567.52E0,1262.925E0,
1	1390.36E0,1380.495E0,	1274.14E0,1484.244E0,	1186.07E0,1585.860E0,
2	1114.88E0,1688.525E0,	1054.63E0,1792.941E0/	
DATA G11 /	1000.0E0,	2073.79E0,1192.936E0,	1960.40E0,1262.293E0,
1	1731.88E0,1384.776E0,	1588.70E0,1487.875E0,	1480.61E0,1587.889E0,
2	1393.68E0,1688.413E0,	1320.03E0,1790.291E0/	
DATA G12 /	1200.0E0,	2512.78E0,1184.813E0,	2357.14E0,1260.858E0,
1	2082.05E0,1383.259E0,	1907.73E0,1487.326E0,	1778.05E0,1587.107E0,
2	1674.23E0,1686.865E0,	1586.33E0,1787.642E0/	
DATA G13 /	1400.0E0,	2965.42E0,1175.307E0,	2760.30E0,1257.989E0,
1	2432.47E0,1382.074E0,	2226.80E0,1489.933E0,	2075.80E0,1586.409E0,
2	1955.33E0,1685.352E0,	1853.38E0,1784.995E0/	

DATA G14 / 1600.0EO, 3433.97EO, 1164.53EO, 3170.87EO, 1253.837EO,
 1 2782.86EO, 1381.242EO, 2545.77EO, 1486.701EO, 2375.82EO, 1585.793EO,
 2 2236.96EO, 1683.872EO, 2121.17EO, 1782.348EO/
 DATA G15 / 1800.0EO, 3921.87EO, 1152.332EO, 3591.34EO, 1248.253EO,
 1 3132.78EO, 1380.778EO, 2864.44EO, 1486.632EO, 2672.07EO, 1585.260EO,
 2 2519.08EO, 1682.426EO, 2389.71EO, 1779.702EO/
 DATA G16 / 2000.0EO, 4434.55EO, 1138.336EO, 4025.84EO, 1240.864EO,
 1 3481.81EO, 1380.692EO, 3182.73EO, 1486.729EO, 2970.49EO, 1584.810EO,
 2 2801.69EO, 1681.012EO, 2658.99EO, 1777.056EO/
 DATA G17 / 2200.0EO, 4979.37EO, 1122.159EO, 4471.88EO, 1233.895EO,
 1 3840.73EO, 1378.038EO, 3505.97EO, 1485.080EO, 3271.12EO, 1583.219EO,
 2 3085.68EO, 1679.026EO, 2930.18EO, 1774.411EO/
 DATA G18 / 2400.0EO, 5565.81EO, 1103.735EO, 4921.76EO, 1227.612EO,
 1 4200.33EO, 1375.616EO, 3829.65EO, 1483.534EO, 3572.20EO, 1581.681EO,
 2 3370.29EO, 1677.062EO, 3202.31EO, 1771.766EO/
 DATA G19 / 2600.0EO, 6208.34EO, 1082.043EO, 5373.43EO, 1222.124EO,
 1 4560.22EO, 1373.439EO, 4153.64EO, 1482.096EO, 3873.69EO, 1580.196EO,
 2 3655.51EO, 1675.119EO, 3475.38EO, 1769.121EO/
 DATA G20 / 2800.0EO, 6935.60EO, 1055.834EO, 5824.61EO, 1217.519EO,
 1 4919.99EO, 1371.516EO, 4477.81EO, 1480.770EO, 4175.53EO, 1578.765EO,
 2 3941.31EO, 1673.198EO, 3749.39EO, 1766.476EO/
 DATA G21 / 3000.0EO, 7830.38EO, 1020.266EO, 6273.03EO, 1213.858EO,
 1 5279.13EO, 1369.856EO, 4802.02EO, 1479.560EO, 4477.62EO, 1577.390EO,
 2 4227.69EO, 1671.299EO, 4024.33EO, 1763.831EO/

APPENDIX D

THERMODYNAMIC PROPERTIES

The thermodynamic state variables used by RELAP5/MOD2 are contained in tabular form within a controlled library. This library was generated by the STH2X water property subroutines transmitted with the base RELAP code release. RELAP5 attaches this library during each execution. Through interpolation the values of pressure, temperature, specific volume, internal energy, entropy, enthalpy, thermal expansion, compressibility, and heat capacity are acquired using a subset of this list and the phase as the independent variables. Single-phase values are stored for 57 temperatures and 36 pressure points. Saturation values for 47 temperatures and 27 pressures are also included in this file.

APPENDIX E

RELAP5/MOD2 INTERNALLY STORED MATERIAL
DEFAULT PROPERTIES

RELAP5/MOD2 has the thermal conductivity and volumetric heat capacity stored internally for gap gas, carbon steel, stainless steel, uranium dioxide, and zirconium. These values may be selected by the user for use in the heat structure heat conduction calculations. If chosen the following values or tables are used.

<u>Material</u>	<u>Temperature (F)</u>	<u>Thermal Conductivity (Btu/hr-ft-F)</u>
1. Gap Gas (constant value)	-	0.41562
2. Carbon Steel (constant value)	-	26.607
3. Stainless Steel	32.	7.5
	1700.	14.506
4. Uranium Dioxide	500.	3.341
	650.	2.671
	800.	2.677
	950.	2.439
	1100.	2.242
	1250.	2.078
	1400.	1.940
	1500.	1.823
	1700.	1.724
	1850.	1.639
	2000.	1.568
	2150.	1.507
	2300.	1.457
	2450.	1.415
	2600.	1.382
3100.	1.323	
3600.	1.333	
4100.	1.406	
4600.	1.538	
5100.	1.730	
5. Zirconium	392.	6.936
	752.	8.092
	1112.	9.827
	1472.	10.983
	1832.	12.717
	2192.	14.451
	2552.	17.341
	2912.	20.809
	3272.	25.433
	3632.	31.792
3992.	39.306	

<u>Material</u>	<u>Temperature (F)</u>	<u>Volumetric Heat Btu/ft³-F</u>
1. Gap Gas (constant value)	-	7.5 · 10 ⁻⁵
2. Carbon Steel (constant value)	-	57.816
3. Stainless Steel	200.	57.114
	300.	59.118
	400.	61.122
	500.	63.126
	600.	64.629
	700.	66.130
	800.	67.134
	1000.	69.138
	2000.	80.160
4. Uranium Dioxide	32.	34.45
	122.	38.35
	212.	40.95
	392.	43.55
	752.	46.80
	2012.	51.35
	2732.	52.65
	3092.	56.55
	3452.	63.05
	3812.	72.80
	4352.	89.70
	4532.	94.25
	4712.	98.15
4892.	100.1	
5144.	101.4	
8000.	101.4	
5. Zirconium	0.	28.392
	1480.	34.476
	1675.	85.176
	1787.5	34.470
	3500.	34.476

This page is intentionally left blank.

APPENDIX F

HEAT TRANSFER REGIMES AND CORRELATIONS IDENTIFICATION

The heat transfer mode, heat transfer correlations, and CHF correlations are identified by a set of flags, and these flags are printed out in the heat slab section of the major edit as MODE. The values of these flags and the corresponding mode/correlations are described below.

Heat Transfer Mode

Mode	Description
1	Single-phase liquid convection at critical and super critical pressure
2	Single-phase liquid convection at subcritical pressure
3	Subcooled nucleate boiling ($T_f < T_{sat} - 0.05$)
4	Saturated nucleate boiling ($T_f \geq T_{sat} - 0.05$)
5	Subcooled transition film boiling
6	Saturated transition film boiling
7	Subcooled film boiling
8	Saturated film boiling
9	Single-phase vapor convection
10	Condensation when void equals one
11	Condensation when void is less than one
12	Air-water mixture heat transfer
13	High AFW spray heat transfer
14	Interpolation between AFW and normal heat slab transfer mode
30-31	NCG condensation degradation

Heat Transfer Correlation Flag

A three digit code, IJK is used to identify the heat transfer correlation. If IJK = 0, EM heat transfer is not used. The first digit, I, represents CHFLCK and FMLOCK; I=0 if CHF has not been exceeded, I=1 if CHF has been exceeded (CHFLCK=T) and I=2 if CHF has been exceeded and $\Delta T_{\text{sat}} \geq 166.667 \text{ K}$ (300 F) (FMLOCK=T). JK represents the heat transfer correlations. In major edits IJK is identified under the heading of EM-MODE-HT. The values of JK and the corresponding correlations are given below.

JK	<u>EM-MODE-HT</u>	<u>Correlation</u>
-	Single-phase liquid	
	1	Dittus-Boelter
	2	Rohsenow-Choi
-	Nucleate Boiling	
	3	Dittus-Boelter
	4	Thom
	5	Thom/Schrock & Grossman interpolation
	6	Schrock & Grossman
	7	Schrock & Grossman/McEligot (steam) interpolation
	8	Schrock & Grossman/Rohsenow-Choi (steam) interpolation
	9	Chen
	10	Chen/McEligot (steam) interpolation
	11	Chen/Rohsenow-Choi (steam) interpolation
	12	Thom/Chen interpolation
	13	Thom/Schrock & Grossman to Chen interpolation

- 14 Schrock & Grossman to Chen interpolation
- 15 Chen/Schrock & Grossman combination to McEligot (steam) interpolation
- 16 Chen/Schrock & Grossman to Rohsenow-Choi (steam) interpolation

- Single-Phase Steam

- 17 McEligot & Radiation
- 18 Rohsenow-Choi & Radiation

- Transition Boiling

- 19 McDonough, Milich and King

- Film Boiling

- 20 Temporary film boiling - CSO/Condie-Bengston IV
- 23 Film boiling - CSO/Condie-Bengston IV

- Condensation

- 31 Dittus-Boelter

CHF Correlation Flag

A three digit code, LMN, is used to identify the CHF correlation. In major edits, it is identified under EM-MODE-CHF. The values of LMN and corresponding correlations are given below.

<u>EM-MODE-CHF</u>	<u>Correlation</u>
<u>High Flow - High Pressure</u>	
100	B&W-2
200	BWC
300	BWCMV
400	BWUMV
500	BWU User-Specified
600	BHTP
700	BHTP User-Specified

High Flow - Low Pressure

10	Interpolation between high pressure and Barnett
20	Barnett
30	Barnett-Modified Barnett Interpolation
40	Modified Barnett

Low Flow

1	High flow - low flow interpolation
2	Low flow (MacBeth) (MacBeth > Griffith)
3	Low flow (Griffith)
4	Minimum value for q_{crit} (90,000 Btu/hr-ft ²) is used

Note: For all flow conditions the CHF value is taken from the transition boiling correlation for $\alpha_g > 0.8$. This condition is identified by adding 50 to the appropriate value of EM-MODE-CHF in the above table. If the transition value of CHF is less than the minimum value of 90,000 Btu/hr-ft², the minimum value is used and 55 is added to EM-MODE-CHF.

This page is intentionally left blank.

APPENDIX G
BENCHMARKS

Two benchmarks are included with this report to verify the RELAP5/MOD2-B&W formulation and implementation. A LBLOCA benchmark, Semiscale MOD1 test S-04-6, and a SBLOCA benchmark, LOFT test L3-5, were performed and are documented in this appendix.

G.1. LBLOCA Benchmark of Semiscale MOD1 Experiment S-04-6

G.1.1. Introduction

Test S-04-6 was one of the 200 percent offset shear double-ended cold leg break tests conducted in the Semiscale MOD1 test facility. RELAP5/MOD2-B&W was used to predict the test, first using the INEL Cycle 36.04 options (base case) and second using the B&W installed evaluation model (EM) options. Both cases predicted higher break mass flow rates than shown by the data, and, as a result, the predicted depressurization rates were higher than the data. The predicted cladding temperature at the peak power location of the high powered rod using the EM option was higher than the Cycle 36.04 prediction. Both cases predicted higher cladding temperatures than measured. From this study it is concluded that the EM option would properly predict the system behavior during the blowdown phase of a PWR large break loss of coolant accident (LBLOCA).

G.1.2. Description of Experiment

An isometric view of the Semiscale MOD1 test facility used for the cold leg break tests is shown in Figure G.1-1. It is a small scale model of a typical four-loop recirculating steam generator PWR. It consists of the following major PWR components: a pressure vessel with the core simulator, lower and upper plenums, and downcomer; an intact loop with a steam generator, a pump and a pressurizer; a broken loop with a simulated steam generator and a simulated pump; emergency coolant systems (ECC) in both loops that included an accumulator, and high and low pressure injection pumps; and a pressure suppression system with a suppression tank.

The configuration of the electrically-heated 40-rod bundle, shown in Figure G.1-2, is typical of a 15 by 15 fuel assembly (0.422 inch rod outside diameter and 0.563 inch pitch) except that the heated length of the test rods is 5.5 feet compared with 12 feet for commercial rods. The bundle has an inlet peaked axial power profile (peak at 26 inches from the bottom of the heated section). Three of the four center rods have a peak power density of 12 kw/ft and the fourth rod is unpowered. Of the remaining 36 rods, 33 rods have a peak power density of 11.46 kw/ft and three rods are unpowered.

The transient was initiated after the system reached steady-state by breaking two rupture assemblies that allowed the flow of the primary fluid into the suppression tank through two blowdown nozzles, each having a break area of 0.00262 ft². The suppression system was maintained at a constant pressure of 34.8 psia. At blowdown initiation, the power to the primary coolant pump was reduced and the pump was allowed to coast down to a speed of 1500 rpm, which was then maintained for the duration of the test. During the transient, the power to the core was automatically controlled to simulate the thermal response of nuclear rods. The measurements made during the transient included pressure, flow, density, and fluid temperatures at different locations in the primary and secondary systems, and surface temperatures at different elevations of the selected heated rods. The sequence of events relative to the transient initiation is given in Table G.1-1.

G.1.3. RELAP5 Input Model

The nodalization of the RELAP5 input model for the Semiscale MOD1 test facility is shown in Figure G.1-32. The nodalization of the primary system is very similar to the RELAP4 model given in Reference 7. The geometry and other needed input information for the primary system was obtained from this RELAP4 model.⁷ The geometry and other input information for the secondary side of

the steam generator were obtained from the RELAP5/MOD0 input model given in Reference 8. The input information obtained from the RELAP4 and the RELAP5/MOD0 input models were verified using the geometry values given in Reference 6.

The RELAP5 base input model consisted of 89 volumes, 98 junctions, and 50 heat structures. Some of the important features of the model are given below.

1. The core was modeled with two channels to account for the radially peaked power profile. The fluid volumes associated with the three high powered rods were modeled as a hot channel. The remaining core fluid volumes were modeled as an average channel. Each channel was axially divided into six volumes in order to make the model consistent with the EM plant model. The axial division coincided with selected axial steps in the power shape curve. Crossflow junctions were used to connect the hot and average channel volumes.
2. The active heater rods in each channel were modeled using ten heat slabs, that is, one heat slab per power step.
3. The pressurizer was modeled using an eight-equal-volume pipe component.
4. The accumulator was modeled using the accumulator component.
5. The high and low pressure pumps were simulated using time-dependent volumes and junctions.
6. The suppression system was modeled as a time-dependent volume.
7. Break nozzles were modeled as trip valves.

8. The homologous curves for the intact loop pump were obtained from the RELAP4 input model.⁷ The measured pump speed versus time data were input to simulate the pump coast down during the transient.
9. The measured power versus time data were input to simulate the electrical power supplied to the heater rods during the transient.
10. The moisture separator on the secondary side of the steam generator was simulated using the separator component.
11. Nonequilibrium and nonhomogeneous options were selected for each volume and junction.
12. The break junctions and the pressurizer surge line junction were treated as choked flow junctions using a discharge coefficient of one.

G.1.3.1. EM Input Options

The following modifications to the base model were made to select the EM options. These options are the same as those used in the EM plant model.

1. The equilibrium option was selected for the core inlet, outlet, and core volumes.
2. The homogeneous option was selected for the core inlet, outlet, and the normal (vertical) core junctions.
3. The EM heat transfer option with the B&W high pressure CHF correlation (B&W-2) was selected for all the core heat slabs. The post-CHF lock-in option was selected that would force permanent film boiling if CHF is exceeded and conditions would permit a return to nucleate boiling.

4. The 90/10 weighting factor was used in the underrelaxation of the interphase heat transfer.

5. Choked Flow Models

Subcooled: Extended Henry-Fauske.

Two-phase and superheated region: Moody/Murdock-Bauman.

Static properties.

Homogeneous option (slip ratio = 1.0).

Quality switching for the subcooled to two-phase transition.

6. The break junctions in the base model were selected as EM choked flow junctions. An additional junction and a time-dependent volume were added at each break plane. These junctions were used to switch the flow from choked flow to a flow calculated by the RELAP5 momentum equations when the system pressure was close to the suppression tank pressure and choked flow was no longer appropriate. The non-choking option was selected for these junctions. When the velocity calculated using the orifice equation is less than the choked junction velocity, the choked junction is closed and the second junction is opened, and will remain open during the remainder of the transient.

G.1.4. Transient Simulation

The base case and the EM case were run with constant boundary conditions to obtain steady-state test conditions. The steam generator secondary side pressure was adjusted to obtain the desired primary system conditions. Once the system reached steady-state, a steady-state post processor was used to replace the assumed initial conditions with the correct steady-state conditions in the input files. The measured and the predicted steady-state conditions are given in Table G.1-2. Trips were used to initiate the sequence of events, given in Table G.1-1, during the transient.

G.1.5. Results and Discussion

The measured and the predicted pressure variations near the vessel side break are shown in Figure G.1-3. Both Cycle 36.04 and the EM predicted lower pressures than the data during the entire transient. The EM calculated a faster depressurization rate than Cycle 36.04. As a result, the pressure near the break location reached the suppression tank pressure at about 18 seconds in the EM case, and at 25.7 seconds in the base case as compared to 37 seconds in the test. The depressurization rate in both cases could be adjusted to match the data by varying the discharge coefficients. However, in the present study no attempt was made to adjust the discharge coefficients.

The pressure response near the pump side break is shown in Figure G.1-4. The predicted pressure response near this break location, using the EM option, was similar to the prediction near the vessel side break. Between 1.0 and 8.0 seconds, the base case predicted a higher pressure than the data. The difference between the measured and the input values of the HPI flow rates near this break location is the cause of this difference. The break plane pressure reached the suppression tank pressure at 15.8 seconds in the EM test case, and 25.6 seconds in the base case as compared to 27.0 seconds in the test.

The pressure responses at other locations in the primary system are shown in Figures G.1-5 through G.1-9. From these figures it can be concluded that the pressure response in the primary system is similar to the pressure response near the vessel side break shown in Figure G.1-3. The Cycle 36.04 pressure response near the broken loop simulated pump suction side, as shown in Figure G.1-6, supports the conclusion made from Figure G.1-4 that the HPI flow rate difference is the cause for the prediction of higher pressure than the data in the 1.0 to 8.0 second time period.

The pressure responses in the intact and the broken loop accumulators, shown in Figures G.1-10 and G.1-11 respectively, are consistent with the primary system pressure response. The sudden drop in measured pressure in the broken loop accumulator at about 2.5 seconds was caused by the opening of a valve in the surge line before the onset of injection.⁷ In the present model, the initial pressure in this accumulator was set to 520 psia as was done in the RELAP4 model given in Reference 7.

The mass flow rates at different locations in the primary system are shown in Figures G.1-12 through G.1-18. In the test, the mass flow rate was estimated from the measured density and the volume flow rate. The mass flow rates given in the data report⁵ were digitized to generate the comparison plots. During the digitalization the oscillations in the original data plots were smoothed out.

Figure G.1-12 shows that, near the vessel side break, both Cycle 36.04 and the EM predicted higher flow rates than the data. Both cases correctly predicted the transition from single-phase conditions to two-phase conditions which occurred at about 2.8 seconds. When the system pressure was close to the suppression tank pressure large spikes were observed in the data as well as in the prediction. These spikes were caused by the movement of liquid slugs from the accumulator injection location to the break. In the EM case, downflow of liquid into the downcomer occurred at about 19.2 seconds. This liquid flashes, thereby, resulting in a large vapor upflow that pushes fluid from the downcomer to the cold legs. The positive spike in the break flow rate (Figure G.1-12) and the negative spike in the flow from the intact loop cold leg to the downcomer, as shown in Figure G.1-17, at about 19.2 seconds were caused by this flashing of liquid in the downcomer.

The data as well as the prediction show that the core inlet flow remains negative during the entire blowdown period as shown in Figure G.1-18. For the first second after the initiation of the transient, both cases predicted higher values than the measured negative flow rate. From 7 to 12 seconds the EM predicted higher negative flow rates than the data and the Cycle 36.04 prediction.

The flow rates from the intact and the broken loop accumulators are shown in Figures G.1-19 and G.1-20, respectively. The starting points for the accumulator injection as well as the flow rates are consistent with the pressure response near the injection location. The spike in the broken loop accumulator flow data was caused by the opening of a valve⁷ and therefore the actual flow did not start until about 3 seconds after transient initiation. The oscillations in the Cycle 36.04 prediction of this accumulator flow were due to the time steps taken by the code. They were larger than those allowed by the Courant limit. Similar oscillations were observed in an EM case when the code used the same time step as in the Cycle 36.04 case. The EM case discussed here was run using time steps which were smaller than that allowed by the Courant limit and it calculated a smooth flow rate as shown in Figure G.1-20.

The density variations near the vessel side and the pump side breaks and near the core inlet are shown in Figures G.1-21, G.1-22, and G.1-23, respectively. The underprediction of density near the vessel side break was due to the prediction of a faster depressurization rate. The spikes in the data as well as in the predictions, during the later part of the transient, were caused by movement of liquid slugs from the ECC injection location to the break. Near the pump side break, the EM underpredicted the density during the entire transient. Cycle 36.04 overpredicted the density from 1.5 to 6.0 seconds and underpredicted it during the remainder of the transient which is consistent with the

pressure prediction shown in Figure G.1-4. Both Cycle 36.04 and the EM overpredicted the density near the core inlet as shown in Figure G.1-23. Higher predicted flows from the core during the early part of the transient and lower predicted core heat transfer are the causes of the high density fluid near the core inlet (Figure G.1-23).

Fluid temperature variations at different locations in the primary system are shown in Figures G.1-24 through G.1-29. The calculated liquid and vapor temperatures are shown in these figures. These figures show that, once the system fluid condition has switched from subcooled liquid to two-phase mixture, the liquid and vapor temperatures generally remain near saturation during the major portion of the blowdown period. During the accumulator injection period, the data as well as the prediction show subcooled liquid and saturated steam at the injection location (Figure G.1-27). As the liquid slugs move toward the break, the fluid conditions along the path change from a saturation condition to saturated steam and subcooled liquid (Figures G.1-25 and G.1-26). The effect of lower core heat transfer during the later part of the transient can be observed in the fluid conditions near the core inlet (Figure G.1-28) and exit (Figure G.1-29).

The cladding temperature variations at the peak power location in the average and the high powered rods are shown in Figures G.1-30 and G.1-31, respectively. From an examination of the data given in Reference 5, it was observed that the cladding temperatures of the rods near the vessel wall were much higher than those of other rods (data D8-27 in Figure G.1-30). The unpowered rods in the bundle could reduce the temperatures of the nearby heated rods. However, test S-04-5, which is the counterpart of test S-04-6 (with all rods powered) showed a similar trend in the results. For most of the inner rods, both tests gave about the same temperatures at the peak power locations. Therefore, only

the cladding temperatures for the inner rods should be used for comparing the data with predictions.

The predicted cladding surface temperatures are shown in Figures G.1-30 and G.1-31. In the test, the thermocouples were located in the creases of the inner sheath. In the model, the cladding was modeled using two radial nodes. Therefore, the inner node temperature would and should be closer to the data. However, in RELAP5 only surface temperatures are stored in the plot file. At steady-state, the calculated temperature of the inner node, in both cases, was found to be close to the data. During the transient the difference between the surface temperature and the inner node temperature was about 10 F. Hence, the surface temperature is sufficient for comparison purposes.

The EM CHF correlations were found to be conservative in predicting DNB. Cycle 36.04 predicted DNB early by about 1 second for the average powered rods and correctly predicted DNB for the high powered rods. The EM predicted DNB early by about 2 seconds for the average powered rods and for the high powered rods the EM predicted DNB within 0.1 seconds after the initiation of the transient whereas DNB in the test occurred at about 3 seconds after the initiation of the transient.

Cycle 36.04 and the EM predicted higher cladding temperatures than the data during the entire transient period. For the high powered rods the EM calculated cladding temperature was much higher than the data as well as that calculated by Cycle 36.04. For the average powered rods the EM calculated cladding temperature was lower than that calculated by Cycle 36.04 after about 11 seconds. The higher core heat transfer predicted by the EM was due to the higher core flow rate prediction.

G.1.6. Summary and Conclusion

Semiscale MOD1 large break LOCA test S-04-6 was simulated using RELAP5/MOD2-B&W with one case using the Cycle 36.04 options and the other using the EM options. In both cases a discharge coefficient of 1.0 was used for both the subcooled and two-phase break flow regimes. The EM options selected in this study are the same as those selected for actual plant modeling. As expected, both cases predicted higher break flow rates, faster system depressurization rates, and higher cladding temperatures than the data; the EM generally predicted higher values for these parameters than Cycle 36.04.

The consistency between the transient behavior predicted by the RELAP5/MOD2-B&W evaluation model version and the test data, given allowances for the effects of the EM discharge and core heat transfer models, supports application of B&W's EM version for conservative calculations of blowdown during large LOCA transients. When applied according to Appendix K requirements, using a spectrum of effective break area-discharge coefficient combinations, RELAP5/MOD2-B&W should prove effective in defining limiting end-of-blowdown conditions.

Table G.1-1. Sequence of Events During Test S-04-6.

<u>Event</u>	<u>Time (sec)</u>
Blowdown Initiated	0.0
ECC Accumulators Initiated	0.0
HPI Pumps Started	0.0
Steam Generator Feedwater and Discharge Valves Closed	1.0
LPI Started	30.0

Table G.1-2. Conditions at Blowdown Initiation.

<u>Parameter</u>	<u>Data</u>	<u>Cycle 36.04</u>	<u>EM</u>
Core Power, kw (Btu/s)	1.44 (1364.86)	1.44	1.44
Cold Leg Fluid Temperature, F	543.0	543.5	543.0
Hot Leg Fluid Temperature, F	610.0	610.3	609.5
Pressurizer Pressure, psia	2252.0	2253.3	2252.6
Pump Speed, RPM	2400.0	2400.0	2400.0
ICL Flow Rate, lbm/s	15.5	15.4	15.4
Steam Generator Pressure, psia	850.0	809.5	803.5
Pressure Suppression Tank Pressure, psia	34.8	34.8	34.8

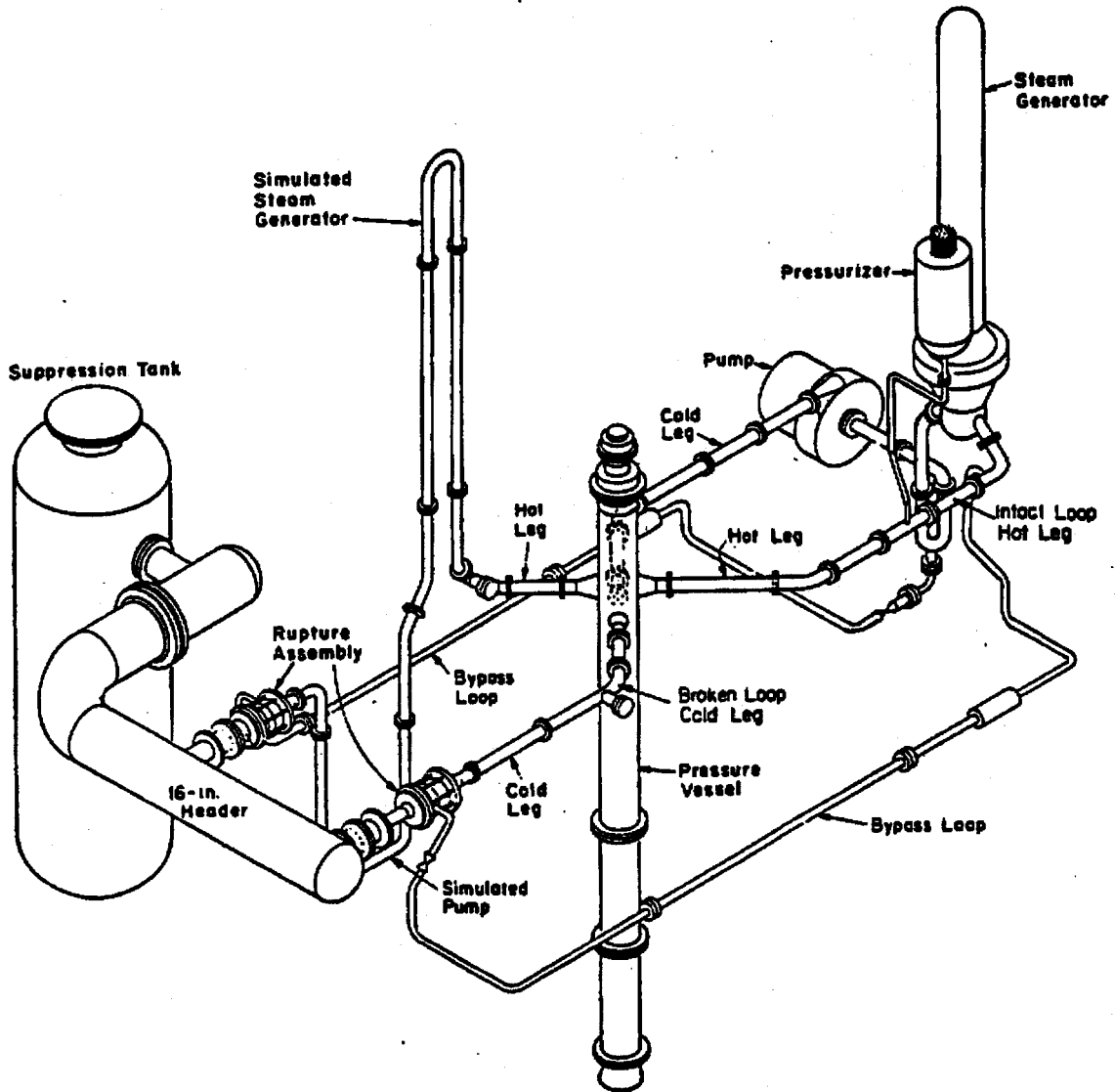


Figure G.1- 1. Semiscale MOD1 Test Facility - Cold Leg Break Configuration.

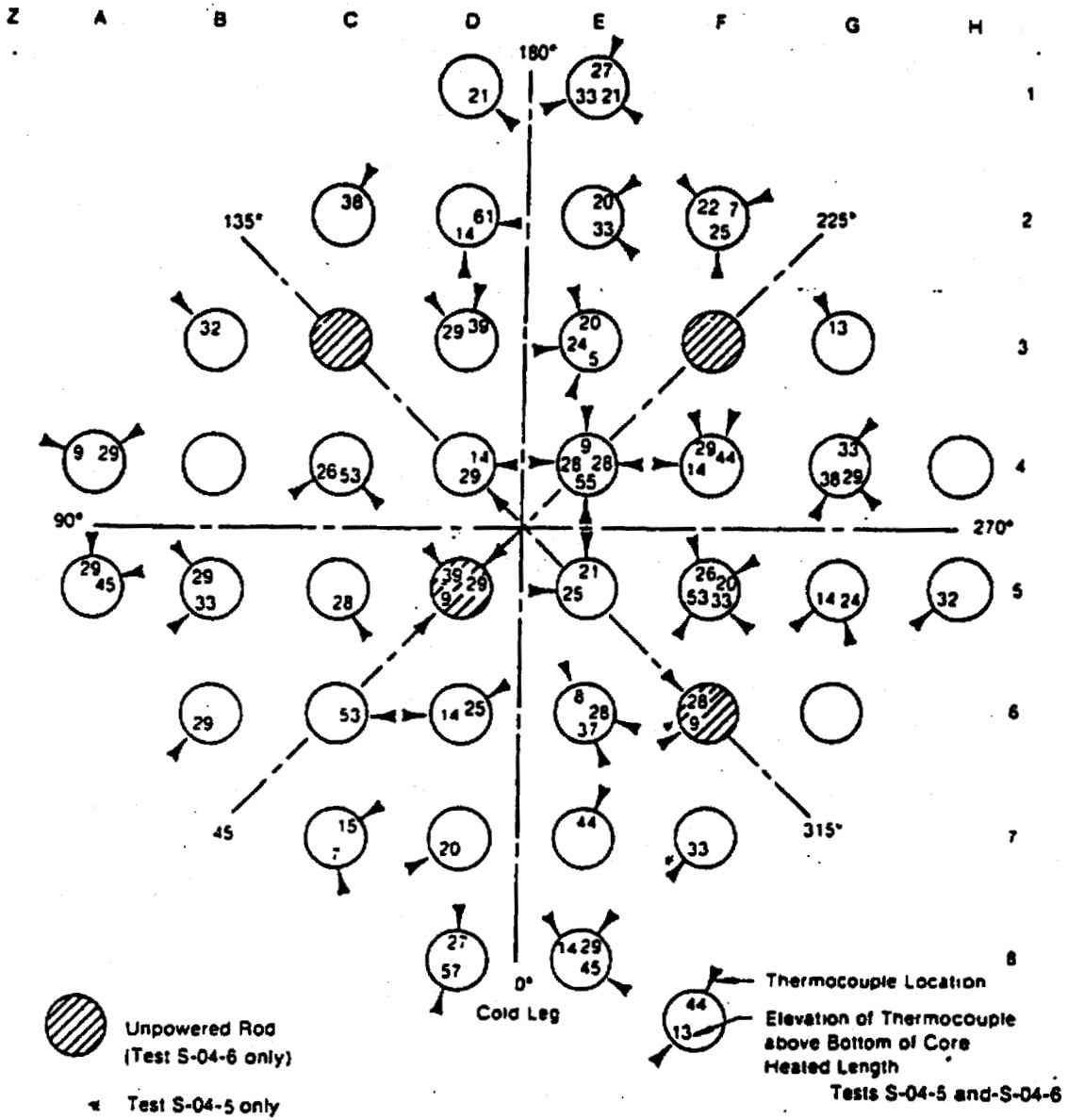


Figure G.1- 2. Semiscale MOD1 Rod Locations for Test S-04-6.

FIGURE G.1-3. SEMISCALE MOD1 TEST S-04-6; PRESSURE NEAR THE VESSEL SIDE BREAK.

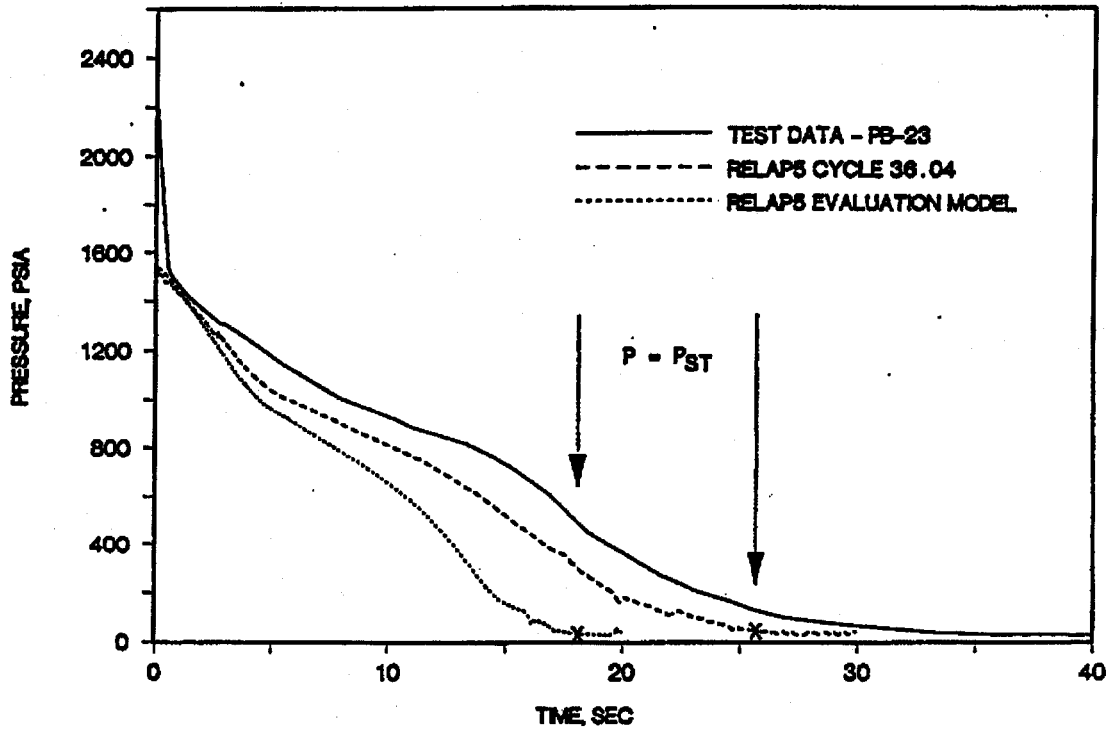


FIGURE G.1-4. SEMISCALE MOD1 TEST S-04-6; PRESSURE NEAR THE PUMP SIDE BREAK.

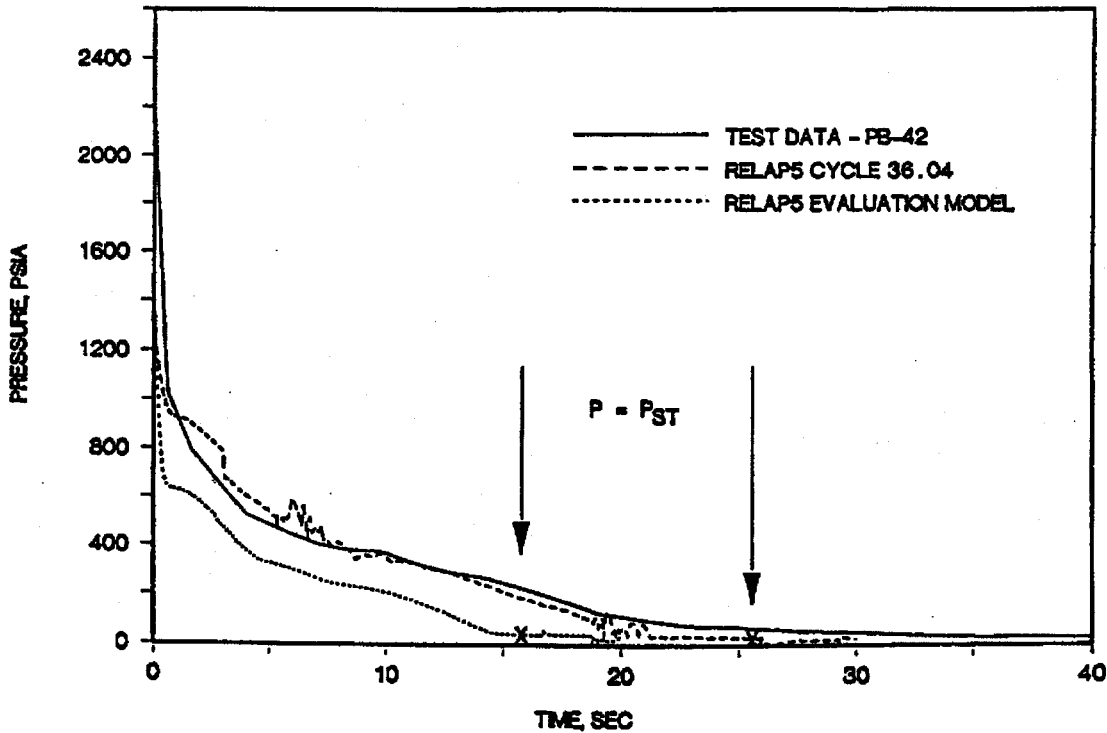


FIGURE G. 1- 5. SEMISCALE MOD1 TEST S-04-6; PRESSURE NEAR THE INTACT LOOP PUMP EXIT.

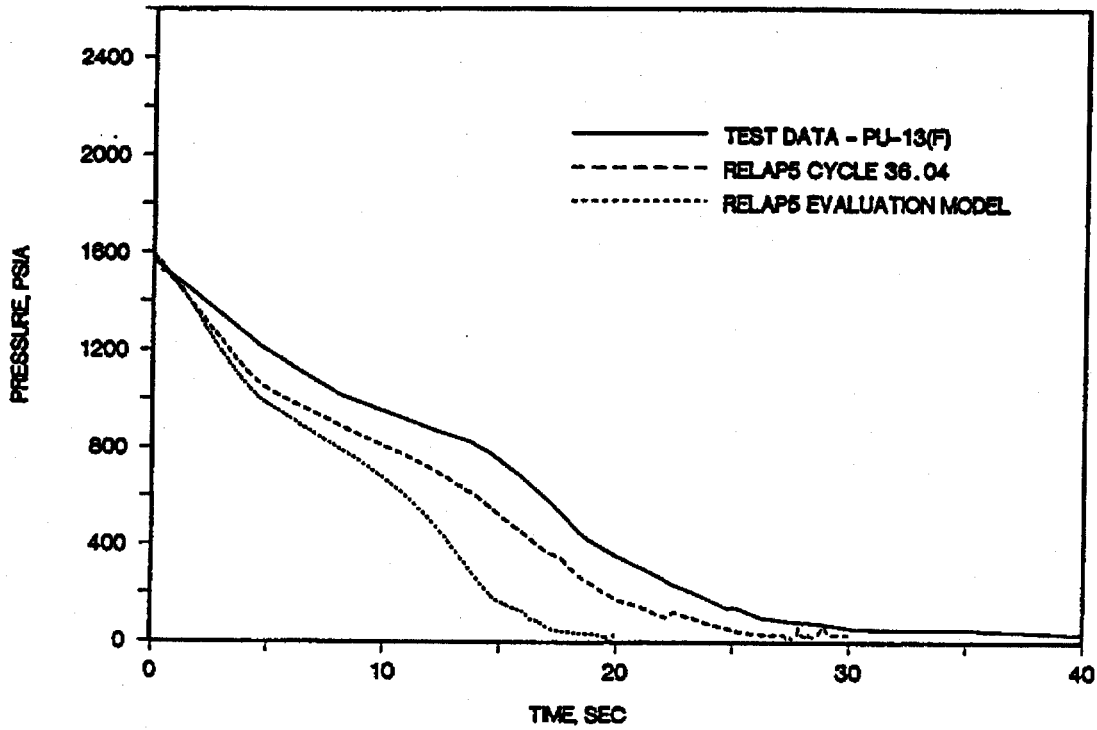


FIGURE G. 1- 6. SEMISCALE MOD1 TEST S-04-6; PRESSURE IN THE BROKEN LOOP NEAR THE PUMP SIMULATOR INLET.

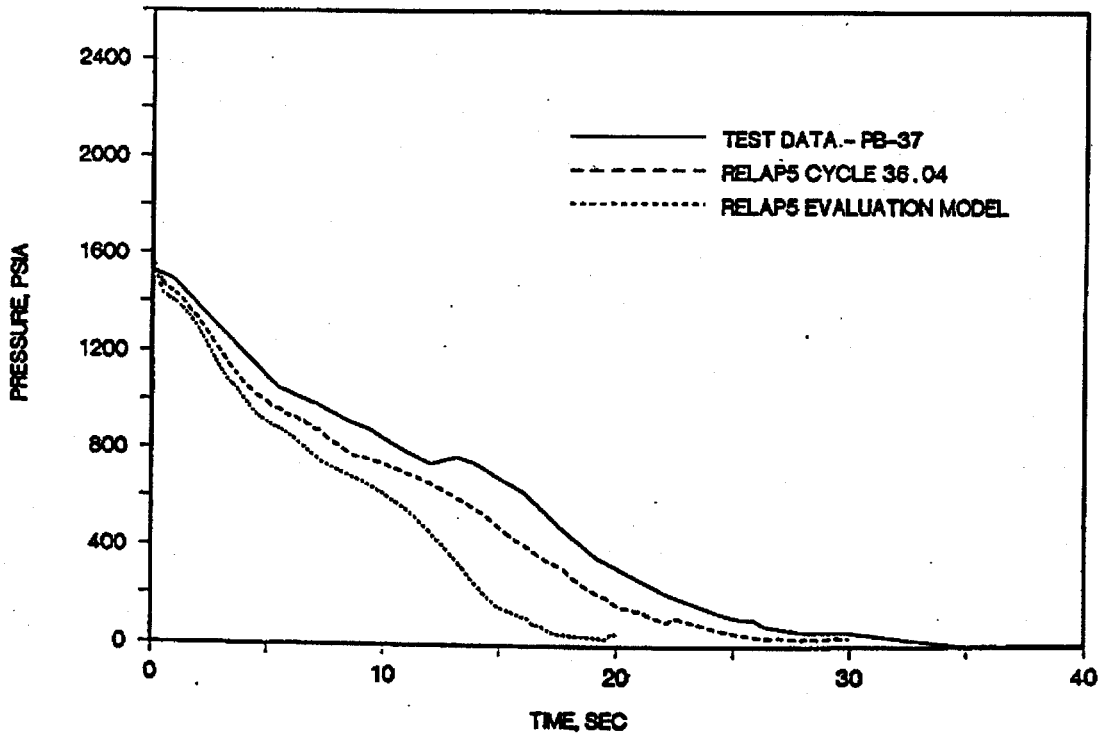


FIGURE G.1-7. SEMISCALE MOD1 TEST S-04-6; PRESSURE IN THE LOWER PLENUM.

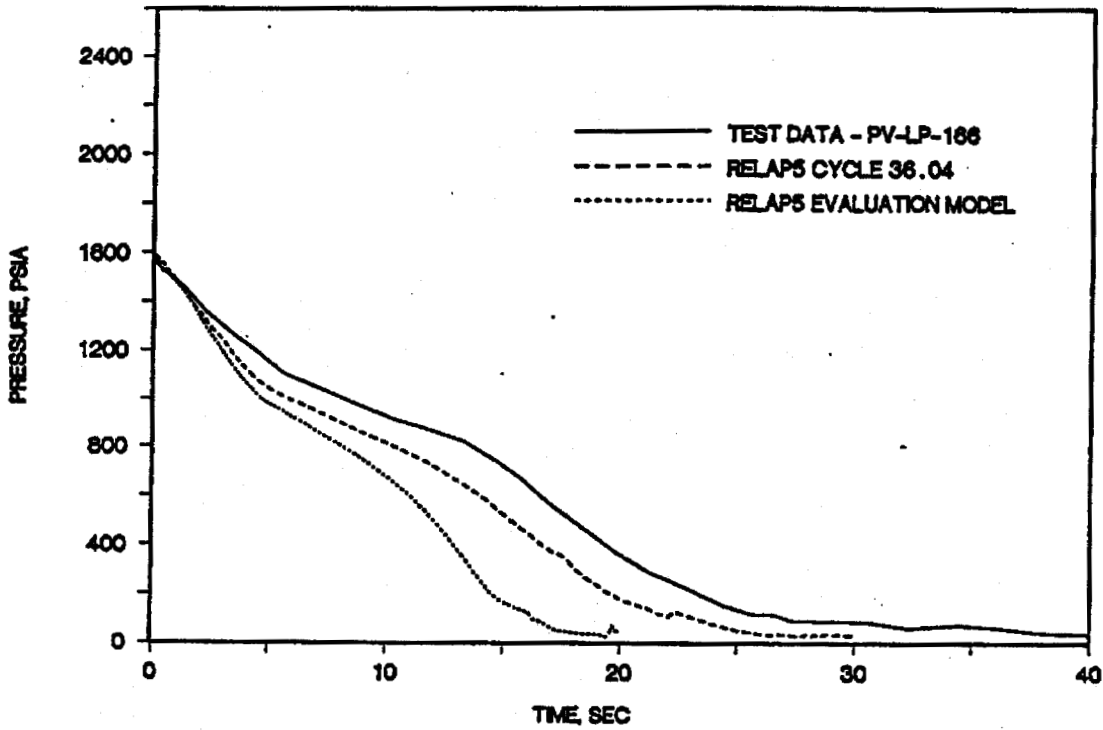


FIGURE G.1-8. SEMISCALE MOD1 TEST S-04-6; PRESSURE IN THE UPPER PLENUM.

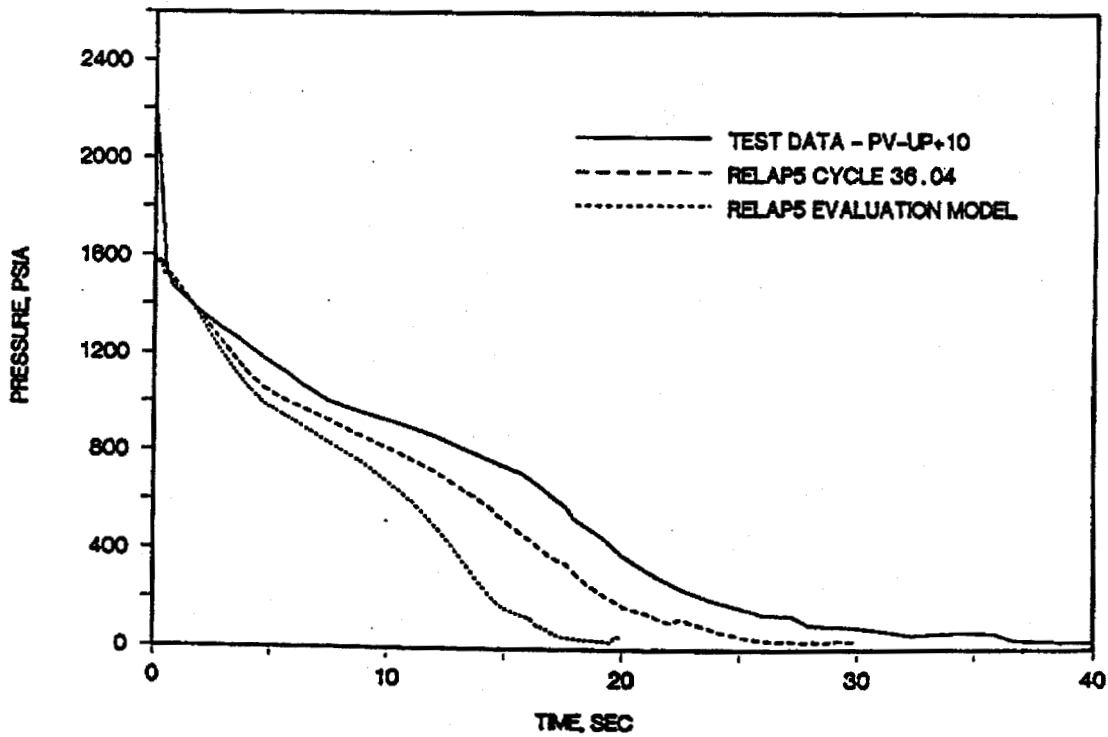


FIGURE G.1-9. SEMISCALE MOD1 TEST S-04-6; PRESSURE NEAR THE TOP OF THE PRESSURIZER.

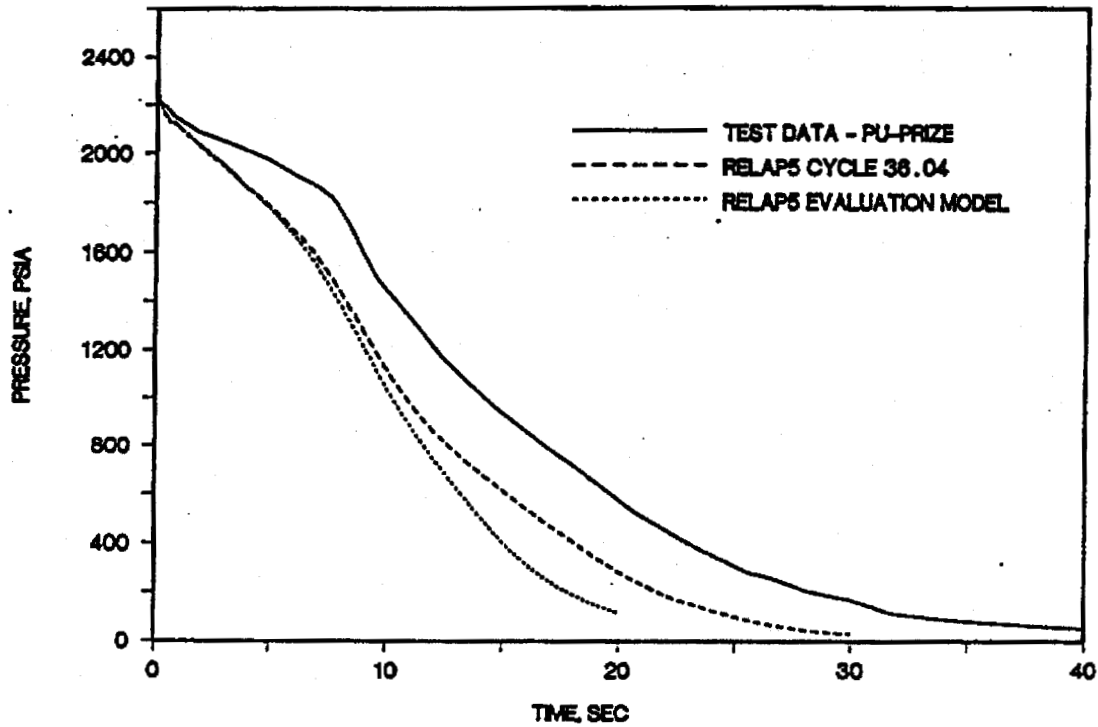


FIGURE G.1-10. SEMISCALE MOD1 TEST S-04-6; PRESSURE IN THE INTACT LOOP ACCUMULATOR.

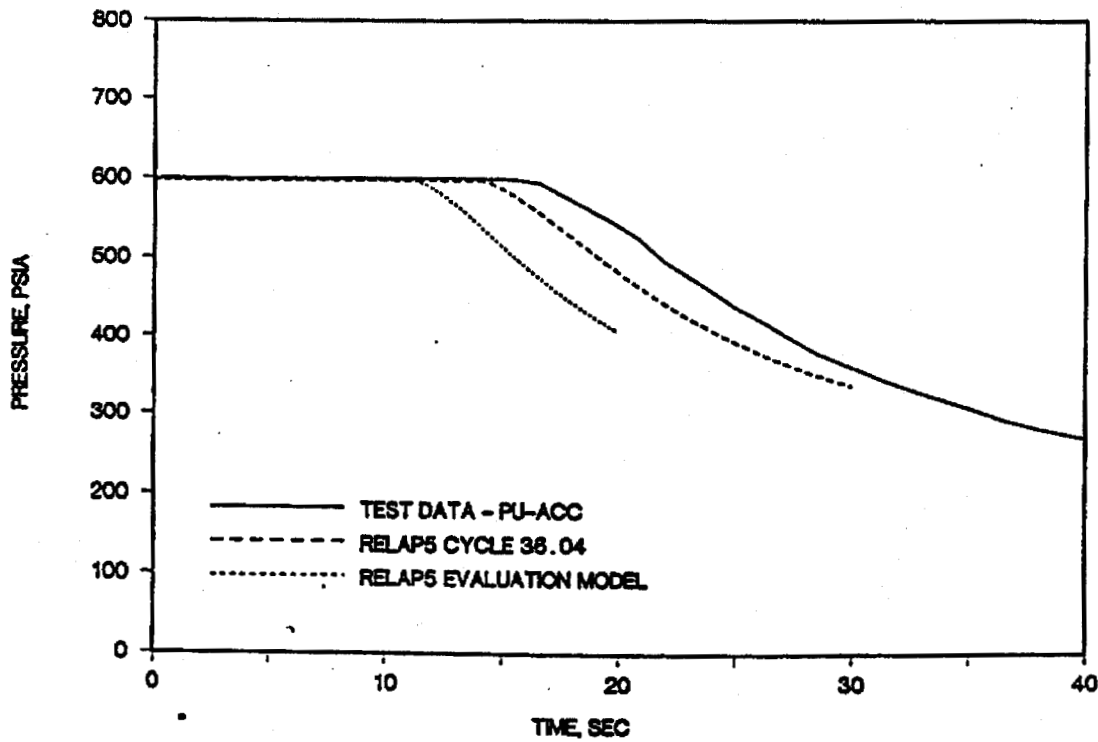


FIGURE G. 1-11. SEMISCALE MOD1 TEST S-04-6; PRESSURE IN THE BROKEN LOOP ACCUMULATOR.

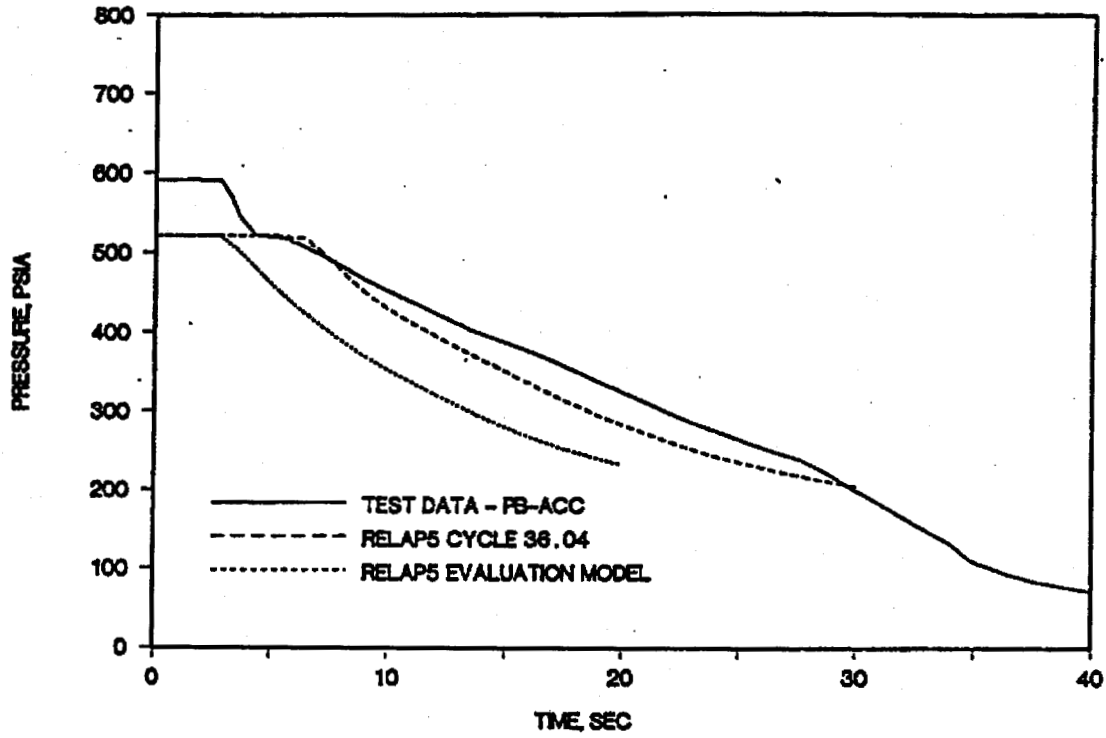


FIGURE G. 1-12. SEMISCALE MOD1 TEST S-04-6; MASS FLOW RATE NEAR THE VESSEL SIDE BREAK.

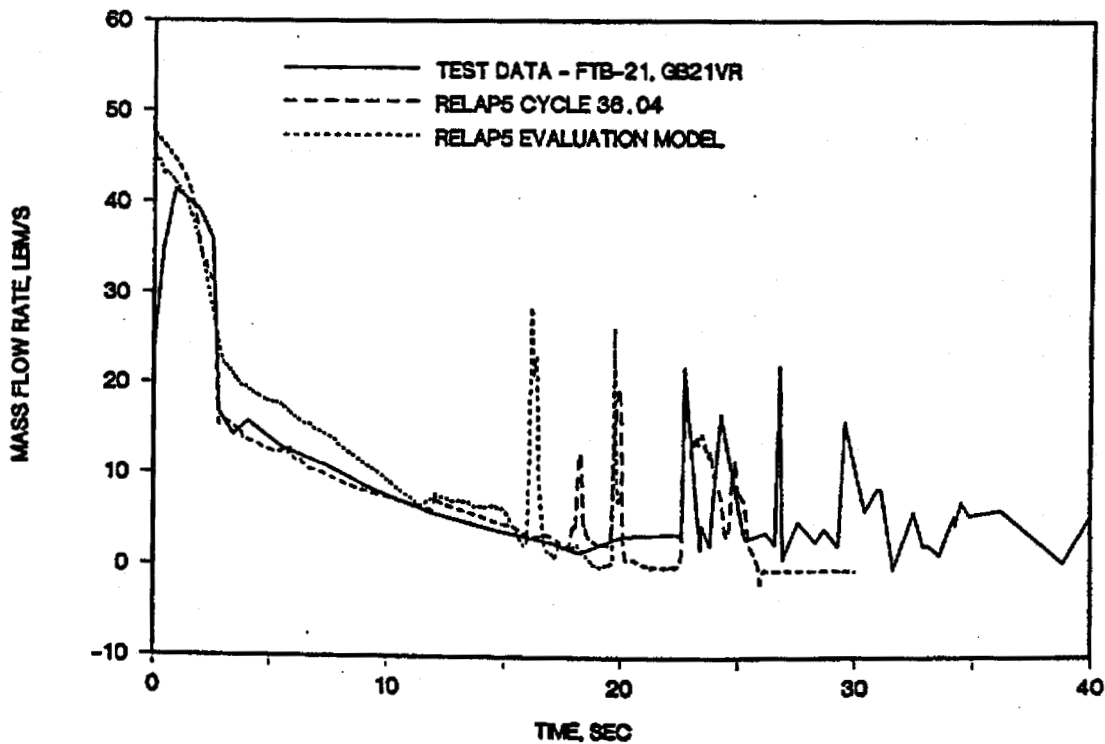


FIGURE G. 1-13. SEMISCALE MOD1 TEST S-04-6; MASS FLOW RATE NEAR PUMP SIDE BREAK (BEFORE ECG INJECTION POINT).

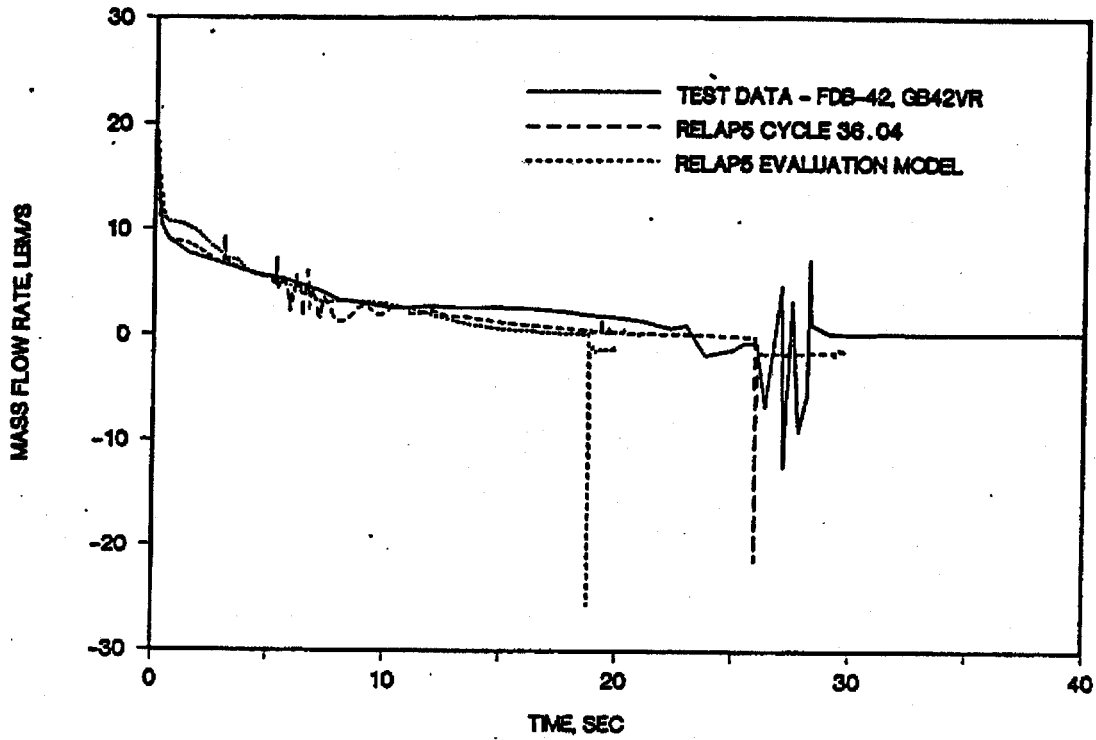


FIGURE G. 1-14. SEMISCALE MOD1 TEST S-04-6; MASS FLOW RATE IN THE INTACT LOOP HOT LEG.

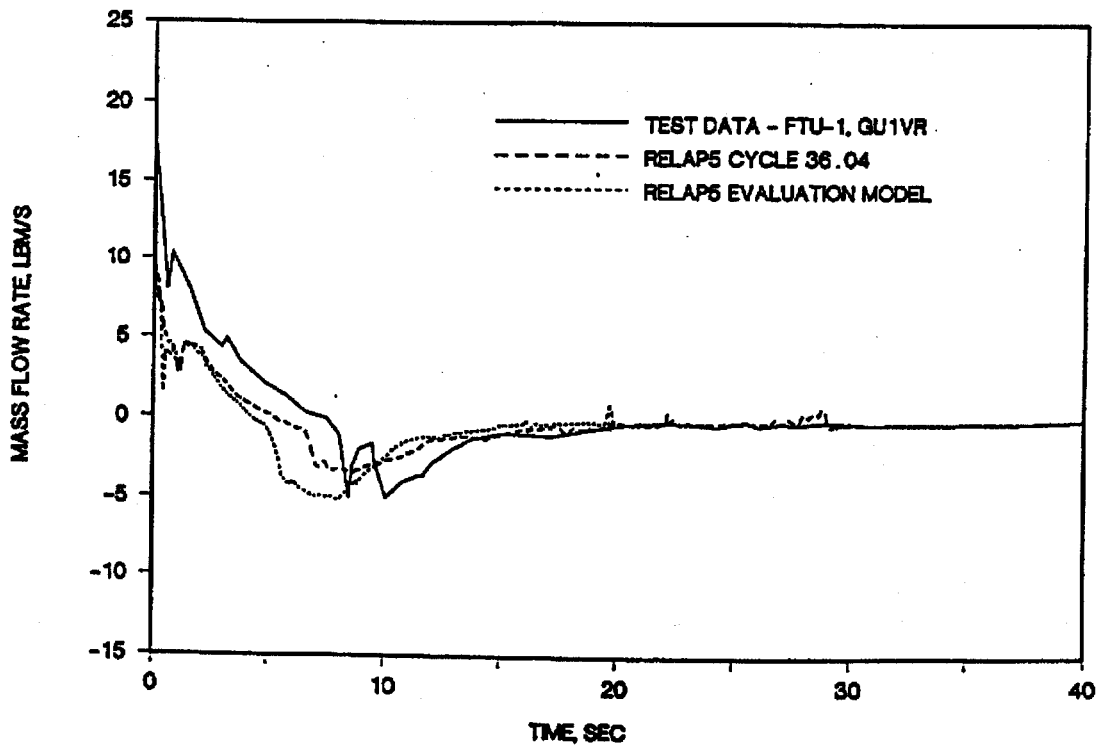


FIGURE G. 1-15. SEMISCALE MOD1 TEST S-04-6; MASS FLOW RATE NEAR THE PUMP SIMULATOR INLET.

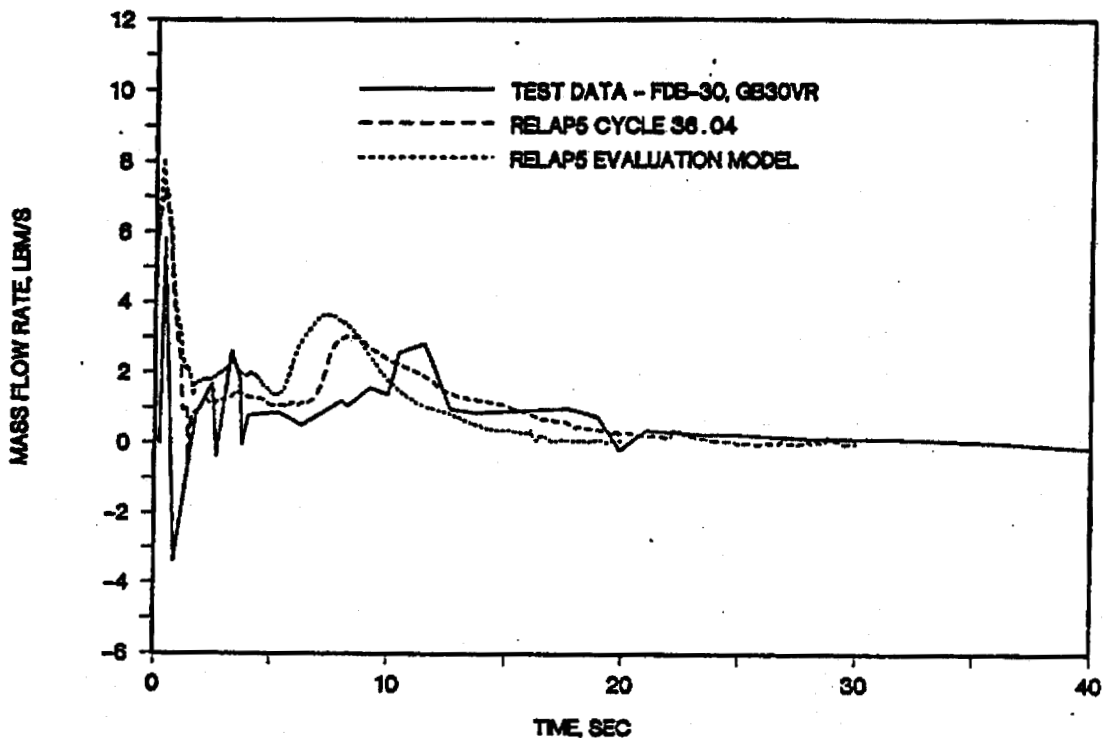


FIGURE G. 1-16. SEMISCALE MOD1 TEST S-04-6; MASS FLOW RATE IN INTACT LOOP COLD LEG (BEFORE ACCUMULATOR INJECTION POINT).

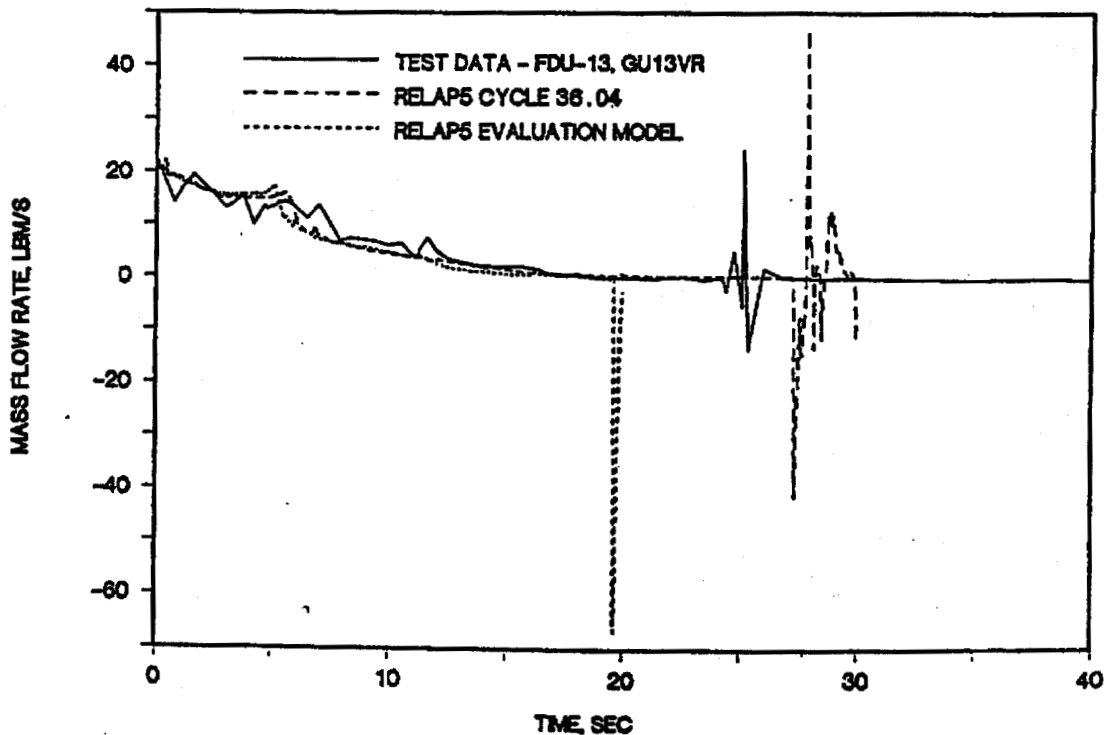


FIGURE G. 1-17. SEMISCALE MOD1 TEST S-04-6; DOWNCOMER INLET FLOW RATE FROM THE INTACT LOOP.

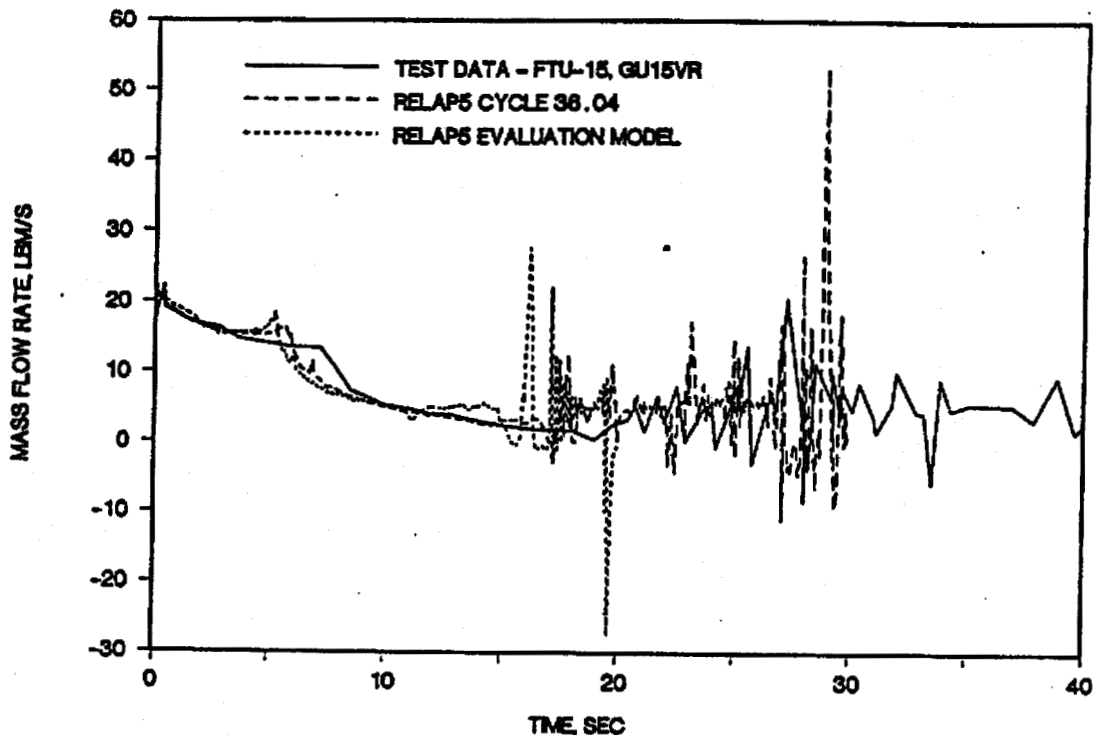


FIGURE G. 1-18. SEMISCALE MOD1 TEST S-04-6; MASS FLOW RATE AT THE CORE INLET.

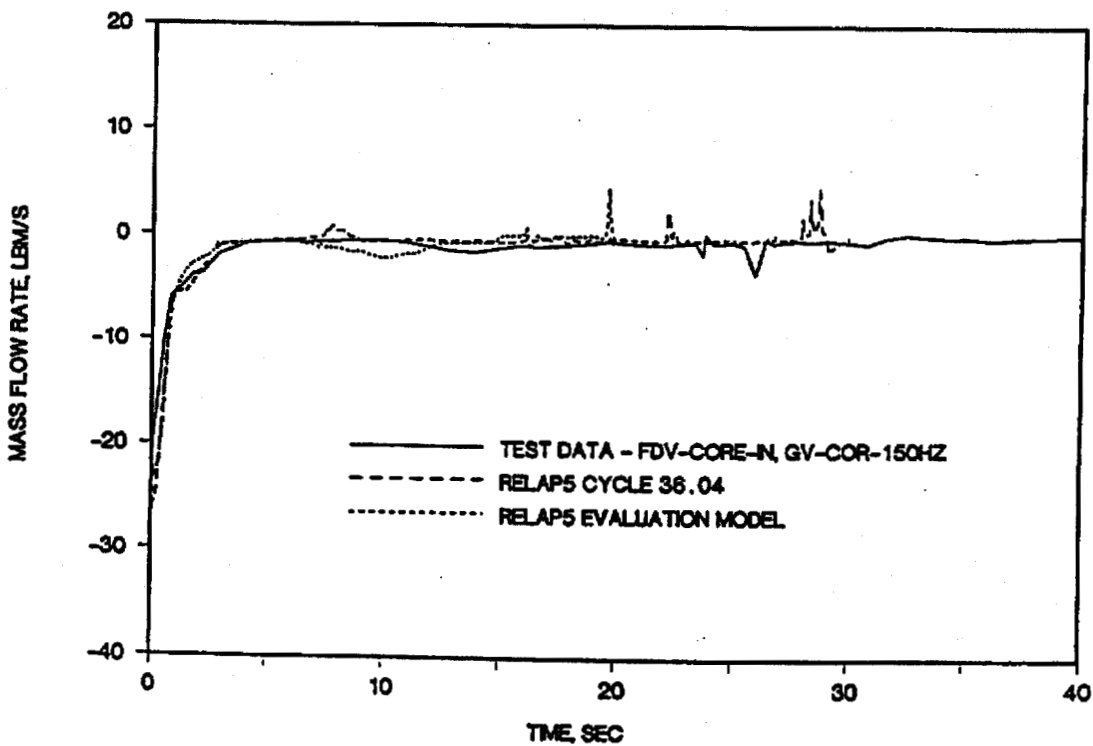


FIGURE G. 1-19. SEMISCALE MOD1 TEST S-04-6; MASS FLOW RATE FROM THE INTACT LOOP ACCUMULATOR.

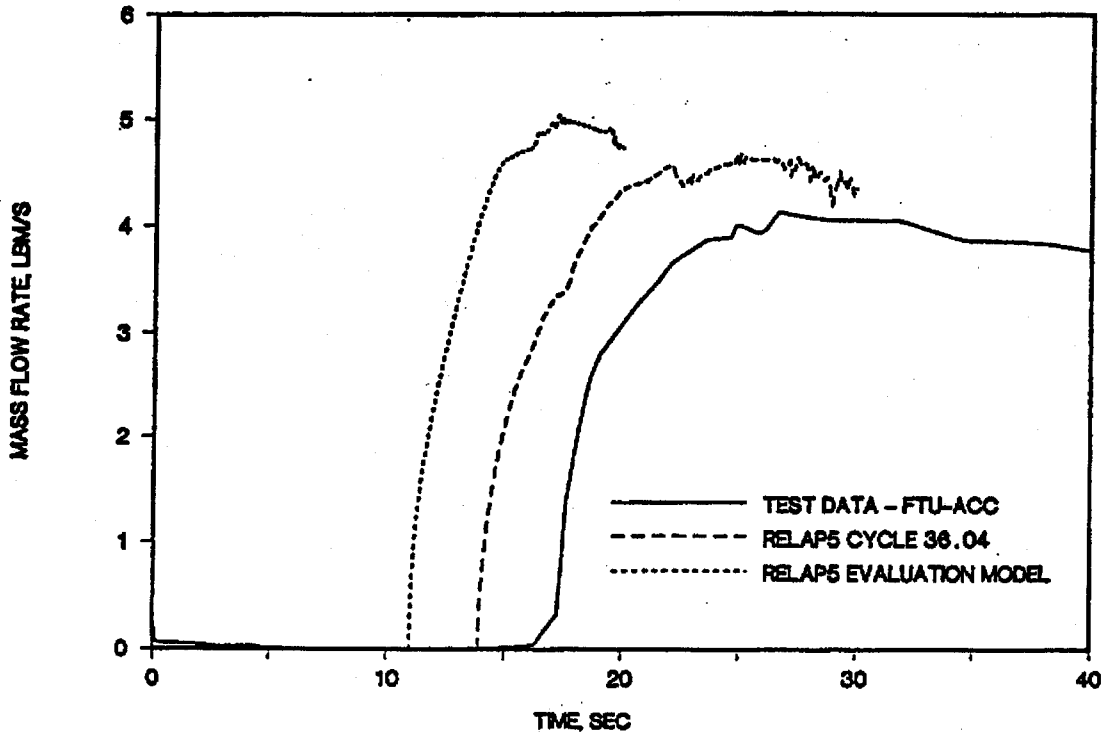


FIGURE G. 1-20. SEMISCALE MOD1 TEST S-04-6; MASS FLOW RATE FROM THE BROKEN LOOP ACCUMULATOR.

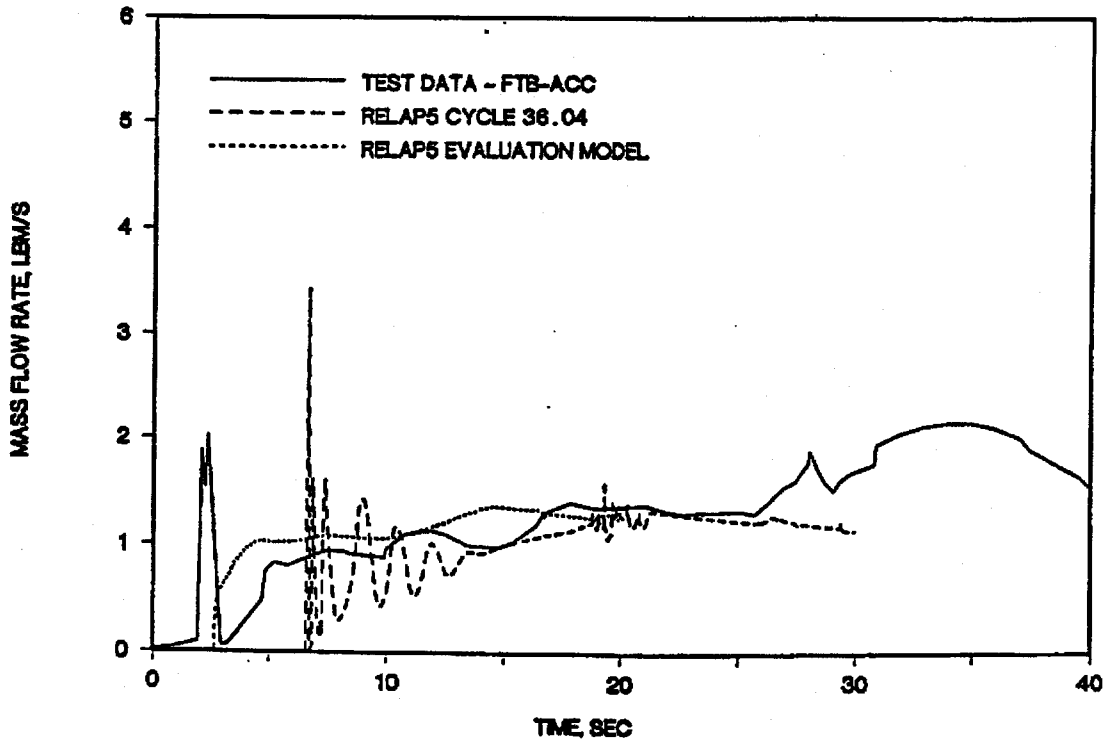


FIGURE G. 1-21. SEMISCALE MOD1 TEST S-04-6; DENSITY NEAR THE VESSEL SIDE BREAK.

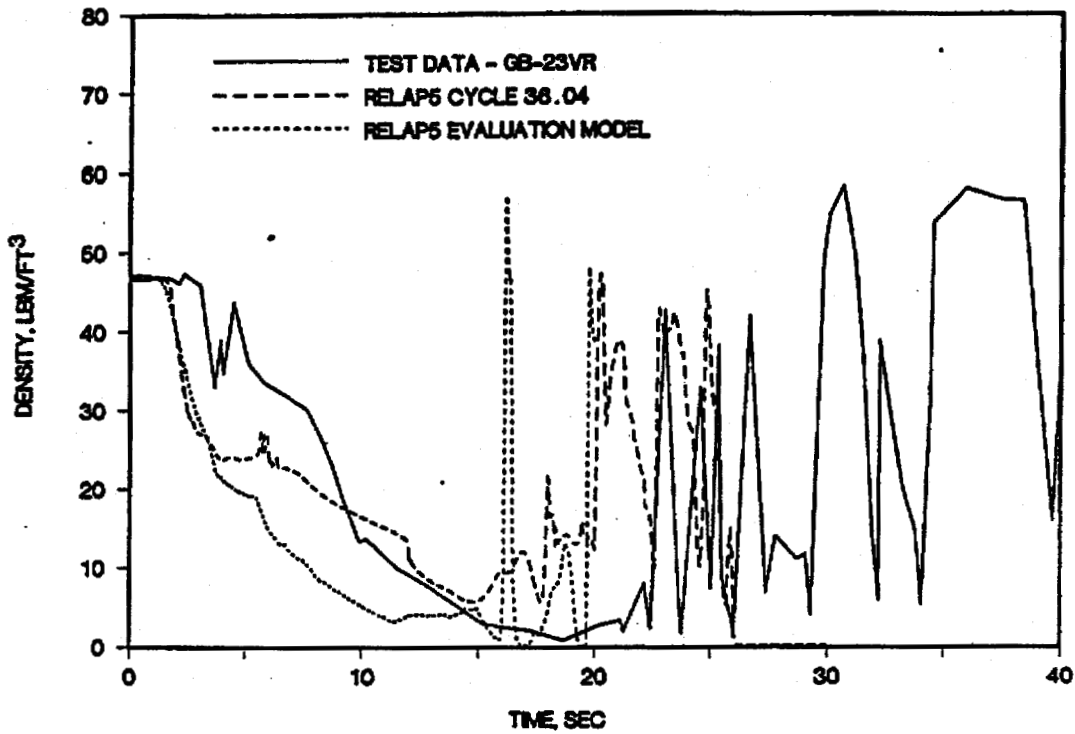


FIGURE G. 1-22. SEMISCALE MOD1 TEST S-04-6; DENSITY NEAR THE PUMP SIDE BREAK (BEFORE THE ECC INJECTION LOCATION).

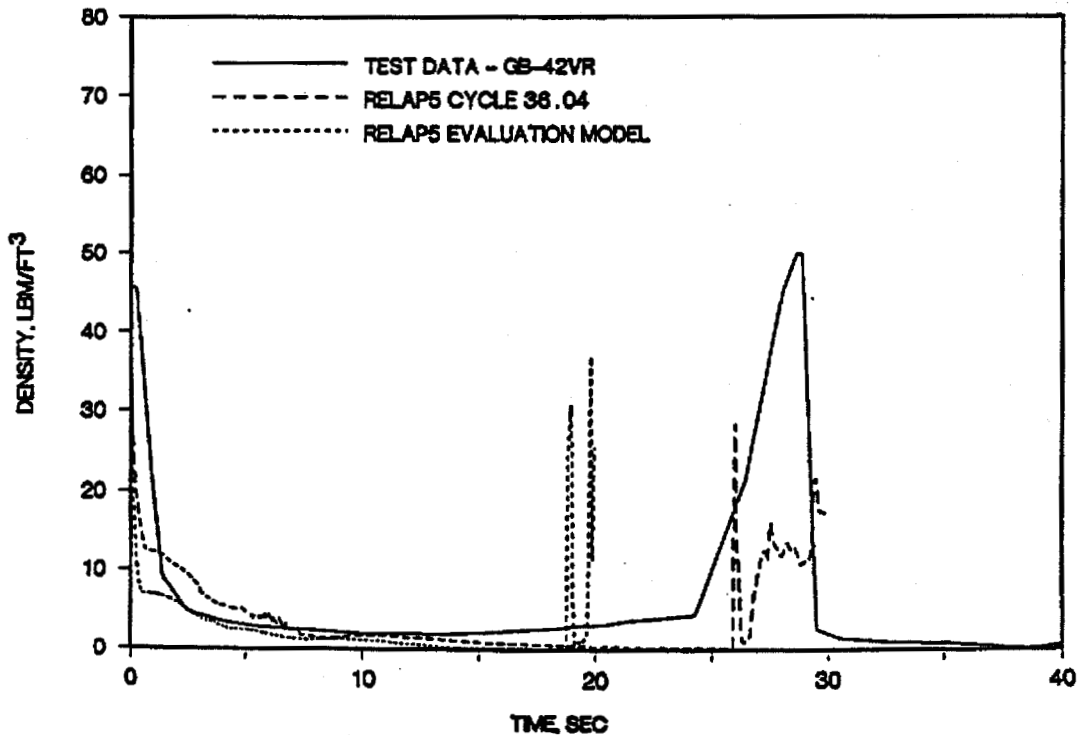


FIGURE G. 1-23. SEMISCALE MOD1 TEST S-04-6; DENSITY NEAR THE CORE INLET.

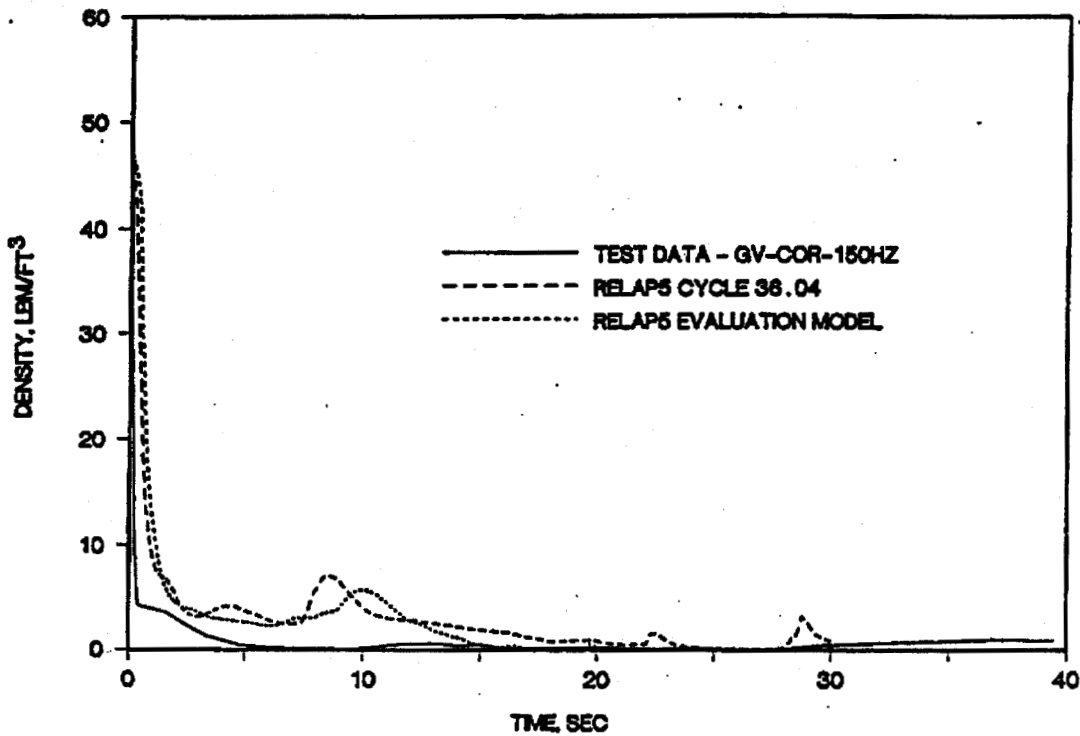


FIGURE G. 1-24. SEMISCALE MOD1 TEST S-04-6; FLUID TEMPERATURE NEAR THE VESSEL SIDE BREAK.

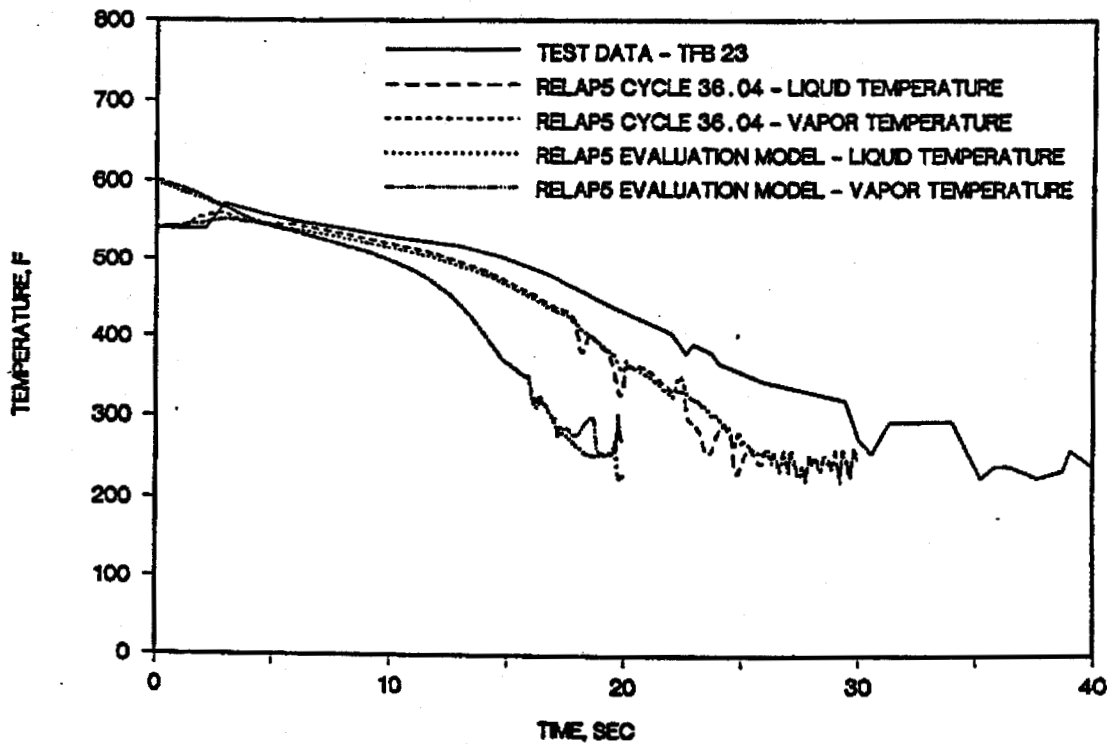


FIGURE G. 1-25. SEMISCALE MOD1 TEST S-04-6; FLUID TEMPERATURE NEAR PUMP SIDE BREAK (BEFORE ECC INJECTION LOCATION).

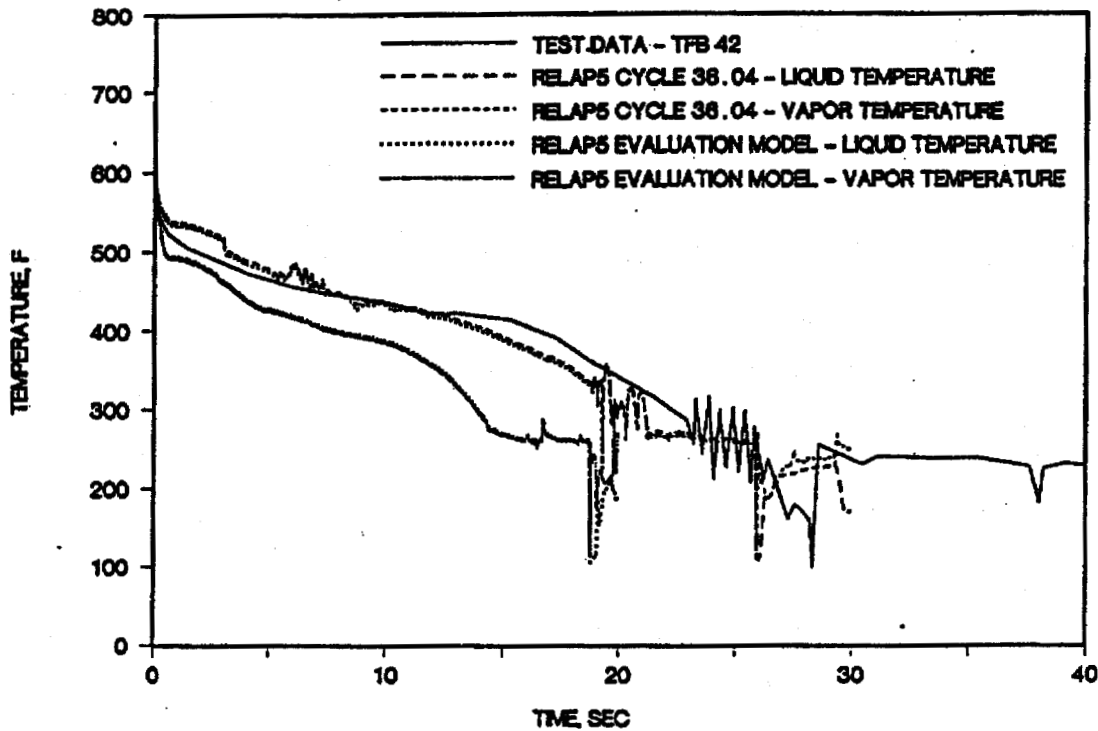


FIGURE G. 1-26. SEMISCALE MOD1 TEST S-04-6; FLUID TEMPERATURE IN THE INTACT LOOP HOT LEG.

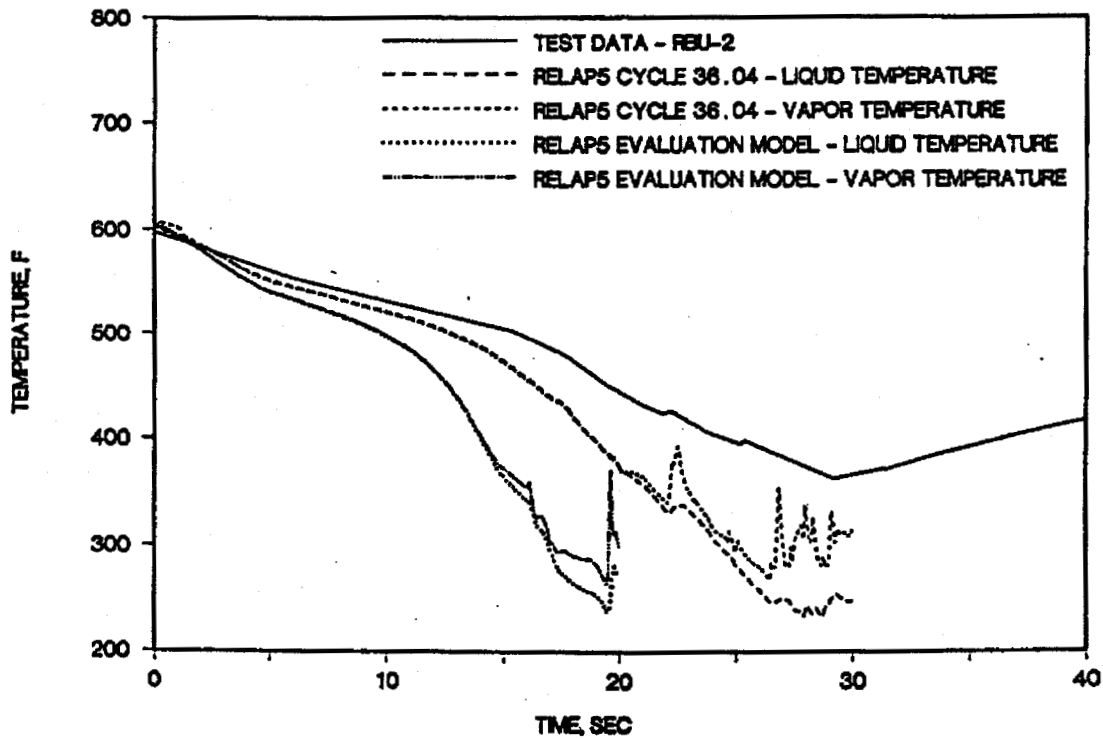


FIGURE G. 1-27. SEMISCALE MOD1 TEST S-04-6; FLUID TEMPERATURE IN INTACT LOOP COLD LEG (NEAR ECC INJECTION POINT).

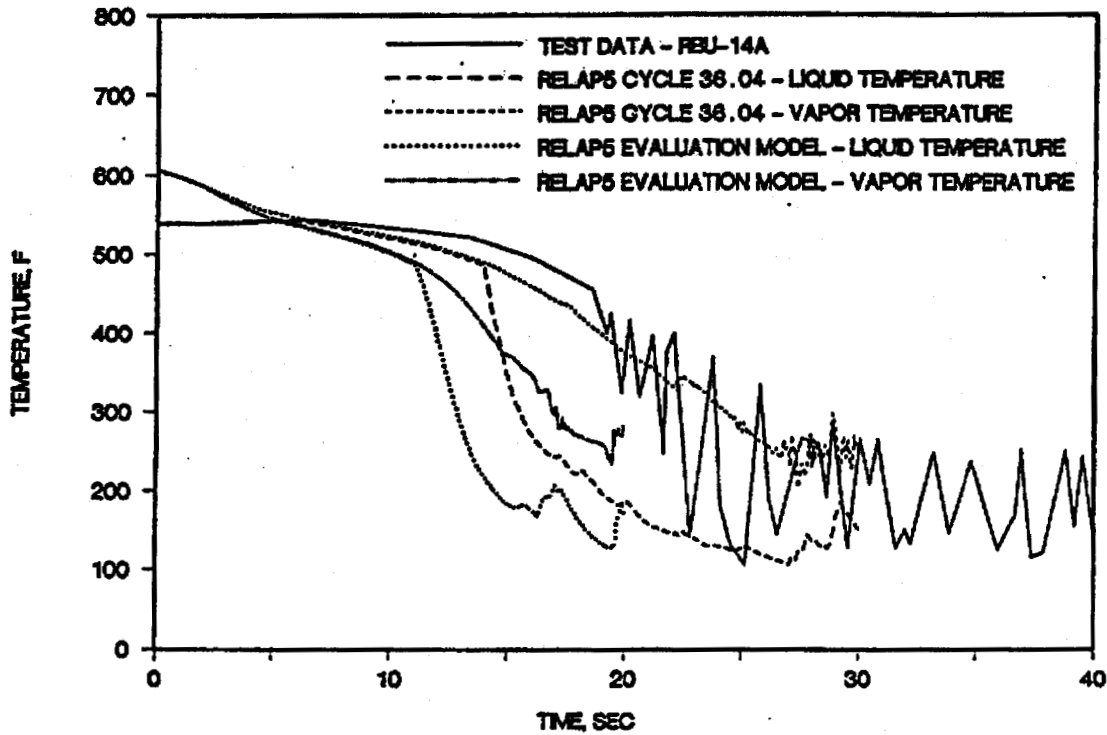


FIGURE G. 1-28. SEMISCALE MOD1 TEST S-04-6; FLUID TEMPERATURE NEAR THE CORE INLET.

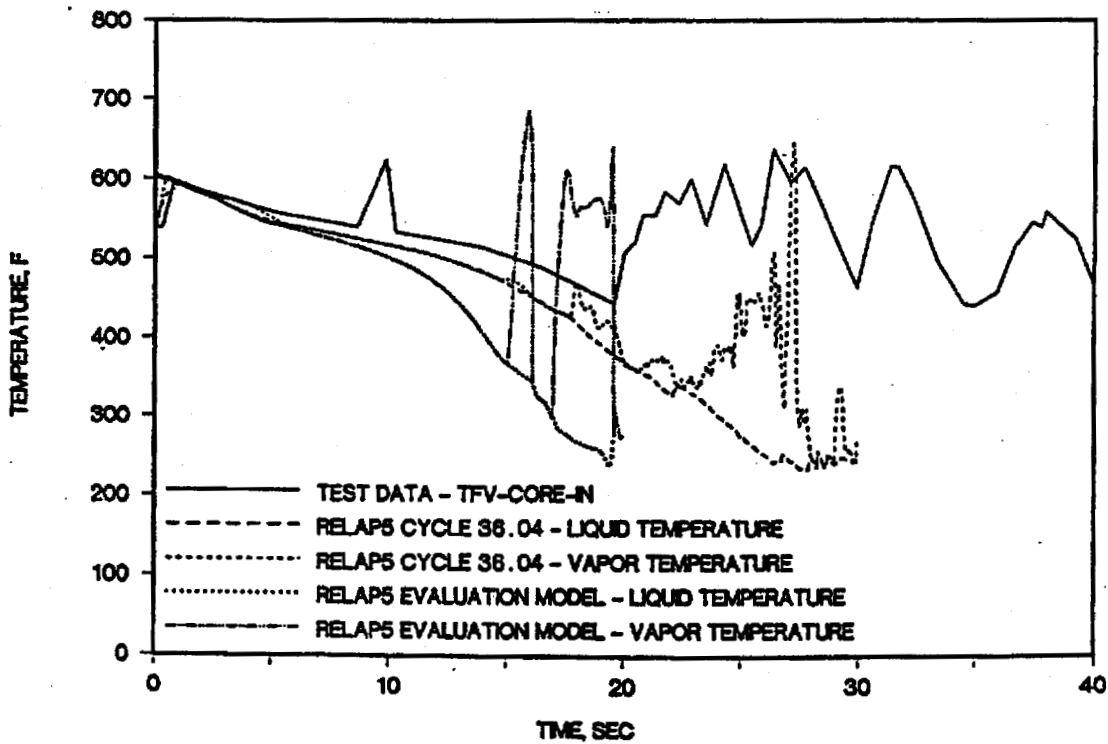


FIGURE G. 1-29. SEMISCALE MOD1 TEST S-04-6; FLUID TEMPERATURE IN UPPER PLENUM.

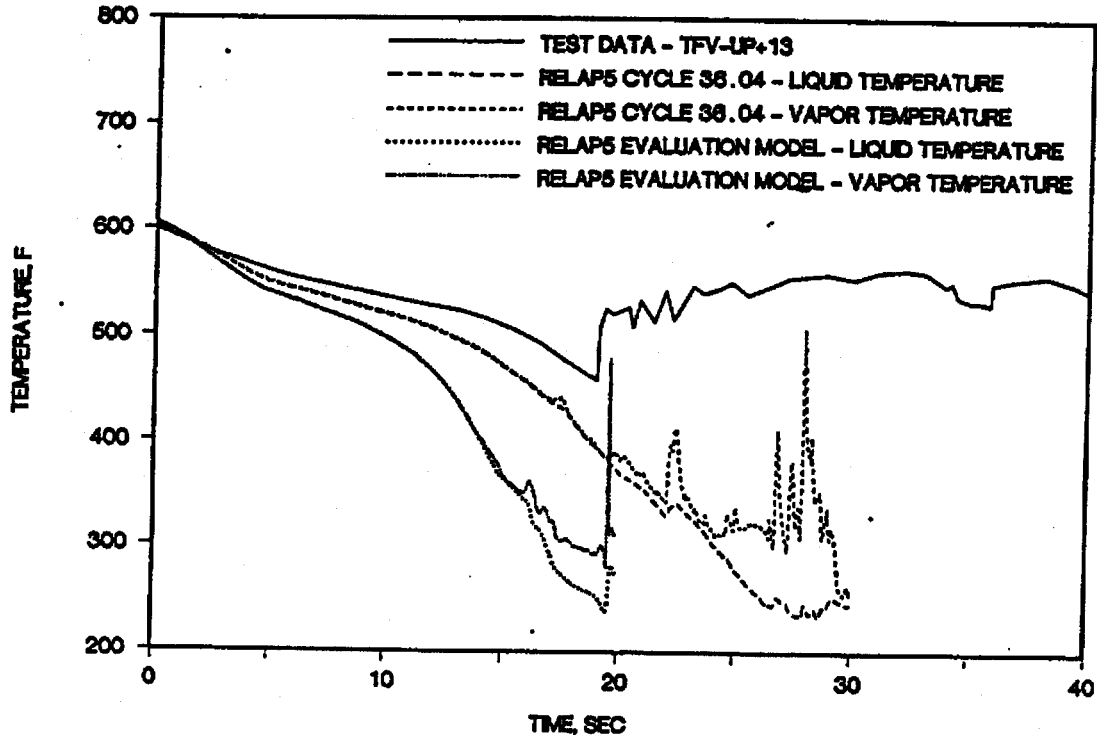


FIGURE G. 1-30. SEMISCALE MOD1 TEST S-04-6; AVERAGE POWER ROD CLADDING TEMPERATURE AT PEAK POWER LOCATION.

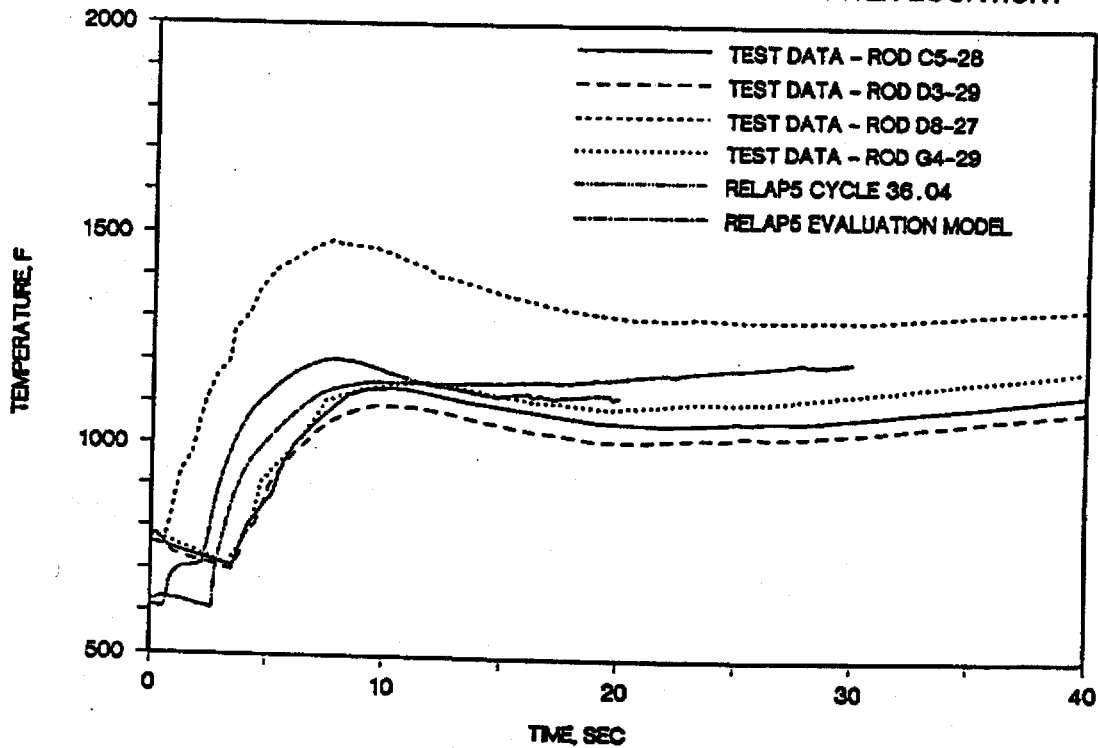
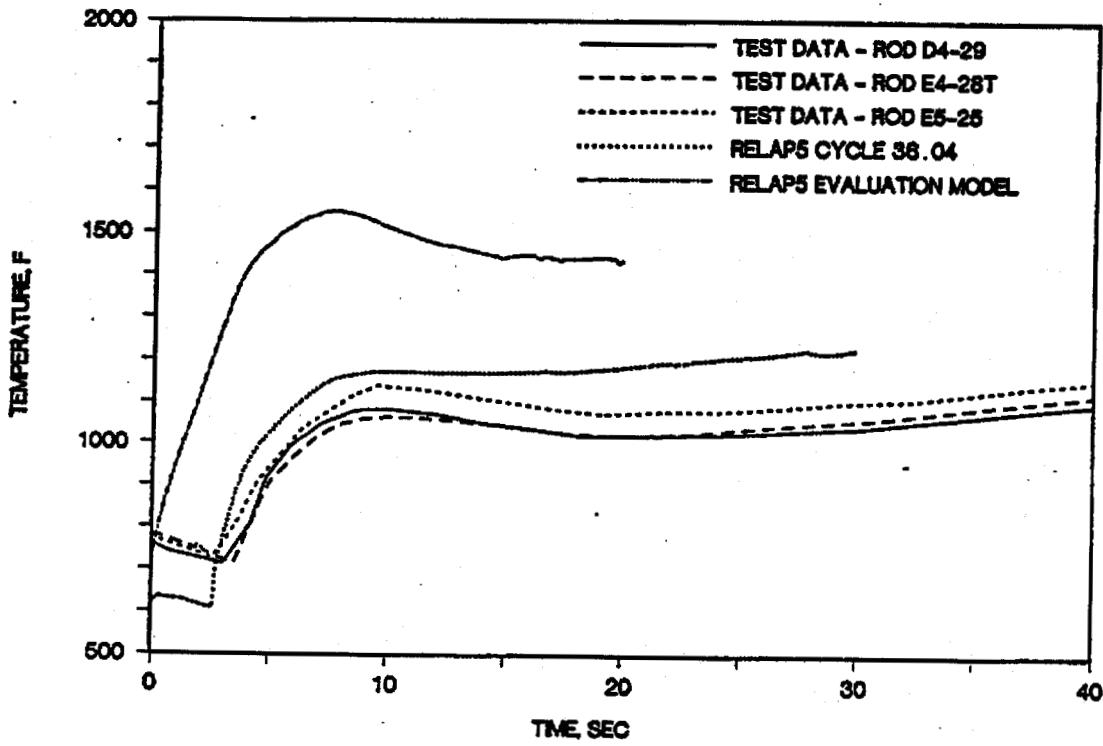


FIGURE G. 1-31. SEMISCALE MOD1 TEST S-04-6; HIGH POWER ROD CLADDING TEMPERATURE NEAR PEAK POWER LOCATION.



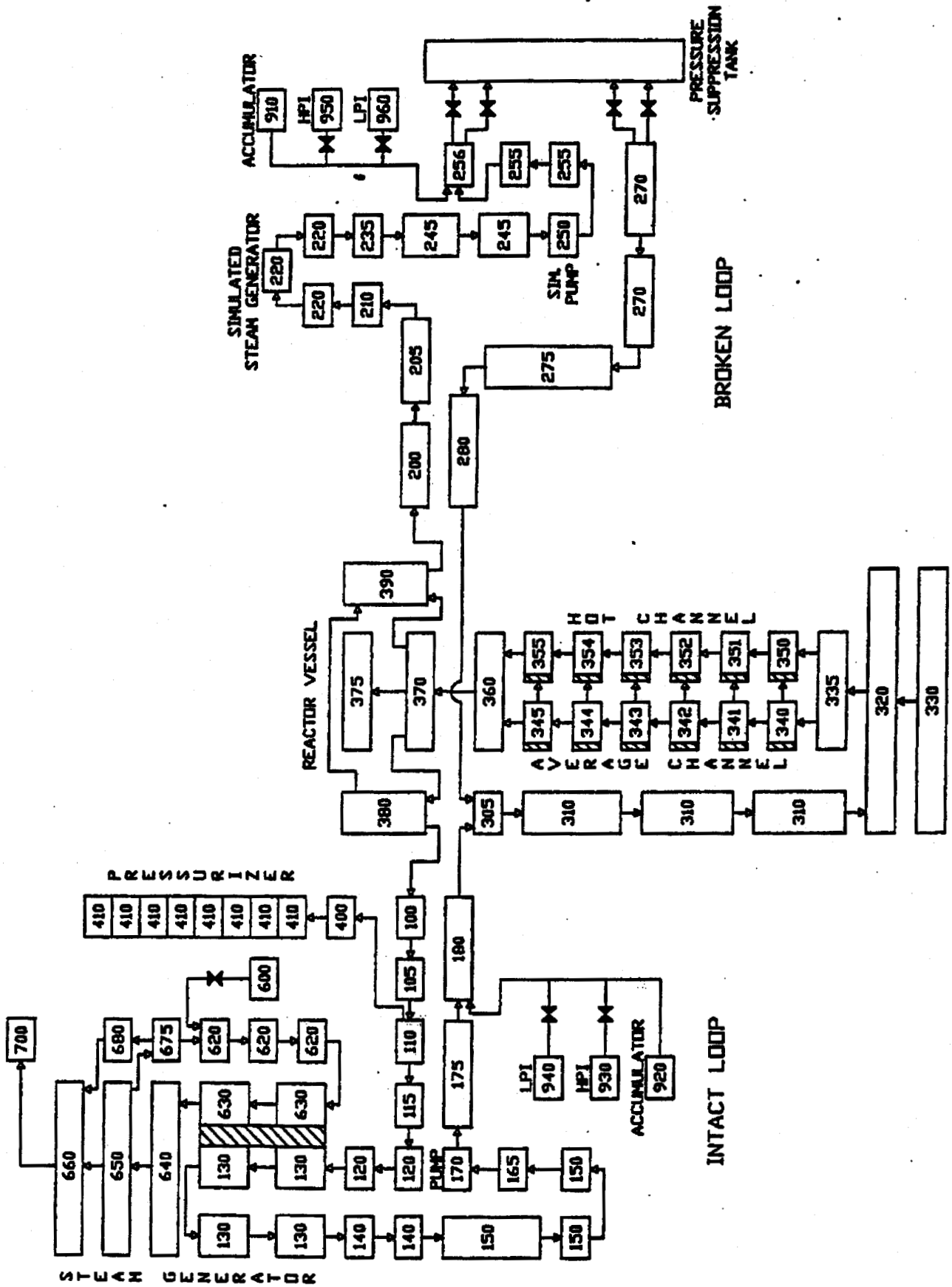


Figure G.1-32. RELAP5 Node and Junction Diagram.

G.2. SBLOCA Benchmark of LOFT Experiment L3-5

Small break LOCA (SBLOCA) events are challenging to predict due to the variety of scenarios which may evolve during a transient. Particularly key to SBLOCA mitigation is continuous core energy removal via the break, steam generator, and absorption through ECCS fluid heating, while maintaining adequate vessel liquid inventory such that clad temperature excursions remain below 2200 F.

Vessel inventory is determined by system boundary flows (HPIS and break) and the liquid distribution within the reactor coolant system. In terms of code models, the system heat transfer, two-phase flow, and choked flow models predominately determine this behavior. Demonstration that these code models are adequate is provided through benchmark calculations. In particular, prediction of integral system transient tests from prototypical PWR scaled facilities provide a good measure of a code's ability to calculate SBLOCA phenomena.

G.2.1. Introduction

LOFT experiment L3-5⁴ was designed to investigate the response of the primary system to a SBLOCA. This experiment addresses the 4-inch diameter equivalent (2.5%) small break transient. The break was located in the intact loop cold leg pipe between the RC pumps and the reactor vessel inlet nozzle. The RC pumps were tripped immediately following leak initiation. This experiment was selected to benchmark the RELAP5/MOD2-B&W computer code because a 4-inch diameter break is characterized by a leak flow exceeding HPIS flow and by a relatively slow system depressurization since the steam generator becomes ineffective in removing decay heat, thereby resulting in a severe system inventory depletion.

The B&W version of RELAP5/MOD2 was benchmarked against the L3-5 experiment to demonstrate the analytical capability of the code

in predicting the various modes of a SBLOCA transient. The RELAP5 model for the L3-5 experiment was obtained from Appendix B of the report EGG-LOFT-5480.² The model was verified against the system design data provided in NUREG/CR-0247³ (LOFT System and Test Description).

Section G.2.2 presents a description of the LOFT L3-5 experiment. The RELAP5 model is provided in section G.2.3 along with minor input changes that are required to achieve stable initial conditions. Section G.2.4 discusses the results of the analysis and compares the test data with the RELAP5 prediction. Conclusions are presented in section G.2.5.

G.2.2. Description of Experiment

The LOFT integral test facility was designed to simulate the major components of a four-loop PWR, thereby producing data on the thermal, hydraulic, nuclear and structural processes expected to occur during a LOCA. As shown in Figure G.2-1, the experimental facility consists of the reactor vessel, intact loop (scaled to represent three operational loops), ECC system, broken loop, and blowdown suppression system. The reactor vessel contains 1300 66-inch long nuclear fuel rods with a total power output of 50 Mwt. The intact loop includes a hot leg, a steam generator, the pressurizer, two parallel RC pumps and a cold leg. The broken loop is primarily used for large LOCA experiments and contains a hot leg, a steam generator, pump simulators, a cold leg, and isolation valves. The ECCS is comprised of the accumulator system, the LPIS and the HPIS.

The L3-5 experiment simulates a small break depressurization with a 0.6374-inch diameter break orifice in the intact loop cold leg between the RC pump and the reactor vessel. The RC pump is tripped at leak initiation. The HPIS is injected into the reactor vessel downcomer, while the accumulator is isolated from the intact loop. The reactor was scrammed approximately 5

seconds before blowdown initiation. When the control rods were fully inserted, the intact cold leg blowdown was initiated. The RC pumps were manually tripped at 0.8 seconds after blowdown initiation. The sequence of events for the experiment is presented in Table G.2-2. HPIS flow was initiated automatically when the primary system pressure dropped to 1900 psia. The leak was isolated at 2309 seconds. The secondary system auxiliary feed pump was started at approximately 2 minutes after scram and was operated for about 30 minutes. The initial plant operating conditions are provided in Table G.2-1.

G.2.3. RELAP5 Model of LOFT L3-5

The RELAP5/MOD2-B&W computer code was used to perform the benchmark analysis of experiment L3-5. This code is based on a one-dimensional, two fluid, nonequilibrium hydrodynamic formulation and uses a finite difference scheme for both fluid paths and heated paths. Inputs for the basic RELAP5 model shown in Figure G.2-2 are contained in Appendix B of the LOFT report. As indicated in the report, this model was used in the post-test analysis of LOFT experiments L3-1, L3-5 and L3-6 by EG&G. The results of the post-test analysis demonstrated that this model can accurately simulate the overall system response to a SBLOCA, including the primary system pressure and inventory.

The nodalization used for the benchmark analysis is shown in Figure G.2-3. It is basically the same as that shown in Figure G.2-2 except minor changes made to the steam generator separator component and the HPIS. In the original nodalization, the separator arrangement shown in Figure G.2-2 is incorrect and results in an elevation discrepancy between the downcomer and the boiler sections. The revised separator model shown in Figure G.2-3 consists of a separator volume (500) and a bypass volume (503). Volume 503 will permit a direct path from the steam dome to the downcomer. The HPIS was injected via the ECCS piping (600) to the RV downcomer in the original model. Volume 600

caused flow instability due to steam backflow from the downcomer. This volume and junction 630 were removed from the original model including the LPIS, which was not used in the experiment. The revised model as shown in Figure G.2-3 permits HPIS injection directly into the downcomer.

The revised model for the L3-5 benchmark analysis consists of 116 volumes, 124 junctions and 120 heat structures. Inputs for the major components have been verified against the design data presented in the LOFT System and Test Description Report (NUREG/CR-0247) to assure that the model closely represents the LOFT system. A steady-state calculation was made to achieve the desired initial conditions. A comparison of the measured initial conditions with the calculated values is presented in Table G.2-1. Considering the discrete nature of steam generator heat transfer in RELAP5, the initialized primary system pressures and temperatures are acceptable for the benchmark analysis.

The transient analysis was performed using the basic Best Estimate (BE) option, INEL's RELAP5/MOD2 version 36.04. The Ransom-Trapp choked flow model with a discharge coefficient of 1.0, nonhomogeneous and nonequilibrium hydrodynamic modeling, and the original system CHF, heat transfer, and fuel pin models were used. The core heat generation was simulated with a tabular input of power versus time. An additional change was made during a restart at 200 seconds. The break nozzle volume, 181 in Figure G.2-2, caused severe leak flow oscillations. This volume is approximately 3.6% of the cold leg volume (180) and was removed at the restart to prevent flow instability. Volume 180 was used as the leak node for the remainder of the analysis.

G.2.4. Transient Calculation

The blowdown was initiated 4.8 seconds after the reactor scram as shown in Table G.2-2, and the RC pumps were tripped 0.8 seconds after the blowdown initiation. The main feedwater flow was

terminated immediately following the reactor trip, and the auxiliary feedwater flow was started 67.8 seconds later. HPIS flow was initiated automatically when the primary system pressure dropped to 1900 psia. The calculated and measured core pressures are shown in Figure G.2-4. The calculated depressurization rate is slower than actually occurred during the initial subcooled phase of the blowdown, but exceeded the experiment thereafter as the primary system approached saturation. The post-test analysis in EGG-LOFT-5480 seems to confirm that RELAP5's Ransom-Trapp model underpredicts leak flow. In addition, the model tends to overpredict low quality two-phase flow, but underpredict high quality mixture flow as it occurred after 150 seconds. This flow characteristic has been verified by hand calculation using the HEM choked flow model with the same inlet conditions. Figure G.2-10 shows the calculated and measured leak node pressures. This figure demonstrates that the leak flowrate has a significant impact on the primary system depressurization rate for the 4-inch diameter equivalent break (2.5%). The short-term and long-term secondary side pressure responses are presented in Figures G.2-5 and G.2-11 respectively. It can be seen that RELAP5 predicted the secondary side pressure response quite well. The pressurizer liquid level is shown in Figure G.2-6. Again, this plot reflects the slower depressurization predicted by RELAP5. The pump coastdown and the loop flow degradation are shown in Figures G.2-7 and G.2-8 respectively. The measured loop flow does not seem to agree with the pump coastdown. This is probably caused by errors in flow measurement that were not quantified during the test.

In the RELAP5 calculation, the pumps coasted down in approximately 29 seconds. Natural circulation was calculated to occur thereafter, and reflux mode circulation was calculated at about 440 seconds. In this mode of cooling, vapor from the reactor core flows upward into the steam generator tubes where it is condensed. The condensate returns via the hot leg pipe to the reactor vessel. The reflux mode continued for the remainder of

the transient because the primary system pressure never dropped below the secondary side pressure due to the benchmarks slower primary system depressurization shown in Figure G.2-10. Injecting the HPIS directly into the primary system instead of the ECC piping resulted in good agreement between the calculated and measured flow rates as shown in Figure G.2-9.

G.2.5. Conclusion

The L3-5 experiment confirmed the dominance of the breakflow as the prime decay heat removal mechanism. Although there is a discrepancy between calculated and measured primary system depressurization as noted previously, the RELAP5 prediction of the L3-5 experiment is quite good. The code predicted the overall system response, including primary and secondary system pressure, pump coastdown, natural circulation, and long term core cooling. Correct characterization of the primary coolant pumps is not imperative to the proper simulation of the test because the pumps coasted down rapidly following the trip. But event times and depressurization rates are dependent upon proper characterization of the leak flow. The experimental data (Figure 35-7 in NUREG/CR-1695) shows a distinct liquid level in the cold leg piping 130 seconds after blowdown initiation. Thus, calculation of this stratification is important for accurate break mass flow calculation.

There are two core bypass flow paths as shown in Figure G.2-2. One is from the inlet annulus to the upper plenum and the other is the reflod assist bypass valve in the broken loop. These paths mitigate the differential pressure that can be developed across the reactor vessel as a result of steam generation in the core, and allow steam venting through the inlet annulus to the break without clearing the loop seal. Continuous primary system depressurization was observed in both the calculation and the test as shown in Figure G.2-10.

The comparison plots provided in the later part of this appendix demonstrate that the RELAP5 code is acceptable for SBLOCA simulation. The overall prediction was quite good confirming the code's predictive ability, which various other RELAP5 users have also observed through integral system SBLOCA calculations of tests from the OTIS, MIST, LOFT, and Semiscale test facilities. Numerous full size PWR plant transient calculations have also confirmed the predictive capabilities of the code. Based on these observations, the code has been demonstrated to be acceptable and reliable in predicting SBLOCA transient behavior for PWR geometries.

Table G.2-1. Initial Conditions for LOFT L3-5.

<u>Parameter</u>	<u>Measured Value *</u>	<u>RELAP5 Model</u>
Primary System Mass Flow Rate (Kg/s)	476.4	484.9
Hot Leg Temperature (K)	576.	579.4
Cold Leg Temperature (K)	558.	560.9
Core Power Level (MW)	49.	48.9
Pressurizer Water Volume (m ³)	0.68	0.66
Pressurizer Pressure (Pa)	14.88E6	14.959E6
Hot Leg Pressure (Pa)	14.86E6	14.945E6 (V105)
SG Secondary Side Flow Rate (Kg/s)	26.4	26.4
SG Secondary Side Pressure (Pa)	5.58E6	5.56E6 (V530)
SG Secondary Side Water Level (m)	3.14	2.758

*Based on Nominal values in Table 2-2 of NUREG/CR-1695.

Table G.2-2. Sequence of Events for LOFT L3-5.

Event	Time (sec)	
	Experiment*	RELAP5
Reactor Scrammed	0.0	0.0
LOCA Initiated	4.8	4.8
RC Pump Tripped	5.6	5.6
HPIS Initiated	8.8	10.6
Pressurizer Emptied	27.0	40.8
RC Pump Coastdown	35.0**	20.0
SG Auxiliary Feedwater Initiated	67.8	67.8
Secondary Side Pressure Exceeded Primary Side	749.8	--
SG Auxiliary Feedwater Terminated	1804.8	--
Leak Isolation	2313.9	1500.0

*Based on data in Table 2-1 of NUREG/CR-1695.

**From Figure 35-45 in NUREG/CR-1695.

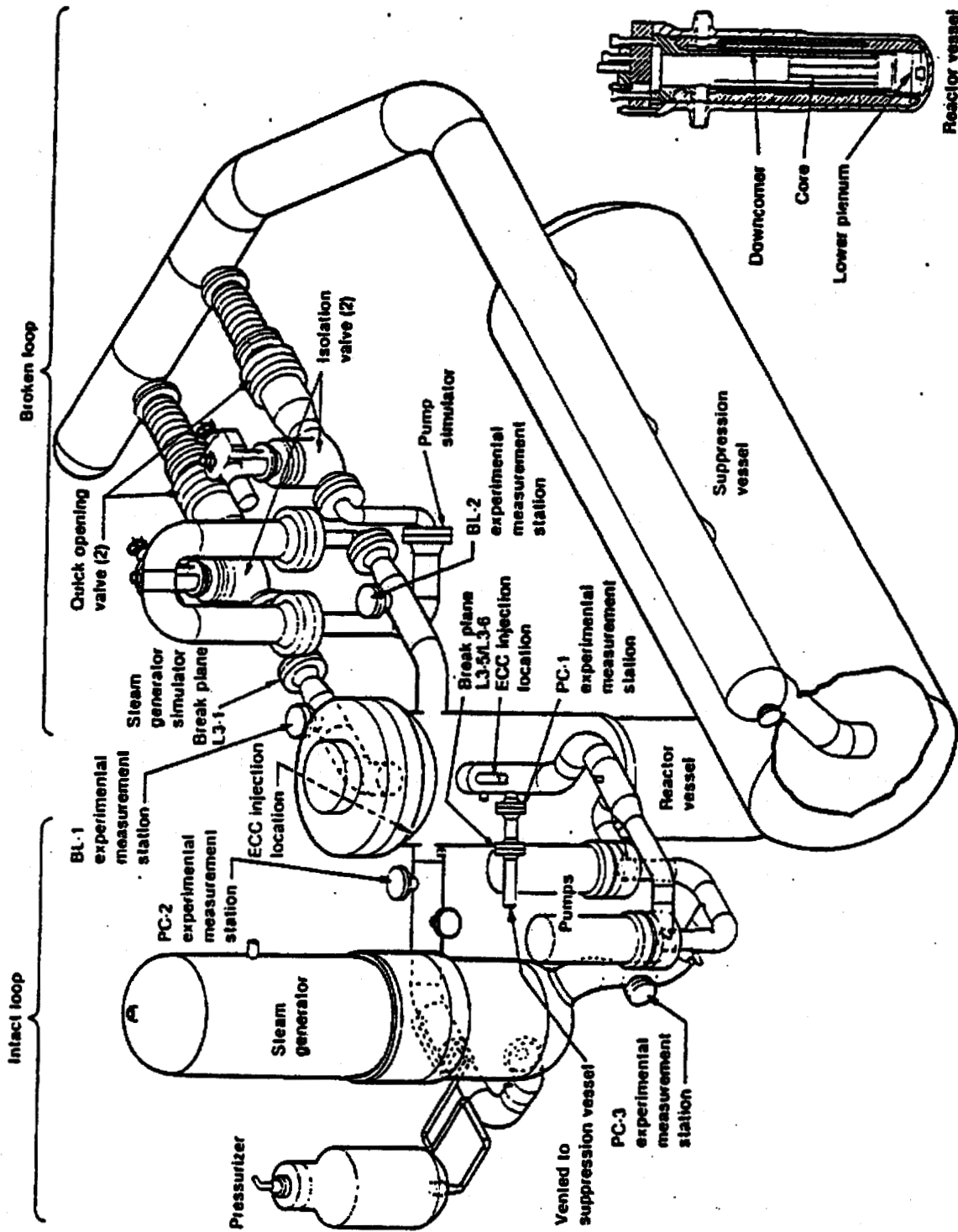


Figure G.2- 1. LOFT System Configuration.

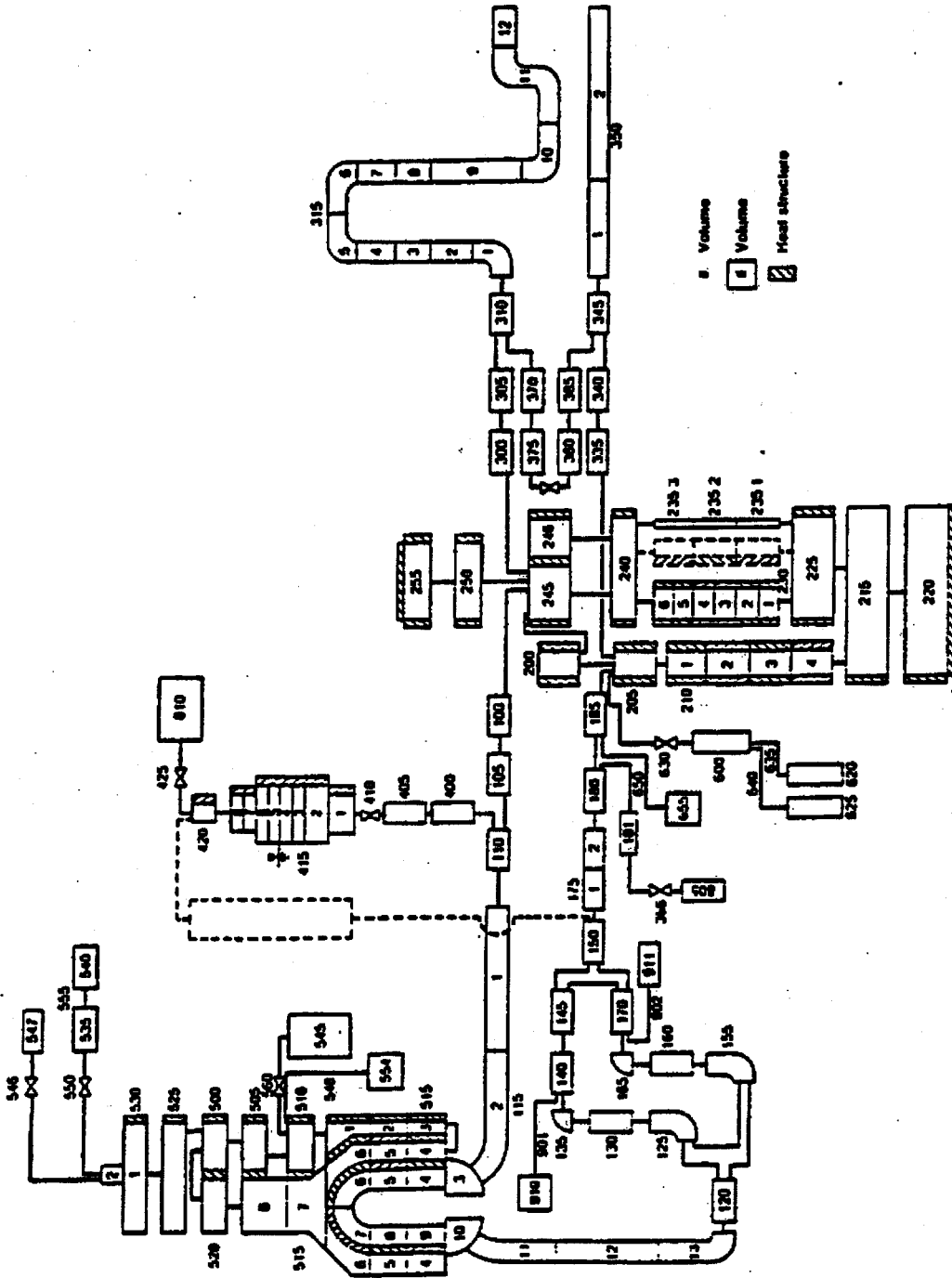


Figure G.2- 2. RELAP5 LOFT Nodalization for Test L-3-5.

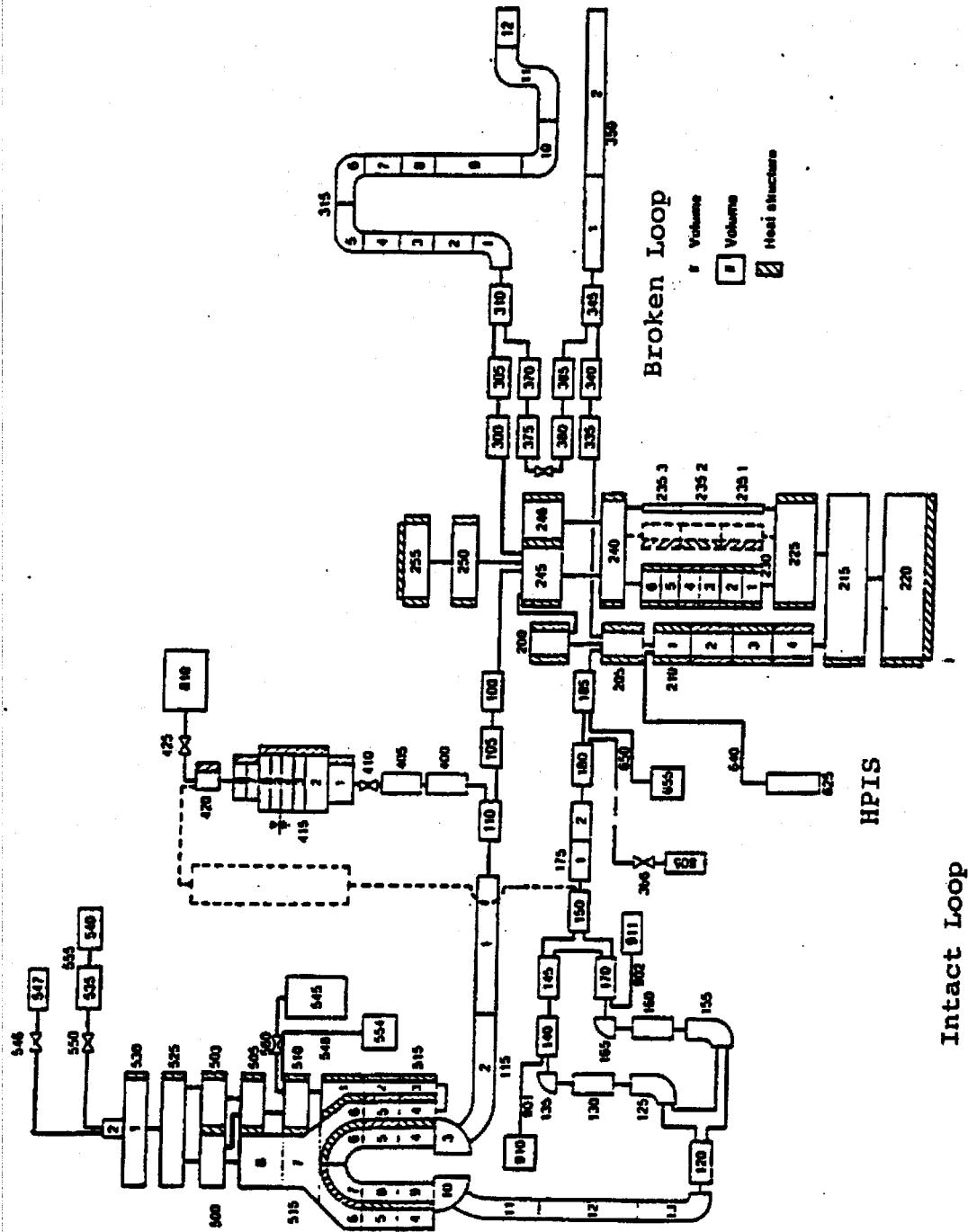


Figure G.2- 3. RELAP5 Nodalization for LOFT Test L-3-5 Benchmark Analysis.

FIGURE G.2- 4. LOFT TEST L-3-5; CORE PRESSURE.

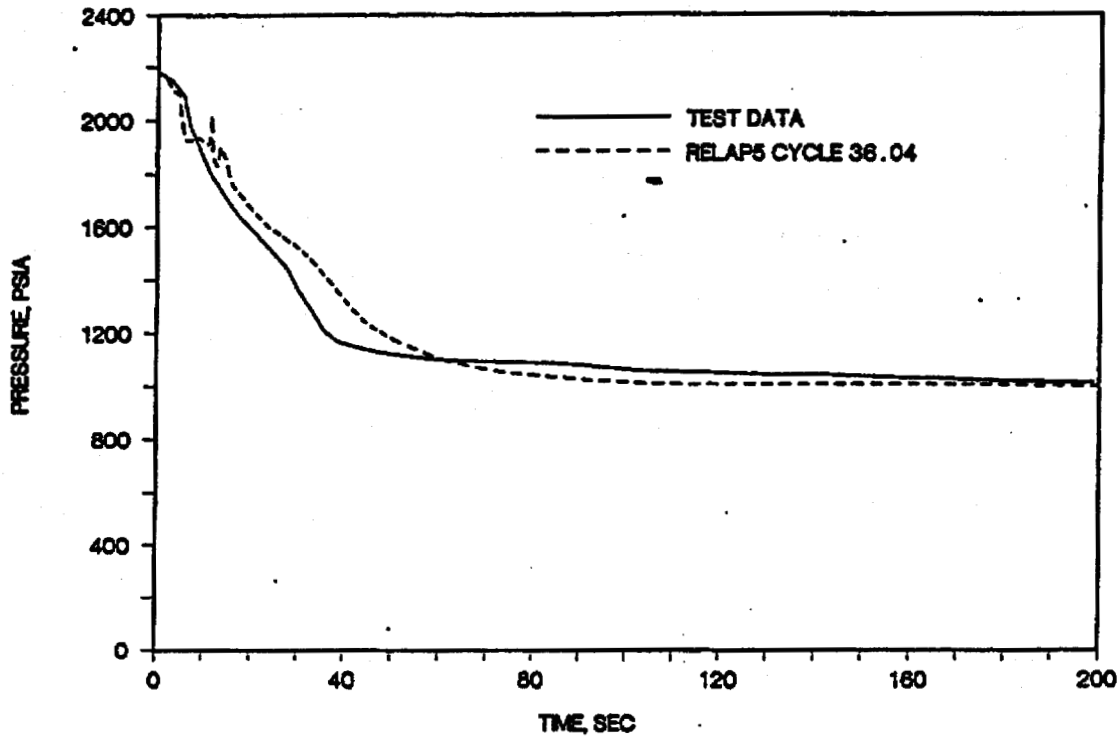


FIGURE G.2- 5. LOFT TEST L-3-5; STEAM GENERATOR PRSSURE.

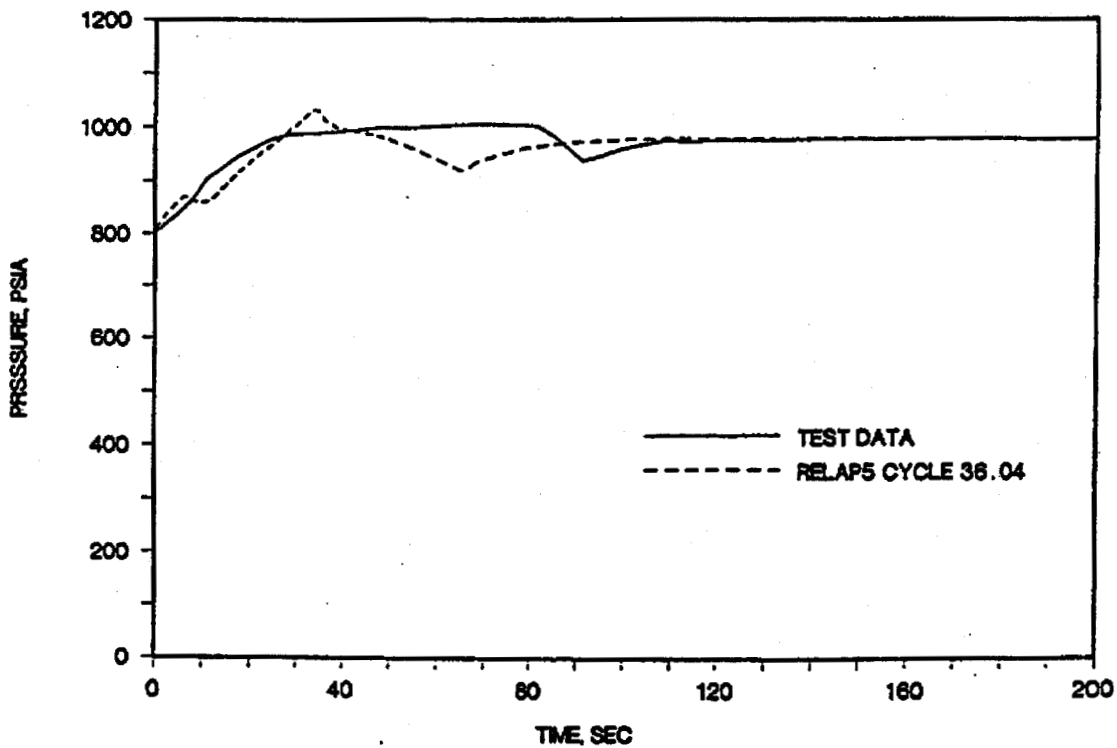


FIGURE G.2-6. LOFT TEST L-3-5; PRESSURIZER WATER LEVEL.

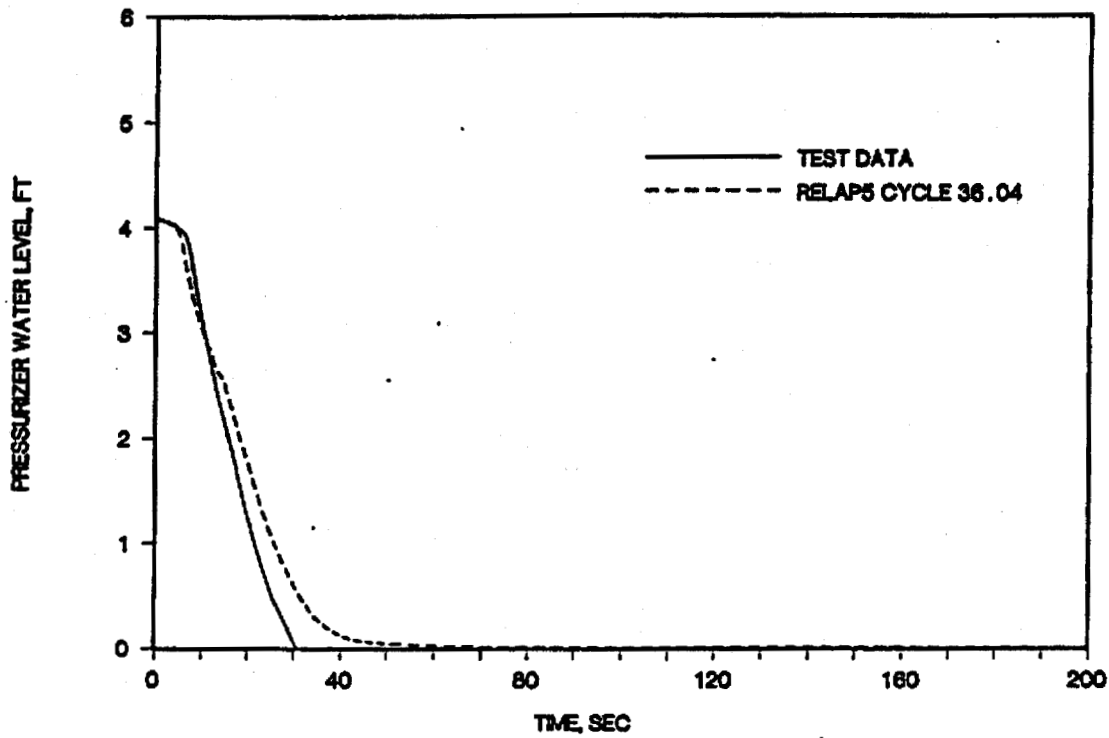


FIGURE G.2-7. LOFT TEST L-3-5; PUMP VELOCITY.

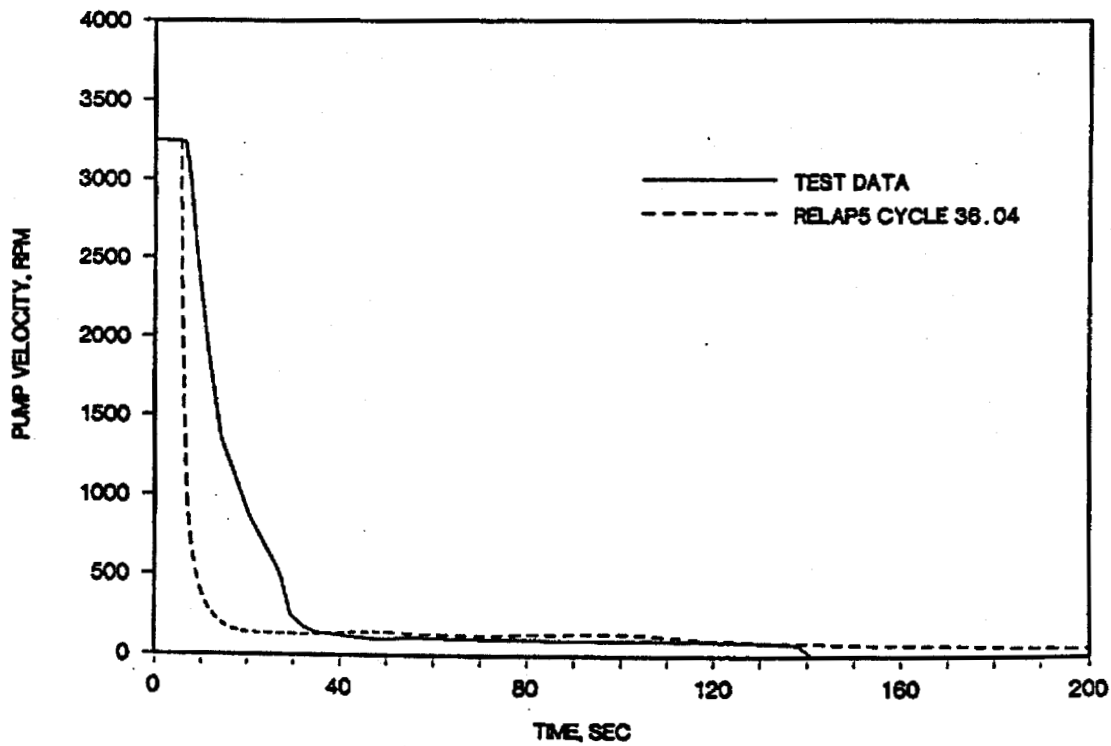


FIGURE G.2- 8. LOFT TEST L-3-5; HOT LEG MASS FLOW RATE.

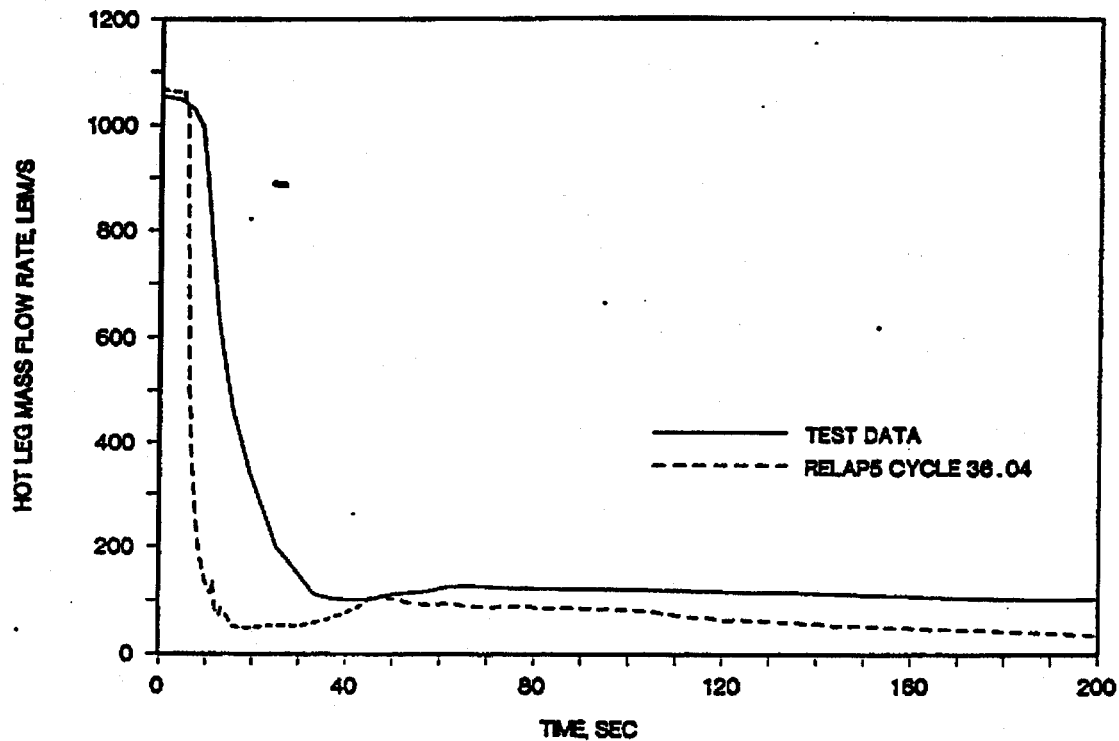


FIGURE G.2- 9. LOFT TEST L-3-5; HPIS MASS FLOW RATE.

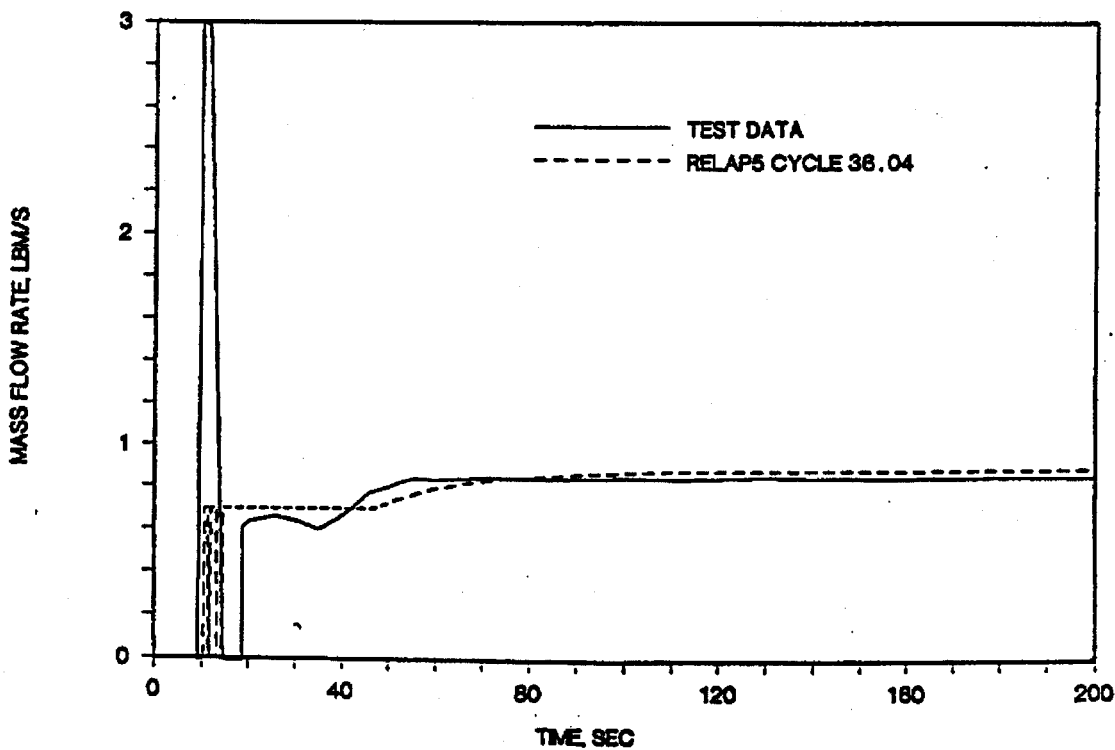


FIGURE G.2-10. LOFT TEST L-3-5; LEAK NODE PRESSURE.

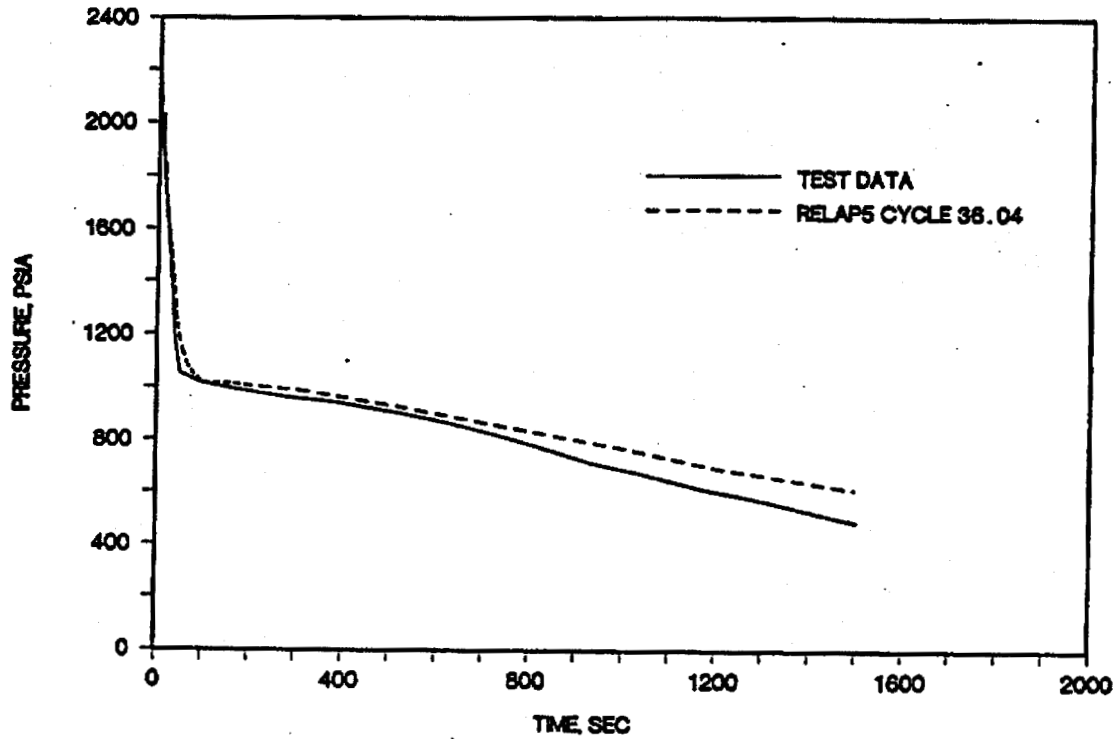
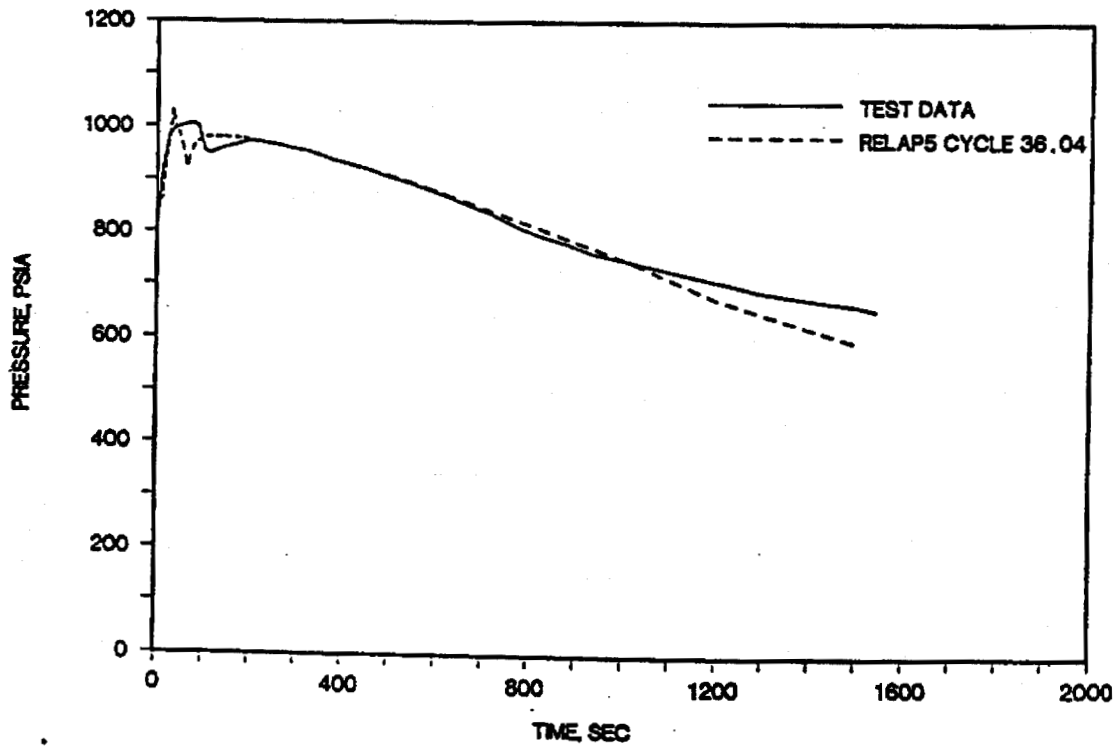


FIGURE G.2-11. LOFT TEST L-3-5; STEAM GENERATOR PRESSURE.



G.3. Conclusion - Large and Small LOCA Benchmark

The B&W benchmark analyses of the large and small LOCA experiments (S-04-6 and L-3-5) show that the B&W RELAP5 code correctly calculates the major system variables during the blowdown, such as the primary and secondary system pressures, leak flows, and ECC injection. These parameters determine the system blowdown rate and mass inventory that significantly affect the fuel cladding temperature behavior during and after the blowdown. With accurately predicted blowdown hydraulic data an overall agreement in the cladding temperature between the calculation and the experiment can be assured. The results of the benchmark presented in the preceding pages have demonstrated that the RELAP5 code is adequate and reliable in predicting overall system thermal hydraulic responses to a LOCA. Furthermore, the results of the S-04-6 benchmark with the EM option indicate that the licensing model predicted a substantially higher cladding temperature and is conservative. The modeling techniques, such as nodalization and time step used in the benchmark analyses are consistent with those used in the PWR plant model. Thus, the benchmark analyses confirm that RELAP5 is adequate and conservative for application to the LOCA simulation in a PWR.

APPENDIX H

WILSON DRAG MODEL BENCHMARKS

Note: This appendix was originally added in its entirety in Revision 2 of BAW-10164, August, 1992.

In this appendix, Wilson drag benchmarks are compared with the NRC-approved code FOAM2 and with small break LOCA experiments performed at the Thermal-Hydraulic Test Facility (THTF), Oak Ridge National Laboratory (ORNL). The Wilson drag model is explained in section 2.1.3 of this topical report. The RELAP5/MOD2-B&W results for steady-state conditions are compared with FOAM2 calculations in Section H.1 and with Oak Ridge THTF data in section H.2; conclusions are given in section H.3.

Comparison of RELAP5/MOD2-B&W with FOAM2 Results

The NRC-approved computer code FOAM2¹⁴⁰ aids in analysis of small break loss-of-coolant accidents (SBLOCA). Its main objective is to determine, based on core void distribution, whether at any time during an SBLOCA transient the water content of the reactor core (as calculated by an appropriate LOCA code, such as RELAP5) is sufficient to cover the entire heated core with a combination of water and steam-water froth. If it determines that the core is uncovered, it calculates the swell level and steaming rate corresponding to the input core water content. If no core uncover occurs, it will, at the user's option, calculate the mass flow and steaming rates.

RELAP5/MOD2-B&W estimates slug drag using the Wilson bubble rise correlation, whereas FOAM2 uses the Wilson bubble rise correlation¹³⁵ to directly calculate the core void distribution. FOAM2 does not include the B&W modification for the flow regime above $\alpha_g^* = 6.526$. Therefore, the core void distribution calculated by RELAP5/MOD2-B&W should be similar to FOAM2 results with potential for deviations at higher void fractions (that is, for $j=3$ in Equation 2.1.3-30.5).

A hypothetical reactor core was modeled as shown in Figure H.1. Low power steady-state RELAP5/MOD2-B&W cases were run for a variety of reactor powers (1.5 to 5.0% of full power) and

pressures (100 to 1600 psia); void profiles were compared with FOAM2 cases with the same water levels as were calculated by RELAP5. A listing of the RELAP5 cases is presented in Table H-1 and compared in Figures H.2 through H.13. RELAP5 data are plotted at the midpoint of each node because RELAP5 calculates an average void fraction for each node. It is assumed that void fraction changes linearly within all nodes, except the first node in which it is assumed that the inlet void fraction is zero.

Figures H.2 through H.13 demonstrate that, for equal core liquid inventories, RELAP5/MOD2-B&W acceptably predicts the void distributions and mixture levels calculated by FOAM2. Differences in mixture level for low pressure cases are caused partly by greater depletion of liquid inventory by RELAP5 at lower elevations, as compared to FOAM2, for which compensation is made at higher elevations.

Comparison with ORNL THTF Experiments ¹⁴¹

The Thermal-Hydraulics Test Facility (THTF) is a large high pressure non-nuclear thermal-hydraulics loop. The facility was designed to simulate the thermal-hydraulics of a small-break loss-of-coolant accident (SBLOCA). The facility configuration is shown in Figure H.14.

The test section bundle contained 60 electrically-heated rods and four unheated rods which simulated control rod guide tubes. Rod diameter and pitch were typical of a 17 x 17 fuel assembly. Further details on the facility configuration and instrumentation is found in Reference 141.

The RELAP5 model for the THTF test loop is shown in Figure H.15. THTF runs 3.09.10i through 3.09.10n and 3.09.10aa through 3.09.10¹⁴¹ were simulated using RELAP5/MOD2-B&W. The test conditions, which were also used as input to RELAP5, are given in

Table H.2. The axial power distribution of the test bundle was uniform.

Comparison of void distributions for all tests are shown in Figure H.16 through H.27. RELAP5/MOD2-B&W tends to predict slightly higher void fractions below the mixture level than the ORNL data. An adjustment has been made of the plots of ORNL data for which dryout occurred (which was true in all cases except 3.09.10i, cc, and ee). In Reference 141, the ORNL data was given at the centerline of intervals between pressure taps. This is appropriate for intervals in which there is a quasi-linear increase in void fraction within the interval, but not appropriate for dryout intervals. Near the dryout point, it is assumed that the void fraction within the dryout interval continued to increase at the same rate as the pre-dryout interval; the mixture level was calculated by determining the point along the extended slope at which the total area under the curve in the dryout interval would match the average void fraction. After making this adjustment, mixture level is quite well predicted.

Figures H.28 through H.33 compare RELAP5 calculated core vapor and cladding temperatures with ORNL THTF data. These figures show that RELAP5 is quite accurate, but slightly conservative in predicting the ORNL temperatures. The dip in the ORNL data at 11.0 ft is caused by grid effects on the heat transfer rate¹⁴¹, which is not accounted for in the RELAP5 model. In case 3.09.10i, an anomolous surface temperature occurs at an elevation of 2.7 meters; this is caused by the overly conservative temperature prediction of the Condie-Bengston IV film boiling correlation used at this point compared to the less conservative predictions of the McEligot single-phase vapor convection correlation applied at higher elevations. Given the overall complexity of the ORNL tests, RELAP5/MOD2-B&W achieved

excellent comparability of mixture level and clad temperature response.

Conclusions

Comparison of RELAP5/MOD2-B&W benchmark cases with equivalent runs using the NRC-approved code FOAM2 and with ORNL THTF small break LOCA experiments shows good agreement between results. It is concluded that the Wilson drag option used to calculate interfacial drag in RELAP5-B&W, does a good job of matching void distributions and mixture levels calculated by the NRC-approved code FOAM2 and measured by ORNL small break LOCA experiments.

Table H.1. FOAM2 Comparison Benchmark Cases.

Case	Power (percent)	Pressure (psia)	Equivalent Water Level (ft)
1	5.0	100	2.77303
2	5.0	200	3.68117
3	5.0	400	3.74587
4	5.0	600	5.15504
5	5.0	800	4.32935
6	5.0	1200	3.95712
7	2.5	100	3.82168
8	2.5	400	4.51021
9	2.5	800	6.38204
10	2.5	1200	6.33372
11	1.5	1200	7.99433
12	1.5	1600	7.34294

Table H.2. ORNL Thermohydraulics Test Facility (THTF)
Benchmark Cases.

Case	Experiment	Pressure (psia)	Power Density (kw/ft)	Mass Flux (lbm/hr/ft ²)
13	3.09.10i	0.68	650	21943.9
14	3.09.10j	0.33	610	9333.4
15	3.09.10k	0.10	580	2306.5
16	3.09.10l	0.66	1090	21461.4
17	3.09.10m	0.31	1010	9313.0
18	3.09.10n	0.14	1030	3395.2
19	3.09.10aa	0.39	590	14938.7
20	3.09.10bb	0.20	560	6961.9
21	3.09.10cc	0.10	520	3706.1
22	3.09.10dd	0.39	1170	14615.7
23	3.09.10ee	0.19	1120	8111.9
24	3.09.10ff	0.08	1090	3561.1

t

Revised Table H.2 shown on page 5-260 per SER instruction on Table 2 (page 5-364).

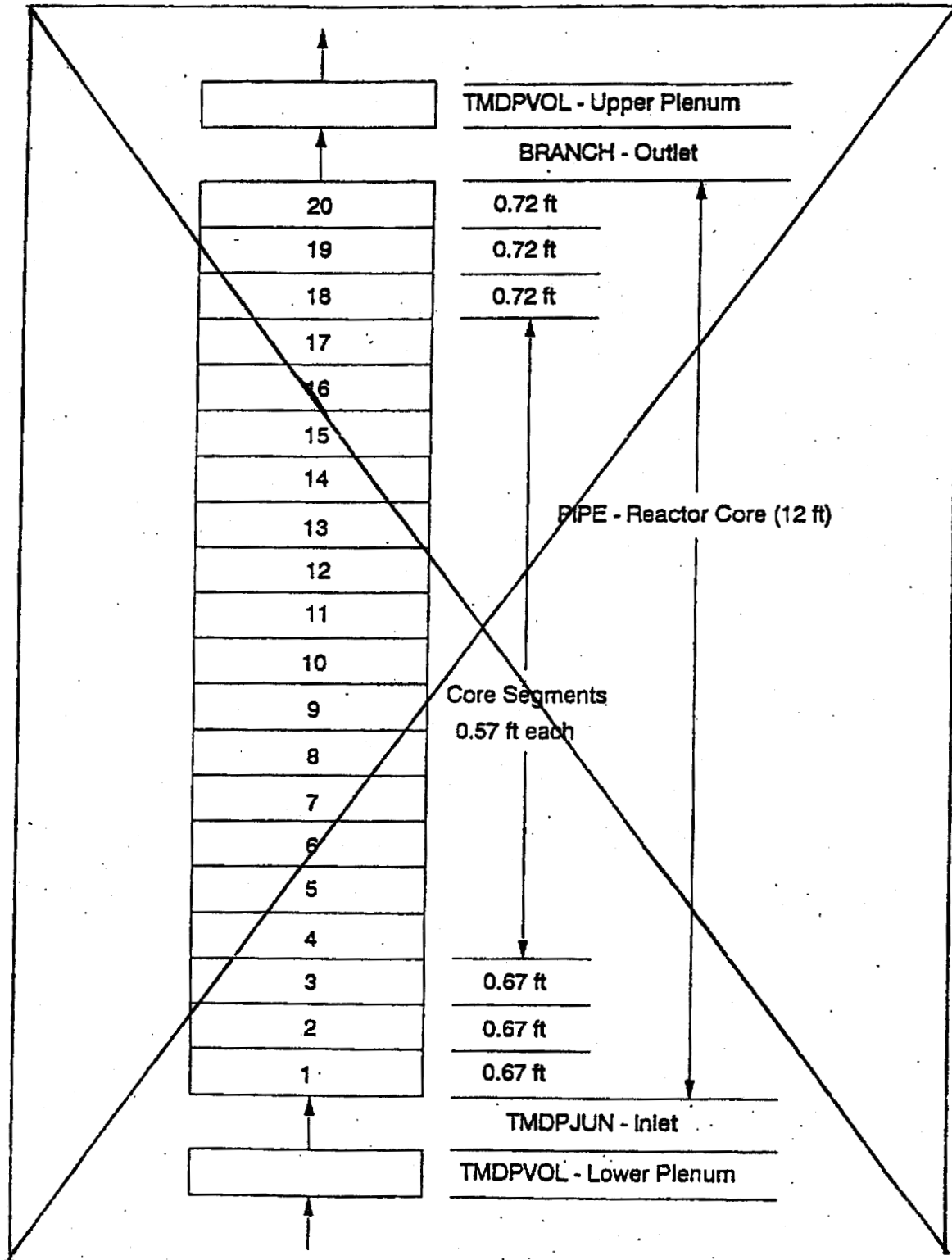


Figure H.1. RELAP5 Model of Hypothetical Reactor Core.

Revised Figure H.1 shown on page 5-257 per SER instruction on Table 2 (page 5-364).

Figure H.2. Comparison of RELAP5 and FOAM2 Predictions:
5% Decay Power, 100 Psia.

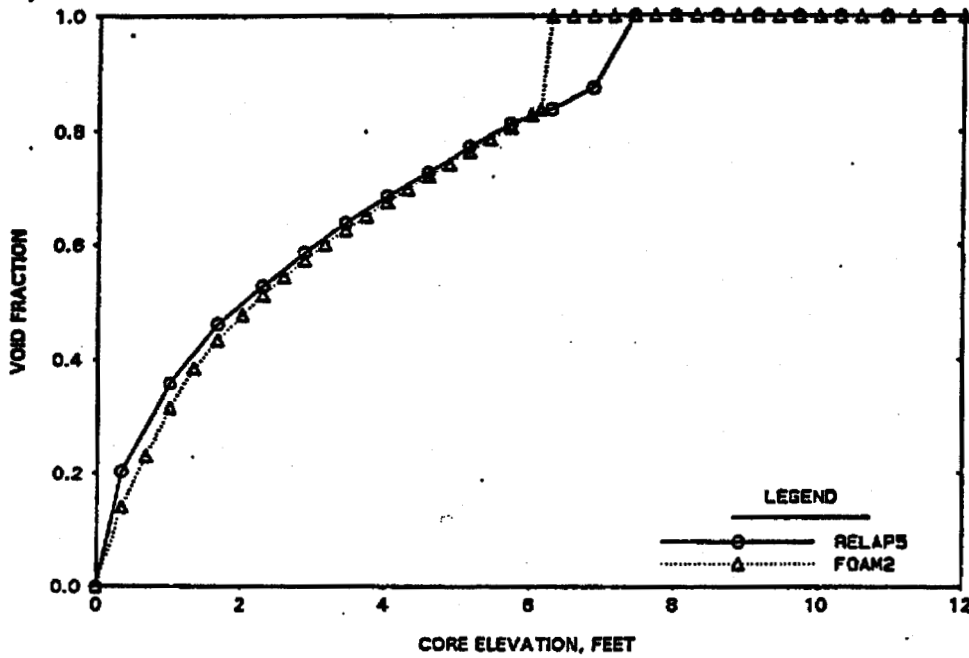


Figure H.3. Comparison of RELAP5 and FOAM2 Predictions:
5% Decay Power, 200 Psia.

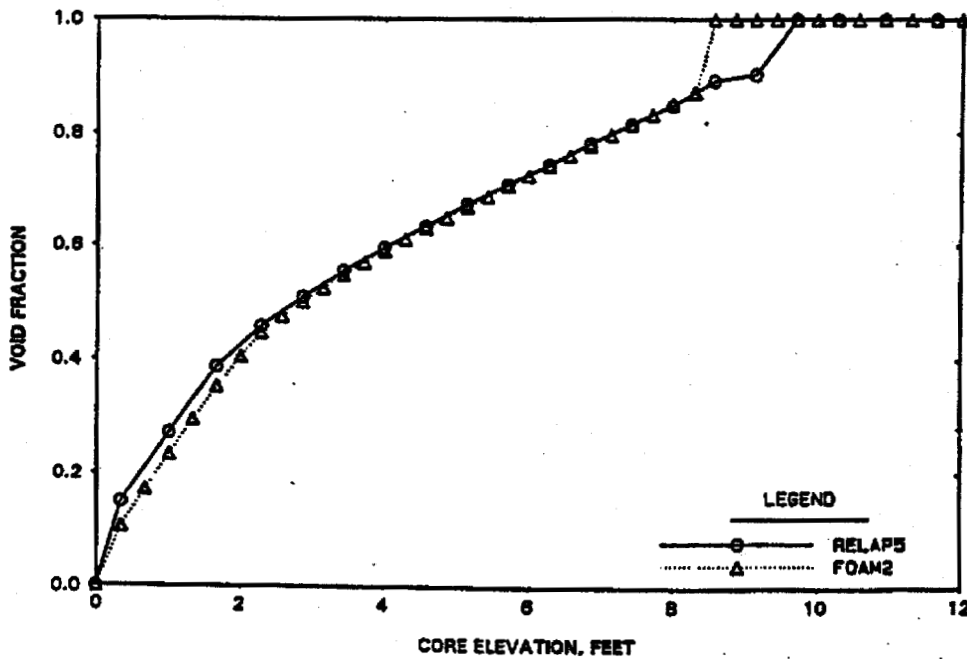


Figure H.4. Comparison of RELAP5 and FOAM2 Predictions:
5% Decay Power, 400 Psia.

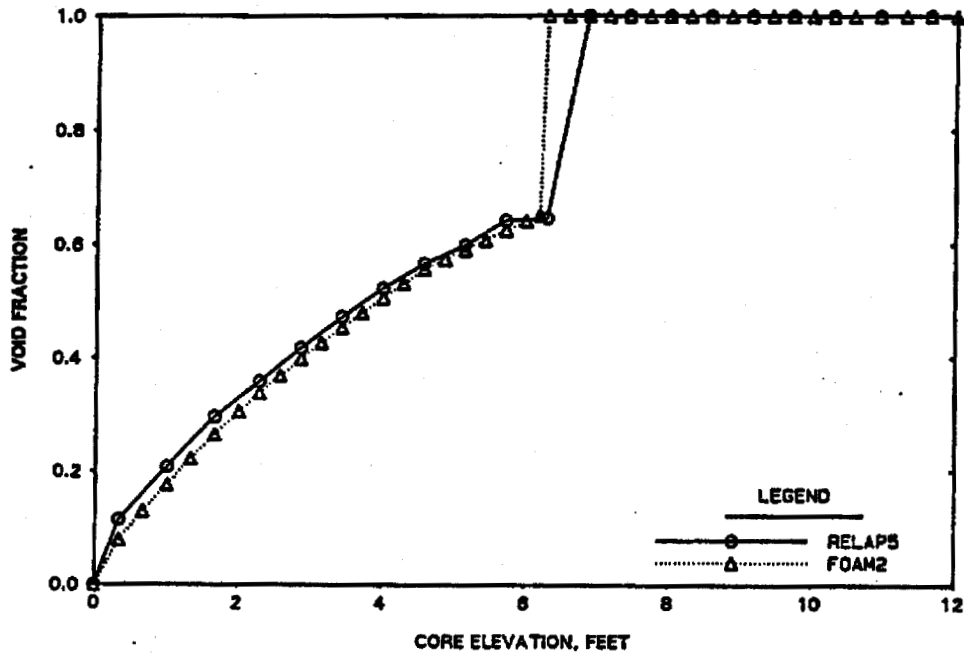


Figure H.5. Comparison of RELAP5 and FOAM2 Predictions:
5% Decay Power, 600 Psia.

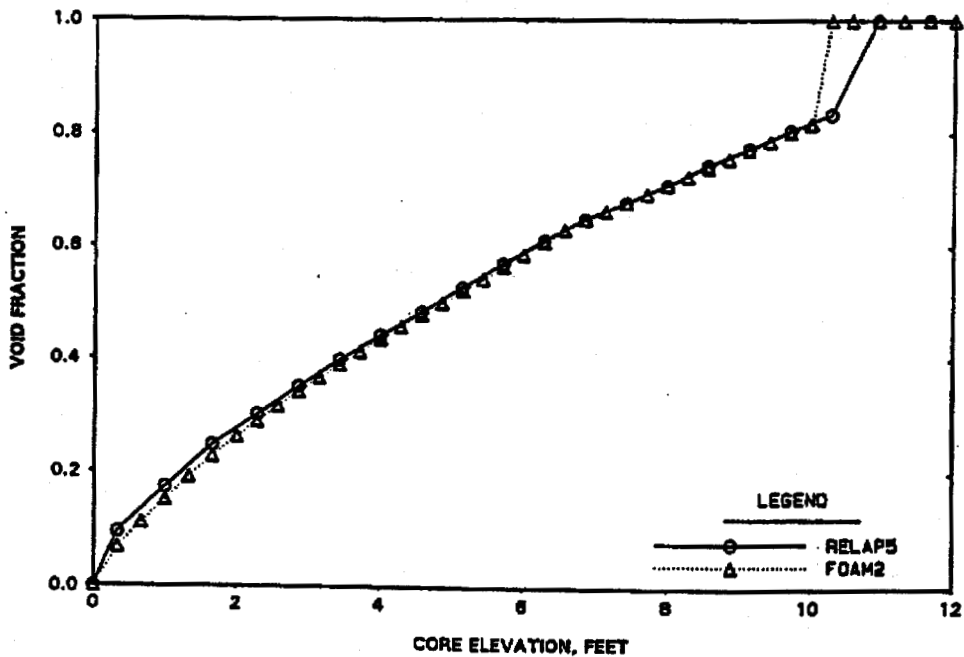


Figure H.6. Comparison of RELAP5 and FOAM2 Predictions:
5% Decay Power, 800 Psia.

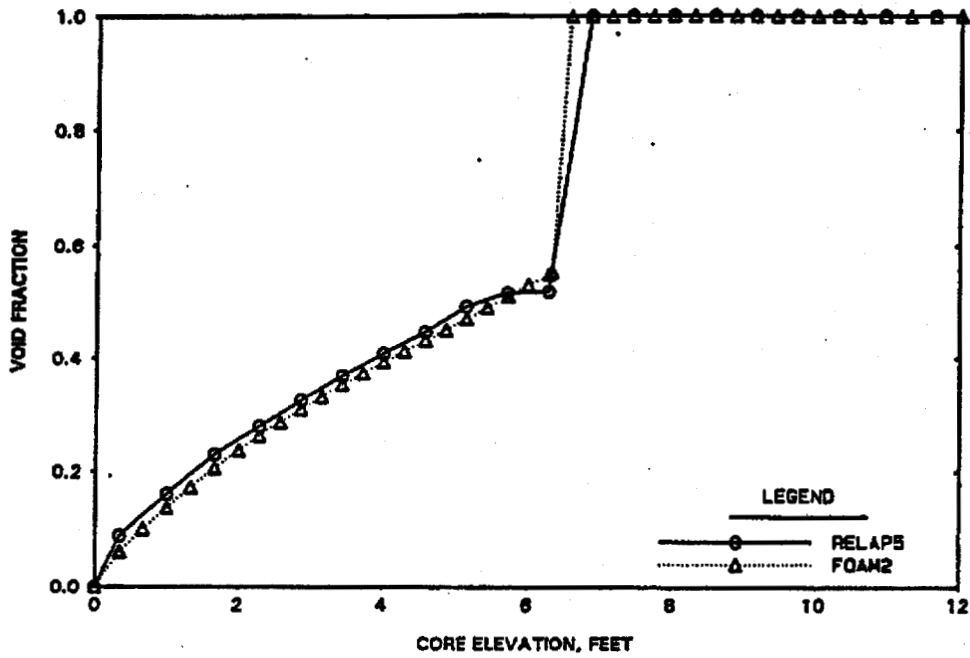


Figure H.7. Comparison of RELAP5 and FOAM2 Predictions:
5% Decay Power, 1200 Psia.

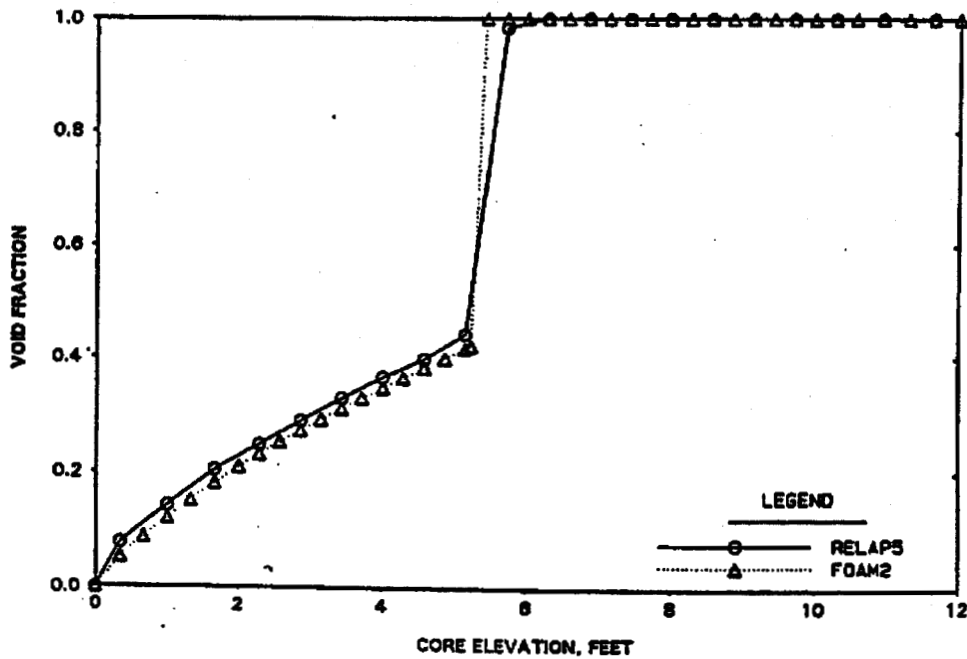


Figure H.8. Comparison of RELAP5 and FOAM2 Predictions:
2.5% Decay Power, 100 Psia.

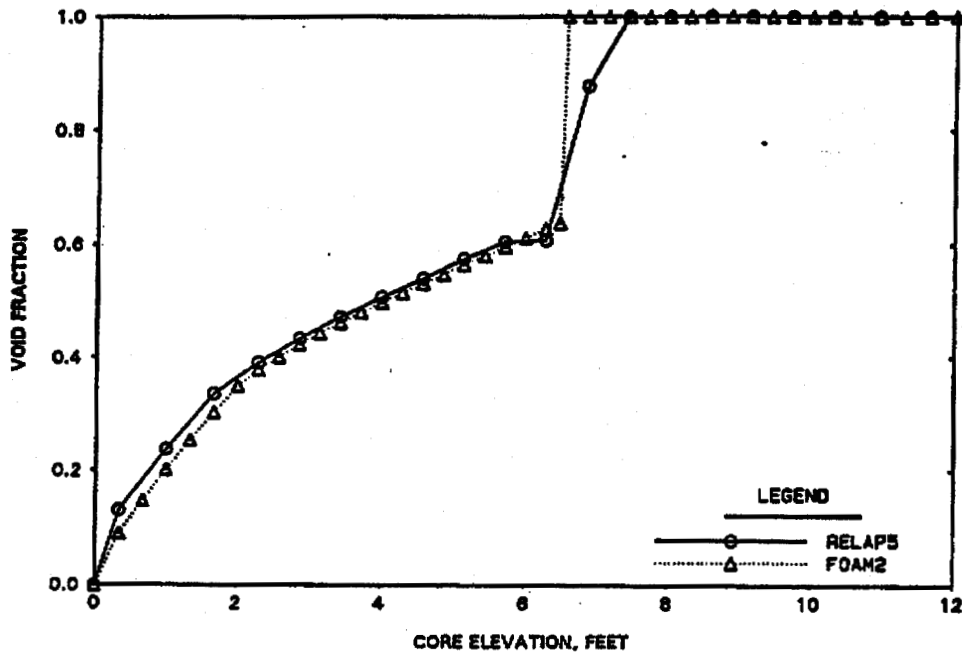


Figure H.9. Comparison of RELAP5 and FOAM2 Predictions:
2.5% Decay Power, 400 Psia.

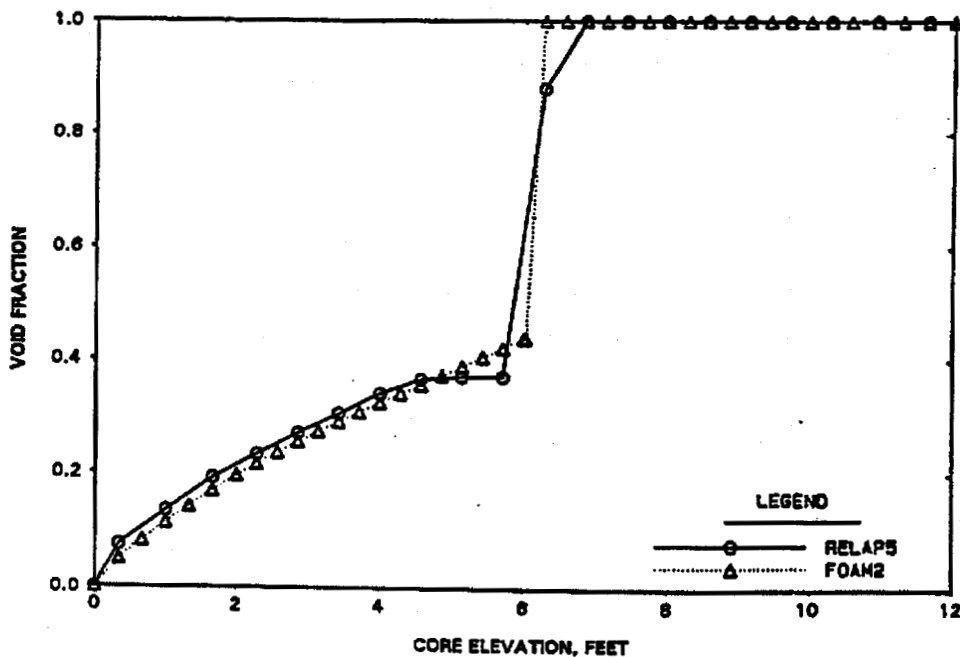


Figure H.10. Comparison of RELAP5 and FOAM2 Predictions:
2.5% Decay Power, 800 Psia.

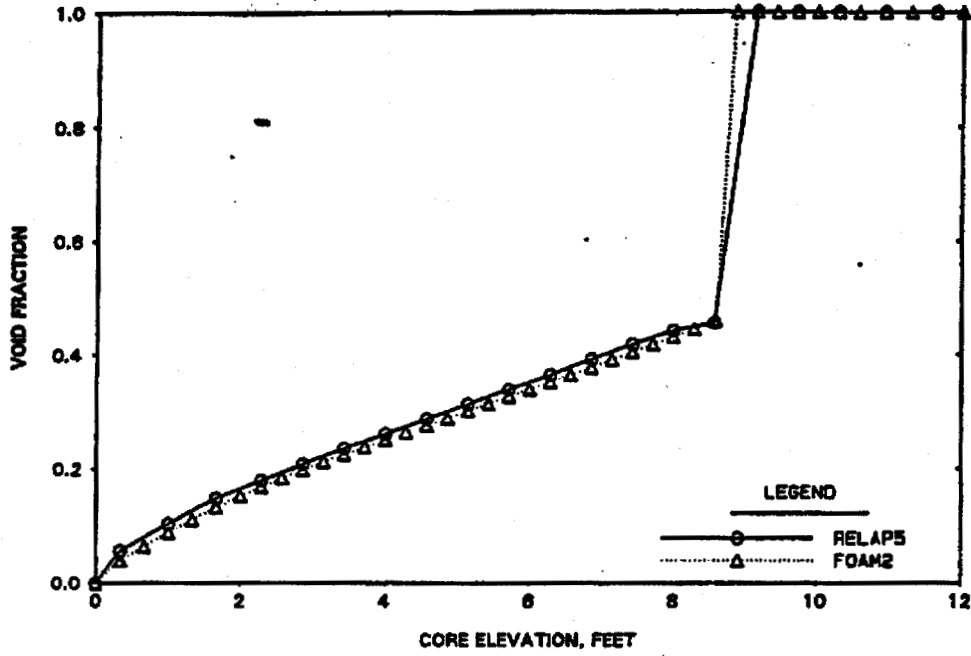


Figure H.11. Comparison of RELAP5 and FOAM2 Predictions:
2.5% Decay Power, 1200 Psia.

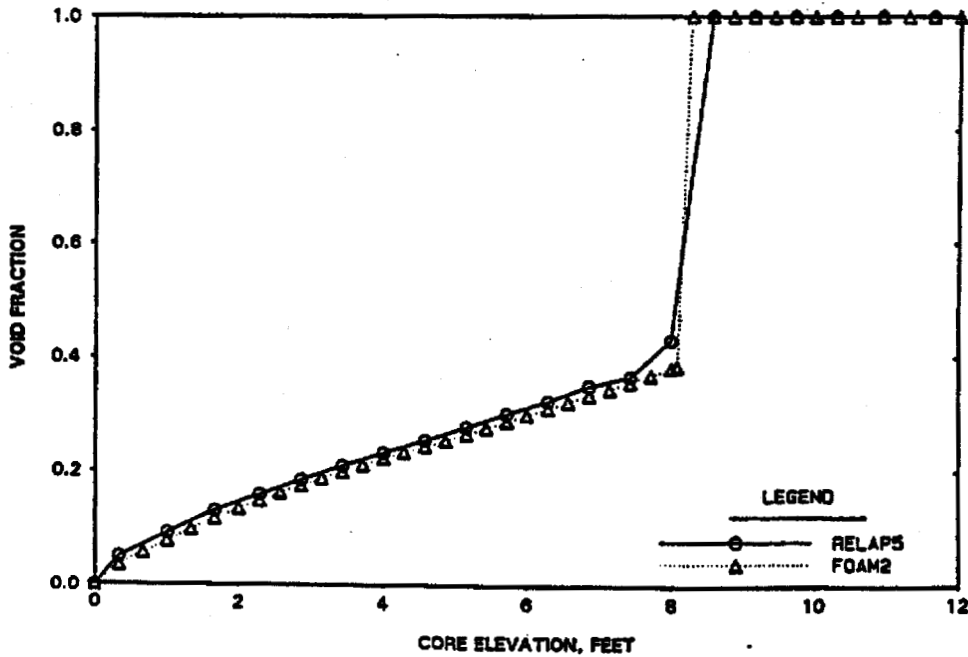


Figure H.12. Comparison of RELAP5 and FOAM2 Predictions:
1.5% Decay Power, 1200 Psia.

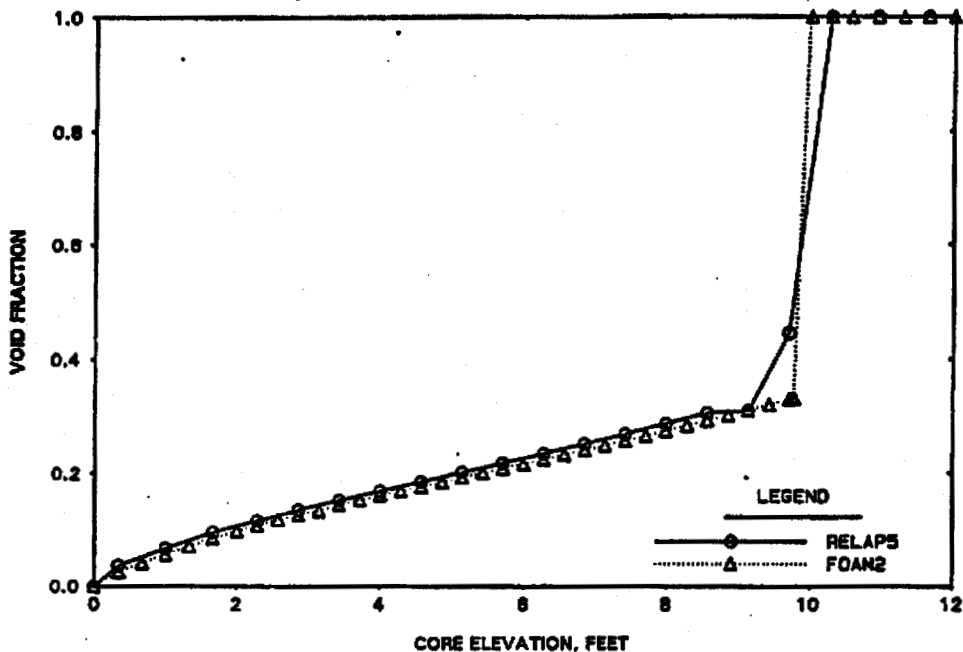
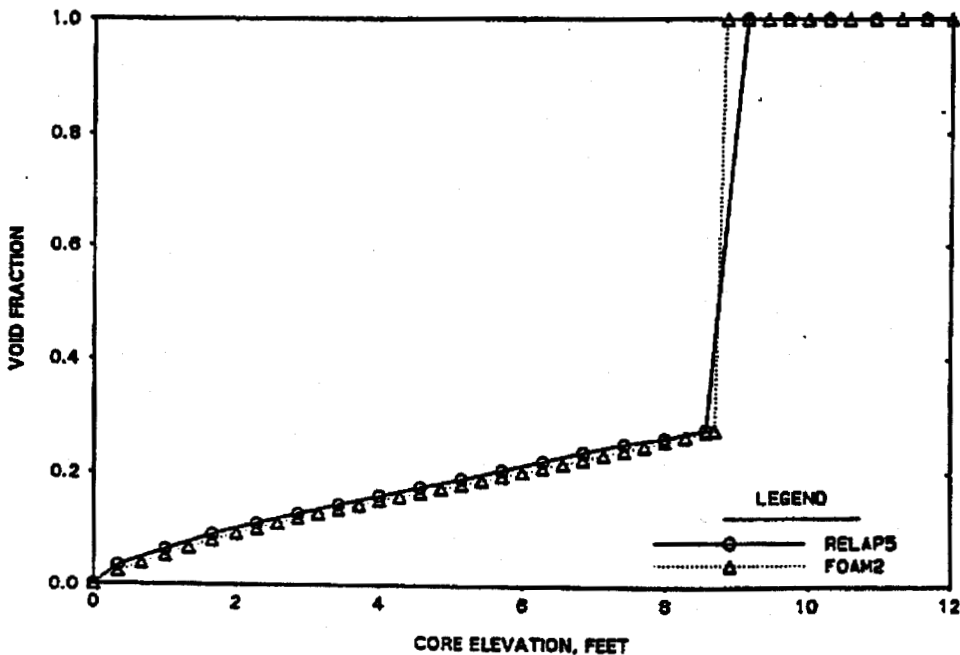


Figure H.13. Comparison of RELAP5 and FOAM2 Predictions:
1.5% Decay Power, 1600 Psia.



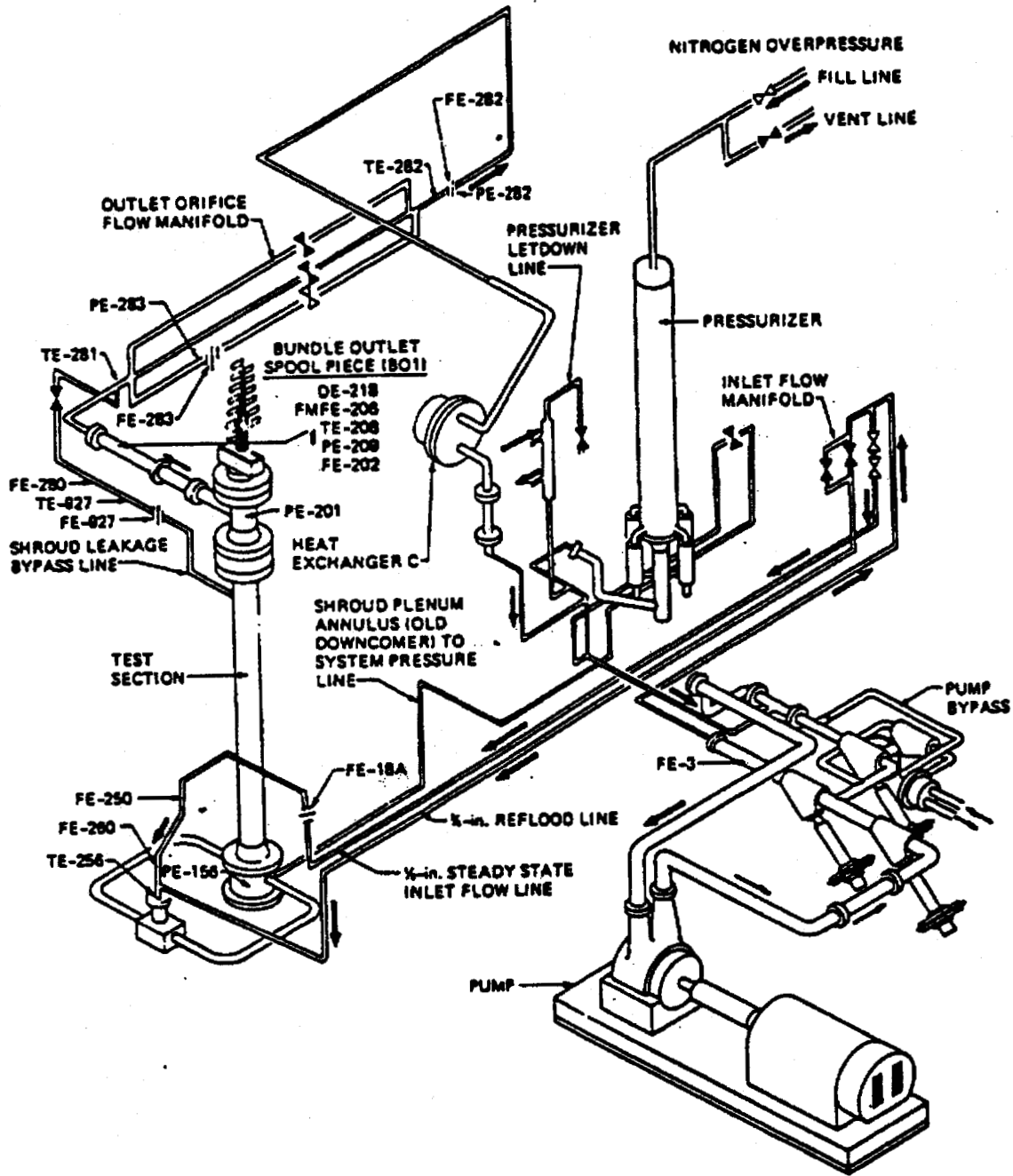


Figure H.14 - THTF in small break test configuration
(Reference 141).

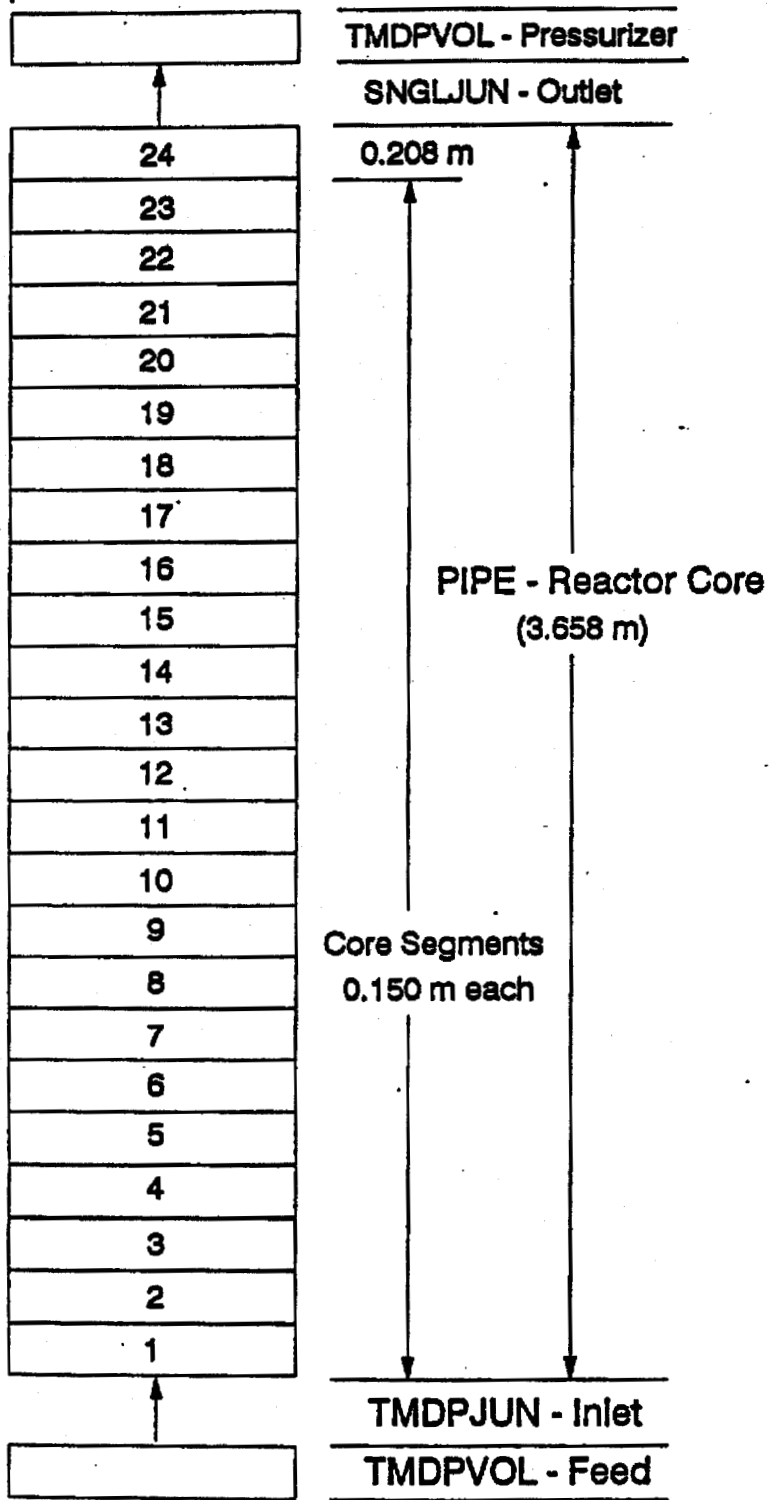


Figure H.15. RELAP Model of ORNL Thermal-Hydraulic Test Facility (THTF).

Figure H.16. Comparison Between RELAP5 Prediction and ORNL Test Data: 0.68 Kw/ft, 650 Psia.

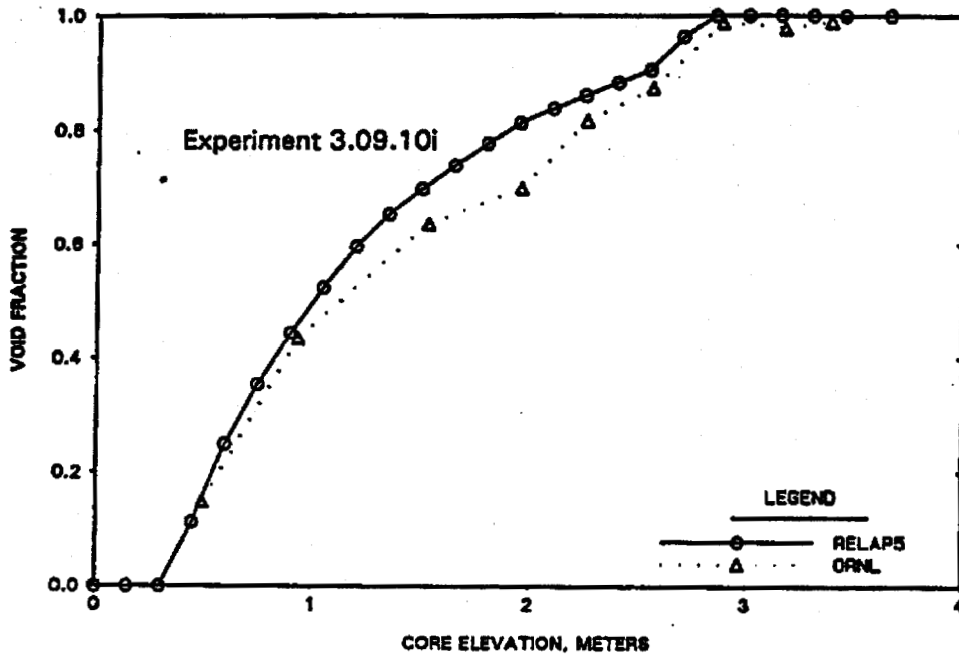


Figure H.17. Comparison Between RELAP5 Prediction and ORNL Test Data: 0.33 Kw/ft, 610 Psia.

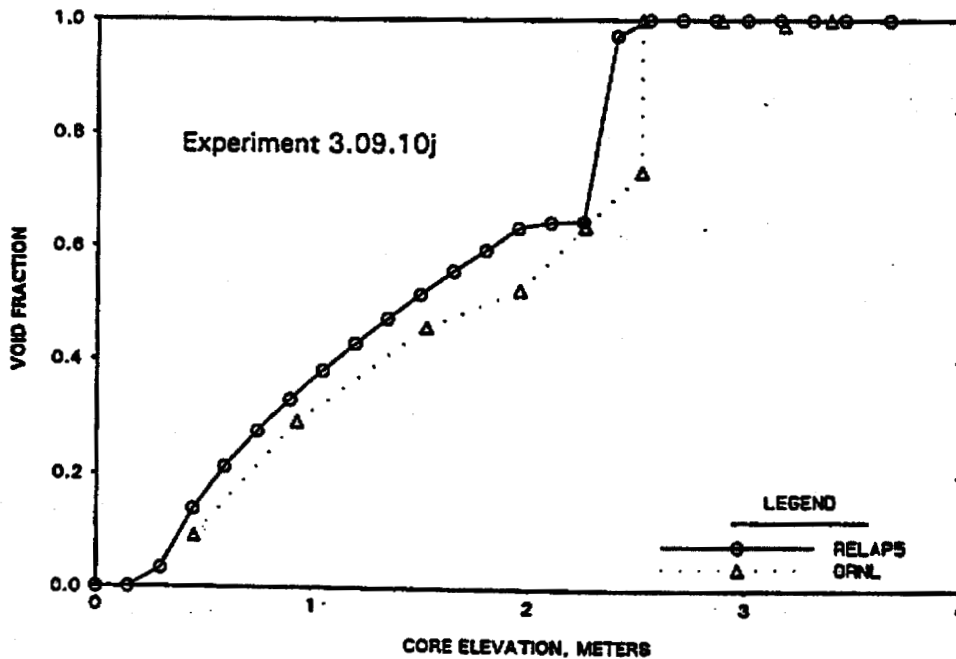


Figure H.18. Comparison Between RELAP5 Prediction and ORNL Test Data: 0.10 Kw/ft, 580 Psia.

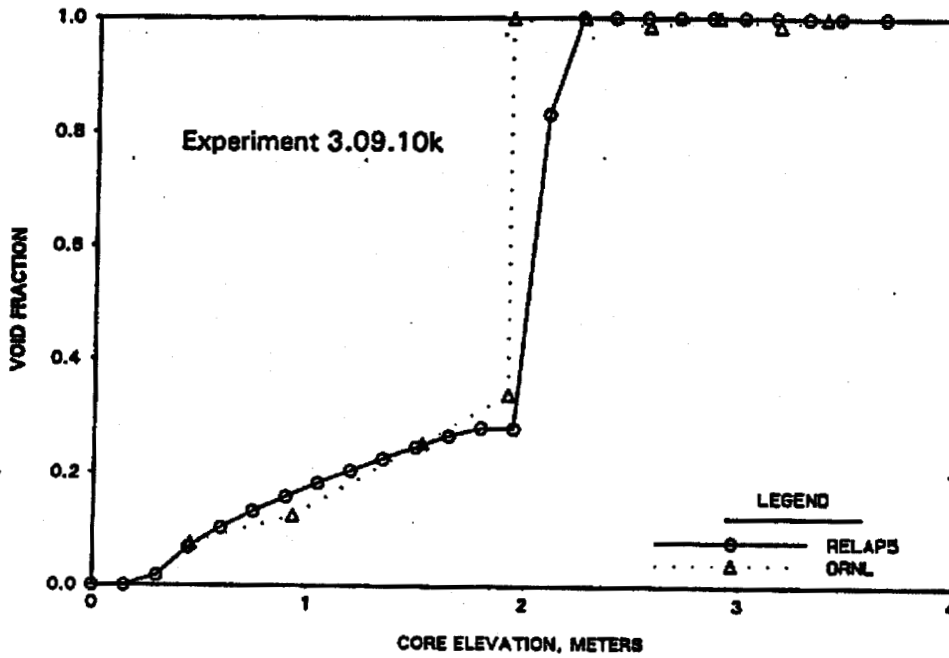


Figure H.19. Comparison Between RELAP5 Prediction and ORNL Test Data: 0.66 Kw/ft, 1090 Psia.

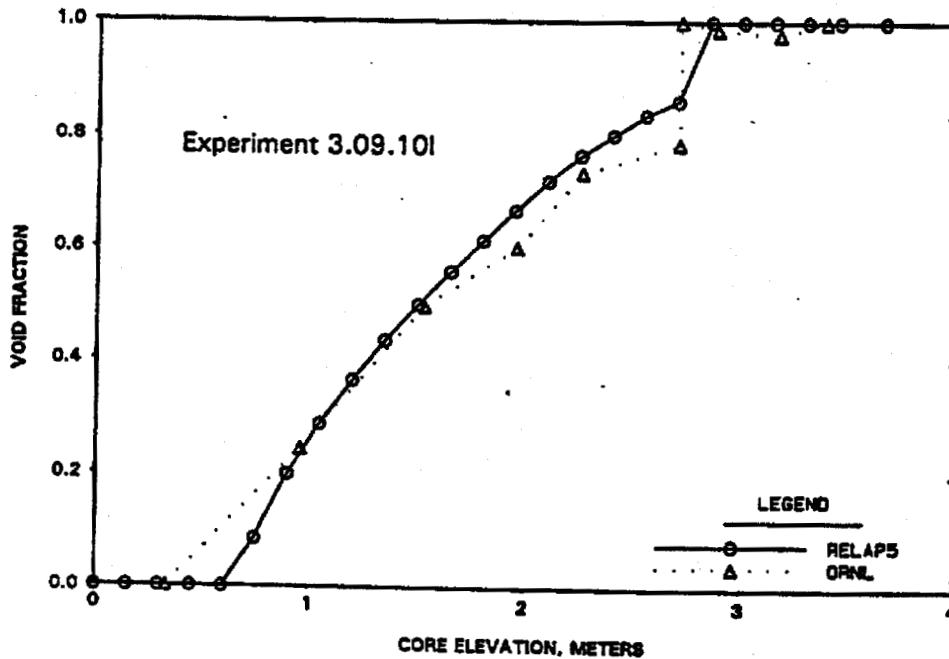


Figure H.20. Comparison Between RELAP5 Prediction and ORNL Test Data: 0.31 Kw/ft, 1010 Psia.

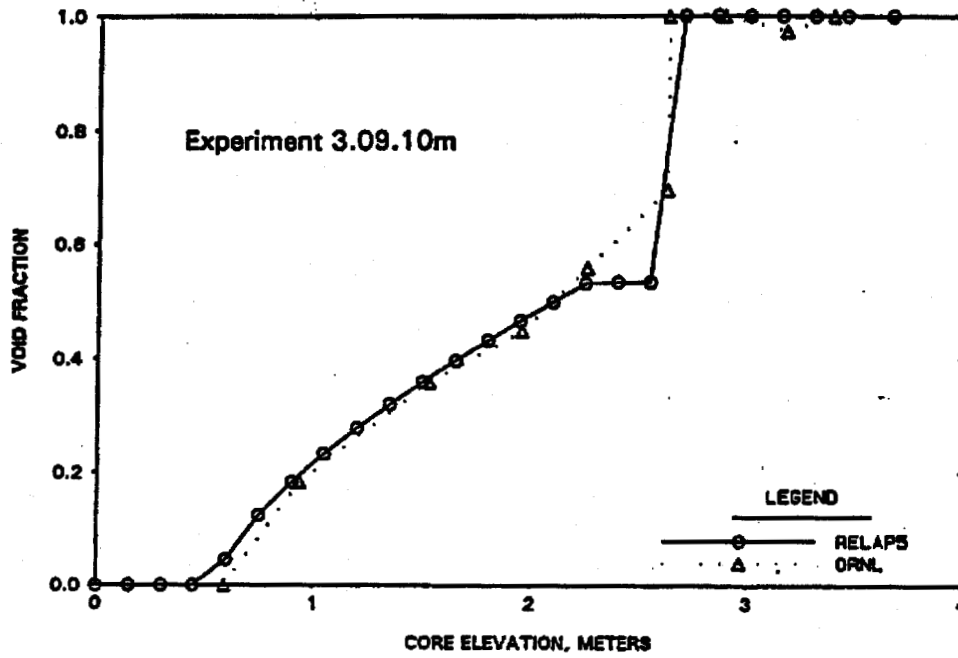


Figure H.21. Comparison Between RELAP5 Prediction and ORNL Test Data: 0.14 Kw/ft, 1030 Psia.

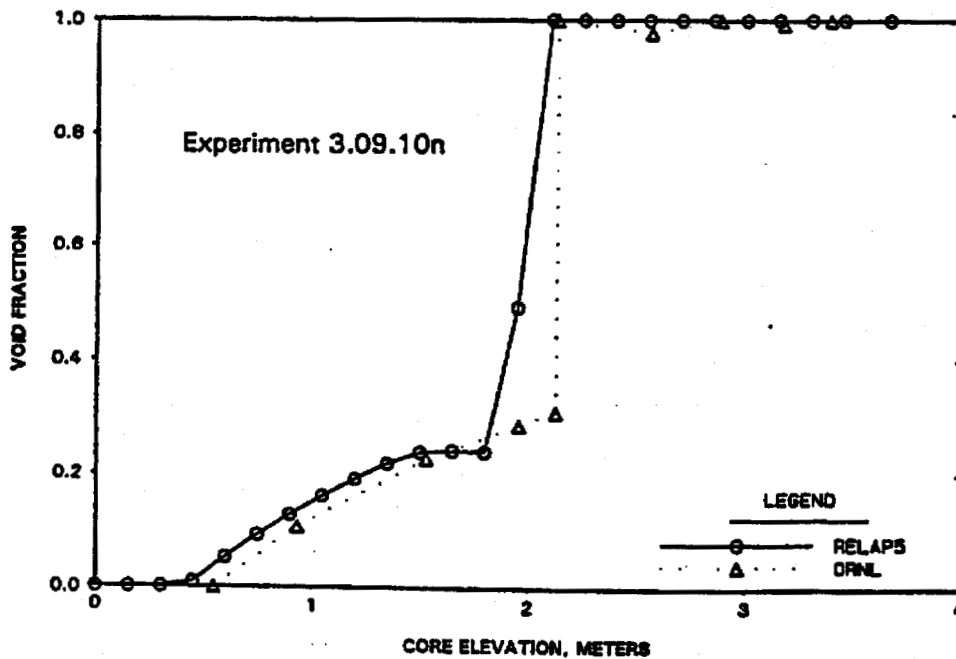


Figure H.22. Comparison Between RELAP5 Prediction and ORNL Test Data: 0.39 Kw/ft, 590 Psia.

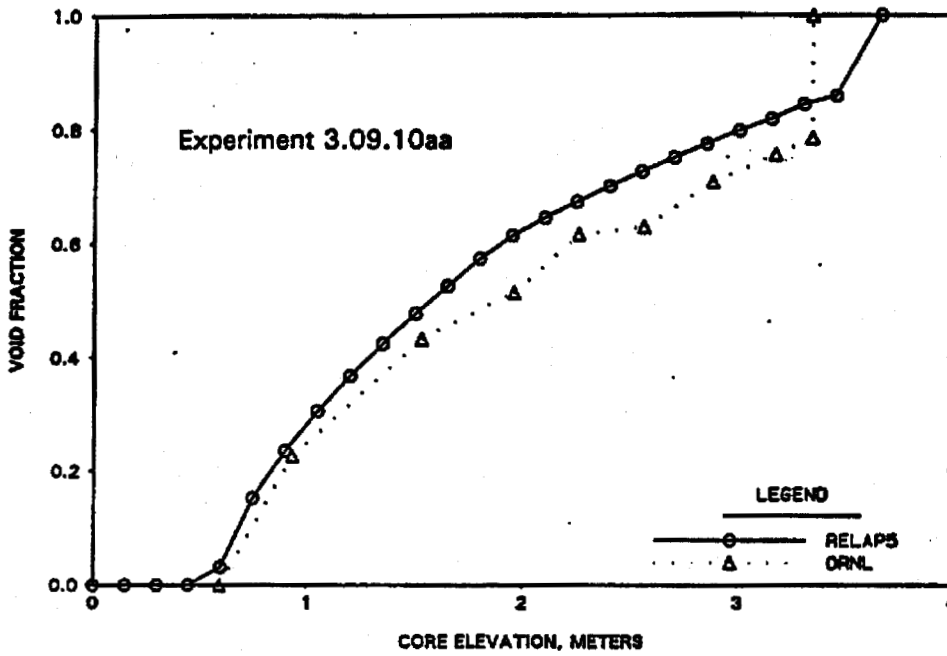


Figure H.23. Comparison Between RELAP5 Prediction and ORNL Test Data: 0.20 Kw/ft, 560 Psia.

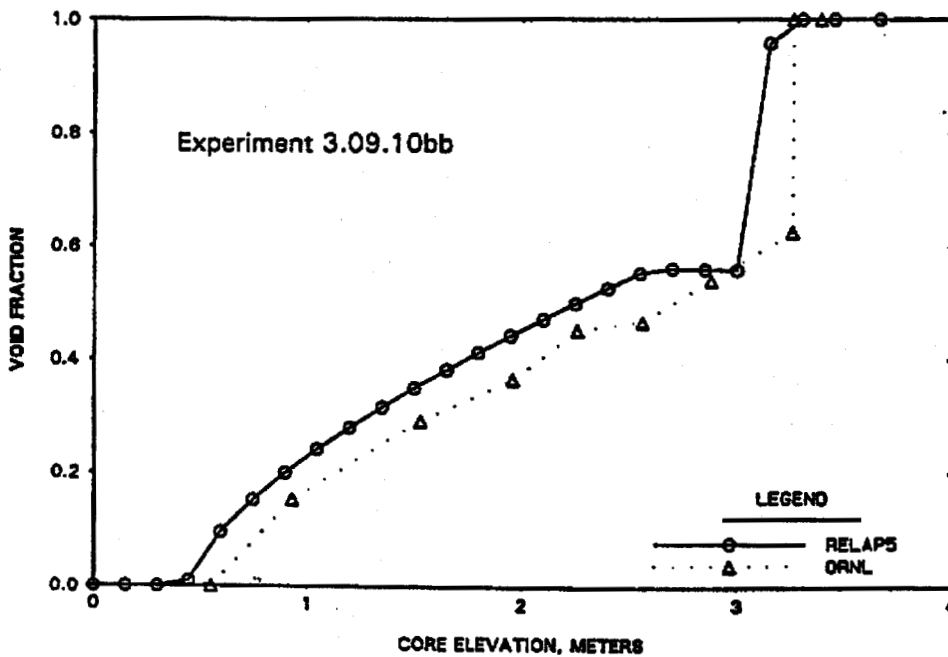


Figure H.24. Comparison Between RELAP5 Prediction and ORNL Test Data: 0.10 Kw/ft, 520 Psia.

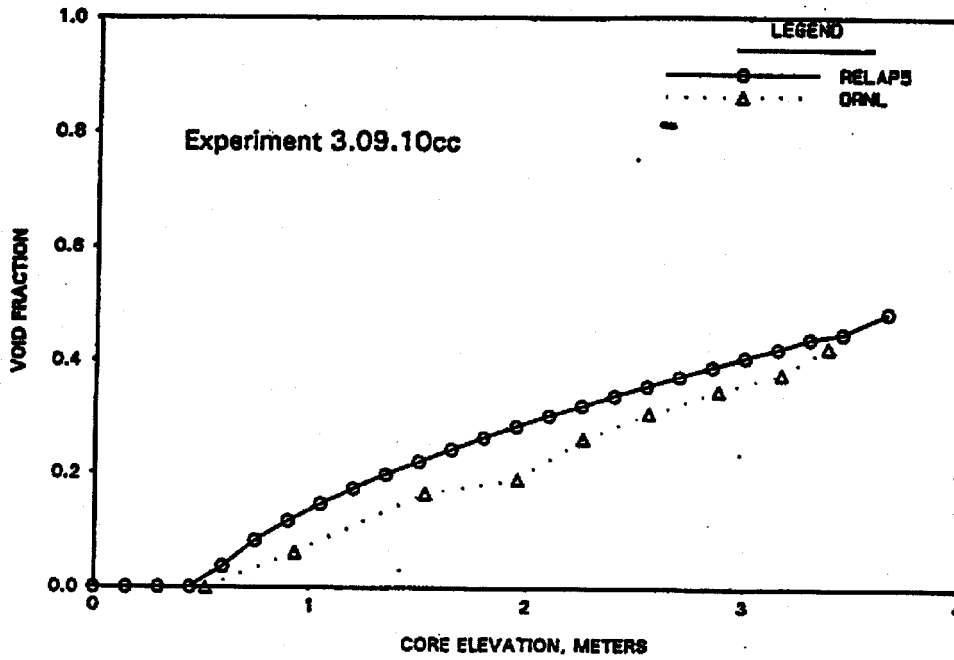


Figure H.25. Comparison Between RELAP5 Prediction and ORNL Test Data: 0.39 Kw/ft, 1170 Psia.

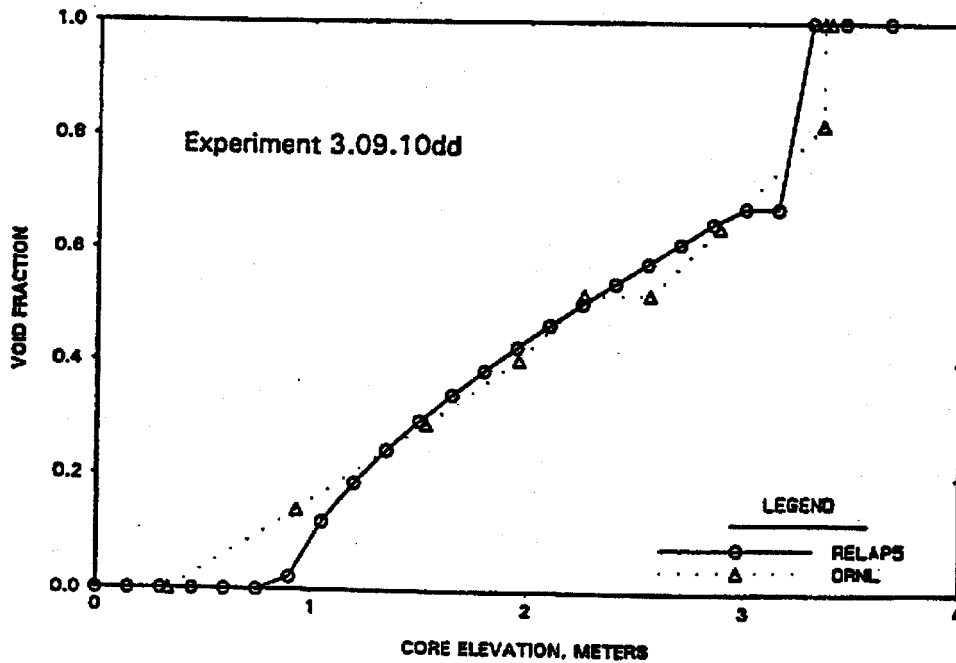


Figure H.26. Comparison Between RELAP5 Prediction and ORNL Test Data: 0.19 Kw/ft, 1120 Psia.

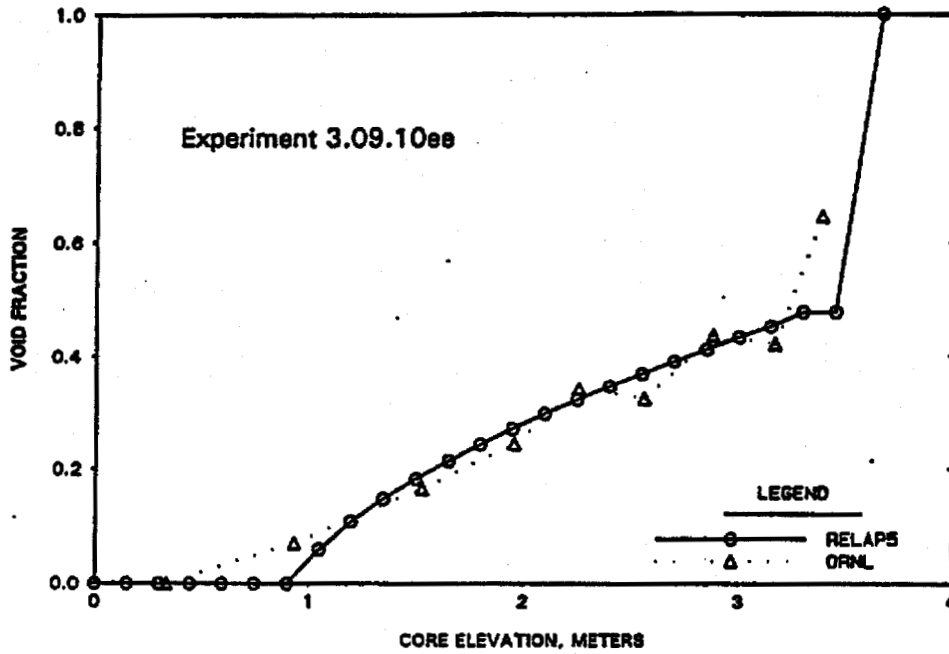


Figure H.27. Comparison Between RELAP5 Prediction and ORNL Test Data: 0.08 Kw/ft, 1090 Psia.

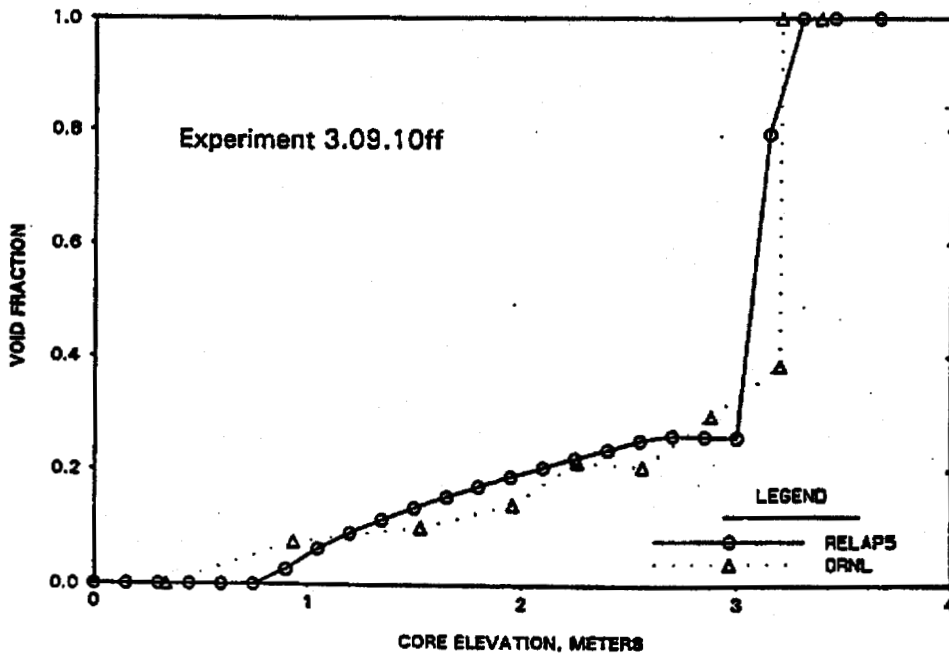


Figure H.28. Comparison Between RELAP5 Prediction and ORNL Test Data: 0.68 Kw/ft, 650 Psia.

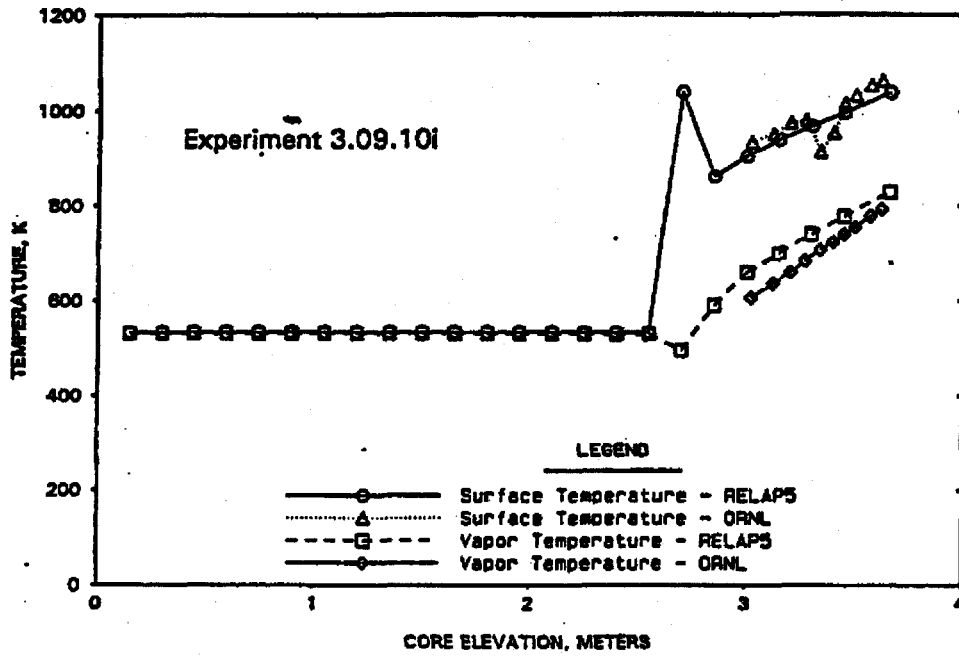


Figure H.29. Comparison Between RELAP5 Prediction and ORNL Test Data: 0.33 Kw/ft, 610 Psia.

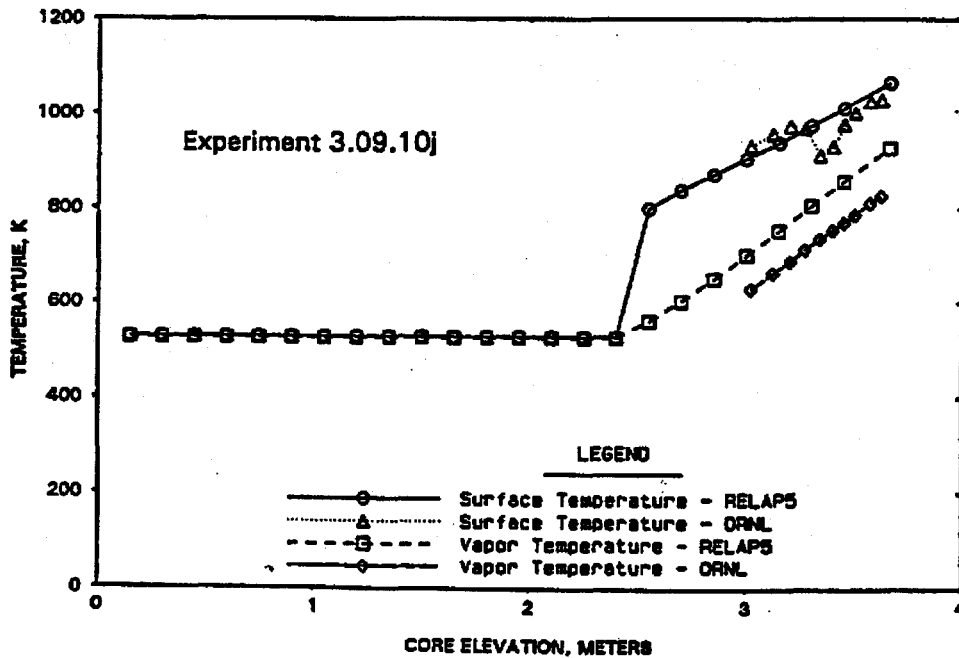


Figure H.30. Comparison Between RELAP5 Prediction and ORNL Test Data: 0.10 Kw/ft, 580 Psia.

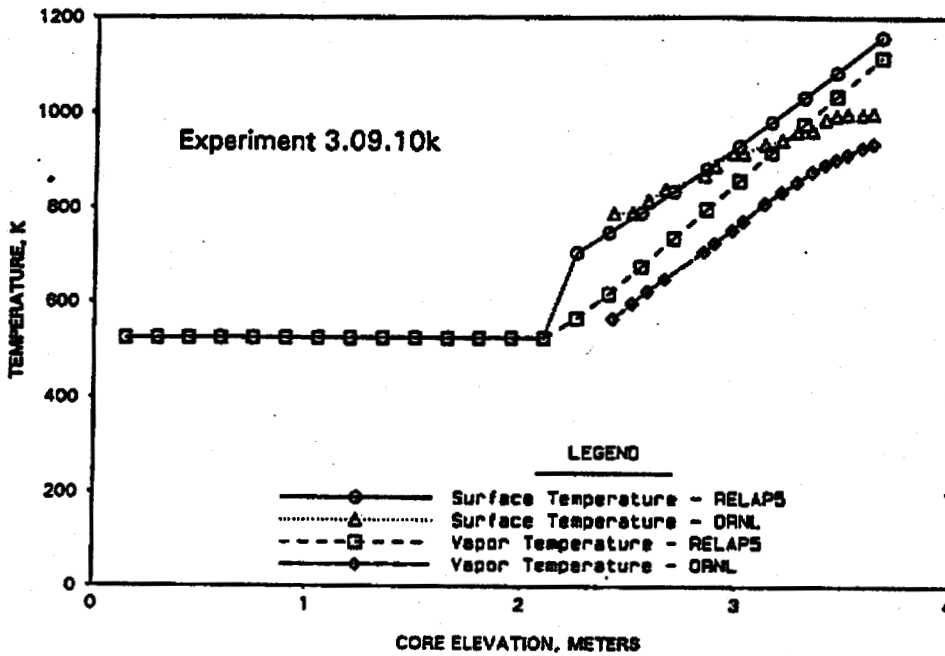


Figure H.31. Comparison Between RELAP5 Prediction and ORNL Test Data: 0.66 Kw/ft, 1090 Psia.

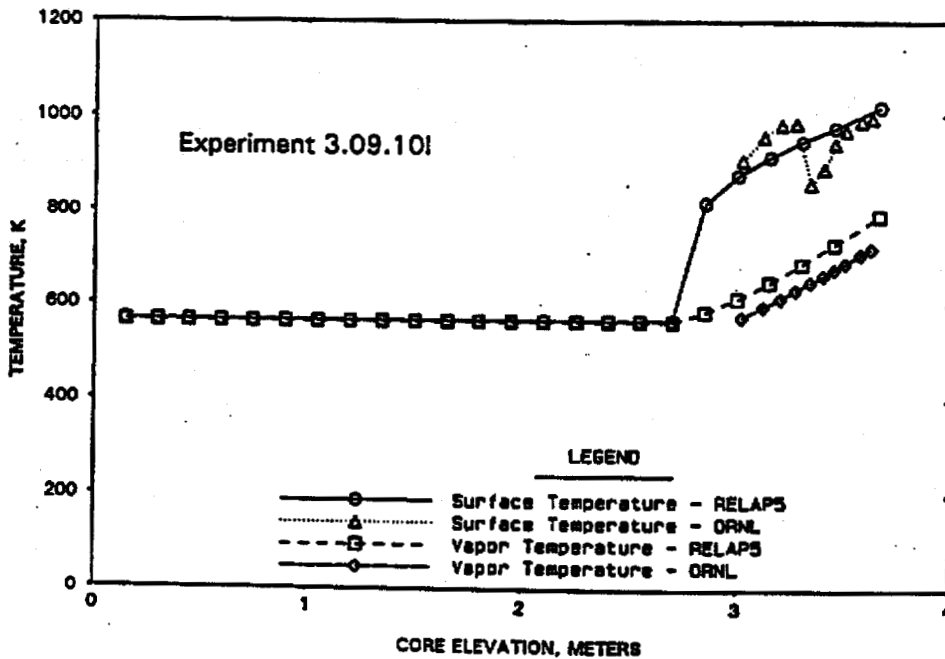


Figure H.32. Comparison Between RELAP5 Prediction and ORNL Test Data: 0.31 Kw/ft, 1010 Psia.

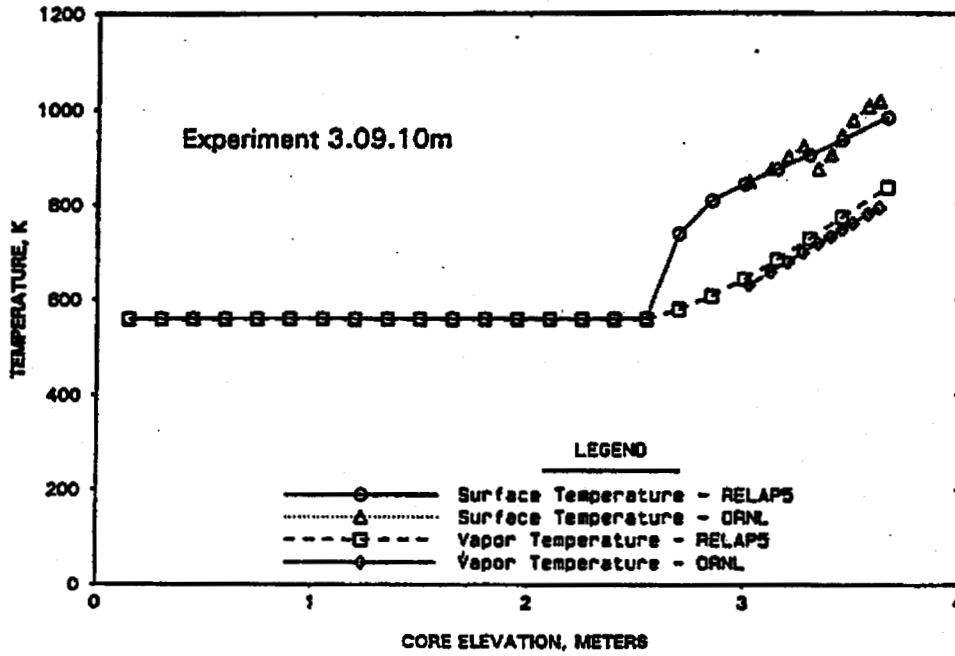
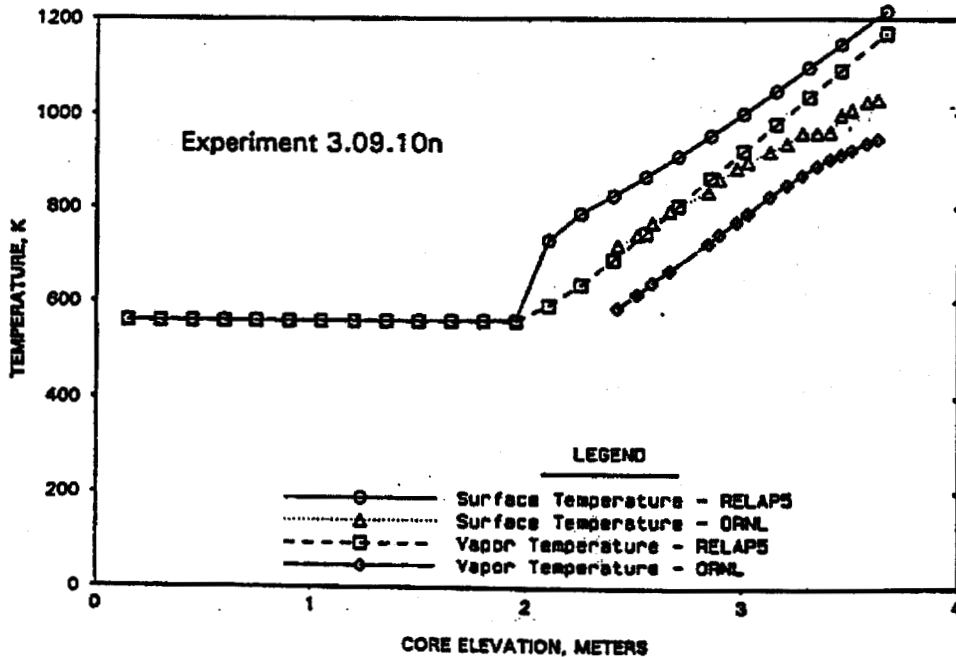


Figure H.33. Comparison Between RELAP5 Prediction and ORNL Test Data: 0.14 Kw/ft, 1030 Psia.



APPENDIX I

BWUMV CRITICAL HEAT FLUX CORRELATION

Note: This appendix was originally added in its entirety in Revision 2 of BAW-10164, August, 1992.

BWNT has developed the BWUMV (B&W Universal - Mixing Vane) CHF correlation for use in SBLOCA analysis. The correlation was generated using the NRC-approved methods in the BWCMV topical report, BAW-10159.¹³⁹ BWUMV is based on the BWCMV database extended to encompass additional data in the mid-flow regime. The correlation is for use with mixing grids.

A brief explanation of the CHF experiments conducted to measure BWUMV data are presented in section I.1, data reduction and derivation of the correlation in section I.2, and conclusions in section I.3.

I.1. Critical Heat Flux Tests

BWUMV is based on published Westinghouse-sponsored CHF experimental data from the Columbia University Heat Transfer Research Facility (HTRF) with supplemental data from tests at the same facility sponsored by Nuclear Fuel Industries (NFI) of Japan. A description of this facility is provided in Reference 140. The Columbia University Heat Transfer Research Facility data (as given in Reference 140) has been used as the basis of other correlations in the past.

In the HTRF tests, the first indication of departure from nucleate boiling (DNB) was used as the one experimentally noted. This practice has been previously found acceptable and conservative by the NRC staff.

Most of the data used to develop BWUMV was previously used to develop BWCMV. The BWCMV database consisted of 70 tests performed for Westinghouse and 4 tests performed for NFI. From the Westinghouse sets only 22 tests (included mixing vane grid cores) qualified for this correlation. All the NFI tests qualified, yielding a total of 26 sets of tests with nearly 1,500 data points. They included six axial flux shapes, three heated

lengths, six grid spacings, six hydraulic diameters, three different grid designs, and both unit and guide tube geometries. For the local thermal-hydraulic conditions, pressure ranged from 1500 to 2400 psia, mass velocity from 1.0 to 3.5 million lbm/hr/ft², and CHF hydrodynamic qualities from -22 to +22 percent. This extensive database fully covers PWR operating ranges for both local and bundle (global) conditions. Further information on the development of BWCMV may be found in Reference 140.

BWUMV used all the BWCMV data plus mid-flow regime data from three additional Westinghouse tests:

I.2. Derivation of Correlation

Because phenomenological models of CHF are not yet sufficiently accurate for most geometries, CHF is measured empirically using experimental facilities approximating reactor geometries. From these experimental measurements, a CHF correlation is derived; this correlation is an empirical regression of the experiments' independent variables. Four steps were used in the derivation of BWUMV:

1. A form of the correlation was chosen that accurately described the CHF data. The database used to derive BWUMV included a wide variety of bundle geometries, tested over a range of conditions (pressure, flow rates, and temperatures) which represent reactor conditions.
2. The level or magnitude of each independent variable for each run of the database was established. Independent variables were classified in two categories: local thermo-hydraulic conditions (such as velocity and quality) and bundle global conditions (such as heated

length and grid position). While global conditions were known, local conditions were calculated based on measured bundle values of flow, power, and system pressure. This was accomplished using the LYNX2 thermal-hydraulic computer code (Reference 141).

3. The correlation was developed; this included sorting of data by flow regime and optimization of the correlation coefficients. BWUMV coefficients were derived by sequential optimization, and verified using the final database.
4. Since BWUMV is an empirical correlation, there is a finite uncertainty associated with it. This uncertainty was quantified in a departure from nucleate boiling ratio (DNBR) design limit, consistent with the specified acceptable fuel design limit of Standard Review Plan 4.4 (NUREG 0800). DNBR is defined as:

$$\text{DNBR} = \frac{q''_{\text{CHF}}}{q''_{\text{actual}}} = \frac{\text{calculated CHF at a given location}}{\text{actual heat flux at that location}} .$$

A DNBR value of 1.0 implies transition to film boiling at that location. The higher the DNBR, the greater the margin to film boiling. Calculation of a DNBR value greater than this design limit provides assurance that there is at least a 95% probability at the 95% confidence level that a departure from nucleate boiling will not occur (95/95 design limit). As the final step in the derivation of the correlation, the 95/95 design limit was calculated and used to verify that the correlation describes CHF accurately and without bias. Verification included visual and numerical checks for bias with respect to all the independent variables.

I.2.1. Correlation Form

The critical heat flux was assumed to depend on three parameters:

$$\begin{aligned} x_1 &= \exp[P / (1000 \cdot Cl_p)], \\ x_2 &= G / (10^6 \cdot Cl_{MF}), \text{ and} \\ x_3 &= X_{eth} \end{aligned}$$

where P is the system pressure in Pa, G is the mass flux in kg/s/m², X_{eth} is the quality at CHF, and Cl_p and Cl_{MF} are the English-to-metric conversion factors for pressure and mass flux, respectively.

Based on the work of Farnsworth¹⁴², a general polynomial form was assumed:

 $\begin{aligned} CHF &= FLS (a_0 + a_1 x_1 + a_2 x_2 + a_3 x_3^2 + a_4 x_1^2 + a_5 x_2 + a_6 x_3 x_3 \\ &+ a_7 x_1 x_2 + a_8 x_1 x_3 + a_9 x_2 x_3 + a_{10} x_1^3 + a_{11} x_2^3 + a_{12} x_3^3 + \\ &+ a_{13} x_1 x_2 x_3) / F \end{aligned}$ 	Revised Equation I-1 shown on Page 5-260 per SER instruction On Table 2 (page 5-364).	I-1
--	---	-----

where FLS is the bundle specific multiplier used in BWCMV and is defined by

 $FLS = e_1 + e_2 L + e_3 S + e_4 L^2 + e_5 LS + e_6 S^2,$ 	I-2
---	-----

Revised Equation I-2 shown on page 5-261 per SER instruction on Table 2 (page 5-364).

in which

- L = heated length,
- S = spacer grid spacing, and
- C_i = empirically determined coefficients.

F is the non-uniform (Tong) factor which is set equal to one in the RELAP5/MOD2-B&W implementation of BWUMV.

From the BWCVM correlation¹³⁹, the empirical coefficients are:

b,c,d,e

I.2.2. Subchannel Analysis

Data reduction was required for the three Westinghouse tests which were not used in BWCVM. The experimental conditions for each of the tests (tests number 121, 160, and 164) are given in Table I.1.¹⁴⁰ Local conditions in each assembly subchannel were calculated using the thermo-hydraulic code LYNX2.¹⁴¹ LYNX2 applies conservation relations at successive axial increments beginning at the channel inlet; downstream increments are considered singly and successively up to the channel exit. The conservation relations used include crossflow between adjacent subchannels. LYNX2 iterates over each axial increment until the differences between current and previous diversion crossflows meet a set convergence criteria. Within each iteration the code solves the conservation and crossflow relations of each subchannel and crossflow boundary.

For the three supplemental tests analyzed, one-eighth of the bundle was analyzed. Westinghouse Test 121 was performed on a 4x4 assembly and was divided into six subchannels as shown in Figure I.1. Westinghouse Tests 160 and 164 were performed with 5x5 assemblies and were divided into six subchannels as shown in

Figure I.2. The dimensions and parameters associated with each assembly are provided in Table I.2.

Based on the axial and radial heat profiles and input of bundle pressure, flow, power, and inlet temperature for each point, local conditions were determined for each assembly as given in Table I.3.

I.2.3 Data Sorting and Coefficient Optimization

When the data points contained in Table I.3 are added to the data points in Reference 139, there are 1527 data points. These data points were used to obtain the coefficients a_0 through a_{13} in Equation I-1 using the methods given in Reference 141. The data points cover the following ranges:

Quality	-0.2160 to 0.6653
Mass Flux (mlbm/hr-ft ²)	0.405 to 3.871
Pressure (psia)	745 to 2455

The following coefficients were determined:

b,c,d,e

I.2.4. Calculation of Design Limit and Verification

The statistical distribution of the mixing vane CHF data is shown in Figure I.3. Four data points were found to have measured-to-

predicted ratios which exceeded three standard deviations and were rejected from the database. The statistics of the remaining 1523 data points were:

Number of data	1523
Mean	1.0018
Standard Deviation	0.1016
Coefficient of Variation	0.1014

The 95/95 departure from nucleate boiling (DNB) design limit was calculated as 1.22.

Figures I.4, I.5, and I.6 show the measured-to-predicted ratios using BWUMV plotted against quality, pressure, and mass velocity, respectively. These figures show no bias of the correlation with respect to the independent variables.

I.3. Conclusions

A new wide-range critical heat flux correlation has been developed based on 70 Westinghouse-sponsored and 4 NFI-sponsored mixing vane-type assembly experiments performed at the Columbia University Heat Transfer Test Facility. The new correlation, called BWUMV, has been demonstrated to have a favorable statistical distribution and to be unbiased relative to quality, pressure, and mass velocity. Based on the data used, BWUMV is applicable to CHF calculations of mixing vane rod assemblies for pressures and flow rates at or above 750 psia, and greater than 4.0×10^5 lbm/hr-ft², respectively.

Table I.1. Geometry of Westinghouse Bundles 121, 160, and 164.

	Bundle Number		
	121	160	164
Total Number of Rods	16	25	25
Number of Heated Rods	16	25	25
Rod Pitch (inches)	0.555	0.496	0.496
Rod Diameter (inches)	0.422	0.374	0.374
Heated Length (inches)	96.0	96.0	168.0
Rod-to-Wall Gap (inches)	0.153	0.100	0.100
Flow Area (square inches)	3.489	3.796	3.796

Table I.2. Local Condition Analysis: Subchannel Parameters.

	Subchannel No.					
	1	2	3	4	5	6
Test No. 121						
Subchannel Type	Corner	Wall	Unit	Wall	Unit	Unit
Flow Area (sq. in.)	0.04877	0.13209	0.08408	0.06605	0.08408	0.02102
Wetted Perimeter (in.)	0.52970	1.21788	0.66288	0.60894	0.66288	0.16572
Heated Perimeter (in.)	0.16572	0.66288	0.66288	0.33144	0.66288	0.16572
Test No. 160						
Subchannel Type	Corner	Wall	Unit	Wall	Unit	Unit
Flow Area (sq. in.)	0.02745	0.08742	0.06808	0.08742	0.13616	0.06808
Wetted Perimeter (in.)	0.43387	1.08347	0.58748	1.08347	1.17495	0.58748
Heated Perimeter (in.)	0.14687	0.58748	0.58748	0.58748	1.17495	0.58748
Test No. 164						
Subchannel Type	Corner	Wall	Unit	Wall	Unit	Unit
Flow Area (sq. in.)	0.02745	0.08742	0.06808	0.08742	0.13616	0.06808
Wetted Perimeter (in.)	0.43387	1.08347	0.58748	1.08347	1.17495	0.58748
Heated Perimeter (in.)	0.14687	0.58748	0.58748	0.58748	1.17495	0.58748

Table I.3. Calculated Local Condition Values.

	Point	Pressure psia	Mass Flux lbm/hr/ft ²	Heat Flux btu/hr/ft ²	Quality
Test 121					
	430	2015	405308	370043	0.2556
	431	2015	721925	461763	0.0969
	432	2015	704141	521065	0.0664
	433	2015	916371	521065	0.0664
Test 160					
Duplicate	786	2115	527956	287300	0.3641
	787	2385	531861	282880	0.3157
	788	1805	541406	311610	0.3265
	789	1515	519832	373490	0.5620
	789	1515	513721	373490	0.6653
	790	2115	532879	335920	0.3127
	791	2405	519639	329290	0.2604
	792	1800	531920	370175	0.4239
	793	1815	516979	397800	0.4586
	794	2075	508498	349180	0.3110
	Test 164				
Duplicate	2055	1000	2554047	601121	0.2000
	2056	1000	3018628	682772	0.1931
	2057	1000	1588414	363385	0.3162
	2058	1000	2035850	647578	0.2044
	2059	1005	2518548	709520	0.1634
	2060	1005	3030165	751754	0.1683
	2060	1005	3050214	611714	0.1980
	2061	1005	1103392	348591	0.4161
	2062	1010	1575738	404069	0.3199
	2063	760	1879028	372631	0.3371
	2064	760	2634649	444754	0.2812
	2065	765	3096974	713744	0.2090

Table I.3 (continued). Calculated Local Condition Values.

	Point	Pressure psia	Mass Flux lbm/hr/ft ²	Heat Flux btu/hr/ft ²	Quality
Test 164 (continued)					
<i>Duplicate</i>	2065	765	3147021	468794	0.2528
	2066	755	1617322	374481	0.3567
	2067	750	2115662	392049	0.3122
	2068	750	1627688	338420	0.3935
	2069	745	1026514	327324	0.4569
	2070	750	1049376	347666	0.4291
	2071	1005	2120543	578597	0.2326
	2072	995	1044837	307906	0.4731
	2073	1005	558151	281092	0.6404
	2074	1000	547973	239483	0.5657
	2075	760	538561	378692	0.4393
	2076	755	545706	232086	0.6060

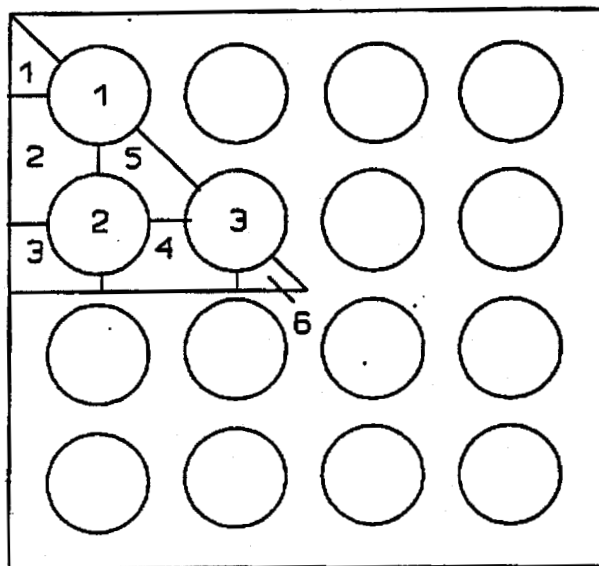


Figure I.1. Subchannel Model for Westinghouse Test 121.

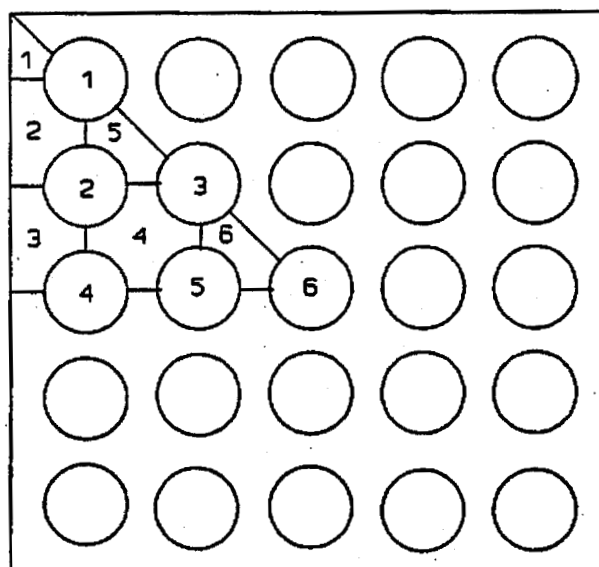


Figure I.2. Subchannel Model for Westinghouse Test 160 and 164.

FIGURE I.3. FREQUENCY DISTRIBUTION OF MIXING VANE CHF DATA.

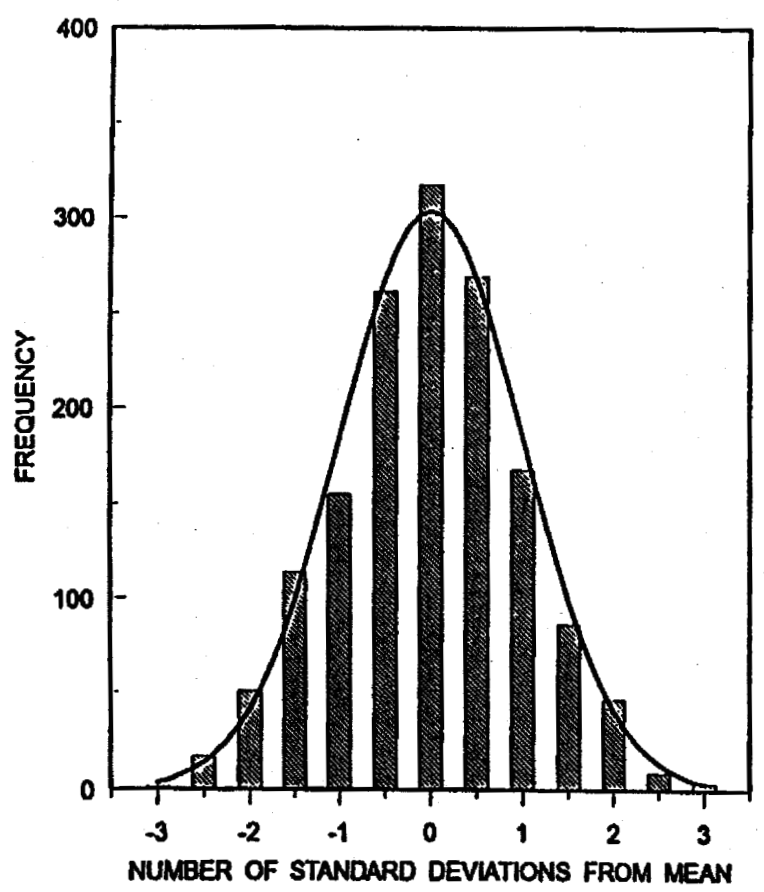


FIGURE I.4. MEASURED-TO-PREDICTED RATIOS OF BWUMV DATA: QUALITY.

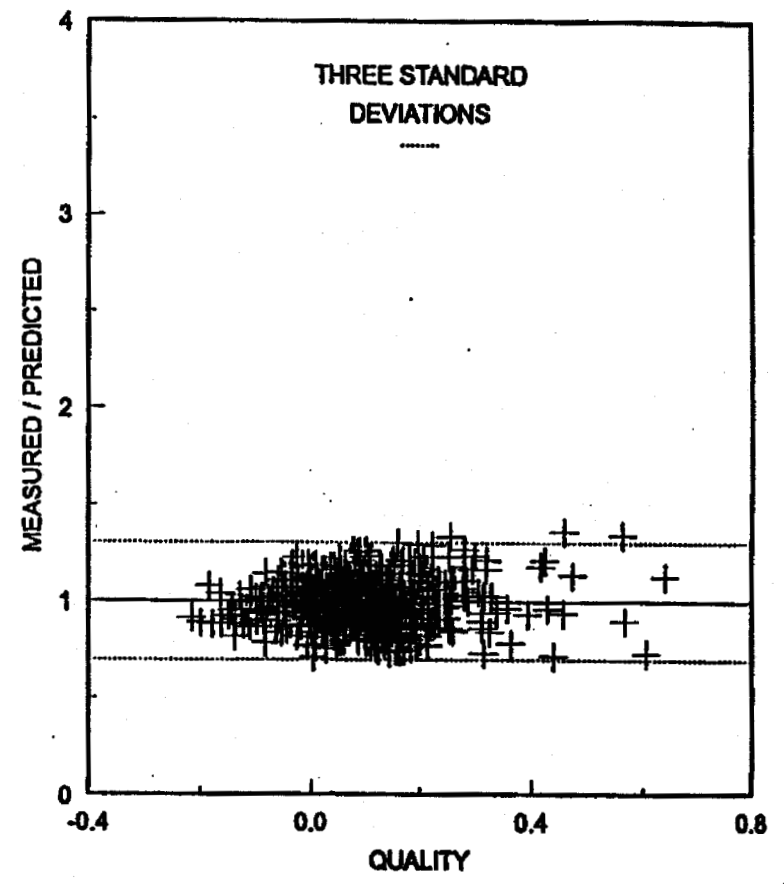


FIGURE I.5. MEASURED-TO-PREDICTED RATIOS OF BWUMV DATA: PRESSURE.

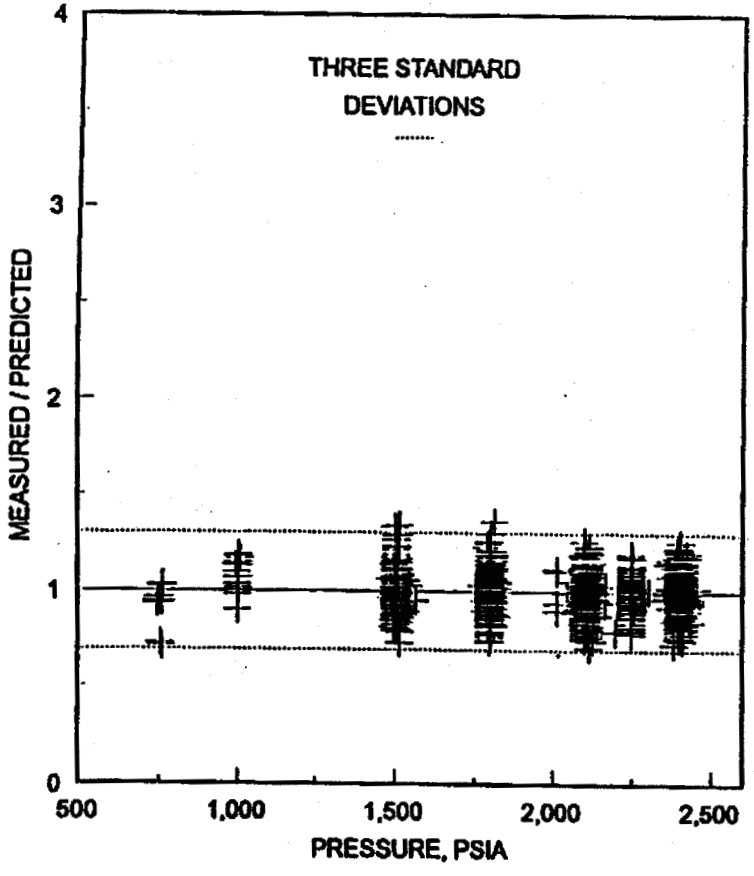
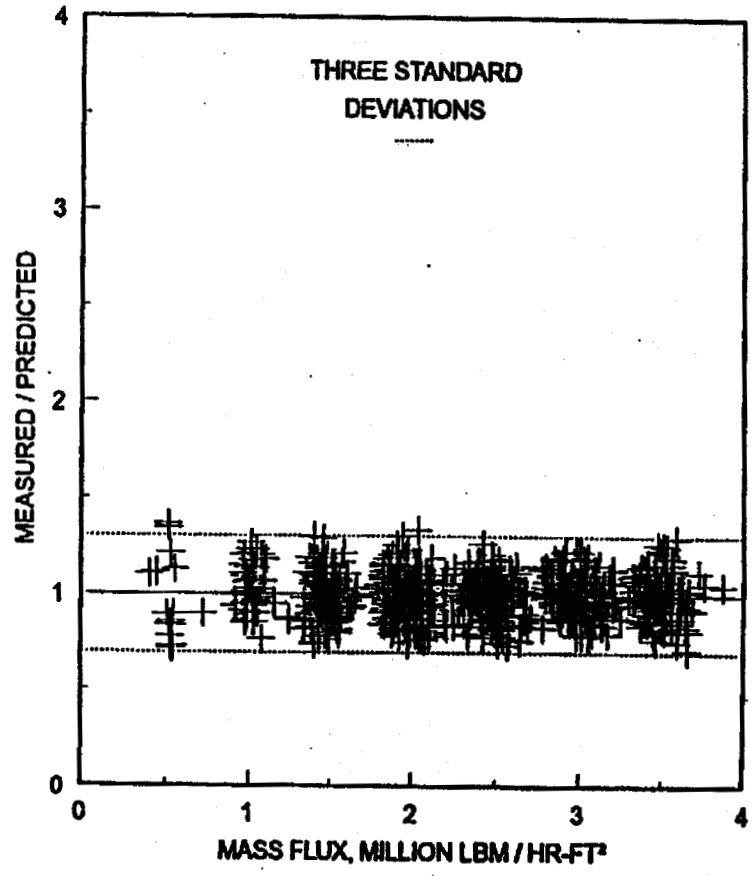


FIGURE I.6. MEASURED-TO-PREDICTED RATIOS OF BWUMV DATA: MASS FLUX.



I-15

Rev. 2
8/92

This page is intentionally left blank.

APPENDIX J

SBLOCA EM BENCHMARK

Note: This appendix was originally added in its entirety in Revision 2 of BAW-10164, August 1992.

Introduction

Test SB-CL-18 was one of the SBLOCA experiments conducted in the ROSA-IV Large Scale Test Facility (LSTF) in 1988. This test was selected for International Standard Problem 26 (ISP-26) for benchmarking various system computer codes including RELAP5/MOD2 by participating organizations. BWNT also selected this test for benchmarking BWNT's version of RELAP5/MOD2 because it provides the various modes of a small break LOCA transient, from an initial system depressurization followed by pump coastdown and loss of two-phase circulation, reflux boiling, loop seal clearing and core level depression, core boiloff, and finally to accumulator injection and core recovering. This test simulates the break area equivalent to 5 percent of the cross sectional area of the pump discharge pipe with no pumped ECC injection.

The RELAP5 model for the ISP-26 program was obtained from EG&G. The model was verified against the system design data provided in Reference 142, and subsequently modified to implement the BWNT SBLOCA EM technology. The BWNT version of RELAP5/MOD2 was benchmarked with the revised model (BAW-10168, Revision 2) to demonstrate the analytical capability of the code in predicting the various modes of a SBLOCA transient. The following sections present a description of the ROSA-IV LSTF test facility, test conditions and calculational model, and a summary of results of the benchmark.

Test Facility

ROSA-IV LSTF, as shown in Figure J.1, is a scaled model representation of a Westinghouse 4-loop PWR plant, with a fluid volume scaling ratio of 1 to 48. The 1 to 1 elevation scaling of the system is preserved because it has a first-order effect on SBLOCA transients. The core is simulated by 1064 electrically heated rods. A comparison of major design parameters of the LSTF

with the PWR is presented in Table J.1. The ROSA-IV system consists of a pressure vessel with two symmetrical loops, each representing two loops of the PWR plant. The pressurizer is connected to the intact loop. A brief description of the major components is provided below.

Pressure vessel:

The pressure vessel consists of an annular downcomer, lower plenum, simulated core with 16-7x7 bundles and 8 semi-crescent bundles on the periphery, and simulated upper plenum and upper head with 8 control rod guide tubes and 10 upper core support columns. Eight 3.4 mm holes are provided in the top flange of the core support barrel to simulate the downcomer-to-upper head bypass flow. An external pipe (1 inch, schedule 160) is used to connect the hot leg pipe to the upper downcomer for simulating hot leg nozzle leakage.

The core consists of 1064 electrically heated rods (9.5 mm OD) and 104 unheated rods (12.2 mm OD) with 9 spacer grids. The active heated length is 3660 mm (12 feet). The axial power distribution is a cosine profile with a 1.5 peak at the midplane.

Steam generator:

The primary side of the steam generator consists of inlet and outlet plenums, tube sheet, and 141 inverted U-tubes (1/48 of the PWR) with an inside diameter of 19.6 mm and a wall thickness of 2.9 mm. There are 9 groups of tubes with various lengths, and the average length is 19.7 m. In the secondary side, feedwater enters at the bottom of the boiler section, and two steam separators above the boiler section are used for moisture separation. The major components outside the steam generator vessel are main and auxiliary feedwater pumps and associated

pipings, steam line and steam isolation valves, and steam condensation system.

Pressurizer:

The pressurizer is a 600 mm ID x 4200 mm height cylindrical vessel with a fluid volume of about 1/48 of the PWR. The pressurizer vessel is connected to the intact loop hot leg pipe by a surgeline (3 inch, schedule 160 pipe). The PORV and safety valves, heater, and spray system were installed to simulate those of the PWR, but they were not activated during the test.

Primary Coolant Pump:

The primary coolant pump is a canned-type centrifugal design. The impeller, casing, and suction and discharge configuration are similar to those of the PWR pump. The pump homologous head and torque curves are presented in Figures 5.2.43 and 5.2.44 of Reference 141.

Primary Coolant Pipe:

The primary loop is a 2x2 equal loop arrangement. Both the hot leg and cold leg pump discharge pipes have an inside diameter of 207 mm, and the inside diameter of the pump suction pipe is 168 mm.

Emergency Core Cooling System:

The ECCS consists of CCI, HPI, RHR and accumulator injection. The pumped ECCS was not activated in this test. The accumulator tank has a volume of 4.8 m³, which is 50 percent larger than the scaled volume of 4 accumulator tanks in the PWR plant. The initial pressure of the cover gas was set at 4.51 MPa (654 psi) consistent with the value used in a PWR plant. There are two accumulator tanks, one each connected via a surgeline (4 inch, schedule 80 pipe) to the pump discharge piping.

Model Description

The ROSA RELAP5 base model was originally developed by EG&G for the ISP-26 program. The model, shown in Figures J.2 and J.3, consists of 166 hydrodynamic volumes, 174 junctions, and 166 heat structures. Volume and junction parameters are calculated with non-equilibrium and non-homogeneous models. Steam generator secondaries, ECC injection, and system environmental heat losses are modelled in detail. The core axial power profile is modelled with six stacked heat structures over six 610 mm long axial fluid volumes. The upper head region is nodalized to allow for junctions to be connected at the elevations of the top of the control rod guide tube and at the elevation of the holes in the guide tube below the upper core support plate. This model was verified against the design data provided in Reference J-1.

For this benchmark the EG&G model was revised to implement the provision of the BWNT SBLOCA calculation model to be proposed in revision 2 of BAW-10168 (The BWNT SBLOCA evaluation model was under revision at the time of this benchmark. The planned release date for the evaluation model was about a month after the release of BAW-10164, Revision 2). Alterations were primarily in primary system nodalization in selected regions. The required changes are discussed below, and the resulting EM nodalization is presented in Figures J.4 and J.5.

The downcomer, component 108, is reduced from 9 to 6 volumes. Volume 1 of component 108 extends from the top of the original volume to the elevation corresponding to the top of the core. Volumes 2, 3, and 4 extend from the top of the core to the bottom of the core, similar to the core baffle region nodalization in a PWR plant model. Volumes 5 and 6 are made equal to the volume lengths of the lower plenum volumes, 120 and 116, respectively. The upper downcomer volumes, 100 and 104 remain unchanged.

The core, component 124, is increased from 6 to 20 volumes, and the original core heat structure is divided into two heat structure groups, one representing 360 high power rods and the other 704 low power rods. Each heat structure is divided into 20 stacked heat structures with axial length equal to the corresponding fluid volume lengths. The core is divided into 20 unequal axial lengths such that each grid is located at the node boundary, and the axial power distribution is modified accordingly. No separate fluid channel is modelled for the high power heat structure because the core fluid temperature measurements indicate good mixing between the high power and low power bundles.

The upper plenum region, components 128, 132 and 136 in the original model, is increased from 3 to 6 volumes, and the heat structure is redistributed in accordance with the volume length.

The steam generator inlet nozzles (components 208-2 and 408-2) are 50 degrees inclined from horizontal (typical of the PWR design). In order to utilize the horizontal flow stratification model, these components are changed from the 50 degree vertical orientation to a 14 degree horizontal orientation to provide adequate draining of water from the steam generator inlet plenum through the hot leg to the pressure vessel.

The two volume nodalization in the steam generator plenum region in the original model is maintained instead of one volume in the plant model, because the LSTF plenum volume is oversized (1/24 of a PWR). The steam generator tubesheet is combined with the upper volume of the plenum region on both inlet and outlet sides. In order to simulate the differential draining of fluid in the steam generator tubes observed in the experiment, the steam generator tube volume is divided into two parallel channels, one representing 78 short tubes (types 1 through 4 in Figure 5.3.4b

of Reference 142), and the other 63 long tubes (types 5 through 9 in Figure 5.3.4b of Reference 142). Each channel contains 16 volumes, eight volumes each on the upflow and downflow sides. The tube heat structures are revised in accordance with the corresponding fluid volume lengths.

The pump suction piping is increased from 9 to 10 volumes (6 for the downflow and 4 for the upflow). The noding changes are primarily in the downflow side (components 232 and 432 for broken and intact loops respectively) including horizontal section of the U-bend to improve spatial representation that affects fluid conditions and timing of the pump suction seal clearing. Volume 1 represents the steam generator outlet nozzle (40 degree bend), and volumes 2 through 5 represent the vertical section of the downflow side with the bottom volume substantially smaller than the others. Volume 6 models the horizontal section of the U-bend. The upflow side (components 236 and 436 for broken and intact loops respectively) is represented by 4 volumes similar to the original model. Heat structures are redistributed accordingly.

The intact loop pump discharge piping is increased from 3 to 4 volumes, and the heat structure is revised accordingly.

The pressurizer surgeline volume is reduced from 3 volumes to 1 volume. The elevation change from the pressurizer outlet to the hot leg is conserved.

The revised model consists of 223 volumes, 233 junctions, and 280 heat structures. Volume and junction parameters are calculated with non-equilibrium and non-homogeneous models similar to the base model except for the core region where equilibrium modeling is used. In addition, the Wilson drag model is applied to vertical volumes in the pressure vessel and primary loops.

Counter current flow limiting (CCFL) is applied to the junctions at the steam generator plenum and tube inlets. The Wallis correlation from Reference 145 is used in the steam generator tube inlet junction, and the CCFL correlation based on the UPTF data from Reference 146 is used in the steam generator plenum inlet junction. The results of the CCFL calculation will be discussed later. The SBLOCA EM heat transfer model is used for the core heat transfer calculation. This model uses the BWUMV CHF correlation to calculate DNB, and permits return to nucleate boiling when rewetting is calculated during the post-DNB period.

A discharge coefficient of 1.1 is used for subcooled flow and two-phase flow up to 70 percent void fraction, and the two-phase coefficient is reduced to 0.77 for void fraction greater than 70 percent. These relative values were used to match a measured flow, and are consistent with the relationship of discharge coefficients with respect to void fraction discussed in Volume 2 Section 4.3.2.3 of BAW-10168, Revision 2.

Results of the Benchmark

The steady-state initial conditions for the benchmark are presented along with the test conditions in Table J.2. To demonstrate model stability relative to time advancement, the EM model was run with a time step advancement of 0.05 seconds (base case) and with a reduced time step of 0.005 seconds. Figures 6 through 10 show the results of the time step study, and confirm that the reduced time step advancement does not change the results. A comparison of the results of the base case (RELAP5/MOD2 EM) with the experimental data identified with instrumentation tag names listed in Reference 142 is presented in Table J.3 and Figures J.11 through J.36 below.

The calculated sequence of major events are presented along with the test data in Table J.3. Due to a facility power limitation,

the initial core power is only 14 percent of the scaled PWR power. To compensate for the power deficiency during the early phase of the transient, the initial core power was maintained for approximately 38 seconds after the reactor scram (8.3 seconds) until it matched the decay power rate based on the initial core power equivalent to the scaled PWR power. Thereafter, the power was reduced in accordance with the decay power curve. The calculation was forced to model this simulation.

The transient was initiated at time zero by opening the leak, and thereby causing a flow of subcooled fluid out the break, resulting in a rapid system depressurization followed by pump coastdown and loss of two-phase circulation. Then, the system enters the reflux cooling mode until clearing of the pump suction seals. The loop seal clearing was accompanied by changes in discharge flow characteristics and system depressurization. Reflux cooling was lost as the primary system depressurized rapidly below the secondary side pressure. Figures J.11, J.12 and J.13 show the leak flow rate, the primary system pressure response, and pressurizer liquid level, respectively. The figures show that the predictions are in good agreement with the experimental results. The secondary system pressure responses are presented in Figures J.14 and J.15. These figures also demonstrate good agreement between the calculations and the experimental results. The pressure perturbation during the early phase of the transient is caused by actuation of relief valves.

The differential pressures for the pump suction downflow and upflow sides in Figures J.16 through J.19 show good agreement in loop seal responses between the calculations and the experimental results. The calculations show that the broken loop seal cleared slightly ahead of the intact loop seal because of its proximity to the leak. But the experimental data seemed to indicate that the both loop seals cleared almost simultaneously. The predicted

time of loop seal clearing is about 16 seconds later than the experiment due to under-prediction of the leak flow. Note that the measured initial differential pressure in the downflow side is approximately 5 KPa higher than that of the calculations. This could be caused by the lower tap instrumentation pipe, for the differential pressure measurement (DPE070/DPE210 in Figure 6.11c of Reference 142), extending below the bottom of the horizontal pipe in the pump suction U-bend. This would be sufficient to produce the additional required static head; but no detailed instrumentation design information is available to confirm the hypothesis.

Figures J.20 and J.21 show differential pressures in the core and downcomer, respectively. The system hydrostatic head balance caused the first core depression during clearing of the pump suction seals. Because of liquid holdup in the steam generator upflow sides, the core level decreased below the level corresponding to the bottom of the pump suction pipe (1.86 m above the bottom of the core). Prior to clearing of the pump suction seals, the remaining fluid in the primary system for core cooling was centered in the pressure vessel and steam generator upflow sides. Following loop seal clearing, the core was reflooded from the bottom by downcomer fluid and from the top by draining of the steam generator upflow side fluid. The second core depression was predicted at 320 seconds, approximately 80 seconds earlier than the experiment.

Since both the experiment and calculation have the same core level depression and downcomer level at their respective time of loop seal clearing (140 seconds for the experiment and 156 seconds for the calculation), and the bottom flooding was not sufficient to match core boil-off, the second core depression was greatly influenced by the top flooding. Figures J.22 through J.25 show differential pressures in the steam generator plenums

and tubes for the upflow side. These plots show the differential pressure in the inlet plenum for the experiment is greater than that for the calculation, and vice-a-versa for the tubes as a result of the system hydrostatic balance. The cross-sectional area of the inlet plenum is approximately four times larger than that of the tubes. Thus, water in the inlet plenums became a major source of coolant for the top flooding. Furthermore, Figures J.22 and J.23, and the differential pressure in the vessel upper plenum in Figure J.26 also show a prolong draining period in the experiment that resulted in delaying the second core depression for approximately 80 seconds. Because the calculated second core depression occurred earlier, and continuous core depression reduced steam generation, this resulted in a faster system depressurization between 350 and 420 seconds as shown in Figure J.12.

Figures J.27 and J.28 show the differential pressures in the steam generator long and short tube groups for the downflow sides. The downflow side drained faster than the upflow side following pump coastdown. Figures J.29 and J.30 show the accumulator flow rates. As a result of the larger depressurization rate calculated during the second core depression (discussed above), the accumulator pressure set point was reached earlier in the calculation than in the experiment. The calculated flow rate is conservatively less than that of the experiment. The increase in accumulator flow after 500 seconds for both the calculation and experiment is caused by a faster system depressurization following quenching of the upper core that reduced steam production.

The temperature responses for various thermocouple locations are presented in Figures J.31 through J.36. Two major core liquid level depressions cause core heater rod temperature excursions. The first of these depressions occurs as a result of loop seal

clearing. Depletion of the core inventory occurs rapidly with water remaining in the steam generator inlet plenum and tubes. That leads to a highly voided core region but not to complete voiding. The retained water prevents superheating within the RELAP control volumes resulting in an underprediction of both vapor and cladding temperatures. Although observable as potentially nonconservative, the underprediction of cladding temperatures at loop seal clearing is not of significant consequence. This phase of SBLOCA has been studied in numerous experiments and consistently found to be of short duration and limited temperature excursion. The more important aspect of core liquid depletion during loop seal clearing is that the inventory during and after the excursion provides the initial liquid inventory for the core boildown phase. Because cladding temperature excursions can only occur at relatively high void fractions, approximately 0.95 or greater, the fact that excursions were calculated demonstrates that the core inventory during and after loop seal clearing was reasonably well predicted. This is further evidenced by the timing of the second temperature excursion.

The second temperature excursion occurred during the core boildown phase. Because this excursion is not limited in duration or extent and is highly dependent on ECCS design and capacity, it is appropriate and significant that the cladding temperature and other controlling parameters be conservatively predicted. Although the temperatures during the experiment were not significant relative to LOCA acceptance criteria, it is evident that the modelling successfully and conservatively established conditions under which the cladding temperature was overpredicted. The heatup period was longer and the temperature excursion higher than the experiment; thereby, confirming the conservatism of the modelling.

The CCFL model was applied to junctions at the steam generator plenum and tube inlets. Figures J.37 through J.39 show the calculated values of j_f^* , j_g^* , and the Wallis constant, C , respectively, at the broken loop steam generator tube inlet. Figures J.40 through J.42 show the CCFL parameters at the broken loop steam generator plenum inlet. In Figures J.39 and J.42, the value for C is set to zero when the flow is co-current. When the flow is counter current, the maximum value for the liquid downflow is limited by the CCFL correlation.

b,c,d,e

From these figures it can be observed that, during the counter current flow period, the RELAP5 calculated flow satisfies the CCFL correlation. In Figure J.39, the calculated constant C exceeds the input value only when the liquid velocity is near zero. Figure J.37 also shows that, from 100 to 140 seconds, the flow in the short tube is co-current and the flow in the long tube is counter current.

Conclusions

RELAP5/MOD2-B&W calculated the major events of the ROSA-IV SB-CL-18 experiment; blowdown, two-phase natural circulation, reflux boiling and liquid holdup, pump suction seal clearing, core liquid level depression, and accumulator injection and core recovery in the proper sequence. The benchmark calculated the overall system responses in good agreement with the experimental data. The code also conservatively predicted heater rod surface temperature during the boil-off phase of the transient.

The SBLOCA EM features and nodalization described in Volume 2 of BAW-10168, Revision 2 are sufficient to meet the calculational needs for the benchmark analysis. The results of the analysis demonstrate that the BWNT version of RELAP5/MOD2 can adequately predict system thermal-hydraulic responses during SBLOCA.

Table J.1. Major Design Parameters of LSTF and PWR.

<u>Items</u>	<u>LSTF</u>	<u>PWR</u>	<u>PWR/LSTF</u>
Pressure, MPa	16	16	1
Hot Leg Temp, K	598	598	1
Cold Leg Temp, K	562	562	1
No. of Fuel Rods	1064	50952	48
Core Height, m	3.66	3.66	1
Core Power, MW	10 [*]	3423	NA [*]
Fluid Volume, m ³	7.23	347	48
Power/Volume, MW/m ³	1.4 [*]	9.9	NA [*]
Core Inlet Flow, Kg/s	48.8 [*]	16700	NA [*]
Downcomer Width, m	0.053	0.26	4.91
Hot Leg Pipe ID, m	0.207	0.737	3.56
No. of Loops	2	4	2
No. of Tubes/SG	141	3382	24
Ave Length of Tubes, m	19.7	20.2	1
CL PS Pipe ID, m	0.168	0.787	4.69
CL PD Pipe ID, m	0.207	0.699	3.37
Acc Pressure, MPa	4.51	4.24	1

* Initial core power is limited to 14 percent of the scaled PWR power. To compensate for the power deficiency during the early phase of the transient, the initial core power was maintained for 47 seconds before power reduction in accordance with the decay power curve.

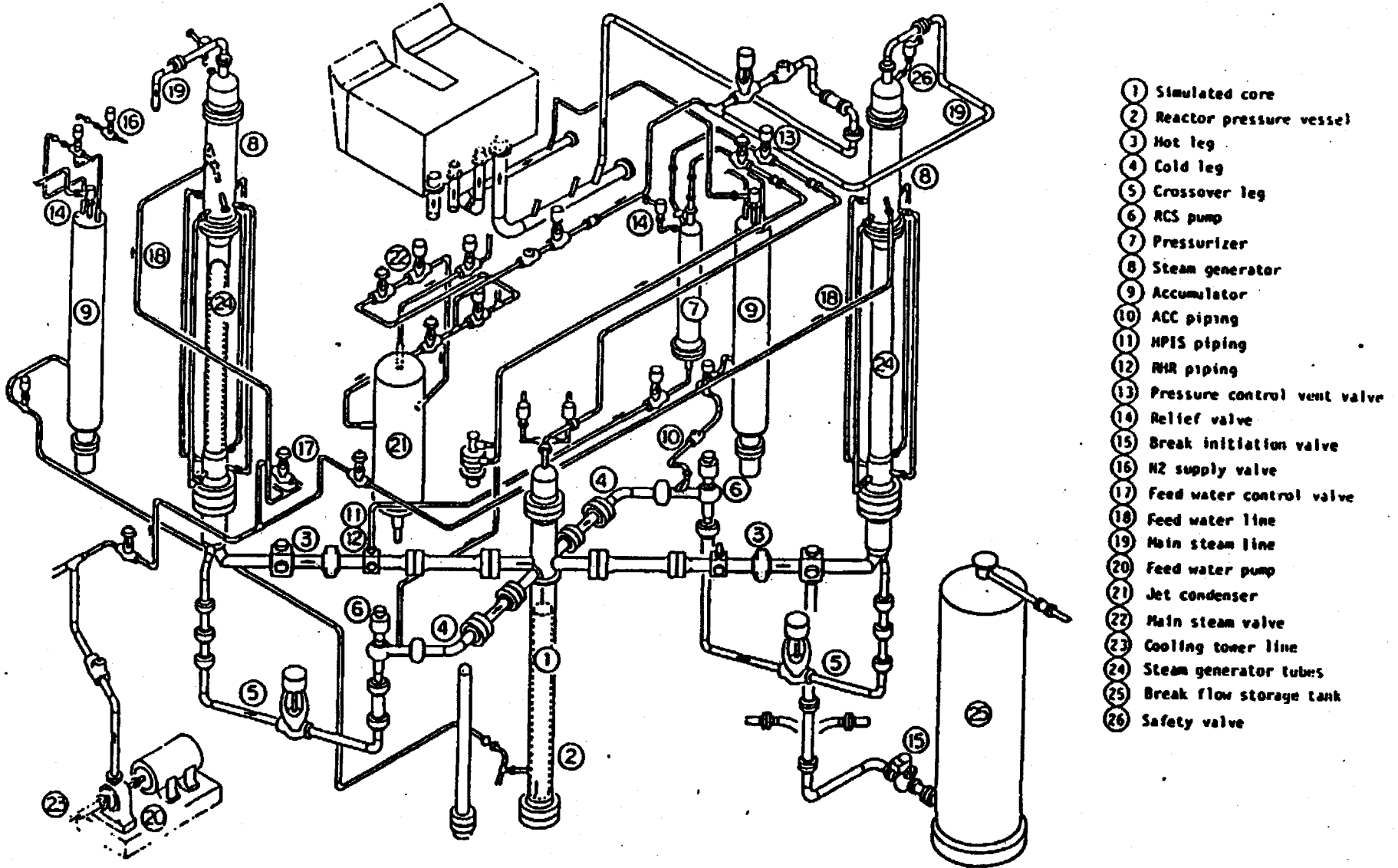
Table J.2. Initial Test Conditions.

<u>Items</u>	<u>Test¹⁴³</u>	<u>RELAP5</u>
Pressurizer Pressure, MPa	15.5	15.5
Hot Leg Fluid Temp. K	599	600
Cold Leg Fluid Temp. K	563	564
Core Power, MW	10	10
Core Inlet Flow, Kg/s	48.7	48.2
Pressurizer Water Level, m	2.7	2.7
Primary Coolant Pump Speed (IL/BL) RPM	769/796	828/828
SG Secondary side Pressure, MPa	7.3	7.3
Steam Flow, Kg/s	2.7	2.8
SG Secondary Side Level, m	10.8	9.0

Table J.3. Sequence of Events.

Events	Time, Seconds	
	Test ¹⁴³	RELAP5
Break Initiation	0.0	0.0
Reactor Scram	9.0	8.3
ESFAS Signal	12.0	12.6
Main Steam Line Isolation	14.0	14.0
Main Feedwater Isolation	16.0	16.0
Pressurizer Empty	25.0	60.0
Loss of Two-Phase Circulation	75.0	107.0
Loop Seal Clearing	140.0	156.0
Accumulator Injection	455.0	430.0
Core Recovered	540.0	560.0

Figure 1. ROSA Large Scale Test Facility Configuration.



- ① Simulated core
- ② Reactor pressure vessel
- ③ Hot leg
- ④ Cold leg
- ⑤ Crossover leg
- ⑥ RCS pump
- ⑦ Pressurizer
- ⑧ Steam generator
- ⑨ Accumulator
- ⑩ ACC piping
- ⑪ HPIS piping
- ⑫ RHR piping
- ⑬ Pressure control vent valve
- ⑭ Relief valve
- ⑮ Break initiation valve
- ⑯ N₂ supply valve
- ⑰ Feed water control valve
- ⑱ Feed water line
- ⑲ Main steam line
- ⑳ Feed water pump
- ㉑ Jet condenser
- ㉒ Main steam valve
- ㉓ Cooling tower line
- ㉔ Steam generator tubes
- ㉕ Break flow storage tank
- ㉖ Safety valve

J-17

Rev. 2
8/92

FIGURE J.2. ROSA NODING DIAGRAM FOR PRESSURE VESSEL

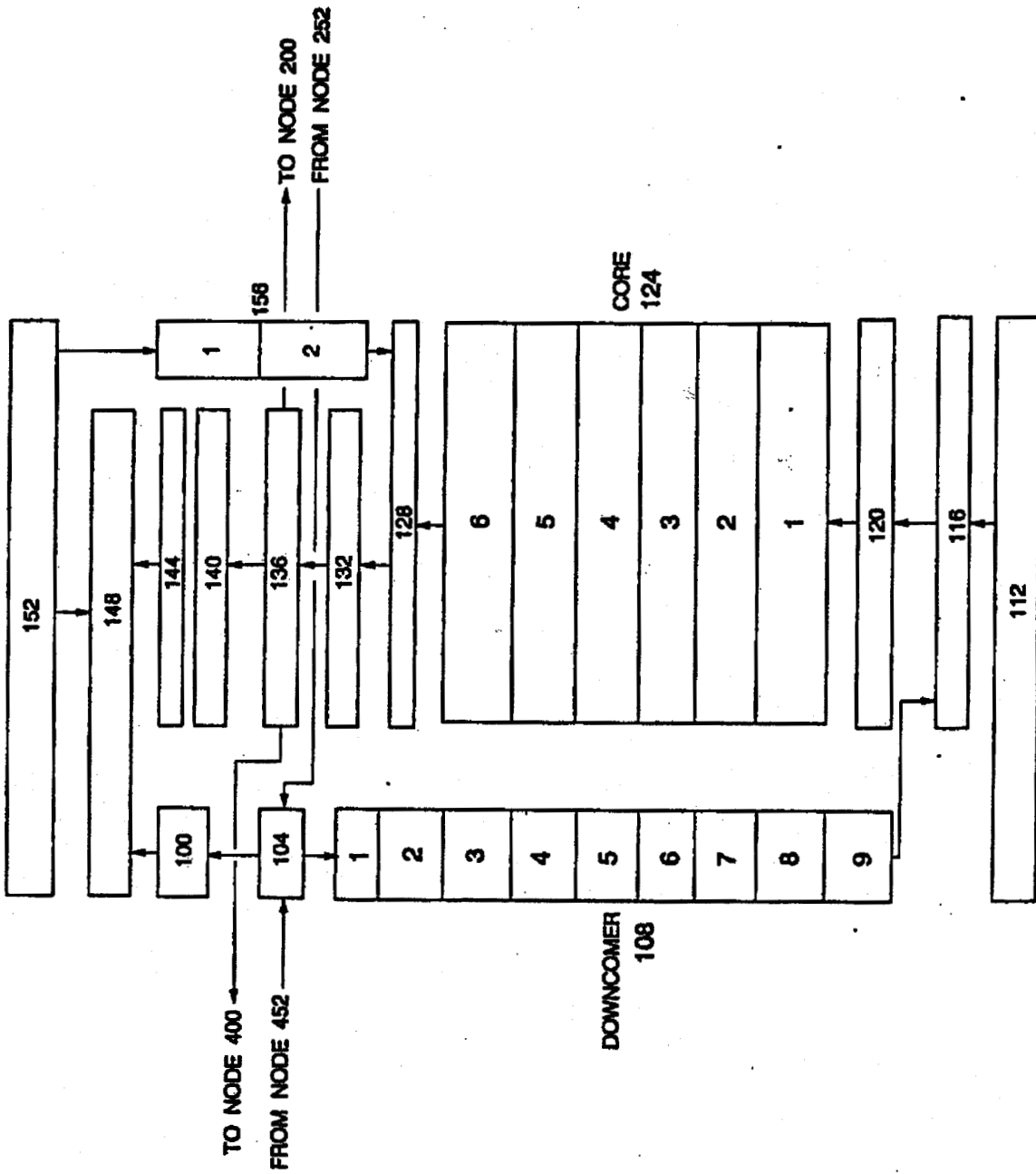
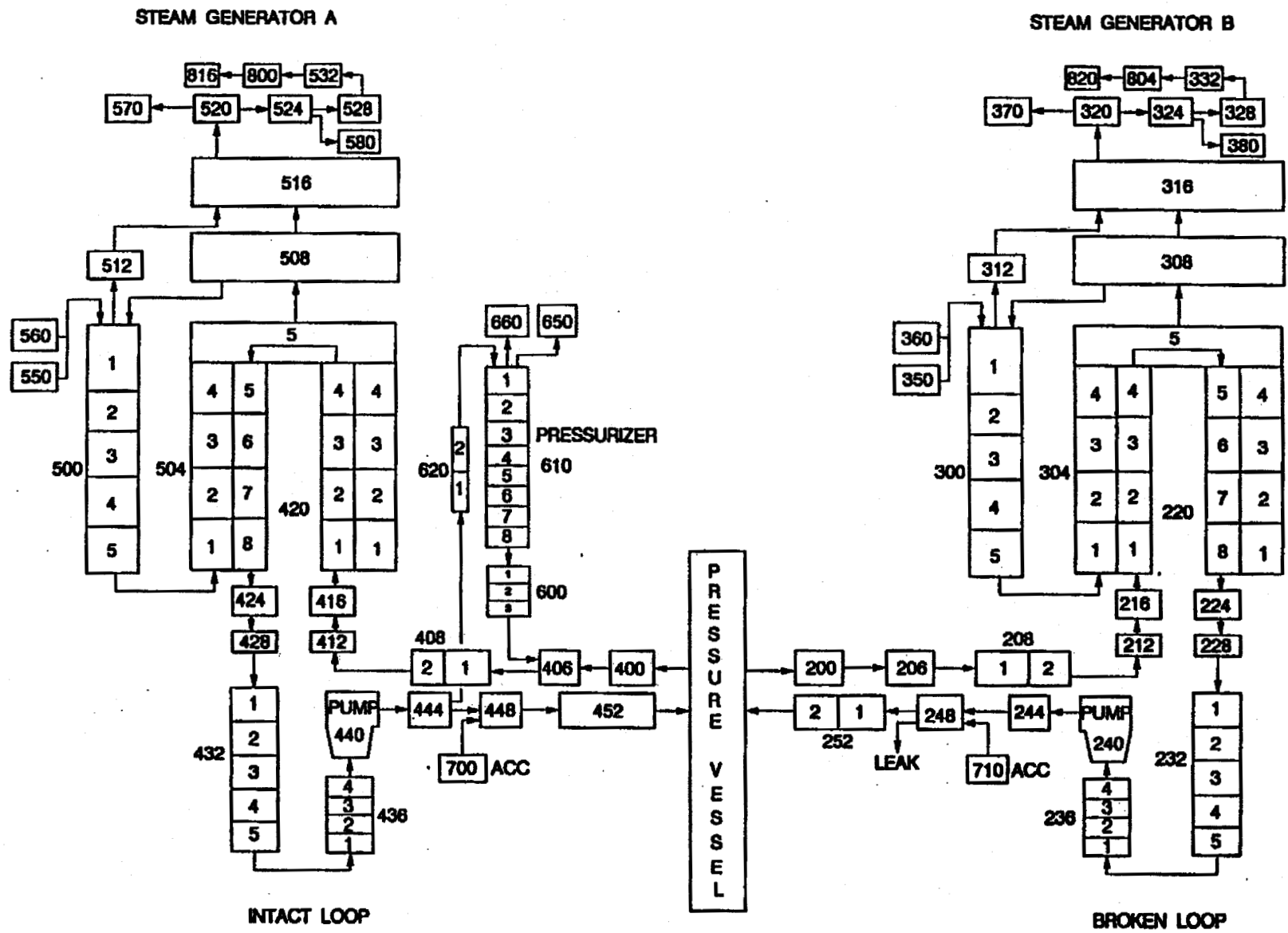


FIGURE J.3. ROSA NODING DIAGRAM FOR PRIMARY LOOPS.



J-19

Rev. 2
8/92

FIGURE J.4. ROSA SBLOCA EM NODING DIAGRAM FOR PRESSURE VESSEL

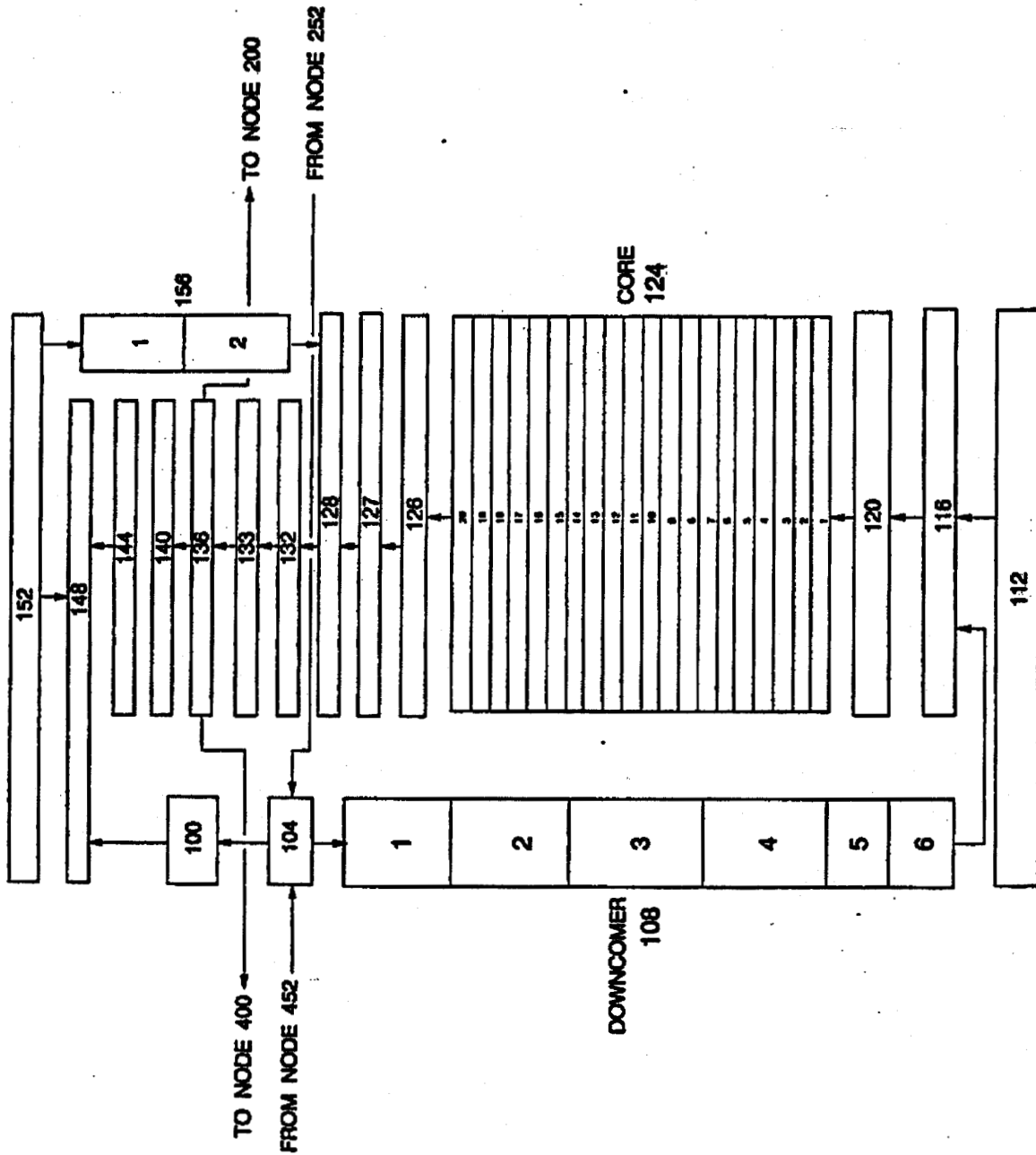


FIGURE J.5. ROSA SBLOCA EM NODING DIAGRAM FOR PRIMARY LOOPS.

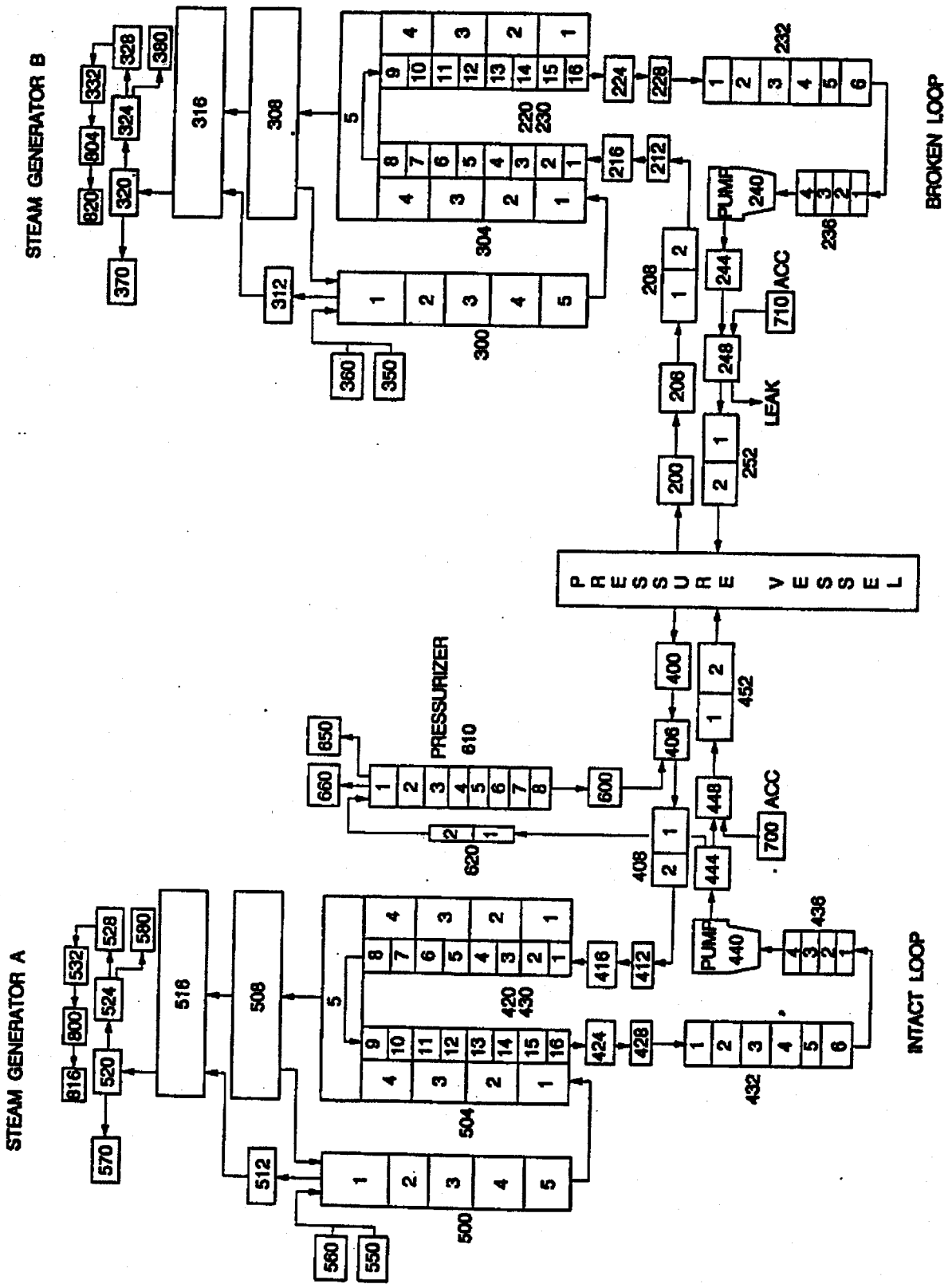


FIGURE J.6. LEAK FLOW RATE.

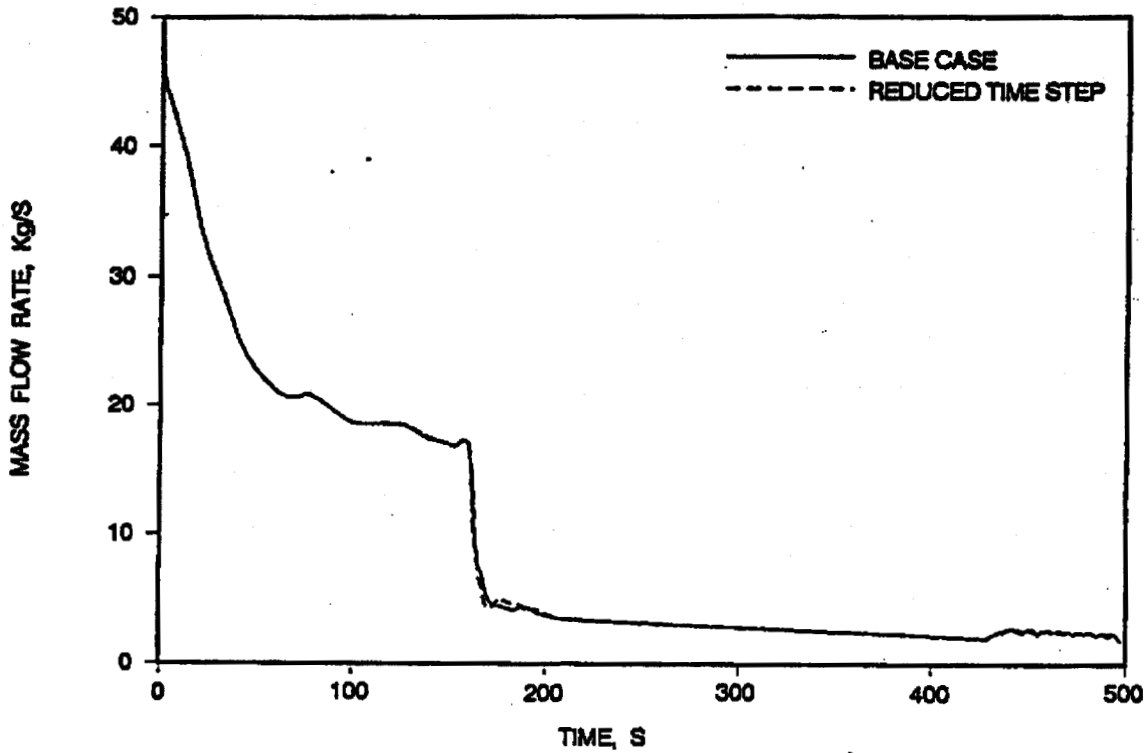


FIGURE J.7. PRIMARY SYSTEM PRESSURE.

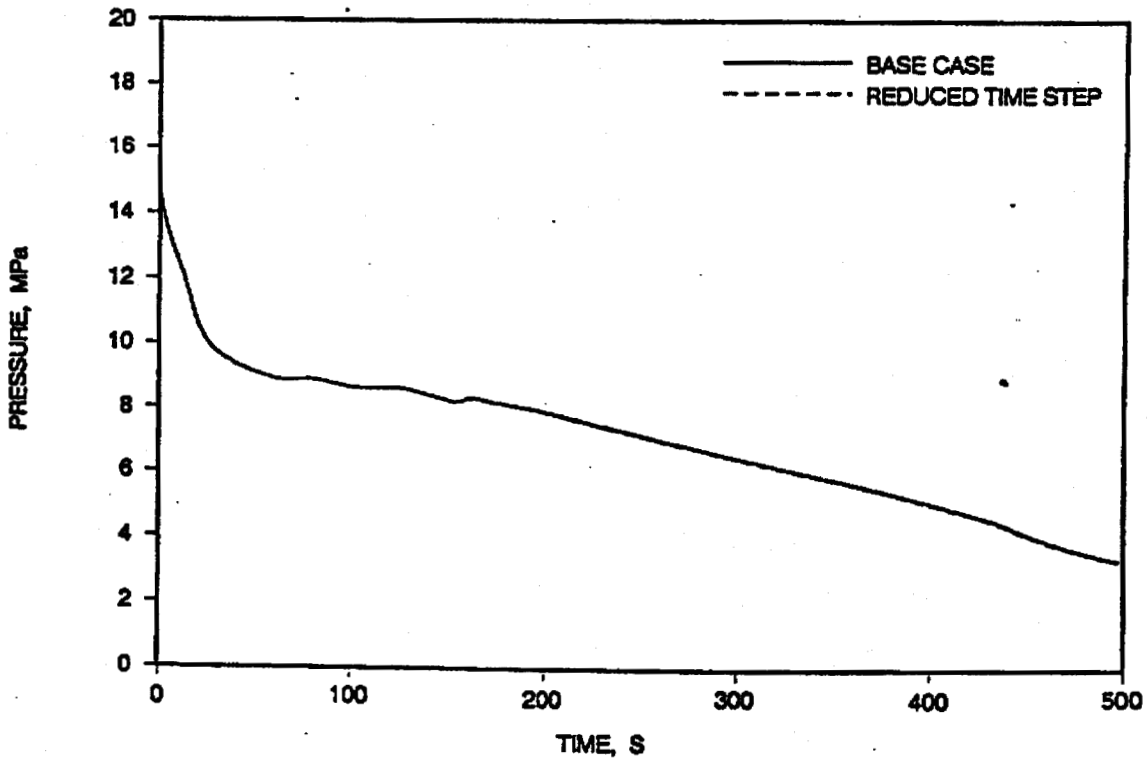


FIGURE J.8. CORE DIFFERENTIAL PRESSURE.

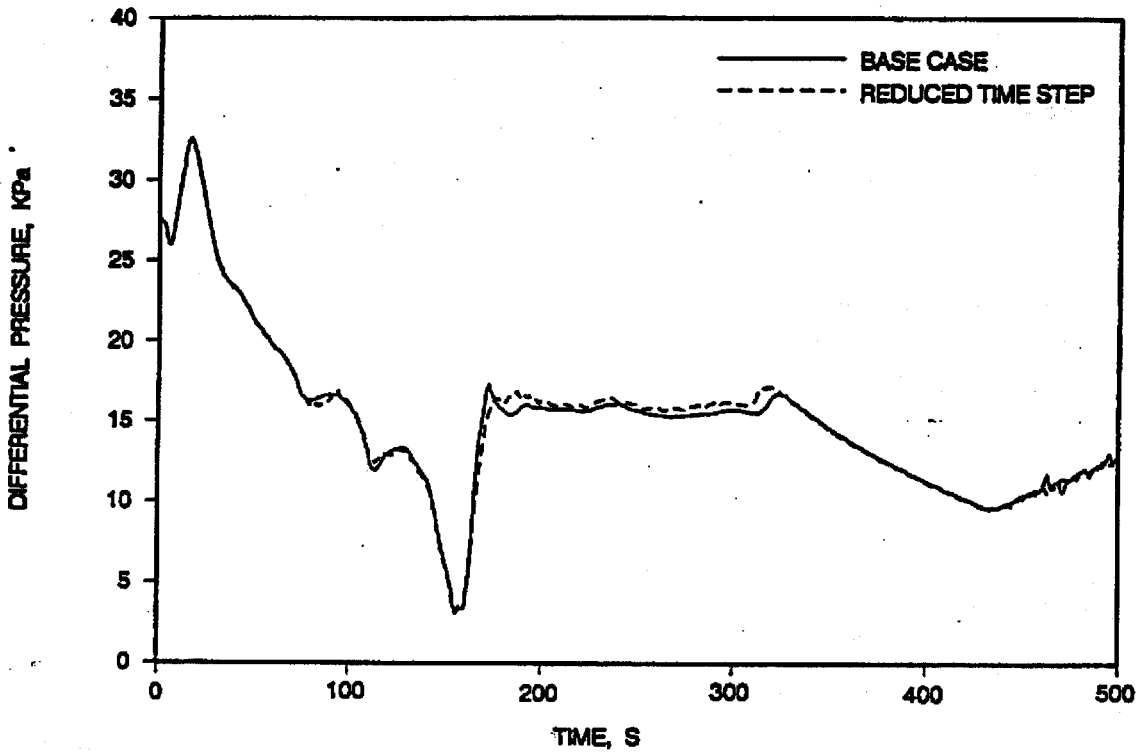


FIGURE J.9. INTACT LOOP PUMP SUCTION SEAL DOWNFLOW DIFFERENTIAL PRESSURE.

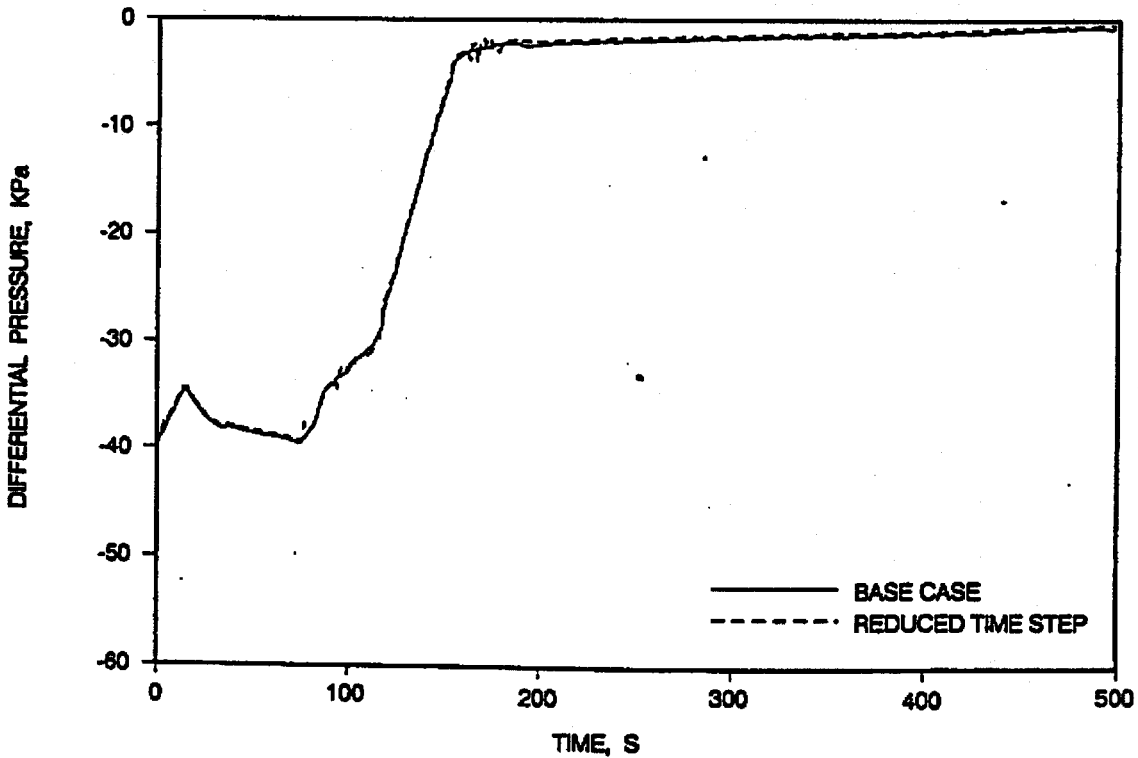


FIGURE J.10. BROKEN LOOP PUMP SUCTION SEAL DOWNFLOW DIFFERENTIAL PRESSURE.

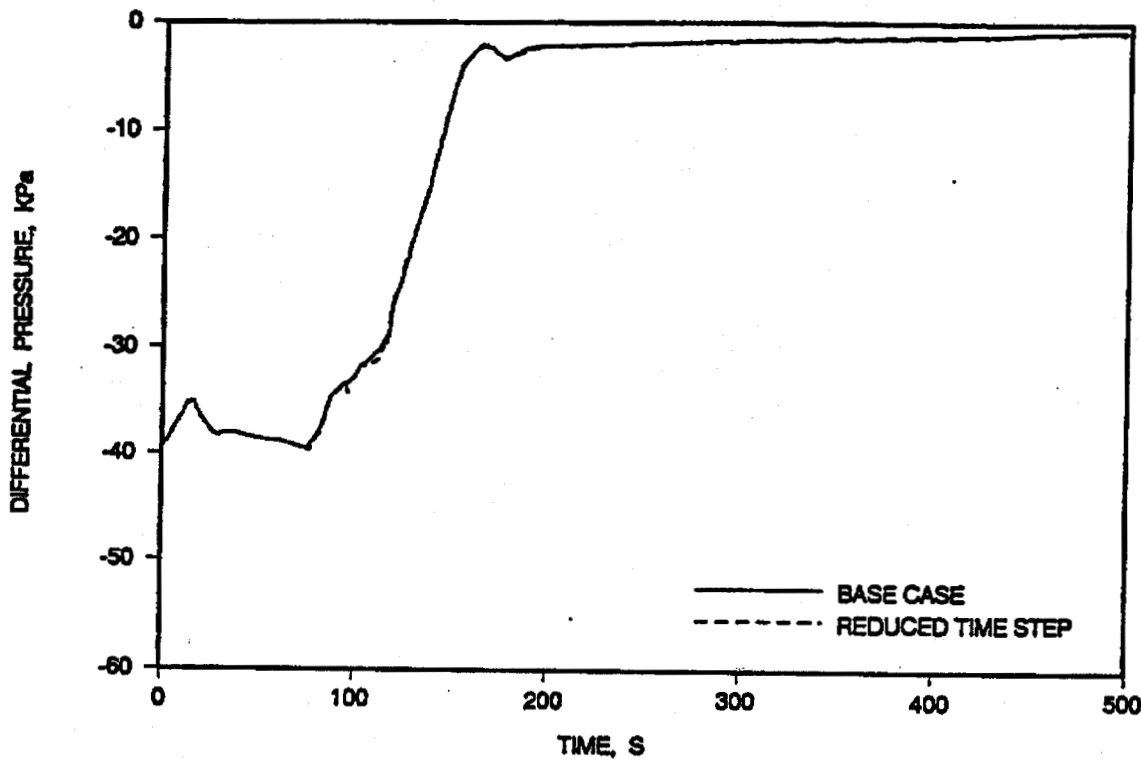


FIGURE J.11. LEAK FLOW RATE.

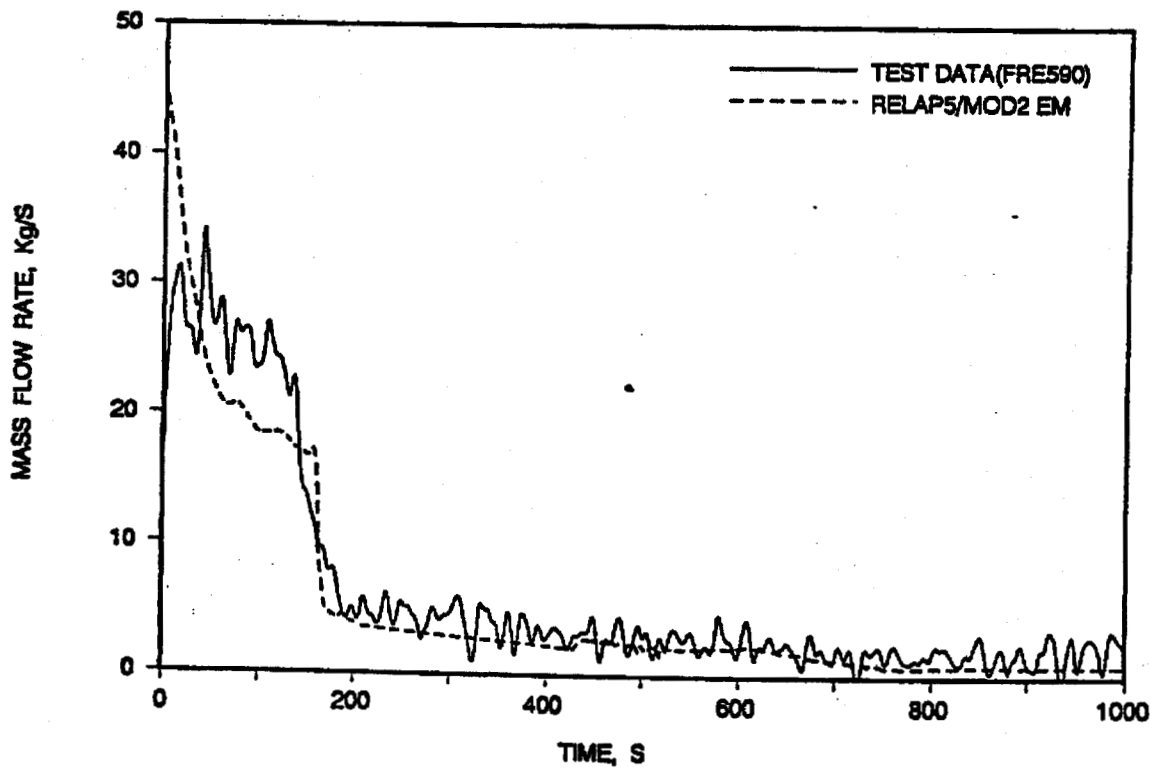


FIGURE J.12. PRIMARY SYSTEM PRESSURE.

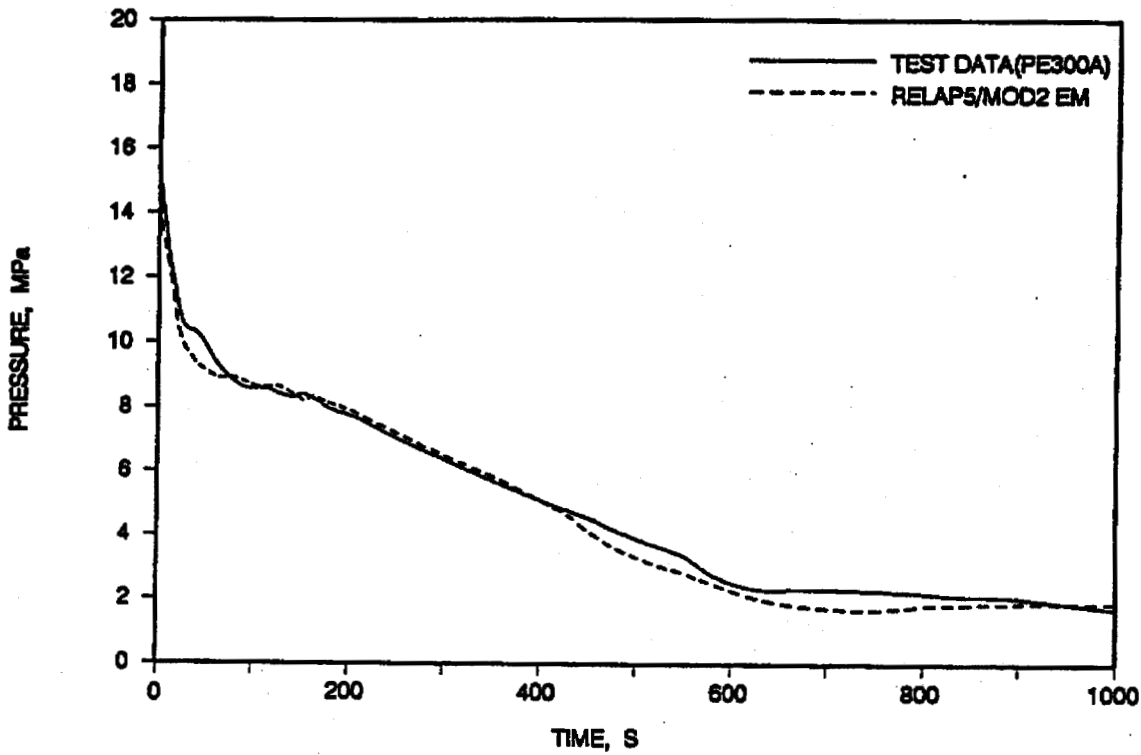


FIGURE J.13. PRESSURIZER LEVEL.

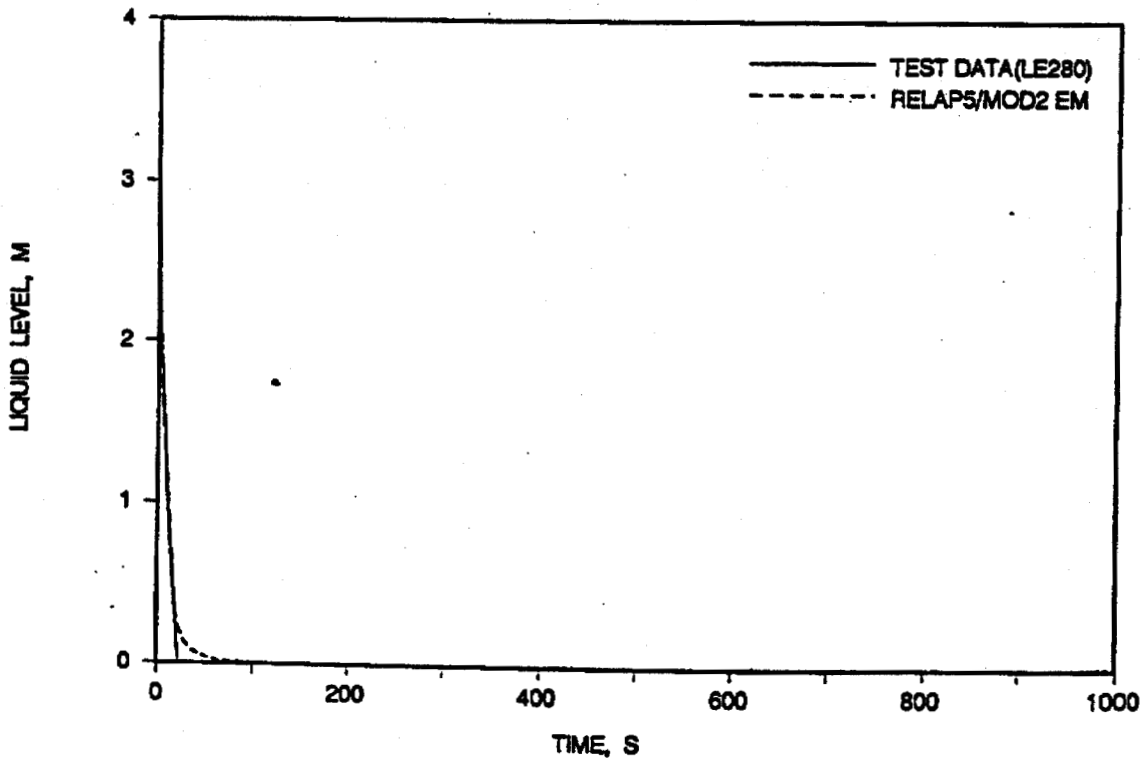


FIGURE J.14. INTACT LOOP STEAM GENERATOR PRESSURE.

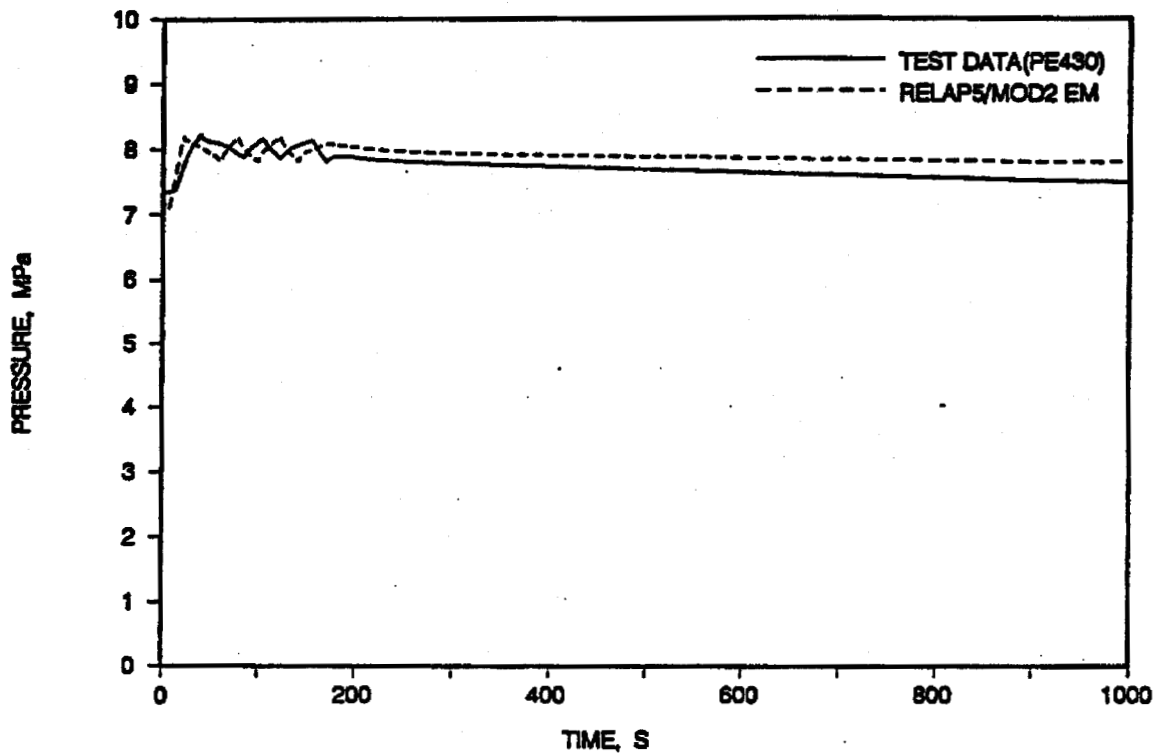


FIGURE J.15. BROKEN LOOP STEAM GENERATOR PRESSURE.

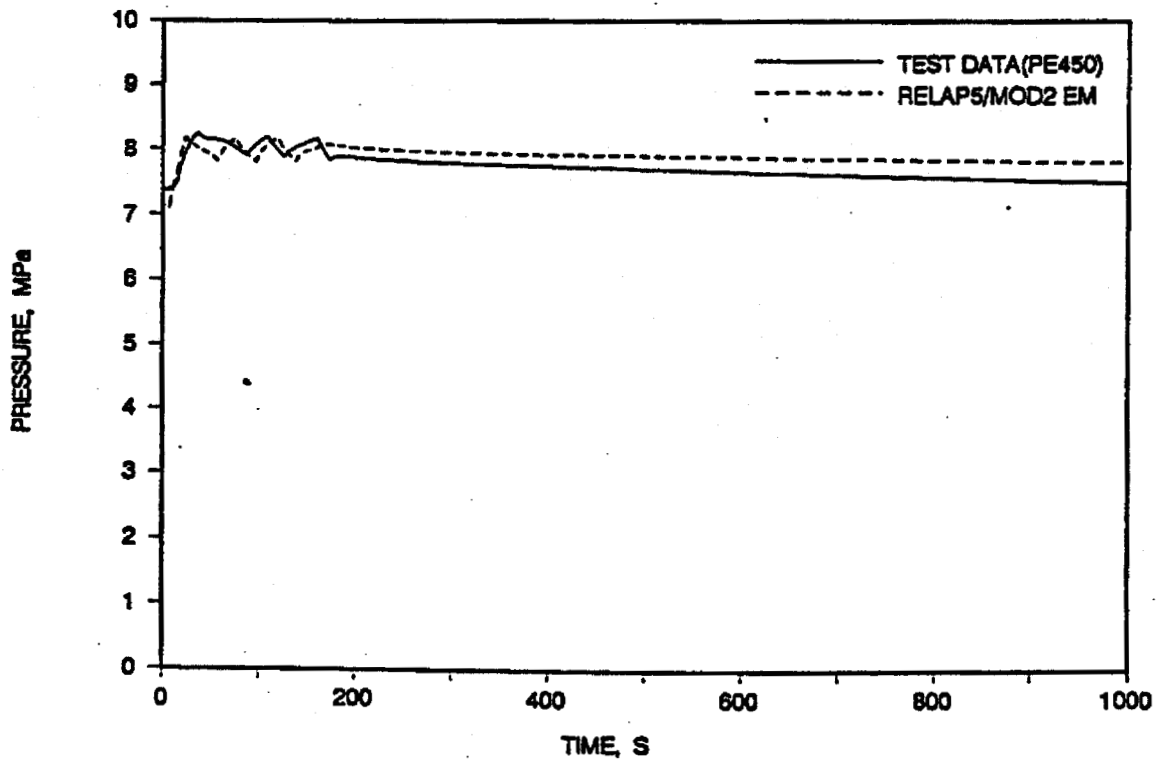


FIGURE J.16. INTACT LOOP PUMP SUCTION SEAL DOWNFLOW DIFFERENTIAL PRESSURE.

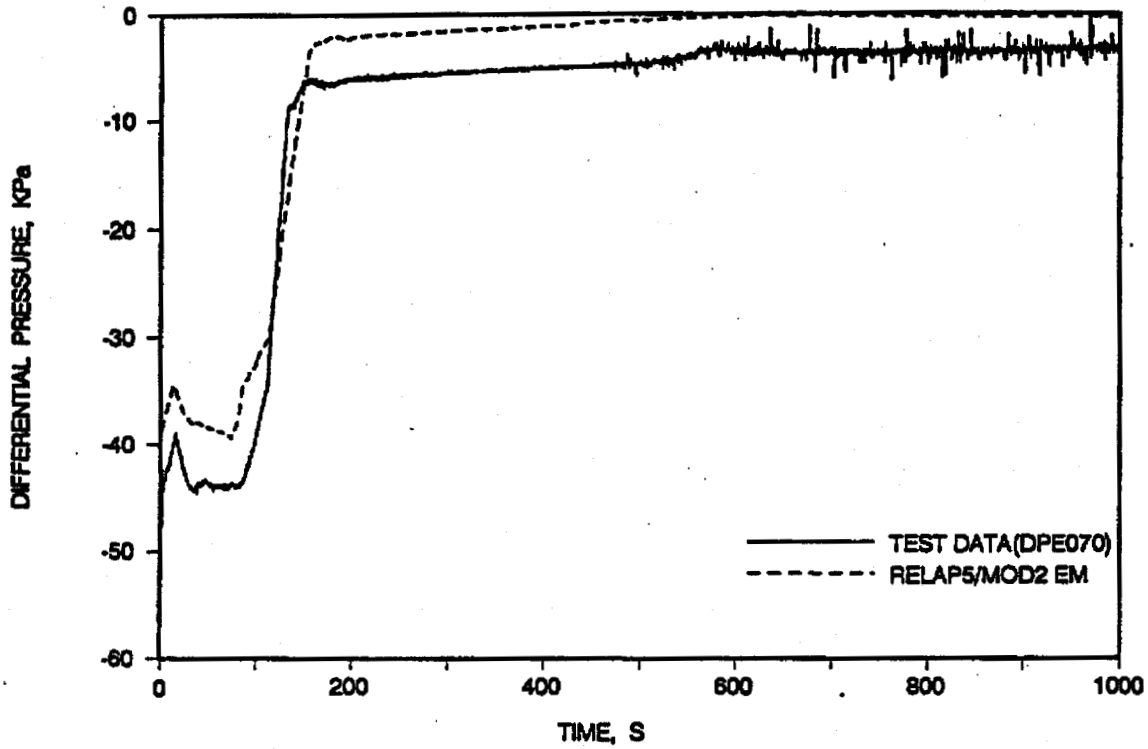


FIGURE J.17. INTACT LOOP PUMP SUCTION SEAL UPFLOW DIFFERENTIAL PRESSURE.

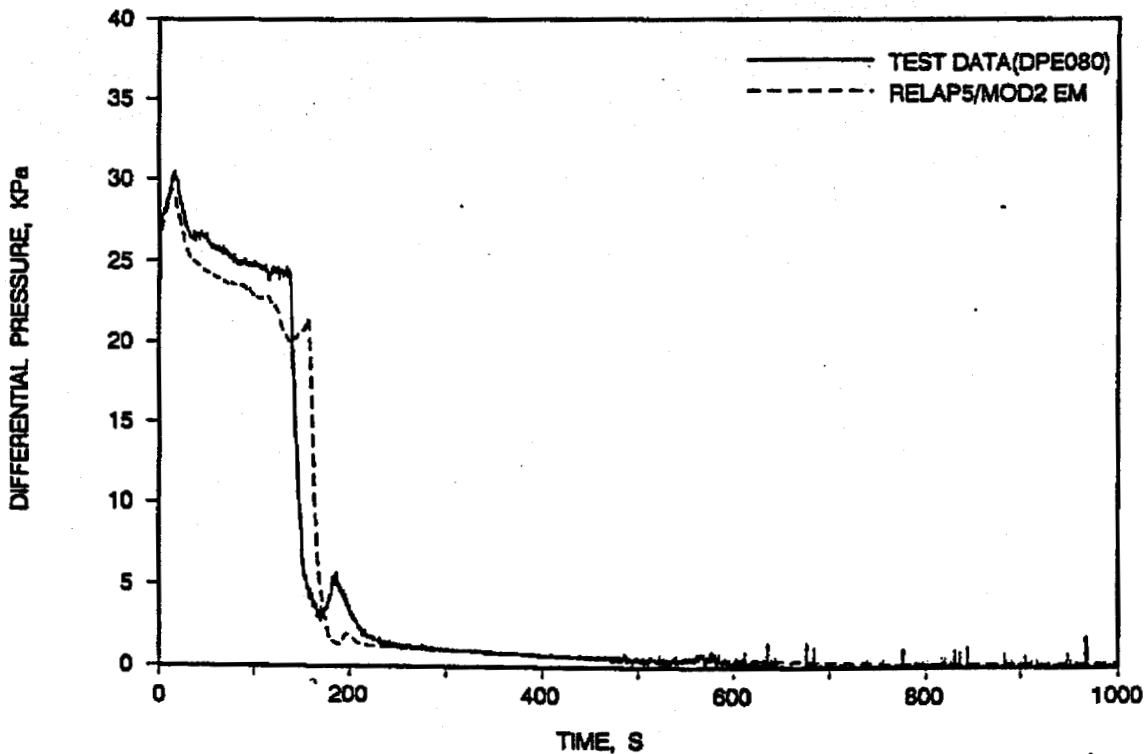


FIGURE J.18. BROKEN LOOP PUMP SUCTION SEAL DOWNFLOW DIFFERENTIAL PRESSURE.

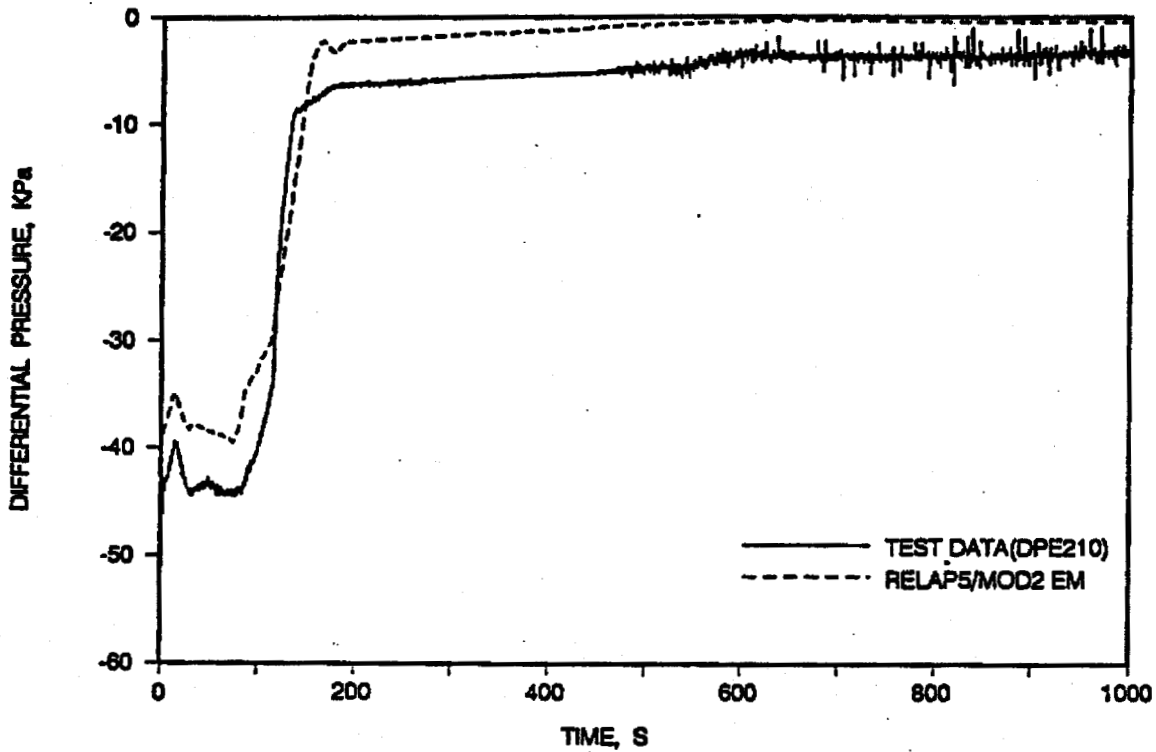


FIGURE J.19. BROKEN LOOP PUMP SUCTION SEAL UPFLOW DIFFERENTIAL PRESSURE.

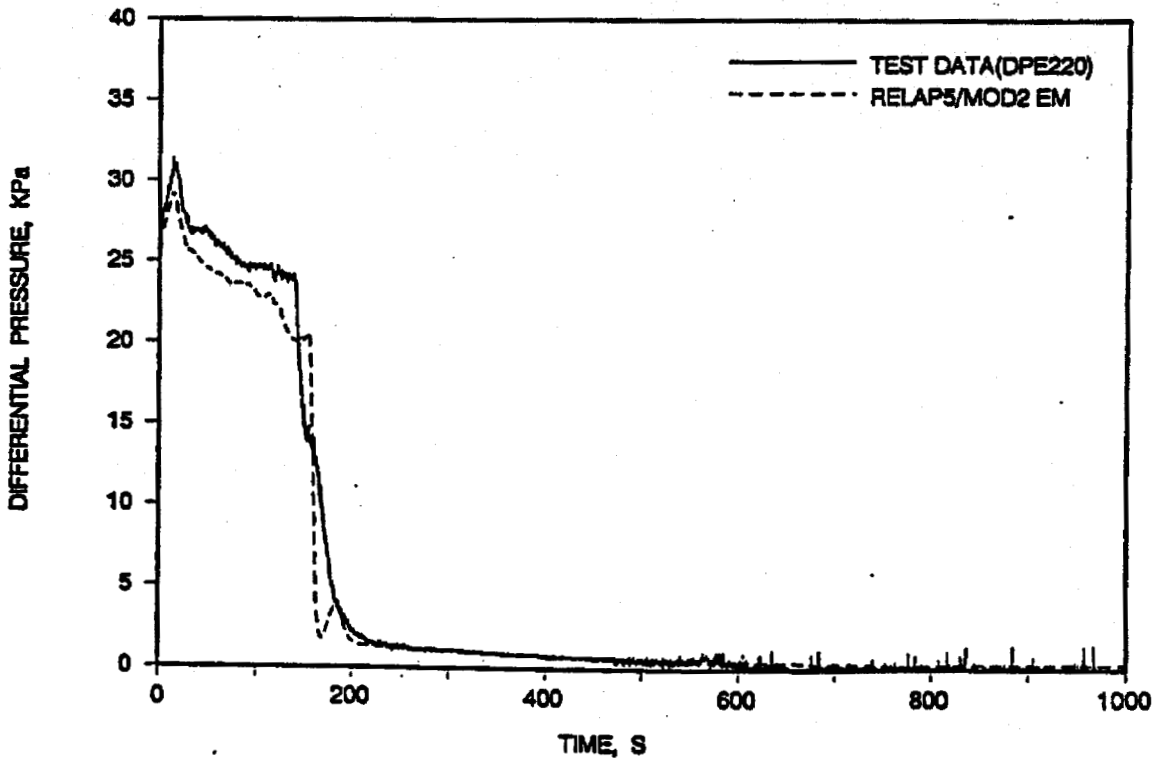


FIGURE J.20. CORE DIFFERENTIAL PRESSURE.

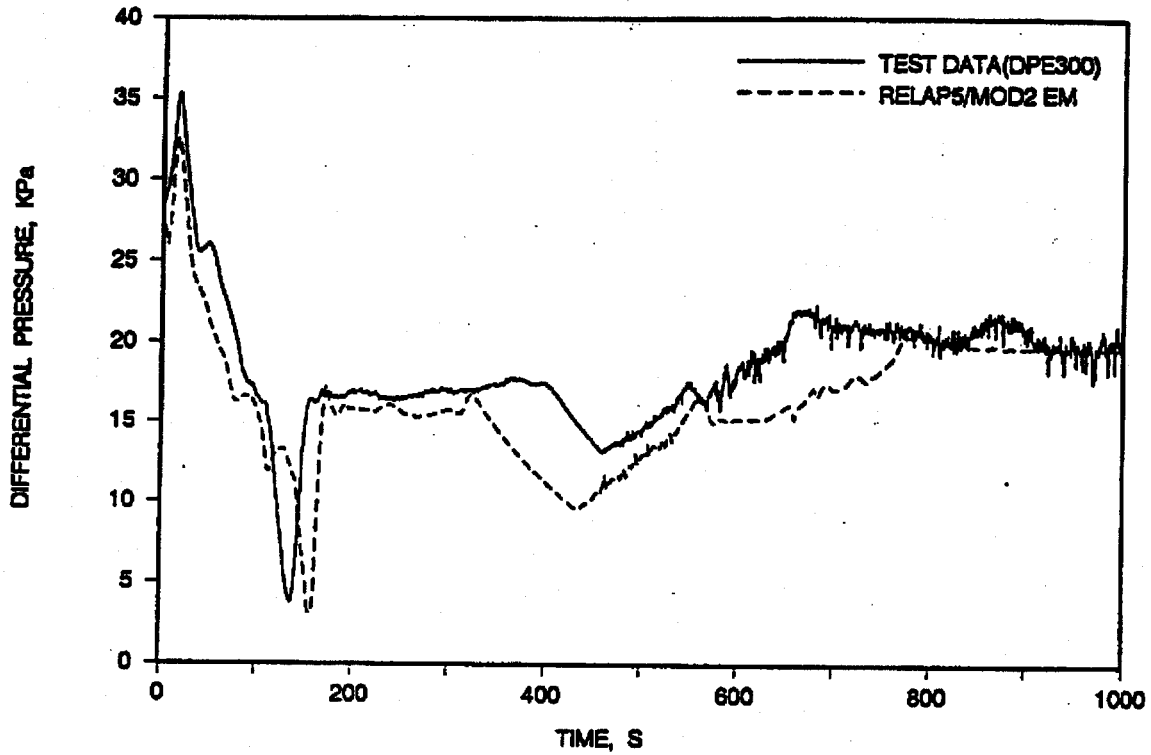


FIGURE J.21. DOWNCOMER DIFFERENTIAL PRESSURE.

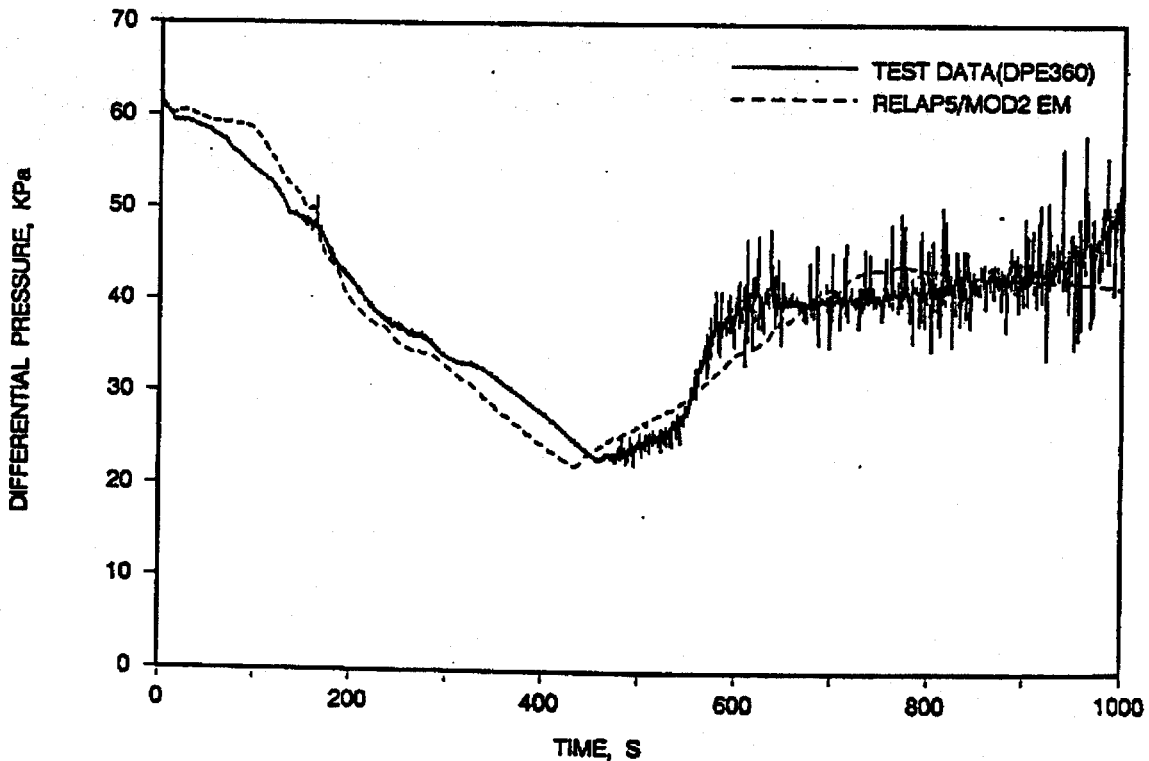


FIGURE J.22. INTACT LOOP STEAM GEN. INLET PLENUM DIFFERENTIAL PRESSURE.

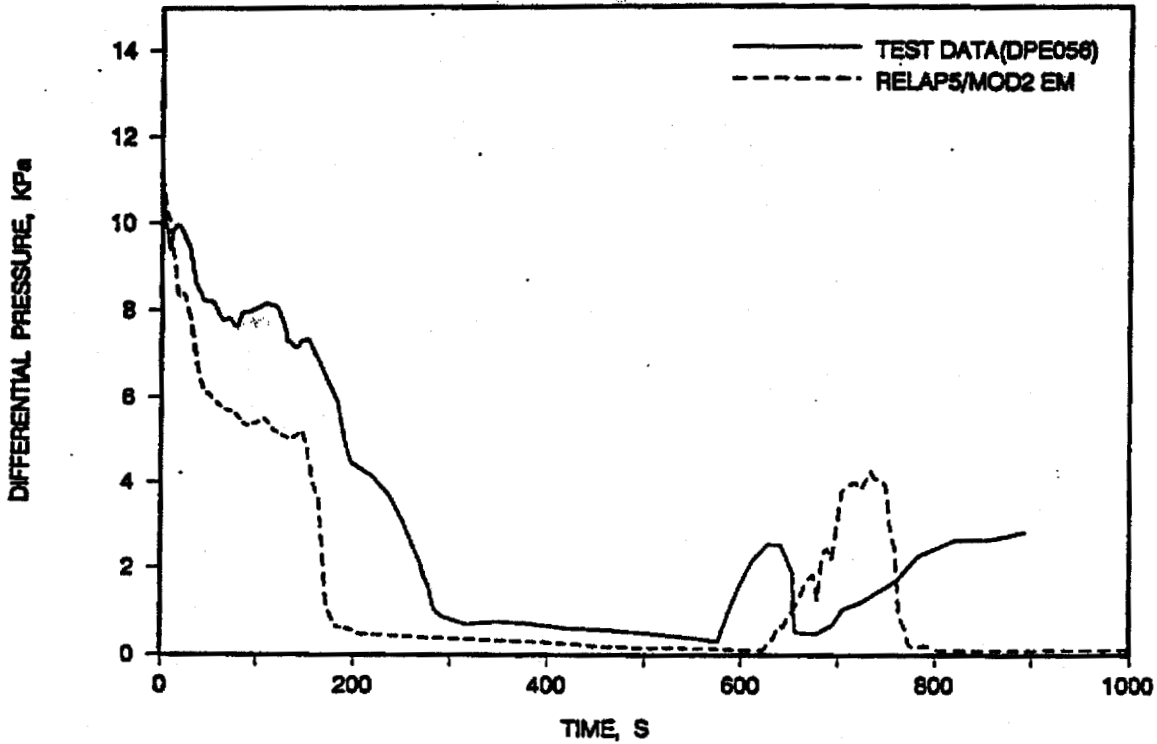
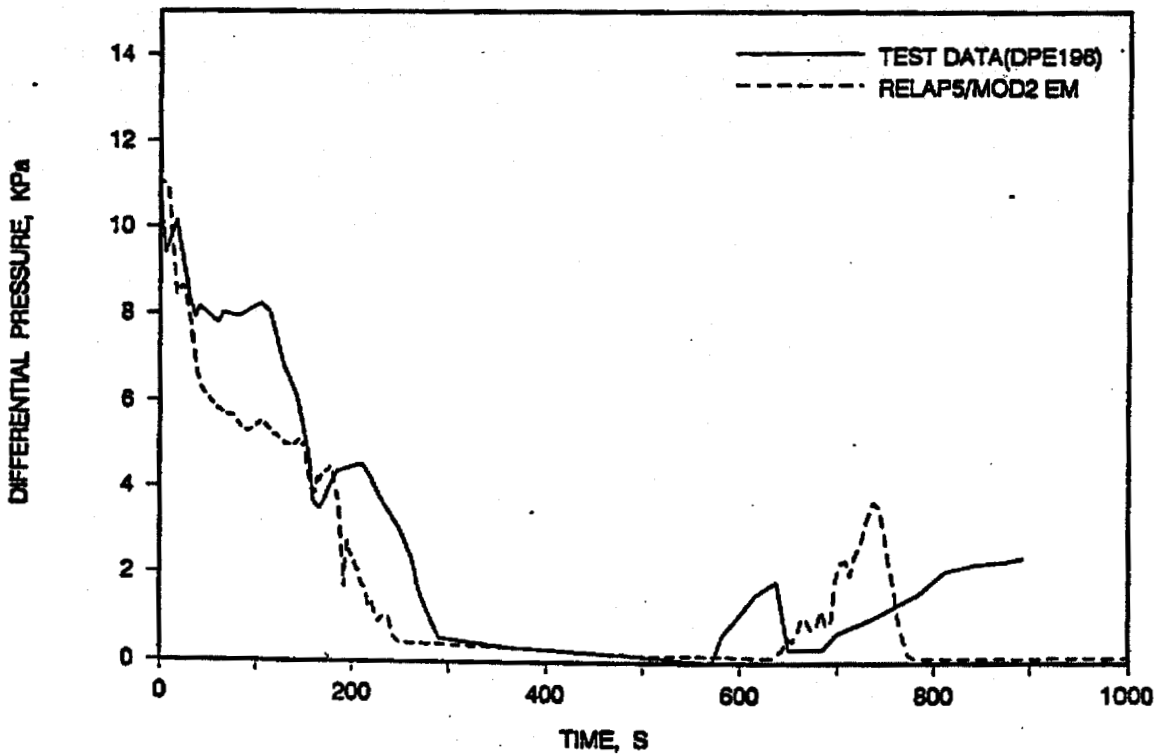


FIGURE J.23. BROKEN LOOP STEAM GEN. INLET PLENUM DIFFERENTIAL PRESSURE.



TIME, S

FIGURE J.24. INTACT LOOP STEAM GEN. TUBE UPFLOW DIFFERENTIAL PRESSURE.

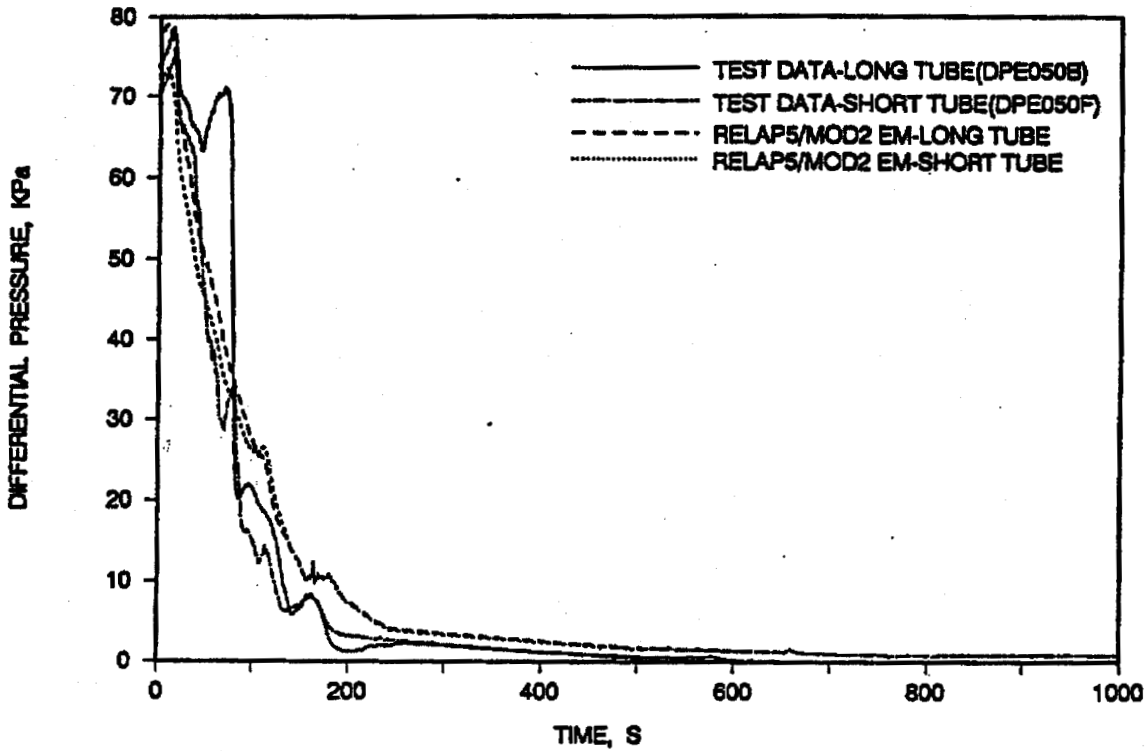


FIGURE J.25. BROKEN LOOP STEAM GEN. TUBE UPFLOW DIFFERENTIAL PRESSURE.

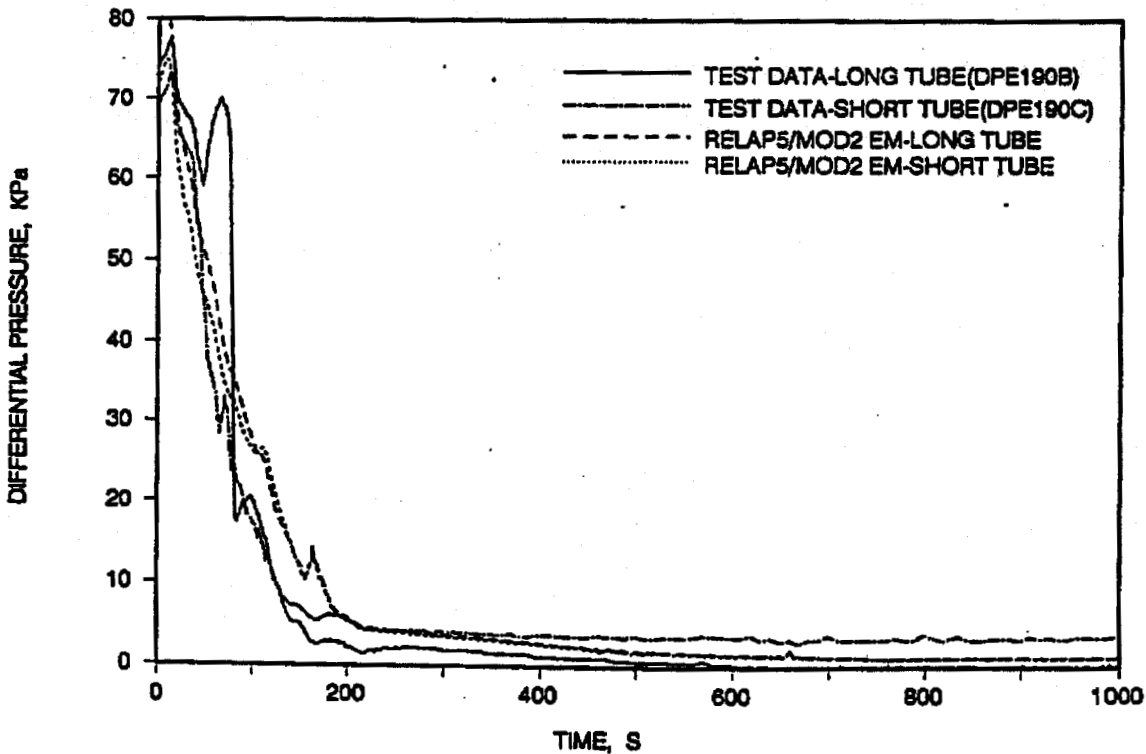


FIGURE J.26. UPPER PLENUM DIFFERENTIAL PRESSURE.

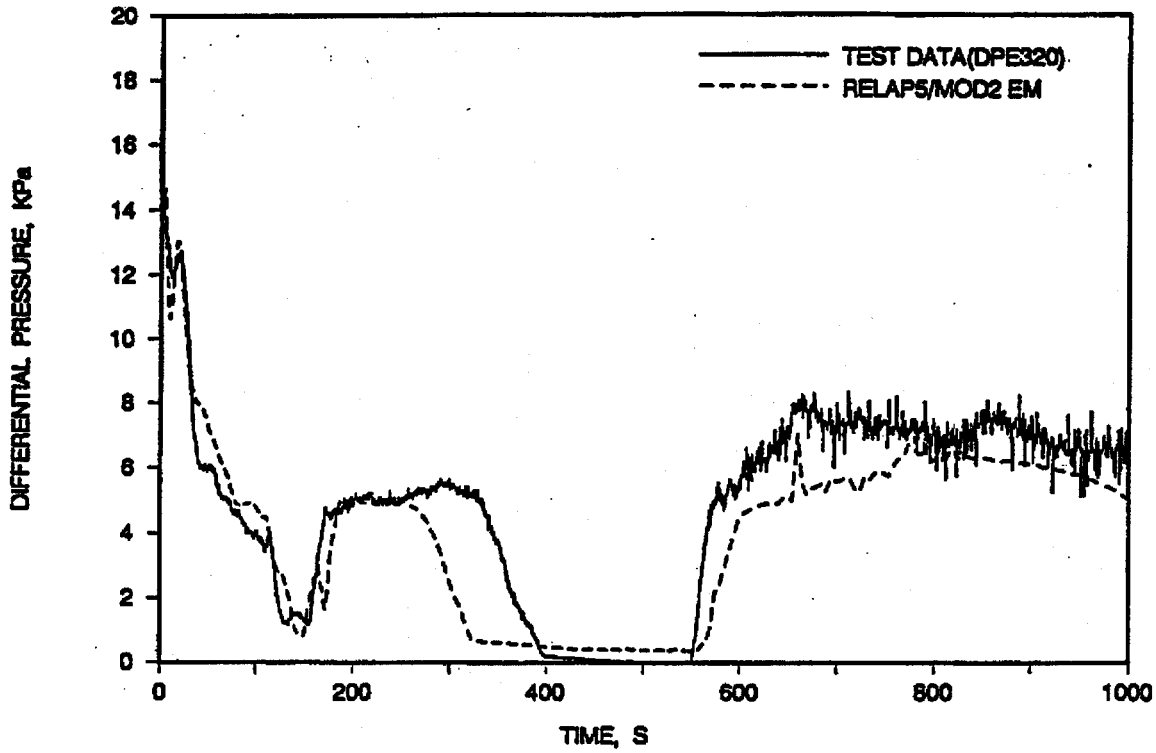


FIGURE J.27. INTACT LOOP STEAM GEN. TUBE DOWNFLOW DIFFERENTIAL PRESSURE.

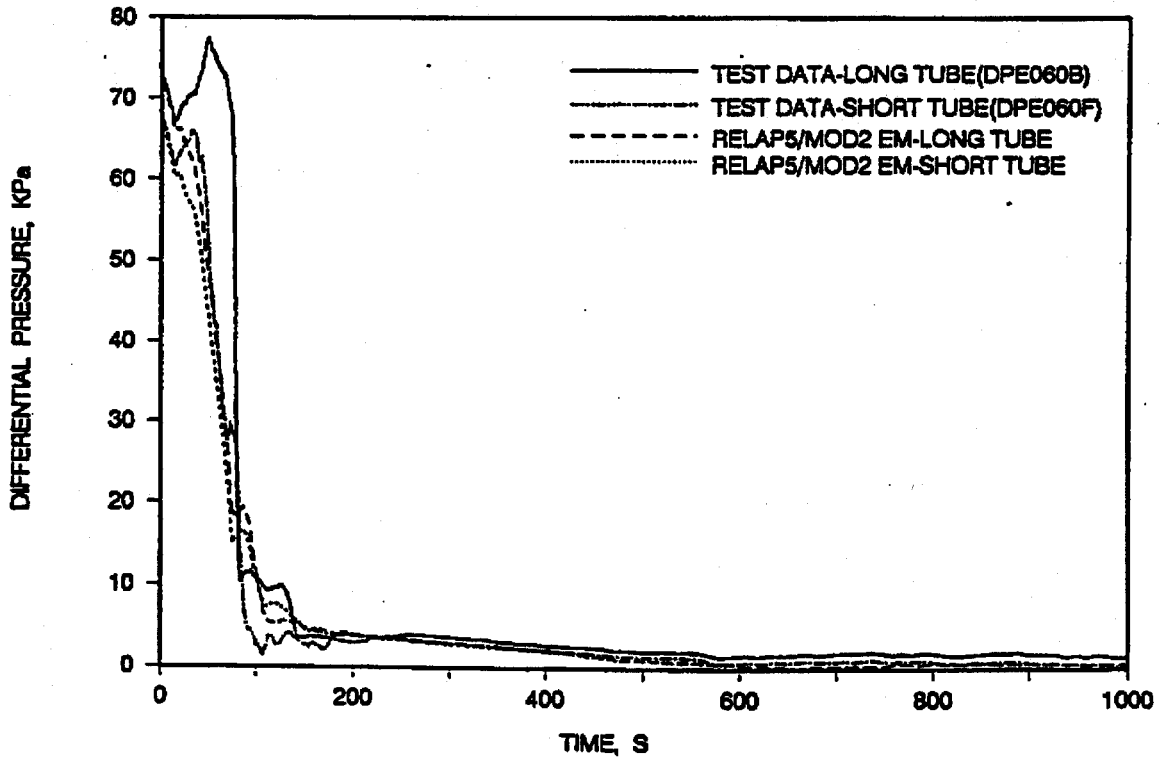


FIGURE J.28. BROKEN LOOP STEAM GEN. TUBE DOWNFLOW DIFFERENTIAL PRESSURE.

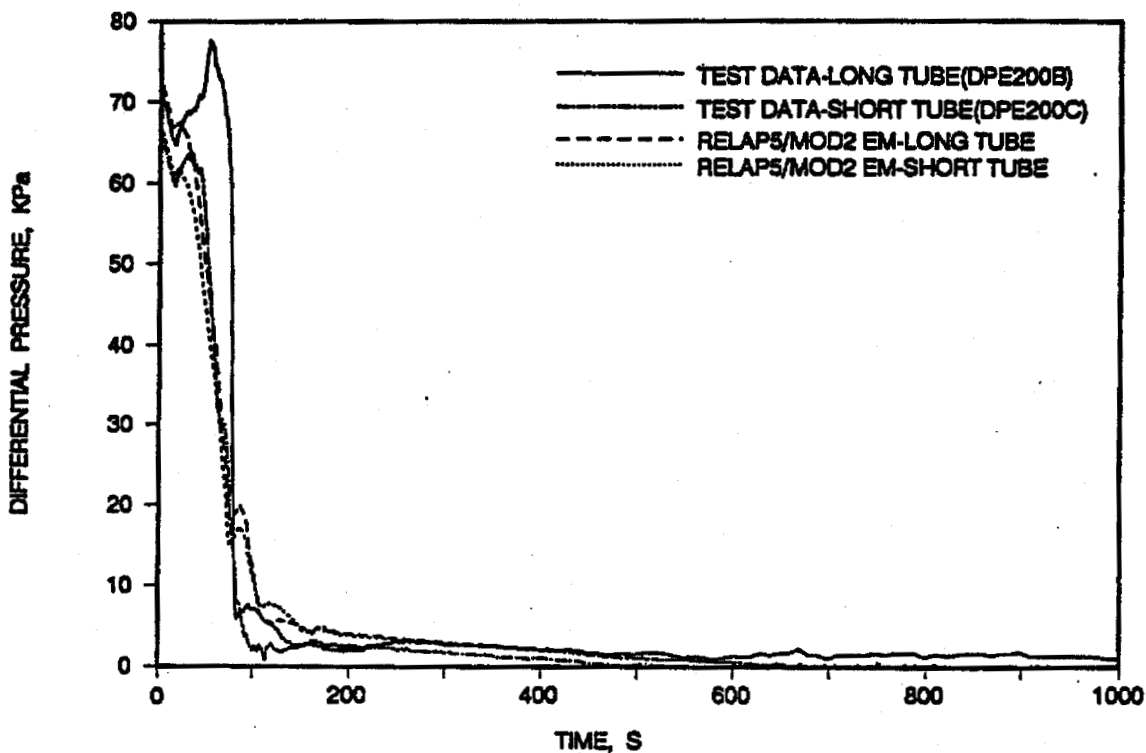


FIGURE J.29. INTACT LOOP ACCUMULATOR FLOW RATE.

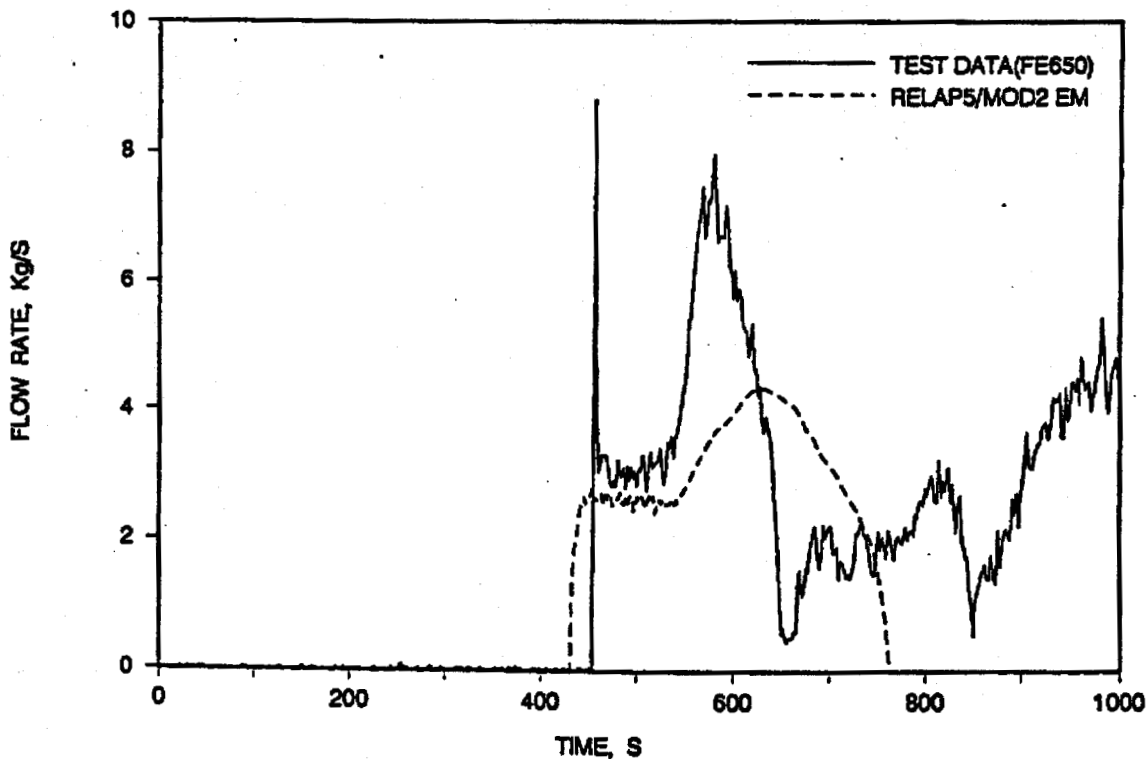


FIGURE J.30. BROKEN LOOP ACCUMULATOR FLOW RATE.

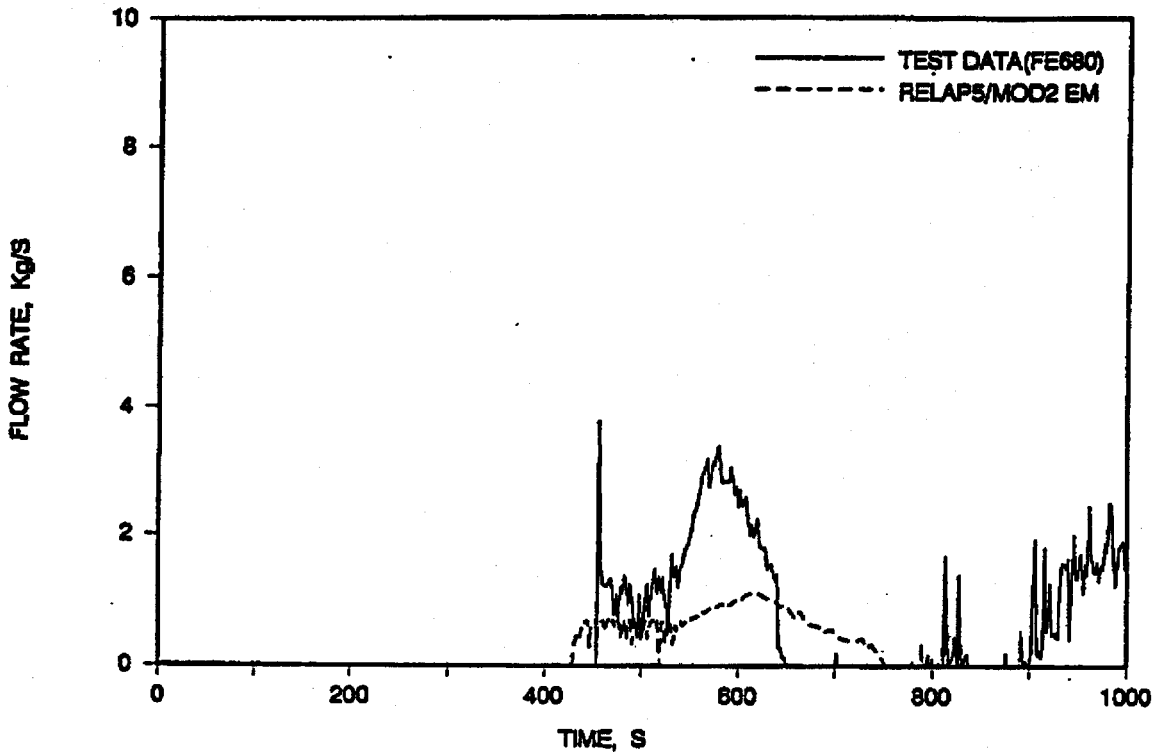
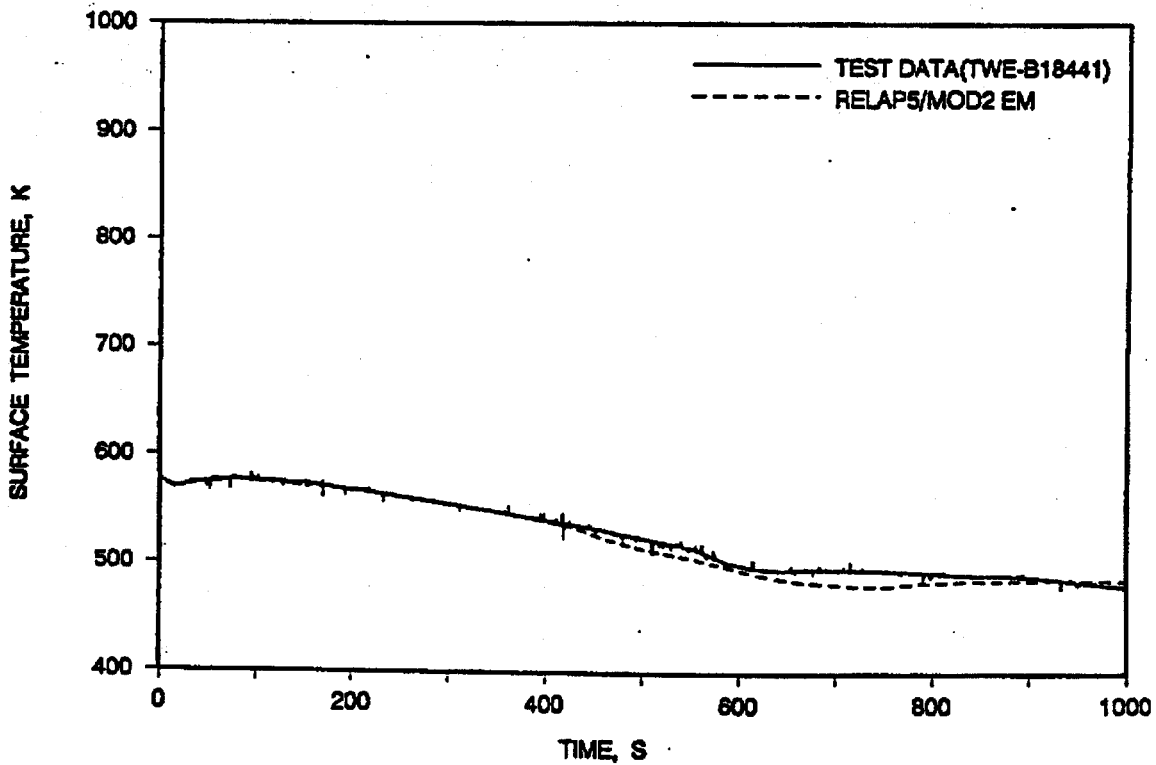


FIGURE J.31. HOT ROD SURFACE TEMPERATURE - ELEV 0.05 M.



TIME, S

FIGURE J.32. HOT ROD SURFACE TEMPERATURE - ELEV 1.018 M.

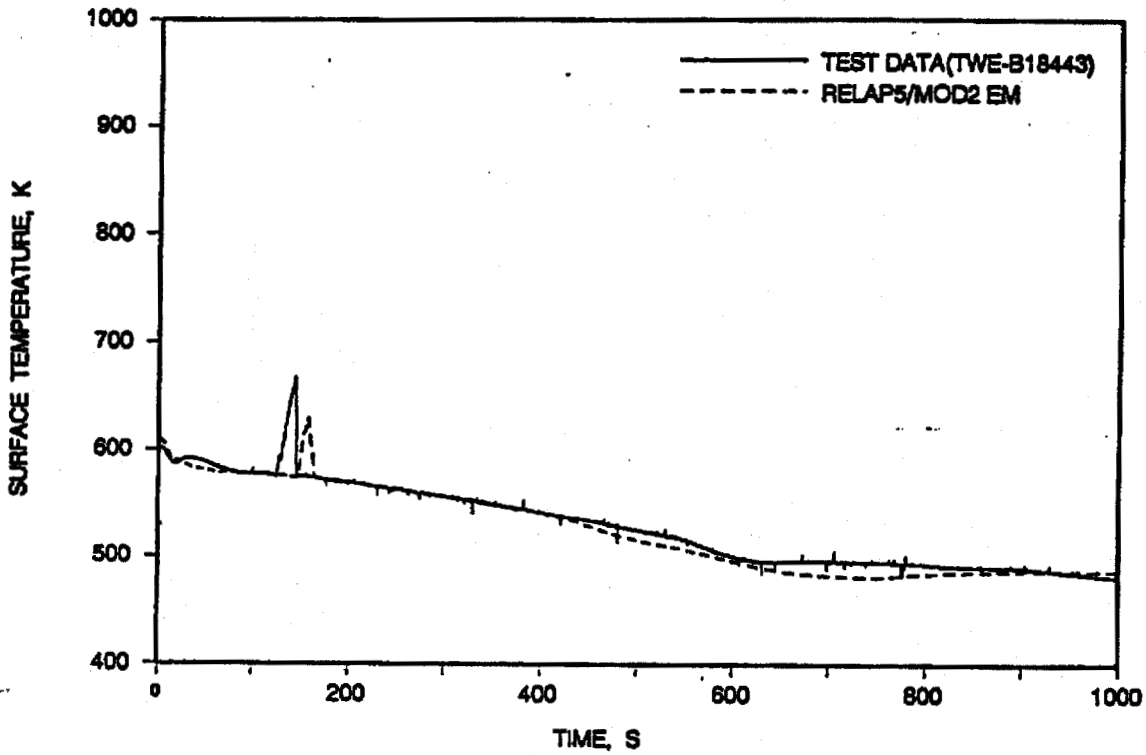


FIGURE J.33. HOT ROD SURFACE TEMPERATURE - ELEV 1.83 M.

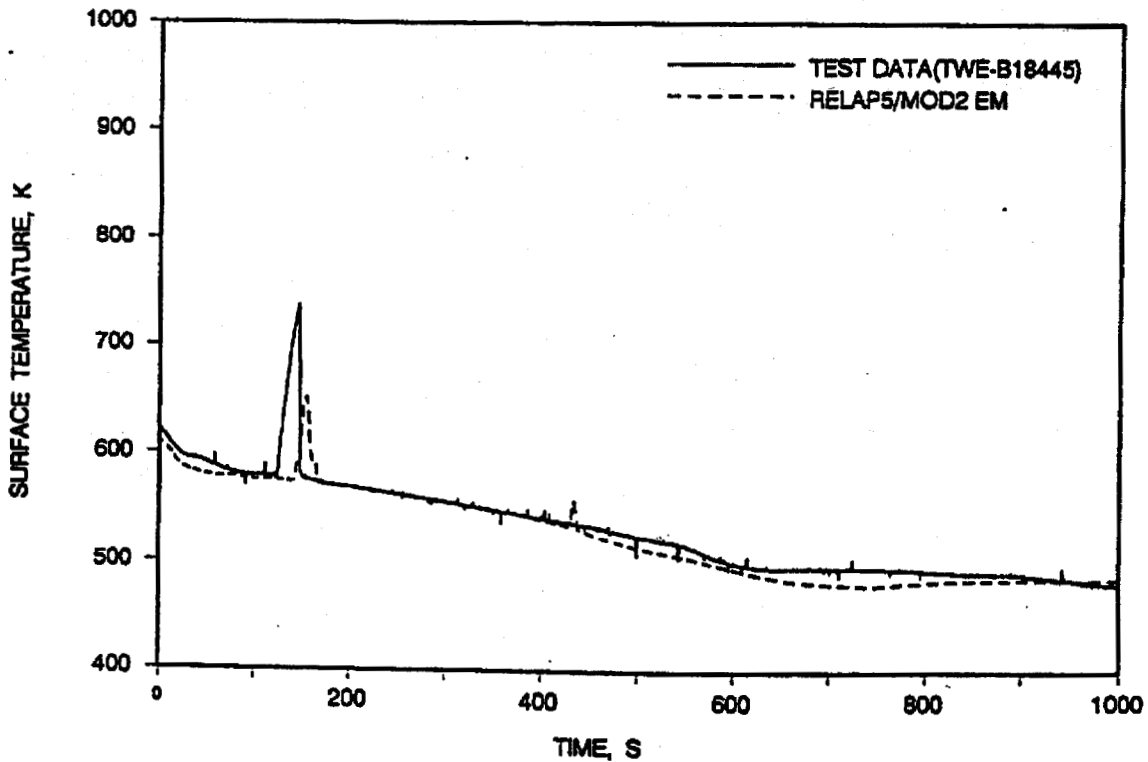


FIGURE J.34. HOT ROD SURFACE TEMPERATURE - ELEV 2.236 M.

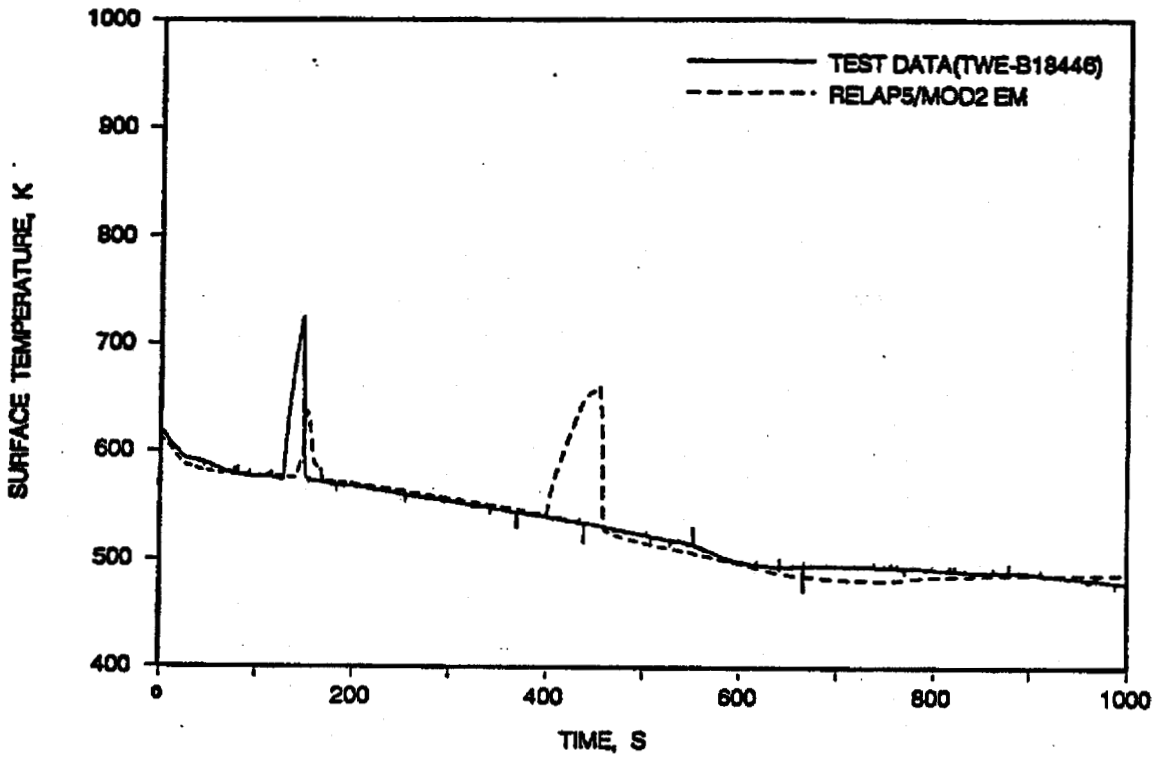


FIGURE J.35. HOT ROD SURFACE TEMPERATURE - ELEV 3.048 M.

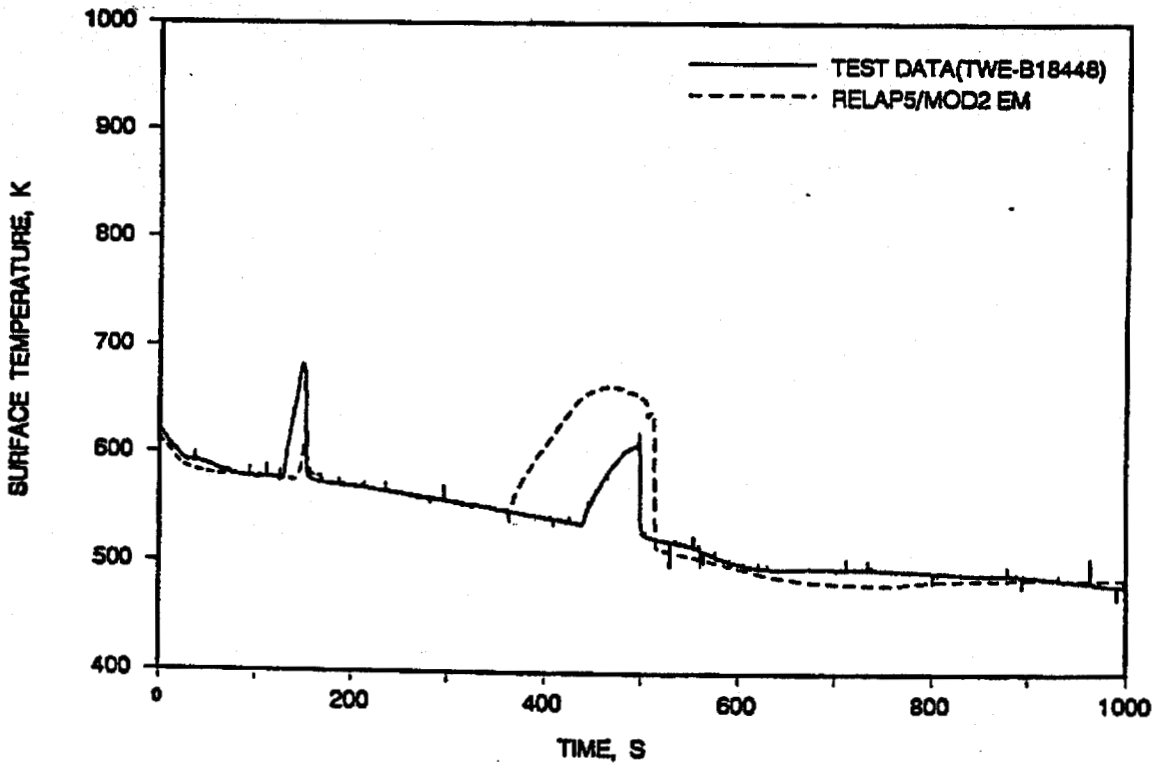


FIGURE J.36. HOT ROD SURFACE TEMPERATURE - ELEV 3.61 M.

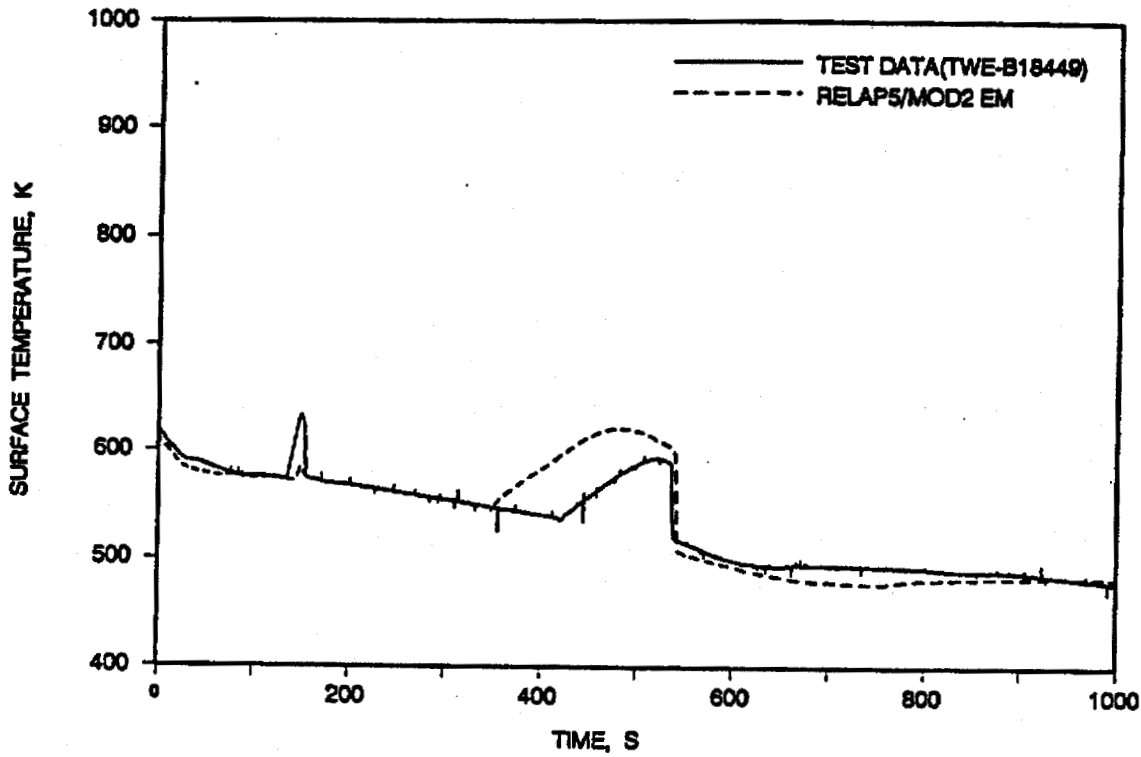


FIGURE J.37. DIMENSIONLESS LIQUID VELOCITY AT STEAM GENERATOR TUBE INLET.

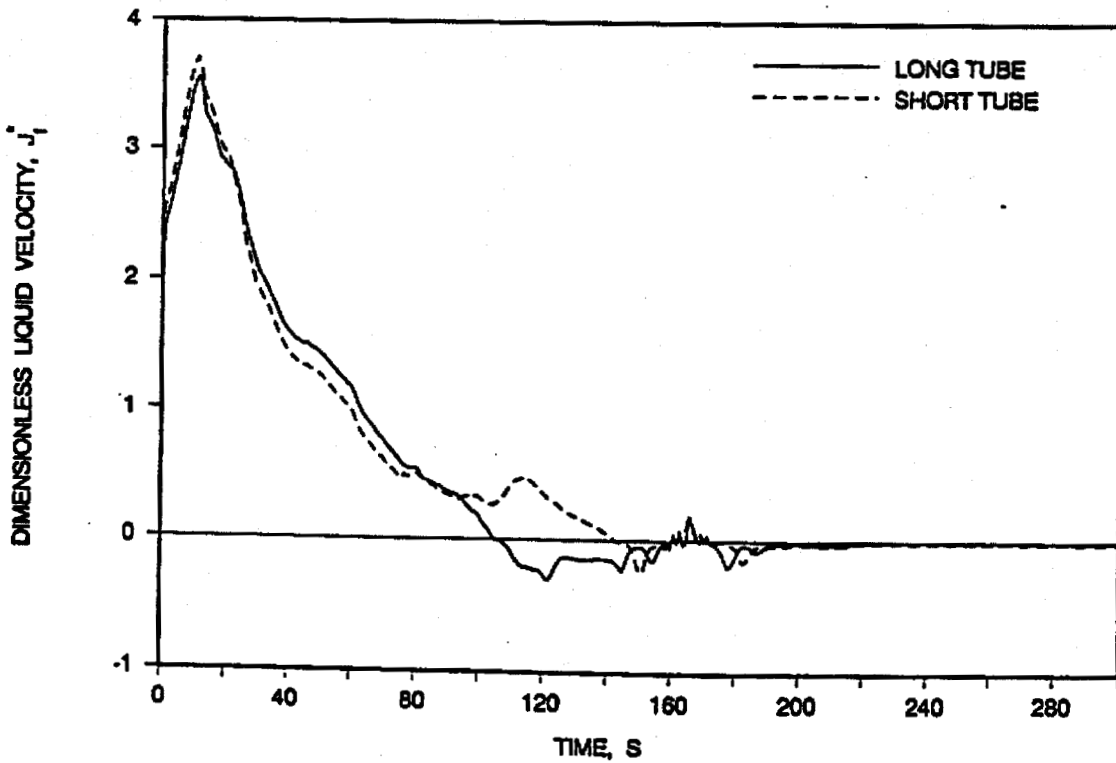


FIGURE J.38. DIMENSIONLESS VAPOR VELOCITY AT STEAM GENERATOR TUBE INLET.

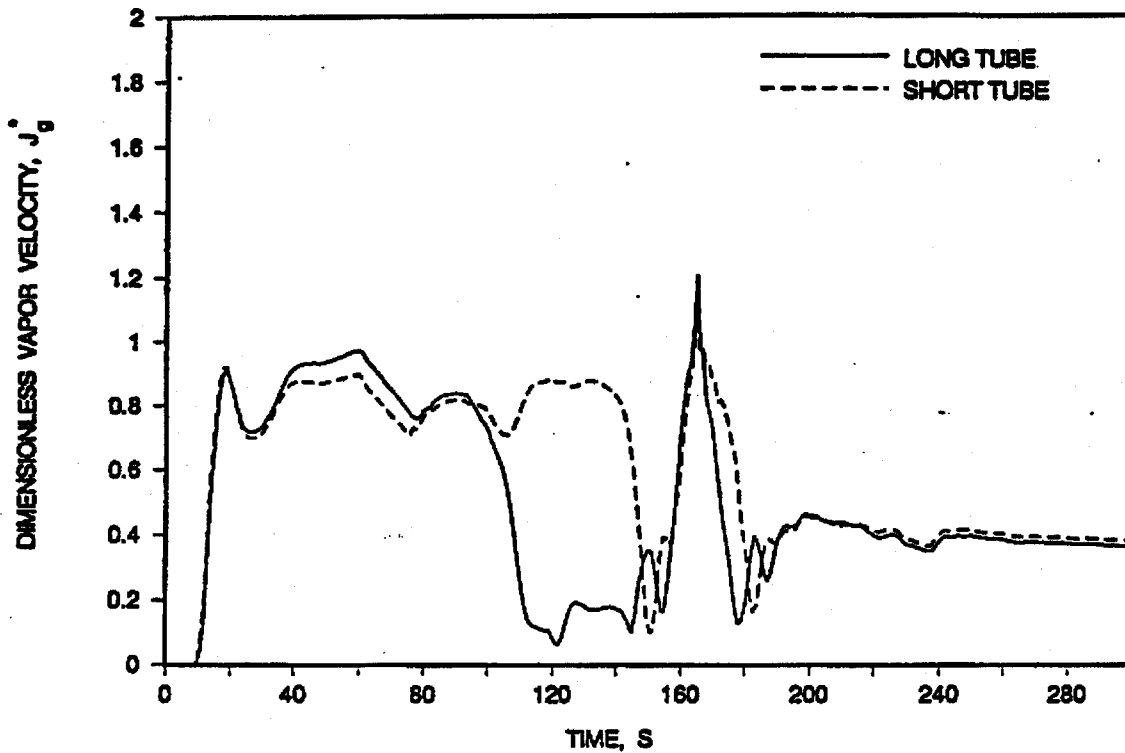


FIGURE J.39. WALLIS CONSTANT AT STEAM GENERATOR TUBE INLET.

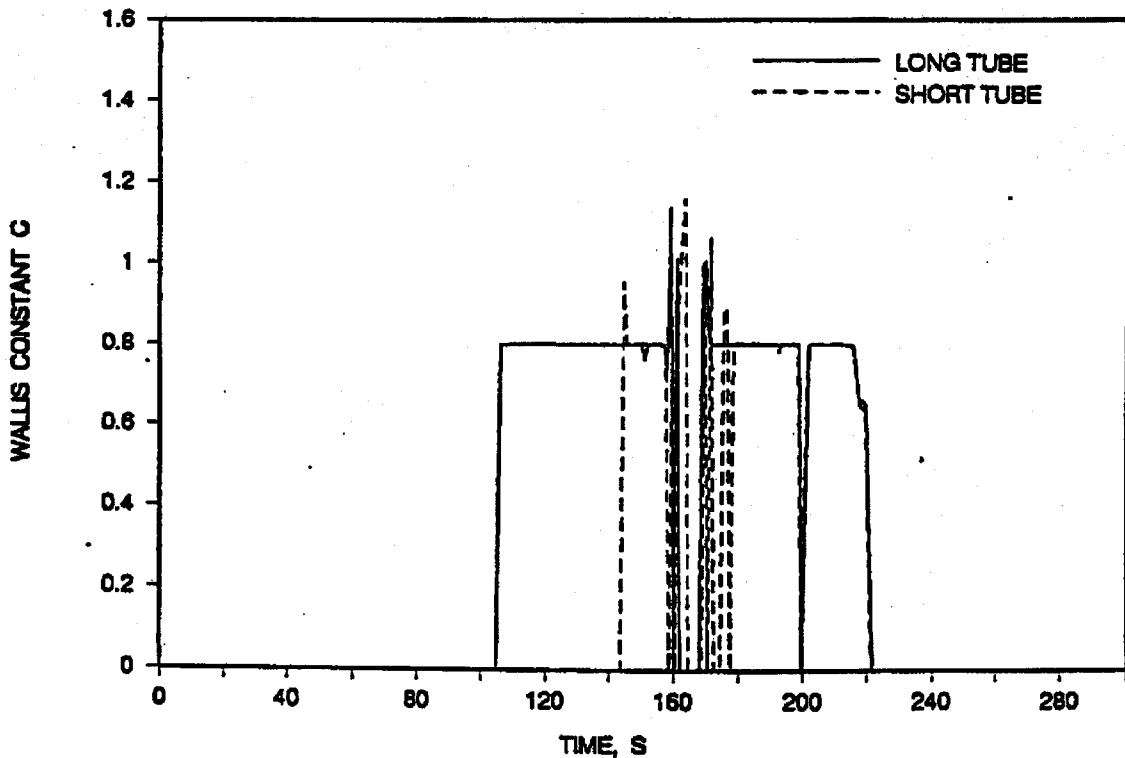


FIGURE J.40. DIMENSIONLESS LIQUID VELOCITY AT STEAM GEN. PLENUM INLET.

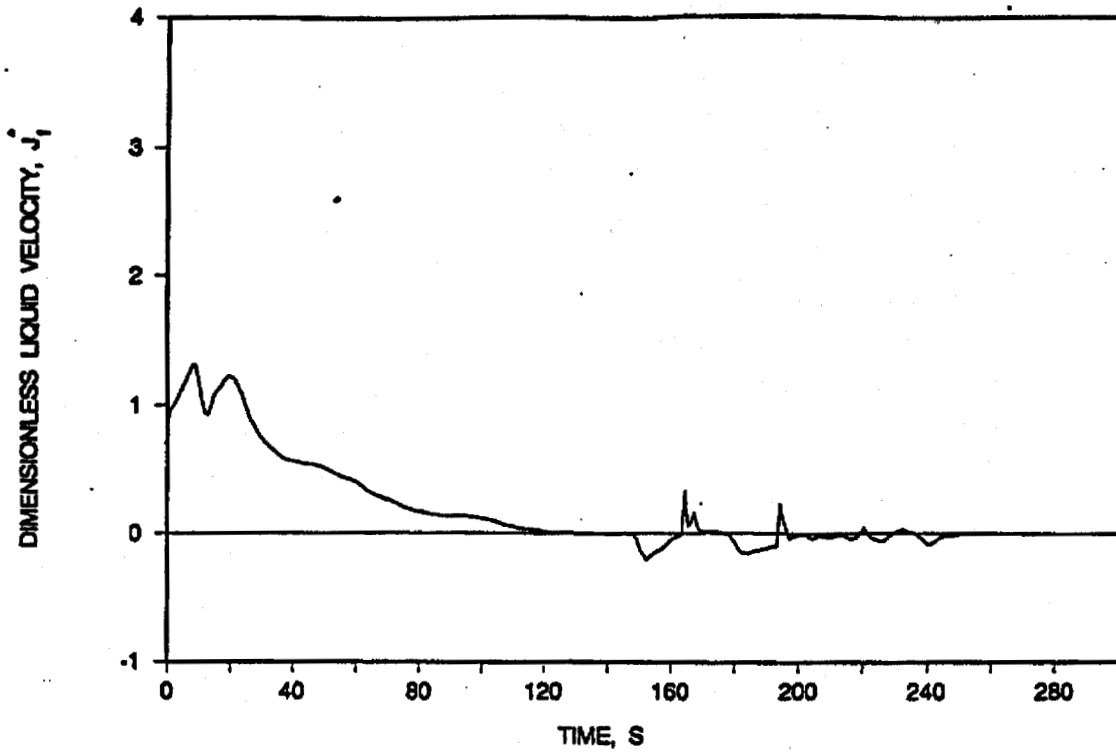


FIGURE J.41. DIMENSIONLESS VAPOR VELOCITY AT STEAM GEN. PLENUM INLET.

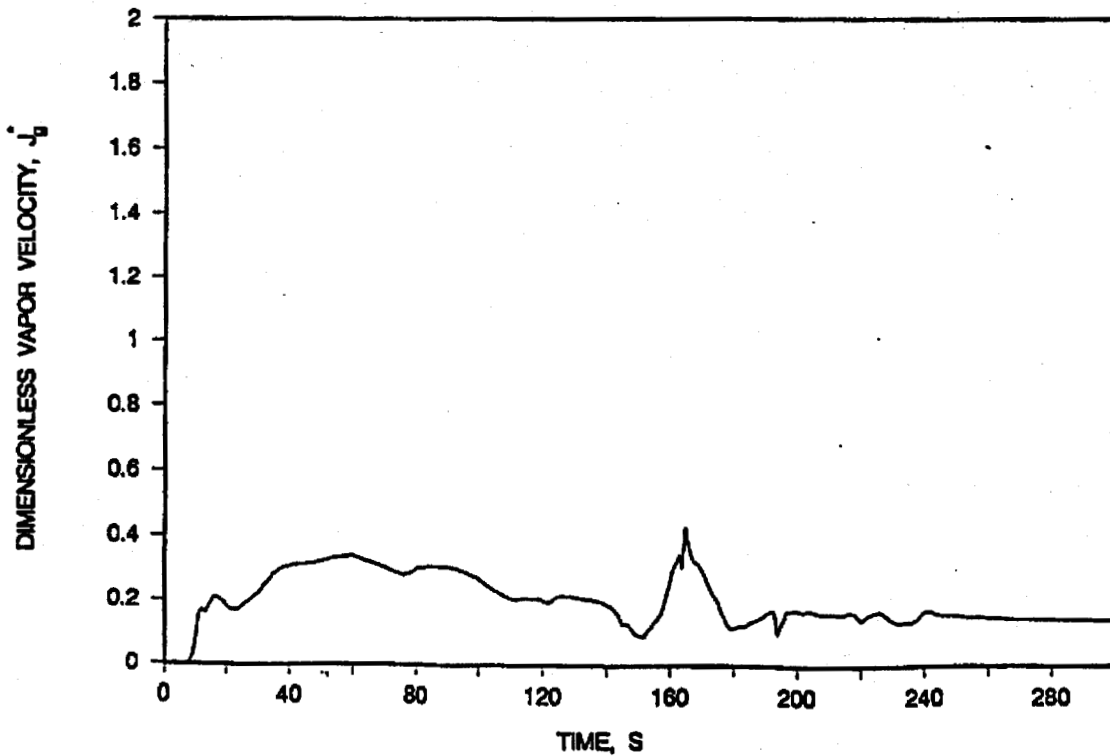
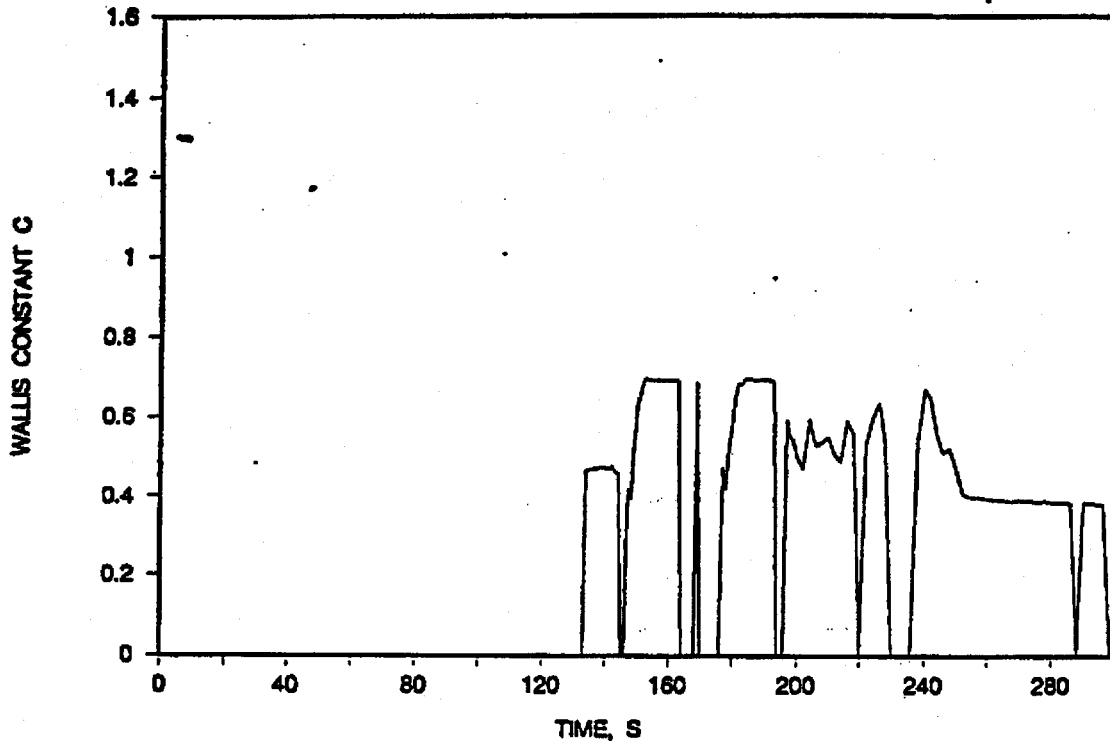


FIGURE J.42. WALLIS CONSTANT AT STEAM GENERATOR PLENUM INLET.



APPENDIX K

19-TUBE OTSG BENCHMARKS

Note: This Appendix was originally added in its entirety in Revision 3 of BAW-10164, October, 1992.

Various benchmarks of the RELAP5/MOD2-B&W code or models have been presented in Appendices G, H, I, and J to verify the code formulation and implementation. They were included to support a variety of licensing applications in nuclear steam supply systems (NSSSs) with U-tube steam generators. These benchmarks demonstrate a general thermal-hydraulic adequacy, for both stand-alone tests and integral system tests, that is applicable to other NSSS designs as well. This appendix is added to include an additional benchmark to augment the existing calculational results, specifically to support licensing analyses of B&W-designed NSSSs.

One of the unique features of the B&W-designed NSSS is the once-through steam generator (OTSG). Accurate prediction of the OTSG performance is required to demonstrate the adequacy of the methods used. This benchmark, against B&W-proprietary data for a 19-tube OTSG, is included to show that the RELAP5/MOD2-B&W formulation and input modeling techniques used to model OTSGs are acceptable for the licensing applications.

K.1. Introduction

Babcock & Wilcox performed numerous tests on model 19-tube and 37-tube once-through steam generators at the Alliance Research Center (ARC) Nuclear Steam Generator Test Facility (NSGTF). The objectives of these tests were to demonstrate the characteristics of B&W-designed steam generators and to provide data for computer code development. BWNT simulated two sets of model 19-tube tests with RELAP5/MOD2-B&W. The first set of benchmarks are to steady-state tests to show the ability of the code to predict the shell side nucleate boiling length at various power levels. The second benchmark is a comparison to a loss-of-feedwater (LOFW) flow test to demonstrate the ability of the code to predict boil-down and refill of a once-through steam generator.

K.2. Facility Description

The ARC NSGTF (Figure K-1) provided the capability of testing steam generators at full system pressure and temperature conditions using water as the test fluid. The primary system of the NSGTF was a closed circuit test loop consisting of a natural gas-fired furnace (simulating reactor heat input to the primary fluid), a pressurizer, flow control valves, flow measuring elements, and a water conditioning system.

The secondary system of the NSGTF was a closed circuit test loop consisting of steam flow control valves, steam flow measuring elements, feedwater heaters, back pressure control valves, a flash tank, circulating pumps, feedwater control valves, feedwater flow measuring elements, feedwater bypass valves, and a water conditioning system.

The model steam generator was a single pass, counterflow, tube and shell heat exchanger (Figure K-2). It consisted of 19 full-length tubes 5/8-inch in diameter spaced on a triangular pitch on 7/8-inch centers. The tube bundle was enclosed in a hexagonal shell 3.935 inches across flats and was held in place by 16 tube support plates spaced at approximately 3-foot intervals. The tube support plates were drilled in a manner to simulate the broached pattern of a full-size tube support plate.

Primary flow entered at the top of the steam generator, flowed downward through the tubes, and exited at the bottom. The secondary fluid was introduced via an external downcomer, entered the tube bundle at the bottom, boiled on the outside of the tubes, and exited at the top. When run in the standard once-through steam generator mode, the feedwater was raised to saturation by mixing it with steam from the tube region via a steam bleed pipe. This bleed pipe simulated the aspirator port in the full size prototype.

K.3. RELAP5/MOD2-B&W Model Description

The 19-tube OTSG was represented with eleven axial control volumes in the primary tube region and the secondary shell region (Figure K-3). Similarly, eleven heat structures simulated the 19 inconel 600 tubes to provide primary-to-secondary heat transfer. The external downcomer was modeled with five axial control volumes that represented the piping from the steam/feedwater mixer region to the tube bundle inlet. Feedwater aspiration was provided by a single junction component that connected the tube bundle region to the external downcomer. Feedwater flow, feedwater temperature, secondary pressure, primary inlet flow, primary inlet temperature, and primary pressure were input as boundary conditions using time-dependent volume and time-dependent junction components.

Special features, available in RELAP5/MOD2-B&W, were employed in the 19-tube OTSG model. First, the Becker critical heat flux correlation was used on the shell side of the tube heat structure to provide a better prediction of the dryout point in the OTSG. Second, the interphase drag in the slug and annular-mist flow regimes was reduced by use of the default multipliers developed for regions of small hydraulic diameters. This model produces results similar to the Wilson bubble rise model for pressures above 200 psia and provides a better prediction of liquid mass in the tube region. Finally, a linear ramp was applied to the Chen boiling suppression factor, S_f , such that it was reduced from the calculated value to zero over a void fraction of 0.99 to 1.0. This prevented the Chen heat transfer coefficient from becoming unrealistically large as the void fraction approached 1.0 on the shell side of the OTSG.

K.4. Comparison to Steady-State Boiling Length Tests

In 1969 the Alliance Research Center performed a series of steady-state tests on the model 19-tube OTSG to determine the nucleate boiling length as a function of scaled power level.¹⁵²

Each test was performed with primary pressure, primary inlet conditions, feedwater conditions, and secondary pressure held constant. The nucleate boiling length (dryout location) was determined from primary tube and secondary side thermocouples.

The boundary conditions for five, 2700 Mwt plant-scaled tests are shown in Table K.1. Using these boundary conditions, a steady-state calculation of each test was performed using RELAP5/MOD2-B&W. Also, for comparison purposes, each test was simulated with RELAP5/MOD2 Cycle 36.05. The calculated boiling lengths are compared to the measured values in Table K.2. and Figure K-4.

The results show that the boiling lengths predicted by RELAP5/MOD2-B&W are in good agreement with the data over the range of simulated power levels. Furthermore, the RELAP5/MOD2-B&W predictions represent a significant improvement over the base RELAP5/MOD2 results at power levels less than 80 percent of scaled full power. This is primarily due to use of the Becker critical heat flux correlation in the RELAP5/MOD2-B&W simulation. That correlation, developed from heated rod bundle dryout data, provides a higher CHF value at reduced feedwater flow rates; whereas, the Biasi-Zuber CHF correlation combination used in RELAP5/MOD2 predicts early dryout in an OTSG as the feedwater flow (power level) decreases.

K.5. Comparison to OTSG LOFW Test

ARC performed several loss-of-feedwater tests on the 19-tube model OTSG.¹⁵³ One LOFW test, Run 29, performed on December 16, 1977, was benchmarked with RELAP5/MOD2-B&W. This test was a loss-of-feedwater from scaled full power conditions consistent with a 2772 Mwt plant.

The model OTSG was initialized to full scaled power consistent with a 2772 Mwt plant. The test was initiated by the simultaneous trip of the feedwater pump and closure of the

feedwater isolation valve. The OTSG was allowed to boil dry. After the OTSG boiled dry, feedwater was turned on by starting the feedwater pump and by opening the feedwater isolation valve.

An attempt was made to hold the primary inlet temperature, primary flow and secondary pressure constant during the test. Primary outlet temperature, secondary steam flow, and secondary steam temperature were measured and recorded during the test.

The RELAP5/MOD2-B&W model was initialized to the test initial conditions shown in Table K.3. The predicted primary and secondary fluid temperatures are compared in Figures K-5 and K-6, respectively, to the measured values just prior to test initiation. The feedwater flow, primary inlet temperature, primary flow, and secondary pressure values that were measured during the test were input as boundary conditions. The calculated steam flow and primary outlet temperature are compared to the measured data in Figures K-7 and K-8, respectively. The code predictions are in good agreement with data, indicating that the calculated heat transfer is similar to that observed during the test.

The differences between observed and calculated results are primarily due to the sudden changes in heat transfer as the control volumes in the tube region systematically dryout and, later, refill. The addition of control volumes in the boiling region would decrease the magnitude of the step changes, but the number of steps would increase. The resulting prediction of primary outlet temperature would be approximately the same as the current prediction.

K.6. Summary and Conclusions

Steady-state performance tests performed on a model 19-tube OTSG were benchmarked with RELAP5/MOD2-B&W and RELAP5/MOD2 Cycle 36.05. Those benchmarks demonstrate that the BWNT slug-drag

model and the Becker critical heat flux correlation properly predict the nucleate boiling length in the OTSG over a wide range of power levels and transient conditions. Furthermore, RELAP5/MOD2-B&W provides a significantly improved prediction of the nucleate boiling length than does RELAP5/MOD2 Cycle 36.05 at power levels less than eighty percent full power.

In addition, a loss-of-feedwater test performed on a model 19-tube OTSG from scaled full power conditions was benchmarked with RELAP5/MOD2-B&W. The code calculation was in good agreement with the measured values of primary outlet temperature and steam flow during the dryout and refill phases of the test.

Therefore, the 19-tube OTSG benchmarks serve two main purposes. First, they validate the OTSG application of the Becker correlation and the BWNT slug and annular-mist drag models. Secondly, they demonstrate that the methods used with RELAP5/MOD2-B&W properly predict the steady-state and transient heat transfer behavior in an OTSG. Together with the other benchmarks they confirm that RELAP5/MOD2-B&W is acceptable for multi-purpose licensing applications in NSSSs with either U-tube or once-through steam generators.

Table K.1. Model 19-Tube OTSG Conditions for Steady-State Boiling Length Tests.

<u>Power Level (Percent)</u>	<u>Feedwater Temperature (F)</u>	<u>Feedwater Flow (lbm/hr)</u>	<u>Prim. Inlet Temperature (F)</u>	<u>Prim. Exit Temperature (F)</u>
------------------------------	----------------------------------	--------------------------------	------------------------------------	-----------------------------------

b, c, d, e				
------------	--	--	--	--

Table K.2 Comparison of Predicted and Measured Boiling Lengths for a 19-Tube Model OTSG.

<u>Power Level (Percent)</u>	<u>Boiling Length, ft.</u>		
	<u>RELAP5/MOD2 Cycle 36.05</u>	<u>RELAP5/MOD2-B&W</u>	<u>Test Data</u>

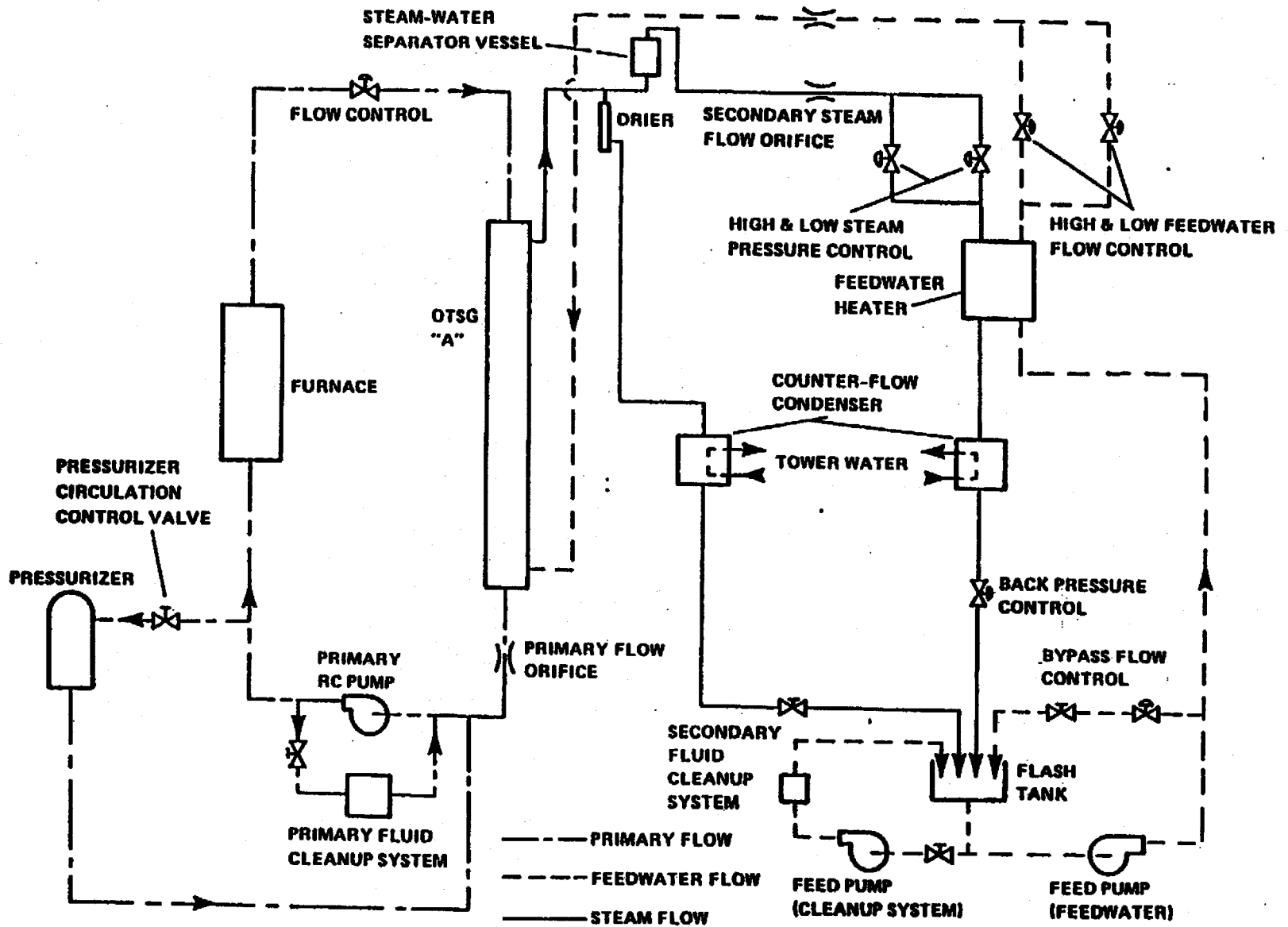
b, c, d, e			
------------	--	--	--

Table K.3. Initial Conditions for 19-Tube Model OTSG LOFW Test.

<u>Parameter</u>	<u>Model OTSG</u>	<u>RELAP5/MOD2-B&W</u>
Primary System Pressure, psia	<div style="border: 1px solid black; width: 100%; height: 100%; display: flex; align-items: center; justify-content: center;"> b,c,d,e </div>	
Primary Inlet Temperature, F		
Primary Exit Temperature, F		
Primary System Flow, lbm/hr		
Secondary System Pressure, psia		
Feedwater Temperature, F		
Steam Discharge Temperature, F		
Feedwater Flow, lbm/hr		
Heat Transfer Rate, Btu/s		

*Input values.

Figure K-1. Schematic Diagram of the Nuclear Steam Generator Test Facility.



K-10

Rev. 3
10/92

Figure K-2. 19-Tube Once-Through Steam Generator and Downcomer.

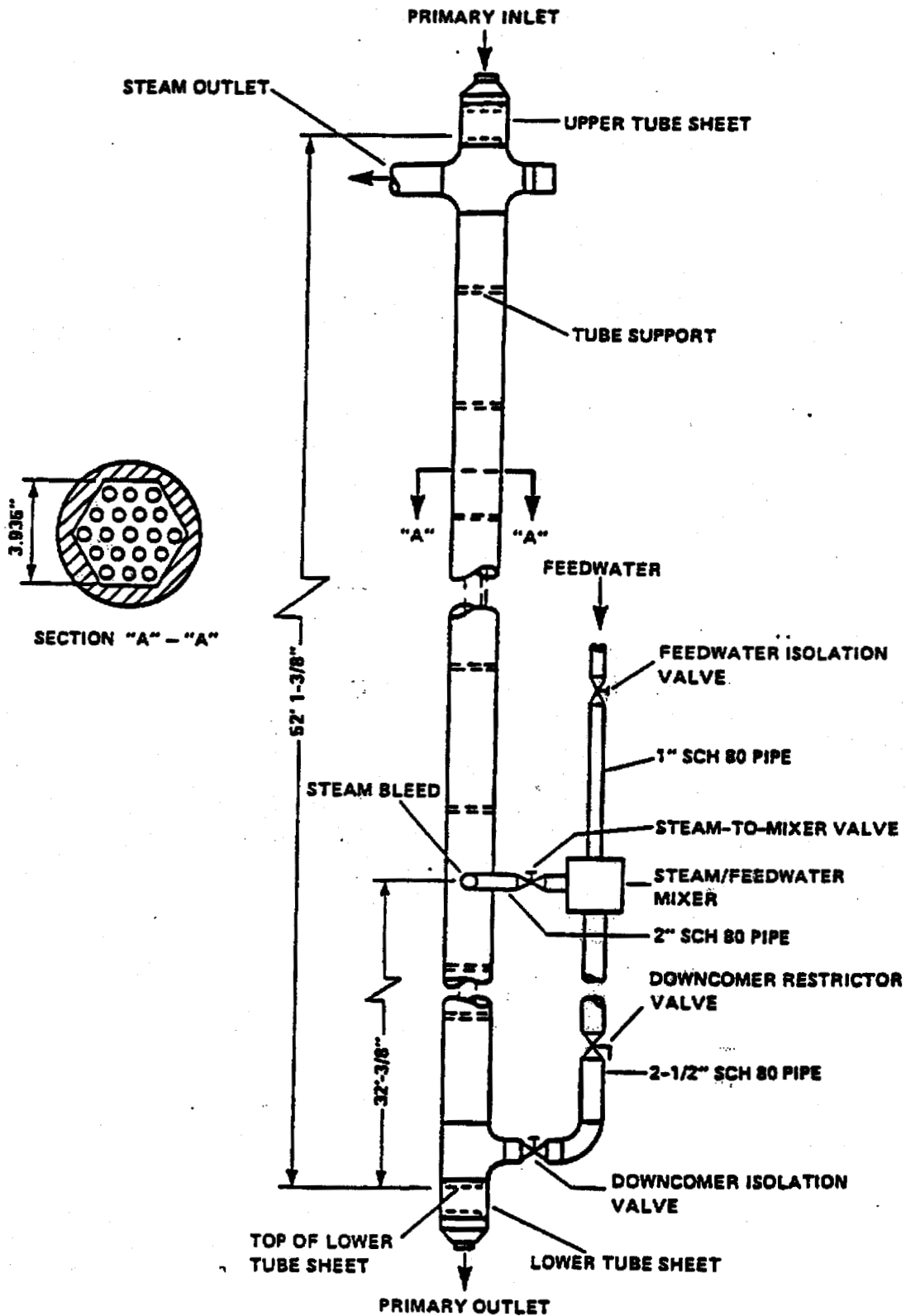
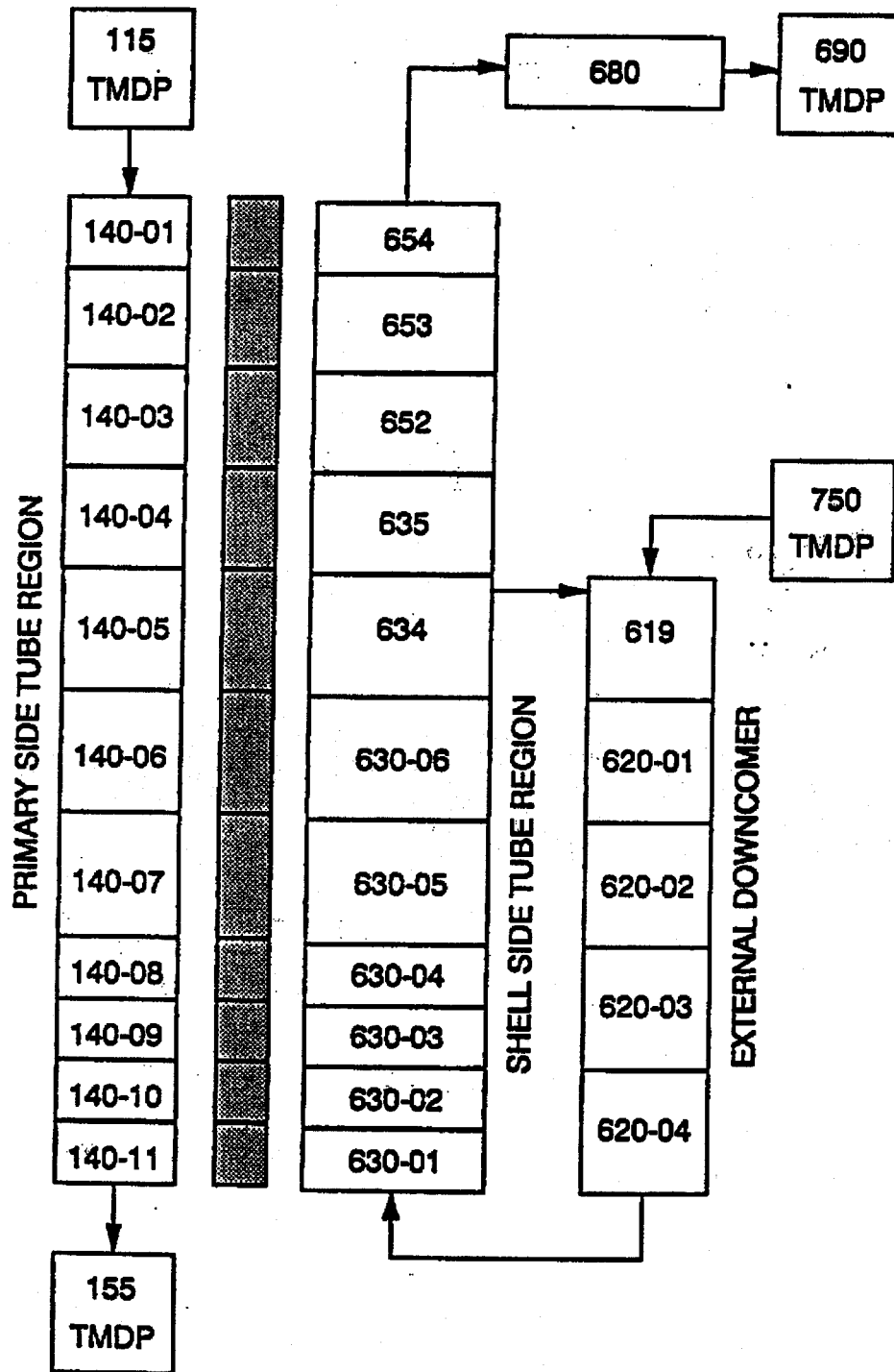


FIGURE K-3. RELAP5/MOD2-B&W MODEL OF 19-TUBE OTSG.



b,c,d,e

b,c,d,e;

b, c, d, e

This page is intentionally left blank.

APPENDIX L

MIST BENCHMARK WITH RELAP5/MOD2-B&W

Note: This Appendix was originally added in its entirety in Revision 3 of BAW-10164, October 1992.

This appendix was added to provide an integral system benchmark of a simulated small break loss-of-coolant accident in a nuclear steam supply system (NSSS) with once-through steam generators (OTSGs). This benchmark of RELAP5/MOD2-B&W code, with the support Appendices G, H, I, J and K, is used to verify the code formulation and implementation. These benchmarks collectively demonstrate a general thermal-hydraulic adequacy, for both stand-alone tests and integral system tests, that is applicable to NSSS designs containing U-tube steam generators or OTSGs.

This benchmark was performed against Multi-Loop Integral System Test facility data. The facility was chosen because it contains all of the unique features of a B&W-designed NSSS. The specific test benchmarked with RELAP5/MOD2-B&W was chosen because the scaled break size corresponds to the worst small break size for B&W-designed plants. The benchmark is included to show that the code formulation and input modeling techniques used to model a scale-model B&W-plant are acceptable for licensing application use.

L.1. Introduction

The Multi-Loop Integral System Test (MIST) facility is a scale model of a Babcock & Wilcox lowered-loop 177 fuel assembly pressurized water reactor. Design, fabrication and testing of the facility was sponsored by Babcock & Wilcox, the Babcock & Wilcox Owners Group (BWO), the Nuclear Regulatory Commission, and the Electric Power Research Institute. The facility was fabricated to provide data on the transient response of B&W PWRs during small-break loss-of-coolant accidents (SBLOCA), steam generator tube ruptures (SGTRs) and feed-and-bleed cooling. The data generated by MIST testing is used to determine the adequacy of thermal-hydraulic computer codes to predict the phenomena exhibited during these events.

To demonstrate that RELAP5/MOD2 adequately predicts the dominant phenomena, the MIST program management group sponsored three pre-test and five post-test predictions.¹⁵⁴ Similarly, the BWOG sponsored several additional RELAP5/MOD2 post-test predictions of MIST tests.¹⁵⁵⁻¹⁶⁰ These benchmarks clearly show that RELAP5/MOD2 properly predicts the phenomena exhibited during SBLOCA and SGTR events. However, in many of the benchmarks the code underpredicted collapsed liquid level in the core region because the code underpredicted the phase slip in the slug flow regime.

Consequently, BWNT modified the RELAP5/MOD2 interphase drag models to reduce the interphase drag forces in the slug and annular-mist flow regimes. The revised models were verified by comparisons to separate effects tests and to core level predictions by the FOAM2 computer code.¹⁶¹ As further justification of this code modification, MIST test 320201 was re-analyzed. The prediction of this scaled 50 cm² pump discharge break test with the revised version of RELAP5/MOD2-B&W is discussed in this Appendix. Section L.2 provides a simple description of the MIST facility. A detailed description is provided in Reference 162. The RELAP5/MOD2-B&W input model is discussed in Section L.3. The results of the revised benchmark are compared to MIST data and to the original RELAP5/MOD2 prediction in Section L.4. A summary and conclusions are provided in Section L.5. References are listed in Section 4 of the main text.

L.2. MIST Facility Description

The MIST facility was a scaled, two-by-four (two hot legs and four cold legs) model of a B&W, lowered-loop, nuclear steam supply system. MIST was designed to operate at plant-typical pressures and temperatures. Experimental data obtained from this facility during post-SBLOCA testing are used for computer code benchmarking.

MIST consisted of two 19-tube once-through steam generators; a reactor vessel with heated core and external downcomer; pressurizer; two hot legs; and four cold legs, each with a scaled reactor coolant pump. Other loop components in MIST included a closed secondary system, four simulated reactor vessel vent valves (RVVVs), a pressurizer power-operated relief valve, hot leg vents and reactor vessel upper-head vents, high pressure injection (HPI), core flood system, and critical flow orifices for scaled leak simulation. The system was also capable of noncondensable gas addition at selected loop sites. The MIST facility is illustrated in Figure L-1.

The reactor coolant system of MIST was scaled according to the following criteria, listed in order of decreasing priority: elevation, post-SBLOCA flow phenomena, component volume, and irrecoverable pressure drop. Consequently, MIST retained full plant elevations throughout the primary system and the steam generator secondaries. Key interfaces were maintained including the hot leg spillover, upper and lower tube sheets of the steam generators, cold leg low point, pump discharge spillover, cold and hot leg nozzle centerlines, core, and points of emergency core cooling system injection. Only the elevations of several non-flow regions were compromised, primarily to optimize power-to-volume scaling. Also, the MIST hot legs and cold legs were oversized with respect to ideal power-to-volume scaling (plant/MIST power ratio is 817). This atypicality was necessary to preserve prototypical two-phase flow characteristics, match irrecoverable pressure losses in the piping, and preserve prototypical cold leg Froude number.

As with any scaled facility, the metal surface area-to-fluid volume ratio of MIST was considerably greater than the plant value. As a result, guard heaters were used, in conjunction with passive insulation, on the steam generator secondaries and on all primary coolant components to minimize model heat losses.

However, the guard heaters did not compensate for all the loop heat losses. Therefore, core power was increased to offset these uncompensated heat losses.

MIST instrumentation was selected and distributed based on input from experimenters and code analysts. This instrument selection process considered the needs of code benchmarking, indications of thermal-hydraulic phenomena, and system closure. MIST instrumentation consisted of measurements of temperature, pressure, and differential pressure. Fluid level and phase indications were provided by optical viewports, gamma densitometers, conductivity probes, and differential pressures. Mass flow rates in the circulation loop were measured using venturis and a cooled thermocouple, and at the system boundaries using Coriolis flowmeters and weigh scales. Approximately 850 MIST instruments were interfaced to a computer-controlled, high-speed data acquisition system.

L.3. RELAP5/MOD2-B&W Model Description

The base RELAP5/MOD2-B&W input model is identical to that used in the original post-test prediction¹⁵⁵ and is discussed in detail in Reference 163. The model simulates all of the MIST primary reactor coolant system piping, active components and ancillary systems. Specifically, the complete model represents the reactor vessel, an external annular downcomer, two hot legs, a pressurizer, two once-through steam generators, four cold legs, four reactor coolant pumps, reactor vessel vent valves, a core flood tank, high point vents, high- and low-pressure emergency core cooling system injection, high elevation auxiliary feedwater, primary and secondary metal mass, and guard heaters.

Special features of the model include the reactor vessel nodding arrangement, the cold leg-to-downcomer connections, and the two-radial region steam generators. The reactor vessel nodding arrangement models the full height core region and the vessel

exit region nodding scheme preserves the two-phase flow splits during boiling pot mode.

The cold legs utilize a double flow path connection to the external reactor vessel downcomer so that counter-current two-phase flow can be predicted. In other words, this connection scheme allows steam from the upper downcomer to enter the cold leg while liquid drains from the cold leg into the lower downcomer.

The final model feature represents the primary steam generator (SG) tube region with two radial regions. One region (three tubes) represents the tubes directly wetted by auxiliary feedwater (AFW) injection on the shell side of the SG. The other region (16 tubes) represents the tubes in contact with secondary steam (dry tubes).

The base RELAP5/MOD2-B&W model was modified for this re-analysis. Most notably, the revised slug drag model was implemented in the core and the shell side of the steam generator. The revised slug drag model is designed for use in these regions where the hydraulic diameters are small and boiling takes place.

In addition to the revised slug drag model, the reactor vessel and downcomer models were modified slightly. The core region was modified so that twenty control volumes represent the full height core instead of the three control volumes used in the original prediction. This increase in core detail is required to maintain consistency with the models used to develop the revised slug drag model. Furthermore, the outer annulus region in the vessel outlet was revised to include three control volumes rather than one so that the mixture level would properly reside below the RVVV during the loop draining period. Also, the RVVV junction was modified to enter the bottom of the upper downcomer control volume to better predict the steam condensation there. This last

modification is consistent with latest MIST benchmark models. A schematic of the RELAP5/MOD2-B&W model of MIST is shown in Figure L-2.

L.4. Prediction of MIST Test 320201 with Revised RELAP5/MOD2-B&W

The original post-test prediction of MIST test 320201 with Version 5.0 of RELAP5/MOD2-B&W is discussed in detail in Reference 155. The models used in this simulation with that code version are identical to those described in Revision 0 of this code topical report. A simple summary of the re-analysis with Version 14.0 is provided here and a comparison is made between the original and revised predictions. The Version 14.0 models used in this simulation are identical to those contained in Revision 3 of this code topical.

L.4.1. MIST Initialization

The MIST facility was capable of only ten percent full-scaled power. Therefore, the facility was initialized to the conditions existing approximately 145 seconds after trip. Consequently, MIST was initialized in natural circulation with the core power equal to 3.5 percent scaled power plus an additional 0.4 percent scaled power for uncompensated heat losses. Other initial conditions were:

1. Primary system pressure corresponding to 22 F core exit subcooling.
2. Pressurizer level five feet above the bottom of the pressurizer.
3. Steam generator pressure of 1010 psia.
4. Steam generator secondary level controlled to five feet above the lower tube sheet by throttling high elevation AFW injection.

The MIST initial conditions for Test 320201 are shown in Table L.1 with the calculated values from the RELAP5/MOD2-B&W model.

L.4.2. Summary of Results

The test was initiated by turning off the pressurizer heaters and opening the leak. When the pressurizer level reached one foot, full HPI flow was started, steam generator secondary refill using full capacity AFW was initiated, the core decay heat ramp was activated, and the RVVV control was placed in automatic.

When the leak was opened the system began a subcooled blowdown. The hot leg and core exit fluid saturated and the primary depressurization rate decreased as the hot fluid flashed. The primary system depressurization continued until the steam produced from flashing of the hot leg fluid interrupted natural circulation at approximately one minute.

The interruption of natural circulation stopped the primary system depressurization because the onset of gross boiling in the core exceeded the volumetric discharge of the break. Steam that was formed in the core collected in the reactor vessel upper head and displaced the mixture level below the RVVV elevation. Steam passed through the RVVVs into the reactor vessel downcomer. As the steam collected in the downcomer, it depressed the liquid level to the cold leg nozzle elevation. With the cold leg nozzles partially uncovered, the rate of condensation of the core steam on the cold HPI liquid in the cold legs increased. Consequently, the primary system depressurization resumed. Shortly thereafter, the depressurization rate increased as the trapped hot leg steam bubble depressed the liquid levels in the SG tubes below the tube sheets, establishing high-elevation boiler-condenser mode (BCM) heat transfer. The depressurization was further augmented as the leak site saturated.

Upon re-establishment of SG heat transfer at three minutes, the primary system depressurization resumed and continued as long as the AFW was flowing. When the secondary levels reached the

control setpoint at eight minutes, AFW flow stopped. Without significant primary-to-secondary heat transfer, the primary system depressurization slowed as the only mode of energy removal was leak-HPI cooling.

The primary system depressurized slowly because of leak-HPI cooling while the SG secondary pressures remained relatively constant. The residual primary-to-secondary heat transfer was offset by steam line heat losses to ambient. Therefore, the SG pressures remained constant. Approximately, twenty-eight minutes after test initiation, the primary system depressurized below the secondary system pressure. At that time, SG secondary side blowdown was initiated. AFW injection reactivated as flashing and boil-off reduced the secondary level below the control setpoint. Consequently, the reactivation of AFW injection re-initiated high elevation BCM heat transfer and the primary system depressurization rate increased. The increase in depressurization rate caused flashing within the primary system. Also, the dramatic increase in primary system steam condensation in the SG tubes caused liquid to relocate from the vessel into the hot legs. Consequently, these two effects caused a decrease in core collapsed liquid level.

As the secondary system blowdown continued, the secondary depressurization rate decreased to a rate limited by the facility condenser. The blowdown rate was sufficient to maintain a primary-to-secondary temperature differential. The resulting primary-to-secondary heat transfer, in combination with leak-HPI cooling, sustained a primary system depressurization for the duration of the event. Reactor vessel collapsed liquid levels increased as flashing decreased and as core flood tank flow suppressed core boiling and aided system refill.

The RELAP5/MOD2-B&W Version 14.0 prediction of primary system pressure is in good agreement with the data (Figure L-3). The

predictions of interruption of natural circulation, high elevation BCM cooling, and leak-HPI cooling are consistent with the observation. The final depressurization caused by SG blowdown is calculated to occur earlier than observed because the MIST operator opened the blowdown valve 2.5 minutes after the primary pressure equalized with the secondary pressure (Table L.2). The SG blowdown was automatically initiated in the simulation when the primary and secondary system pressures equalized.

The response predicted by Version 14.0 was similar to the Version 5.0 prediction. As expected, the change in the interphase drag had little impact on the primary system pressure response. However, the Version 14.0 prediction showed a later actuation of the SG blowdown and a better primary system pressure prediction during the blowdown. The delayed blowdown occurred because the Version 14.0 prediction of the "A" SG pressure was lower than the Version 5.0 prediction when AFW was terminated (Figure L-4). The pressure was lower because the revised MIST model used in the Version 14.0 prediction had subcooled liquid in the pressurizer surge line and lower head. Since the fluid entering the hot leg was colder, less flashing occurred, reducing two-phase natural circulation. The net result was less heat transfer to the secondary system. The Version 5.0 prediction exhibited a lower primary pressure during the blowdown because the secondary level swell was overpredicted, providing more primary-to-secondary heat transfer than was observed in the test.

The reactor vessel collapsed liquid level predicted by Version 14.0 was also in good agreement with MIST data (Figure L-5). During the test, the reactor vessel mixture level quickly fell below the RVVVs and stabilized above the hot leg nozzles. This mixture level translated to a collapsed liquid level of approximately 19 feet above the upper face of the lower SG tube sheet. Both post-test predictions showed the same behavior.

However, the Version 5.0 simulation underpredicted the collapsed liquid level because it overpredicted the void fractions in the mixture region. The Version 14.0 prediction, with the revised slug drag model and finer core nodding, provided an excellent calculation of collapsed liquid level for the same approximate mixture level. Furthermore, the revised prediction properly calculated reactor vessel collapsed liquid level during the SG blowdown phase of the transient. The collapsed liquid level decreased during this phase as flashing in the reactor vessel increased the void fraction in the mixture region.

In addition to an improved reactor vessel liquid level prediction, the Version 14.0 post-test prediction also displayed an improved SG secondary collapsed liquid level prediction (Figure L-6). RELAP5/MOD2-B&W Version 5.0 overpredicted the secondary level swell during the SG blowdown, resulting in significant carryout of liquid. The Version 14.0 prediction incorporated the revised slug drag model in the SG tube region. The revised slug drag model significantly reduced the level swell and produced a collapsed liquid level calculation that was in good agreement with the data. Furthermore, the accurate calculation of mixture level by Version 14.0 during the SG blowdown provided an accurate calculation of primary-to-secondary heat transfer and gave an improved primary pressure prediction as compared to the Version 5.0 results.

L.5. Summary and Conclusions

A post-test prediction of MIST test 320201, a scaled 50 cm² cold leg pump discharge break, was performed with Version 14.0 of the RELAP5/MOD2-B&W computer code. The models employed in that prediction are identical to those contained in Version 19.0, and described in this revision to the code topical. The calculation included the BWNT modified interphase drag modeling in the reactor vessel and steam generator secondary components to reduce the calculated interphase drag force in the slug flow regime.

The results were compared to the MIST test data and the original post-test prediction that was performed with Version 5.0 of RELAP5/MOD2-B&W.

That comparison showed the calculated primary and secondary pressure responses were in good agreement with the data and were similar to the original predictions. However, the reduced interphase drag forces predicted by Version 14.0 provided a significant improvement in calculated collapsed liquid levels in the reactor vessel and the steam generator secondary as compared to the Version 5.0 calculations. Furthermore, the collapsed liquid levels predicted by Version 14.0 are in excellent agreement with the MIST data. Therefore, it is concluded that the revised slug drag model is appropriate for use in regions of small hydraulic diameter.

This benchmark demonstrates the accuracy and adequacy of the RELAP5/MOD2-B&W code for prediction of the phenomena expected to occur during a postulated SBLOCA in a plant with OTSGs. In combination with the other benchmark cases, it confirms that the RELAP5/MOD2-B&W code is appropriate for licensing applications of B&W-designed NSSSs.

Table L.1. Comparison of MIST Initial Conditions to RELAP5/MOD2-B&W Values.

<u>Parameter, Units</u>	<u>MIST Value</u>	<u>RELAP5/MOD2-B&W Value</u>
Primary Pressure, psia	1730.0	1726.5
Secondary Pressure, psia	1010.0	1010.0
Core Exit Temperature, F	592.0	593.4
SG Exit Temperature, F	551.0	550.3
Core Exit Subcooling, F	22.0	22.0
Core Power, Btu/s	117.0	119.5
Pressurizer Level, ft	5.0	5.0
SG Secondary Level, ft	4.8	5.0
Core Flow Rate, lbm/s	1.86	1.86

Revised Table L.1 shown on page 5-285 per SER instruction on Table 2 (page 5-364).

Table L.2. Sequence of Events.

<u>Event</u>	<u>MIST Observation Seconds</u>	<u>Ver 5.0 Prediction Seconds</u>	<u>Ver 14.0 Prediction Seconds</u>
Leak opened	0	0	0
Primary saturates	12	31	34
Pzr level reaches one foot (HPI, AFW, and DH ramp started)	30-42	60	57
Hot leg U-bend voiding interrupts natural circ. (Loop A/Loop B)	54/42	85/130	130/90
High elev BCM begins (Loop A/Loop B)	170/175	180/185	180/180
Break saturates	190	130	140
Secondary refilled and AFW shutoff (SG A/SG B)	480/480	490/440	480/480
Primary and secondary pressures equalize	1560	1500	1650
Secondary blowdown	1710	1500	1650
CFT injection begins	1920	1680	1800

Revised Table L.2 shown on page 5-288 per SER instruction on Table 2 (page 5-364).

Figure L-1. MIST Facility

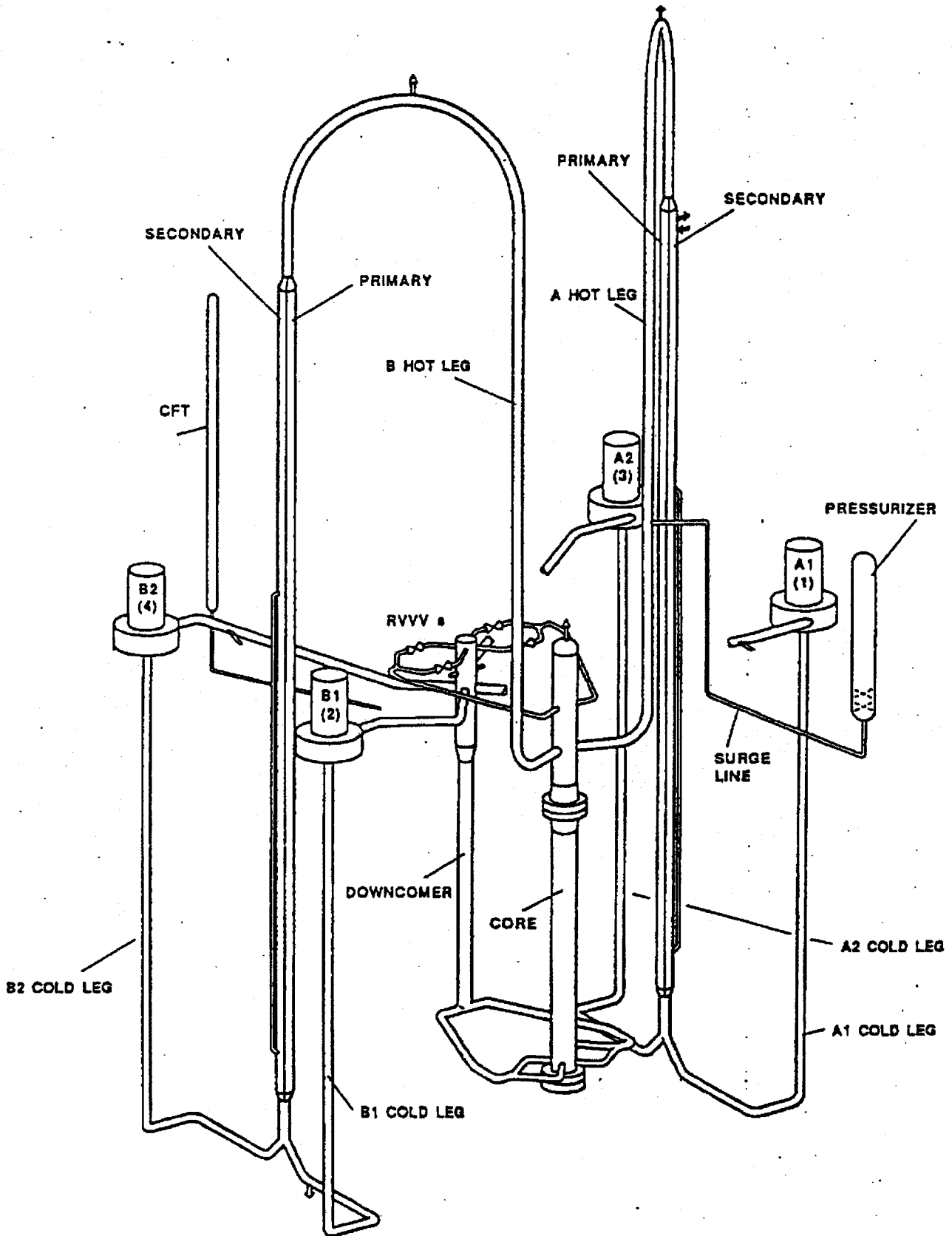


FIGURE L-2. RELAP5/MOD2-B&W MODEL OF THE MIST FACILITY.

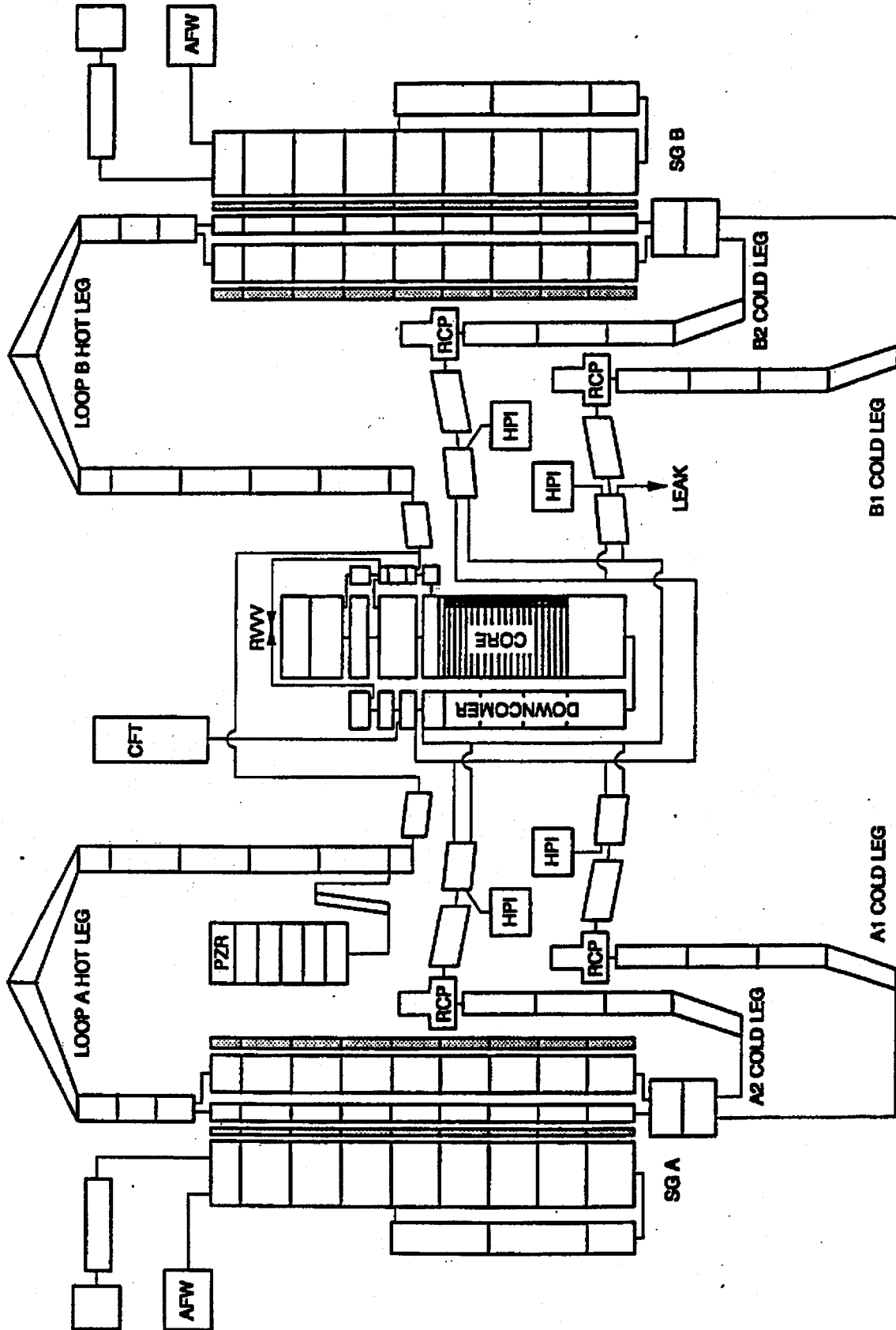


FIGURE L-3. COMPARISON OF PREDICTED AND OBSERVED PRIMARY PRESSURES FOR MIST TEST 320201.

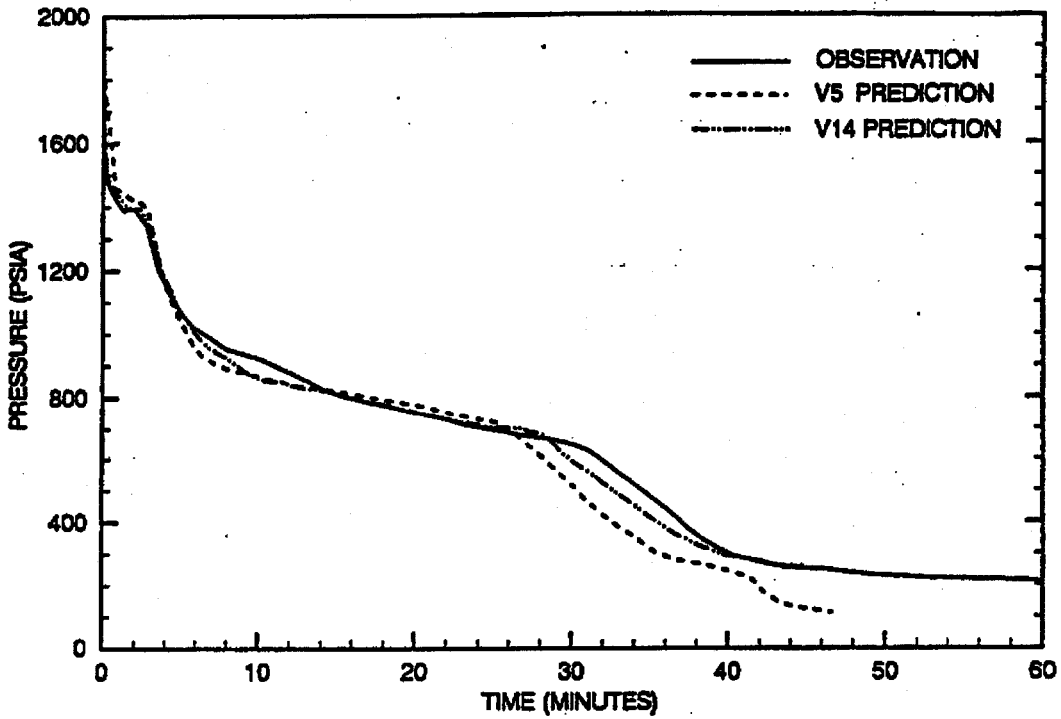


FIGURE L-4. COMPARISON OF PREDICTED AND OBSERVED SECONDARY SYSTEM PRESSURES FOR MIST TEST 320201.

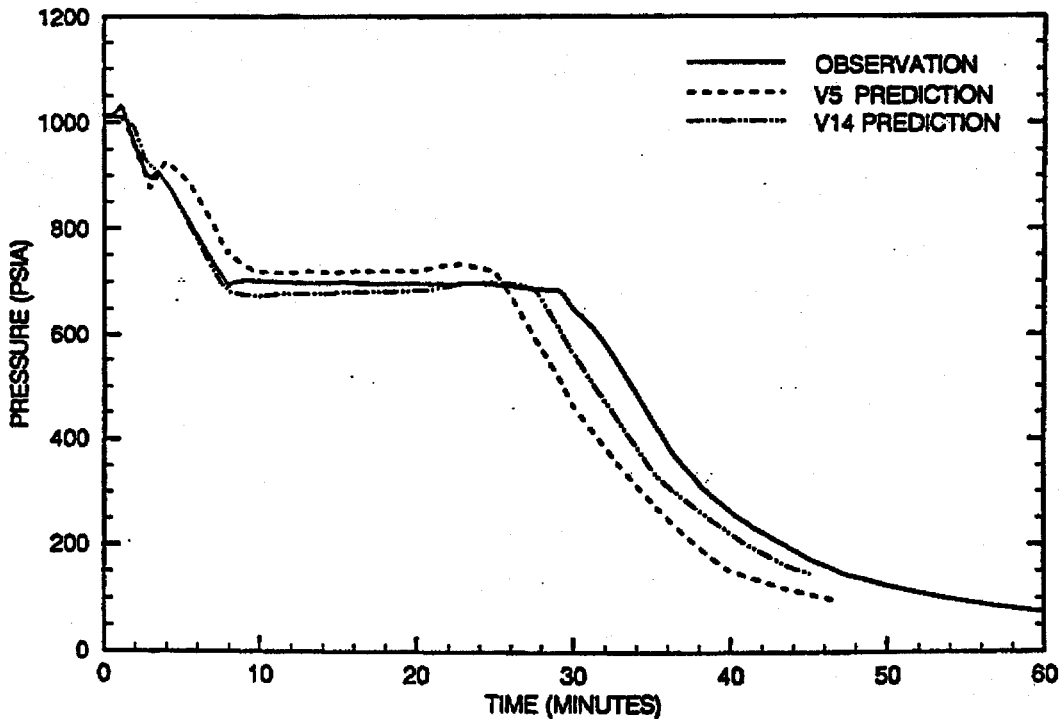


FIGURE L-5. COMPARISON OF PREDICTED AND OBSERVED REACTOR VESSEL LIQUID LEVELS FOR MIST TEST 320201.

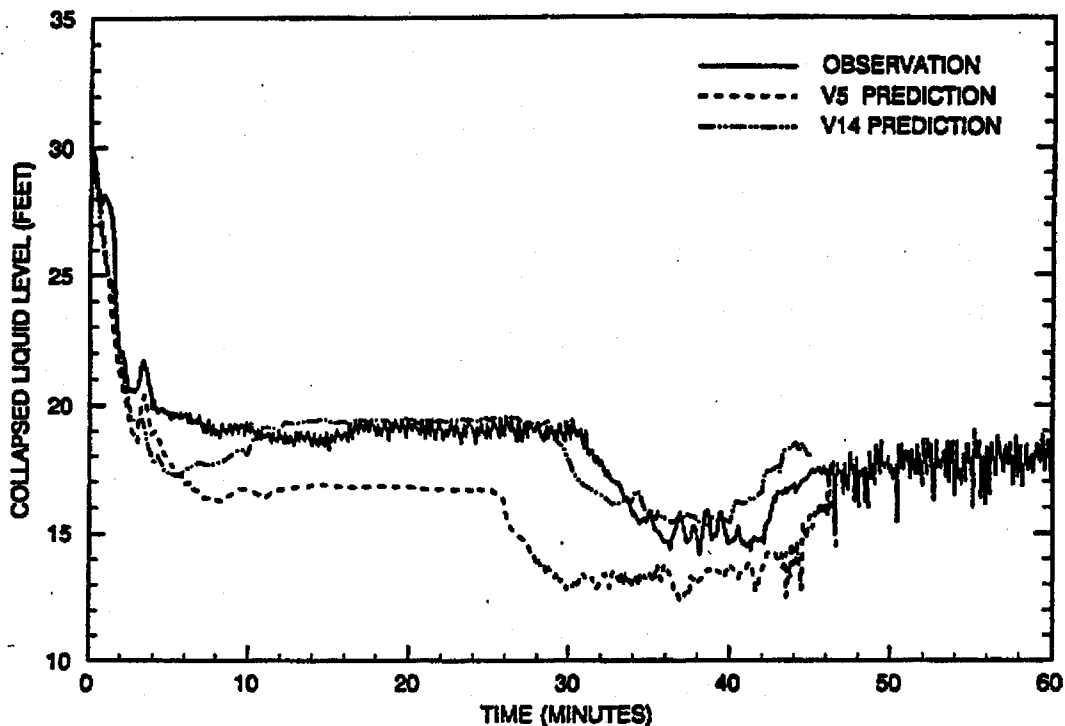


FIGURE L-6. COMPARISON OF PREDICTED AND OBSERVED SG SECONDARY LIQUID LEVELS FOR MIST TEST 320201.

